

# Transactions of the ASME®

## HEAT TRANSFER DIVISION

Chairman, R. GREIF  
Secretary, G. P. PETERSON  
Technical Editor, R. VISKANTA (1995)  
Associate Technical Editors,  
Y. BAYAZITOGU (1995)  
S. H. CHAN (1997)  
V. K. DHIR (1996)  
A. FAGHRI (1996)  
W. L. GROSSHANDLER (1995)  
C. E. HICKOX, JR. (1995)  
Y. JALURIA (1996)  
J. R. LLOYD (1995)  
M. F. MODEST (1996)  
R. A. NELSON, JR. (1996)  
T. J. RABAS (1997)  
T. W. SIMON (1995)  
K. VAFAI (1997)  
B. W. WEBB (1997)

## BOARD ON COMMUNICATIONS

Chairman and Vice President  
R. D. ROCKE

## Members-at-Large

T. BARLOW, N. H. CHAO, A. ERDMAN,  
G. JOHNSON, L. KEER, W. MORGAN,  
E. M. PATTON, S. PATULSKI, R. E. REDER,  
S. ROHDE, R. SHAH, F. WHITE,  
J. WHITEHEAD

## OFFICERS OF THE ASME

President, P. J. TORPEY  
Executive Director,  
D. L. BELDEN  
Treasurer,  
R. A. BENNETT

## PUBLISHING STAFF

Mng. Dir., Publ.,  
CHARLES W. BEARDSLEY  
Managing Editor,  
CORNELIA MONAHAN  
Sr. Production Editor,  
VALERIE WINTERS  
Production Assistant,  
MARISOL ANDINO

Transactions of the ASME, *Journal of Heat Transfer* (ISSN 0022-1481) is published quarterly (Feb., May, Aug., Nov.) for \$185.00 per year by The American Society of Mechanical Engineers, 345 East 47th Street, New York, NY 10017. Second class postage paid at New York, NY and additional mailing offices. POSTMASTER: Send address changes to Transactions of the ASME, *Journal of Heat Transfer*, c/o THE AMERICAN SOCIETY OF MECHANICAL ENGINEERS, 22 Law Drive, Box 2300, Fairfield, NJ 07007-2300.

CHANGES OF ADDRESS must be received at Society headquarters seven weeks before they are to be effective. Please send old label and new address.

PRICES: To members, \$40.00, annually;  
to nonmembers, \$185.00.

Add \$30.00 for postage to countries outside the United States and Canada.

STATEMENT from By-Laws. The Society shall not be responsible for statements or opinions advanced in papers or . . . printed in its publications (B7.1, para. 3).

COPYRIGHT © 1995 by The American Society of Mechanical Engineers. Authorization to photocopy material for internal or personal use under circumstances not falling within the fair use provisions of the Copyright Act is granted by ASME to libraries and other users registered with the Copyright Clearance Center (CCC) Transactional Reporting Service provided that the base fee of \$3.00 per article is paid directly to CCC, 222 Rosewood Dr., Danvers, MA 01923. Request for special permission or bulk copying should be addressed to Reprints/Permission Department. INDEXED by Applied Mechanics Reviews and Engineering Information, Inc. Canadian Goods & Services Tax Registration #126148048.

# Journal of Heat Transfer

Published Quarterly by The American Society of Mechanical Engineers

VOLUME 117 • NUMBER 1 • FEBRUARY 1995

## TECHNICAL PAPERS

### Heat Conduction

- 8 A Unified Field Approach for Heat Conduction From Macro- to Micro-Scales  
D. Y. Tzou
- 17 Transient Temperature During Pulsed Excimer Laser Heating of Thin Polysilicon Films Obtained by Optical Reflectivity Measurement  
X. Xu, C. P. Grigoropoulos, and R. E. Russo
- 25 Heat Generation and Transport in Submicron Semiconductor Devices  
K. Fushinobu, A. Majumdar, and K. Hijikata

### Forced Convection

- 32 Holographic Interferometry Study of Spatially Periodic Heat Transfer in a Channel With Ribs Detached From One Wall  
Tong-Miin Liou, Wen-Bin Wang, and Yuan-Jen Chang
- 40 A Correlation for Heat Transfer and Wake Effect in the Entrance Region of an In-Line Array of Rectangular Blocks Simulating Electronic Components  
M. Molki, M. Faghri, and O. Ozbay
- 47 Local Heat Transfer in Axially Feeding Radial Flow Between Parallel Disks  
A. T. Prata, C. D. M. Pilichi, and R. T. S. Ferreira
- 54 Heat Transfer and Pressure Drop Characteristics of Spirally Fluted Annuli: Part I—Hydrodynamics  
S. Garimella and R. N. Christensen
- 61 Heat Transfer and Pressure Drop Characteristics of Spirally Fluted Annuli: Part II—Heat Transfer  
S. Garimella and R. N. Christensen
- 69 Heat Transfer Coefficients in an Orthogonally Rotating Duct With Turbulators  
Shou-Shing Hsieh and Ying-Jong Hong
- 79 Heat Transfer From an Asymmetrically Heated Channel Partially Enclosing a Rotating Disk  
R. R. Schmidt and P. Patel
- 85 Turbulence Dissipation in a Free-Surface Jet of Water and Its Effect on Local Impingement Heat Transfer From a Heated Surface: Part 1—Flow Structure  
D. H. Wolf, R. Viskanta, and F. P. Incropera
- 95 Turbulence Dissipation in a Free-Surface Jet of Water and Its Effect on Local Impingement Heat Transfer From a Heated Surface: Part 2—Local Heat Transfer  
D. H. Wolf, R. Viskanta, and F. P. Incropera
- 104 Mechanisms of Heat Transfer Enhancement of Gas-Solid Fluidized Bed: Estimation of Direct Contact Heat Exchange From Heat Transfer Surface to Fluidized Particles Using an Optical Visualization Technique  
Y. Kurosaki, I. Satoh, and T. Ishize

### Natural and Mixed Convection

- 113 Effect of Imposed Wall Temperature Oscillations on the Stability of Natural Convection in a Square Enclosure  
Q. Xia, K. T. Yang, and D. Mukutmoni
- 121 Natural Convection in an Inclined Fluid Layer With a Transverse Magnetic Field: Analogy With a Porous Medium  
P. Vasseur, M. Hasnaoui, E. Bilgen, and L. Robillard
- 130 Study of Natural Convection in an Enclosure Bounded by Two Concentric Cylinders and Two Diametric Planes  
J. Sarr, C. Mbow, H. Chehouani, B. Zeghmati, S. Benet, and M. Daguene
- 138 Velocity Statistics of Round, Fully Developed, Buoyant Turbulent Plumes  
Z. Dai, L. K. Tseng, and G. M. Faeth

- 138 Velocity Statistics of Round, Fully Developed, Buoyant Turbulent Plumes  
Z. Dai, L. K. Tseng, and G. M. Faeth

### ***Radiative Transfer***

- 146 In-Depth Absorption of Externally Incident Radiation in Nongray Media  
S. S. Manohar, A. K. Kulkarni, and S. T. Thynell
- 152 Computational Evaluation of Approximate Rayleigh-Debye-Gans/Fractal-Aggregate Theory for the Absorption and Scattering Properties of Soot  
T. L. Farias, M. G. Carvalho, Ü. O. Köylü, and G. M. Faeth
- 160 Dependent Scattering Properties of Woven Fibrous Insulations for Normal Incidence  
Sunil Kumar and S. M. White

### ***Boiling Heat Transfer***

- 167 Subcooled Flow Film Boiling Across a Horizontal Cylinder: Part I—Analytical Model  
X. S. Chou and L. C. Witte
- 175 Subcooled Flow Film Boiling Across a Horizontal Cylinder: Part II—Comparison to Experimental Data  
X. S. Chou, S. Sankaran, and L. C. Witte
- 179 Stratified Flow Film Boiling Inside Horizontal Tubes  
A. M. C. Chan
- 185 An Experimental Study of Flow Boiling Heat Transfer in Rib-Roughened Tube Annuli  
Shou-Shing Hsieh and Mao-Yu Wen

### ***Heat Pipes***

- 195 The Interfacial Thermodynamics of Micro Heat Pipes  
L. W. Swanson and G. P. Peterson
- 202 Two-Dimensional Rotating Heat Pipe Analysis  
C. Harley and A. Faghri
- 209 Analysis of Asymmetric Disk-Shaped and Flat-Plate Heat Pipes  
K. Vafai, N. Zhu, and W. Wang

## **TECHNICAL NOTES**

- 219 Heat Conduction in an Energy-Generating Slab Subject to a Nonuniform Heat Transfer Coefficient  
G. F. Jones, E. V. McAssey, Jr., and B. W. Yang
- 222 Heat Transfer Across a Bilayer Composite Cylinder With Partial Debonding  
C. Y. Wang
- 224 Agitation and Heat Transfer Studies in Suspensions  
A. Ramasubramanian and S. K. Pandey
- 226 Three-Fluid Heat Exchanger Effectiveness—Revisited  
D. P. Sekulić and I. Kmečko
- 229 Turbulent Mixed Convection Heat and Mass Transfer in a Wetted Channel  
Wei-Mon Yan
- 234 Unsteady Conjugated Mixed Convection in a Vertical Channel  
Wei-Mon Yan and Kuan-Tzong Lee
- 238 Buoyancy Effect on the Flow Reversal of Three-Dimensional Developing Flow in a Vertical Rectangular Duct—A Parabolic Model Solution  
C.-H. Cheng, C.-J. Weng, and W. Aung
- 241 On the Superposition Rule for Configuration Factors  
K. G. T. Hollands
- 245 Saturated Flow Boiling Heat Transfer in Internally Spirally Knurled/Integral Finned Tubes  
Mao-Yu Wen and Shou-Shing Hsieh
- 248 Toward a Universal Critical Heat Flux (CHF) Correlation for Uniformly Heated Round Tubes  
G. A. Tingate

## **ANNOUNCEMENTS**

- 2 Journal of Heat Transfer Referees—1994
- 7 Recognition of Exemplary Service by Reviewers
- 16 Change of address form for subscribers
- 252 Announcement and call for papers: ISROMAC-6
- 253 First announcement and call for papers: 5th International Symposium on Thermal Engineering and Science for Cold Regions
- 254 Information for authors

# A Unified Field Approach for Heat Conduction From Macro- to Micro-Scales

D. Y. Tzou

Associate Professor,  
Department of Mechanical Engineering,  
University of New Mexico  
Albuquerque, NM 87131  
Mem. ASME

*A universal constitutive equation between the heat flux vector and the temperature gradient is proposed to cover the fundamental behaviors of diffusion (macroscopic in both space and time), wave (macroscopic in space but microscopic in time), phonon-electron interactions (microscopic in both space and time), and pure phonon scattering. The model is generalized from the dual-phase-lag concept accounting for the lagging behavior in the high-rate response. While the phase lag of the heat flux captures the small-scale response in time, the phase lag of the temperature gradient captures the small-scale response in space. The universal form of the energy equation facilitates identifications of the physical parameters governing the transition from one mechanism (such as diffusion or wave) to another (the phonon-electron interaction).*

## Introduction

High-rate heating is a rapidly emerging area in heat transfer. Associated with shortening of the response time, the *nonequilibrium* thermodynamic transition and the *microscopic* effects in the energy exchange are two important issues to be faced. An equilibrium state in thermodynamic transitions, first of all, needs time to be established. Should the response time be comparable or even shorter than that required to establish an equilibrium state, physical mechanisms reflecting the nonequilibrium thermodynamic transition must be addressed in the high-rate model. The relaxation time proposed by Chester (1963) provides a typical example. The relaxation concept based on the critical frequency of molecular collisions places the thermal wave behavior originally hypothesized by Morse and Feshbach (1953), Cattaneo (1958), and Vernotte (1958, 1961) on a firm physical foundation. The phase-lag concept proposed by Tzou (1992a, 1993), in essence, is the same effort addressing the nonequilibrium thermodynamic transition from a *macroscopic* point of view. The average concept employed in the macroscopic approach may lose its physical support associated with shortening of the response time. The two-step model (Anisimov et al., 1974; Brorson et al., 1987, 1990; Fujimoto et al., 1984; Elsayed-Ali et al., 1987; Elsayed-Ali, 1991; Qiu and Tien, 1992) is an example where the phonon-electron interaction dominates the short-time heat transfer before diffusion, a macroscopically averaged behavior, occurs. This is especially true for short-pulse laser heating on metal films, because the response time is on the order of picoseconds which is comparable with the phonon-electron thermal relaxation time, the microscopic effect of phonon-electron interaction must be incorporated for a successful prediction of the surface reflectivity. Including the equation of phonon radiative transfer (EPRT) governing the microscale heat transfer in dielectric thin films (Majumdar, 1993), the microscale factors in high-rate heating have been outlined in a special session of *Fundamental Issues in Small-Scale Heat Transfer* at the 1992 ASME Winter Annual Meeting (Bayazitoglu and Peterson, 1992). The microscale effects in high-rate heating processes, obviously, have attracted a lot of attention in the heat transfer society.

When switching from a macroscopic to a microscopic approach, however, a difficulty encountered by practical engineers may be the lack of sufficient knowledge in statistical thermodynamics and mechanics that are required for the microscopic anal-

yses. This seriously limits the rigorous development of the microscale model because the micromechanics itself may take months to years to become fully acquainted with. An effort interfacing the macroscopic and the microscopic approaches is evidently needed for promoting the rapid growth of this emerging area.

Bearing in mind that the macroscopic concepts are already familiar to practicing engineers, this work takes the following challenge: Is it possible to provide a *macroscopic* description that can also capture the *microscopic* effect of phonon-electron interactions? More aggressively, is it possible to establish a *universal* model that can describe all the fundamental behaviors in diffusion, thermal wave, phonon-electron interactions and pure phonon scattering (Guyer and Krumhansl, 1966) associated with shortening of the response time? What are the physical parameters governing the transition of these physical mechanisms when space and time scales shift in physical observations? By viewing the microscopic effects as *retarding* sources to the heat transfer process on a macroscopic level, I shall generalize the single-phase-lag concept employed in the thermal wave theory (Tzou, 1992a, 1993) to provide possible answers to these questions.

## The Generalized Lagging Response

I propose to lump the microstructural effects into the delayed response in *time* in the macroscopic formulation. Exemplified by the microscopic two-step model in laser heating, the temperature of the metal lattice may remain undisturbed while the energy exchange between phonons and free electrons is taking place. Relative to the time at which the electron gas starts to receive the photon energy from the laser source, therefore, increase of the lattice temperature is delayed due to the phonon-electron interactions on the microscopic level. A macroscopic *lagging* (or delayed) response between the temperature gradient and the heat flux vector seems to be a possible outcome due to such progressive interactions. Introducing *two* phase lags to both the heat flux vector ( $\vec{q}$ ) and the temperature gradient ( $\nabla T$ ), I propose the following constitutive equation to describe the lagging behavior:

$$\vec{q}(\vec{r}, t + \tau_q) = -K \nabla T(\vec{r}, t + \tau_T) \quad (1)$$

The equation shows that the temperature gradient established across a material volume located at a position  $\vec{r}$  at time  $t + \tau_T$  results in a heat flux to flow at a different instant of time  $t + \tau_q$ . The phase lags  $\tau_q$  and  $\tau_T$  are both positive and assumed to be intrinsic properties of the medium. In order to combine with the energy equation where all the physical quantities occur at the

Contributed by the Heat Transfer Division for publication in the JOURNAL OF HEAT TRANSFER. Manuscript received by the Heat Transfer Division October 1993; revision received April 1994. Keywords: Conduction, High-Temperature Phenomena, Thermodynamics and Second Law. Associate Technical Editor: Y. Bayazitoglu.

same instant of time, I further make a Taylor series expansion to Eq. (1) with respect to  $t$ . This gives

$$\begin{aligned} \vec{q}(\vec{r}, t) + \tau_q \frac{\partial \vec{q}}{\partial t}(\vec{r}, t) \\ \cong -K \left\{ \nabla T(\vec{r}, t) + \tau_T \frac{\partial}{\partial t} [\nabla T(\vec{r}, t)] \right\} \end{aligned} \quad (2)$$

where both phase lags  $\tau_q$  and  $\tau_T$  are assumed small, implying that the nonlinear terms in  $\tau$  are negligible. Equation (2) is now combined with the energy equation<sup>1</sup>:

$$-\nabla \cdot \vec{q}(\vec{r}, t) = C_p \frac{\partial T}{\partial t}(\vec{r}, t). \quad (3)$$

Eliminating the heat flux vector,<sup>2</sup> I obtain:

$$\begin{aligned} \nabla^2 T + \tau_T \frac{\partial}{\partial t} (\nabla^2 T) \\ = \frac{1}{\alpha} \frac{\partial T}{\partial t} + \frac{\tau_q}{\alpha} \frac{\partial^2 T}{\partial t^2} \quad (T \text{ representation}). \end{aligned} \quad (4)$$

Eliminating the temperature, on the other hand, results in the following equation:

$$\begin{aligned} \nabla(\nabla \cdot \vec{q}) + \tau_T \frac{\partial}{\partial t} [\nabla(\nabla \cdot \vec{q})] \\ = \frac{1}{\alpha} \frac{\partial \vec{q}}{\partial t} + \frac{\tau_q}{\alpha} \frac{\partial^2 \vec{q}}{\partial t^2} \quad (\vec{q} \text{ representation}). \end{aligned} \quad (5)$$

For the case of  $\tau_T = 0$ , Eqs. (4) and (5) reduce to the thermal wave equations in heat conduction (Cattaneo, 1958; Vernotte, 1958, 1961; Baumeister and Hamill, 1969). The coefficient  $\tau_q/\alpha$  in front of the wave terms in both equations is defined as  $1/C^2$ , with  $C$  being the thermal wave speed (Chester, 1963). The thermal wave behavior is thus captured by the phase lag of the heat flux vector ( $\tau_q$ ). For  $\tau_q = \tau_T = 0$ , Eq. (1) reduces to the Fourier law in heat conduction and Eq. (4) reduces to the classical diffusion equation. In the presence of both phase lags, obviously, Eq. (4) (and hence the generalized constitutive Eq. (1)) describes a more general behavior than wave and diffusion. The  $\vec{q}$  representation (Eq. (5)), due to the complicated relation be-

<sup>1</sup> Though not required in the framework of the extended irreversible thermodynamics (Jou et al., 1988; Tzou, 1993), Coleman and his colleagues (1982, 1986) showed that the internal energy must contain a term proportional to heat flux squared for a *pure* wave behavior to exist in heat conduction. Equation (3) does not incorporate this feature due to mixed behavior of waves (represented by  $\tau_q$ ) and the microstructural effect ( $\tau_T$ ). As shown by Bai and Lavine (1992), however, incorporating the flux-dependent internal energy into the energy equation does not change the temperature solutions much should the physical domain be sufficiently large to hold the continuum hypothesis.

<sup>2</sup> All the thermal properties are assumed constant for simpler correlations to the two-step model. Combination of Eqs. (2) and (3) is performed with reference to the observation time  $t$  at which the energy Eq. (3) is written. *Different* physical behavior of heat propagation results (refer to the appendix), if the reference time is shifted.

tween the heat flux vector and the temperature gradient shown by Eq. (2), is more convenient to use for problems involving heat-flux specified boundary conditions. At the initial stage of exploring the fundamental characteristics of temperature depicted by Eq. (4), however, I shall focus attention on the  $T$  representation in this work.

## The Phonon-Electron Interactions

Equation (4) contains a mixed derivative term, second order in space and first order in time, which may result from the effect of phonon-electron interactions in the two-step model. I demonstrate this important correspondence by examining the microscopic two-step energy equations (Anisimov et al., 1974; Qiu and Tien, 1992):

$$C_e \frac{\partial T_e}{\partial t} = \nabla \cdot (K \nabla T_e) - G(T_e - T_l) \quad (\text{heating of electron gas}) \quad (6)$$

$$C_l \frac{\partial T_l}{\partial t} = G(T_e - T_l) \quad (\text{phonon-electron interactions}). \quad (7)$$

For metals, externally supplied photons first increase the temperature of the electron gas as represented by Eq. (6). Through the phonon-electron interactions, the second step, the hot electron gas then heats up the metal lattice as represented by Eq. (7). The energy exchange between phonons and electrons is characterized by the coupling factor  $G$ :

$$G = \frac{\pi^4 (n_e v_s k)^2}{K}. \quad (8)$$

The coupling factor depends on the number density of free electrons per unit volume ( $n_e$ ), the Boltzmann constant ( $k$ ), and the speed of sound  $v_s$ :

$$v_s = \frac{k}{2\pi h} (6\pi^2 n_a)^{-1/3} T_D. \quad (9)$$

The phonon-electron coupling factor, through the speed of sound, further depends on the Planck constant ( $h$ ), the atomic number density per unit volume ( $n_a$ ), and the Debye temperature ( $T_D$ ). The *s-band* approximation employed by Qiu and Tien (1992) provides an accurate estimate for the number density of free electrons in pure metals.

Equations (6) and (7) can be combined by eliminating the electron-gas temperature ( $T_e$ ):

$$\nabla^2 T_l + \frac{\alpha_e}{C_E^2} \frac{\partial}{\partial t} (\nabla^2 T_l) = \frac{1}{\alpha_E} \frac{\partial T_l}{\partial t} + \frac{1}{C_E^2} \frac{\partial^2 T_l}{\partial t^2} \quad (\text{metal lattice}). \quad (10)$$

## Nomenclature

$C$  = volumetric heat capacity, J/m<sup>3</sup> K  
 $C_E$  = equivalent thermal wave speed, m/s  
 $G$  = electron-phonon coupling factor, W/m<sup>3</sup> K  
 $h$  = Planck constant, Js  
 $k$  = Boltzmann constant, J/K  
 $K$  = thermal conductivity, W/m K  
 $l$  = length of the one-dimensional solid,  $\mu\text{m}$   
 $n$  = volumetric number density, 1/m<sup>3</sup>

$N$  = number of terms in truncation  
 $p$  = Laplace transform parameter  
 $t$  = time, s  
 $T$  = absolute temperature, K  
 $v_s$  = speed of sound, m/s  
 $x$  = space variable,  $\mu\text{m}$   
 $\alpha$  = thermal diffusivity, m<sup>2</sup>/s  
 $\beta$  = dimensionless time  
 $\delta$  = dimensionless distance  
 $\theta$  = dimensionless temperature

$\tau$  = phase lag or relaxation time, s  
 $\omega$  = frequency in the Fourier transform domain

## Subscripts and Superscripts

$a$  = atom  
 $e$  = electron  
 $E$  = equivalent properties  
 $l$  = lattice  
 $q$  = heat flux vector  
 $T$  = temperature gradient

Eliminating the lattice temperature ( $T_l$ ), on the other hand, yields

$$\nabla^2 T_e + \frac{\alpha_e}{C_E^2} \frac{\partial}{\partial t} (\nabla^2 T_e) = \frac{1}{\alpha_E} \frac{\partial T_e}{\partial t} + \frac{1}{C_E^2} \frac{\partial^2 T_e}{\partial t^2} \quad (\text{electron gas}). \quad (11)$$

Although diffusion is assumed for heat transfer through the electron gas, a wave term (the second-order derivative with respect to time) is still present in both equations. The *equivalent* thermal diffusivity and thermal wave speed are defined as

$$\alpha_E = \frac{K}{C_e + C_l} \quad \text{and} \quad C_E = \sqrt{\frac{KG}{C_e C_l}} \quad (12)$$

in these equations. In the case that the number density of free electrons ( $n_e$ ) approaches infinity (refer to Eq. (8)), the coupling factor  $G$  approaches infinity, and the equivalent thermal wave speed in Eq. (12) approaches infinity. Since the number density of free electrons is a fraction of the valence electrons (Qiu and Tien, 1992) which is finite, the wave behavior (small-scale response in time) must be present in company with the phonon-electron interactions (microscale response in space).

Equation (10) or (11) accounting for the *microscopic* phonon-electron interactions has exactly the same form as Eq. (4) employing the *macroscopic* dual-phase-lag concept.<sup>3</sup> Comparing the coefficients in Eqs. (4) and (10), I have

$$\alpha = \alpha_E, \quad \tau_T = \frac{\alpha_e}{C_E^2}, \quad \tau_q = \frac{\alpha_E}{C_E^2}. \quad (13)$$

In terms of the microscopic properties, alternately,

$$\alpha = \frac{K}{C_e + C_l}, \quad \tau_T = \frac{C_l}{G}, \quad \tau_q = \frac{1}{G} \left[ \frac{1}{C_e} + \frac{1}{C_l} \right]^{-1}. \quad (14)$$

The effect of phonon-electron interactions (*microscopic*) vanishes when the coupling factor ( $G$ ) approaches infinity, implying that both phase lags  $\tau_q$  and  $\tau_T$  (*macroscopic*) approach zero. Equation (4) reduces to the classical diffusion equation in this case and the assumption of instantaneous thermodynamic equilibrium is retrieved. Should the values of  $\alpha$ ,  $\tau_q$ , and  $\tau_T$  be related to the microscopic properties shown by Eq. (14), on the other hand, the *macroscopic* approach reduces to the *microscopic* two-step model. While the phase lag of the heat flux vector ( $\tau_q$ ) captures the thermal wave behavior, a small-scale response in time, the phase lag of the temperature gradient ( $\tau_T$ ) captures the effect of phonon-electron interactions, a microscale response in space. The dual-phase-lag concept is thus capable of capturing the small-scale response in both space and time. For further emphasizing such a macroscopic to microscopic correspondence, I calculate the values of  $\alpha$ ,  $\tau_q$ ,  $\tau_T$ , and  $C_E$  for copper (Cu), silver (Ag), gold (Au), and lead (Pb) based on the  $G$  values obtained experimentally by Elsayed-Ali et al. (1987), Brorson et al. (1990), and Groeneveld et al. (1990). The results are shown in Table 1.

In passing, it should be noted that the correlation between the dual-phase-lag model (Eq. (4)) and the two-step model (Eq. (10)) is made within the merit of the two-step model represented by Eqs. (6) and (7). Should the ballistic electron component in the short-time heat transport be included (Qiu and Tien, 1993), for example, Eqs. (6) and (7) have different forms and Eq. (10) for the lattice temperature becomes much more involved. The correspondence shown in Table 1 no longer holds in this case. Another example is negligence of the temperature gradient in the metal lattice shown by Eq. (7). Should heat transport in a *thick*

<sup>3</sup> The correlation to the two-step model is confined to the case of constant thermal properties in this work. For the electron gas with temperature-dependent heat capacity, the correlation can be obtained in the same manner. The effective heat capacity in the dual-phase-lag model, however, is governed by a first-order ordinary differential equation in time due to such complexity.

**Table 1** Equivalent thermal diffusivity ( $\alpha_E$ ), phase lags ( $\tau_q$  and  $\tau_T$ ), and thermal wave speed ( $C_E$ );  $C_e = 2.1 \times 10^4$  J/m<sup>3</sup> K at room temperature; ps = picosecond, ns = nanosecond

	$K$ W/mK	$C_l$ J/m <sup>3</sup> K $\times 10^6$	$G$ W/m <sup>3</sup> K $\times 10^6$	$\alpha_E$ m <sup>2</sup> /s $\times 10^{-4}$	$\tau_T$ ps	$\tau_q$ ps	$C_E$ m/s $\times 10^4$	$l^2/\alpha_E$ ns	$\tau_T$ $\times 10^4$	$\tau_q$ $\times 10^5$
Cu	386	3.4	4.8	1.1283	70.833	0.4348	1.6109	8.8629	7.992	4.906
Ag	419	2.5	2.8	1.6620	89.286	0.7438	1.4949	6.0168	14.839	12.361
Au	315	2.5	2.8	1.2495	89.286	0.7438	1.2961	8.0032	11.156	9.293
Pb	35	1.5	12.4	0.2301	12.097	0.1670	1.1738	43.459	0.278	0.384

medium be intended, Eq. (7) may include a second-order derivative in space. The resulting equation governing the lattice temperature shall include both the second and the fourth order spatial derivatives, blemishing the correspondence established in Table 1.

### The Pure Phonon Field in Dielectric Crystals

Guyer and Krumhansl (1966) employed the normal-process collision operator to solve the linearized Boltzmann equation for the pure phonon field in dielectric crystals. By neglecting the electronic conduction and the other interactions in which momentum is lost from the phonon system, they proposed a rather complicated constitutive relation between the heat flux vector and the temperature gradient,

$$\frac{\partial \vec{q}}{\partial t} + \frac{c^2 C_p}{3} \nabla T + \frac{1}{\tau_R} \vec{q} = \frac{\tau_N c^2}{5} [\nabla^2 \vec{q} + 2\nabla(\nabla \cdot \vec{q})] \quad (15)$$

where  $c$  is the average speed of the phonons,  $\tau_R$  stands for the relaxation time for the umklapp processes in which momentum is lost from the phonon system (the momentum-nonconserving processes), and  $\tau_N$  the relaxation time for normal processes in which momentum is conserved in the phonon system. All the quantities in Eq. (15) are at the same instant of time and Eq. (15) is ready to combine with the energy Eq. (3). Eliminating the heat flux vector, I have

$$\nabla^2 T + \frac{9\tau_N}{5} \frac{\partial}{\partial t} (\nabla^2 T) = \frac{3}{\tau_R c^2} \frac{\partial T}{\partial t} + \frac{3}{c^2} \frac{\partial^2 T}{\partial t^2}. \quad (16)$$

It comes to my attention that Eq. (16) was already derived by Joseph and Preziosi (1989), though in a slightly different form. But two typos, missing  $C_p$  ( $\gamma$  in terms of their symbols) in their Eq. (4.2a) and an extra  $C_p$  ( $\gamma$ ) in the denominator of the coefficient  $\nabla^2 \theta$  in their Eq. (4.3), seem to exist. These typos, of course, do not affect their elegant treatment on the subject matter at all. Again, Eq. (16) has an identical form to Eq. (4) in the generalized model. Comparing the corresponding coefficients, I have

$$\alpha = \frac{\tau_R c^2}{3}, \quad \tau_T = \frac{9\tau_N}{5}, \quad \tau_q = \tau_R. \quad (17)$$

While the phase lag of the heat flux vector ( $\tau_q$  in the universal model) is exactly the same as the relaxation time for the momentum-nonconserving processes ( $\tau_R$  in the pure phonon field), the phase lag of the temperature gradient ( $\tau_T$ ) displays a simple stretch of the relaxation time ( $\tau_N$ ) for the normal processes conserving the momentum in the phonon system. Such simple correlations result from the fact that both models describe the *macroscopic* response between the heat flux vector and the temperature gradient. The thermal diffusivity, on the other hand, provides a more complicated relationship. The major complexity lies in that the pure phonon scattering field represented by Eq. (15) does not reduce to the Fourier's law under steady state while the proposed universal model does.

## A One-Dimensional Example

Equation (4) is the universal energy equation describing the general behaviors of diffusion ( $\tau_q = \tau_T = 0$ ), thermal wave propagation ( $\tau_T = 0$ ), phonon–electron interactions and pure phonon scatterings ( $\tau_q \neq 0$  and  $\tau_T \neq 0$ ). When the space and time scales shift in physical observations, Eq. (4) captures the physical mechanisms governing the thermal responses in different scales and there is no need to switch from one model to another associated with shortening of the response time. The experience dependency involved in the model switching is thus removed.

I shall provide a one-dimensional example here to illustrate the universality of the model, Eq. (4). Benefiting from the *single* energy equation, I especially emphasize the transition of temperature patterns from one mechanism (such as diffusion or wave) to another (the phonon–electron interactions or pure phonon scatterings). Two initial conditions are needed due to presence of the wave term in Eq. (4). I consider an initial temperature  $T_0$  in the solid and impose an initial *time-rate* change of temperature,  $\dot{T}_0$ , for studying the *rate effect* later. Mathematically, these conditions can be expressed as

$$T = T_0, \quad \frac{\partial T}{\partial t} = \dot{T}_0 \quad \text{at } t = 0. \quad (18)$$

For application to the problems of short-pulse laser heating on metal films, the solid is assumed to have a finite dimension  $l$ . The left end at  $x = 0$  is suddenly raised to a temperature  $T_w$  while the right end at  $x = l$  remains at a zero temperature gradient:

$$T = T_w \quad \text{at } x = 0, \quad \frac{\partial T}{\partial x} = 0 \quad \text{at } x = l. \quad (19)$$

The zero-gradient boundary condition is taken from Qiu and Tien (1992), which implies that  $q + \tau_T(\partial q/\partial t) = 0$  in the present model, referring to Eq. (2). It does not necessarily imply an insulated boundary condition ( $q = 0$ ).

I further introduce the following dimensionless variables:

$$\theta = \frac{T - T_0}{T_w - T_0}, \quad \delta = \frac{x}{l}, \quad \beta = \frac{t}{(l^2/\alpha)} \quad (20)$$

for a systematic study. The reference time,  $l^2/\alpha$ , is defined as the diffusion time because it deals with the macroscopic diffusivity. The energy Eq. (4), the initial conditions (18), and the boundary conditions (19) thus become

$$\frac{\partial^2 \theta}{\partial \delta^2} + z_T \frac{\partial^3 \theta}{\partial \delta^2 \partial \beta} = \frac{\partial \theta}{\partial \beta} + z_q \frac{\partial^2 \theta}{\partial \beta^2}$$

$$\text{with } z_T = \frac{\tau_T}{(l^2/\alpha)} \quad \text{and} \quad z_q = \frac{\tau_q}{(l^2/\alpha)} \quad (21)$$

$$\theta = 0 \quad \text{and} \quad \frac{\partial \theta}{\partial \beta} = \dot{\theta}_0 \quad \text{at } \beta = 0 \quad (22)$$

$$\theta = 1 \quad \text{at } \delta = 0 \quad \text{and} \quad \frac{\partial \theta}{\partial \delta} = 0 \quad \text{at } \delta = 1 \quad (23)$$

where  $\dot{\theta}_0 = \dot{T}_0(l^2/\alpha)/(T_w - T_0)$ , the dimensionless initial temperature rate. The parameters  $z_T$  and  $z_q$  in Eq. (21) weigh the relative importance of the lagging times (in both the temperature gradient and the heat flux vector) to the diffusion time. They are the physical parameters governing the transition of the physical mechanisms. The universal approach proposed here can thus be viewed as a one-step, two-parameter model.

The Laplace transform solution satisfying Eqs. (21)–(23) is easily obtained:

$$\bar{\theta}(\delta; p) = \frac{1}{p} \left\{ A + (1 - A) \frac{\cosh[(1 - \delta)B]}{\cosh[B]} \right\}$$

$$\text{with } A = \frac{z_q \dot{\theta}_0}{1 + z_q p}, \quad B = \sqrt{\frac{p(1 + z_q p)}{1 + z_T p}}. \quad (24)$$

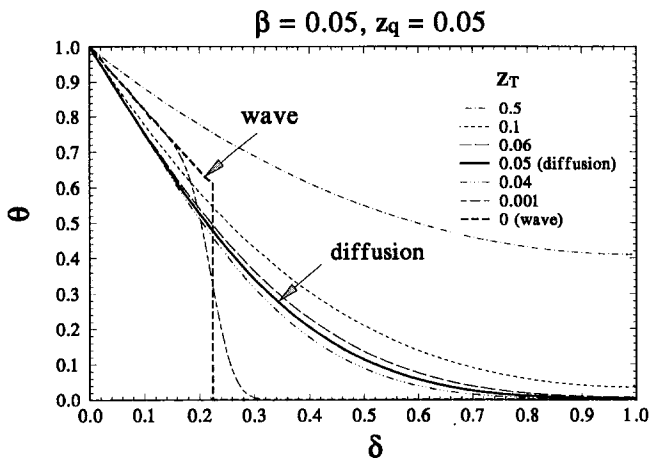


Fig. 1 Evolution of the universal model into diffusion, classical thermal wave, and phonon–electron interaction models—the effect of the phase lag of the temperature gradient:  $\beta = 0.05$  and  $z_q = 0.05$

The branch points resulting from the mixed-derivative term in Eq. (21) prevent me from obtaining an analytical inversion. The Bromwich contour of integrations results in an improper integral and a numerical evaluation is still unavoidable. Therefore, I invoke the numerical algorithm developed previously (Tzou et al., 1994) for the purpose of inversion. Since all the details, including the conditions for the fast convergence of the algorithm, were discussed previously, I only summarize the result here:

$$\theta(\delta, \beta) = \frac{e^{\gamma\beta}}{\beta} \left[ \frac{\bar{\theta}(\delta, \gamma)}{2} + \text{Re} \sum_{n=1}^N (-1)^n \bar{\theta} \left( \delta, \gamma + \frac{i n \pi}{\beta} \right) \right] \quad (25)$$

Equation (25) is actually the Riemann sum approximation of the *Fourier* integral transformed from the Laplace inversion integral. The quantity  $\gamma$  is the real value in the Bromwich cut from  $\gamma - i\infty$  to  $\gamma + i\infty$ . For a faster convergence, the value of  $\gamma$  satisfies the relation

$$\gamma\beta \cong 4.7 \quad (26)$$

with  $\beta$  being the dimensionless physical time. At  $\beta = 0.05$ , for example, a value of 94 should be selected for  $\gamma$  in Eq. (26). This is an important characteristic in the present algorithm for a faster convergence.

**(a) Transition Mechanisms.** I shall assume a zero initial temperature rate for the time being to study the transition mechanisms associated with the lagging response in terms of  $\tau_T$  and  $\tau_q$ . The emphasis, however, is placed on the effect of  $\tau_T$  since the effect of  $\tau_q$  has been well understood in the development of the classical thermal wave theory (Chester, 1963; Tzou, 1992a for example). Inserting Eq. (24) with  $\dot{\theta}_0 = 0$  into Eq. (25), the temperature distributions in the physical space are obtained by the finite sum of the series. Figure 1 shows the result with the Cauchy error norm being controlled below  $10^{-10}$  for all cases. A small value of time,  $\beta = 0.05$ , is selected for avoiding the effect of wave reflection<sup>4</sup> from the boundary at  $\delta = 1$ . The value of  $z_q$  is fixed at 0.05 while the value of  $z_T$  increases from zero to 0.5. The curve with  $z_T = 0$  corresponds to the thermal wave solution:

<sup>4</sup>The abrupt increase of temperature due to arrival of thermal wavefront results from mathematical idealizations. As discussed by Tzou et al. (1994), the physical scale for this phenomenon to occur is on an atomic level where the continuum hypothesis no longer holds. Also, Bai and Lavine (1993) showed that the sharp wavefront (and hence the temperature overshooting due to wave reflection) diminishes should a more realistic boundary condition be applied. Regardless of these deficiencies, however, the temperature overshooting due to wave reflections is kept in this study because it is consistent with the mathematical model.

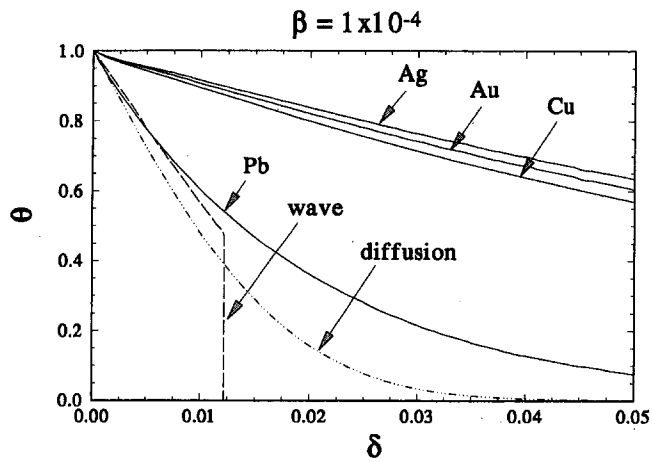


Fig. 2 Temperature distributions in thin films of Ag, Au, Cu, and Pb according to the values of  $z_q$  and  $z_T$  shown in Table 1;  $z = 6.736 \times 10^{-5}$  for the classical wave solution;  $\beta = 0.0001$

refer to Eq. (21). A sharp wavefront exists at  $\delta = \beta/\sqrt{z_q}(x = Ct)$  which is approximately 0.2236 according to the chosen parameters. As the value of  $z_T$  deviates slightly from zero to 0.001, implying the gradual activation of the microscale effect, the sharp wavefront is *destroyed* and the heat-affected zone extends deeper into the medium to  $\delta \approx 0.31$ . The abrupt drop of temperature in  $0.15 \leq \delta \leq 0.31$  levels off when  $\tau_T$  further increases to 0.04.

When  $z_T$  approaches  $z_q$ , i.e.,  $\tau_T = \tau_q$  and  $z_T = z_q = 0.05$ , I note that the distribution approaches the result of *diffusion*. This becomes evident by arranging Eq. (4) in the following form:

$$\left(1 + \tau \frac{\partial}{\partial t}\right) \left(\nabla^2 T - \frac{1}{\alpha} \frac{\partial T}{\partial t}\right) = 0 \quad (27)$$

with  $\tau \equiv \tau_q = \tau_T$ . The diffusion equation,

$$\nabla^2 T - \frac{1}{\alpha} \frac{\partial T}{\partial t} = 0, \quad (28)$$

is indeed a particular solution of Eq. (27). A more general condition for the reduction of the universal model to diffusion, therefore, is  $\tau_q = \tau_T$  (not necessarily equal to zero), which implies a trivial shift of the observation time from 0 to  $\tau$  in Eq. (1). No phase lag exists between the heat flux vector and the temperature gradient in this case.

The temperature level exceeds those of diffusion and wave as the value of  $z_T$  exceeds that of  $z_q$ . The amount increases with the value of  $z_T$  and the heat-affected zone significantly stretches into the solid. In fact, a larger heat-affected zone is the main reason for the success of the two-step model (in predicting the surface reflectivity of metal films, Qiu and Tien, 1992), which has been nicely absorbed in the phase lag of the temperature gradient in the present model. Once the wave behavior diminishes, as a general trend in Fig. 1 for  $z_T \geq 0.04$ , the temperature level increases with the value of  $z_T$ . Recognizing that the diffusion term,  $\partial\theta/\partial\beta$ , in Eq. (21) provides damping to the heat flow, this behavior becomes evident because the mixed-derivative term,  $\partial^3\theta/\partial\beta\partial\delta^2$ , appears on the different side of the equation, which provides a "negative" damping, a counterbalanced effect to diffusion, to heat propagation.

Within the context of the dual-phase-lag concept, I intend to show the temperature distributions for the existing materials whose phase lags are known. Figure 2 displays the results for Ag, Au, Cu, and Pb based on their values of  $z_q$  and  $z_T$  calculated in Table 1. I also provide the results of diffusion ( $z_T = z_q$ ) and wave ( $z_T = 0$  and  $z_q = 6.736 \times 10^{-5}$ , the averaged value of the four materials) for comparisons. Even for the short-time response

at  $\beta = 0.0001$ , the classical wave theory significantly underestimates the temperature levels and the heat-affected zones for Ag, Au, and Cu because it does not incorporate the microscale effect in *space*. The Pb curve seems to be closer to the wave solution near the suddenly heated boundary ( $0 \leq \delta \leq 0.005$ ). This is due to the larger value of  $G$  (and hence a weaker effect of microstructures) for lead as given in Table 1. The classical diffusion theory deviates the most from these models because it does not incorporate any small-scale effect. For  $\beta = 0.0001$  shown in Fig. 2, I note that the corresponding response time ( $t$ ) is on the order of microseconds. This is a result inheriting from the boundary condition, Eq. (23), indicating that the boundary temperature is raised to  $T_w$  in *no time*, i.e., right at  $\beta = 0^+$ . A more appropriate formulation for describing the time history of the lattice temperature should involve heat flux rather than temperature in Eq. (23). The response time thus obtained will be longer due to the delayed response between the exterior heat flux and the interior temperature gradient.

Large deviations (from the classical wave theory) shown in Fig. 2 indicate that the small-scale response in space and time cannot be separated and must be accommodated as an entirety. Although the wave theory aims to capture the small-scale response in time (in terms of  $\tau_q$ ), it does not seem to be complete until the microscale response in *space* (in terms of  $\tau_T$ ) is implemented. I further emphasize that the effects of  $\tau_q$  and  $\tau_T$  enters *simultaneously* associated with shortening of the response time. According to Eq. (14), it does not seem possible that one can assume a nonzero value for  $\tau_q$  yet idealize a zero value for  $\tau_T$  under any physically admissible values of  $G$ ,  $C_e$ , and  $C_l$ .

(b) **The Effect of  $\tau_T$  in the Short-Time Response.** Figure 3 shows the evolution of the local temperature at the middle point,  $\delta = 0.5$ , in the time history. Again, the solutions for wave ( $z_T = 0$  and  $z_q = 0.05$ ) and diffusion ( $z_T = z_q = 0.05$ ) are provided for comparison. Due to the finite speed of heat propagation in the wave theory, the temperature at the middle point starts to increase when  $\beta = \delta\sqrt{z_q} \approx 0.112$ . The first reflection of thermal waves causes a temperature jump at  $\beta = 0.335$  (the first reflection) while the second reflection at  $\beta = 0.559$  does not have a noticeable effect. This is due to the strong damping from the diffusion behavior (Tzou, 1992b, c). When the value of  $\tau_T$  increases to 0.001, although the sharp wavefront is destroyed, the first "reflection" still causes a local fluctuation at  $\beta = 0.335$ . All the wave features disappear as the value of  $z_T$  becomes large. At  $z_T = 0.5$ , for example, an *immediate* increase of temperature starts from  $\beta = 0$  and nothing happens at the instants of arrival of the "reflected waves." Both the generalized model and the wave

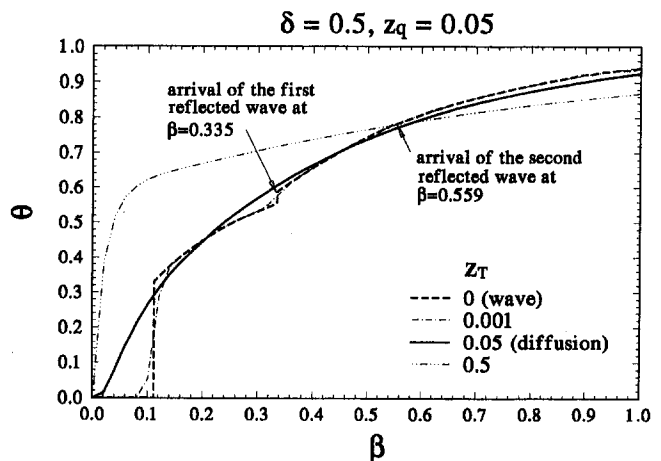


Fig. 3 Effect of the phase lag of the temperature gradient ( $\tau_T$ ) on the long-time behavior of the temperature at the middle point of the solid ( $\delta = 0.5$ )

theory approach diffusion when the response time is sufficiently long. For  $z_q = 0.05$  and  $z_T = 0$  (the thermal wave theory), this occurs when  $\beta \geq 4$ . For  $z_T = 0.5$ , on the other hand, this occurs when  $\beta \geq 150$ . The phase lag of the temperature gradient ( $\tau_T$ ) thus produces two major effects: It significantly exaggerates the temperature level in the short-time transient and it lengthens the merging time to diffusion.

**(c) The Rate Effect.** The initial temperature rate may result from the initial heating provided to the solid. It competes with the combined effect of damping (from diffusion and the phase lag of the temperature gradient) and produces additional effects in the short-time response. The coefficient  $A$  in Eq. (24) is non-zero for  $\dot{\theta}_0 \neq 0$ . By using the full form of Eq. (24) in the numerical Laplace inversion, I obtain the rate responses for  $\dot{\theta}_0 = 5, 25,$  and  $50$ . For the same values of  $\beta$  (0.05) and  $z_q$  (0.05) used previously, the results are displayed in Fig. 4. Under a moderate rate, say  $\dot{\theta}_0 = 5$  shown by the curves of  $z_T = 0.05$  and  $0.5$  in Fig. 4(b), the temperature levels increase with  $z_T$ . This is the same behavior as that in the absence of the initial temperature-rate shown in Fig. 4(a). When the initial rate increases to 25, Fig. 4(c), the temperature distribution with  $z_T = 0.5$  remains at the reference level ( $\theta = 1$ ) while the temperatures in the neighborhood of the wall at  $\delta = 0$  start to decrease when the value of  $z_T$  increases. The rate effect in this case dominates over the combined effect of damping and reverses the qualitative trend in Fig. 1 where no initial rate is present. Also, the field temperature may exceed the wall temperature ( $\theta = 1$ ) when the initial temperature rate is sufficiently high. This behavior becomes more pronounced when the value of  $\dot{\theta}_0$  further increases to 50 as shown in Fig. 4(d). No matter how high the initial heating rate is, the microstructural effect (currently interpreted as the phase lag in the temperature gradient  $\tau_T$ ) destroys the wave structure in heat propagation. A slight deviation of  $\tau_T$  from zero, as shown in Fig. 4, destroys the sharp wavefront and reduces the peak values of temperature.

In the presence of an initial temperature rate, also, I note that the result of diffusion is *no longer* retrieved by the special case with  $z_T = z_q$ . In fact, the classical diffusion model is not com-

patible with the initial condition describing a temperature rate due to absence of a wave term in the energy equation.

### Microscale Effect in Superfluid Liquid Helium

Bearing in mind that the phase lag of the temperature gradient smoothes out the sharp wavefront, I revisit the experimental result obtained by Bertman and Sandiford (1970). They emanated an electrical pulse from a generator, providing a pulse of heat to the superfluid liquid helium sample at about 1 K. The electrical pulse simultaneously triggers the oscilloscope, and the temperature at the *fixed* measuring point in the sample was recorded by a resistance thermometer. The oscilloscope trace recorded in their experiment is shown in Fig. 5. The temperature at the fixed measuring point rises and falls sharply at a certain time after the heat pulse is applied to the end of the sample. The authors attributed this rapid change in temperature to heat flow by wave propagation. No scale in the temperature and the time axes was given and the experimental result is qualitative.

In employing the dual-phase-lag concept to explain this phenomenon, I attribute the lagging response of the temperature gradient to the *inert behavior* of molecules under such a low temperature (about 1 K). For a closer simulation to the laboratory conditions, I replace the zero-gradient boundary condition in Eq. (19) by  $T = 0$ , the undisturbed initial temperature, at  $x = l$  and impose a thermal pulse described by  $T = T_w dlt(t)$  with  $dlt(\cdot)$  denoting the Dirac delta function, at  $x = 0$ . The dimensionless form of the boundary conditions thus becomes

$$\theta = dlt(\beta) \text{ at } \delta = 0 \text{ and } \theta = 0 \text{ at } \delta = 1 \quad (29)$$

where  $\theta = T/T_w$  while  $\beta$  and  $\delta$  defined in Eq. (20) remain the same. The initial conditions, including the zero initial temperature rate ( $\dot{\theta}_0 = 0$ ), are given by Eq. (22). The transformed temperature corresponding to Eq. (24) is

$$\bar{\theta}(\delta; p) = \frac{\sinh[(1-\delta)B]}{\sinh[B]} \quad (30)$$

in the present case. Substituting Eq. (30) into Eq. (25) with the values of  $\beta$  and  $\gamma$  satisfying Eq. (26), I obtain the temperature

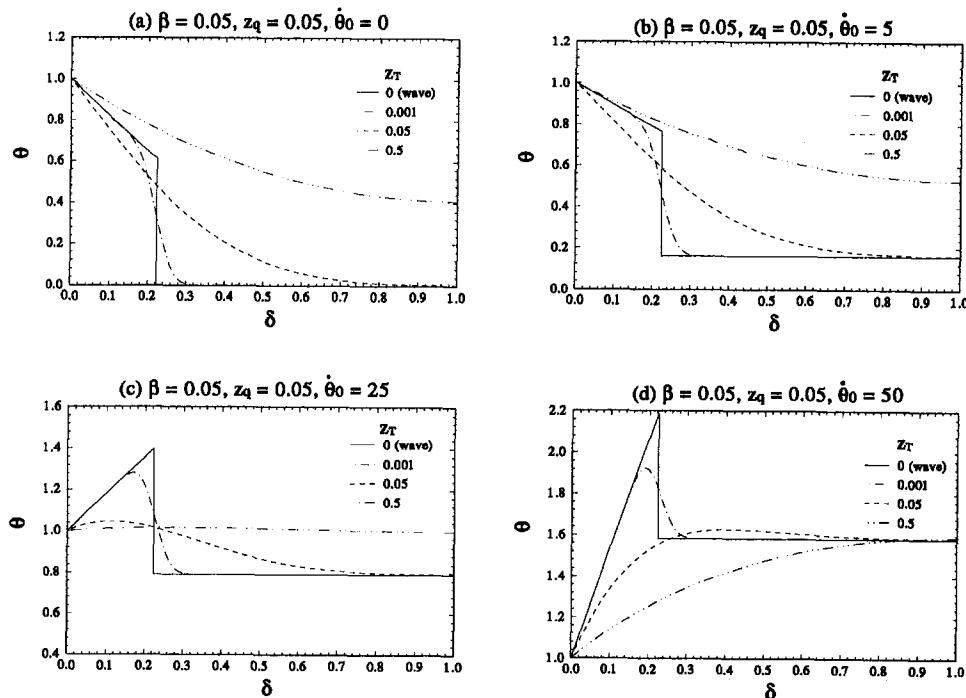


Fig. 4 Effect of the initial temperature rate ( $\dot{\theta}_0$ ) on the temperature distributions: (a)  $\dot{\theta}_0 = 0$ , (b)  $\dot{\theta}_0 = 5$ , (c)  $\dot{\theta}_0 = 25$ , and (d)  $\dot{\theta}_0 = 50$



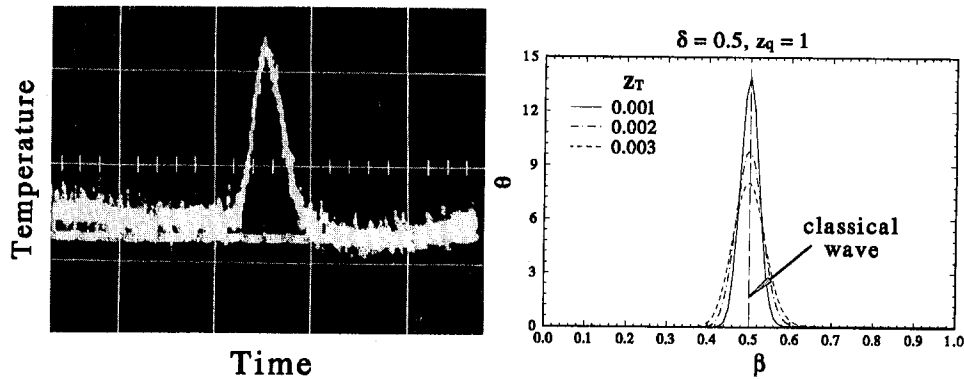


Fig. 5 The rapid but finite response of temperature upon arrival of the wavefront—the effect of the phase lag of the temperature gradient. The scanned picture is from the results obtained by Bertman and Sandiford (1970).

distribution in the physical space. For  $z_q = 1$ , I plot the time history of the temperature developed at the middle point of the solid ( $\delta = 0.5$ ) in the same Fig. 5. In order to avoid the undesirable wave reflections from the opposite wall at  $\delta = 1$ , I restrict the time domain within  $0 \leq \beta \leq \sqrt{z_q} = 1$ .<sup>5</sup> The classical wave solution is denoted by the dashed line at  $\beta = 0.5$ . It represents a sudden increase of temperature to infinity, inherited from the thermal pulse approximated by a delta function, upon arrival of the sharp wavefront.

In the presence of the phase lag of the temperature gradient, the temperature at  $\beta = 0.5$  becomes bounded as evidenced by the curves with  $z_T$  being 0.001, 0.002 and 0.003 in Fig. 5. As the value of  $z_T$  increases, clearly, the peak value of temperature decreases and the rise-time becomes earlier while the decay-time becomes later. These behaviors make the envelope of temperature smoother, a special feature in the experimental result shown in Fig. 5. From a macroscopic point of view, the lagging response of the temperature gradient seems to explain this phenomenon well.

No pulse like a delta function (Eq. (29)) could exist in reality. The temperature pulse shown in Fig. 5, consequently, may result from the finite pulse duration in Bertman and Sandiford's experiment.<sup>6</sup> Due to the absence of these data in their work, unfortunately, a quantitative assessment for such an effect is impossible. In comparison with the classical thermal wave theory, however, it is clear that the inert behavior of molecules at 1 K (expressed in terms of the phase lag  $\tau_T$  in the present model) results in a pulse shape with a smaller amplitude and a wider span in time.

## Conclusion

Based on the generalized concept of dual-phase-lag in both the heat flux vector ( $\tau_q$ ) and the temperature gradient ( $\tau_T$ ), a universal model for heat conduction has been proposed in this work. The model reduces to diffusion, thermal wave, the phonon-electron interaction, and the pure phonon scattering models under special values of  $\tau_q$  and  $\tau_T$ . I summarize the various correspondences in Table 2 for an overview. Evidently, the universal model covers a wide range of physical responses from microscopic to macroscopic scales in both space and time. When the response time becomes short and the microscale effect becomes important, therefore, there is no need to switch from one model to another

<sup>5</sup> According to the classical wave theory, the wavefront arrives at  $\delta$  at  $\beta = \delta\sqrt{z_q}$ . For  $\delta = 1$ , the dimensionless length of the solid,  $\sqrt{z_q}$ , is the time required for the one-way propagation without reflection.

<sup>6</sup> Since the heat pulse is generated electrically (on the order of 300 K) and the sample is liquid helium (1 K) in Bertman and Sandiford's experiment, temperature rise at the heated boundary is expected to decay very rapidly due to such a large temperature difference. The sudden temperature increase described by the delta function in Eq. (29), consequently, may be a close approximation.

that not only depends heavily on experience but may result in inconsistencies due to different physical basis in different models. In view of the dual-phase-lag concept represented by Eqs. (1)–(4), an important value of the proposed model lies in its simplicity. The derivation is straightforward and the macroscopic approach is what practical engineers are already familiar with. Extending from the single-phase-lag concept in the classical thermal wave theory (Tzou, 1992a, 1993) to the dual-phase-lag concept proposed in this work, indeed, is intuitive and consistent. With regard to its broad equivalence to the representative models shown in Table 2, however, this simple extension is able to capture several important effects in the microscopic response. The dual-phase-lag concept proposed hereby, therefore, makes the transition from a macroscopic analysis to a microscopic evaluation much smoother and more efficient. It facilitates an immediate involvement of practical engineers in the rapid growth of the high-rate, small-scale heat transfer.

In addition to the theoretical contact with the existing models, correlation to the experimental result of a rapidly varying but continuous profile of temperature (Fig. 5) seems very promising for the future development of the model. The classical thermal wave theory, to the closest extent, describes a temperature ripple propagating with a finite width (Vick and Özişik, 1983). The infinite response of temperature in time upon arrival of the sharp wavefront is an unresolved issue in its framework. The lagging response of the temperature gradient in the present model seems to explain such a rapid but finite response well.

I further emphasize that the small-scale response in time may not be separable from the microscale response in space. Although the classical thermal wave theory addresses the short-time behavior in heat conduction, it does not capture the finite response of temperature shown in Fig. 5. The rising time and the decay time at a fixed point in space, as reflected by the dashed line in

Table 2 Correspondence of the universal model to diffusion, thermal wave, and phonon-electron interactions in terms of  $\tau_q$  and  $\tau_T$

Universal Model	Diffusion*	Classical Wave	Phonon-Electron Interactions	Pure Phonon Field
$\tau_q$	0	$\frac{\alpha}{c^2}$	$\frac{1}{G}(\frac{1}{C_e} + \frac{1}{C_l})^{-1}$	$\tau_x$
$\tau_T$	0	0	$\frac{C_l}{G}$	$\frac{9}{5}\tau_x$
$\alpha$	$\alpha$	$\alpha$	$\frac{K}{C_e + C_l}$	$\frac{c^2\tau_x}{3}$

[\*] Reduction to diffusion under  $\tau_q = \tau_T = 0$  is only valid for a zero initial temperature-rate.

Fig. 5, are simply too fast according to the thermal wave model. All these evidences, including the large deviations from the wave solutions shown in Fig. 2, strongly suggest that the microscopic effect in space must be taken into account along with the small-scale response in time. Equation (14), the correlations of  $\tau_q$  and  $\tau_T$  to the microscopic properties in the two-step model, supports this argument on a firm physical basis.

Lastly, the microscale interactions between phonons and electrons and the inert behavior of molecules at low temperatures are two physical factors resulting in the macroscopic lagging response in the present model. The microvoids in porous media might display the same behavior. Especially for solids containing dense microvoids or microcracks, the air trapped inside these closures may effectively retard the heat flow in the presence of a temperature gradient (Tzou, 1991a, b). I am currently working with my colleagues to verify the dual phase lag concept in the laboratory. The dual phase lags for powder metallurgical materials seem to be on the order of submilliseconds, while those for sand and concrete with weaker internal structures are on the order of several tens of seconds. Of course, their values depend strongly on the porosity of the solid medium. I shall report these experimental results in the near future.

### Acknowledgments

This work has been accomplished in the course of research supported by the National Science Foundation under Grant No. MSS-9200993 with the University of New Mexico.

### References

Anisimov, S. I., Kapeliovich, B. L., and Perel'man, T. L., 1974, "Electron Emission From Metal Surfaces Exposed to Ultra-short Laser Pulses," *Soviet Physics JETP*, Vol. 39, pp. 375–377.

Bai, C., and Lavine, A. S., 1992, "Non-equilibrium Hyperbolic Type Heat Conduction Equation," *ASME HTD-Vol. 200*, pp. 87–92.

Bai, C., and Lavine, A. S., 1993, "Thermal Boundary Conditions for Hyperbolic Heat Conduction," *ASME HTD-Vol. 253*, pp. 37–44.

Baumeister, K. J., and Hamill, T. D., 1969, "Hyperbolic Heat Conduction Equation—A Solution for the Semi-infinite Body Problem," *ASME JOURNAL OF HEAT TRANSFER*, Vol. 91, pp. 543–548.

Bayazitoglu, Y., and Peterson, G. P., eds., 1992, *Fundamental Issues in Small-Scale Heat Transfer*, ASME HTD-Vol. 227.

Bertman, B., and Sandiford, D. J., 1970, "Second Sound in Solid Helium," *Scientific America*, Vol. 222, pp. 92–101.

Brorson, S. D., Fujimoto, J. G., and Ippen, E. P., 1987, "Femtosecond Electron Heat-Transport Dynamics in Thin Gold Film," *Physical Review Letters*, Vol. 59, pp. 1962–1965.

Brorson, S. D., Kazeroonian, A., Mooder, J. S., Face, D. W., Cheng, T. K., Ippen, E. P., Dresselhaus, M. S., and Dresselhaus, G., 1990, "Femtosecond Room-Temperature Measurement of the Electron-Phonon Coupling Constant  $\lambda$  in Metallic Superconductors," *Physical Review Letters*, Vol. 64, pp. 2172–2175.

Cattaneo, C., 1958, "A Form of Heat Conduction Equation Which Eliminates the Paradox of Instantaneous Propagation," *Compte Rendus*, Vol. 247, pp. 431–433.

Chester, M., 1963, "Second Sound in Solids," *Physical Review*, Vol. 131, pp. 2013–2015.

Coleman, B. D., Fabrizio, M., and Owen, D. R., 1982, "On the Thermodynamics of Second Sound in Dielectric Crystals," *Archive for Rational Mechanics and Analysis*, Vol. 80, pp. 135–158.

Coleman, B. D., Fabrizio, M., and Owen, D. R., 1986, "Thermodynamics and the Constitutive Relations for Second Sound in Crystals," *New Perspectives in Thermodynamics*, J. Serrin, ed., pp. 171–185.

Elsayed-Ali, H. E., Norris, T. B., Pessot, M. A., and Mourou, G. A., 1987, "Time-Resolved Observation of Electron-Phonon Relaxation in Copper," *Physical Review Letters*, Vol. 58, pp. 1212–1215.

Elsayed-Ali, H. E., 1991, "Femtosecond Thermorefectivity and Thermotransmissivity of Polycrystalline and Single-Crystalline Gold Films," *Physical Review B*, Vol. 43, pp. 4488–4491.

Flik, M. I., and Tien, C. L., 1990, "Size Effect on the Thermal Conductivity of High- $T_c$  Thin-Film Superconductors," *ASME JOURNAL OF HEAT TRANSFER*, Vol. 112, pp. 872–881.

Frankel, J. I., Vick, B., and Özişik, M. N., 1985, "Flux Formulation of Hyperbolic Heat Conduction," *Journal of Applied Physics*, Vol. 58, pp. 3340–3345.

Fujimoto, J. G., Liu, J. M., and Ippen, E. P., 1984, "Femtosecond Laser Interaction With Metallic Tungsten and Non-equilibrium Electron and Lattice Temperature," *Physical Review Letters*, Vol. 53, pp. 1837–1840.

Groeneveld, R. H. M., Sprik, R., Wittebrood, M., and Legendijk, A., 1990, "Ultrafast Relaxation of Electrons Probed by Surface Plasmons at a Thin Silver Film," in: *Ultrafast Phenomena VII*, C. B. Harris et al., ed., Springer, Berlin, pp. 368–370.

Guyer, R. A., and Krumhansl, J. A., 1966, "Solution of the Linearized Phonon Boltzmann Equation," *Physical Review*, Vol. 148, pp. 766–780.

Joseph, D. D., and Preziosi, L., 1989, "Heat Waves," *Review of Modern Physics*, Vol. 61, pp. 41–73.

Joseph, D. D., and Preziosi, L., 1990, "Addendum to the Paper on Heat Waves," *Review of Modern Physics*, Vol. 62, pp. 375–391.

Jou, D., Casas-Vazquez, and Lebon, J., 1988, "Extended Irreversible Thermodynamics," *Reports on Progress in Physics*, Vol. 51, pp. 1105–1179.

Majumdar, A., 1993, "Microscale Heat Conduction in Dielectric Thin Films," *ASME JOURNAL OF HEAT TRANSFER*, Vol. 115, pp. 7–16.

Morse, P. M., and Feshbach, H., 1953, *Methods of Theoretical Physics*, Vol. 1, McGraw-Hill, New York.

Qiu, T. Q., and Tien, C. L., 1992, "Short-Pulse Laser Heating on Metals," *International Journal of Heat and Mass Transfer*, Vol. 35, pp. 719–726.

Qiu, T. Q., and Tien, C. L., 1993, "Heat Transfer Mechanisms During Short-Pulse Laser Heating of Metals," *ASME JOURNAL OF HEAT TRANSFER*, Vol. 115, pp. 835–841.

Tzou, D. Y., 1989a, "On the Thermal Shock Wave Induced by a Moving Heat Source," *ASME JOURNAL OF HEAT TRANSFER*, Vol. 111, pp. 232–238.

Tzou, D. Y., 1989b, "Shock Wave Formation Around a Moving Heat Source in a Solid With Finite Speed of Heat Propagation," *International Journal of Heat and Mass Transfer*, Vol. 32, pp. 1979–1987.

Tzou, D. Y., 1990a, "Thermal Shock Waves Induced by a Moving Crack," *ASME JOURNAL OF HEAT TRANSFER*, Vol. 112, pp. 21–27.

Tzou, D. Y., 1990b, "Thermal Shock Waves Induced by a Moving Crack—A Heat Flux Formulation," *International Journal of Heat and Mass Transfer*, Vol. 33, pp. 877–885.

Tzou, D. Y., 1991a, "The Effect of Internal Heat Transfer in Cavities on the Overall Thermal Conductivity," *International Journal of Heat and Mass Transfer*, Vol. 34, pp. 1839–1846.

Tzou, D. Y., 1991b, "A Universal Model for the Overall Thermal Conductivity of Porous Media," *Journal of Composite Materials*, Vol. 25, pp. 1064–1084.

Tzou, D. Y., 1992a, "Thermal Shock Phenomena Under High-Rate Response in Solids," in: *Annual Review of Heat Transfer*, Chang-Lin Tien, ed., Hemisphere Publishing Inc., Washington, DC, Chap. 3, pp. 111–185.

Tzou, D. Y., 1992b, "Thermal Resonance Under Frequency Excitations," *ASME JOURNAL OF HEAT TRANSFER*, Vol. 114, pp. 310–316.

Tzou, D. Y., 1992c, "Damping and Resonance Characteristics of Thermal Waves," *ASME Journal of Applied Mechanics*, Vol. 59, pp. 862–867.

Tzou, D. Y., 1993, "An Engineering Assessment to the Relaxation Time in the Thermal Wave Theory," *International Journal of Heat and Mass Transfer*, Vol. 36, pp. 1845–1851.

Tzou, D. Y., Özişik, M. N., and Chiffelle, R. J., 1994, "The Lattice Temperature in the Microscopic Two-Step Model," *ASME JOURNAL OF HEAT TRANSFER*, Vol. 116, pp. 1034–1038.

Vernotte, P., 1958, "Les Paradoxes de la Théorie Continue de l'Équation de la Chaleur," *Compte Rendus*, Vol. 246, pp. 3154–3155.

Vernotte, P., 1961, "Some Possible Complications in the Phenomena of Thermal Conduction," *Compte Rendus*, Vol. 252, pp. 2190–2191.

Vick, B., and Özişik, M. N., 1983, "Growth and Decay of a Thermal Pulse Predicted by the Hyperbolic Heat Conduction Equation," *ASME JOURNAL OF HEAT TRANSFER*, Vol. 105, pp. 902–907.

## APPENDIX

### Different Behavior of Heat Propagation Associated With Shift in Time Scales

Three characteristic times are involved in the proposed model: The *physical time* ( $t$ ) at which conservation of energy is applied for describing heat conduction across the material volume, the *delayed time* ( $t + \tau_T$ ) at which the temperature gradient is established across the same material volume, and the *delayed time* ( $t + \tau_q$ ) at which heat flows through. Since the model is concerned with the lagging response *in time*, shift of the time scales must be carefully performed to preserve the desired behavior in heat propagation. The gist is that the physical quantities involved in the constitutive equation and the energy equation must occur at the same instant of time (for the purpose of combination) and refer to the same reference of time (for consistent description). Equation (4) results from the combination of Eqs. (2) and (3) with reference to the observation time  $t$ . Should one make a time shift from  $t$  to  $t + \tau_T$ , i.e., letting

$$t^* = t + \tau_T, \quad (\text{A.1})$$

the constitutive Eq. (1) describing the lagging response becomes

$$\dot{q}(\vec{r}, t^* + \tau) = -K \nabla T(\vec{r}, t^*), \quad \text{with } \tau = \tau_q - \tau_T, \quad (\text{A.2})$$

while the energy equation originally established at time  $t$  changes to

$$-\nabla \cdot \vec{q}(\vec{r}, t^* - \tau_T) = C_p \frac{\partial T(\vec{r}, t^* - \tau_T)}{\partial t^*} \quad (\text{A.3})$$

which occurs at  $t^* - \tau$ . In the time frame referring to  $t^*$ , Eq. (A.1) bears resemblance to the Cattaneo–Vernotte equation for the classical thermal wave. However, the energy equation (A.3) resulting from the time-shift from  $t$  to  $t^*$  *destroys* the wave structure. There are *still* three characteristic times,  $t^*$ ,  $t^* + \tau$ , and  $t^* - \tau_T$  existing in Eqs. (A.2) and (A.3). Expanding them with reference to  $t^*$  results

$$\vec{q}(\vec{r}, t^*) + \tau \frac{\partial \vec{q}(\vec{r}, t^*)}{\partial t^*} = -K \nabla T(\vec{r}, t^*) \quad (\text{A.4})$$

$$-\nabla \cdot \vec{q}(\vec{r}, t^*) + \tau_T \frac{\partial}{\partial t^*} [\nabla \cdot \vec{q}(\vec{r}, t^*)] = C_p \left[ \frac{\partial T(\vec{r}, t^*)}{\partial t^*} - \tau_T \frac{\partial^2 T(\vec{r}, t^*)}{\partial t^{*2}} \right]. \quad (\text{A.5})$$

Unlike Eq. (4), unfortunately, the heat flux vector cannot be eliminated from Eqs. (A.4) and (A.5) in the time-frame  $t^*$ , im-

plying the need to solve the two equations simultaneously for  $\vec{q}$  and  $T$ . A proper manipulation on Eqs. (A.4) and (A.5), however, yields an informative result:

$$\nabla^2 T(\vec{r}, t^*) = \frac{1}{\alpha} \frac{\partial T(\vec{r}, t^*)}{\partial t^*} - \frac{\tau_T}{\alpha} \frac{\partial^2 T(\vec{r}, t^*)}{\partial t^{*2}} - \frac{\tau_q}{\alpha} \frac{\partial}{\partial t^*} [\nabla \cdot \vec{q}(\vec{r}, t^*)]. \quad (\text{A.6})$$

Even though Eq. (A.4) resembles the Cattaneo–Vernotte equation for thermal waves, the wave behavior *vanishes* due to the negative sign in front of the wave term and the additional term involving the time derivative and the spatial gradient of the heat flux vector. Equation (1) describing the delayed response, therefore, should not be confused with the *single* phase lag model (see Tzou, 1989a, b, 1990a, b, 1992a, for a parallel treatment) in the thermal wave theory.

When dealing with differential equations with time delay, in summary, I recommend the use of physical time  $t$  at which conservation of energy is applied to describe the process of heat transfer. Other quantities occurred at different instants of time are referred to the physical time  $t$  by making the Taylor series expansion provided that the delay time is small comparing to the physical time of observation.

X. Xu<sup>1</sup>

C. P. Grigoropoulos

Department of Mechanical Engineering,  
University of California,  
Berkeley, CA 94720

R. E. Russo

Energy and Environment Division,  
Lawrence Berkeley Laboratory,  
Berkeley, CA 94720

# Transient Temperature During Pulsed Excimer Laser Heating of Thin Polysilicon Films Obtained by Optical Reflectivity Measurement

*The transient reflectivity of a continuous wave (CW) HeNe laser was measured during the pulsed excimer laser heating of thin polysilicon films at the nanosecond time scale. Polysilicon films with thicknesses from 0.1 to 0.4  $\mu\text{m}$  were deposited by Low-Pressure Chemical Vapor Deposition (LPCVD) on thermally oxidized crystalline silicon wafers. The complex refractive index of these films at the HeNe laser wavelength ( $\lambda_{\text{probe}} = 0.6328 \mu\text{m}$ ) was measured in the temperature range from 300 K to approximately 1400 K by combined ellipsometric and normal incidence reflectivity measurements. Numerical heat transfer and optical reflectivity analysis based on the measured optical properties of polysilicon films were conducted. The calculated reflectivity histories were compared with the experimental results to reveal the transient temperature field.*

## I Introduction

Polycrystalline silicon (polysilicon) is used in the electronics industry as gate metal in metal-oxide-semiconductor (MOS) transistors (Kamins, 1988). Thin polysilicon films have shown good potential for fabrication of novel, high-speed devices, having three-dimensional architecture and increased circuit packing density (Tsaur, 1986). Advances in electronic film deposition and in selective etching techniques have enabled the emergence of a new class of micromechanical devices, sensors, and actuators (Howe, 1985). Pulsed laser irradiation is employed in semiconductor processing applications, including surface cleaning, annealing, and synthesis of compound films. As these applications become more demanding, a thorough understanding of the fundamental heat transfer phenomena involved is critical. Despite their importance, few in-situ temperature measurements have been reported. It is noted that infrared thermometry is difficult to apply at short time scales, because of the relatively slow time response of infrared sensitive detectors, which are usually slower than 1  $\mu\text{s}$ , and the limited strength of the electrical response of the faster detectors for measurements in the nanosecond time scale. Also, in the case of semitransparent films, the thermal emission is a volumetric effect, thus complicating the experimental signal interpretation and analysis. Optical techniques can provide noninvasive measurements of the transient temperature field. Park et al. (1993) reported an optical transmission technique for in-situ probing excimer laser heating of 0.2- $\mu\text{m}$ -thick amorphous silicon (a-Si) films on transparent fused quartz substrates. Time-resolved optical transmission and reflection measurements have been reported for the irradiation of crystalline silicon (c-Si), on sapphire structures in the nanosecond (Lowndes, 1982; Lowndes and Jellison, 1984) and picosecond (Lompre et al., 1983) time domains.

The development of optical temperature measurement techniques has been limited by lack of data on the high-temperature material radiative properties. The structure of silicon films pre-

pared by chemical vapor deposition depends on the deposition conditions. It is well known that the thin film optical properties are strongly influenced by the presence of grain boundaries, disordered regions, and inhomogeneities on the microstructural scale of 10–10,000  $\text{\AA}$  (Aspnes, 1982). The complex refractive index of thin polysilicon films is a strong function of the deposition conditions and the post-processing annealing procedure (Kamins, 1988; Harbecke et al., 1984; Montaudon et al., 1985). The optical properties of thin polysilicon films have been measured by ellipsometry from room temperature to about 1400 K (Xu and Grigoropoulos, 1993). Polysilicon films of thickness in the range of 0.1 to 0.4  $\mu\text{m}$  were used in the experiment. This investigation focused on a structure commonly used in electronics microfabrication: polysilicon-silicon dioxide-silicon substrate. The HeNe laser wavelength ( $\lambda_{\text{probe}} = 0.6328 \mu\text{m}$ ) was selected, because HeNe lasers are frequently used as probes in in-situ experimental investigations. For example, in the work by Grigoropoulos et al. (1991b), a HeNe laser probe was scanned over a thin polysilicon film heated by a CW argon-ion laser beam, in order to map the temperature-induced steady, spatial reflectivity distribution.

The transient optical reflectivity and transmissivity measurements are based on the variation of the materials complex refractive index with temperature. Interference effects significantly enhance the variation of the thin film reflectivity with temperature, so that the sensitivity of the temperature measurement is increased. This effect was demonstrated (Xu et al., 1993) for the transient reflectivity of thin polysilicon films during continuous wave (CW) laser annealing. In this work, the optical reflection technique for in-situ monitoring of the transient temperature field during pulsed excimer laser heating of thin polysilicon films is developed and verified. Data on the thin film complex refractive index at high temperatures are employed in the calculation of the sample transient reflectivity response and the experimental signal analysis. A numerical conductive heat transfer model for the transient temperature field in the thin film structure is applied. Transient reflectivity is calculated and compared with the experimentally measured values to yield the temperature field. To the authors' knowledge, this is the first work that demonstrates temperature measurements in thin films at the nanosecond time scale, based on accurate high-temperature optical property data over the entire temperature range achieved in the experiment.

<sup>1</sup>Current address: School of Mechanical Engineering, Purdue University, West Lafayette, IN 47907.

Contributed by the Heat Transfer Division for publication in the JOURNAL OF HEAT TRANSFER. Manuscript received by the Heat Transfer Division May 1993; revision received May 1994. Keywords: Laser Processing, Materials Processing, and Manufacturing Processes, Radiation. Associate Technical Editor: M. Modest.

## II Experimental Procedure

### II.1 Measurement of Optical Properties of Thin Polysilicon Films.

Thin oxide layers of thickness in the range of 0.1  $\mu\text{m}$  were thermally grown on crystalline silicon substrates by keeping the reaction temperature at 900°C and controlling the reaction time. An automatic ellipsometer was used to determine the thickness and the refractive index of the oxidation layer, with an accuracy of 1 Å and 0.001, respectively, according to the instrument manufacturer's specification (Table 1). After the oxidation process, a silicon layer was deposited onto the SiO<sub>2</sub> layer by LPCVD, at a temperature of 580°C. The polysilicon film thicknesses,  $d_{\text{p-Si}}$ , varied from about 0.1  $\mu\text{m}$  to 0.4  $\mu\text{m}$ . Following the silicon deposition, the samples were annealed in dry nitrogen at a temperature of 1050°C for 30 minutes. The microstructure of the sample was studied by cross-sectional TEM (Transmission Electron Microscopy). It was found that the annealed sample has a polycrystalline structure. The grain sizes are between 200 and 700 Å, which are randomly distributed across the thin film. Although the grain size distribution could vary across the thin film for some materials (Graebner et al., 1992), such a behavior was not observed in the polysilicon samples used in this experiment. Thicker polysilicon films (1.2  $\mu\text{m}$ ) deposited at the same conditions as in this experiment do not show grain size distribution either (Kruevitch et al., 1992). Using an Alpha-step 200 profilometer, the rms roughness of both the polysilicon film and the oxidized crystal silicon wafer was found to be approximately 30 Å. This roughness is much smaller than the laser wavelengths used in the experiment, so that the sample surface can be considered to be optically smooth.

Ellipsometric and normal incidence reflectivity measurements were used to determine the optical constants at the wavelength of 0.6328  $\mu\text{m}$ , as well as the thickness of the polysilicon film. The detailed description of the experimental apparatus and the ellipsometric measurement procedure, including a systematic error analysis, have been given by Xu and Grigoropoulos (1993).

To determine the absorption of the excimer laser light, the refractive index of poly-Si at the excimer laser light ( $\lambda_{\text{exc}} = 0.248 \mu\text{m}$ ) was measured by a Variable-Angle-Spectroscopic-Ellipsometer. The accuracy of this measurement is about  $\pm 0.1$  for  $n$  and  $\pm 0.1$  for  $k$ . This refractive index value was verified by measuring the normal reflectivity  $R_{\text{exc}}$  of the polysilicon films, using a Perkin-Elmer Lambda 6 UV-VIS-NIR Spectrophotometer.

**II.2 Transient Reflectivity Measurement During Pulsed Laser Heating of Polysilicon Films.** The experimental setup for the transient reflectivity measurement is shown in Fig. 1. A pulsed KrF excimer laser ( $\lambda_{\text{exc}} = 0.248 \mu\text{m}$ ) is used as a heating

**Table 1 Sample thickness and complex refractive index at  $\lambda_{\text{probe}} = 0.6328 \mu\text{m}$**

Sample	Thickness of SiO <sub>2</sub> Layer ( $\mu\text{m}$ )	Thickness of Poly-Si Layer ( $\mu\text{m}$ )	$n_0$	$n_1 \times 10^4$	$k_0$	$T_0$ °C
# 1	0.1183	0.097	4.02	3.47	0.0425	756
# 2	0.1226	0.250	4.11	4.31	0.0328	569
# 3	0.1186	0.412	4.10	4.30	0.0311	608
Crystalline Silicon (Jellison and Burke, 1986)			3.88	5.0	0.018	447

source. The pulse duration of the excimer laser beam is measured to be 52 ns, using a fast silicon PIN photodiode with a rise and fall time of less than 1 ns and a digitizing oscilloscope with a 1 GHz sampling speed (1 ns time resolution). The laser pulse energy is monitored by an energy meter, which receives the laser light reflected from a beam splitter. Accurate knowledge of the power intensity of the excimer laser light incident on the sample is critical for temperature calculations. The light emitted from the aperture of the excimer laser has a poor uniformity, with a spatial intensity variation larger than 100 percent over the 90 percent central portion of the beam profile. A tunnel-type beam homogenizer made of polished aluminum is used to improve the uniformity of the laser beam profile. The output light from the homogenizer has a spatial uniformity within 10 percent. A series of lenses is used to image the output excimer laser light from the homogenizer onto the sample surface at normal incidence. The area of excimer laser beam spot at the sample surface is approximately 0.5 cm<sup>2</sup>.

A 0.1 mW continuous wave (CW) unpolarized HeNe laser is used as a probing light source for the reflectivity measurement. The HeNe laser beam is focused onto the sample surface by a spherical lens at the center of the excimer laser irradiated area. Using the technique described by Grigoropoulos (1991a), the  $1/e$  intensity diameter of the probing laser spot is measured to be approximately 50  $\mu\text{m}$ . By measuring the relative distances between the HeNe laser source, the probing laser beam spot at the sample surface, and the detector, the angle of incidence of the HeNe probing laser was determined to be  $\theta = 38$  deg with an accuracy of  $\pm 0.5$  deg. The reflected light of the HeNe laser beam is focused onto a fast silicon PIN photodiode. The fast digitizing oscilloscope is used for recording the transient reflectivity signals. The accuracy in the absolute reflectivity measurement is estimated to be  $\delta R = 0.01$ , while the fractional error in the laser pulse fluence measurement,  $\delta F/F = \pm 10$  percent. The connecting cables, the detectors, and the electronic components were carefully shielded to avoid the strong RF interference from the excimer laser.

## Nomenclature

$C_p$ = specific heat	$N$ = number of discrete elements in the stratified layer structure (Fig. 3)	$\theta$ = angle of incidence of probing laser beam
$d$ = thickness		$\lambda$ = wavelength
$d_p$ = absorption penetration depth		$\rho$ = density
$F$ = laser pulse fluence	$Q_{ab}$ = power flux absorbed by the thin silicon layer	<b>Subscripts</b>
$i = \sqrt{-1}$	$R$ = reflectivity	$c$ = calculated result
$I$ = incident laser light intensity	$T$ = temperature	exc = excimer laser
$K$ = thermal conductivity	$T_0$ = fitting constant	$m$ = measured result
$k_0$ = fitting constant for the imaginary part of the complex refractive index	$T_\infty$ = ambient temperature	$ox$ = naturally oxidized layer
$k$ = imaginary part of the complex refractive index	$t$ = time	$p$ = transverse magnetic wave
$n$ = real part of the complex refractive index	$t_l$ = length of laser pulse	p-Si = polysilicon
$n_0, n_1$ = fitting constants for the real part of the complex refractive index	$t_p$ = time of occurrence of peak laser pulse intensity	probe = probing laser
$\hat{n}$ = complex refractive index	$x$ = coordinate in the normal to the sample surface direction	$s$ = transverse electric wave
	$\gamma$ = absorption coefficient	Si = silicon wafer
	$\delta$ = uncertainty of measurement	SiO <sub>2</sub> = thermal oxidation layer on crystalline silicon substrate

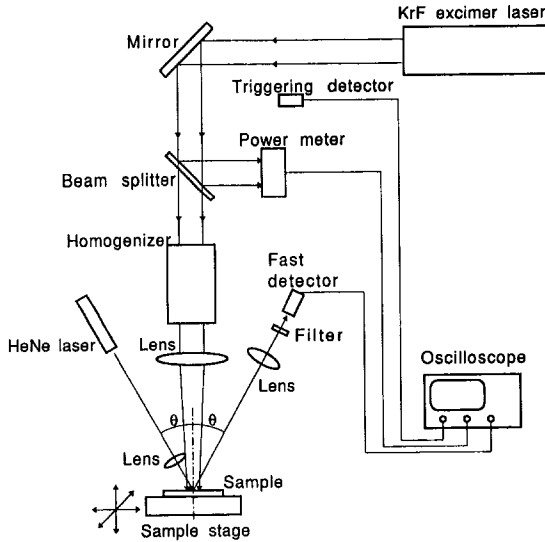


Fig. 1 Experimental setup for transient reflectance measurement

A 0.5 mW linearly polarized HeNe laser was also used in some experiments, with the direction of light polarization adjusted so that the incident probing laser beam was *p*-polarized. The probing laser beam angle of incidence in this experiment,  $\theta = 16.7$  deg.

### III Heat Transfer Modeling

The temperature profile penetration into the sample is of the order of  $1 \mu\text{m}$ . Comparing this penetration depth with the excimer laser beam size ( $0.5 \text{ cm}^2$ ), it can be assumed that the heat transfer at the center of the laser beam is essentially one dimensional. For the nanosecond time scales considered in this work, nonequilibrium and non-Fourier thermal wave effects are negligible. For temperatures below the melting temperature, the conductive heat transfer in the solid silicon layer is given by:

$$\rho C_p \frac{\partial T}{\partial t} = \frac{\partial}{\partial x} \left( K \frac{\partial T}{\partial x} \right) + Q_{ab}(x, t) \quad (1)$$

In the equation above,  $x$  is the coordinate normal to the sample surface ( $x = 0$ ),  $\rho$  is the density,  $T$  is the temperature,  $C_p$  is the specific heat at constant pressure, and  $K$  is the thermal conductivity. The variation with temperature given by Touloukian (1970) for the bulk material thermal properties was considered. The optical constants measured in this work (see next section) yield an absorption coefficient,  $\gamma$  ( $= 4\pi k_{\text{exc}}/\lambda_{\text{exc}}$ ) of approximately  $1 \times 10^6 \text{ cm}^{-1}$ . This absorption corresponds to an optical penetration depth ( $d_p = 1/\gamma$ ) in the thin film on the order of ten nanometers, in contrast to the Nd:YAG laser ( $\lambda = 0.532 \mu\text{m}$ ) and Ruby laser ( $\lambda = 0.694 \mu\text{m}$ ) absorption in silicon films, which is strongly modified by wave interference (Grigoropoulos et al., 1993). Thus, the excimer laser irradiation does not penetrate into the oxidized layer and the underlying silicon substrate. The optical property data for crystalline silicon at elevated temperatures (Jellison and Modine, 1982) show little dependence on temperature in the ultraviolet (UV) range. To the authors' knowledge, no temperature dependent optical properties for polysilicon in the UV range have been reported in the literature. It is assumed in this work that the polysilicon complex refractive index at the excimer laser wavelength,  $\lambda_{\text{exc}} = 0.248 \mu\text{m}$  is constant with temperature.

The laser energy is transferred to the lattice on the order of  $10^{-12}$ – $10^{-11}$  second and can be treated as an internal volumetric heat source. The energy absorption,  $Q_{ab}(x, t)$ , follows an exponential decay in the material:

$$Q_{ab}(x, t) = (1 - R_{\text{exc}})\gamma I(t)e^{-\gamma x} \quad (2)$$

Measurements of the laser-pulse temporal profile,  $I(t)$  (Fig. 2), have shown that the pulse fluence,  $F$ , is distributed in a triangular shape, with the pulse length,  $t_l = 52 \text{ ns}$ , and the peak intensity occurring at  $t_p = 10 \text{ ns}$ .

$$I(t) = \frac{2Ft}{t_l t_p} \quad 0 < t < t_p$$

$$I(t) = \frac{2F(t_l - t)}{t_l(t_l - t_p)} \quad t_p < t < t_l$$

$$I(t) = 0 \quad t_l < t \quad (3)$$

Convection and radiation losses are negligible, in view of the high incident laser intensities (of the order of  $10^{11} \text{ W/m}^2$ ) and the short time scales considered in this problem. The temperature penetration in the structure is small, so that the bottom substrate surface remains at the ambient temperature,  $T_\infty$ .

$$\left. \frac{\partial T}{\partial x} \right|_{x=0} = 0 \quad (4a)$$

$$T(x = d_{\text{p-si}} + d_{\text{SiO}_2} + d_{\text{Si}}) = T_\infty \quad (4b)$$

Initially the structure is isothermal, at the ambient temperature:

$$T(t = 0) = T_\infty \quad (4c)$$

Continuity of both temperature and heat flux is applied at the film/oxidation layer and oxide layer/silicon substrate interfaces.

The heat conduction is solved numerically by an implicit finite difference algorithm. A depth of  $x = 50 \mu\text{m}$  is sufficient to contain the temperature field penetration for the time duration considered in this work. Figure 3 shows a schematic of the stratified layer structure. In both the heat transfer and the optical response calculations, the polysilicon film, the  $\text{SiO}_2$  layer, and the silicon substrate were subdivided into  $N_{\text{p-si}} = 50$ ,  $N_{\text{SiO}_2} = 20$ ,  $N_{\text{Si}} = 100$  discrete elements, respectively. These discretizations are sufficient to capture the temperature field and the optical property variation accurately. Once the temperature field is solved, the optical reflectivity can be calculated using thin film optics. The temperature field variation with depth induces changes in the complex refractive index of polysilicon film at the  $\lambda_{\text{probe}} = 0.6328 \mu\text{m}$  wavelength. Such changes were accounted for in the picosecond irradiation of thin crystalline silicon (c-Si) films (Lompre et al., 1983) by assuming an average temperature for fitting the measured optical properties. In this study, the semiconductor film is treated as a stratified multilayer structure (Jacobsson, 1965; Born and Wolf, 1980; Knittl, 1976) composed of thin layers of varying complex refractive index. The refractive index of the dielectric  $\text{SiO}_2$  layer varies little with temperature and is assumed to be a constant in the calculation. The underlying crystalline

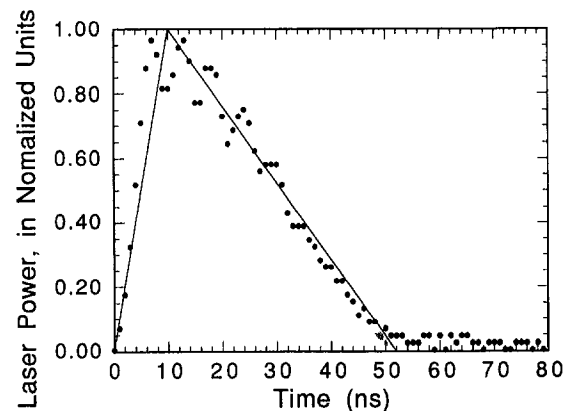


Fig. 2 Measured pulse shape of excimer laser

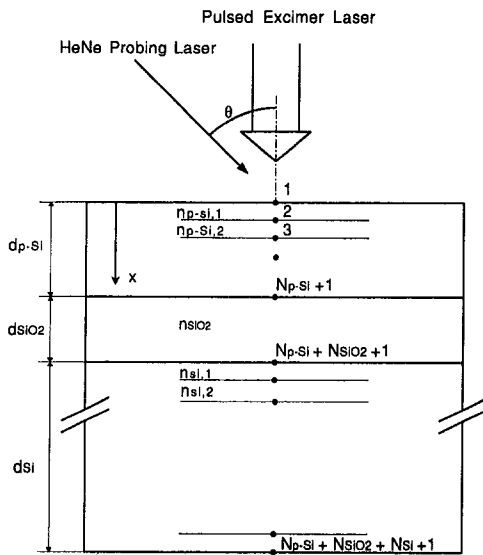


Fig. 3 Sample structure

silicon substrate is treated as a stratified structure of varying complex refractive index, in a manner similar to the polysilicon layer discretization, using the results of Jellison and Burke (1986) for the c-Si optical properties. The detailed optical calculation is shown in Appendix I.

#### IV Results and Discussion

##### IV.1 Results of the Optical Properties Measurement.

Measurement of the optical properties of the polysilicon samples is performed from room temperature to about 1400 K. The measured refractive indices of the 0.097, 0.250, and 0.412- $\mu\text{m}$ -thick polysilicon films are shown in Fig. 4. The real part of the refractive index,  $n$ , increases linearly with temperature and the imaginary part,  $k$ , increases exponentially with temperature. The components of the refractive index,  $n$  and  $k$ , of the thicker samples (Sample #2,  $d_{p-si} = 0.250 \mu\text{m}$ , and Sample #3,  $d_{p-si} = 0.412 \mu\text{m}$ ) are very close. The real part of the refractive index,  $n$ , of the sample with 0.097  $\mu\text{m}$  (Sample #1) thickness has lower values, and the imaginary part,  $k$ , increases slower with temperature. The uncertainties in these results (Xu and Grigoropoulos, 1993), are  $\delta d_{p-si} = 10 \text{ \AA}$ ,  $\delta n/n = 1$  percent, and  $\delta k/k = 5$  percent. These measurements are verified by (a) normal reflectivity data at high temperatures and (b) the angular variation of the reflectivity at a temperature of 300°C. Calculations based on the thin film refractive indices and thicknesses derived in this work show good agreement with the experimental results (Figs. 5a, 5b).

The values of  $n$  are fitted linearly and values of  $k$  are fitted exponentially for temperature  $T$  measured in °C:

$$n = n_0 + n_1 \times T \quad (6a)$$

$$k = k_0 \times \exp(T/T_0) \quad (6b)$$

The fitting parameters  $n_0$ ,  $n_1$ ,  $k_0$ , and  $T_0$  for the three samples are listed in Table 1. For comparison, the corresponding parameters for the complex refractive index of the crystalline silicon are also given in this table. The measured polysilicon complex refractive indices are used for calculating the reflectivity at the HeNe laser wavelength.

The complex refractive indices of polysilicon films measured at the  $\lambda_{exc} = 0.248 \mu\text{m}$  wavelength are shown in Table 2. These values are different from the polysilicon complex refractive index,  $\hat{n}_{exc} = 1.6 + i2.5$ , extracted from the room temperature dielectric function spectra given by Bagley et al. (1981). This difference could be attributed to the deposition conditions used for the polysilicon sample preparation. Also, it is noted that the three

samples tested in this work have quite different refractive indices. The room temperature normal reflectivities calculated using the ellipsometrically measured refractive indices are close to the reflectivities measured by the spectrophotometer (Table 2). The measured complex refractive indices are used in the calculation of the excimer laser radiation absorption of the polysilicon samples.

**IV.2 Results of the Transient Reflectivity Measurement.** Figures 6(a) and 6(b) show the comparison between the calculated and the measured reflectivities of Sample #2 ( $d_{p-si} = 0.250 \mu\text{m}$ ), and Sample #3 ( $d_{p-si} = 0.412 \mu\text{m}$ ) heated by the pulsed excimer laser. The laser fluencies are fixed at  $F = 0.17 \text{ J/cm}^2$ . The results of the reflectivity measurement were obtained from an unpolarized HeNe laser beam at an angle of incidence,  $\theta = 38$  deg. The interference effect of the HeNe laser light in the thin film results in the reflectivity increases, followed by a drop as the temperature is increased. The reflectivity minimum at about 43 ns corresponds to the peak surface temperature during the heating. As can be seen in the figures, the numerical model captures the experimental trend accurately.

Figures 7(a), 7(b), and 7(c) show another set of calculated and measured reflectivity of Sample #1, Sample #2, and Sample #3, respectively. The excimer laser fluency,  $F = 0.155 \text{ J/cm}^2$ , and a  $p$ -polarized HeNe laser beam with the angle of incidence of  $\theta = 16.7$  deg is used for reflectivity measurement. Good agreement is achieved between the calculated and measured reflectivity histories.

The transient temperature profile development during the excimer laser heating is of primary interest. The calculated temperature profiles across the sample are shown in Fig. 8 for Sample #3 ( $d_{p-si} = 0.412 \mu\text{m}$ ). The temperature gradient in the  $\text{SiO}_2$  layer is much larger than that in the polysilicon layer. This is due to the lower thermal diffusivity of the  $\text{SiO}_2$  layer. Figure 9 shows the transient surface temperatures histories for three samples. The differences of the peak temperatures of three samples are due to the different optical absorption of the samples, and the effect of the  $\text{SiO}_2$  layer.

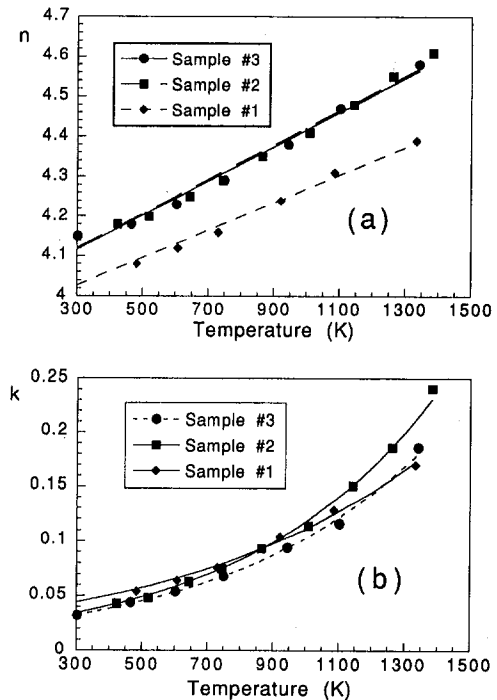


Fig. 4 Optical constants of LPCVD polysilicon films deposited at 580°C: (a) real part of the complex refractive index; (b) imaginary part of the complex refractive index

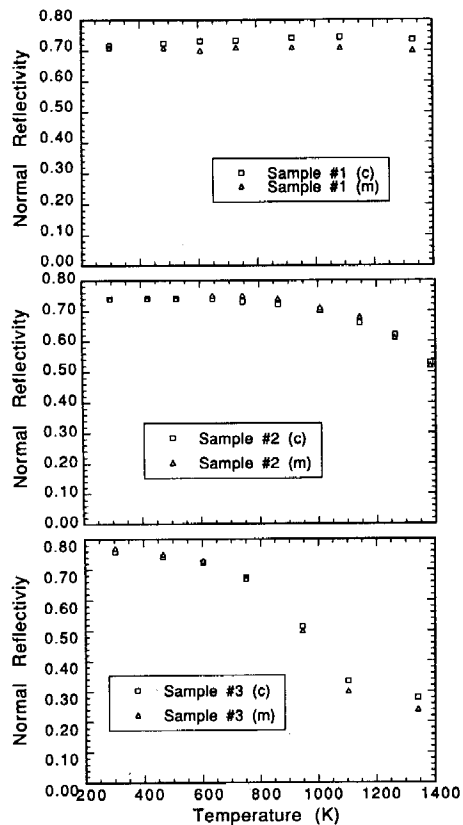


Fig. 5(a) Measured and calculated temperature dependence of normal incidence reflectivity

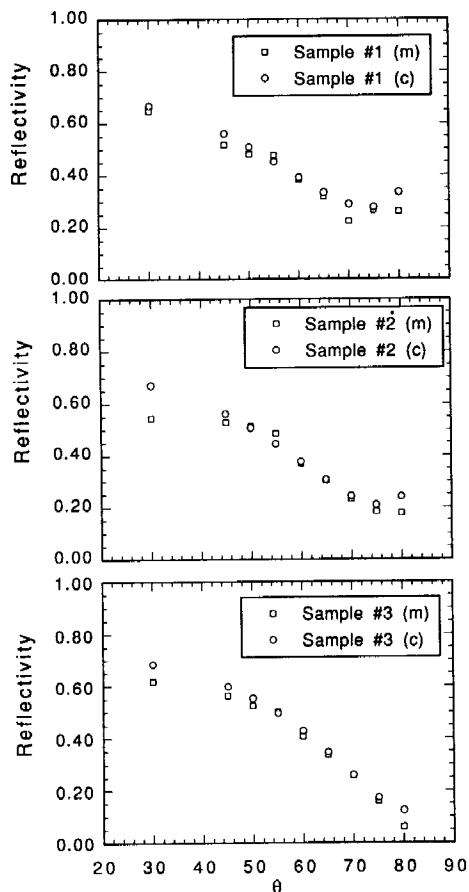


Fig. 5(b) Measured and calculated angular variation of the reflectivity for unpolarized HeNe laser light. The samples are maintained at a temperature of 300°C using a standard heater assembly.

Table 2 Components of the complex refractive index and normal reflectivity of polysilicon at  $\lambda_{exc} = 0.248 \mu\text{m}$ ;  $m$  = measured reflectivity;  $c$  = reflectivity calculated from the measured refractive index

Sample	$n_{exc}$	$k_{exc}$	Reflectivity (m)	Reflectivity (c)
# 1	1.1	3.1	0.72	0.69
# 2	0.85	2.6	0.65	0.67
# 3	1.2	2.8	0.58	0.62

The accuracy of the calculated surface temperature is determined by (a) the experimental uncertainties in the transient reflectivity measurement, (b) the accuracy of the temperature dependence of complex refractive index of polysilicon films at the probing laser light wavelength, (c) the accuracy in the measured thickness of thin polysilicon film, and (d) the neglect of the deviation of the thermal conductivity of thin film material from the bulk, and the neglect of a possible thermal boundary resistance. The complex refractive index measurements have accuracies of  $\delta n/n = 1$  percent and  $\delta k/k = 5$  percent in the temperature range from 300 K to 1400 K. On the other hand, the thickness of the thin polysilicon film is determined with accuracy of  $\pm 10 \text{ \AA}$ . These two effects combined cause an error of  $\pm 0.015$  in the reflectivity calculation. The maximum error for the reflectivity is thus estimated to be  $\pm 0.025$  including the uncertainty in the reflectivity measurement ( $\pm 0.01$ ). Numerical calculation is performed to estimate the effect of this uncertainty of reflectivity measurement on the accuracy of temperature determination. Figure 10 shows the correspondence between the calculated maximum surface temperature rise and minimum reflectivity of Sample #3 using the  $p$ -polarized probing HeNe laser at an angle of incidence  $\theta = 16.7$  deg. It can be seen that the reflectivity error of  $\pm 0.025$  will cause a variation of the maximum surface temperature of about 50 K. Similar accuracies were obtained for other samples.

The effect of the reduction of thermal conductivity and the boundary resistance is considered. It has been shown (Lambro-

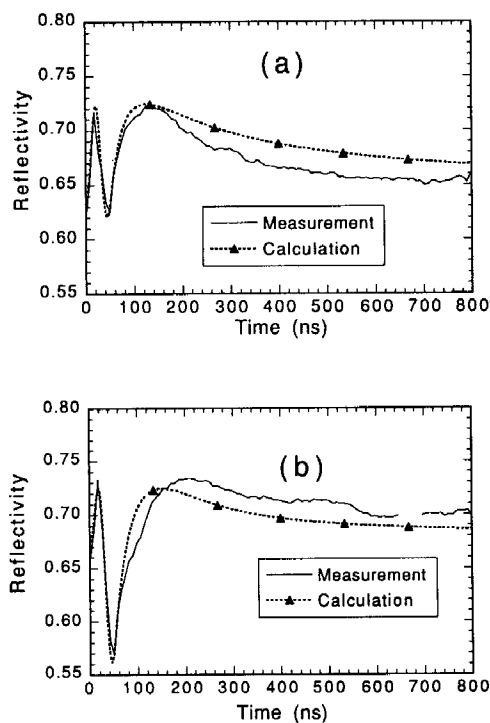


Fig. 6 Computed and measured transient reflectivity of (a) Sample #2 ( $d_{p-si} = 0.250 \mu\text{m}$ ); (b) Sample #3 ( $d_{p-si} = 0.412 \mu\text{m}$ ). The excimer laser fluence  $F = 0.17 \text{ J/cm}^2$ . The angle of incidence of the unpolarized HeNe probing laser beam  $\theta = 38$  deg.



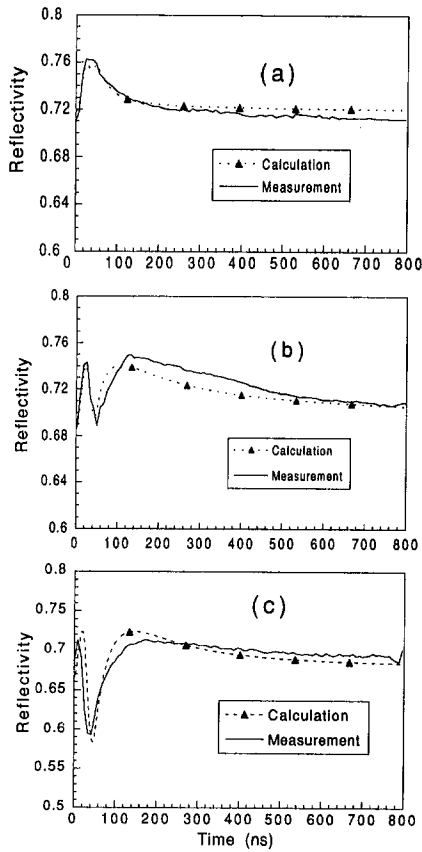


Fig. 7 Computed and measured transient reflectivity of (a) Sample #1 ( $d_{p-Si} = 0.097 \mu\text{m}$ ); (b) Sample #2 ( $d_{p-Si} = 0.250 \mu\text{m}$ ); (c) Sample #3 ( $d_{p-Si} = 0.412 \mu\text{m}$ ). The excimer laser fluence  $F = 0.155 \text{ J/cm}^2$ . The angle of incidence of the  $p$ -polarized HeNe probing laser beam  $\theta = 16.7 \text{ deg}$ .

poulos et al., 1991; Mastrangelo and Muller, 1988), that the thermal conductivity of the thin film is less than that of the bulk material when the smallest dimension (thin film thickness or the grain size) in the thin film material is comparable to the mean free path of heat carriers. The experimental results (Goodson et al., 1993) show that the effective conductivity (which accounts for the boundary resistance) of thin  $\text{SiO}_2$  films with thickness around  $0.1 \mu\text{m}$ , and which were annealed at a temperature of  $1400 \text{ K}$ , is reduced by approximately 23 percent from its bulk value. The thermal conductivity of thin polysilicon films is also expected to be smaller than the bulk value. Mastrangelo and Muller (1988) reported a reduction of thermal conductivity of heavily

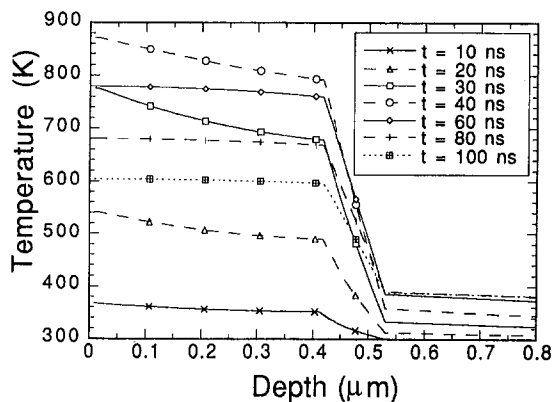


Fig. 8 Computed temperature profile across the thin film,  $d_{p-Si} = 0.412 \mu\text{m}$ . The excimer laser pulse fluence  $F = 0.155 \text{ J/cm}^2$ .

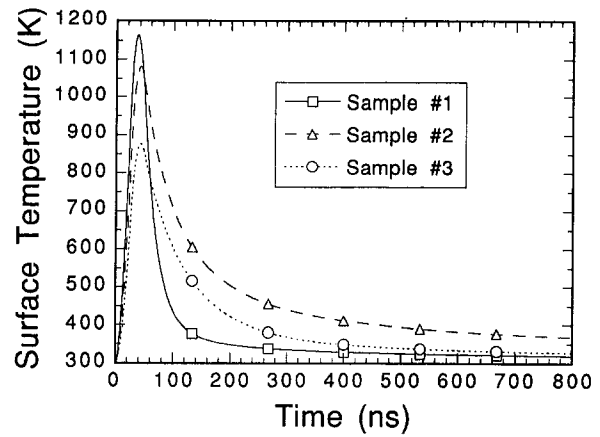


Fig. 9 Computed surface temperature variation with time. The excimer laser fluence  $F = 0.155 \text{ J/cm}^2$ .

doped,  $1.3\text{-}\mu\text{m}$ -thick polysilicon films by a factor of four from the thermal conductivity of bulk crystalline silicon. Numerical calculation is performed to estimate the deviation of the temperature determination using the reduced thermal conductivity. Reduced values of thermal conductivities of both the polysilicon film and the  $\text{SiO}_2$  film are used in the calculation. The thermal conductivity of  $\text{SiO}_2$  is reduced by 23 percent and the thermal conductivity of polysilicon is reduced by a factor of four from the thermal conductivity of bulk silicon in the calculation. It is noted that the  $\text{SiO}_2$  films in the sample tested in this work are thermally grown and annealed at high temperatures, with expected microstructure and thermal properties closer to the bulk values than LPCVD films. In order to match the reflectivity curve produced by the experiment and the calculation results using bulk values, the laser fluence is reduced by about 10 percent in the calculation that employs the reduced thermal conductivities. This reduction of the fluency is within the experimental uncertainties of the laser fluency measurement. Table 3 compares the calculation results of maximum surface temperatures using the bulk and reduced thermal conductivities. It can be seen that the difference between the maximum temperature obtained by using the bulk and the thin film properties is less than  $20 \text{ K}$  for all three samples. Therefore, the total experimental uncertainty of the temperature measurement is less than  $90 \text{ K}$ .

It must be pointed out that use of inaccurate optical properties and film thickness for the polysilicon layer does not allow correct calculation and analysis of the reflectivity signal.

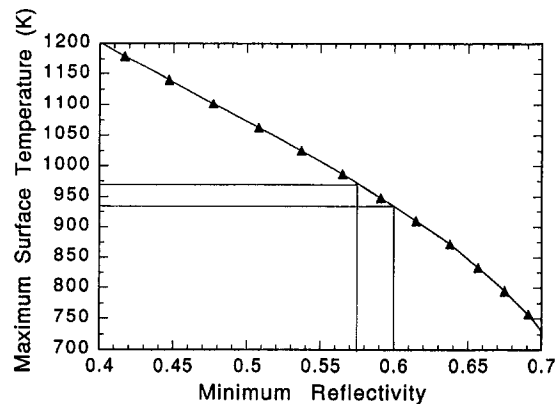


Fig. 10 Relation between minimum reflectivity and maximum surface temperature rise, of Sample #3. The angle of incidence of the  $p$ -polarized HeNe probing laser beam,  $\theta = 16.7 \text{ deg}$ .

Even small changes in the polysilicon optical constants drastically alter the reflection response for the HeNe probing laser wavelength due to wave interference effects. Figure 11(a) shows the reflectivity dependence for unpolarized HeNe laser light incident onto samples maintained at uniform temperature, at an angle of incidence,  $\theta = 38$  deg. These curves were calculated using the thin film complex refractive index data measured in this work. Figure 11(b) shows the reflectivity under the same conditions, but using the optical properties of bulk silicon (Jellison and Burke, 1986, Table 1), which were extrapolated for temperature,  $T > 700^\circ\text{C}$ . It can be seen that calculation of the optical response based on bulk values does not produce the experimental reflectivity behavior. It is noted that while the reflectivities for Sample #1 ( $d_{p\text{-Si}} = 0.097 \mu\text{m}$ ) exhibit similar trends, the temperature dependence of the reflectivity for the thicker samples (Samples #2, #3) is entirely different when crystalline properties are used (Fig. 11b) rather than the directly measured values (Fig. 11a). By the same reasoning, variations of the thin film thickness of the order of 10 nm can change the sample reflection characteristics due to optical interference effects (Xu et al., 1993).

## V Conclusions

The transient temperature field of thin polysilicon films of thickness in the range of 0.1 to 0.4  $\mu\text{m}$  during pulsed excimer laser heating has been studied. Polarized and unpolarized continuous wave HeNe lasers were used as probes for absolute transient reflectivity measurement. The complex refractive index of the polysilicon films was determined statically by combined ellipsometric and normal incidence reflectivity measurements in the temperature range from 300 K to approximately 1400 K. The room temperature complex refractive index of the excimer laser wavelength was measured by spectroscopic ellipsometry. These measurements were used for modeling the transient reflectivity during pulsed laser heating on the nanosecond time scale. Good agreement was obtained between the experimental results and the calculation. The temporal variation of the measured reflectivity enables experimental probing of the transient temperature field. The experimental uncertainties of the temperature determination is estimated to be less than 90 K, considering both the accuracy of reflectivity measurement and the uncertainties of the thermal properties. The present work verifies a general experimental procedure for in-situ monitoring of fast thermal processes that is based on knowledge of the temperature dependence of the thin film complex refractive index.

## Acknowledgments

Support by the National Science Foundation under Grant No. CTS-9210333 is gratefully acknowledged. R. Russo acknowledges the support by the U.S. Department of Energy, Office of Basic Energy Sciences, Division of Chemical Sciences, under contract #DE-AC03-76SF00098. The authors thank Dr. Michael Rubin, and Dr. Reto Furler of Lawrence Berkeley Laboratory for measuring UV optical properties. The help of Xiang Zhang, Hee K. Park, and Mark Shannon of the Department of Mechanical Engineering of the University of California at Berkeley on conducting the experimental work is appreciated.

**Table 3 Comparison of maximum surface obtained by using bulk thermal properties and reduced thermal properties**

	Sample #1	Sample #2	Sample #3
Maximum T, using bulk properties	1255 K	1006 K	891 K
Maximum T, using reduced properties	1274 K	1025 K	905 K

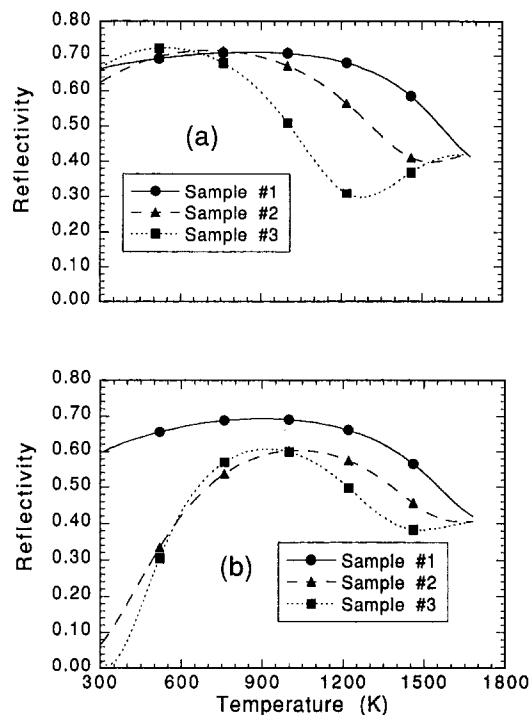


**Fig. 11 Temperature dependence of reflectivity for unpolarized HeNe laser light, at an angle of incidence of 38 deg: (a): calculation results using the optical properties measured in this work; (b): calculation results using the optical properties of bulk silicon (Jellison and Burke, 1986)**

## References

- Aspnes, D. E., 1982, "Optical Properties of Thin Films," *Thin Solid Films*, Vol. 89, pp. 249–262.
- Bagley, B. G., Aspnes, D. E., Adams, A. C., and Mogab, C. J., 1981, "Optical Properties of Low-Pressure Chemically Vapor Deposited Silicon Over the Energy Range 3.0–6.0 eV," *Applied Physics Letters*, Vol. 38, No. 1, pp. 56–58.
- Born, M., and Wolf, W., 1980, *Principles of Optics*, 6th ed., Pergamon, Exeter, pp. 55–60, 611–624.
- Graebner, J. E., Jin, S., Kammlott, G. W., Herb, J. A., and Gardinier, C. F., 1992, "Unusually High Thermal Conductivity in Diamond Films," *Applied Physics Letters*, Vol. 60, pp. 1576–1578.
- Goodson, K. E., Flik, M. I., Su, L. T., and Antoniadis, D. A., 1993, "Annealing-Temperature Dependence of the Thermal Conductivity of CVD Silicon-Dioxide Layers," *ASME HDT-Vol. 253*, pp. 29–36.
- Grigoropoulos, C. P., Dutcher, W. E., Jr., and Emery, A. F., 1991a, "Experimental and Computational Analysis of CW Argon Laser Melting of Thin Silicon Films," *ASME JOURNAL OF HEAT TRANSFER*, Vol. 113, pp. 21–29.
- Grigoropoulos, C. P., Dutcher, W. E., Jr., and Barclay, K. E., 1991b, "Radiative Phenomena in CW Laser Annealing," *ASME JOURNAL OF HEAT TRANSFER*, Vol. 113, pp. 657–662.
- Grigoropoulos, C. P., Park, H. K., and Xu, X., 1993, "Modeling of Pulsed Laser Irradiation of Thin Silicon Films," *International Journal of Heat and Mass Transfer*, Vol. 36, No. 4, pp. 919–924.
- Harbecke, G., Krausbauer, L., Steigmeier, E. F., Widmer, A. E., Kappert, H. F., and Neugebauer, G., 1984, "Growth and Physical Properties of LPCVD Polycrystalline Silicon Films," *Journal of the Electrochemical Society*, Vol. 131, pp. 675–682.
- Howe, R. T., 1985, "Polycrystalline Silicon Micromachining," in: *Micromachining and Micropackaging of Transducers*, C. D. Fung et al., eds., Elsevier, New York, pp. 169–187.
- Jacobsson, R., 1965, "Light Reflection From Films of Continuously Varying Refractive Index," in: *Progress in Optics*, Vol. 5, E. Wolf, ed., North-Holland, Amsterdam, pp. 247–286.
- Jellison, G. E., Jr., and Modine, F. A., 1982, "Optical Absorption of Silicon Between 1.6 and 4.7 eV at Elevated Temperatures," *Applied Physics Letters*, Vol. 41, pp. 180–182.
- Jellison, G. E., Jr., and Burke, H. H., 1986, "The Temperature Dependence of the Refractive Index of Silicon at Elevated Temperatures at Several Laser Wavelengths," *Journal of Applied Physics*, Vol. 60, No. 2, pp. 841–843.
- Kamins, T. I., 1988, *Polycrystalline Silicon for Integrated Circuit Applications*, Kluwer Academic Publishers, Boston.
- Knittl, Z., 1976, *Optics of Thin Films*, Wiley, Prague, Czechoslovakia, pp. 182–282.
- Krulevitch, P., Johnson, G. C., and Howe, R. T., 1992, "Stress and Microstructure in Phosphorus Doped Polycrystalline Silicon," *Material Research Society Symposium Proceedings*, Vol. 276, pp. 79–84.

Lambropoulos, J. C., Jacobs, S. D., Burns, S. J., Shaw-Klein, L., and Hwang, S.-S., 1991, "Thermal Conductivity of Thin Films: Measurement and Microstructural Effects," *Thin Film Heat Transfer: Properties and Process*, ASME HTD-Vol. 184, pp. 21–31.

Lompere, L. A., Liu, J. M., Kurz, H., and Bloembergen, N., 1983, "Time-Resolved Temperature Measurement of Picosecond Laser Irradiated Silicon," *Applied Physics Letters*, Vol. 43, No. 2, pp. 168–170.

Lowndes, D. H., 1982, "Time-Resolved Optical Transmission and Reflectivity of Pulsed-Ruby-Laser Irradiated Crystalline Silicon," *Physical Review Letters*, Vol. 48, No. 4, pp. 267–271.

Lowndes, D. H., and Jellison, G. E., Jr., 1984, "Time Resolved Measurements During Pulsed Laser Irradiation of Silicon," in: *Semiconductors and Semimetals*, Vol. 23, R. F. Wood, C. W. White, and R. T. Young, ed., Academic, Orlando, pp. 313–404.

Mastrangelo, C. H., and Muller, R. S., 1988, "Thermal Diffusivity of Heavily Doped Low Pressure Chemical Vapor Deposited Polycrystalline Silicon Films," *Sensors and Materials*, Vol. 3, pp. 133–142.

Montaudon, P., Debroux, M. H., Ferrieu, F., and Vareille, A., 1985, "Optical Characterization of Polycrystalline Silicon Before and After Thermal Oxidation," *Thin Solid Films*, Vol. 125, pp. 235–241.

Park, H. K., Xu, X., Grigoropoulos, C. P., Do, N., Klees, L., Leung, P. T., and Tam, A. C., 1993, "Transient Optical Transmission Temperature Measurement in Excimer-Laser Irradiation of Amorphous Silicon Films," *ASME JOURNAL OF HEAT TRANSFER*, Vol. 115, pp. 178–183.

Touloukian, Y. S., 1970, *Thermophysical Properties of Matter: Thermal Conductivity*, IFI/Plenum, New York.

Tsaur, B. Y., 1986, "Assessment of Silicon on Insulator Technologies for VLSI," *Proceedings of the Materials Research Society*, A. Chiang et al., eds., Vol. 53, MRS, Pittsburgh, pp. 365–373.

Xu, X., and Grigoropoulos, C. P., 1993, "High Temperature Radiative Properties of Thin Polysilicon Films at the  $\lambda = 0.6328 \mu\text{m}$  Wavelength," *International Journal of Heat and Mass Transfer*, Vol. 36, No. 17, pp. 4163–4172.

Xu, X., Taylor, S. L., Park, H. K., and Grigoropoulos, C. P., 1993, "Transient Heating and Melting Transformation in Argon-Ion Laser Irradiation of Polysilicon Films," *Journal of Applied Physics*, Vol. 73, No. 12, pp. 8088–8096.

## APPENDIX I

### Thermal Properties

The solid silicon properties vary with temperature (Touloukian, 1970):

$$K_{\text{Si}}(T) = 2.99 \times 10^4 / (T - 99) \quad (\text{W/m/K}) \quad (\text{A.1})$$

$$\rho_{\text{Si}}(T) C_{p,\text{Si}}(T) = (1.474 + 0.17066T/300) \times 10^6 \quad (\text{J/m}^3/\text{K}) \quad (\text{A.2})$$

The thermal properties of  $\text{SiO}_2$  are assumed temperature independent:

$$K_{\text{SiO}_2} = 1.4 \text{ W/m/K}, \quad \rho_{\text{SiO}_2} = 2200 \text{ kg/m}^3,$$

$$C_{p,\text{SiO}_2} = 1200 \text{ J/kg}.$$

The reduced thermal conductivities used for comparing the maximum temperature calculated using bulk thermal properties and thin film properties:

$$K_{\text{Si}}(T) = 2.0 \times 10^4 / (T - 99) \quad (\text{W/m/K})$$

$$K_{\text{SiO}_2} = 1.0 \text{ W/m/K} \quad (\text{A.3})$$

## APPENDIX II

### Thin Film Optics

Utilizing the formalism of the characteristic transmission matrix, the lumped structure reflectivity and transmissivity can be obtained. The  $i$ th layer of thickness  $d_i$ , which may be absorbing, having a complex refractive index,  $\hat{n}_i = n_i - ik_{\text{ext},i}$ , is represented by the transmission matrix  $M_i$ :

$$M_i = \begin{pmatrix} \cos\left(\frac{2\pi}{\lambda} \hat{n}_i d_i\right) & \frac{i}{\hat{n}_i} \sin\left(\frac{2\pi}{\lambda} \hat{n}_i d_i\right) \\ i\hat{n}_i \sin\left(\frac{2\pi}{\lambda} \hat{n}_i d_i\right) & \cos\left(\frac{2\pi}{\lambda} \hat{n}_i d_i\right) \end{pmatrix} \quad (\text{A.4})$$

The multilayer transmission matrix,  $M$ , is:

$$M = \prod_{i=1}^{IT} M_i \quad (\text{A.5})$$

$IT$  is the number of nodes in the sample structure. For both  $p$  and  $s$  polarized light, the reflection Fresnel coefficients,  $r$ , is:

$$r = \frac{(M(1, 1) + M(1, 2)\hat{n}_s)\hat{n}_a - (M(2, 1) + M(2, 2)\hat{n}_s)}{(M(1, 1) + M(1, 2)\hat{n}_s)\hat{n}_a + (M(2, 1) + M(2, 2)\hat{n}_s)} \quad (\text{A.6})$$

The reflectivity  $R$  is calculated as

$$R = |r|^2 \quad (\text{A.7})$$

The reflectivity of the unpolarized light is calculated as:

$$R = (R_p + R_s)/2 \quad (\text{A.8})$$

K. Fushinobu<sup>1</sup>  
Graduate Student.

A. Majumdar  
Associate Professor.

Department of Mechanical and  
Environmental Engineering,  
University of California, Santa Barbara,  
Santa Barbara, CA 93106

K. Hijikata  
Professor,  
Tokyo Institute of Technology,  
Department of Mechano-Aerospace  
Engineering,  
Tokyo, Japan

# Heat Generation and Transport in Submicron Semiconductor Devices

*The reduction of semiconductor device size to the submicrometer range leads to unique electrical and thermal phenomena. The presence of high electric fields (order of  $10^7$  V/m) energizes the electrons and throws them far from equilibrium with the lattice. This makes heat generation a nonequilibrium process. For gallium arsenide (GaAs), energy is first transferred from the energized electrons to optical phonons due to strong polar coupling. Since optical phonons do not conduct heat, they must transfer their energy to acoustic phonons for lattice heat conduction. Based on the two-step mechanism with corresponding time scales, a new model is developed to study the process of nonequilibrium heat generation and transport in a GaAs metal semiconductor field effect transistor (MESFET) with a gate length of  $0.2 \mu\text{m}$ . When 3 V is applied to the device, the electron temperature rise is predicted to be more than 1000 K. The effect of lattice heating on electrical characteristics of the device shows that the current is reduced due to decrease in electron mobility. The package thermal conductance is observed to have strong effects on the transient response of the device.*

## Introduction

Heat removal from semiconductor devices and electronic packages has been a critical issue in the design of LSI chips. The typical heat dissipation rate of recent LSI chips is in the range of  $1 \sim 10 \text{ W/cm}^2$ . Future trends indicate that LSI chips with heat dissipation rate of about  $100 \text{ W/cm}^2$  are possible. For such high heat dissipation rates, it would be necessary to consider not only macroscopic heat transfer mechanisms for effective heat removal from the chip, but also microscopic optimum device designs for the reduction of the heat dissipation rate itself. It is, therefore, important to understand the mechanism of heat generation and transport phenomena at the device level.

Design of semiconductor devices based on electrical characteristics is a well-established field (Sze, 1981; Snowden, 1988). These simulations give the electrical characteristics, such as the current-voltage characteristics, electron number density distribution, etc. Some other researchers (Curtice and Yun, 1981; Cook and Frey, 1982; Zhou and Ferry, 1992; Yoganathan and Banerjee, 1992) have proposed numerical calculations that include electron energy transport effect. They, however, have assumed that the lattice temperature does not change during device operation. Since heat transport in semiconductors is dominated by the lattice and not by the electrons, this approximation may not be realistic. Wang (1985) has developed a model including lattice energy transport equation. However this model does not consider the phonon dispersion relations and the resulting differential behavior of phonon modes.

Figure 1 shows a schematic diagram of the heat generation mechanism in a metal-semiconductor field effect transistor (MESFET). When a voltage is applied across the drain and the source, electrons are accelerated from the source, and flow under the channel into the drain. For MESFETs, a typical applied voltage of about 1 V and a typical length of the gate channel  $\approx 1 \mu\text{m}$  result in an electric field of  $\approx 10^4 \text{ V/cm}$ . With new advances in nanofabrication techniques, the further reduction in gate length can produce fields as high as  $10^6 \text{ V/cm}$ . Under such high electric

fields, the electrons become highly energetic. Heat generation in semiconductor devices occurs due to collisions between these electrons and the lattice. Due to collisions, the lattice gains energy from the electrons, and the lattice temperature increases. With the change of the lattice temperature, scattering rate of the electrons and the lattice is also altered and the electron transport is in turn affected. Therefore thermal and electrical characteristics have an influence on each other and must be treated as a coupled problem.

The aim of this study is to consider the nonequilibrium nature of the electrons and the phonons to show the thermal and the electrical characteristics in submicron MESFETs. We choose MESFET made of gallium arsenide (GaAs) for our study since it is an integral component in signal processing and communication circuits.

In Section 2, the physics and operating principle of GaAs MESFETs are discussed. Section 3 shows the computational method of this work, and Section 4 discusses the results. Finally, Section 5 states the conclusions.

## Physics of Heat Generation and Transport

As shown in Fig. 1, GaAs MESFETs have the active layer deposited on the semi-insulating substrate. The active layer is *n*-doped and has higher electron concentration and electrical conductivity than the semi-insulating layer. The source, drain, and gate contacts are formed by metal. Although each of the source and drain contacts has negligible contact resistance, the gate contact makes an electrostatic potential barrier (Schottky barrier) at the metal semiconductor contact without an external bias voltage (Sze, 1981). The former is called *ohmic contact*, while the latter is called *Schottky contact*. The physics of the Schottky barrier is such that an effective negative potential is induced on the contact. This makes electrons move away from the region under the gate contact to the surroundings. Thus a *depletion region*, where the electron number density is much smaller than the rest of the active layer, is formed and the channel where electrons can go through becomes narrow. When a drain to source voltage ( $V_{ds}$ ) is applied, most of the drain current ( $I_d$ ) flows in this narrow channel between the depletion region and the semi-insulating substrate.

The thickness of the depletion region can be controlled by the gate voltage ( $V_g$ ). If a negative  $V_g$  is applied, the electrostatic

<sup>1</sup> Present address: Post-doctoral researcher, University of California, Berkeley, CA 94720.

Contributed by the Heat Transfer Division for publication in the JOURNAL OF HEAT TRANSFER. Manuscript received by the Heat Transfer Division January 1993; revision received February 1994. Keywords: Electronic Equipment, Numerical Methods. Associate Technical Editor: L. S. Fletcher.

potential barrier at the gate becomes higher, which results in a bigger depletion region thickness. Therefore, a smaller channel imposes higher electrical resistance between drain to source. The drain to source current of MESFETs is controlled in this manner.

Heat generation in semiconductor devices occurs due to the collisions between the electrons and the lattice. The electrons gain energy from the applied electric field and can become very energetic. In general, applying an electric field causes a deviation of the statistical distribution function of electrons from the equilibrium Fermi-Dirac distribution (Shah, 1992). Although, strictly speaking, an electron temperature cannot be defined for the nonequilibrium distribution, an effective electron temperature,  $T_e$ , can be defined for the purpose of energy transport analysis. Such energetic electrons are called hot electrons (Ferry, 1991). Under high electric fields, the electron temperature becomes higher than the lattice temperature. During collision with the lattice, each of these hot electrons either emits or absorbs a quantum of lattice vibrational energy called a *phonon*. For heat generation, the phonon emission rate is higher than the absorption rate.

Figure 2 shows the phonon dispersion relations for GaAs, which contains two types of crystal vibration: optical mode and acoustic mode. The optical mode corresponds to the Ga and As atoms vibrating against or in opposite directions to each other, whereas the acoustic mode corresponds to that when they move in the same direction. Each mode has one longitudinal polarization and two transverse polarizations. The longitudinal optical (LO) mode couples most strongly with electrons due to polar interactions, explained as follows. Since the chemical bond of Ga and As is slightly ionic it forms an electric dipole. The LO vibrations, where the atoms vibrate against each other, produce an oscillating dipole, which interacts strongly with electrons. Photoexcitation studies (Lin et al., 1988; Peterson and Lyon, 1990) have shown that when a laser pulse excites electrons in GaAs, the dominant mechanism of electron energy relaxation is electron-LO phonon scattering. Through this process, the energetic electrons give their energy to the lattice and create LO phonons. In other words, the LO phonon temperature can increase due to energy transfer from electrons. This is the mechanism of lattice heating in GaAs.

The net generation of LO phonons can push its population well above the equilibrium value. The increase in the number of LO phonons can be high enough to the point the electron-LO phonon scattering rates are altered (Joshi and Ferry, 1989; Carrillo and Rodriguez, 1991). The change in electron scattering rate affects the electron transport in a device and therefore alters the device electrical characteristics.

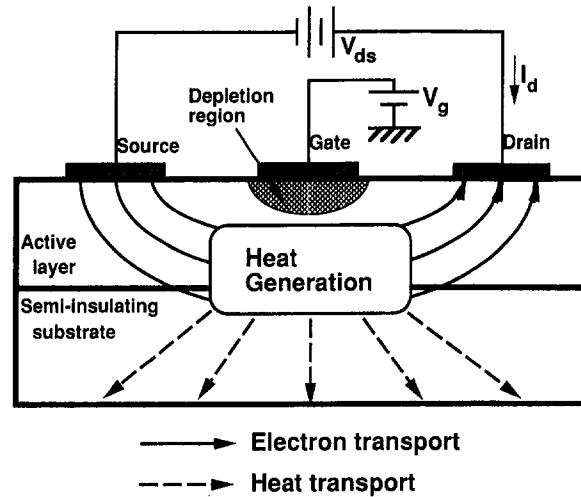


Fig. 1 Schematic diagram of heat generation and transport in MESFETs

The group velocity,  $v_g$ , of each mode is equal to the slope of the dispersion curves,  $v_g = d\omega/dK$ , where  $\omega$  is the vibrational frequency and  $K$  is the wave vector. It is clear from Fig. 2 that the group velocity of the optical mode is close to zero. Therefore, although electrons can transfer energy to the LO phonons, this mode *cannot* conduct heat since the thermal conductivity  $\kappa = \frac{1}{3}Cv_g l$ , where  $C$  is the specific heat and  $l$  is the mean free path. Therefore, this mode must transfer its energy to the acoustic mode vibrations. The acoustic phonons propagate at the speed of sound and are the dominant mode of heat conduction in GaAs. The mechanism of heat generation in GaAs is therefore a two-step process: electrons to LO phonons, LO phonons to acoustic phonons.

The predominant factor of the thermal effect on the electrical transport is due to the temperature dependent nature of the electron mobility. The electron mobility  $\mu$  is defined to be a proportionality constant between the electron drift velocity  $v_d$  and the applied electric field strength  $E$  (Sze, 1981). When an electric field is applied to a semiconductor, electrons respond to the field and start motion. Charged-particle (in our study, electrons) motion in response to an applied electric field is called *drift* (Pierret, 1989). Although the microscopic motion of these electrons is affected by the scattering process with other carriers, ionized impurities, etc., and becomes quite complicated, we can define drift

## Nomenclature

$c$  = speed of light in vacuum =  $2.99792 \times 10^8$  m/s  
 $C$  = heat capacity per unit volume,  $J/m^3 K$   
 $e$  = elementary charge =  $1.60218 \times 10^{-19}$  C  
 $\mathbf{E}$  = electric field (vector), V/m  
 $h$  = heat transfer coefficient,  $W/m^2 K$   
 $\hbar$  = reduced Planck constant =  $1.05457 \times 10^{-34}$  J s  
 $\mathbf{J}$  = current density (vector),  $A/m^2$   
 $k_B$  = Boltzmann constant =  $1.38066 \times 10^{-23}$  J/K  
 $L_g$  = gate length, m  
 $m_e$  = electron rest mass =  $9.10939 \times 10^{-31}$  kg  
 $m^*$  = electron effective mass =  $0.066 \times m_e$ , kg

$n$  = electron number density,  $1/m^3$   
 $N_D$  = doping concentration of the active layer,  $1/m^3$   
 $t$  = time, s  
 $\Delta t$  = time step, s  
 $T$  = temperature, K  
 $v_d$  = electron drift velocity, m/s  
 $\mathbf{v}$  = electron average velocity (vector), m/s  
 $V$  = voltage, V  
 $w$  = average electron energy, J  
 $W$  = energy, J/m<sup>3</sup>  
 $x, y$  = spatial coordinates, m  
 $\epsilon_0$  = permittivity in vacuum =  $10^7/(4\pi c^2)$ , F/m  
 $\epsilon_s$  = permittivity in GaAs =  $\epsilon_r \epsilon_0$ , F/m  
 $\epsilon_r$  = low-frequency dielectric constant of GaAs = 12.8

$\epsilon_r^\infty$  = high-frequency dielectric constant of GaAs = 10.9  
 $\kappa$  = thermal conductivity, W/mK  
 $\mu$  = electron mobility,  $m^2/V s$   
 $\rho$  = density,  $kg/m^3$   
 $\tau$  = relaxation time, s  
 $\phi_B$  = Schottky barrier height, V

## Subscripts

$A$  = acoustic phonon  
 $ds$  = drain to source  
 $e$  = electron  
 $g$  = gate  
 $l$  = lattice  
 $LO$  = LO phonon

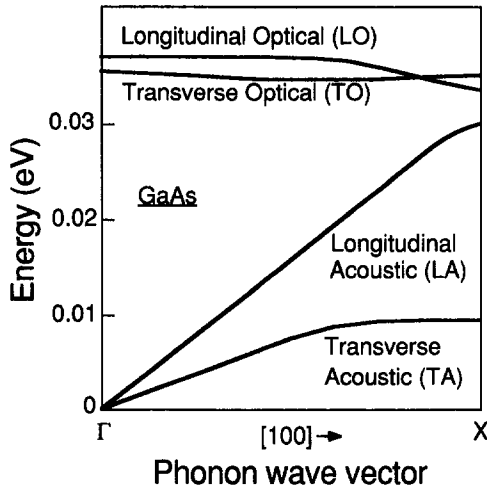


Fig. 2 Phonon dispersion relations in GaAs

velocity  $v_d$  as an average velocity of overall motion of electrons. The drift velocity and the electric field have the following relationship:

$$v_d = \mu E \quad (1)$$

At low electric field,  $\mu$  is constant and  $v_d$  is proportional to  $E$ . However, as the electric field becomes higher, the proportionality between  $v_d$  and  $E$  is no longer sustained. Figure 3 shows the typical relationship between  $v_d$  and  $E$  in GaAs. The electron mobility is also written as follows (Kittel, 1986):

$$\mu = e\tau_m/m^* \quad (2)$$

where  $e$  is the elementary charge,  $\tau_m$  is the electron momentum relaxation time, and  $m^*$  is the electron effective mass. The relaxation time  $\tau_m$  is a function of both the electron temperature and lattice temperature (Wolfe et al., 1989). Therefore any change in electron or lattice temperature changes the electron mobility and thus the electrical characteristics of the device.

It is clear that the thermal and electrical behavior of the device is highly coupled and a rigorous device simulation must consider not only the electron transport but also a consideration of the thermal behavior, that is, the LO phonons and the acoustic phonons.

### Governing Equations

We calculate a two-dimensional MESFET structure shown in Fig. 4. Taking into account the lack of equilibrium between electrons, LO phonons, and acoustic phonons, the following set of the energy equations can be derived from the first law of the thermodynamics:

Electrons:

$$\frac{\partial W_e}{\partial t} + \nabla \cdot \mathbf{q}_e + n\mathbf{v} \cdot (e\mathbf{E}) = \left( \frac{\partial W_e}{\partial t} \right)_c \quad (3)$$

LO Phonons:

$$\frac{\partial W_{LO}}{\partial t} = - \left( \frac{\partial W_e}{\partial t} \right)_c + \left( \frac{\partial W_{LO}}{\partial t} \right)_c \quad (4)$$

Acoustic Phonons:

$$\frac{\partial W_A}{\partial t} + \nabla \cdot \mathbf{q}_A = - \left( \frac{\partial W_{LO}}{\partial t} \right)_c \quad (5)$$

where  $W$  is the energy per unit volume,  $\mathbf{q}_e$  and  $\mathbf{q}_A$  are the energy flux of the electrons and the acoustic phonons, respectively, and  $t$  is time. Note that due to zero group velocity, there is no heat

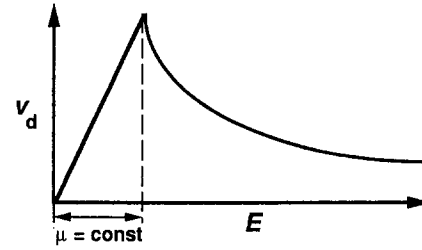


Fig. 3 Typical electron drift velocity: electric field relationship in GaAs

flux of LO phonons and hence there is no divergence term in the left-hand side of Eq. (4). The right-hand side term,  $(\partial W_j/\partial t)_c$ , of each equation represent the energy transfer rate due to collisions, where the suffix  $j$  denotes either  $e$  (electron), LO (LO phonon), or A (acoustic phonon). The third term of the right-hand side of Eq. (3) represents the work done by the applied electric field.

The particle and the momentum conservation equations of the electrons are expressed as follows (Blotekjaer, 1970):

$$\frac{\partial n}{\partial t} + \nabla \cdot (n\mathbf{v}) = 0 \quad (6)$$

$$\begin{aligned} \frac{\partial (nm^*\mathbf{v})}{\partial t} + \nabla \cdot \{ \mathbf{v}(nm^*\mathbf{v}) \} \\ = -en\mathbf{E} - \nabla(nk_B T_e) - \frac{nm^*\mathbf{v}}{\tau_m} \end{aligned} \quad (7)$$

where  $n$  is the electron number density,  $\mathbf{v}$  is the average velocity of electrons,  $\mathbf{E}$  is the local electric field,  $k_B$  is the Boltzmann constant, and  $T_e$  is the local electron temperature. Note that the current density  $\mathbf{J}$  can be written as  $\mathbf{J} = -en\mathbf{v}$ . In Eq. (6), we assume that there is no source or sink of electrons in the medium. In the left-hand side of Eq. (7), the first term is the rate of change of the electron momentum, the second term is the convective term. In the right-hand side, the first term is the drift term, the second term represents the force exerted by the electron pressure (Blotekjaer, 1970), and the last term is the rate of momentum change due to collisions.

The electric field is found by solving the Poisson equation

$$\nabla^2 V = -e(N_D - n)/\epsilon_s \quad (8)$$

where  $V$  is the voltage,  $\epsilon_s$  is the permittivity in GaAs,  $N_D$  is the doping concentration, and the field is

$$\mathbf{E} = -\nabla V \quad (9)$$

The permittivity in GaAs is calculated as  $\epsilon_s = \epsilon_r \epsilon_0$ , where  $\epsilon_r$  is the dielectric constant of GaAs, and  $\epsilon_0$  is the permittivity in vacuum. Here, we assume that all the donors are ionized, and the permittivity in GaAs is uniform and independent of position.

In order to solve this system of equations, we need the following constitutive relations. The heat fluxes of the electrons and the acoustic phonons are written as

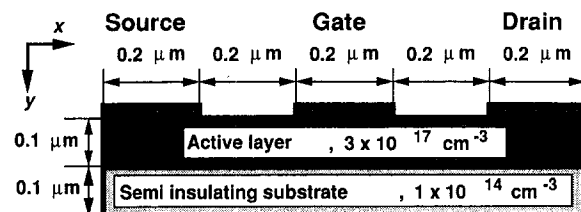


Fig. 4 Two-dimensional MESFET structure for calculation

$$\mathbf{q}_e = n\mathbf{w}\mathbf{v} + nk_B T_e \mathbf{v} - \kappa_e \nabla T_e \quad (10)$$

$$\mathbf{q}_A = -\kappa_A \nabla T_A \quad (11)$$

where  $\kappa_e$  and  $\kappa_A$  are the thermal conductivities of the electrons and the acoustic phonons, respectively. In Eq. (10), the first term of the right-hand side is the energy transport due to the electron motion, and the second term is the work performed by the electron pressure (Blotekjaer, 1970). The third term is energy transport by thermal diffusion. The average electron energy,  $w$ , is written as,

$$w = 3k_B T_e / 2 + m^* v^2 / 2 \quad (12)$$

where  $v^2 = |\mathbf{v}|^2$ . In Eq. (12), the first term is the internal energy and the second term is the kinetic energy.

The collision terms in Eq. (3), (4), and (5) are expressed as

$$\left( \frac{\partial W_e}{\partial t} \right)_c = - \frac{n(3k_B T_e / 2 + m^* v^2 / 2 - 3k_B T_{LO} / 2)}{\tau_{e-LO}} \quad (13)$$

$$\left( \frac{\partial W_{LO}}{\partial t} \right)_c = -C_{LO} \frac{T_{LO} - T_A}{\tau_{LO-A}} \quad (14)$$

where  $T_{LO}$  is the  $LO$  phonon temperature,  $\tau_{e-LO}$  is the energy relaxation time between electrons and  $LO$  phonons,  $C_{LO}$  is the  $LO$  phonon heat capacity per unit volume,  $T_A$  is the acoustic phonon temperature, and  $\tau_{LO-A}$  is the energy relaxation time between  $LO$  phonons and acoustic phonons.

With these constitutive relations and Eqs. (6) and (7), the energy conservation equations, Eqs. (3), (4), and (5), reduce to

$$\frac{\partial T_e}{\partial t} + \nabla \cdot (\mathbf{v} T_e) = \frac{1}{3} T_e \nabla \cdot \mathbf{v} + \frac{2}{3nk_B} \nabla \cdot (\kappa_e \nabla T_e) + \frac{m^* v^2}{3k_B} \left( \frac{2}{\tau_m} - \frac{1}{\tau_{e-LO}} \right) - \frac{T_e - T_{LO}}{\tau_{e-LO}} \quad (15)$$

$$C_{LO} \frac{\partial T_{LO}}{\partial t} = \frac{3}{2} nk_B \frac{T_e - T_{LO}}{\tau_{e-LO}} + \frac{nm^* v^2}{2\tau_{e-LO}} - C_{LO} \frac{T_{LO} - T_A}{\tau_{LO-A}} \quad (16)$$

$$C_A \frac{\partial T_A}{\partial t} = \nabla \cdot (\kappa_A \nabla T_A) + C_{LO} \frac{T_{LO} - T_A}{\tau_{LO-A}} \quad (17)$$

In the derivation of Eq. (15), the time derivative of the voltage is neglected.

The momentum conservation equation can be further simplified (Yoganathan and Banerjee, 1992) by neglecting the transient and inertia terms of the left-hand side of Eq. (7). Thus in conjunction with Eq. (2), Eq. (7) becomes

$$\mathbf{v} - \mu \mathbf{E} - \frac{\mu}{en} \nabla (nk_B T_e) = 0 \quad (18)$$

Substituting Eq. (18) into Eq. (6), we get

$$\frac{\partial n}{\partial t} - \nabla \cdot (n\mu \mathbf{E}) - \nabla \cdot \left\{ \frac{\mu}{e} \nabla (nk_B T_e) \right\} = 0 \quad (19)$$

We solve Eqs. (8), (15), (16), (17), and (19) simultaneously to obtain voltage, electron temperature,  $LO$  phonon temperature, acoustic phonon temperature, and the electron number density.

The physical properties needed for the computations are given in Table 1. The electronic thermal conductivity (Bhandari and Rowe, 1988) contains the parameter  $r$  (Wolfe et al., 1989), which is a function of  $T_{LO}$  and varies between  $-0.37$  for  $T_{LO} = 300$  K and  $0.5$  for  $T_{LO} = 1500$  K. Taking into account the insignificant electron (Bhandari and Rowe, 1988) and  $LO$  phonon contribution to the thermal conductivity, the experimental data of thermal conductivity of GaAs can be regarded as the contribution of only acoustic phonons. We used a curve fit of the experimental data (INSPEC, 1986) to get the correlation given in Table 1. All the  $LO$  phonons are assumed to have one frequency and therefore Einstein's model is used to approximate the heat

Table 1 Properties of GaAs used in the calculations

Physical Property	Expression
Electron Thermal Conductivity, $\kappa_e$ [W/m-K]	$\kappa_e = (nk_B^2 \tau_m T_e / m^*)^{(r+2.5)}$
Acoustic Phonon Thermal Conductivity, $\kappa_A$ [W/m-K]	$\kappa_A = A_1 / T_A^{1.2}$ ; $A_1 = 5.44 \times 10^4$ W-K <sup>0.2</sup> /m ( $N_D = 10^{14}$ cm <sup>-3</sup> ) $A_1 = 4.04 \times 10^4$ W-K <sup>0.2</sup> /m ( $N_D = 3 \times 10^{17}$ cm <sup>-3</sup> )
LO-phonon Specific Heat, $C_{LO}$ [J/m <sup>3</sup> -K]	$C_{LO} = 3.06 \times 10^5 - 2.40 \times 10^4 (\theta_{LO} / T_{LO})^{1.940}$ for $300 \text{ K} < T_{LO} < 1500 \text{ K}$ ; $\theta_{LO} = \hbar \omega_{LO} / k_B$
Acoustic Phonon Specific Heat, $C_A$ [J/m <sup>3</sup> -K]	$C_A = 9.17 \times 10^5 - 4.40 \times 10^4 (\theta_{LO} / T_{LO})^{1.948}$ for $300 \text{ K} < T_A < 1500 \text{ K}$ ; $\theta_D = 344 \text{ K}$
Drift velocity, $v_d$ [m/s]	$v_d = \mu E = \mu_0 (300 / T_{LO}) E$ for $E < E_{th}$ ; $\mu_0 = 8500$ cm <sup>2</sup> /V-s $v_d = (A_2 / E) + v_s$ for $E > E_{th}$ ; $A_2 = \mu_0 (300 / T_{LO}) E_{th}^2 - v_s E_{th}$ , $v_s = 6.67 \times 10^5 (300 / T_{LO})$ m/s; $E_{th} = 3.3 \times 10^5$ V/m at 300 K

capacity (Kittel, 1986). The heat capacity of the acoustic phonons can be calculated using the Debye model (Kittel, 1986) where the Debye temperature  $\theta_D$  is equal to 344 K for GaAs (Landolt, 1982).

The drift velocity,  $v_d$ , in GaAs is a function of the temperature and the doping concentration as well as of electric field. There exists a threshold field  $E_{th}$  below which the drift velocity increases linearly with the field and the mobility remains constant. For fields higher than  $E_{th}$ , the drift velocity decreases with increasing field and then finally reaches a constant saturation value for very high fields. We model this behavior as shown in Table 1. Here  $\mu$  is the electron mobility as a function of  $T_{LO}$  and  $N_D$ , which varies as  $T_{LO}^{-1}$  for  $n$ -type GaAs near room temperature and  $\mu_0$  is the mobility of GaAs at 300 K (Sze, 1981). The saturation velocity  $v_s$  is essentially independent of  $N_D$  and is inversely proportional to lattice temperature (Sze, 1981; Kramer and Mircea, 1975). Although  $E_{th}$  is a weak function of temperature (Blakemore, 1982), it is assumed to be a constant given in Table 1, which is the value at 300 K. It must be noted that the drift velocity decreases with increasing lattice temperature in both regimes. However, when  $T_{LO}$  increases, the electron temperature also increases, thus resulting in more energetic and faster electrons.

The energy relaxation time between the electrons and the  $LO$  phonons  $\tau_{e-LO}$  is equal to 0.1 ps (Collins and Yu, 1984). While the energy relaxation time between the  $LO$  phonons and the acoustic phonons  $\tau_{LO-A}$  is reported to have a rather wide range (Lugli et al., 1989), we choose 8 ps for our calculation. The electron momentum relaxation time is expressed as (Wolfe et al., 1989)

$$\tau_m = 4\tau_0 \Gamma(r + 2.5) / (3\sqrt{\pi}) \quad (20)$$

where  $\Gamma(r + 2.5)$  is the gamma function, and

$$\tau_0 = \frac{9.61 \times 10^{-15} \epsilon_r \epsilon_r^\infty \{ \exp(\theta_{LO} / T_{LO}) - 1 \}}{\{ \epsilon_r - \epsilon_r^\infty \} \theta_{LO}^{1/2} (\theta_{LO} / T_{LO})^r} \left( \frac{m_e}{m^*} \right)^{1/2} \quad (21)$$

where  $m_e$  is the electron rest mass.

## Computational Method

We use finite difference methods to discretize the set of governing equations in a two-dimensional MESFET structure. A central difference method is used to discretize the whole set of equations, except for the second term of the left-hand side of Eq. (15) where the first-upwind scheme is applied. A square uniform mesh is used over the entire computational domain. As we showed before (Fushinobu and Majumdar, 1992), any spatial mesh in a semiconductor must have a spacing of less than the Debye length (Sze, 1981). The Debye length  $L_D$  is a measure of how abruptly the free carrier concentration can change in space, and is written as:

$$L_D = \sqrt{(\epsilon_r k_B T) / (e^2 N_D)} \quad (22)$$

For instance,  $L_D$  is equal to 7.8 nm for  $N_D = 3 \times 10^{17} \text{ cm}^{-3}$  at  $T = 300 \text{ K}$ . We use a 6.7 nm mesh for the entire computational domain.

The boundary conditions are given as follows. For voltage, constant values are given at the source, gate, and drain contact (Dirichlet condition), and zero gradient normal to the boundary (zero electric field) is given at the rest of the boundary (Neumann condition). Note that at the gate contact, the sum of the Schottky barrier height,  $\phi_B = -0.8 \text{ V}$  (Sze, 1981), and the external gate voltage  $V_g$  is applied as the boundary condition. For LO phonon and acoustic phonon temperatures, constant heat transfer coefficient  $h$  is given at the top and bottom boundaries. Although  $h$  value is varied to see the effect on the results (Fig. 8), a typical value is  $h = 10^3 \text{ W/m}^2\text{K}$ . An adiabatic condition is applied at the other boundaries because many FETs are arranged together and each boundary is assumed to be symmetric in real LSIs. An adiabatic boundary condition is applied for electron temperature at the entire boundary, too. For the electron number density,  $n = N_D$  is given at each of the source and the drain contact, and zero particle flux normal to the boundary is applied at the rest of boundary.

We solve Eqs. (8), (15), (16), (17), and (19) simultaneously. A fully implicit method is used for the time-marching scheme. At each time step, the Incomplete LU Decomposition Conjugate Gradient Squared (ILUCGS) method (Watanabe et al., 1989) is used to solve the Poisson equation. An ILUCGS method is also used for matrix inversion of each of Eqs. (15), (17), and (19) at each time step.

We developed a *trot-gallop technique* for the time-marching scheme, in which we use two different time steps  $\Delta t_t$  (*trot* stage) and  $\Delta t_g$  (*gallop* stage) for iteration, where  $\Delta t_t < \Delta t_g$ . Since  $\tau_{e-LO} = 0.1 \text{ ps}$ , we observed that when we solve *electron energy equation part* (Eqs. (8), (15), and (19)) with a time step bigger than 0.01 ps, the results showed physically unrealistic behavior. At the same time, since  $\tau_{LO-A} = 8 \text{ ps}$ , the *lattice part* (Eqs. (16) and (17)) allows a rather larger time step. Also, the electron part can reach steady state much faster than the lattice part. Although  $\Delta t = 0.01 \text{ ps}$  would work for both lattice and electron equations, it is very time consuming to reach steady state for the lattice, since the relaxation time is 8 ps. To circumvent this problem, the *trot-gallop technique* solves the whole set of equations with the time step  $\Delta t_t$  until a quasi-steady state is reached for  $T_e$  (*trot* stage). Note that due to the slow response of the lattice part to the applied electric field, their effect on the electron part is negligible at this time level, and quasi-steady state can be achieved. Then, only the lattice part is solved with the bigger time step  $\Delta t_g$  (*gallop* stage), and then all equations are again solved with the time step  $\Delta t_t$  (*trot* stage). This procedure is repeated. The time steps  $\Delta t_t$  and  $\Delta t_g$  we choose are equal to 0.01 ps and 4.5 ps, respectively.

All the results shown below are of a GaAs MESFET with gate length  $L_g = 0.2 \mu\text{m}$ . The doping concentration of the active layer and the semi-insulating substrate are  $3 \times 10^{17} \text{ cm}^{-3}$  and  $1 \times 10^{14} \text{ cm}^{-3}$ , respectively. The thickness of the active layer and the semi-insulating substrate are both equal to 0.1  $\mu\text{m}$ .

The effect of the time step and the mesh size on the drain current are examined in order to validate the current values ( $\Delta t$

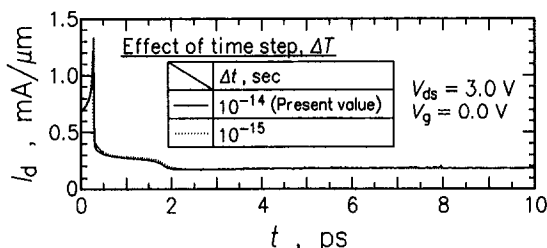


Fig. 5 Effect of the time step on the drain current ( $V_{ds} = 3 \text{ V}$ ,  $V_g = 0 \text{ V}$ )

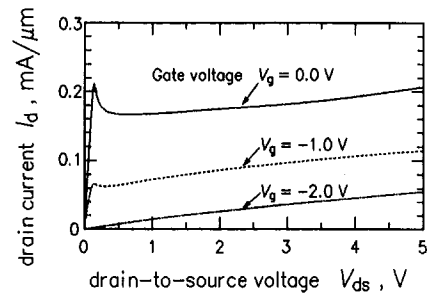


Fig. 6 Current-voltage characteristics of a  $0.2 \mu\text{m}$  gate length MESFET

$= 0.01 \text{ ps}$  and  $\Delta x = \Delta y = 6.7 \text{ nm}$ ). The computed drain current is plotted in Fig. 5 for different time steps,  $10^{-14} \text{ s}$  ( $=0.01 \text{ ps}$ ) and  $10^{-15} \text{ s}$  ( $=0.001 \text{ ps}$ ), and the two curves match very well. The comparison between two mesh sizes, 6.7 nm and 3.3 nm, gives the same results. The steady-state drain currents are computed to be 0.1827  $\text{mA}/\mu\text{m}$  (6.7 nm mesh) and 0.1828  $\text{mA}/\mu\text{m}$  (3.3 nm mesh), respectively. The results in the following session are thus independent of the time step and the mesh size.

## Results and Discussion

Figure 6 shows a calculated current-voltage characteristic. The unit of the ordinate,  $\text{mA}/\mu\text{m}$ , means the drain to source current per 1  $\mu\text{m}$  gate width. The gate width is the length of the gate contact normal to the  $x$ - $y$  plane defined in Fig. 4. It is clear that  $I_d$  saturates when  $V_{ds}$  is increased. Also, when  $V_g$  is increased, the channel size is decreased, thus decreasing  $I_d$ . Another interesting feature is that the current values show peaks around  $V_{ds} = 0.14 \text{ V}$ . Since  $\nu_d$  in Fig. 3 has a peak value at  $E = 3.3 \times 10^5 \text{ V/m}$ , the electric current, which is proportional to  $\nu_d$ , is also expected to have a peak value.

Figure 7 shows the distributions of (a) voltage,  $V$ , (b) electron number density divided by the doping concentration of the active layer,  $n/N_D$ , (c) Joule heating rate,  $\mathbf{J} \cdot \mathbf{E}$ , (d) electron temperature,  $T_e$ , (e) LO phonon temperature,  $T_{LO}$ , and (f) acoustic phonon temperature,  $T_A$ . The applied drain to source voltage  $V_{ds} = 3 \text{ V}$ , and the gate voltage  $V_g = 0 \text{ V}$ . Time level is  $t = 5 \text{ ns}$ .

In Fig. 7(a), each contour line step is 0.3 V and the dashed lines denote negative values of the potential. We can see in Fig. 7(a) that for even  $V_g = 0 \text{ V}$ , the voltage under the gate contact becomes negative due to the Schottky barrier. From this figure, we can also see that the major voltage drop occurs at the drain side of the channel under the gate. This means that the electric field in this region is higher than in the rest of the medium.

The line step in Fig. 7(b) is  $0.1 \times (n/N_D)$ . The depletion region can be clearly seen in this figure. This makes the current channel under the depletion region narrow. Since the channel is narrow, the current density becomes large in the channel.

Since the current density  $\mathbf{J}$  and the electric field  $\mathbf{E}$  become higher in the gate channel, it is expected that the Joule heating rate is the highest around the region. Figure 7(c) shows the distribution of the Joule heating rate due to the applied voltage. The line step is  $5 \times 10^{15} \text{ W/m}^3$ . One can clearly see that the Joule heating rate has a strong peak at the drain side of the active layer, as expected. It should be noted that the maximum value reaches about  $4 \times 10^{16} \text{ W/m}^3$ . With this extremely high Joule heating rate, we can expect a high temperature increase at this location.

Figure 7(d) shows the distribution of local electron temperature  $T_e$ . The line step is 100 K. We can find a local hot spot at the drain side of the channel under the depletion region, with maximum temperature increase 1370 K. Note that it is not at the center of the channel due to the big potential drop at the drain side of the gate channel.

Figures 7(e, f) show the distribution of the LO phonon and acoustic phonon temperature, respectively. The line step is 1 K.



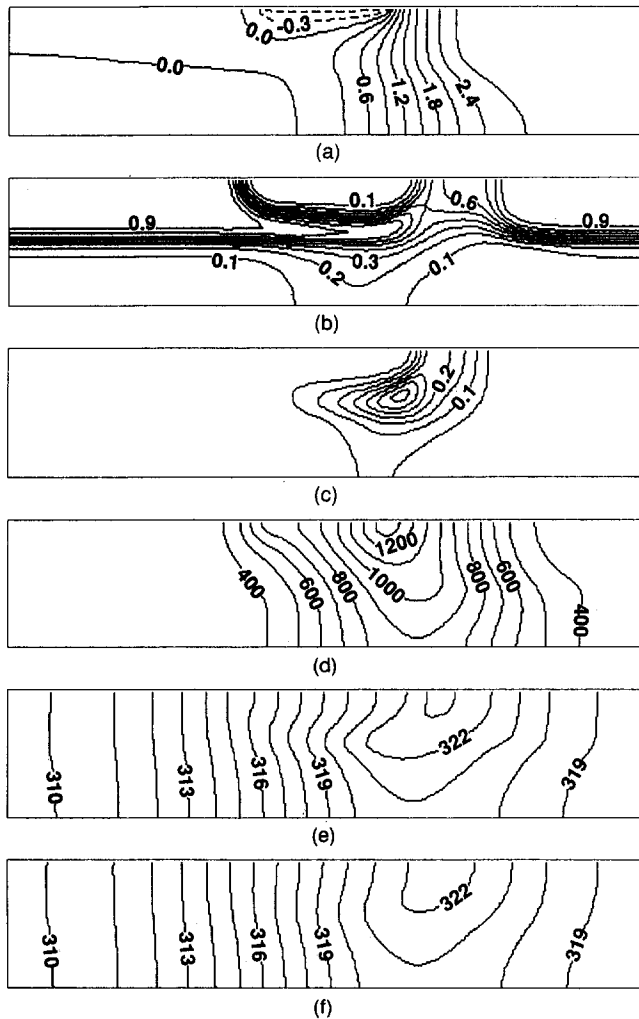


Fig. 7 Calculated result ( $V_{ds} = 3$  V,  $V_g = 0$  V,  $t = 5$  ns): (a) potential, V; (b) reduced electron number density,  $n/N_D$ ; (c) heat generation rate,  $J \cdot E$ ,  $\times 10^{17}$  W m $^{-3}$ ; (d) LO phonon temperature,  $T_{LO}$ , K; (e) LO phonon temperature,  $T_{LO}$ , K; (f) acoustic phonon temperature,  $T_A$ , K

At this time ( $t = 5$  ns), the electron temperature is much higher than the phonon temperatures. It can be understood that due to the applied high electric field, the electrons gain energy and become hot quickly; then the energy is transferred to the phonons and raises the phonon temperatures gradually. The acoustic phonon temperature distribution shows that there is a hot region at the drain side near the gate. Recent experimental measurement of temperature within a device also indicates this behavior (Majumdar et al., 1992; Lai et al., 1993). It is also observed that the acoustic phonon temperature gradient within the device is small compared with that of the electron temperature. This is due to the difference of the thermal conductivities. At 300 K and  $n/N_D = 1$ , the thermal conductivities of the electrons and the acoustic phonons in the active layer are  $\kappa_e = 0.161$  W/mK, and  $\kappa_A = 42.9$  W/mK, respectively. Consequently, the gradient of  $T_A$  becomes smaller than  $T_e$ , and the acoustic phonon temperature increase becomes spatially more uniform within the device. This behavior is also shown in the experimental measurement (Majumdar et al., 1992; Lai et al., 1993). The LO phonon temperature distribution is similar to that of acoustic phonon temperature. This can be understood by considering Eq. (19). The LO phonon temperature is determined by the energy transfer rate from the electrons and to the acoustic phonons. Each of these rates is a function of either  $C_e$  or  $C_{LO}$ . The electron heat capacity is  $C_e = 3nk_B/2 = 6.21$  W/m $^3$ K, and  $C_{LO}$  is equal to  $2.57 \times 10^5$  W/m $^3$ K at 300 K. About four orders of magnitude difference between the heat

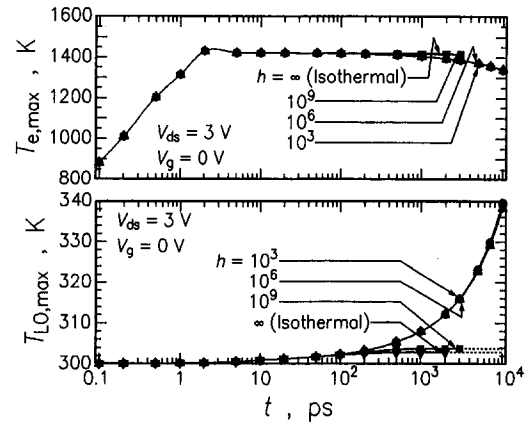


Fig. 8 Effect of heat transfer coefficient on temperature

capacities of the electrons and the LO phonons indicates smaller temperature difference between  $T_{LO}$  and  $T_A$  than between  $T_e$  and  $T_{LO}$ .

The value of the heat transfer coefficient  $h$  is fixed in the above-mentioned computation. However, this value is expected to have an effect on the results. Figure 8 shows the effect of  $h$  on the LO phonon temperature. As expected, the LO phonon temperature  $T_{LO}$  becomes lower and reach steady state faster as  $h$  is increased. The acoustic phonon temperature  $T_A$  shows same tendency. The electron temperature, on the other hand, drops when  $h$  is small due to the energy transfer to the lattice.

Although we use the trot-gallop technique discussed before, the time constant for the lattice to reach steady state is too long to follow with our time steps  $\Delta t_i$  and  $\Delta t_g$ . However, since the temperature fields of both  $T_{LO}$  and  $T_A$  are somewhat uniform, as discussed in the last paragraph, an assumption of uniform increase of  $T_{LO}$  and  $T_A$  may suffice to show roughly the lattice temperature effect on the electrical characteristics. Figure 9 shows the phonon temperature ( $T_{LO}$ ,  $T_A$ ) effect on the drain to source current  $I_d$ . Here, the LO phonon ( $T_{LO}$ ) and the acoustic phonon ( $T_A$ ) temperatures are set to be equal ( $=T_l$ , where the suffix  $l$  denotes the lattice) and uniform in the entire device. Solid circles denote  $I_d$  for various lattice temperatures. It can be seen that  $I_d$  is reduced by 25 percent with a 100 K increase of  $T_l$ . An open triangle denotes the results without thermal analysis (Eqs. (15), (16) and (17)). This also reduces  $I_d$ . These results suggest that the electrical performance cannot be predicted without thorough thermal analysis.

## Conclusions

In this study, we have developed a simple model to study the heat generation and transport mechanism and their effect on the

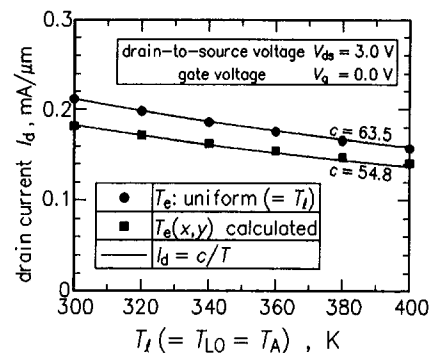


Fig. 9 Effect of the lattice (LO phonon, acoustic phonon) temperature on the electrical characteristics ( $V_{ds} = 3$  V,  $V_g = 0$  V)

electrical performance in a GaAs MESFET. Taking into account the nonequilibrium nature of the electrons and the phonons, a set of the particle, momentum, and energy conservation equations of the electrons and the energy conservation equations of  $LO$  phonons and acoustic phonons were developed and solved numerically.

Calculated results showed that at time level  $t = 5$  ns, the electron temperature  $T_e$  is much higher than the  $LO$  phonon temperature  $T_{LO}$  and the acoustic phonon temperature  $T_A$ . Therefore energy gained from the applied electric field is initially given to the electrons and increase the electron temperature more than 1200 K, and then gradually transferred to the phonons thereby raising the phonon temperatures.

The results also showed that there is a hot spot in a device at the drain side of the gate channel. This is due to the high electric field and the large current density in this region. This result suggests that it is important to reduce the locally higher electric field and to keep the current density as uniform as possible. An optimum position of a gate contact can be investigated by computation as in the present study to minimize the heat generation in a device.

The phonon temperature increase seems to have considerable effect on the electrical performance of the GaAs MESFET. This means that an electrical analysis without thermal consideration is not sufficient to predict electrical performance.

## Acknowledgments

We appreciate the help of Professor D. K. Ferry and Dr. J. Zhou at Arizona State University for their kind advice and discussions. We also would like to thank J. Lai and A. Padmanabhan for their discussions. This work was supported by the National Science Foundation through grant No. CTS-9215818 and partly supported by a Grant-in-Aid for Developmental Scientific Research (No. 01850047) from the Ministry of Education in Japan. AM also acknowledges the help of NSF through the Young Investigators Award. KF acknowledges the help of the Japan Society for the Promotion of Science.

## References

Bhandari, C. N., and Rowe, D. M., 1988, *Thermal Conduction in Semiconductors*, Wiley, New York.  
 Blakemore, J. S., 1982, "Semiconductor and Other Major Properties of Gallium Arsenide," *J. Appl. Phys.*, Vol. 53, pp. R123–R181.  
 Blotekjaer, K., 1970, "Transport Equations for Electrons in Two-Valley Semiconductors," *IEEE Trans. Electron Devices*, Vol. ED-17, pp. 38–47.

Carrillo, J. L., and Rodriguez, M. A., 1991, "Model for Hot-Electron Phenomena: Theory and General Results," *Phys. Rev. B*, Vol. 44, pp. 2934–2945.  
 Collins, C. L., and Yu, P. Y., 1984, "Generation of Nonequilibrium Optical Phonons in GaAs and Their Application in Studying Intervalley Electron-Phonon Scattering," *Phys. Rev. B*, Vol. 30, pp. 4501–4515.  
 Cook, R. T., and Frey, J., 1982, "Two-Dimensional Numerical Simulation of Energy Transport Effects in Si and GaAs MESFETs," *IEEE Trans. Electron Devices*, Vol. ED-29, pp. 970–977.  
 Curtice, W. R., and Yun, Y.-H., 1981, "A Temperature Model for the GaAs MESFET," *IEEE Trans. Electron Devices*, Vol. ED-28, pp. 954–962.  
 Ferry, D. K., 1991, *Semiconductors*, Macmillan, New York.  
 Fushinobu, K., and Majumdar, A., 1992, "Thermal and Electrical Modeling of Sub-micron MESFETs," *Thermal Science and Engineering*, Vol. 1, pp. 1–10.  
 INSPEC, 1986, *Properties of Gallium Arsenide*, EMIS Data Reviews Series No. 2, New York.  
 Joshi, R. P., and Ferry, D. K., 1989, "Hot-Phonon Effects and Interband Relaxation Process in Photoexcited GaAs Quantum Wells," *Phys. Rev. B*, Vol. 39, pp. 1180–1187.  
 Kittel, C., 1986, *Introduction to Solid State Physics*, 6th ed., Wiley, New York.  
 Kramer, B., and Mircea, A., 1975, "Determination of Saturated Electron Velocity in GaAs," *Appl. Phys. Lett.*, Vol. 26, pp. 623–625.  
 Lai, J., Carrejo, J. P., and Majumdar, A., 1993, "Thermal Imaging and Analysis at Sub-micrometer Scales Using the Atomic Force Microscope," *Heat Transfer on the Microscale*, ASME HTD-Vol. 253, pp. 13–20.  
 Landolt, H., 1982, *Numerical Data and Functional Relationships in Science and Technology*, Vol. III/17a, Springer-Verlag, New York.  
 Lin, W., Schoenlein, R. W., Fujimoto, J. G., and Ippen, E. P., 1988, "Femtosecond Absorption Saturation Studies of Hot Carriers in GaAs and AlGaAs," *IEEE J. Quantum Electronics*, Vol. 24, pp. 267–275.  
 Lugli, P., Bordone, P., Reggiani, L., Rieger, M., Kocevar, P., and Goodnick, S. M., 1989, "Monte Carlo Studies of Nonequilibrium Phonon Effects in Polar Semiconductors and Quantum Wells. I. Laser Photoexcitation," *Phys. Rev. Lett.*, Vol. 39, pp. 7852–7865.  
 Majumdar, A., Carrejo, J. P., and Lai, J., 1992, "Thermal Imaging Using the Atomic Force Microscope," *Appl. Phys. Lett.*, Vol. 62, pp. 2501–2503.  
 Peterson, C. L., and Lyon, S. A., 1990, "Observation of Hot-Electron Energy Loss Through the Emission of Phonon-Plasmon Coupled Modes in GaAs," *Phys. Rev. Lett.*, Vol. 65, pp. 760–763.  
 Pierret, R. F., 1989, *Advanced Semiconductor Fundamentals, Modular Series on Solid State Devices*, Vol. VI, Addison-Wesley, Boston, MA.  
 Shah, J., 1992, *Hot Carriers in Semiconductor Nanostructures: Physics and Applications*, Academic Press, New York.  
 Snowden, C. M., 1988, *Semiconductor Device Modeling*, Peregrinus, London.  
 Sze, S. M., 1981, *Physics of Semiconductor Devices*, 2nd ed., Wiley, New York.  
 Wang, C. T., 1985, "A New Set of Semiconductor Equations for Computer Simulation of Submicron Devices," *Solid-State Electronics*, Vol. 28, pp. 783–788.  
 Watanabe, T., Natori, M., and Oguni, T., 1989, *Fortran 77 ni yoru suuchi keisan software* [in Japanese], Maruzen Co., Ltd., Tokyo.  
 Wolfe, C. M., Holonyak, N., Jr., and Stillman, G. E., 1989, *Physical Properties of Semiconductors*, Prentice Hall, New Jersey.  
 Yoganathan, S., and Banerjee, S. K., 1992, "A New Decoupled Algorithm for Nonstationary, Transient Simulations of GaAs MESFET's," *IEEE Trans. Electron Devices*, Vol. 39, pp. 1578–1587.  
 Zhou, J.-R., and Ferry, D. K., 1992, "Simulation of Ultra-Small GaAs MESFET Using Quantum Moment Equations," *IEEE Trans. Electron Devices*, Vol. 39, pp. 473–478.

# Holographic Interferometry Study of Spatially Periodic Heat Transfer in a Channel With Ribs Detached From One Wall

Tong-Miin Liou

Professor.  
Mem. ASME

Wen-Bin Wang

Graduate Student.

Yuan-Jen Chang

Graduate Student.

Department of Power Mechanical  
Engineering,  
National Tsing Hua University,  
Hsinchu, Taiwan 30043

*The effects of clearance ratio ( $C/H$ ) and Reynolds number ( $Re$ ) on the turbulent heat transfer and friction in a rectangular duct with ribs detached from one wall were characterized quantitatively using laser holographic interferometry and pressure measurements. The investigated flow was periodic in space both hydrodynamically and thermally.  $C/H$  and  $Re$  were varied from 0.25 to 1.5 and  $5 \times 10^3$  to  $5 \times 10^4$ , respectively. The obtained interferograms, local ( $Nu$ ) and average ( $\bar{Nu}$ ) Nusselt number, and thermal performance ( $\bar{Nu}_p/\bar{Nu}_s^*$ ) allowed the critical  $C/H$  characterizing different mechanisms of heat transfer augmentation to be identified and allowed a comparison of  $Nu$ ,  $\bar{Nu}$ , and  $\bar{Nu}_p/\bar{Nu}_s^*$  among the detached ribbed duct, the attached ribbed duct, and the smooth duct to be made. It was found that the detached ribbed geometry has the advantage of eliminating the hot spots behind the attached ribs. Optimal clearance ratios for heat transfer enhancement between the present periodic detached ribs and previous single detached cylinder were also compared. Furthermore, compact heat transfer and friction correlations were developed for a detached ribbed duct for the first time.*

## Introduction

Ducts with rib-disturbed walls are often adopted in heat exchange systems for augmentation of the heat transfer (Han et al., 1985; Metzger et al., 1990; Bergles, 1988; Liou and Hwang, 1992a, b). The main feature in modeling this kind of flow field is that an equivalent roughness factor often cannot be assumed for the discrete ribs since the ribs disturb the core flow significantly (Davalath and Bayazitoglu, 1987; Liou et al., 1993a). To promote the advancement of computational simulations on the ribbed-channel flows (Liou et al., 1992; Acharya et al., 1993), detailed measurements of the flow structure and local temperature distribution over the repeated ribs are imperative. Moreover, previous heat transfer (Liou and Hwang, 1992a) and fluid flow (Liou et al., 1993a) studies indicated that for the solid ribs attached on the walls, the heat transfer locally deteriorated immediately behind the ribs. To remove the local heat transfer deterioration in the rear concave corners of the attached solid ribs, heat transfer measurements in a channel with perforated ribs mounted on the walls have been performed (Hwang and Liou, 1993) and the results showed that perforated ribs could eliminate the aforementioned heat transfer deterioration. The present paper focuses on the friction and heat transfer measurements in a rectangular duct with periodic solid ribs positioned at a small distance from one wall. The detached solid ribs are adopted as a possible alternative to the perforated ribs for manufacturing concern.

For works on detached ribbed duct flows, many of the previous studies were concerned with the fluid flow around a circular (Bearman and Zdravkovich, 1978; Oyakawa and Mabuchi, 1983; Marumo et al., 1985; Taniguchi and Miyakoshi, 1990), a triangular (Kamemoto et al., 1984), and a square (Suzuki et al., 1993a, b) cylinder near a plane wall. Among these studies, additional heat transfer measurements were made by Oyakawa and Mabuchi (1983) and Marumo et al. (1985) and computations by

Suzuki et al. (1993a, b). Their major results related to the present work are: (1) Heat transfer deterioration that occurs just downstream of an attached cylinder can be removed by displacing the cylinder a small distance from the wall; (2) heat transfer augmentation is most effective when the ratio  $C/H$  of the clearance (between the cylinder and the wall) and the cylinder diameter is 0.5; (3) the enhancement disappears far downstream from the cylinder (Marumo et al., 1985). This third point suggests that to maintain an effectively enhanced heat transfer over a long surface, cylinders must be placed in an array at an appropriate streamwise pitch.

For multiple detached ribs, Kawaguchi et al. (1985) investigated the heat transfer promotion with a number of circular cylinders positioned in a line and near one wall at various streamwise pitches by measuring the heat transfer coefficient. However, they did not conclude a specific value of the spatial pitch between cylinders for the optimum heat transfer enhancement. Oyakawa et al. (1986) studied how the heat transfer augmentation in the fully developed region is affected by the geometric shape (a straight band plate, an angled band plate, and a  $T$  band plate) and clearance of the turbulence promoters, which are set in a staggered arrangement near two opposite walls of a rectangular duct. The roles of the Karman vortex shedding and reattachment were documented in detail. Some shapes of turbulence promoters were found to provide a marked improvement in thermal performance as compared with previously reported cylinder case. Karniadakis et al. (1988) revisited Reynolds' analogy for the geometry similar to that used by Kawaguchi et al. (1985) at Reynolds numbers ranging from 100 to 525. They found that small-cylinder supercritical eddy-promoter flows roughly preserve the convective-diffusive Reynolds analogy. It thus follows from the transport stability theory that eddy-promoter laminar flows achieve the same heat transfer rates as lower Reynolds number plane-channel turbulent flows while incurring significantly less dissipation. For duct flows with a staggered array of circular cylinders near two opposite walls, Yao et al. (1987, 1989) found that after the first three cylinders, an almost fully developed state was attained thermally and hydrodynamically and that an averaged Nusselt number more than three times larger relative to that in the smooth duct flow can be achieved. Moreover, the measured distribution

Contributed by the Heat Transfer Division for publication in the JOURNAL OF HEAT TRANSFER. Manuscript received by the Heat Transfer Division September 1993; revision received April 1994. Keywords: Augmentation and Enhancement, Heat Exchangers, Turbulence. Associate Technical Editor: T. W. Simon.

of the local Nusselt number was found to be similar in shape regardless of the Reynolds number ( $8 \times 10^3 < Re < 6 \times 10^4$ ).

As far as the experimental techniques are concerned, hot-wire anemometers and flow visualization methods were respectively used to characterize the flow field quantitatively and qualitatively, and thermocouples were used to measure the temperature distribution in the aforementioned works. The present paper employs nonintrusive laser holographic interferometry (LHI) for quantitative measurements of the local heat transfer coefficients in a rectangular duct with a rib array located near one wall and placed transverse to the streamwise direction. The paper also addresses the following: (1) For duct flows with a detached rib array, no data have been reported for square ribs. Laminar flow and heat transfer studies were previously performed with only a single detached rib. The present study thus focuses on the turbulent heat transfer and friction in a duct with a detached square-rib array. (2) Heat transfer enhancement is most effective as  $C/H = 0.5$  for the single detached cylinder case. It is important in the present study to determine how this optimal value of  $C/H$  is influenced by the rib shape and the presence of consecutive ribs. (3) Semi-empirical correlations of fully developed heat transfer and friction in terms of the clearance ratio and Reynolds number are developed in the present paper for a duct with detached ribs. Such correlations have not been proposed in the past for ducts with a detached rib array, and may be helpful for the design of related devices such as compact heat exchangers and internal cooling passages of the turbine blades.

## Experimental Program and Conditions

**Apparatus.** Figure 1 shows the overall arrangement of the present real-time holographic interferometer. The laser used is an argon-ion laser, Spectra-Physics Model 2000. After passing through a shutter, the laser beam is divided into two equal components by a beam splitter. One beam, the reference beam, bypasses the test section and is expanded and filtered by a spatial filter. The expanded wave is subsequently collimated to a planar wave by a collimated lens. The other beam, the object beam, is also expanded, filtered, and collimated to a planar wave by a spatial filter and a collimating lens. Both the planar waves fall onto the holographic plate with an angle of 30 deg. Before the ribbed wall is heated, the hologram is exposed so that the comparison wave is recorded. When the planar object wave passes through the heated test section, it is distorted as a result of the refractive index field generated by local temperature variation in

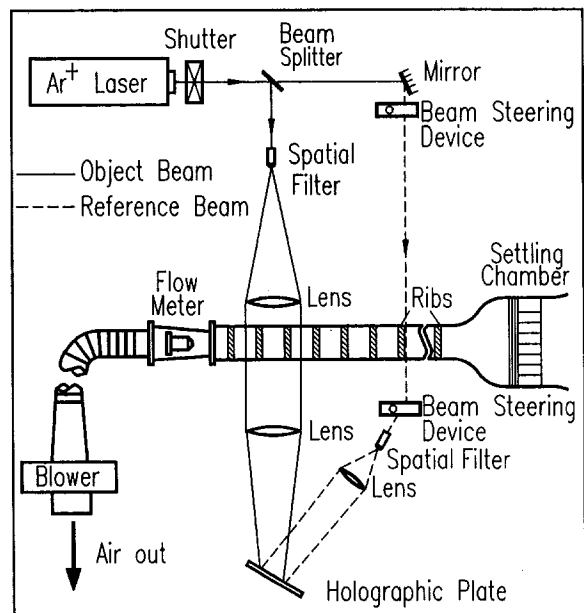


Fig. 1 Schematic drawing of overall experimental system

the test section. The distorted object wave passes through the hologram where it interferes continuously with the comparison beam reconstructed by the reference wave. Thus an instantaneous interference field forms behind the hologram plate. A combination of the holographic film plate holder and a liquid gate is used to provide in-place development of the film plate as required for subsequent real-time work. The photographic emulsion 8E56, made by Agfa-Gevaert Ltd., is found to be a suitable recording material for combining a good compromise between light sensitivity and resolution. To adjust the unwanted interference fringes caused by a shrinkage of the photographic emulsion in the developed and fixed processes, the liquid gate associated with the film plate holder is mounted on a multi-axis micropositioning base. This arrangement is designed to provide submicron positioning of the hologram in linear (three orthogonal axes) and rotational directions. The instantaneous interference field is digitized by a CCD camera (COHU, Model 6400), which allows 512 pixel resolution with 256 gray levels per pixel, and recorded

## Nomenclature

$A$  = half-width of channel  
 $B$  = half-height of channel  
 $C$  = clearance between rib and wall  
 $c_p$  = specific heat at constant pressure  
 $D_e$  = hydraulic diameter =  $4B/(1 + B/A)$   
 $f$  = (Darcy) friction factor  
 $H$  = rib height  
 $h$  = heat transfer coefficient  
 $k_f$  = air conductivity  
 $m$  = mass flow rate  
 $Nu$  = local Nusselt number  
 $\overline{Nu}$  = average Nusselt number  
 $\overline{Nu}_p$  = periodic fully developed average Nusselt number for the ribbed duct  
 $\overline{Nu}_s$  = average Nusselt number for the smooth duct (at the same mass flow rate)

$\overline{Nu}_s^*$  = average Nusselt number for the smooth duct (at the same pumping power)  
 $P$  = pressure  
 $Pi$  = rib pitch  
 $Pr$  = Prandtl number  
 $Q$  = quantity of heat given to air from entrance to the considered cross section of the duct  
 $q_{conv}$  = local convective heat transfer flux from the wall  
 $Re$  = Reynolds number  
 $T$  = temperature of air  
 $T_b$  = local bulk mean temperature of air  
 $T_m$  = air temperature at duct inlet (i.e., room temperature)  
 $T_w$  = local wall temperature  
 $\overline{T}_b$  = average bulk mean temperature of air

$\overline{T}_w$  = average wall temperature  
 $U$  = axial mean velocity  
 $X$  = axial coordinate ( $X = 0$  at inlet reference, Fig. 2)  
 $X_w$  = axial coordinate ( $X = 0$  at rib rear edge, Fig. 2)  
 $X_h$  = axial coordinate for heated test section, Fig. 2  
 $Y$  = transverse coordinate, Fig. 2  
 $Z$  = spanwise coordinate, Fig. 2  
 $\rho$  = air density

## Subscripts

$b$  = bulk mean  
 $cr$  = critical  
 $N$  = rib index  
 $s$  = smooth  
 $w$  = wall

on a VHS videocassette recorder for storage and further image processing.

In addition to the flow field temperature measured by LHI, the wall temperature of the test section is measured by copper-constantan thermocouples (i.e.,  $T$  type). The junction-bead of the thermocouple is about 0.15 mm in diameter. The temperature signals are transferred to a hybrid recorder (Yokogawa, DA-2500) with 30 channels. All of the data are then sent to a PC-AT via GPIB interface. The preprocessing of the raw data can be carried out by use of a built-in BASIC program by which the nondimensional parameter can be calculated. The static pressure at the test section is measured by a microdifferential transducer (Kyowa), which is connected to pressure taps. The measured pressure signals are subsequently amplified by an amplifier (Kyowa WGA-200) and read from a digital readout.

**Test Section.** The airflow is drawn into the test section from a temperature-controlled laboratory by a centrifugal blower (Fig. 1), which is situated in a service corridor outside the laboratory to minimize vibration. The coordinate system, construction, and dimension of the test duct are sketched in Fig. 2. The test duct, as shown in Fig. 2, is 1600 mm long and has a rectangular cross section of 160 mm by 40 mm ( $YZ$  plane). The sharp-edged aluminum ribs investigated are 160 mm in length and 5.2 mm in width and height ( $H/De = 0.08$  or  $H/2B = 0.13$ ) and positioned at a distance  $C$  from the bottom wall (stainless-steel sheet, 0.3 mm in thickness) of the test duct. The rib angle-of-attack and pitch-to-height ratio are 90 deg and 10, respectively. Thermofoils of thickness 0.18 mm are attached uniformly between the aluminum plate and a 6-mm-thick fiberglass board to insure good contact. In addition, a piece of Bakelite wood (30 mm in thickness) is used to prevent heat loss from the back side of the heated plate. The thermal resistance of the glue (0.13 mm thick or less), used at each of the above-mentioned interfaces, is negligible (less than 2 percent). For wall temperature measurements, as shown in Fig. 2, the region of optical view is instrumented with 60 thermocouples distributed along the spanwise centerline ( $Z = 0$ ) of the heated plate. Two Pitot tubes situated at  $X/De = 11.8$  and 14.2 are used to measure the static pressure drop for the fully developed duct flows. The pressure drop of the present work is based on the unheated flow conditions.

**Experimental Conditions.** The parameters investigated include the Reynolds number (based on the hydraulic diameter and cross-sectional bulk mean velocity of the ribbed duct), from 5000 to 50,000, and the channel-wall-rib clearance to rib height ratio,  $C/H = 0, 0.25, 0.38, 0.58, 1.0,$  and  $1.5$ . The majority of temperature measurements were done for the region between the 15th and 17th ribs ( $148 \leq X/H \leq 171$  or  $12 \leq X/De \leq 14$  or  $2.5 \leq X_h/De \leq 4.5$ , Fig. 2) where the air flow was both hydrodynamically (Liou and Lin, 1988) and thermally (Han, 1988; Liou and Hwang, 1992b) fully developed. The hydrodynamic and thermal periodicity based on the present friction factor and local Nusselt number distributions are within 4.3 and 3.2 percent, respectively. The two dimensionality of the actual temperature field, and thermal boundary conditions of the test section were described in detail in Liou and Hwang (1992a), and will not be elaborated on in the present paper.

**Data Analysis and Uncertainty.** The entire investigated temperature field is revealed by the infinite-fringe interferometry, which enables the calculations of local and average heat transfer coefficients (Hauf and Grigull, 1970). The significant errors of the interferometry usually encountered are the end effect and the refraction effect errors. By using the interferometry error analysis suggested by Goldstein (1976), it is found that the resulting errors in the fringe shift due to the end and refraction effects are about 6 percent and 4 percent, respectively. The convection heat transfer coefficient of the heated wall can be presented in terms of the local Nusselt number  $Nu$ , which is defined as

$$Nu = h \cdot D_e / k_f = -(dT/dY)_w \cdot D_e / (T_w - T_b) \quad (1)$$

where  $(dT/dY)_w$  is determined by curve fitting, based on a least-squares method through the near-wall values for temperature and fringe shift;  $T_w$  is read from the thermocouple output;  $2a$  and  $T_b$  is calculated from an energy balance,  $T_b = T_{in} + Q/(m \cdot c_p)$ , where  $Q$  is the quantity of heat given to air from entrance to the considered cross section of the duct and can be obtained by the integrated form of  $\int_0^x [k_f \cdot (dT/dY)_w \cdot 2A] \cdot dX$ . The maximum uncertainty of the local Nusselt number is estimated to be less than 8.1 percent for all of the cases by the uncertainty estimation method of Kline and McClintock (1953). The average Nusselt number for the periodically fully developed region is evaluated by the following equation:

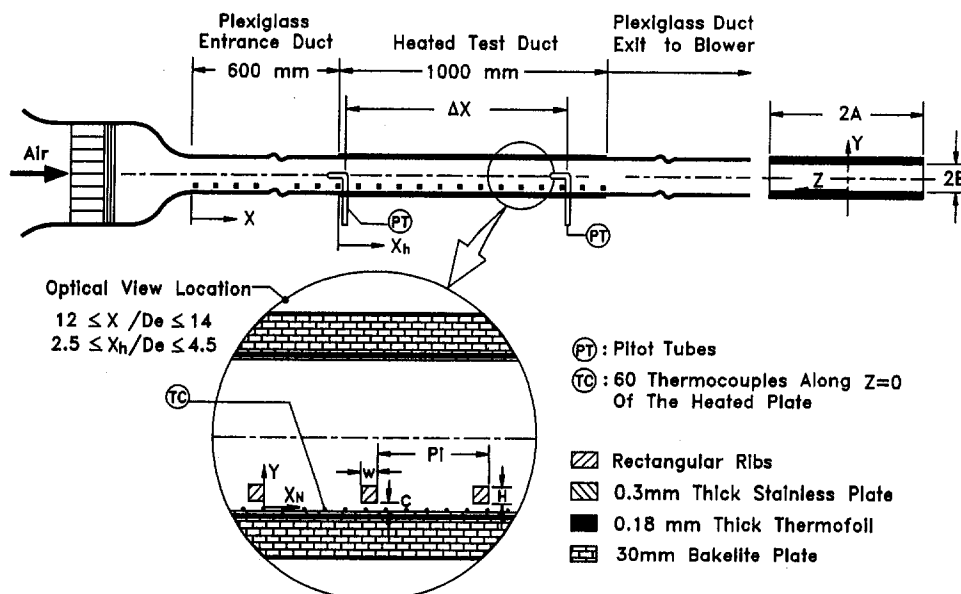


Fig. 2 Coordinate system, construction, and dimension of test duct

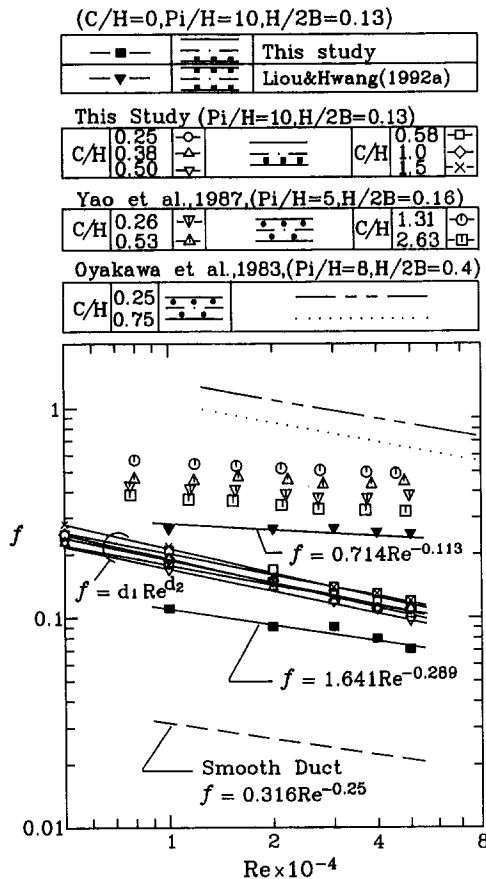


Fig. 3 Friction factor versus Reynolds number

$$\overline{Nu}_p = q_{conv} \cdot D_e / [k_f \cdot (\overline{T}_w - \overline{T}_b)] \quad (2)$$

where  $q_{conv}$  is the convective heat flux from the wall and is estimated by subtracting the heat loss from the supplied electrical input,  $\overline{T}_w$  is the average wall temperature in one rib pitch, and  $\overline{T}_b$  is the average bulk mean temperature of air. The maximum uncertainty of  $\overline{Nu}_p$  is estimated to be less than 9.8 percent. The local Nusselt number of the present study is normalized by the Nusselt number for fully developed turbulent flow in smooth circular tubes correlated by Dittus and Boelter (1930) as:

$$Nu/\overline{Nu}_s = Nu / (0.023 \cdot Re^{0.8} \cdot Pr^{0.4}) \quad (3)$$

The following equation is used to calculate the Darcy friction factor of the periodically fully developed flow:

$$f = [(-\Delta P/\Delta X) \cdot D_e] / (\rho \cdot U^2/2) \quad (4)$$

In this expression,  $\Delta P/\Delta X$  is an axial pressure gradient, which is evaluated by taking the ratio of the pressure difference and the distance of two successive Pitot tubes. The maximum uncertainty of  $f$  is estimated to be less than 7.3 percent.

## Results and Discussion

**Average Friction Factor.** Figure 3 depicts the Reynolds number dependence of average friction factor for periodic fully developed duct flows with various wall-rib clearance to rib height ratios. Some previous results made by other researchers for different rib geometries and arrangements are also included in Fig. 3 for comparison. All the curves show a decrease of  $f$  with increasing  $Re$  and an increase of  $f$  by displacing the ribs a small distance from the wall for both one-wall and double-wall ribbed duct flows. The reason for the latter trend is partly that for the present case the detached ribs have four wetted surfaces, whereas

the attached ribs have three wetted surfaces. More specifically, Fig. 3 indicates that for the present one-wall ribbed duct flows a small distance displacement of the ribs from the wall increases the friction loss approximately 5.5–7.5 and 1.6–1.9 times over those of the smooth wall case and the ribbed wall case with ribs attached to the wall, respectively, for the test ranges of  $C/H$ ,  $Pi/H$ , and  $Re$ .

The effects of the Reynolds number ( $5 \times 10^3 \leq Re \leq 5 \times 10^4$ ) and the clearance between the rib and the wall ( $0.25 \leq C/H \leq 1.5$ ) on the average friction factor for the present test conditions can be correlated by the following expression:

$$f = 7.96 \cdot Re^{-0.40} \cdot (C/H)^{-0.06} \quad (5)$$

where the constants are obtained by curve fitting, based on a least-squares method through the measured data shown in Fig. 3. The maximum deviations of the measured data from these correlation are  $\pm 9.8, 9.0, 9.1, 4.1, 9.9$ , and  $9.0$  percent for  $C/H = 0.25, 0.38, 0.50, 0.58, 1.0$ , and  $1.5$ , respectively.

**Interference Patterns.** Figures 4 and 5 show typical examples of the holographic interferograms at various clearances and Reynolds numbers, respectively. The mean flow direction is from left to right. For small clearance  $C/H = 0.25$  (Fig. 4b), the fringe patterns near the rib top and behind the rib are more similar to those for the attached rib case ( $C/H = 0$ , Fig. 4a, Liou et al., 1993b) since the fluid flows at a lower velocity through the smaller gap between the rib and wall. This subsequently turns upward immediately downstream of the gap exit, as shown by

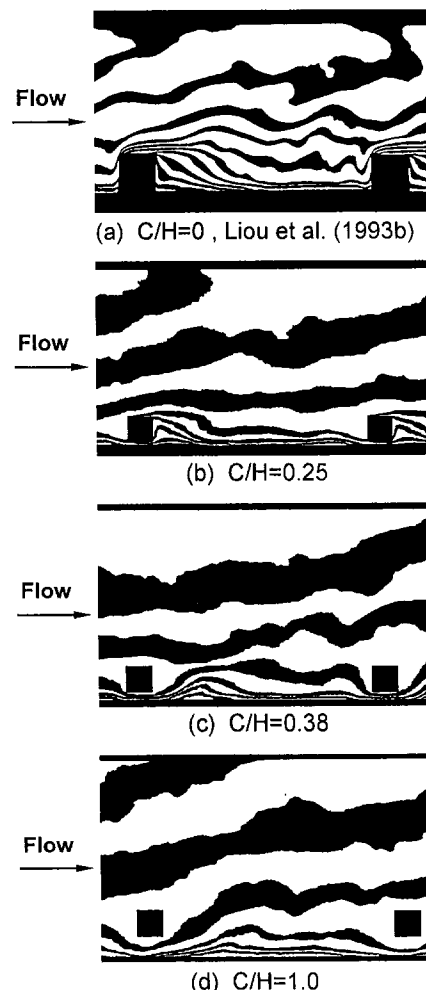


Fig. 4 Variation of the holographic interferogram with various  $C/H$  for  $Re = 5000, Pi/H = 10, H/2B = 0.13$ , and  $-2 \leq X_n/H \leq 11.2$

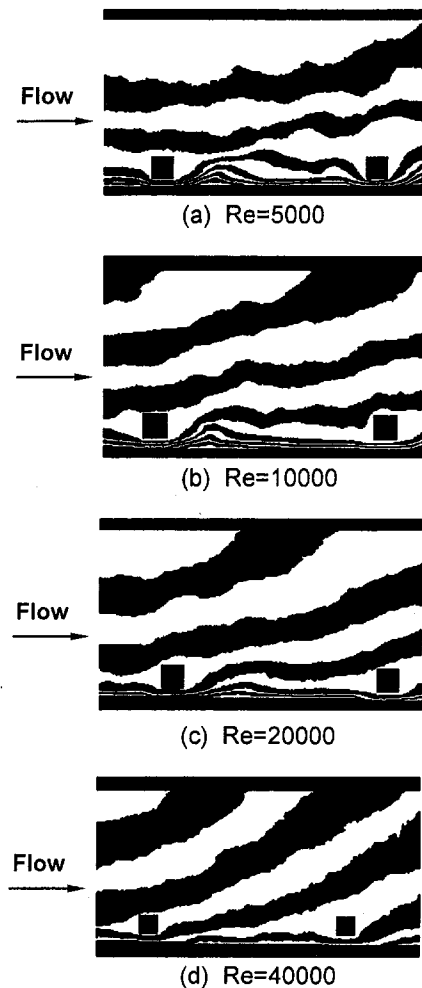


Fig. 5 Variation of the holographic interferogram with Reynolds number for  $C/H = 0.38$ ,  $Pi/H = 10$ ,  $H/2B = 0.13$ , and  $-2 \leq X_N/H \leq 11.2$

the significantly distorted fringe in Fig. 4(b), due to the entrainment of the recirculating flow behind the rib. Consequently, a large amount of heat can be transferred from the heated wall to the rib from which heat is further convected by the core fluid near the rib top and recirculating fluid near the rib rear face in the way similar to the attached rib case. For  $C/H > 0.25$ , Figs. 4(c, d), the gap is large enough to play the role of a nozzle, as evidenced by the contraction and expansion of the interference fringes in front of, beneath, and behind the rib. A large amount of heat conducted from the heated wall has, therefore, been convected by the fluid that is accelerated through the gap between the rib base and the heated wall. This is noted by the increased number of thin fringes and the narrow fringe spacings and, in turn, the steep temperature gradients around the rib base and near the heated wall. Hence, there is a reduction of heat transfer rate on the rib top and rib rear face for  $C/H = 0.38$  and 1.0. On the other hand, the wake flow behind the detached rib tends to restrain the wall jet from spreading out. The wall jet shear layer and the associated turbulent transport enhancement thus remain adjacent to the heated wall for the central and latter part of the inter-rib region ( $0 < X_N/H < 9$ ), as can be judged from the dense fringes in the corresponding regions. This rationale illustrates the difference in fringe patterns between cases of  $C/H = 0-0.25$  and  $C/H = 0.38-1.0$  and suggests the existence of a critical clearance ratio ( $0.25 < (C/H)_{cr} < 0.38$ ) above which the heat transfer from the rib surface to the core fluid is insignificant and the forced convection enhancement in the clearance region as well as turbulent transport enhancement in the inter-rib

region near the heated wall play the main role for the overall heat transfer augmentation. A comparison of Figs. 4(c, d) further reveals that the temperature gradients near the heated wall and, in particular, between the rib base and the heated wall decrease with increasing  $C/H$ . This is because the convective heat transfer and hence the flow acceleration through the gap decreases with increasing  $C/H$ . It should be pointed out that the aforementioned results are valid for the test ranges of Reynolds number and clearance ratio,  $5 \times 10^3 \leq Re \leq 5 \times 10^4$  and  $0 \leq C/H \leq 1.5$ .

The effect of Reynolds number on the fringe pattern is depicted in Fig. 5 for the case of  $C/H = 0.38$ . It is seen that the number of fringes between the rib and the heated wall decreases with increasing Reynolds number due to the reduction in the difference between the  $T_w$  and  $T_b$  in the periodic fully developed flow regime with increasing  $Re$  (Liou and Hwang, 1992a, b).

**Local Heat Transfer.** From the information of the whole-field air temperature distributions provided by the interferograms, the centerline local heat transfer coefficient of the heated wall can be calculated. Figure 6 shows the distributions of the local Nusselt number ratio along the wall for various  $C/H$ . The Reynolds number, rib pitch-to-height ratio, and rib-to-channel height ratio are fixed at values of 20,000, 10, and 0.13, respectively. It is noticed that the hot spots ( $Nu/Nu_s < 1$ ) around the concave corners behind the attached ribs ( $C/H = 0$ ) (Liou and Hwang, 1992a) do not occur with the detached-ribbed wall ( $C/H \neq 0$ ). The average level of heat transfer enhancement ( $Nu/Nu_s > 1$ ) increases as  $C/H$  increases from  $C/H = 0$  to  $C/H = 0.38$ . Beyond  $C/H = 0.38$ , the level of  $Nu/Nu_s$  decreases with increasing  $C/H$ . The reason for this trend has been addressed in the last section.  $C/H = 0.38$  provides the highest enhancement of wall heat transfer among the tested  $C/H$  due to the corresponding highest forced convection resulting from the highest acceleration of the flow between the rib base and the heated wall. This value of  $C/H$  is different from the optimal value  $C/H = 0.5$  reported previously for a flat plate boundary layer disturbed by a single detached cylinder without considering the interaction between consecutive ribs (Marumo et al., 1985). It is also noted in Fig. 6 that the heat transfer enhancements are comparable between the present duct flow with detached ribs on one wall and the previous duct flow with a staggered array of cylinders (Yao et

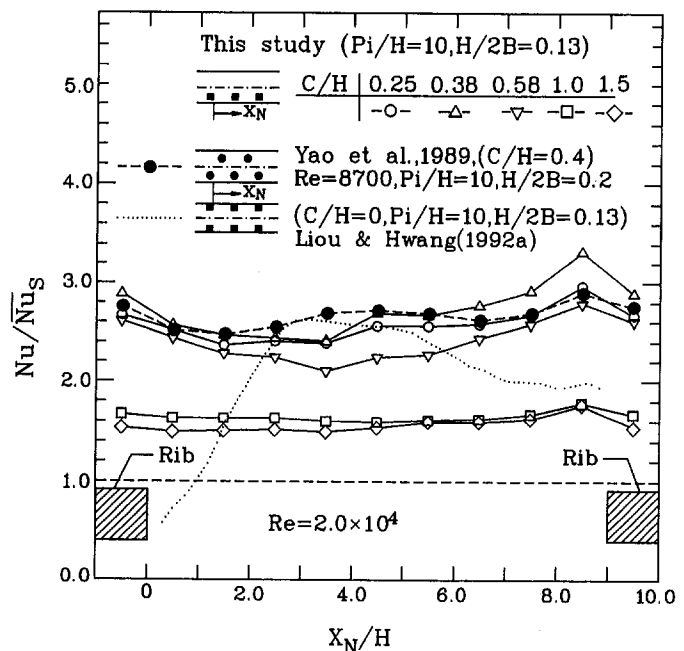


Fig. 6 Distributions of local centerline Nusselt number ratio along the heated wall for various  $C/H$

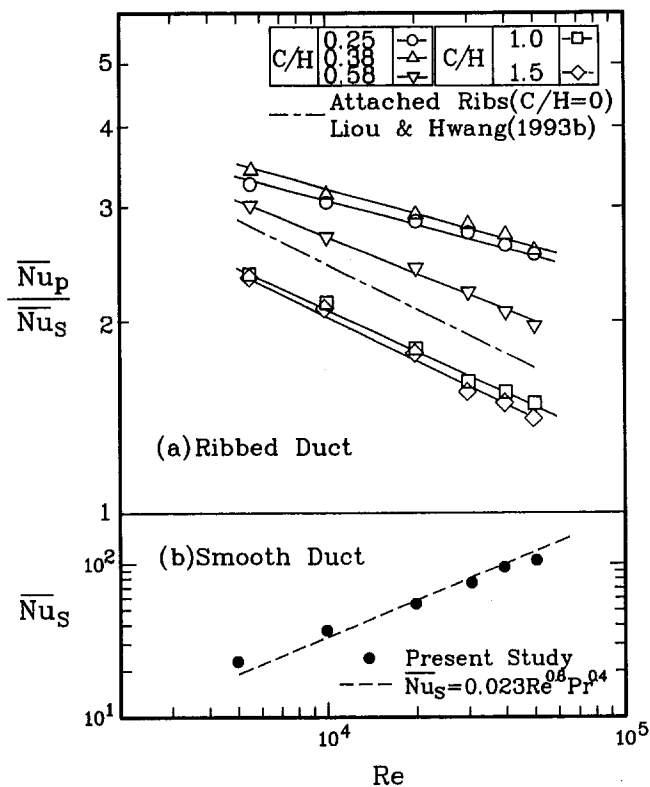


Fig. 7 Reynolds number dependence of the average centerline Nusselt number ratio: (a) ribbed duct with various  $C/H$ ; (b) smooth duct

al., 1987) at nearly the same  $C/H = 0.38-0.4$  and  $Pi/H = 10$  although the Reynolds number and rib height are different. Both cases reveal two major local peak values of  $Nu/Nu_s$ . One is located at about  $X_N/H = 8.5$  (close to the rib's bottom salient) and the other at the half rib width  $X_N/H = -0.5$  beneath the rib. Both the temperature gradient and mean velocity gradient are steep due to an approach of the shear layer to the rib wall by sudden contraction of the flow around the rib's bottom salient and to the enhanced forced convection of the flow's acceleration through the gap, as judged by the qualitative observation of the fringe distributions in the corresponding regions.

**Average Nusselt Number.** The Reynolds number dependence of the average centerline Nusselt number ratio for various  $C/H$  is plotted in Fig. 7, where the average Nusselt number is nondimensionalized by the Dittus-Boelter correlation, which provides a good representation of the present data for a smooth duct. It can be seen that ribbed duct flows with  $C/H = 0-1.5$  all give rise to substantial enhancement relative to the smooth duct, ranging from 50 to 240 percent. The extent of the enhancement is larger at lower Reynolds numbers. As addressed in the last section, the average Nusselt number ratio for the  $C/H = 0.38$  case is the highest enhancement, ranging from 170 to 240 percent. Beyond  $C/H = 0.38$ ,  $Nu/Nu_s$  decreases with increasing  $C/H$ . The most significant conclusion that can be drawn from Fig. 7 is that for  $C/H > 0.58$  of the tested  $C/H$  the average Nusselt number ratios are lower than those of the attached rib case,  $C/H = 0$  (Liou and Hwang, 1993b). The explanation of this fact is as follows: For larger clearance between the heated wall and the ribs, the forced convection by the fluid flowing through the clearance is weaker and the extended surfaces provided by the ribs do not effectively, as compared with the attached rib case, transfer the heat to the core fluid due to a reduction of heat conduction from the heated wall to the detached ribs caused by the presence of the larger clearance. In other words, for the detached ribs with  $C/H > 0.58$  the ribs act more practically as a turbulator only.

With the values presented in Fig. 7, the average Nusselt number ratios for the duct flows with detached ribs can be further correlated in terms of the rib and flow parameters as below:

$$\overline{Nu}_p / \overline{Nu}_s = 9.33 \cdot Re^{-0.16} \cdot (C/H)^{-0.32}$$

$$(5 \times 10^3 \leq Re \leq 5 \times 10^4, 0.25 \leq C/H \leq 1.5) \quad (6)$$

where the constants are obtained by curve fitting, based on a least-squares method through the measured data shown in Fig. 7. The maximum deviations of the experimental data from the Eq. (6) are  $\pm 1.1, 4.0, 5.0, 1.8,$  and  $4.1$  percent for  $C/H = 0.25, 0.38, 0.58, 1.0,$  and  $1.5$ , respectively.

**Thermal Performance.** In the present study, the thermal performance is evaluated by comparing the average heat transfer coefficient for a duct with detached ribs with those for a smooth duct without ribs and for a duct with attached ribs (Liou and Hwang, 1993b) per unit pumping (or blowing) power for a constant heat transfer surface. In order to impose the constraint of equal pumping power, it is necessary to find the relationship between the Reynolds number relative to the ribbed duct ( $Re$ ) and the corresponding Reynolds number for the smooth duct (proportional to  $f^{1/3} \cdot Re$ ) that yields the same pumping power (Liou and Hwang, 1992b). The relationship obtained is plotted in Fig. 8. As expected from Fig. 3, a ribbed duct has to be operated at a lower Reynolds number because of increasing friction loss. For ribbed ducts, the detached-rib case has to be operated at a slightly lower Reynolds number than the attached-rib case to keep equal pumping power. It is also noted that for the detached-rib case the difference between the two Reynolds numbers is only slightly dependent on the clearance ratio  $C/H$ .

The pumping power required to feed the fluid through the duct is proportional to  $f \cdot Re^3$ . Thus in Fig. 9 the performance shown by the ratio of  $\overline{Nu}_p / \overline{Nu}_s^*$  is plotted against  $f^{1/3} \cdot Re$ , where  $\overline{Nu}_s^*$  is the average Nusselt number for a smooth duct with the flow rate at which the pumping power is the same as that obtained in the ribbed duct. The calculation of the  $\overline{Nu}_s^*$  had been described in detail by Liou and Hwang (1992b). It is clear in this figure that the improvement in the Nusselt number ratio of the duct with detached ribs and  $C/H < 0.58$  is more pronounced than that of the duct with attached ribs. For  $C/H > 0.58$ , the thermal performance of the duct with detached ribs is lower than that of the duct with attached ribs. It should be further noted that at the higher Reynolds number range the thermal performance is even poorer ( $\overline{Nu}_p / \overline{Nu}_s^* < 1$ ) in comparison with that of the smooth

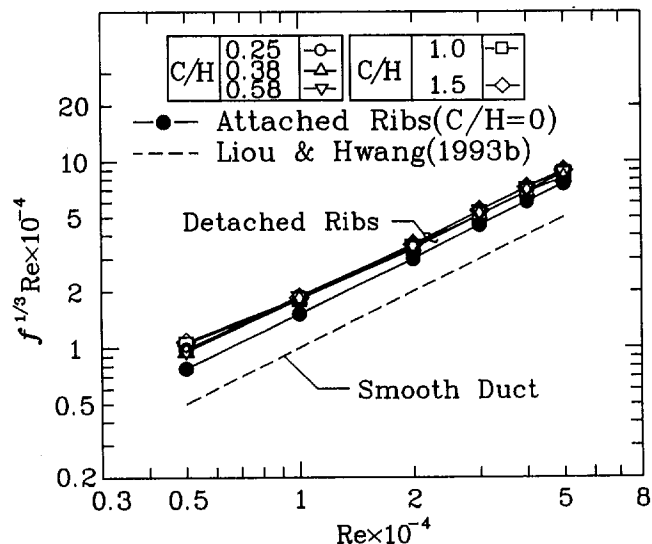


Fig. 8 Relationship between  $Re$  for ribbed ducts and  $f^{1/3} \cdot Re$  for smooth ducts under equal pumping power constraint



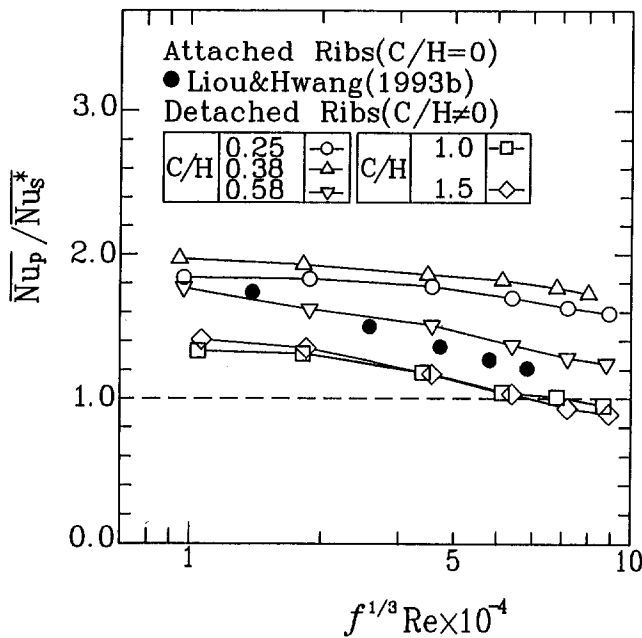


Fig. 9 Performances of the detached and attached ribbed ducts under a constant pumping power constraint

duct. Consequently, the usage of the detached ribs at the low Reynolds number range and with  $C/H < 0.58$  is recommended. For the present tested conditions, a thermal performance improvement as high as 100 percent, relative to a smooth duct, can be achieved with the  $C/H = 0.38$  case.

### Concluding Remarks

This paper has presented experimental results for turbulent heat transfer and friction in the periodic-fully developed region of a 4:1 aspect ratio rectangular duct with square ribs displaced a small distance from one of the walls. The main parameters studied are the clearance ratio and Reynolds number. The new and significant information presented here is that: (1) There exists a critical clearance ratio, as evidenced by the LHI interferograms, above which the heat transfer augmentation is mainly achieved by the enhanced forced convection and turbulent transport along the heated wall; (2) there exists a critical clearance ratio below which the heat transfer augmentation is attributable to the extended surfaces provided by the ribs and the approaching of the separated shear layer from the rib top toward the heated wall; (3) there exists a critical clearance ratio, below which the average Nusselt number and thermal performance at a constant pumping power for the duct flow with detached ribs are higher than with attached ribs; (4) there exists a critical clearance ratio above which the trend is reversed and, moreover, the thermal performance for the detached ribbed ducts is even poorer than for the smooth ducts at the high Reynolds number range. These characteristics are useful references of practical applications and tests of computational models. Furthermore, compact correlations of the friction and heat transfer in terms of the clearance ratio and Reynolds number for duct flows with detached ribs are obtained for the first time.

The hot spots around the concave corners behind the attached ribs, reported previously, are found to be absent for the present duct flows with detached ribs. Heat transfer augmentation for a flat plate boundary layer disturbed by a single detached cylinder was reported previously by others to be most effective as  $C/H = 0.5$ . The present study shows that the effects of multiple detached ribs and rib shape modulate this value to  $C/H = 0.38$  among the tested  $C/H$ . For  $C/H = 0.38$  the heat transfer and thermal performance enhancement over the smooth duct can at-

tain values as high as 170 to 240 percent and 80 to 100 percent, respectively, for the test range of Reynolds number.

### Acknowledgments

Support for this work was provided by the National Science Council of the Republic of China under contract No. NSC82-0401-E007-289.

### References

- Acharya, S., Dutta, S., Myrum, T. A., and Baker, R. S., 1993, "Periodically Developed Flow and Heat Transfer in a Ribbed Duct," *International Journal of Heat and Mass Transfer*, Vol. 36, No. 8, pp. 2069–2082.
- Bearman, P. W., and Zdravkovich, M. M., 1978, "Flow Around a Circular Cylinder Near a Plane Boundary," *Journal of Fluid Mechanics*, Vol. 89, Part 1, pp. 33–47.
- Bergles, A. E., 1988, "Some Perspectives on Enhanced Heat Transfer—Second-Generation Heat Transfer Technology," *ASME JOURNAL OF HEAT TRANSFER*, Vol. 110, pp. 1082–1096.
- Davalath, J., and Bayazitoglu, Y., 1987, "Forced Convective Cooling Across Rectangular Blocks," *ASME JOURNAL OF HEAT TRANSFER*, Vol. 109, pp. 321–328.
- Dittus, F. W., and Boelter, L. M. K., 1930, *Publications on Engineering*, Vol. 2, University of California at Berkeley, p. 443.
- Goldstein, R. J., 1976, "Optical Measurement of Temperature," *Measurement in Heat Transfer*, 2nd ed., E. R. G. Eckert and R. J. Goldstein, eds., Hemisphere, Washington, DC, pp. 241–294.
- Han, J. C., Park, J. S., and Lei, C. K., 1985, "Heat Transfer Enhancement in Channels With Turbulence Promoters," *ASME Journal of Engineering for Gas Turbines and Power*, Vol. 107, pp. 628–635.
- Han, J. C., 1988, "Heat Transfer and Friction Characteristics in Rectangular Channels With Rib Turbulators," *ASME JOURNAL OF HEAT TRANSFER*, Vol. 110, pp. 321–328.
- Hauf, W., and Grigull, U., 1970, "Optical Methods in Heat Transfer," *Advances in Heat Transfer*, Vol. 6, J. P. Hartnett and T. F. Irvine, Jr., eds., Academic Press, New York, pp. 133–136.
- Hwang, J. J., and Liou, T. M., 1993, "Augmented Heat Transfer in a Rectangular Channel With Permeable Ribs Mounted on the Wall," *ASME JOURNAL OF HEAT TRANSFER*, in press.
- Kamemoto, K., Oda, Y., and Masahiro, A., 1984, "Characteristics of the Flow Around a Bluff Body Near a Plane Surface," *Bulletin of JSME*, Vol. 27, No. 230, pp. 1637–1643.
- Karniadakis, G. E., Mikic, B. B., and Patera, A. T., 1988, "Minimum Dissipation Transport Enhancement by Flow Destabilization: Reynolds' Analogy Revisited," *Journal of Fluid Mechanics*, Vol. 192, pp. 365–391.
- Kawaguchi, Y., Suzuki, K., and Sato, T., 1985, "Heat Transfer Promotion With a Cylinder Array Located Near the Wall," *International Journal of Heat and Fluid Flow*, Vol. 6, No. 4, pp. 249–255.
- Kline, S. J., and McClintock, F. A., 1953, "Describing Uncertainties on Single-Sample Experiments," *Mechanical Engineering*, Vol. 75, Jan., pp. 3–8.
- Liou, T. M., and Lin, J., 1988, "Measurements of Turbulent Flow in a Duct With Repeated Ribs Applied to Two Opposite Walls," *Journal of the Chinese Institute of Engineers*, Vol. 11, No. 4, pp. 319–326.
- Liou, T. M., and Hwang, J. J., 1992a, "Turbulent Heat Transfer Augmentation and Friction in Periodic Fully Developed Channel Flows," *ASME JOURNAL OF HEAT TRANSFER*, Vol. 114, pp. 56–64.
- Liou, T. M., and Hwang, J. J., 1992b, "Developing Heat Transfer and Friction in a Ribbed Rectangular Duct With Flow Separation at Inlet," *ASME JOURNAL OF HEAT TRANSFER*, Vol. 114, pp. 565–573.
- Liou, T. M., Hwang, J. J., and Chen, S. H., 1992, "Turbulent Transport Phenomena in a Channel With Periodic Rib Turbulators," *AIAA Journal of Thermophysics and Heat Transfer*, Vol. 6, No. 3, pp. 513–521.
- Liou, T. M., Wu, Y. Y., and Chang, Y., 1993a, "LDV Measurements of Periodic Fully Developed Main and Secondary Flows in a Channel With Rib-Disturbed Walls," *ASME Journal of Fluids Engineering*, Vol. 115, pp. 109–114.
- Liou, T. M., Hwang, J. J., and Chen, S. H., 1993b, "Simulation and Measurement of Enhanced Turbulent Heat Transfer in a Channel With Periodic Ribs on One Principal Wall," *International Journal of Heat and Mass Transfer*, Vol. 36, No. 2, pp. 507–517.
- Marumo, E., Suzuki, K., and Sato, T., 1985, "Turbulent Heat Transfer in a Flat Plate Boundary Layer Disturbed by a Cylinder," *International Journal of Heat and Fluid Flow*, Vol. 6, No. 4, pp. 241–248.
- Metzger, D. E., Fan, C. S., and Yu, Y., 1990, "Effects of Rib Angle and Orientation on Local Heat Transfer in Square Channels With Angled Roughness Ribs," *Compact Heat Exchangers, A Festschrift for A. L. London*, Hemisphere, Washington, DC.
- Oyakawa, K., and Mabuchi, I., 1983, "Fluid Flow and Heat Transfer in a Parallel Plate Duct Containing a Cylinder," *Bulletin of JSME*, Vol. 48, No. 432, pp. 1509–1519.
- Oyakawa, K., Shinzato, T., and Mabuchi, I., 1986, "Effect on Heat Transfer Augmentation of Some Geometric Shapes of a Turbulence Promoter in a Rectangular Duct," *Bulletin of JSME*, Vol. 29, No. 256, pp. 3415–3420.
- Suzuki, H., Inoue, Y., Nishimura, T., Fukutani, K., and Suzuki, K., 1993a, "Unsteady Flow in a Channel Obstructed by a Square Rod (Crisscross Motion of Vortex)," *International Journal of Heat and Fluid Flow*, Vol. 14, pp. 2–9.

Suzuki, H., Fukutani, K., Takishita, T., and Suzuki, K., 1993b, "Flow and Heat Transfer Characteristics in a Channel Obstructed by a Square Rod Mounted in Asymmetric Positions," *Proceedings of the 6th International Symposium on Transport Phenomena in Thermal Engineering*, Seoul, Korea, pp. 353-358.

Taniguchi, S., and Miyakoshi, K., 1990, "Fluctuating Fluid Forces Acting on a Circular Cylinder and Interference With a Plane Wall," *Experiments in Fluids*, Vol. 9, pp. 197-204.

Yao, M., Nakatani, M., and Suzuki, K., 1987, "An Experimental Study on Pressure Drop and Heat Transfer in a Duct With a Staggered Array of Cylinders," *ASME-JSME Thermal Engineering Joint Conference*, P. J. Marto and I. Tanasawa, eds., Vol. 5, pp. 189-196.

Yao, M., Nakatani, M., and Suzuki, K., 1989, "Flow Visualization and Heat Transfer Experiments in a Duct With a Staggered Array of Cylinders," *Experimental Thermal and Fluid Science*, Vol. 2, pp. 193-200.

# A Correlation for Heat Transfer and Wake Effect in the Entrance Region of an In-Line Array of Rectangular Blocks Simulating Electronic Components

**M. Molki**

Professor,  
Department of Mechanical Engineering,  
Esfahan University of Technology,  
Esfahan, Iran

**M. Faghri**

Professor,  
Fellow ASME

**O. Ozbay**

Department of Mechanical Engineering  
and Applied Mechanics,  
University of Rhode Island,  
Kingston, RI 02881

*An experimental investigation is carried out to study heat transfer in the entrance region of an array of rectangular heated blocks. The focus of the work is on the entrance heat transfer coefficients and the associated thermal wake effects. The experiments were performed with air as the working fluid. The geometric parameters of the array were varied in the range identified with  $B/L = 0.5$ ,  $S/L = 0.128-0.33$ , and  $H/L = 0.128-1$ . The Reynolds number, based on the height above the blocks and the fluid mean velocity in the bypass channel, ranged from 3000 to 15,000. The adiabatic heat transfer coefficients and thermal wake effects are correlated for the entrance region. These correlations are incorporated into a user-friendly FORTRAN program, which can be used by the engineers to predict the working temperatures of the components of circuit boards with similar layout. A typical computer output indicated that the mean deviation between the measured and predicted temperatures is 11.0 percent.*

## Introduction

An experimental investigation is carried out to measure and to correlate the convective heat transfer coefficient and thermal wake effect in the entrance region of an array of rectangular blocks. The correlations presented in this paper are intended to be used by the practitioners to predict the temperature of the electronic components, which have a similar geometric layout and especially short entrance lengths. The range of parameters employed in this work is close to that often encountered in the computer industry.

The subject of heat transfer in arrays of rectangular blocks, especially for the periodic fully developed flow, has been addressed by many investigators. Sparrow et al. (1982, 1983) have reported heat transfer and pressure drop in arrays of rectangular blocks with barriers and missing blocks. They used a mass transfer technique with the heat-mass analogy to obtain the so-called adiabatic heat transfer coefficient. The focus of their work was to study the effect of the missing block and barriers on thermal-hydraulic behavior of the array.

Arvizu and Moffat (1982) have discussed a superposition approach for predicting the temperature distribution in a regular array of cubical elements. Another related work on the subject is a paper by Wirtz and Dykshoorn (1984) in which some information is provided about heat transfer in the entry region of a sparse array of elements.

In a series of experimental investigations, Moffat and his group have extensively studied various aspects of thermal-hydraulic behavior of the arrays of electronic components (Moffat et al., 1985; Moffat and Anderson, 1988; Anderson and Moffat, 1990, 1991). The overall objective of their effort has been to develop the techniques and the data bases needed to predict the operating temperature of the blocks. They have also emphasized the very crucial point that the adiabatic heat transfer coefficients, which are reported in the electronics cooling literature, should be used

in reference to the adiabatic fluid temperature. Other relevant studies are those reported by Sridhar et al. (1990), Faghri et al. (1991), Wirtz and Chen (1991), Kang (1992), and a review article by Peterson and Ortega (1990). Despite all the useful information and data available in the aforementioned references, a concise and convenient correlation for temperature prediction is not seen in the open literature, especially for short channels encountered in electronic equipment.

There are several novel aspects to the present work that have not been addressed by other investigators. The focus of this paper is on the entrance heat transfer coefficients and the associated thermal wake effects. The data are successfully brought together by defining modified parameters, and they are presented by simple correlations. These correlations are subsequently incorporated into a simple algorithm to estimate the operating temperature of a circuit board with random heating.

The present work is part of a major program, which is aimed at gaining a better understanding of heat transfer and fluid flow in the entrance of the arrays of rectangular blocks. These efforts are performed both experimentally and numerically, and they are intended to provide sufficient information for predicting the temperatures of the electronic components. The experimental pressure drop and the numerical results have been reported earlier (Molki et al., 1993; Faghri et al., 1994), and this paper is mainly concerned with the heat transfer aspect of the problem.

In the present study, an array of rectangular blocks is positioned along the lower wall of a rectangular duct. These blocks, which represent a model for the modular electronic components, are arranged in an in-line fashion. The geometric variables, namely the block dimension ( $L$ ), the block height ( $B$ ), the interblock spacing ( $S$ ), and the height of the flow passage between the block and the opposite wall of the duct ( $H$ ), are varied in such a manner that  $B/L = 0.5$ ,  $S/L = 0.128$  and  $0.33$ , and  $H/L = 0.128, 0.25, 0.50, 0.75, 0.765$ , and  $1$ . The working fluid is air, and the Reynolds number based on  $H$  and the air velocity in the bypass channel (i.e., the channel formed between the top surface of blocks and the opposite wall of the duct) ranges from 3000 to 15,000.

Attention is now turned to a full description of the work. First, the experimental apparatus will be described, followed by a pre-

Contributed by the Heat Transfer Division for publication in the JOURNAL OF HEAT TRANSFER. Manuscript received by the Heat Transfer Division July 1993; revision received April 1994. Keywords: Electronic Equipment, Forced Convection. Associate Technical Editor: Y. Jaluria.

sentation of the data reduction, uncertainty analysis, and the heat transfer results.

## The Experimental Setup and Procedure

The experimental apparatus consists of a bell-mouth inlet, a flow development section (591 mm), test section (343 mm), a flow redevelopment section (591 mm), a venturimeter, a control valve, and a blower. The test section and the corresponding upstream and downstream ducts have a rectangular cross section. The width of the cross section is 178 mm, but the height, i.e.,  $H + B$  in Fig. 1(a), depending on the dimensions of the array, varies from 19.1 to 50.8 mm. The laboratory air is drawn into the apparatus through the bell-mouth inlet, and after flowing through the test section (Fig. 1) and the related flow passages, it exits the flow circuit through the blower operating in suction mode.

The air flow is adjusted by the main control valve. There is also available a bypass valve, which is used for fine adjustments. The flow rate is measured by a precalibrated venturimeter, which is located downstream from the test section and before the main control valve.

The rectangular blocks of the test section are made of copper and are positioned along the lower wall in an in-line arrangement. The geometry of the test section, as noted in Fig. 1, is identified with  $S$ ,  $H$ ,  $L$ , and  $B$ . In this investigation,  $S$  ranged from 6.4 to 8.4 mm,  $H$  from 6.4 to 25.4 mm,  $L$  from 25.4 to 49.8 mm, and  $B$  from 12.7 to 25.4 mm. From the combination of these dimensions, seven test sections were fabricated, which could readily be identified with their respective dimensionless geometric parameters  $B/L = 0.5$ ,  $S/L = 0.128$  and  $0.33$ , and  $H/L = 0.128$ ,  $0.25$ ,  $0.255$ ,  $0.50$ ,  $0.75$ ,  $0.765$ , and  $1$ . With this arrangement, the number of copper rectangular blocks along and across a given test section was either  $5 \times 3$  or  $8 \times 5$ . In addition, a number of dummy plexiglass blocks of the same dimensions were positioned downstream of the last copper block to eliminate possible extraneous effects. The air pressure is measured by pressure taps (not shown in the figure) along the wall of the test section. Details of the location of pressure taps and the pressure drop correlations are reported by the authors elsewhere (Molki et al., 1993).

As shown in Fig. 1(c), a thermofoil heater is attached to the bottom of the copper block. To minimize the heat losses, a layer of silica powder was placed at the bottom between the thermofoil heater and the plexiglass lower wall. This arrangement was repeated for all copper blocks of the array. Moreover, the outside surfaces of the test section, including the upstream and downstream ducts, were completely wrapped and insulated by 100 mm of common glass wool insulation.

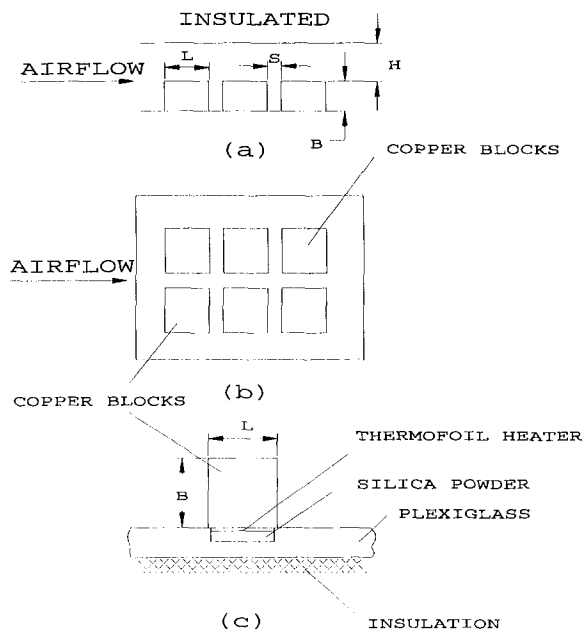


Fig. 1 Schematic of the test section: (a) side view, (b) top view, (c) a typical heated block

The blocks used in this study were made of electrolytic grade copper, which has a high thermal conductivity. This ensured that the temperature gradient in the module would be negligible and a few temperature sensors would be sufficient to estimate its average temperature. The thermistors were embedded in grooves cut on the surface of the copper module and kept in place by a special adhesive. Two thermistors were positioned at the side, and one was at the top of the module.

Before the onset of a data run, the proper test section is selected and assembled. Then, to prevent air from leaking into the test section, all suspected joints are sealed by silicon rubber and thoroughly tested for leaks with the aid of soap solution. Subsequently, the flow and power to thermofoil heater are turned on and adjusted for a predetermined Reynolds number. It takes typically 30 minutes to warm up the apparatus.

In a typical data run, only one copper block is heated at a time and the remaining blocks are adiabatic. The input power of the thermofoil heater is adjusted at such a level that the temperature difference between the block and ambient remain constant. This temperature difference varies from 30 to 50°C, depending on the run. Once the heated block reaches steady state, the various pa-

## Nomenclature

$B$  = block height, mm, Fig. 1  
 $C_D$  = flow coefficient of venturimeter  
 $D_h$  = hydraulic diameter =  $2W(H + B)/(W + H + B)$ , mm  
 $h$  = mean heat transfer coefficient for a rectangular block, Eq. (1)  
 $H$  = distance between top surface of blocks and the opposite wall, mm, Fig. 1  
 $L$  = plane dimension of square block, mm, Fig. 1  
 $Nu$  = Nusselt number =  $hL/k$   
 $\dot{Q}$  = rate of heat convection, W, Eq. (2)  
 $R$  = thermofoil electrical resistance,  $\Omega$ , Eq. (2)

$Re$  = Reynolds number =  $VH/\nu$   
 $S$  = interblock spacing, mm, Fig. 1  
 $T$  = temperature, °C  
 $V$  = voltage across the thermofoil heater, Eq. (2), air mean velocity in the bypass channel  
 $W$  = duct width = 178 mm  
 $X$  = axial coordinate;  $X = 0$  at the leading edge of the first block  
 $\theta$  = wake effect, Eqs. (5)–(9)  
 $\nu$  = kinematic viscosity of air

### Superscripts

+ = modified parameter, Eqs. (4), (6), and (7)

### Subscripts

$a1$  = refers to adiabatic temperature of the first block behind the heated block, Eq. (5)  
 $aN$  = refers to adiabatic temperature of the  $N$ th block behind the heated block  
 $fd$  = refers to periodic fully developed, Eq. (4)  
 $fN$  = refers to flanking column, Eq. (9)  
 $h$  = refers to heated block, Eq. (5)  
 $in$  = refers to inlet condition, Eq. (1)  
 $N$  = refers to the  $N$ th block behind the heated block, Eq. (8)  
 $sh$  = refers to self heating  
 $we$  = refers to wake effect

rameters are recorded. These parameters are block surface temperature by three surface-mounted thermistors, inlet air temperature (typically 20 to 25 ± 0.1°C), air temperature downstream of the test section (usually 1°C higher than the inlet temperature, ± 0.1), pressure drop across the venturimeter (0.05017 to 9.80 ± 1 × 10<sup>-5</sup> mm Hg), inlet pressure of the venturimeter relative to ambient (0.01 to 13 ± 1 × 10<sup>-5</sup> mm Hg), ambient barometric pressure (740 to 770 ± 0.1 mm Hg), thermfoil heater voltage (5 to 35 ± 0.3 V), and resistance of the thermfoil heater (30 to 32 ± 0.3 Ω). Except for the barometric pressure, all other pressures were measured by a pressure transducer and an electronic manometer. All pressure and temperature readings were performed by an IBM PC. The computer scanned the temperature and pressure signals at a scan rate of (50/22) per second.

### Data Reduction

The convective heat transfer coefficient is evaluated from

$$h = \frac{\dot{Q}}{A(T_h - T_m)} \quad (1)$$

where

$$\dot{Q} = \frac{V^2}{R} - (\text{conduction losses} + \text{radiation losses}) \quad (2)$$

In these equations,  $\dot{Q}$  is the rate of heat convection from the heated block to air stream,  $A$  is surface area of the block,  $T_h$  mean surface temperature of the block,  $T_m$  inlet air temperature,  $V$  voltage across the thermfoil heater, and  $R$  is the thermfoil electrical resistance.

Conduction losses were evaluated from a two-dimensional and three-dimensional numerical simulation of heat transfer in the copper block and the adjacent walls. However, due to low thermal conductivity of plexiglass, the effect of longitudinal conduction through the base board was negligible. Radiation losses were estimated from a simplified model where the heated block is treated as a small radiating object surrounded by a large environment. The results suggested that the conduction losses were 10 percent of  $V^2/R$ , and the radiation losses, with an emissivity value of 0.15 for copper, were always less than 1 percent of  $V^2/R$ . The  $h$  values were subsequently nondimensionalized and expressed in terms of Nusselt number with the conventional definition,  $Nu = hL/k$ .

The heat transfer results will be presented in terms of Reynolds number,  $Re = VH/\nu$ , based on mean air velocity,  $V$ , in the bypass channel above the blocks and the dimension  $H$  (Fig. 1a). The velocity  $V$  is obtained by dividing the air volume flow rate, as measured by the venturimeter, by  $W \times H$  ( $W = 178$  mm).

### Uncertainty Analysis

Prior to the onset of the experimental runs, the venturimeter was calibrated with the aid of a laminar-flow element. The parameters recorded during the calibration process and the respective uncertainties are: barometric pressure, ± 0.1 mm Hg, venturimeter inlet gage pressure, ± 10<sup>-5</sup> mm Hg, pressure drop across the venturimeter, ± 10<sup>-5</sup> mm Hg, pressure drop across the laminar-flow element, ± 10<sup>-5</sup> mm Hg, and inlet air temperature, ± 0.1°C. In addition to these values, the uncertainty of laminar-flow element is estimated as ± 1 percent of volume flow rate. From these values, the uncertainty of venturimeter coefficient is found to be ± 0.027, resulting in a venturi coefficient of  $C_D = 0.971 \pm 2.8$  percent.

The block surface temperatures were measured by thermistor. The thermistor is an extremely sensitive device, and consistent performance within 0.01°C may be anticipated with proper calibration (Holman, 1984). The thermistors used in this work were #44033 elements, made by Omega Engineering Inc., with a standard resistance of 2252 Ω at 25°C, and an accuracy of ± 0.1°C.

Other variables used to evaluate the final uncertainties are: duct width, ± 0.1 mm, dimension  $H$  (Fig. 1a), ± 0.1 mm, block height  $B$ , ± 0.1 mm, inlet and throat diameters of venturimeter, ± 0.1 mm, test section gage pressure, ± 10<sup>-5</sup> mm Hg, block surface temperature, ± 0.1°C, thermfoil voltage, ± 0.3 V, and thermfoil resistance, ± 0.3 Ω. The numbers identified with "±" are the precision limits. These are based on the smallest interval between scale markings (least count) of the respective instruments. The sensitivity coefficients were evaluated using the data reduction FORTRAN program. The results were then combined through the root-sum-square expression to obtain uncertainty. The bias limit for instruments was negligible. Using the guidelines of Kline (1985) and Abernethy et al. (1985), the mean uncertainty of  $Re$  and  $Nu$  is estimated as 2.3 and 4.8 percent, with the maximum uncertainty being 2.7 and 7.9 percent. The uncertainties of other parameters are given in the figure captions.

### Results and Discussion

The entrance region adiabatic heat transfer coefficients are presented in Figs. 2 and 3. The ordinate is nondimensionalized with the periodic fully developed Nusselt number,  $Nu_{fd}$ , at the Reynolds number corresponding to the same set of data. The coordinate  $X$  is measured along the flow with  $X = 0$  corresponding to the leading edge of the first block. The family of curves in Fig. 2 is for  $S/L = 0.128$  and  $H/L$  ranges from 0.128 to 0.765, while those in Fig. 3 are for  $S/L = 0.33$  and  $H/L = 0.25$  to 1. It is evident from the figures that the distribution of  $Nu/Nu_{fd}$  is almost independent of Reynolds number and  $H/L$ . A careful examination of the numerical value of the individual data points shows that the mean deviation of data from the best fit (solid lines) is 5.3 percent, and the maximum deviation does not exceed 10.4 percent.

The family of curves seen in Figs. 2 and 3 shows a common trend. Starting with a relatively large value, the Nusselt number decreases rapidly and approaches the fully developed value. This trend is reminiscent of heat transfer coefficient in the entrance region of a duct. However, in addition to the high-temperature

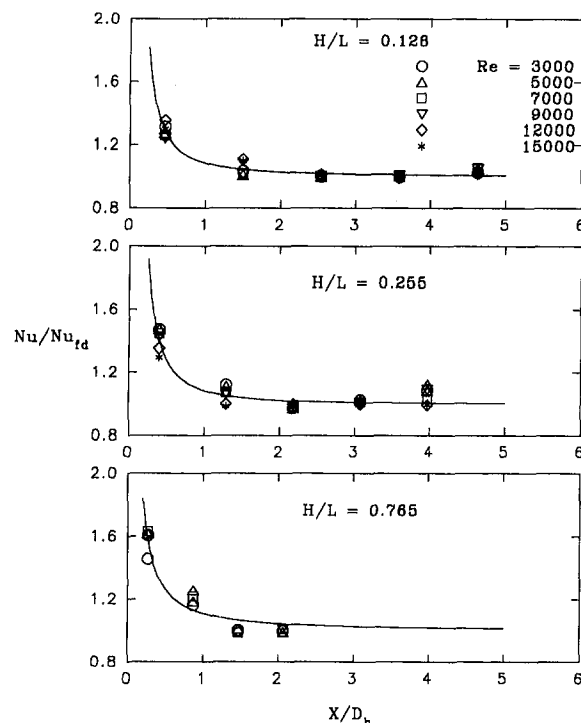


Fig. 2 Entrance adiabatic heat transfer coefficients for  $S/L = 0.128$  (mean and maximum uncertainty = 16.1, 44.2 percent)

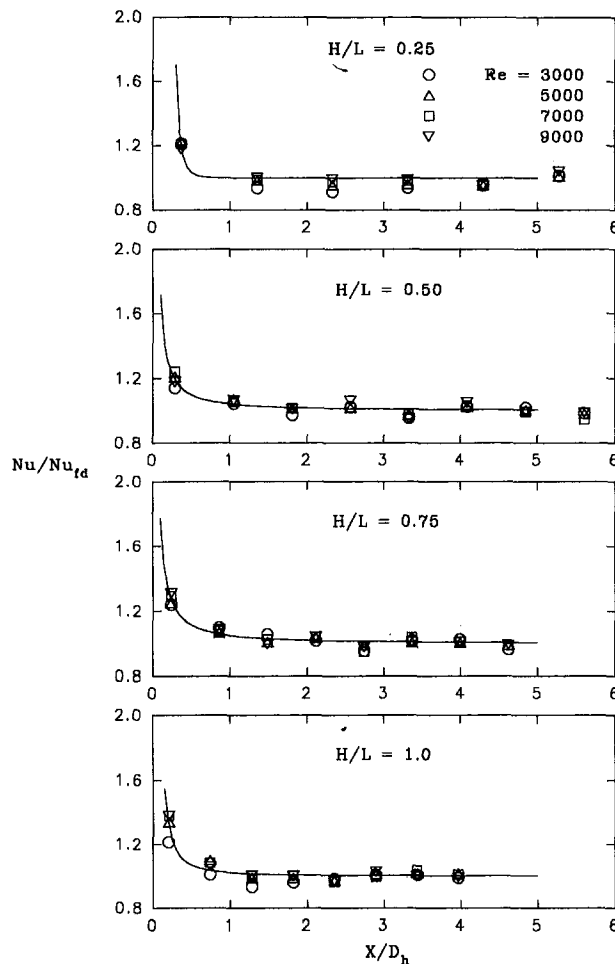


Fig. 3 Entrance adiabatic heat transfer coefficients for  $S/L = 0.33$  (mean and maximum uncertainty = 16.1, 44.2 percent)

gradients at the entrance, there exists a strong flow separation zone on the first block of the array (Molki et al., 1993). This flow separation has an enhancing effect on the block-averaged heat transfer coefficients reported in Figs. 2 and 3. It should be noted that the extent of enhancement is even more pronounced at special locations such as the line of reattachment.

The data reported in Figs. 2 and 3, a total of 176 points, are presented in Fig. 4. Also shown in this figure are the results of Anderson and Moffat (1990) for  $H/L = 0.102$ – $0.735$ ,  $S/L = 0.273$ , and  $B/L = 0.204$ . Despite all the differences between the two investigation, it is seen that all data follow a certain trend. This suggests that a curve fit to all data may be a proper way of representing the Nusselt number in the entrance region of the array. The solid line in Fig. 4 is the least-squares best fit to the data with the equation

$$\frac{Nu}{Nu_{fd}} = 1 + 0.0786 \left( \frac{X}{D_h} \right)^{-1.099} \quad (3)$$

The mean and maximum deviations of data from this equation are, respectively, 4.8 and 19.8 percent, while the mean and maximum experimental uncertainties are estimated as 16.1 and 44.2 percent. These figures suggest that Eq. (3) is a possible correlation for  $Nu/Nu_{fd}$ . According to this equation, if the  $Nu/Nu_{fd} = 1.01$  marks the beginning of the periodic fully developed region, then the entrance region of the array is identified with  $0 \leq X/D_h \leq 6.53$ . Therefore, Eq. (3) is particularly useful when  $X \leq 6.53D_h$ . Otherwise, the fully developed results can be used.

To facilitate the use of Eq. (3) in practical applications, the periodic fully developed Nusselt numbers had to be written in a

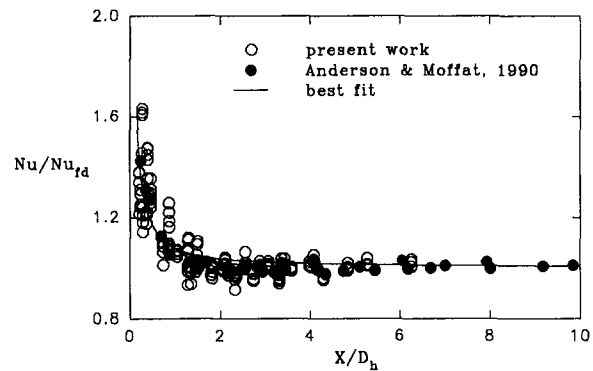


Fig. 4 Entrance adiabatic heat transfer coefficients for all data and comparison with literature (mean and maximum uncertainty = 16.1, 44.2 percent)

convenient way. After extensive examination of data and several curve-fitting attempts, a modified Nusselt number emerged as  $Nu_{fd}^+ = 2.819 Nu_{fd} Re^{-0.607} (S/L)^{-0.295}$  which is presented in Fig. 5. Also seen in this figure are the results from the literature. The figure suggests that the modified Nusselt number is a suitable parameter, which correlates the data fairly well. The correlation is obtained from a least-squares curve fit to all data with the equation

$$Nu_{fd}^+ = 0.968 \left( \frac{H}{L} \right)^{-0.670} \quad (4)$$

The mean and maximum deviation of data from Eq. (4) are, respectively, 12.8 and 41.1 percent.

The effect of buoyancy is negligible in the highly turbulent flow of the present investigation, and it is not included in this correlation. It has been shown by Kang et al. (1990) that when  $Gr/Re^{5/2}$  is less than 0.9, the flow is dominated by forced convection. For a set of typical data (namely, heat generation,  $Q = 9.843$  W, Reynolds number = 5000,  $H/L = 0.765$ ,  $B/L = 0.5$ , measured temperature =  $61.82^\circ\text{C}$ , air inlet temperature =  $27.57^\circ\text{C}$ , see Fig. 10), and using the notation of Kang et al. (1990), we find  $Gr = 4.52 \times 10^6$ ,  $Re = 3952$ , and  $Gr/Re^{5/2} = 0.0046$ . Therefore, the buoyancy is indeed negligible.

There are a number of differences between the present results and those of literature as seen in Figs. 4 and 5. Anderson and Moffat (1990) performed their experiments for  $H/L = 0.102$  to  $0.735$ ,  $S/L = 0.273$ , and  $B/L = 0.204$ , while those of Sridhar

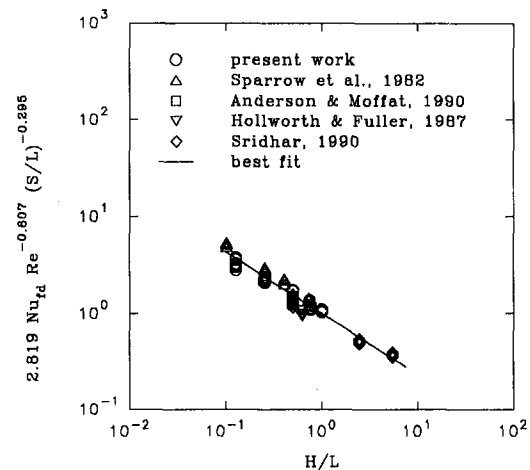


Fig. 5 Distribution of the modified periodic fully developed Nusselt number (mean and maximum uncertainty = 7.8, 15.0 percent)

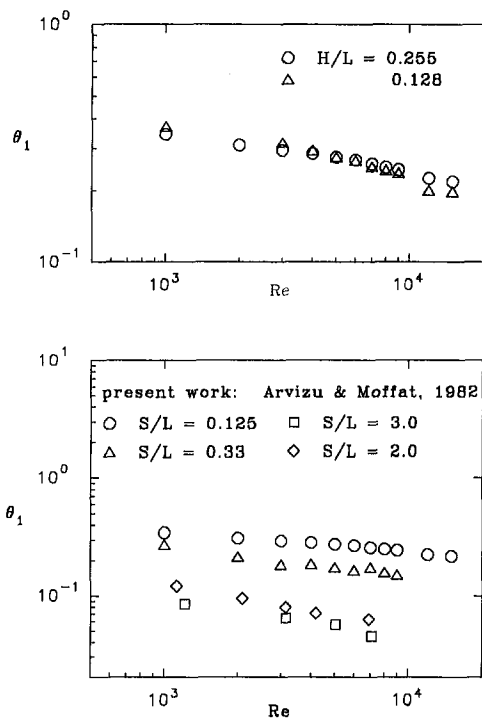


Fig. 6 Thermal wake effect for the first adiabatic block (mean and maximum uncertainty = 1.4, 2.8 percent)

(1990) were  $H/L = 0.5$  to  $5.5$ ,  $S/L = 0.33$  to  $0.5$ , and  $B/L = 0.5$ . Sparrow et al. (1982) did not use the electrically heated blocks in their experiments; instead, they employed a mass transfer technique and the heat-mass analogy to obtain the heat transfer coefficients. Their experiments were conducted for  $H/L = 0.625$ ,  $S/L = 0.25$ , and  $B/L = 0.375$ . On the other hand, the Hollworth and Fuller (1987) results in Fig. 5 are measured for a staggered array of blocks with  $H/L = 0.25$  and  $0.5$ ,  $S/L = 1.0$ , and  $B/L = 0.25$ . Despite all these differences, it is noteworthy that the modified Nusselt number has correlated the data well. Therefore, Eqs. (3)–(4) are suggested as a complete set of correlations for the adiabatic heat transfer coefficient in array of heated blocks.

The adiabatic temperature of the first block situated immediately behind the heated block is presented in Fig. 6 as a function of  $Re$  with  $H/L$  and  $S/L$  as parameters. This dimensionless temperature, or the so-called wake effect, is defined as

$$\theta_1 = \frac{T_{a1} - T_{in}}{T_h - T_{in}} \quad (5)$$

In this equation,  $T_{a1}$ ,  $T_{in}$ , and  $T_h$  are, respectively, the adiabatic (unheated) temperature of the first block, the inlet air temperature, and the temperature of the heated block. It is evident from the figure that the effect of  $H/L$  on  $\theta_1$  is negligible. However, the effect of the interblock spacing,  $S/L$ , is somewhat important. In fact, increasing  $S/L$  shifts the location of the first adiabatic block farther away from the thermal wake of the heated block and, therefore, the temperature is reduced. The results of Arvizu and Moffat (1982) for  $S/L = 2.0$  and  $3.0$ , Wirtz and Dykshoorn (1984) for  $S/L = 1$ , and Sridhar et al. (1990) for  $S/L = 0.33$ , are also consistent with this observation.

Defining the modified wake effect according to

$$\theta_1^+ = 2.680 \theta_1 Re^{0.168} \quad (6)$$

the results are brought together in Fig. 7. In this figure, the solid line is the curve fit to all data with the equation

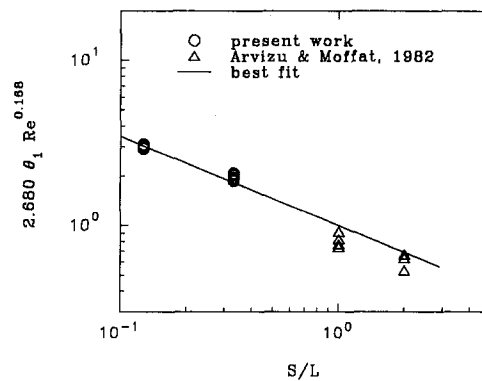


Fig. 7 Modified wake function (mean and maximum uncertainty = 28.3, 30.1 percent)

$$\theta_1^+ = 0.998 \left( \frac{S}{L} \right)^{-0.540} \quad (7)$$

The mean and maximum deviation of data from the solid line are, respectively, 6.3 and 34.4 percent. The uncertainty analysis indicates that the mean and maximum experimental uncertainty of  $\theta_1^+$  are 28.3 and 30.1 percent, respectively. Since the mean deviation is well within the mean uncertainty and the maximum deviation and uncertainty have comparable values, it may be suggested that Eq. (6) be considered for the range  $0.125 \leq S/L \leq 3.0$ , which extends beyond the range of  $S/L$  in the present investigation.

The wake effect for other downstream blocks is presented in Fig. 8. In this figure,  $\theta_N$  is defined as  $\theta_N = (T_{aN} - T_{in}) / (T_h - T_{in})$ . Here, the subscript  $N$  refers to the  $N$ th adiabatic block situated downstream of the heated block, with  $N = 0$  corresponding to the heated block itself. During the wake effect experiments, the heated block was located at the centerline and at either the first (leading) or at the third row of the array. The experimental runs were also carried out for different geometries. As evidenced from the data in Fig. 8, the location of the heated block and the geometry does not have a marked effect on the distribution of  $\theta_N / \theta_1$ .

There are a number of investigators who have correlated the  $\theta_N / \theta_1$  data as  $1/N$  (e.g., Arvizu and Moffat, 1982; Moffat et al., 1985; Sridhar et al., 1990) or  $(1/N)^m$  where  $m$  is a function of  $Re$  (Wirtz and Dykshoorn, 1984). The major difficulty with this correlation is that when the number of blocks is large ( $N \rightarrow \infty$ ),  $1/N$  approaches zero. In an insulated duct with a number of heated blocks, the temperature of the downstream adiabatic blocks approaches the mean temperature of the air flow, which is somewhat higher than the inlet temperature. Therefore, a suitable correlation incorporates this limiting case. In the light of the foregoing discussion, the wake effects are correlated as

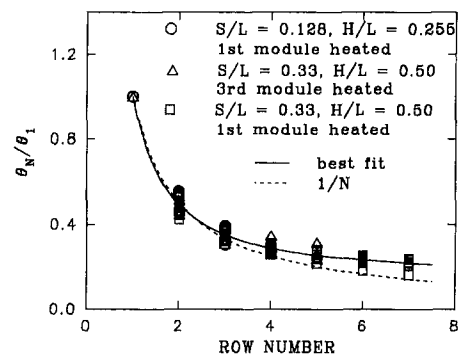


Fig. 8 Thermal wake effect for other downstream blocks (mean and maximum uncertainty = 4.0, 44.0 percent)

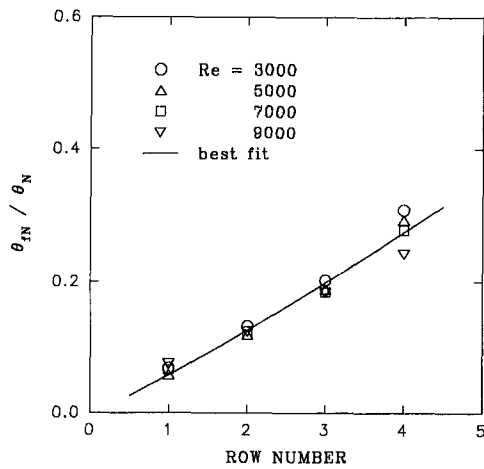


Fig. 9 Thermal wake effect for the blocks in the flanking columns (mean and maximum = 13.0, 16.0 percent)

$$\frac{\theta_{fN}}{\theta_N} = 0.151 + 0.849N^{-1.314} \quad (8)$$

Figure 8 shows that Eq. (8) is a better fit to data than  $1/N$ .

Attention is next turned to the wake effect on the blocks situated in the flanking columns of the heated block. In Fig. 9, the ordinate,  $\theta_{fN}/\theta_N$ , is the ratio of the wake effect for the flanking block at the same row, i.e.,  $\theta_{fN} = (T_{fN} - T_{in})/(T_h - T_{in})$ , to  $\theta_N$  defined earlier. It is seen from the figure that farther away from the heated block,  $\theta_{fN}$  increases with respect to  $\theta_N$  and is independent of Re. In the range of  $N = 1$  to 4,  $\theta_{fN}$  varies from 5.8 to 27.5 percent of  $\theta_N$ .

The wake effect for the flanking column may be represented by

$$\frac{\theta_{fN}}{\theta_N} = 0.0575N^{1.128} \quad (9)$$

which is a least-squares fit to all data. The mean and maximum deviation of data from this equation are, respectively, 7.8 and 22.6 percent, while the mean and maximum uncertainty are 13.0 and 16.0 percent.

Next, attention is turned to the application of these correlations for predicting the temperature of the circuit-board elements. The application is limited to the geometry and the range of parameters considered in this paper. However, they can also be used as a first approximation for a wider range of geometry and parameters in practical problems.

### Application of the Proposed Correlations

Based on the aforementioned correlations, a marching procedure is proposed for estimating the operating temperature of elements in a circuit-board with random heating using the superposition approach (Arvizu and Moffat, 1982). In this procedure, the temperature of each block is considered to be composed of two components. One is due to self heating ( $\Delta T_{sh} = T_h - T_a$ ), the other is due to the thermal wake of the upstream heated blocks ( $\Delta T_{we}$ ). It should be noted that every downstream block is affected by the thermal wake of every upstream block situated in the same column or in the flanking columns. Therefore, the thermal wake component will be evaluated from the summation of the wake effects of all the upstream heated blocks.

The algorithm is started by providing the geometric parameters (number of rows and columns,  $L, B, S, H, W$ ), air inlet velocity,  $V_{in}$ , inlet air temperature,  $T_{in}$ , and power dissipation in each block. These values are used to obtain  $S/L, H/L, X/D_h$ , and Re. Then, the temperatures are computed according to the following steps:

1 Adiabatic heat transfer coefficient,  $h$ , is obtained from Eqs. (3)–(4) for all blocks of the array.

2 Operating temperatures of the blocks in the first row are evaluated from: (Power – heat losses) =  $hA(T_h - T_a)$ , where Power is the heat generation within the block. It should be noted that the adiabatic temperature of the blocks situated in the first row is equal to the inlet air temperature, i.e.,  $T_a = T_{in}$ .

3 Wake effect of the heated blocks on all downstream blocks situated in the same column, i.e.,  $\Delta T_{we,s} = T_{aN} - T_{in}$ , is obtained from Eqs. (5)–(8). In this way, for every downstream block a different  $\Delta T_{we,s}$  value is evaluated and assigned to that block.

4 Wake effect of the heated blocks on the flanking columns is evaluated from Eq. (9). Only one column to the left and one to the right of the respective heated block is considered. The wake effect on other columns has been found to be negligible. In this manner, two additional wake effects, namely  $\Delta T_{we,l}$  and  $\Delta T_{we,r}$ , are found and assigned to the block. In this procedure, for heated blocks in the first row, three  $\Delta T$ 's are assigned to each of the blocks situated downstream.

5 The adiabatic temperatures of the blocks in the second row are estimated from  $T_a = \Delta T_{we} + T_{in}$ , where  $\Delta T_{we} = \sum \Delta T_{we,i}$ , and  $i = s, l, r$ .

6 Consider the second row of heated blocks. Using the adiabatic temperatures of the previous step, repeat steps (2)–(5) to find the operating temperatures of the blocks in the second row and their respective wake effects on downstream blocks. At the end of every cycle of iteration, the adiabatic temperature of the blocks in the next row is obtained from all the previously obtained  $\Delta T_{we,i}$ 's according to step (5).

This procedure is incorporated into a user-friendly FORTRAN program, which is available from one of the authors (MF) upon request. A sample output from this computer program is shown in Fig. 10. The figure shows the top view of the array. The cross-hatched blocks are heated, while the remaining blocks are adiabatic. The first of the four numbers on the heated blocks is the power generation in watts. This number is not seen for the un-

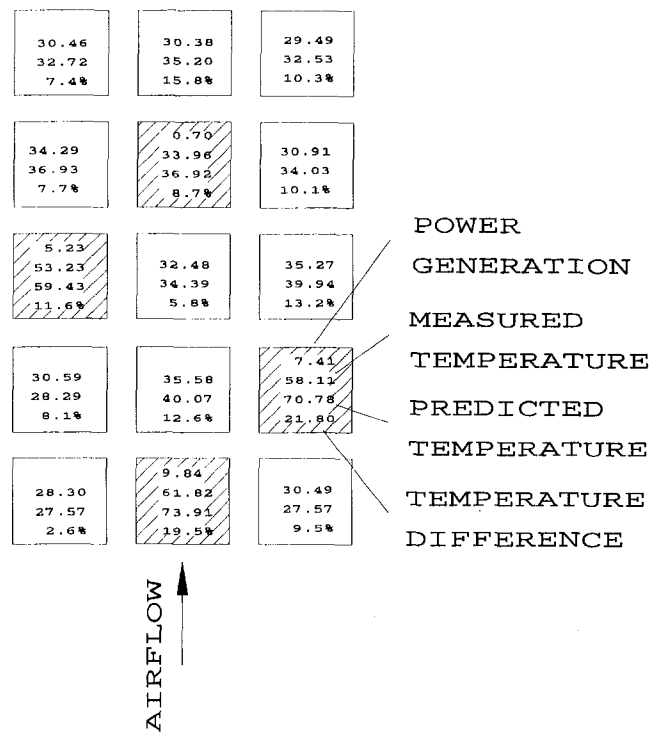


Fig. 10 A typical temperature prediction for the elements of a circuit board. The data are for  $L = 49.8$  mm,  $B = 25.4$  mm,  $S = 6.4$  mm,  $H = 38.1$  mm,  $V_{in} = 1.24$  m/s, and  $T_{in} = 27.57^\circ\text{C}$ , corresponding to  $S/L = 0.128$ ,  $H/L = 0.765$ ,  $B/L = 0.5$ , and  $Re = 5000$ .



heated blocks. The last three numbers on the heated and unheated blocks indicate the measured and computed temperatures in °C, and their difference, respectively. Examination of difference percentages indicates that the difference between experiment and prediction is in the range from 2.6 to 21.8 percent, and the mean difference is 11.0 percent.

The viability of using adiabatic heat transfer coefficient in a situation where there is considerable recirculation is best reflected by the final results in Fig. 10. As is evident from the figure, the agreement between measured and predicted temperatures is fairly good. Therefore, it is unlikely that recirculation and conduction losses at the base of the heated blocks would have a noticeable impact on temperature predictions.

### Concluding Remarks

The research reported here is an experimental investigation of heat transfer in the entrance region of an in-line array of heated blocks. The study is aimed at obtaining the adiabatic heat transfer coefficient and thermal wake effects, so that the operating temperature of the real circuit boards with a similar geometric layout can be estimated. However, since the real electronic components are irregular both in placement and size, the results reported in this paper may not be applicable to highly irregular layouts. In all of the experiments, the working fluid was air.

The entrance heat transfer coefficients revealed that  $Nu/Nu_{fd}$  is a function  $X/D_h$ , and its dependence on geometric parameters and Reynolds number is within the limits of the experimental uncertainty. These coefficients were successfully correlated by defining a modified Nusselt number. The correlation is obtained by a curve-fitting procedure that includes the data from other investigators, and thus is expected to be valid over a wider range than that of the present work.

Temperature measurements indicated that the thermal wake effect,  $\theta_1$ , for the first adiabatic block behind the heated block is a function of  $Re$  and  $S/L$ , and it is insensitive to  $H/L$ . A modified wake effect,  $\theta_1^*$ , absorbed the effect of  $Re$  and correlated the results as a function of  $S/L$ .

The wake effects for other blocks, when presented as  $\theta_N/\theta_1$ , are found to be independent of the position of the heated block and geometry. It was further found that the commonly employed  $1/N$  function is not a good representation of the  $\theta_N/\theta_1$  distribution. Instead, it was correlated as  $0.151 + 0.849 N^{-1.314}$ , which gives a more realistic asymptotic value for  $\theta_N/\theta_1$  when  $N \rightarrow \infty$ . Correlations were also found for the blocks situated in the flanking columns.

The present correlations are incorporated into a FORTRAN program to predict the operating temperatures of the circuit boards of similar geometry with random heating. The results indicate that the temperatures can be predicted with sufficient accuracy for practical application.

### Acknowledgments

This work was supported by a grant from IBM corporation. The authors are particularly grateful to Dr. R. Schmidt for his

support and encouragement. Dr. M. Molki gratefully acknowledges the support of Esfahan University of Technology during his sabbatical leave. The preliminary measurements by A. Ray at the early stage of this work are gratefully acknowledged.

### References

- Abernethy, R. B., Benedict, R. P., and Dowdell, R. B., 1985, "ASME Measurement Uncertainty," *ASME Journal of Fluids Engineering*, Vol. 107, pp. 161–164.
- Anderson, A. M., and Moffat, R. J., 1990, "A New Type of Heat Transfer Correlation for Air Cooling of Regular Arrays of Electronic Components," *Proceedings of ASME Winter Annual Meeting*, pp. 27–39.
- Anderson, A. M., and Moffat, R. J., 1991, "Direct Air Cooling of Electronic Components: Reducing Component Temperatures by Controlled Thermal Mixing," *ASME JOURNAL OF HEAT TRANSFER*, Vol. 113, pp. 56–62.
- Arvizu, D. E., and Moffat, R. J., 1982, "The Use of Superposition in Calculating Cooling Requirements for Circuit Board Mounted Electronic Components," *Proceedings of the 32nd Electronic Components Conference, IEEE*, Vol. 32, pp. 133–144.
- Faghri, M., Ray, A., and Sridhar, S., 1991, "Entrance Heat Transfer Correlation for Air Cooling of Arrays of Rectangular Blocks," *Heat Transfer Enhancement in Electronics Cooling*, ASME HTD-Vol. 183, pp. 19–23.
- Faghri, M., Molki, M., Chrupcala, J., and Asako, Y., 1994, "Entrance Analysis of Turbulent Flow in an Array of Heated Rectangular Blocks," *Proceedings of IEEE InterSociety Conference on Thermal Phenomena*, pp. 198–205.
- Hollworth, B. R., and Fuller, H. A., 1987, "Heat Transfer and Pressure Drop in a Staggered Array of Air-Cooled Components," *Proceedings of the International Symposium on Cooling Technology Equipment*, Honolulu, HI, pp. 732–748.
- Holman, J. P., 1984, "Experimental Methods for Engineers," 4th ed., McGraw-Hill, New York, p. 294.
- Kang, B. H., Jaluria, Y., and Tewari, S. S., 1990, "Mixed Convection Transport From an Isolated Heat Source Module on a Horizontal Plate," *ASME JOURNAL OF HEAT TRANSFER*, Vol. 112, pp. 653–661.
- Kang, S. S., 1992, "The Thermal Wake Function for Rectangular Electronic Modules," *Proc. National Heat Transfer Conference*, Open Forum, San Diego, CA.
- Kline, S. J., 1985, "The Purposes of Uncertainty Analysis," *ASME Journal of Fluids Engineering*, Vol. 107, pp. 153–160.
- Moffat, R. J., Arvizu, D. E., and Ortega, A., 1985, "Cooling Electronic Components: Forced Convection Experiments With an Air-Cooled Array," *Heat Transfer in Electronic Equipment*, ASME HTD-Vol. 48, pp. 17–27.
- Moffat, R. J., and Anderson, A. M., 1988, "Applying Heat Transfer Coefficient Data to Electronics Cooling," presented at the ASME Winter Annual Meeting, Chicago, IL.
- Molki, M., Faghri, M., and Ozbay, O., 1993, "A New Correlation for Pressure Drop in Arrays of Rectangular Blocks in Air-Cooled Electronic Units," *Natural and Forced Convection*, ASME HTD-Vol. 237, pp. 75–81.
- Peterson, G. P., and Ortega, A., 1990, "Thermal Control of Electronic Equipment," in: *Advances in Heat Transfer*, Vol. 20, pp. 181–305.
- Sparrow, E. M., Niethammer, J. E., and Chaboki, A., 1982, "Heat Transfer and Pressure Drop Characteristics of Arrays of Rectangular Modules Encountered in Electronic Equipment," *Int. J. Heat Mass Transfer*, Vol. 25, pp. 961–973.
- Sparrow, E. M., Vemuri, S. B., and Kadle, D. S., 1983, "Enhanced and Local Heat Transfer, Pressure Drop, and Flow Visualization for Arrays of Block-like Electronic Components," *Int. J. Heat Mass Transfer*, Vol. 26, pp. 689–699.
- Sridhar, S., 1990, "Heat Transfer and Fluid Flow Behavior in Arrays of Rectangular Blocks Encountered in Electronic Equipment," M.S. Thesis, Department of Mechanical Engineering and Applied Mechanics, University of Rhode Island.
- Sridhar, S., Faghri, M., and Lessmann, R. C., 1990, "Heat Transfer Behavior Including Thermal Wake Effects in Forced Air Cooling of Arrays of Rectangular Blocks," *ASME HTD-Vol. 153*, pp. 15–26.
- Wirtz, R. A., and Dykshorn, P., 1984, "Heat Transfer From Arrays of Flat Packs in a Channel Flow," *Proceedings of the Fourth Annual International Electronics Packaging Society*, Baltimore, MD, pp. 247–256.
- Wirtz, R. A., and Chen, Weiming, 1991, "Laminar-Transitional Convection From Repeated Ribs in a Channel," *Heat Transfer in Electronic Equipment*, ASME HTD-Vol. 171, pp. 89–94.

# Local Heat Transfer in Axially Feeding Radial Flow Between Parallel Disks

A. T. Prata

C. D. M. Pilichi

R. T. S. Ferreira

Department of Mechanical Engineering,  
Federal University of Santa Catarina,  
88040-900 Florianópolis, SC—Brazil

*Experiments and computations were performed to determine the local heat transfer in radial flows between parallel concentric disks. The flow is supplied axially by a feeding orifice placed in one of the disks and becomes radial after being deflected by the frontal disk. The frontal disk is kept isothermal and the other solid surfaces washed by the flow are kept adiabatic. Local heat transfer coefficients were determined using the naphthalene sublimation technique and the analogy between heat and mass transfer. Computations were performed using a finite volume methodology. The local Nusselt number distribution showed a valley at the stagnant region in front of the feeding orifice and a peak at the diffuser entrance where the flow impinges on the frontal disk prior to becoming radial. Depending on the Reynolds number and on the gap between the disks a secondary peak was observed in the diffuser region. The secondary peak is believed to be caused by nonparallelism or unsteadiness of the flow field and was not captured by the numerical model.*

## Introduction

Radial flows between parallel and concentric disks are of great interest in engineering and science. Some examples of technological applications related to radial flows are air thrust bearings, aerosol impactors, and electro-discharge machines. From the fundamental point of view radial flows present some unresolved issues. The concept of fully developed flow, when applied to radial diffusers, despite its use, is still not completely explored and leads to physical inconsistencies (Bird et al., 1960, p. 122). Also unresolved are the different patterns that the flow may assume as the Reynolds number is increased. Some authors believe that from a parallel configuration the flow separates at a given critical Reynolds number and that separation occurs periodically and alternately from the diffuser walls causing the formation of a vortex street (Mochizuki and Yang, 1985). Other works have reported flow separation under steady-state regime (Raal, 1978; Langer et al., 1990).

In the present work the attention is focused on radial flow with axial feeding. For this configuration the diffuser is fed axially through an existing orifice in one of the disks. The main motivation for this research is to understand the heat transfer in reed-type valves usually encountered in hermetic compressors. As the piston goes up and down the valves are subjected to different pressures on their sides causing the valves to open or close. For a detailed study on the pressure distribution along valve reeds of hermetic compressors reference is made to Ferreira et al. (1987, 1989).

In addition to the hydrodynamic problem, also very important is the thermal problem associated with compressor valves. As the fluid is sucked inside the cylinder, its specific volume is increased due to heat transfer from the suction valve. This results in a decrease of the compressor volumetric efficiency and is an undesirable effect. Despite its importance, very few works have dealt with heat transfer in radial diffusers (Kreith, 1966; Mochizuki and Yao, 1983; Mochizuki et al., 1983; Mochizuki and Yang, 1987). None of these works have dealt with radial flow with axial feeding as is the case here.

A schematic view of the flow geometry of the present work is presented in Fig. 1. As observed in the figure the flow is supplied

through the feeding orifice and after being deflected by the frontal disk the flow becomes radial. The fluid temperature at the orifice entrance is  $T_e$ , and the frontal disk is kept at constant temperature  $T_w$ . The orifice walls as well as the leeward disk are adiabatic. In a compressor valve system the frontal disk represents the valve reed and the main objective here is to determine the local heat transfer from the heated disk to the fluid as it passes through the diffuser. The situation is axisymmetric and therefore the local heat transfer is only function of the radial location.

In what follows both experiments and computations will be performed. In the experimental work mass transfer measurements will be made instead of direct heat transfer measurements. According to the analogy between the two processes, mass transfer can be regarded as heat transfer in the present situation. For the mass transfer use will be made of the naphthalene sublimation technique (Souza Mendes, 1991). Numerical solutions of the equations that describe the fluid flow and the heat transfer will also be presented. The computations will be performed using the finite volume methodology of Patankar (1980).

## Experimental Technique

The determination of the heat transfer coefficient and the local Nusselt number was achieved by performing mass transfer experiments. The mass transfer experiments were carried out using naphthalene sublimation.

The usual definition of the local heat and mass transfer coefficients are, respectively,

$$h = q/(T_w - T_f) \quad \text{and} \quad K = \dot{m}/(\rho_w - \rho_f) \quad (1)$$

where  $T$  is temperature,  $\rho$  is vapor density,  $q$  is heat flux, and  $\dot{m}$  is mass flux. The subscripts  $w$  and  $f$  refer, respectively, to conditions at wall and free stream.

To reproduce in the mass transfer experiments the desired boundary conditions shown in Fig. 1, the surface of the frontal disk is substituted by a solid naphthalene surface and the adiabatic surfaces are perfectly simulated by a metallic surface (non subliming surface). Air flowing adjacent to the solid naphthalene surface causes mass transfer from the wall to the airstream in the same manner that heat would be transferred from a heated surface. The mass transfer is essentially isothermal and the density of the naphthalene vapor at the surface can be regarded as uniform and equal to the saturated value at the surface temperature. A constant value of  $\rho_w$  perfectly reproduces the prescribed temperature  $T_w$  in the heat transfer situation, provided that  $T_w$  is not

Contributed by the Heat Transfer Division for publication in the JOURNAL OF HEAT TRANSFER. Manuscript received by the Heat Transfer Division March 1993, revision received March 1994. Keywords: Augmentation and Enhancement, Flow Separation, Forced Convection. Associate Technical Editor: A. Faghri.

so high as to induce an effective blowing velocity at the surface. In the present situation  $T_w$  was the ambient temperature, which prevented this phenomenon from occurring.

To obtain  $K$  from Eq. (1) it is necessary to measure the local sublimation rate  $\dot{m}$ . This is achieved by evaluating the surface depression due to the mass transfer, which is given by

$$\Delta z = \dot{m} \Delta t / \rho_s \quad (2)$$

where  $\Delta z$  is the surface depression,  $\rho_s$  is the density of the solid naphthalene ( $\rho_s = 1.146 \times 10^3 \text{ kg/m}^3$  from Sogin, 1958) and  $\Delta t$  is the time interval associated with  $\Delta z$ . Knowing how  $\Delta z$  varies along the radial location allows the evaluation of the local mass transfer coefficient, and, therefore, the local Sherwood number.

## Experimental Setup and Procedure

The experimental setup was mounted inside a windowless laboratory to provide a better temperature control of the air (working fluid) during the experimental run, which was kept under  $0.5^\circ\text{C}$  for all runs.

Laboratory air was drawn into a circular duct and was allowed to attain a fully developed hydrodynamic regime before reaching the test section where the radial diffuser was located. The airflow rate was controlled through two valves (coarse and fine flow adjusting). From the radial diffuser the flow expanded into a Plexiglas chamber of prismatic shape and hexagonal cross section. This chamber was important to assure that the flow between the diffuser disks was radial and axisymmetric. The flow adjusting valves, the flow developing tube, and the Plexiglas chamber were all mounted on a base table.

One of the six lateral sides of the prismatic chamber allowed access to the test section, which was placed inside the chamber. At one of the two faces of the chamber air entered the flow developing section and at the other face a flexible tubing sucked the air from inside the chamber to a rigid duct with a previously calibrated orifice for mass flow rate measurements. After the orifice was placed the blower operating in the suction mode and venting the naphthalene-laden air to the exterior of the laboratory.

The feeding orifice, as indicated in Fig. 1, was placed at the end of the flow developing section and inside the Plexiglas chamber. The frontal disk was concentric and parallel to the feeding orifice, and was held in place by a positioning device composed of four moving tables: three for linear displacements and one for angular displacements. During the experimental run the gap between the disks was controlled using a displacement transducer. For all runs the maximum variation observed was less than  $5 \mu\text{m}$ .

The local mass transfer rate  $\dot{m}$  was determined through measurements of the naphthalene surface depression  $\Delta z$  (Eq. 2). A computerized coordinate table made by Carl Zeiss, model ZMC 550 (Carl Zeiss, 1987), was employed to determine  $\Delta z$ . The

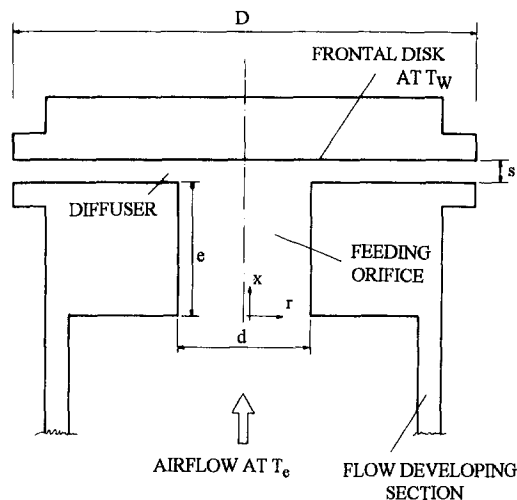


Fig. 1 Flow geometry of radial diffuser with axial feeding

naphthalene sublimation depths were on the order of  $40 \mu\text{m}$  and the resolution of the coordinate table was  $\pm 1 \mu\text{m}$ . The depth gage had a spherical 8 mm tip made of ruby, and the force associated with the measurements was 0.2 N and constant. The coordinate table was totally automated, which allowed a large number of measurements to be taken (40 locations) in a short time interval (180 s). The radius of the circular contact area between the gage and the naphthalene surface was estimated assuming a Hertz relation for elastic contact and was 0.08 mm. Therefore, the gage head size had little impact on both the sublimation depth uncertainty and the uncertainty associated with the  $x, y$  location. For some typical runs the overall mass change of the naphthalene was also measured with a Sartorius balance and compared with the sublimation depth measurements integrated over the coated surface. The deviation between the weighed and integrated results varied between 6 and 8 percent.

The first step for each experimental run was to adjust the desired airflow rate and the gap between the diffuser disks. To determine the zero reference gap use was made of a steel sphere with diameter of 3.960 mm. This sphere was suspended by a fine thread (glued to the sphere) and placed in different positions between the disks. By adjusting the micrometric table that supported the frontal disk it was possible to assure the parallelism between the disks. The concentricity and alignment of the disks were achieved using a mask. The uncertainty in the gap between the disks was estimated to be 0.03 mm.

After the gap had been adjusted to a desired value, the blower was turned on. Through a displacement transducer the gap was controlled and corrected to account for deformations of the Plexiglas chamber.

## Nomenclature

$D$ = diameter of frontal disk, m	$s$ = Gap between the diffuser disks, m	$\Delta z$ = naphthalene surface depression, m
$\mathcal{D}$ = diffusion coefficient, $\text{m}^2/\text{s}$	$Sc$ = Schmidt number	$\mu$ = absolute viscosity, $\text{kg}/(\text{m s})$
$d$ = diameter of feeding orifice, m	$Sh$ = Sherwood number, Eq. (3)	$\nu$ = kinematic viscosity, $\text{m}^2/\text{s}$
$e$ = length of feeding orifice, m	$T$ = temperature, K	$\rho$ = density, $\text{kg}/\text{m}^3$
$K$ = mass transfer coefficient, $\text{m/s}$	$\Delta t$ = time interval, s	$\phi$ = naphthalene vapor density
$\dot{M}$ = airflow rate in the test section, $\text{kg/s}$	$U, V$ = axial and radial velocity components	<b>Subscripts</b>
$\dot{m}$ = naphthalene mass flux, $\text{kg}/(\text{m}^2 \text{ s})$	$u, v$ = axial and radial velocity components, $\text{m/s}$	$e$ = refer to entrance conditions
$P$ = pressure	$X, R$ = axial and radial coordinates	$f$ = refer to free-stream conditions
$p$ = pressure, Pa	$x, r$ = axial and radial coordinates, m	$s$ = refer to solid
$Re$ = Reynolds number, Eq. (5)		$w$ = refer to wall conditions

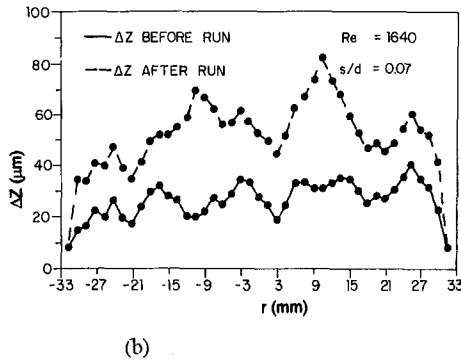
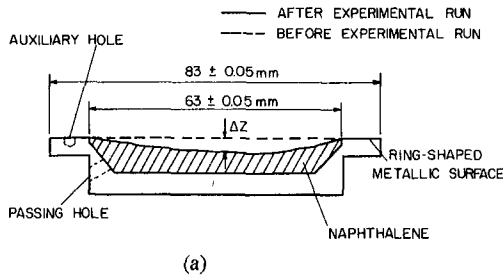


Fig. 2 Typical surface depression due to naphthalene sublimation; (a) schematic view of frontal disk; (b) local surface depression measurements

The naphthalene surface was fabricated from casting solid naphthalene (98.5 percent pure). Molten naphthalene was poured into an aluminum mold cavity and allowed to solidify. Care was taken to assure that the active surface had a glasslike smoothness. The frontal disk had a total diameter of 83 mm, and 63 mm was covered with cast naphthalene. The outer ring-shaped surface of 20 mm was used to adjust the alignment and parallelism of the frontal disk using the steel sphere as previously described. Additionally, it also served as a reference for the surface depression measurements when the disk was placed on the coordinate table; a small auxiliary hole allowed the depth gage to always find the same locations on the active surface.

Measurements of the naphthalene surface profiles were taken before and after the exposure to the airflow rate. After being placed on the coordinate table and the auxiliary reference hole being located manually, all data were taken automatically. The machine was programmed to measure the surface depression in 40 points along the disk diameter. The points were equally spaced 1.5 mm apart covering the total diameter of the naphthalene circle. A typical surface depression measurement is shown in Fig. 2. It is seen in the figure that despite all care that was taken the naphthalene surface was rather irregular. To obtain reliable data, the surface depression measurements before and after the experimental run had to be taken precisely at the same location. The uncertainty associated with the  $x$ ,  $y$  location of the depth gage was estimated to be 0.05 mm.

Depending on the airflow rate and on the gap between the disks, the experimental run elapsed from one to two hours. To account for the mass transfer during times that the run was not in progress, an after-run was always performed. Therefore, for each experimental run, three surface depression measurements were taken, and the actual sublimation depth was obtained as  $(z_2 - z_1) - (z_3 - z_2)$ , where  $z_i$  is the surface depression of the  $i$ th measurement (first, second, and third). A typical time duration for making the first surface depression measurement and for assembling the frontal disk in the test section was 537 s. A typical experimental run lasted 6993 s and to disassemble the frontal disk and make additional surface measurements required 612 s.

For this typical case a typical surface depression was 29.5  $\mu\text{m}$  and the extraneous mass transfer during assembling, disassembling, and transportation corresponded to a surface depression of 2.6  $\mu\text{m}$ .

Once the surface depression was measured, the mass transfer rate and the local mass transfer coefficient were obtained from Eqs. (2) and (1), respectively. In turn, the local Sherwood number was calculated as

$$\text{Sh} = Ks/\bar{v} = \rho_s \Delta z s / [(\rho_w - \rho_f) \Delta t \bar{v}] \quad (3)$$

where  $s$  is the gap between the disks (see Fig. 1) and  $\bar{v}$  is the diffusion coefficient of the naphthalene vapor into air obtained from a well-established form for correlating diffusion coefficients (Reid et al., 1987),

$$\bar{v} = 2.8965 \times 10^{-5} T^{1.75} / p \quad [\text{m}^2/\text{s}] \quad (4)$$

in which  $T$  (in K) and  $p$  (in  $\text{N/m}^2$ ) are the temperature and pressure at the test section. The constant in Eq. (4) was evaluated using the value of  $\bar{v}$  at  $T = 25^\circ\text{C}$  and  $p = 1$  atm. From  $\bar{v}$  the Schmidt number was calculated as  $\text{Sc} = \nu/\bar{v}$  where  $\nu$  is the air kinematic viscosity in the test section.

In the literature (for example Souza Mendes, 1991) the value of  $\text{Sc} = 2.5$  is usually adopted in naphthalene experiments. However, as the air relative humidity varies from 0 to 100 percent,  $\text{Sc}$  varies from 2.5 to 2.6, respectively. Thus, in the numerical solutions to be described shortly, use was made of the precise value of  $\text{Sc}$  corresponding to each experimental run.

In Eq. (3)  $\rho_w$  is the saturated value of the naphthalene vapor density at the mass transfer surface (function of the surface temperature) and  $\rho_f$  is the naphthalene vapor density in the free stream (bulk value) at each radial location. The value of  $\rho_f$  varies along the diffuser radius according to the amount of naphthalene that is sublimed.

The Reynolds number used to characterize the airflow rate was based on the diameter of the feeding orifice,  $d$ , (see Fig. 1) and given by

$$\text{Re} = 4 \dot{M} / \mu \pi d \quad (5)$$

where  $\dot{M}$  is the airflow rate in the test section. There was no need to correct the airflow rate for the naphthalene sublimation since the former was around  $10^4$  greater than the later.

The uncertainty analysis associated with the experimental results was performed according to the methodology described by Moffat (1982). Typical values of the measured parameters and their uncertainties are presented in Table 1.

### Numerical Methodology

The comparison between experiments and computations provided means of detecting small imperfections in the experimental setup and procedure. For the present study the results are very sensitive to existing misalignments and the main purpose of the computational model was to validate the experimental results.

For the present situation the flow is assumed to be laminar and axisymmetric. Considering the fluid properties to be constant, the hydrodynamic and mass transfer problem can be described in cylindrical coordinates as

$$\partial(RU)/\partial X + \partial(RV)/\partial R = 0 \quad (6)$$

Table 1 Typical values of measured parameters and their uncertainties

Parameter	Typical value	Uncertainty, percent
Re	700	7.8
Sh	2.23	13.5
Sc	2.60	0.1
s/d	0.07	2.1

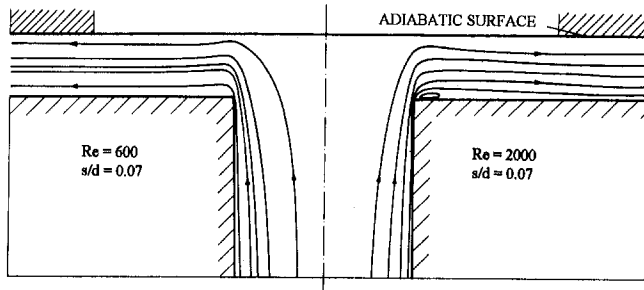


Fig. 3 Streamline maps for  $s/d = 0.07$  and  $Re = 600$  and  $2000$

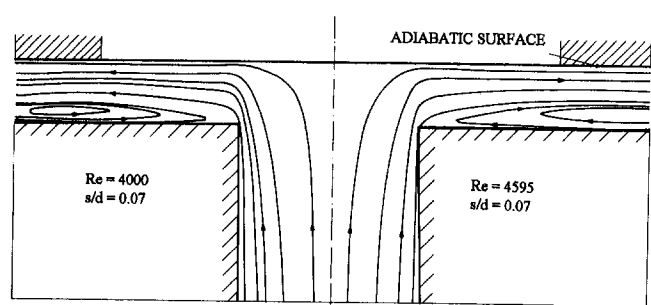


Fig. 4 Streamline maps for  $s/d = 0.07$  and  $Re = 4000$  and  $4595$

$$U \partial U / \partial X + V \partial U / \partial R = -\partial P / \partial X + \nabla^2 U \quad (7)$$

$$U \partial V / \partial X + V \partial V / \partial R = -\partial P / \partial R + \nabla^2 V - V / R^2 \quad (8)$$

$$U \partial \phi / \partial X + V \partial \phi / \partial R = (1 / Sc) \nabla^2 \phi \quad (9)$$

where  $\nabla^2$  is the Laplace operator in cylindrical coordinates and

$$X = x/s, \quad R = r/s$$

$$U = us/v, \quad V = vs/v$$

$$P = ps^2/\rho v^2, \quad \phi = \rho/\rho_w \quad (10)$$

The upstream boundary of the computation domain was located at the entrance of the feeding orifice (see Fig. 1 for the origin of the  $x, r$  coordinate system). At the end of the flow developing section the air entered the feeding orifice, which had a smaller diameter. This contraction in the flow domain introduced a radial velocity component that could be expected to affect the flow in the diffuser. Deschamps et al. (1987) showed that for small gaps between the diffuser disks ( $s/d < 0.1$ ), the flow in the diffuser was insensitive to the velocity boundary condition at the orifice entrance provided that the mass flow rate remained the same. Several tests were performed here to detect the influence of the axial and radial components of the entrance velocity on the local Sherwood number. It was found that the mass transfer problem was unaffected by entrance effects. The other boundary conditions for the hydrodynamic problem were the symmetry boundary condition at  $r = 0$ , the nonslip boundary condition at the solid walls and local parabolic boundary condition at the diffuser exit (upwinding as discussed by Bottaro, 1990). Tests performed with an expanded domain validated the outflow boundary condition: Except at the very exit where the streamlines appeared somewhat distorted, overall, the main features of the flow field were well captured by imposing the local parabolic condition even in a recirculation region.

At the orifice entrance the value of the naphthalene vapor density was zero, which yielded  $\phi = 0$ . For the naphthalene-coated surface (frontal disk)  $\phi = 1$  and at the metallic walls  $\partial \phi / \partial n = 0$ , where  $n$  is the normal to the surface. A symmetry boundary condition was used at the orifice axis and a local parabolic boundary condition (upwinding) was prescribed at the diffuser exit. At the higher Reynolds numbers investigated the inflow at the diffuser exit drew in fresh fluid from outside the domain. For those cases  $\phi = 0$  whenever  $V < 0$ , otherwise  $\partial \phi / \partial r = 0$ .

The differential equations (6)–(9) together with the boundary conditions were integrated using the finite volume methodology described by Patankar (1980). The coupling between velocity and pressure was performed through the SIMPLER algorithm (Patankar, 1980). A total of 2710 grid points was employed for discretizing the flow region; 1120 points were placed in the orifice and 1590 in the diffuser. Those points were hand placed with higher concentration in the regions of steeper velocity gradients. Prior to deciding the final configuration of the computational mesh, it was necessary to perform several tests. Computations of the local Sherwood number versus the radial location made with 4900 grid points (80 percent more points than that adopted here)

when plotted and compared with those obtained using the 2710 grid points presented no visual difference. Further assessments of the accuracy of the computations were obtained by comparing the numerical and analytical solutions for purely radial flows. For the fluid flow problem comparisons were made for low Reynolds number (lubrication approximation) as well as for high Reynolds number flow assuming fully developed regime. For the mass transfer problem, the comparisons were made for fully developed regime where the local Sherwood number as a function of the  $Re$  and  $Sc$  can be obtained analytically through the method of separation of variables. Good agreement always prevailed between the numerical and the analytical solutions, and in general the deviations decreased as the radial location increased. For example, for  $Re = 4000$ ,  $Sc = 2.60$  and  $s/d = 0.01$ , the deviations in the Sherwood number at  $r/s = 140$  ( $r/d = 1.4$ ) and  $r/s = 150$  ( $r/d = 1.5$ ) were, respectively, 6 and 2 percent. In this comparison it should be kept in mind that for the analytical solution some approximations were introduced and the deviations observed might not be associated exclusively with inaccuracy of the numerical methodology.

## Results and Discussion

For all cases investigated the feeding orifice diameter,  $d$ , and length,  $e$ , were 20 mm. Two gaps between the diffuser disks were explored,  $s = 1.4$  and 2.0 mm, corresponding to  $s/d = 0.07$  and 0.1, respectively. The Reynolds number according to Eq. (5) varied from 600 to 4595. At the entrance of the diffuser proper, the Reynolds number based on the gap between the disks,  $Re_s = \rho \bar{u} s / \mu$ , is four times smaller than  $Re$  as defined in Eq. (5). For increasing values of  $r$ ,  $Re_s$  decreases assuring that for the range of  $Re$  values investigated here the flow was laminar throughout the diffuser. For  $Re = 4595$ , for example, the  $Re_s$  values at the entrance and exit of the diffuser were, respectively, 1149 and 365.

The presentation and discussion of the experimental and numerical results will be made in terms of heat transfer. However, it should be kept in mind that in what follows the expressions “heat transfer” and “mass transfer” are interchangeable.

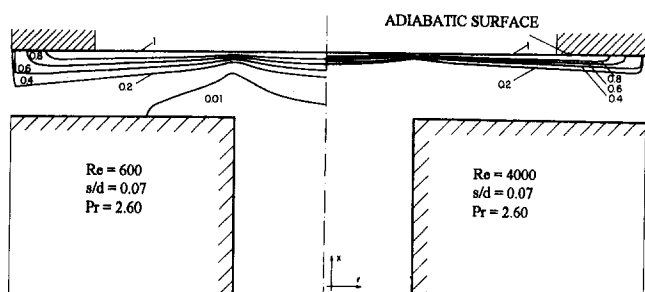


Fig. 5 Isothermal maps for  $s/d = 0.07$  and  $Re = 600$  and  $4000$

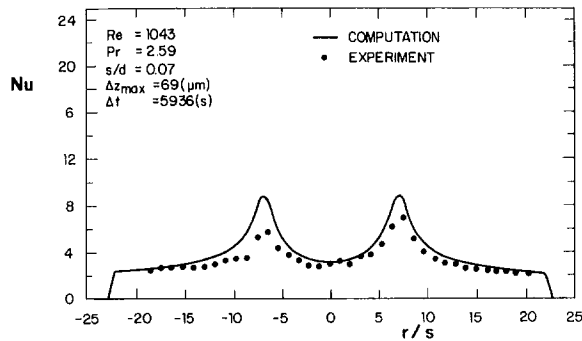


Fig. 6 Local Nusselt number as a function of radial location;  $s/d = 0.07$  and  $Re = 1043$

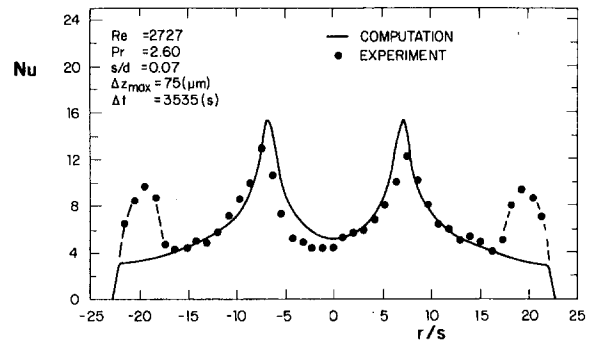


Fig. 8 Local Nusselt number as a function of radial location;  $s/d = 0.07$  and  $Re = 2727$

Streamline maps for  $s/d = 0.07$  and  $Re = 600, 2000, 4000,$  and  $4595$  are shown in Figs. 3 and 4. The first thing to be observed is that these figures as well as Fig. 5 are not to scale: The distance between the disks was enlarged by a factor of five. As seen in the figures, the flow enters axially through the feeding orifice and after being deflected by the frontal disk it becomes radial. Depending on the Reynolds number, the fluid particles are unable to follow the rapid change in the contour of the surface as they pass from the feeding orifice to the diffuser. The existing sharp corner causes the flow to separate from the surface. For  $Re = 600$  the flow separation was not captured in the numerical solution and for  $Re = 2000$  only a small recirculation zone (annular bubble) is seen. As the Reynolds number increases the recirculation zone increases and eventually it occupies all the region of the leeward disk. From Fig. 4 it is seen that for  $Re = 4000$  the fluid particles that separate from the wall at the diffuser entrance leave the solution domain without reattaching to the disk. As the Reynolds number increases further the region occupied by the recirculation zone increased along the axial direction, which can be seen by comparing the two sides of Fig. 4.

Isothermal maps are shown in Fig. 5 for  $s/d = 0.07$  and  $Re = 600$  and  $4000$ . For  $Re = 4000$  the isotherms are packed more closely to the heated frontal disk indicating higher temperature gradients and in turn higher local Nusselt numbers, as expected. An interesting aspect to be noted is the proximity of the isotherms to the frontal disk where the diffuser proper starts ( $r = d/2$ ). As will be seen shortly, this corresponds to a peak in the local Nusselt number and is caused by the flow acceleration as it turns from the feeding orifice to enter the diffuser and impinges on the frontal disk.

The adiabatic surfaces shown in Figs. 3–5 correspond to the part of the frontal disk that are not covered by naphthalene (the ring-shaped metallic surface shown in Fig. 2). The computation domain was extended up to the end of the adiabatic surface to reproduce the experimental situation and to minimize the influence of the outflow boundary condition on the region of interest.

Results for the local Nusselt number are presented in Figs. 6 to 11. Figures 6 to 8 are for  $s/d = 0.07$  and Figs. 9 to 11 are for  $s/d = 0.1$ . For each value of  $s/d$  the figures are presented in order of increasing values of the Reynolds number. In analyzing these figures it should be kept in mind that for  $s/d = 0.07$  the feeding orifice comprises the region  $-7.14 \leq r/s \leq 7.14$ , and for  $s/d = 0.1$  the region  $-5 \leq r/s \leq 5$ . At  $r/s = 7.14$  for  $s/d = 0.07$  and  $r/s = 5$  for  $s/d = 0.1$  the fluid enters into the diffuser proper. For low values of the Reynolds number the curves present a single peak as  $r/s$  increases from the center to the exit of the diffuser. As  $Re$  increases a secondary peak starts to be observed.

The stagnant region is represented by the valley on the local Nusselt number profiles. As the flow enters into the diffuser region the fluid particles impinge on the frontal disk yielding the heat transfer peaks observed in all the figures. Those peaks precisely occur at the entrance of the diffuser, that is,  $r/s = 7.14$  for  $s/d = 0.07$ , and  $r/s = 5$  for  $s/d = 0.1$ . For low Reynolds number, as the flow progresses in the radial direction, the increase in the flow cross-sectional area causes the velocity to decrease yielding smaller values of  $Nu$ , which decrease asymptotically. For higher values of the Reynolds number a secondary peak is observed in the local Nusselt number profile. As seen from Figs. 8, 10, and 11, after the first peak the decrease in the local Nusselt number associated with the decrease in the outflow velocity is arrested and  $Nu$  increases once again, attains a maximum, and then begins a steady decrease. As seen from the comparison between computation and experiments, the secondary peak was not captured by the numerical model. In the absence of the secondary peak a very good agreement prevailed between experiment and computation. The sharp decrease of  $Nu$  at the exit is due to a single point measured on the metallic disk outside the naphthalene-coated surface and is of no relevance.

An overall appraisal of the figures indicates that the local Nusselt number increases with increasing values of  $Re$ . Additionally, for a fixed Reynolds number,  $Nu$  increases as the gap between the disks increases. The secondary peak is more affected by  $Re$

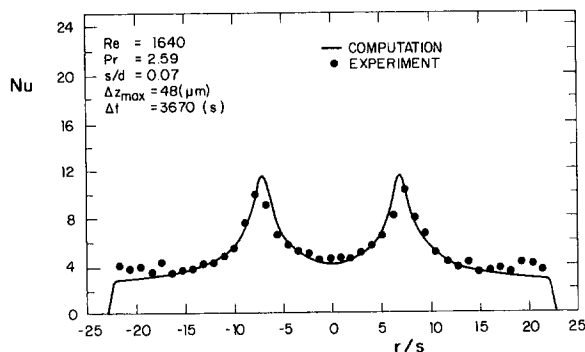


Fig. 7 Local Nusselt number as a function of radial location;  $s/d = 0.07$  and  $Re = 1640$

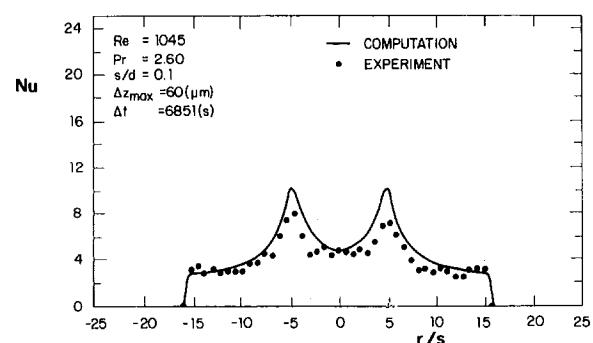


Fig. 9 Local Nusselt number as a function of radial location;  $s/d = 0.1$  and  $Re = 1045$

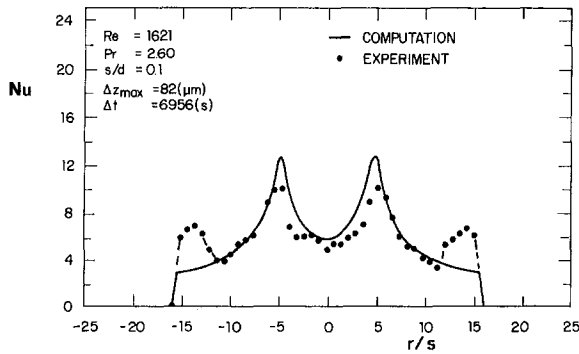


Fig. 10 Local Nusselt number as a function of radial location;  $s/d = 0.1$  and  $Re = 1621$

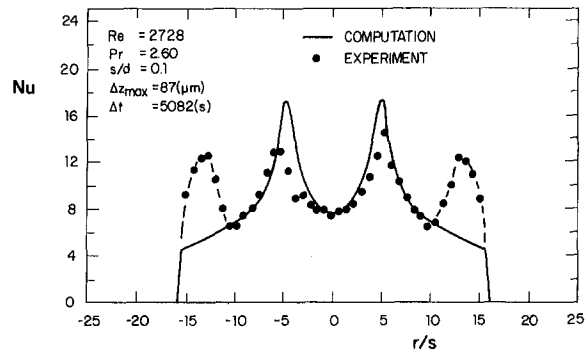


Fig. 11 Local Nusselt number as a function of radial location;  $s/d = 0.1$  and  $Re = 2728$

and  $s/d$  values than the primary peak. It can be seen from Figs. 7 and 10, both for approximately the same value of Reynolds number, that the gap between the disks has a great influence on the secondary peak. From those figures it is seen that as the gap increased by 43 percent (from 0.07 to 0.1), the primary peak increased by 9 percent whereas the secondary peak increased by 67 percent. Furthermore, the secondary peak moves upstream as  $Re$  and  $s/d$  increases.

The occurrence of the secondary peak is unexpected and suggests that at the peak location the flow is no longer parallel (i.e., the flow may be separated) or has become unsteady. The disagreement between computation and experiment at the location of the secondary peak is a further evidence of the nonparallelism or unsteadiness of the flow. This is so because the numerical solutions predicted a parallel flow configuration for the fluid particles that washed the frontal disk and temporal terms were not included in the numerical model.

An attempt was made to relate the occurrence of the secondary peak with existing information in the open literature. However, due to major differences in the flow geometry a direct comparison with published results was not possible.

It is known that the existence of an adverse pressure gradient in radial flows, due to the increase of the flow cross-sectional area, can cause flow separation (Mochizuki and Yang, 1985; Raal, 1978; Langer et al., 1990). Due to the flow separation, local heat transfer peaks similar to those observed here have been reported by Mochizuki and Yao (1983) for purely radial flows. It was observed that at certain radial locations laminar flow separations occur periodically and alternately from both disk walls and that the separation points agree well with the points where local Nusselt number starts to increase toward a secondary peak. On the basis of their results, Mochizuki and Yao concluded that the upturn of the  $Nu$  curve was due to the strong mixing caused by the periodic flow separation and subsequent formation of a vortex street.

In order to correlate the results obtained here in a manner similar to that reported by Mochizuki and Yao (1983), Fig. 12 was prepared. In this figure the dimensionless radial location corresponding to the position where the local Nusselt number starts to increase toward the secondary peak is plotted against a modified Reynolds number that incorporates the dimensionless gap between the disks as suggested by Mochizuki and Yao. It is seen from Fig. 12 that irrespective of  $s/d$  the location of the upturn of the  $Nu$  curve seems to correlate with  $Re(s/d)$ . According to the figure secondary peaks are expected to appear for situations lying above the curve.

The values of  $(r - d/2)/s$  corresponding to the upturn of the  $Nu$  curve obtained here and presented in Fig. 12 are considerably smaller than those of Mochizuki and Yao (1983). It is believed that the sharp corner at the end of the feeding orifice and the entrance of the diffuser plays an important role in the mechanism associated with the occurrence of the sec-

ondary peak. Further research is required to shed more light into this phenomenon.

For completeness, mention may be made of the local Nusselt number distribution associated with a single round jet impinging normally on a flat surface. There, for small separation between nozzle and plate, the distribution is characterized by a secondary peak similar to the ones observed in the present work (Martin, 1977). However, for the jet the secondary peak is attributed to turbulence effects, which is not the case here.

## Conclusions

The present work presented experimental and computational results for local heat transfer in radial flow between parallel and concentric disks. The flow is supplied axially by a feeding orifice placed in one of the disks. After being deflected by the frontal disk the flow is forced through the gap between the disks and becomes radial. Except for the frontal disk that is kept at a constant temperature, all other walls washed by the flow are maintained adiabatic. At the entrance of the feeding orifice the temperature is constant and the main focus of this work is to determine the heat transfer between the fluid and the frontal disk for various Reynolds number and gaps between disks.

The flow throughout radial diffusers as the one considered here can be considered the basic problem for performance analysis of various engineering applications. Thrust bearings, aerosol impactors, and electro-discharge machining are some technological applications of radial flows. For the present work motivation came from valve systems of reciprocating hermetic compressors. In such compressors heat transfer from the suction valve to the refrigerant is highly undesirable as it represents losses in the compressor volumetric efficiency.

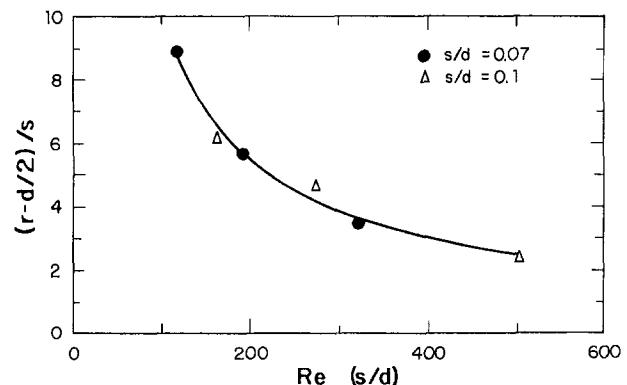


Fig. 12 Dimensional radial location corresponding to the position where the local Nusselt number starts to increase toward the secondary peak plotted as a function of  $Re(s/d)$ .

The heat transfer experiments were performed indirectly using the existing analogy between heat and mass transfer. In particular, the naphthalene sublimation technique was employed. Local sublimation rates of naphthalene were obtained by measuring surface depression. Values of surface depression were converted into local mass transfer coefficients, and, thereafter, into local Sherwood numbers (or Nusselt numbers). For compressor applications a Prandtl number correction has to be used. A way of proceeding is to normalize the Sherwood number results as  $Sh/Sc^n$ , where  $n \cong \frac{1}{3}$ . For the computations the flow was assumed to be laminar, steady, and axisymmetric. The governing equations were solved using a finite volume methodology.

Results were presented for two ratios between disk gap and feeding orifice diameter,  $s/d = 0.07$  and  $0.1$ . The Reynolds number based on the mass flow rate and the feeding orifice diameter was varied from 600 to 4595. For small values of the Reynolds number, the distribution of the local Nusselt number along the radius was characterized by a valley, a peak, and a monotonic decrease. The valley was associated with the stagnant region in front of the feeding orifice. As the flow changes its direction from axial to radial, it impinges on the frontal disk causing a peak in the local Nusselt number profile. The flow then progresses between the disks in the radial direction, and due to the increase in the flow cross-sectional area the outflow velocity decreases causing an asymptotic decrease in the local Nusselt number.

For higher values of the Reynolds number, the decrease in the local Nusselt number along the diffuser was arrested and a secondary peak was observed. The radial location corresponding to the position of the upturn of the local Nusselt number toward the secondary peak was successfully correlated with a modified Reynolds number given by  $Re(s/d)$ . Secondary peaks are expected to appear for situations lying above the curve of  $(r - d/2)/s$  versus  $Re(s/d)$ . In the absence of the secondary peak a very good agreement prevailed between experiments and computation. The secondary peak was not captured by the numerical model. It is believed that the occurrence of secondary peaks is due to nonparallelism (i.e., separation) or unsteadiness of the flow field, and that it is affected by the presence of the axial flow at the diffuser entrance.

### Acknowledgments

Support for this work from the Brazilian Compressor Industry, EMBRACO S.A., is gratefully acknowledged. Special thanks

goes to EMBRACO engineer Rinaldo Puff for helping in designing the experimental setup.

### References

- Bird, R. B., Stewart, W. E., and Lightfoot, E. N., 1960, *Transport Phenomena*, Wiley, New York.
- Bottaro, A., 1990, "Note on Open Boundary Conditions for Elliptic Flows," *Num. Heat Transfer*, Part B, Vol. 18, pp. 243–256.
- Carl Zeiss Geschäftsbereich Industrielle Messtechnik, 1987, *CNC Coordinate Measuring Machines With Universal 3D Probe Head*.
- Deschamps, C. J., Prata, A. T., and Ferreira, R. T. S., 1987, "Influence of the Feeding Orifice Length on the Flow in Radial Diffusers" [in Portuguese], *IX Brazilian Congress of Mechanical Engineering*, Florianópolis, SC, Vol. I, pp. 335–338.
- Ferreira, R. T. S., Prata, A. T., and Deschamps, C. J., 1987, "Laminar Fluid Flow in Compressor Valves—Numerical and Experimental Results," *ASME FED-Vol. 62*, pp. 33–38.
- Ferreira, R. T. S., Deschamps, C. J., and Prata, A. T., 1989, "Pressure Distribution Along Valve Reeds of Hermetic Compressors," *Exp. Thermal and Fluid Sci.*, Vol. 2, pp. 201–207.
- Kreith, F., 1966, "Transport de Chaleur et de Masse dans un Ecoulement Radial Entre Deux Disques Paralleles Fixes, ou Tourant a la Meme Vitesse," *Int. J. Heat Mass Transfer*, Vol. 9, pp. 265–272.
- Langer, C. A., Prata, A. T., and Ferreira, R. T. S., 1990, "Flow Separation and Bifurcation in Radial Diffusers" [in Portuguese], *3rd Brazilian Thermal Science Meeting*, Itapema, SC, Vol. 1, pp. 357–362.
- Martin, H., 1977, "Heat and Mass Transfer Between Impinging Gas Jets and Solid Surfaces," in: J. P. Hartnett and T. F. Irvine, Jr., eds., *Advances in Heat Transfer*, Academic Press, New York, Vol. 13, pp. 1–60.
- Mochizuki, S., Yang, W. J., Yagi, Y., and Ueno, M., 1983, "Heat Transfer Mechanisms and Performance in Multiple Parallel Disk Assemblies," *ASME JOURNAL OF HEAT TRANSFER*, Vol. 105, pp. 598–604.
- Mochizuki, S., and Yao, M., 1983, "Flow Separation and Heat Transfer in Radial Flows Between Two Parallel Disks," *Trans. Japan Soc. Mech. Eng.*, Vol. 49, pp. 426–432.
- Mochizuki, S., and Yang, W. J., 1985, "Self-Sustained Radial Oscillating Flows Between Parallel Disks," *J. Fluid Mech.*, Vol. 154, pp. 377–397.
- Mochizuki, S., and Yang, W. J., 1987, "Local Heat Transfer Performance and Mechanisms in Radial Flow Between Parallel Disks," *J. Thermophysics*, Vol. 1, pp. 112–116.
- Moffat, R. J., 1982, "Contribution to the Theory of Single-Sample Uncertainty Analysis," *ASME Journal of Fluids Engineering*, Vol. 104, pp. 250–260.
- Patankar, S. V., 1980, *Numerical Heat Transfer and Fluid Flow*, Hemisphere, Washington DC.
- Raal, J. D., 1978, "Radial Source Flow Between Parallel Disks," *J. Fluid Mech.*, Vol. 85, pp. 401–416.
- Reid, R. C., Prausnitz, J. M., and Sherwood, T. K., 1987, *The Properties of Gases and Liquids*, 3rd ed., Mc-Graw Hill, New York.
- Sogin, H. H., 1958, "Heat Transfer From Surfaces of Non-uniform Temperature Distribution, Part 1: Laminar Transfer From Isothermal Heat Poles on a Flat Plate," AFOSR TN-58-930, ASTIA Doc. No. 205095.
- Souza Mendes, P. R., 1991, "The Naphthalene Sublimation Technique," *Exp. Thermal and Fluid Sci.*, Vol. 4, pp. 510–523.



# Heat Transfer and Pressure Drop Characteristics of Spirally Fluted Annuli: Part I—Hydrodynamics

S. Garimella

Assistant Professor,  
Mechanical and Aeronautical  
Engineering Department,  
Western Michigan University,  
2076 Kohrman Hall,  
Kalamazoo, MI 49008  
Mem. ASME

R. N. Christensen

Professor,  
Mechanical Engineering Department,  
The Ohio State University,  
206 W. Eighteenth Ave.,  
Columbus, OH 43210  
Mem. ASME

*This paper is the first of two papers that present the results of a comprehensive study of heat transfer and pressure drop in annuli with spirally fluted inner tubes for the laminar, transition, and turbulent flow regimes. To understand the underlying physical phenomena responsible for heat transfer enhancement, flow mechanisms documented elsewhere are combined with pressure drop measurements to propose friction factor correlations for the low  $Re$  range ( $Re < 800$ ) and the high  $Re$  range ( $800 < Re < 43,500$ ). Friction factors were found to be functions of the flute depth, pitch and angle, and the annulus radius ratio. These correlations are used in the second paper to develop Nusselt number correlations in terms of the fluted annulus friction factor. Transition in these annuli occurred in the  $310 < Re < 1000$  range. In Part II of this study, this early transition is shown to be responsible, in part, for significant heat transfer enhancement. Friction factor increases were typically between 1.1 and 2.0 in the laminar regime, and up to 10 in the turbulent regime. These enhancement values can be used in conjunction with heat transfer enhancement values reported in Part II to determine appropriate ranges of applicability for spirally enhanced annuli.*

## Introduction

Single-phase heat transfer coefficients may be increased by artificially roughened surfaces, inlet vortex generators, vibration of the surface, application of electrostatic fields, and modifications to the duct cross section and surface. Many of these techniques typically increase the heat transfer coefficient through a change in flow patterns. In the recent past, some attention has been given to heat transfer augmentation by means of spiral flutes, grooves, and ridges on heat exchanger tubes. A spiral element on the surface is believed to enhance convective heat transfer by introducing swirl into the bulk flow and/or periodic disruption of the boundary layer at the tube surface due to repeated changes in the surface geometry. Several geometric parameters such as the bore diameter, envelope diameter, flute depth, pitch, and the number of starts, must be specified to define a spirally enhanced geometry completely as shown in Fig. 1. A change in any of these dimensions affects the flow and heat transfer characteristics of the tube. While some research has been done on similar geometries, there are deficiencies in the understanding of heat transfer and pressure-drop characteristics of spirally fluted geometries.

The objective of the present two-part study is to experimentally investigate the heat transfer and friction characteristics of annuli formed by placing a spirally fluted tube inside a smooth outer tube (see Fig. 1). This paper, Part I, addresses the hydrodynamic aspects, which explain the underlying physical phenomena responsible for heat transfer enhancement: Flow mechanisms documented elsewhere are combined with pressure drop measurements to propose friction factor correlations. These correlations are used in the second paper (Garimella and Christensen, 1995) to develop Nusselt number correlations in terms of the fluted annulus friction factor. Friction factor increases over the

corresponding smooth-annulus values can be used in conjunction with heat transfer enhancement values reported in Part II to determine the pressure drop penalty that will be incurred to effect a desired increase in heat transfer.

## Previous Work

Heat transfer and friction in tubes with repeated-rib roughness was investigated by Webb et al. (1971). They developed a friction-factor correlation based on the law-of-the-wall similarity for sand-grain type roughness. Watkinson et al. (1973, 1975a, 1975b) conducted studies on integral internally finned tubes for turbulent water and air flow, and laminar oil flow. Their results indicate that the high-spiral fin tubes result in the highest Nusselt number enhancements, followed by low-spiral fin tubes, and straight-fin tubes, respectively. They also found that transition occurs at lower  $Re$  values (250 to 1500) than for smooth tubes. Marto et al. (1979) demonstrated that the heat transfer coefficient and friction factor inside tubes are enhanced when spiral corrugations are introduced on the tube wall. They found that the heat transfer coefficient and friction factor are higher for tightly spaced or deep grooves because at low pitch values, the flow patterns change from predominantly swirling motion to predominantly turbulent mixing.

A survey of heat transfer and friction factor studies for spirally fluted tubing was conducted by Bergles (1980). For laminar internal heat transfer in heating, a maximum increase in the heat transfer coefficient and friction factor of 200 percent was reported. For turbulent internal flow, several studies were quoted with improvements of up to 400 percent above the plain tube heat transfer coefficients, but the pressure drop was as much as 10 times higher than for plain tubes. Flow in an annulus formed by a fluted inner tube and a smooth outer tube was identified as the configuration for which "more data are sorely needed . . .".

Heat transfer and pressure drop for tubes with single- and multiple-helix internal ridging were investigated by Withers (1980a, b). An empirical correlation for friction factor in terms of the Reynolds number  $Re$  and a set of adjustable constants was proposed. Nakayama et al. (1983) conducted an experimental investigation of heat transfer augmentation for water flowing

Contributed by the Heat Transfer Division and presented at the 28th National Heat Transfer Conference, San Diego, California, August 9–12, 1992. Manuscript received by the Heat Transfer Division August 1993; revision received March 1994. Keywords: Augmentation and Enhancement, Flow Visualization, Forced Convection. Associate Technical Editor: W. A. Fiveland.

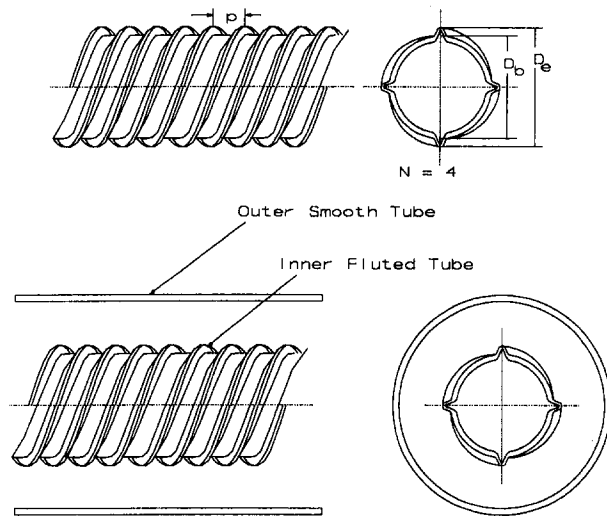


Fig. 1 Fluted-tube annulus

through spirally ribbed tubes in the turbulent regime. They postulated that at low helix angles, the flow near the wall follows the rib profiles, while at high helix angles, it crosses the ribs. At intermediate angles, the flow changes from swirl-dominated flow to cross-over flow.

Ravigururajan and Bergles (1985) proposed generalized correlations for turbulent flow in several internally ribbed tube geometries based on data cited by most of the above-mentioned investigators. They commented that in many of the studies employing sand-grain roughness analyses and the heat transfer-momentum analogy, the effects of pitch and helix angle, if included, were only as adjustments or "afterthoughts." They questioned the validity of these approaches due to the presence of significantly different swirl flow mechanisms in these geometries and chose a statistical approach to correlate data from many different studies.

Richards et al. (1987) presented pressure drop and heat transfer results for turbulent flow of water in fluted tubes as individual correlations of friction factor and Nusselt number for each tube. Garimella et al. (1988) conducted a survey of heat transfer and pressure-drop augmentation for turbulent flow in spirally enhanced tubes. A geometric parameter known as severity ( $\phi =$

$e^2/pD$ ) was used to characterize Nusselt number and friction-factor enhancements. An increase in  $e$  or a decrease in  $p$  or  $D$ , keeping other dimensions constant, yields a geometry that departs further from that of a plain tube. Three functions were defined, namely, heat transfer enhancement ( $e_h = Nu_f/Nu_s$ ), friction-factor enhancement ( $e_f = f_f/f_s$ ), and enhancement efficiency ( $\xi = e_h/e_f$ ), and the dependence of each of these functions on severity was investigated. Severity was found to be a good correlating parameter for data for over 60 different tubes from many previous studies. They showed that in turbulent flow, the friction-factor increase is usually much larger than the corresponding increase in heat transfer.

Few of the studies cited above address heat transfer and fluid friction in fluted geometries through the entire range of flow regimes and geometric combinations. Most of the above investigations focused only on the turbulent flow regime, but it is equally important that similar investigations be performed for the laminar and transition flow regimes, especially because heat transfer coefficients are inherently lower in the laminar and transition regimes than those for turbulent flow. Also, for the design of a heat exchanger, friction factors and heat transfer coefficients for the tube side and the annulus side are *equally important* in the determination of length and pressure drops. However, prior studies have not investigated enhancement in annuli. The present study addresses these deficiencies in the literature on spirally fluted geometries.

## Experimental Approach and Procedures

The experimental apparatus used for these tests is described briefly here. Further details can be found in the study by Garimella (1990). Nine fluted tubes, selected to achieve an adequate variation in all the relevant geometric variables, were used for the pressure-drop tests. Each tube was placed in different smooth outer tubes, which enabled the testing of annuli with different radius ratios. A matrix of all the annuli for which pressure-drop tests were conducted is presented in Table 1. Smooth-tube annuli were also tested for benchmarking purposes.

A schematic of the flow loop and the test sections used for the pressure-drop tests is presented in Fig. 2. City water was supplied to a settling tank equipped with an overflow line. In this tank, any dissolved air escaped to the atmosphere. In addition, the overflow line ensured a constant level and, therefore, a constant pressure head at the inlet to the pumps. From the settling tank, water flowed to two pumps connected in parallel. One or two of the pumps were used at any given time, depending on the specific

## Nomenclature

$A_c$ = cross-sectional area = $\pi(D_{o,i}^2 - D_{v,o}^2)/4$ , mm <sup>2</sup>	$L_{hy}^+$ = $L/D_h Re$	$\Delta P$ = pressure drop, Pa
$D_b$ = bore diameter, mm	$\dot{m}$ = mass flow rate, kg/s	$\Delta x$ = error in variable $x$ , absolute value
$D_e$ = envelope diameter, mm	$N$ = number of flute starts	$\epsilon_x$ = uncertainty in variable $x$ , fraction
$D_h$ = hydraulic diameter = $(D_{o,i} - D_{v,o})$ , mm	$Nu$ = Nusselt number = $hD_h/k$	$\theta$ = flute helix angle = $\tan^{-1}(\pi D_{v,o}/Np)$
$D_v$ = volume-based fluted tube diameter, mm	$p$ = flute pitch, mm	$\theta^*$ = nondimensional flute angle = $\theta/90$
$D_{o,i}$ = inner diameter of the outer tube, mm	$p^*$ = nondimensional flute pitch = $p/D_{v,o}$	$\xi$ = enhancement efficiency = $e_h/e_f$
$e$ = flute depth = $(D_e - D_b)/2$ , mm	$Re$ = Reynolds number = $\rho VD_h/\mu$	$\mu$ = viscosity, kg/s · m
$e_f$ = friction-factor increase = $f_f/f_s$	$Re_{crit,L}$ = lower critical Reynolds number	$\rho$ = density, kg/m <sup>3</sup>
$e_h$ = heat transfer enhancement = $Nu_f/Nu_s$	$Re_{crit,U}$ = upper critical Reynolds number	$\phi$ = severity = $e^2/pD$
$e^*$ = nondimensional flute depth = $e/D_{v,o}$	$r^*$ = annulus radius (diameter) ratio = $D_{v,o}/D_{o,i}$	
$f$ = friction factor = $(2\Delta PD_h/\rho V^2 L)$	$t$ = tube wall thickness, mm	
$FB$ = flute base, mm	$V$ = flow velocity, m/s	
$L$ = tube length between pressure taps, m	$Vol.$ = volume, m <sup>3</sup>	
	$W$ = volumetric flow rate, m <sup>3</sup> /s	
	$x$ = representative variable	

## Subscripts

$a$ = annulus, annulus side, augmented
$f$ = friction factor, fluted
$h$ = hydraulic, heat transfer
$i$ = inner
$o$ = outer
$s$ = smooth
$t$ = tube, tube side

Table 1 Test matrix for pressure-drop measurements

Annulus	Inner Tube						Outer Tube
	D <sub>i</sub> mm	D <sub>e,o</sub> mm	D <sub>b,o</sub> mm	D <sub>v,o</sub> mm	P mm	N	D <sub>o,i</sub> mm
A01T01	19.050	18.796	11.227	12.243	13.259	3	25.273
A02T01	19.050	18.796	11.227	12.243	13.259	3	29.972
A01T02	19.050	19.812	15.494	17.399	6.223	5	25.273
A02T02	19.050	19.812	15.494	17.399	6.223	5	29.972
A01T04	19.050	21.082	13.970	16.281	13.259	3	25.273
A02T04	19.050	21.082	13.970	16.281	13.259	3	29.972
A01T05	12.700	14.224	9.271	10.185	13.259	3	25.273
A03T05	12.700	14.224	9.271	10.185	13.259	3	23.622
A04T05	12.700	14.224	9.271	10.185	13.259	3	20.447
A01T06	15.875	17.145	11.125	12.116	11.735	3	25.273
A03T06	15.875	17.145	11.125	12.116	11.735	3	23.622
A04T06	15.875	17.145	11.125	12.116	11.735	3	20.447
A01T07	15.875	16.154	10.312	12.040	6.629	4	25.273
A03T07	15.875	16.154	10.312	12.040	6.629	4	23.622
A04T07	15.875	16.154	10.312	12.040	6.629	4	20.447
A02T08	25.400	26.670	19.050	19.964	15.240	4	29.972
A05T08	25.400	26.670	19.050	19.964	15.240	4	40.894
A01T09	15.875	16.637	11.684	12.725	8.230	4	25.273
A03T09	15.875	16.637	11.684	12.725	8.230	4	23.622
A04T09	15.875	16.637	11.684	12.725	8.230	4	20.447
A01T10	12.700	12.827	8.890	9.804	6.096	4	25.273
A03T10	12.700	12.827	8.890	9.804	6.096	4	23.622
A04T10	12.700	12.827	8.890	9.804	6.096	4	20.447

NOTES:  
D<sub>s</sub> = Original smooth-tube diameter  
D<sub>e,o</sub> = Outer envelope diameter  
D<sub>b,o</sub> = Outer bore diameter  
p = Flute pitch (space between consecutive flutes)  
N = Number of flute starts  
D<sub>o,i</sub> = Inner diameter of outer smooth tube  
Annulus Number A\*\*T\*\* refers to outer smooth tube number A\*\* and inner fluted tube number T\*\*; e.g., A04T10 refers to outer tube number 4 and inner tube number 10.

flow rate requirements. A magnetic flowmeter was installed between the control valves and the inlet to the test section. After flowing through the annulus side of the test section, the water flowed through a valve into the drain. The test section consisted of a 2.438-m-long annulus formed by placing a fluted tube with plain ends into a smooth outer tube. Two pressure taps were mounted on the outer tube to measure the differential pressure drop across the length of the annulus. A detail of these pressure taps is also shown in Fig. 2. The taps were designed specifically to minimize potential errors due to local circumferential pressure variations. Six holes, 60° apart, were drilled into the outer tube of the annulus at each of the two axial locations. Water from the annulus flowed out through these holes into a jacket brazed to the outer tube, thus equalizing the pressure from six circumferential locations. The tap conveying the pressure to the transducer was screwed on to this outer jacket.

The magnetic flowmeter was capable of measuring flow rates in the range  $1.199 \times 10^{-6} \text{ m}^3/\text{s}$  to  $1.793 \times 10^{-3} \text{ m}^3/\text{s}$ . The pressure taps were located near the inlet and the outlet of the test section. The upstream tap was located 0.914 m from the inlet of the annulus to ensure fully developed flow. Information about entrance lengths for flow in smooth annuli is available in Kakac et al. (1987). For laminar flow, the entrance length  $L_{hy}^+ = (L/D_h \text{ Re})$  varies from 0.0175 to 0.0109 for radius ratios of  $0.1 < r^* < 0.75$ . Thus, for a value of  $D_h = 12.7 \text{ mm}$ , where  $D_h = (D_o - D_i)$ , and  $\text{Re} = 2000$ , the maximum value of the entrance length would be 444.5 mm for a smooth annulus. For turbulent developing flow,  $L/D_h$  values of 15 suffice for establishing fully developed flow. These values are much smaller than the 0.914 m provided in the test section.

Two differential pressure transducers, with maximum  $\Delta P$ s of  $37.36 \times 10^3 \text{ Pa}$  and  $689.5 \times 10^3 \text{ Pa}$ , were used to measure pressure drops. The low and high  $\Delta P$  transducers had accuracies of  $\pm 0.2$  and  $\pm 0.25$  percent of the calibrated span, respectively. The low  $\Delta P$  transducer was further calibrated to an accuracy of  $\pm 12.44 \text{ Pa}$ . The tests were conducted for 23 different annuli up to the flow rate that could be sustained by the system, about 1.512 kg/s, with the corresponding pressure drops being up to  $241.3 \times 10^3 \text{ Pa}$ , depending on the annulus being tested.

### Data Analysis

The Reynolds number was calculated from the measured volumetric flow rate based on the hydraulic diameter,  $D_h$ . The flow velocity was calculated using the cross-sectional area,  $A_c$ . It should be noted that the fluted tube does not have a circular cross section, and previous investigators have arbitrarily chosen the envelope diameter,  $D_e$ , the bore diameter,  $D_b$ , or a mean of the two to represent the tube. In the present study, a diameter that represented the actual average cross-sectional area of the fluted tube was chosen. The volume of water required to fill a given length of tubing was measured. From the length of tubing, and the measured volume, the volume-based diameter,  $D_{v,i}$  was calculated as follows:

$$D_{v,i} = \sqrt{\frac{4 \text{ Vol}}{\pi L}} \quad (1)$$

The volumetric outside diameter,  $D_{v,o}$ , which is the quantity of interest for the annulus side, is calculated by adding twice the

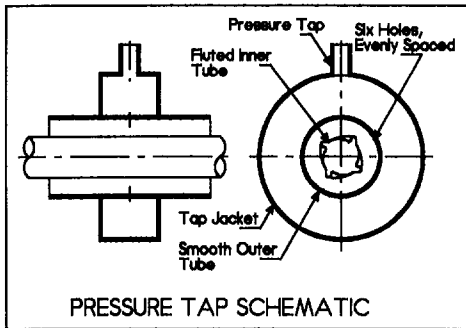
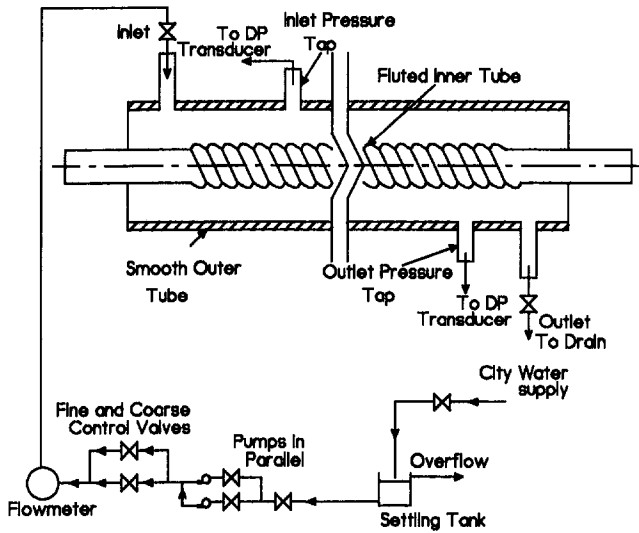


Fig. 2 Flow loop and test section for pressure-drop testing

tube thickness ( $t$ ) to  $D_{v,i}$ . While  $D_{v,o}$  is an accurate representation of the fluted tube diameter, in practice, it can only be calculated after the tube has been fabricated, which limits its applicability to tube specification. Therefore, a model was developed to calculate the volumetric diameter in terms of geometric features such as the tube bore and envelope diameters, number of flutes, and flute pitch. The cross-sectional area may be approximated as the sum of the clear bore area, and the area within the flutes, each flute being approximated as a triangle with the height equal to the flute depth, as shown in Fig. 3. This approximation for the tube cross-sectional area yields the following expression for  $D_{v,i}$ :

$$D_{v,i} = \sqrt{D_{b,i}^2 + \frac{N(D_{e,i} - D_{b,i})FB}{\pi}} \quad (2)$$

where  $FB$  refers to the portion of the tube circumference occupied by an individual flute:

$$FB = \frac{(1 - R)\pi D_{b,i}}{N} \quad (3)$$

Further details of the derivation of this model for  $D_v$  are available in Garimella (1990). The trough-to-circumference ratio,  $R$ , used in the equation above, can either be obtained through detailed measurements of the tube profile, or estimated from visual inspection. This model for the fluted tube diameter was validated by comparing the value of  $D_v$  calculated using this model with the values obtained by measuring the volume of water within the tube. For 15 tubes with widely varying geometries, the error was typically less than 3 percent.

Darcy friction factors were computed based on the above-mentioned definition of the hydraulic diameter,  $D_h$ . The flute depth,

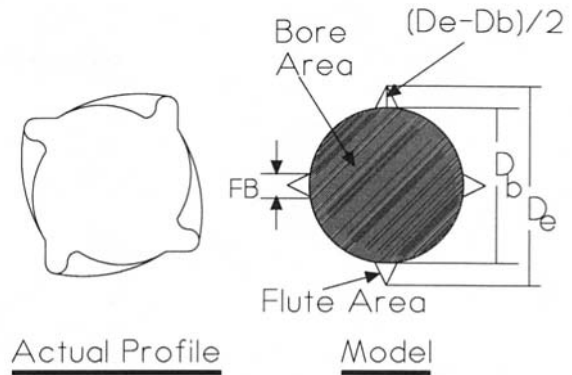


Fig. 3 Volumetric diameter of a fluted tube

$e$ , pitch,  $p$ , and the number of flute starts,  $N$ , were nondimensionalized using the tube volumetric outside diameter,  $D_{v,o}$ . The nondimensional flute helix angle  $\theta^*$  (with respect to the tube axis) was used to represent  $N$ . Annuli formed by different outer tubes for the same inner fluted tube were characterized by the radius ratio,  $r^*$ .

The uncertainties in the reported values for  $f$  were estimated using the compounding-of-errors technique (Kline and McClintock, 1953). Let  $\epsilon_x$  represent the fractional error in any variable,  $x$ , with absolute error,  $\Delta x$ . A sensitivity equation can be written as follows:

$$\epsilon_{f_f}^2 = \epsilon_{\Delta P}^2 + \epsilon_{D_h}^2 + 4\epsilon_V^2 + \epsilon_L^2 \quad (4)$$

As an example of this analysis for the annulus A01T02, uncertainties in the measurement of the volume of water, and the length and thickness of the tube, translated to an error in  $D_{v,o}$  of 0.03 mm. The error in the annulus cross-sectional area was calculated to be 5.12 mm<sup>2</sup>. The error in the flow velocity is composed of the error in  $A_c$  and the error in the flow rate measurement. This yields an error in  $V$  of 0.082 m/s (at  $Re = 20,802$ ). The error in  $D_h$  was calculated to be 0.131 mm. The error in the pressure drop was 74.7 Pa. Combining these errors, the uncertainty in  $f$  values calculated from the measured pressure drops is estimated to be  $\pm 4.3$  percent at  $Re = 20,802$ . At the lower  $Re$  values, due to the small magnitudes of the pressure drops (and a measurement uncertainty of 12.4 Pa), the uncertainty in the friction factor is higher: 9.4 percent at  $Re = 455$ .

## Results

Results from the validation tests on smooth-tube annuli with radius ratios of 0.636, 0.754 and 0.806 are presented in Fig. 4.

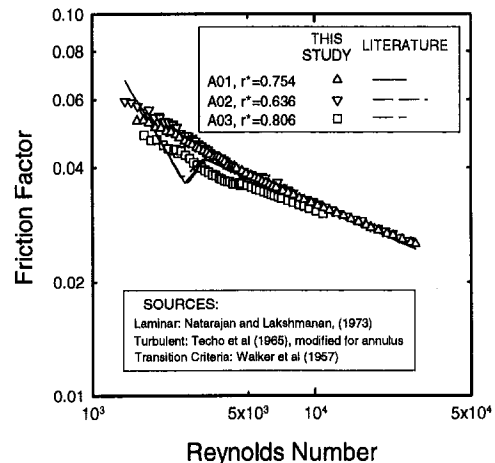


Fig. 4 Friction factors for smooth-tube annuli

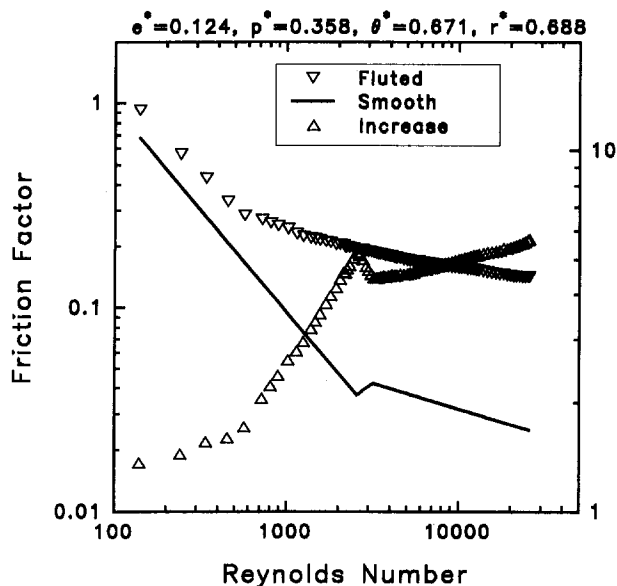


Fig. 5 Friction factors for annulus A01T02

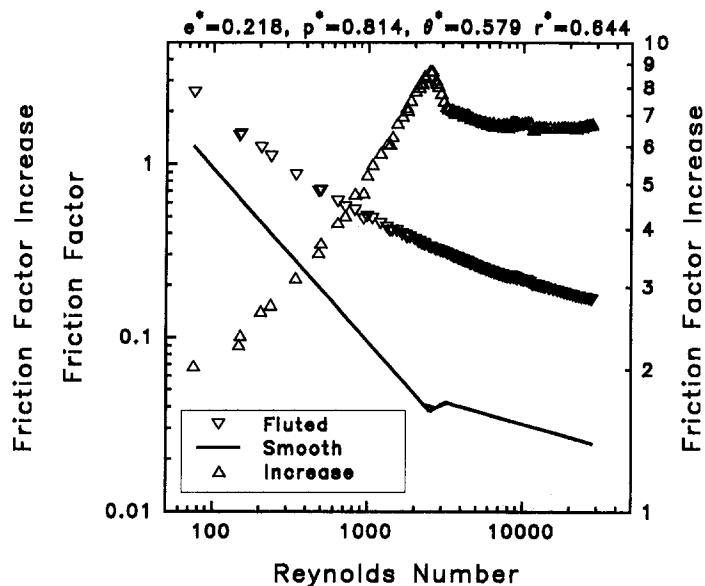


Fig. 6 Friction factors for annulus A01T04

Measured values and values obtained from the literature are presented for the Reynolds number range  $1408 < Re < 28227$ . For the laminar regime, the correlation developed by Natarajan and Lakshmanan (1973) was used as a reference. For the turbulent regime, the correlation developed by Techo et al. (1965) for smooth tubes, with an appropriate modification for the annular geometry suggested by Kakac et al. (1987) was used. Transition occurs in smooth annuli between the lower critical  $Re$  ( $2090 < Re_{crit,L} < 2775$ , depending on  $r^*$ ) and the upper critical  $Re$  ( $2960 < Re_{crit,U} < 3300$ ) according to Walker et al. (1957). Because friction factors for this region are somewhat indeterminate, logarithmically interpolated values between the laminar and turbulent values at  $Re_{crit,L}$  and  $Re_{crit,U}$  were used to represent this region. It can be seen from Fig. 4 that there is good agreement between the smooth annulus friction factors obtained here and the corresponding values in the literature.

Sample graphs for the friction factors in fluted annuli, the corresponding smooth-annulus values, and the ratio of the two, are presented in Figs. 5 and 6. In Figs. 5 and 6, the ordinates on the left and right sides refer to the friction factor, and friction-factor increase, respectively. In Fig. 5 for A01T02, the curve for  $f_f$  is almost parallel to the corresponding  $f_s$  curve in the low  $Re$  range up to  $Re \approx 600$ . At this value of  $Re$ , the slope undergoes an abrupt transition, representing a change in the flow characteristics. The transition  $Re$  value is much lower than the value expected for a smooth annulus ( $2560 < Re < 3190$  at  $r^* = 0.688$ , Walker et al., 1957). This change is also clearly reflected in the friction-factor increase graph. The increase in the low  $Re$  range is about 1.5 times the smooth-annulus value.

In the high  $Re$  range, the  $f_f$  graph is "flatter" than the  $f_s$  graph, resulting in a friction-factor increase graph that has a positive slope. Also, the enhancement in this regime is much higher, between four and six times the smooth-annulus value. In the neighborhood of  $Re \approx 2500$ , the small region of rapid slope changes in the friction-factor increase graph is due to the indeterminate nature of  $f_s$  in this region. Figure 6 for Annulus A01T04 is similar to Fig. 5 in most respects. The notable difference, however, is that transition between low  $Re$  and high  $Re$  friction factors is gradual (see especially the graph of friction factor increase versus  $Re$ ), and no single value for  $Re$  may be identified as the "critical  $Re$ " value. Across the test matrix, both types of transition were exhibited, with the departure from laminar behavior occurring without exception at much lower  $Re$  values than for smooth annuli.

Friction factors for annuli formed by one tube, T04, are presented in Fig. 7, which illustrates the effect of using different outer smooth tubes with the same fluted tube (i.e., varying  $r^*$ ). The larger value of  $r^*$  corresponds to a tighter annulus and results in a higher value of the friction factor. In addition, transition appears to occur in a more gradual manner as  $r^*$  is increased. This is because a greater fraction of the flow is in swirl at the higher  $r^*$  values.

The results described above were used to develop correlations for friction factor in fluted-tube annuli. Results of flow visualization tests conducted by Garimella (1990) were also used to develop a rationale for the correlation procedure. In those tests, it was found that the flow in this geometry is not a mere perturbation of smooth-annulus flow through surface roughness; therefore, law-of-the-wall similarity and other such approaches toward

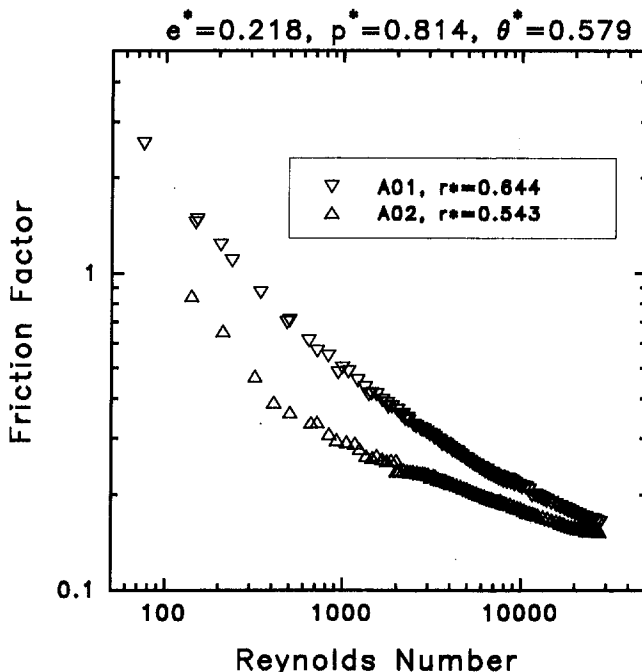


Fig. 7 Friction factors for tube O4

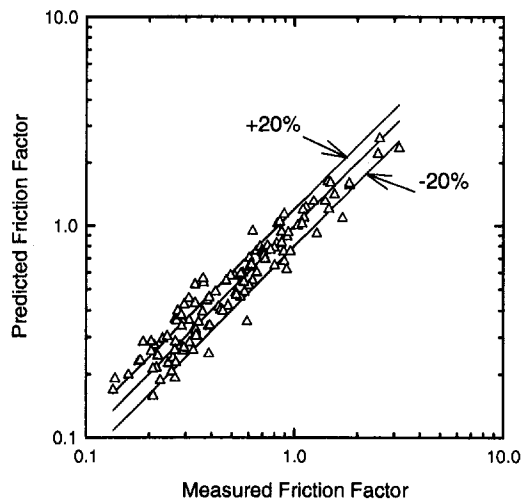


Fig. 8 Friction-factor correlation:  $Re < 800$

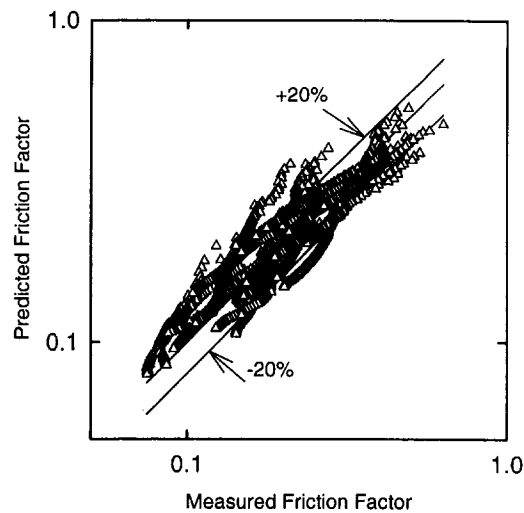


Fig. 9 Friction-factor correlation:  $Re > 800$

data correlation are not justifiable on a fundamental basis. The fluid does not flow in clearly demarcated trough and crest zones near the wall, and a purely axial flow away from the wall. In fact, it flows in a spiral pattern at an angle to the tube axis that is *different from the flute helix angle*. Moreover, flow that begins in the trough does not continue to stay in the same trough for any appreciable distance. It alternately crosses over between the trough and the crest as it flows spirally in the annulus. Therefore, a correlation technique based on models that simply superimpose flow in different zones of the geometry (troughs and crests, or near fluted wall and near smooth wall) is not likely to be successful. A statistical approach, similar to that used by Ravigururajan and Bergles (1985) for spirally enhanced geometries was used in the present study.

Results from the flow visualization and pressure-drop tests in this study showed that a Reynolds number of 800 adequately delineates laminar and turbulent flow in fluted-tube annuli (see also Garimella, 1990, and Garimella and Christensen, 1993). Therefore, the 1947 data points were divided into two sets: (a) low Re data:  $Re < 800$  (120 points), and (b) high Re data:  $Re > 800$  (1827 points). The fluted friction factor  $f_f$  was represented as a product of  $f_s$  and an augmentation function dependent on the geometry and the Reynolds number. For smooth annuli, Natarajan and Lakshmanan (1973) have proposed the following laminar-flow correlation:

$$f_s = \frac{96r^{*0.035}}{Re} \quad (5)$$

The fluted-annulus friction factor can be written as:

$$f_f = f_s [1 + a_0 Re^{C_1(e^*, p^*, r^*, \theta^*)} e^* C_2(Re, p^*, r^*, \theta^*) p^* C_3(Re, e^*, r^*, \theta^*) \times \theta^* C_4(Re, e^*, p^*, r^*) r^* C_5(Re, e^*, p^*, \theta^*)] \quad (6)$$

where the term in brackets is the augmentation function, and  $C_1, \dots, C_5$  are functions of the geometric parameters. The cross effects between all the variables and the parameters were first included as evidenced by the appearance of several parameters in the exponents of the respective variables in this equation. A commercially available program that uses nonlinear regression techniques (Marquardt–Levenberg algorithm) was used to correlate the data in this form. After a series of successively improved models, the following equation was chosen as the best fit:

$$f_f = \frac{96r^{*0.035}}{Re} [1 + 101.7 Re^{0.52} e^{*1.65+2.00\theta^*} r^{*5.77}] \quad (7)$$

The correlation above predicted 68 percent of the low Re data

(120 points) within  $\pm 20$  percent. Measured friction factors and the values predicted by this equation are compared in Fig. 8.

The high Re data were correlated using the same steps that were used for the low Re data. The following correlation (Techo et al., 1965) is applicable for turbulent flow in smooth tubes:

$$f_s = 4 \left[ 1.7372 \ln \left( \frac{Re}{1.964 \ln Re - 3.8215} \right) \right]^{-2} \quad (8)$$

Kakac et al. (1987) suggested the following multiplier for the Techo et al. correlation, which would enable prediction of smooth-annulus friction factors in the range  $5000 < Re < 10^7$ :

$$f_{s,a} = f_{s,t} (1 + 0.0925r^*) \quad (9)$$

where the subscript  $s, a$  refers to a smooth annulus, and the subscript  $s, t$  refers to a smooth tube. The correlation is only valid for  $Re > 5000$ . However, for the fluted annulus, friction factor and flow visualization tests showed that transition from laminar behavior occurred at much lower Re values. Therefore, it was assumed that this equation, coupled with the appropriate augmentation function, could be used for lower Re values ( $Re \geq 800$ ). Thus:

$$f_f = 4 \left[ 1.7372 \ln \left( \frac{Re}{1.964 \ln Re - 3.8215} \right) \right]^{-2} \times (1 + 0.0925r^*) e_f \quad (10)$$

where  $e_f$  is the enhancement function for the fluted annulus and is similar in form to Eq. (6) for the laminar correlation. After implementing the curve-fitting process, the following enhancement function for the high Re range ( $800 < Re < 43,500$ ) friction factors was obtained:

$$e_f = (1 + 222 Re^{0.09} e^{*2.40} p^{*-0.49} \theta^{*-0.38} r^{*2.22}) \quad (11)$$

The correlation above predicted 73 percent of the high Re data (1827 points) within  $\pm 20$  percent. A comparison of the measured and predicted friction factors is presented in Fig. 9. This correlation is used in the second part of this study (Garimella and Christensen, 1995) to correlate the heat transfer data in terms of the fluted annulus friction factor, thus illustrating the interdependence of fluid flow and thermal phenomena. The correlations above are valid for:

$$\begin{aligned} 0.124 < e^* < 0.309 \\ 0.358 < p^* < 1.302 \\ 0.431 < \theta^* < 0.671 \\ 0.388 < r^* < 0.688 \end{aligned}$$

## Comparison With Previous Studies

The results of the present study are now compared with those obtained by previous investigators for similar geometries. Because the enhanced annulus has received no attention in the past, direct quantitative comparisons are not feasible. However, results from the present study, especially those related to transitions and enhancements over smooth geometries, can be qualitatively compared with previous studies. In the present study, transition between laminar and turbulent behavior occurred in the range  $300 < Re < 1000$ . The terms laminar and turbulent are used here to facilitate comparison: flow in a fluted annulus is fundamentally different from that in a smooth annulus. Tangential velocities are present at almost all Re values. It is shear between these components and the bulk axial flow that leads to transition at very low Re values. These transitions were documented by Garimella (1990) through visual techniques, and were corroborated here through analyses of the pressure-drop data. In some cases, the transition was gradual, and no single Re value could be characterized as the critical Re. In other cases, transition Re values were identified. For a smooth annulus, transition is initiated in the range  $2090 < Re_{crit,L} < 2775$ , and the flow becomes fully turbulent in the range  $2960 < Re_{crit,U} < 3300$  (Walker et al., 1957). Thus, using a fluted inner tube causes transition at much lower Re values than for smooth annuli. Similar observations were made by Watkinson et al. (1975b) for tubes with spiral internal fins, who reported that transition occurred in the range  $250 < Re < 1500$ .

In the present study, friction factors in the laminar regime were typically found to be between 1.1 and 2.0 times the smooth annulus values. (A few cases showed an increase of up to 3.5 times the smooth values). Bergles (1980) reported laminar  $e_f$  values of up to 2, which agrees well with the results of the present study. In the turbulent regime, friction-factor increases ( $e_f$ ) of up to 10 times were observed in the present study, with a typical value being in the range  $4 < e_f < 5$ . Marto et al. (1979) reported  $e_f$  values of up to 10 for turbulent flow, some of their tubes being similar to the fluted tubes used in this study. They also found that  $e_f$  increases with an increase in flute depth or a decrease in flute pitch. Both these findings are similar to the results for the present study. Another feature of their results was that the friction factor becomes relatively independent of the Reynolds number for very deeply fluted tubes. For many of the annuli tested in the present study, the slope of the fluted annulus  $f - Re$  graph was flatter than that of the corresponding smooth annulus (see Fig. 5). Bergles (1980) reported turbulent  $e_f$  values of up to 10 for similar tubes. The survey of spirally enhanced tubes in turbulent flow by Garimella et al. (1988) showed  $e_f$  values as high as 30. Thus,  $e_f$  values for spirally fluted annuli reported here are in the range of values reported in previous studies on spirally enhanced tubes.

## Conclusions

This study represents a comprehensive investigation of friction-factor enhancement in spirally fluted annuli over all three flow regimes. A wide variation in all the relevant geometric parameters was also achieved. Correlations were developed for friction factors by using measured data and previously observed flow mechanisms. The effects of geometry and flow-related variables were modeled. The results are in general agreement with the limited literature in this area. The study focused on the annulus side, which has typically been ignored by most investigators. The following specific conclusions were drawn:

- Friction-factor increases over smooth-annulus values were typically between 1.1 and 2.0 for laminar flow, and up to 10 for turbulent flow.
- The annulus radius ratio is an important parameter in determining the fluted-annulus friction factor:  $e_f$  increases with an increase in  $r^*$ .

- Transition in fluted annuli occurs at much lower Re values ( $300 < Re < 1000$ ) than for smooth annuli.
- Friction-factor data were correlated in two regimes:  $Re < 800$  and  $800 < Re < 43,500$ , by developing augmentation functions with respect to smooth-annulus values in terms of dimensionless geometric and flow parameters.

The results from this study serve as the basis for the understanding of heat transfer in spirally fluted annuli. The flow regimes and the respective transitions identified here using friction factor data are used to interpret Nusselt number variations and the friction factor correlations developed here are incorporated into the Nusselt number correlations in the second part of this study (Garimella and Christensen, 1995).

## Acknowledgments

The research reported in this paper was supported by the Gas Research Institute. The fluted tubes were supplied by  $\Delta T$  Ltd. of Tulsa, OK.

## References

- Bergles, A. E., 1980, *Heat Transfer Characteristics of Turbotec Tubing*, Heat Transfer Laboratory Report HTL-24 ISU-ERI-Ames-81018, Iowa State University, Ames, IA.
- Garimella, S., Chandrachud, V., Christensen, R. N., and Richards, D. E., 1988, "Investigation of Heat Transfer and Pressure Drop Augmentation for Turbulent Flow in Spirally Enhanced Tubes," *ASHRAE Transactions*, Vol. 94, Part 2.
- Garimella, S., 1990, "Experimental Investigation of Heat Transfer and Pressure Drop Characteristics of Annuli With Spirally Fluted Inner Tubes," Ph.D. Dissertation, The Ohio State University, Columbus, OH.
- Garimella, S., and Christensen, R. N., 1995, "Heat Transfer and Pressure Drop Characteristics of Spirally Fluted Annuli: Part II—Heat Transfer," *ASME JOURNAL OF HEAT TRANSFER*, Vol. 117, this issue, pp. 61–68.
- Kakac, S., Shah, R. K., and Aung, W., 1987, *Handbook of Single-Phase Convective Heat Transfer*, Wiley, New York, pp. 3–92, 4–132.
- Kline, S. J., and McClintock, 1953, "Describing Uncertainties in Single-Sample Experiments," *Mechanical Engineering*, Vol. 75, Jan., pp. 3–8.
- Marto, P. J., Reilly, R. J., and Fenner, J. H., 1979, "An Experimental Comparison of Enhanced Heat Transfer Condenser Tubing," in: *Advances in Enhanced Heat Transfer*, ASME, New York, pp. 1–9.
- Nakayama, W., Takahashi, K., and Daikoku, T., 1983, "Spiral Ribbing to Enhance Single-Phase Heat Transfer Inside Tubes," *ASME-JSME Thermal Engineering Joint Conference Proceedings*, Honolulu, HI, Vol. 1, pp. 365–372.
- Natarajan, N. M., and Lakshmanan, S. M., 1973, "Laminar Flow Through Annuli: Analytical Method for Calculation of Pressure Drop," *Indian Chem. Eng.*, Vol. 15, pp. 50–53.
- Ravigururajan, T. S., and Bergles, A. E., 1985, "General Correlations for Pressure Drop and Heat Transfer for Single-Phase Turbulent Flow in Internally Ribbed Tubes," in: *Augmentation of Heat Transfer in Energy Systems*, ASME HTD-Vol. 52, pp. 9–20.
- Richards, D. E., Grant, M., and Christensen, R. N., 1987, "Turbulent Flow and Heat Transfer Inside Doubly-Fluted Tubes," *ASHRAE Transactions*, Vol. 93, Pt. 2.
- Techo, R., Tickner, R. R., and James, R. E., 1965, "An Accurate Equation for the Computation of the Friction Factor for Smooth Pipes From the Reynolds-Number," *J. Appl. Mech.*, Vol. 32, p. 443.
- Walker, J. E., Whan, G. A., and Rothfus, R. R., 1957, "Fluid Friction in Non-circular Ducts," *AIChE Journal*, Vol. 3, No. 4, pp. 484–489.
- Watkinson, A. P., Miletti, D. L., and Tarassoff, P., 1973, "Turbulent Heat Transfer and Pressure Drop in Internally Finned Tubes," *AIChE Symposium Series*, Vol. 69, No. 131, pp. 94–103.
- Watkinson, A. P., Miletti, D. L., and Kubanek, G. R., 1975a, "Heat Transfer and Pressure Drop of Forge-Fin Tubes in Turbulent Air Flow," *Proceedings of the ASHRAE Semi-Annual Meeting*, ASHRAE, New York, Vol. 81, Part 1, pp. 330–349.
- Watkinson, A. P., Miletti, D. L., and Kubanek, G. R., 1975b, "Heat Transfer and Pressure Drop of Internally Finned Tubes in Laminar Oil Flow," *Proceedings of the AIChE-ASME Heat Transfer Conference*, ASME, New York, Paper No. 75-HT-41.
- Webb, R. L., Eckert, E. R. G., and Goldstein, R. J., 1971, "Heat Transfer and Friction in Tubes With Repeated-Rib Roughness," *Int. J. Heat Mass Transfer*, Vol. 14, pp. 601–617.
- Withers, J. G., 1980a, "Tube-Side Heat Transfer and Pressure Drop for Tubes Having Helical Internal Ridging With Turbulent/Transitional Flow of Single-Phase Fluid. Part 1. Single-Helix Ridging," *Heat Transfer Engineering*, Vol. 2, No. 1, pp. 48–58.
- Withers, J. G., 1980b, "Tube-Side Heat Transfer and Pressure Drop for Tubes Having Helical Internal Ridging With Turbulent/Transitional Flow of Single-Phase Fluid. Part 2. Multiple-Helix Ridging," *Heat Transfer Engineering*, Vol. 2, No. 2, pp. 43–50.

# Heat Transfer and Pressure Drop Characteristics of Spirally Fluted Annuli: Part II—Heat Transfer

**S. Garimella**

Assistant Professor,  
Mechanical and Aeronautical  
Engineering Department,  
Western Michigan University,  
2076 Kohrman Hall,  
Kalamazoo, MI 49008  
Mem. ASME

**R. N. Christensen**

Professor.  
Mechanical Engineering Department,  
The Ohio State University,  
206 W. Eighteenth Ave.,  
Columbus, OH 43210  
Mem. ASME

*This paper is the second of two papers that present the results of a comprehensive study of heat transfer and pressure drop in annuli with spirally fluted inner tubes for the laminar, transition, and turbulent flow regimes. Fourteen fluted tubes with varying geometries were studied, with up to three outer smooth tubes for each fluted tube. Flow patterns and transitions between flow regimes investigated through visualization tests, friction factor data (from Part I), and tube surface-temperature measurements were used to explain the enhancement phenomena. The fluted inner tubes induced a significant degree of swirl in the flow, and transition occurred in the  $310 < Re < 1000$  range. A Nusselt number correlation was developed in terms of the fluted annulus friction factor developed in Part I and geometric parameters. Nusselt numbers were between 4 and 20 times the smooth annulus values in the low  $Re$  range, while turbulent enhancements were between 1.1 and 4.0. These enhancement values can be used in conjunction with friction factor increase values reported in Part I to determine appropriate ranges of applicability for spirally enhanced annuli.*

## Introduction

Single-phase heat transfer coefficients may be increased by artificially roughened surfaces, inlet vortex generators, vibration of the surface, application of electrostatic fields, and modification of the duct cross section and surface. Many of these techniques increase the heat transfer coefficient through a change in flow patterns. In the recent past, some attention has been given to heat transfer augmentation by means of spiral flutes, grooves, and ridges on heat exchanger tubes. A spiral element on the surface is believed to enhance convective heat transfer by introducing swirl into the bulk flow and/or periodic disruption of the boundary layer at the tube surface due to repeated changes in the geometry. Several geometric parameters such as the bore diameter, envelope diameter, ridge or flute depth, pitch and shape, and the number of starts, must be specified to define a spirally enhanced geometry completely. These dimensions are shown in Fig. 1. A change in any of these dimensions affects the flow and heat transfer characteristics of the tube. While some research has been done by previous investigators on similar geometries, there are deficiencies in the understanding of heat transfer and pressure drop characteristics of spirally fluted geometries. The objective of the present two-part study is to experimentally investigate heat transfer and friction characteristics of annuli formed by placing a spirally fluted tube inside a smooth outer tube (see Fig. 1). Part I of this study (Garimella and Christensen, 1995) addressed the hydrodynamic aspects, which explain the underlying physical phenomena responsible for heat transfer enhancement. Flow mechanisms and pressure drop measurements were used to propose friction factor correlations. It is shown in this paper, Part II, that these fluted-annulus friction factor correlations can be used in conjunction with heat transfer data to develop Nusselt number correlations. Heat transfer enhancements over the corresponding smooth-annulus values can be compared with the friction factor increases reported in Part I to determine the pressure drop penalty that will be incurred to effect a desired increase in heat transfer.

## Previous Work

A comprehensive review of the literature on spiral enhancement of heat transfer in ducts was presented in Part I of this study (Garimella and Christensen, 1995) and also in the Dissertation by Garimella (1990). In Part I of this study, flow mechanisms and pressure drop in annuli with spirally fluted inner tubes were investigated for the laminar, transition, and turbulent regimes. From the variation of friction factor as a function of Reynolds number, it was shown that transition in these annuli occurs in the  $310 < Re < 1000$  range. Friction factor increases in the laminar regime were typically between 1.1 and 2.0, while enhancements of up to 10 were recorded in the turbulent regime. The friction factors were found to be functions of flute depth, pitch and angle, and the annulus radius ratio. Two different friction factor correlations for  $Re < 800$ , and  $Re > 800$ , respectively, were proposed. Garimella and Christensen (1993) also conducted investigations of the flow mechanisms in annuli with different types of spirally enhanced inner tubes through visualization tests using dye injection. Detailed temperature profile measurements were also made on the crests and troughs of the tube surface to investigate potential circumferential, axial, and spiral variations. It was found that the fluted inner tubes induced a significant degree of swirl in the flow. Spirally ribbed and spirally indented tubes induced progressively smaller degrees of swirl. The primary conclusion from these investigations was that the fluid does not flow exclusively in trough and crest zones near the enhanced-tube wall and in a purely axial flow away from the wall, but rather in a spiral pattern, alternately crossing over between the trough and crest. Their tests also confirmed the conclusion from friction factor data that transition in these annuli occurs in the range  $310 < Re < 1000$ .

Previous studies have not addressed heat transfer in spirally enhanced geometries through the entire range of flow regimes and geometric combinations. Also, heat transfer coefficients for the tube side and the annulus side are equally important in the determination of tube-in-tube heat exchanger lengths, but prior studies have not investigated enhancement in annuli. The present study attempts to address these deficiencies in the literature by obtaining an understanding of heat transfer characteristics of fluted-tube annuli for a wide range of geometric and flow parameters.

Contributed by the Heat Transfer Division and presented at the ASME Winter Annual Meeting, New Orleans, Louisiana, November 28–December 3, 1993. Manuscript received by the Heat Transfer Division August 1993; revision received March 1994. Keywords: Augmentation and Enhancement, Forced Convection, Heat Exchangers. Associate Technical Editor: W. A. Fiveland.



## Experimental Approach and Procedures

Fourteen fluted tubes, selected to achieve a wide variation in all the relevant geometric variables, were used for the heat transfer tests. The tube geometries tested here cover an even greater range than was included in Part I (Garimella and Christensen, 1995) for the pressure drop tests, thus extending the range of nondimensional parameters for which the results are applicable. Each tube was placed in up to three different smooth outer tubes, which enabled the testing of annuli with different radius ratios. The annuli were tested as counterflow tube-in-tube heat exchangers. Smooth-tube annuli were also tested for benchmarking purposes.

To achieve the objectives of this study, a test rig that allowed testing over a wide range of flow rates was required. It was essential that temperature changes in the individual fluid streams, and the approach temperature differences used for the calculation of LMTDs, were large enough to minimize errors due to measurement inaccuracies. Electric heating from the tube side or the tube wall itself was deemed impractical because of the convoluted fluted tube geometry and the high heat-duty requirement (up to 66 kW, or a linear flux of 26 kW/m in the test section) for the high Re test points. Steam condensation on the tube side could not be used because for laminar flow on the annulus side, the low flow rate causes the cold fluid to approach the hot-side temperature within a very short distance. Thus, a substantial part of the heat exchanger does not contribute to heat transfer but is erroneously included in the heat transfer area calculations. Near the outlet of the annulus side, the water could start boiling. Thus, this method was not suitable.

Laminar and turbulent heat transfer tests with reasonable temperature changes in the respective streams, as well as between the hot and cold side, can be performed by using single-phase water on both sides of the heat exchanger. An appropriately controlled tube-side inlet temperature and mass flow rate would provide a high enough ratio of  $h_t/h_a$  without causing an excessive temperature rise in the annulus fluid or the "dead heat exchanger" zone described above. As the annulus-side flow rate is increased to achieve the turbulent Re values, the tube-side flow rate can also be increased to maintain high values of  $h_t/h_a$ . Considering these factors, this method was chosen for conducting the heat transfer tests. This method does, however, require a means of calculating  $h_t$  with an accuracy that depends on the specific value of  $h_t/h_a$  in question. For the laminar tests, where this ratio is very high, errors even as high as  $\pm 300$  percent or more in the

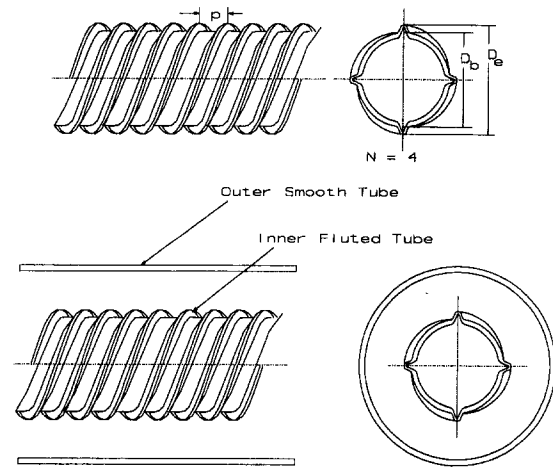


Fig. 1 Fluted-tube annulus: focus of current study

calculated values of  $h_t$  are acceptable and do not significantly affect the resulting value of  $h_a$ . For the turbulent flow tests, relatively smaller errors are tolerable. A correlation for turbulent Nusselt numbers in spirally augmented tubes proposed by Ravigururajan and Bergles (1985) satisfied these criteria and was used to calculate the tube-side coefficient, and thus deduce the annulus-side coefficient from measured UA values.

The flow loop and the test section used in this study are shown in Fig. 2. A city-water supply line and a supply of steam were used for the tests. The city water line was split into two different streams. One stream was used as the cold water inlet to the annulus side of the test section. The other stream was mixed with an appropriate amount of steam to provide the desired flow rate of hot water at the required inlet temperature. The steam and cold water from the outlets of V2 and V3 were conveyed to the inlet of the tube side through a long serpentine section of piping, which ensured complete mixing of the water and the steam upstream of the heat-exchanger inlet valve (V4). The hot water passed through the heat exchanger and exited to the drain. Cold water from the outlet of valve V1 was supplied to the combination of coarse and fine control valves VC and VF, from which it flowed through a magnetic flowmeter. This measured flow rate was used to calculate the heat duty in the heat exchanger and the

## Nomenclature

$A_c$  = cross-sectional area =  $\pi(D_{o,i}^2 - D_{v,o}^2)/4$   
 $C_p$  = specific heat  
 $D_b$  = bore diameter  
 $D_e$  = envelope diameter  
 $D_h$  = annulus hydraulic diameter =  $(D_{o,i} - D_{v,o})$   
 $D_{o,i}$  = inner diameter of the outer smooth tube  
 $D_v$  = volume-based fluted tube diameter  
 $e$  = flute depth =  $(D_e - D_b)/2$   
 $e_f$  = friction factor increase =  $f_f/f_s$   
 $e_h$  = heat transfer enhancement =  $Nu_f/Nu_s$   
 $e^*$  = nondimensional flute depth =  $e/D_{v,o}$   
 $f$  = friction factor =  $(2\Delta PD_h/\rho V^2 L)$   
 $FB$  = flute base  
 $h$  = heat transfer coefficient  
 $k$  = thermal conductivity

$L$  = tube length  
 $LMTD$  = log-mean temperature difference  
 $\dot{m}$  = mass flow rate  
 $N$  = number of flute starts  
 $Nu$  = Nusselt number =  $hD_h/k$   
 $p$  = flute pitch  
 $p^*$  = nondimensional flute pitch =  $p/D_{v,o}$   
 $Pr$  = Prandtl number =  $\mu C_p/k$   
 $Q$  = heat duty  
 $R$  = heat transfer resistance  
 $Re$  = Reynolds number  
 $r^*$  = annulus radius ratio =  $D_{v,o}/D_{o,i}$   
 $T$  = temperature  
 $t$  = tube wall thickness  
 $U$  = overall heat transfer coefficient  
 $V$  = flow velocity  
 $Vol.$  = volume

$\Delta T$  = temperature difference  
 $\epsilon_x$  = uncertainty in variable  $x$   
 $\theta$  = flute helix angle =  $\tan^{-1}(\pi D_{v,o}/Np)$   
 $\theta^*$  = nondimensional flute helix angle =  $\theta/90$   
 $\mu$  = viscosity  
 $\rho$  = density  
 $\phi$  = severity =  $e^2/pD$

## Subscripts

$a$  = annulus, annulus-side, augmented  
 $f$  = friction factor, fluted  
 $h$  = hydraulic, heat transfer  
 $i$  = inner, inlet  
 $o$  = outer, outlet  
 $s$  = smooth  
 $t$  = tube, tube-side  
 $tot$  = total  
 $w$  = wall

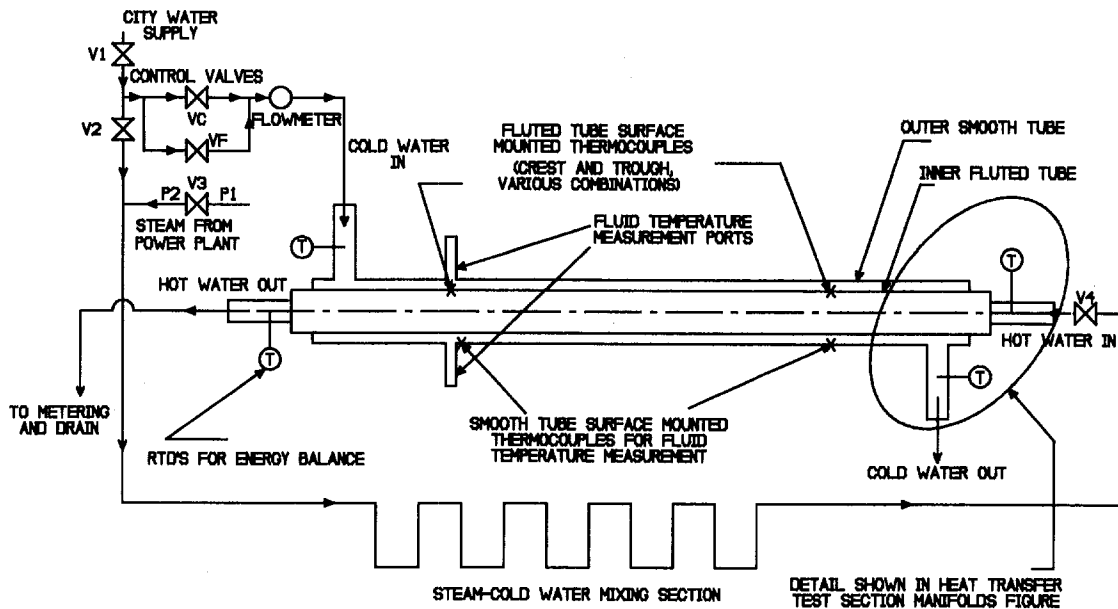


Fig. 2 Heat transfer test facility

calculation of annulus  $Re$ . (Manually collected tube-side flow rates were used to ensure energy balances.) After passing through the flowmeter, the cold water flowed through the counterflow heat-exchange test section and exited to the drain.

The test section consisted of a 2.44-m-long heat exchanger, insulated on the outside, formed by placing a fluted tube inside a smooth outer tube. A detail of the manifolds that housed the inlets/outlets, thermocouple and RTD connections is shown in Fig. 3. The RTDs measured inlet and outlet temperatures of the tube side and the annulus side for overall energy balance. Thermocouple ports (for T-type thermocouples) were also provided 213 mm from the ends of the inner tube. Temperatures measured at these locations provided experimental confirmation of the establishment of fully developed flow. Eight 24-gage thermocouples were also welded to the fluted tube surface to measure temperature variations at the wall of the fluted tube. These measurements were used to propose flow mechanisms in the annulus, as

reported earlier by Garimella and Christensen (1993). Numerical values and graphs of temperatures as a function of time were displayed and recorded on a computer to allow confirmation of steady state. Further details of the experimental apparatus are available in Garimella (1990). During the tests, the ratio of tube-side to annulus-side flow was kept at about five whenever feasible. Because the annulus-side flow area was typically larger than that of the tube side, this ratio of mass-flow rates resulted in an even higher ratio of heat transfer resistances. This control strategy helped in minimizing the sensitivity of the deduced  $h_a$  values to errors in the tube-side correlations.

### Data Analysis

The techniques used to reduce the data from the 45 annuli tested in this study are described here. The Reynolds number was calculated from the measured flow rate based on the hydraulic

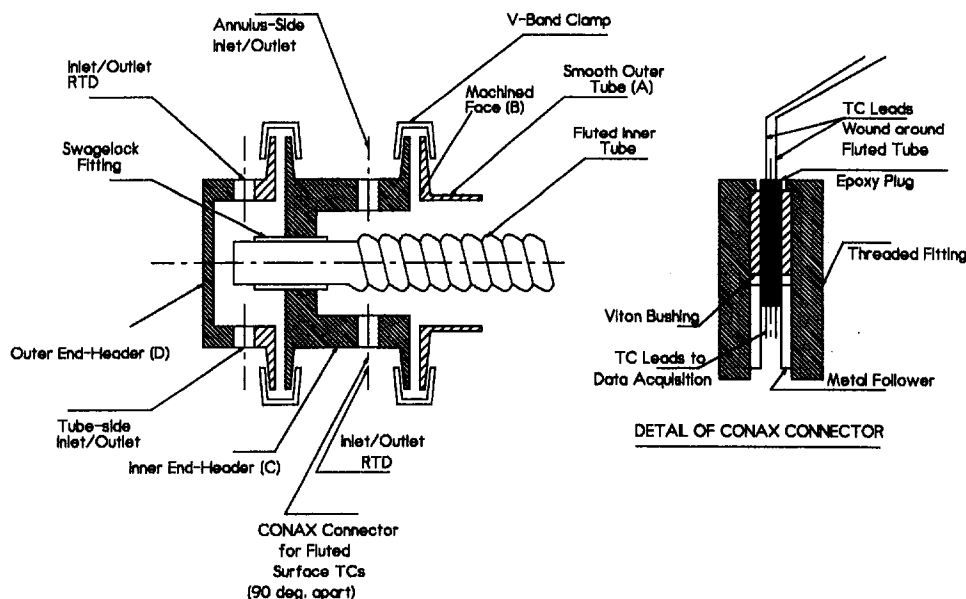


Fig. 3 Heat transfer test section manifolds

diameter,  $D_h$ . The flow velocity was calculated using the cross-sectional flow area,  $A_c$ . It should be noted that the fluted tube does not have a circular cross section; therefore, a diameter that represented the average cross-sectional area of the fluted tube was calculated from the volume of water required to fill a given length of tubing as follows:

$$D_{v,i} = \sqrt{\frac{4 \text{Vol}}{\pi L}} \quad (1)$$

The volumetric outside diameter,  $D_{v,o}$ , which is the quantity of interest for the annulus side, is calculated by adding twice the tube thickness ( $t$ ) to  $D_{v,i}$ . To facilitate tube specification, a model was developed to calculate the volumetric diameter in terms of geometric features such  $D_o$ ,  $D_e$ ,  $p$ , and  $N$ . The cross-sectional area was approximated as the sum of the clear bore area, and the area within the flutes, each flute being approximated as a triangle with the height equal to the flute depth, which yields the following expression for  $D_{v,i}$ :

$$D_{v,i} = \sqrt{D_{b,i}^2 + \frac{N(D_{e,i} - D_{b,i})FB}{\pi}} \quad (2)$$

where  $FB$  refers to the portion of the tube circumference occupied by an individual flute. Further details of the derivation of this model for  $D_v$  are available in the first paper (Garimella and Christensen, 1995) and also in Garimella (1990). This model was validated by comparing the value of  $D_v$  calculated using this model with the values obtained by measuring the volume of water within the tube. For 15 tubes with widely varying geometries, the error was typically less than 3 percent. The flute depth and pitch were nondimensionalized using the volumetric diameter,  $D_{v,o}$ . The nondimensional helix angle  $\theta^*$  (with respect to the tube axis) was used to represent the number of flute starts,  $N$ . Annuli formed by choosing different outer tubes for the same inner fluted tube may be differentiated by the radius ratio,  $r^*$ .

The heat duties of the two fluid streams were calculated from the flow rates and the temperature changes in the respective streams from the inlet to the outlet. The discrepancy between  $Q_a$  and  $Q_i$  was less than 3 percent for about 90 percent of the data points. If there was a large discrepancy between these values, the specific data point was discarded. The log-mean temperature difference (LMTD) is given by:

$$\text{LMTD} = \frac{(T_{h,i} - T_{c,o}) - (T_{h,o} - T_{c,i})}{\ln [(T_{h,i} - T_{c,o}) / (T_{h,o} - T_{c,i})]} \quad (3)$$

where the subscripts  $h$  and  $c$  refer to the hot and cold fluids, respectively. From the heat duty and the LMTD, the overall heat transfer coefficient  $UA_{\text{tot}}$  was calculated as follows:

$$UA_{\text{tot}} = \frac{Q_{\text{tot}}}{\text{LMTD}_{\text{tot}}} \quad (4)$$

where the subscript tot refers to the total heat exchanger defined by fluid inlets and outlets. As mentioned above, several other thermocouples on the tube-side and annulus-side were installed at a distance of 213 mm from each end of the heat exchanger to determine the significance of end effects. Heat duties, LMTDs, and  $UAs$  were also calculated using the equations shown above for this "fully developed" heat exchanger for each data point for all the annuli. The  $UA$  for this shorter heat exchanger coincided with the  $UA_{\text{tot}}$  for the total heat exchanger within the limits of accuracy of measurement for all the data, implying that end effects were negligible.

The overall  $U$  value ( $UA/\pi D_{v,o}L$ ) is comprised of the conductance of the tube side, the tube wall, and the annulus side. Tube-side flow was always maintained in the turbulent regime, and the corresponding tube-side  $Nu$  is given by Ravigururajan and Bergles (1985) as follows:

$$\frac{Nu_o}{Nu_i} = \{1 + [2.64 \text{Re}^{0.036} e^{*0.212} p^{*-0.21} \times (\theta^*)^{0.29} \text{Pr}^{-0.024}]^7\}^{1/7} \quad (5)$$

The nondimensionalization in this correlation is with respect to the inside envelope diameter,  $D_{e,i}$ . The resulting Nusselt number was converted to the  $D_v$  basis consistent with the present study.  $Nu_i$  in the above equation is the Petukhov and Popov (1963) correlation:

$$Nu_i = \frac{(f_s/8) \text{Re} \text{Pr}}{1 + 12.7\sqrt{f_s/8}(\text{Pr}^{2/3} - 1)} \quad (6)$$

where  $f_s$  is the smooth-tube friction factor (Petukhov, 1970; Darcy form):

$$f_s = 4[1.58 \ln(\text{Re}) - 3.28]^{-2} \quad (7)$$

These correlations were applied to calculate the tube-side heat transfer coefficient based on the fluted-tube outer volumetric diameter as follows:

$$h_{t,o} = \frac{Nu_i k}{D_{v,i}} \left(\frac{D_{v,i}}{D_{v,o}}\right) \quad (8)$$

The tube wall presents the following resistance to heat transfer:

$$R_w = \frac{D_{v,o}}{2k_w} \ln\left(\frac{D_{v,o}}{D_{v,i}}\right) \quad (9)$$

From the overall heat transfer coefficient and the resistances of the tube side and the tube wall, the heat transfer coefficient of the annulus was calculated from the following equation:

$$\frac{1}{U} = \frac{1}{1/h_{t,o} + R_w + 1/h_a} \quad (10)$$

Uncertainties in the reported values of  $Nu$  were estimated using the compounding-of-errors technique (Kline and McClintock, 1953). Uncertainties in the measurement of the volume of water, and the length and thickness of the tube, translated to a 0.05 mm error in  $D_{v,o}$ . The error in the annulus cross-sectional area (annulus A150T04) was calculated to be 5.16 mm<sup>2</sup>, and the error in the hydraulic diameter was 0.254 mm. The uncertainty in the calculation of  $Nu$  is composed of two major components, uncertainty in  $U$ , and uncertainty in deriving  $Nu$  from  $U$ , and the  $h_t$  predictions. The sensitivity equation for  $U$  in terms of the mass flow rate, fluid temperature rise, tube surface area, and the LMTD may be written as follows:

$$\epsilon_U^2 = \epsilon_m^2 + \epsilon_{\Delta T}^2 + \epsilon_A^2 + \epsilon_{\text{LMTD}}^2 \quad (11)$$

For a sample data point with  $\text{Re} = 19,095$ , with a temperature rise in the annulus of 9.28°C, and LMTD of 34.61°C (individual temperature measurement error of  $\pm 0.28^\circ\text{C}$ ), the uncertainty in  $U$  was estimated to be  $\pm 4.36$  percent. A simplified version of the relationship in between uncertainties in the overall resistance and the components is as follows:

$$\epsilon_{R(a)}^2 = \left[ \epsilon_{R(\text{tot})} \frac{R(\text{tot})}{R(a)} \right]^2 + \left[ \epsilon_{R(t)} \frac{R(t)}{R(a)} \right]^2 \quad (12)$$

where  $R$  is the resistance to heat transfer, and subscripts tot,  $t$ , and  $a$  refer to the overall, tube side, and annulus side, respectively. The ratio of  $R_a$  to  $R_t$  in this case was 2.8. This implies that  $R_{\text{tot}}/R_a$  is 3.8/2.8, or 1.36. Substituting into the equation above, we have:

$$\epsilon_{R(a)}^2 = 1.84\epsilon_{R(\text{tot})}^2 + \frac{1}{7.84}\epsilon_{R(t)}^2 \quad (13)$$

From the correlation by Ravigururajan and Bergles (1985), the uncertainty in the tube-side resistance may be conservatively estimated to be  $\pm 25$  percent. By combining this with the uncer-

tainty in  $U$  calculated above, the uncertainty in the annulus-side  $Nu$  is  $\pm 10.7$  percent.

## Results

Two smooth-tube annuli were tested to validate the test procedures and analysis techniques. The results are presented in Fig. 4. The literature values for these annuli were obtained from Kays and Leung (1963). These investigators present turbulent heat transfer data for  $Re > 5000$ . Nusselt numbers for  $Re < 5000$  are not available. Therefore, the data from Kays and Leung were correlated by the authors and the resulting equation was assumed also to apply for  $Re$  values between 3000 and 5000, with the recognition that the potential for error for  $Re < 5000$  would be high. The correlation used was as follows:

$$Nu_{a,s} = 0.025 Re^{0.78} Pr^{0.48} p^*^{-0.14} \quad (14)$$

where the subscript  $a, s$  refers to a smooth annulus. Error bands for this equation are also plotted in Fig. 4. The graphs show good correspondence between test results and the literature values.

A sample graph of the Nusselt numbers for the fluted annuli formed by tubes of different flute depths, keeping other geometric parameters almost constant, is shown in Fig. 5. (A matrix depicting the range of geometries covered in this study is presented in Table 1.) Corresponding smooth-annulus values from the literature are also plotted for reference. It should be noted that the fluid Prandtl number changed during the test due to changing inlet/outlet temperatures; therefore, part of the variation/scatter in  $Nu$  is due to this property variation. Figure 5 shows that the slope of the  $Nu$  versus  $Re$  graph is almost constant, even at the low  $Re$  ( $Re \approx 1000$ ) end. There is no transition region (in the range of tested  $Re$  values  $700 < Re < 40,000$ ) as would be expected for the smooth annuli. This was the case for all the annuli tested in this study. The Nusselt number for a smooth annulus, on the other hand, remains at the laminar value up to  $2090 < Re < 2775$  (Walker et al., 1957), the exact  $Re$  value depending on the annulus radius ratio. Thus, increases in Nusselt number of up to 20 are possible in the low  $Re$  region by using fluted annuli. In the turbulent regime, the enhancement is in the range  $1.5 < e_h < 4$ . The Nusselt number is higher for annuli with deeply fluted tubes, which is to be expected.

The effect of  $p^*$  on  $Nu$  (keeping other geometric parameters almost constant) is shown in Fig. 6. As  $p^*$  increases (fewer flutes

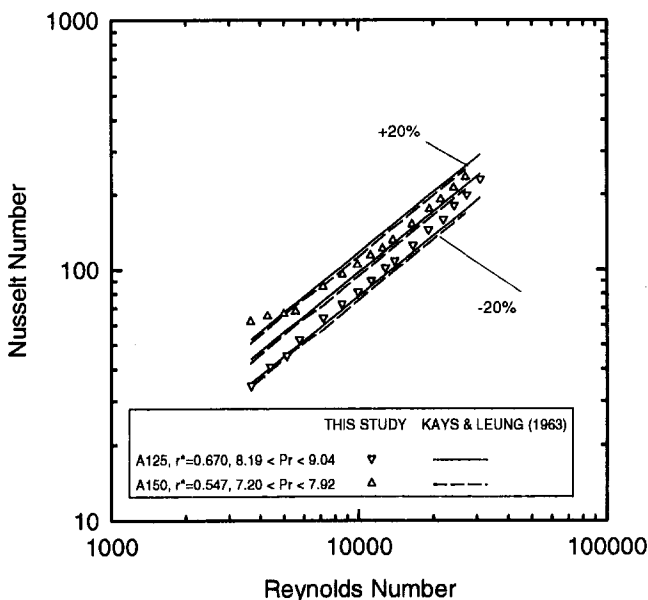


Fig. 4 Results for the confirmatory heat transfer tests

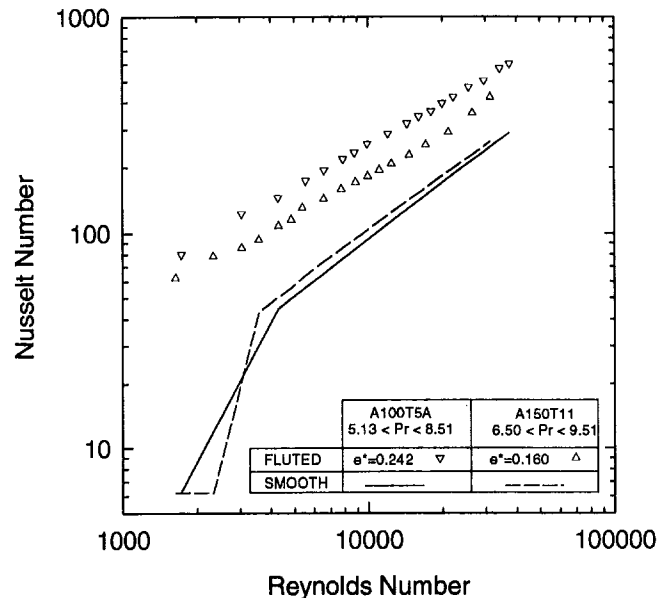


Fig. 5 Effect of flute depth on Nusselt number

per unit length),  $Nu$  decreases. Once again, this is to be expected from literature on similar geometries. Tubes with shallow, sparsely spaced flutes approach the smooth-tube limit; therefore,  $Nu$  is lowest for these tubes. Over the test matrix, it was found that even very gently fluted tubes help in establishing swirl flow, thereby enhancing heat transfer, especially for low Reynolds numbers.

Nusselt numbers for annuli formed by Tube 12 and three outer smooth tubes are shown in Fig. 7. For all values of  $r^*$ ,  $Nu_f$  is larger than  $Nu_s$ ; however,  $Nu_f$  is smaller for tighter annuli. In the graphs discussed above, a change in  $e^*$  or  $p^*$  simply reflects a change in the enhancement geometry; equal  $Re$  values even for different  $e^*$  or  $p^*$  imply comparison at the same bulk fluid velocities. However, in this case, different  $r^*$  values at the same  $Re$  correspond to different bulk fluid velocities due to the different annulus gaps. The same holds true for the transformation between  $Nu$  and the heat transfer coefficient. Therefore, even though  $Nu_f$  is smaller for large values of  $r^*$ , the heat transfer coefficient at the same bulk fluid flow rate is actually larger for these tight annuli, as would be expected. The apparently anomalous behavior displayed in Fig. 7 is, therefore, mainly due to the definition of  $Nu$ ,  $Re$ , and  $r^*$ . Also, heat transfer enhancement requires that the flow be not only disturbed (which increases friction), but also that the fluid and energy be transported away from the fluted surface to the bulk flow. For very tight annuli, swirl and recirculation might be occurring at the same global location, which increases the dissipative friction factor without necessarily transporting the energy downstream. In addition, for the same flute depth, the flow degenerates to flow over fully rough surfaces much more readily when the  $r^*$  value is large, because the ratio of flute depth to the annulus gap is higher for these cases.

## Data Correlation

Flow visualization and qualitative heat transfer testing (Garimella and Christensen, 1993) showed that the flow in this geometry is not a mere perturbation of smooth-annulus flow through surface roughness; therefore, law-of-the-wall similarity and other such approaches toward data correlation are neither justifiable on a fundamental basis, nor likely to yield successful correlations. The fluid does not flow exclusively in clearly demarcated trough and crest zones near the

Table 1 Range of geometric parameters investigated

A No	D <sub>s,o</sub>	D <sub>e,o</sub>	D <sub>b,o</sub>	D <sub>v,o</sub>	N	p	D <sub>o,j</sub>	e	e*	p*	θ*	r*
A200T01	19.05	18.80	11.23	12.59	3	13.25	47.50	3.785	0.301	1.052	0.498	0.265
A150T01	19.05	18.80	11.23	12.59	3	13.25	34.80	3.785	0.301	1.052	0.498	0.362
A125T01	19.05	18.80	11.23	12.59	3	13.25	28.45	3.785	0.301	1.052	0.498	0.443
A200T02	19.05	19.81	15.49	16.24	5	6.22	47.50	2.159	0.133	0.383	0.652	0.342
A150T02	19.05	19.81	15.49	16.24	5	6.22	34.80	2.159	0.133	0.383	0.652	0.467
A125T02	19.05	19.81	15.49	16.24	5	6.22	28.45	2.159	0.133	0.383	0.652	0.571
A200T04	19.05	21.08	13.97	14.75	3	13.25	47.50	3.556	0.241	0.899	0.548	0.310
A150T04	19.05	21.08	13.97	14.75	3	13.25	34.80	3.556	0.241	0.899	0.548	0.424
A125T04	19.05	21.08	13.97	14.75	3	13.25	28.45	3.556	0.241	0.899	0.548	0.518
A200T05	12.70	14.22	9.27	10.25	3	13.25	47.50	2.477	0.242	1.293	0.433	0.216
A100T5B	12.70	14.22	9.27	10.25	3	13.25	22.10	2.477	0.242	1.293	0.433	0.464
A100T5A	12.70	14.22	9.27	10.25	3	13.25	22.10	2.477	0.242	1.293	0.433	0.464
A150T06	15.88	17.15	11.13	11.99	3	11.72	34.80	3.010	0.251	0.978	0.522	0.345
A125T06	15.88	17.15	11.13	11.99	3	11.72	28.45	3.010	0.251	0.978	0.522	0.421
A100T06	15.88	17.15	11.13	11.99	3	11.72	22.10	3.010	0.251	0.978	0.522	0.543
A150T07	15.88	16.15	10.31	11.25	4	6.63	34.80	2.921	0.260	0.589	0.590	0.323
A125T07	15.88	16.15	10.31	11.25	4	6.63	28.45	2.921	0.260	0.589	0.590	0.395
A100T07	15.88	16.15	10.31	11.25	4	6.63	22.10	2.921	0.260	0.589	0.590	0.509
A200T08	25.40	26.67	19.05	20.38	4	15.24	47.50	3.810	0.187	0.748	0.516	0.429
A150T08	25.40	26.67	19.05	20.38	4	15.24	34.80	3.810	0.187	0.748	0.516	0.586
A150T09	15.88	16.64	11.68	12.59	4	8.24	34.80	2.477	0.197	0.654	0.558	0.362
A125T09	15.88	16.64	11.68	12.59	4	8.24	28.45	2.477	0.197	0.654	0.558	0.443
A100T09	15.88	16.64	11.68	12.59	4	8.24	22.10	2.477	0.197	0.654	0.558	0.570
A125T10	12.70	12.83	8.89	9.60	4	6.10	28.45	1.969	0.205	0.635	0.567	0.337
A100T10	12.70	12.83	8.89	9.60	4	6.10	22.10	1.969	0.205	0.635	0.567	0.434
A200T11	19.05	21.72	16.26	17.10	3	23.45	47.50	2.731	0.160	1.371	0.415	0.360
A150T11	19.05	21.72	16.26	17.10	3	23.45	34.80	2.731	0.160	1.371	0.415	0.491
A125T11	19.05	21.72	16.26	17.10	3	23.45	28.45	2.731	0.160	1.371	0.415	0.601
A200T12	19.05	19.94	16.38	17.17	4	15.24	47.50	1.778	0.104	0.888	0.461	0.361
A150T12	19.05	19.94	16.38	17.17	4	15.24	34.80	1.778	0.104	0.888	0.461	0.493
A125T12	19.05	19.94	16.38	17.17	4	15.24	28.45	1.778	0.104	0.888	0.461	0.604
A200T13	19.05	28.07	15.62	16.20	1	60.96	47.50	6.223	0.384	3.762	0.443	0.341
A150T13	19.05	28.07	15.62	16.20	1	60.96	34.80	6.223	0.384	3.762	0.443	0.466
A200T14	19.05	24.38	15.49	16.91	2	43.54	47.50	4.445	0.263	2.575	0.349	0.356
A150T14	19.05	24.38	15.49	16.91	2	43.54	34.80	4.445	0.263	2.575	0.349	0.486
A125T14	19.05	24.38	15.49	16.91	2	43.54	28.45	4.445	0.263	2.575	0.349	0.594
A200T15	19.05	25.40	17.40	18.16	1	121.9	47.50	4.001	0.220	6.714	0.279	0.382
A150T15	19.05	25.40	17.40	18.16	1	121.9	34.80	4.001	0.220	6.714	0.279	0.522
Min Val	12.70	12.83	8.89	9.60	1	6.10	22.10	1.778	0.104	0.383	0.279	0.216
Max Val	25.40	28.07	19.05	20.38	5	121.9	47.50	6.223	0.384	6.714	0.652	0.604
Avg Val	17.80	19.88	13.57	14.51	3	22.97	34.46	3.158	0.222	1.467	0.492	0.437

Annulus A\*\*\*T\*\* refers to the smooth outer tube diameter A\*\*\* and fluted inner tube number T\*\*; e.g., A200T15 refers to an annulus with outer smooth tube O.D. = 2.00" (50.8 mm) and inner fluted tube number 15.

wall and a purely axial flow away from the wall. Fluid flow occurs in a spiral pattern at an angle to the tube axis *different from the flute helix angle*. Moreover, flow that begins in the trough does not continue in the same trough for any appreciable distance. It alternately crosses over between the trough and the crest as it flows spirally in the annulus. Some previous investigations (Ravigururajan and Bergles, 1985) of spirally enhanced geometries have used a statistical approach to correlate friction factors and Nusselt numbers, which appears warranted in the present situation.

In correlating heat transfer data for smooth tubes, several investigators have used an equation that incorporates the corresponding friction factor. One such example is the Petukhov and Popov (1963) correlation. Because Nusselt numbers for the fluted annuli showed a departure from laminar behavior at Reynolds numbers as low as 700, it was assumed that such an approach would be applicable for 700 < Re < 40000, with a few modifications. The following fluted annulus turbulent friction factor correlation developed in the first part of this study by Garmella and Christensen (1995) was used for correlation of Nusselt number:

$$f_f = 4 \left[ 1.7372 \ln \left( \frac{Re}{1.964 \ln Re - 3.8215} \right) \right]^{-2} \times (1 + 0.0925r^*)e_f \quad (15)$$

where  $e_f$  is the fluted annulus friction enhancement function:

$$e_f = (1 + 222 Re^{0.09} e^{*2.40} p^{*-0.49} \theta^{*-0.38} r^{*2.22}) \quad (16)$$

Modifying terms that are functions of Re,  $e^*$ ,  $p^*$ ,  $\theta^*$ , and  $r^*$  were incorporated as multipliers to account for the fact that using the fluted friction factor in the equation might not, by itself, capture all the heat transfer phenomena in fluted annuli. These modifiers account for the difference in enhancement of friction factor and the enhancement of Nusselt number as discussed above in terms of the flow mechanisms. The resulting correlation for  $Nu_f$  was as follows:

$$Nu_f = \left[ \frac{(f_f/8) Re Pr}{1 + 9.77 \sqrt{f_f/8} (Pr^{2/3} - 1)} \right] \times (Re^{-0.20} e^{*-0.32} p^{*-0.28} r^{*-1.64}) \quad (17)$$

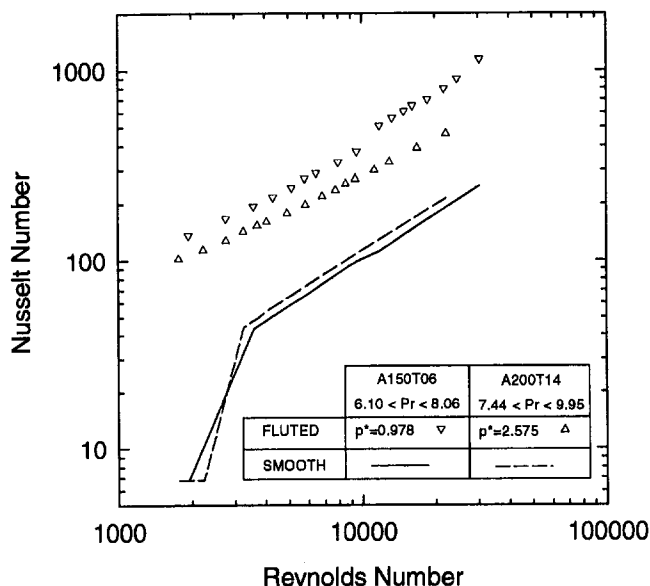


Fig. 6 Effect of flute pitch on Nusselt number

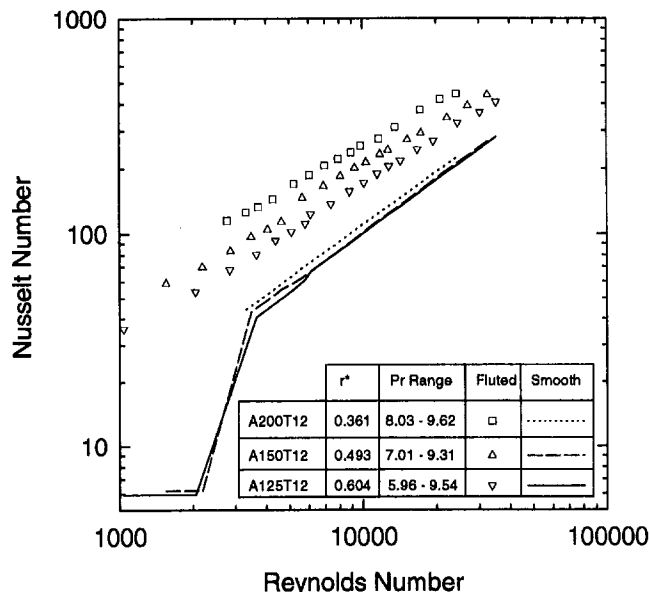


Fig. 7 Effect of annulus radius ratio on Nusselt number

A comparison of the measured Nusselt numbers and the values predicted by this equation is presented in Fig. 8. This correlation predicts 84 percent of the 642 measured Nusselt numbers within  $\pm 20$  percent. The correlation is valid for the following range of parameters:

$$0.104 < e^* < 0.384$$

$$0.383 < p^* < 6.714$$

$$0.279 < \theta^* < 0.652$$

$$0.216 < r^* < 0.604$$

$$700 < Re < 40,000$$

$$4.37 < Pr < 10.31$$

### Comparison With Previous Studies

Nusselt numbers for fluted annuli were reported above, and correlations were developed to predict them in terms of flow and geometry-related variables. Because the enhanced annulus has received no attention in the past, direct quantitative comparisons are not feasible. However, results from the present study, especially those related to flow patterns, transitions, and enhancements over smooth geometries can be qualitatively compared with previous work.

In the present study, it was shown that the graphs of Nu versus Re maintain a constant slope to Re values as low as 700, indicating a departure from laminar behavior at these low Re values. This is consistent with the earlier work by Garimella and Christensen (1993, 1995), who used friction factor data, flow visualization, and fluted-tube surface-temperature variations to demonstrate that transition occurred in the range  $300 < Re < 1000$ . For a smooth annulus, transition is initiated in the range  $2090 < Re_{crit,L} < 2775$ , and the flow becomes fully turbulent in the range  $2960 < Re_{crit,U} < 3300$  (Walker et al., 1957). Thus, using a fluted inner tube causes transition to be initiated at much lower Re values than for smooth annuli. Similar observations were made by Watkinson et al. (1975b) for tubes with spiral internal fins. They reported that transition typically occurred in the range  $250 < Re < 1500$ .

Nusselt numbers for  $Re < 3300$  were found to be between 4 and 20 times the smooth annulus values. In the turbulent regime, Nusselt number increases ( $e_h$ ) of between 1.1 and 4.0 were observed. The enhancement in the turbulent regime decreased with

an increase in Re. The Nusselt number enhancement was higher for larger values of  $e^*$ , but decreased with an increase in  $p^*$  or  $r^*$ . Some similarities exist between these results and the literature for spirally enhanced tubes. Watkinson et al. (1973, 1975a, 1975b) reported  $e_h$  values in the range 1.15 to 1.95 for turbulent flow of air and water in high-spiral finned tubes, and found that  $e_h$  was high for low values of  $p^*$  and for relatively lower Re values. In laminar flow, they obtained heat transfer enhancements of 8 to 224 percent and concluded that spiralling caused a stronger effect in laminar flow than in turbulent flow. Marto et al. (1979) obtained  $e_h$  values between 1.6 and 5.1, with a similar geometric dependence ( $e_h$  higher for low  $p^*$  and high  $e^*$ ). Bergles (1980) reported a 200 percent increase for laminar flow, and up to a 400 percent increase for the turbulent case. The survey by Garimella et al. (1988) showed that turbulent  $e_h$  values were between 1 and 3.5 for a wide variety of spirally enhanced ge-

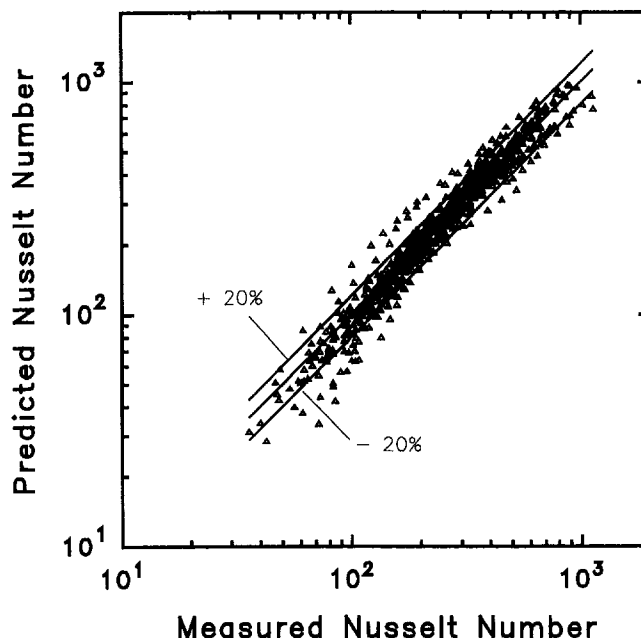


Fig. 8 Nusselt number correlation

ometries. The present study is in complete agreement with these results.

## Conclusions

Heat transfer in fluted-tube annuli for the Reynolds number range  $700 < Re < 40,000$  was investigated in this study. A wide variation in all the relevant geometric parameters was achieved. Qualitative insights gained from flow-visualization tests and local-temperature-variation measurements were used to explain the heat transfer data. Correlations were developed for Nusselt numbers using the measured data and postulated flow mechanisms. The effects of geometry and flow-related variables were modeled. The results of this study are in general agreement with the limited literature in this area. This study represents the first comprehensive investigation, with justification on a hydrodynamic basis, of enhancement characteristics of a wide variety of spirally fluted annuli. The study focused on the annulus side, which has been ignored by most investigators. The most significant finding of the present study is that in the *low Re range*, using fluted inner tubes in an annulus causes enhancements in heat transfer that are up to seven times greater than the corresponding increase in friction factor. Specifically:

- Nusselt numbers in spirally fluted annuli are between 4 and 20 times higher than the corresponding smooth-annulus values in laminar flow due to the induced swirl flow. For turbulent flow, the enhancement is between 1.1 and 4.0.
- The fluted annulus Nusselt number increases with an increase in flute depth, and with a decrease in flute pitch and annulus radius ratio.
- Turbulent behavior was exhibited for  $Re$  values as low as 700.
- A Nusselt number correlation was developed in terms of the fluted annulus friction factor and geometric parameters. This correlation predicted 84 percent of the 642 data points within  $\pm 20$  percent.

## Acknowledgments

The research reported in this paper was supported by the Gas Research Institute, Chicago, IL. The fluted tubes were supplied by  $\Delta T$  Ltd. of Tulsa, OK.

## References

- Bergles, A. E., 1980, "Heat Transfer Characteristics of Turbotec Tubing," Heat Transfer Laboratory Report HTL-24 ISU-ERI-Ames-81018, Iowa State University, Ames, IA.
- Garimella, S., Chandrachood, V., Christensen, R. N., and Richards, D. E., 1988, "Investigation of Heat Transfer and Pressure Drop Augmentation for Turbulent Flow in Spirally Enhanced Tubes," *ASHRAE Transactions*, Vol. 94, Part 2, pp. 1119–1131.
- Garimella, S., 1990, "Experimental Investigation of Heat Transfer and Pressure Drop Characteristics of Annuli With Spirally Fluted Inner Tubes," Ph.D. Dissertation, The Ohio State University, Columbus, OH.
- Garimella, S., and Christensen, R. N., 1993, "Experimental Investigation of Fluid Flow Mechanisms in Annuli With Spirally Fluted Inner Tubes," *ASHRAE Transactions*, Vol. 99, Part 1, pp. 1205–1216.
- Garimella, S., and Christensen, R. N., 1995, "Heat Transfer and Pressure Drop Characteristics of Spirally Fluted Annuli: Part I—Hydrodynamics," *ASME JOURNAL OF HEAT TRANSFER*, Vol. 117, this issue, pp. 54–60.
- Kays, W. M., and Leung, E. Y., 1963, "Heat Transfer in Annular Passages: Hydrodynamically Developed Flow With Arbitrarily Prescribed Heat Flux," *Int. J. Heat Mass Transfer*, Vol. 6, pp. 537–557.
- Kline, S. J., and McClintock, 1953, "Describing Uncertainties in Single-Sample Experiments," *Mechanical Engineering*, Vol. 75, Jan., pp. 3–8.
- Marto, P. J., Reilly, R. J., and Fenner, J. H., 1979, "An Experimental Comparison of Enhanced Heat Transfer Condenser Tubing," in: *Advances in Enhanced Heat Transfer*, ASME, New York, pp. 1–9.
- Petukhov, B. S., 1970, "Heat Transfer and Friction in Turbulent Pipe Flow With Variable Physical Properties," in: *Advances in Heat Transfer*, T. F. Irvine and J. P. Hartnett, Vol. 6, Academic Press, New York, pp. 503–564.
- Petukhov, B. S., and Popov, V. N., 1963, "Theoretical Calculation of Heat Exchange and Frictional Resistance in Turbulent Flow in Tubes of an Incompressible Fluid With Variable Physical Properties," *High Temperature*, Vol. 1, pp. 69–83.
- Ravigururajan, T. S., and Bergles, A. E., 1985, "General Correlations for Pressure Drop and Heat Transfer for Single-Phase Turbulent Flow in Internally Ribbed Tubes," in: *Augmentation of Heat Transfer in Energy Systems*, ASME HTD-Vol. 52, pp. 9–20.
- Walker, J. E., Whan, G. A., and Rothfus, R. R., 1957, "Fluid Friction in Non-circular Ducts," *AIChE Journal*, Vol. 3, No. 4, pp. 484–489.
- Watkinson, A. P., Miletta, D. L., and Tarassoff, P., 1973, "Turbulent Heat Transfer and Pressure Drop in Internally Finned Tubes," *AIChE Symposium Series*, Vol. 69, No. 131, pp. 94–103.
- Watkinson, A. P., Miletta, D. L., and Kubanek, G. R., 1975a, "Heat Transfer and Pressure Drop of Forge-Fin Tubes in Turbulent Air Flow," *Proceedings of the ASHRAE Semi-Annual Meeting*, ASHRAE, New York, Vol. 81, Part 1, pp. 330–349.
- Watkinson, A. P., Miletta, D. L., and Kubanek, G. R., 1975b, "Heat Transfer and Pressure Drop of Internally Finned Tubes in Laminar Oil Flow," *Proceedings of the AIChE-ASME Heat Transfer Conference*, ASME, New York, Paper No. 75-HT-41.

# Heat Transfer Coefficients in an Orthogonally Rotating Duct With Turbulators

**Shou-Shing Hsieh**

Professor and Chairman,  
Mem. ASME

**Ying-Jong Hong**

Former Graduate Student.

Department of Mechanical Engineering,  
National Sun Yat-Sen University,  
Kaohsiung, Taiwan, 80424

*Experiments were conducted to determine the influence of rotation on local heat transfer coefficient for the turbulent flow in a short square duct ( $L/D_H = 15$ ) with a pair of opposite rib-roughened walls. The ribs are configured in an in-line arrangement with an attack angle of 90 deg to the main flow. The coolant used was air with the flow direction in the radially outward direction. The Reynolds numbers ranged from 5000 to 25,000; the rib pitch-to-height ratio was 5; and the rib height-to-hydraulic diameter ratio was kept at a value of 0.20. The rotation number range was 0 to 0.5. Local Nusselt number variations along the duct were determined over the trailing and leading surfaces. In addition, local heat transfer measurements on all sides of a typical rib as well as on a typical exposed base surface between two consecutive ribs in a fully developed region were conducted at various rotational speeds. It is shown that the Coriolis acceleration tends to improve the heat transfer due to the presence of strong secondary flow. Centripetal buoyancy is shown to influence the heat transfer response with heat transfer being suppressed on both leading and trailing surfaces as the wall-to-coolant temperature difference is increased with other controlling parameters hold constant. Results are also compared with previous investigations. It was found that the results agree very well with those reported by other works in this field.*

## Introduction

In modern gas turbine airfoil designs, increased speeds, pressures, and temperatures are used to increase thrust/weight ratios and to reduce the specific fuel consumption. As a result, the turbine blades are subjected to increased heating loads in addition to increased levels of stress. Internal convective cooling is usually required to reduce the blade metal temperatures and thereby increase the durability of the blade. The heat transfer from the blade surface to the internal cooling air is significantly enhanced when the internal passages are roughened with ribs located at discrete positions along the passage wall. Geometric parameters such as passage aspect ratio, rib height-to-hydraulic diameter, pitch-to-height ratio, angle of attack, and the manner in which the ribs are positioned with respect to each other have pronounced effects on both local and overall heat transfer coefficients.

Experimental results on fully developed turbulent flow for the stationary case have been widely reported for a variety of geometric variations. Interested readers are referred to the work done by Burggraf (1970), Han et al. (1985), Metzger et al. (1987), Hsieh and Hong (1989), and Hong and Hsieh (1993). However, in actual operating conditions, the rotor blade rotates at high speeds. In the presence of rotation, the Coriolis and centripetal accelerations generate secondary flows that, especially in a rib-roughened passage of high blockage ratio, can change the flow structure and heat transfer behavior significantly. In addition to those pertinent geometric parameters for the stationary case mentioned above, the following parameters play an important role in the study of an orthogonally rotating test section: Rotation number,  $Ro$ , rotational Reynolds number,  $Re_\Omega$ , and rotational Rayleigh number,  $Ra_\Omega$ . Results of several investigations have been reported for rotating passages with smooth walls. Heat transfer enhancement was studied with the use of rib turbulators in the stationary case but it has not been treated in the rotating system before 1990. It is only in recent years that literature pertinent to

this type of problem has begun to surface, for example, Taslim et al. (1991a, 1991b).

The phenomena of the Coriolis force induced secondary flow have prompted many investigators to study the flow field generated in unheated, rotating circular and rectangular passages without consideration of the interaction of the Coriolis and centripetal buoyancy force. This topic has been studied in many investigations, e.g., the analytical works by Hart (1971), Moore (1967) and Rothe and Johnston (1979); and the experimental works by Wagner and Velkoff (1972) and Johnston et al. (1972). These investigators have documented strong secondary flows and have identified aspects of flow stability that produce streamwise-oriented, vortex-like structures in the flow of rotating radial passages. Recently, Morris and Ayhan (1979, 1982) advocated the significance of the centrifugal-buoyancy effect. Based on these experimental results, buoyancy forces would be expected to cause significant changes in the heat transfer in turbine blade coolant passages and be strongly dependent on flow direction (radially inward flow or radially outward flow).

The combined effects of Coriolis and buoyancy forces on heat transfer have been studied by a number of investigators. Heat transfer in rotating, smooth wall models has been investigated by Mori et al. (1971), Johnson (1978), Morris and Ayhan (1979, 1982), Lokai and Gunchenko (1979), Clifford et al. (1984), Iskakov and Trushin (1985), and Guidez (1989). Large increases and decreases in local heat transfer were found by some investigators to occur under certain conditions of rotation while other investigators showed lesser effects. Analysis of these results does not show consistent trends. The inconsistency of the previous results is attributed to differences in the measurement techniques, models, and test conditions.

Most recently, experiments were conducted by Wagner et al. (1992) to determine the effects of buoyancy and Coriolis forces on heat transfer in rotating supertine passages with trips normal to the flow. Their experiments were conducted with a large-scale, multipass, heat transfer model with both radially inward and outward flow. They found that the heat transfer rate on the trailing wall increases but the heat transfer rate decreases on the leading side of the passage near the inlet (i.e.,  $x/D < 6$ ) with increasing rotation number. Subsequently, Johnson et al. (1994) conducted experiments with trip strips skewed 45 deg to the flow direction.

Contributed by the Heat Transfer Division for publication in the JOURNAL OF HEAT TRANSFER. Manuscript received by the Heat Transfer Division December 1992; revision received March 1994. Keywords: Augmentation and Enhancement, Forced Convection, Turbines. Associate Technical Editor: R. J. Simoneau.



They found that the heat transfer with skewed trip strips is less sensitive to buoyancy than the heat transfer in models with either smooth walls or normal trip strips.

Table 1 lists the previous experimental investigations on heat transfer in channels with orthogonal mode rotation. One can find that studies in most of the previous works are concerned with circular pipes, and recent studies pertain to triangular (Clifford et al., 1984; Harasgama and Morris, 1988; Wagner et al., 1991a, b), and rectangular (Guidez, 1989; Soong et al. 1991) ducts. In practice the utilizations of the circular, triangular, and rectangular ducts are all possible in a turbine blade. Because of the shape of the turbine airfoil, the internal cooling passages often possess triangular cross section in the leading edge, and square or rectangular in the midchord and trailing edge.

The objective of this study was to investigate the combined effects of rotation and rib roughness on the local heat transfer distribution in channels with two opposite rib-roughened walls in developing and fully developed regions for Reynolds number from 5000 to 25,000. A duct of aspect ratio  $AR = 1$  at rotational speeds up to 1000 rpm is studied. For the test channel, the aluminum ribs with a square cross section were glued periodically to the leading and trailing side walls so that the ribs on opposite walls were all parallel with an attack angle of 90 deg and in an in-line arrangement. The rib height-to-hydraulic diameter ratio ( $e/D_H$ ) was 0.20; the rib pitch-to-height ratio ( $p/e$ ) was 5.0. Air was the working fluid, and the air flow was radially outward in the test section. Two wall adiabatic and two wall constant heat flux were the boundary conditions. This arrangement is closer to the actual turbine blade since in multiple cooling passage blades there exists a large temperature gradient between the adjacent (trailing-wall and side-wall or leading-wall and side-wall). Results of the heat transfer coefficient distributions on the leading and trailing ribbed walls were presented and discussed. The physical limitations of the device result in  $e/D_H = 0.2$  and  $p/e = 5$  and only top and bottom walls were roughened and heated.

## Experimental Apparatus and Test Procedure

Measurements were carried out in an open-circuit low speed rotating wind tunnel. A schematic of the experimental apparatus is shown in Fig. 1. A 2 hp d-c motor is used to drive an overhung rotor arm via a toothed pulley. The constructional details of the test section is shown in Fig. 2. The test channel was constructed of two 5.0-mm-thick heated ribbed aluminum walls and two 5.0-mm-thick unheated plexiglass walls with 50.0-mm-thick fiberglass insulation covering the test section on all four sides to minimize heat losses to the environment. The active heated length of the test section was 300 mm. Since the test section with cross section of 20.0 mm  $\times$  20.0 mm corresponds to hydraulic diameter of 20.0 mm; this gave a nominal length/effective diameter

ratio of 15. The test section was located on the rotor arm so that the eccentricity of the midspan position was 300 mm. For the case of ribbed channel tests, the aluminum ribs of a square cross section were glued onto the leading and trailing plates of the foil-heated channel so that the rib turbulators on opposite walls were all parallel with a prescribed repeated distribution. For the test section, the location of the first rib from the test section inlet is 20.0 mm. The air used for the test fluid was blown through the test section via a rotating seal assembly in the radially outward direction with a 2 kW centrifugal blower. A 40.0-mm-dia pipe, equipped with a 36.0-mm-dia orifice plate ( $C_0 = 0.68$ ) was used to measure mass flow rate. After passing through the orifice plate, the air enters the plenum cylinder in the hollow shaft and it flows through the straightener fixed in the interior of the shaft to eliminate the initial swirl before entering the square duct. The Reynolds numbers based on the channel hydraulic diameter ( $D_H$ ) ranged from 5000 to 25,000.

Electrical power was supplied to the woven heaters for the entire test section through a pair of power slip-rings mounted on the main shaft; the power supplied is monitored on a "Cambridge" wattmeter. Each heater could be independently controlled by a variac transformer and provided a controllable constant heat flux for the entire test plate. The nearly constant heat flux experiment was conducted for the ribbed walls because of its simplicity of construction and ease of operation. After applying power to the test section, the time required for the loop to reach steady state (the variation of Nusselt number is less than 1 percent in 20 minutes) was between 50 and 60 minutes. A copper/constantan thermocouple (AWG40, T type) is centrally located at the inlet of the plenum space to measure the temperature of the inlet air. An insulated mixing chamber made of plexiglass is attached to the exit plane. A pair of staggered grids are installed in the chamber to mix the flow prior to venting to atmosphere. The bulk mean temperature of the cooling air at the outlet of the test channel was thus taken and calculated with two thermocouples inside the chamber.

Experimental data were taken on the trailing and leading surfaces of the test section in both rotating and stationary modes. Rotational speeds of 200, 400, 600, 800, and 1000 rpm were set either in the counterclockwise or clockwise direction shown in Fig. 2. The two rotational directions allowed data to be taken on both the trailing and leading surfaces of the test section.

Under a typical test case at fixed Reynolds number and rotational speed, but with varying heat transfer settings, it was possible to vary the rotational Rayleigh number systematically with other parameters kept to within 2 percent of the stated values.

The main rotor assembly comprising main shafting, rotor arm, and heated test section was mounted between two self-aligning

## Nomenclature

$A$  = projected area  
 $AR$  = aspect ratio =  $H/D$   
 $C_0$  = discharge coefficient  
 $C_p$  = specific heat  
 $D$  = width of channel  
 $D_H$  = hydraulic diameter  
 $e$  = rib height  
 $G$  = mass flow rate  
 $H$  = height of channel or midspan eccentricity  
 $h$  = heat transfer coefficient  
 $k_f$  = thermal conductivity of air at film temperature  
 $L$  = test channel length  
 $Nu$  = Nusselt number =  $hD_H/k_f$   
 $\bar{Nu}$  = mean Nusselt number

$Nu_{r,s}$  = local Nusselt number of rotating smooth duct  
 $Nu_{r,r}$  = local Nusselt number of stationary roughened duct  
 $p$  = pitch  
 $Pe$  = Peclet number =  $Re_H Pr$   
 $Pr$  = Prandtl number =  $\nu/\alpha$   
 $Q_t$  = the total power input to the test section  
 $Ra_{\Omega}$  = rotational Rayleigh number =  $H\Omega^2\beta\Delta T D_H^2 Pr/\nu^2$   
 $Re_H$  = Reynolds number based on hydraulic diameter =  $UD_H/\nu$   
 $Re_{\Omega}$  = rotational Reynolds number =  $\Omega D_H^2/\nu$   
 $Ro$  = rotation number =  $Re_{\Omega}/Re_H$

$T$  = local temperature  
 $T_{av}$  = bulk mean air temperature  
 $T_{bx}$  = local bulk mean air temperature  
 $T_f$  = film temperature =  $(T_w + T_{bx})/2$   
 $T_w$  = wall temperature  
 $T_0$  = inlet temperature  
 $T_{\infty}$  = ambient temperature  
 $\Delta T$  = temperature difference  
 $U_m$  = mean velocity of the working fluid  
 $W$  = width of channel  
 $\alpha$  = thermal diffusivity =  $k/\rho C_p$   
 $\beta$  = volume expansion coefficient  
 $\nu$  = viscosity  
 $\rho$  = density of working fluid  
 $\Omega$  = rotational speed

**Table 1 Existing data for experimental investigations on cooling channels with orthogonal mode rotation**

Investigators	Physical Geometry	Boundary Condition	Rotation Number	Reynolds Number	Smooth/Roughened Channel	Developing / Fully Developed	Parameters Investigated	Flow Direction	Local/Mean Nu
Mori et al. (1971)	Straight Circular Tube	UWT	0-0.5	1,000 10,800	Smooth Channel	FD	Re, Ro, Re <sub>Ω</sub>	Radially Outward Flow	Mean
Lokai and Limanskii(1975)	Straight Circular Tube	UHF	0-0.03	9,000 40,000	Smooth Channel	FD	Re, Ro, L/d	Radially Outward Flow	Mean
Metzger and Stan (1977)	Straight Circular Tube	UWT	0-0.5	700 3,100	Smooth Channel	D/FD	Re, Ro, Re <sub>Ω</sub> L/d	Radially Outward Flow	Mean
Morris and Ayhan (1979)	Straight Circular Tube	UHF	0-0.23	5,000 15,000	Smooth Channel	D/FD	Re, Re <sub>Ω</sub> , Ra <sub>Ω</sub> , ε, L/d	Radially Outward Flow	Local/ Mean
Morris and Ayhan (1982)	Straight Circular Tube	UHF	0-0.23	5,000 15,000	Smooth Channel	D/FD	Re, Re <sub>Ω</sub> , Ra <sub>Ω</sub> , ε, L/d	Radially Outward Flow	Local/ Mean
Clifford et al. (1984)	Triangular Duct	UHF	0-0.19	6,800 38,000	Smooth Channel	D/FD	Re, Re <sub>Ω</sub> , Ra <sub>Ω</sub>	Radially Outward Flow	Local/ Mean
Harasgama and Morris(1988)	Circular, Triangular and Square Duct	UHF	0-0.103	7,000 25,000	Smooth Channel	D/FD	Re, Ro, Re <sub>Ω</sub> , Ra <sub>Ω</sub> , ε	Radially Inward/ Outward Flow	Local/ Mean
Guidez (1989)	Wide Rectangular Duct	UHF	0-0.40	17,000 41,000	Smooth Channel	D	Re, Ro, Re <sub>Ω</sub>	Radially Outward Flow	Local
Taslim et al. (1991a)	Square and Wide Rectangular Ducts	UHF	0-0.10	15,000 50,000	Roughened Channel (Staggered)	D/FD	Re, Ro, ε/D <sub>H</sub> , Re <sub>Ω</sub>	Radially Outward Flow	Local
Taslim et al. (1991b)	Square and Wide Rectangular Ducts	UHF	0-0.30	15,000 50,000	Roughened Channel (criss-cross)	FD	Re, Ro, ε/D <sub>H</sub> , Re <sub>Ω</sub> , γ	Radially Outward Flow	Local
Morris and Ghavami-Nasr(1991)	Narrow Rectangular Duct	UHF	0-0.50	10,000 25,000	Smooth Channel	D/FD	Re, Ro, Ra <sub>Ω</sub> z/d	Radially Outward Flow	Local
Soong et al. (1991)	Square and Rectangular Duct	UWT	0-0.43	700 20,000	Smooth Channel	FD	Re, Re <sub>Ω</sub> , Ra <sub>Ω</sub> γ	Radially Outward Flow	Mean
Wagner et al. (1991a)	Square Duct	UWT	0-0.48	12,500 50,000	Smooth Channel	FD	Re, Ro, Δρ/p R/D, Gr/Re <sup>2</sup>	Radially Outward Flow	Local
Wagner et al. (1991b)	Square Duct	UWT	0-0.48	50,000 500,000	Smooth Serpentine Channel	D/FD	Re, Ro, Δρ/p R/D, Gr/Re <sup>2</sup>	Radially Inward/ Outward Flow	Local
Wagner et al. (1991c)	Square Duct	UWT	0-0.35	25,000	Roughened(normal) Serpentine Channel	D/FD	Re, Ro, Δρ/p R/D, Gr/Re <sup>2</sup>	Radially Inward/ Outward Flow	Local
Johnson et al. (1992)	Square Duct	UWT	0-0.35	12,500 75,000	Roughened(skew) Serpentine Channel	D/FD	Re, Ro, Δρ/p R/D, Gr/Re <sup>2</sup>	Radially Inward/ Outward Flow	Local
Yang et al. (1992)	Square Duct	UHF	0-0.042	44,000 110,000	Smooth Serpentine Channel	D/FD	Re, Ro, Ra <sub>Ω</sub>	Radially Inward/ Outward Flow	Local
Present Study	Square Duct	UHF	0-0.50	5,000 25,000	Roughened Channel (in-line)	D/FD	Re, Ro, Re <sub>Ω</sub> , Ra <sub>Ω</sub>	Radially Outward Flow	Local

bearings and it driven by means of a controlled d-c motor. The rotational speed can be detected by a "Conch" photo-electric tachometer and adjusted by a feedback controller to reach the present speed. A total of 28 AWG40 T-type thermocouples were placed in strategic locations to measure the local wall temperature. Fourteen thermocouples are installed along the axial centerlines of the ribbed walls to determine the streamwise wall tem-

perature distributions, which is found adequate after comparing with those of Han et al. (1985). Fourteen other thermocouples were positioned along the axial centerlines of one typical rib surface as well as along a typical exposed base surface between two consecutive ribs in the fully developed region. Detailed distributions of thermocouples are shown in Fig. 2. The thermocouple beads were carefully imbedded into the wall and then ground

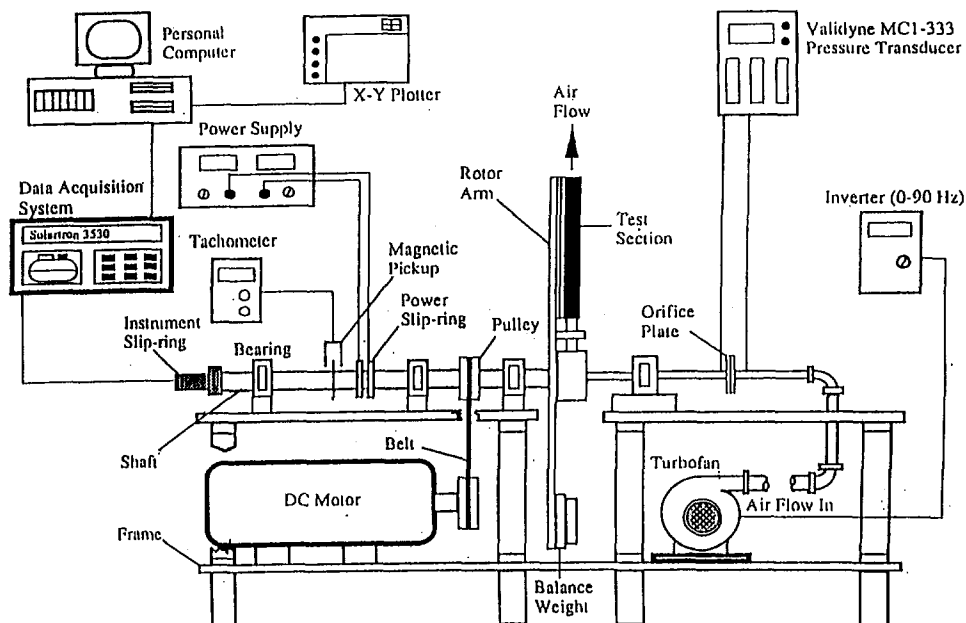


**Fig. 1 Schematic of experimental apparatus and instruments (side view)**

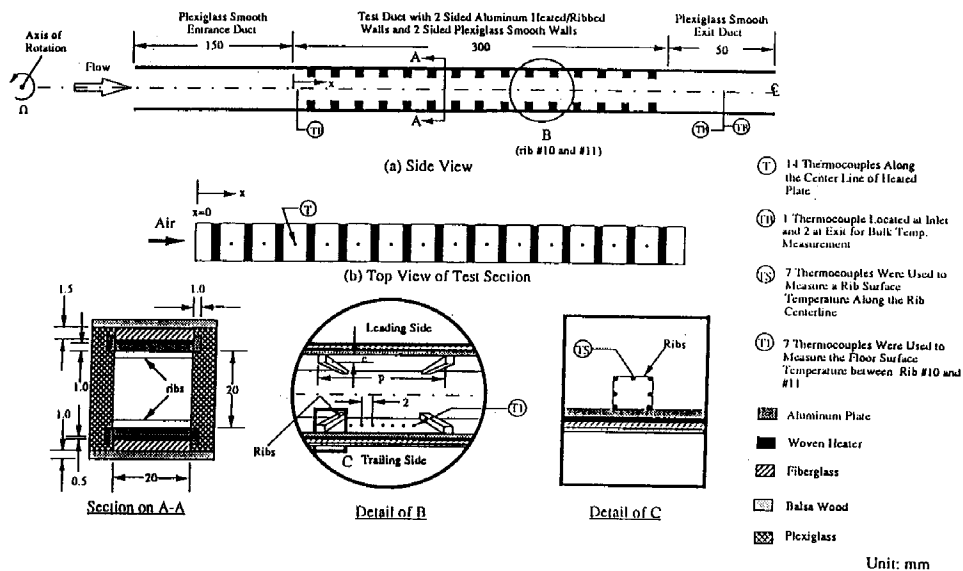


Fig. 2 Detailed thermocouple locations and dimensions of the test section (in-line type)

flat to ensure that they were underneath the surface. The positioning accuracy of the thermocouple bead was  $\pm 0.1$  mm. A Schlumberger Solartron 3530 Data Logger was interfaced with an IBM PC/AT for data acquisition. The temperature readings from the rotating test piece are transferred to the stationary recorder through an instrumentation slip-ring assembly attached at the end of the shaft. The slip-ring assembly has 18 rings; its permitted speed for continuous duty is 3000 rpm. Experimental data were written on magnetic disk storage for subsequent processing and analysis.

### Data Reduction

The major aim of the study was to measure experimentally the local heat transfer on the leading and trailing surfaces of this rotating square channel and to assess the effect of rotation on an otherwise ducted flow forced convection problem. Heat transfer was quantified using the customary Nusselt number. In order to determine the local Nusselt number, it is necessary to obtain the axial variation of heat flux from the channel wall and the locally prevailing difference between the wall temperature and the bulk mean temperature of the coolant. The local heat transfer coefficient was determined by dividing the local net heat input to the coolant by the projected heated surface area and the temperature difference between the local heated surface temperature and the calculated local bulk mean coolant temperature:

$$h(x) = Q_{\text{net}} / [A(T_w - T_{bx})] \quad (1)$$

where the local net heat flux ( $Q_{\text{net}}$ ) is the electrical power generated from the heaters, which is calculated from heating voltage and current measurements subtracting heat loss to the outside of the test channel. Heat loss measurements were obtained with no coolant flow and constant electrical power supplied under steady-state conditions with rotation, identical to the heat transfer  $Q_{\text{net}}$  experiments, but without coolant flow. The heat losses to the outside of the test channel ranged from 11 to 24 percent of the total heat supplied for stationary heat transfer levels. The local bulk mean air temperature,  $T_{bx}$ , used in Eq. (1) was calculated from an energy balance through each set of heated surfaces. The local bulk mean temperature was determined by marching along the test section and calculating the temperature rise due to the net heat addition to the coolant, which is defined as  $T_{bx} = T_0 + \Sigma Q_{\text{net}} / (GC_p)$ , where  $\Sigma Q_{\text{net}}$  is the summation of net heat given to air from the entrance to the considered cross section of the duct

along the downstream distance. Over the range of test conditions, the inlet bulk mean air temperature (room temperature) was kept between 27 and 30°C. One thing needs to be mentioned here that, since the aluminum plates were used as the test walls, the present results in the entrance region may suffer certain wall conduction problems even though the axial conduction effect was corrected in present study. Consequently, the results in this region are somewhere between "average" and "local" instead of local heat transfer coefficients.

The local values of the thermophysical properties of the testing fluid (i.e., air) were obtained at the local film temperature ( $T_f$ ),  $T_f = 0.5(T_w(x) + T_{bx})$ . Local heat transfer results are presented in terms of Nusselt numbers as

$$\text{Nu}(x) = h(x)D_H/k_f \quad (2)$$

where  $D_H$  is the hydraulic diameter,  $k_f$  is the thermal conductivity of air. It should be noted that the value of  $\text{Nu}(x)$  at the same cross section varies between the sidewalls of the flow passage (see, for example, Yang et al., 1992, and Wagner et al., 1991a, b). The leading and trailing walls have different flow conditions. It should be noted that heat transfer coefficient is measured on the turbulated wall, but the turbulators themselves are not covered by the heaters, and hence fin-type effects are not investigated.

### Uncertainty Analysis

A conservative estimate of the accuracy of the temperature measurement is  $\pm 0.5^\circ\text{C}$  (20/1 odds) due to the inaccuracies in the thermocouples, the data acquisition system, and the connections in the slip ring. The voltage was measured by a Hewlett Packard 3466A digital multimeter with a maximum uncertainty of  $\pm 1.2$  percent (20/1 odds). Current was measured by an AC ammeter with a maximum uncertainty of  $\pm 1.5$  percent (20/1 odds). This procedure resulted in a maximum uncertainty of  $\pm 2.7$  percent in the calculated power inputs.

The uncertainty for heat flux is found to be within 4.1 percent. The uncertainty associated with the length scale used in the data reduction was  $\pm 0.1$  mm (20/1 odds). The thermophysical properties of the air were assigned an uncertainty of  $\pm 3.0$  percent. It was found that, for the minimum flow rate, which was the worst case, the uncertainty for Reynolds number was about 6.2 percent. These uncertainties would result in the typical uncertainty of Nusselt number of about 8.5 percent for Reynolds number larger

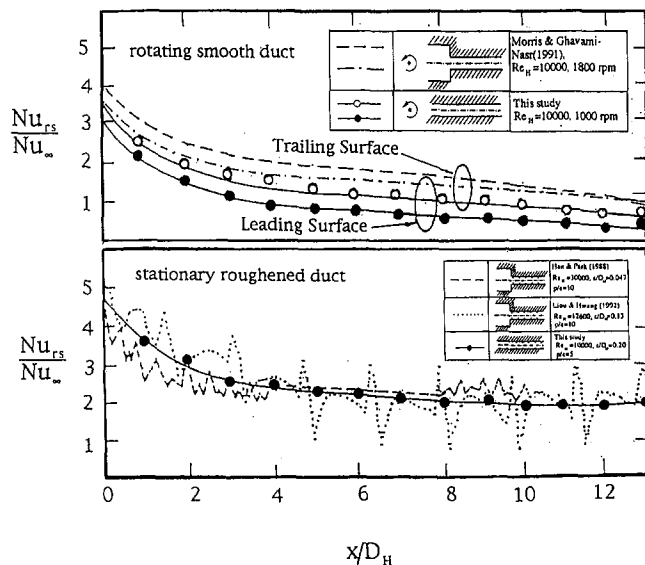


Fig. 3 Local Nusselt number ratio versus  $x/D_H$  in stationary roughened and rotating smooth ducts

than 10,000 using the uncertainties estimated procedure described by Kline and McClintock (1953) and modified by Moffat (1988). The maximum uncertainty, however, could be up to 23 percent for the lower heat transfer coefficient at the lowest Reynolds number tested ( $Re_H = 5,000$ ). The uncertainty of the Nusselt number (or heat transfer coefficient) is influenced mainly by the wall-to-bulk temperature difference and the net heat flux from each heater.

## Results and Discussion

The Nusselt number inside a rotating roughened channel is governed by the flow rate, rotational speed, wall-to-bulk mean temperature differences, aspect ratio, duct length, rib pitch-to-height ratio, rib height-to-hydraulic diameter ratio, streamwise distance from the inlet, and eccentricity. For a duct of fixed length, aspect ratio, rib pitch-to-height ratio, rib height-to-hydraulic diameter ratio, and eccentricity, the Nusselt number can be expressed as a function of  $Re_H$ ,  $x/D_H$ ,  $Ro$ ,  $Re_\Omega$ ,  $Ra_\Omega$ . In other words,

$$Nu = f(Re_H, x/D_H, Ro, Ra_\Omega) \quad (3)$$

where  $Ro = Re_\Omega/Re_H$  is the rotation number,  $Ra_\Omega = H\Omega^2\beta\Delta T D_H^2 Pr/\nu^2$  is the rotational Rayleigh number. In the present study the properties  $k$ ,  $\nu$ , and  $Pr$  are all assumed as constants due to the low wall-to-bulk mean temperature differences for the inlet to the outlet of the flow.

**Rotating Smooth and Stationary Roughened Duct.** Before initiating experiments with the rotating roughened channel, the local Nusselt numbers were determined for rotating smooth and stationary roughened ducts and compared with the results given in the relevant literature, as shown in Fig. 3. The local heat transfer results are presented as the streamwise distributions of the Nusselt number ratio,  $Nu_{rs}/Nu_\infty$  and  $Nu_{sr}/Nu_\infty$ , respectively. Data reported by Morris and Ghavami-Nasr (1991) were based on the local measurements of the flow in a rotating smooth channel with a sharp entrance. Han and Park (1988) and Liou and Hwang (1992) obtained results for a turbulent flow in a square roughened channel with a sharp entrance by using the thermocouple technique. In this study, both test ducts exhibit the effects of a thermal entrance region, i.e., decreasing  $Nu_0$  with increasing non-dimensional distance,  $x/D_H$ , from the entrance. In addition, it can also be seen from Fig. 3 that the results of Han and Park (1988)

and Liou and Hwang (1992) are slightly oscillatory in shape. This is due to the nature that the flow separates from the rib top wall when it passes a rib (which cause a peak in  $Nu$ ) and then reattaches to the wall in the interrib region (and this cause a local maximum value). Because of the limitation of the measurement channels through the slip-ring, the wall temperatures were measured only at the midway of the interrib region, such that the phenomena were not visible in this study. These (the results of rotating-smooth and stationary roughened duct) all confirmed that the processed data gave good agreement with previously published data. So, the results of stationary roughened duct can serve as the baseline data to evaluate the effects of rotation.

## Nusselt Number Distributions of Rotating Roughened Duct.

The distributions of the local Nusselt number of the rotating ribbed-duct flows at various rotational speeds along the length of the duct are presented in Figs. 4 and 5, respectively. In each figure, the local Nusselt numbers corresponding to a succession of axial stations  $x$  are plotted as a function of the dimensionless axial coordinate  $x/D_H$ . Results are presented for both trailing and leading surfaces. An overall examination of these figures reveals that the heat transfer coefficient distributions exhibit a definite trend with the highest value at the beginning of the test section and decrease monotonically with increasing downstream distance, eventually reaching a fully developed value ( $x/D_H \geq 6$ ) except for the case of  $Re_H = 5000$  with  $Re_\Omega$

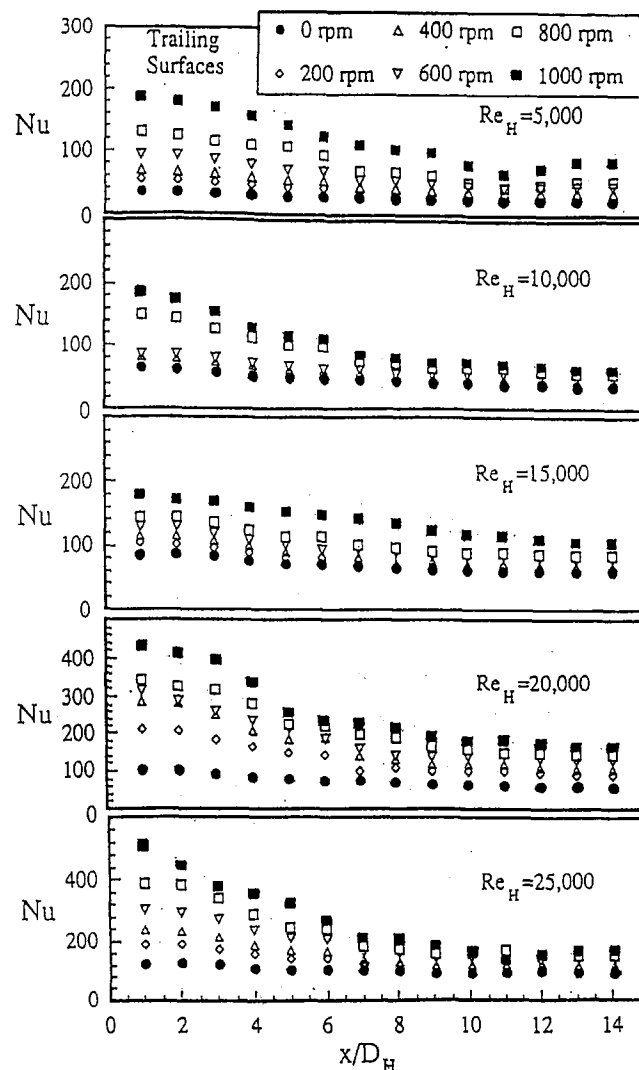


Fig. 4 Local heat transfer variation at different rotational speeds (trailing surfaces)

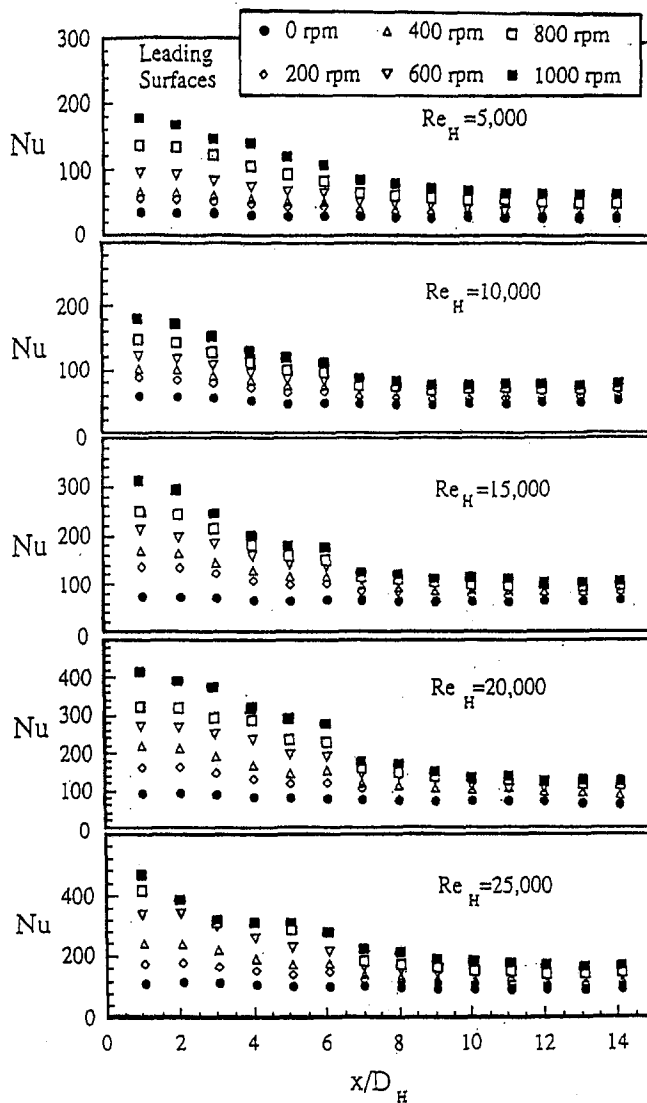


Fig. 5 Local heat transfer variations at different rotational speeds (leading surfaces)

= 1000 (it seems that there is no difference between the rotating and the stationary cases). Several jumps appear in some cases (e.g.,  $Re = 20,000$  and  $Re = 25,000$ ). These are perhaps due to uncertainty and inaccuracies in measurements. While the relatively large initial values of  $Nu$  are due to the large temperature gradients near the leading edge of the test duct inlet, the growth of thermal boundary layer and resulting decrease in temperature gradients is responsible for the subsequent lower values of  $Nu$ . It can be seen from Figs. 4 and 5 that an increase in  $Re_H$  and rotational speed (or  $Ro$ ) causes a significant increase in  $Nu$  for both trailing and leading surfaces. Furthermore, a comparison of Figs. 4 and 5 reveals that when the experiments were operated with rotation the heat transfer on the trailing surface of the duct can be significantly enhanced relative to the leading surface of the duct. This, of course, is consistent with a number of previously published smooth-duct works with other cross sections. This is due to the presence of a Coriolis-driven cross-stream secondary flow. Consequently, the flow pattern is reconstructed, which causes relatively cold working fluid from the central region to spiral onto the trailing surface, and thus stimulates enhanced cooling. Additionally, the coolant near the trailing surface of the channel is also believed to be influenced by the wall shear layers due to rotation. The large increase in the heat transfer from the trailing surface is attributed to a combination of these effects.

The lesser increases in the heat transfer coefficient on the leading surface are attributed, for the most part, to the cross-stream flow patterns as well as the stabilization of the near-wall flow on it (Johnston et al., 1972). The cross-stream flows cause heated, near-wall fluid from the trailing and sidewall surfaces to stay near the leading side of the cooling air passage resulting in lesser heat transfer augmentation. The net increases in the heat transfer coefficient are mainly owing to the large-scale development of the Coriolis generated secondary flow cells.

Figures 6 and 7 show the variation of local Nusselt numbers along the rib forward-facing side, top wall, backward-facing side and the floor surface between two consecutive ribs in the fully developed region (between rib #10 and #11). It can be seen from these figures that the values of  $Nu$  have a peak on the front convex corner of the rib, and monotonically increase along the streamwise direction on the floor, reaching a local maximum near the front concave corner of the downstream rib. These results are consistent with the behavior reported by Hong and Hsieh (1993) where the  $ple = 5.31$ . Previous studies of flow over repeated transverse ribs (e.g., Hsieh and Hong, 1989) indicate that for  $p/e > 6-8$  the separated shear layers produced by the ribs reattach on the floor between two adjacent ribs. The shear layer reattachment phenomena are unsteady in nature, and time-averaged observations in these studies have indicated that the floor reattach-

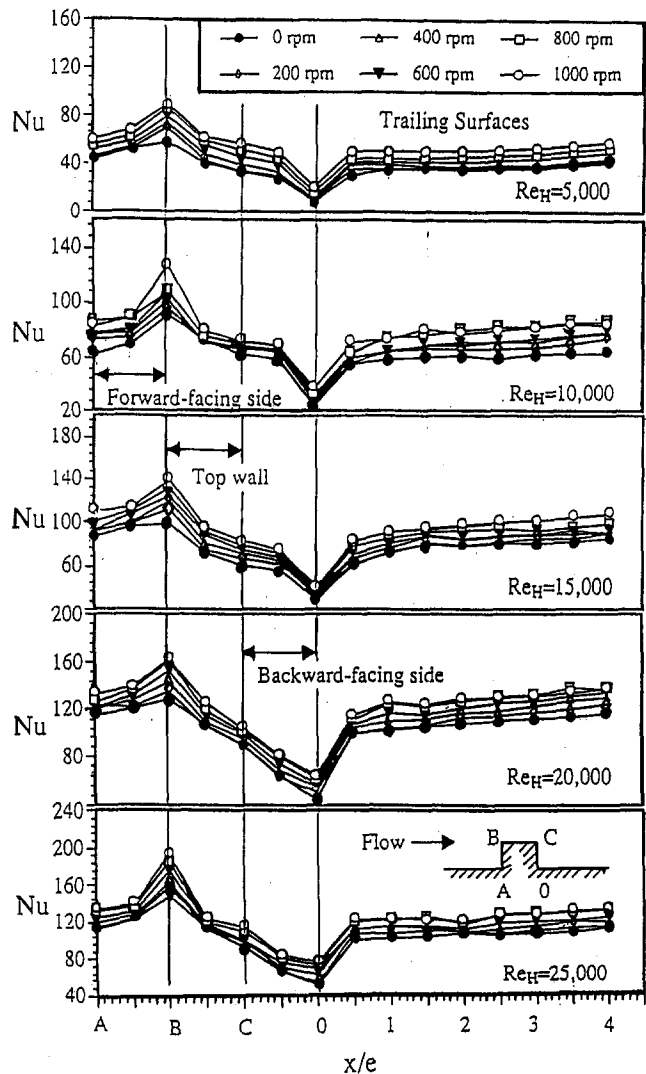


Fig. 6 Local Nusselt number distribution between two consecutive ribs for different rotational speeds at various Reynolds number (trailing surface)

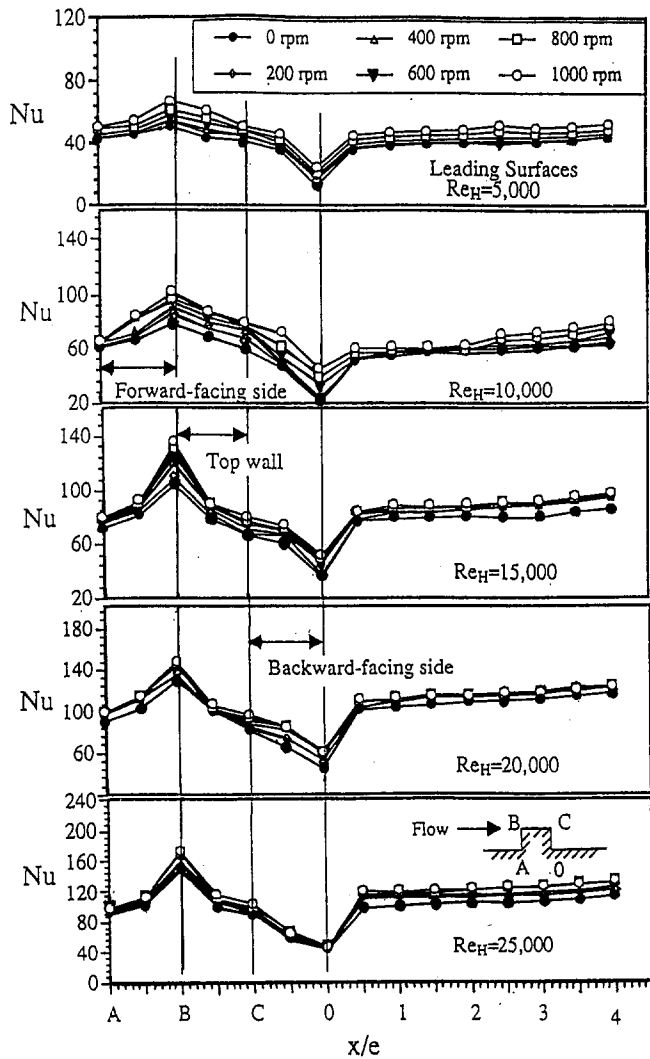


Fig. 7 Local Nusselt number distribution between two consecutive ribs for different rotational speeds at various Reynolds number (leading surface)

ment is typically located at 3 to 5 rib-heights downstream of the rib rear face. The high level of turbulence generated near the shear layer reattachment results in the local maximum of heat transfer in the region. The results of Taslim et al. (1991a) support this view. In contrast, for the case of  $p/e = 5$ , the previous studies indicate that the separated shear layer either just reattaches on the forward-facing side of downstream rib or skims over the cavity altogether. As a result, the near-wall region between two adjacent ribs is filled with a recirculating bubble, and the heat transfer displays characteristics shown in Figs. 6 and 7. In addition, the local maximum of  $Nu$  just ahead of the downstream rib may be attributable to the flow unsteadiness in the region. It can be seen that, from Figs. 6 and 7, there is no reattachment point between two adjacent ribs in the present configuration.

For a rotating duct, heat transfer from the rib surfaces themselves varies significantly between the different rib surfaces, as shown in Figs. 6 and 7. On the forward-facing side, the heat transfer mechanism involves shear layer impingement, at least near the top portion of the surface. On the backward-facing side wall, heat transfer generally decreases progressively from the rib convex corner to the rib concave corner. The recirculating flow region immediately adjacent to the backward-facing side wall is responsible for this heat transfer distribution. In both trailing and leading surfaces, at a fixed  $Ro$ , Nusselt number increases as Reynolds number increases. This is because higher Reynolds

numbers correspond to higher air mean velocity, which results in higher Nusselt number. When rotational speed is increased, the magnitude and width of the recirculation zone increase at the leading surface and decrease at the trailing surface. But, the strength of secondary flow increased with increasing rotational speed, which counterbalances the recirculation zone effect and hence, enhances the energy exchange between the roughened wall and the core flow. Therefore, the heat transfer coefficients for trailing and leading surfaces were continuously promoted comparing with those of stationary case.

**Reynolds Number Effect.** Based on the local heat transfer distributions, it is found that the local Nusselt number distributions become flat after  $x/D_H > 6.0$ . Therefore, the heat transfer in the region with  $x/D_H > 6.0$  was used to provide the average Nusselt numbers, and in the present study the average Nusselt number are only based on the average values in the region between  $x/D_H = 10.0$  and  $x/D_H = 12.0$ . Figures 8(a, b) illustrated the variation of the mean Nusselt number with Reynolds number at various rotational Reynolds numbers for trailing and leading surfaces, respectively. The Dittus-Boelter equation for stationary smooth duct and data from Soong et al. (1991) at  $Re_\Omega = 300$  were plotted for comparison. As expected, the average Nusselt number increases with increasing Reynolds number. The results also show that for a given Reynolds number, the average Nusselt number decreases with increasing rotational Reynolds number for both trailing and leading surfaces. In Fig. 8, a comparison of  $Nu$  distribution between the stationary ribbed-duct flow and the rotating one reveals that the maximum heat transfer augmentation is 35 percent on the trailing surface at  $Re_\Omega = 2480$  while the minimum enhancement is about 13 percent on the leading surface at  $Re_\Omega = 496$  for the test ranges of  $Re_H$ . The results shown in Fig. 8 generally agree with the previous data of fully developed flow for rotating constant wall temperature smooth-duct with  $Re_\Omega = 300$  reported by Soong et al. (1991).

**Rotation Number Effect.** Figure 9 shows the variation of Nusselt number versus rotation number at different rotational

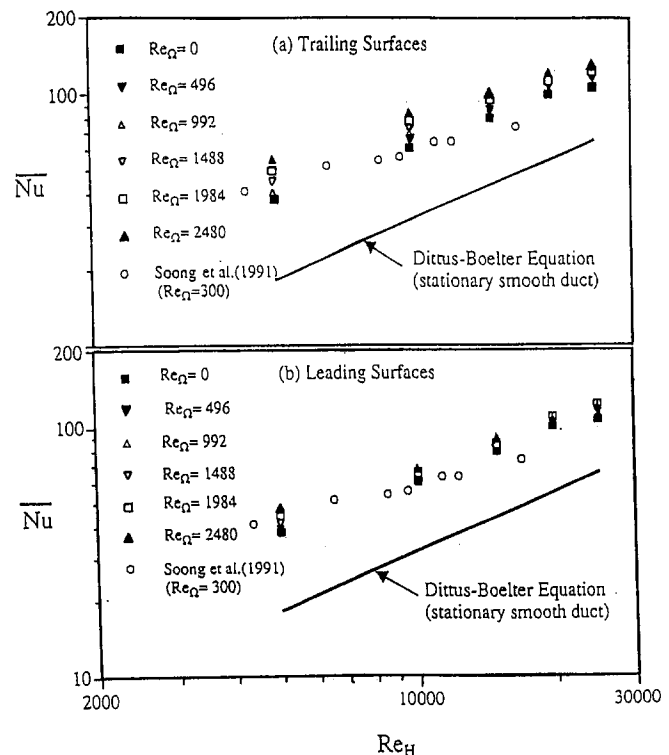


Fig. 8 Mean Nusselt number versus Reynolds number in rotating square duct

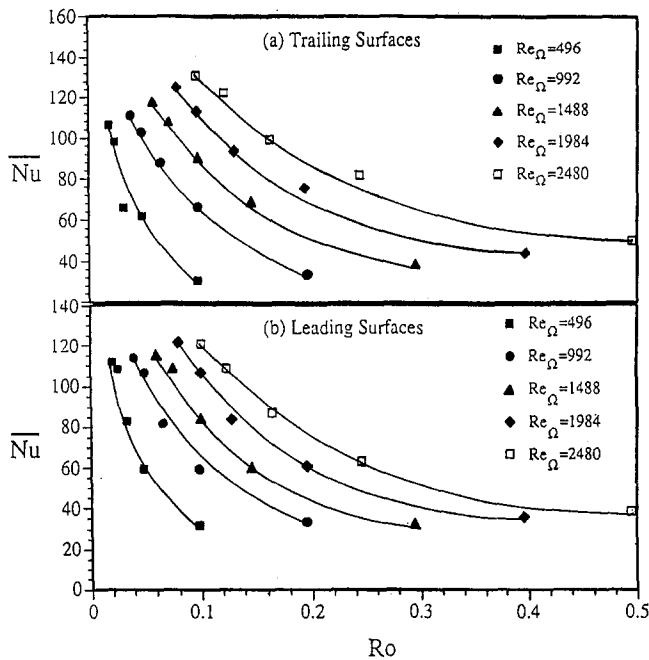


Fig. 9 Variation of Nusselt number with rotation number at different rotational Reynolds number for (a) trailing surfaces, (b) leading surfaces

Reynolds numbers for both trailing and leading surfaces. For a specific rotational Reynolds number (i.e., the value of  $\Omega$  is constant), it is seen that Nusselt number decreases with increasing rotation number for both surfaces. The reason for this is that with angular velocity  $\Omega$  fixed, a higher rotational number corresponds to a lower value of  $U_m$ , which in turn corresponds to a lower Nusselt number. This is because the flow capacity (in terms of Reynolds number generally) reflects the heat transport capacity from the surrounding. It can be seen from Fig. 9 that the Nusselt number decreases more rapidly with increasing rotational number at lower rotational Reynolds number that at high rotational Reynolds number. This indicates that the influence of the Coriolis force is relative weak at lower rotational speed and, there, the Reynolds number plays a dominant role. As rotational speed increases, on the other hand, the Coriolis force plays a dominant role gradually. These results agree quite well with the data reported by Taslim et al. (1991a, b).

**Rotational Reynolds Number Effect.** Figure 10 demonstrates the variation of mean Nusselt number with the rotational Reynolds number over trailing and leading surfaces at five different Reynolds numbers. Previous data from Taslim et al. (1991a) for square-duct with staggered-type ribs ( $e/D_H = 0.133$ ,  $0.25$ ,  $p/e = 10$ , and  $Re_H = 16,600, 19,300, 24,800$ ) and Mori et al. (1971) for smooth circular-duct were also plotted. It can be observed that the Nusselt number increases as the rotational Reynolds number increases. This trend coincides very well with the data of Mori et al. (1971) and Lokai and Limanskii (1975) (not shown here). It is speculated that this behavior is due to the increase of the development of the secondary flow with increasing  $Re_\Omega$  and interact with the buoyant, stabilized near-wall flow field, which adversely affect the heat transfer coefficient in a radially outward flow. This, however, is not the case for Taslim et al. (1991a), where they show a quite different tendency. In their study, the Nusselt number first increases as the rotation Reynolds number increases until it reaches a maximum and then, with the exception of the lowest Reynolds number ( $Re_H = 16,600$ ) on the trailing surface, the Nusselt number decreases with  $Re_\Omega$ . This discrepancy may be attributed to different geometric configurations. In their study, a larger pitch-to-rib height ratio ( $p/e = 10$ ) was adopted, in which the interaction between

secondary flow generated by rotation and the wall shear layer induced by ribs may be suppressed as the rotational speed increased. Furthermore, the Nusselt number decrease may also be due to the rotational buoyancy effect. This impaired the heat transfer significantly. Nevertheless, compared with the stationary case, for the range of rotation numbers tested, the heat transfer coefficient is enhanced on both leading and trailing surfaces for these investigations which is also different from those of Wagner et al. (1992) and Zhang et al. (1993). They showed that, for outward flow, heat transfer is enhanced with rotation at the trailing surface, but degraded with rotation at the leading surface. These could be due to the following two significant differences in our experiments. First, it appears that the present configuration discharges directly out of the end of the rotating passage with no return leg, which means no bend and no back pressure. Second, our ribs are higher than normal and closer spaced than normal, causing a jetting action between two consecutive ribs. Moreover, as can be seen from these figures, the slopes of the trailing surfaces are larger than the leading surfaces. This indicates that the influences of rotational speed on heat transfer enhancement are more on the trailing surface than on the leading surface.

**Centripetal-Buoyancy Effect.** As rotation number ( $Ro$ ) is referred to the Coriolis acceleration, so rotational Rayleigh number ( $Ra_\Omega$ ) is to the centripetal-buoyancy force. The Coriolis acceleration induces a secondary flow, and the resulting increased movement in the fluid region near the wall tends to increase the heat transfer coefficient. Buoyancy force, however, can have an opposite effect, as proposed by Morris and Ayhan (1979) for radially outward flow. The rotational Rayleigh number is similar to the Rayleigh number associated with free convection effects due to the earth's gravity except that, in the present case, the centripetal acceleration at the midsection plane of the test channel has been used. When the flow is radially outward, the buoyancy situation is analogous to a vertical duct influenced by the earth's field and having a downward flow. It is not easy to separate the Coriolis and the centripetal buoyancy effects in an experimental condition at a

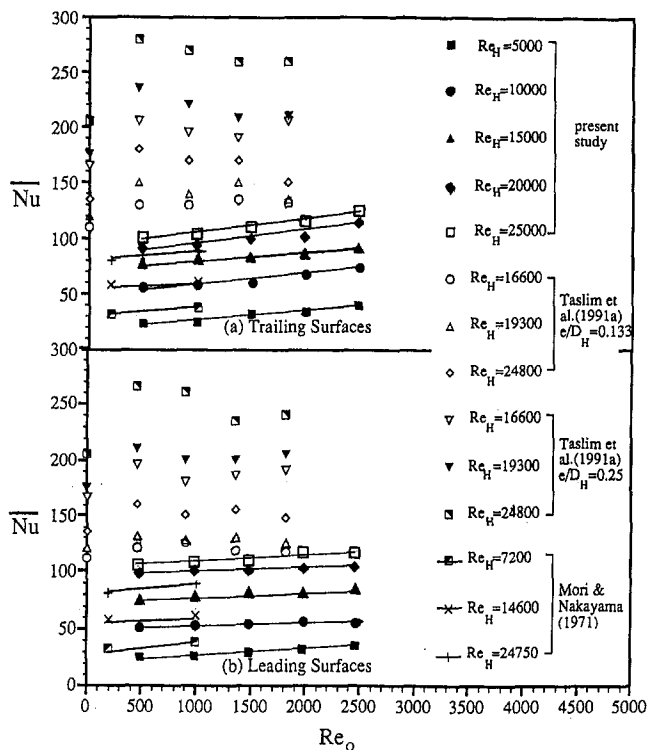


Fig. 10 Nusselt number versus rotational Reynolds number at various Reynolds number and compared with previous investigations

given Reynolds number. This fact was also found in this study. In the present study, different heat flux settings are used to generate different buoyancy effects while keeping the other parameters unchanged. The measurements were performed at five different Reynolds number for both trailing and leading surfaces, as shown in Figs. 11 and 12, respectively. In these figures, the mean Nusselt number is plotted against the quotient  $Ra_{\Omega}/Re_H^2$  (i.e., the local level of wall to fluid bulk mean temperature difference) at a specific Reynolds number and rotation number. The physical significances for the present rotating duct, which are highlighted in these figures, are threefold. First, at a specified Reynolds number and rotation number, which is equivalent to fixing the rotational speed of the test duct, the mean level of heat transfer is systematically reduced as  $Ra_{\Omega}/Re_H^2$  increases, i.e., there is an adverse effect of centrifugal buoyancy on heat transfer. For radially outward flow from the rotation axis in a heated duct in orthogonally rotation, the higher temperature region near the wall would create a buoyancy force acting toward the axis of rotation in opposition to the axial pumping pressure. This can reduce the axial velocity near the wall and decrease the heat transfer coefficient. The axial buoyancy component thus opposes the customary forced convection, resulting in an impediment to heat transfer. This finding is different from those of Wagner et al. (1991a, b) in which they indicated the buoyancy force has positive effect on the Nusselt numbers on both leading and trailing walls. This is because, as previously stated, the present test sections

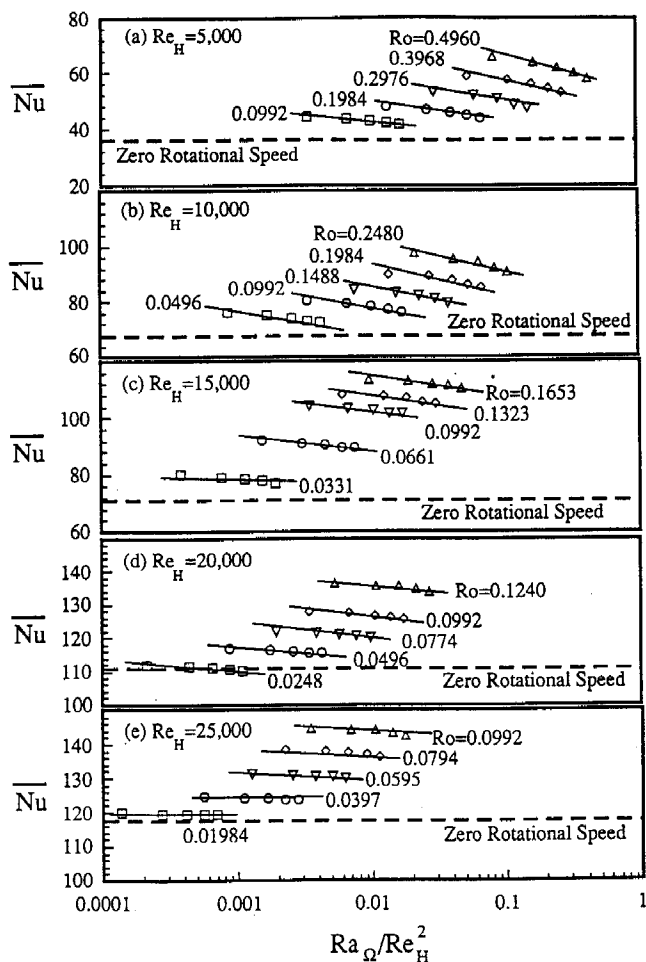


Fig. 11 Centripetal-buoyancy effect on heat transfer in a square roughened duct (trailing surface)

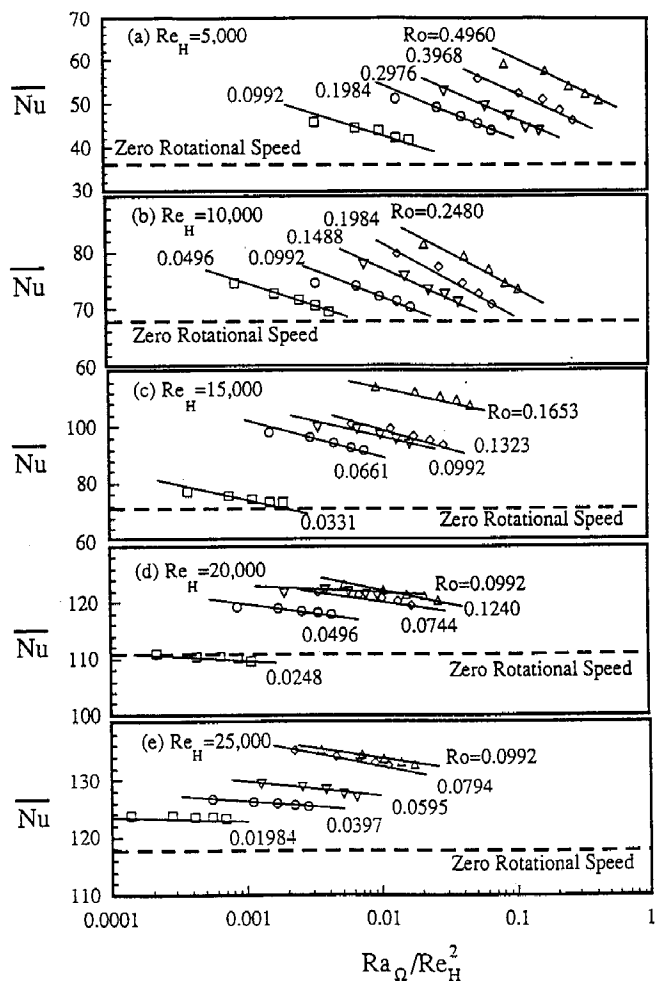


Fig. 12 Centripetal-buoyancy effect on heat transfer in a square roughened duct (leading surface)

seem to have a wall conduction problem. Nevertheless, the present result suggests that, for this condition of radial outward flow, the rotational induced free convection would tend to oppose the beneficial effects of the Coriolis acceleration. Second, the adverse effect of the  $Ra_{\Omega}/Re_H^2$  tends to diminish as the Reynolds number increases. This indicates that, in the high Reynolds number regime, the role of the rotational Rayleigh number would no longer be as important as the Reynolds number is. Furthermore, at a fixed value of the Reynolds and rotational Rayleigh numbers the heat transfer increases with increases in the rotation number, which is a measure of the relative influence of the Coriolis force.

These results agree with those reported by Morris and Aghan (1979), Clifford et al. (1984), and Harasgama and Morris (1988) for rotating smooth channel. In spite of this, Guidez (1989) reported a mean Nusselt number increase with an increase in centripetal-buoyancy force. This is because, in his paper,  $Ro$  is not a control variable, which caused the resulting heat transfer characteristics to be dependent on  $Ro$  instead of buoyancy effect. This can also be seen from present data with a change of  $Ro$ . However, it should be emphasized that, in the design context, the serious overprediction in heat transfer would result if the effect of the centripetal buoyancy was not taken into consideration.

### Concluding Remarks

The present experimental investigation provides turbulent heat transfer data of an orthogonally rotating square ribbed-duct. The



distributions of the local Nusselt number of the rotating ribbed-duct flows at various rotational speeds along the length of the duct are presented for both trailing and leading surfaces. These figures reveal that the heat transfer coefficient distributions measured/calculated exhibit a definite trend with the highest value at the beginning of the test section and decrease monotonically with increasing downstream distance, eventually reaching a fully developed value ( $x/D_H > 6$ ). Besides, a significant enhancement in heat transfer is achieved in a rotating ribbed-duct.

The variation of local Nusselt numbers along the rib forward-facing side, top wall, backward-facing side, and the floor surface between two consecutive ribs in the fully developed region (between ribs #10 and #11) are also demonstrated. It can be seen from these figures that the values of Nu have a peak on the front convex corner of the rib, and monotonically increase along the streamwise on the floor, reaching a local maximum near the front concave corner of the downstream rib. The trend in both rotating and stationary roughened ducts was found almost the same with some difference in the values of the heat transfer coefficients.

Based on the results from the present experiments with normal ribs in rotating, radial, square coolant passage, the following conclusions may be drawn:

1 For a specific rotational Reynolds number (i.e., the value of  $\Omega$  is constant), the Nusselt number decreases with increasing rotation number for both surfaces. Moreover, the Nusselt number decrease more rapidly with increasing rotational number at low rotational Reynolds number than that at high rotational Reynolds number.

2 Increasing the rotational speed causes a significant increase in heat transfer on the trailing surfaces but a lesser increase on the leading surfaces. For a specified Reynolds and rotational Reynolds number, for instance,  $Re_H = 10,000$  and  $Re_\Omega = 992$ , an enhancement of about 25 percent for trailing surface and 17 percent for leading surface in heat transfer coefficient due to rotation is observed.

3 A comparison of  $\bar{Nu}$  distribution between the stationary ribbed-duct flow and the rotating one reveals that the maximum heat transfer augmentation is 35 percent on the trailing surface at  $Re_\Omega = 2480$  while the minimum enhancement is about 13 percent on the leading surface at  $Re_\Omega = 496$  for the test ranges of  $Re_H$ .

4 The Coriolis-induced secondary flow can provide a beneficial effect on the heat transfer enhancement while the centripetal-buoyancy presents an adverse effect. Both of these effects will diminish in a strong forced flow field. But the buoyancy effect diminishes faster than the Coriolis effect as Reynolds number is larger than 20,000.

## Acknowledgments

Revision assistance in conducting several modification measurements as well as for preparation of manuscript from Messrs. Der-Yuan Li and Chun-Jen Weng is sincerely appreciated.

## References

- Burggraf, F., 1970, "Experimental Heat Transfer and Pressure Drop With Two-Dimensional Turbulence Promoter Applied to Two Opposite Walls of a Square Tube," in: *Augmentation of Convective Heat and Mass Transfer*, E. E. Bergles and R. L. Webb, eds., ASME, New York, pp. 70–79.
- Clifford, R. J., Harasgama, S. P., and Morris, W. D., 1984, "An Experimental Study of Local and Mean Heat Transfer in a Triangular-Sectional Duct Rotating in the Orthogonal Mode," *ASME Journal of Engineering for Gas Turbines and Power*, Vol. 106, pp. 661–667.
- Guidez, J., 1989, "Study of the Convective Heat Transfer in a Rotating Coolant Channel," *ASME Journal of Turbomachinery*, Vol. 111, pp. 43–50.
- Han, J. C., Park, J. S., and Lei, C. K., 1985, "Heat Transfer Enhancement in Channels With Turbulence Promoters," *ASME Journal of Engineering for Gas Turbines and Power*, Vol. 107, pp. 628–635.
- Han, J. C., and Park, J. S., 1988, "Developing Heat Transfer in Rectangular Channels With Rib Turbulators," *International Journal of Heat and Mass Transfer*, Vol. 31, pp. 183–195.
- Harasgama, S. P., and Morris, W. D., 1988, "The Influence of Rotation on the Heat Transfer Characteristics of Circular, Triangular, and Square-Sectioned Coolant

- Passages of Gas Turbine Rotor Blades," *ASME Journal of Turbomachinery*, Vol. 110, pp. 44–50.
- Hart, J. E., 1971, "Instability and Secondary Motion in Rotating Channel Flow," *J. Fluid Mech.*, Vol. 45, No. 2, pp. 341–351.
- Hong, Y. J., and Hsieh, S. S., 1993, "Heat Transfer and Friction Factor Measurements in Ducts With Staggered and In-Line Ribs," *ASME JOURNAL OF HEAT TRANSFER*, Vol. 115, pp. 58–65.
- Hsieh, S. S., and Hong, Y. J., 1989, "Separating Flow Over Repeated Surface Mounted-Ribs in a Square Duct," *AIAA Journal*, Vol. 27, pp. 770–775.
- Iskakov, K. M., and Trushin, V. A., 1985, "The Effect of Rotation on Heat Transfer in the Radial Cooling Channels of Turbine Blades," *Thermal Engineering*, Vol. 32, pp. 93–96.
- Johnson, B. V., 1978, "Heat Transfer Experiments in Rotating Radial Passages With Supercritical Water," *Proc. ASME Winter Annual Meeting*.
- Johnson, B. V., Wagner, J. H., Steuber, G. D., and Yeh, F. C., 1994, "Heat Transfer in Rotating Serpentine Passages With Trips Skewed to the Flow," *ASME Journal of Turbomachinery*, Vol. 116, pp. 112–123; NASA TM 105581.
- Johnston, J. P., Halleen, R. M., and Lezius, D. K., 1972, "Effects of Spanwise Rotation on the Structure of Two-Dimensional Fully Developed Turbulent Channel Flow," *J. Fluid Mech.*, Vol. 56, No. 3, pp. 533–557.
- Kline, S. J., and McClintock, F. A., 1953, "Describing Uncertainties in Single-Sample Experiments," *Mechanical Engineering*, Vol. 75, Jan., pp. 3–8.
- Liou, T. M., and Hwang, J. J., 1992, "Turbulent Heat-Transfer Augmentation and Friction in Periodic Fully-Developed Channel Flows," *ASME JOURNAL OF HEAT TRANSFER*, Vol. 114, pp. 56–64.
- Lokai, V. I., and Limanskii, A. S., 1975, "Influence of Rotation on Heat Transfer in Radial Cooling Channels of Turbine Blades," *Izvestiya VUZ. Aviatstionnaya Tekhnika*, Vol. 18, pp. 69–72.
- Lokai, V. I., and Gunchenko, E. I., 1979, "Heat Transfer Over the Initial Section of Turbine Blade Cooling Channels Under Conditions of Rotation," *Thermal Engineering*, Vol. 26, pp. 93–95.
- Metzger, D. E., and Stan, R. L., 1977, "Entry Region Heat Transfer in Rotating Radial Tubes," *Proc. AIAA 15th Aerospace Science Meeting*, pp. 77–89.
- Metzger, D. E., Vedula, R. D., and Breen, D. D., 1987, "The Effect of Rib Angle and Length on Convection Heat Transfer in Rib-Roughened Triangular Ducts," *Proceedings of the 1987 ASME/JSME Thermal Engineering Joint Conference*, Vol. 3, pp. 327–333.
- Moffat, R. J., 1988, "Describing the Uncertainties in Experimental Results," *Experimental Thermal and Fluid Science*, Vol. 1, pp. 3–17.
- Moore, J., 1967, "Effects of Coriolis on Turbulent Flow in Rotating Rectangular Channels," M.I.T. Gas Turbine Laboratory Report No. 89.
- Mori, Y., Fukada, T., and Nakayama, W., 1971, "Convective Heat Transfer in a Rotating Radial Circular Pipe (2nd Report)," *Int. J. Heat Mass Transfer*, Vol. 14, pp. 1807–1824.
- Morris, W. D., and Ayhan, T., 1979, "Observations on the Influence of Rotation on Heat Transfer in the Coolant Channels of Gas Turbine Rotor Blades," *Proc. Inst. Mech. Engrs.*, Vol. 193, pp. 303–311.
- Morris, W. D., and Ayhan, T., 1982, "An Experimental Study of Turbulent Heat Transfer in the Tube Which Rotates About an Orthogonal Axis," *Proc. XIV ICHMT Symposium on Heat and Mass Transfer in Rotating Machinery*, Dubrovnik, Yugoslavia, Aug. 30–Sep. 3.
- Morris, W. D., and Ghavami-Nasr, G., 1991, "Heat Transfer Measurements in Rectangular Channels With Orthogonal Mode Rotation," *ASME Journal of Turbomachinery*, Vol. 113, pp. 339–345.
- Rothe, P. H., and Johnston, J. P., 1979, "Free Shear Layer Behavior in Rotating System," *ASME Journal of Fluids Engineering*, Vol. 101, pp. 117–120.
- Siegel, R., and Howell, J. R., 1981, *Thermal Radiation Heat Transfer*, 2nd ed., McGraw-Hill, New York.
- Soong, C. Y., Lin, S. T., and Hwang, G. J., 1991, "An Experimental Study of Convective Heat Transfer in Radially Rotating Rectangular Ducts," *ASME JOURNAL OF HEAT TRANSFER*, Vol. 113, pp. 604–611.
- Taslim, M. E., Rahman, A., and Spring, S. D., 1991a, "An Experimental Investigation of Heat Transfer Coefficients in a Spanwise Rotating Channel With Two Opposite Rib-Roughened Walls," *ASME Journal of Turbomachinery*, Vol. 113, pp. 75–82.
- Taslim, M. E., Bondi, L. A., and Kercher, D. M., 1991b, "An Experimental Investigation of Heat Transfer in an Orthogonally Rotating Channel Roughened With 45 deg Criss-Cross Ribs on Two Opposite Walls," *ASME Journal of Turbomachinery*, Vol. 113, pp. 346–353.
- Wagner, J. H., Johnson, B. V., and Hajek, T. J., 1991a, "Heat Transfer in Rotating Passages With Smooth Walls and Radial Outward Flow," *ASME Journal of Turbomachinery*, Vol. 113, pp. 42–51.
- Wagner, J. H., Johnson, B. V., and Kopper, F. C., 1991b, "Heat Transfer in Rotating Serpentine Passages With Smooth Walls," *ASME Journal of Turbomachinery*, Vol. 113, pp. 321–330.
- Wagner, J. H., Johnson, B. V., Graziani, R. A., and Yeh, F. C., 1992, "Heat Transfer in Rotating Serpentine Passages With Trips Normal to the Flow," *ASME Journal of Turbomachinery*, Vol. 114, pp. 847–857; NASA TM 103758.
- Wagner, R. E., and Velkoff, H. R., 1972, "Measurements of Secondary Flows in a Rotating Duct," *ASME Journal of Engineering for Power*, Vol. 94, pp. 261–270.
- Yang, W. J., Zhang, N., and Chiou, J., 1992, "Local Heat Transfer in a Rotating Serpentine Flow Passage," *ASME JOURNAL OF HEAT TRANSFER*, Vol. 114, pp. 354–361.
- Zhang, N., Chiou, J., Fann, S., and Yang, W. J., 1993, "Local Heat Transfer Distribution in a Rotating Serpentine Rib Roughened Flow Passage," *ASME JOURNAL OF HEAT TRANSFER*, Vol. 115, pp. 560–567.

# Heat Transfer From an Asymmetrically Heated Channel Partially Enclosing a Rotating Disk

R. R. Schmidt

Senior Engineer,  
Large Scale Computing Division,  
IBM Corporation,  
Poughkeepsie, NY 12601  
Assoc. Mem. ASME

P. Patel

Mechanical Engineering Student,  
New Jersey Institute of Technology,  
Newark, NJ 07102

*Experiments have been performed to determine the heat transfer from an asymmetrically heated channel partially enclosing a vertically oriented rotating disk. Parallel rectangular surfaces enclose the rear portion of a disk (slightly less than  $1/2$  of the disk is enclosed) allowing air to enter and exit the perimeter of the channel, except the rear vertical portion bridging the two parallel surfaces. The experiments encompassed data runs where one of the parallel walls was isothermal and the other was adiabatic. The experiments encompassed a range of spacings between the rotating disk and the adjacent parallel surfaces and a range of rotational speeds varying by a factor of 30. The experiments were performed using the naphthalene sublimation technique. From the experimental results a dimensionless correlation equation suitable for predicting average heat and mass transfer coefficients of the enclosing surfaces for various rotational Reynolds numbers and disk-to-wall spacings was deduced. Finally, to gain some insight into the air flow pattern along the enclosing walls, a visual flow technique was employed, the results of which will be described herein.*

## Introduction

There are many applications in industry that use parallel fin heat sinks attached to heat-producing components in order to increase the area whereby heat is transferred and the component temperature is reduced. In many of these situations forced air is ducted to the parallel fin heat sink from an air-moving device. The assembly, made up of an air-moving device, ducting, and a heat sink, can consume significant space within the overall hardware system.

In an effort to improve the heat transfer performance of a parallel fin heat sink and at the same time provide an assembly that will significantly reduce the space required to provide this performance, a novel design of a parallel fin heat sink integrated with a "disk fan" has been proposed, as shown in Fig. 1. This paper studies the basic heat transfer characteristics of this assembly by focusing on a single disk rotating between two parallel fin surfaces. Obviously, the flow pattern and thereby the heat transfer will be affected by adjacent disks, but this study will serve as a basis to which further research on this subject can be compared.

Several papers investigate the flow phenomena in the vicinity of a rotating disk either partially enclosed (Kreith et al., 1963, 1959; Maroti et al., 1960; Metzger, 1970; Richardson and Saunders, 1963; Soo, 1958) with parallel side walls or fully enclosed (Daily and Nece, 1960; Nece and Daily, 1960) with parallel side walls and a rim shroud. In addition several of these papers (Kreith et al., 1963, 1959; Metzger, 1970; Richardson and Saunders, 1963) show the degradation in heat transfer on the rotating disk as the spacing between the side wall and disk decrease. However, none of these investigations, nor the authoritative survey of Kreith (1968), which covers many rotational heat transfer configurations, provide any information on the heat transfer occurring at the surfaces enclosing the disk. The investigation described in this paper is the first phase of experiments in understanding the heat transfer on surfaces enclosing a rotating disk.

In the presentation of the results, the convective transfer coefficients for each disk-to-side wall spacing are plotted separately at first and then brought together in a common correlation, which encompasses various spacings and Reynolds numbers tested.

## The Experiments

These experiments were performed utilizing the naphthalene sublimation technique. This technique was employed because it affords smaller extraneous losses, higher measurement accuracy, and simpler fabrication and assembly than does the corresponding heat transfer experiment. Furthermore, it enables a standard boundary condition (analogous to uniform wall temperature) to be readily obtained.

The mass transfer results can be transformed to heat transfer results using the well-established analogy between the two processes. The conversion from mass transfer results to heat transfer results can be obtained by employing the following relationships:

$$Nu = f(Re, Pr, X_i), Sh = f(Re, Sc, X_i) \quad (1)$$

where the function  $f$  is the same for both processes ( $X_i$  denotes geometric parameters). In the correlation of heat and mass transfer data, Eq. (1) becomes

$$Nu = Pr^m g(Re, X_i), Sh = Sc^m g(Re, X_i) \quad (2)$$

so that

$$Nu = (Pr/Sc)^m Sh \quad (3)$$

**Experimental Apparatus.** A schematic diagram of the experimental apparatus is presented in Fig. 2. The main components of the apparatus are a vertically oriented disk, the rear portion of which is enclosed by two parallel surfaces, one active in the mass transfer process. To complete the enclosure a vertical surface bridges the two parallel surfaces at the rear of the disk. Therefore, the perimeter of the channel formed by the parallel surfaces is entirely open to air entering and exiting except the vertical surface bridging the two parallel surfaces at the rear of the disk.

The disk was made of aluminum with a diameter of 130 mm and a thickness of 0.8 mm. The flatness of the disk was within 0.05 mm TIR as measured by a dial indicator. A center hole in the disk is to allow the disk to be mounted to the end of a motor

Contributed by the Heat Transfer Division for publication in the JOURNAL OF HEAT TRANSFER. Manuscript received by the Heat Transfer Division April 1993; revision received November 1993. Keywords: Finned Surfaces, Mass Transfer, Moving Boundaries. Associate Technical Editor: A. Faghri.

shaft. The end of the shaft of the motor was reduced in diameter to facilitate mating the disk to the shaft. A threaded bolt screwed to the end of the shaft was used to affix the disk tightly to the shaft.

The shaft was attached to a variable speed motor in which angular speeds ranged from 100 to 3000 rpm. Periodic measurements of the rotational speeds by both optical and electromechanical tachometers verified their constancy. Both instruments typically agreed to within one rpm of each other.

The drive system for the rotating disk consists of three components: Electro Craft Model E19-2 servomotor, Electro Craft Model MAX-400 servocontroller, and power source with enabling and speed controls. The controller could drive the motor in either direction, at speeds up to 5000 rpm. For these experiments the disk was only rotated in a direction to force air out the top of the parallel surfaces enclosing the disk. The speed control is a potentiometer, which sends a voltage to the servocontroller, and is set by monitoring the shaft with a tachometer.

The motor and parallel surfaces enclosing the disk were mounted to a vertical 1-in.-thick aluminum plate affixed to a laboratory table. The massive aluminum plate was chosen to provide an essentially vibration-free platform for mounting the motor.

The parallel surface nearest the motor could be adjusted to provide different disk-to-wall spacings with a series of spacers. The other parallel wall, active in mass transfer, was designed so that it could be removed and accurately reset in place in a matter of seconds, thus making efficient use of the naphthalene sublimation technique. Because the end collar of the shaft extended beyond the naphthalene surface, a frame was designed into which the naphthalene mold could be easily inserted. This frame was attached to a linear motion slide plate and micrometer that would allow the frame to be quickly and accurately positioned. The frame was also designed to enclose the rear of the naphthalene test element during the test run. This design eliminated any extraneous mass transfer that could occur during the test run from an opening in the back of the naphthalene test element used in the casting process.

Figure 3 shows the naphthalene surface relative to the rotating disk.

**Mass Transfer Surface.** The procedure used for casting the naphthalene surface will be described with the aid of Fig. 4. To obtain a smooth naphthalene surface from which mass transfer occurs, the aluminum frame mold is placed face down on a smooth optical glass plate. Once the naphthalene is melted in a beaker, the molten naphthalene is poured into the mold cavity through an opening in the back of the frame. When the naphthalene had solidified, the frame is briskly tapped to dislodge the solidified naphthalene from the glass plate, leaving an exposed naphthalene surface whose finish is comparable to that of the glass.

**Instrumentation and Experimental Procedure.** The quantities measured for each data run include the mass of the naph-

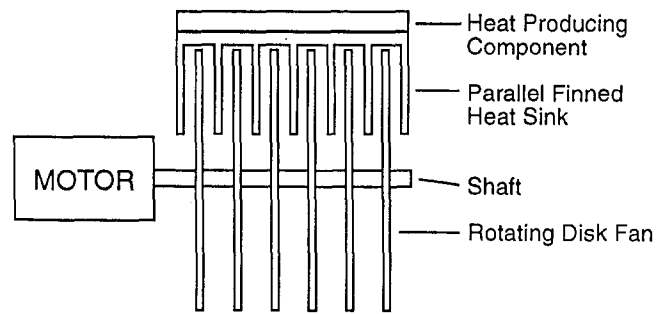


Fig. 1 Integrated "disk fan" and parallel fin heat sink

thalene test element (both before and after the run), the temperature of the naphthalene, the room ambient pressure, and the duration of the test run. In addition, each run was characterized by the rotational speed of the disk and a gap between the disk and mass transfer surface. In all cases the disk was symmetrically positioned between the parallel side walls.

The mass of the test element was measured by a Mettler analytical balance with a resolving power of 0.1 mg and a capacity of 160 g. Typically, the change of mass during a run was in the 20 to 30 mg range.

The temperature of the naphthalene was measured with a calibrated thermocouple embedded at the surface of the naphthalene, placed there during the molding process. (Copper-constantan thermocouples used throughout this research were calibrated to a quartz thermometer having an accuracy of 0.05°C.) The thermocouple was attached to a Fluke data logger Model 2280A, which was in turn connected to an IBM PC-XT that provided a time-averaged temperature. Temperatures were measured every 30 seconds and then averaged over the length of the test run. Temperature variations during all test runs varied by less than 0.2°C.

The rotational speed of the shaft was preset by a potentiometer on the servocontroller. As stated previously, each setting was calibrated with tachometers and checked periodically for constancy.

To initiate a data run, the test element is first cast, enclosed in an impermeable plastic bag to minimize naphthalene sublimation, and placed near the test apparatus to begin the thermal equilibration process. Immediately before the test run the test element is weighed and then inserted into the apparatus for the start of the test run. The naphthalene mold, once fabricated, was never touched with the fingers but grasped through the use of surgical gloves. The test run is begun with the rotational speed of the disk preset. The duration of the run was selected to limit the average sublimation-related change in the naphthalene surface to less than 0.0010 cm.

Once the test element is weighted immediately following the test run, a further weighing was carried out to determine a cor-

## Nomenclature

$C$  = coefficient in Sh, Re relation  
 $D$  = diameter of disk  
 $D_h$  = hydraulic diameter of channel, Eq. (9)  
 $\mathcal{D}$  = naphthalene-air diffusion coefficient  
 $f$  = friction factor, Eq. (8)  
 $G$  = gap between disk and mass transfer surface, Fig. 2  
 $H$  = channel height, Fig. 3  
 $K$  = mass transfer coefficient, Eq. (4)  
 $L$  = channel length, Fig. 3

$\dot{m}$  = mass transfer per unit time and area  
 $Nu$  = Nusselt number  
 $n$  = exponent in Sh, Re relation  
 $Pr$  = Prandtl number  
 $R$  = radius of disk  
 $Re_r$  = rotational Reynolds number, Eq. (5)  
 $Re$  = channel-flow Reynolds number, Eqs. (7) and (8)  
 $Sc$  = Schmidt number  
 $Sh$  = Sherwood number =  $KR/\mathcal{D}$

$t$  = disk thickness  
 $X_i$  = geometric parameters  
 $\mu$  = viscosity  
 $\nu$  = kinematic viscosity  
 $\rho$  = density  
 $\rho_{nw}$  = naphthalene vapor density at surface  
 $\rho_{n\infty}$  = naphthalene vapor density in ambient  
 $\omega$  = angular velocity

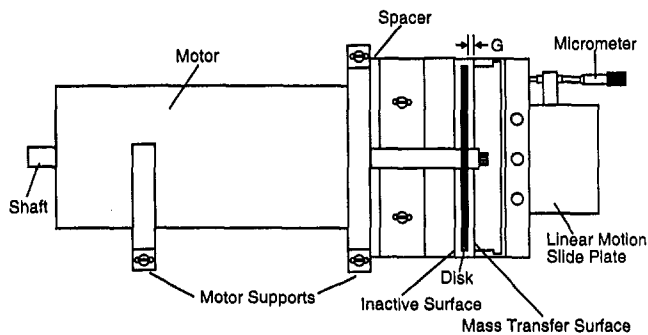


Fig. 2 Schematic sketch of 130-mm-dia rotating disk assembly

rection for any extraneous mass transfer that might have occurred in the period between the first and second weighings. All of the steps that had been performed between the two weighings were repeated, but the motor was never turned on. A third weighing was then made, and this yielded a correction factor in the 1.5 to 4 percent range.

Additional experiments were performed to determine the time for the naphthalene, once cast, to stabilize at the room temperature. These experiments, performed with a thermocouple embedded in the naphthalene, showed that the naphthalene stabilized to the room temperature in 1.5 hours. Based on this data all test runs were made only after the test element remained in the vicinity of the test apparatus for at least 2 hours.

To further maintain temperature stability of the naphthalene test element, the analytical balance for measuring the weight of the test element before and after the test run was located in the same laboratory room as the test apparatus.

The experiments were run in a laboratory room in which an auxiliary blower was activated during the test run to assure that accumulations of any naphthalene vapor within the room were negligible.

The flow pattern near the naphthalene wall was observed by replacing the active mass transfer wall and its supporting structure with a wall of clear plexiglass and attaching a matrix of thin threads to the plexiglass wall and then photographing their motion. A single thread was passed through an eye of a needle and inserted into each of a series of holes drilled into the plexiglass and then affixed with glue injected into the hole with a hot glue gun. Each thread was cut to an approximate length of 10 mm.

**Supplemental Thermal Experiments.** Since the accuracy of the naphthalene temperature is crucial (an error of  $1^{\circ}\text{C}$  in naphthalene temperature results in approximately a 10 percent error in heat transfer coefficient), a number of preliminary tests were performed to establish the method for measuring the temperature of the naphthalene accurately and to assure that any extraneous heating effects were minimized. Investigation of the extraneous heating of the naphthalene focused on the heat generated by the motor.

Temperature measurements throughout the apparatus showed that the heat generated by the motor could be transferred to the naphthalene by three different thermal paths. One of the thermal paths occurs when the motor conducts heat through its supports, into the vertical aluminum mounting plate and finally to the parallel surfaces, heating the naphthalene and the surrounding air. Another thermal path occurs from the motor to the shaft and finally to the rotating disk thereby heating the air surrounding the disk and possibly the naphthalene. Finally, convection currents were evident in the vicinity of the heated motor, which showed that some heated air could be ingested into the parallel channel enclosing the disk. All three effects were found to be dependent on the rotational speed and length of operation of the motor.

It was determined that by limiting the time of a test run, yet keeping it long enough to obtain adequate mass loss, that the

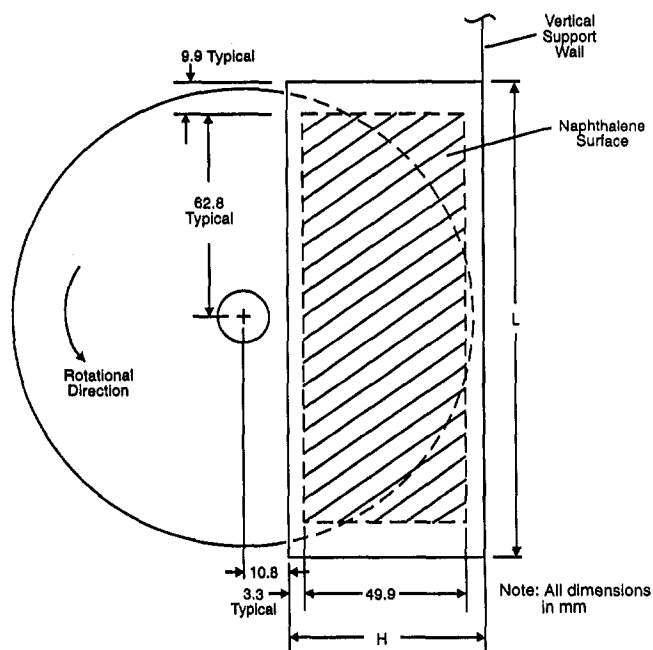


Fig. 3 Schematic sketch of naphthalene surface relative to 130-mm-dia rotating disk

naphthalene temperature could be maintained to less than  $0.2^{\circ}\text{C}$  variation over the length of the test run. This variation includes the temperature depression (approximately  $0.15^{\circ}\text{C}$ ) effect at the surface of the naphthalene due to absorption of latent heat from the surroundings. The convection currents in the vicinity of the motor and their effect on the naphthalene were eliminated by erecting a vertical wall of cardboard between the motor and test section.

In addition to these temperature effects in which thermal tests were performed, frictional heating resulting from the rotation of the disk was also examined analytically. Calculations were performed that showed that the outer perimeter of the disk would rise less than  $0.1^{\circ}\text{C}$  for the highest rotational speeds tested.

**Data Reduction.** The measured change of mass during a data run, divided by the duration of the run and by the naphthalene

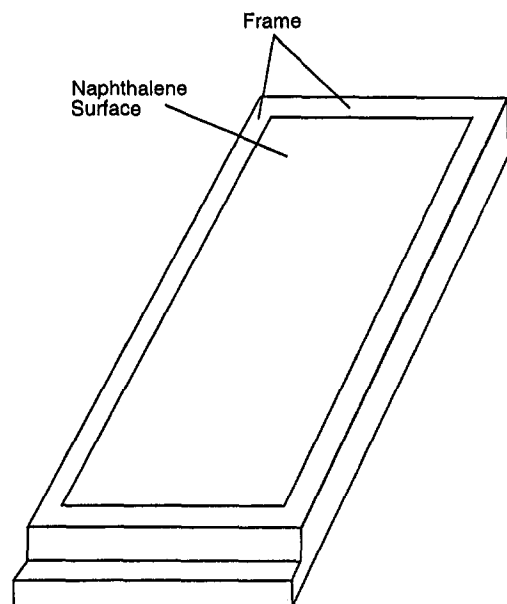


Fig. 4 Naphthalene test surface and its surrounding frame

surface area, yields the average mass flux  $\dot{m}$ . With  $\dot{m}$  as input, the average mass transfer coefficient  $K$  and Sherwood number  $Sh$  are given as

$$K = \dot{m}/(\rho_{nw} - \rho_{n\infty}), \quad Sh = KR/\mathcal{D} \quad (4)$$

Although several geometric variables exist in the problem studied, the radius ( $R$ ) was selected as the characteristic length in the Sherwood number for three reasons: (1) consistency with published literature on heat/mass transfer from rotating disk, (2) the radius is constant throughout the experimental study and graphic display of mass transfer results truly depict changes in mass transfer coefficients, and finally (3) a lack of knowledge of the effects of varying the other geometric parameters from which the "best" parameter could then be selected.

In defining  $K$ , the driving potential for mass transfer was taken to be the difference between the densities of the naphthalene vapor at the active wall and the ambient outside the flow passage. The naphthalene vapor pressure at the surface–fluid interface is uniform along the flow passage. The Sogin vapor pressure–temperature relation (Sogin, 1958) was used to evaluate the vapor pressure with the measured naphthalene temperature as input. The naphthalene vapor density at the active wall,  $\rho_{nw}$ , was computed using the perfect gas law with temperature and vapor pressure as inputs. The naphthalene vapor density for the ambient,  $\rho_{n\infty}$ , is zero for the tests.

The mass diffusion coefficient  $\mathcal{D}$ , which appears in the Sherwood number, was eliminated by means of the Schmidt number,  $Sc = \nu/\mathcal{D}$ , with the result that  $Sh = (KR/\nu)Sc$ . The value of the Schmidt number is 2.5 for naphthalene diffusion in air (Sogin, 1958).

The absolute viscosity, which appears in the evaluation of the Sherwood and Reynolds numbers, was evaluated as a function of the naphthalene surface temperature for pure air, and the density was evaluated at the measured barometric pressure.

It is to be expected that the angular velocity  $\omega$  of the disk will play a key role in establishing the value of the Sherwood number. A Reynolds-number-like dimensionless group was formulated in which the disk radius,  $R$ , was used as the characteristic length since it was common to all test runs. Thus,

$$Re_r = \rho\omega R^2/\mu \quad (5)$$

## Results and Discussion

The experimental mass transfer data obtained are shown in Fig. 5 where the Sherwood number for the active side wall surface is plotted as a function of spacing ratio ( $G/D$ ) with the rotational Reynolds number as the parameter. Experimental mass transfer data were obtained for spacing ratios of 0.0077, 0.0115, and 0.0154, which are equivalent to distances between the rotating disk and side wall surfaces of 1 mm, 1.5 mm, and 2 mm, respectively. It is clear from the figure that the Sherwood number for the side wall increases with the rotational Reynolds number and that at each spacing ratio, the data are well correlated by a power-law relation of the form  $Sh = C Re^n$ , where the  $C$  and  $n$  values are listed adjacent to the respective lines.

The data for the various spacing ratios are arranged in decreasing order with increasing spacing ratios. In effect, the momentum imparted to the fluid by the rotating disk diminishes in influence on the stationary side wall as the wall moves further away from the disk. However, as shown in Fig. 5, the data for rotational Reynolds number below 10,000 showed no appreciable differences for the three spacing ratios tested.

For comparison purposes the results of Sparrow and Gregg (1959) for the mass transfer from a rotating disk without any enclosing surfaces, commonly denoted as a free or isolated disk, are shown in Fig. 5. Additionally, the results of Kreith et al. (1963) for mass transfer from a 130-mm-dia rotating disk with parallel enclosing surfaces at spacing ratios identical to two of those tested in the current investigation are also shown. Several

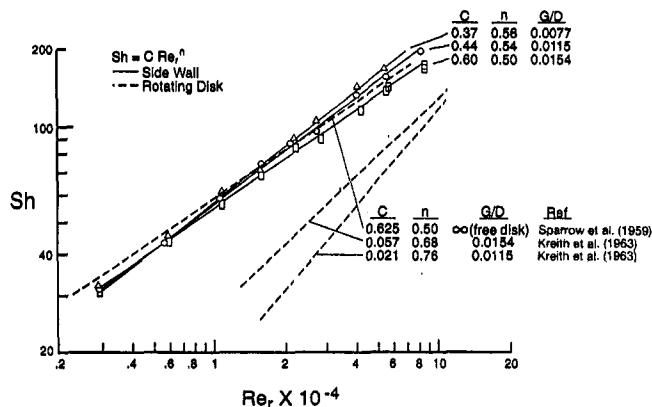


Fig. 5 Sherwood number versus rotational Reynolds numbers at various spacing ratios

observations can be made on comparing the mass transfer from the rotating disk to that from the stationary side wall. First, it is somewhat surprising that the mass transfer from the stationary surface measured in this study are nearly the same as that of a free rotating disk. For some spacing ratios and rotational Reynolds numbers the mass transfer results from the side wall are actually higher than that of the rotating disk. In comparing the results for both the disk and stationary surfaces for spacing ratios of 0.0154 (2 mm gap) and 0.0115 (1.5 mm gap) the results for the side wall are significantly higher than those from the rotating disk. For example, at a rotational Reynolds number of 20,000 and a spacing ratio of 0.0154 (2 mm gap) the mass transfer results from the side wall are approximately 80 percent higher than that of the disk. Not only that, but the change in mass transfer with spacing ratio significantly affects the disk mass transfer while minimum effects on the side wall are evident.

The investigation by Richardson and Saunders (1963) may aid in understanding this observed phenomenon. An isolated rotating disk can be considered a source of a radial jet, which has a tangential velocity component at all radii. Experiments with disks of the form used in the present research showed that vortices formed as the boundary layers on the disk surfaces flowed over the sharp edges of the rim of the disk. In the region radially just beyond the rim of the disk considerable entrainment occurs, and according to Richardson and Saunders (1963), this entrainment extends radially outward by about 40 percent of the disk radius. When stationary surfaces larger than the disk are brought close to the disk, gross flow instabilities can occur beyond the disk. This region beyond the disk then may contribute significantly to the heat transfer on the stationary wall so that the overall heat transfer when compared to the rotating disk is greater. Of course, this hypothesis must be verified with further experimental work.

The commonality of the equations describing the parallel side wall mass transfer suggested a further correlation in which  $C$  and  $n$  were functions of the spacing between the disk and side wall surfaces. Such a general correlation is shown in Fig. 6, where the equation of the correlation line is

$$Sh = 13.09 (G/D)^{0.75} Re_r^{0.26(G/D)^{-1.6}} \quad (6)$$

Of the 32 data points plotted in Fig. 6, 29 lie within 4 percent of the line. Three points deviate up to 5.7 percent from the best fit line. The correlation coefficient for the regression curve is 0.998. Thus Eq. (6) can be regarded as an excellent representation of the data.

A photograph illustrating the flow pattern is shown in Fig. 7. Various disk-to-wall spacings and rotational speeds were examined but no noticeable differences in the flow pattern as indicated by the position of the threads were observed. In addition, any oscillatory motion of the threads was almost nonexistent. As with all the studies reported herein, the disk rotation was in the coun-

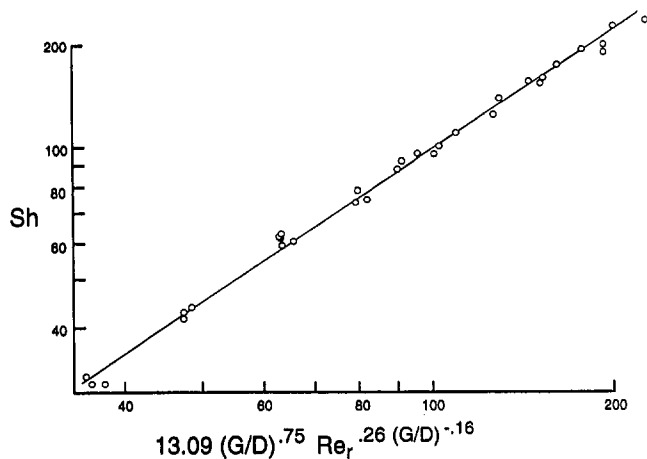


Fig. 6 Comparison of experimental data with the dimensionless correlation equation for mass transfer from a surface partially enclosing a rotating disk

terclockwise direction. As evident in the photograph the flow in the lower half of the channel exhibited flow velocities that, for the most part, were tangential to the disk rotation, these velocities being imparted by the tangential friction drag at the surface of the disk. Flow is drawn in at the bottom of the channel beyond the disk and in a tangential direction as evident by the two threads (faintly visible) attached at the bottom of the channel. Flow exited the upper half of the channel essentially in a vertical direction, except for the flow near the top of the disk, which appeared to be exiting the channel at an angle of approximately 45 deg to the horizontal. The basic flow pattern then appears as tangential inflow in the lower half of the channel with vertical outflow at the top half of the channel.

As noted in the introduction, this research is focused on understanding the heat transfer characteristics of a series of disks rotating between fins of a parallel finned heat sink. This design could be a replacement for a standard air moving device cooling a finned heat sink. Therefore, it is desirable to compare the present results with those for forced convection heat transfer in a rectangular channel with the parallel side walls defined by the inactive and active walls in the present research. Among the available correlations, the Gnielinski modification (Gnielinski, 1976) of the well-established Petukhov–Popoc equation covers the widest Reynolds number range ( $Re > 2300$ ) because it spans both the transition and turbulent regimes. According to Gnielinski, the average Nusselt number for a channel of length  $L/D_h$  is given by

$$Nu = \frac{(f/8)(Re - 1000) Pr [1 + (D_h/L)^{2/3}]}{1 + 12.7(f/8)^{1/2}(Pr^{2/3} - 1)} \quad (7)$$

where

$$f = [1.82 \log(Re) - 1.64]^{-2} \quad (8)$$

The hydraulic diameter of the channel,  $D_h$ , is defined by

$$D_h = \frac{4(2G + t)H}{(2G + t) + 2H} \quad (9)$$

For mass transfer, the Nusselt and Prandtl numbers appearing in Eq. (7) are replaced by the Sherwood and Schmidt numbers. In addition heat transfer coefficients from heating of one wall of a rectangular duct have been shown by Sparrow (1966) to be about 20 percent lower than that of equal heating represented by the Gnielinski correlation. To account for this reduction in heat transfer the right-hand side of Eq. (7) is decreased by 20 percent. With these changes and after setting  $Sc = 2.5$  for naphthalene sublimation in air, Eq. (7) provides the value of  $Sh$  for given

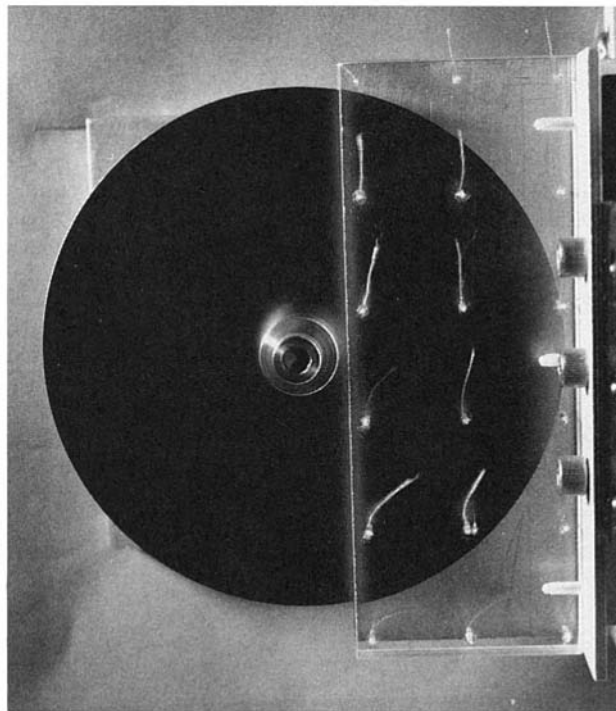


Fig. 7 Photograph of the flow pattern near the stationary side wall partially enclosing a rotating disk

values of  $Re$  and  $L/D_h$ . Then Eq. (7) can be used to find the channel-flow Reynolds number  $Re$ , which yields the same Sherwood number as was obtained at a given value of rotational Reynolds number  $Re_r$  in the present experiments.

Since only slight differences in mass transfer coefficients existed over the range of spacing ratios, the equivalent channel-flow Reynolds numbers are plotted in Fig. 8 as a function of rotational Reynolds number  $Re_r$ , for only the middle spacing ratio, namely, 0.0115 (1.5 mm gap). This figure shows that the channel Reynolds numbers are quite high, an order of magnitude higher than conventional flows through parallel fin heat sinks of this type. In addition the channel Reynolds number suggests the flows are turbulent in nature. Most likely a portion of the flow passing over the side wall is laminar and a portion turbulent. As the

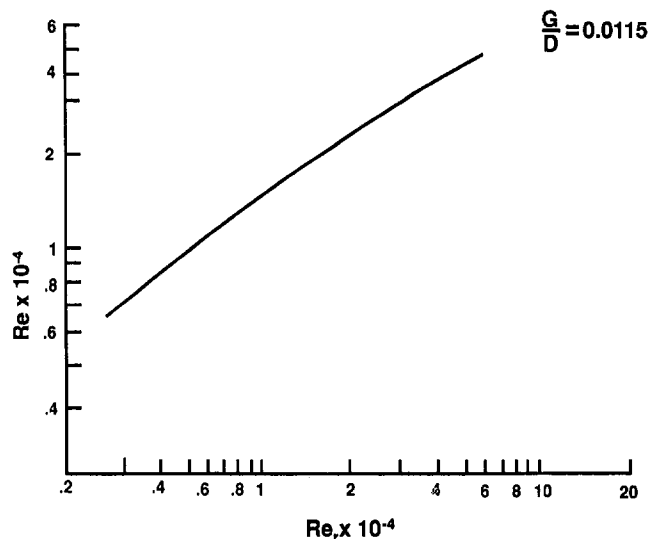


Fig. 8 Values of channel Reynolds number  $Re$  and rotational Reynolds number  $Re_r$ , which yield the same Sherwood number

rotational Reynolds number increases the laminar region decreases while the turbulent region increases.

Finally, attention is turned to the analysis of the errors in the present research. As shown in Eq. (6) three primary variables are used in correlating the data,  $Sh$ ,  $Re_r$ , and  $G/D$ . The uncertainties in these three variables may be divided into two major types: (1) experimental uncertainties, and (2) fluid property uncertainties. These uncertainties can be summarized as follows: naphthalene and fluid temperatures  $\pm 0.2^\circ\text{C}$ , sublimed mass  $\pm 0.1$  mg, surface area of naphthalene  $\pm 1.4$  percent, run duration time  $\pm 2$  s, rotational disk speed  $\pm 1$  rpm, disk diameter  $\pm 0.4$  percent, disk to wall gap  $\pm 0.05$  mm, and fluid kinematic viscosity  $\pm 1.5$  percent. If the same level of accuracy is desired in the three primary variables as in the individual components used in computing this result, then the proper method of combining individual errors is with the mean-square error (Scarborough, 1962) or root-sum square formula (Doebelin, 1975). For example, the rotational Reynolds number can be expressed by

$$Re_r = \frac{\omega R^2}{\nu} \quad (10)$$

Then the uncertainty in  $Re_r$  is given by

$$\left(\frac{\partial Re_r}{Re_r}\right) = \sqrt{\left(\frac{\partial \omega}{\omega}\right)^2 + \left(2\frac{\partial R}{R}\right)^2 + \left(\frac{\partial \nu}{\nu}\right)^2} \quad (11)$$

Substitution of the estimated uncertainties of the variables in the right-hand side of the equation above yields an uncertainty interval in rotational Reynolds number of  $\pm 1.5$  to  $\pm 1.8$  percent depending on the rotational speed of the disk. Using the same technique the uncertainty interval in the Sherwood number is  $\pm 2.5$  percent and in  $G/D \pm 5$  percent for the 1 mm gap ( $G$ ) and  $\pm 2.5$  percent for the 2 mm gap ( $G$ ).

### Concluding Remarks

It still remains to relate the mass transfer results to heat transfer. According to the analogy, at a fixed Reynolds number and fixed geometric parameters, the Sherwood and Nusselt numbers are equal when the Schmidt number for the mass transfer process equals the Prandtl number for the heat transfer process. Thus, with regard to the present experiments, where  $Sc = 2.5$ ,

$$Nu = Sh \quad \text{for} \quad Pr = 2.5 \quad (12)$$

The generalization of the thus-obtained Nusselt number results for  $Pr = 2.5$  to other Prandtl numbers will now be considered. From the flow visualization results presented in a preceding section of the paper suggest that the flow is of the boundary layer type. For such flows,  $Nu \sim Pr^{1/3}$  for  $Pr \geq 0.7$ . Therefore, from Eq. (3) the Nusselt number for an arbitrary Prandtl number can be related by

$$Nu = 9.64 Pr^{1/3} (G/D)^{0.75} Re_r^{0.26(G/D)^{-16}} \quad (13)$$

For a  $Pr = 0.7$  for air this relationship becomes

$$Nu = 8.56 (G/D)^{0.75} Re_r^{0.26(G/D)^{-16}} \quad (14)$$

### References

- Daily, J. W., and Nece, R. E., 1960, "Chamber Dimension Effects on Induced Flow and Frictional Resistance of Enclosed Rotation Disks," *ASME Journal of Basic Engineering*, Vol. 82, pp. 217-232.
- Doebelin, E. O., 1975, *Measurement Systems*, McGraw-Hill, New York, p. 64.
- Gnielinski, V., 1976, "New Equations for Heat and Mass Transfer in Turbulent Pipe and Channel Flow," *Int. Chem. Engng.*, Vol. 16, pp. 359-368.
- Kreith, F., Taylor, J. H., and Chong, J. P., 1959, "Heat and Mass Transfer From a Rotating Disk," *ASME JOURNAL OF HEAT TRANSFER*, Vol. 81, pp. 95-104.
- Kreith, F., Doughman, E., and Kozlowki, H., 1963, "Mass and Heat Transfer From an Enclosed Rotating Disk With and Without Source Flow," *ASME JOURNAL OF HEAT TRANSFER*, Vol. 85, pp. 153-163.
- Kreith, F., 1968, "Convection Heat Transfer in Rotating Systems," *Advances in Heat Transfer*, Vol. 5, T. F. Irvine and J. P. Hartnett, eds., Academic Press, New York, pp. 129-251.
- Maroti, L. A., Deak, G., and Kreith, F., 1960, "Flow Phenomena of Partially Enclosed Rotation Disks," *ASME Journal of Basic Engineering*, Vol. 82, pp. 539-552.
- Metzger, D. E., 1970, "Heat Transfer and Pumping on a Rotating Disk With Freely Induced and Forced Cooling," *ASME Journal of Engineering for Power*, Vol. 92, pp. 342-348.
- Nece, R. E., and Daily, J. W., 1960, "Roughness Effects on Frictional Resistance of Enclosed Rotating Disks," *ASME Journal of Basic Engineering*, Vol. 82, pp. 553-562.
- Richardson, P. D., and Saunders, O. A., 1963, "Studies of Flow and Heat Transfer Associated With a Rotating Disc," *Journal of Mechanical Engineering Science*, Vol. 5, No. 4, pp. 336-342.
- Scarborough, J. B., 1962, *Numerical Mathematical Analysis*, 5th ed., The John Hopkins Press, p. 489.
- Sogin, H. H., 1958, "Sublimation From Disks to Airstreams Flowing Normal to Their Surfaces," *Trans. ASME*, Vol. 80, pp. 61-71.
- Soo, S. L., 1958, "Laminar Flow Over an Enclosed Rotating Disk," *Trans. ASME*, Vol. 80, pp. 287-296.
- Sparrow, E. M., and Gregg, J. L., 1959, "Heat Transfer From a Rotating Disk to Fluids of Any Prandtl Number," *ASME JOURNAL OF HEAT TRANSFER*, Vol. 81, pp. 249-251.
- Sparrow, E. M., Lloyd, J. R., and Hixon, C. W., 1966, "Experiment on Turbulent Heat Transfer in an Asymmetrically Heated Rectangular Duct," *ASME JOURNAL OF HEAT TRANSFER*, Vol. 88, pp. 170-174.

# Turbulence Dissipation in a Free-Surface Jet of Water and Its Effect on Local Impingement Heat Transfer From a Heated Surface: Part 1—Flow Structure

D. H. Wolf<sup>1</sup>

R. Viskanta

F. P. Incropera

Heat Transfer Laboratory,  
School of Mechanical Engineering,  
Purdue University,  
West Lafayette, IN 47907

*This study investigates the relationship between jet turbulence and local impingement heat transfer for a free-surface, planar jet of water. Employing a thermal anemometer system, measurements of the mean velocity and turbulence intensity are reported at different streamwise and spanwise locations throughout the jet. The flow conditions at the nozzle discharge were controlled by using different nozzle designs (parallel-plate and converging) and flow manipulators (wire grid and screens). Measurements of the velocity gradient along the impingement surface, known to influence heat transfer from analytical considerations of a laminar impinging jet, were also made for the same sets of nozzle conditions. The test matrix also included variations in the Reynolds number (23,000 and 46,000) and distance from the nozzle discharge to the surface (0 to 30 nozzle widths). The local heat transfer results corresponding to the flow structure measurements are reported in Part 2 of this paper.*

## Introduction

Convective cooling of high-heat flux surfaces through single or multiple jet impingement is becoming increasingly common in physical situations where large rates of heat transfer are required. The cooling of microelectronic components, neutron beam dumps, and processed metals are only a few of the high-flux applications currently facing thermal engineers. Of the different types of jet systems (*submerged*: gas-into-gas or liquid-into-liquid; *free-surface*: liquid-into-gas), the free-surface arrangement is the least understood, despite its many current uses. Investigations of submerged jets are numerous and all-encompassing, addressing both the hydrodynamic and thermal aspects of such systems (see reviews by Martin, 1977; Polat et al., 1989; Kataoka, 1990; Jambunathan et al., 1992; Viskanta, 1993). By contrast, due to difficulties in obtaining flow measurements within the jet, posed largely by the need to cross the liquid/gas interface, investigations of free-surface jets have been largely confined to heat transfer results. This lack of hydrodynamic information has forced investigators to rely largely on laminar, analytical results, coupled with conjecture about the effects of jet turbulence, to interpret heat transfer data.

Analytically, a laminar, impinging jet may be treated as a subset of the broader problem associated with an infinite, uniform, laminar flow past a wedge, where the included angle is variable. Falkner and Skan (1931) developed similarity transformations applicable to this flow geometry with constant thermophysical properties. If the included angle of the wedge is increased to a value of  $\pi$ , the Falkner–Skan analysis predicts heat transfer from a planar surface at constant temperature to an impinging jet of infinite extent. This solution may also be applied to a jet of finite width ( $w_j$ ) at locations very near the stagnation point (Vader et al., 1991). Levy (1952) has shown that the Falkner–Skan anal-

ysis is the same for both a constant temperature and a heat flux boundary condition, as long as the wedge angle is equal to  $\pi$ . Hence, for a laminar, planar jet that impinges on a constant temperature or constant heat flux surface, the convection coefficient at the stagnation point  $h(0)$  is given by

$$h(0) = 0.570 \frac{k_f}{w_j} \left( \frac{C}{\nu} \right)^{1/2} \text{Pr}^{0.375} \quad (1)$$

where the Prandtl number dependence is based on the analytical results of Evans (1962), and  $C$  is the free-stream velocity gradient along the impingement surface

$$C = \frac{d\bar{U}_\infty}{dx} \quad (2)$$

When scaled in terms of the average jet velocity ( $\bar{V}_j$ ) and jet width ( $w_j$ ), Eq. (1) may be presented in dimensionless form as

$$\text{Nu}_j = 0.570 G^{1/2} \text{Re}_j^{1/2} \text{Pr}^{0.375} \quad (3)$$

where  $G$  is the dimensionless velocity gradient ( $G = Cw_j/\bar{V}_j$ ). The parameter  $G$ , although it arises directly from the governing equations, has seldom been acknowledged in experimental investigations. Rather, the quantity  $G^{1/2}$  has typically been absorbed in the correlated constant. The experimental investigation of a circular, free-surface jet by Pan et al. (1992) is the exception, where the functional dependence of  $G$  was correlated.

For conditions where the flow is turbulent, several authors reporting on heat transfer at the stagnation region of both a cylinder in crossflow (Kestin and Wood, 1971; Lowery and Vachon, 1975) and a submerged, impinging jet (Hoogendoorn, 1977; van der Meer, 1991) have contended that the foregoing laminar relationship may be modified to include the influence of the flow's turbulence intensity  $\tilde{v}$ , yielding a dependence of the form

$$\text{Nu}_j = f(G, \text{Re}_j, \text{Pr}, \tilde{v}) \quad (4)$$

where independent increases in  $\tilde{v}$  were shown to yield increases in the stagnation line Nusselt number, although the relationship was not demonstrated to be limitless.

<sup>1</sup>Current address: Owens-Corning Science & Technology Center, 2790 Columbus Rd., Granville, OH 43023.

Contributed by the Heat Transfer Division for publication in the JOURNAL OF HEAT TRANSFER. Manuscript received by the Heat Transfer Division July 1993; revision received February 1994. Keywords: Jets, Turbulence. Associate Technical Editor: A. Faghri.



Thus far, nearly all of the investigations pertaining to free-surface, jet impingement heat transfer have correlated the Nusselt number in terms of the Reynolds and Prandtl numbers only. Recent reviews of the free-surface, jet impingement literature underscore this point (Faggiani and Grassi, 1990a, 1990b; Vader et al., 1991). As a result, data reported by different investigators are not in agreement. Several investigators (Zumbrunnen et al., 1989; Wolf et al., 1990; Stevens and Webb, 1991; Vader et al., 1991) have speculated about the importance of both the velocity gradient and turbulence intensity on convective transport in the stagnation region of a jet.

To the authors' knowledge, the only published work that has examined the relationship depicted in Eq. (4) for a free-surface jet was the investigation performed by Webb and his co-workers. They presented, as companion papers, the effects of various nozzle configurations on the turbulence intensity and velocity gradient at impingement (Stevens et al., 1992) and on the stagnation-zone heat transfer (Pan et al., 1992). Their measurements were made on a circular, free-surface jet of water that was generated by either a fully developed pipe-type nozzle, a contoured orifice, or a sharp-edged orifice with and without upstream damping screens.

Their investigation used a pseudo-radial turbulence intensity (ratio of the radial rms fluctuating velocity to the mass-averaged jet velocity at the nozzle discharge) as the figure-of-merit to characterize the influence of turbulence on impingement heat transfer. The correlation of their results is

$$Nu_d = 1.115 Re_d^{0.53} G^{0.63} \left( \frac{u'}{\bar{V}_n} \right)^{-0.022} \quad (5)$$

where  $Nu_d$  is the stagnation point Nusselt number based on nozzle diameter  $d_n$ ,  $Re_d$  is the Reynolds number based on  $\bar{V}_n$  and  $d_n$ ,  $G$  is the dimensionless radial velocity gradient at the stagnation point, and  $u'$  is the radial rms fluctuating velocity. This correlation indicates virtually no dependence of the stagnation point Nusselt number on the turbulence level, at least as gaged by the radial component.

This investigation explores the functional relationship depicted by Eq. (4) for a free-surface, planar jet of water. Although limitations with the experimental apparatus precluded variations of the Prandtl number, the remaining independent variables ( $G$ ,  $Re_j$ , and  $\bar{v}$ ) were investigated, and their functional relationship to the convection coefficient was assessed. Specifically, Part 1 of this report presents the results of turbulence measurements obtained following ejection from a nozzle but prior to impingement and

velocity gradient measurements obtained in proximity to the jet's stagnation point. Part 2 of this report presents single-phase heat transfer measurements taken locally along the impingement surface and correlation of the results. The test matrix included variations in the Reynolds number ( $23,000 \leq Re_n \leq 46,000$ ), nozzle-to-surface spacing ( $2 \leq y/w_n \leq 30$ ), turbulence intensity ( $0.012 \leq \bar{v} \leq 0.055$ ), and velocity gradient ( $0.79 \leq G \leq 1.13$ ). The turbulence intensity and velocity gradient were controlled by different nozzle designs and turbulence manipulators.

## Experimental Methods and Apparatus

Figure 1 shows the essential features of the velocimetry measurements as well as the coordinate system. The technique chosen to measure the streamwise mean and rms velocities within the jet was a constant temperature thermal anemometer system (Dantec, Model 55M01), where the sensing element was a conical hot-film probe (TSI, Model 1230W). The hot-film probe was mounted in a stainless steel support tube, which was bent at a 90° angle to allow access from a direction transverse to the mean flow. The 90° bend was 95 mm (9.4 nozzle widths) downstream of the sensing element to preclude flow disturbances. The support tube was mounted in a positioning assembly, which enabled accurate movement of the probe in both the transverse ( $x$ ) and longitudinal ( $y$ ) directions.

Selection of the conical hot-film probe, in lieu of the more common hot-wire or cylindrical hot-film geometries, was based on the unique flow conditions of this study. Use of a hot wire in a water flow with velocities in the range of 2 to 4 m/s would have been impractical because of the wire's fragility (5  $\mu$ m wire diameter). The cylindrical hot-film probe, although more durable, was plagued with turbulent vortex shedding from the aft portion of the cylinder, because its Reynolds number based on cylinder diameter (70  $\mu$ m) was too large. The vortex shedding would cause the anemometer to sense turbulence even in a laminar bulk flow. Although the literature describing thermal anemometry measurements in liquids with velocities in excess of 1 m/s is small compared to measurements in gases, there exists a well-accepted consensus that difficulties from eddy shedding and contamination may be eliminated by using a hot-film probe of conical geometry (Resch, 1970; Morrow and Kline, 1971; Warschauer et al., 1974; Hinze, 1975). Likewise, several investigators have successfully demonstrated the accuracy of this type of probe for liquid flows (Friehe and Schwarz, 1969; Rodriguez et al., 1970; Resch, 1970; Warschauer et al., 1974).

## Nomenclature

$AR$  = aspect ratio of a rectangular channel (nozzle)  
 $C$  = free-stream velocity gradient along the impingement surface =  $dU_\infty/dx$   
 $d$  = screen-wire diameter  
 $d_n$  = diameter of a circular nozzle  
 $D_h$  = hydraulic diameter  
 $g$  = gravitational acceleration  
 $G$  = dimensionless free-stream velocity gradient =  $Cw_j/\bar{V}_j$   
 $h$  = local convection heat transfer coefficient =  $q''/[T_w - T_f]$   
 $k_f$  = thermal conductivity of the liquid  
 $M$  = screen-mesh length  
 $Nu_d$  = stagnation point Nusselt number =  $h(0)d_n/k_f$   
 $Nu_j$  = stagnation point Nusselt number =  $h(0)w_j/k_f$

$P$  = local pressure along the impingement surface  
 $Pr$  = Prandtl number  
 $q''$  = surface heat flux  
 $Re_d$  = Reynolds number =  $\bar{V}_n d_n/\nu$   
 $Re_j$  = Reynolds number =  $\bar{V}_j w_j/\nu$   
 $Re_n$  = Reynolds number =  $\bar{V}_n w_n/\nu$   
 $Re_M$  = Reynolds number =  $\bar{V}M/\nu$   
 $T_f$  = liquid temperature  
 $T_w$  = local temperature on the wet side of the heated surface  
 $u, v, w$  = fluctuating components of velocity  
 $u', v', w'$  = root-mean-square (rms) fluctuating components of velocity  
 $\bar{u}, \bar{v}, \bar{w}$  = turbulence intensity =  $u'/\bar{U}, v'/\bar{V}, w'/\bar{W}$

$U, V, W$  = instantaneous components of velocity  
 $\bar{U}, \bar{V}, \bar{W}$  = mean components of velocity  
 $\bar{U}_\infty$  = mean inviscid velocity along the impingement surface  
 $\bar{V}_j$  = mass-averaged jet velocity at a distance  $y$  from the nozzle exit =  $(\bar{V}_n^2 + 2gy)^{1/2}$   
 $\bar{V}_n$  = mass-averaged jet velocity at the nozzle discharge  
 $w_j$  = jet width at a distance  $y$  from the nozzle exit =  $w_n \bar{V}_n/\bar{V}_j$   
 $w_n$  = nozzle width  
 $x, y, z$  = orthogonal coordinate directions with origin at the center of the nozzle outlet  
 $\nu$  = kinematic viscosity  
 $\rho$  = density of the liquid

To assess the suitability of this type of probe for the measurements of this investigation, experiments were conducted *inside* the parallel-plate nozzle and compared to results for a parallel-plate channel (Hussain and Reynolds, 1975). Due to the large size of the probe relative to the nozzle width, measurements could not be obtained near the wall and were thus limited to the central 80 percent of the nozzle. Agreement with the results of Hussain and Reynolds was within 2 percent for the mean velocity and 12 percent for the turbulence intensity, both of which were considered acceptable.

The voltage output from the anemometer was read digitally by a variable-gain, 12-bit *A/D* converter. The mean and rms fluctuating velocities were computed from 10,000 data sampled at varying acquisition rates depending on the bulk velocity of the flow. The number of data was chosen to achieve a statistically large ensemble. The acquisition rate was selected such that the length of the sampling interval would allow approximately 10,000 large-scale eddies to pass the hot-film probe, with approximately one data point obtained for each eddy. An approximate estimate for the time required for a large-scale eddy to be advected past the probe was obtained from the ratio of the flow's characteristic length ( $w_n$ ) to its characteristic velocity ( $\bar{V}_n$ ). For a fixed nozzle width of 10.2 mm and average nozzle velocities of 2 and 4 m/s, the approximate time interval that the probe was located within a single eddy was 2.5 or 5.0 ms; hence, the acquisition rate was either 200 samples/s for the low-velocity case ( $\bar{V}_n = 2.0$  m/s) or 400 samples/s for the high-velocity case ( $\bar{V}_n = 4.0$  m/s) (sampling intervals of 50 and 25 seconds, respectively). Although these specific sampling rates were used consistently for all experiments, the rms velocities were found to be insensitive to sampling rate provided that the sampling was done slowly enough to avoid multiple readings being taken within a single eddy.

The only data conditioning that was applied to the measured anemometer signal was done to correct for the presence of air bubbles in the jet flow. It was observed that, at certain locations within the jet, large voltage spikes would be superimposed on the typical fluctuating voltage signal. The spikes, negative with respect to the mean voltage and typically more than ten times larger than the turbulence-induced fluctuations, were caused by air bubbles that were entrained into the flow following ejection from the nozzle. A good description of the air entrainment phenomenon is given by Hoyt and Taylor (1977), with particularly revealing photographs being presented in a later publication by the same authors (Taylor and Hoyt, 1983). The large voltage change resulted from an air bubble striking the hot film and causing its temperature to rise momentarily. This increase in temperature was sensed by the bridge circuitry, which in turn decreased the bridge voltage in an attempt to lower the film temperature. The number of these spikes in a given time interval increased with increasing streamwise distance (*y* coordinate) away from the nozzle exit, increasing lateral distance (*x* coordinate) toward the free interface, and increasing Reynolds number for a fixed probe location. Voltage records (10,000 samples long) containing fewer than 100 spikes were accepted as usable data sets, and the voltage spikes were removed from the record prior to processing. Those sets with more than 100 spikes were rejected. This criterion is predicated on the premise that spurious data exceeding 1 percent of the data record (100 spikes in 10,000 samples) would have made the extraction of accurate velocimetry data more difficult. Since the voltage spikes were an artifact of the bubbles and not the turbulence, they were removed from the data set prior to computing the mean and rms fluctuating velocities. All results presented in this paper that are based on conditioned data are indicated with a vertical tick drawn through the data point (i.e., unconditioned ■; conditioned ■). The bubbles, present in the pre-impinging jet, would also clearly be present at impingement. However, this investigation did not examine the influence of the air bubbles on impingement heat transfer.

Spectral analysis of the anemometer voltage revealed a periodic oscillation in the flow with a frequency of approximately 18 Hz. Diagnostic tests on the entire flow system revealed that the pulsation existed as far upstream as the pump and may in fact have been induced by the pump. No effort was made to eliminate this pulsation from the flow, because the core interest of this study was to investigate the effect of turbulence, as gaged by the turbulence intensity, on the impingement heat transfer. Any velocity fluctuations in the flow, whether they be regular (pulsation) or random (turbulence), would also be present during the heat transfer measurements and would each have its respective impact on the thermal transport. Hence, the presence of this low-frequency pulsation was not viewed as intrusive, as it might be in a pure fluid mechanical investigation, but rather as an artifact of the system that was present for both turbulence and heat transfer measurements.

The magnitude of the pulsation was small relative to the natural turbulence level for all the flow conditions to be discussed except for the low-Reynolds-number, converging nozzle case. This flow condition generated very low levels of naturally induced turbulence, which accentuated the vibration's influence on the flow. This influence will be discussed further as it pertains to the results for the converging nozzle. More quantitative details concerning the pulsation are presented by Wolf (1993).

The fluid consisted of demineralized, deionized water (specific resistance  $>10$  M $\Omega$ -cm) that was continuously passed through a 5  $\mu$ m, cartridge-type filter to remove any small-scale sediment. All the turbulence measurements were obtained with the anemometer operating at an overheat ratio of 0.05. For the fixed fluid temperature of 25°C, this overheat ratio corresponded to an operating film temperature of 49°C and a temperature difference between the film and fluid of 24°C. This overheat ratio was chosen because it provided sufficient sensitivity while still maintaining a relatively low film temperature to avoid generating bubbles (vapor or noncondensable gases) at the film surface. The temperature of the water for both experiments and calibrations was held constant to within  $\pm 0.05^\circ\text{C}$  of 25°C to avoid thermal drift in the signal. Calibration of the hot-film anemometer was achieved by placing the probe within a laminar, cylindrical jet of known velocity, which was produced at a sharp-edged orifice located at the bottom of a tank of water. The relationship between the height of the water and the velocity at the orifice was derived from Bernoulli's equation with the application of a measured loss coefficient (Wolf, 1993).

The primary nozzle was a parallel-plate channel with rectangular cross-sectional dimensions of 10.2 mm  $\times$  102 mm ( $D_h = 18.5$  mm;  $AR = 10$ ) and an axial length of 935 mm ( $50.6D_h$ ;  $92w_n$ ). In addition to considering the natural turbulence that results from the fully developed channel flow, several techniques were adopted either to mechanically manipulate the turbulence that existed at the outlet of the parallel-plate channel or to use a completely different low-turbulence nozzle. The mechanical manipulators consisted of two different types of screens and a wire grid. The low-turbulence nozzle consisted of a converging section to damp upstream disturbances and an outlet geometry that was identical to that of the parallel-plate nozzle.

The screens and wires were attached to the nozzle as shown in Fig. 1. A holder was designed to fit over the outlet of the parallel-plate nozzle while still maintaining the inside channel dimensions of 10.2 mm  $\times$  102 mm. The manipulator would then be in intimate contact with the exit of the nozzle proper and would be followed by a 12.7 mm long section prior to ejection. This extra nozzle length was intended to avoid air entrainment at the manipulator. Table 1 provides all of the characteristics related to the two screens.

A wire grid was chosen as a turbulence manipulator because it generates vortices with their axes parallel to that of the wire. This feature was attractive because it allowed for the generation of vortices that would be aligned with the direction of the velocity gradient on the impingement surface. The ability of such a flow

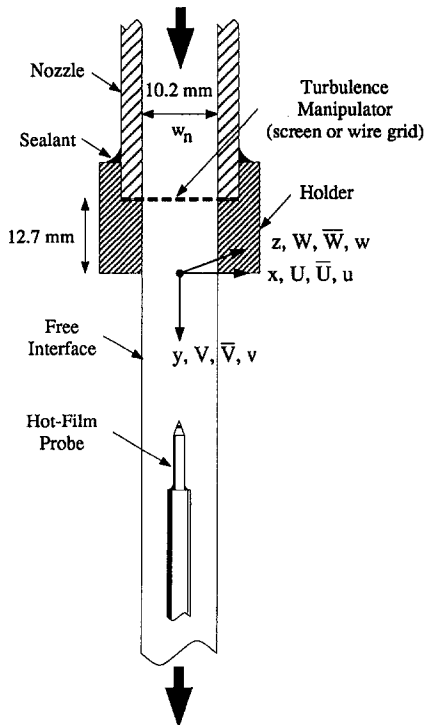


**Fig. 1 Schematic of nozzle exit showing the arrangement employed to introduce turbulence manipulators into the flow, the hot-film probe, and some associated nomenclature**

condition to enhance stagnation point heat transfer has been widely reported, as, for example, by VanFossen and Simoneau (1987) for cylinders in crossflow. The wire grid consisted of an array of wires (0.508 mm diameter on 2.54 mm centers) that were positioned in a plane (the  $x$ - $z$  plane with the wires oriented parallel to the  $x$  axis) normal to the jet flow. Wire size selection was based on guidelines obtained from the archival literature that addressed the phenomenon of heat transfer augmentation through vortex stretching in a stagnated flow (Wolf, 1993).

A converging nozzle was also used in order to achieve very low turbulence levels. It is well established that subjecting a fluid to rapid acceleration (favorable pressure gradient) induces substantial damping of the streamwise turbulent component. Sizable pressure gradients in internal flows may be achieved through large contraction ratios. Investigations on systems of this type have shown transition from fully developed turbulent flow to a near-laminar state (Hoyt and Taylor, 1985). The converging nozzle used in this investigation was the same as that used by Vader et al. (1991), which employed a 5:1 contraction ratio over an axial length  $6\frac{1}{2}$  times the inlet width. The outlet geometry, however, was the same as that of the parallel-plate nozzle (10.2 mm  $\times$  102 mm).

Independent of nozzle configuration, the flow condition corresponding to the lowest Reynolds number (23,000) and largest distance from the nozzle exit ( $30w_n$ ) was the most susceptible to changes in the geometry of the jet's cross section due to surface tension forces, which act to minimize the free surface area (i.e., convert the cross section from rectangular to circular). While the influence of surface tension could clearly be seen for this flow condition in the form of rounded jet corners, it did not influence the measurement domain, which was far-removed from the corners. The measurements were made in the  $x$ - $y$  plane located centrally with respect to the jet's depth of 102 mm.

The free-stream velocity along the impingement surface  $\bar{U}_\infty$  was inferred from knowledge of the static pressure  $P$  by virtue of Euler's equation, which gives

$$\bar{U}_\infty(x) = \left( \frac{2(P(0) - P(x))}{\rho} \right)^{1/2} \quad (6)$$

Static pressure measurements were taken along the impingement surface with a wall tap (0.15 mm diameter) located on a flat, acrylic plate that was translated beneath the jet. The free-stream velocity increases linearly in the region  $0 \leq x/w_j \leq 1$ ; hence, the static pressure was measured within this region and used with Eq. (6) to compute the local free-stream velocity. These results were then subjected to a linear least-squares fit, which yielded the desired velocity gradient at the stagnation point.

Since the velocity  $\bar{U}_\infty$  was inferred from the static pressure measured at the wall, which is equal to the static pressure at the edge of the viscous boundary layer (i.e.,  $\partial P/\partial y = 0$  within the boundary layer), the velocity gradients correspond to those present at the edge of the viscous boundary layer. This distinction is important in light of recent measurements by Stevens et al. (1992), which showed, albeit for a circular jet, that  $G$  was a function of the  $y$  coordinate outside of the viscous boundary layer.

The uncertainties associated with the turbulence and velocity gradient measurements have been assessed in accordance with the method suggested by Kline and McClintock (1953) and Moffat (1988). The worst-case overall uncertainties (based on the root-sum-square of the precision and bias limits) are  $\pm 3$ ,  $\pm 5$ , and  $\pm 9$  percent for  $\bar{V}$ ,  $\bar{v}$ , and  $G$ , respectively. Details of the analysis are provided by Wolf (1993).

## Experimental Results

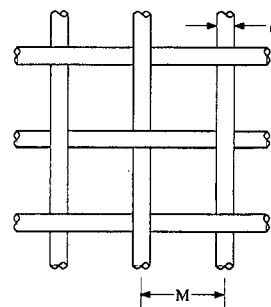
**Mean Velocity and Turbulence Intensity Within the Jet.** This section provides selected mappings of the mean and rms fluctuating velocities within the  $x$ - $y$  plane of the jet. Results presented in this paper are limited to those needed to interpret and correlate the heat transfer data of the companion paper. Correlation of the data will be based on use of the turbulence intensity  $\bar{v}$  at the centerline of the jet as the appropriate figure-of-merit to characterize the effects of turbulence on impingement heat transfer. Hence, only one set of profiles will be presented for the mean velocity and turbulence intensity across the jet width, with greater attention given to the evolution of hydrodynamic conditions along the centerline of the jet. Complete mappings of  $\bar{V}$  and

**Table 1 Specifications of the screens used as turbulence manipulators**

Screen Mesh	M (mm)	d (mm)	M/d	Solidity	$Re_M$	
					at $\bar{V}_n = 2$ m/s	at $\bar{V}_n = 4$ m/s
30 $\times$ 30	0.847	0.165	5.13	35.2%	1900	3800
40 $\times$ 40	0.635	0.165	3.85	45.2%	1420	2840

$$Re_M = \frac{\bar{V}_n M}{\nu}$$

$$\text{Solidity} = \frac{\text{Solid Area}}{\text{Total Area}}$$



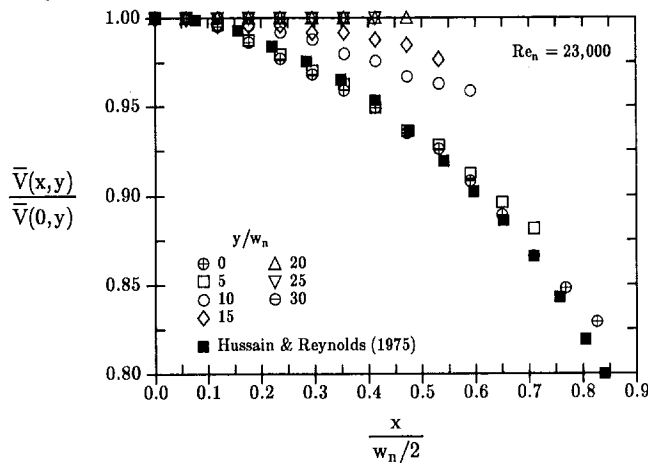


Fig. 2 The streamwise mean velocity profiles across the jet width as a function of the streamwise distance from the nozzle exit for the open nozzle condition and  $Re_n = 23,000$

$\bar{v}$  within the jet are provided by Wolf (1993) for each of the nozzle configurations.

The velocity mappings are subdivided in terms of nozzle type and nozzle-exit condition. For the parallel-plate channel, results are reported for nozzle-exit conditions that are either open (no turbulence manipulators) or involve screens or a wire grid. Since the converging nozzle was intended to provide low-turbulence results relative to the parallel-plate channel, no turbulence manipulators were used (the exit condition was open). Data were obtained at nozzle Reynolds numbers ( $Re_n$ ) of 23,000 and 46,000. The lateral extent of the mappings that follow were often limited by either the free surface, which moves closer to the jet centerline as the flow is accelerated under gravity, or by air bubbles, which were entrained at the free surface and would strike the probe.

**Mean Velocity.** The mean velocity profile for the parallel-plate nozzle with an open exit condition is given in Fig. 2 for the low-Reynolds-number case. The mean velocity data of Hussain and Reynolds (1975) for fully developed, turbulent channel flow is also provided for comparison. The streamwise mean velocity is normalized with respect to the mean velocity at the jet centerline and is presented as a function of the spanwise coordinate ( $x$ ) and parameterized with respect to the streamwise coordinate ( $y$ ). The profile is most nonuniform at the nozzle exit ( $y/w_n = 0$ ), where it retains the primary features of fully developed channel flow, and within the first five nozzle widths from the exit, it remains essentially the same, at least within the spanwise limits of the data ( $2x/w_n \leq 0.83$  at  $y/w_n = 0$  and  $2x/w_n \leq 0.71$  at  $y/w_n = 5$ ). However, at distances beyond  $5w_n$ , the profile begins a gradual transition to a completely uniform condition at approximately 20 nozzle widths. The only other known investigation to report similar velocimetry data was that of Stevens and Webb (1992), who monitored the acceleration of a jet's free surface. The present results, however, are too far removed from the free surface to lend themselves to direct comparison.

Figures 3 and 4 are summaries of all of the centerline mean velocity data as a function of streamwise distance and nozzle condition for the low and high Reynolds numbers, respectively. The solid curve in each of these figures is the estimate of the local mass-averaged velocity (the jet velocity,  $\bar{V}_j$ ) based on an initial value of  $\bar{V}_n$  that is accelerated as a solid body [ $\bar{V}_j(y) = (\bar{V}_n^2 + 2gy)^{1/2}$ ]. The mass-averaged velocity at the nozzle discharge  $\bar{V}_n$  was either 2.0 m/s (Fig. 3,  $Re_n = 23,000$ ) or 4.0 m/s (Fig. 4,  $Re_n = 46,000$ ), independent of the nozzle exit condition. The average jet velocity  $\bar{V}_j$  is the parameter used in all of the heat transfer correlations presented in the companion paper, primarily because of its simplicity. Independent of nozzle type or exit con-

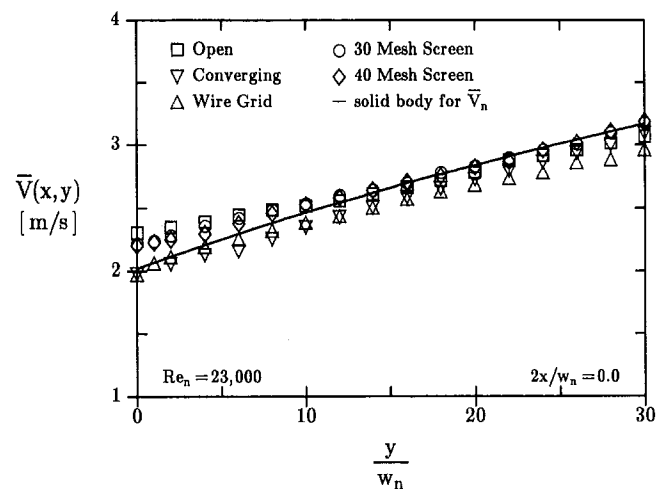


Fig. 3 The evolution of the absolute mean velocity with streamwise distance at a spanwise location of  $2x/w_n = 0.0$  for all nozzle conditions and  $Re_n = 23,000$

dition, the jet velocity may be computed with basic system parameters (volume flow rate, nozzle exit area, and nozzle-to-surface spacing) that would be readily available to the designer of an impingement cooling scheme. The maximum variation between the centerline mean velocity and  $\bar{V}_j$  never exceeded 15 percent.

For both Reynolds numbers, the mean velocity increases with streamwise distance. The two predominant mechanisms that affect this velocity are gravitational acceleration and viscous shear internal to the jet (the shear at the interface between the water and air is negligible). The effect of gravity is to increase the mean velocity with streamwise distance and may be approximated by the following solid-body expression:

$$\bar{V}(x, y) = (\bar{V}(x, 0)^2 + 2gy)^{1/2} \quad (7)$$

The effect of viscous shear is to flatten the mean velocity profile with streamwise distance. Due to the no-slip condition at the boundary, the fluid at the edge of the jet is zero immediately prior to leaving the nozzle ( $y = 0$ ). Thereafter, shear forces increase the mean velocity of the fluid at the liquid/gas interface, at the expense of a reduction in local velocities internal to the jet, ul-

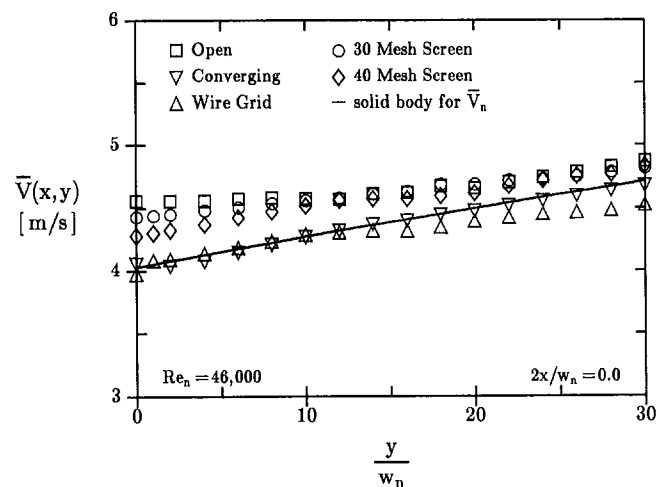


Fig. 4 The evolution of the absolute mean velocity with streamwise distance at a spanwise location of  $2x/w_n = 0.0$  for all nozzle conditions and  $Re_n = 46,000$

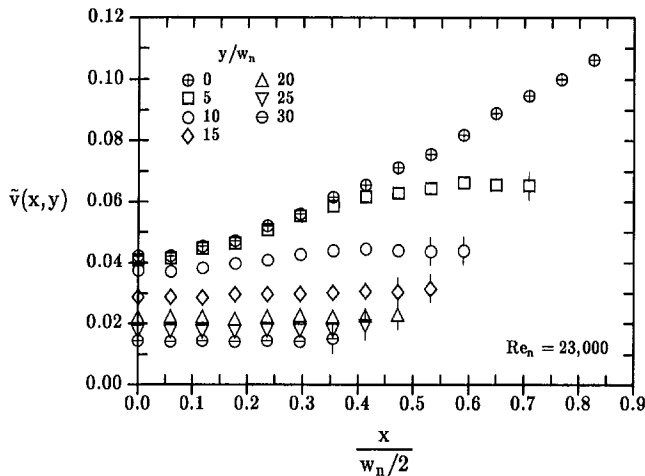


Fig. 5 The streamwise turbulence intensity profiles across the jet width as a function of the streamwise distance from the nozzle exit for the open nozzle condition and  $Re_n = 23,000$

timately resulting in a more uniform velocity profile (Fig. 2). Depending on the spanwise location in the jet, the gravitational and shear forces may operate cocurrent or countercurrent to one another. At the centerline of the jet, for example, these two forces oppose one another until the velocity profile becomes flat, at which time, the gravitational force acts alone.

The spread in centerline mean velocities at the nozzle discharge ( $y/w_n = 0$ ) is due to the different upstream nozzle conditions. While the nozzle Reynolds number  $Re_n$  based on the mass-averaged velocity ( $\bar{V}$ ) was fixed, the centerline velocity at the nozzle exit [ $\bar{V}(0, 0)$ ] varied in accordance with the degree of nonuniformity in the velocity profile. For the converging nozzle, where the mean velocity profile was uniform,  $\bar{V}(0, 0)$  was approximately equal to  $\bar{V}_n$  (the solid line); for the open, parallel-plate nozzle, where the mean velocity profile was nonuniform,  $\bar{V}(0, 0)$  exceeded  $\bar{V}_n$  by approximately 14 percent.

Differences in accelerations over the streamwise length of  $30w_n$  are due to the aforementioned competing mechanisms of gravitational acceleration and viscous shear. For a fixed Reynolds number, those nozzle configurations that yield the most uniform velocity profile at the nozzle exit also have the largest relative acceleration. The mean velocity for the converging nozzle, which yielded the most uniform mean velocity profile at the nozzle exit, experiences the largest relative acceleration. Conversely, the mean velocity for the open, parallel-plate nozzle, which yielded the most nonuniform profile at the nozzle exit, experiences the smallest relative acceleration, since the gravitational acceleration is competing with local deceleration caused by the viscous shear within the jet. The results of Figs. 3 and 4 plotted relative to the mean velocity at  $y/w_n = 0$  are available elsewhere (Wolf, 1993).

**Turbulence Intensity.** Figure 5 shows the turbulence intensity profile for the same nozzle condition and Reynolds number as Fig. 2. The turbulence intensity is most nonhomogeneous at the nozzle exit ( $y/w_n = 0$ ), where it increases monotonically from approximately 4 percent at the centerline of the jet to approximately 10 percent as the nozzle wall and spanwise limits of the data are approached. After a streamwise distance of five nozzle widths, the turbulence intensity begins to decay and become more homogeneous in the outer regions of the jet ( $2x/w_n > 0.4$ ). With increasing streamwise distance, the turbulent decay and homogeneity penetrate deeper into the core of the jet such that, by 15 to 20 nozzle widths, the turbulence is completely homogeneous and of an intensity that is approximately 30 percent below the centerline level at the nozzle exit.

To understand better the transport of turbulent kinetic energy (an approximate measure of  $v'^2$ ) throughout the jet, some insight is sought from the relation governing conservation of the kinetic

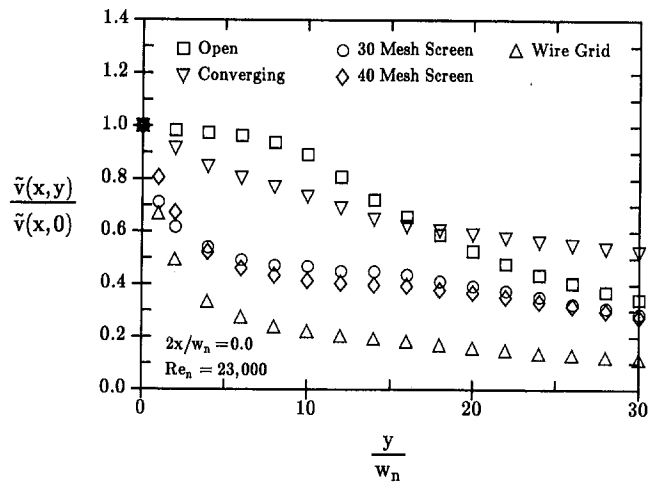


Fig. 6 The evolution of the normalized turbulence intensity with streamwise distance at a spanwise location of  $2x/w_n = 0.0$  for all nozzle conditions and  $Re_n = 23,000$

energy. Hinze (1975) shows that the conservation of turbulent kinetic energy may be demarcated in terms of the following mechanisms: (a) the change that results from unsteadiness in the mean flow and advective transport by the mean motion, (b) diffusion, (c) production, (d) viscous transport, and (e) viscous dissipation. Internal to the nozzle, all five of these mechanisms (except for the unsteady part of term a) contribute to the overall distribution of energy. Following ejection, however, energy production (term c) is approximately zero, since the mean velocity profile quickly becomes uniform (Fig. 2), and the viscous transport of turbulent energy (term d) is negligible everywhere except near a solid surface (Bradshaw, 1971). Hence, the transport of turbulent energy in the jet is governed only by advection (the steady part of term a), diffusion (term b), and viscous dissipation (term e). The outcome is that the turbulent kinetic energy will be redistributed throughout the flow by advection and diffusion (i.e., the turbulence becomes more homogeneous) and will be dissipated by viscous shear (i.e., the turbulence decays). The mappings of the turbulence intensity shown in Fig. 5 support this argument.

Figures 6 and 7 show the turbulence intensity relative to the value at the nozzle exit as a function of streamwise distance and nozzle configuration for the low and high Reynolds numbers,

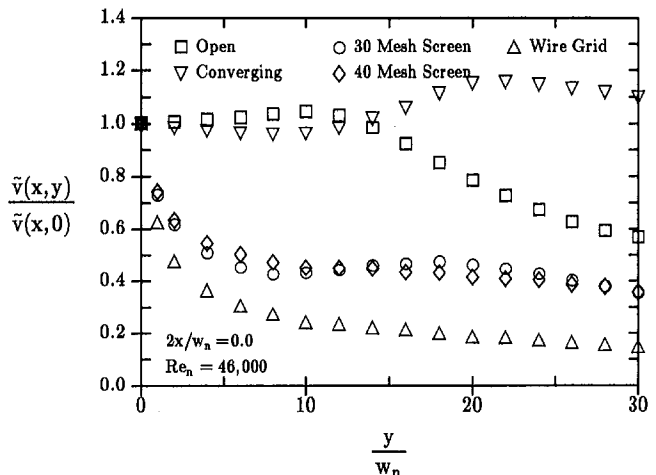


Fig. 7 The evolution of the normalized turbulence intensity with streamwise distance at a spanwise location of  $2x/w_n = 0.0$  for all nozzle conditions and  $Re_n = 46,000$

respectively. These figures demonstrate the vastly different turbulent characteristics that exist among the various flows. All the results involving turbulence manipulators (wire grid and screens) exhibit very rapid decay rates immediately downstream of the nozzle exit. In the absence of a manipulator (open parallel-plate nozzle and converging nozzle), the overall decay rate is much slower and, in some instances, even exhibits local enhancements in the turbulence level with streamwise distance.

For both the wire grid and the screens at both Reynolds numbers, the turbulence intensity decreases by more than a factor of two within a distance of  $6w_n$  from the nozzle exit; thereafter, the decay rate is much more gradual. This precipitous decline in the turbulence level is caused by a level of viscous dissipation that greatly exceeds advection and diffusion because of the small-scale turbulent structures created by the manipulator. In an unmanipulated flow, the turbulent energy undergoes a natural cascade from its inception with large-scale structures to its dissipation with small-scale structures. This transfer of energy occurs incrementally over the entire spectrum of eddy sizes from the largest to the smallest. A wire grid or screen, however, disrupts this spectrum of different sizes, favoring length scales that are on the order of the wire or mesh dimension. In doing so, the natural cascade is interrupted and a majority of the turbulent energy is funneled into smaller length scales where dissipation is most apt to occur. This condition induces rapid decay in the turbulence level until a natural spectrum of sizes redevelops, at which point the decay rate declines. This entire process of an initially rapid decay rate followed by a gradual decay is apparent in Figs. 6 and 7 and is consistent with previous results obtained for decay downstream of a screen (Groth and Johansson, 1988).

For the open, parallel-plate nozzle, the rate of turbulence dissipation resulting from a normal process of energy cascading is much smaller at the nozzle discharge than for the manipulated flows and is of similar magnitude as the turbulent transport mechanisms of diffusion and advection. The interaction of these three mechanisms affect the turbulence in a manner quite different from the dissipation-dominated, manipulated flows such that the evolution of the turbulence intensity at the jet centerline is divided into two general regions, independent of Reynolds number. The first region ( $y/w_n \lesssim 10$  in the case of the parallel-plate nozzle), hereafter called the equilibrium region, is one in which the turbulence intensity remains essentially constant with streamwise distance. The second region ( $y/w_n \gtrsim 10$ ), hereafter called the decay region, is one in which the turbulence intensity declines monotonically with streamwise distance.

The equilibrium region is so named because the mechanisms of advection/diffusion and dissipation of the turbulent energy are opposing one another. From Fig. 5, it is clear that the turbulence intensity (and hence, the turbulent kinetic energy) is highest in regions close to the free interface and lowest at the jet centerline. This unbalanced distribution results in the diffusion of turbulent energy toward the jet centerline. Concurrently, the turbulent kinetic energy is also advected downstream by the bulk fluid motion. These mechanisms serve to increase the turbulence intensity near the core of the jet at the expense of a decline in the turbulence intensity at the outer regions. Simultaneous to this advection/diffusion process, viscous dissipation of the turbulence contributes to a decline of the energy level throughout the jet. Hence, locally at the jet centerline, a pseudo-equilibrium develops, where advection/diffusion is enriching the region with turbulent energy, while viscous dissipation is depleting the region of energy. In some cases, as for the high-Reynolds-number data shown in Fig. 7, advection/diffusion apparently dominates the energy exchange, such that the turbulence intensity actually increases locally by about 6 percent over the first eight nozzle widths. For the low-Reynolds-number case, however, a monotonic decline exists over the first ten nozzle widths, but at a much lower rate than the decline beyond  $10w_n$ .

The decay region is so named because the viscous dissipation of turbulent energy dominates and the turbulence level decays

rapidly and monotonically. At the streamwise distance of approximately  $10w_n$ , the diffusion of turbulent kinetic energy is essentially nil. This result is shown clearly in Fig. 5, where the turbulence is nearly homogeneous for distances of  $y/w_n > 10$ . Hence, for streamwise distances beyond  $10w_n$ , the turbulent kinetic energy (and turbulence intensity) decays quickly, as evidenced in Fig. 6.

Much like the transport of the turbulent kinetic energy described for the parallel-plate nozzle with an open exit condition, similar mechanisms are believed to apply for the high Reynolds number, converging nozzle (Fig. 7). For  $y/w_n < 10$ , the turbulence is predominantly governed by viscous dissipation and the turbulence level decreases. At  $y/w_n \approx 10$ , the effects of a redistribution (advection/diffusion-driven) in the turbulent kinetic energy influences the local turbulence level. Profiles of the turbulence intensity with respect to the lateral coordinate  $x$  showed the turbulence at the nozzle exit to be highly nonhomogeneous at the outer regions of the jet. This nonuniformity results in the diffusion of turbulent kinetic energy inward toward the jet centerline while the energy is simultaneously being advected downstream. Once the turbulence is completely homogeneous, the redistribution of the turbulent kinetic energy ceases (probably at  $y/w_n \approx 20$ ) and the turbulence undergoes viscous dissipation only.

For the low-Reynolds-number, converging nozzle, the turbulence intensity behavior (Fig. 6) is quite different from that at the higher Reynolds number (Fig. 7). Specifically, the turbulence intensity declines monotonically with streamwise distance for the low-Reynolds-number case. The different behavior between the two Reynolds numbers is due to the previously discussed, low-frequency ( $\sim 18$  Hz) pulsation present in the flow loop. This low-amplitude pulsation was too small to influence flow conditions significantly other than results for the low-Reynolds-number, converging nozzle. For this case, the pulsation is a dominant factor in the flow and governs the decay rate. Influences such as the diffusion of turbulent energy from other regions of the jet, which is seen to augment the turbulence level for the other unmanipulated flows (Figs. 6 and 7), are weak relative to the pulsation. At the other test conditions, the natural turbulence of the flow exceeded, often significantly, the pulsation level (Wolf, 1993).

The results from Figs. 6 and 7 have been replotted in Figs. 8 and 9 in terms of the actual value of the turbulence intensity for the low and high Reynolds numbers, respectively. This representation reveals the levels of turbulence generated by each nozzle configuration relative to the other. At the nozzle exit, the range of turbulence levels is the largest, with the wire grid generating

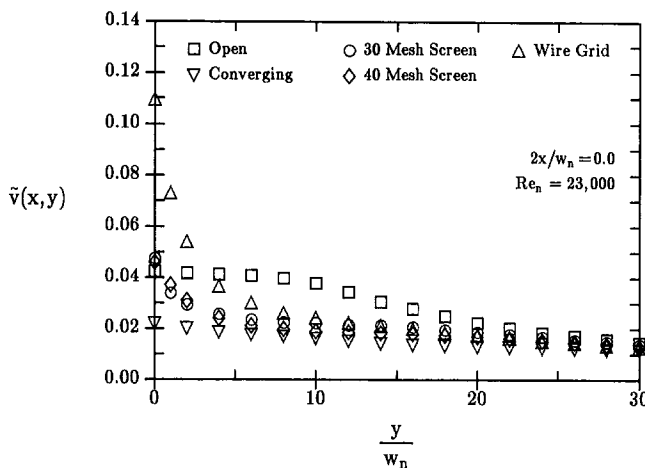


Fig. 8 The evolution of the absolute turbulence intensity with streamwise distance at a spanwise location of  $2x/w_n = 0.0$  for all nozzle conditions and  $Re_n = 23,000$

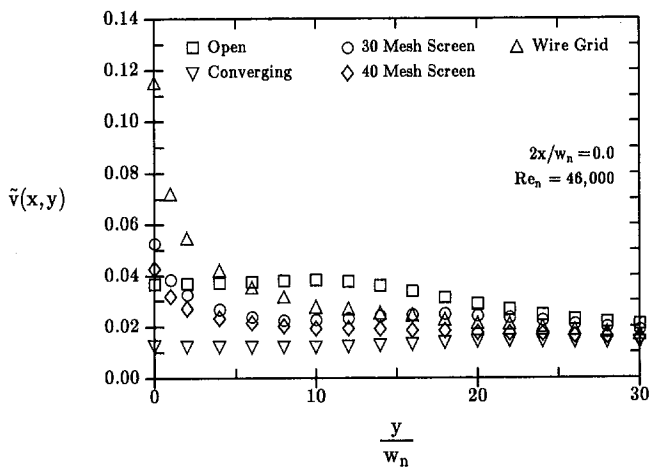


Fig. 9 The evolution of the absolute turbulence intensity with streamwise distance at a spanwise location of  $2x/w_n = 0.0$  for all nozzle conditions and  $Re_n = 46,000$

the most turbulence at levels greater than 10 percent of the mean velocity. The wire grid-generated turbulence decays very rapidly, and for streamwise distances greater than approximately  $5w_n$ , the maximum turbulence is exhibited by the open, parallel-plate nozzle. Despite significantly different levels of turbulence at the nozzle exit, all the nozzle conditions decay to turbulence levels of 1 to 2 percent at  $30w_n$ , independent of the Reynolds number.

Figures 8 and 9 clearly demonstrate that, for cooling arrangements where the nozzle-to-surface spacing is  $\geq 5w_n$ , the unmanipulated, parallel-plate nozzle will deliver the highest turbulence levels to the impingement zone. This behavior is in contrast to what one might intuitively expect; namely, that mechanical devices positioned at the nozzle exit will enhance the impingement turbulence level over the unmanipulated jet and, in turn, provide the greatest amount of augmentation of the surface heat transfer. Moreover, the fact that the open nozzle produces the most turbulent jet for the majority of separation distances has the added benefit of simple, maintenance-free operation (no added pressure loss, no reliability concerns such as contaminants clogging a screen, etc.).

In the interest of space limitations, distributions of  $\tilde{v}$  as a function of  $y/w_n$  for  $2x/w_n > 0$  have been omitted. However, the streamwise trends of  $\tilde{v}$  at transverse locations away from the jet centerline were, in general, similar to the results presented heretofore at the jet centerline. Complete mappings are available elsewhere (Wolf, 1993).

Finally, it is important to emphasize that the manner in which the results are presented in Figs. 6–9 for the manipulated flows (wire grid and screens) is somewhat arbitrary, in that they depend on where the manipulator was located relative to the nozzle exit. For those results, the manipulator was positioned 12.7 mm upstream of the nozzle exit (Fig. 1), which corresponds to 20 wire diameters for the wire grid and 15 and 20 mesh lengths for the 30- and 40-mesh screens. If the manipulator had been closer to the exit, the turbulence intensity would have been higher at the nozzle exit, since the distance presently available for turbulent decay (12.7 mm) would be smaller. Therefore, trends of quantities nondimensionalized by their initial values will vary depending on the choice of the initial location relative to the manipulator. This does not, however, take away from the aforementioned, general conclusion that turbulence from the manipulated flows was dissipated much more rapidly than turbulence from the unmanipulated flows.

**Velocity Gradient Along the Impingement Surface.** The test matrix for the heat transfer measurements to be discussed in Part 2 of this paper contained 70 elements (2 Reynolds numbers

$\times 5$  nozzle-exit conditions  $\times 7$  nozzle-to-surface spacings). The turbulence measurements needed to correspond to each of these conditions in the test matrix are given in Figs. 8 and 9. It would follow that measurements of the velocity gradient should also be performed for each of these conditions. However, measurement of the velocity gradient by the previously described technique was an arduous task. To obtain a single velocity gradient, approximately 3 hours of manual data sampling was required due to the lengthy transients that existed with the manometer system. For this reason, measurements were initially limited to the extremes of the nozzle-to-surface spacing to determine the necessity of obtaining data at the intermediate spacings. This initially limited the test matrix for the velocity gradient to 20 elements (i.e., 2 Reynolds numbers, 5 nozzle exit conditions, 2 nozzle-to-surface spacings:  $y/w_n = 2$  and 30).

Figure 10(a) shows the free-stream velocity distributions along the impingement surface for the open, parallel-plate nozzle as a function of the low and high Reynolds numbers and the two nozzle-to-surface spacings. The dimensionless slope of each respective distribution ( $G$ ) is also listed in the figure and is the result of a linear least-squares fit of the data. While the effect of the Reynolds number on the velocity gradient is small [ $<3$  percent and consistent with the findings of Stevens et al. (1992)], the influence of the nozzle-to-surface spacing is much more significant (30–40 percent). The spacing influences the velocity gradient solely through its effect on the mean velocity profile

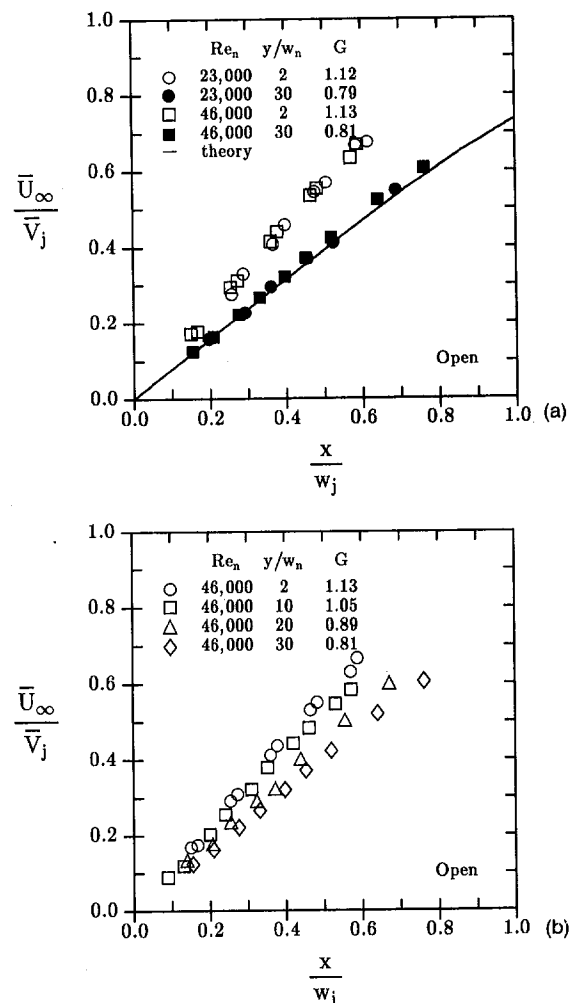


Fig. 10 Free-stream velocity along the impingement surface for the parallel-plate nozzle with an open exit condition showing the effect of (a) Reynolds number and (b) nozzle-to-surface spacing

within the jet. For small nozzle-to-surface spacings, the nonuniformity in the velocity profile present at the nozzle discharge is preserved within the first two nozzle widths downstream. The mean velocity distributions presented in Fig. 2 support this claim. However, for large nozzle-to-surface spacings, the mean velocity profile becomes nearly uniform. Note the similarity between the profiles for the large nozzle-to-surface spacings and the theoretically derived profile for a uniform velocity distribution (Milne-Thomson, 1955). Several investigators (Scholtz and Trass, 1970; Sparrow and Lee, 1975; Deshpande and Vaishnav, 1982; van der Meer, 1987) have shown that the strength of the velocity gradient on the impingement surface increases with the degree of nonuniformity in the jet's mean velocity profile. In particular, Sparrow and Lee (1975) report the dimensionless velocity gradient at the stagnation point to be nearly four times larger for a near-parabolic velocity profile than for a uniform velocity profile. Such large differences in the velocity gradient would not be expected here, however, since the fully developed turbulent velocity profile at the nozzle discharge is much flatter than a laminar, parabolic profile.

Distributions similar those of Fig. 10(a) have been obtained by Wolf (1993) for the other nozzle conditions, and two common features were revealed: (1)  $G$  is independent of the Reynolds number, and (2)  $G$  decreases with increasing nozzle-to-surface spacing, albeit marginally in some cases where the initial velocity profile was very uniform (i.e., the converging nozzle). Moreover, with the exception of the open-ended, parallel-plate nozzle,  $G$  is nearly invariant with respect to the nozzle-to-surface spacing. Hence, for the open-ended condition only, additional experiments were performed at a few of the intermediate separation distances in an attempt to establish an approximate relationship between  $G$  and  $y/w_n$ .

Figure 10(b) shows the velocity distributions for the high Reynolds number case at separation distances of  $2w_n$ ,  $10w_n$ ,  $20w_n$ , and  $30w_n$ . The results indicate monotonic decreases in the velocity gradient with increasing nozzle-to-surface spacing (i.e., increasing uniformity in the jet's mean velocity profile). The four values of  $G$  corresponding to the four separation distances are approximately linear (to within  $\pm 5$  percent) with respect to the nozzle-to-surface spacing. Although this favorable agreement is encouraging, there is no evidence to support that the physical relationship between  $G$  and  $y/w_n$  is precisely linear. Rather, this relationship provided adequate support for the approximation that velocity gradients at separation distances between  $2w_n$  and  $30w_n$  may be linearly interpolated to within about 5 percent. Tabulation of the velocity gradients for all of the 70 matrix conditions may be found elsewhere (Wolf, 1993).

## Summary

Measurements of the mean velocity and turbulence intensity within the jet and the velocity gradient along the impingement surface have been reported for various nozzle configurations. In general, the mean velocity profile across the jet width was fairly uniform, independent of the nozzle exit condition, distance from the nozzle discharge, and Reynolds number. This behavior is attributed to the fact that the flow was fully turbulent. Lateral profiles of the turbulence intensity revealed that the large, non-homogeneous levels of turbulence present at the nozzle exit eventually become more homogeneous with streamwise distance and decay to levels of about 1 percent after 30 nozzle widths from the discharge. With the exception of regions close to the nozzle exit (within five nozzle widths), the parallel-plate nozzle with an open exit condition yielded the highest levels of turbulence. Flows involving turbulence manipulators (wires and screens), although exhibiting very high initial turbulence levels (as high as 12 percent), experience large rates of turbulent decay such that, within about five to ten nozzle widths, the turbulence intensity declined to approximately 2 percent. The velocity gradient along the impingement surface was shown to be insensitive to

the Reynolds number and to vary approximately linearly with the nozzle-to-surface spacing.

## Acknowledgments

This work was supported by the National Science Foundation under grant numbers CTS-8912831 and CTS-9307232.

## References

- Bradshaw, P., 1971, *An Introduction to Turbulence and Its Measurement*, Pergamon Press, Oxford, pp. 24–28.
- Deshpande, M. D., and Vaishnav, R. N., 1982, "Submerged Laminar Jet Impingement on a Plane," *Journal of Fluid Mechanics*, Vol. 114, pp. 213–236.
- Evans, H. L., 1962, "Mass Transfer Through Laminar Boundary Layers—Further Similar Solutions to the  $B$ -Equation for the Case  $B = 0$ ," *International Journal of Heat and Mass Transfer*, Vol. 5, pp. 35–57.
- Faggiani, S., and Grassi, W., 1990a, "Impinging Liquid Jets on Heated Surfaces," *Proceedings of the Ninth International Heat Transfer Conference*, Vol. 1, pp. 275–285.
- Faggiani, S., and Grassi, W., 1990b, "Round Liquid Jet Impingement Heat Transfer: Local Nusselt Numbers in the Region With Non Zero Pressure Gradient," *Proceedings of the Ninth International Heat Transfer Conference*, Vol. 4, pp. 197–202.
- Falkner, V. M., and Skan, S. W., 1931, "Some Approximate Solutions of the Boundary Layer Equations," *Philosophical Magazine*, Vol. 12, pp. 865–896.
- Friehe, C. A., and Schwarz, W. H., 1969, "The Use of Pitot-Static Tubes and Hot-Film Anemometers in Dilute Polymer Solutions," *Viscous Drag Reduction, Proceedings of the Symposium on Viscous Drag Reduction*, C. S. Wells, ed., Plenum Press, New York, pp. 281–296.
- Groth, J., and Johansson, A. V., 1988, "Turbulence Reduction by Screens," *Journal of Fluid Mechanics*, Vol. 197, pp. 139–155.
- Hinze, J. O., 1975, *Turbulence*, 2nd ed., McGraw-Hill, New York, pp. 72, 143–144.
- Hoogendoorn, C. J., 1977, "The Effect of Turbulence on Heat Transfer at a Stagnation Point," *International Journal of Heat and Mass Transfer*, Vol. 20, pp. 1333–1338.
- Hoyt, J. W., and Taylor, J. J., 1977, "Turbulence Structure in a Water Jet Discharging in Air," *Physics of Fluids*, Vol. 20, No. 10, pp. S253–S257.
- Hoyt, J. W., and Taylor, J. J., 1985, "Effect of Nozzle Boundary Layer on Water Jets Discharging Into Air," *Jets and Cavities—International Symposium*, ASME, New York, pp. 93–100.
- Hussain, A. K. M. F., and Reynolds, W. C., 1975, "Measurements in Fully-Developed Turbulent Channel Flow," *ASME Journal of Fluids Engineering*, Vol. 97, pp. 568–580.
- Jambunathan, K., Lai, E., Moss, M. A., and Button, B. L., 1992, "A Review of Heat Transfer Data for Single Circular Jet Impingement," *International Journal of Heat and Fluid Flow*, Vol. 13, pp. 106–115.
- Kataoka, K., 1990, "Impingement Heat Transfer Augmentation Due to Large Scale Eddies," *Proceedings of the Ninth International Heat Transfer Conference*, G. Hetsroni, ed., Vol. 1, pp. 255–273.
- Kestin, J., and Wood, R. T., 1971, "The Influence of Turbulence on Mass Transfer From Cylinders," *ASME JOURNAL OF HEAT TRANSFER*, Vol. 93, pp. 321–327.
- Kline, S. J., and McClintock, F. A., 1953, "Describing Uncertainties in Single-Sample Experiments," *Mechanical Engineering*, Vol. 75, Jan., pp. 3–8.
- Levy, S., 1952, "Heat Transfer to Constant-Property Laminar Boundary-Layer Flows With Power-Function Free-Stream Velocity and Wall-Temperature Variation," *Journal of the Aeronautical Sciences*, Vol. 19, pp. 341–348.
- Lowery, G. W., and Vachon, R. I., 1975, "The Effect of Turbulence on Heat Transfer From Heated Cylinders," *International Journal of Heat and Mass Transfer*, Vol. 18, pp. 1229–1242.
- Martin, H., 1977, "Heat and Mass Transfer Between Impinging Gas Jets and Solid Surfaces," *Advances in Heat Transfer*, T. F. Irvine, Jr. and J. P. Hartnett, eds., Academic Press, New York, Vol. 13, pp. 1–60.
- Milne-Thomson, L. M., 1955, *Theoretical Hydrodynamics*, 3rd ed., Macmillan Company, New York, pp. 279–289.
- Moffat, R. J., 1988, "Describing the Uncertainties in Experimental Results," *Experimental Thermal and Fluid Science*, Vol. 1, pp. 3–17.
- Morrow, T. B., and Kline, S. J., 1971, "The Evaluation and Use of Hot-Wire and Hot-Film Anemometers in Liquids," Stanford University, Report MD-25.
- Pan, Y., Stevens, J., and Webb, B. W., 1992, "Effect of Nozzle Configuration on Transport in the Stagnation Zone of Axisymmetric, Impinging Free-Surface Liquid Jets: Part 2—Local Heat Transfer," *ASME JOURNAL OF HEAT TRANSFER*, Vol. 114, pp. 880–886.
- Polat, S., Huang, B., Mujumdar, A. S., and Douglas, W. J. M., 1989, "Numerical Flow and Heat Transfer Under Impinging Jets: A Review," *Annual Review of Numerical Fluid Mechanics and Heat Transfer*, C. C. Tien and T. C. Chawla, eds., Hemisphere, New York, Vol. 2, pp. 157–197.
- Resch, F. J., 1970, "Hot-Film Turbulence Measurements in Water Flow," *Journal of the Hydraulics Division of ASCE*, Vol. 96, No. HY3, Proceedings Paper 7177, pp. 787–800.
- Rodriguez, J. M., Patterson, G. K., and Zakin, J. L., 1970, "Effects of Probe Geometry on Turbulence Measurements in Liquids Using Hot-Film Anemometry," *Journal of Hydraulics*, Vol. 4, pp. 16–21.
- Scholtz, M. T., and Trass, O., 1970, "Mass Transfer in a Nonuniform Impinging Jet," *AIChE Journal*, Vol. 16, No. 1, pp. 82–96.



- Sparrow, E. M., and Lee, L., 1975, "Analysis of Fluid Field and Impingement Heat/Mass Transfer Due to a Nonuniform Slot Jet," *ASME JOURNAL OF HEAT TRANSFER*, Vol. 97, pp. 191–197.
- Stevens, J., and Webb, B. W., 1991, "Local Heat Transfer Coefficients Under an Axisymmetric, Single-Phase Liquid Jet," *ASME JOURNAL OF HEAT TRANSFER*, Vol. 113, pp. 71–78.
- Stevens, J., and Webb, B. W., 1992, "Measurements of the Free Surface Flow Structure Under an Impinging, Free Liquid Jet," *ASME JOURNAL OF HEAT TRANSFER*, Vol. 114, pp. 79–84.
- Stevens, J., Pan, Y., and Webb, B. W., 1992, "Effect of Nozzle Configuration on Transport in the Stagnation Zone of Axisymmetric, Impinging Free-Surface Liquid Jets: Part 1—Turbulent Flow Structure," *ASME JOURNAL OF HEAT TRANSFER*, Vol. 114, pp. 874–879.
- Taylor, J. J., and Hoyt, J. W., 1983, "Water Jet Photography—Techniques and Methods," *Experiments in Fluids*, Vol. 1, pp. 113–120.
- Vader, D. T., Incropera, F. P., and Viskanta, R., 1991, "Local Convective Heat Transfer From a Heated Surface to an Impinging, Planar Jet of Water," *International Journal of Heat and Mass Transfer*, Vol. 34, pp. 611–623.
- van der Meer, T. H., 1987, "Heat Transfer From Impinging Flame Jets," Doctoral Thesis, Technical University of Delft, The Netherlands.
- van der Meer, T. H., 1991, "Stagnation Point Heat Transfer From Turbulent Low Reynolds Number Jets and Flame Jets," *Experimental Thermal and Fluid Science*, Vol. 4, pp. 115–126.
- VanFossen, G. J., Jr., and Simoneau, R. J., 1987, "A Study of the Relationship Between Free-Stream Turbulence and Stagnation Region Heat Transfer," *ASME JOURNAL OF HEAT TRANSFER*, Vol. 109, pp. 10–15.
- Viskanta, R., 1993, "Heat Transfer to Impinging Isothermal Gas and Flame Jets," *Experimental Thermal and Fluid Science*, Vol. 6, pp. 111–134.
- Warschauer, K. A., Vijge, J. B. A., and Boschloo, G. A., 1974, "Some Experiences and Considerations on Measuring Turbulence in Water With Hot Films," *Applied Scientific Research*, Vol. 29, pp. 81–98.
- Wolf, D. H., Viskanta, R., and Incropera, F. P., 1990, "Local Convective Heat Transfer From a Heated Surface to a Planar Jet of Water With a Nonuniform Velocity Profile," *ASME JOURNAL OF HEAT TRANSFER*, Vol. 112, pp. 899–905.
- Wolf, D. H., 1993, "Turbulent Development in a Free-Surface Jet and Impingement Boiling Heat Transfer," Ph.D. Thesis, Purdue University, West Lafayette, IN.
- Zumbrunnen, D. A., Incropera, F. P., and Viskanta, R., 1989, "Convective Heat Transfer Distributions on a Plate Cooled by Planar Water Jets," *ASME JOURNAL OF HEAT TRANSFER*, Vol. 111, pp. 889–896.

# Turbulence Dissipation in a Free-Surface Jet of Water and Its Effect on Local Impingement Heat Transfer From a Heated Surface: Part 2—Local Heat Transfer

D. H. Wolf<sup>1</sup>

R. Viskanta

F. P. Incropera

Heat Transfer Laboratory,  
School of Mechanical Engineering,  
Purdue University,  
West Lafayette, IN 47907

*This paper presents local heat transfer data for a planar, free-surface jet of water impinging normal on a uniformly heated surface. The hydrodynamic conditions of the jet were altered through the use of different nozzle types (parallel-plate and converging) and flow manipulators (wire grid and screens) to investigate the relationship between jet turbulence and local impingement heat transfer. The flow structures for each of the various nozzle conditions are reported in a companion paper (Wolf et al., 1995), and results are used in this paper to interpret their effect on local heat transfer. In addition to qualitative interpretations, correlations are developed for both the onset of transition to turbulence and the dimensionless convection coefficient at the stagnation point. Higher levels of jet turbulence are shown to induce transition to a turbulent boundary layer at smaller streamwise distances from the stagnation point. The effect of streamwise turbulence intensity on the convection coefficient is shown to scale approximately as the one-quarter power.*

## Introduction

The review of literature pertaining to laminar impingement heat transfer and the effects of free-stream turbulence on impingement heat transfer discussed in the first paper (Wolf et al., 1995) suggested that the dimensionless convection coefficient at the stagnation point  $Nu_j (=hw_j/k_f)$  has the following dependence:

$$Nu_j = f(G, Re_j, Pr, \tilde{v}) \quad (1)$$

where  $G$  is the dimensionless velocity gradient at the stagnation point,  $Re_j$  is the Reynolds number,  $Pr$  is the Prandtl number, and  $\tilde{v}$  is the streamwise turbulence intensity. This paper reports the local, single-phase heat transfer measurements along the impingement surface for conditions corresponding to the turbulence and velocity gradient measurements of the first paper. The relative effects of the velocity gradient, Reynolds number, and turbulence level on the stagnation point heat transfer are assessed through multivariate correlating techniques.

## Experimental Methods and Apparatus

A schematic of the experimental apparatus used to obtain the heat transfer data is shown in Fig. 1. The system was designed to obtain nonintrusive measurements of the local convection coefficient through knowledge of the surface heat flux ( $q''$ ), free-stream fluid temperature ( $T_f$ ), and local wall temperature ( $T_w$ ).

The various nozzle types and flow manipulators were the same as those described in the first paper. The jet of water descended normal to a uniformly heated strip (Haynes Alloy 230) that was

35.7 mm wide, 260 mm long, and 0.775 mm thick. The plate was subjected to direct current, Joulean heating over 112 mm of its total length by a power supply with peak output of 15 kW (1500 A at 10 V). The nozzle-to-surface spacing ( $H$ ) was varied within the range of  $2 \leq H/w_n \leq 30$ . The jet (free-stream) temperature was measured with a thermocouple mounted in a plenum chamber that preceded the nozzle entrance and was held constant at 25°C for all experiments. The average jet velocity ( $\bar{V}_j$ ) and width ( $w_j$ ) were based on conditions at the nozzle exit ( $\bar{V}_n$  and  $w_n$ ) but were corrected for gravitational acceleration by expressions of the form

$$\bar{V}_j = (\bar{V}_n^2 + 2gH)^{1/2} \quad (2)$$

$$w_j = w_n[\bar{V}_n/\bar{V}_j] \quad (3)$$

where

$$\bar{V}_n = \dot{Q}/A_n \quad (4)$$

The wall temperature ( $T_w$ ) and heat flux ( $q''$ ) distributions on the upper (wet) surface of the plate were not measured directly but were obtained from the solution of the steady-state energy equation within the solid. The solution requires knowledge of the boundary conditions and the amount of energy generated within the plate from Joulean heating.

The boundary condition at the lower (dry) face of the plate was obtained from temperatures measured by thermocouples in contact with the surface ( $T_m$ ) and located along the direction of flow ( $x$  coordinate). Fibrous insulation encapsulated the thermocouples, furnishing a near-adiabatic surface as an additional boundary condition at the same face. Measurement of the voltage difference across the plate, coupled with the geometry and electrical resistivity, provides sufficient information to infer the local volumetric heating.

The instrumentation located on the dry side of the heater's midline consisted of 22 in-line thermocouples that were flanked on both ends by the positive and negative leads of the voltage probe. Each thermocouple (chromel-alumel of diameter 0.127

<sup>1</sup>Current address: Owens-Corning Science & Technology Center, 2790 Columbus Rd., Granville, OH 43023.

Contributed by the Heat Transfer Division for publication in the JOURNAL OF HEAT TRANSFER. Manuscript received by the Heat Transfer Division July 1993; revision received February 1994. Keywords: Augmentation and Enhancement. Forced Convection, Jets. Associate Technical Editor: A. Faghri.

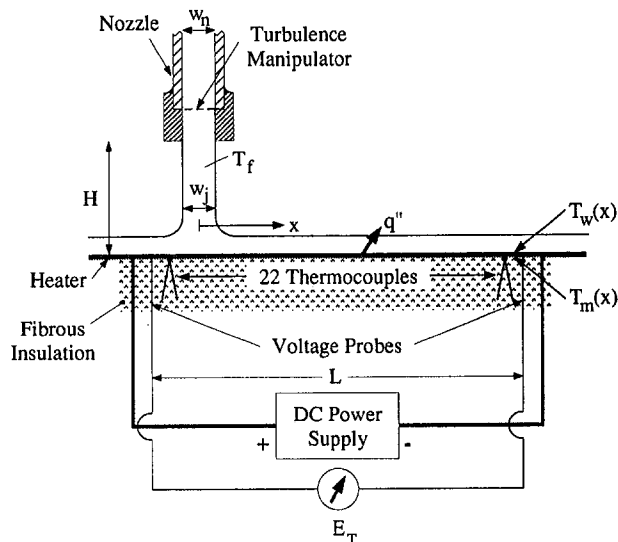


Fig. 1 Schematic of experimental apparatus for heat transfer measurements

mm) and voltage lead (copper of diameter 0.127 mm) were welded to the heater surface to ensure intimate contact. Each of the electrically insulated leads from a particular thermocouple departed from the bead in the spanwise direction and was epoxied to the surface to provide structural support and to inhibit heat losses along the wire. The spacing between each thermocouple was approximately 4.9 mm but varied slightly due to the limited tolerances associated with welding. The precise locations of the thermocouples and voltage probes were determined after completion of the welding process by viewing the dry side of the heater under a toolmaker's microscope and recording the respective positions. Experiments performed on this apparatus by Vader et al. (1991a) with thermocouples offset from the heater centerline have verified that the temperature gradient normal to the midline is small.

## Nomenclature

$A_n$  = nozzle discharge area  
 $C$  = free-stream velocity gradient along the impingement surface =  $d\bar{U}_\infty/dx$   
 $d_n$  = diameter of a circular nozzle  
 $d_w$  = wire diameter  
 $E$  = electromotive force (EMF)  
 $E_m$  = measured thermocouple EMF  
 $E_t$  = thermal thermocouple EMF  
 $E_o$  = Ohmic thermocouple EMF  
 $E_T$  = total EMF applied to the heater between the voltage probes  
 $g$  = gravitational acceleration  
 $G$  = dimensionless free-stream velocity gradient =  $Cw_j/\bar{V}_j$   
 $h$  = local convection heat transfer coefficient =  $q''/(T_w - T_f)$   
 $H$  = distance between the nozzle discharge and the impingement surface  
 $H_w$  = distance between the wire grid and the impingement surface  
 $k_f$  = thermal conductivity of the liquid  
 $Nu_d$  = stagnation point Nusselt number =  $h(0)d_n/k_f$

$Nu_j$  = stagnation point Nusselt number =  $h(0)w_j/k_f$   
 $(Nu_j)_0$  = stagnation point Nusselt number based on laminar, analytical solution  
 $Pr$  = Prandtl number  
 $q''$  = surface heat flux  
 $\dot{Q}$  = volume flow rate  
 $Re_c$  = critical Reynolds number =  $\bar{V}_j x_c/\nu$   
 $Re_d$  = Reynolds number =  $\bar{V}_n d_n/\nu$   
 $Re_j$  = Reynolds number =  $\bar{V}_j w_j/\nu$   
 $Re_n$  = Reynolds number =  $\bar{V}_n w_n/\nu$   
 $Re_x$  = critical Reynolds number =  $\bar{U}_\infty x_c/\nu$   
 $S$  = grid-wire spacing  
 $T_f$  = liquid temperature  
 $T_{film}$  = film temperature =  $(T_w + T_f)/2$   
 $T_m$  = local measured temperature on the dry side of the heated surface  
 $T_w$  = local temperature on the wet side of the heated surface

$u', v', w'$  = root-mean-square (rms) fluctuating components of velocity  
 $\tilde{u}, \tilde{v}, \tilde{w}$  = turbulence intensity =  $u'/\bar{U}, v'/\bar{V}, w'/\bar{W}$   
 $\bar{U}, \bar{V}, \bar{W}$  = mean components of velocity  
 $\bar{U}_\infty$  = mean inviscid velocity along the impingement surface  
 $\bar{V}_j$  = mass-averaged jet impingement velocity  
 $\bar{V}_n$  = mass-averaged jet velocity at the nozzle discharge  
 $w_j$  = jet width  
 $w_n$  = nozzle width  
 $x, y, z$  = orthogonal coordinate directions with origin at the center of the nozzle outlet  
 $x_c$  = value of  $x$  for incipient boundary layer turbulence  
 $\Delta L$  = distance between thermocouple leads at the thermocouple bead  
 $\nu$  = kinematic viscosity

The use of thermocouples that were welded to the heater surface is in contrast with the technique employed in previous investigations by the authors (Vader et al., 1991a, 1991b; Wolf et al., 1990), which utilized an approach whereby the thermocouples were spring-loaded against the heater surface, but not welded. This approach of using spring-loaded thermocouples was abandoned due to problems associated with achieving good and consistent thermal contact between each thermocouple and the heater surface. These problems were overcome by moving to a welding technique, for which the intimate thermal contact between the heater surface and the thermocouple was certain.

The only problem associated with welding thermocouples to a current-carrying body is that the measured EMF ( $E_m$ ) will consist of two parts: the thermal EMF ( $E_t$ ), which is a function of the temperature difference between the surface and reference junction, and an Ohmic EMF ( $E_o$ ), which occurs because the two wires comprising the thermocouple junction are not at the same electrical potential on the heater. It can be shown [see Wolf (1993)] that, for a particular heated length and a particular thermocouple, the Ohmic EMF is constant if the total applied voltage ( $E_T$ ) is constant, which will be the case for all of the results presented here. What is needed is a technique by which to measure the Ohmic EMF.

Although two different techniques for determining  $E_o$  were identified (Dutton and Lee, 1959; Davenport et al., 1962), this investigation adopted another approach where, for a fixed thermal EMF ( $E_t$ ), and total EMF ( $E_T$ ), the polarity of the total EMF would be changed such that the absolute value of the Ohmic EMF would be constant but the sign would vary in accordance with the polarity. The thermal EMF was held constant simply by cooling the heater with the impinging jet. The choice of jet parameters (i.e., nozzle type, Reynolds number, separation distance, water temperature) was not important, provided they were held constant. For one choice of polarity, the measured EMF ( $E_m^{(-)}$ ) would be below the thermal EMF ( $E_t$ ) by an amount equal to the Ohmic EMF ( $E_o$ ) for that thermocouple, i.e.,

$$E_m^{(-)} = E_t - E_o \quad (5)$$

For the opposite polarity, the measured EMF ( $E_m^{(+)}$ ) would be above  $E_t$  by an amount equal to  $E_o$  for that thermocouple, i.e.,

$$E_m^{(+)} = E_i + E_o \quad (6)$$

By taking the difference of Eqs. (5) and (6), the Ohmic EMF is given by

$$E_o = (E_m^{(+)} - E_m^{(-)})/2 \quad (7)$$

This expression provides a means to measure the Ohmic EMF  $E_o$  for each thermocouple for a given  $E_T$ .

The results reported here were obtained at a single heat flux of  $0.5 \text{ MW/m}^2$ , which corresponds to a total applied voltage  $E_T$  of 3.2 V. Equation (7) was evaluated for each thermocouple at this fixed value of  $E_T$ . The actual values used for  $E_o$  were the average of ten independent measurements for each thermocouple. The magnitude of the Ohmic EMF varied significantly ( $0.044 \leq E_o \leq 2.0 \text{ mV}$ , which corresponds to temperatures in the range of  $1.1 - 50^\circ\text{C}$ ) from thermocouple to thermocouple due to differences in the distance  $\Delta L$  between thermocouple lead wires at the bead that arose during the welding process ( $1.5 \leq \Delta L \leq 70 \mu\text{m}$ ). However, the maximum variation in any given value of  $E_o$  throughout these ten measurements never exceeded  $\pm 0.010 \text{ mV}$ , which corresponds to an associated maximum uncertainty in the temperature as a result of this correction of  $\pm 0.25^\circ\text{C}$ .

The analysis of uncertainties associated with the heat transfer measurements, as well as the turbulence and velocity gradient measurements of the prior study, has been performed in accordance with the method suggested by Kline and McClintock (1953) and Moffat (1988), and details are provided elsewhere (Wolf, 1993). The overall uncertainties are based on the root-sum-square of the precision and bias limits and are: convection coefficient ( $h$ ),  $\pm 7$  percent; average jet velocity ( $\bar{V}_j$ ),  $\pm 2$  percent; jet width ( $w_j$ ),  $\pm 2$  percent; Nusselt number ( $Nu_j$ ),  $\pm 7$  percent; Reynolds number ( $Re_j$ ),  $\pm 3$  percent. Repeatability of the convection coefficient was commonly achieved to within  $\pm 5$  percent, which is within the precision limit for that quantity.

## Experimental Results

**Local Heat Transfer.** Heat transfer measurements along the impingement surface are reported in terms of the local convection coefficient  $h(x)$  defined as

$$h(x) = \frac{q''}{T_w(x) - T_j} \quad (8)$$

where  $q''$  is the surface heat flux,  $T_w$  is the local wall temperature, and  $T_j$  is the jet temperature. Distributions are provided as a function of the Reynolds number ( $Re_n = 23,000$  and  $46,000$ ), nozzle exit condition (open, 30-mesh screen, 40-mesh screen, wire grid, and converging), and nozzle-to-surface spacing ( $2 \leq H/w_n \leq 30$ ). The jet temperature  $T_j$  and surface heat flux  $q''$  were held constant at  $25^\circ\text{C}$  and  $0.5 \text{ MW/m}^2$ , respectively, for all the experiments. The spatial coordinate along the impingement surface  $x$  is nondimensionalized by the jet width  $w_j$ . This width is more appropriate than the nozzle width  $w_n$  because it represents the local length scale at impingement.

Figures 2(a) and 2(b) show typical distributions of the surface temperature and convection coefficient for both the low and high Reynolds numbers at a nozzle-to-surface spacing of  $2w_n$ . Shown schematically at the top of Fig. 2(a) is the jet configuration, which is scaled to correspond to the dimensions on the abscissa. Because the surface heat flux  $q''$  is a constant, the distributions of the surface temperature difference ( $T_w - T_j$ ) and the convection coefficient ( $h$ ) are mirror images of one another [see Eq. (8)]. The symbols ( $\square$ ,  $\circ$ , etc.) shown in this figure and all of the spatial distributions in this paper represent the  $x$  locations corresponding to the thermocouples on the dry side of the heater.

For a fixed Reynolds number, the boundary layer conditions govern the shape of the respective distributions shown in Fig. 2. Consider the results of the larger Reynolds number. At the stag-

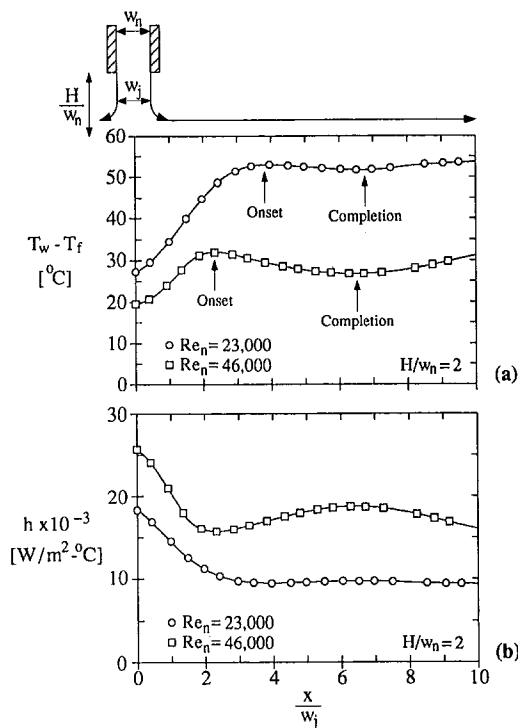


**Fig. 2 Distributions of (a) surface temperature and (b) convection coefficient as a function of the Reynolds number at  $H/w_n = 2$ . The arrows designated by *onset* and *completion* indicate the approximate locations of the onset and completion of the transition from a laminar to a turbulent boundary layer.**

nation point ( $x/w_j = 0$ ), the thermal and hydrodynamic boundary layer thicknesses are characterized by minima and the surface temperature is a minimum. As the flow is accelerated downstream, the laminar boundary layer thicknesses increase, thereby increasing the thermal resistance between the wall and low-temperature, free-stream fluid. Hence, the heat transfer coefficient and surface temperature decrease and increase, respectively. The boundary layers near the stagnation point are laminar, despite a turbulent, impinging flow. This behavior is characteristic of flows accelerating from a stagnation point due to a favorable pressure gradient. The favorable pressure gradient is effective in damping boundary layer instabilities that may be initiated by the free-stream flow and therefore in delaying the transition to turbulence.

Eventually, the pressure gradient approaches zero and the local Reynolds number ( $=\bar{U}_\infty x/\nu$ ) becomes large enough to permit amplification of boundary layer instabilities and transition to turbulence. At the onset of transition, low-temperature liquid from the free stream is mixed within the boundary layer, inducing a local drop in the surface temperature. Farther downstream, the transition to turbulence is completed, and the turbulent boundary layer continues its growth, resulting in a second increase in the surface temperature. All of this is consistent with prior investigations (Zumbrunnen et al., 1989; Wolf et al., 1990; Vader et al., 1991b).

The main objective of this investigation was to establish a relationship between the jet turbulence level, velocity gradient at the stagnation line, and the local convection coefficient along the impingement surface. The distributions of the convection coefficient that follow are presented for 20 of the 70 elements of the test matrix (2 Reynolds numbers  $\times$  5 nozzle-exit conditions  $\times$  2 of 7 nozzle-to-surface spacings). Results for each of the five nozzle exit conditions are plotted in a particular figure for a given Reynolds number and nozzle-to-surface spacing. The two nozzle-to-surface spacings for which results are presented are at the extremes of the matrix (i.e.,  $H/w_n = 2$  and  $30$ ) but provide a rep-

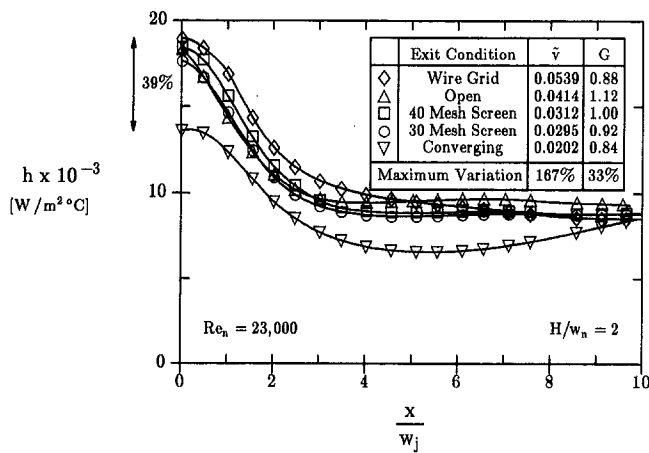


Fig. 3 Effect of nozzle-exit condition on the local convection coefficient for  $Re_n = 23,000$  and  $H/w_n = 2$

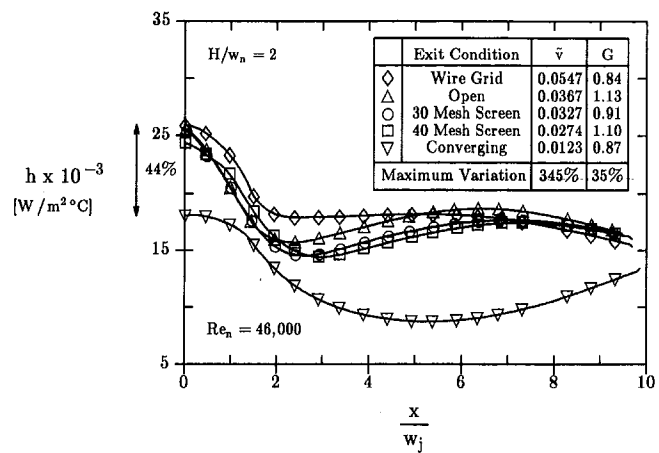


Fig. 5 Effect of nozzle-exit condition on the local convection coefficient for  $Re_n = 46,000$  and  $H/w_n = 2$

representative picture of the overall effects of  $H/w_n$ . Distributions for the five intermediate spacings are provided by Wolf (1993).

Figures 3 and 4 show the local convection coefficient at  $Re_n = 23,000$  for the separation distances of  $2w_n$  and  $30w_n$ , and Figs. 5 and 6 show the local convection coefficient for  $Re_n = 46,000$  at the same two separation distances. In the legends of each figure, the centerline turbulence intensity  $\bar{v}$  and dimensionless stagnation line velocity gradient  $G$ , as presented by Wolf et al. (1995), are listed for the streamwise location in the jet corresponding to the prescribed value of  $H/w_n$ . Below the tabulated values for  $\bar{v}$  and  $G$  are the respective percentages by which the largest tabulated value of the quantity exceeds the smallest tabulated value. On the left-hand side of each figure, the percentage by which the largest convection coefficient exceeds the smallest convection coefficient at the stagnation point is presented. These results provide an approximate indication of the effects of turbulence level and velocity gradient on the convection coefficient at the stagnation point.

Common to all of the results is the monotonic trend of increasing  $h(0)$  with increasing  $\bar{v}$ , independent of  $G$ . Although a quantitative relationship between these parameters will be developed in the following section, one can qualitatively see from Figs. 3–6 that substantial variations in the turbulence level (for example, 167 percent for the results shown in Fig. 3) correspond to relatively moderate differences in the convection coefficient at the stagnation point (39 percent for Fig. 3). Moreover, the variations in the turbulence intensity, velocity gradient, and local convec-

tion coefficient generally decrease with increasing nozzle-to-surface spacing. The range of turbulence intensities among the various exit conditions was shown in Figs. 8 and 9 of the first paper as a function of the streamwise distance from the nozzle discharge. The results indicated that jet turbulence levels, although vastly different near the mouth of the nozzle, ultimately decayed to a level of 1 to 2 percent after a distance  $30w_n$  from the nozzle exit, independent of the Reynolds number and exit condition. These small variations in the turbulence level and velocity gradient (for example, 24 and 14 percent, respectively, for the results shown in Fig. 4) result in correspondingly small variations in the convection coefficient at the stagnation point (10 percent for Fig. 4).

Note that, for a fixed Reynolds number, the effect of separation distance on the stagnation line convection coefficient is small (compare Figs. 3 and 4 for  $Re_n = 23,000$  and Figs. 5 and 6 for  $Re_n = 46,000$ ), despite declines in both the turbulence intensity and velocity gradient with decreasing nozzle-to-surface spacing. In fact, the low Reynolds number results given in Figs. 3 and 4 show a slight increase in convection coefficient for increasing  $H/w_n$ . This apparent anomaly is driven by the influence of the jet width on the convection coefficient. As the correlation of these results will show,  $h \sim w_j^{-1}$ . The jet width  $w_j$  declines with increasing separation distance due to gravitational acceleration [see Eq. (3)].

Consider now the effect of the jet turbulence level on the convection coefficient distribution downstream of the stagnation point. For virtually all of the test conditions, these distributions

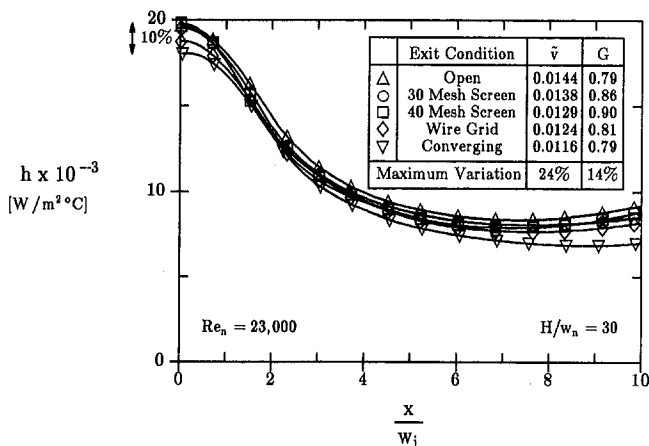


Fig. 4 Effect of nozzle-exit condition on the local convection coefficient for  $Re_n = 23,000$  and  $H/w_n = 30$

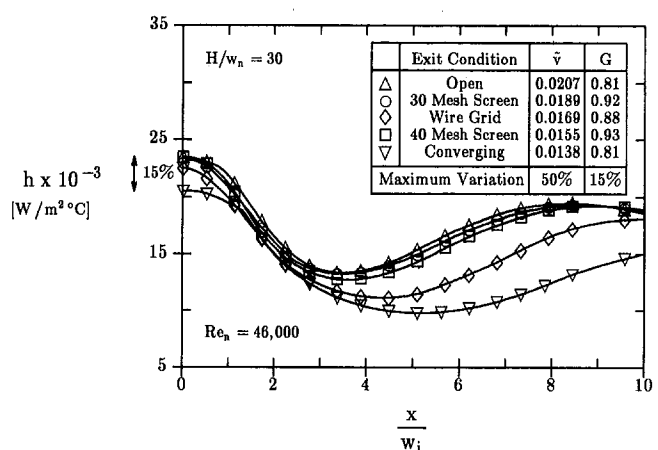


Fig. 6 Effect of nozzle-exit condition on the local convection coefficient for  $Re_n = 46,000$  and  $H/w_n = 30$

exhibited the same trend with respect to  $\bar{v}$  as at the stagnation point, namely, the higher the jet turbulence level, the greater the convective heat transfer along the surface. In fact, at some locations, differences between the low and high convection coefficients exceeded those at the stagnation point. This behavior is most evident for the higher Reynolds number results (see Fig. 5 at  $x/w_j \approx 6$ , for example).

These larger differences in the convection coefficient downstream of the stagnation point are mainly the result of different locations for the onset of turbulence within the boundary layer. Consider Fig. 5, for example, which provides distributions for the high Reynolds number at the smallest nozzle-to-surface spacing ( $2w_n$ ). The high-turbulence jet corresponds to the wire grid. The onset of transition (as indicated by a local minimum in  $h$ ) for this jet occurs at approximately  $2w_j$  and, completion of the transition (as indicated by a local maximum in  $h$ ) occurs at roughly  $6w_j$ . The onset of transition induces mixing within the boundary layer such that cooler fluid from the free stream is transported to the surface, thereby locally increasing the heat transfer rate. In contrast, for the low-turbulence jet corresponding to the converging nozzle, the transition to a turbulent boundary layer is initiated at approximately  $5w_j$  and is not completed within the limits of the measurement domain ( $10w_j$ ).

For virtually all the test conditions, the onset of transition to turbulence occurs at locations closer to the stagnation point as the level of jet turbulence rises. The transition from a laminar to turbulent flow may be expressed in terms of a local Reynolds number

$$\text{Re}_c = \frac{\bar{V}_j x_c}{\nu} \quad (9)$$

where  $\text{Re}_c$  is the critical Reynolds number indicating the onset of transition,  $\bar{V}_j$  is the average jet velocity,  $x_c$  is the distance from the stagnation point corresponding to the first minimum in the convection coefficient, and  $\nu$  is the kinematic viscosity evaluated at the local film temperature [equal to the average of the jet temperature  $T_j$  and the local surface temperature  $T_w(x)$ ]. This definition of the local Reynolds number is approximate in that it assumes  $\bar{V}_j$  to be equal to the local free-stream velocity  $\bar{U}_\infty$ . For all the data presented, the onset to transition occurred at locations where  $x/w_j \geq 2.3$ . Measurements of the free-stream velocity, similar to those presented in Fig. 10 of the first paper but for larger  $x/w_j$ , indicate that the velocity is very nearly equal to the jet velocity at these streamwise distances; hence,  $\text{Re}_c$  should be a good estimate of the local Reynolds number.

Figure 7 shows the critical Reynolds number as a function of the turbulence intensity for 68 of the 70 test cases [no onset to transition occurred within  $0 \leq x/w_j \leq 10$  for the wire grid at  $\text{Re}_n = 23,000$  and  $H/w_n = 2$  (Fig. 3) or for the 40-mesh screen at  $\text{Re}_n = 23,000$  and  $H/w_n = 10$  (not shown)]. The data clearly indicate that the critical Reynolds number declines with increasing jet turbulence, or, for a fixed average jet velocity, the onset to turbulence occurs closer to the stagnation point with increasing  $\bar{v}$ . These trends have been reported by others for flows with (Driest and Blumer, 1963) and without pressure gradients (Gazley, 1953).

Specifically, Driest and Blumer developed a semi-empirical relation for the local Reynolds number at transition as a function of the free-stream turbulence intensity and pressure gradient. They adapted their model to account for the wedge-type laminar flows analyzed by Falkner and Skan (1931). For a wedge angle equal to  $\pi$ , flow conditions are similar to those in the stagnation region of an impinging jet, and Driest and Blumer arrived at a relationship that predicted decreasing critical Reynolds number with increasing free-stream turbulence intensity  $\bar{u}$ . However, direct comparison with the results of Fig. 7 is precluded, since the turbulence intensity outside the boundary layer  $\bar{u}$  is unknown for this investigation.

Finally, note that for the high-Reynolds-number results (Figs. 5 and 6), all the convection coefficient distributions collapse to

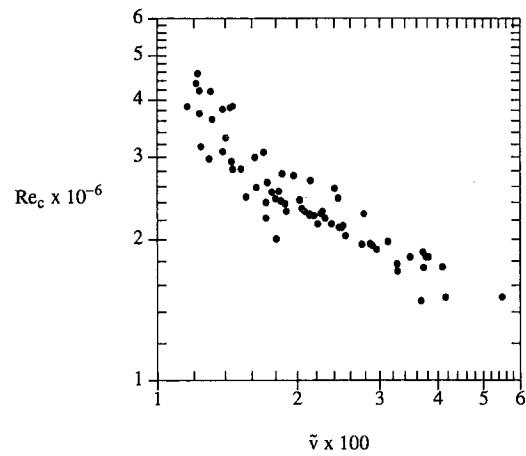


Fig. 7 Effect of turbulence intensity at the jet centerline upon impingement on the critical Reynolds number

a single curve after the transition to turbulence is complete. This trend is independent of the nozzle configuration and the nozzle-to-surface spacing. This behavior is not evident at the lower Reynolds number (or for the converging nozzle at the higher Reynolds number), since the transition to turbulence is never completed within the measurement domain.

The velocimetry measurements reported in the first paper indicated that the influence of the wire grid on the flow field became negligible within the first two nozzle widths after ejection. This result was implicitly supported by the heat transfer measurements, which showed the wire grid to perform best, albeit marginally, at the nozzle-to-surface spacing of  $2w_n$  (see Figs. 3 and 5). One reason that the effects of the wire grid were not sustained for a longer distance from the nozzle discharge was because the wires were positioned 12.7 mm (25 wire diameters) upstream of the exit; hence, significant decay occurred prior to ejection. The wires were positioned within the nozzle to avoid air entrainment at the free interface, which would have made the turbulence measurements unachievable.

One final set of experiments was conducted with the wire grid positioned close to the impingement surface, but detached from the nozzle, thereby avoiding significant decay of the vorticity. However, accompanying turbulence measurements downstream of the grid could not be obtained because of air entrainment. Figure 8 shows the two arrangements of the wire grid (in-line and staggered) relative to the heater centerline. The wires were oriented parallel to the post-impingement flow direction, which is normal to the plane of the diagram in Fig. 8.

Figures 9 and 10 show the convection coefficient distributions as a function of the wire-to-surface spacing for the low and high Reynolds numbers, respectively. In both cases, the nozzle-to-surface spacing is  $10w_n$ . The benchmark results provided for the open nozzle and the wire grid also correspond to a separation distance of  $10w_n$ . All results for the detached wire grid indicate enhanced heat transfer over the benchmark conditions in the stagnation region, as well as at most downstream locations. At the low Reynolds number, enhancements over the open-nozzle condition range from 6 to 32 percent, while at the high Reynolds number, enhancements range from 19 to 36 percent.

The effects of the wire grid arrangement (in-line or staggered) and wire-to-surface spacing on the convection coefficient in the stagnation region appear to depend on the Reynolds number. For example, the low-Reynolds-number results indicate that the stagnation point heat transfer increases monotonically with decreasing wire-to-surface spacing and is largest for the staggered arrangement. The maximum variation in  $h(0)$  among these conditions is approximately 25 percent. In contrast, the high Reynolds number results have a maximum variation in  $h(0)$  of

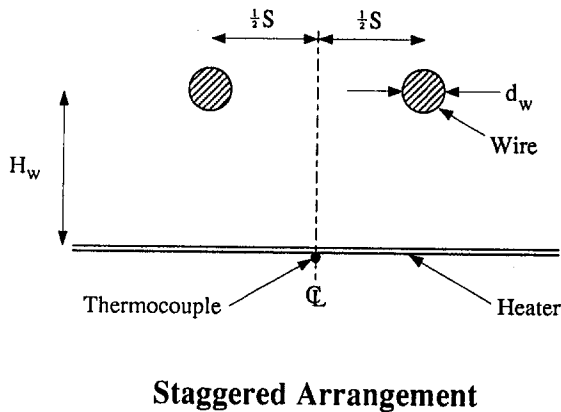
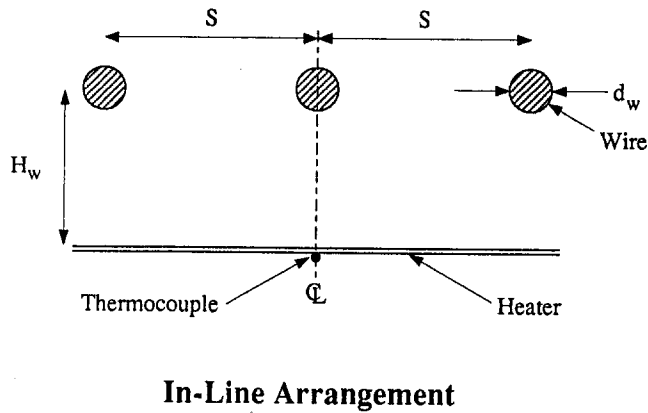


**Fig. 8** Schematic depicting placement of the wire grid relative to the thermocouple locations on the heater for those experiments where the grid was detached from the nozzle

less than 15 percent. Moreover, the trends observed at the low Reynolds number, namely that of increasing  $h(0)$  with decreasing  $H_w$  and of the staggered arrangement outperforming the in-line case, are not consistently exhibited at the high Reynolds number. Initial concerns that this lack of consistency was the result of random measurement error were dispelled by a complete set of repeatability measurements that closely matched the data of Figs. 9 and 10.

The local convection coefficient for the low Reynolds number is invariant with respect to grid arrangement and wire-to-surface spacing at locations downstream of the stagnation point ( $x/w_j \approx 2$ ). The same spatial region for the high Reynolds number data show a slight, but monotonic, variation of increasing convection coefficient with decreasing  $H_w$ . This trend was also evident in the repeatability results.

Independent of Reynolds number, all the distributions decline monotonically with increasing distance from the stagnation point. This behavior is in contrast to virtually all the distributions presented heretofore, which exhibited local minima and maxima in response to the onset and completion, respectively, of boundary-layer transition to turbulence. It may, therefore, be concluded that, over the region  $0 \leq x/w_j \leq 10$ , the boundary layer has not undergone transition; hence, it is either laminar or turbulent throughout. Since experimental limitations precluded auxiliary testing to explicitly reveal the state of the boundary layer, identification of a laminar boundary layer from the data of Figs. 3–6 was implicitly based on transition phenomena. However, similar inferences cannot be made from the results of Figs. 9 and 10.

**Correlation of Data.** The Nusselt number at the stagnation point is defined as

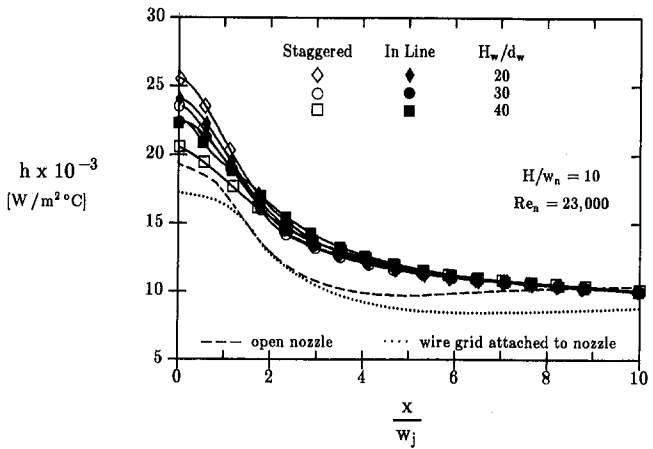


**Fig. 9** Effect of the wire grid arrangement and wire-to-surface spacing on the local convection coefficient for  $Re_n = 23,000$  and  $H/w_n = 10$

$$Nu_y = \frac{h(0)w_j}{k_f} \quad (10)$$

where  $h(0)$  is the convection coefficient at  $x/w_j = 0$ ,  $w_j$  is the jet width, and  $k_f$  is the thermal conductivity of the fluid evaluated at the film temperature,  $[T_{ilm} = \frac{1}{2}(T_w(0) + T_f)]$ . It is correlated in terms of the jet Reynolds number  $Re_j$ , which is defined as

$$Re_j = \frac{\bar{V}_j w_j}{\nu} \quad (11)$$

where  $\bar{V}_j$  is the average jet velocity prescribed by Eq. (2) and  $\nu$  is the kinematic viscosity of the fluid evaluated at the film temperature. Since mass conservation requires that  $\bar{V}_n w_n = \bar{V}_j w_j$  and the viscosity used to compute the nozzle Reynolds number  $Re_n (= \bar{V}_n w_n / \nu)$  is evaluated at the temperature of the nozzle discharge,  $T_f$ , the only difference between  $Re_j$  and  $Re_n$  is the temperature at which the kinematic viscosity  $\nu$  is evaluated. For the nozzle Reynolds numbers of 23,000 and 46,000, the corresponding jet Reynolds numbers were, on the average, 30,800 and 58,100, respectively (slight variations in these values resulted from different values of  $T_w(0)$ ). As indicated previously,  $Re_j$  is more representative of hydrodynamic conditions at impingement.

Values for the dimensionless velocity gradient  $G$  and the turbulence intensity  $\bar{v}$  used in the correlation were the same as those given in Figs. 8–10 of the first paper. The Prandtl number  $Pr$  was evaluated at the stagnation point film temperature and was nearly constant for all of the measurements ( $4.03 \leq Pr \leq 4.86$ ),

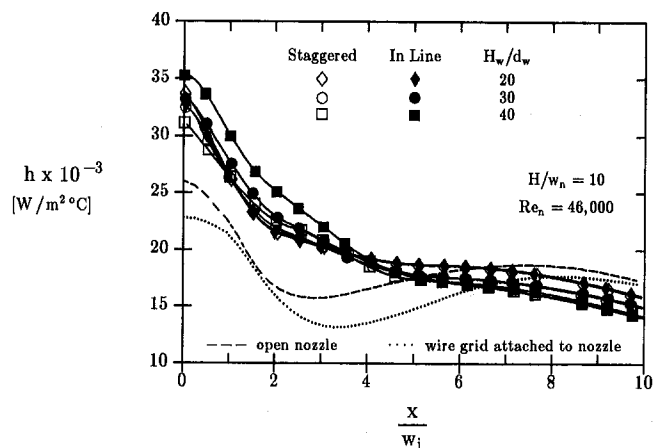


**Fig. 10** Effect of the wire grid arrangement and wire-to-surface spacing on the local convection coefficient for  $Re_n = 46,000$  and  $H/w_n = 10$

thereby preventing correlation of its functional relationship to  $Nu_j$ . Hence, an exponent of 0.4 was assigned to maintain consistency with other correlations (0.33–0.42) for jet impingement (McMurray et al., 1966; Downs and James, 1987; Zumbrennen et al., 1989; Vader et al., 1991b).

Correlations of the form  $Nu_j = f(Re_j, Pr)$  have been proposed by many investigators (McMurray et al., 1966; Metzger et al., 1974; Zumbrennen et al., 1989; Wolf et al., 1990; Vader et al., 1991b) and was attempted as a first approach in this study. The least-squares fit of the 70 data from this investigation, albeit at only two Reynolds numbers, yielded the following relation:

$$Nu_j = 0.202 Re_j^{0.620} Pr^{0.4} \quad (12)$$

which correlated all of the data to within  $\pm 33$  percent and had a 95 percent confidence interval of  $\pm 26$  percent (i.e., 19 out of 20 data lie within an interval of  $\pm 26$  percent of the correlation). Clearly, the two parameters ( $Re_j$  and  $Pr$ ) are, alone, insufficient to predict the stagnation point Nusselt number adequately.

The second approach to correlating the data assumed that  $Nu_j$  was directly proportional to each of the independent variables raised to some power,

$$Nu_j = C Re_j^m G^n \bar{v}^p Pr^{0.4} \quad (13)$$

However, one drawback to this approach is that, for  $\bar{v} = 0$ , the correlation does not reduce to the limiting condition for laminar flow, which is of the form (Wolf et al., 1995)

$$(Nu_j)_0 = 0.570 G^{1/2} Re_j^{1/2} Pr^{0.375} \quad (14)$$

That is, a correlation in the form of Eq. (13) would indicate that the Nusselt number is zero for a laminar jet, which is clearly unrealistic. The merit of using Eq. (13), however, is that it provides a simple means of assessing the relative contributions of each independent variable through the magnitudes of the exponents.

When it is assumed that  $Nu_j = f(Re_j, G, Pr, \bar{v})$ , the following correlation results from a multivariate, least-squares fit of the data:

$$Nu_j = 0.849 Re_j^{0.584} G^{0.360} \bar{v}^{0.263} Pr^{0.4} \quad (15)$$

This expression correlated all 70 of the data to within  $\pm 10$  percent, had a 95 percent confidence interval of  $\pm 7.3$  percent, and is based on data within the ranges  $29,900 \leq Re_j \leq 61,200$ ,  $0.79 \leq G \leq 1.13$ , and  $0.0116 \leq \bar{v} \leq 0.0547$ . The correlation and data are shown in Fig. 11.

Of the three independent parameters correlated ( $Re_j$ ,  $G$ , and  $\bar{v}$ ), the range of the dimensionless velocity gradient  $G$  is relatively narrow (a factor of 1.4 between smallest and largest values) when compared to either the Reynolds number (a factor of 2.0) or the turbulence intensity (a factor of 4.7). For this reason, the dependence of  $Nu_j$  on  $G^{0.360}$  is presented with some reservation. Alternatively, if the dependence of  $G^{1/2}$  that resulted from the laminar, analytical solution is forced, the resulting correlation is

$$Nu_j = 0.839 Re_j^{0.581} G^{1/2} \bar{v}^{0.246} Pr^{0.4} \quad (16)$$

which correlates all of the data to within  $\pm 11$  percent and has a 95 percent confidence interval of  $\pm 7.6$  percent. In comparison to Eq. (15), neither the exponents nor the quality of the fit have changed significantly by forcing the  $G$  dependence, which lends support to the argument that its range is probably too small to determine its influence on  $Nu_j$  accurately.

The dependence of the Nusselt number on the turbulence intensity is approximately  $Nu_j \sim \bar{v}^{0.25}$ , independent of whether Eq. (15) or (16) is considered. This relationship reveals that an increase in the jet turbulence level by a factor of two will increase the stagnation point heat transfer by only 19 percent. From the viewpoint of commercial applications, this enhancement would likely be too small to warrant the additional requirements associated with use of turbulence-augmenting schemes (increased

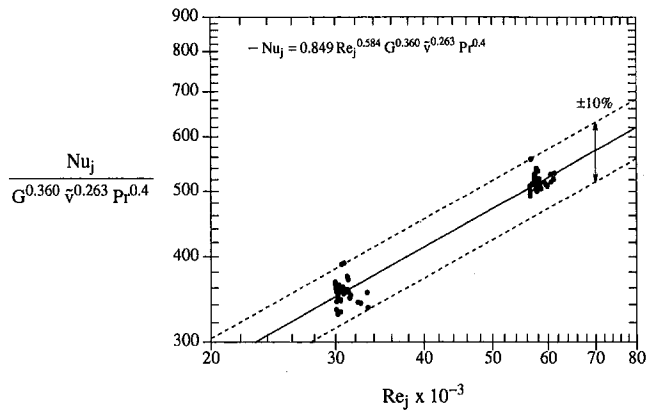


Fig. 11 Correlation of stagnation point Nusselt number assuming that  $Nu_j = f(Re_j, G, Pr, \bar{v})$

pressure drop and maintenance of the manipulators, as well as close nozzle-to-surface spacings to minimize the effects of viscous decay).

In contrast to the measurements of Stevens et al. (1992) and Pan et al. (1992), which were obtained for circular free-surface jets and used a pseudo-radial turbulence intensity (ratio of the radial rms fluctuating velocity to the mass-averaged jet velocity) as the figure-of-merit, this investigation uses the streamwise intensity  $\bar{v}$  to characterize the contribution of turbulence to impingement heat transfer. This quantity was measured at a distance from the nozzle discharge that would correspond to the nozzle-to-surface spacing but in the absence of an impingement surface. Therefore, in contrast to the work of Stevens et al. (1992) and Pan et al. (1992), which involved turbulence measurements with an impinging surface, any influence that impingement would have on the jet turbulence level is not represented in the data of this study.

The correlation proposed by Pan et al. (1992) is of the form

$$Nu_d = 1.115 Re_d^{0.53} G^{0.63} \left( \frac{u'}{\bar{V}_n} \right)^{-0.022} \quad (17)$$

where  $Nu_d$  is the stagnation point Nusselt number based on the nozzle diameter  $d_n$ ,  $Re_d$  is the Reynolds number based on  $\bar{V}_n$ , and  $d_n$ ,  $G$  is the dimensionless radial velocity gradient at the stagnation point, and  $u'$  is the radial rms fluctuating velocity. The functional relationships depicted in this expression differ from those given by Eq. (15). Most notably, the correlation indicates virtually no dependence of the stagnation point Nusselt number on the turbulence level, at least as gaged by the radial component. This apparent disagreement may be the result of either (1) the different components of the fluctuating velocity that were used to correlate the data, or (2) the fact that turbulence measurements were, in one case, made in the presence of an impingement surface and, in the other, with a nonimpinging jet.

The literature addressing heat transfer in the stagnation zone of a bluff body (cylinder, sphere, airfoil, etc.) typically attributes the enhancement to vortex amplification induced by the accelerating flow along the surface of the body. This mechanism was first postulated by Suter et al. (1963) and has been experimentally substantiated by others (Sadeh and Brauer, 1980, 1981; VanFossen and Simoneau, 1987). One of the consequences of vortex amplification is that the rms fluctuating velocity in the direction of the impinging flow (i.e., normal to the bluff body) increases considerably within some small distance of the surface (on the order of boundary layer thicknesses) prior to impact (Tran and Taulbee, 1989; Sadeh and Brauer, 1981; Sadeh and Sullivan, 1980; Sadeh et al., 1970). Hence, the turbulence data of this report represent the pre-impingement flow and are not necessarily of the same magnitude as experienced at the edge of the boundary layer on the surface.



Tran and Taulbee (1989) have numerically shown that the rms fluctuating velocity normal to the impinging flow (i.e., parallel to the surface of the bluff body) changes only slightly as the flow approaches the surface. For the coordinate system of this study, the implication is that the  $v$  component of the fluctuating velocity would experience a significant enhancement, while the  $u$  component measured by Stevens et al. (1992) would not. As indicated by Pan et al. (1992), the  $v$  component of the rms fluctuating velocity may therefore be the more appropriate figure-of-merit. This argument is only valid if one assumes that the vortex amplification mechanism, which is responsible for heat transfer enhancement at the stagnation point of a bluff body, is also applicable to circular and planar, free-surface jets.

Yet another approach to correlation of the stagnation point Nusselt number is one in which the limiting condition for the Nusselt number of a laminar jet ( $\tilde{v} = 0$ ) is forced to comply with the laminar, analytical solution of Eq. (14). One such formulation that has a phenomenological basis was developed by Smith and Kueth (1966) for heat transfer at the stagnation point of a cylinder. They invoked the boundary layer equations for incompressible flow near the stagnation point but modified the diffusion terms by including equivalent eddy momentum and thermal diffusivities to account for turbulence. The eddy diffusivities were assumed to be proportional to the free-stream turbulence and to distance from the wall, and using a similarity transformation to solve the conservation equations, the following expression was obtained for the Nusselt number:

$$\frac{Nu}{(Nu)_0} = 1 + f(\tilde{v} Re^{1/2}) \quad (18)$$

This relationship satisfies the limiting condition in that it defaults to the laminar result  $(Nu)_0$  when  $\tilde{v} = 0$ . Numerous subsequent investigations involving stagnation point heat transfer (Kestin and Wood, 1971; Lowery and Vachon, 1975; Hoogendoorn, 1977; Hargrave et al., 1985; Mehendale et al., 1990) adopted this relationship and, for simplicity, assumed the function  $f$  to be a polynomial.

Figure 12 shows the results of this investigation plotted in accordance with the format suggested by Eq. (18). Also plotted is the following least-squares, polynomial fit of the data:

$$\frac{Nu_j}{(Nu_j)_0} = 1 + 10.2 \left( \frac{\tilde{v} Re_j^{1/2}}{100} \right) - 30.3 \left( \frac{\tilde{v} Re_j^{1/2}}{100} \right)^2 \quad (19)$$

where  $(Nu_j)_0$  is given by Eq. (14). This expression correlated all of the data to within  $\pm 13$  percent, had a 95 percent confidence interval of  $\pm 8.0$  percent, and is based on data within the ranges  $154 \leq (Nu_j)_0 \leq 261$  and  $2 \leq \tilde{v} Re_j^{1/2} \leq 13$ .

Despite the fact that this correlation satisfies the limiting condition and collapses most of the data to within 10 percent, it has its shortcomings. Phenomenologically, this expression is only valid for a *turbulent boundary layer*. Recall that its origin was based on the boundary layer equations, where the turbulent transport of momentum and heat was incorporated into the diffusion terms. The evidence is clear, however, that the boundary layer at the stagnation point of a bluff body is laminar. Turbulence in the free stream is known to induce a three dimensionality to what would otherwise be a two-dimensional, laminar boundary layer. It is the laminar, three-dimensional effects that are believed to augment heat transfer, not a turbulent boundary layer. Also, the polynomial fit in terms of the quantity  $\tilde{v} Re_j^{1/2}$  is a contrived function that, albeit convenient, has no physical significance to this problem. The results shown in Fig. 12 could have been correlated with a variety of different functions, so long as the independent variable in those functions was  $\tilde{v} Re_j^{1/2}$ .

Figure 12 also shows the correlation developed by Hoogendoorn (1977) for a circular, impinging jet of air. The large difference in turbulence-induced enhancements between the present results and those of Hoogendoorn are apparent. Although the differences in jet geometry (planar versus circular) and ambient

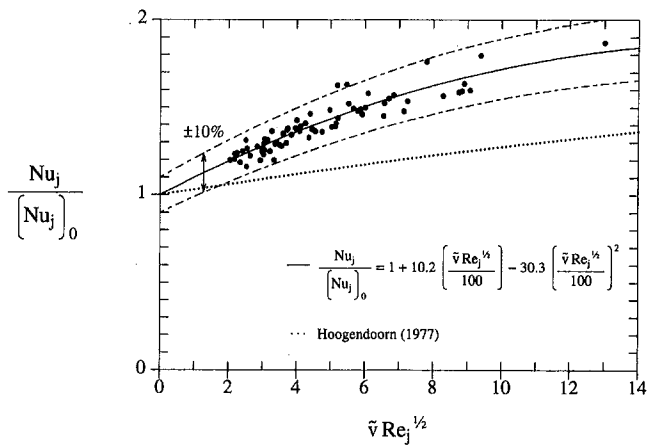


Fig. 12 Correlation of stagnation point Nusselt number relative to the laminar, analytically derived Nusselt number

surroundings (free-surface versus submerged) could be expected to yield some disparity in the correlated results, the large magnitude of the disagreement shown in Fig. 12 seems too large to be reconciled by such factors. Rather, this lack of agreement may imply that the format of Eq. (18) is not universal to all impinging flows.

## Summary

Local heat transfer results have been reported for a uniformly heated surface subjected to an impinging, free-surface jet of water. The hydrodynamics of the jet were altered by using either a parallel-plate or converging nozzle in conjunction with a wire grid or screen positioned at the nozzle discharge. Despite stream-wise turbulence intensities within the jet that differed by as much as 345 percent, the influence on the stagnation point convection coefficient was limited to enhancements of less than 44 percent. Correlation of a 70-point test matrix, spanning nearly a factor of five in the jet's turbulence intensity, yielded approximately a one-quarter power dependence of the stagnation point convection coefficient on the turbulence intensity. The level of jet turbulence was also shown to influence the transition from a laminar to turbulent boundary layer in the post-impingement flow. The local Reynolds number at the onset of boundary layer transition declined monotonically with increasing levels of jet turbulence.

## Acknowledgments

This work was supported by the National Science Foundation under grant numbers CTS-8912831 and CTS-9307232.

## References

- Davenport, M. E., Magee, P. M., and Leppert, G., 1962, "Thermocouple Attachment to a Direct-Current Heater," *ASME JOURNAL OF HEAT TRANSFER*, Vol. 84, pp. 187–188.
- Downs, S. J., and James, E. H., 1987, "Jet Impingement Heat Transfer—A Literature Survey," ASME Paper No. 87-HT-35.
- Driest, E. R. van, and Blumer, C. B., 1963, "Boundary Layer Transition: Free-Stream Turbulence and Pressure Gradient Effects," *AIAA Journal*, Vol. 1, pp. 1303–1306.
- Dutton, R., and Lee, E. C., 1959, "Surface-Temperature Measurement of Current-Carrying Objects," *ISA Journal*, Vol. 6, No. 12, pp. 49–51.
- Falkner, V. M., and Skan, S. W., 1931, "Some Approximate Solutions of the Boundary Layer Equations," *Philosophical Magazine*, Vol. 12, pp. 865–896.
- Gazley, C., 1953, "Boundary-Layer Stability and Transition in Subsonic and Supersonic Flow," *Journal of the Aeronautical Sciences*, Vol. 20, pp. 19–28.
- Hargrave, G. K., Fairweather, M., and Kilham, J. K., 1985, "Turbulence Enhancement of Stagnation Point Heat Transfer on a Body of Revolution," *International Journal of Heat and Fluid Flow*, Vol. 6, pp. 91–98.
- Hoogendoorn, C. J., 1977, "The Effect of Turbulence on Heat Transfer at a Stagnation Point," *International Journal of Heat and Mass Transfer*, Vol. 20, pp. 1333–1338.

- Kestin, J., and Wood, R. T., 1970, "The Mechanism Which Causes Free-Stream Turbulence to Enhance Stagnation-Line Heat and Mass Transfer," *Proceedings of the Fourth International Heat Transfer Conference*, U. Grigull and E. Hahne, eds., Elsevier, Amsterdam, Vol. II, FC2.7.
- Kestin, J., and Wood, R. T., 1971, "The Influence of Turbulence on Mass Transfer From Cylinders," *ASME JOURNAL OF HEAT TRANSFER*, Vol. 93, pp. 321–327.
- Kline, S. J., and McClintock, F. A., 1953, "Describing Uncertainties in Single-Sample Experiments," *Mechanical Engineering*, Vol. 75, Jan., pp. 3–8.
- Lowery, G. W., and Vachon, R. I., 1975, "The Effect of Turbulence on Heat Transfer From Heated Cylinders," *International Journal of Heat and Mass Transfer*, Vol. 18, pp. 1229–1242.
- McMurray, D. C., Myers, P. S., and Ueyhara, O. A., 1966, "Influence of Impinging Jet Variables on Local Heat Transfer Coefficients Along a Flat Surface With Constant Heat Flux," *Proceedings of the Third International Heat Transfer Conference*, AIChE, New York, Vol. II, pp. 292–299.
- Mehendale, A. B., Han, J. C., and Ou, S., 1990, "Influence of High Mainstream Turbulence on Leading Edge Heat Transfer," *AIAA/ASME Thermophysics and Heat Transfer Conference—Heat Transfer in Turbulent Flow*, R. S. Amano et al., eds., ASME HTD-Vol. 138, pp. 27–35.
- Metzger, D. E., Cummings, K. N., and Ruby, W. A., 1974, "Effects of Prandtl Number on Heat Transfer Characteristics of Impinging Liquid Jets," *Proceedings of the Fifth International Heat Transfer Conference*, JSME, Tokyo, Vol. II, pp. 20–24.
- Moffat, R. J., 1988, "Describing the Uncertainties in Experimental Results," *Experimental Thermal and Fluid Science*, Vol. 1, pp. 3–17.
- Pan, Y., Stevens, J., and Webb, B. W., 1992, "Effect of Nozzle Configuration on Transport in the Stagnation Zone of Axisymmetric, Impinging Free-Surface Liquid Jets: Part 2—Local Heat Transfer," *ASME JOURNAL OF HEAT TRANSFER*, Vol. 114, pp. 880–886.
- Sadeh, W. Z., Suter, S. P., and Maeder, P. F., 1970, "An Investigation of Vorticity Amplification in Stagnation Flow," *Z. Angew. Math. Phys.*, Vol. 21, pp. 717–742.
- Sadeh, W. Z., and Brauer, H. J., 1980, "A Visual Investigation of Turbulence in Stagnation Flow About a Circular Cylinder," *Journal of Fluid Mechanics*, Vol. 99, pp. 53–64.
- Sadeh, W. Z., and Sullivan, P. P., 1980, "Turbulence Amplification in Flow About an Airfoil," *ASME Paper No. 80-GT-111*.
- Sadeh, W. Z., and Brauer, H. J., 1981, "Coherent Substructure of Turbulence Near the Stagnation Zone of a Bluff Body," *Journal of Wind Engineering and Industrial Aerodynamics*, Vol. 8, pp. 59–72.
- Smith, M. C., and Kueth, A. M., 1966, "Effects of Turbulence on Laminar Skin Friction and Heat Transfer," *Physics of Fluids*, Vol. 9, pp. 2337–2344.
- Stevens, J., Pan, Y., and Webb, B. W., 1992, "Effect of Nozzle Configuration on Transport in the Stagnation Zone of Axisymmetric, Impinging Free-Surface Liquid Jets: Part 1—Turbulent Flow Structure," *ASME JOURNAL OF HEAT TRANSFER*, Vol. 114, pp. 874–879.
- Suter, S. P., Maeder, P. F., and Kestin, J., 1963, "On the Sensitivity of Heat Transfer in the Stagnation-Point Boundary Layer to Free-Stream Vorticity," *Journal of Fluid Mechanics*, Vol. 16, pp. 497–520.
- Tran, L. T., and Taulbee, D. B., 1989, "Prediction of Stagnation Point Heat Transfer With Free Stream Turbulence," *Proceedings of the 1989 National Heat Transfer Conference—Heat Transfer in Convective Flows*, R. K. Shah, ed., ASME HTD-Vol. 107, pp. 27–34.
- Vader, D. T., Incropera, F. P., and Viskanta, R., 1991a, "A Method for Measuring Steady Local Heat Transfer to an Impinging Liquid Jet," *Experimental Thermal and Fluid Science*, Vol. 4, pp. 1–11.
- Vader, D. T., Incropera, F. P., and Viskanta, R., 1991b, "Local Convective Heat Transfer From a Heated Surface to an Impinging, Planar Jet of Water," *International Journal of Heat and Mass Transfer*, Vol. 34, pp. 611–623.
- VanFossen, G. J., Jr., and Simoneau, R. J., 1987, "A Study of the Relationship Between Free-Stream Turbulence and Stagnation Region Heat Transfer," *ASME JOURNAL OF HEAT TRANSFER*, Vol. 109, pp. 10–15.
- Wolf, D. H., Viskanta, R., and Incropera, F. P., 1990, "Local Convective Heat Transfer From a Heated Surface to a Planar Jet of Water With a Nonuniform Velocity Profile," *ASME JOURNAL OF HEAT TRANSFER*, Vol. 112, pp. 899–905.
- Wolf, D. H., 1993, "Turbulent Development in a Free-Surface Jet and Impingement Boiling Heat Transfer," Ph.D. Thesis, Purdue University, West Lafayette, IN.
- Wolf, D. H., Viskanta, R., and Incropera, F. P., 1995, "Turbulence Dissipation in a Free-Surface Jet of Water and Its Effect on Local Impingement Heat Transfer From a Heated Surface: Part 1—Flow Structure," *ASME JOURNAL OF HEAT TRANSFER*, Vol. 117, pp. 85–94.
- Zumbrunnen, D. A., Incropera, F. P., and Viskanta, R., 1989, "Convective Heat Transfer Distributions on a Plate Cooled by Planar Water Jets," *ASME JOURNAL OF HEAT TRANSFER*, Vol. 111, pp. 889–896.

# Mechanisms of Heat Transfer Enhancement of Gas-Solid Fluidized Bed: Estimation of Direct Contact Heat Exchange From Heat Transfer Surface to Fluidized Particles Using an Optical Visualization Technique

Y. Kurosaki  
Professor,  
Mem. ASME

I. Satoh  
Associate Professor.

Department of Mechanical and Intelligent  
Systems Engineering,  
Tokyo Institute of Technology  
O-okayama, Meguro-ku, Tokyo 152,  
Japan

T. Ishize  
Printing Development Center,  
Fuji-Xerox Co., Ltd.,  
2274 Hongo, Ebina-shi, Kanagawa  
243-04, Japan

*This paper deals with mechanisms of heat transfer in a gas-solid fluidized bed. Heat transfer due to heat exchange by direct contact from a heat transfer tube immersed in the bed to fluidized particles was studied by means of visualization of contact of the fluidized particles to the heat transfer surface. The results show that the duration of contact of fluidized particles was almost uniform over the tube circumference and was hardly affected by the flow rate of fluidizing gas. On the other hand, the contact frequency between the particles and heat transfer tube was evidently influenced by the gas flow rate and particle diameter, as well as the location on the tube circumference. Using the visualized results, the amount of heat conducted to fluidized particles during the contact was estimated. This result showed that unsteady heat conduction to the fluidized particles plays an important role in the heat transfer, especially at the condition of incipient fluidization.*

## Introduction

**1 Modeling of Heat Transfer in Gas Fluidizing Bed.** It is well known that fluidized beds have an excellent heat transfer performance. Many applications of fluidized beds involve heat transfer to or from immersed tubes and tube bundles. The rate of heat transfer between a fluidized bed and a tube depends upon a number of factors, including the properties of the bed material, bed and tube geometries, and the fluidization state. Measurements of heat transfer between fluidized beds and immersed tubes have been performed by many investigators, and many correlations are reported in the literature.

A number of researchers have arrived at semi-empirical relations for the heat transfer coefficient of the tubes immersed in fluidized beds. The models that have been proposed in cases where the contribution due to radiation is insignificant are classified into four groups:

**1 Film Model** (for example, Heerden et al., 1953): In this model, a fluid film is considered adjacent to the heat transfer surface. The fluid film constitutes the principal thermal resistance to heat transfer, and the fluidized particles scour away the limiting film and increase heat transfer.

**2 Packet Model** (Mickley and Fairbanks, 1960): This model treats the fluid-solid medium (packet or emulsion) that comes into contact with the heat transfer surface as homogeneous, and assigns it the average thermal properties of the bed at incipient fluidization. The packet model utilizes an unsteady-state ap-

proach and is based on the "surface renewal" concept that accounts for particle convective transport.

**3 Single-Particle Model** (Botterill and Williams, 1963): This model recognizes the heterogeneity of the fluidized media and considers transient conduction between the heat transfer surface and a contacting spherical particle immersed in fluid. In this model, however, long particle residence times, wherein the depth of heat penetration has exceeded one particle diameter, are assumed, and details of the contact behavior have not been studied.

**4 Gas Convection Model** (Baskakov and Suprum, 1972): This model focuses on the importance of gas-convective heat transfer for fluidization of large particles or elevated pressure operation.

Numerous empirical correlations for heat transfer coefficients have been proposed based upon the models described above. It is important to know the transient local contact characteristics between the fluidized particles and heat transfer surface so as to determine the propriety of the empirical correlations and their basic models. A few measurements of contact dynamics have been reported (Ozkayrak and Chen, 1978; Chandran and Chen, 1982) and these reports showed the contact behavior between the "emulsion" of the fluidized particles and the heat transfer surface. In order to obtain a better understanding of the heat transfer mechanisms of fluidized beds, however, the results reported previously are insufficient, because heat transfer between individual particles (as opposed to considerations of a bulk "emulsion" of fluidized particles) and the heat transfer surface cannot be examined by using these results.

**2 Heat Transfer Through Particles Around the Heat Transfer Surface.** Thermal energy transferred to the individual particles around a heat transfer surface finally diffuses into the fluidizing gas flow. From the microscopic view point, however,

Contributed by the Heat Transfer Division for publication in the JOURNAL OF HEAT TRANSFER. Manuscript received by the Heat Transfer Division August 1993; revision received April 1994. Keywords: Augmentation and Enhancement, Measurement Techniques, Packed and Fluidized Beds. Associate Technical Editor: R. Viskanta.

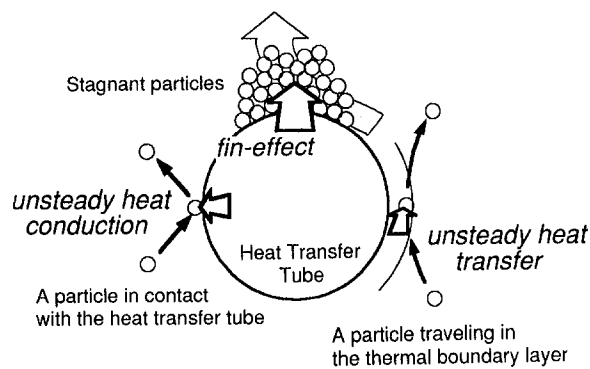


Fig. 1 Classification of heat transfer to particles around the heat transfer surface

the process of heat transfer through particles around heat transfer surface can be separated into the following three categories (see Fig. 1):

(i) *Direct-Contact Heat Exchange*: Thermal energy is directly transferred to a particle, which is in contact with the heat transfer surface, through the contact area. After a certain contact duration, the particle moves apart from the heat transfer surface, so that the thermal energy diffuses into gas flow.

(ii) *Convection to the Particles Adjacent to Heat Transfer Surface*: Thermal energy is indirectly transferred to particles traveling in the thermal boundary layer around heat transfer surface. The particles do not come in contact with the heat transfer surface.

(iii) *Fin Effect Due to Stagnant Particles*: When particles stay on the heat transfer surface for a long duration, the penetration length of heat exceeds the particle diameter. In this case, convective heat transfer at the particle surface is predominant. That is, the stagnant particles on the heat transfer surface act as an "extended surface."

In the present study, the authors have measured contact duration and frequency between individual particles and a heat transfer tube immersed in a fluidized bed employing an optical visualization technique. In this measurement, only the particles being in contact with a surface for a short period were counted. Thus the aforementioned direct-contact heat exchange from the heat transfer surface to the fluidized particles could be estimated by using the measured contact behavior. The relations between the direct contact heat exchange and measured heat transfer augmentations were also discussed.

## Nomenclature

$A$  = contact area between a particle and heat transfer surface,  $m^2$   
 $c_p$  = specific heat of particle,  $J/kg\ K$   
 $D$  = diameter of the heat transfer tube,  $m$   
 $d_p$  = particle diameter,  $m$   
 $k_g$  = thermal conductivity of gas phase,  $W/m\ K$   
 $N$  = contact frequency of particles,  $1/m^2\ s$   
 $Nu$  = Nusselt number =  $hD/k_g$   
 $Nu_p$  = Nusselt number due to direct contact heat exchange between heat transfer surface and fluidized particles (see Eq. (5))

$Nu_m$  = circumferentially average Nusselt number  
 $Nu_{cont}$  = Nusselt number showing thermal resistance of the contact area =  $(1/R)d_p/k_g$   
 $Q_p$  = amount of heat conducted to a particle,  $J$   
 $q_p$  = heat flux due to direct contact heat exchange between heat transfer surface and fluidized particles,  $W/m^2$   
 $R$  = thermal resistance of the contact region per unit projected area of a single particle,  $m^2\ K/W$

$Re_{mf}$  = Reynolds number based on the minimum fluidization velocity =  $U_{mf}D/\nu$   
 $T_b$  = mean temperature of the bed,  $K$   
 $T_p$  = time-dependent particle temperature,  $K$   
 $T_w$  = local wall temperature of the heat transfer surface,  $K$   
 $t_c$  = contact duration of a particle,  $s$   
 $U_{mf}$  = minimum fluidization velocity of particles,  $m/s$   
 $\rho$  = density of a particle,  $kg/m^3$   
 $\tau$  = thermal time constant of a particle (see Eq. (2)),  $s$

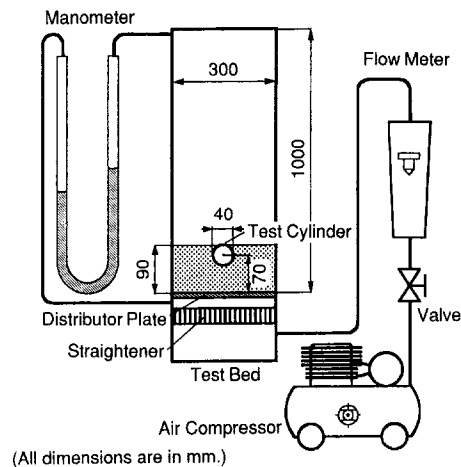


Fig. 2 Experimental apparatus

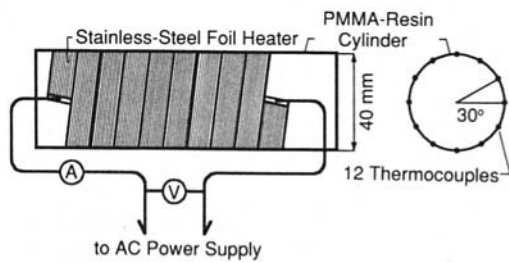
## Experimental Apparatus

**1 Fluidized Bed.** The measurements of the contact behavior and heat transfer augmentation were all performed in the same experimental (i.e., small scale) fluidized bed. Figure 2 is a schematic diagram of the experimental apparatus used in this study. The test bed was made with transparent PMMA resin plate, so as to observe the fluidizing state of particles in it. The cross section of the test bed is  $100\ mm \times 300\ mm$  and its height is  $1000\ mm$ . At the bottom of the test bed, a distributor plate, which was a felt cloth sandwiched between two punched metal plates, was installed to support the particles.

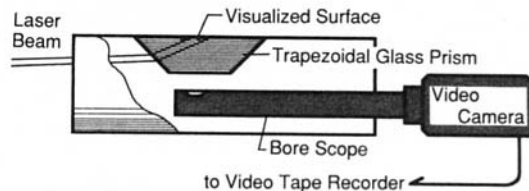
An air flow and spherical glass beads were used as the fluidizing fluid flow and fluidized particles, respectively. In this study, glass beads of three different diameters ( $200\ \mu m$ ,  $400\ \mu m$ , and  $600\ \mu m$ ) were used to examine the effects of particle size on the heat transfer mechanisms of fluidized beds. The static bed height of the particles was  $90\ mm$  and maintained constant through the experiments. Measurements of both heat transfer and contact behavior are performed on a horizontal circular cylinder (O.D.  $40\ mm$ ) immersed in the fluidized bed. The test cylinder was placed  $70\ mm$  above the distributor plate.

**2 Test Cylinders.** In the present study, two test cylinders were prepared for the measurements of heat transfer and contact behavior. The details of these test cylinders are shown in Fig. 3.

For the heat transfer measurement, a heated circular cylinder (Fig. 3a) was immersed in the fluidized bed. The cylinder made



(a) Test cylinder for heat transfer measurements.



(b) Test cylinder for observation of contact behaviors.

Fig. 3 Test cylinders

with PMMA resin is heated under the condition of uniform heating flux by passing an AC current through a stainless-steel foil heater (30  $\mu\text{m}$  thick, 10 mm  $\times$  790 mm). The surface temperature distributions of the test cylinder were measured by 12 copper-constantan thermocouples welded on the back surface of the foil heater. Only the time-averaged surface temperature was measured and transient heat transfer characteristics were not examined. In order to obtain the time-averaged temperature, the output of the thermocouples was electrically smoothed by using a low-pass filter of 1 Hz cutoff, and the remaining fluctuation was averaged for 10 seconds on the data acquisition system. The resolution of the thermometer used in this study was 0.1 K, and the uncertainty of heat transfer coefficient due to the thermometer resolution was less than  $\pm 2$  percent.

The contact behavior between the fluidized particles and a circular tube immersed in the fluidized bed was obtained by employing an optical visualization technique. As shown in Fig. 3(b), a trapezoidal glass prism is installed in a hole bored in the wall of a PMMA resin cylinder (O.D. 40 mm). The outer surface of the glass prism corresponds to the visualized surface, and the inner flat surface parallel to the outer face is the visualizing window. The outer surface is illuminated by a laser beam (He-Ne laser,  $\lambda = 632.8$  nm).

When the fluidized particle is not in contact with the outer surface of the glass prism, the incident laser beam is reflected totally at the glass-air boundary. This means that nothing is observed in the visualization window. If a particle comes into contact with the visualized surface, a part of the reflected laser leaks into the particle through the contact area (see Fig. 4). The particle in contact with the visualized surface is illuminated by scattering of the leaked light and is visible through the window (inner surface of the glass prism). The key to this optical technique is that only the particle in contact with the tube (prism) surface can be observed. The contact behavior of the particles was recorded on a VCR system.

**3 Experimental Conditions.** The heat transfer and contact behavior were measured in the region near the minimum fluidization condition. The minimum fluidization velocity  $U_{mf}$  depends upon the particle diameter, and is 0.064 m/s, 0.19 m/s, and 0.33 m/s for 200  $\mu\text{m}$ , 400  $\mu\text{m}$ , and 600  $\mu\text{m}$  glass beads, respectively. These minimum fluidization velocities were determined from the characteristics of pressure

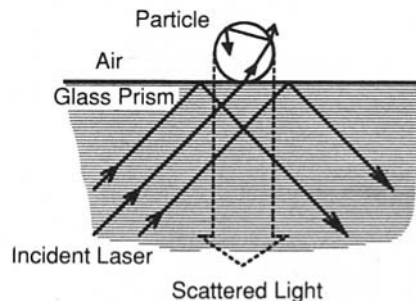
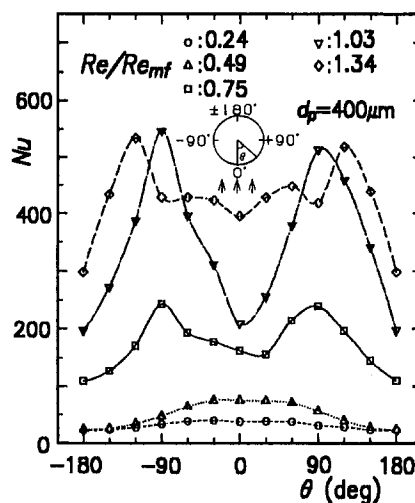
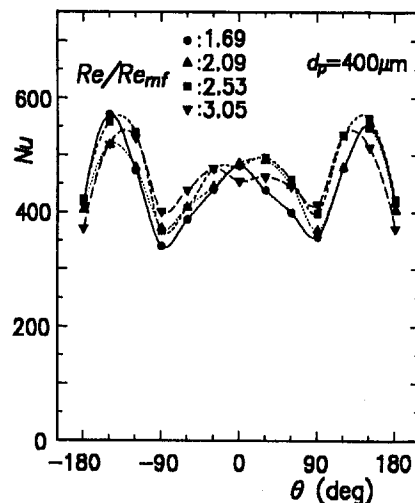


Fig. 4 Principles of the visualization of contact

drop across the test bed; the minimum fluidization velocity was determined as the gas velocity at which the whole particles in the bed are supported by the gas flow and thus the

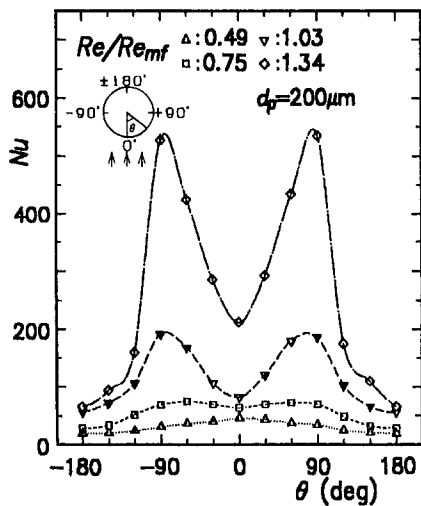


(a) The case of low gas flow rate.

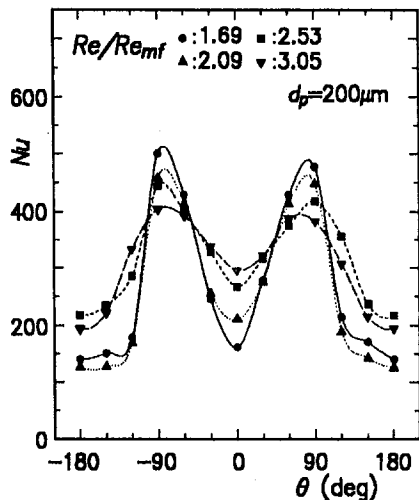


(b) The case of high gas flow rate.

Fig. 5 Local heat transfer coefficient around a horizontal tube immersed in a fluidized bed ( $d_p = 400 \mu\text{m}$ )



(a) The case of low gas flow rate.



(b) The case of high gas flow rate.

Fig. 6 Local heat transfer coefficient around a horizontal tube immersed in a fluidized bed ( $d_p = 200 \mu\text{m}$ )

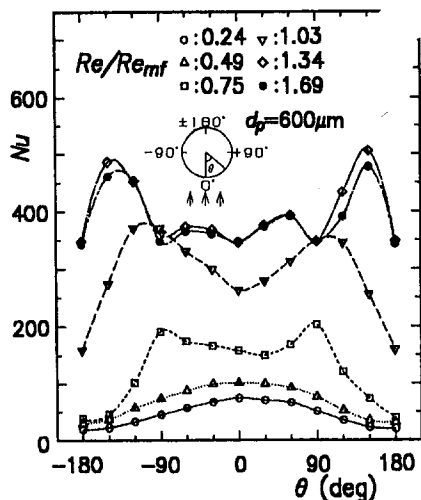


Fig. 7 Local heat transfer coefficient around a horizontal tube immersed in a fluidized bed ( $d_p = 600 \mu\text{m}$ )

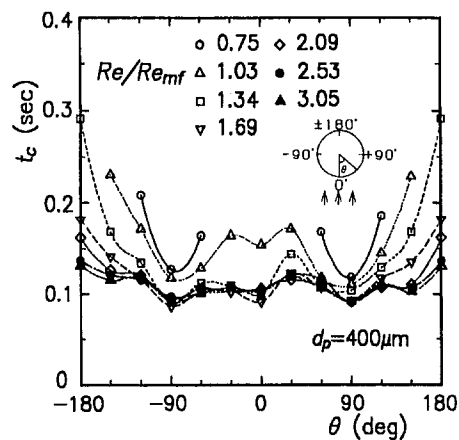


Fig. 8 Local contact duration of a particle around a tube immersed in a fluidized bed ( $d_p = 400 \mu\text{m}$ )

pressure drop due to particles becomes independent on the gas velocity. The fluidization gas (air) velocity was varied in the range from  $0.2U_{mf}$  to  $3U_{mf}$  for each particle diameter. Under the circumstances, the particles start to move at the region under the test cylinder even when the gas velocity is slower than  $U_{mf}$ . This is explained by the fact that the hydrodynamic thickness of the particle layer in this region becomes shallow since the weight of particles on the cylinder is supported by the cylinder. The particles used in the present study belong to the *group B* particle of Geldart's classification (Geldart, 1973), and all measurements were carried out in the "bubbling" state.

For measuring the heat transfer characteristics, the maximum wall temperature was maintained less than  $50^\circ\text{C}$  so that the effects of radiation heat transfer would be insignificant. We were careful to avoid factors of asymmetry of particle fluidization such as inclination of the bed, nonuniformity of the distributor plate, etc., so as to achieve appropriate measurements of heat transfer characteristics and particle contact behaviors. As shown in the following sections, however, circumferential distributions of heat transfer coefficient and particle contact behaviors were slightly asymmetric with respect to the centerline of bed. The authors believe that the slight asymmetry of measured data was not an essential problem for discussing the microscopic mechanisms of fluidized bed heat transfer, because the measurements of both heat transfer and particle contact behaviors were performed under

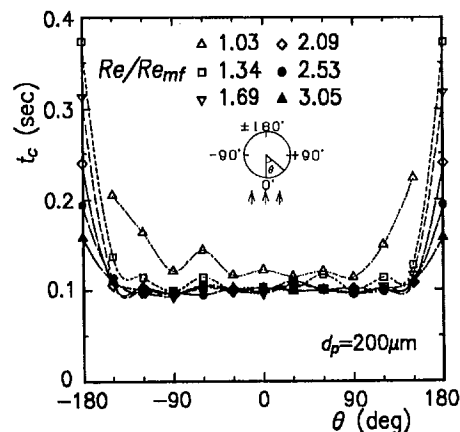


Fig. 9 Local contact duration of a particle around a tube immersed in a fluidized bed ( $d_p = 200 \mu\text{m}$ )

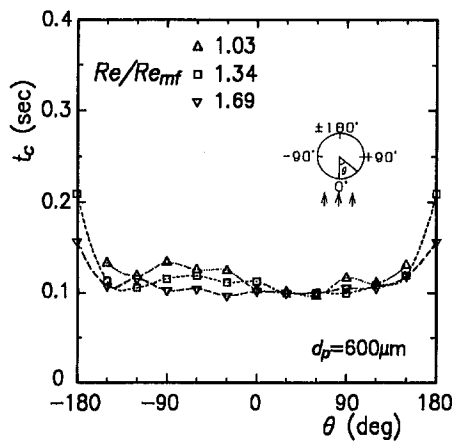


Fig. 10 Local contact duration of a particle around a tube immersed in a fluidized bed ( $d_p = 600 \mu\text{m}$ )

identical bed conditions, i.e., in the same bed with the same distributor plate.

## Results and Discussion

**1 Heat Transfer Characteristics.** Figure 5 shows local heat transfer coefficients around a horizontal circular cylinder immersed in the experimental bed; the results measured for  $400 \mu\text{m}$  glass particles are shown in this figure.

When the fluidizing gas flow is slow ( $Re/Re_{mf} < 1.1$ ), heat transfer around a tube immersed in the fluidized bed is enhanced in both side portions ( $\theta = \pm 90$  deg) of the tube. Evident heat transfer augmentation can be observed even if the gas velocity is lower than the minimum fluidization velocity (i.e.,  $Re/Re_{mf} < 1$ ). This heat transfer augmentation is due to the passing of bubbles near the side portions of the heat transfer tube.

As the gas velocity increases over the minimum fluidization velocity ( $Re/Re_{mf} > 1.1$ ), heat transfer enhancement at the front stagnation point ( $\theta = 0$  deg) also becomes remarkable while the heat transfer coefficients of the side portions are hardly affected by the gas velocity. This is explained by the fact that, as the gas velocity increases, the portion of tube wall in contact with "bubbly" fluidized particles expands in both the upstream and downstream directions. A careful inspection of Fig. 5 shows that the positions where the local heat transfer coefficient is maximal move slightly toward the downstream stagnation point of the tube as the gas flow rate increases.

Figures 6 and 7 show the local heat transfer coefficients measured for  $200 \mu\text{m}$  and  $600 \mu\text{m}$  particles, respectively. As shown in these figures, the distribution profiles of local heat transfer

coefficients measured for larger and smaller particles depend upon the relative fluidizing gas flow rate  $Re/Re_{mf}$  in a manner similar to the profile for  $400 \mu\text{m}$  particles. This means that, under our experimental conditions, the fluidization states of the particles of three different diameters are quite similar when the relative fluidizing gas velocities  $Re/Re_{mf}$  are identical. As shown in Figs. 6 and 7, the positions where the local heat transfer coefficient for these particles is maximal were affected by the relative gas flow rate  $Re/Re_{mf}$  in a manner similar to the ones for  $400 \mu\text{m}$  particles; the maximum positions move toward the downstream stagnation point of tube as the gas velocity  $Re/Re_{mf}$  increases. Comparing Figs. 5–7, however, one can easily find that the displacement of the maximum position of local heat transfer coefficients becomes evident as the particle diameter increases even if the relative gas flow rate  $Re/Re_{mf}$  is fixed. This is explained by the fact that the absolute gas velocity increases with increasing the particle size for the fixed  $Re/Re_{mf}$  since the minimum fluidization gas velocity  $Re_{mf}$  depends upon the particle size.

**2 Contact Behaviors.** Using the contact behavior between the fluidized particles and tube surface recorded by a VCR system, the contact duration of single particles and contact frequency of fluidized particles were measured on a local basis.

The contact duration  $t_c$  was evaluated by measuring the period wherein a particle was observed on the TV frame; contact periods of 50 individual particles or more were measured and the results were averaged so as to determine the local contact duration for a certain fluidization state. The minimum resolution of the measured contact period is limited by the frame-renewal frequency of the VCR, which is 60 frames/s. On the other hand, the contact frequency  $N$  of the fluidized particles was measured by counting the number of particles visualized in the TV frame for 10 seconds; since the observation surface is magnified so as to identify individual particles, the size of a TV frame corresponds to  $6.7 \text{ mm} \times 5 \text{ mm}$  on the observation surface. The contact frequency per unit area per unit time was obtained from the number of visualized particles. The authors feared that the contact frequency of fluidized particles was slightly underestimated because the contact particles were counted in the limited visualized area by naked eyes. That is, in this study, stagnant particles on the visualized surface could not be counted because of the limitation of the naked eye; these particles tend to fluctuate on the surface, and therefore the corresponding particles were hardly recognized in successive TV frames by naked eyes. The omission of these particles results in the underestimation of contact frequency, but we believe that influence of the omission on the contact frequency is negligibly small since the number of stagnant particles were not so large.

Figure 8 shows the circumferential distributions of the local contact duration. The results measured for  $400 \mu\text{m}$  particles are shown in this figure. The local contact duration between a particle

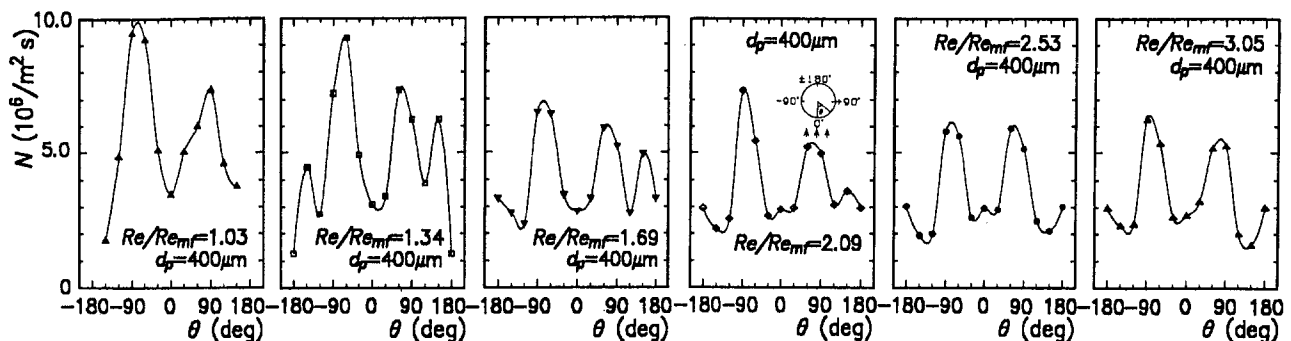


Fig. 11 Circumferential distributions of local contact frequency around a tube immersed in a fluidized bed ( $d_p = 400 \mu\text{m}$ )

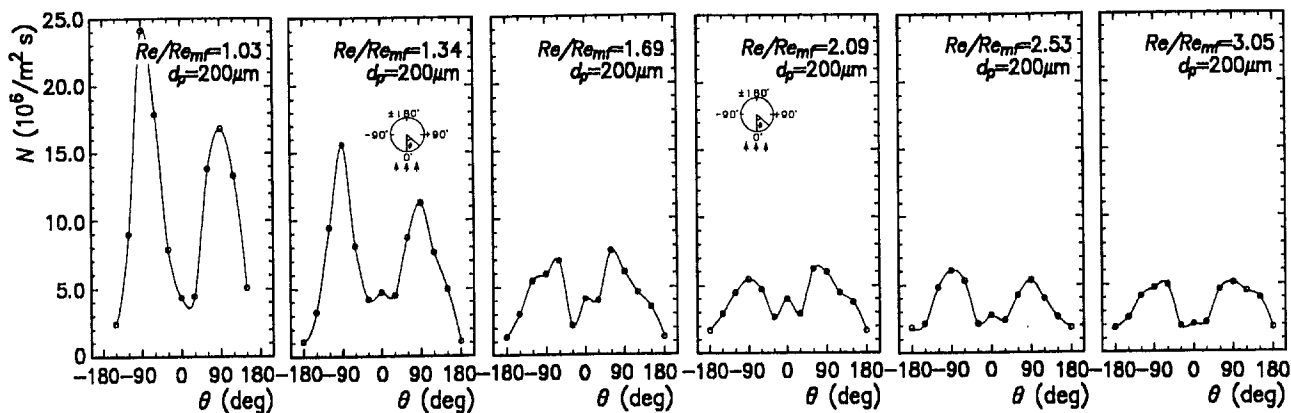


Fig. 12 Circumferential distributions of local contact frequency around a tube immersed in a fluidized bed ( $d_p = 200 \mu\text{m}$ )

and the tube surface immersed in the bed was almost 0.1 s, uniform over the tube circumference except for the front and back stagnation points, and was hardly affected by the fluidizing gas flow rate  $Re/Re_{mf}$ . The locations at which the particles remained in somewhat longer contact with the tube wall corresponded to the regions where the particles move less violently, and these regions decreased with increasing gas flow rate.

The contact durations measured for smaller ( $200 \mu\text{m}$ ) and larger ( $600 \mu\text{m}$ ) particles are shown in Figs. 9 and 10. Comparisons of these three figures (Figs. 8, 9, and 10) clearly show that, in our experimental conditions, the contact behavior for the different particle diameters was almost identical both qualitatively and quantitatively. This means that the fluidization states of our experimental bed can be correlated with the relative gas flow rate  $Re/Re_{mf}$  and are almost similar even if the particle diameter varies in the range from  $200 \mu\text{m}$  to  $600 \mu\text{m}$ .

On the other hand, the contact frequency of the fluidized particles was evidently influenced by both particle size and fluidizing gas flow rate. Figures 11, 12, and 13 show the circumferential distributions of contact frequency measured for  $400 \mu\text{m}$ ,  $200 \mu\text{m}$ , and  $600 \mu\text{m}$  particles, respectively. After the bed was fully fluidized ( $Re/Re_{mf} > 1$ ), the contact frequency of the fluidized particles decreased with increasing relative gas flow rate  $Re/Re_{mf}$  and/or the particle diameter, over the entire tube circumference. This behavior is explained by the change of number density of the fluidized particles. Namely, the number density decreases with increasing average void fraction of the bed and the particle size. As shown in these figures, the local contact frequency was distinctly larger at both side portions of the tube ( $\theta = \pm 90 \text{ deg}$ ). These portions of the tube circumference correspond to the re-

gion where bubbles (the "void phase") pass at the highest frequency, with correspondingly violent particle motion. It should be pointed out that the distribution profiles of local contact frequency bore a resemblance to the profiles of local heat transfer augmentation (see Figs. 5, 6, and 7), especially when the fluidizing gas velocity is low. This result suggests the importance of direct contact heat exchange between fluidized particles and heat transfer surface in the total heat transfer.

**3 Estimation of Direct Contact Heat Exchange.** As mentioned in the Introduction, the heat transfer augmentation described above results from the following two heat transfer mechanisms: (1) the disturbance of thermal boundary layer or the increase of turbulent intensity of the gas flow due to interaction between the fluidizing fluid flow and fluidized particles, and (2) the transient heat exchange between fluidized particles and the heat transfer surface. Moreover, the later mechanism can be separated into two microscopic mechanisms: (2a) the unsteady heat "conduction" due to physical contact, and (2b) the transient "convective" heat exchange between particles and thermal boundary layer around the heat transfer surface. From the measured heat transfer characteristics, however, the contribution ratios of these heat transfer mechanisms to the total heat transfer augmentation of fluidized beds cannot be evaluated.

There have been a number of reports concerning the unsteady heat conduction between particles and a surface or between two individual particles. For example, Sun and Chen (1988) studied the heat exchange between impacting spherical particles or a particle and a surface. In this study, the impact was considered to be elastic, and unsteady heat conduction through the time varying contact area during the impact was analyzed. The authors (Kurosaki et al., 1990) also studied the unsteady heat exchange between a heat transfer surface and solid particles laden in an impinging air jet. We carried out heat transfer experiments under different direct-contact heat exchange thermal conditions while holding the contributions of other heat transfer augmentation mechanisms constant, and the results were compared with numerical ones so that the particle contacting period and the contribution of direct-contact heat exchange can be inversely examined. Indeed these results enable us to estimate the amount of heat conducted to or from the particles under the prescribed contact pressure, but they are not applicable for the purpose of this study since we could not determine neither the contact pressure nor the contact area of particles from the measured contact behavior of particles.

Under the circumstances, contact Nusselt number (or contact thermal resistance) reported by Decker and Glicksman (1981) is effective for estimating the unsteady heat exchange between a flat surface and a particle; both thermal resistance and the contact

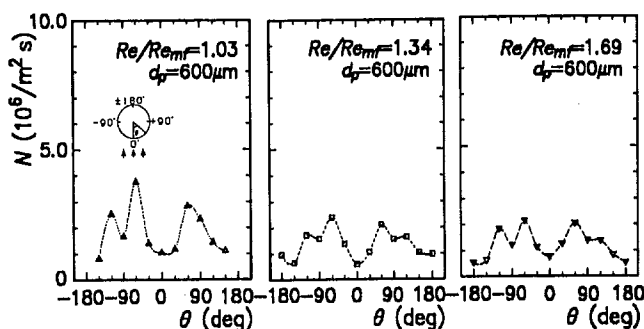


Fig. 13 Circumferential distributions of local contact frequency around a tube immersed in a fluidized bed ( $d_p = 600 \mu\text{m}$ )



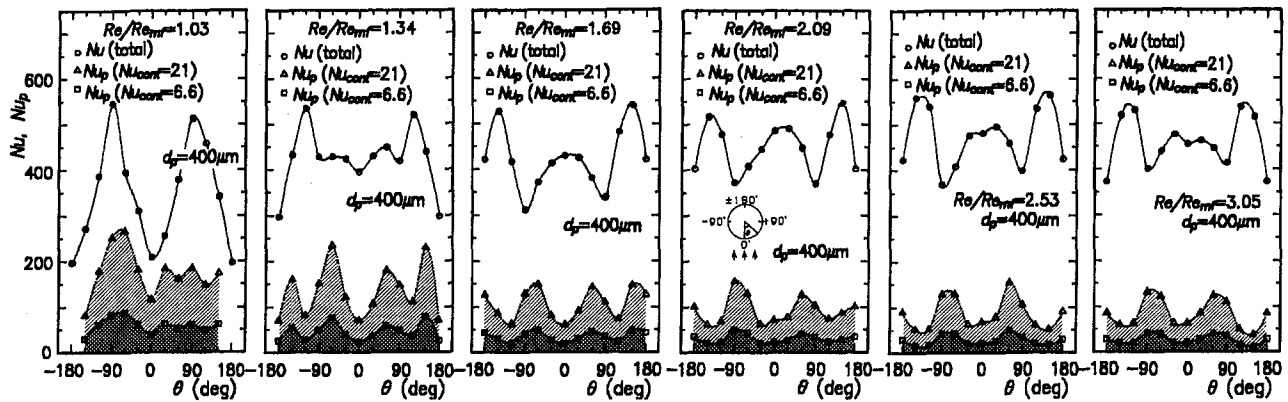


Fig. 14 Heat transfer due to direct contact heat exchange between heat transfer surface and fluidized particles ( $d_p = 400 \mu\text{m}$ )

area of a particle were estimated from their analytical results. Decker and Glicksman calculated the apparent thermal resistance of the contact area between a rough spherical particle and a flat surface, and they indicated the thermal resistance using "contact" Nusselt number ( $Nu_{\text{cont}} = (1/R)d_p/k_g$ ). In their report, heat flux due to contact heat transfer was averaged in the particle projection area; this means that the projection area of a particle ( $= \pi d_p^2/4$ ) can be substituted for the contact area  $A$ .

Neglecting the temperature distribution within a particle (i.e., assuming the particle as the lumped-heat-capacity), the average temperature of particle  $T_p$  can be easily obtained as a function of the contact duration  $t_c$ :

$$T_p(t_c) = (T_w(\theta) - T_b)(1 - \exp(-t_c/\tau)) + T_b \quad (1)$$

where  $T_w(\theta)$  is the local wall temperature of the heat transfer tube, and  $T_b$  shows the initial temperature of a particle and is assumed to be equal to the bed mean temperature. The thermal time constant  $\tau$  is determined as follows:

$$\tau = \rho_p c_p \pi d_p^3 R / 6A \quad (2)$$

where  $A$  shows the contact area between a particle and heat transfer surface, and  $R$  is the thermal resistance of the contact area. Using the contact Nusselt number, the thermal time constant  $\tau$  can be evaluated as

$$\tau = 2\rho_p c_p d_p^2 / 3 Nu_{\text{cont}} k_g \quad (2')$$

From the results of Decker and Glicksman, the contact Nusselt number for the particles and heat transfer surface used in the

present study can be estimated in the range from 6.6 to 21. The amount of heat conducted to a single particle  $Q_p$  is

$$Q_p = \pi \rho_p c_p d_p^3 (T_p(t_c) - T_b) / 6. \quad (3)$$

Local heat flux  $q_p$  due to conductive heat transfer between the fluidized particles and heat transfer surface is evaluated by using the local contact frequency  $N(\theta)$ :

$$q_p(\theta) = Q_p \times N(\theta) \quad (4)$$

The Nusselt number  $Nu_p$ , which shows the heat transfer augmentation due to direct-contact heat conduction to the fluidized particles, is

$$Nu_p(\theta) = \frac{q_p(\theta)}{(T_w(\theta) - T_b) k_g} \quad (5)$$

It should be noted that the procedure described above underestimates the amount of heat conducted to the particles in contact with the heat transfer surface. That is, in the present procedure, heat transfer to a single particle can be estimated with Eq. (3), and particle-to-particle heat transfer was not taken into account.

Figures 14, 15, and 16 show the circumferential distributions of the local Nusselt number  $Nu_p$  due to direct contact heat transfer estimated by the procedure described above. The estimated Nusselt number  $Nu_p$  depends upon the contact thermal resistance (i.e., the contact Nusselt number  $Nu_{\text{cont}}$ ), but the lightly shaded regions of these figures involve the actual heat transfer augmentation due to the direct contact heat exchange.

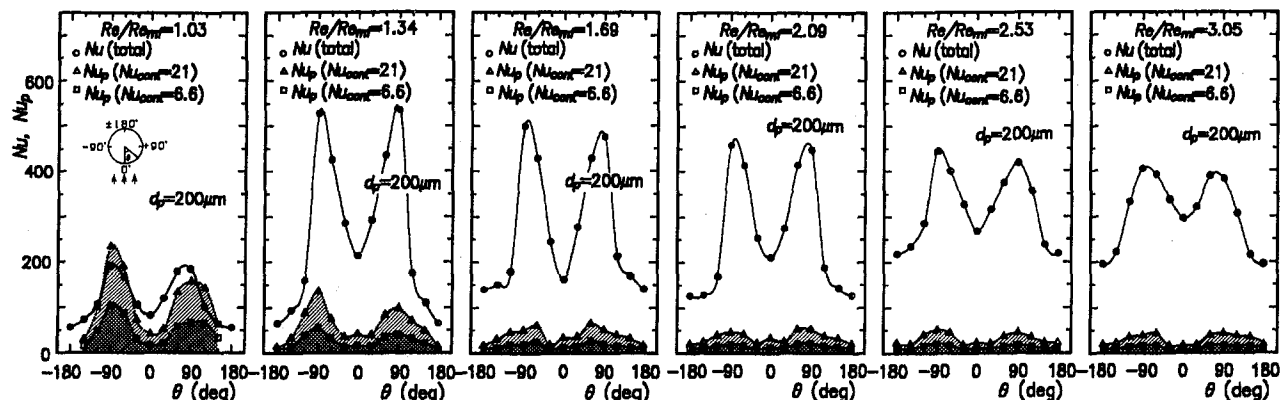


Fig. 15 Heat transfer due to direct contact heat exchange between heat transfer surface and fluidized particles ( $d_p = 200 \mu\text{m}$ )

In these figures, the circumferential distributions of heat transfer coefficients (Nusselt numbers) measured in the experimental bed are also shown for a reference purpose. When the relative gas flow rate  $Re/Re_{mf}$  was small (i.e.,  $Re/Re_{mf} \sim 1$ ), the heat transfer augmentation due to direct-contact heat exchange occupied a major part of the total heat transfer enhancement. The contribution ratio of direct contact heat transfer decreased, however, with increase in the gas flow rate. This is explained by the fact that the contact frequency between fluidized particles and heat transfer surface decreases with the average void fraction of the bed. This behavior of  $Nu_p$  was more evident in the results with small particles (Fig. 15) than with large ones (Fig. 16).

The heat transfer augmentations due to direct contact heat exchange were circumferentially averaged and compared with the average heat transfer coefficients in Fig. 17; the vertical axis of this figure  $Nu_{pm}/Nu_m$  shows the relative contribution ratio of the direct contact heat exchange to total heat transfer of the bed. As shown in this figure, the direct contact heat exchange between fluidized particles and heat transfer surface played an important role for enhancing heat transfer of the bed at incipient fluidization. The importance of the direct contact heat exchange increased with decrease in the particle diameter. However, the contribution of direct contact heat exchange decreased rapidly with increase in the fluidizing gas flow rate  $Re/Re_{mf}$ , and asymptotically approached a lower value. In this region (i.e., under the fully fluidized condition), the direct contact heat exchange contributed only 5–20 percent to the total heat transfer of the bed. That is, unsteady “convective” heat transfer to fluidized particles and/or increase of the turbulent intensity of gas flow due to fluidized particles is the dominant mechanism of heat transfer in the fully fluidized condition.

### Concluding Remarks

In this paper, the authors reported the duration and frequency of contact between a fluidized particle and the heat transfer surface in a fluidized bed, which were measured by employing an optical visualization technique, and we estimated the direct contact heat exchange between them. The results showed that heat exchange through direct contact between particles and the exchanger pipe plays an important role for enhancing heat transfer of the bed at incipient fluidization, but the importance decreases rapidly with increase in both fluidizing gas flow rate and particle size.

These results clearly show that one dominant mechanism of heat transfer changes place with the other as the operating conditions of the bed changes. In this sense, the models or correlations proposed previously, which have usually been based upon a single predominant heat transfer mechanism, cannot describe accurately the heat transfer characteristics of fluidized beds for

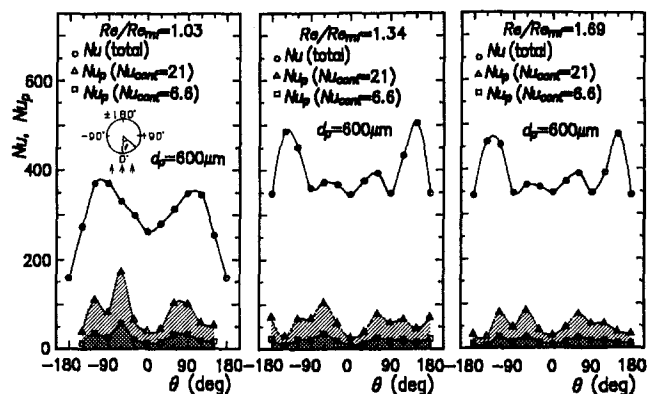
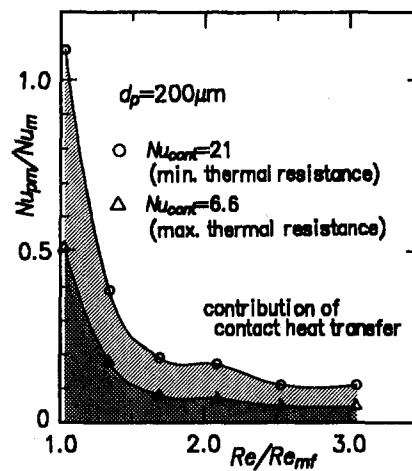
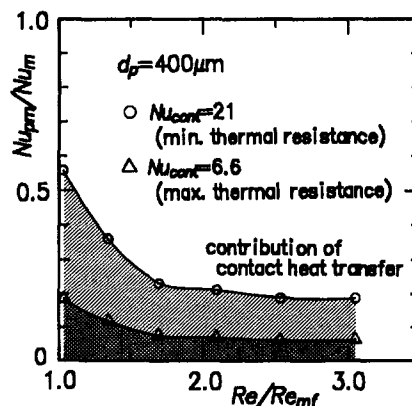


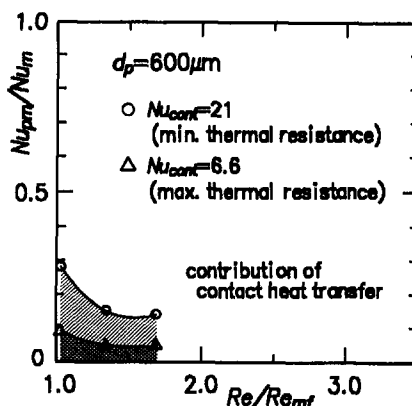
Fig. 16 Heat transfer due to direct contact heat exchange between heat transfer surface and fluidized particles ( $d_p = 600 \mu\text{m}$ )



(a)  $d_p = 200 \mu\text{m}$ .



(b)  $d_p = 400 \mu\text{m}$ .



(c)  $d_p = 600 \mu\text{m}$ .

Fig. 17 Relative contribution ratios of the direct contact heat exchange to total heat transfer of a fluidized bed

wide operating conditions. Therefore, it is important to develop a model wherein several heat transfer mechanisms are taken into account in parallel so as to make accurate predictions of the heat transfer characteristics of fluidized beds.

### References

- Baskakov, A. P., and Suprum, V. M., 1972, "Determination of the Convective Component of the Heat Transfer Coefficient to a Gas in a Fluidized Bed," *Int. Chem. Eng.*, Vol. 12, No. 2, pp. 324–326.

- Botterill, J. S. M., and Williams, J. R., 1963, "The Mechanism of Heat Transfer to Gas-Fluidized Beds," *Trans. Int. Chem. Eng.*, Vol. 41, p. 217.
- Chandran, R., and Chen, J. C., 1982, "Bed Surface Contact Dynamics for Horizontal Tubes in Fluidized Beds," *AIChE J.*, Vol. 28, No. 6, p. 907.
- Decker, N. A., and Glicksman, L. R., 1981, "Conduction Heat Transfer at the Surface of Bodies Immersed in Gas Fluidized Beds of Spherical Particles," *AIChE Symp. Ser.*, Vol. 208, No. 77, pp. 341-349.
- Geldart, D., 1973, "Types of Gas Fluidization," *Powder Technol.*, Vol. 7, pp. 285-292.
- Heerden, C. van Nobel, A. P. P., and van Krevelen, D. W., 1993, "Mechanism of Heat Transfer in Fluidized Beds," *Ind. Eng. Chem.*, Vol. 45, No. 6, pp. 1237-1242.
- Kurosaki, Y., Satoh, I., Kameoka, Y., and Annmo, Y., 1990, "Mechanisms of Heat Transfer Enhancement Around the Stagnation Point of an Impinging Air Jet Laden With Solid Particles," *Heat Transfer 1990 (Proc. 9th Int. Heat Transfer Conf.)*, Vol. 4, pp. 95-100.
- Mickley, H. S., and Fairbanks, D. F., 1960, "Mechanism of Heat Transfer to Fluidized Beds," *AIChE J.*, Vol. 1, pp. 374-384.
- Ozkayrak, T. F., and Chen, J. C., 1978, "Average Residence Times of Emulsion and Void Phases at the Surface of Heat Transfer Tubes in Fluidized Beds," *AIChE Symp. Ser.*, Vol. 74, No. 174, p. 334.
- Sun, J., and Chen, M. M., 1988, "A Theoretical Analysis of Heat Transfer Due to Particle Impact," *Int. J. Heat Mass Transfer*, Vol. 31, No. 5, pp. 969-975.

# Effect of Imposed Wall Temperature Oscillations on the Stability of Natural Convection in a Square Enclosure

Q. Xia

Cooper Industries,  
Cameron Forged Products Division,  
Houston, TX 77240

K. T. Yang

Department of Aerospace and Mechanical  
Engineering,  
University of Notre Dame,  
Notre Dame, IN 46556

D. Mukutmoni

Adapco, Ltd.,  
Melville, NY 11747

*The present numerical study is directed toward buoyancy-driven laminar flows in a two-dimensional square enclosure with differential heating at the vertical walls. The top and bottom walls are insulated. A time-dependent temperature varying sinusoidal perturbation is imposed on the hot vertical wall. The cold vertical wall is maintained at a constant temperature. The fluid is air with a Prandtl number of 0.72. Computations were carried out at one imposed frequency, which is of the same order as the first natural frequency of the system. It was found that the perturbations destabilized the flow in that higher amplitudes lead to lower critical Rayleigh numbers for the flow transitions. Computations spanned four regimes: periodic, quasi-periodic with two frequencies, quasi-periodic with three-frequencies, and chaotic.*

## Introduction

The vertical differentially heated square-enclosure problem has been extensively studied in the past and has even been used as a model problem for benchmarking numerical solutions (de Vahl Davis, 1983). It is known that for relatively small Rayleigh numbers (less than  $10^5$ ), the flow is essentially unicellular. For higher Rayleigh numbers, secondary and tertiary flows occur. The flow becomes oscillatory for even higher Rayleigh numbers as a result of boundary layer instabilities and an internal hydraulic jump near the corner of the cavity (Yang, 1988; Paolucci and Chenoweth, 1989).

According to published literature, the physics of the flow field in the steady-state regime is quite well understood and a broad consensus exists. Steady laminar flow in the cavity was found to occur up to a Rayleigh number of  $10^9$  for air ( $Pr = 0.71$ ) and up to  $10^{11}$  for water ( $Pr = 7.0$ ) for a square cavity (Henkes, 1990). Unsteady natural convection is a more controversial issue. Paolucci and Chenoweth (1989) performed numerical simulations for air and concluded that for aspect ratios less than 0.5 and greater than 3, the first time-dependent instability is due to the boundary layers along the isothermal cold and hot walls. For aspect ratios between the same two limits, it was concluded that periodic motion was due to internal waves near the departing corners. The internal waves, it was postulated, resulted from an internal "hydraulic jump" as the fluid turns the corner.

Ivey's (1984) experiments with glycerol and water in an enclosure of aspect ratio unity had earlier suggested the same "hydraulic jump" mechanism. Schladow (1990) performed direct numerical simulations for a Rayleigh number of  $2 \times 10^9$ , an aspect ratio of unity, and a Prandtl number of 7.1. His results refuted the hydraulic jump mechanism and tended to suggest that it was no more than a complex recirculating zone near the corners. The oscillations were a consequence of instabilities in the thermal boundary layer.

Direct numerical simulations that transcended the oscillatory regime have been performed by Paolucci (1990). Two-dimensional natural convection for an air-filled enclosure was simulated at a Rayleigh number of  $10^{10}$  and an aspect ratio of unity in the fully turbulent regime. But again, as it is now generally

known (Nieuwstadt, 1990), the dynamics of turbulent flows is inherently three dimensional, implying that two-dimensional simulations are fundamentally unrealistic. In all fairness, it can be claimed that for differentially heated cavities, the physics of unsteady natural convection is not unequivocally clear in contrast to steady convection that occurs at lower Rayleigh numbers.

The purpose of this investigation is not only to look into the physics of natural convection in the side-heated enclosure, but also to see if the flow field and heat transfer can be manipulated to achieve desirable goals. To that end, a sinusoidal perturbation in the temperature is imposed on the hot wall. No doubt other means of flow control are available, such as using baffles (Bajorek and Lloyd, 1982). The present investigation is, however, restricted to the effect of temperature perturbations on the flow, especially its instabilities. The previous results of this investigation have already been communicated (Xia and Yang, 1990). A similar study has been undertaken by Kazmierczak and Chinoda (1992). They investigated the effect of time periodic boundary conditions on one of the vertical walls of a square cavity. The simulations were, however, restricted to very few cases for a fluid Prandtl number of 7, and the emphasis was placed on the resulting heat transfer characteristics.

The present study is an investigation of the unsteady phenomena for different Rayleigh numbers and for different perturbation amplitudes. Due to limited computer resources, the study is reported for one particular imposed frequency only. It is chosen in the general area of the first natural frequency or the frequency at which the steady flow first becomes oscillatory in the case of a steady differentially heated vertical cavity (Paolucci and Chenoweth, 1989). This is done to increase the probability of interaction between the natural and imposed modes of oscillation. It is also to be noted that, despite the two-dimensional nature of the present study, it is expected that the results should yield much physical insight to the flow bifurcation phenomena under the effect of periodic wall temperature perturbations.

## Governing Equations and Formulation

The geometry of the square enclosure is shown in Fig. 1. The fluid under consideration is air with  $Pr = 0.72$ . The left wall at  $x = 0$  is isothermal and subjected to a sinusoidal temperature perturbation. The right wall is maintained at a constant lower temperature. The upper and lower surfaces are insulated. The  $x$  and  $y$  coordinates were scaled by  $H$ , the enclosure height; the velocities were scaled by  $\alpha/H$ ; the time scaled by  $H^2/\alpha$ ; and the

Contributed by the Heat Transfer Division for publication in the JOURNAL OF HEAT TRANSFER. Manuscript received by the Heat Transfer Division February 1993; revision received March 1994. Keywords: Enclosure Flows, Flow Instability, Natural Convection. Associate Technical Editor: J. R. Lloyd.

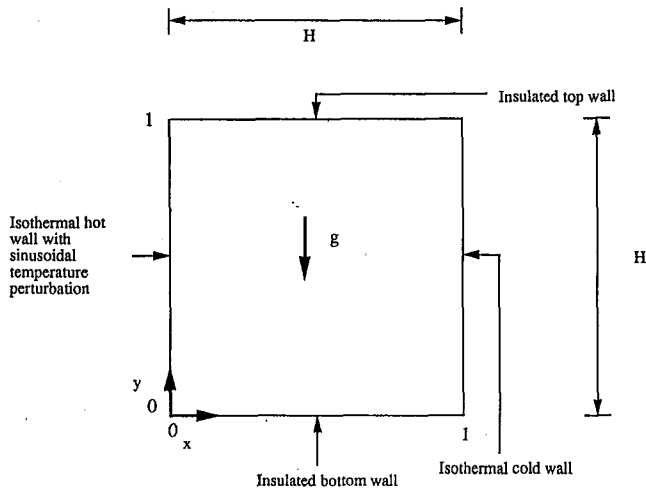


Fig. 1 Geometry of the enclosure

pressure difference between the total pressure and the equilibrium hydrostatic pressure in the absence of a temperature gradient scaled by  $\rho\alpha^2/H^2$ . The temperature was nondimensionalized as  $T = (\bar{T} - \bar{T}_C)/\Delta\bar{T}$  where  $\Delta\bar{T} = \bar{T}_{Hm} - \bar{T}_C$ . The thermal diffusivity is  $\alpha$  and  $\rho$  is the fluid density. The nondimensionalized governing equations using the Boussinesq approximation are the following (Yang, 1988):

$$\nabla \cdot \vec{U} = 0 \quad (1)$$

$$\frac{\partial u}{\partial t} + \nabla \cdot (u\vec{U}) = -\frac{\partial p}{\partial x} + \text{Pr}\nabla^2 u \quad (2)$$

$$\frac{\partial v}{\partial t} + \nabla \cdot (v\vec{U}) = -\frac{\partial p}{\partial y} + \text{Pr}\nabla^2 v + \text{Ra}\text{Pr}T \quad (3)$$

$$\frac{\partial T}{\partial t} + \nabla \cdot (T\vec{U}) = \nabla^2 T \quad (4)$$

The boundary conditions are

$$y = 0, 1, \quad 0 \leq x \leq 1, \quad u = v = 0, \quad \frac{\partial T}{\partial y} = 0 \quad (5)$$

$$x = 0, \quad u = v = 0, \quad T = 1 + \epsilon \sin(\omega_0 t) \quad (6)$$

$$x = 1, \quad u = v = 0, \quad T = 0 \quad (7)$$

where  $\epsilon$  is a nondimensional amplitude of the temperature perturbation, Ra is the Rayleigh number,  $g\beta\Delta\bar{T}H^3/\alpha\nu$ , and  $\omega_0$  is a nondimensional frequency of the imposed temperature perturbation, which is defined as  $\bar{\omega}_0 H^2/\alpha$ , where  $\bar{\omega}_0$  is the dimensional frequency.

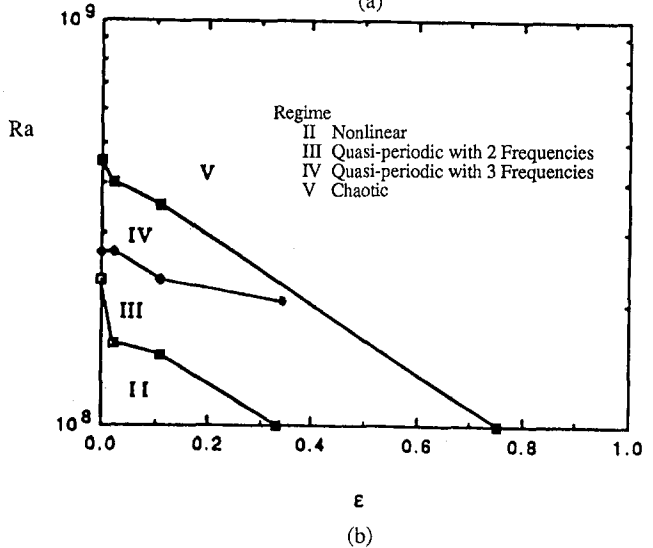
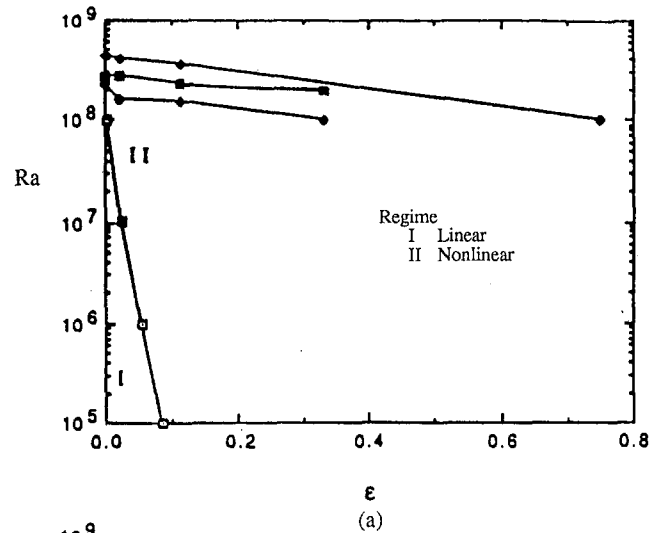


Fig. 2 Flow regime maps

The governing equations set in two dimensions are solved using the control volume method for the primitive variable formulation. The grid is nonuniform and staggered. The QUICK scheme, which is a third-order accurate interpolation formula for the advection terms (Leonard, 1983) was used for the computations. Other than the improved accuracy of the scheme, it is now fully established that QUICK minimizes false diffusion

The governing equations set in two dimensions are solved using the control volume method for the primitive variable formulation. The grid is nonuniform and staggered. The QUICK scheme, which is a third-order accurate interpolation formula for the advection terms (Leonard, 1983) was used for the computations. Other than the improved accuracy of the scheme, it is now fully established that QUICK minimizes false diffusion

## Nomenclature

$g$  = acceleration due to gravity,  $\text{m/s}^2$   
 $H$  = height and width of enclosure,  $\text{m}$   
 $p$  = nondimensional pressure  
 $\text{Pr}$  = Prandtl number =  $\nu/\alpha$   
 $\text{Ra}$  = Rayleigh number =  $g\beta\Delta\bar{T}H^3/(\nu\alpha)$   
 $T$  = nondimensional temperature  
 $\bar{T}_C$  = cold wall temperature,  $\text{K}$   
 $\bar{T}_{Hm}$  = mean hot wall temperature,  $\text{K}$   
 $t$  = nondimensional time  
 $\vec{U}$  = nondimensional velocity vector  
 $u$  = nondimensional velocity in the  $x$  direction

$u_R$  = dimensional reference velocity,  $\text{m/s}$   
 $v$  = nondimensional velocity in the  $y$  direction  
 $x$  = nondimensional  $x$  coordinate  
 $y$  = nondimensional  $y$  coordinate  
 $\alpha$  = thermal diffusivity,  $\text{m}^2/\text{s}$   
 $\beta$  = volumetric coefficient of expansion,  $1/\text{K}$   
 $\Delta\bar{T}$  = temperature difference =  $\bar{T}_C - \bar{T}_{Hm}$ ,  $\text{K}$   
 $\epsilon$  = nondimensional amplitude of perturbation

$\nu$  = kinematic viscosity,  $\text{m}^2/\text{s}$   
 $\rho$  = density,  $\text{kg}/\text{m}^3$   
 $\omega$  = nondimensional frequency of oscillation =  $\bar{\omega}H^2/\alpha$   
 $\omega_0$  = imposed nondimensional frequency of oscillation =  $\bar{\omega}_0 H^2/\alpha$   
 $\bar{\omega}$  = dimensional frequency,  $\text{rad/s}$   
 $\tilde{\omega}$  = nondimensional frequency of oscillation =  $\bar{\omega}H/u_R$   
 $\tilde{\omega}_1$  = nondimensional frequency of oscillation at first bifurcation  
 $\tilde{\omega}_2$  = nondimensional frequency of oscillation at second bifurcation

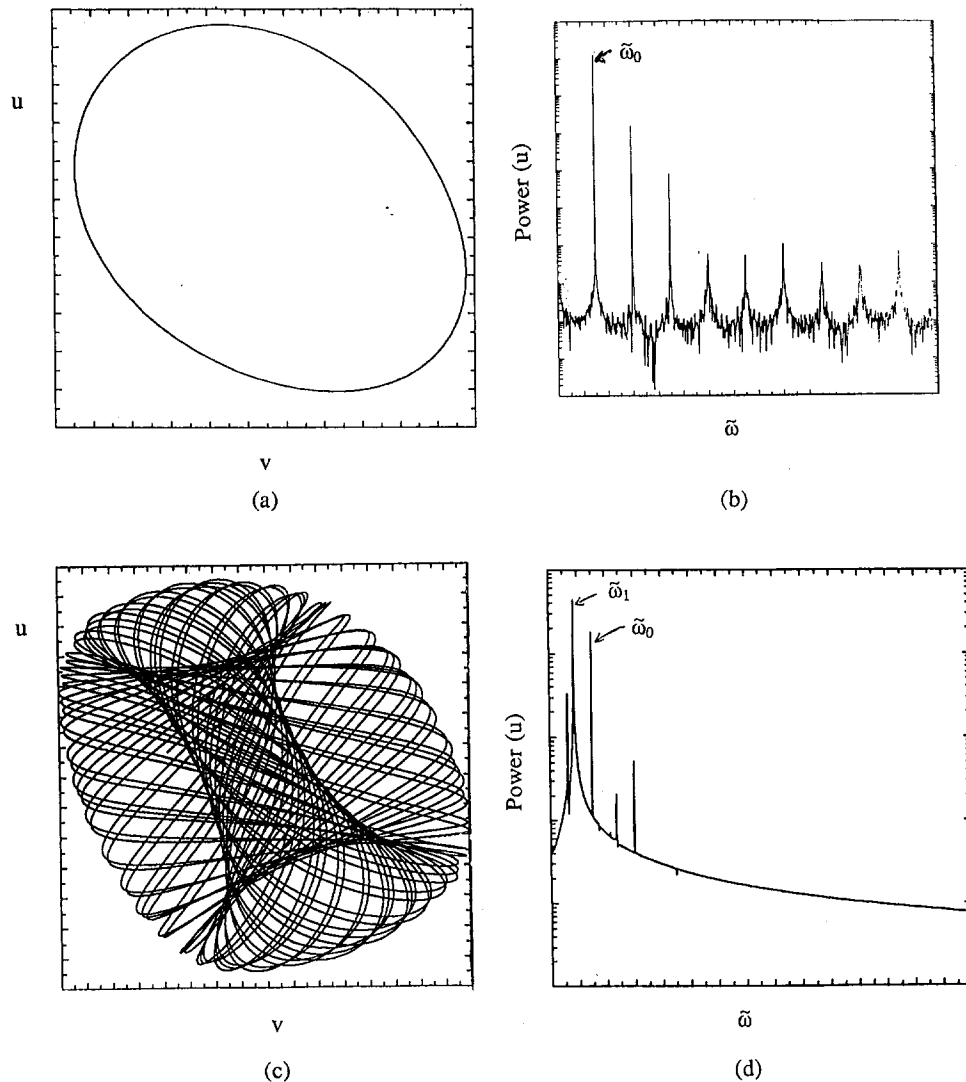


Fig. 3 (a) Phase trajectory; (b) frequency spectra for  $Ra = 10^8$ ,  $\epsilon = 0.02$ ,  $\tilde{\omega}_0 = 3.0$ ; (c) phase trajectory; (d) frequency spectra for  $Ra = 2 \times 10^8$ ,  $\epsilon = 0.02$ ,  $\omega_0 = 3.0$

(Leonard, 1988). This is crucial for bifurcation studies since accurate modeling of the unsteady phenomena is essential.

It was determined that a  $60 \times 60$  grid with five cells inside the thermal boundary layer was a good compromise between accuracy and computing resources. The cells inside the boundary layer are of uniform size, whereas the cell sizes outside are in a geometric ratio with the largest cell next to the centerline. The grid is symmetric about the centerlines in the  $x$  and  $y$  directions. This is so chosen because the temperature and velocity fields are known to have similar symmetries in the steady-state regimes. Validation studies for the code have been reported earlier (Xia and Yang, 1990).

## Results

In the present study, the effect of a perturbation of the hot wall temperature on the velocity and temperature field is studied parametrically for different Rayleigh numbers and amplitudes of the temperature perturbation. The effect of the frequency is not a part of this study. Here it is convenient to introduce another nondimensional frequency  $\tilde{\omega}$  defined as  $\tilde{\omega} = \bar{\omega}H/u_R$ , where  $u_R$  is a constant dimensional reference velocity utilized to reduce the computational effort (Yang and Lloyd, 1985). As a result, the relation between the two nondimensional frequencies is simply  $\tilde{\omega} = \omega(\alpha/Hu_R)$ . In the present study,  $u_R$  is chosen such that the

quantity  $(Hu_R/\alpha)$  is of the order of 800. The computations here are based on one imposed nondimensional frequency of  $\tilde{\omega}_0 = 3.0$ , which, as will be shown later, lies between the first and second bifurcation frequencies of the zero-perturbation ( $\epsilon = 0$ ) case. As mentioned previously, this is chosen to increase the probability of interaction between the natural and imposed modes of oscillation. At this low imposed frequency, the effect of the oscillation is likely to be felt over the entire cavity. For higher frequencies, the effect in the cavity is restricted to a small shear layer close to the wall, as indicated by Xia and Yang (1990).

A response is deemed linear if the amplitude of heat flux or temperature is proportional to the amplitude of the imposed temperature perturbation. Typically, this is the case for perturbation amplitudes that are relatively small. For the nonlinear regime, this simple direct proportion is no longer valid. The boundary between linear and nonlinear regime in the  $Ra-\epsilon$  plane has already been reported by Xia and Yang (1990). In this paper we cover the so-called nonlinear regime by detailed computations in the  $Ra-\epsilon$  plane. The results are summarized in Fig. 2 by a flow regime map parameterized by the Rayleigh number and the amplitude of perturbation for a nondimensional imposed frequency of three. Figure 2(b) represents an enlarged map in the region for  $Ra = 10^8$  to  $10^9$  for clarity. The map divides the whole region into five different flow regimes: I—linear response flow; II—nonlinear response flow with self-induced higher harmonics;

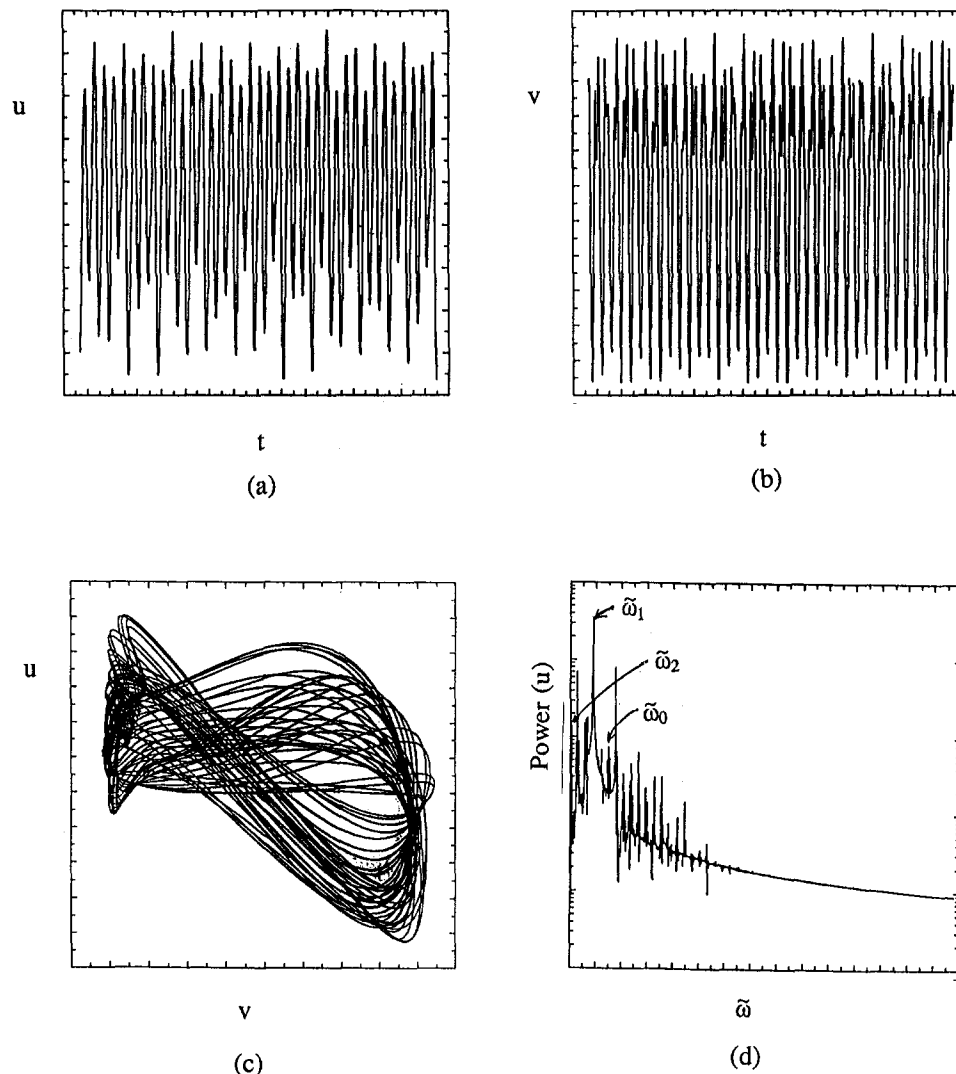


Fig. 4 (a) Time series for  $u$  velocity; (b) time series for  $v$  velocity; (c) phase trajectory; (d) frequency spectra for  $Ra = 2.9 \times 10^8$ ,  $\epsilon = 0.02$ ,  $\tilde{\omega}_0 = 3.0$

III—quasi-periodic flow with two independent frequencies; IV—quasi-periodic flow with three independent frequencies; V—chaotic flow. It should, however, be emphasized here that the demarcation between regimes I and II is superficial in that theoretically regime I blends into regime II continuously and no clear boundary is discernible, as already pointed out by Xia and Yang (1990).

Due to limitations in computing resources, the flow regime map shown in Fig. 2 has been constructed from a relatively small number of cases. It is possible that the boundaries between the different flow regimes would have taken a more complex structure with additional points in the  $Ra$ - $\epsilon$  plane. For instance, the boundary between regime IV and V is a result of just four points. It must therefore be cautioned that the boundary contours in Fig. 2 should only be interpreted qualitatively.

**Flow Regimes.** For air in a square side-heated cavity without imposed temperature oscillations, Paolucci and Chenoweth (1989) discovered that the transition to chaos follows the Ruelle-Takens-Newhouse scenario. The sequence is the following: Steady-State  $\rightarrow$  Periodic  $\rightarrow$  Quasi-Periodic  $\rightarrow$  Chaotic. The present study intends to document the qualitative and quantitative effects of the additional frequency forced onto the system. The dynamic behavior of the system was examined by looking at the power spectra and the phase trajectories of some local

variables. Since the aspect ratio is small, the qualitative dynamic behavior of the system is independent of the location and the variable chosen. In other words, any variable at any location represents the dynamic behavior of the system as a whole. In this case, the power spectra of the  $u$  velocity at the location (0.03, 0.93) was selected for all the power spectra shown. All the phase trajectories shown in this paper are between the  $u$  and  $v$  velocities at the same spatial location.

The results shown in Fig. 2 were obtained by adopting the following procedure: (1) For a given  $\epsilon$  increase the Rayleigh number until the onset of chaos. (2) Repeat step 1 for a different  $\epsilon$  (which is higher). (3) For a given  $Ra$ , increase amplitude until the onset of chaos. As mentioned in Mukutmoni and Yang (1993a, 1993b), the calculation sequence is important because of the sensitivity of the solutions to initial conditions.

**First Bifurcation ( $\epsilon = 0.02$ ).** For  $\epsilon = 0.02$ , the initial runs were started at a Rayleigh number of  $10^7$  and then progressively increased. The flow and temperature field is oscillatory as a consequence of the perturbation. The only frequency present in the system is the one imposed, along with its higher harmonics, if any. At sufficiently higher Rayleigh numbers the system itself generates additional frequencies. The first frequency  $\tilde{\omega}_1$ , generated by the system, appears in the power spectra at a Rayleigh number of  $1.6 \times 10^8$ . The frequency in nondimensional terms is

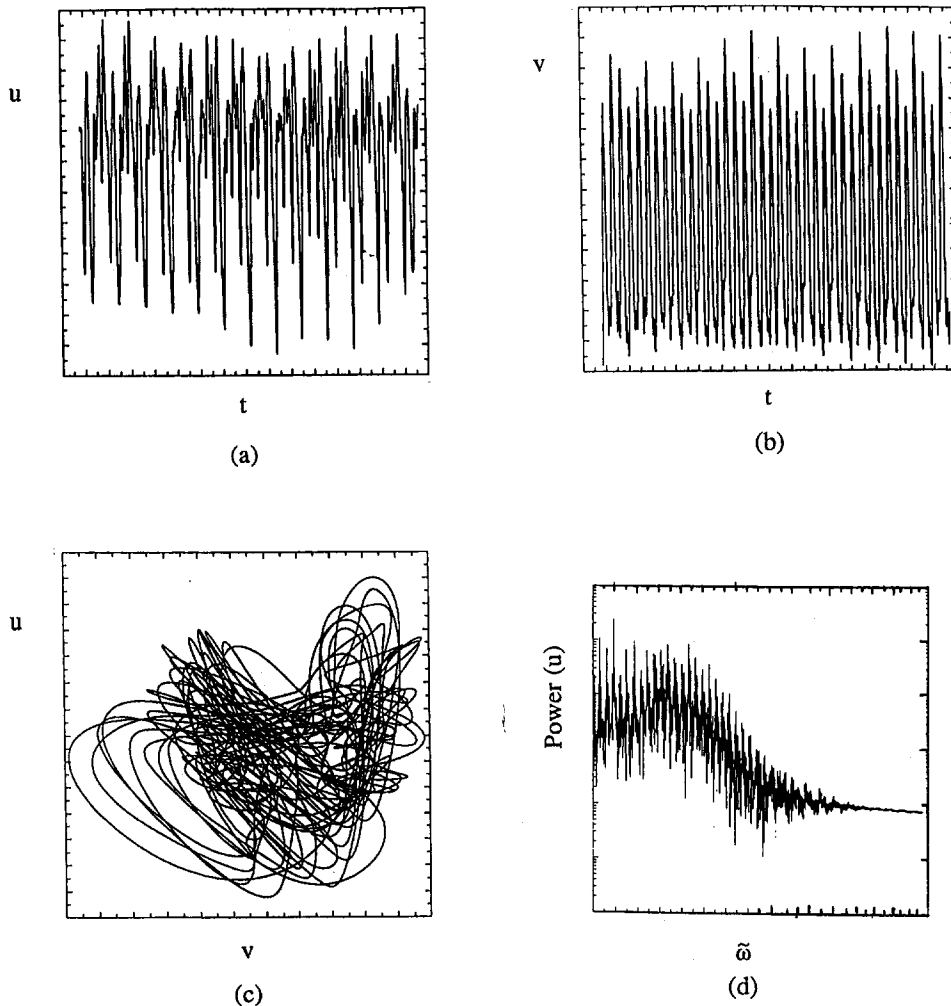


Fig. 5 (a) Time series for  $u$  velocity; (b) time series for  $v$  velocity; (c) phase trajectory; (d) frequency spectra for  $Ra = 4.0 \times 10^8$ ,  $\epsilon = 0.02$ ,  $\tilde{\omega}_0 = 3.0$

$\tilde{\omega}_1 = 1.664$ . This is of the same order as the imposed frequency of 3.0. The frequency ratio, however, is not a simple proportion. It therefore seems that the flow is quasi-periodic. The dynamic nature of the flow must be confirmed by phase trajectories.

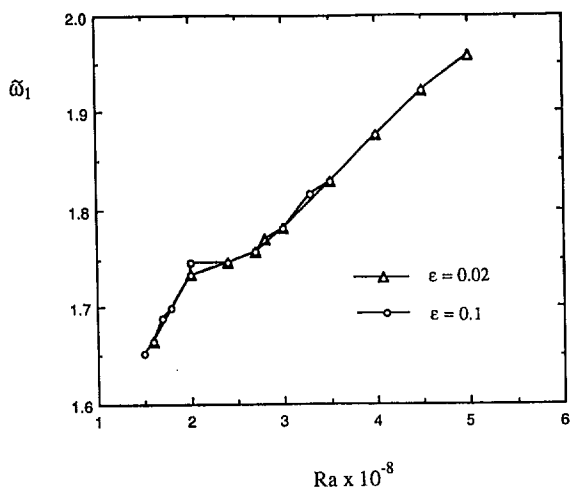


Fig. 6 The first generated frequency ( $\tilde{\omega}_1$ ) as a function of the Rayleigh number

The flow is subcritical at  $Ra = 1.0 \times 10^8$ . The phase trajectory and frequency is shown in Fig. 3(a, b). The frequency spectra (Fig. 3(b)) show the fundamental frequency  $\tilde{\omega}_0$  and its higher harmonics. The phase trajectory shows a simple closed trajectory that represents an asymptotic oscillatory state with one frequency.

The supercritical flow is shown for  $Ra = 2.0 \times 10^8$  in Figs. 3(c, d). The frequency spectra (Fig. 3(d)) now portray the independent frequencies  $\tilde{\omega}_0$  and  $\tilde{\omega}_1$  as well as the multiples and linear combinations of the two. The phase trajectory (Fig. 3(c)) clearly shows what looks like an obvious projection of a torus onto a two-dimensional plane. That is a tell-tale signature of quasi-periodicity. It implies that the frequencies  $\omega_0$  and  $\omega_1$  must necessarily be incommensurate.

**Further Bifurcations.** As the Rayleigh number is increased further, yet another frequency is added to the system. This corresponds to the boundary between regions III and IV. The second independent frequency ( $\tilde{\omega}_2$ ) generated by the system appears at a Rayleigh number of  $2.7 \times 10^8$ . The value of the frequency is 0.152. The time series, phase trajectories, and the frequency spectra of the postbifurcation regime are shown in Fig. 4(a-d). The power spectra indicate that the effects of the naturally generated frequencies  $\tilde{\omega}_1$  and  $\tilde{\omega}_2$  are now overwhelming. The amplitudes of  $\tilde{\omega}_1$  and  $\tilde{\omega}_2$  are much larger than that at  $\tilde{\omega}_0$ . Also,  $\tilde{\omega}_2$  is much smaller than  $\tilde{\omega}_1$ .

Figures 5(a, b) show respectively the phase trajectory and the frequency spectra at a Rayleigh number of  $4.0 \times 10^8$ . The



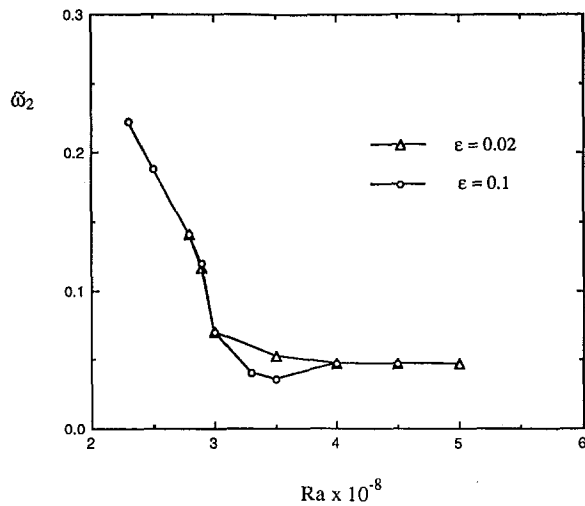


Fig. 7 The second generated frequency ( $\tilde{\omega}_2$ ) as a function of the Rayleigh number

frequency spectra do appear to have some dominant frequencies. Nevertheless, the most significant feature of the spectra is the presence of broad band components particularly in the low-frequency range. The phase trajectory resembles a tangle of cobwebs. It appears that the trajectory never repeats itself. This is confirmed by the time series of the variables in Figs. 5(c, d).

At this point, the flow can no longer be described in terms of a small number of well-defined characteristic frequencies; it is best described as chaotic or weakly turbulent. It certainly is aperiodic. The time series must be analyzed further to determine whether the flow is truly chaotic. One needs to estimate the Liapunov exponents. The calculated Liapunov exponent using the algorithm due to Wolf et al. (1985) at this Rayleigh number indicates that the exponent is positive.

The Liapunov exponent quantifies the average rate of convergence or divergence of nearby trajectories. A positive Liapunov exponent is tantamount to chaos. It is difficult to pin down the onset of chaos because the estimate of the Liapunov exponent using time series data is inherently uncertain (30 to 40 percent error is expected). To the best of our knowledge, chaos occurs between  $3.5 \times 10^8$  and  $4.0 \times 10^8$ .

To summarize, the Ruelle-Takens-Newhouse scenario was observed for  $\epsilon = 0.02$  i.e., Periodic (one frequency)  $\rightarrow$  Quasi-Periodic (two frequencies)  $\rightarrow$  Quasi-Periodic (three-frequencies)  $\rightarrow$  Chaotic. In the absence of a forcing frequency ( $\epsilon = 0$ ), the same scenario was observed. However, quantitative changes were found to occur. The first frequency  $\tilde{\omega}_1 = 6.04$  was generated at  $Ra = 2.3 \times 10^8$ . The second frequency  $\tilde{\omega}_2 = 0.598$  occurred at  $Ra = 2.7 \times 10^8$ . The changes observed are quantitative rather than qualitative. Transition to chaos was found to occur between a Rayleigh number of  $3.5 \times 10^8$  and  $4.0 \times 10^8$ . Thus, the critical Rayleigh numbers and the frequencies themselves are somewhat different. It is interesting to note that the critical Rayleigh number for the transition to chaos was relatively unchanged.

**Higher Amplitudes of Perturbation.** For  $\epsilon = 0.1$ , the first bifurcation occurs at  $Ra = 1.5 \times 10^8$  and  $\tilde{\omega}_1 = 1.65$ . The second bifurcation occurs at  $Ra = 2.3 \times 10^8$  and  $\tilde{\omega}_2 = 0.22$ . Chaos sets in at  $Ra = 3.5 \times 10^8$ . Based on the numerical experiments so far one can see that as the amplitude is increased the critical Rayleigh number decreases. The frequencies themselves ( $\omega_1$  and  $\omega_2$ ) are a strong function of the perturbation amplitude. The scenario (Ruelle-Takens-Newhouse) is nevertheless unchanged.

Table 1 Bifurcation frequencies  $\omega_1$  and  $\omega_2$  at  $Ra = 3 \times 10^8$  with  $\epsilon = 0$

Study	First Bifurcation Frequency $\omega_1$	Second Bifurcation Frequency $\omega_2$
Present	629.2	6707
Paolucci & Chenoweth (1989)	737.7	8856
Henkes (1990)	661.7	9118

In a further set of numerical experiments, the Rayleigh number and frequency are fixed and the amplitude is progressively increased. In the process, the effects of large amplitudes are examined.  $Ra = 10^8$ ,  $\epsilon = 0.001$  was found to be in the linear regime (I in Fig. 2). As the amplitude is increased, the flow regime moves from region I to region II. The system generates its own frequency at  $\epsilon = 0.33$  with  $\tilde{\omega}_1 = 1.57$ . Chaos sets in at  $\epsilon = 0.75$ . No evidence of  $\tilde{\omega}_2$  was observed. The route to chaos has thus been altered when the amplitudes were sufficiently large. Rather than going through two successive Hopf bifurcations, we have a situation wherein one Hopf bifurcation is followed directly by transition to chaos.

The complete set of simulation results is not stated in detail. Instead, they are summarized in Fig. 2(a, b) for convenience and brevity. Figure 2(b) is simply an enlarged portion of Fig. 2(a) in the high-Rayleigh-number end.

#### Rayleigh Number Effect on Bifurcation Frequencies.

Having discussed the bifurcations occurring in the flow, we now address the flow behavior between the bifurcations. Figures 6 and 7 show respectively the frequencies  $\omega_1$  and  $\omega_2$  as a functions of the Rayleigh number for two different perturbation amplitudes. Curiously, the behavior of  $\tilde{\omega}_2$  is qualitatively different from  $\tilde{\omega}_1$ . Whereas  $\tilde{\omega}_1$  increases with increasing Rayleigh number,  $\tilde{\omega}_2$  decreases and then levels off with an increase in Rayleigh number.

We now compare some of the results for  $\tilde{\omega}_0 = 0$  with numerical results that have been published. The numerical results of the same case with no forcing ( $\epsilon = 0$ ) have already been reported by Paolucci and Chenoweth (1989) and Henkes (1990). It is therefore natural that we compare our results with theirs. The comparison, indicated in Table 1, shows reasonable agreement in frequencies (the only yardstick available for

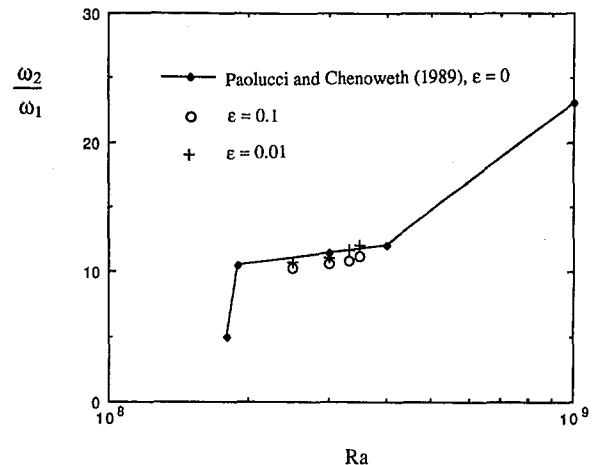


Fig. 8 Frequency ratio as a function of the Rayleigh number

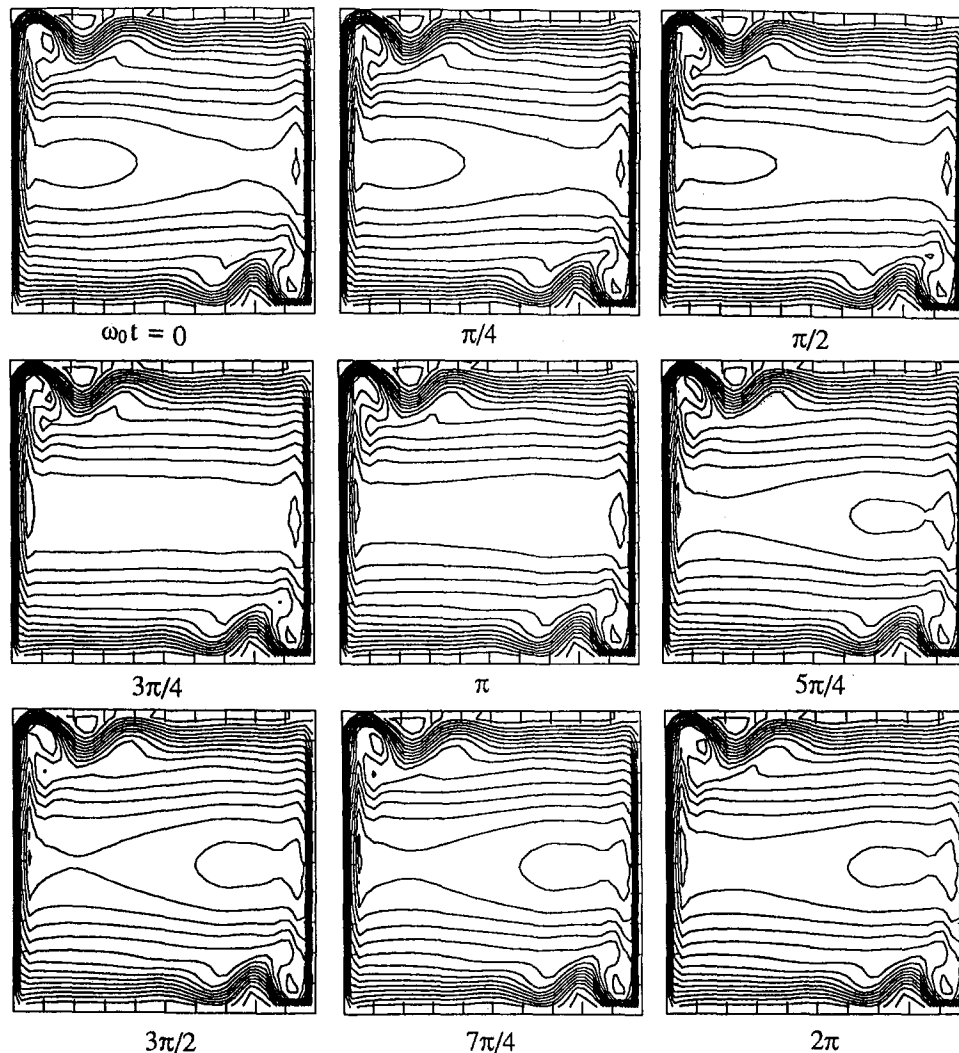


Fig. 9 The oscillating flow field over one complete cycle of the imposed frequency ( $\omega_0$ ):  $Ra = 2.0 \times 10^8$ ,  $\epsilon = 0.02$

comparison). Here the nondimensional frequencies  $\omega_1$  and  $\omega_2$  are compared at a Rayleigh number of  $3 \times 10^8$ . Note that the dimensionless frequencies were defined differently in their studies and to facilitate comparison the frequencies were scaled in a consistent manner. In view of the fact that bifurcation frequencies are known to be sensitive to the details of the numerical methods, the differences shown in Table 1 are not all unexpected. Figure 8 compares the frequency ratios  $\omega_1/\omega_2$  with the results of Paolucci and Chenoweth (1989). The agreement is quite reasonable. The critical Rayleigh numbers for these two bifurcations are  $2 \times 10^8$  and  $2.5 \times 10^8$ , respectively. The corresponding numbers from Paolucci and Chenoweth (1989) are  $1.93 \times 10^8$  and  $2.55 \times 10^8$ , respectively.

**Flow Mechanism.** In order to find how the frequency was generated, one must take a closer look at the flow field. Figures 9 and 10 show the flow field over a complete cycle of imposed oscillation ( $\omega_0$ ) and system natural oscillation ( $\omega_1$ ), respectively ( $Ra = 2 \times 10^8$ ,  $\epsilon = 0.02$ ). A closer inspection of Fig. 9 reveals that the hot upper and cold lower corner regions complete one cycle and are therefore dominated by  $\omega_0$ . The rest of the cavity is dominated by the other frequency and do not complete the cycle. Figure 10 shows the opposite. The core of the cavity appears to repeat itself but the corners do not. Thus, the core regions are dominated by  $\omega_1$ .

From Fig. 10, a closer look shows that traveling waves are also moving along the heated and cooled vertical walls. This is highly

suggestive of a boundary layer type of instability (Tollmien-Schlichting waves). However, a hydraulic jump type of instability cannot be absolutely ruled out since the existing hydraulic jump phenomenon may or may not be a direct consequence of the traveling waves.

## Conclusions

An extensive parametric study has been carried out to investigate the qualitative and quantitative effect of wall temperature oscillations on the velocity and temperature field. The parameters were restricted to the Rayleigh number and amplitude of perturbation. The computational results were consistent with zero amplitude results available in the literature (Paolucci and Chenoweth, 1989). Some of the major findings are the following:

- 1 The imposed forcing oscillations decrease the critical Rayleigh numbers. But the route to chaos follows the Ruelle-Takens-Newhouse scenario with the exception of very large amplitudes, in which case only one Hopf bifurcation was observed.
- 2 The frequency generated by the system during each bifurcation is a strong function of the Rayleigh number. It also depends strongly on the amplitude of the imposed forcing oscillations.
- 3 The first bifurcation results primarily from the instability of the wall and corner flows; the traveling waves

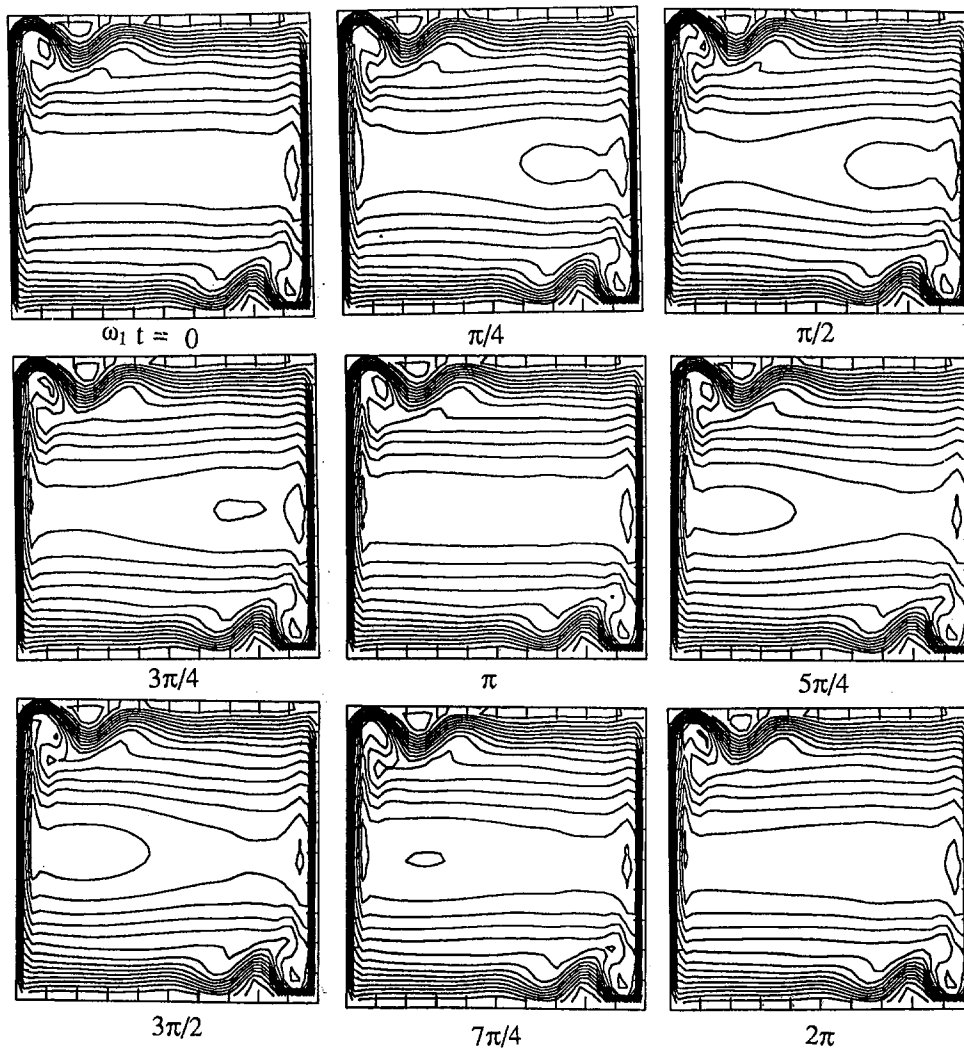


Fig. 10 The oscillating flow field over one complete cycle of the first generated frequency ( $\omega_1$ ):  $Ra = 2.0 \times 10^8$ ,  $\epsilon = 0.02$

along the walls are the likely mechanisms for this instability.

## References

- Bajorek, S. M., and Lloyd, J. R., 1982, "Experimental Investigation of Natural Convection in Partitioned Enclosures," *ASME JOURNAL OF HEAT TRANSFER*, Vol. 104, pp. 527–532.
- De Vahl Davis, G., 1983, "Natural Convection of Air in a Square Cavity: A Benchmark Numerical Solution," *International Journal of Numerical Methods in Fluids*, Vol. 3, pp. 249–264.
- Henkes, R. A. W. M., 1990, "Natural Convection Boundary Layers," Ph.D. Thesis, Delft University, Delft, Netherlands.
- Ivey, G. A., 1984, "Experiments on Transient Natural Convection in a Cavity," *Journal of Fluid Mechanics*, Vol. 144, pp. 389–401.
- Kazmierczak, M., and Chinoda, Z., 1992, "Buoyancy-Driven Flow in an Enclosure With Time Periodic Boundary Conditions," *International Journal of Heat and Mass Transfer*, Vol. 35, No. 6, pp. 1507–1518.
- Leonard, B. P., 1983, "A Convectively Stable, Third-Order Accurate Finite-Difference Method for Steady Two-Dimensional Flow and Heat Transfer," *Numerical Properties and Methodologies in Heat Transfer*, T. M. Shih, ed., Hemisphere Publishing Corporation, Washington, DC, pp. 211–226.
- Leonard, B. P., 1988, "Elliptic Systems: Finite-Difference Method IV," in: *Handbook of Numerical Heat Transfer*, W. J. Minkowycz, E. M. Sparrow, G. E. Schneider, and R. H. Fletcher, eds., Wiley, New York, pp. 347–378.
- Mukutmoni, D., and Yang, K. T., 1993a, "Rayleigh–Bénard Convection in a Small Aspect Ratio Enclosure: Part I—Bifurcation to Oscillation Convection," *ASME JOURNAL OF HEAT TRANSFER*, Vol. 115, pp. 360–366.
- Mukutmoni, D., and Yang, K. T., 1993b, "Rayleigh–Bénard Convection in a Small Aspect Ratio Enclosure: Part II—Bifurcation to Chaos," *ASME JOURNAL OF HEAT TRANSFER*, Vol. 115, pp. 367–376.
- Nieuwstadt, F. T. M., 1990, "Direct and Large-Eddy Simulation of Free Convection," *Proceedings of the 9th International Heat Transfer Conference*, Jerusalem, Israel, Vol. 1, pp. 37–47.
- Paolucci, S., and Chenoweth, D. R., 1989, "Transition to Chaos in a Differentially Heated Vertical Cavity," *Journal of Fluid Mechanics*, Vol. 201, pp. 379–410.
- Paolucci, S., 1990, "Direct Numerical Simulation of Two-Dimensional Turbulent Natural Convection in an Enclosed Cavity," *Journal of Fluid Mechanics*, Vol. 215, pp. 229–262.
- Schladow, S. G., 1990, "Oscillatory Motion in a Side-Heated Cavity," *Journal of Fluid Mechanics*, Vol. 213, pp. 589–610.
- Wolf, A., Swift, J. B., Swinney, H. L., and Vastano, J. A., 1985, "Determining Liapunov Exponents From a Time Series," *Physica 16D*, pp. 285–317.
- Xia, Q., and Yang, K. T., 1990, "Linear Response of the Temperature and Flow Fields in a Square Enclosure to Imposed Wall Temperature Oscillations," *Proceedings of the 9th International Heat Transfer Conference*, Jerusalem, Israel, Vol. 3, pp. 271–276.
- Yang, K. T., and Lloyd, J. R., 1985, "Turbulent Buoyant Flow in Vented Simple and Complex Enclosures," in: *Natural Convection—Fundamentals and Applications*, W. Aung, S. Kakac, and R. Viskanta, eds., Hemisphere Publishing Corporation, Washington, DC, pp. 303–329.
- Yang, K. T., 1988, "Transitions and Bifurcations in Laminar Buoyant Flows in Confined Enclosures," *ASME JOURNAL OF HEAT TRANSFER*, Vol. 110, pp. 1191–1204.

# Natural Convection in an Inclined Fluid Layer With a Transverse Magnetic Field: Analogy With a Porous Medium

P. Vasseur

M. Hasnaoui

E. Bilgen

L. Robillard

Ecole Polytechnique de Montréal,  
Mechanical Engineering Department,  
C.P. 6079, St. A, Montréal, P.Q. H3C 3A7  
Canada

*In this paper the effect of a transverse magnetic field on buoyancy-driven convection in an inclined two-dimensional cavity is studied analytically and numerically. A constant heat flux is applied for heating and cooling the two opposing walls while the other two walls are insulated. The governing equations are solved analytically, in the limit of a thin layer, using a parallel flow approximation and an integral form of the energy equation. Solutions for the flow fields, temperature distributions, and Nusselt numbers are obtained explicitly in terms of the Rayleigh and Hartmann numbers and the angle of inclination of the cavity. In the high Hartmann number limit it is demonstrated that the resulting solution is equivalent to that obtained for a porous layer on the basis of Darcy's model. In the low Hartmann number limit the solution for a fluid layer in the absence of a magnetic force is recovered. In the case of a horizontal layer heated from below the critical Rayleigh number for the onset of convection is derived in term of the Hartmann number. A good agreement is found between the analytical predictions and the numerical simulation of the full governing equations.*

## Introduction

Several aspects of natural convection of an electrically conducting fluid in magnetic fields have been studied extensively over the past 20 years or so. The interest in such problems stems from their importance in such areas as the design of magneto-hydrodynamic generators, pumps and accelerators, the process of manufacturing semiconducting material and the use of liquid metals as the coolant medium in a variety of nuclear reactors involving the presence of strong magnetic fields. To improve design in the manufacturing and operational processes, a better understanding of the interaction between magnetic fields and convection is of importance.

The natural convection boundary-layer flow on a hot vertical plate, in the presence of a strong cross magnetic field, has been discussed by several authors (Singh and Cowling, 1963; Kuiken, 1970; Wilks, 1976; Hunt and Wilks, 1981). Using asymptotic series expansions, an analytical solution for this problem was derived by Wilks (1976). Details of heat transfer coefficients were obtained for the Prandtl number of order unity. This solution was extended to the low Prandtl range by Hunt and Wilks (1981). It was found that the rate of heat transfer, near the leading edge of the plate, increases as the Prandtl number decreases.

Two-dimensional natural convection in a fluid heated from below in the presence of an imposed vertical magnetic field has been studied by Weiss (1981). The pattern of bifurcation from the static solution and the connection between small-amplitude theory and nonlinear convection was considered for the case of Pr equal to unity. His work is, however, limited to stress-free boundaries, which are more plausible in astrophysical than in laboratory applications. Tabeling (1982) studied, with a linearized theory, stationary convective instability in rectangular boxes of finite extent. The relationship between the flow patterns of the Bénard cells and the direction of an external magnetic field is discussed. When the magnetic field

is horizontally applied, calculations show transition from transversal to longitudinal rolls as the magnitude of the field is increased.

The case of a square cavity with vertical walls at constant temperatures, the horizontal walls being insulated, has been studied numerically by Ozoe and Maruo (1987). Results were obtained for  $10^4 \leq Ra \leq 10^6$ ,  $1 \leq Ha \leq 10^3$ , and for  $Pr = 0.054$ . A correlation equation was derived by those authors for the average heat transfer as a function of the Hartmann, Rayleigh, and Prandtl numbers. The same problem was extended to the three-dimensional situation by Ozoe and Okada (1989). It was found that the convective flow can be mostly suppressed by the imposition of a horizontal magnetic field perpendicular to the heated vertical wall. However, a field horizontal but parallel to the heated surface was observed to be least effective in suppressing the circulation flow. Magneto-hydrodynamic free convection of an electrically conducting fluid, in a rectangular enclosure ( $A = 1$  and  $2$ ) with two side walls maintained at uniform heat flux condition, has been studied by Venkatachallappa and Subbaraya (1993). Numerical results show that with the application of an external magnetic field, aligned with gravity, the temperature and velocity fields are significantly modified. For sufficiently large magnetic field strength the convection was found to be suppressed for all values of Grashof number.

Recently, an analytical solution to the problem of buoyancy-driven flow in a two-dimensional shallow cavity with a transverse magnetic field has been proposed by Garandet et al. (1992). It was demonstrated that, in the high Hartmann number limit, the velocity gradient in the core was constant outside the two Hartmann layers at the vicinity of the walls normal to the magnetic field. The recirculating part of the flow was studied by means of a series expansion.

In this paper the effect of a transverse magnetic field on the natural convection, in an inclined fluid layer, is studied with a two-dimensional Navier-Stokes equation including Lorentz force terms. The thermal conditions are uniform heating and cooling through opposite walls. An analytical solution, valid for a shallow layer ( $A \gg 1$ ), is developed using a parallel flow approximation. The results of the analysis are also verified through numerical calculations.

Contributed by the Heat Transfer Division for publication in the JOURNAL OF HEAT TRANSFER. Manuscript received by the Heat Transfer Division June 1993; revision received September 1993. Keywords: Natural Convection. Associate Technical Editor: J. R. Lloyd.

## Geometric Configuration and Set of Equations

The study domain is an inclined two-dimensional cavity of dimensions  $L' \times H'$ , and infinite extent in the  $z'$  direction, as shown in Fig. 1. The long sides are subjected to uniform heat flux  $q'$ , while the short end walls are adiabatic. A magnetic field  $\vec{B}'$  is applied perpendicularly to the long sides. The thermophysical properties of the fluid at a reference temperature  $T'_0$  are assumed to be constant, except for the density in the buoyancy term in the momentum equation (Boussinesq approximation).

Neglecting the effect of Joule heating and viscous dissipation on heat transfer and also assuming that the induced magnetic field is very small compared to  $\vec{B}'$ , the governing equations for continuity, momentum transfer, heat transfer, and electric charge transfer are:

$$\nabla \cdot \vec{V}' = 0 \quad (1)$$

$$\frac{\partial \vec{V}'}{\partial t'} + (\vec{V}' \cdot \nabla) \vec{V}' = -\frac{1}{\rho_0} \nabla p' + \frac{1}{\rho_0} \vec{J}' \times \vec{B}' + \nu \nabla^2 \vec{V}' - \beta(T' - T'_0) \vec{g} \quad (2)$$

$$\frac{\partial T'}{\partial t'} + (\vec{V}' \cdot \nabla) T' = \alpha \nabla^2 T' \quad (3)$$

$$\nabla \cdot \vec{J}' = 0 \quad \vec{J}' = \sigma'(-\nabla \Phi' + \vec{V}' \times \vec{B}') \quad (4)$$

In these equations,  $\sigma'$  stands for the electrical conductivity,  $\Phi'$  for the electric potential, and  $-\nabla \Phi'$  for the associated electric field. As discussed by Garandet et al. (1992), for a two-dimensional case, Eq. (4) for the electric potential reduces to  $\nabla^2 \Phi' = 0$ . The unique solution is  $\nabla \Phi' = 0$  since there is always an electrically insulating boundary around the enclosure. It follows that the electric field vanishes everywhere.

The pressure terms appearing in Eq. (2) are eliminated in the usual way by taking the curl for both sides. In the two-dimensional frame of Fig. 1 the governing equations Eqs. (1)–(3) reduce to

$$\frac{\partial}{\partial t} \nabla^2 \Psi + J(\Psi, \nabla^2 \Psi) = \text{Ra Pr} \left[ \sin \phi \frac{\partial T}{\partial x} + \cos \phi \frac{\partial T}{\partial y} \right] - \text{Ha}^2 \text{Pr} \frac{\partial v}{\partial x} + \text{Pr} \nabla^4 \Psi \quad (5)$$

$$\frac{\partial T}{\partial t} + J(\Psi, T) = \nabla^2 T \quad (6)$$

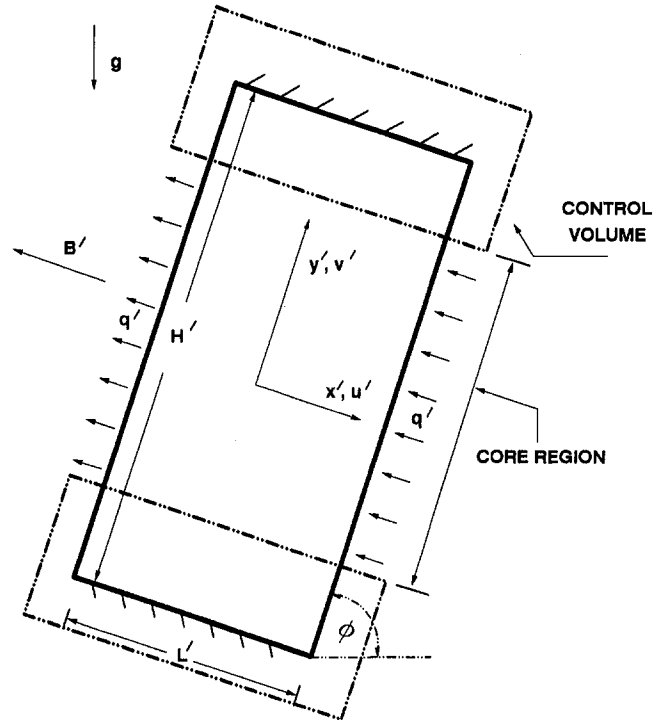


Fig. 1 Definition sketch

$$u = \frac{\partial \Psi}{\partial y} \quad v = -\frac{\partial \Psi}{\partial x} \quad (7)$$

where  $J(f, g) = f_x g_y - f_y g_x$

The nondimensional groups appearing in these equations are the Rayleigh number  $\text{Ra} = g\beta q' L'^4 / k\alpha\nu$ , the Hartmann number  $\text{Ha} = B' L' (\sigma' / \rho_0 \nu)^{1/2}$ , and the Prandtl number  $\text{Pr} = \nu / \alpha$ .

Equations (5)–(7) have been reduced to dimensionless form by introducing the following scales:

$$\left. \begin{aligned} (x, y) &= (x', y') / L' & (u, v) &= (u', v') / (\alpha / L') \\ T &= (T' - T'_0) / \Delta T' & \Delta T' &= (q' L' / k) \\ t &= t' \alpha / L'^2 \end{aligned} \right\} \quad (8)$$

where the symbols are defined in the nomenclature and primes denote dimensional variables.

## Nomenclature

$A$  = aspect ratio =  $H'/L'$   
 $B'$  = applied magnetic field  
 $C$  = dimensionless temperature gradient along  $y$  direction  
 $Da$  = Darcy number  
 $g$  = acceleration due to gravity  
 $H'$  = height of the system  
 $Ha$  = Hartmann number =  $B' L' (\sigma' / \rho_0 \nu)^{1/2}$   
 $\vec{J}'$  = electric current  
 $k$  = thermal conductivity of the fluid  
 $L'$  = thickness of the system  
 $Nu$  = Nusselt number, Eq. (11)  
 $p'$  = pressure  
 $Pr$  = Prandtl number =  $\nu / \alpha$   
 $q'$  = constant heat flux  
 $R$  = magnetic Rayleigh number =  $\text{Ra} / \text{Ha}^2$

$\text{Ra}$  = Rayleigh number =  $(g\beta q' L'^4) / (k\nu\alpha)$   
 $\text{Ra}_C$  = critical Rayleigh number  
 $T$  = dimensionless temperature =  $(T' - T'_0) / (q' L' / k)$   
 $T'_0$  = reference temperature at  $x' = y' = 0$   
 $\Delta T'$  = characteristic temperature difference =  $q' L' / k$   
 $\Delta T$  = dimensionless temperature difference at  $y = 0$ ,  $(T'_{(1/2,0)} - T'_{(-1/2,0)})$   
 $\vec{V}'$  = velocity vector  
 $u, v$  = dimensionless velocities in  $x$  and  $y$  directions =  $(u', v') L' / \alpha$   
 $x, y$  = dimensionless Cartesian coordinates =  $(x', y') / L'$

$\alpha$  = thermal diffusivity of fluid medium  
 $\beta$  = coefficient of thermal expansion of fluid  
 $\theta$  = dimensionless temperature  
 $\nu$  = kinematic viscosity  
 $\rho_0$  = density at temperature  $T'_0$   
 $\sigma'$  = electrical conductivity  
 $\Phi'$  = electric potential  
 $\phi$  = angle of inclination of the enclosure

### Subscript

$C$  = critical value

### Superscript

' = dimensional variables

The thermal boundary conditions are

$$x = \pm 1/2 \quad \frac{\partial T}{\partial x} = 1 \quad (9a)$$

$$y = \pm A/2 \quad \frac{\partial T}{\partial y} = 0 \quad (9b)$$

where  $A = H'/L'$  is the enclosure aspect ratio.

The hydrodynamic boundary conditions are

$$x = \pm 1/2 \quad \Psi = \frac{\partial \Psi}{\partial x} = 0 \quad (10a)$$

$$y = \pm A/2 \quad \Psi = \frac{\partial \Psi}{\partial y} = 0 \quad (10b)$$

Equations (5)–(7) together with boundary conditions (9)–(10) complete the formulation of the problem. The governing parameters are  $Ra$ ,  $Ha$ ,  $Pr$ ,  $A$ , and  $\phi$ .

The heat transfer rate across the system can be expressed in terms of a Nusselt number at  $y = 0$ , defined as

$$Nu = \frac{1}{\Delta T} \quad (11)$$

where  $\Delta T = (T_{(1/2,0)} - T_{(-1/2,0)})$  is the dimensionless temperature differences between thermally active walls.

### Analytical Solution

An approximate solution to the present problem can be obtained on the basis of the parallel flow approximation developed by Cormack et al. (1974) and used by Bejan and Tien (1978), Vasseur et al. (1987, 1989), and Sen et al. (1987, 1988). This approximation, valid for shallow cavities ( $A \gg 1$ ), suggests that the velocity and temperature distributions in the core region of the fluid layer are of the form

$$\Psi(x, y) \approx \Psi(x) \quad (12)$$

$$T(x, y) \approx Cy + \theta(x) \quad (13)$$

where  $C$  is an unknown but constant temperature gradient in the  $y$  direction. Because of the turning flow at the end regions, the boundary condition, Eq. (9b), cannot be exactly satisfied by the parallel flow approximation. Taking  $\Psi = 0$  at  $x = \pm 1/2$ , however, assures that the net flow in the  $y$  direction is zero. Instead of specifying thermal conditions at the ends, an equivalent energy flux condition is used (Bejan, 1983):

$$C = \int_{-1/2}^{1/2} v\theta \Big|_y dx \quad (14)$$

Using the approximations (12) and (13), the steady-state form of the governing Eqs. (5) and (6) can be reduced to ordinary differential equations

$$-\frac{d^4v}{dx^4} - Ha^2 \frac{d^2v}{dx^2} + RaCv \sin \phi = 0 \quad (15)$$

$$\frac{d^2\theta}{dx^2} = Cv \quad (16)$$

Solutions to Eqs. (15) and (16) satisfying boundary conditions (9a) and (10a) are

$$v = B(\sinh dx \cos ex - \alpha_0 \cosh dx \sin ex) \quad (17)$$

$$\theta = B\beta_0(\alpha_0 \sinh dx \cos ex + \cosh dx \sin ex) + \frac{vHa^2}{2Ra \sin \phi} - Cx \cot \phi \quad (18)$$

where

$$d = \frac{Ha}{2} \sqrt{\gamma + 1} \quad e = \frac{Ha}{2} \sqrt{\gamma - 1} \quad \gamma = \frac{2}{Ha^2} \sqrt{RaC \sin \phi}$$

$$B = \frac{Ha^2 \gamma (1 + C \cot \phi)}{2CD} \quad \beta = \sqrt{\gamma^2 - 1} \quad \beta_0 = \frac{Ha^2 \beta}{2Ra \sin \phi} \quad (19)$$

$$D = \alpha_1 \cosh d/2 \cos e/2 + \alpha_2 \sinh d/2 \sin e/2$$

$$\alpha_0 = \cot e/2 \tanh d/2 \quad \alpha_1 = d + e\alpha_0 \quad \alpha_2 = e - d\alpha_0$$

To obtain an equation for the constant  $C$ , condition (14) together with Eqs. (17)–(19) can be used to give

$$\frac{B^2 Ha^2}{8RaC \sin \phi} [(1 - \alpha_0^2)F + 2\alpha_0 G + (1 + \alpha_0^2)H + 2\alpha_0(B - \alpha_0)] + \frac{2B \cot \phi}{\gamma Ha^2} \left[ D - \frac{4de}{d^2 + e^2} E \right] + 1 = 0 \quad (20)$$

where

$$E = \alpha_0 \sinh d/2 \cos e/2 + \cosh d/2 \sin e/2$$

$$F = \beta_1 \sinh d \cos e + \beta_2 \cosh d \sin e$$

$$G = \beta_2 \sinh d \cos e - \beta_1 \cosh d \sin e$$

$$H = \frac{de - e \sinh d + d \sin e}{de}$$

$$\beta_1 = -\frac{4d}{\gamma Ha^4} (d^2 - 3e^2) \quad \beta_2 = -\frac{4e}{\gamma Ha^4} (3d^2 - e^2)$$

Equation (20) can readily be solved numerically to obtain  $C$  for given values of  $Ra$ ,  $Ha$ , and  $\phi$ , after which the velocity and temperature distributions are given by Eqs. (17)–(19).

Substituting Eq. (18) into Eq. (12) yields the Nusselt number as

$$Nu = \frac{1}{2BE\beta_0 - C \cot \phi} \quad (21)$$

It is noticed that this approximate solution is independent of the Prandtl number. This is a consequence of the parallel flow approximation ( $A \gg 1$ ) for which the inertia terms (the left-hand terms in Eq. (5)) are identically nil. The resulting approximate governing Eqs. (15) and (16), and the corresponding solution, are thus independent of  $Pr$ . Nevertheless, the fact that the present solution is independent of  $Pr$  does not imply that it is valid for any value of  $Pr$ . In fact, it has been demonstrated in the past, on scaling grounds, by Gill (1966) and more recently by Patterson and Imberger (1980), that the inertia terms in Eq. (5) are negligible for  $Pr = O(1)$  or greater fluids. Consequently, the present solution is valid implicitly for  $Pr \geq 1$ . Thus, it is expected to be valid in the case of ionized gases ( $Pr \approx O(1)$ ) but not for liquid metals ( $Pr \ll 1$ ) for which the inertia terms are known to be important and the parallel flow approximation inadequate.

**1 The Vertical System.** The case of a vertical layer ( $\phi = 90^\circ$ ) is considered in this section. Of particular interest is the boundary layer regime for which  $Ra \rightarrow \infty$ . An asymptotic analysis of Eqs. (17)–(21) shows that the flow and temperature fields and Nusselt number are given respectively by

$$v = \sqrt{\frac{Ra}{C}} \frac{1}{d} \sinh d\bar{x} e^{-e\bar{x}} \quad (22)$$

$$T = Cy - \frac{vHa^2}{2Ra} + \frac{2e}{\sqrt{C} Ra} \cosh d\bar{x} e^{-e\bar{x}} \quad (23)$$

$$\text{Nu} = \frac{1}{4e(C \text{Ra})^{-1/2}} \quad (24)$$

$$\frac{2e(\text{Ra}C)^{5/2}}{\text{Ra}^2[\text{Ha}^2 + \sqrt{\text{Ra}C}]} = 1 \quad (25)$$

where  $\bar{x} = (x - \frac{1}{2})$  and

$$d = \frac{1}{2}[\text{Ha}^2 - 2\sqrt{\text{Ra}C}]^{1/2}$$

$$e = \frac{1}{2}[\text{Ha}^2 + 2\sqrt{\text{Ra}C}]^{1/2}$$

Equations (22)–(25) can be considered for the two following limits:

(i) *The Low Hartmann Limit:  $\text{Ha} \ll 1$ .* In the low  $\text{Ha}$  limit an asymptotic analysis of this solution shows that the flow and temperature fields and Nusselt number are given respectively by

$$v = (\sqrt{2d})^3 e^{-d\bar{x}} \sin d\bar{x} \quad (26)$$

$$T = \frac{1}{\sqrt{2d}} y + \frac{1}{d} e^{-d\bar{x}} \cos d\bar{x} \quad (27)$$

$$\text{Nu} = \frac{d}{2} \quad (28)$$

$$d^9 = \frac{\text{Ra}^2}{32} \quad (29)$$

which is in agreement with the results obtained by Kimura and Bejan (1984) for the boundary layer flow within a vertical fluid layer in the absence of a magnetic field.

(ii) *The High Hartmann limit  $\text{Ha} \gg 1$ .* An asymptotic analysis of Eqs. (22)–(25) when  $\text{Ha} \gg 1$  yields the following results:

$$v = p^{3/2}(e^{-p\bar{x}} - e^{-\text{Ha}\bar{x}}) \quad (30)$$

$$T = \frac{y}{\sqrt{p}} + \frac{1}{p} e^{-p\bar{x}} \quad (31)$$

$$\text{Nu} = \frac{p}{2} \quad (32)$$

$$p = \text{Ra}^{2/5} \text{Ha}^{-4/5} = R^{2/5} \quad (33)$$

The velocity profile, Eq. (30), indicates that the effect of viscosity, in the high Hartmann limit, cannot be neglected in a thin layer of thickness  $\text{Ha}^{-1}$  near the solid boundary.

In fact, the solution of Eq. (15), in the absence of the viscous term  $d^4v/dx^4$ , yields the following velocity profile:

$$v = p^{3/2} e^{-p\bar{x}} \quad (34)$$

while Eqs. (31)–(33) remain the same. Corresponding to the neglect of viscosity, Eq. (34) does not satisfy the boundary condition  $v = 0$  at  $x = 0$ .

It is interesting to mention that Eqs. (31)–(34) are equivalent to the results predicted by Bejan (1983) while solving the boundary layer equations, for the case of a vertical porous layer, using Darcy's model, i.e., for a low-porosity porous medium. In fact, there is an analogy between the bulk resistance exerted by the magnetic drag in a fluid layer and the bulk resistance exerted by the solid matrix in a fluid saturated porous layer.

In the case of porous medium,  $R$  is a Darcy–Rayleigh number defined as

$$R = \frac{g\beta KL^2 q'}{k\alpha\nu} \quad (35)$$

where  $K$  is the permeability of the porous medium.

In the present problem, the retarding effect of the magnetic field is equivalent to that resulting from the presence of a solid matrix in a porous medium having a permeability

$$K = \frac{L'^2}{\text{Ha}^2} = \frac{\mu}{B'\sigma'} \quad (36)$$

Hereafter,  $R = \text{Ra}/\text{Ha}^2$  will be referred to as the magnetic Rayleigh number while the solution to Eq. (15), for  $\text{Ha} \rightarrow \infty$  and in the absence of viscous boundary effects, is the asymptotic solution. It is noted that the effect of the Hartmann number  $\text{Ha}$  in the present problem is similar to that of the Darcy number  $\text{Da} = K/L'^2$  in a porous medium. From Eq. (36) it is seen that both numbers are related by  $\text{Ha} = (\text{Da})^{-1/2}$ .

**2 The Horizontal System Heated From Below.** The particular case of a horizontal system heated from below can be deduced by expanding this solution for small  $\phi$ , or more simply by solving the governing Eqs. (5)–(7) for  $\phi = 0$ . This yields

$$u = \frac{\text{Ra}C}{\text{Ha}^2} \left[ x - \frac{\sinh \text{Ha}x}{2 \sinh \text{Ha}/2} \right] \quad (37)$$

$$\theta = \frac{\text{Ra}C^2}{2\text{Ha}^2} \left[ \frac{x^3}{6} - x \left( \frac{1}{4} - \frac{\coth \text{Ha}/2}{\text{Ha}} \right) - \frac{\sinh \text{Ha}x}{\text{Ha}^2 \sinh \text{Ha}/2} \right] + x \quad (38)$$

$$C = \pm \frac{\text{Ha}^2}{\text{Ra}} \sqrt{\frac{1 - \text{Ra}z_1/\text{Ha}^2}{z_2}} \quad (39)$$

$$\text{Nu} = \frac{1}{1 - \frac{\text{Ra}C^2}{\text{Ha}^2} z_1} \quad (40)$$

where

$$z_1 = \frac{1}{12} - \frac{\coth \text{Ha}/2}{2\text{Ha}} + \frac{1}{\text{Ha}^2} \quad (41)$$

$$z_2 = \frac{-1}{120} + \frac{2}{\text{Ha}^4} + \frac{(\sinh \text{Ha} - \text{Ha})}{8\text{Ha}^3 \sinh^2 \text{Ha}/2} + \frac{\coth \text{Ha}/2}{12a^3} (\text{Ha}^2 - 6) - \frac{\coth^2 \text{Ha}/2}{4\text{Ha}^2} \quad (42)$$

Equation (39) indicates that when the Rayleigh number  $\text{Ra}$  is below a critical value  $\text{Ra}_c$ ,  $C = 0$ , i.e., the fluid is at rest and heat transfer is through conduction alone. However, when  $\text{Ra}$  is above  $\text{Ra}_c$ , there are two convective solutions representing clockwise and counterclockwise circulations. Substituting  $\text{Ra} = \text{Ra}_c$  and  $C = 0$  into Eq. (39) it is found that the critical Rayleigh number for the onset of motion is given by

$$\text{Ra}_c = \frac{\text{Ha}^2}{z_1} \quad (43)$$

This prediction of the critical Rayleigh number is correctly obtained from the present parallel-flow analysis because the convection that occurs under the present thermal boundary conditions is at zero wave number (Sparrow et al., 1964).

(i) *The low Hartmann limit  $\text{Ha} \ll 1$ .* In the low  $\text{Ha}$  limit, a power series expansion of these equations gives

$$u = \frac{\text{Ra}C}{24} (4x^3 - x) \quad (44)$$

$$T = Cy + x \left[ 1 - \frac{\text{Ra}C^2}{120} \left( x^4 - \frac{5}{6} x^2 + \frac{5}{16} \right) \right] \quad (45)$$

$$C = \pm \frac{1}{Ra} \sqrt{504(Ra - 720)} \quad (46)$$

$$Nu = \frac{1}{3/10 + \frac{504}{Ra}} \quad (47)$$

$$Ra_c = 720 \quad (48)$$

which are identical to the equations obtained by Vasseur et al. (1987) in the absence of a magnetic field. The critical Rayleigh number was given by Sparrow et al. (1964).

(ii) *The High Hartmann limit:  $Ha \gg 1$ .* As  $Ha \rightarrow \infty$  an asymptotic analysis of Eqs. (37) to (42) yields

$$u = \frac{RC}{2} \left[ \frac{e^{Ha(x-1/2)}}{2} - x \right]; \quad 0 \leq x \leq 1/2 \quad (49)$$

$$T = Cy + x \left[ 1 + \frac{RC^2}{24} (4x^2 - 3) \right] \quad (50)$$

$$C = \frac{1}{R} \sqrt{10(R - 12)} \quad (51)$$

$$Nu = \frac{1}{1/6 + 10/R} \quad (52)$$

$$R_c = 12 \quad (\text{i.e., } Ra_c = 12Ha^2) \quad (53)$$

The asymptotic solution, obtained by solving Eq. (15) in the absence of the viscous term  $d^4v/dx^4$ , yields

$$u = \frac{RC}{2} x \quad (54)$$

which corresponds to the linear velocity profile predicted by the Darcy model for a porous layer. Also, it is noted that in the case of a horizontal porous layer heated from below by a constant heat flux, a critical Rayleigh number  $R_c = 12$  was predicted by Nield (1968) on the basis of a linear stability theory.

### Numerical Method

The numerical solution of governing Eqs. (1) to (3) is obtained by using a finite-difference procedure—the SIMPLER method (Patankar, 1980). The control volume formulation used in this algorithm ensures continuity of the convective and diffusive fluxes as well as overall momentum and energy conser-

vation. The computer code was validated with the limiting solution obtained by Vasseur et al. (1987) in the absence of the magnetic drag ( $Ha = 0$ ). The comparison was observed to be very good with a maximum deviation with less than 1.5 percent.

The hybrid scheme was used and various tests showed that  $41 \times 61$  grids were generally adequate to describe correctly the flow and heat transfer. However, grids of  $61 \times 81$  were also used at high Ra numbers to obtain the flow details near the boundaries. A staggered grid was used for velocity to avoid wavy pressure and velocity fields. The relaxation parameter was varied from 0.4 for small Ra numbers to 0.05 for large Ra. The number of iterations was between 100 and 500 depending on Ra and Ha numbers. The convergence criterion was based on the corrected pressure field. When the corrected terms were small enough the computation was stopped. The following criterion convergence was used:

$$\sum_{i=1}^{i_{\max}} \sum_{j=1}^{j_{\max}} |r_{ij}| \leq \epsilon \quad (55)$$

where  $r_{ij}$  is the source term in the pressure correction equation and  $\epsilon \leq 0.00001$ .

In the absence of a magnetic field it has been demonstrated by Vasseur et al. (1987) that the parallel flow approximation gives a reasonable prediction for the flow and heat transfer provided that the aspect ratio is made greater than 2. For this reason all the numerical results presented here were obtained for a cavity with  $A = 4$ . Also the Prandtl number was fixed at  $Pr = 0.72$  and the results are expected to be valid for  $Pr \geq 1$  since the problem is weakly dependent on this parameter as long as it is of order one or greater (Gill, 1966; Kimura and Bejan, 1984; Vasseur et al., 1987). Thus, in the limit of a thin layer the problem is only governed by three parameters: Ra (or R), Ha, and  $\phi$ . The effects of these parameters on the flow and temperature fields will now be discussed.

### Results and Discussion

In this section, some representative results are presented to illustrate the effects of the various controlling parameters. Both the cases of vertical ( $\phi = 90^\circ$ ) and horizontal ( $\phi = 0^\circ$ ) cavities will be first presented. Then, the effect of the inclination angle  $\phi$  will be discussed.

Figure 2 illustrates typical streamline and isotherm patterns for a vertical cavity ( $\phi = 90^\circ$ ) for  $Ra = 10^6$  and  $Ha = 0, 20,$  and  $100$ , respectively. Figure 2(a) shows the results obtained with

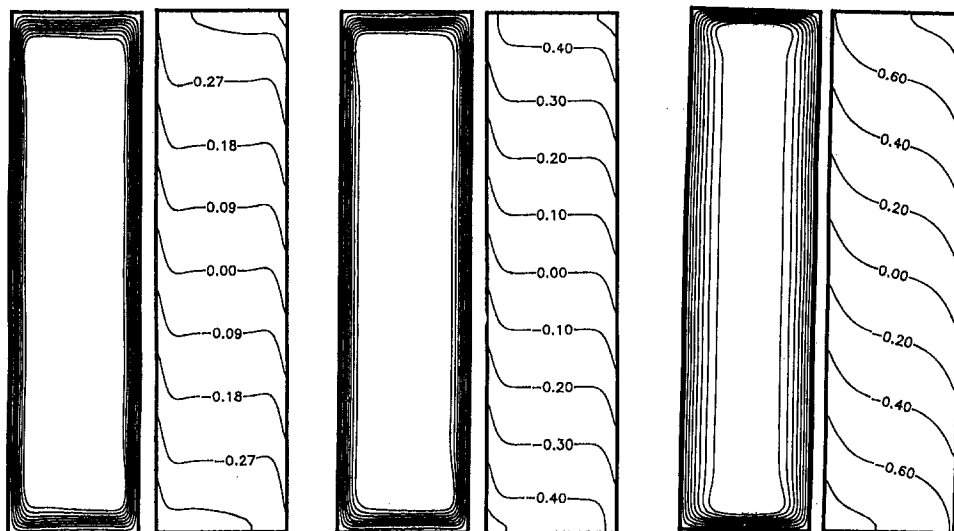


Fig. 2 Numerical solution for the flow and temperature fields for a vertical cavity,  $Ra = 10^6$ : (a)  $Ha = 0$ ,  $\Psi_{\max} = 6.59$ ; (b)  $Ha = 20$ ,  $\Psi_{\max} = 5.34$ ; (c)  $Ha = 100$ ,  $\Psi_{\max} = 2.67$



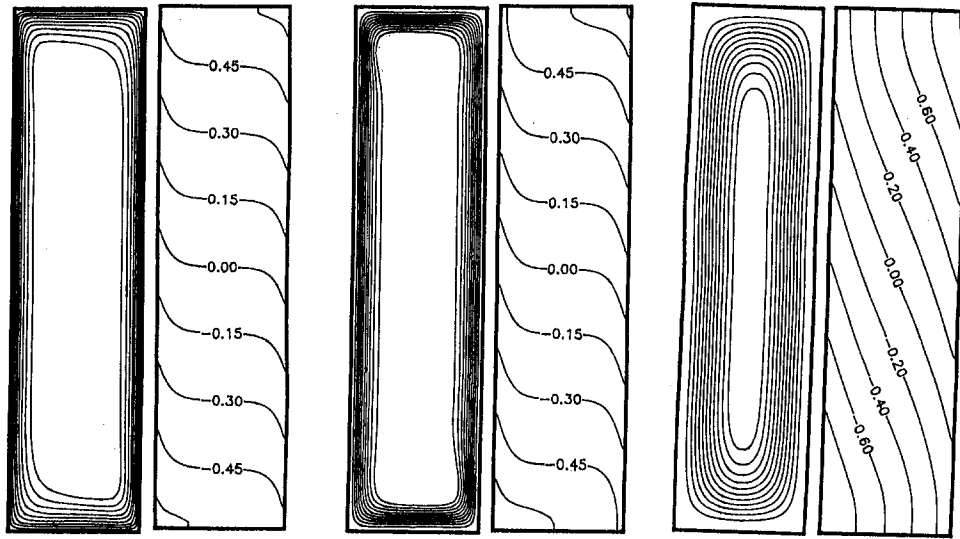


Fig. 3 (a) Numerical solution for the flow and temperature fields for a vertical cavity,  $R = 500$ , (a)  $Ha = \infty$ ,  $\Psi_{\max} = 4.25$ ; (b)  $Ha = 20$ ,  $\Psi_{\max} = 3.84$ ; (c)  $Ha = 1$ ,  $\Psi_{\max} = 0.78$

$Ha = 0$ , i.e., in the absence of a magnetic field. This situation has been studied in the past by Kimura and Bejan (1984) and Vasseur et al. (1987). The resulting flow regime is characterized by a boundary layer of constant thickness and a motionless fluid in the core region of the cavity. Also, the parallelism of the flow and the existence of a linear thermal stratification, as postulated in the analytical solution of the preceding section, are clearly illustrated by the flow and temperature patterns of Fig. 2(a). These features, which differ considerably from those observed in a slot with isothermal walls, result from the constant heat flux boundary conditions considered here. The retarding effects of magnetic drag on the present flow pattern are demonstrated in Fig. 2(b, c) for  $Ha = 20$  and  $100$ , respectively. It is seen that for a given  $Ra$ , as the Hartmann number is increased, the convective circulation within the cavity is more and more inhibited. Thus  $\Psi_{\max} = 6.59$  for  $Ha = 0$ ,  $5.34$  for  $Ha = 20$ , and  $2.67$  for  $Ha = 100$ .

Another way to look at this problem is to vary the Hartmann number  $Ha$  for a fixed value of the magnetic Rayleigh number  $R$ . This is illustrated in Figs. 3(a-c) for  $R = 500$  and  $Ha = \infty$ ,  $100$ ,  $20$ , and  $1$ , respectively. The case with  $Ha = \infty$ , Fig. 3(a), was obtained by solving numerically the governing Eq. (5) in the absence of the viscous terms (i.e.,  $\nabla^4 \Psi = 0$ ). For this asymptotic situation, the only resistance to the flow is due to the retarding effects of the magnetic drag. By analogy with a porous medium, this corresponds to the case of a pure Darcy medium, characterized by a low porosity. In such a medium, the viscous terms, responsible for the boundary effects, are negligible and the only resistance to the flow is due to the presence of the solid matrix. Naturally, for such a model, due to the neglect of the viscous terms, the fluid is "allowed" to slip on a given solid boundary. In general, when the viscous effects are accounted for, this asymptotic limit will be reached, for a given value of  $R$ , provided that  $Ha$  is made large enough. Naturally, as  $Ha$  is decreased, the boundary effects on the flow become more and more important and slow down the fluid in the neighborhood of the walls. This is illustrated in Figs. 3(b, c) where the streamlines are observed to become more and more sparsely spaced near the solid boundaries. As a result, the overall strength of the circulation is considerably reduced with a decrease of  $Ha$ . Thus  $\Psi_{\max} = 4.25$  when  $Ha = \infty$ ,  $\Psi_{\max} = 3.84$  when  $Ha = 20$ , and  $\Psi_{\max} = 0.78$  when  $Ha = 1$ . This follows from the fact that the boundary frictional resistance becomes gradually more important as  $Ha$  decreases and adds to the bulk drag induced by the magnetic field. By anal-

ogy with a porous medium, this situation is similar to the one predicted by the Brinkman-extended Darcy model (with  $Da = Ha^{-2}$ ) for which the no-slip boundary condition is considered (see for instance Vasseur et al., 1987).

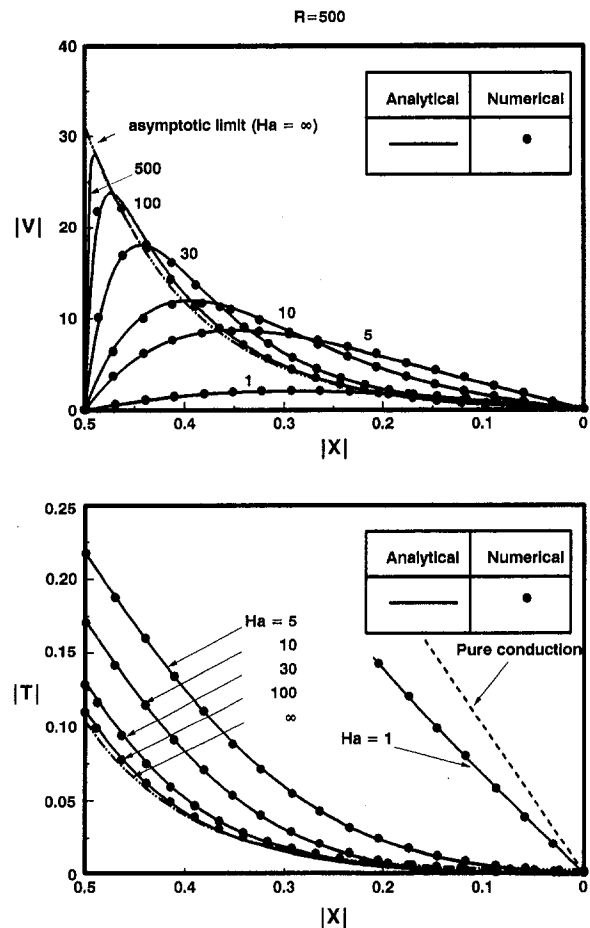


Fig. 4 The velocity and temperature profiles at midheight of a vertical enclosure as a function of the Hartmann number  $Ha$  for  $R = 300$ : (a) velocity; (b) temperature

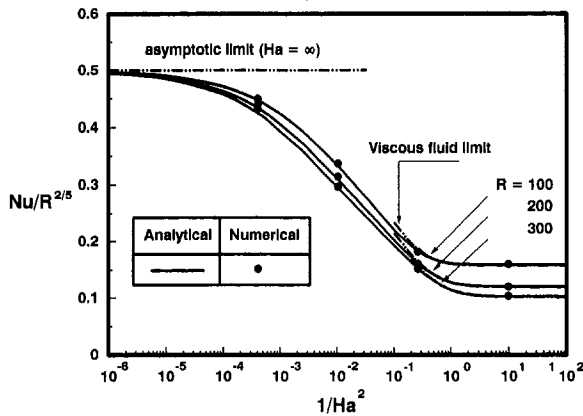


Fig. 5 Effect of the Hartmann number  $Ha$  on the Nusselt number for a vertical cavity for  $R = 100, 200,$  and  $300$

Figures 4(a, b) show the vertical velocity and temperatures profiles at midheight of the cavity for  $R = 300$  and various values of  $Ha$ . The present analytical solution, depicted by solid lines, is seen to agree well with the numerical results. In general, Fig. 4(a) indicates that the velocity increases from zero at the wall to a peak, in a region called viscous sublayer, and then drops back to zero at the center of the cavity ( $x = 0.5$ ). All the curves for the temperature profiles, Fig. 4(b), have a constant slope at  $x = 0$  since a constant heat flux is imposed on the thermally active walls. With the asymptotic solution ( $Ha \rightarrow \infty$ ), the thickness of the viscous sublayer is nil since, due to the neglect of the viscous effects, the peak velocity is located on the wall. The only resistance to the flow is the magnetic drag; the convective motion within the cavity is maximum. Figures 4(a, b) indicate that, for  $Ha \geq 100$  the asymptotic solution is a good approximation for this limit. However, as the value of  $Ha$  is decreased, the boundary frictional resistance becomes gradually more important and adds to the bulk magnetic drag. The position of the maximum velocity shifts away from the wall, resulting in a thicker viscous sublayer, the strength of the flow circulation is reduced, and the temperature of the wall increases significantly. Hence, when  $Ha = 1$ , the convective motion is very weak and the temperature profile is almost that of a pure conduction regime.

In Fig. 5 the Nusselt number is plotted against the Hartmann number for  $R = 100, 200,$  and  $300$ . The Nusselt number is normalized with respect to  $R^{2/5}$ , i.e., half the value predicted by the asymptotic solution ( $Ha \rightarrow \infty$ ), Eq. (32). When  $Ha$  is high enough ( $Ha \geq 10^3$ ), i.e., when the only resistance to the flow is due to magnetic drag, all the curves tend asymptotically toward  $Nu/R^{2/5} = 0.5$ . As the Hartmann number is decreased, the value of the heat transfer drops significantly since the convective flow is progressively inhibited by the combined action of the magnetic drag and the viscous boundary effects. When  $Ha$  is low enough, the only resistance to the flow results from the boundary effects and the pure viscous fluid solution, Eq. (28) is recovered.

The case of a horizontal fluid layer ( $\phi = 0^\circ$ ) heated from below will now be discussed. Plots of  $u^* = u/RC$  are given in Fig. 6 for various values of  $Ha$ . The asymptotic solution for  $Ha \rightarrow \infty$  is the linear velocity profile predicted by Darcy's law in the case of a porous layer with a low porosity (Vasseur et al., 1989). For  $Ha = 100$ , Fig. 6 indicates that a constant velocity prevails everywhere in the cavity except in a thin layer (Hartmann layer) near the wall where the effect of viscosity cannot be neglected. As  $Ha$  decreases the thickness of the Hartmann layer increases progressively, giving rise, for low values of  $Ha$ , to the cubic profiles reported in the literature for a fluid layer in the absence of magnetic force (Bejan and Tien, 1978). The results of Fig. 6 are similar to those obtained by Garandet et al. (1992) for the case of a horizontal fluid cavity, heated isothermally from the sides, with a transverse magnetic field.

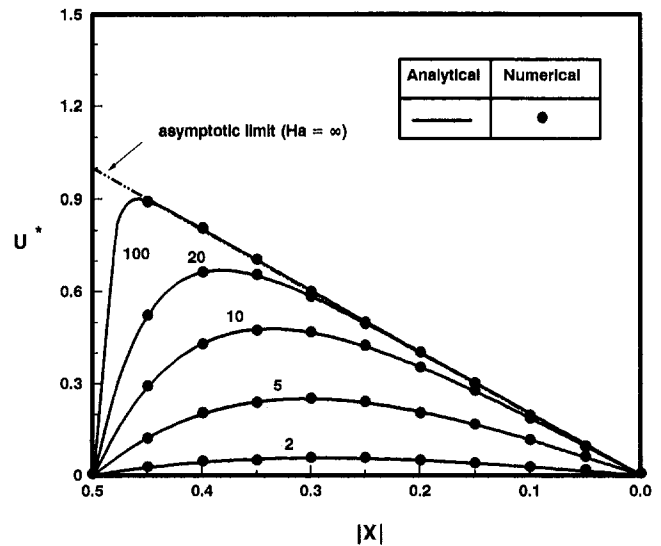


Fig. 6 Normalized velocity profiles in a horizontal cavity as a function of the Hartmann number  $Ha$

The dependence of the Nusselt number  $Nu$  on  $Ra$  and  $Ha$  for a horizontal cavity heated from below is presented in Fig. 7. For this situation it has been demonstrated that the critical Rayleigh number for the onset of convection was given by Eq. (43). Thus, for each Hartmann number considered in Fig. 7  $Nu \rightarrow 1$  (pure conduction solution) as  $Ra \rightarrow Ra_c$ . In the absence of a magnetic field ( $Ha = 0$ )  $Ra_c = 720$  while it is 127496.81 when  $Ha = 100$ . For a given  $Ha$ , after the onset of convection, the heat transfer is seen to increase first sharply with  $Ra$ . However, for large values of  $Ra$  each curve in Fig. 7 is seen to tend asymptotically toward  $Nu = \text{const}$ . This result is a consequence of the particular thermal boundary conditions considered here. For  $Ha = 0$  the asymptotic value  $Nu = 10/3$  was obtained in the past by Vasseur et al. (1989). An increase of  $Ha$  results in an increase of this asymptotic limit.

Figure 8 presents the results for Nusselt number  $Nu$  as a function of the angle of inclination  $\phi$  for  $R = 500$  and various  $Ha$ . The Nusselt number is maximum, independently of the inclina-

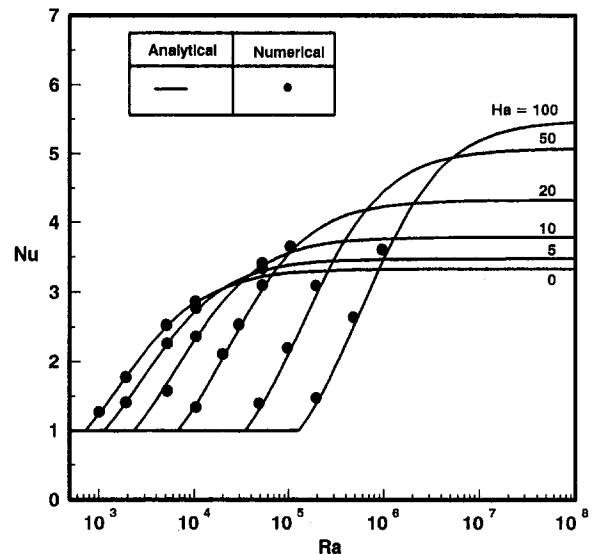


Fig. 7 Nusselt number as a function of the Rayleigh number  $Ra$  for selected values of the Hartmann number  $Ha$  for a horizontal cavity heated from below

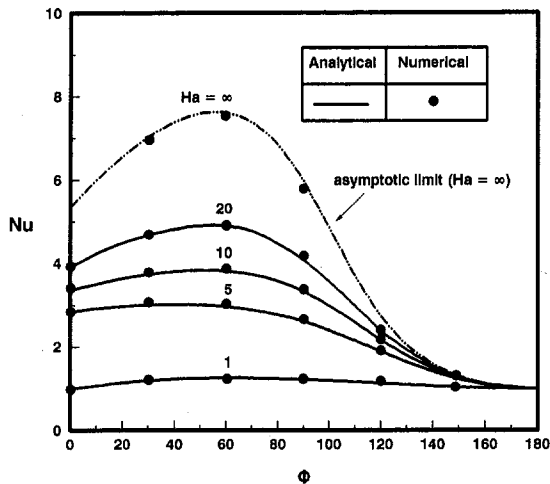


Fig. 8 Effect of inclination angle  $\phi$  and the Hartmann number  $Ha$  on the Nusselt number  $Nu$  for  $R = 500$

tion, for the asymptotic limit. As discussed earlier, for  $Ha \rightarrow \infty$  the only resistance to the flow is due to the magnetic drag and the resulting convective heat transfer is maximum. As the value of  $Ha$  is decreased, the heat transfer is reduced, for a given inclination  $\phi$ , since the viscous effects add to the magnetic drag to slow down the fluid circulation within the cavity. Thus, when  $Ha = 1$  the Nusselt number approaches unity, indicating a pure conduction regime. For a given  $Ha$  it is observed from Fig. 8 that, as  $\phi$  increases from 0 to 180°,  $Nu$  starts to increase with  $\phi$ , passes through a peak, and begins to decrease. A similar trend has been observed in the past for an inclined fluid layer in the absence of magnetic force (Vasseur et al., 1987).

## Conclusions

The purpose of this work was to study the two-dimensional natural convection in an inclined cavity under a uniform transverse magnetic field. An approximate analytical solution was developed, in the limit of a thin layer ( $A \gg 1$ ), that predicts the dependence of the Nusselt number on the Rayleigh and Hartmann numbers and the angle of inclination of the layer. The main conclusions of the present analysis are:

(i) An analogy exists between the flow in a fluid layer, subjected to a transverse magnetic field, and the flow in a fluid-saturated porous layer modeled according to the Brinkman-extended Darcy equations. The retarding forces, exerted by the magnetic drag, play a role similar to the flow resistance due to the presence of the solid matrix in a porous medium. Moreover, the high Hartmann limit ( $Ha \rightarrow \infty$ ), where the viscous boundary effects can be neglected and the only resistance to the flow results from the magnetic drag, is equivalent to the Darcy limit ( $Da \rightarrow 0$ ) in a porous medium with a low porosity, where also the boundary effects are negligible and the only resistance to the flow is exerted by the solid matrix. In both cases, as  $Ha$  decreases (or  $Da$  increases) the boundary frictional resistance becomes gradually more important and adds to the bulk resistance induced by the magnetic drag (or by solid matrix). For sufficiently low values of  $Ha$  (or high values of  $Da$ ) the pure fluid situation is recovered.

(ii) In the case of a vertical enclosure the heat transfer in the boundary layer regime varies with  $R^{2/5}$  in the high Hartmann limit. This result is in agreement with the finding of Kimura and Bejan (1984). In the low Hartmann limit it varies with  $R^{2/9}$  as predicted by Bejan (1983) for a fluid layer in the absence of a magnetic field.

This perfect analogy with the Brinkman porous layer is in fact restricted to parallel flow, that is, to flow with only one

velocity component, this latter being at nonzero angle with the magnetic field. As a matter of fact, the magnetic resistance occurs only in a direction perpendicular to the magnetic field so that an "infinite permeability" exists for the velocity component parallel to the magnetic field. The  $u'$  velocity component of Fig. 1 is parallel to the magnetic field and differs from zero only in the end region (termed control volume in that figure). As observed numerically, the shear layers near the short end walls of the cavity are sometimes characterized by relatively high velocities (see for instance Fig. 2c). Finally one must also bear in mind that Brinkman flows are inertia-free whereas some inertia effects are present for general non-parallel fluid flows with curved streamlines.

(iii) The effect of the magnetic drag on the critical Rayleigh number for the onset of motion in a horizontal layer heated from below is predicted by the present theory. Here again the actual results follow the trend obtained in the past for a porous layer modeled according to the Brinkman-extended Darcy equations.

The main features of the approximate analytical solution have been tested by a numerical solution of the full governing equations in the range  $0 \leq R \leq 500$ ,  $1 \leq Ha \leq 500$ , and  $0 \leq \phi \leq 180$  deg. A good agreement was found between the parallel flow approximation and the numerical simulation.

## Acknowledgments

This work was supported in part by the National Sciences and Engineering Research Council of Canada and jointly by the FCAR Government of Quebec.

## References

- Bejan, A., and Tien, C. L., 1978, "Natural Convection in a Horizontal Porous Medium Subjected to an End-to-End Temperature Difference," *ASME JOURNAL OF HEAT TRANSFER*, Vol. 100, pp. 191–198.
- Bejan, A., 1983, "The Boundary Layer Regime in a Porous Layer With Uniform Heat Flux From the Side," *Int. J. Heat Mass Transfer*, Vol. 26, pp. 1339–1346.
- Cormack, D. E., Leal, L. G., and Imberger, J., 1974, "Natural Convection in a Shallow Cavity With Differentially Heated End Walls, Part I, Asymptotic Theory," *J. Fluid Mechanics*, Vol. 65, pp. 209–230.
- Garandet, J. P., Alboussiere, T., and Moreau, R., 1992, "Buoyancy Driven Convection in a Rectangular Enclosure With a Transverse Magnetic Field," *Int. J. Heat Mass Transfer*, Vol. 35, pp. 741–748.
- Gill, A. E., 1966, "The Boundary-Layer Regime for Convection in a Rectangular Cavity," *J. Fluid Mechanics*, Vol. 26, pp. 515–536.
- Hunt, R., and Wilks, G., 1981, "Low Prandtl Number Magnetohydrodynamic Natural Convection in a Strong Cross Field," *Numerical Heat Transfer*, Vol. 4, pp. 303–316.
- Kimura, S., and Bejan, A., 1984, "The Boundary Layer Natural Convection Regime in a Rectangular Cavity With Uniform Heat Flux From the Side," *ASME JOURNAL OF HEAT TRANSFER*, Vol. 106, pp. 98–103.
- Kuiken, H. K., 1970, "Magnetohydrodynamic Free Convection in a Strong Cross Field," *J. Fluid Mechanics*, Vol. 40, pp. 21–38.
- Nield, D. A., 1968, "Onset of Thermolaline Convection in a Porous Medium," *Water Resources Research*, Vol. 4, pp. 535–560.
- Ozoe, H., and Maruo, E., 1987, "Magnetic and Gravitational Natural Convection of Melted Silicon—Two-Dimensional Numerical Computations in the Rate of Heat Transfer," *JSM International Journal*, Vol. 30, pp. 774–784.
- Ozoe, H., and Okada, K., 1989, "The Effect of the Direction of the External Magnetic Field on the Three-Dimensional Natural Convection in a Cubical Enclosure," *Int. J. Heat Mass Transfer*, Vol. 32, pp. 1939–1954.
- Patankar, S. V., 1980, *Numerical Heat Transfer and Fluid Flow*, Hemisphere, Washington, DC.
- Patterson, J., and Imberger, J., 1980, "Unsteady Natural Convection in a Rectangular Cavity," *J. Fluid Mechanics*, Vol. 100, pp. 65–86.
- Sen, M., Vasseur, P., and Robillard, L., 1987, "Multiple Steady States for Unicellular Natural Convection in an Inclined Porous Layer," *Int. J. Heat Mass Transfer*, Vol. 30, pp. 2097–2113.
- Sen, M., Vasseur, P., and Robillard, L., 1988, "Parallel Flow Convection in a Tilted Two-Dimensional Porous Layer Heated From All Sides," *Phys. Fluids*, Vol. 31, pp. 3480–3487.
- Singh, K., and Cowling, T. G., 1963, "Thermal Convection in Magnetohydrodynamics," *Quart. J. Mech. Applied Math.*, Vol. XVI, pp. 17–31.
- Sparrow, E. M., Goldstein, R. J., and Jonsson, U. K., 1964, "Thermal Instability in a Horizontal Fluid Layer: Effect of Boundary Conditions and Nonlinear Temperature Fields," *J. Fluid Mechanics*, Vol. 18, pp. 513–528.
- Tabelling, P., 1982, "Convective Flow Patterns in Rectangular Boxes of Finite Extent Under an External Magnetic Field," *J. Physique*, Vol. 43, pp. 1295–1303.
- Vasseur, P., Robillard, L., and Sen, M., 1987, "Unicellular Convective Motion in an Inclined Fluid Layer With Uniform Heat Flux," *Bifurcation Phenomena in Thermal Processes and Convection*, ASME HTD-Vol. 94, pp. 23–29.

Vasseur, P., Wang, C. H., and Sen, M., 1989, "The Brinkman Model for Natural Convection in a Shallow Porous Cavity With Uniform Heat Flux," *Numerical Heat Transfer*, Vol. 15, pp. 221–242.

Venkatachalappa, M., and Subbaraya, C. K., 1993, "Natural Convection in a Rectangular Enclosure in the Presence of a Magnetic Field With Uniform Heat Flux From the Side Walls," *Acta Mechanica*, Vol. 96, pp. 13–26.

Weiss, N. O., 1981, "Convection in an Imposed Magnetic Fluid. Part 1. The Development of Nonlinear Convection," *J. Fluid Mechanics*, Vol. 108, pp. 247–272.

Wilks, G., 1976, "Magnetohydrodynamic Free Convection About a Semi-infinite Vertical Plate in a Strong Cross Field," *J. Appl. Math. Phys.*, Vol. 27, pp. 621–631.

---

J. Sarr

C. Mbow

Laboratoire de Thermodynamique et  
Energétique,  
Université de Perpignan,  
52 Ave. de Villeneuve,  
66860 Perpignan, France

H. Chehouani

Laboratoire de Physique Appliquée,  
Université de Perpignan,  
52 Ave. de Villeneuve,  
66860 Perpignan, France

B. Zeghmati

I. U. T.,  
Rue Engel Gros, B. P. 527,  
90 016 Belfort Cedex, France

S. Benet

Laboratoire de Physique Appliquée,  
Université de Perpignan,  
52 Ave. de Villeneuve,  
66860 Perpignan, France

M. Daguene

Laboratoire de Thermodynamique et  
Energétique,  
Université de Perpignan,  
52 Ave. de Villeneuve,  
66860 Perpignan, France

# Study of Natural Convection in an Enclosure Bounded by Two Concentric Cylinders and Two Diametric Planes

*The two-dimensional heat transfer induced by free laminar convection in an enclosure is numerically investigated in this work. A constant wall heat flux is applied on the inner cylinder while the outer is maintained at a uniform temperature, the others walls being adiabatic. The influence of the modified Grashof number ( $10^2 \leq Gr \leq 10^6$ ) and an aspect  $F_r$  on convective motion and heat transfer is examined. A comparison of the heat transfer between different fluids such as air, ammonia-liquid, and carbon dioxide-liquid is also displayed. Holographic interferometry is used to visualize the temperature field within the enclosure and to confirm the two-dimensional behavior of the convective flow. The results show that maximum heat transfer is found for  $F_r = 1$ , when the Grashof number is up to  $10^3$ , and the conduction regime is reached for a modified Grashof number less than  $10^3$ . On the other hand, the average Nusselt number increases with the Prandtl number,  $F_r = 1$ .*

## I Introduction

The study of convective heat transfer in cavities is of considerable interest, in connection with a great variety of problems in industrial engineering. The annular enclosure is of particular significance because of its applications as thermal exchanger for energy conversion. Examples of possible applications include the study of the heat waste of hot fluid in industrial heating and sterilization processes.

Many mathematical correlations suitable for engineering prediction of heat transfer rates are available for the case of transient or steady-state regimes in rectangular shapes (Wilkes and Churchill, 1966; Samuels and Churchill, 1967; Torrance, 1968; Kublbeck et al., 1980; Chadwick et al., 1991) or enclosures bounded by two concentric cylinders (Mack and Bishop, 1986; Kuehn and Goldstein, 1976a, 1976b; Rao et al., 1985; Tsui and Tremblay, 1984; Ranganathan, 1988; Castrejon and Spalding, 1988). Most of the investigations so far are for the plain annuli or for annuli with radial spacers (Shilston and Probert, 1978; Kwon et al., 1982). In these works, the authors studied generally the influence of the Grashof number and the ratio of radii. A few investigations are on partial sector-shaped enclosures. Al-Ani

and Nansteel (1993) studied experimentally a fluid-filled partial circular sector where the radial surfaces were heated and cooled isothermally, while the remaining circumferential surfaces were insulated.

In the present study, the investigations are on an identical partial sector, which is symmetric with respect to the vertical axis and is subjected to different boundary conditions (Fig. 1). The purpose of the present paper is to report an investigation of transient laminar natural convection in this enclosure and to study, more particularly, the influence of the angle between the two insulated diametric planes.

A conformal transformation (Lavrentiev and Chabat, 1972) is used to reduce the curvilinear enclosure into a rectangular field, in order to facilitate writing the expression for the boundary conditions. The governing equations are formulated in terms of vorticity and stream function and are solved with the aid of the ADI method (Wilkes and Churchill, 1966; Samuels and Churchill, 1967; Torrance, 1968; Kublbeck et al., 1980; Peaceman and Rachford, 1955; Vafai and Javad, 1991; Carnahan et al., 1969; Nogotov, 1978; Roache, 1982).

## II Problem Statement and Governing Equations

Viscous dissipation, thermal radiation, and compressibility effects are neglected. The fluid properties are constants, except the density in the motion equation, the variation of which is treated by using the Boussinesq approximation. We assume that the

Contributed by the Heat Transfer Division for publication in the JOURNAL OF HEAT TRANSFER. Manuscript received by the Heat Transfer Division December 1992; revision received February 1994. Keywords: Enclosure Flows, Natural Convection, Numerical Methods. Associate Technical Editor: Y. Jaluria.

problem is laminar and two dimensional and the study is performed in a plane orthogonal to the cylindrical axis.

An adapted conformal mapping is used to transform the curvilinear enclosure into a rectangular domain. Considering the following expressions:

$$f(z) = \log\left(\frac{z}{a}\right) = \phi(x, y) + i\psi(x, y),$$

with  $z = x + iy$  and  $i^2 = -1$ , (1)

the governing equations can be formulated with respect to  $(\phi, \psi)$  coordinates.

Since the present study is concerned essentially with the effects of heat flux on the convective flow, it is convenient to introduce the following set of dimensionless variables:

$$\tilde{\omega} = \frac{b^2 \text{Gr}^{-1/2}}{\nu} \omega, \quad \tilde{\Omega} = \frac{\Omega}{\nu}, \quad \tilde{t} = \frac{\nu \text{Gr}^{1/2}}{b^2} t$$

$$\tilde{U} = \frac{b \text{Gr}^{-1/4}}{\nu} U, \quad \tilde{V} = \frac{b \text{Gr}^{-1/4}}{\nu} V,$$

$$\tilde{T} = \frac{g\beta b^3 \text{Gr}^{-3/4}}{\nu^2} (T - T_2) \quad (2)$$

where  $U, V$ , and  $T$ , respectively, denote the velocity components and the temperature of the fluid.  $T_2$  is the temperature of the outer cylinder;  $\text{Gr}$  is the modified Grashof number;  $\omega$  and  $\Omega$  are, respectively, the vorticity and the stream function;  $b$  is the characteristic length of the problem.

The use of the vorticity and stream function allows us to write the differential system of equations as:

$$\tilde{\omega} = -\frac{1}{e^{2\phi}} \left( \frac{\partial^2 \tilde{\Omega}}{\partial \phi^2} + \frac{\partial^2 \tilde{\Omega}}{\partial \psi^2} \right) \quad (3)$$

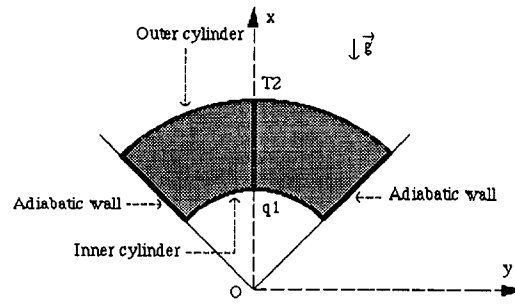


Fig. 1 Enclosure geometry

$$\frac{\partial F}{\partial \tilde{t}} + \frac{1}{e^\phi} \left( \tilde{U} \frac{\partial F}{\partial \phi} + \tilde{V} \frac{\partial F}{\partial \psi} \right)$$

$$= \frac{G}{e^\phi} \left( \frac{\partial \tilde{T}}{\partial \phi} \cos \psi - \frac{\partial \tilde{T}}{\partial \psi} \sin \psi \right) + \frac{1}{\text{Pe}^{2\phi}} \left( \frac{\partial^2 F}{\partial \phi^2} + \frac{\partial^2 F}{\partial \psi^2} \right) \quad (4)$$

with:

$$\tilde{U} = \frac{1}{e^\phi} \frac{\partial \tilde{\Omega}}{\partial \psi} \quad \text{and} \quad \tilde{V} = -\frac{1}{e^\phi} \frac{\partial \tilde{\Omega}}{\partial \phi} \quad (5)$$

$F = \tilde{\omega}, G = 1$ , and  $P = 1$  for motion equation;  $F = \tilde{T}, G = 0$ , and  $P = \text{Pr}$  for energy equation.

The preceding set of dimensionless equations is subjected to the following initial and boundary conditions,  $\phi$  and  $\psi$  being the dimensionless coordinates, respectively, in the vertical and horizontal transformed field:

$$\tilde{t} = 0, \quad \text{for } \phi_1 \leq \phi \leq \phi_N, \psi_1 \leq \psi \leq \psi_M: \tilde{\omega}(\phi, \psi, 0) = 0,$$

$$\tilde{\Omega}(\phi, \psi, 0) = 0, \quad \tilde{T}(\phi, \psi, 0) = \frac{g\beta b^3 \text{Gr}^{-3/4}}{\nu^2} (T_0 - T_2) \quad (6)$$

## Nomenclature

$a$  = parameter in conformal transformation (1), m  
 $b$  = characteristic length =  $a \text{Gr}^{1/4}$ , m  
 $D_h$  = hydraulic diameter, m  
 $F$  = symbolic function for vorticity or temperature  
 $F_r$  = aspect ratio defined in the transformed field (Eq. (17))  
 $g$  = acceleration due to gravity,  $\text{m s}^{-2}$   
 $G$  = symbolic parameter in parabolic Eq. (4)  
 $\text{Gr}$  = modified Grashof number =  $g\beta b^4 q_1 / (\nu^2 \lambda)$   
 $m$  = integer  
 $n$  = time increment  
 $\text{Nu}$  = Nusselt number (Eq. (8))  
 $p$  = iteration number  
 $P$  = symbolic parameter in parabolic Eq. (4)  
 $\text{Pr}$  = Prandtl number =  $\nu/\alpha$   
 $q^*$  = heat flux, W  
 $q_1$  = heat flux density imposed on inner cylindrical wall,  $\text{W m}^{-2}$   
 $R$  = radius of cylinder, m  
 $\text{Re}_h$  = horizontal cell Reynolds number =  $|\tilde{U}|P \exp(\phi_k) \Delta\phi$   
 $\text{Re}_v$  = vertical cell Reynolds number =  $|\tilde{V}|P \exp(\phi_k) \Delta\psi$

$T$  = temperature, K  
 $T_0$  = initial temperature, K  
 $T_2$  = temperature of outer cylindrical wall, K  
 $t$  = time, s  
 $u, v$  = velocity components in Cartesian system,  $\text{m s}^{-1}$   
 $U$  = horizontal velocity component in the transformed field =  $(1/ae^\phi)(-y(\partial/\partial x) + x(\partial/\partial y))\Omega$   
 $V$  = vertical velocity component in the transformed field =  $-(1/ae^\phi)(x(\partial/\partial x) + y(\partial/\partial y))\Omega$   
 $x, y$  = coordinates in Cartesian system, m  
 $z$  = complex variable  
 $\alpha$  = thermal diffusivity,  $\text{m}^2 \text{s}^{-1}$   
 $\beta$  = coefficient of thermal expansion,  $\text{K}^{-1}$   
 $\delta_k^k$  = Kronecker symbol  
 $\Delta t$  = time increment, s  
 $\Delta\phi, \Delta\psi$  = grid spacings in  $f$  and  $y$  directions, respectively  
 $\gamma$  = relaxation factor in S.O.R. algorithm (Eq. (10))  
 $\nu$  = kinematic viscosity,  $\text{m}^2 \text{s}^{-1}$

$\phi$  = dimensionless coordinate in vertical transformed field  
 $\psi$  = dimensionless coordinate in horizontal transformed field  
 $\Omega$  = stream function, such that  $u = \partial\Omega/\partial y$  and  $v = -\partial\Omega/\partial x$ ,  $\text{m}^2 \text{s}^{-1}$   
 $\omega$  = vorticity =  $(\partial v/\partial x - \partial u/\partial y)$ ,  $\text{s}^{-1}$

### Subscripts/Superscripts

0 = value at initial time  
1 = value on inner cylinder or on right adiabatic wall  
cond = due to pure conduction  
dim = dimension value  
 $j, k$  = space subscripts of grid points in  $y$  and  $f$  directions, respectively  
 $M$  = value on left adiabatic wall  
max = maximum value  
 $n, N$  = time superscript and value on outer cylinder, respectively  
opt = optimum

### Signs

$\bar{X}$  = average value  
 $\tilde{X}$  = dimensionless value (Eq. (2))

where  $T_0$  is the initial temperature of the system.

$\tilde{t} > 0$ :

$$\begin{aligned} \tilde{U}(\phi, \psi, \tilde{t}) = \tilde{V}(\phi, \psi, \tilde{t}) = 0, \quad \tilde{\Omega}(\phi, \psi, \tilde{t}) = \text{const for} \\ \phi = \phi_1, \quad \phi = \phi_N, \quad \psi = \psi_1, \quad \psi = \psi_M \\ \tilde{\omega}(\phi, \psi, \tilde{t}) = -\frac{1}{\exp(2\phi)} \left( \frac{\partial^2 \tilde{\Omega}(\phi, \psi, \tilde{t})}{\partial \phi^2} + \frac{\partial^2 \tilde{\Omega}(\phi, \psi, \tilde{t})}{\partial \psi^2} \right) \\ \text{for } \phi = \phi_1, \quad \phi = \phi_N, \quad \psi = \psi_1, \quad \psi = \psi_M \\ \frac{\partial \tilde{T}(\phi_1, \psi, \tilde{t})}{\partial \phi} = -\exp(\phi_1), \quad \tilde{T}(\phi_N, \psi, \tilde{t}) = \tilde{T}_2 = 0, \\ \frac{\partial \tilde{T}(\phi, \psi_1, \tilde{t})}{\partial \psi} = \frac{\partial \tilde{T}(\phi, \psi_M, \tilde{t})}{\partial \psi} = 0 \end{aligned} \quad (7)$$

The Nusselt number on the active walls may be expressed in terms of dimensionless variables as

$$\begin{aligned} \text{Nu}(\phi_k, \psi) = \frac{q^*}{q_{\text{cond}}^*} = \frac{(-1)^{k+N}(\phi_N - \phi_1)}{\Delta \tilde{T}(\phi_k, \psi)} \frac{\partial \tilde{T}(\phi_k, \psi)}{\partial \phi} \\ \text{and } \bar{\text{Nu}}(\phi_k) = \frac{1}{(\psi_M - \psi_1)} \int_{\psi_1}^{\psi_M} \text{Nu}(\phi_k, \psi) d\psi \end{aligned} \quad (8)$$

with:

$$\begin{aligned} \Delta \tilde{T}(\phi_k, \psi) = (\tilde{T}(\phi_N, \psi) - \tilde{T}(\phi_1, \psi)) \delta_k^1 \\ + (\tilde{T}(\phi_1, \psi) - \tilde{T}(\phi_N, \psi)) \delta_k^N \\ \delta_k^k = 1, \quad \delta_{k'+k}^k = 0 \quad \text{and } k, k' = \{1, N\} \end{aligned}$$

### III Numerical Analysis

A rectangular network of  $N$  nodes along the  $\phi$  axis and  $M$  nodes along the  $\psi$  axis is used to establish grid points, with  $\Delta\phi$  and  $\Delta\psi$  as grid spacings:

$$\phi_k = \phi_1 + (k-1)\Delta\phi \quad \text{and} \quad \psi_j = \psi_1 + (j-1)\Delta\psi \quad (9)$$

The time is expressed by:  $\tilde{t}^n = n\Delta\tilde{t}$ .

In order to solve the elliptic stream function Eq. (3), the method of successive over-relaxation (Bejan, 1984) is used:

$$\begin{aligned} \tilde{\Omega}_{k,j}^{p+1} = \tilde{\Omega}_{k,j}^p + \frac{\gamma}{2 \left[ 1 + \left( \frac{\Delta\phi}{\Delta\psi} \right)^2 \right]} \left\{ \tilde{\Omega}_{k+1,j}^p + \tilde{\Omega}_{k-1,j}^{p+1} \right. \\ + \left( \frac{\Delta\phi}{\Delta\psi} \right)^2 \tilde{\Omega}_{k,j+1}^p + \left( \frac{\Delta\phi}{\Delta\psi} \right)^2 \tilde{\Omega}_{k,j-1}^{p+1} \\ \left. - 2 \left[ 1 + \left( \frac{\Delta\phi}{\Delta\psi} \right)^2 \right] \tilde{\Omega}_{k,j}^p + (\Delta\phi)^2 \tilde{\omega}_{k,j} \exp(2\phi_k) \right\} \end{aligned} \quad (10)$$

with  $p$  = iteration number,  $\gamma$  = relaxation factor.

The velocity components (5) are calculated with a central finite-difference approximation of the stream function (David and David, 1977). The finite-difference approximations to parabolic Eq. (4), to be used consecutively over two half time steps, each of duration  $\Delta\tilde{t}/2$ , according to the ADI method, are:

$$\begin{aligned} \frac{F_{k,j}^{n+1/2} - F_{k,j}^n}{\Delta\tilde{t}/2} + \frac{1}{\exp(\phi_k)} \\ \times \left( \tilde{U}_{k,j}^n \frac{F_{k+1,j}^{n+1/2} - F_{k-1,j}^{n+1/2}}{2\Delta\phi} + \tilde{V}_{k,j}^n \frac{F_{k,j+1}^n - F_{k,j-1}^n}{2\Delta\psi} \right) \\ = \frac{G}{\exp(\phi_k)} \left( \cos \psi_j \frac{\tilde{T}_{k+1,j}^{n+1/2} - \tilde{T}_{k-1,j}^{n+1/2}}{2\Delta\phi} - \sin \psi_j \frac{\tilde{T}_{k,j+1}^n - \tilde{T}_{k,j-1}^n}{2\Delta\psi} \right) \\ + \frac{1}{P \exp(2\phi_k)} \left( \frac{F_{k+1,j}^{n+1/2} - 2F_{k,j}^{n+1/2} + F_{k-1,j}^{n+1/2}}{(\Delta\phi)^2} \right. \\ \left. + \frac{F_{k,j+1}^n - 2F_{k,j}^n + F_{k,j-1}^n}{(\Delta\psi)^2} \right) \end{aligned} \quad (11)$$

and

$$\begin{aligned} \frac{F_{k,j}^{n+1} - F_{k,j}^{n+1/2}}{\Delta\tilde{t}/2} + \frac{1}{\exp(\phi_k)} \\ \times \left( \tilde{U}_{k,j}^n \frac{F_{k+1,j}^{n+1/2} - F_{k-1,j}^{n+1/2}}{2\Delta\phi} + \tilde{V}_{k,j}^n \frac{F_{k,j+1}^n - F_{k,j-1}^n}{2\Delta\psi} \right) \\ = \frac{G}{\exp(\phi_k)} \left( \cos \psi_j \frac{\tilde{T}_{k+1,j}^{n+1/2} - \tilde{T}_{k-1,j}^{n+1/2}}{2\Delta\phi} - \sin \psi_j \frac{\tilde{T}_{k,j+1}^n - \tilde{T}_{k,j-1}^n}{2\Delta\psi} \right) \\ + \frac{1}{P \exp(2\phi_k)} \left( \frac{F_{k+1,j}^{n+1/2} - 2F_{k,j}^{n+1/2} + F_{k-1,j}^{n+1/2}}{(\Delta\phi)^2} \right. \\ \left. + \frac{F_{k,j+1}^n - 2F_{k,j}^n + F_{k,j-1}^n}{(\Delta\psi)^2} \right) \end{aligned} \quad (12)$$

Equations (11) and (12) are implicit in the  $\phi$  and  $\psi$  directions, respectively, and yield tri-diagonal systems, which are solved with the aid of the Thomas algorithm (Gourdin and Boumahrat, 1983), when they are applied to every point.

In the classical ADI method, the gradients of temperature in the vorticity equation and the velocity components  $\tilde{U}$  and  $\tilde{V}$  are treated as constants, at any grid point, over a time step (Wilkes and Churchill, 1966; Samuels and Churchill, 1967; Torrance and Churchill, 1968). To obtain transient results, an iterative process is worked out with the previous variables, at every time step  $\Delta\tilde{t}$ .

In order to factorize the systems of equations, it is necessary to work with diagonal matrices, so that two restrictions on the time step  $\Delta\tilde{t}$  are assumed:

$$\Delta\tilde{t} < \frac{2P \exp(2\phi_k)(\Delta\phi)^2}{\text{Re}_u - 2} \quad \text{if } \text{Re}_u > 2 \quad (13)$$

$$\Delta\tilde{t} < \frac{2P \exp(2\phi_k)(\Delta\psi)^2}{\text{Re}_v - 2} \quad \text{if } \text{Re}_v > 2 \quad (14)$$

where  $\text{Re}_u$  and  $\text{Re}_v$  are respectively the horizontal and the vertical cell Reynolds numbers.

Wall values of stream function, heat flux, temperature, and Nusselt number are obtained by using a three-point discretization. For the stream function, Taylor series expansions are used to calculate the vorticity at the walls. The mean temperature of the fluid is determined by means of Simpson's rule (Holman, 1985).

It has been observed that steady state occurs when the following convergence criterion is satisfied for both temperature and vorticity:

$$\frac{\text{MAX } |F_{k,j}^{n+1} - F_{k,j}^n|}{\text{MAX } |F_{k,j}^{n+1}|} < 0.5 \times 10^{-5} \quad (15)$$

where MAX defines the maximum value of the function and  $n$  is the time increment.

In order to solve the elliptic equation, a similar criterion is applied about the stream function:

$$\frac{\text{MAX } |\tilde{\Omega}_{k,j}^{p+1} - \tilde{\Omega}_{k,j}^p|}{\text{MAX } |\tilde{\Omega}_{k,j}^{p+1}|} < 10^{-4},$$

where  $p$  is the iteration number. (16)

The whole procedure for solving governing Eqs. (3), (4), and (5) is performed in terms of a second-order accuracy.

An aspect ratio allowing regular rectangular domains in the transformed field is defined by the following expression:

$$F_r = \frac{\log(R_N/R_1)}{\psi_M - \psi_1} \quad (17)$$

where  $R_N$  and  $R_1$  are, respectively, the radii of the outer and inner cylinders.

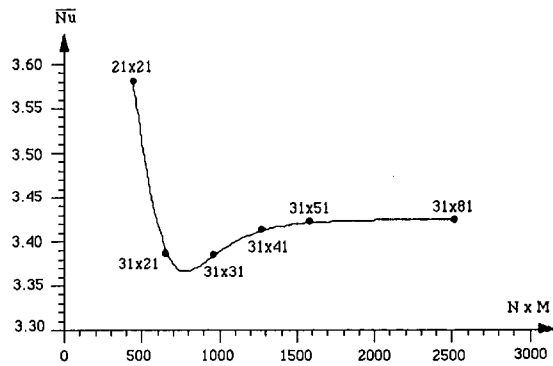


Fig. 2 Variations of mean Nusselt number versus grid system for  $F_r = 1/5$  and  $Gr = 10^6$

#### IV Numerical Results and Discussions

In order to observe the symmetric behavior of the fluid, numerical simulations were performed on configurations that are symmetric with respect to the vertical axis, for aspect ratios varying from 0.2 to 1 and for  $10^2 \leq Gr \leq 10^6$ .

**Computational Details.** Various combinations of regular mesh sizes were used to select one that produces grid-independent results. Initially, the number of grids in the angular direction was set to a constant value to examine the grid dependency of the results for the number of grids in the radial direction. The number of grids was varied from 21 to 31, 41 and 51 in the radial direction, and from 21 to 31, 41, 51 and 81 in the angular direction.

The calculation performed on a  $31 \times 51$  relative to  $41 \times 41$  grid system resulted in a 3.60 percent change in the mean Nusselt number  $\bar{Nu}$ , for  $F_r = 1/2$  and  $Gr = 10^6$ , 4.12 percent for  $F_r = 1/3$  and  $Gr = 10^6$ , and 3.42% for  $F_r = 1/5$  and  $Gr = 10^6$ . For  $Gr = 10^6$ , the calculation performed on a  $31 \times 51$  grid relative to a  $51 \times 51$  grid system yielded a 5.51 percent change in the mean Nusselt number, for  $F_r = 1/3$  and 5.01 percent for  $F_r = 1/5$ .

The results reported in the paper were mainly obtained with the grids ranging from  $21 \times 21$  to  $31 \times 51$ , depending on the aspect ratio and the Grashof number, which were considered to represent a reasonable compromise between accuracy and computing cost. For instance, as shown in Fig. 2, for  $F_r = 1/5$  and  $Gr = 10^6$ , the difference in the mean Nusselt number is less than 1 percent between using the  $31 \times 51$  and  $31 \times 81$  grids.

The numerical computations have been carried out on a VAX/VMS 4200. The CPU time required generally depends on the problem. For example, for a Grashof number of  $10^6$  and  $F_r = 1/5$ , 1 h 37 min of CPU time was required to reach convergent and steady-state solution, with the basic grid of  $31 \times 51$ . The time and the storage required were respectively about 6.3 s per time step and 131 Ko. By iterating several times over each time step, to get accurate transient results, 4 h 17 min of CPU time was required.

It was determined that a time increment less than  $\tilde{t} = 0.1$  had to be used in order to obtain a time step-independent solution.

**Comparison With Previous Results.** Our numerical scheme was applied on a horizontal annulus, where the inner cylinder was heated by the application of a constant heat flux and the outer cylinder was isothermally cooled (Ranganathan, 1988), in order to compare our results with those of the literature (fluid = air and  $b = R_N - R_1$ ). The algorithm was also applied on a horizontal annulus with isothermal walls. We discovered excellent agreement with Ranganathan (1988), Tsui and Tremblay (1984), and Rao et al. (1985) as shown in Table 1. Thus, the relative difference between calculated mean Nusselt numbers was less than 3.5 percent for all cases presented.

Table 1 Comparison of mean Nusselt number with previous results: (a) Tsui and Tremblay (1984); (b) Rao et al. (1985); (c) Ranganathan (1988)

$R_N/R_1$	Gr	NxM	Nu (a)	Present num.	% diff.
1.2	$0.732 \times 10^3$	21x21	1.00	1.000	+ 0.00
1.5	$0.262 \times 10^5$	31x51	1.88	1.911	+ 1.65
2.0	$0.100 \times 10^6$	31x51	1.64	1.674	+ 2.07
2.0	$0.880 \times 10^6$	31x51	3.08	3.077	- 0.10
-----	Ra	-----	----- (b)	-----	-----
2.0	$0.500 \times 10^6$	31x51	5.776	5.869	+ 1.61
-----	-----	-----	----- (c)	-----	-----
1.2	$0.100 \times 10^6$	31x51	2.499	2.466	- 1.32
1.33	$0.100 \times 10^6$	31x51	2.744	2.835	+ 3.32
1.5	$0.100 \times 10^6$	31x51	3.092	3.182	+ 2.91

**Summary of Principal Runs.** Air was used for these applications (physical properties in Bejan, 1984) and the other data are:

- radius of the inner cylinder:  $R_1 = 0.10$  m
- temperature of the outer cylinder:  $T_2 = 293$  K

Calculations were performed for 16 combinations of the aspect ratio  $F_r$ , the modified Grashof number  $Gr$ , and the ratio of radii  $R_N/R_1$ . A summary of the cases studied is presented in Table 2. In each case, calculations were performed until  $\bar{Nu}$  no longer varied significantly with time.

**Study of Unsteady State.** To display transient results, a typical set of the variations of streamlines and isotherms with the time is shown in Fig. 3, for the conditions of run 14 (Table 2).

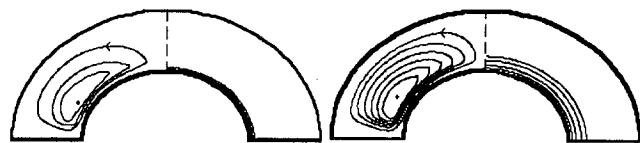
**Variation of Streamlines and Isotherms.** In order to plot the results an auxiliary program was written, with the aid of the subroutine named SEARCH2 (Chuen-yen, 1979). Figure 3 shows that the streamlines start symmetrically on the heated cylinder, near the adiabatic walls. These curves expand and the centers of rotation move away from the wall with increasing time. In the beginning, the motion is induced by fluid particles heated by the inner cylinder. These particles become lighter and go up to the isothermal wall along the symmetric axis; they are cooled on this wall and go down hugging the walls. For moderate and low values of the heat flux applied on the inner cylinder, two eddies rotating in opposite directions are obtained.

For small times, the isotherms are parallel to one other and they are located near the heated wall. This is due to the predominance of the conduction. With increasing time and according to the heat flux applied on the inner cylinder, the isotherms move away and gradually approach a steady state with a conduction-dominant regime, when the Grashof number is relatively small,

Table 2 Summary of principal runs

Run	$F_r$	N X M	Gr	$\bar{Nu}$	$D_h$ (m)	$R_N/R_1$
01	1/1	21 x 21	$10^2$	1.00	$0.41985 \times 10^{-1}$	1.4177
02	1/1	31 x 51	$10^4$	1.31	$0.41985 \times 10^{-1}$	1.4177
03	1/1	31 x 51	$10^5$	2.70	$0.41985 \times 10^{-1}$	1.4177
04	1/1	31 x 51	$10^6$	5.42	$0.41985 \times 10^{-1}$	1.4177
05	1/2	21 x 21	$10^2$	1.00	$0.55886 \times 10^{-1}$	1.4177
06	1/2	31 x 51	$10^4$	1.25	$0.55886 \times 10^{-1}$	1.4177
07	1/2	31 x 51	$10^5$	2.59	$0.55886 \times 10^{-1}$	1.4177
08	1/2	31 x 51	$10^6$	4.41	$0.55886 \times 10^{-1}$	1.4177
09	1/3	21 x 51	$10^2$	1.00	$0.62819 \times 10^{-1}$	1.4177
10	1/3	31 x 51	$10^4$	1.16	$0.62819 \times 10^{-1}$	1.4177
11	1/3	31 x 51	$10^5$	2.37	$0.62819 \times 10^{-1}$	1.4177
12	1/3	31 x 51	$10^6$	4.04	$0.62819 \times 10^{-1}$	1.4177
13	1/5	21 x 21	$10^2$	1.00	0.14652	1.8745
14	1/5	31 x 51	$10^4$	1.10	0.14652	1.8745
15	1/5	31 x 51	$10^5$	1.98	0.14652	1.8745
16	1/5	31 x 51	$10^6$	3.42	0.14652	1.8745

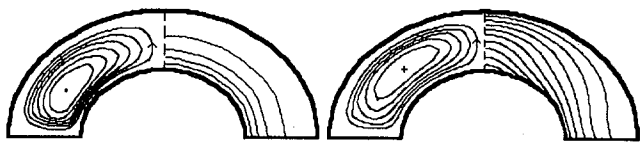




$\tilde{t} = 0.1$   $\tilde{t} = 0.5$

$|\tilde{\Omega}| : 0.47 \times 10^{-4}, 0.3 \times 10^{-4}, 0.2 \times 10^{-4}, 0.1 \times 10^{-4}$   $|\tilde{\Omega}| : 0.0071, 0.006, 0.005, 0.004, 0.003, 0.002, 0.001$

$\bar{T}_{\text{bot} \rightarrow \text{top}} : 0.055, 0.040, 0.025, 0.005$   $\bar{T}_{\text{bot} \rightarrow \text{top}} : 0.8, 0.6, 0.4, 0.2, 0.1, 0.002, 0.001$



$\tilde{t} = 2.5$   $\tilde{t} = \infty$

$|\tilde{\Omega}| : 0.75, 0.6, 0.5, 0.4, 0.3, 0.2, 0.1$   $|\tilde{\Omega}| : 3.1, 2.5, 2.0, 1.5, 1.0, 0.5$

$\bar{T}_{\text{bot} \rightarrow \text{top}} : 1.4, 1.0, 0.6, 0.2$   $\bar{T}_{\text{bot} \rightarrow \text{top}} : 4.5, 4.0, 3.5, 3.0, 2.5, 2.0, 1.5, 1.0, 0.5$

**Fig. 3** Variations of streamlines and isotherms versus dimensionless time for  $F_r = 1/5$  and  $Gr = 10^4$

or with a convection-dominant regime for a greater Grashof number.

In all cases, the present investigation clearly established the symmetry of the flow with respect to the midaxial plane of the enclosure.

**Accuracy of the Numerical Scheme.** The convergence, as well as the accuracy, of the numerical method are checked by comparing mean Nusselt numbers at the inner and the outer cylindrical walls.

Both mean transient Nusselt numbers,  $\bar{Nu}_i$  and  $\bar{Nu}_o$ , against time,  $t$ , are plotted in Figs. 4 and 5 corresponding, respectively, to the cases of runs 14 and 16. As  $t$  increases, both  $Nu_i$  and  $Nu_o$  approach their steady-state values. It should be noted that, in theory for a purely two-dimensional flow field, based on a simple energy balance, their asymptotic values should converge to the same value. As shown in Fig. 4, for  $Gr = 10^4$  and  $F_r = 1/5$ , the deviation is so small that it cannot be visually detected. In fact, due to the numerical techniques involved, for all cases studied, the relative difference between the inner and the outer

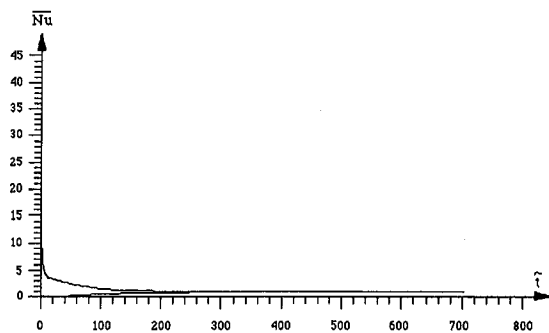


**Fig. 4** Variations of mean Nusselt number on cylindrical external and on cylindrical internal walls versus dimensionless time for  $Gr = 10^4$  and  $F_r = 1/5$

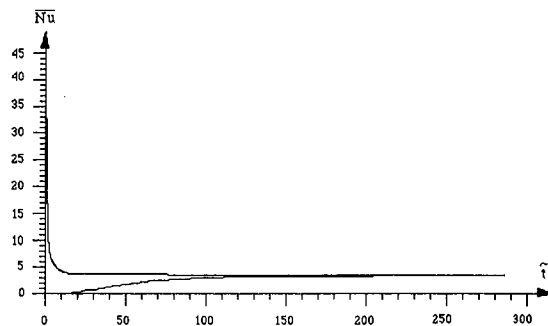


**Fig. 5** Variations of mean Nusselt number on cylindrical external and on cylindrical internal walls versus dimensionless time for  $Gr = 10^6$  and  $F_r = 1/5$

mean Nusselt numbers at convergence differ somewhat and are found to be less than 1 percent.

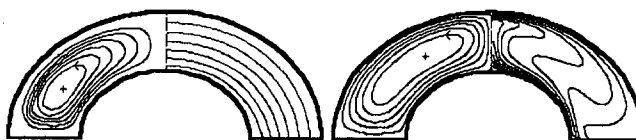
The steady state and the unsteady state are clearly distinguished. For  $F_r = 1/5$ , this separation occurs for  $\tilde{t} \approx 190$ , when  $Gr = 10^4$ , and for  $\tilde{t} \approx 110$ , when  $Gr = 10^6$ .

**Study of the Steady State.** To analyze the steady-state results, the conditions of runs 1, 4, 5, 8, 13, and 16 (Table 2) are used.

**Streamlines and Isotherms.** At steady state, for moderate and low values of the heat flux, it should be noted that the central point of streamlines remains approximately equidistant to the symmetric axis and to the two cylindrical walls, as shown in Figs. 6, 7, and 8. From these considerations we can deduce that thermal transfer appears balanced between active walls, for two-cellular flow. The values of the stream function grow in the same direction as the Grashof number.

When the heat flux applied on the inner cylinder is high and  $F_r = 1/1$ , it should be noted that a secondary recirculation zone appears in the lower corners of the enclosure. There is therefore a transition regime and the formation of a four-cellular flow (Fig. 9).

For  $Gr = 10^2$  the isotherms are roughly parallel to each other. For this case, the temperature increases from the outer cylinder to the heated wall and the conduction on the heated wall is the dominant regime. The convection transfer is relatively insignificant and that is why the values of the stream function are very low. For greater Grashof numbers, the isotherms are symmetrically transformed with respect to the vertical axis. They are strongly modified and become as a ‘‘mushroom’’ at the end. The distribution of the temperature is now more complex. These deformations of the isotherms agree with the direction of the rotation of streamlines. For a two-cellular flow, the fluid particles leaving the heated wall in the neighborhood of the symmetric axis generate a motion and the isotherms become ‘‘round-shouldered’’ and move away from the wall at this point.



(a)  $|\tilde{\Omega}| : 39.96 \times 10^{-3}, 30 \times 10^{-3}, 25 \times 10^{-3}, 20.10^{-3}, 15 \times 10^{-3}, 10 \times 10^{-3}, 5 \times 10^{-3}$  (b)  $|\tilde{\Omega}| : 26.6, 22.0, 17.0, 12.0, 7.0, 2.0$

$\bar{T}_{\text{bot} \rightarrow \text{top}} : 1.2, 1.0, 0.8, 0.6, 0.4, 0.2$   $\bar{T}_{\text{bot} \rightarrow \text{top}} : 5.0, 4.5, 4.0, 3.5, 3.0, 2.5, 2.0, 1.5, 1.0, 0.5$

**Fig. 6** Dimensionless streamlines and isotherms at steady state for  $F_r = 1/5$  and (a)  $Gr = 10^2$ ; (b)  $Gr = 10^6$

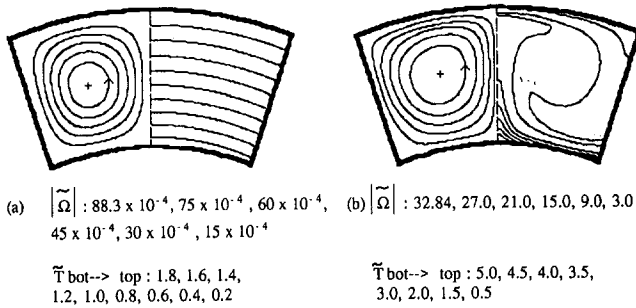


Fig. 7 Dimensionless streamlines and isotherms at steady state for  $F_r = 1/2$  and (a)  $Gr = 10^2$ ; (b)  $Gr = 10^6$

**Local Nusselt Number.** In the heated wall, the local Nusselt number is smaller in the vicinity of the symmetric axis, except for the four-cellular flow, which generates a counterrotating region in the bottom of the enclosure (Figs. 10 and 11).

In the isothermal wall, for a given Grashof number, Figs. 10 and 11 show that thermal exchanges are larger in the vicinity of the symmetric axis, and that they increase with the density of the heat flux imposed on the inner cylinder. However, we note that the distribution of heat exchanges is better if  $F_r = 1/1$ . In the preceding figures, the tops of bell-shaped curves are wider when the aspect ratio increases. For  $F_r = 1/5$  and  $Gr = 10^4$ , for example, parts of the isothermal wall located in the angular intervals 0–0.7 and 2.4–3.14 rad take part in convective heat exchange less than for  $Gr = 10^2$ . These “dead” zones are still located in the corners and their sizes are reduced when the heat flux density increases but they are more important for smaller aspect ratios. According to this observation, the heat transfer seems better for greater aspect ratios.

**Mean Nusselt Number.** In order to compare with more accuracy all the configurations which have been studied, it is suitable to present the variations of the mean Nusselt number  $Nu = (Nu_i + Nu_N)/2$ .

Figure 12 shows quasi-linear curves until the Grashof number is approximately  $10^3$ , which corresponds to the upper bound of the conduction regime. For a Grashof number up to  $10^3$ , the different curves are clearly distinct. From these results we can deduce that convective heat exchange increases with the aspect ratio for Grashof numbers up to  $10^3$ . This conclusion agrees with the observations developed before.

**Influence of the Fluid on the Heat Transfer.** Subsequent runs have been performed to analyze the effect of the fluid on heat transfer. Two liquids were used for this purpose (carbon dioxide

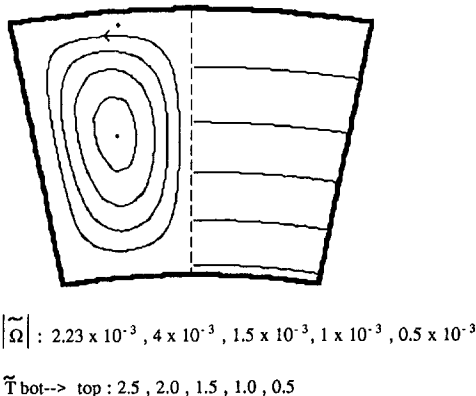


Fig. 8 Dimensionless streamlines and isotherms at steady state for  $F_r = 1/1$  and  $Gr = 10^2$

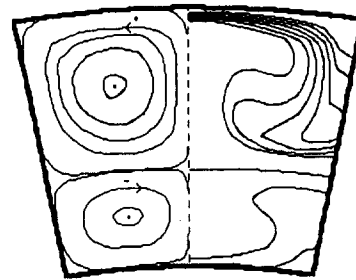


Fig. 9 Dimensionless streamlines and isotherms at steady state for  $F_r = 1/1$  and  $Gr = 10^6$

and ammonia, physical properties in Holman, 1985) with  $F_r$  of 1/1. Figure 13 shows that the mean Nusselt number increases with the Prandtl number, when the heat transfer coefficient increases naturally with the thermal conductivity. It should be noted that the conduction regime does not occur for the ammonia and the carbon dioxide for the tested values.

## V Experimental Study

Holographic interferometry was used to visualize the temperature field within the enclosure. The purpose of the experimental study was to verify the two-dimensional behavior of the convective flow and to compare theoretical temperature fields and interferograms. Of the available holographic techniques, the real-time method was chosen for these experiences. The evaluation of the recorded interference pictures of the temperature field in the test section was accomplished by the known interferometer equation reported by Sarr (1993).

**Apparatus.** The experimental apparatus is shown in Fig. 14. This consists of a 5.4 cm o.d., 50 cm long, copper inner cylinder and 10.5 cm i.d. copper outer cylinder. The ends of the annulus between these two cylinders were kept open and thus, the test section was filled with air as the test fluid. An electric heater made of 1 mm o.d., 1000 cm long, nichrome wire wrapped around a steel rod was inserted in the inner tube. The upper part of the system was brazed with a water jacket so that the outer cylinder is cooled to maintain the tube surface temperature uni-

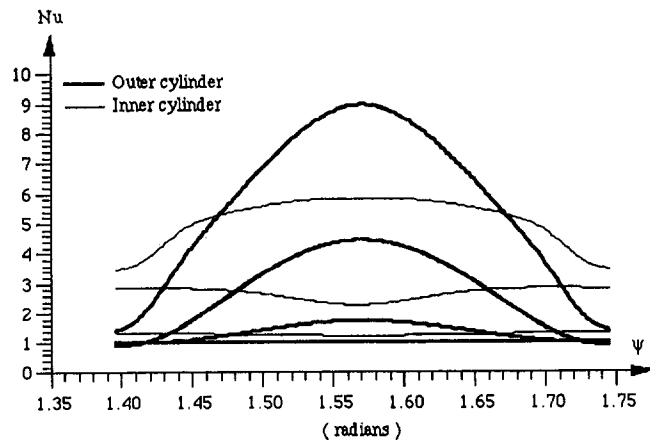


Fig. 10 Angular variations of local Nusselt number on cylindrical walls for  $F_r = 1/1$  and for different modified Grashof numbers,  $Gr_{top-bottom}$ :  $10^6$ ,  $10^5$ ,  $10^4$ , and  $10^2$

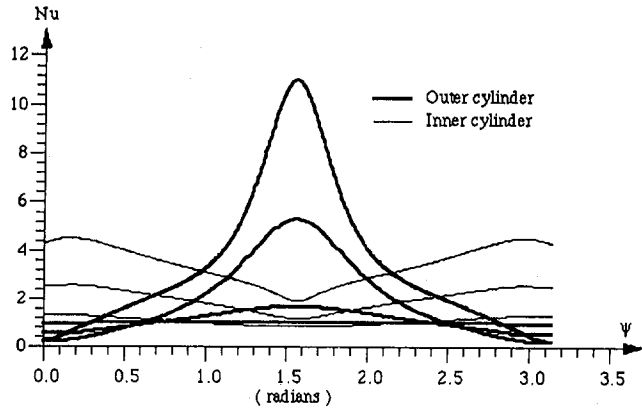


Fig. 11 Angular variations of local Nusselt number on cylindrical walls for  $F_r = 1/5$  and for different modified Grashof numbers,  $Gr_{top-bottom}$ :  $10^6$ ,  $10^5$ ,  $10^4$ , and  $10^2$

form, with the aid of a thermal regulating unit. The temperature stability of the outer cylinder was on the order of 0.1 K. Five chromel-alumel thermocouples were embedded in both cylindrical walls at several locations to measure the surfaces temperatures. The lower part of the test section was insulated with a polystyrene foam insulation.

**Experimental Results.** The temperature of the outer cylinder used for all the experiences is  $T_2 = 295.5$  K, corresponding to the ambient temperature, and the test section described above allows us an enclosure with  $F_r = 0.21$  and  $R_N/R_1 = 1.94$ .

Since one of the main objectives of this paragraph is to provide experimental evidence about the basic flow patterns arising in this kind of flow, the results to be presented here involve the variation of the Grashof number.

The Grashof number was varied by changing the heat flux imposed on the inner cylinder. Figure 15 (a) shows a comparison between the experimental temperature field and the theoretical predictions for temperature field, for  $Gr = 711,757$ . The predicted isothermal lines correspond respectively to the bright interference fringes of the interferogram, numbered in increasing order, from the isothermal wall to the inner cylinder. The temperature difference between two bright interference fringes is about 0.72 K. It may be seen in this figure that the agreement between the experimental and numerical isotherms is fairly good. The predicted isotherms are seen to be similar to the experimental isotherms. For greater Grashof numbers, a better level of qualitative and quantitative agreement is seen between the interfero-

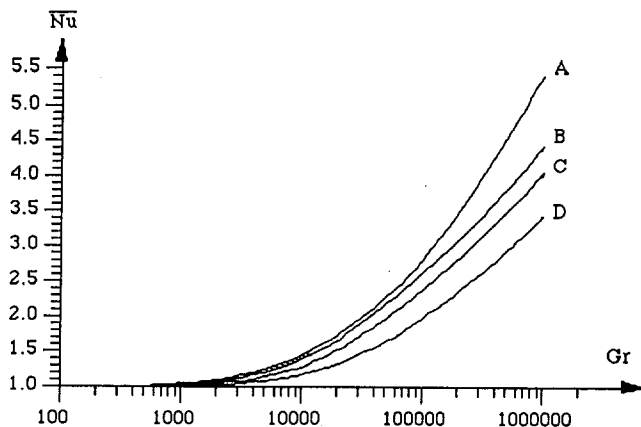


Fig. 12 Mean Nusselt number versus modified Grashof numbers for different aspect ratios  $F_r$ : (A) 1/1; (B) 1/2; (C) 1/3; (D) 1/5

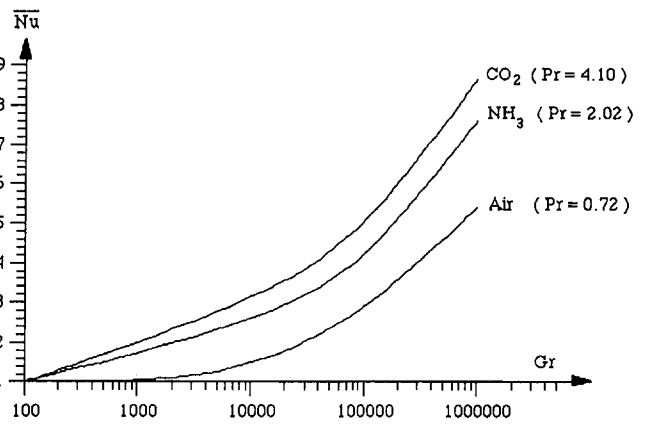


Fig. 13 Mean Nusselt number versus modified Grashof numbers for different fluids with an aspect ratio of  $F_r = 1/1$

metric data and the predicted isotherms for  $Gr = 973,882$  and  $Gr = 1,251,314$ , seen in Figs. 15 (b) and 15 (c), respectively.

The presence of a thermal boundary layer with isotherms clustered near the region of high heat transfer along the cylindrical walls is evident.

For all cases studied, the end effects are seen to be negligible and the two-dimensional behavior of the convective flow was observed. Thus, for  $Gr = 1,251,314$ , only one fringe should be observed, located 1 cm outside the test section.

The discrepancies between the experimental and numerical results occur for low Grashof numbers. In these cases, the flow velocities induced in the enclosure are very low and are therefore disturbed by the ambient conditions. The experimental results may be improved by getting under control the atmospheric conditions.

## Conclusion

At any time, for moderate and low values of the heat flux, the analysis of the stream function shows that a two-cellular flow pattern symmetric to the vertical axis is formed: a negative clockwise eddy and a positive counterclockwise.

When the heat flux applied on the inner cylinder is high and  $F_r = 1/1$ , a transition regime and a four-cellular flow will form due to a counterrotating region in the bottom of the enclosure.

For the steady-state regime and for  $Gr = 10^2$  the values of the stream function are very low and the isotherms are roughly parallel. For a greater Grashof number, the values of the stream function increase quickly and the isotherms are transformed and become as a "mushroom." For any aspect ratio, the conduction is the dominant heat transfer regime for a Grashof number less than  $10^3$ . For a Grashof number up to  $10^3$ , the mean Nusselt number increases with the aspect ratio.

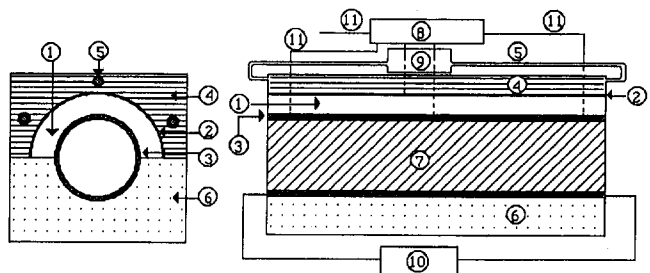
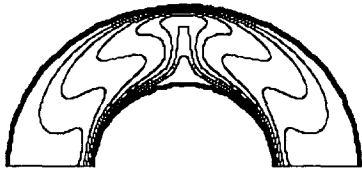


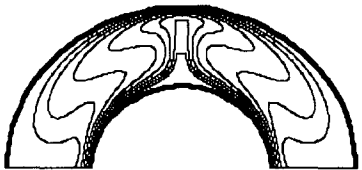
Fig. 14 Experimental apparatus: (1) test section, (2) outer cylinder, (3) inner cylinder, (4) water jacket, (5) cooling water tubes, (6) polystyrene foam insulation, (7) resistance heaters, (8) multipoint data recorder, (9) pump and thermal regulator, (10) rotary transformer, (11) thermocouples



(a)  $Gr = 711\,757$ ,  $q_1 = 37.2\text{ W/m}^2$



(b)  $Gr = 973\,882$ ,  $q_1 = 50.9\text{ W/m}^2$



(c)  $Gr = 1\,251\,314$ ,  $q_1 = 65.4\text{ W/m}^2$

**Fig. 15 Interferograms and corresponding predicted temperature fields at steady state for various Grashof numbers**

For  $F_r = 1$ , a comparison of the heat transfer by using air, ammonia–liquid, and carbon dioxide–liquid enables us to deduce that the mean Nusselt number is increasing with the Prandtl number.

Holographic interferometry permitting the validation of the theoretical model shows a good agreement between the predicted and experimental isotherms.

## References

- Al-Ani, N., and Nansteel, M. W., 1993, "Natural Convection in a Partial Sector-Shaped Enclosure: Experimental Results," *ASME JOURNAL OF HEAT TRANSFER*, Vol. 115, pp. 133–139.
- Bejan, A., 1984, *Convection Heat Transfer*, A Wiley-Interscience Publication, Wiley, New York.
- Carnahan, B., Luther, H. A., and Wilkes, J. O., 1969, *Applied Numerical Methods*, Wiley, New York.

Castrejon, A., and Spalding, D. B., 1988, "An Experimental and Theoretical Study of Transient Free-Convection Flow Between Horizontal Concentric Cylinders," *Int. J. Heat Mass Transfer*, Vol. 31, No. 2, pp. 273–284.

Chadwick, M. L., Webb, B. W., and Heaton, H. S., 1991, "Natural Convection From Two-Dimensional Discrete Heat Sources in a Rectangular Enclosure," *Int. J. Heat Mass Transfer*, Vol. 34, No. 7, pp. 1679–1793.

Chuen-Yen, C., 1979, *An Introduction to Computational Fluid Mechanics*, Wiley, New York.

David, R. C., and David, G. L., 1977, *Heat Transfer Calculations Using Finite Difference Equations*, Applied Sciences Publishers LTD, London.

Euvrard, D., 1990, "Résolution Numérique des Equations aux Dérivées Partielles," 2nd ed., Masson, Paris.

Gourdin, A., and Boumahrat, M., 1983, *Méthodes Numériques Appliquées*, Lavoisier TEC & DOC, Paris.

Holman, J. P., 1985, *Heat Transfer*, 5th ed., McGraw-Hill, New York.

Kubbeck, K., Merker, G. P., and Straub, J., 1980, "Advanced Numerical Computation of Two-Dimensional Time-Dependent Free Convection in Cavities," *Int. J. Heat Mass Transfer*, Vol. 23, pp. 203–217.

Kuehn, T. H., and Goldstein, R. J., 1976a, "An Experimental and Theoretical Study of Natural Convection in the Annulus Between Horizontal Concentric Cylinders," *J. Fluid Mech.*, Vol. 74, No. 4, pp. 695–719.

Kuehn, T. H., and Goldstein, R. J., 1976b, "Correlating Equations for Natural Convection Heat Transfer Between Horizontal Circular Cylinders," *Int. J. Heat Mass Transfer*, Vol. 19, pp. 1127–1134.

Kwon, S. S., Kuehn, T. H., and Lee, T. S., 1982, "Natural Convection in the Annulus Between Horizontal Circular Cylinders With Three Axial Spacers," *ASME JOURNAL OF HEAT TRANSFER*, Vol. 104, pp. 118–124.

Lavrentiev, M., and Chabat, B., 1972, *Méthodes de la théorie des fonctions d'une variable complexe*, Editions MIR, Moscow.

Mack, R., and Bishop, E. H., 1986, "Natural Convection Between Horizontal Concentric Cylinders for Low Rayleigh Numbers," *Quart. Journ. Mech. and Applied Math.*, Vol. 21, No. 2, pp. ???–???

Nogotov, E. F., 1978, *Applications of Numerical Heat Transfer*, McGraw-Hill, New York.

Peaceman, D. W., and Rachford, H. H., 1955, "The Numerical Solution of Parabolic and Elliptic Differential Equations," *J. Soc. Ind. Appl. Math.*, Vol. 3, No. 1, pp. 28–41.

Ranganathan, K., 1988, "Study of Natural Convection in Horizontal Annuli," *Int. J. Heat Mass Transfer*, Vol. 31, No. 6, pp. 1137–1148.

Rao, Y. F., Miki, Y., Fukuda, K., Tanaka, K., and Hasegawa, S., 1985, "Flow Patterns of Natural Convection in Horizontal Cylindrical Annuli," *Int. J. Heat Mass Transfer*, Vol. 28, pp. 705–714.

Roache, P. J., 1982, *Computational Fluid Dynamics*, Hermosa Publ., Albuquerque, NM.

Samuels, M. R., and Churchill, S. W., 1967, "Stability of Fluid in a Rectangular Region Heated From Below," *AIChE J.*, Vol. 13, No. 1, pp. 77–85.

Sarr, J., 1993, "Contribution à l'Etude de la Convection Naturelle dans une Enceinte Fermée Limitée par deux Cylindres Concentriques Horizontaux et deux Plans Diamétraux," Thèse de Doctorat, Université de Perpignan, France.

Shilston, M. J., and Probert, S. D., 1978, "Effects of Horizontal and Vertical Spacers on the Heat Transfer Across a Horizontal, Annular, Air-Filled Cavity," *Applied Energy*, Vol. 4, pp. 21–27.

Torrance, K. E., 1968, "Comparison of Finite-Difference Computations of Natural Convection," *Journal of Research of the National Bureau of Standards—B. Mathematical Sciences*, Vol. 72B, No. 4, Oct., pp. 281–300.

Tsui, Y. T., and Tremblay, B., 1984, "On Transient Natural Convection Heat Transfer in the Annulus Between Concentric, Horizontal Cylinders With Isothermal Surfaces," *Int. J. Heat Mass Transfer*, Vol. 27, No. 1, pp. 103–111.

Vafai, K., and Javad, E., 1991, "An Investigation of Transient Three-Dimensional Buoyancy-Driven Flow and Heat Transfer in a Closed Horizontal Annulus," *Int. J. Heat Mass Transfer*, Vol. 34, No. 10, pp. 2555–2570.

Wilkes, J. O., and Churchill, S. W., 1966, "The Finite-Difference Computation of Natural Convection in a Rectangular Enclosure," *AIChE J.*, Vol. 12, No. 1, pp. 161–166.

# Velocity Statistics of Round, Fully Developed, Buoyant Turbulent Plumes

Z. Dai

Graduate Student Research Assistant.

L. K. Tseng<sup>1</sup>

Research Fellow.

G. M. Faeth

Professor.  
Fellow ASME

Department of Aerospace Engineering,  
The University of Michigan,  
Ann Arbor, MI 48109-2118

*An experimental study of the structure of round buoyant turbulent plumes was carried out, limited to conditions within the fully developed (self-preserving) portion of the flow. Plume conditions were simulated using dense gas sources (carbon dioxide and sulfur hexafluoride) in a still air environment. Velocity statistics were measured using laser velocimetry in order to supplement earlier measurements of mixture fraction statistics using laser-induced iodine fluorescence. Similar to the earlier observations of mixture fraction statistics, self-preserving behavior was observed for velocity statistics over the present test range (87–151 source diameters and 12–43 Morton length scales from the source), which was farther from the source than most earlier measurements. Additionally, the new measurements indicated that self-preserving plumes are narrower, with larger mean streamwise velocities near the axis (when appropriately scaled) and with smaller entrainment rates, than previously thought. Velocity statistics reported include mean and fluctuating velocities, temporal power spectra, temporal and spatial integral scales, and Reynolds stresses.*

## Introduction

The structure of round buoyant turbulent plumes in still and unstratified environments is an important fundamental problem that has attracted significant attention since the classical study of Rouse et al. (1952). However, recent work has highlighted the need for more information about buoyant turbulent plumes in order to address effects of turbulence/radiation interactions (Kounalakis et al., 1991), and to help benchmark models of buoyant turbulent flows (Dai et al., 1994). Thus, the objective of the present investigation was to measure mean and fluctuating velocity properties in round buoyant turbulent plumes in order to supplement earlier measurements of mean and fluctuating scalar properties (mixture fractions) in these flows, due to Dai et al. (1994). The fully developed region, where effects of the source have been lost and the properties of the flow become self-preserving, was emphasized due to its fundamental importance for simplifying both theoretical considerations and the interpretation of the measurements (Tennekes and Lumley, 1972), even though few practical plumes reach these conditions.

Several reviews of turbulent plumes have appeared (Chen and Rodi, 1980; Kotsovinos, 1985; List, 1982; Papanicolaou and List, 1987, 1988); therefore, the discussion of past studies will be brief. The earliest work emphasized the development of similarity relationships for flow properties within fully developed (self-preserving) buoyant turbulent plumes (Rouse et al., 1952; Morton et al., 1956; Morton, 1959). Subsequently, many workers reported observations of mean properties at self-preserving conditions; however, the various determinations of centerline values and flow widths generally were not in good agreement (Abraham, 1960; Chen and Rodi, 1980; Dai et al., 1994; George et al., 1977; Kotsovinos, 1985; Kotsovinos and List, 1987; Mizushima et al., 1979; Nakagome and Hirata, 1977; Ogino et al., 1980; Papanicolaou and List, 1987, 1988; Papantoniou and List, 1989; Peterson and Bayazitoglu, 1992; Seban and Behnia, 1976; Shabir and George, 1992; Zimin and Frik, 1977). Papanicolaou and List (1987, 1988), Papantoniou and List (1989), and Dai et al.

(1994) attribute these discrepancies mainly to problems of fully reaching self-preserving conditions, with conventional experimental uncertainties serving as a contributing factor.

Self-preserving round buoyant turbulent plume conditions are reached when streamwise distances from the plume source are large in comparison to two characteristic length scales, as follows: (1) the source diameter, as a measure of conditions where effects of source disturbances have been lost; and (2) the Morton length scale, as a measure of conditions when the buoyant features of the flow are dominant. For general buoyant jet sources, the Morton length scale is defined as follows (Morton, 1959; List, 1982; Papanicolaou and List, 1988):

$$l_M = M_0^{3/4} / B_0^{1/2} \quad (1)$$

For round plumes with uniform properties defined at the source (similar to the present experiments), the source specific momentum flux,  $M_0$ , and the source buoyancy flux,  $B_0$ , are defined as follows (List, 1982; Dai et al., 1994):

$$M_0 = (\pi/4) d^2 u_0^2 \quad (2)$$

$$B_0 = (\pi/4) d^2 u_0 g |\rho_0 - \rho_\infty| / \rho_\infty \quad (3)$$

where an absolute value of the density difference has been used in Eq. (3) to account for both rising and falling plumes. Substituting Eqs. (2) and (3) into Eq. (1) then yields the following expression for  $l_M$  for round plumes that have uniform properties at the source:

$$l_M = (\pi/4)^{1/4} (\rho_\infty d u_0^2 / (g |\rho_0 - \rho_\infty|))^{1/2} \quad (4)$$

The ratio,  $l_M/d$ , is proportional to the source Froude number, defined as follows for conditions analogous to those of Eq. (4) (List, 1982):

$$Fr_0 = (4/\pi)^{1/4} l_M/d = (\rho_\infty u_0^2 / (g |\rho_0 - \rho_\infty| d))^{1/2} \quad (5)$$

The source Froude number is a convenient measure of the dominance of buoyancy at the source, e.g.,  $Fr_0 = 0$  and  $\infty$  for purely buoyant and for purely nonbuoyant sources, respectively.

Papanicolaou and List (1987, 1988) suggest that buoyancy-dominated conditions for mean and fluctuating quantities are reached for  $(x - x_0)/l_M$  greater than roughly 6 and 14, respectively, which has been satisfied by most past measurements seeking results at self-preserving conditions (Dai et al., 1994). However, aside from the measurements of Papantoniou and List (1989) and Dai et al. (1994), to be discussed subsequently, ex-

<sup>1</sup> Current address: School of Mechanical Engineering, Purdue University, West Lafayette, IN.

Contributed by the Heat Transfer Division for publication in the JOURNAL OF HEAT TRANSFER. Manuscript received by the Heat Transfer Division November 1993; revision received April 1994. Keywords: Natural Convection, Plumes, Turbulence. Associate Technical Editor: Y. Jaluria.

isting measurements of radial profiles of mean and fluctuating properties in buoyant turbulent plumes have been limited to  $(x - x_0)/d$  in the range 6–62, with most measurements emphasizing the lower end of this range, see Papanicolaou and List (1987, 1988), Shabbir and George (1992), George et al. (1977), Ogino et al. (1980), Nakagome and Hirata (1977), and Peterson and Bayazitoglu (1992), among others. This range of normalized streamwise distances is rather small to achieve self-preserving conditions, based on findings for nonbuoyant round turbulent jets where values of  $(x - x_0)/d$  greater than roughly 40 and 100 are required to achieve self-preserving profiles of mean and fluctuating properties, respectively (Hinze, 1975; Tennekes and Lumley, 1972). Similar behavior for round buoyant turbulent plumes recently has been established by Papantoniou and List (1989) and Dai et al. (1994). These measurements were limited to scalar properties and found that self-preserving mean and fluctuating mixture fractions (i.e., the mass fraction of source material in a sample) only were achieved at  $(x - x_0)/d$  and  $(x - x_0)/l_M$  greater than roughly 100 and 10, respectively. These results also showed that self-preserving buoyant turbulent plumes were narrower, with larger mean and fluctuating scalar properties at the axis (when appropriately scaled), than earlier reported measurements of self-preserving scalar properties made closer to the source. Finally, it seems likely that self-preserving behavior for other properties only is achieved at comparable conditions.

The preceding discussion suggests that existing measurements of mean and fluctuating velocities within round buoyant turbulent plumes probably involve transitional plumes. Thus, the objective of the present investigation was to extend the scalar property measurements of Papantoniou and List (1989) and Dai et al. (1994) to consider mean and fluctuating velocity properties within the self-preserving region of round buoyant turbulent plumes. Present test conditions were identical to those of Dai et al. (1994), and involved source flows of carbon dioxide and sulfur hexafluoride in still air at room temperature and atmospheric pressure. This approach yields downwardly flowing negatively buoyant plumes in still and unstratified environments, and allows straightforward specification of the buoyancy flux within the test plumes.

## Experimental Methods

**Test Apparatus.** Description of the experimental apparatus will be brief; see Dai et al. (1994) for more details. The test plumes were within a screened enclosure (which could be traversed to accommodate rigidly mounted instrumentation) that was mounted within an outer enclosure. The plume sources were

long round tubes that could be traversed in the vertical direction within the inner enclosure for measurements at various streamwise distances from the source. The ambient air within the enclosures was seeded with oil drops (roughly  $1 \mu\text{m}$  nominal diameter) for laser velocimetry (LV) measurements of velocities, using several multiple jet spray generators (TSI, model 9306) that discharged above the screened top of the outer enclosure. In the self-preserving region where present measurements were made, maximum mixture fractions were less than 6 percent; therefore, effects of concentration bias (because only the ambient air was seeded) were negligible.

**Instrumentation.** Dual-beam, frequency-shifted LV was used for the velocity measurements, based on the 514.5 nm line of an argon-ion laser. The optical axis of the LV passed horizontally through the flow with signal collection at right angles to the optical axis to yield a measuring volume having a diameter of  $400 \mu\text{m}$  and a length of  $260 \mu\text{m}$ . A darkened enclosure as well as a laser line filter in front of the detector were used to minimize effects of background light. Various orientations of the plane of the laser beams were used to find the three components of mean and fluctuating velocities, as well as the Reynolds stress, as described by Lai and Faeth (1987).

The detector output was amplified and processed using a burst counter signal processor (TSI, model 1980B). The low-pass filtered analog output of the signal processor was sampled at equal time intervals in order to avoid problems of velocity bias, while directional ambiguity and bias were controlled by frequency shifting. The detector output was sampled at rates more than twice the break frequency of the low-pass filter in order to control alias signals. Seeding levels were controlled so that effects of step noise contributed less than 3 percent to determinations of velocity fluctuations, based on measurements of temporal spectra to be discussed later. Experimental uncertainties (95 percent confidence) were mainly governed by finite sampling time limitations and are estimated to be less than 5 and 13 percent for mean and fluctuating velocities, respectively; the corresponding uncertainties for Reynolds stresses are estimated to be less than 16 percent.

**Test Conditions.** The experiments involved carbon dioxide and sulfur hexafluoride plumes as summarized in Table 1. For  $(x - x_0)/d \geq 87$ , where self-preserving conditions were observed, the Kolmogorov microscales of velocity fluctuations were less than  $350 \mu\text{m}$ ; therefore, the spatial resolution of present measurements was not sufficient to resolve the smallest scales of turbulence. Present source conditions were identical to those of Dai et al. (1994), however, the locations of the virtual origins of

## Nomenclature

$B_0$ = source buoyancy flux, Eq. (3)	$l_f, l_u$ = characteristic plume radii based on $\bar{f}$ and $\bar{u}$	$x$ = streamwise distance
$d$ = source diameter	$l_M$ = Morton length scale, Eqs. (1) and (4)	$\eta$ = dimensionless radial distance, Eq. (15)
$E_i(n)$ = temporal power spectral density of velocity component $i$	$M_0$ = source-specific momentum flux, Eq. (2)	$\nu$ = kinematic viscosity
$E_0$ = entrainment constant, Eq. (19)	$n$ = frequency	$\rho$ = density
$f$ = mixture fraction	$Q$ = plume volumetric flow rate	$\tau_f, \tau_u$ = temporal integral scales of $f'$ and $u'$
$F(r/(x - x_0))$ = scaled radial distribution of $\bar{f}$ in self-preserving region	$r$ = radial distance	<b>Subscripts</b>
$Fr_0$ = source Froude number, Eq. (5)	$Re_0$ = source Reynolds number = $u_0 d / \nu_0$	$c$ = centerline value
$g$ = acceleration of gravity	$u$ = streamwise velocity	$0$ = initial value or virtual origin location
$k_f, k_u$ = plume width coefficients based on $\bar{f}$ and $\bar{u}$	$U(r/(x - x_0))$ = scaled radial distribution of $\bar{u}$ in self-preserving region	$\infty$ = ambient value
	$v$ = radial velocity	<b>Superscripts</b>
	$w$ = tangential velocity	$\bar{(\quad)}$ = time-averaged mean value
		$(\quad)'$ = root-mean-squared fluctuating value

**Table 1 Summary of test conditions<sup>a</sup>**

Source Properties	CO <sub>2</sub>	SF <sub>6</sub>
Density (kg/m <sup>3</sup> )	1.75	5.87
Kinematic viscosity (mm <sup>2</sup> /s)	8.5	2.6
Diameter (mm)	9.7	6.4
Average velocity (m/s)	1.74	1.89
Reynolds number, Re <sub>0</sub>	2000	4600
Froude number, Fr <sub>0</sub>	7.80	3.75
Morton length scale, $\hat{L}_M/d$	7.34	3.53
Virtual origin, based on $\bar{f}, x_0/d^b$	12.7	0.0
Virtual origin, based on $\bar{u}, x_0/d$	0.0	0.0

<sup>a</sup>Flow directed vertically downward in still air with an ambient pressure, temperature, density and kinematic viscosity of 99 ± 0.5 kPa, 297 ± 0.5 K, 1.16 kg/m<sup>3</sup> and 14.8 mm<sup>2</sup>/s. Source passage length-to-diameter ratios of 50:1.

<sup>b</sup>Based on the measurements of Dai et al. (1994).

the carbon dioxide plume, based on  $\bar{f}$  from Dai et al. (1994) and based on  $\bar{u}$  for the present measurements, were not identical. It was beyond the scope of the present investigation to study the reasons for different locations of these virtual origins; however, such behavior is not surprising because the initial conditions and Prandtl/Schmidt numbers are not the same for mixture fractions and velocities.

### Self-Preserving Scaling

The general state relationship for density as a function of mixture fraction, assuming ideal gas behavior, is given as follows for the present plume flows (Dai et al., 1994):

$$\rho = \rho_\infty / (1 - f(1 - \rho_\infty / \rho_0)) \quad (6)$$

Then, noting that  $f \ll 1$  in the self-preserving region, Eq. (6) can be linearized as follows:

$$\rho = \rho_\infty + f\rho_\infty(1 - \rho_\infty / \rho_0), f \ll 1 \quad (7)$$

Under present assumptions, conservation principles and the state relationship for density imply that the buoyancy flux is conserved for buoyant turbulent plumes. Then mean streamwise velocities and mixture fractions can be scaled as follows in the self-preserving region, where flow properties are independent of source properties like  $d$  and  $u_0$  (List, 1982):

$$\bar{u}((x - x_0)/B_0)^{1/3} = U(r/(x - x_0)) \quad (8)$$

$$\bar{f}gB_0^{-2/3}(x - x_0)^{5/3} |d \ln \rho / df|_{f=0} = F(r/(x - x_0)) \quad (9)$$

For present conditions, it can be seen from Eq. (7) that

$$|d \ln \rho / df|_{f=0} = |\rho_0 - \rho_\infty| / \rho_0 \quad (10)$$

is a measure of the buoyancy potential with the extent of mixing. As before, an absolute value has been used in Eq. (10) to account for both rising and falling plumes. The  $x_0$  in Eqs. (8) and (9) are the virtual origins for  $\bar{u}$  and  $\bar{f}$ , respectively, as noted in Table 1. The  $U(r/(x - x_0))$  and  $F(r/(x - x_0))$  are appropriately scaled radial profile functions of mean streamwise velocities and mixture fractions, which become universal functions in the self-preserving region far from the source where Eq. (7) applies. Equations (8) and (9) were used to extrapolate present measurements of mean mixture fractions and velocities along the axis to find the corresponding values of the virtual origins, as discussed earlier.

### Results and Discussion

**Mean Velocities.** The evolution of mean and fluctuating mixture fractions from source to self-preserving conditions has been

considered by Dai et al. (1994). Present measurements of velocity properties were limited to the region where self-preserving behavior was observed for mean and fluctuating mixture fractions; namely,  $(x - x_0)/d \geq 87$  and  $(x - x_0)/l_M \geq 12$ . Within this region, velocity properties also were observed to be self-preserving. Present measurements of mean streamwise velocities for the self-preserving region are illustrated in Fig. 1. The scaling parameters of Eq. (8) are used in the figure so that the ordinate is equal to  $U(r/(x - x_0))$ . The variation of  $U(r/(x - x_0))$  is seen to be universal within experimental uncertainties over the range of the measurements, as anticipated for self-preserving flow. In contrast, results at smaller values of  $(x - x_0)/d$ , not shown in Fig. 1, exhibited broader profiles and smaller values of  $U(0)$ , analogous to the behavior of  $\bar{f}$  observed by Dai et al. (1994) in the transitional region of buoyant turbulent plumes.

Within the self-preserving region, present radial profiles of mean streamwise velocities are reasonably approximated by a Gaussian fit, similar to past work (Rouse et al., 1952; Papanicolaou and List, 1988; Ogino et al., 1980; Nakagome and Hirata, 1977; Shabbir and George, 1992; George et al., 1977) as follows:

$$U(r/(x - x_0)) = U(0) \exp\{-k_u^2(r/(x - x_0))^2\} \quad (11)$$

where

$$k_u = (x - x_0)/l_u \quad (12)$$

and  $l_u$  is a characteristic plume radius where  $\bar{u}/\bar{u}_c = \exp(-1)$ . The best fit of the present data in the self-preserving region yielded  $U(0) = 4.3$  and  $k_u^2 = 93$ , with  $l_u/(x - x_0) = 0.10$ . The resulting correlation is seen to be a good representation of the measurements illustrated in Fig. 1.

Present measurements of mean streamwise velocities in the self-preserving region of turbulent plumes yield narrower profiles with larger values near the axis (when appropriately scaled) than

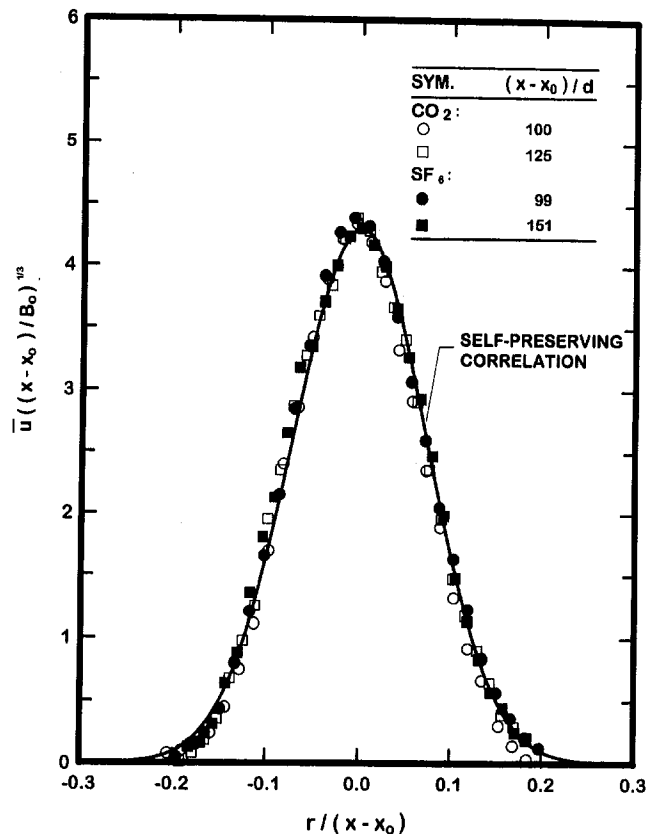


**Fig. 1 Radial profiles of mean streamwise velocities in self-preserving buoyant turbulent plumes**

earlier results obtained at smaller distances from the source. This behavior is quantified in Table 2, where the range of streamwise distances considered for measurements of radial profiles of self-preserving plume properties, and the corresponding reported values of  $k_u^2$ ,  $U(0)$ , and  $l_u/(x - x_0)$ , are summarized for representative past studies and associated earlier work from the same laboratories. Past measurements generally satisfy the criterion for buoyancy-dominated flow, i.e.,  $(x - x_0)/l_M > 6$  (Papanicolaou and List, 1987, 1988). However, except for the present study, the measurements were obtained at values of  $(x - x_0)/d$  that normally are not associated with self-preserving conditions for jetlike sources. Somewhat like the tendency for transitional plumes to have broader profiles than the self-preserving region, mentioned earlier, the values of  $k_u^2$  tend to increase as the maximum streamwise position considered is increased, exhibiting an increase of 40 percent for the range of conditions given in Table 2. This yields a corresponding reduction of the characteristic plume radius of 40 percent, and an increase of  $U(0)$  of 25 percent, when approaching self-preserving conditions over the range considered in Table 2.

Present measurements of radial profiles of mean radial velocities are illustrated in Fig. 2. The scaling parameters used in the figure for  $\bar{v}$  and radial distance provide universal plots within the self-preserving region as well as a check of the internal consistency of the present measurements of  $\bar{u}$  and  $\bar{v}$ . This behavior can be seen from conservation of mass in the self-preserving region where the variation of density is small, e.g.:

$$r \partial \bar{u} / \partial x + \partial r \bar{v} / \partial r = 0 \quad (13)$$

Integrating Eq. (13), noting that  $r \bar{v} = 0$  at  $r = 0$ , then yields:

$$r \bar{v} / ((x - x_0) \bar{u}_c) = \int_0^\eta ((x - x_0) / \bar{u}_c) (\partial \bar{u} / \partial x) \eta d\eta \quad (14)$$

where

$$\eta = r / (x - x_0) \quad (15)$$

The integral on the right-hand side of Eq. (14) can be evaluated for self-preserving conditions after substituting from Eqs. (8) and (11) for  $\bar{u}$  and  $\bar{u}_c$ . This yields:

$$r \bar{v} / ((x - x_0) \bar{u}_c) = (5/6 k_u^2) [(1 + 6 k_u^2 \eta^2 / 5) \times \exp(-k_u^2 \eta^2) - 1] \quad (16)$$

which demonstrates the universality of the scaled value of  $r \bar{v}$  as a function of  $\eta$  within the self-preserving region. Finally, adopting  $k_u^2 = 93$  from present measurements (see Table 2) yields the plot based on the mean streamwise velocity measurements illustrated in Fig. 2.

The measurements of  $\bar{v}$  illustrated in Fig. 2 exhibit universal behavior for the two test plumes, as anticipated for the self-preserving region. Additionally, the measurements of  $\bar{v}$  also are consistent with present measurements of  $\bar{u}$ , based on good agreement with the correlation found from  $\bar{u}$  through the continuity equation. This check is important because  $\bar{v}$  is small, roughly an order

**Table 2 Summary of self-preserving buoyant turbulent plume velocity properties<sup>a</sup>**

Source	Medium	$(x-x_0)/d$	$(x-x_0)/R_M$	$k_u^2$	$R_u/(x-x_0)$	$U(0)$	$(\bar{u}/\bar{u}_c)$	$E_0^b$
Present study	gaseous	87-151	12-43	93	0.10	4.3	0.22	0.086
Papanicolaou and List (1988)	liquid	22-62	9-62	90	0.11	3.9	0.25	0.088
Shabbir and George (1992)	gaseous	10-25	6-15	58	0.13	3.4	0.32	0.109
George et al. (1977)	gaseous	8-16	6-12	55	0.14	3.4	0.28	0.112
Ogino et al. (1980)	liquid	6-36	5-15	51	0.14	3.4	...	0.117
Nakagome and Hirata (1977)	gaseous	5-13	∞	48	0.14	3.9	0.25	0.120

<sup>a</sup>Round turbulent plumes in still, unstratified environments. Range of streamwise distances are for conditions where quoted self-preserving properties were found from measurements over the cross section of the plumes. Entries are ordered in terms of decreasing  $k_u^2$ .

<sup>b</sup>Found from Eq. (20).

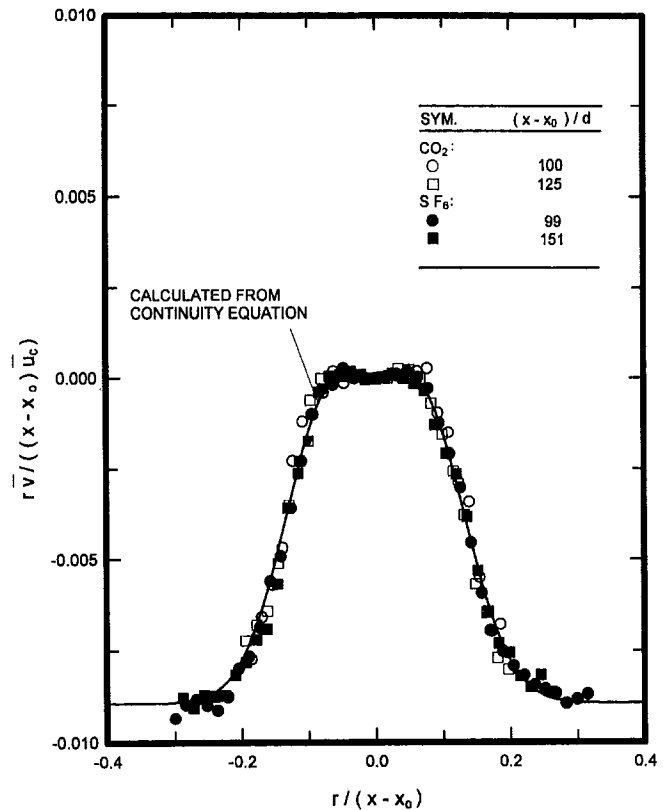


**Fig. 2 Radial profiles of mean radial velocities in self-preserving buoyant turbulent plumes**

of magnitude smaller than  $\bar{v}'$ , so that it is difficult to measure due to its rather low signal-to-noise ratios.

The asymptotic values of  $r \bar{v}$  at large absolute values of  $\eta$  are proportional to the entrainment constant of the plumes, which is important for integral theories of plume scaling and as a measure of turbulent mixing rates (Morton, 1959; Morton et al., 1956). Entrainment behavior can be seen by integrating Eq. (13) to obtain an expression for the rate of change of the volumetric flow rate within the plumes at self-preserving conditions where the density of the flow is nearly constant:

$$d/dx \int_0^\infty r \bar{u} dr = dQ/dx = -(r \bar{v})_\infty \quad (17)$$

An estimate of  $(r \bar{v})_\infty$  can be found from the measurements of mean streamwise velocities through Eq. (16), as follows:

$$-(r \bar{v})_\infty / ((x - x_0) \bar{u}_c) = 5 / (6 k_u^2) \quad (18)$$

In view of the agreement between measurements of  $r \bar{v}$  and Eq. (16), discussed earlier, Eq. (18) provides a reasonable estimate of entrainment properties. Then, noting that  $k_u^2 = 93$ , Eq. (18) yields  $-(r \bar{v})_\infty / ((x - x_0) \bar{u}_c) = 0.0090$ .

Actual entrainment constants have values that depend on the characteristic radius and velocity used in their definition (Morton, 1959). For present purposes, it is convenient to use  $l_u$  and  $\bar{u}_c$  as the radius and velocity scales so that the entrainment constant,  $E_0$ , is defined as follows:

$$dQ/dx = E_0 l_u \bar{u}_c \quad (19)$$

Then, an expression for  $E_0$  can be found in terms of measurements of mean streamwise velocities from Eqs. (12), (17), (18) and (19), as follows:

$$E_0 = 5 / (6 k_u) \quad (20)$$



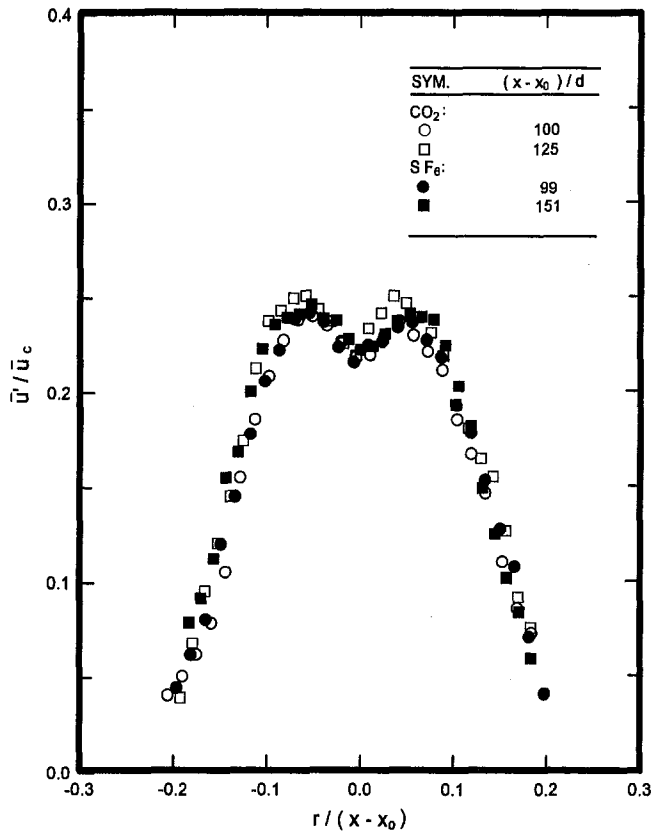


Fig. 3 Radial profiles of streamwise velocity fluctuations in self-preserving buoyant turbulent plumes

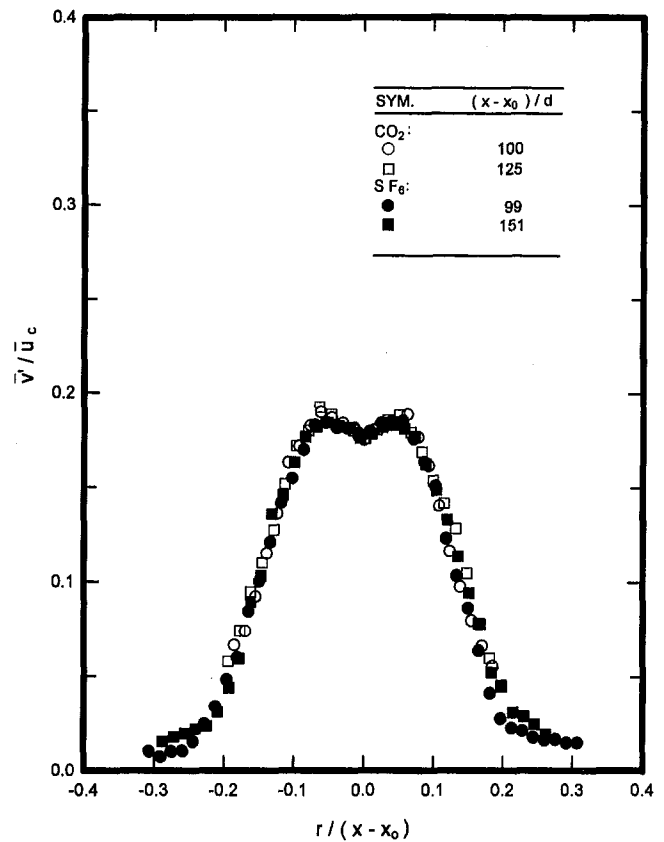


Fig. 4 Radial profiles of radial velocity fluctuations in self-preserving buoyant turbulent plumes

Values of  $E_0$  found from Eq. (20) are summarized in Table 2 for various existing measurements. The main trend of the data is for  $E_0$  to decrease as self-preserving conditions are approached at large distances from the source, with  $E_0$  decreasing roughly 40 percent over the range of existing measurements.

**Velocity Fluctuations.** Radial profiles of streamwise, radial, and tangential velocity fluctuations for the self-preserving region of the two sources,  $(x-x_0)/d \geq 87$  and  $(x-x_0)/l_M \geq 12$ , are illustrated in Figs. 3–5. It is seen that over the range of streamwise distances considered, the profiles are universal within experimental uncertainties. Results at smaller distances (not shown in Figs. 3–5), however, exhibited broader profiles, analogous to the other mean and fluctuating properties within the transitional region of buoyant turbulent plumes. The magnitude of streamwise turbulence intensities near the axis, however, actually decreases slightly during the latter stages of development of the transitional plumes. This behavior appears to be due to the increase of mean velocities near the axis (when appropriately scaled) as the self-preserving region of the flow is approached. Thus, present estimates of  $(\bar{u}'/\bar{u})_c = 0.22$  generally are lower than values in the range 0.25–0.32 observed earlier for transitional plumes, see Table 2.

The presence of the dip in streamwise velocity fluctuations near the axis for the self-preserving region, seen in Figs. 3–5, is similar to the behavior of nonbuoyant jets, see Papanicolaou and List (1988) and references cited therein, and is expected because turbulence production is reduced near the axis due to symmetry. In contrast, Dai et al. (1994) did not observe a corresponding dip near the axis for mixture fraction fluctuations, within self-preserving buoyant turbulent plumes, which they attribute to buoyancy/turbulence interactions because such dips are observed in nonbuoyant turbulent jets (Becker et al., 1967). Another unusual effect of buoyancy is that streamwise turbulence intensities near

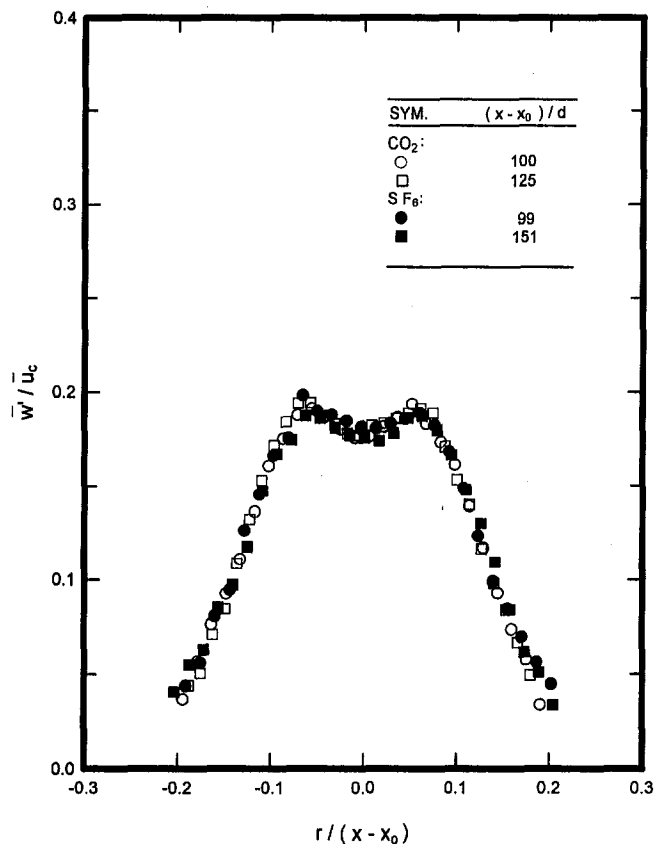


Fig. 5 Radial profiles of tangential velocity fluctuations in self-preserving buoyant turbulent plumes

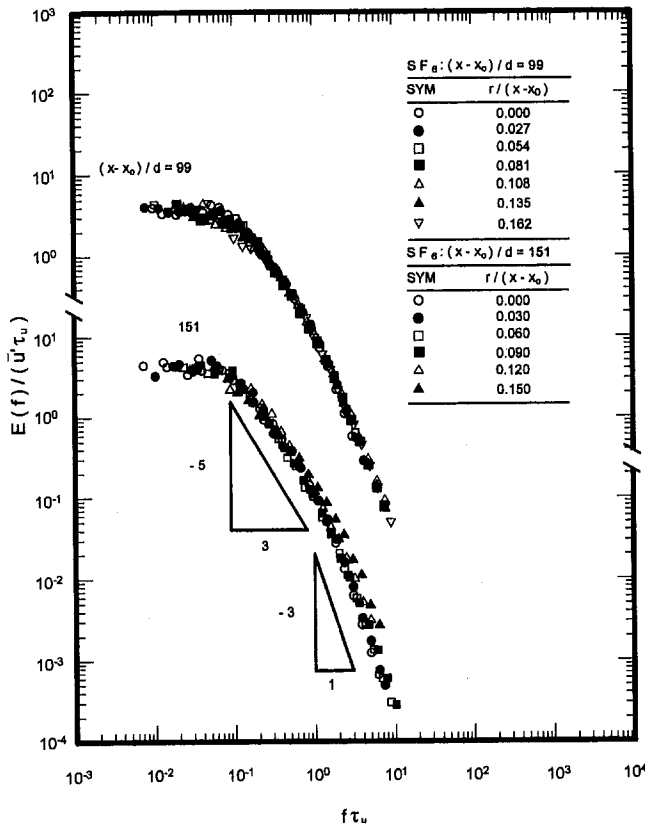


Fig. 6 Temporal power spectra of streamwise velocity fluctuations in the self-preserving portion of buoyant turbulent sulfur hexafluoride plumes

the axis of self-preserving plumes are slightly lower than for nonbuoyant jets, 0.22 in comparison to 0.25, see Papanicolaou and List (1988) for a discussion of existing turbulent jet data. Thus, buoyancy/turbulence interactions simultaneously act to reduce velocity fluctuation intensities, and to increase mixture fraction fluctuation intensities, near the axis of self-preserving turbulent plumes, in comparison to values found for nonbuoyant jets. Other properties of the velocity fluctuations in the self-preserving region of buoyant turbulent plumes are qualitatively similar to nonbuoyant turbulent jets (List, 1982). For example,  $\bar{v}' \approx \bar{w}'$  throughout the self-preserving region, while the outer edge of the flow is nearly isotropic, e.g.,  $\bar{u}' \approx \bar{v}' \approx \bar{w}'$  for  $r/(x - x_0) \geq 0.2$ . In contrast, the flow exhibits greater anisotropy near the axis, e.g.,  $\bar{u}' \approx 1.25\bar{v}' \approx 1.25\bar{w}'$  for  $r/(x - x_0) < 0.1$ . Finally, the region of peak values of  $\bar{u}'$ ,  $\bar{v}'$  and  $\bar{w}'$  is nearly the same, e.g.,  $r/(x - x_0)$  of roughly 0.05.

Some typical temporal power spectra of streamwise velocity fluctuations for the self-preserving region of the sulfur hexafluoride plumes are illustrated in Fig. 6. Results for the self-preserving region of the carbon dioxide plumes are similar. The spectra are relatively independent of radial position, when normalized in the manner of Fig. 6. The spectra initially decay according to the  $-5/3$  power of frequency, analogous to the well-known inertial-convection region for scalar property and velocity fluctuations in nonbuoyant turbulence (Tennekes and Lumley, 1972). At higher frequencies, however, there is a prominent region where the spectra decay according to the  $-3$  power of frequency, which has been observed before but only in buoyant turbulent flows (Dai et al., 1994; Mizushima et al., 1979; Papanicolaou and List, 1987, 1988). This region has been called the inertial-diffusive subrange, where the variation of the local rate of dissipation of velocity fluctuations in buoyant flows is due to buoyancy-generated inertial forces rather than viscous forces. This effect is plausible due to the progressive increase in the span of the inertial range

as  $(x - x_0)/d$ , or the plume Reynolds number, increases. For example, the intersections of the  $-5/3$  and  $-3$  subranges occur at higher values of  $n\tau_u$ , and  $(x - x_0)/d$  increases; similar behavior has been observed for mixture fraction fluctuations in the self-preserving region of buoyant turbulent plumes (Dai et al., 1994). At higher frequencies, power spectral densities should become smaller as the Kolmogorov scale is approached. However, present measurements could not resolve this region due to seeding limitations, which introduced effects of step noise.

The measured values of the temporal integral scales are illustrated in Fig. 7 for the self-preserving region of the two plumes. Additionally, streamwise spatial integral scales have been found from the temporal integral scale data using Taylor's hypothesis, e.g.,  $\Lambda_{ux} = \bar{u}'\tau_u$ , and are plotted in Fig. 7 as well. Self-preserving normalization has been used for both integral scales, similar to past treatment of integral scales relevant to mixture fraction fluctuations (Dai et al., 1994). Both integral scales approximate universal behavior for self-preserving conditions when plotted in the manner of Fig. 7. The spatial integral scale for streamwise velocity,  $\Lambda_{ux}$ , exhibits a slight reduction near the axis, which is not observed for spatial integral scales associated with mixture fraction fluctuations. The increase of  $\tau_u$  near the edge of the flow is similar to the behavior of  $\tau_f$  observed by Dai et al. (1994); this increase is caused by smaller mean velocities near the edge of the flow, combined with relatively uniform spatial integral scales, through Taylor's hypothesis,

**Reynolds Stress.** Present measurements of Reynolds stress for the self-preserving region of the two plumes are illustrated in Fig. 8. The measurements are seen to exhibit universal behavior throughout the self-preserving region, with  $\overline{u'v'} = 0$  at  $r = 0$ , and then increasing to a maximum value near  $r/(x - x_0) = 0.05$  (in the absolute sense), before decreasing to zero once again at large  $r$ . Notably, the region of the maximum Reynolds stress in Fig. 8 roughly corresponds to the region of maximum velocity fluctuations in Figs. 3-5.

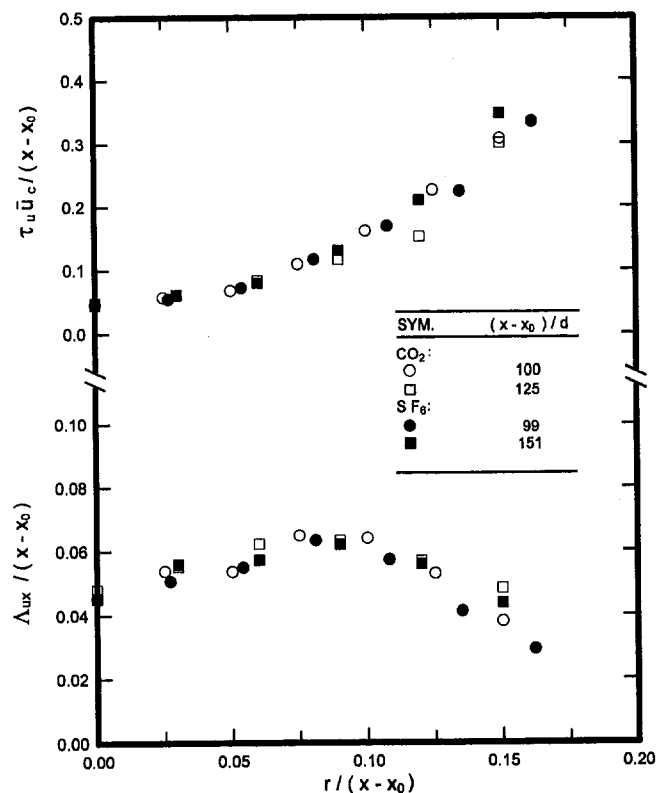


Fig. 7 Temporal and spatial integral scales of streamwise velocity fluctuations in self-preserving buoyant turbulent plumes

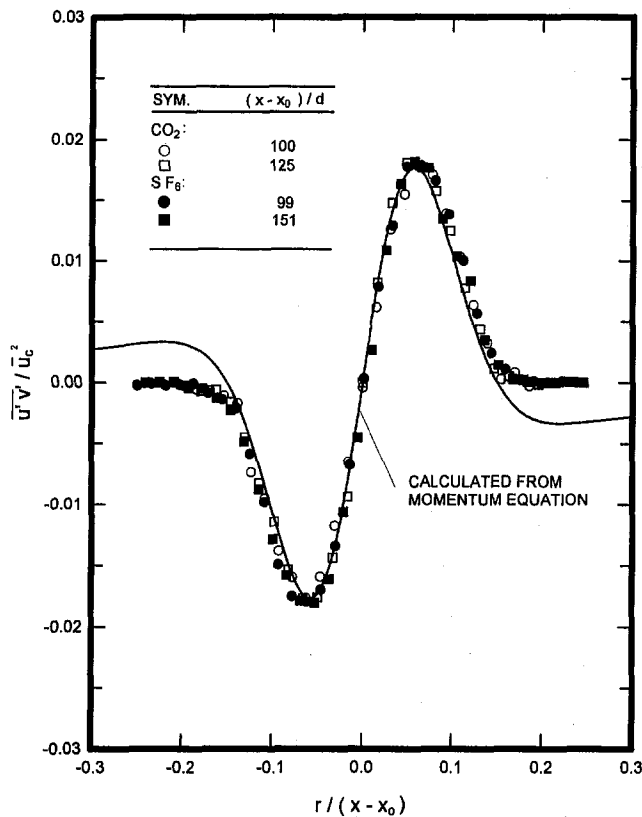


Fig. 8 Radial profiles of Reynolds stress in self-preserving buoyant turbulent plumes

The consistency of measured values of Reynolds stress with other measurements of mean and fluctuating quantities was evaluated, similar to the conservation of mass considerations for  $\bar{v}$ , discussed earlier. Imposing the approximations of a thin, boundary-layer-like plume flow, self-preserving conditions so that density variations are small, and neglecting viscous stresses in comparison to turbulent stresses, there results:

$$\bar{u}\partial\bar{u}/\partial x + \bar{v}\partial\bar{u}/\partial r = \partial/\partial x(\bar{v}'^2 - \bar{u}'^2) + g(1 - \rho_0/\rho_0)\bar{f} - \partial/\partial r(r\overline{u'v'})/r \quad (21)$$

Then, integrating Eq. (21), assuming  $(\bar{u}'^2 - \bar{v}'^2)/\bar{u}^2 \ll 1$ , and using the present correlations for  $\bar{u}$  and  $\bar{v}$  and the correlation for  $\bar{f}$  from Dai et al. (1994), all for the self-preserving portion of the flow, yields the following expression for Reynolds stresses:

$$\overline{u'v'}/\overline{u_c}^2 = (F(0)/(2\eta k_f^2 U(0)^2))(1 - \exp(-k_f^2 \eta^2)) + (\eta + 1/(3\eta k_u^2)) \exp(-2k_u^2 \eta^2) - 1/(3k_u^2 \eta^2) - \bar{u}\bar{v}/\overline{u_c}^2 \quad (22)$$

Equation (22) also is plotted in Fig. 8. In general, this relationship is in good agreement with the measurements, implying reasonably good internal consistency of the present data. The main discrepancies between Eq. (22) and present measurements of Reynolds stresses are observed near the edge of the flow. This difficulty is mainly thought to be due to errors in the fits of mean velocities and mixture fractions by Gaussian functions near the edge of the flow.

## Conclusions

Velocity statistics were measured in round buoyant turbulent plumes in still and unstratified air, in order to supplement earlier measurements of mixture fraction statistics for these flows due to Dai et al. (1994). The test conditions involved buoyant jet

sources of carbon dioxide and sulfur hexafluoride to give  $\rho_0/\rho_\infty$  of 1.51 and 5.06 and source Froude numbers of 7.80 and 3.75, respectively, with  $(x - x_0)/d$  in the range 87–151 and  $(x - x_0)/l_M$  in the range 12–43. The major conclusions of the study are as follows:

1 Present measurements yielded distributions of mean streamwise velocities in self-preserving plumes that were up to 40 percent narrower, with larger mean streamwise velocities near the axis (when appropriately scaled), and smaller entrainment rates, than earlier results in the literature. The reason for these differences is that the earlier measurements were limited to  $(x - x_0)/d \leq 62$ , which is not a sufficient distance from the source to observe self-preserving behavior. Notably, these observations confirm the earlier results of Dai et al. (1994) concerning the requirements for self-preserving buoyant turbulent plume behavior, based on measurements of mixture fraction statistics.

2 Radial profiles of velocity fluctuations in self-preserving buoyant turbulent plumes and nonbuoyant turbulent jets are similar: the streamwise component exhibits a dip near the axis with intensities at the axis of roughly 22 percent for buoyant turbulent plumes, and there is a tendency toward isotropic behavior near the edge of the flow. This behavior is in sharp contrast to mixture fraction statistics where mixture fraction fluctuations within buoyant turbulent plumes do not exhibit a dip near the axis, unlike nonbuoyant turbulent jets. Effects of buoyancy/turbulence interactions causing this contrasting behavior for velocity and mixture fraction statistics clearly merit further study.

3 The temporal power spectra of streamwise velocity and mixture fraction fluctuations are qualitatively similar: The low-frequency portions scale in a robust manner even in the transitional plume region, there is an inertial region where the spectra decay according to the  $-5/3$  power of frequency, and there is an inertial-diffusive region at higher frequencies where the spectra decay according to the  $-3$  power of frequency. The inertial-diffusive region has been observed by others for buoyant flows but is not observed in nonbuoyant flows; thus, the inertial-diffusive region is an interesting buoyancy/turbulence interaction that merits further study.

4 Past evaluations of turbulence models for buoyant turbulent flows, based on the assumption of self-preserving behavior for earlier measurements within buoyant turbulent plumes, should be reconsidered. In particular, present measurements suggest that such evaluations were compromised by effects of flow development because past measurements generally involved transitional plumes.

## Acknowledgments

This research was supported by the United States Department of Commerce, National Institute of Standards and Technology, Grant No. 60NANBID1175, with H. R. Baum of the Building and Fire Research Laboratory serving as Scientific Officer.

## References

- Abraham, G., 1960, "Jet Diffusion in Liquid of Greater Density," *ASCE J. Hyd. Div.*, Vol. 86, pp. 1–13.
- Becker, H. A., Hottel, H. C., and Williams, G. C., 1967, "The Nozzle-Fluid Concentration Field of the Round, Turbulent, Free Jet," *J. Fluid Mech.*, Vol. 30, pp. 285–303.
- Chen, C. J., and Rodi, W., 1980, *Vertical Turbulent Buoyant Jets: A Review of Experimental Data*, Pergamon Press, Oxford, p. 16.
- Dai, Z., Tseng, L.-K., and Faeth, G. M., 1994, "Structure of Round, Fully Developed, Buoyant Turbulent Plumes," *ASME JOURNAL OF HEAT TRANSFER*, Vol. 116, pp. 409–417.
- George, W. K., Jr., Alpert, R. L., and Tamanini, F., 1977, "Turbulence Measurements in an Axisymmetric Buoyant Plume," *Int. J. Heat Mass Trans.*, Vol. 20, pp. 1145–1154.
- Hinze, J. O., 1975, *Turbulence*, 2nd ed., McGraw-Hill, New York, pp. 175–319.
- Kotsovinos, N. E., 1985, "Temperature Measurements in a Turbulent Round Plume," *Int. J. Heat Mass Trans.*, Vol. 28, pp. 771–777.
- Kotsovinos, N. E., and List, E. J., 1977, "Turbulent Buoyant Jets. Part 1. Integral Properties," *J. Fluid Mech.*, Vol. 81, pp. 25–44.

- Kounalakis, M. E., Sivathanu, Y. R., and Faeth, G. M., 1991, "Infrared Radiation Statistics of Nonluminous Turbulent Diffusion Flames," *ASME JOURNAL OF HEAT TRANSFER*, Vol. 113, pp. 437–445.
- Lai, M.-C., and Faeth, G. M., 1987, "A Combined Laser-Doppler Anemometer/Laser-Induced Fluorescence System for Turbulent Transport Measurements," *ASME JOURNAL OF HEAT TRANSFER*, Vol. 109, pp. 254–256.
- List, E. J., 1982, "Turbulent Jets and Plumes," *Ann. Rev. Fluid Mech.*, Vol. 14, pp. 189–212.
- Mizushima, T., Ogino, F., Veda, H., and Komori, S., 1979, "Application of Laser-Doppler Velocimetry to Turbulence Measurements in Non-isothermal Flow," *Proc. Roy. Soc. London*, Vol. A366, pp. 63–79.
- Morton, B. R., Taylor, G. I., and Turner, J. S., 1956, "Turbulent Gravitational Convection From Maintained and Instantaneous Sources," *Proc. Roy. Soc. London*, Vol. A234, pp. 1–23.
- Morton, B. R., 1959, "Forced Plumes," *J. Fluid Mech.*, Vol. 5, pp. 151–163.
- Nakagome, H., and Hirata, M., 1977, "The Structure of Turbulent Diffusion in an Axisymmetrical Thermal Plume," *Heat Transfer and Turbulent Buoyant Convection*, D. B. Spalding and N. Afgan, eds., McGraw-Hill, New York, pp. 367–372.
- Ogino, F., Takeuchi, H., Kudo, I., and Mizushima, T., 1980, "Heated Jet Discharged Vertically in Ambients of Uniform and Linear Temperature Profiles," *Int. J. Heat Mass Trans.*, Vol. 23, pp. 1581–1588.
- Papanicolaou, P. N., and List, E. J., 1987, "Statistical and Spectral Properties of Tracer Concentration in Round Buoyant Jets," *Int. J. Heat Mass Trans.*, Vol. 30, pp. 2059–2071.
- Papanicolaou, P. N., and List, E. J., 1988, "Investigation of Round Vertical Turbulent Buoyant Jets," *J. Fluid Mech.*, Vol. 195, pp. 341–391.
- Papantoniou, D., and List, E. J., 1989, "Large Scale Structure in the Far Field of Buoyant Jets," *J. Fluid Mech.*, Vol. 209, pp. 151–190.
- Peterson, J., and Bayazitoglu, Y., 1992, "Measurements of Velocity and Turbulence in Vertical Axisymmetric Isothermal and Buoyant Plumes," *ASME JOURNAL OF HEAT TRANSFER*, Vol. 114, pp. 135–142.
- Rouse, H., Yih, C. S., and Humphreys, H. W., 1952, "Gravitational Convection From a Boundary Source," *Tellus*, Vol. 4, pp. 201–210.
- Seban, R. A., and Behnia, M. M., 1976, "Turbulent Buoyant Jets in Unstratified Surroundings," *Int. J. Heat Mass Trans.*, Vol. 19, pp. 1197–1204.
- Shabbir, A., and George, W. K., 1992, "Experiments on a Round Turbulent Buoyant Plume," NASA Technical Memorandum 105955.
- Tennekes, H., and Lumley, J. L., 1972, *A First Course in Turbulence*, M.I.T. Press, Cambridge, MA.
- Zimin, V. D., and Frik, P. G., 1977, "Averaged Temperature Fields in Asymmetrical Turbulent Streams Over Localized Heat Sources," *Izv. Akad. Nauk. SSSR, Mekhanika Zhidkosti Gaza*, Vol. 2, pp. 199–203.

# In-Depth Absorption of Externally Incident Radiation in Nongray Media

S. S. Manohar

A. K. Kulkarni

S. T. Thynell

Department of Mechanical Engineering,  
The Pennsylvania State University,  
University Park, PA 16802

*During flame spread along a surface, the thermal radiation emitted by high-temperature combustion products supports the advancement of the flame front. To model the response of the solid to the externally incident radiation, it is necessary to consider the spectral variation of radiative properties of the solid. For highly absorbent solids, such as wood or particle board, almost all of the externally incident radiation is absorbed at or very near the surface. However, for highly semitransparent materials, such as a plastic material whose surface is not clean, the externally incident radiation is absorbed both at the surface and within the material. In this work, the objective is to study both theoretically and experimentally the importance of in-depth radiation. A transient, one-dimensional model is formulated and solved numerically. The spectral radiative properties employed in the radiation model have been obtained from separate experiments on polymethylmethacrylate (PMMA), a clear plastic. The model demonstrates the importance of in-depth absorption. Model results exhibit the same trend as those revealed in experiments for the rise in surface temperature of the sample.*

## Introduction

The rate of flame spread along a surface depends upon the rate at which the surface just ahead of the pyrolysis front reaches its pyrolysis temperature. The effects from both thermal radiation and convection cause rapid heating of the unpyrolyzed surface to the pyrolysis temperature. If the flame contains a high concentration of soot and if the flame temperature is 1500 K or higher, the effects of thermal radiation are of particular importance. Examples of such situations include, among others, the case of burning walls within confined spaces where surrounding flames constitute a strong source of external radiation (Kulkarni, 1990; Ito et al., 1992) and emission from plumes of burning liquid pools (Klassen et al., 1992). To model the thermal response of semitransparent materials exposed to externally incident radiation, it is necessary to consider the effects of in-depth absorption, which includes spectral variation of the radiative properties.

Park and Tien (1990) performed a detailed analysis of the heating up and ignition of solid fuels subjected to radiation that included volumetric radiation absorption in both the gaseous and solid phases. For in-depth absorption in the solid, they used a gray model with a constant value of  $100 \text{ cm}^{-1}$  for the absorption coefficient. A nongray radiation model was employed by Song and Viskanta (1990) to study heating of ice by external radiation using a multiband, spectrally dependent absorption coefficient. Using a gray model, Finlayson et al. (1987) studied temperature profiles caused by in-depth absorption in polymeric solids and compared them to the opaque case. For clear plastics, such as polymethylmethacrylate (PMMA), the absorption coefficient is highly wavenumber dependent and much smaller (i.e., the radiation is absorbed much deeper inside the solid). As a result, it is necessary to measure the spectral variation of the absorption coefficient accurately in order to model the volumetric absorption of the incident radiation.

Flame spread driven by externally incident radiation has been studied experimentally and theoretically (Saito et al., 1989; Fernandez-Pello, 1977). However, these models treated the medium as opaque. Such an assumption results in a more rapid rise in

surface temperature and consequently in a greater rate of predicted flame spread. On the other hand, in-depth absorption results in distribution of the incident radiant energy within the material, and hence the surface temperature rises at a lower rate. Consequently, upward flame spread will be slower on a semitransparent medium.

In order to improve the predictive capabilities of ignition and flame spread across semitransparent materials, it is important to account for a spectral variation of the in-depth radiation absorption in the model. In particular, prediction of surface temperature requires detailed treatment of the interfacial conditions between the gas and solid phases. PMMA is a material commonly used in many practical applications as well as in flammability testing. The objective of the present work is to study the effects of in-depth radiation absorption on the surface temperature of a semitransparent material, using PMMA as an example. Analysis for a problem of one-dimensional, transient conduction with volumetric spectral radiation absorption is carried out and solved numerically to determine the surface temperature. The model accounts for spectral variation of the absorption coefficient and reflectivity. These properties are determined for PMMA using a Fourier transform infrared (FTIR) spectrometer. Experiments are conducted to measure the surface temperature of PMMA slabs subjected to a range of flux levels of externally incident radiation. The effect of in-depth absorption is then evaluated by comparing surface temperature histories of semitransparent slabs with clear versus absorbing front surfaces obtained from both model and experiments.

## Mathematical Model

**Assumptions.** A schematic of the model is shown in Fig. 1. The medium considered is either semitransparent or opaque. In a real fire situation, the surface well above the pyrolysis front may be clear initially, but becomes covered with a layer of soot as combustion progresses. Hence, it is necessary to consider one situation when the surface is clear and the other when the surface is covered with a layer of soot or dust. When the surface is covered with a layer of soot, most of the external radiation is absorbed at the surface, but the soot layer may reradiate some of this energy into the semitransparent medium and into the surroundings. However, if the medium is opaque, reradiation takes place into the surroundings only. When the surface is free of soot or dust, in-depth absorption takes place in the case of a semi-

Contributed by the Heat Transfer Division for publication in the JOURNAL OF HEAT TRANSFER. Manuscript received by the Heat Transfer Division January 1993; revision received March 1994. Keywords: Conjugate Heat Transfer, Fire/Flames, Radiation. Associate Technical Editor: W. L. Grosshandler.

transparent medium, whereas the opaque medium either reflects or absorbs the incident radiant energy at the surface. Based on this description, the mathematical model considers the following four cases:

- Case 1: The front surface is clear, and the medium is semi-transparent.
- Case 2: The front surface is clear, and the medium is opaque.
- Case 3: The front surface is absorbing (soot-covered), and the medium is semitransparent.
- Case 4: The front surface is absorbing (soot-covered), and the medium is opaque.

The difference in the thermal response between case 1 and case 2 illustrates the effect of in-depth absorption for clear samples, and the difference in the thermal response between case 3 and case 4 reveals a similar effect for surface-absorbing samples. The purpose of the proposed model is to predict the thermal response of the semitransparent or opaque medium. It employs the following set of assumptions:

- 1 The temperature distribution within the medium is one dimensional and transient.
- 2 The front surface at  $x = 0$  is subjected to externally incident radiation and convection.
- 3 The back surface at  $x = L$  is insulated and neither receives nor reflects any thermal radiation.
- 4 The externally incident radiation is diffuse.
- 5 Emission of thermal radiation from and scattering within the semitransparent medium is neglected.
- 6 The soot layer is a perfect emitter and a perfect absorber of thermal radiation.
- 7 In the surface temperature measurements, the external flux is not truly hemispherical. Hence, the normal spectral reflectivity obtained from measurements of PMMA has been used for the hemispherical spectral reflectivity.
- 8 The spectral emissive power of the external source (heated panel) is based on calibration measurements at the sample location, gray emissivity of the panel's surface, and temperature measurements of the panels.
- 9 Properties of PMMA are independent of temperature in the range of interest.
- 10 Properties of surrounding air are temperature dependent.

Some of these assumptions require further explanation. Regarding assumption 1, the length and width of a slab or wall material is usually much greater than its thickness in most applications of interest; therefore, the parameters of interest do not vary significantly with length or width. Assumption 3 is based on the fact that thermal-wave penetration is not deep for thick samples (typically 19 mm) employed in our relatively short duration experiments, and that the absorption of the incident radiation in PMMA is nearly complete at a depth of about 4 mm for the wavenumbers of interest (Daikoku et al., 1991). Reradiation from the medium will be most important very close to the surface, where the surface temperature is the highest. To justify assumption

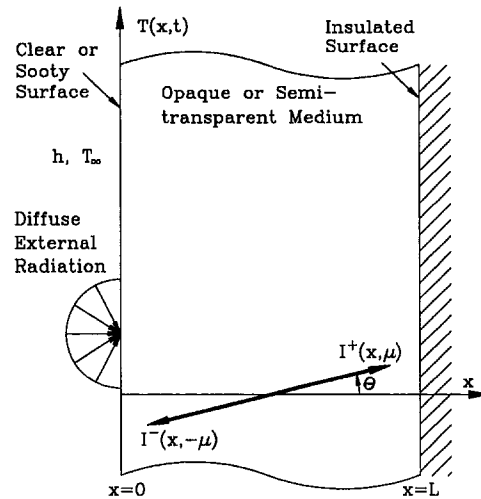


Fig. 1 Schematic of mathematical model

tion 5, the total forward intensity was compared to the reradiated intensity very close to the surface and was found to be less than 10 percent for the worst case scenario of the highest sample temperature and lowest external flux. For further justification of assumptions and more details, please refer to Manohar (1992).

**Formulation.** The energy equation within the solid is given by

$$k \frac{\partial^2 T}{\partial x^2} - S(x) = \rho C_p \frac{\partial T}{\partial t}, \quad 0 < x < L, \quad t > 0,$$

with initial condition

$$T = T_i, \quad 0 \leq x \leq L, \quad t = 0$$

and boundary condition

$$\frac{\partial T}{\partial x} = 0, \quad x = L, \quad t > 0.$$

The boundary conditions at  $x = 0, t > 0$ , are as follows:

Case 1: *Semitransparent solid with clear surface*

$$h(T_\infty - T) = -k \frac{\partial T}{\partial x}$$

Case 2: *Opaque solid with clear surface*

$$\int_0^\infty (1 - \rho_\nu) q_{e,\nu} d\nu + h(T_\infty - T) = -k \frac{\partial T}{\partial x}$$

Because the surface reradiation term is expected to be small for samples with clear surfaces, it is not included in this energy bal-

## Nomenclature

$a$  = absorption coefficient,  $m^{-1}$   
 $C$  = specific heat,  $J kg^{-1} K^{-1}$   
 $E$  = emissive power,  $W m^{-2}$   
 $h$  = heat transfer coefficient,  $W m^{-2} K^{-1}$   
 $I$  = radiation intensity,  $W sr^{-1} cm m^{-2}$   
 $k$  = thermal conductivity,  $W m^{-1} K^{-1}$   
 $L$  = thickness of slab,  $m$   
 $q$  = heat flux,  $W m^{-2}$   
 $T$  = temperature,  $K$ ; also, total transmittance  
 $\bar{T}$  = dimensionless temperature

$t$  = time,  $s$   
 $x$  = distance,  $m$   
 $\bar{x}$  = dimensionless distance  
 $\alpha$  = absorptivity  
 $\theta$  = angle of directional radiation  
 $\lambda$  = wavelength,  $\mu m$   
 $\mu$  =  $\cos \theta$  (see Fig. 1)  
 $\nu$  = wavenumber,  $cm^{-1}$   
 $\rho$  = density,  $kg m^{-3}$ ; also, reflectivity when subscripted  
 $\tau$  = transmittance of medium

## Subscripts

$b$  = blackbody  
 $e$  = external  
 $i$  = initial  
 $p$  = at constant pressure  
 $\infty$  = ambient  
 $\lambda, \nu$  = spectral

## Superscripts

$-$  = backward  
 $+$  = forward

ance. This also ensures that the same amount of energy is deposited on the opaque and semitransparent solids; consequently, the difference in surface temperature between cases 1 and 2 is due to in-depth absorption.

Case 3: *Semitransparent solid with surface covered with soot*

$$q_e + h(T_\infty - T) - 2E_b[T(0, t)] = -k \frac{\partial T}{\partial x}$$

Case 4: *Opaque solid with surface covered with soot:*

$$q_e + h(T_\infty - T) - E_b[T(0, t)] = -k \frac{\partial T}{\partial x}$$

The source term in Eq. (1) is

$$S(x) = -\frac{\partial q_r}{\partial x},$$

and for the opaque medium, it is

$$S(x) = 0.$$

In order to estimate the convective heat transfer, it is necessary to determine the heat transfer coefficient. The Nusselt number is determined using a correlation for a vertical surface at constant temperature (Churchill and Chu, 1975) since variation of temperature along the surface is not significant. During the experiments, however, the surface temperature is expected to vary from about 298 to 570 K; therefore, variable properties of air are used. For a semitransparent medium, the equation of transfer for a non-scattering and nonemitting medium is given by (Siegel and Howell, 1981),

$$\mu \frac{\partial I_\nu(x, \mu)}{\partial x} + a_\nu I_\nu(x, \mu) = 0, \quad 0 < x < L, \quad -1 \leq \mu \leq 1.$$

The radiation intensity is split into a forward  $I^+$  and backward direction  $I^-$ . The boundary conditions at  $x = 0$  and  $x = L$ , corresponding to the two cases involving a semitransparent medium described above are given by

$$\text{Case 1: } I_\nu^+(0) = (1 - \rho_\nu) q_{e,\nu} / \pi$$

$$\text{Case 2: } I_\nu^+(0) = E_{b,\nu}[T(0, t), \nu] / \pi$$

and, for both cases,  $I_\nu^-(L, -\mu) = 0, \mu > 0$ .

The solution to the radiation problem is immediately found as

$$I_\nu^+(x, \mu) = I_\nu^+(0) \exp(-a_\nu x / \mu), \quad \mu > 0,$$

$$I_\nu^-(x, -\mu) = 0, \quad \mu > 0.$$

Integration over all solid angles and wavenumbers yields an expression for the source term of the form

$$S(x) = 2\pi \int_0^\infty a_\nu I_\nu^+(0) E_2(a_\nu x) d\nu$$

where  $E_2(a_\nu x)$  is the exponential integral function. Spectral absorption coefficient and reflectivity are determined experimentally, as discussed in the following section. Finally, a solution to the transient heat conduction problem is obtained using the Crank-Nicholson scheme. The resulting finite-difference equations were solved using a Digital VAX computer.

## Experiments

Two series of experiments were conducted: radiation property measurements for input to the model, and transient surface temperature measurements for a slab in the presence of strong external radiation to verify the model.

**Absorption Coefficient and Reflectivity.** The mathematical model requires input of the spectral absorption coefficient and reflectivity of the surface. These properties were deduced from transmittance measurements for PMMA slabs of different thick-

ness, using an FTIR spectrometer. A wavenumber range from 12,000 to 500  $\text{cm}^{-1}$  was covered through two different combinations of detector and beam splitter. A potassium bromide beam-splitter was used with a mercury-cadmium-telluride (MCT) detector, and a quartz beam splitter was used with a lead selenide detector. Details of the FTIR experiments can be found from Manohar (1992). The data reduction procedure discussed below is similar to that used by Myers et al. (1983).

The spectral data obtained using the spectrometer represent the total transmittance ( $T_\nu$ ), that is, it accounts for multiple reflections within the semitransparent medium. To deduce the transmissivity ( $\tau_\nu$ ) and reflectivity ( $\rho_\nu$ ), one employs the relationship (Siegel and Howell, 1981),

$$\tau_\nu = \frac{-(1 - \rho_\nu)^2 + \sqrt{(1 - \rho_\nu)^4 + 4T_\nu^2 \rho_\nu^2}}{2T_\nu \rho_\nu^2}.$$

Transmittance data ( $T_\nu$ ) for at least two different sample thicknesses are necessary in order to solve for the two unknowns ( $a_\nu$ ) and ( $\rho_\nu$ ) at each wavenumber. The resulting pair of nonlinear, simultaneous equations is readily solved using the available software NEQNF (IMSL, 1984). Data for three different combinations of sample thicknesses were obtained and values were averaged. The repeatability of the transmittance data was verified by conducting additional experiments for another set of samples of the same thickness. Finally, the absorption coefficient,  $a_\nu$ , is calculated from

$$\tau_\nu = \exp(-a_\nu L).$$

**Surface Temperature Measurements.** In order to verify the accuracy of the model discussed earlier, experiments were carried out to determine the rise of surface temperature on two sets of PMMA samples subjected to a range of heat fluxes. In the first set, clear samples were used. In the second set, samples were covered with a flat black paint to simulate the presence of a layer of soot.

Figure 2 shows the experimental setup. A 12 cm  $\times$  12 cm  $\times$  1.9 cm PMMA sample was mounted in a sample holder. The sides and back face of the sample holder were insulated with ceramic fiber and then mounted on a steel framework. The sample was then subjected to external radiation by radiant panels placed in front of it. The power supplied to the radiant panels was varied with a silicon control rectifier (SCR) controller.

Four grooves of the depth approximately equal to the thermocouple bead diameter were cut into the sample, two on the front face and two on the back face. Thermocouples of 100  $\mu\text{m}$  diameter were mounted in these grooves. A few drops of a vol-

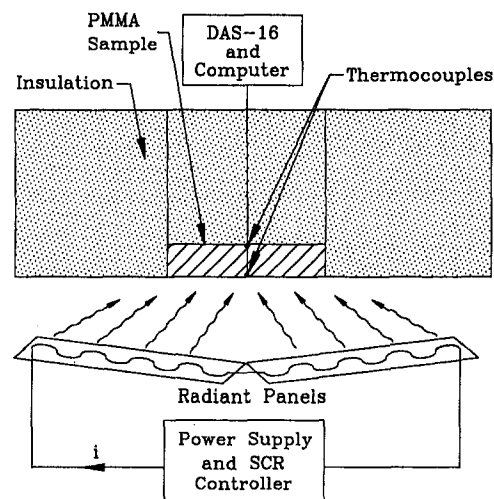


Fig. 2 Schematic of experimental setup

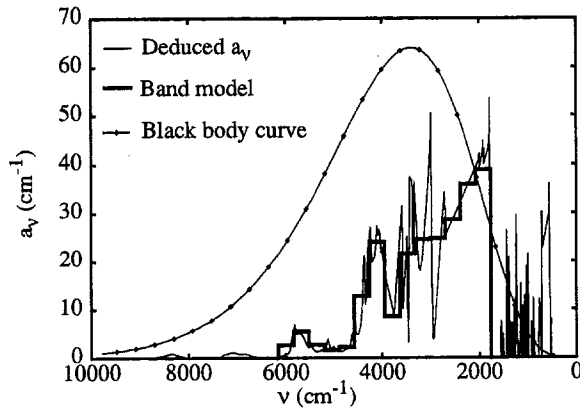


Fig. 3 Spectral absorption coefficient and the 14-band model. The superimposed blackbody curve shows the distribution of energy in this wavenumber regime.

atile solution added to the grooves then dissolved a small amount of PMMA. A thin layer of PMMA formed on the thermocouple bead and its wires; this ensured that the temperature read by the thermocouple was essentially that of the surface of the sample. The thermocouples were connected to a digital data acquisition system.

The error in surface temperature measurements was mainly due to the size of the junction and the uncertainty in positioning the thermocouple junction at the surface (about 0.5 mm), and the magnitude depended on the temperature gradient at the surface (between 6 to 40 deg per mm for heat flux between 3.7 and 16.2 kW/m<sup>2</sup>). In addition, there is an error due to difference in emissivities of thermocouple junction and PMMA surface, an error in measuring the heat flux itself (about 10 to 20 percent depending on heat flux level), and scatter in data (about 1.5 deg). Thus, the surface temperature data are accurate to within  $\pm 5$  to  $\pm 25$  deg. Since there are uncertainties in the model due to inexact property data and other assumptions, it is important to compare the data and model calculations *qualitatively*, while model calculations at various conditions can be compared *quantitatively*. The experiments were conducted primarily to observe any obvious relative effects of in-depth absorption on temperature profiles, and to observe the general trends of temperature at various conditions.

## Results and Discussion

**Radiation Properties.** The FTIR data obtained for clear PMMA samples revealed a relatively low transmittance in the near- and mid-infrared wavenumber ranges, from 1000 to 3000 cm<sup>-1</sup>, compared to wavenumbers over 4000 cm<sup>-1</sup>. Transmittance for soot-covered samples was found to be negligible compared to that of the clear samples due to high absorption in the soot layer on the surface. Figures 3 and 4 show the deduced spectral absorption coefficient and reflectivity, respectively. The absorption coefficient data in the region 1000 to 3000 cm<sup>-1</sup> show a number of spikes. This may be explained by examining the molecular structure of PMMA. The monomer unit of PMMA is C<sub>5</sub>H<sub>8</sub>O<sub>2</sub>. The region around 1000 cm<sup>-1</sup> corresponds to the bending of C-H, C-O-C, and C=O groups and the twisting frequencies of the methyl (CH<sub>3</sub>) and methylene (CH<sub>2</sub>) groups. The region around 3000 cm<sup>-1</sup> corresponds to the stretching frequency of the C-H bond in the methyl group (Silverstein et al., 1981). This region also has a high reflectivity, which explains the low transmittance values.

Figure 3 also shows the blackbody radiation spectrum at 1000 K and the 14-band model for the absorption coefficient. It should be noted that only 25 percent of the incident energy from a source having an equivalent blackbody emission at 1000 K is contained

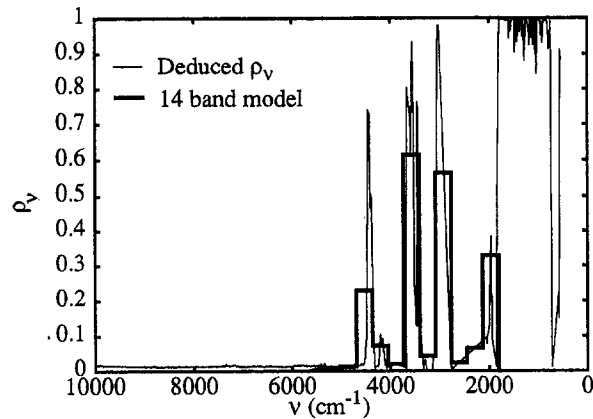


Fig. 4 Spectral reflectivity and the 14-band model

in the spectrum above 3300 cm<sup>-1</sup>. On the other hand, the spectral absorption coefficient changes in a highly nonlinear manner with the wavenumber, then rapidly diminishes above 3300 cm<sup>-1</sup>. The band model range is selected in such a way that below 1775 cm<sup>-1</sup> and above 6250 cm<sup>-1</sup> absorption of radiant energy changes from a volumetric to a surface phenomenon because the transmittance is negligible in those regions. The range between these two values is divided into 14 equal intervals, and within each interval the absorption coefficient is uniform. It should be noted that the in-depth absorption depends on both the spectral distribution of incident radiation and the spectral properties of the absorbing medium. Therefore, a carefully selected multiband model must be used in addressing the radiation problem. Table 1 shows the details of the experimentally determined band model used in the present problem.

**Surface Temperature Measurements.** Experiments were carried out for clear and blackened samples, using five different heat fluxes ranging from 3.7 to 23.2 kW/m<sup>2</sup>. Experimental data were recorded until either steady state was reached or the surface of the sample was completely covered with bubbles. Figure 5 shows the measured surface temperature of clear and surface-blackened PMMA samples for a heat flux of 16.2 kW/m<sup>2</sup>; results at other heat fluxes are not shown here for brevity. At the lowest level of heat flux (3.7 kW/m<sup>2</sup>), bubbles did not form at the surface of the PMMA sample before the surface temperature began to reach the steady-state value asymptotically. With an in-

Table 1 A 14-band model for spectral absorption coefficient and reflectivity

Wavenumber range (cm <sup>-1</sup> )	Absorption coefficient (cm <sup>-1</sup> )	Reflectivity
1800 - 2122	38.95	0.33
2122 - 2444	35.85	0.066
2444 - 2766	28.64	0.024
2766 - 3088	24.74	0.5643
3088 - 3410	24.53	0.0431
3410 - 3732	21.65	0.6151
3732 - 4054	8.70	0.019
4054 - 4376	24.07	0.0732
4376 - 4698	12.77	0.2301
4698 - 5020	2.26	0.013
5020 - 5342	1.70	0.0099
5342 - 5664	2.74	0.0097
5664 - 5986	5.55	0.0092
5986 - 6308	2.68	0.0061



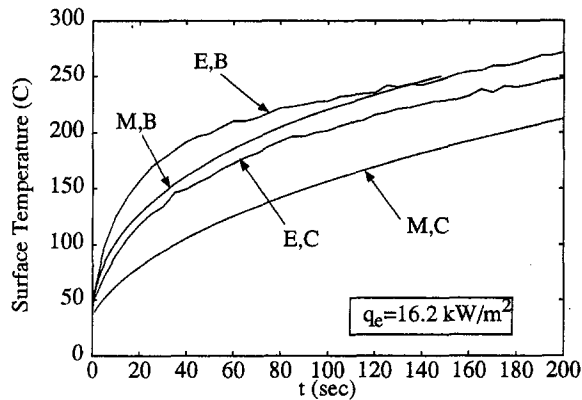


Fig. 5 Comparison between surface temperatures obtained by model and measured in experiments for clear and blackened surfaces at an external heat flux of 16.2 kW/m<sup>2</sup>. E = Experiment, M = Model, C = Clear surface, B = Blackened surface.

crease in the external flux, the rate of temperature rise became far more pronounced, with bubbles forming rapidly just beneath the surface. Because of convective loss at the surface and in-depth absorption, the highest temperature in the solid occurs at an interior location, not at the surface. Therefore, formation of bubbles under the surface is an indication of in-depth absorption. Recovered samples showed bubble formation just beneath the surface. For blackened PMMA samples, the general nature of the temperature rise was the same as in the clear samples. However, as the temperature of the surface increased, the time required for bubble formation at the surface decreased. This is to be expected, since a larger fraction of the externally incident radiation is absorbed by the blackened PMMA surface compared to the clear PMMA surface.

**Analytical Results.** For a given surface condition (clear or blackened) and heat flux, the difference between the opaque and semitransparent cases represents the effect of in-depth radiation absorption. Figure 6 shows the effect of in-depth absorption by comparison of profiles in dimensionless position and temperature,

$$\bar{T} = \frac{T - T_i}{(q/kA)\sqrt{\alpha t}}$$

and

$$\bar{x} = \frac{x}{\sqrt{\alpha t}}$$

The choice of dimensionless parameters is based on the classical solution for conduction in a semi-infinite medium with constant heat flux (Holman, 1986). Results of in-depth temperature distribution in opaque and semitransparent slabs subjected to fluxes of 3.7 kW/m<sup>2</sup> and 16.2 kW/m<sup>2</sup> at  $t = 125$  s, and a flux of 3.7 kW/m<sup>2</sup> at 2000 s, are presented in Fig. 6. The back face temperature of the slab at 125 s is essentially unchanged, indicating virtually no penetration of thermal wave to the back face. Thus, at shorter durations, the slab behaves like a semi-infinite medium and the dimensionless variables adequately predict the temperature distribution. However, the dimensionless variables are in general not appropriate in the present problem for three main reasons. First, the back surface temperature starts increasing significantly at relatively longer times and/or at higher fluxes encountered in the present problem (see, for example, results at  $t = 2000$  s, Fig. 6). Second, the external radiation is wavelength dependent, and so are surface reflectance and in-depth absorption properties. The actual amount of energy for a given incident flux, therefore, is not the same for an opaque slab and a semitrans-

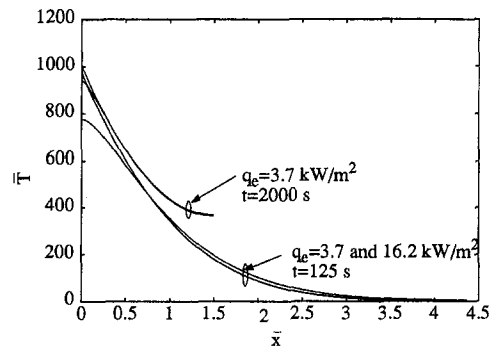


Fig. 6 Thermal wave penetration in dimensionless temperature and position coordinates. Profiles at  $t = 125$  s for the two fluxes coincide within the line thickness. In each set, the profile with lower surface temperature corresponds to the semitransparent medium and higher surface temperature corresponds to the opaque medium.

parent slab at different depths. Finally, the convective heat loss from the front surface depends on the surface temperature, which is different for the opaque and semiinfinite cases. Therefore, the remaining results are presented in actual variables.

Figure 7 shows the temperature profiles obtained for semitransparent and opaque media for different heat fluxes. Since in-depth absorption distributes energy within the solid, the surface temperature is expected to rise at a slower rate. The temperature profiles intersect just below the surface because the total energy deposited into the solid is the same, except for the convective loss. (Since the surface temperatures are different, the convective loss from the opaque medium is greater than that of the semitransparent medium; therefore, the two curves do not meet later.)

In applications such as upward flame spread, the heat-up time (time required to reach a critical temperature) is an important parameter. Figure 8 shows the effect of in-depth absorption on the rise of surface temperature at two different fluxes. As a representative case for the clear samples, the time required for the surface temperature to reach 150°C for the clear surface is recorded in Table 2 for several heat fluxes. A temperature of 150°C is selected because bubble formation does not occur at this temperature. At low heat fluxes, the difference is on the order of 10 percent. The temperature rise for both media is slow, and the surface temperature asymptotically reaches steady state. At higher heat fluxes, however, there is a significant increase in the heat-up time for the semitransparent sample, which requires more than twice the time to reach 150°C at a heat flux level of 16.2 kW/m<sup>2</sup> compared to the opaque sample. Clearly, a semitransparent medium will support upward flame spread at a slower pace than a similar opaque medium.

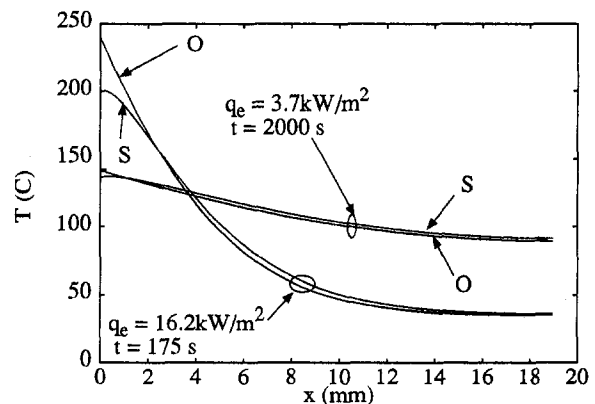


Fig. 7 Theoretical temperature profiles at two different conditions. O = Opaque medium, S = Semitransparent medium.

For blackened samples, it is observed that there is practically no difference in the rise of surface temperature for the two media. Both absorb the externally incident flux at the surface. Energy reradiated inward by the semitransparent medium's blackened surface is then absorbed in depth. This fraction of energy does not noticeably affect the surface temperature. The time required for the surface to reach a critical temperature is virtually the same. For the cases considered in this work, in-depth absorption does not significantly affect the thermal response of media with blackened surfaces.

**Comparison With Experiments.** The model results are compared to experiments in Fig. 5. Examination of this figure reveals a discrepancy between the model prediction and experiments. There are several reasons for this discrepancy. First, the model uses measured values of the heat flux. The temperature rise is extremely sensitive to the heat flux, and a small error in determining the heat flux significantly affects the heat-up time. Second, the model assumes temperature-independent properties for PMMA. Nonetheless, the model does predict the same trends as those established in the experiments.

When there is a fire in a confined space, a surface may be subjected to external radiation from surrounding burning walls before actually igniting. However, once combustion has been initiated, the surface is rapidly covered with soot. In the case of semitransparent materials, it will be important to account for in-depth absorption while analyzing heat up time. After ignition, however, the medium can effectively be considered opaque if there is soot deposition.

## Conclusions

An analysis has been carried out to determine the effects of in-depth absorption of externally incident radiation. The radiation model considered the spectral variation of the absorption coefficient, which was obtained from FTIR spectroscopy experiments. Surface temperature results from the model were also compared with those obtained from experiments on PMMA. Based on the results for PMMA slabs under external radiation, the following conclusions have been reached:

1 For clear surfaces, the rise of surface temperature is affected by in-depth absorption. Heat-up times are significantly longer for semitransparent media as opposed to opaque media. Upward flame spread on semitransparent media is, therefore, expected to be slower than on opaque media.

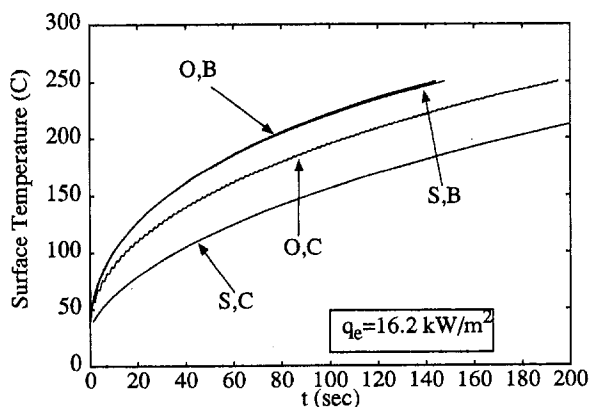


**Fig. 8** Rise of surface temperature for a PMMA slab. The difference between the clear and the opaque media represents the effect of in-depth absorption. External heat flux is  $16.2 \text{ kW/m}^2$ . O = Opaque medium, S = Semitransparent medium, C = Clear surface, B = Blackened surface.

**Table 2** Time required for surface temperature to reach  $150^\circ\text{C}$  for samples with clear surface

Flux ( $\text{kW/m}^2$ )	Time for semitransparent medium (s)	Time for opaque medium (s)	% difference (based on time for opaque medium)
3.7	2332	2130	9.5
6.8	662	513	29.0
12.5	155	95	63.1
16.2	91	49	85.7
23.1	46	19	142.1

2 For a blackened surface, opaque and semitransparent media have nearly the same surface temperature rise. Semitransparent media may thus be considered opaque for upward flame spread purposes when the surface is covered with soot or dust.

3 The radiation problem required the use of a fourteen-band model for PMMA to represent the spectral variation of surface reflectivity and absorption coefficient in order to adequately account for heating under external radiation.

4 The theoretical model demonstrates the same trends as the experiments.

## Acknowledgments

S. S. Manohar and A. K. Kulkarni gratefully acknowledge the support received from the National Institute of Standards and Technology under contract No. 60NANB8D0849. S. T. Thynell appreciates the support received from the Office of Naval Research under contract N00014-91-J-4116 with Dr. G. D. Roy serving as the contract monitor.

## References

- Churchill, S. W., and Chu, H. S., 1975, "Correlating Equations for Laminar and Turbulent Free Convection From a Vertical Plate," *Int. J. Heat Mass Transfer*, Vol. 18, pp. 1323-1329.
- Daikoku, M., Venkatesh, S., and Saito, K., 1991, private communication.
- Fernandez-Pello, A. C., 1977, "Upward Laminar Flame Spread Under the Influence of Externally Applied Thermal Radiation," *Comb. Sci. Technol.*, Vol. 17, pp. 87-98.
- Finlayson, E. U., Aung, W., and Kashiwagi, T., 1987, "Theoretical Models for Combined Radiation-Conduction in Polymeric Solids Heated by External Radiative Flux," *Proceedings of the 1987 ASME-JSME Thermal Engineering Joint Conference*, Honolulu, HI.
- Holman, J. P., 1986, *Heat Transfer*, 6th ed., McGraw-Hill, New York, p. 138.
- IMSL (International Mathematical and Statistical Libraries), 1984, 9th ed., GNB Bldg., 7500 Ballaire Blvd., Houston, TX 77036.
- Ito, A., Saito, K., and Inamura, T., 1992, "Holographic Interferometry Temperature Measurements in Liquids for Pool Fires Supported on Water," *ASME JOURNAL OF HEAT TRANSFER*, Vol. 114, pp. 944-949.
- Klassen, M., Sivathanu, Y. R., and Gore, J. P., 1992, "Simultaneous Emission Absorption Measurements in Toluene-Fueled Flames: Mean and rms Properties," *Combust. Flame*, Vol. 90, pp. 34-44.
- Kulkarni, A. K., 1990, "Heat Feedback in Vertical Wall Fires," *Experimental Heat Transfer*, Vol. 3, pp. 411-426.
- Manohar, S. S., 1992, "In-Depth Radiation Absorption in Semitransparent Materials," Master of Science Thesis, Mechanical Engineering, The Pennsylvania State University, University Park, PA.
- Myers, V. H., Ono, A., and DeWitt, D. P., 1983, "A New Method for Measuring Optical Properties of Semitransparent Materials at High Temperatures," presented at the 18th AIAA Thermophysics Conference, held in Montreal, Canada.
- Park, S. H., and Tien, C. L., 1990, "Radiation Induced Ignition of Solid Fuels," *Int. J. Heat Mass Transfer*, Vol. 33, pp. 1511-1520.
- Saito, K., Williams, F. A., Wichman, I. S., and Quintiere, J. G., 1989, "Upward Turbulent Flame Spread on Wood Under External Radiation," *ASME JOURNAL OF HEAT TRANSFER*, Vol. 111, pp. 438-445.
- Siegel, R., and Howell, J. R., 1981, *Thermal Radiation Heat Transfer*, 2nd ed., Hemisphere, New York.
- Silverstein, R. M., Bassler, G. C., and Morrill, T. C., 1981, *Spectrometric Identification of Organic Compounds*, 4th ed., Wiley, New York.
- Song, B., and Viskanta, R., 1990, "Deicing of Solids Using Radiant Heating," *AIAA Journal of Thermophysics and Heat Transfer*, Vol. 4, pp. 311-317.

# Computational Evaluation of Approximate Rayleigh–Debye–Gans/Fractal-Aggregate Theory for the Absorption and Scattering Properties of Soot

T. L. Farias  
Graduate Student.

M. G. Carvalho  
Professor.  
Mem. ASME

Mechanical Engineering Department,  
Instituto Superior Técnico,  
1096 Lisbon, Portugal

Ü. Ö. Köylü  
Research Fellow.

G. M. Faeth  
Professor.  
Fellow ASME

Department of Aerospace Engineering,  
The University of Michigan,  
Ann Arbor, MI 48109-2118

*A computational evaluation of an approximate theory for the optical properties of soot is described, emphasizing the small-angle (Guinier) regime. The approximate theory (denoted RDG-FA theory) is based on the Rayleigh–Debye–Gans scattering approximation while treating soot as mass-fractal aggregates of spherical primary particles that have constant diameters and refractive indices. The approximate theory was evaluated by more exact predictions from the solution of the volume integral equation formulation of the governing equations, using the method of moments, and based on the ICP algorithm of Iskander et al. (1989). Numerical simulations were used to construct statistically significant populations of soot aggregates having appropriate fractal properties and prescribed numbers of primary particles per aggregate. Optical properties considered included absorption, differential scattering, and total scattering cross sections for conditions typical of soot within flame environments at wavelengths in the visible and the infrared. Specific ranges of aggregate properties were as follows: primary particle optical size parameters up to 0.4, numbers of primary particles per aggregate up to 512, mean fractal dimensions of 1.75, mean fractal prefactors of 8.0, and refractive indices typical of soot. Over the range of the evaluation, ICP and RDG-FA predictions generally agreed within numerical uncertainties (ca. 10 percent) within the Guinier regime, complementing similar performance of RDG-FA theory in the power-law regime based on recent experiments. Thus, the use of approximate RDG-FA theory to estimate the optical properties of soot appears to be acceptable—particularly in view of the significant uncertainties about soot optical properties due to current uncertainties about soot refractive indices.*

## Introduction

Soot is present within most practical nonpremixed hydrocarbon-fueled flames, which affects their structure, radiation, and pollutant emission properties (Köylü and Faeth, 1993). Thus, the absorption and scattering (optical) properties of soot are needed to predict the continuum radiation properties of soot and to interpret nonintrusive optical measurements to find soot concentrations and structure. Soot optical properties are a challenging problem, however, due to the complexity of soot structure. For example, while soot generally consists of small spherical primary particles that individually satisfy the Rayleigh scattering approximation, these primary particles combine into branched aggregates that exhibit neither Rayleigh nor Mie scattering behavior (Dalzell et al., 1970; Jullien and Botet, 1987; Köylü and Faeth, 1993). However, a potentially useful approximate theory for soot optical properties (denoted RDG-FA theory in the following) recently has been developed, based on the Rayleigh–Debye–Gans (RDG) scattering approximation while assuming that soot aggregates are mass-fractal objects (Jullien and Botet, 1987; Martin and Hurd, 1987; Dobbins and Megaridis, 1991; Köylü and Faeth, 1994a). In particular, the approximate RDG-FA theory provides a computationally tractable way of treating complex populations of soot aggregates having widely varying numbers of primary particles per aggregate that must be considered for

practical applications (Köylü and Faeth, 1993, 1994a). Nevertheless, past theoretical and experimental evaluations of RDG-FA theory have not been definitive due to computational and experimental limitations (Köylü and Faeth, 1993, 1994a, b). Thus, the objective of the present investigation was to complete an additional theoretical evaluation of RDG-FA theory for soot, based on computations using a more exact theory (that unfortunately is not tractable for estimates of the optical properties of practical soot aggregates) for populations of mass-fractal aggregates having prescribed properties.

Although RDG-FA theories have been applied to estimate soot scattering properties and to interpret scattering measurements in order to find soot structure properties (Dobbins et al., 1990; Puri et al., 1993; Sorensen et al., 1992), there are significant uncertainties about some of the approximations of the theory for soot aggregates. In particular use of the RDG approximation requires that both  $|m - 1| \ll 1$  and  $2x_p|m - 1| \ll 1$  (Bohren and Huffman, 1983; Kerker, 1969; van de Hulst, 1957), which is questionable due to the large refractive indices of soot. Additionally, Berry and Percival (1986) argue that RDG theory should be effective for mass-fractal objects having  $D_f < 2$ , which is true for soot aggregates, when

$$N \ll x_p^{-D_f} \quad (1)$$

or if this criterion is not satisfied, when

$$x_p \ll \left[ \frac{|m^2 - 1| 2^{1-D_f} (D_f (D_f + 1))^{D_f/2}}{3(D_f - 1)(2 - D_f)} \right]^{1/(D_f - 3)} \quad (2)$$

The first criterion is rarely satisfied for soot aggregates. The second criterion generally requires  $x_p \ll 0.15$ , which also is not sat-

Contributed by the Heat Transfer Division for publication in the JOURNAL OF HEAT TRANSFER. Manuscript received by the Heat Transfer Division December 1993; revision received April 1994. Keywords: Combustion, Fire/Flames, Radiation. Associate Technical Editor: W. L. Grosshandler.

ified for a very wide range of soot properties, particularly in the visible portion of the spectrum, which usually is used for optical measurements of soot structure. Finally, recent computational studies suggest significant effects of multiple scattering for large soot aggregates, which is ignored when the RDG approximation is used (Berry and Percival, 1986; Chen et al., 1990; Ku and Shim, 1992a, b; Nelson, 1989). Thus, additional evaluation of RDG-FA theory is required before it can be recommended for predictions of soot optical properties.

In spite of these concerns about RDG-FA theory, however, recent experimental evaluations of the approach have been encouraging. These evaluations involved comparing RDG-FA scattering predictions, based on measured soot structure properties from thermophoretic sampling and analysis by transmission electron microscopy, with in situ scattering measurements for the same soot aggregate population. This work involved both large soot aggregates in the fuel-lean (overfire) region of buoyant turbulent diffusion flames, which emphasized the large-angle (power-law) scattering regime (Köylü and Faeth, 1994a), and small soot aggregates in the fuel-rich (underfire) region of laminar diffusion flames, which emphasized the small-angle (Guinier) scattering regime (Köylü and Faeth, 1994b). The predictions and measurements agreed within experimental uncertainties for both the power-law and Guinier regimes. This finding was reasonably definitive within the power-law regime, where the soot aggregate fractal properties that dominate aggregate scattering properties could be found accurately from structure measurements. The evaluation was less definitive in the Guinier regime, however, due to difficulties of accurately measuring both scattering properties at small angles and the higher moments of the aggregate size distribution function (e.g.,  $\bar{N}^2$ ) that dominate scattering properties at small angles (Köylü and Faeth, 1994a, b). This limitation is unfortunate because multiple-scattering effects that could compromise the use of RDG-FA theory are most significant in the Guinier regime (Nelson, 1989).

Existing computer simulations of the optical properties of soot also do not provide an adequate basis for evaluating RDG-FA scattering theory. In particular, problems of computational tractability for past computer simulations imply that they either involve fundamentally accurate solutions for small nonfractal aggregates where effects of multiple and self-induced scattering are small, or approximate solutions having uncertain accuracy for the large soot aggregates of interest for practical flames (Köylü and Faeth, 1993). Additionally, existing computations have been limited to relatively small samples of both orientations of given aggregates and aggregate configurations, raising questions about the statistical significance of the results (Köylü and Faeth, 1993).

To summarize, while the approximate RDG-FA approach offers a promising treatment of the optical properties of practical

soot aggregates, past experimental and theoretical evaluations have not provided a definitive assessment of the approach over the full range of interest. In particular, although acceptable performance of RDG-FA theory has been established in the power-law regime, comparable assessment in the Guinier regime has not been achieved. Thus, the objective of the present investigation was to undertake a theoretical evaluation of RDG-FA theory, emphasizing the Guinier regime. The evaluation was based on computations using the ICP approach of Iskander et al. (1989), which provides a more exact treatment of aggregate scattering in the Guinier regime than RDG-FA theory, by including effects of multiple and self-induced scattering. Problems of defining the higher moments of the size distribution functions of polydisperse aggregates during experiments were avoided by using numerical simulations to generate aggregates having prescribed sizes and mass-fractal properties.

## Theoretical Methods

**RDG-FA Scattering Theory.** The RDG-FA scattering theory is based on methods described by Freltoft et al. (1986), Jullien and Botet (1987), Lin et al. (1989), Martin and Hurd (1987), and Dobbins and Megaridis (1991). Present considerations, however, will be limited to the extended version due to Köylü and Faeth (1994a), which allows for the presence of the power-law regime when finding total scattering cross sections because this regime is important for large aggregates. The major assumptions of this approach with respect to soot aggregate physical properties are as follows: spherical primary particles have constant diameters, primary particles have uniform refractive indices, primary particles just touch one another, and the aggregates are mass-fractal objects. Justifications of these assumptions for soot aggregates are discussed by Köylü and Faeth (1993, 1994a).

The mass fractal approximation for aggregates of constant-diameter spherical primary particles implies the following relationship between the number of primary particles in an aggregate,  $N$ , and the radius of gyration of the aggregate,  $R_g$  (Jullien and Botet, 1987):

$$N = k_f (R_g/d_p)^{D_f} \quad (3)$$

The fractal dimension and prefactor in Eq. (3),  $D_f$  and  $k_f$ , appear to be relatively universal properties of soot aggregates, e.g., recent measurements for a variety of soot in flame environments indicate  $D_f = 1.77$  and  $k_f = 8.1$ , with standard deviations of 2 and 10 percent, respectively (Köylü and Faeth, 1993, 1994a, b). Thus, Eq. (3) provides a critical relationship between  $N$ , a quantity that is readily measured, and  $R_g$ , an important parameter required by RDG scattering theory.

## Nomenclature

$C$ = optical cross section	$k_f$ = fractal prefactor, Eq. (3)	$\rho_v^s$ = depolarization ratio
$d_e$ = equivalent sphere diameter	$m$ = refractive index of object = $n + i\kappa$	<b>Subscripts</b>
$d_i$ = diameter of object $i$	$n$ = real part of refractive index of object	$a$ = absorption
$d_p$ = primary particle diameter	$N$ = number of primary particles in an aggregate	$e$ = optically equivalent object
$D_f$ = mass fractal dimension, Eq. (3)	$q$ = modulus of scattering vector = $(4\pi/\lambda) \sin(\theta/2)$	$h$ = horizontal polarization
$E(m)$ = refractive index function = $\text{Im}((m^2 - 1)/(m^2 + 2))$	$R_g$ = radius of gyration of an object	$i$ = property of primary particle $i$
$f(qR_g)$ = aggregate form factor, Eq. (5)	$x_i$ = optical size parameter based on $d_i$ ; $x_i = \pi d_i/\lambda$	$ij$ = incident ( $i$ ) and scattered ( $j$ ) polarization directions
$F(m)$ = refractive index function = $ (m^2 - 1)/(m^2 + 2) ^2$	$\theta$ = angle of scattering from forward direction	$s$ = total scattering
$g(\lambda, R_g, D_f)$ = aggregate total scattering factor, Eq. (8)	$\kappa$ = imaginary part of refractive index of object	$v$ = vertical polarization
$i$ = $(-1)^{1/2}$	$\lambda$ = wavelength of radiation	<b>Superscripts</b>
$k$ = wave number = $2\pi/\lambda$		$a$ = aggregate property
		$p$ = primary particle property
		$(\bar{\quad})$ = mean value over aggregate size distribution

In addition to the RDG approximation, it is also assumed that the primary particles are small enough to satisfy the Rayleigh scattering approximation as individual particles. This is reasonable because primary particle optical size parameters generally are less than 0.4 for soot in the visible and infrared wavelength ranges, which implies that the total scattering and absorption cross sections of individual primary particles are within 1 and 5 percent, respectively, of estimates based on the Rayleigh scattering approximation for refractive indices typical of soot (Köylü and Faeth, 1993). This yields the following expressions for the absorption and scattering cross sections of individual primary particles (Bohren and Huffman, 1983; Kerker, 1969):

$$C_a^p = 4\pi x_p^3 E(m)/k^2, \\ C_s^p = 8\pi x_p^6 F(m)/(3k^2), \quad C_w^p = x_p^6 F(m)/k^2 \quad (4)$$

In Eq. (4), and the following equations, subscripts for differential scattering cross sections denote the direction of polarization vectors with respect to the scattering plane defined by the light source, the aggregate and the observer:  $v$  and  $h$  designate polarization vectors normal and parallel to this plane while the first and second subscripts designate incident and scattered light.

Under the RDG approximation, differential scattering cross sections for aggregates of a given size (after averaging over all orientations of each aggregate within a statistically significant monodisperse aggregate population) satisfy the following formulas (Kerker, 1969):

$$C_{vw}^a(\theta) = C_{hh}^a(\theta)/\cos^2 \theta = N^2 C_{vw}^p f(qR_g) \quad (5)$$

The form factor,  $f(qR_g)$ , is expressed as follows in the Guinier and power-law regimes (Freltoft et al., 1986; Jullien and Botet, 1987; Lin et al., 1989; Martin and Hurd, 1987):

$$f(qR_g) = \exp(-(qR_g)^2/3), \quad \text{Guinier regime} \quad (6)$$

$$f(qR_g) = (qR_g)^{-D_f}, \quad \text{power-law regime} \quad (7)$$

Adopting the proposal of Dobbins and Megaridis (1991), the boundary between the Guinier and power-law regimes is taken to be  $(qR_g)^2 = 3D_f/2$ , which is chosen to match the value and the derivative of  $f(qR_g)$  where the two regimes meet. The total scattering cross section then becomes:

$$C_s^a = N^2 C_s^p g(\lambda, R_g, D_f) \quad (8)$$

where  $g(\lambda, R_g, D_f)$  has different forms if the power-law regime is reached for  $\theta \leq 180$  deg, or not; see Köylü and Faeth (1994a) for these expressions. It also is assumed that absorption is not affected by aggregation, while the extinction cross section is the sum of the absorption and scattering cross sections by definition, i.e.,

$$C_a^a = NC_a^p, \quad C_e^a = C_a^a + C_s^a \quad (9)$$

The corresponding formulation for a polydisperse aggregate population, which is not needed here, can be found from Köylü and Faeth (1994a).

**ICP Scattering Theory.** Ku and Shim (1992a, b) review theories of aggregate optical properties more accurate than the RDG approximation. Various methods are considered but those of Borghese et al. (1984), Jones (1979a, b), Purcell and Pennypacker (1973), and Iskander et al. (1989) are emphasized. Borghese et al. (1984) developed an exact solution for the optical properties of clusters of spheres but this approach is computationally intensive and its practical accuracy is limited by the truncation of series expansions. The popular Jones (1979a, b) formulation, after correction of errors found by Kumar and Tien (1989) and Ku (1991), only includes multiple-scattering terms up to second order (based on the reciprocal of the distance between primary particles) and it was found to be less reliable than the rest. The Iskander et al. (1989) and Purcell and Pennypacker (1973) formulations both include multiple-scattering terms up to

third order in the reciprocal distance between primary particles; however, the latter formulation omits a self-interaction term that can be significant for practical aggregates. Based on these considerations, Ku and Shim (1992b) conclude that the ICP formulation of Iskander et al. (1989) was superior to the rest; therefore, this approach was adopted for the present calculations.

The soot aggregate structure approximations of the ICP and RDG-FA calculations were the same. In addition, each primary particle constituted an ICP computational cell, which implies that individual primary particles satisfy the Rayleigh scattering approximation, i.e., the internal electrical fields of primary particles are assumed to be uniform. This approximation is reasonable because errors are less than 10 percent for cross sections and near-forward scattering when  $x_p < 0.8|(m^2 + 5)/(2m^2 + 1)|$ , taking individual primary particles to be ICP computational cells (Ku and Shim, 1992b). The refractive index factor in this expression is roughly unity for soot, so that present calculations satisfied the criterion with a significant margin for  $x_p \leq 0.4$ .

The ICP approach involves first determining the internal field of each primary particle, and then finding the optical cross sections resulting from these fields. The formulation for these calculations is lengthy and Iskander et al. (1989) and Ku and Shim (1992b) should be consulted for details. Present results were obtained as averages obtained over various orientations of individual aggregates with respect to the direction of the incident field (in equally spaced spherical coordinate angles) and over populations of fractal aggregates of specified size,  $N$ , unless otherwise noted.

**Simulation of Aggregates.** Mountain and Mulholland (1988) generated aggregates using a simulation of cluster/cluster aggregation based on solution of the Langevin equations. This approach yields fractal aggregates that satisfy the power-law relationship of Eq. (3) with  $1.7 < D_f < 1.9$  and  $k_f$  circa 5.5, for  $N > 10$ . These sample aggregates subsequently were used by Chen et al. (1990) for ICP calculations of aggregate scattering properties. However, a larger sample of aggregates was required for the present work, and it was desired to have  $1.7 < D_f < 1.8$  and  $k_f$  circa 8.0 in order to correspond to recent observations of the fractal properties of soot aggregates (Köylü and Faeth, 1992, 1994a, b). As a result, an alternative aggregate simulation was used during the present investigation. The present numerical simulations of aggregates sought to create populations of aggregates by cluster/cluster aggregation, following Jullien and Botet (1987). The process started with individual and pairs of primary particles, which then were attached to each other randomly, assuming uniform distributions of the point and orientation of attachment but rejecting configurations where primary particles intersected. This procedure was continued in order to form progressively larger aggregates, but with the additional restriction that the aggregates should have  $1.7 < D_f < 1.8$  and  $k_f$  circa 8 for  $N > 8$ . It was observed that  $D_f$  fell naturally in the range 1.6–1.9 for  $N > 48$  during these simulations; therefore, few cluster/cluster combinations were rejected for inappropriate fractal properties when larger aggregates were constructed. Similarly, for  $D_f$  in the range 1.7–1.8, the value of  $k_f$  fell naturally near  $k_f = 8.0$  for statistically significant populations of aggregates.

Projected images of typical aggregates constructed using the present simulation are illustrated in Fig. 1 for  $N = 16, 64$ , and 256, which cover the range of mean aggregate sizes observed in nonpremixed flames (Köylü and Faeth, 1992, 1993, 1994a, b). The appearance of the aggregates varies considerably with the direction of projection, and from aggregate to aggregate within a population of given size. Nevertheless, the simulated aggregates are qualitatively similar to both past experimental observations of soot aggregates (Dalzell et al., 1970; Jullien and Botet, 1987; Köylü and Faeth, 1992, 1994a, b) and other numerical simulations of soot aggregates (Chen et al., 1990; Jullien and Botet, 1987; Mountain and Mulholland, 1988; Nelson, 1989). Combined with their prescribed fractal properties, this suggests

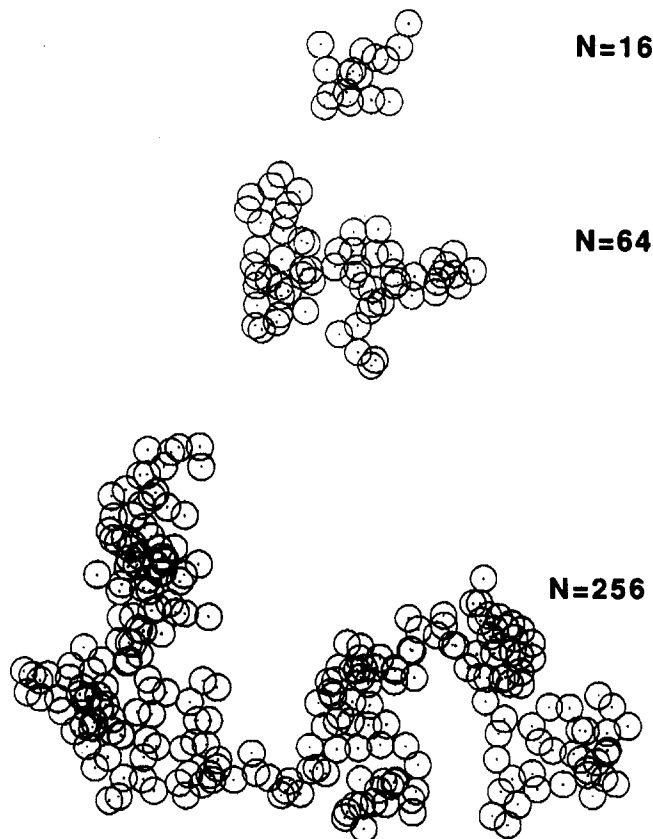


Fig. 1 Projected images of typical aggregates used in the computations for  $N = 16, 64,$  and  $256$

that the present simulated aggregate populations are reasonably representative of the structure of the soot aggregates found in flame environments.

## Results and Discussion

### Evaluation of ICP Predictions

**Spherelike Aggregate.** The ICP algorithm was checked by computing the scattering properties of spherelike aggregates, and comparing these results with Mie scattering predictions for an optically equivalent sphere. The configuration of the spherelike aggregate was similar to the arrangement considered by Purcell and Pennypacker (1973) and Ku and Shim (1992b), involving 136 spherical primary particles in a cubical lattice with the aggregate having a spherical outer boundary. For this arrangement, each primary sphere is bounded by a cube having an edge length of  $d_p$ , so that the diameter of the equivalent sphere is given by  $d_e = (6N/\pi)^{1/3} d_p$ , or  $d_e = 6.38 d_p$  for  $N = 136$ . In order to apply Mie scattering predictions to this aggregate, the following Maxwell-Garnett relationship was used to find the effective refractive indices for the equivalent sphere,  $m_e$ , noting that the volume fraction of the primary particle within its surrounding cubical volume is  $\pi/6$  (Ku and Shim, 1992b):

$$(m_e^2 - 1)/(m_e^2 + 2) = (\pi/6)(m^2 - 1)/(m^2 + 2) \quad (10)$$

The present calculations were carried out for various values of  $x_p$  with  $m = 1.60 + 0.60i$ , which is a typical value of the complex refractive index of soot (Charalampopoulos, 1992). This implies  $m_e = 1.33 + 0.25i$  from Eq. (10).

Predictions of normalized differential scattering patterns,  $k^2 C_{vv}^a(\theta)$ , as a function of  $\theta$  and  $x_p$ , are illustrated in Fig. 2 for the spherelike aggregate. The results include Mie scattering predictions for an equivalent sphere, as well as ICP predictions for

both a single orientation and averaged over 128 orientations of the aggregate. At small angles, within the Guinier regime, effects of orientation averaging are small and the agreement between the Mie and ICP predictions is excellent for the full range of  $x_p$  considered ( $x_p \leq 0.5$ ). This behavior agrees with the small-angle criterion for ICP cell sizes of Ku and Shim (1992b), discussed earlier, and helps to justify the use of ICP predictions to evaluate RDG-FA theory in the Guinier regime. ICP also yields similar performance for the complete range of scattering angles for  $x_p \leq 0.25$ . At large angles for  $x_p = 0.5$ , however, effects of orientation averaging become more important, as discussed subsequently, and there are considerable discrepancies between ICP and Mie scattering predictions, which are caused by truncation errors due to excessively large ICP cell sizes. Thus, the use of ICP to estimate the differential scattering properties of aggregates having large  $x_p$  is questionable at large angles.

**Fractal Aggregates.** The next issues to be established are the number of orientations (in spherical coordinate angles, as noted earlier) of individual aggregates, and the number of individual aggregates, that should be averaged in order to obtain statistically significant ICP predictions. The required numbers of realizations increased with increasing  $N$ ,  $m$ , and  $x_p$ ; therefore, effects of averaging are illustrated in Fig. 3 for  $N = 256$ ,  $m = 1.57 + 0.57i$ , and  $x_p = 0.4$ , which represents a conservative condition for present calculations and a typical refractive index of soot (Charalampopoulos, 1992). The results shown include  $vv$  scattering patterns for a single realization (a particular aggregate and orientation) as well as average values and standard deviations for 128 orientations of one aggregate and single orientations (each) of a population of 128 aggregates. The results for a single realization exhibit a complex scattering pattern, particularly at larger scat-

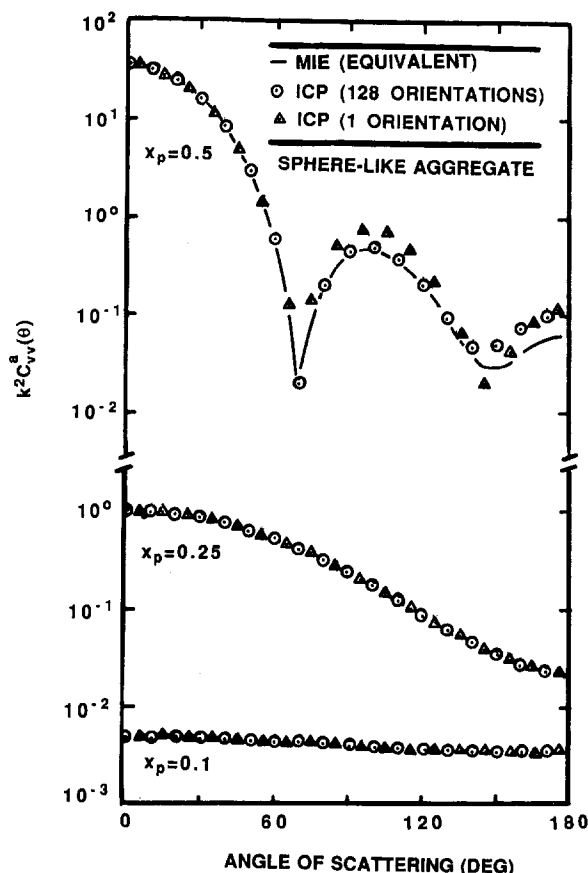


Fig. 2 Normalized  $vv$  scattering patterns for a spherelike aggregate, computed using ICP and Mie scattering for an equivalent sphere ( $N = 136$ ,  $m = 1.60 + 0.60i$ ,  $m_e = 1.33 + 0.25i$ ,  $x_e = 6.38x_p$ )

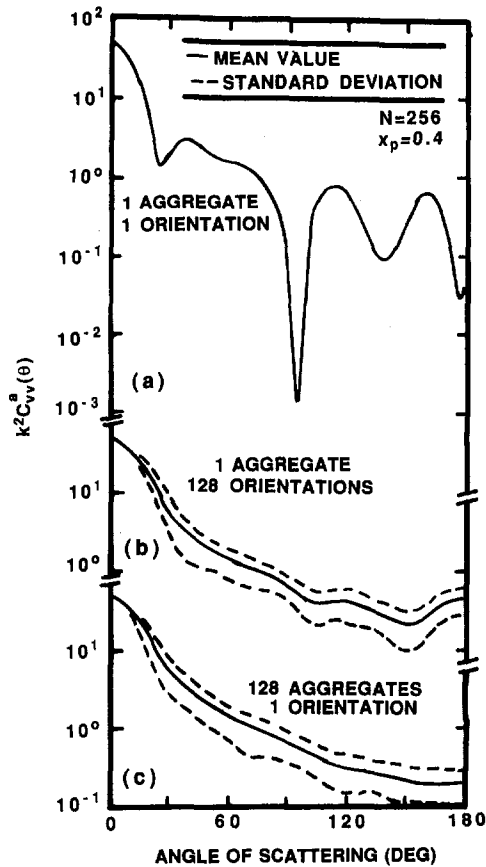


Fig. 3 Normalized  $vv$  scattering patterns for fractal aggregates computed using ICP ( $N = 256$ ,  $D_f = 1.72$ ,  $k_f = 8.0$ ,  $\lambda = 514.5$  nm,  $m = 1.57 + 0.57i$  and  $x_p = 0.4$ ): (a) results for a single aggregate and orientation, (b) results for a single aggregate averaged over 128 orientations, (c) results for a single orientation averaged over 128 aggregates

tering angles, due to interference effects for this particular aggregate array and incident wave propagation direction. Naturally, such patterns are not observed for scattering from practical soot aggregates because aggregate orientations are random and scattering patterns involve averages over very large aggregate populations.

The smoothing of scattering patterns due to averaging is evident from the results considering orientation and aggregate averaging in Fig. 3. Thus, the scattering patterns based on averages decay smoothly, and optical properties are relatively independent of the method of averaging, at small and moderate angles ( $\theta < 30$  deg), which is critical for present evaluation of RDG-FA theory. Oscillations begin to appear with increasing angle, particularly when only one aggregate is considered; nevertheless, the performance of ICP for  $x_p = 0.4$  is suspect at these conditions in any event, based on the results discussed in connection with Fig. 2. Similarly, the standard deviations of the cross sections over the sample populations progressively increase with increasing scattering angle. This latter behavior is similar to results found by Mountain and Mulholland (1988) for RDG scattering calculations using numerically simulated populations of aggregates, and reflects the increasing importance of the aggregate arrangement as the scattering angle increases. For example, under the RDG scattering approximation, the form factor is nearly unity in the small-angle (Guinier) scattering regime and scattering mainly depends upon the number of primary particles in the aggregates, see Eq. (6). In contrast, the form factor depends strongly on the aggregate arrangement through the values of  $R_g$  and  $D_f$  in the large-angle (power-law) scattering regime; see Eq. (7). Thus, the largest angle controls the requirements for sam-

pling to achieve statistically significant ICP predictions of differential scattering patterns.

Based on the previous considerations, 64 aggregates, each sampled at 16 orientations, were used to obtain a numerical uncertainty (95 percent confidence) less than 10 percent for ICP predictions of differential scattering cross sections at 180 deg. Fewer realizations were required to obtain statistically significant absorption and total scattering cross sections. Thus, using as few as four orientations of eight aggregates still yielded numerical uncertainties (95 percent confidence) less than 5 percent for ICP predictions of these two cross sections. Naturally, these estimates do not include effects of deficiencies of ICP predictions at large angles and  $x_p$ , noted earlier.

#### Evaluation of RDG-FA Predictions

**Differential Scattering Cross Sections.** Figure 4 is an illustration of RDG-FA and ICP predictions of  $C_{vv}^a(\theta)/(NC_w^p)$  as a function of the radiation momentum,  $qd_p$ , for aggregates having  $D_f = 1.75$ ,  $k_f = 8.0$ ,  $m = 1.57 + 0.57i$ , and  $x_p$  up to 0.4 for  $\lambda = 514.5$  nm. The results for large  $x_p$  represent severe conditions: rather large primary particles, refractive indices typical of soot, and a wavelength provided by argon-ion lasers that frequently is used for nonintrusive measurements of soot properties. Results are plotted for aggregates of various size, considering  $N = 16$ , 64, and 256—the last representing a reasonable limit for ICP calculations in view of current computer capabilities and the sampling requirements needed to achieve the computational uncertainties stated earlier, and representative of maximum mean aggregate sizes observed in nonpremixed flames (Köylü and Faeth, 1992, 1993, 1994a, b). The predictions are terminated at values of  $qd_p$  that correspond to  $\theta = 180$  deg.

The RDG-FA results illustrated in Fig. 4 exhibit extended Guinier regimes for the range of aggregate properties considered, reaching  $C_{vv}^a(\theta)/(NC_w^p) = N$  at small values of  $qd_p$ , as anticipated from Eqs. (5) and (6). It is seen that there are progressively larger regions of power-law behavior, where the slopes of the RDG-FA plots approach  $-D_f$  according to Eqs. (5) and (7), as both  $x_p$  and  $N$  increase. This can be explained by noting that the maximum value of  $qd_p = 4x_p$  at  $\theta = 180$  deg, which implies a greater range of  $qd_p$  as  $x_p$  increases, while the boundary between the Guinier and power-law regimes can be represented as  $qd_p = (3D_f/2)^{1/2}(k_f/N)^{1/D_f}$ , which implies smaller values of  $qd_p$  at the onset of the power-law regime as  $N$  increases for given aggregate fractal properties. Another feature of the normalization used in Fig. 4 is that the RDG-FA results become universal in the power-law regime for given aggregate fractal properties. This can be seen by eliminating  $R_g$  from Eqs. (5) and (7), using Eq. (3), to yield the following relationship for the power-law regime:

$$C_{vv}^a(\theta)/(NC_w^p) = k_f(qd_p)^{-D_f} \quad (11)$$

Thus, RDG-FA predictions only depend on the values of the fractal properties and  $qd_p$  within the power-law regime, and reach an intercept of  $k_f = 8.0$  at  $qd_p = 1$  if this value of  $qd_p$  is within the power-law regime.

For the conditions considered in Fig. 4, the comparison between ICP and RDG-FA predictions is excellent throughout the Guinier regime. For example, the maximum discrepancy between the two predictions within the Guinier regime is roughly 15 percent for forward scattering at  $x_p = 0.4$  and  $N = 256$  (see Fig. 4c). Additionally, discrepancies at other conditions within the Guinier regime generally are less than 10 percent, with comparable agreement over the entire available range of scattering angles for  $x_p \leq 0.2$  (see Figs. 4a, b). Thus, for the range of conditions where ICP predictions are reliable, in view of the results discussed in connection with Fig. 2, RDG-FA predictions seem generally satisfactory based on agreement with ICP predictions.

The comparison between RDG-FA and ICP predictions is less satisfactory in the power-law regime for  $x_p = 0.4$  (see Fig. 4c); however, this behavior does not imply a deficiency of RDG-FA

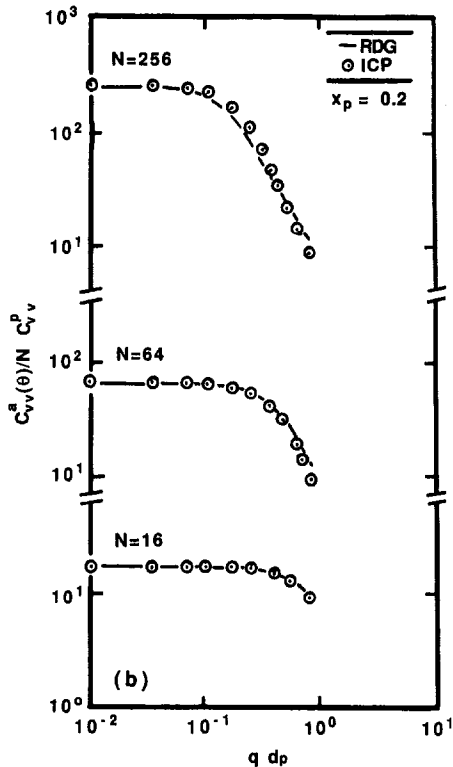
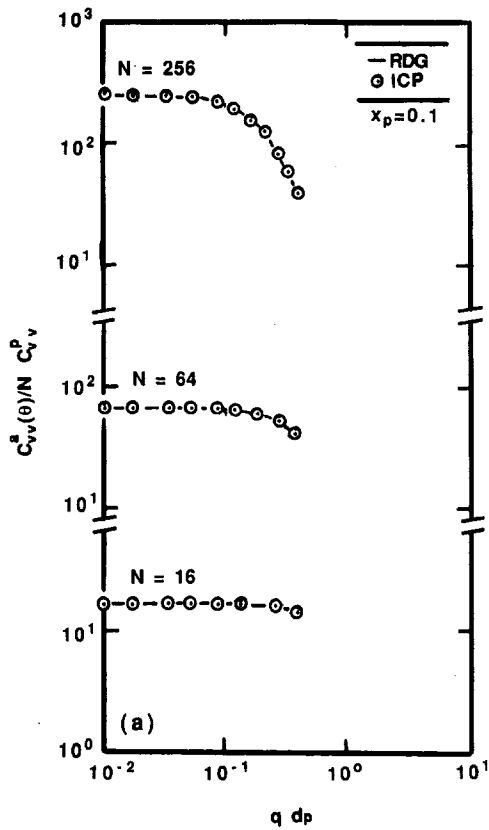


Fig. 4 Normalized  $vv$  scattering cross sections as a function of the radiation momentum for fractal aggregates of various size, computed using the ICP and RDG-FA methods ( $D_f = 1.75$ ,  $k_f = 8.0$ ,  $\lambda = 514.5$  nm,  $m = 1.57 + 0.57i$ ): (a)  $x_p = 0.1$ , (b)  $x_p = 0.2$ , (c)  $x_p = 0.4$

theory. In particular, past experimental evaluations in the power-law regime are reasonably definitive and indicate satisfactory performance for RDG-FA theory (Köylü and Faeth, 1994a, b), as noted earlier. In contrast, ICP predictions are not very satis-

factory at large angles and  $x_p$  due to truncation errors, as discussed in connection with Fig. 2. The main problem is that ICP overestimates the rate of decrease of  $C_{vv}^a(\theta)$  with increasing  $q d_p$  for soot aggregates in the power-law regime. This behavior yields slopes of the ICP plots in Fig. 4(c) that are greater than  $-D_f$  from Eq. (11), which contradicts a well-established property of soot aggregates having an extended power-law regime (Köylü and Faeth, 1993, 1994a, b).

Normalized differential scattering patterns found from both the ICP and RDG-FA theories are illustrated in Fig. 5. The results are plotted as  $k^2 C_{vv}^a(\theta)$  in order to highlight effects of aggregate size on differential scattering patterns. The aggregate properties for these calculations are the same as Fig. 4, except that only the worst-case condition,  $x_p = 0.4$ , has been illustrated. For the properties used to construct Fig. 5, scattering is in the power-law regime at 90 deg for the RDG-FA predictions. Then evaluating  $C_{vv}^a(\theta)$  at 0 and 90 deg from Eqs. (5)–(7) yields:

$$\begin{aligned} C_{vv}^a(0 \text{ deg})/C_{vv}^a(90 \text{ deg}) \\ = C_{hh}^a(0 \text{ deg})/C_{hh}^a(90 \text{ deg}) = N(2\sqrt{2}x_p)^{D_f}/k_f \end{aligned} \quad (12)$$

Thus, Eq. (12) explains the increase of the normalized  $vv$  and  $hh$  scattering cross sections in the forward-scattering direction seen in Fig. 5 as  $N$  is increased, as well as a corresponding increase when  $x_p$  is increased, which is not illustrated in the figure. Similarly, within the power-law regime, Eqs. (5) and (7) yield:

$$\begin{aligned} C_{vv}^a(\theta)/C_{vv}^a(90 \text{ deg}) = C_{hh}^a(\theta)/(\cos^2 \theta C_{vv}^a(90 \text{ deg})) \\ = (\sqrt{2} \sin(\theta/2))^{-D_f} \end{aligned} \quad (13)$$

Thus, Eq. (13) implies that variations of  $vv$  and  $hh$  differential scattering cross sections with scattering angle are controlled by  $D_f$  in the power law regime.

The RDG-FA predictions of  $C_{hh}^a(\theta)$  in Fig. 5 were corrected for effects of depolarization ratios by analogy to Rayleigh scattering theory (Rudder and Bach, 1968) using the approach of

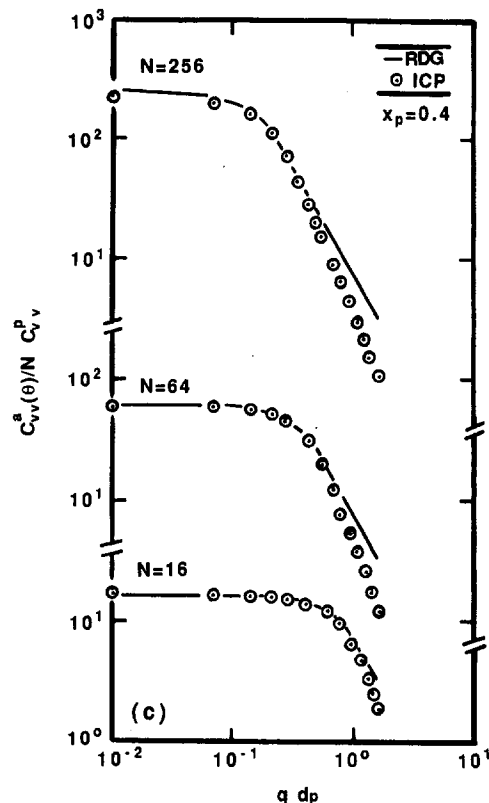


Fig. 4. (Continued)



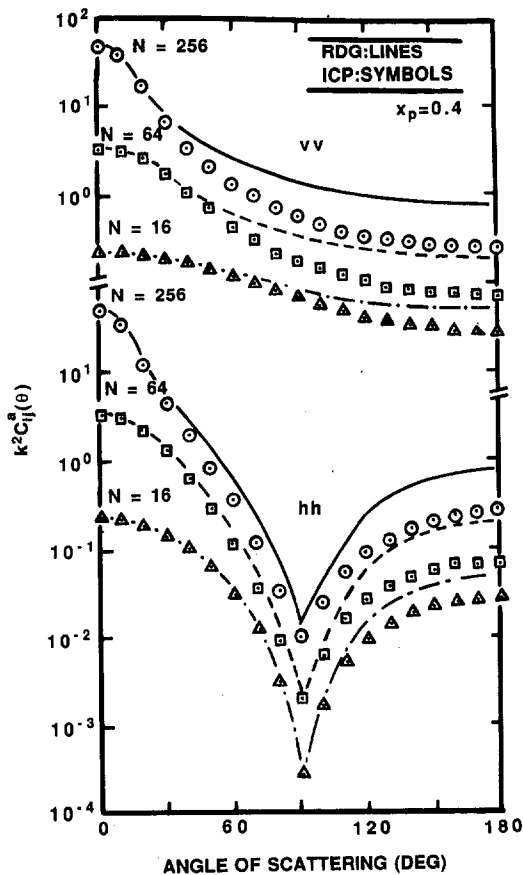


Fig. 5 Normalized scattering patterns for fractal aggregates of various size, computed using the ICP and RDG-FA methods ( $D_f = 1.75$ ,  $k_f = 8.0$ ,  $\lambda = 514.5$  nm,  $m = 1.57 + 0.57i$ , and  $x_p = 0.4$ )

Köylü and Faeth (1994a). These corrections were based on depolarization ratios,  $\rho_v^a = 0.0035, 0.0071, 0.0113$ , for  $N = 16, 64$ , and  $256$ , respectively, from the ICP predictions. After correcting  $C_{hh}^a(\theta)$  for RDG-FA predictions in this manner, the agreement between RDG-FA and ICP predictions in Fig. 5 is within numerical uncertainties throughout the Guinier regime (roughly  $\theta < 20, 40$ , and  $90$  deg for  $N = 256, 64$ , and  $16$ , respectively). As discussed earlier, ICP predictions underestimate scattering levels at larger angles due to truncation errors at large  $x_p$ , accounting for the discrepancies between the two predictions in this region. However, results similar to Fig. 5 indicated good agreement between the two theories at all angles for  $x_p \leq 0.2$ , similar to the findings illustrated in Fig. 4.

Effects of refractive indices on the comparison between ICP and RDG-FA predictions also were considered. The variations of  $m$  were carried out by taking  $n = 1 + \kappa$  and  $|m - 1| = 0.2, 0.4$ , and  $0.8$ . This procedure yields progressively increasing refractive indices with the largest values corresponding to typical values for soot in the visible wavelength range (Charalampopoulos, 1992). Other properties of these calculations were similar to the results illustrated in Figs. 4 and 5. The comparison between ICP and RDG-FA predictions of the differential scattering cross sections as refractive indices varied was similar to results discussed in connection with Figs. 4 and 5. In particular, the agreement between the two predictions was within numerical accuracies at small and moderate angles (roughly  $\theta < 30$  deg), while ICP predictions tended to underestimate scattering levels at large angles where they are less reliable.

**Absorption and Total Scattering.** The last phase of the present evaluation of RDG-FA theory was to consider absorption and total scattering cross sections. Figure 6 is an illustration of nor-

malized absorption and total scattering cross sections from the ICP and RDG-FA predictions plotted as a function of  $N$  for various values of  $x_p$ . The other parameters of these calculations were similar to Figs. 4 and 5; that is,  $D_f = 1.75$ ,  $k_f = 8.0$ ,  $\lambda = 514.5$  nm and  $m = 1.57 + 0.57i$ . As noted earlier, reduced sampling requirements to obtain statistically significant values of these cross sections allowed maximum values of  $N$  up to 512 to be considered for the ICP predictions.

The ICP predictions of normalized absorption cross sections,  $C_s^a/(NC_s^p)$ , remain within 10 percent of unity for the conditions illustrated in Fig. 6, even including questionable values for  $x_p = 0.4$  at large  $N$ . This is in good agreement with RDG-FA predictions where this ratio is unity from Eq. (9), i.e., the absorption of primary particles in aggregates is identical to the absorption of individual primary particles. In contrast, both predictions of  $C_s^a/(NC_s^p)$  increase with increasing  $N$ , with the rate of increase gradually decreasing as  $N$  increases. This latter effect is observed because fractal aggregate scattering becomes saturated at large  $N$  for  $D_f < 2$ ; in contrast, for  $D_f > 2$ ,  $C_s^a/(NC_s^p)$  continues to increase without bound as  $N$  increases (Berry and Percival, 1986; Dobbins and Megaridis, 1991). In particular, RDG-FA theory yields the following expression for  $C_s^a/(NC_s^p)$  at large  $N$  (Köylü and Faeth, 1994a):

$$C_s^a/(NC_s^p) = k_f(4x_p)^{-D_f}(3/(2 - D_f) - 12/((6 - D_f)(4 - D_f))) \quad (14)$$

Thus, for given fractal properties,  $C_s^a/(NC_s^p)$  is independent of  $N$  for large  $N$ , with this plateau value tending to decrease as  $x_p$  increases. Present predictions in Fig. 6 do not extend to large enough values of  $N$  to reach the plateau condition; however, both predictions are in good agreement over the range of conditions that are illustrated for  $x_p \leq 0.2$ . In contrast, problems with ICP predictions at large angles for  $x_p = 0.4$  (see Fig. 5) cause greater discrepancies between the two theories for large  $N$ . Similar calculations over the range of refractive indices considered yielded the same general behavior.

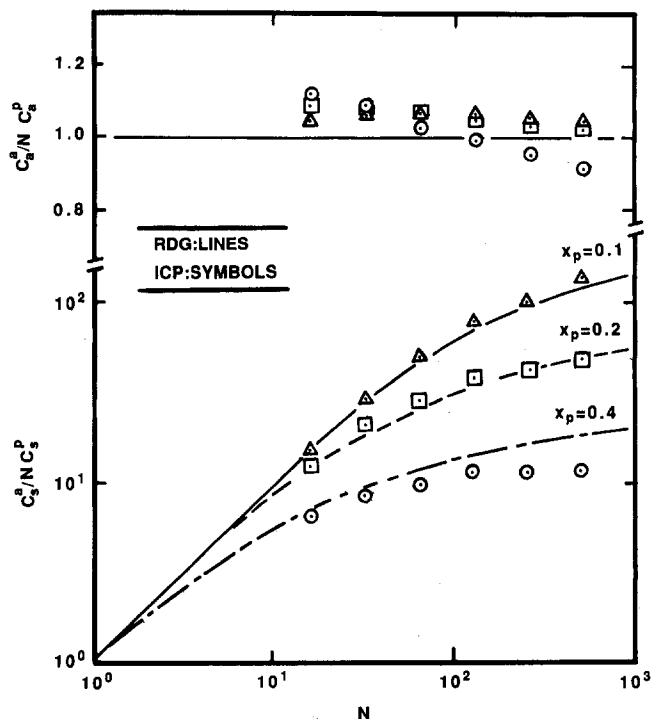


Fig. 6 Normalized absorption and total scattering cross sections as a function of aggregate size for fractal aggregates having various  $x_p$ , computed using the ICP and RDG-FA methods ( $D_f = 1.75$ ,  $k_f = 8.0$ ,  $\lambda = 514.5$  nm,  $m = 1.57 + 0.57i$ )

## Conclusions

An evaluation of an approximate RDG-FA theory for the optical properties of soot aggregates, emphasizing the Guinier regime, was completed based on predictions using the more precise ICP theoretical approach due to Iskander et al. (1989). Conditions considered during the evaluation were selected to approximate the properties of soot aggregates in the visible and near-infrared portions of the spectrum, as follows:  $x_p$  up to 0.4,  $N$  up to 512,  $D_f = 1.75$ ,  $k_f = 8.0$  and refractive indices typical of soot. The main conclusions of the study are as follows:

1 RDG-FA and ICP predictions of absorption cross sections, and of differential scattering cross sections within the Guinier regime, generally agreed within numerical uncertainties (ca. 10 percent) over the range of the evaluation. Combined with reasonable performance of RDG-FA predictions during recent experimental evaluations (Köylü and Faeth, 1994a, b), these results suggest that RDG-FA theory should replace other approximate theories of soot optical properties, such as Rayleigh scattering and Mie scattering for an equivalent sphere, which have not been very effective during recent experimental and computational evaluations (Köylü and Faeth, 1993, 1994a, b).

2 Present calculations using the ICP approach were not satisfactory at large scattering angles for aggregates having  $x_p > 0.25$ , based on evaluations using Mie scattering predictions for a spherulike aggregate and well-established RDG-FA predictions in the power-law regime for soot aggregates. This difficulty is due to the truncation errors caused by excessively large ICP cell sizes and might be avoided by dividing each primary particle in an aggregate into several ICP cells. This approach, and other methods of treating large aggregates having large  $x_p$ , merit further study.

3 Effects of aggregate size mainly dominate scattering properties in the Guinier regime, while the power-law regime exhibits nearly universal behavior independent of aggregate size. Thus, forward-scattering properties, rather than dissymmetry ratios, provide the most reliable indication of aggregate size for large aggregates where scattering properties are dominated by the power-law regime.

4 Variations of refractive indices over the range typical of current uncertainties about these properties yielded far greater variations of optical cross sections than uncertainties concerning RDG-FA predictions for the aggregate properties considered during the present investigation. Thus, current uncertainties about soot refractive indices are the main limitation for accurate estimates of the continuum radiation properties of soot, and the application of nonintrusive optical diagnostics to measure soot concentrations and structure.

## Acknowledgments

One of the authors (T.L.F.) would like to acknowledge scholarship support under the JNICT-CIENCIA BOLSAS Program (BD/860/90-IB). Two of the authors (Ü.Ö.K. and G.M.F.) would like to acknowledge support from the Building and Fire Research Laboratory of the National Institute of Standards and Technology (Grant No. 60NANB1D1175) and the Microgravity Combustion Science Program of NASA (Contract No. NAG3-1245). The collaboration between Instituto Superior Técnico and the University of Michigan is sponsored by AGARD Support Project P-101.

## References

Berry, M. V., and Percival, I. C., 1986, "Optics of Fractal Clusters Such as Smoke," *Optica Acta*, Vol. 33, pp. 577–591.

- Bohren, C. F., and Huffman, D. R., 1983, *Absorption and Scattering of Light by Small Particles*, Wiley, New York, pp. 477–482.
- Borghese, F., Denti, P., Saija, R., Toscano, G., and Sindoni, O. I., 1984, "Multiple Electromagnetic Scattering From a Cluster of Spheres. I. Theory," *Aerosol Sci. Tech.*, Vol. 3, pp. 227–235.
- Charalampopoulos, T. T., 1992, "Morphology and Dynamics of Agglomerated Particulates in Combustion Systems Using Light Scattering Techniques," *Prog. Energy Combust. Sci.*, Vol. 18, pp. 13–45.
- Chen, H. Y., Iskander, M. F., and Penner, J. E., 1990, "Light Scattering and Absorption by Fractal Agglomerates and Coagulations of Smoke Aerosols," *J. Modern Optics*, Vol. 37, pp. 171–181.
- Dalzell, W. H., Williams, G. C., and Hottel, H. C., 1970, "A Light Scattering Method for Soot Concentration Measurements," *Combust. Flame*, Vol. 14, pp. 161–170.
- Dobbins, R. A., Santoro, R. J., and Semerjian, H. G., 1990, "Analysis of Light Scattering From Soot Using Optical Cross Sections for Aggregates," *Twenty-Third Symposium (International) on Combustion*, The Combustion Institute, Pittsburgh, PA, pp. 1525–1532.
- Dobbins, R. A., and Megaridis, C. M., 1991, "Absorption and Scattering of Light by Polydisperse Aggregates," *Appl. Optics*, Vol. 30, pp. 4747–4754.
- Freltoft, T., Kjems, J. K., and Sinha, S. K., 1986, "Power-Law Correlations and Finite Size Effects in Silica Particle Aggregates Studied by Small-Angle Neutron Scattering," *Physical Review B*, Vol. 33, pp. 269–275.
- Iskander, M. F., Chen, H. Y., and Penner, J. E., 1989, "Optical Scattering and Absorption by Branched Chains of Aerosols," *Appl. Optics*, Vol. 28, pp. 3083–3091.
- Jones, A. R., 1979a, "Electromagnetic Wave Scattering by Assemblies of Particles in the Rayleigh Approximation," *Proc. Roy. Soc. London*, Vol. A366, pp. 111–127.
- Jones, A. R., 1979b, "Scattering Efficiency Factors for Agglomerates of Small Spheres," *J. Phys. D: Appl. Phys.*, Vol. 12, pp. 1661–1672.
- Jullien, R., and Botet, R., 1987, *Aggregation and Fractal Aggregates*, World Scientific Publishing Co., Singapore, pp. 46–60.
- Kerker, M., 1969, *The Scattering of Light*, Academic Press, New York, pp. 414–486.
- Köylü, Ü. Ö., and Faeth, G. M., 1992, "Structure of Overfire Soot in Buoyant Turbulent Diffusion Flames at Long Residence Times," *Combust. Flame*, Vol. 89, pp. 140–156.
- Köylü, Ü. Ö., and Faeth, G. M., 1993, "Radiation Properties of Flame-Generated Soot," *ASME JOURNAL OF HEAT TRANSFER*, Vol. 115, pp. 409–417.
- Köylü, Ü. Ö., and Faeth, G. M., 1994a, "Optical Properties of Overfire Soot in Buoyant Turbulent Diffusion Flames at Long Residence Times," *ASME JOURNAL OF HEAT TRANSFER*, Vol. 116, pp. 152–159.
- Köylü, Ü. Ö., and Faeth, G. M., 1994b, "Optical Properties of Soot in Buoyant Laminar Diffusion Flames," *ASME JOURNAL OF HEAT TRANSFER*, Vol. 116, pp. 971–979.
- Ku, J. C., 1991, "Correction for the Extinction Efficiency Factors Given in the Jones Solution for Electromagnetic Scattering by Agglomerates of Small Spheres," *J. Phys. D: Appl. Phys.*, Vol. 24, pp. 71–75.
- Ku, J. C., and Shim, K.-H., 1992a, "Optical Diagnostics and Radiative Properties of Simulated Soot Agglomerates," *ASME JOURNAL OF HEAT TRANSFER*, Vol. 113, pp. 953–958.
- Ku, J. C., and Shim, K.-H., 1992b, "A Comparison of Solutions for Light Scattering and Absorption by Agglomerated or Arbitrarily-Shaped Particles," *J. Quant. Spect. and Rad. Trans.*, Vol. 47, pp. 201–220.
- Kumar, S., and Tien, C. L., 1989, "Effective Diameter of Agglomerates for Radiative Extinction and Scattering," *Combust. Sci. Tech.*, Vol. 66, pp. 199–216.
- Lin, M. Y., Lindsay, H. M., Weitz, D. A., Ball, R. C., Klein, R., and Meakin, P., 1989, "Universality of Fractal Aggregates as Probed by Light Scattering," *Proc. Roy. Soc. London*, Vol. A423, pp. 71–87.
- Martin, J. E., and Hurd, A. J., 1987, "Scattering From Fractals," *J. Appl. Cryst.*, Vol. 20, pp. 61–78.
- Mountain, R. D., and Mulholland, G. W., 1988, "Light Scattering From Simulated Smoke Agglomerates," *Langmuir*, Vol. 4, pp. 1321–1326.
- Nelson, J., 1989, "Test of a Mean Field Theory for the Optics of Fractal Clusters," *J. Modern Optics*, Vol. 36, pp. 1031–1057.
- Purcell, E. M., and Pennypacker, C. R., 1973, "Scattering and Absorption of Light by Nonspherical Dielectric Grains," *Astrophys. J.*, Vol. 186, pp. 705–714.
- Puri, R., Richardson, T. F., Santoro, R. J., and Dobbins, R. A., 1993, "Aerosol Dynamic Processes of Soot Aggregates in a Laminar Ethene Diffusion Flame," *Combust. Flame*, Vol. 92, pp. 320–333.
- Rudder, R. R., and Bach, D. R., 1968, "Rayleigh Scattering of Ruby-Laser Light by Neutral Gases," *J. Opt. Soc. Amer.*, Vol. 58, pp. 1260–1266.
- Sorensen, C. M., Cai, J., and Lee, N., 1992, "Test of Static Structure Factors for Describing Light Scattering From Fractal Soot Aggregates," *Langmuir*, Vol. 8, pp. 2064–2069.
- van de Hulst, H. C., 1957, *Light Scattering by Small Particles*, Dover Publications, New York.

# Dependent Scattering Properties of Woven Fibrous Insulations for Normal Incidence

Sunil Kumar

Department of Mechanical Engineering,  
Polytechnic University,  
333 Jay Street,  
Brooklyn, NY 11201

S. M. White

Thermal Protection Materials Branch,  
NASA Ames Research Center,  
Moffett Field, CA 94035

*The scattering properties of woven fibrous materials are examined in this paper and a simple model is presented to account for the interactions between the scattered radiation from different individual fibers. The case of a normally incident plane electromagnetic wave is considered. Fiber sizes in the Rayleigh regime are considered for developing closed-form solutions. Previous studies in the literature that have addressed the scattering properties of fibrous materials have mostly ignored the effect of constructive or destructive addition of scattered waves from individual fibers, the exception being the case of parallel fibers. The difference in the effects of interference on scattering properties of parallel fibers and of woven fabrics arises from the additional interaction of radiation scattered from mutually perpendicular fibers in the latter case, which further complicates the analysis.*

## Introduction

In a previous paper (White and Kumar, 1990) it has been demonstrated, both experimentally and analytically, that interference between the scattered waves from a collection of parallel fibers has a significant effect on the scattering characteristics. In this study the analysis is extended to include woven fibrous materials where the fibers are oriented in two distinct perpendicular directions in the plane normal to the incident direction. Such configurations are encountered in high-temperature fabrics that are used as thermal insulation for atmospheric entry vehicles, such as the Space Shuttle Orbiter component of the Space Transportation System (STS), and may be used on Aeroassisted Space Transfer Vehicles (ASTVs) (Pitts and Murbach, 1986; Walberg, 1988). These materials are ceramic blankets woven from silica, aluminoborosilicate, or silicon carbide fibers.

Figure 1 shows a scanning electron micrograph (SEM) of a typical silica glass fabric, woven from a high-purity silica known as Astroquartz II. Silica glass fibers are relatively stiff and brittle, but they can be woven into fabrics with relatively little twisting or bending. Over most of the surface of such a woven material, the fibers are nearly parallel in one plane with a second plane of perpendicular fibers immediately behind the first plane. The highly ordered closely spaced parallel geometry of the fibers in a yarn or fabric affects the radiative transfer significantly by enhancing interference effects.

Classical independent theory for studying such systems assumes that each fiber acts independently in the absorption and scattering of radiation, unaffected by the presence of other fibers (Kerker, 1981; Bohren and Huffman, 1983). Departure from the assumption of the independent theory originates from the mechanisms of coherent addition (i.e., constructive/destructive interference) of the far-field scattered electromagnetic radiation and the interparticle effects in the near field. Discussions of these mechanisms are found in studies of dense systems containing small spherical particles (Tien and Drolen, 1987; Kumar and Tien, 1990; Ma et al., 1990; Al-Nimr and Arpacı, 1992), agglomerates (Kumar and Tien, 1989; Ku and Shim, 1991; Koylu and Faeth, 1993), and unidirectional parallel fibers (White and Kumar, 1990; Lee, 1990, 1992).

For fibers that are oriented parallel to each other with their axes normal to the direction of incidence, radiation is scattered in the plane perpendicular to the fiber axes that contains the incident radiation. The scattered radiation from individual parallel fibers interferes at all angles within the scattering plane and the interference can be accounted for by a simple multiplicative correction factor (White and Kumar, 1990). This simple correction factor may also be obtained from the general, more mathematically complex, formulation of Lee (1990, 1992). When two sets of perpendicular fiber orientations are present (as in fabrics) the scattering takes place in the two corresponding perpendicular planes due to the radial nature of the propagation of the scattered radiation. Whereas the interference within these individual planes can be accounted for by the multiplicative correction factor, an interference between the radiation fields in the two mutually perpendicular planes occurs in the forward and backward directions and has to be separately modeled. This correction is an additive one.

The present paper presents a simple methodology for modeling the interference effects in the far field and develops simple closed-form expressions for the scattering properties for fibrous media of small size parameters. Since the emphasis is to obtain simple closed-form solutions, the approach adopted is of tracking the phase of the scattered radiation from individual fibers and evaluating the phase cancellations and additions in the far field. This is in contrast with detailed mathematical examinations of the interference phenomena via rigorous electromagnetic theory analysis that includes the far field. This would yield very complicated mathematical results, which would not be practical for use in engineering applications.

## Analysis

In the previous study of White and Kumar (1990) the effects of far-field interference on scattering from parallel fibers for normally incident radiation were accounted for by defining a correction factor  $F(\gamma)$  so that the scattering from  $N$  fibers is written in terms of the independent scattering value as

$$I_{sN}(\gamma) = NI_{si}(\gamma)F(\gamma), \quad (1)$$

where  $I_s$  is the scattered intensity, the subscript  $N$  indicates  $N$  fibers, the subscript  $i$  indicates independent scattering from a single fiber, and  $\gamma$  is the angle between the forward scattering direction and the direction under consideration in the scattering plane normal to the fiber. In the independent scat-

Contributed by the Heat Transfer Division for publication in the JOURNAL OF HEAT TRANSFER. Manuscript received by the Heat Transfer Division June 1993; revision received April 1994. Keywords: Radiation, Radiation Interactions. Associate Technical Editor: M. F. Modest.

tering assumption  $F(\gamma)$  is unity, i.e., the scattered intensity from a collection of fibers is obtained by algebraically summing up the scattered intensity from each fiber and each fiber is assumed to be uninfluenced by the presence of the other fibers (near-field effects are neglected). The correction factor  $F$  takes into account the phase cancellation and addition of the scattered electromagnetic waves from different fibers. For simplicity of notation,  $F$  and  $I$  are written as functions only of  $\gamma$  here, although they depend on other variables as described below. Both  $F$  and  $I$  depend on the size parameter  $\alpha$  and the refractive index  $m$  of the fiber material. The size parameter  $\alpha$  equals  $\pi d/\lambda$ , where  $d$  is the fiber diameter and  $\lambda$  is the wavelength of incident radiation. The refractive index  $m = n + i\kappa$ ,  $n$  being the index of refraction and  $\kappa$  the index of absorption, in turn depends on both the wavelength and the temperature. The correction factor  $F$  also is a function of the clearance parameter  $c (= a/\lambda)$ , where  $a$  is the clearance between fibers.

The above-mentioned definition of a correction factor is possible for the case of parallel fibers because the scattering from two different incident waves of parallel and perpendicular polarizations, respectively, do not interfere. However, for the case of fabrics where there exist two sets of fibers in two different orientations, the same incident polarization is parallel to one set of fibers and perpendicular to the other. The two sets of resultant scattered fields, which are a combination of scattering due to two different polarizations, interfere with each other in the forward and backward directions only. Thus, a simple correction factor cannot be defined because the correction is now a function of the relative magnitudes of scattering from the two different sets of fibers. Also since independent theory does not predict such cross-polarization effects, the multiplicative form of correction factor cannot be defined. Instead the cross-polarization component has to be modeled as a new additive term.

In order to evaluate these complicated interference effects, the expressions for scattering from one fiber are first written. With reference to Fig. 2, a horizontal fiber located at the origin is first considered. If the incident wave is polarized perpendicular to the fiber,  $\mathbf{E}_{\text{inc}} = E_0 \mathbf{e}_x \exp(ikz)$ , the asymptotic scattered field at a large radial distance  $r$  (in a cylindrical geometry) from the fiber axis in the plane perpendicular to the fiber is (Bohren and Huffman, 1983)

$$\begin{aligned} \mathbf{E}_s &= -E_0 e^{-i\pi/4} \sqrt{\frac{2}{\pi kr}} \exp(ikr) \sum_n (-1)^n e^{in(\pi-\theta)} a_n \mathbf{e}_\theta, \\ &= E_0 \frac{1}{\pi} \sqrt{\frac{\lambda}{r}} \mathbf{X}(\theta) \exp(ikr). \end{aligned} \quad (2a)$$

The second expression defines the scattering function  $\mathbf{X}(\theta)$  for simplicity and represents the summation over  $n$  term in the first expression. If the incident beam is polarized parallel to the fiber,  $\mathbf{E}_{\text{inc}} = E_0 \mathbf{e}_y \exp(ikz)$ , the scattered field is similarly

$$\begin{aligned} \mathbf{E}_s &= -E_0 e^{-i\pi/4} \sqrt{\frac{2}{\pi kr}} \exp(ikr) \sum_n (-1)^n e^{in(\pi-\theta)} b_n \mathbf{e}_y, \\ &= E_0 \frac{1}{\pi} \sqrt{\frac{\lambda}{r}} \mathbf{Y}(\theta) \exp(ikr). \end{aligned} \quad (2b)$$

The scattering function  $\mathbf{Y}(\theta)$  in the second expression is defined for simplicity. The index  $n$  in the above-mentioned expressions is summed from  $-\infty$  to  $+\infty$ . Here  $k$  is the propagation constant ( $= 2\pi/\lambda$ ), and  $a_n, b_n$  are the expansion coefficients where  $a_{-n} = a_n$  and  $b_{-n} = b_n$  (Bohren and Huffman, 1983).

In order to capture the far-field interference effects, the value of  $r$  is changed to reflect the position of each fiber with respect to a common origin as well as to account for the actual distance traveled by the incident and scattered waves from each fiber. Also, the energy per unit area normal to propagation direction of the scattered wave is computed from the Poynting vector  $\mathbf{S}$

$$\begin{aligned} \mathbf{S} &= \text{Re} \left\{ \frac{k}{2\omega\mu_0} \sum_i \sum_j \mathbf{E}_{sij} \times \mathbf{e}_r \times \text{conj}(\mathbf{E}_{sij}) \right\}, \\ &= \text{Re} \left\{ \frac{k}{2\omega\mu_0} \sum_i \sum_j \mathbf{E}_{sij} \cdot \text{conj}(\mathbf{E}_{sij}) \right\} \mathbf{e}_r, \\ &= \text{Re} \left\{ \frac{k}{2\omega\mu_0} |E_0|^2 \frac{\lambda}{\pi^2 r} \sum_i \sum_j \mathbf{Z}_j \cdot \text{conj}(\mathbf{Z}_i) \right. \\ &\quad \left. \times \exp(ik(\mathbf{e}_z - \mathbf{e}_r) \cdot (\mathbf{r}_j - \mathbf{r}_i)) \right\} \mathbf{e}_r, \end{aligned} \quad (3)$$

## Nomenclature

$a$  = clearance between fibers,  $\mu\text{m}$   
 $A$  = scaled distance between fiber centers, coplanar case =  $1 + a/d$   
 $a_n, b_n$  = expansion coefficients for scattered fields  
 $c$  = clearance parameter =  $a/\lambda$   
 $C$  = cross-polarization correction factor  
 $\text{conj}$  = complex conjugate  
 $d$  = fiber diameter,  $\mu\text{m}$   
 $\mathbf{e}$  = unit vector  
 $\mathbf{E}$  = electric field  
 $f$  = solid volume fraction  
 $F$  = dependent scattering correction factor  
 $g$  = scaled local fiber number density  
 $H$  = total number of horizontal fibers (parallel to  $y$  axis)  
 $I$  = intensity,  $\text{W/m}^2 \cdot \mu\text{m} \cdot \text{str}$   
 $k$  = propagation constant =  $2\pi/\lambda$   
 $m$  = complex refractive index =  $n + i\kappa$

$n$  = index of refraction  
 $N$  = total number of fibers =  $H + V$   
 $Q$  = efficiency  
 $\mathbf{r}$  = position vector in the plane perpendicular to fiber  
 $R$  = scaled distance =  $r/d$   
 $\text{Re}$  = real part of complex number  
 $\mathbf{S}$  = Poynting vector,  $\text{W/m}^2 \cdot \mu\text{m}$   
 $V$  = total number of vertical fibers (parallel to  $x$  axis)  
 $x, y, z$  = vertical, horizontal, and incident directions  
 $\mathbf{X}, \mathbf{Y}$  = scattering functions defined by Eq. (2)  
 $\alpha$  = size parameter =  $\pi d/\lambda$   
 $\gamma$  = dummy angle for angle from incident direction in plane normal to fiber  
 $\theta$  = angle from incident direction in vertical plane  
 $\kappa$  = index of absorption  
 $\lambda$  = wavelength,  $\mu\text{m}$

$\mu_0$  = magnetic permeability of air  
 $\phi$  = angle from incident direction in horizontal plane  
 $\Phi$  = scattering phase function  
 $\omega$  = angular velocity

## Subscripts

$a$  = absorption  
 $\text{bck}$  = backward  
 $e$  = extinction  
 $\text{fw}$  = forward  
 $h$  = horizontal  
 $i$  = from one individual fiber in independent scattering  
 $\text{inc}$  = incident  
 $j, k, l$  = fiber specifications  
 $N$  = from  $N$  fibers  
 $s$  = scattering  
 $r$  = radial direction  
 $v$  = vertical  
 $x, y, z$  = along vertical, horizontal, incident directions

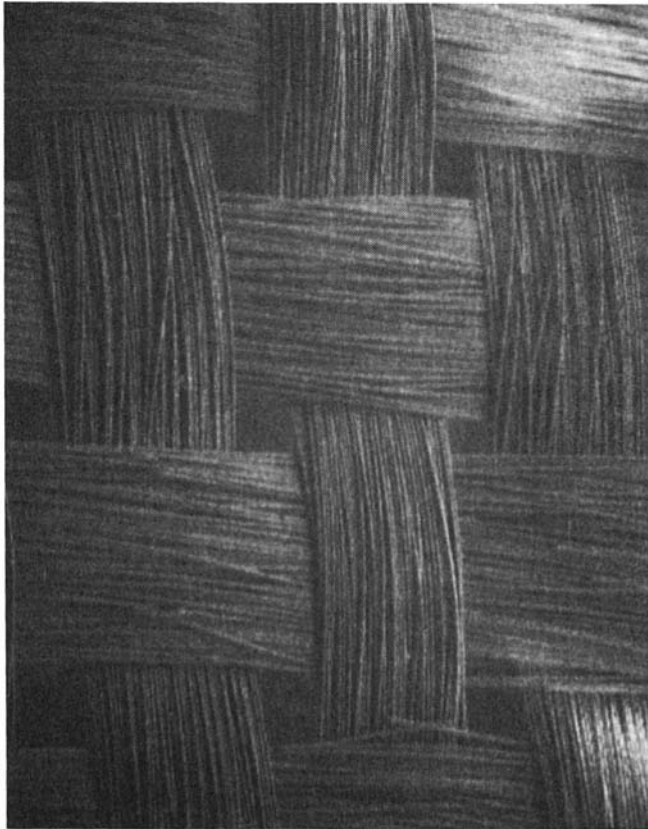


Fig. 1 Scanning Electron Micrograph (SEM) showing the weave of ceramic fabric No. 525 woven from 9 μm silica fibers

where  $Z$  is  $X$  or  $Y$  depending on the fiber it corresponds to and on the polarization of the incident wave. The summations (represented by indices  $l$  and  $j$ ) are carried out over the total number of fibers in the system. The position vectors  $\mathbf{r}_l$  and  $\mathbf{r}_j$  reflect the positions of the fiber centers. Implicit in the last equation above is the assumption that  $r \gg r_j$ , and consequently  $|\mathbf{r} - \mathbf{r}_j| = r$  and  $(|\mathbf{r} - \mathbf{r}_j| - |\mathbf{r} - \mathbf{r}_l|) \approx \mathbf{e}_r \cdot (\mathbf{r}_l - \mathbf{r}_j)$ . Here "conj" indicates complex conjugate,  $\omega$  is the angular velocity of the incident wave, and  $\mu_0$  is the magnetic permeability of air. The corresponding scattered intensity is given by

$$I = |S| \frac{r}{d}. \quad (4)$$

The physical case under consideration consists of an incoherent beam of light that is incident normally on the set of  $V$  vertical fibers and  $H$  horizontal fibers. All the fibers have the same diameter and are made of the same material. Using the above-mentioned expressions and separating each summation into two subsummations over the horizontal and vertical fibers, the following is obtained after straightforward, albeit tedious, algebraic manipulations:

$$I_{sN}(\theta, \phi) = VI_{si}(\phi)F(\phi)[\delta(\theta) + \delta(\pi - \theta)] + HI_{si}(\theta)F(\theta) \times [\delta(\phi) + \delta(\pi - \phi)] + VHI_{inc}[C_{fw}\delta(\theta)\delta(\phi) + C_{bck}\delta(\pi - \theta)\delta(\pi - \phi)]. \quad (5)$$

The number of vertical fibers is denoted by  $V$  and the horizontal by  $H$ , and the total number  $N = V + H$ . For independent scattering theory the value of  $F$  is unity and the effects of cross-polarization interference are neglected, yielding  $I_{sN} = NI_{si}$ .

The delta functions in the above-mentioned expression are a consequence of the cylindrical form of scattered waves. The scattered field from the horizontal cylinder propagates radially out-

ward from the fiber axis along the vertical plane containing the incident beam. Similarly the scattered field from the vertical fibers is contained in the horizontal plane having the incident beam. Since the polarized components of the scattered fields oscillate transversely in different planes perpendicular to their radial propagation direction, the two sets of waves do not interfere except in the forward and backward directions. Within each set of waves in the horizontal and vertical planes, respectively, interference takes place as described by White and Kumar (1990) and is accounted for by the correction factor  $F$ . In the forward and backward directions the additional cross-polarization correction factors  $C$  are defined as

$$C_{fw} = \frac{1}{\pi\alpha} [\mathbf{X}(0) \cdot \text{conj}(\mathbf{Y}(0)) + \mathbf{Y}(0) \cdot \text{conj}(\mathbf{X}(0))], \\ = \frac{1}{\pi\alpha} \sum_n \sum_m [\text{conj}(a_n)b_m + a_n \text{conj}(b_m)], \quad (6a)$$

$$C_{bck} = \frac{1}{\pi\alpha} [\mathbf{X}(\pi) \cdot \text{conj}(\mathbf{Y}(\pi)) + \mathbf{Y}(\pi) \cdot \text{conj}(\mathbf{X}(\pi))] \\ \times \frac{1}{HV} \sum_{j=1}^V \sum_{l=1}^H \cos(2k(z_j - z_l)), \\ = \frac{-1}{\pi\alpha} \sum_n \sum_m (-1)^{n+m} [\text{conj}(a_n)b_m + a_n \text{conj}(b_m)] \\ \times \frac{1}{HV} \sum_{j=1}^V \sum_{l=1}^H \cos(2k(z_j - z_l)). \quad (6b)$$

Similarly the independent scattering intensity and scattering efficiency are defined as (Bohren and Huffman, 1983)

$$I_{si}(\gamma) = I_{inc} \frac{1}{2\pi\alpha} \{ |\mathbf{X}(\gamma)|^2 + |\mathbf{Y}(\gamma)|^2 \}, \\ = I_{inc} \frac{1}{2\pi\alpha} \sum_n \sum_m [a_n \text{conj}(a_m) + b_n \text{conj}(b_m)] \\ \times \exp(-i(n - m)\gamma), \quad (7a)$$

$$Q_{si} = \frac{1}{\alpha} \{ |a_0|^2 + |b_0|^2 + 2 \sum_{n=1}^{\infty} [|a_n|^2 + |b_n|^2] \}. \quad (7b)$$

Since the phase of the scattered waves is proportional to the distance from the fiber centers and the incident phases,  $F(\gamma)$  is given by (White and Kumar, 1990)

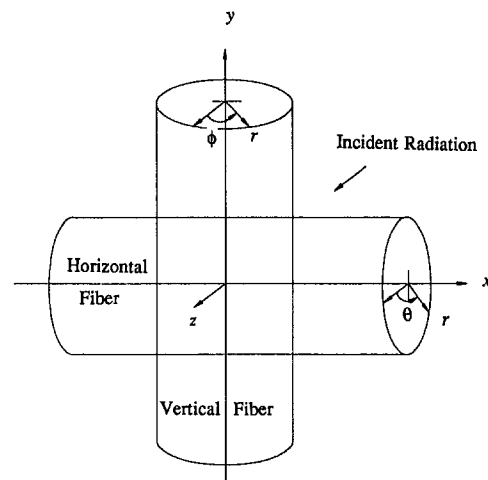


Fig. 2 Schematic of the model and position vectors in the fiber system

$$F(\gamma) = \frac{1}{M} \operatorname{Re} \sum_{k=1}^M \sum_{j=1}^M \exp\left(i \frac{2\pi}{\lambda} (\mathbf{e}_z - \mathbf{e}_r) \cdot (\mathbf{r}_j - \mathbf{r}_k)\right), \quad (8)$$

where unit vector  $\mathbf{e}_z$  is in the forward direction,  $\mathbf{e}_r$  is the unit vector along the radial direction of observation in the plane perpendicular to the fibers and is at an angle  $\gamma$  from forward direction, and  $\mathbf{r}_j$  and  $\mathbf{r}_k$  are the position vectors of the centers of the fibers  $j$  and  $k$ . Figure 2 shows the coordinate system. The vectors  $\mathbf{e}_z$ ,  $\mathbf{e}_r$ ,  $\mathbf{r}_j$ ,  $\mathbf{r}_k$  lie in the same plane that is perpendicular to the fiber axis and contains the incident direction.  $M$  is either  $V$  or  $H$  depending on whether  $\gamma$  is  $\phi$  or  $\theta$ . The dot product in the above-mentioned equation represents the difference in the total distance traveled by the waves from a common origin to the detector after being scattered by fibers  $j$  and  $k$ . If the  $M$  fibers are very closely packed so that all the scattered waves add constructively in the forward direction, then  $F(0) = M$ , and the intensity in the forward direction, cf. Eq. (1), is  $I_{sN}(0) = N^2 I_{si}(0)$  (the opposite extreme from independent scattering), where  $N = M$  for this case.

The scattering efficiency  $Q_s$  is the ratio of the total energy scattered by the fiber to the total energy intercepted by the fiber. The scattering efficiency is evaluated by integrating the scattered intensity over all angles. In this expression, the independent scattering efficiency from a single fiber  $Q_{si}$  is a well-known function from independent scattering theory. It is used to normalize the scattering efficiency for simplicity. That is, to isolate mathematically the effect of interference on the scattering efficiency, the ratio of the dependent scattering efficiency of the fiber system ( $= (H + V)Q_{sN}$ ) to that of the collection of fiber in the independent scattering assumption ( $= (H + V)Q_{si}$ ) is presented as follows:

$$\frac{Q_{sN}}{Q_{si}} = \left[ H \int_0^{2\pi} \Phi_i(\theta) F(\theta) d\theta + V \int_0^{2\pi} \Phi_i(\phi) F(\phi) d\phi \right] \times \frac{1}{2\pi} \frac{1}{H + V} + (C_{fw} + C_{bck}) \frac{HV}{Q_{si}(V + H)}, \quad (9)$$

Here  $\Phi_i$  is the scattering phase function of an individual fiber and  $\theta$  is the angle between the scattered and incident directions. The phase function is evaluated by using the independent scattering theory, and is a known function of the scattering angle  $\theta$  or  $\phi$  and the size parameter  $\alpha$ . To obtain the last term in the above-mentioned equation, it is assumed that the finite number of fibers are closely packed so that the scattered waves from each fiber interact with those of every other fiber in the forward and backward-scattering directions. For systems with a large number of the fibers, this equation has to be modified, as is considered later in the paper.

The previous expressions are general ones, as long as the near-field effects are negligible. If such effects are significant they have to be included via additional correction terms or appropriate models. Near-field effects may be neglected if the Rayleigh-Gans assumptions are met. These are  $|m - 1| \ll 1$  and  $2\alpha|m - 1| \ll 1$  (Bohren and Huffman, 1983; Lee, 1992). However, the expressions developed here may be used even if near-field effects are present, as long as the near-field corrections are in the form of multiplicative correction factors (Kumar and Tien, 1990).

Simplifying assumptions can be used to obtain closed-form solutions, which offer a great improvement in computational efficiency over the complex numerical integration required otherwise. Several closed-form expressions are presented below for different cases in the Rayleigh regime. The independent phase function asymptotes to the first term in the infinite series containing even powers of the size parameter  $\alpha$  for small values of the size parameter:

$$\Phi_i(\gamma) = \frac{|m^2 + 1|^2 + 4 \cos^2 \gamma}{|m^2 + 1|^2 + 2}, \quad \alpha \ll 1, \quad (10a)$$

$$= \frac{2}{3}(1 + \cos^2 \gamma), \quad \alpha \ll 1, \quad m \approx 1. \quad (10b)$$

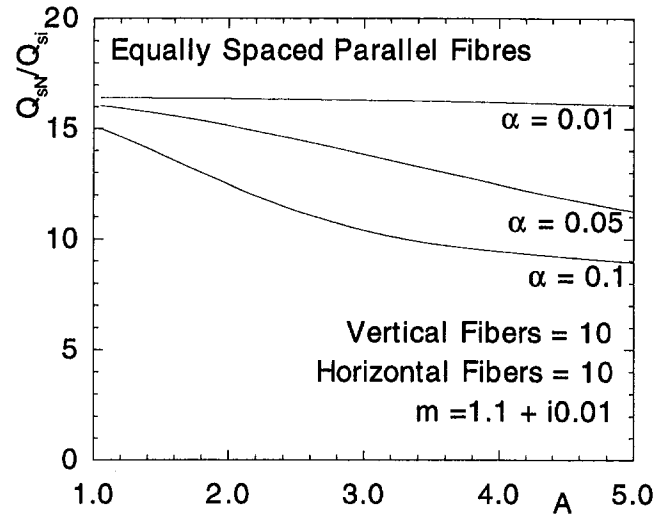


Fig. 3 Effect of fiber spacing on the scattering efficiency  $Q_{sN}$  for evenly spaced fibers in one plane ( $A$  = scaled distance between coplanar fiber axes)

Similarly, retaining the leading order the expansion coefficients asymptote to ( $\alpha \ll 1$ )

$$a_0 = \frac{-i\pi\alpha^4(m^2 - 1)}{32}, \quad b_0 = \frac{-i\pi\alpha^2(m^2 - 1)}{4},$$

$$a_1 = \frac{-i\pi\alpha^2 m^2 - 1}{4(m^2 + 1)}, \quad b_1 = \frac{-i\pi\alpha^4(m^2 - 1)}{32}. \quad (11)$$

For larger size parameters the phase function and the expansion coefficients are more complicated. The cross-polarization interference correction factors and the independent scattering efficiency can be written for small size parameters as ( $\alpha \ll 1$ )

$$C_{fw} = \frac{2}{\pi\alpha} [\operatorname{conj}(a_1)b_0 + a_1\operatorname{conj}(b_0)],$$

$$= \frac{\pi}{4} \alpha^3 \frac{|m^2 - 1|^2}{|m^2 + 1|^2} \operatorname{Re}(m^2 + 1), \quad (12a)$$

$$C_{bck} = C_{fw} \frac{1}{HV} \sum_{j=1}^H \sum_{l=1}^V \cos(2k(z_j - z_l)), \quad (12b)$$

$$Q_{si} = \frac{\pi^2 \alpha^3}{16} \frac{|m^2 - 1|^2}{|m^2 + 1|^2} [2 + |m^2 + 1|^2]. \quad (12c)$$

Here, too, only the leading order terms have been retained.

Two representative geometries for the fibers in a given plane are presented below. In either case, the woven material is modeled as a horizontally oriented layer on top of a vertically oriented layer of fibers. These cases represent a simple idealized geometry, which yields a relatively simple closed-form solution for the dependent scattering efficiency. A more realistic but complicated geometry would require a more complicated numerical evaluation of the scattering efficiency. The fibers in one plane are considered to be either evenly spaced at a fixed, known distance apart or to be aligned parallel to one another in three-dimensional space, having a random distribution of spacings between them. In the second case, the probability of finding a fiber on a given angular ray is given by a probability distribution, and the interference effect of that fiber on scattering decreases functionally as a Bessel function, so the integration over space is carried out to the limit of infinity. These results are presented in the following sections.

**Finite Number of Evenly Spaced Coplanar Fibers.** If the horizontal and vertical fibers are arranged in plane layers where

the fibers are equidistant in the plane, the following mathematical form of  $F$  is obtained (White and Kumar, 1990):

$$F(\gamma) = 1 + \frac{1}{M} \sum_{k=1}^M \sum_{\substack{j=1 \\ j \neq k}}^M \cos(2\alpha A(k-j) \sin \gamma). \quad (13)$$

Here the ratio of the fixed distance between the centers of adjacent fibers to the diameter of the fibers is represented by  $A (= 1 + a/d)$ .  $F(\gamma)$  becomes more oscillatory as the size parameter  $\alpha$  increases. For smaller  $\alpha$  the scattered radiation from these closely spaced fibers always adds constructively since the different scattered waves emanate from points that are very close to one another and hence  $F$  is smoother at smaller  $\alpha$ . For small size parameters, the expression for dependent scattering efficiency is readily integrated by using Eqs. (9), (10a), (12b), and (13) as

$$\begin{aligned} \frac{Q_{sN}}{Q_{si}} = \frac{1}{V+H} & \left\{ \sum_{k=1}^V \sum_{\substack{j=1 \\ j \neq k}}^V \left[ J_0(2\alpha A_v(k-j)) \right. \right. \\ & + \frac{2}{|m^2 + 1|^2 + 2} J_2(2\alpha A_v(k-j)) \left. \right] \\ & + \sum_{k=1}^H \sum_{\substack{j=1 \\ j \neq k}}^H \left[ J_0(2\alpha A_h(k-j)) \right. \\ & + \frac{2}{|m^2 + 1|^2 + 2} J_2(2\alpha A_h(k-j)) \left. \right] \left. \right\} \\ & + \frac{2C_{fw} VH}{Q_{si}(V+H)} + 1. \quad (14) \end{aligned}$$

It has been assumed in the second to last term in this equation that all horizontal and vertical fibers are in the same plane and thus  $C_{bck} = C_{fw}$  where  $C_{fw}$  is obtained from Eq. (12a). This approximation is a good representation for loosely woven fabrics. If the two planes are at a fixed distance  $\rho$  apart then the term  $2C_{fw}$  has to be replaced by  $C_{fw}(1 + \cos(2k\rho))$ , as indicated by Eq. (12b). Here, too, it has been assumed that the scattered waves from each fiber interact in the forward and backward directions with those from every other fiber (cf. Eq. (9)).

**Large Fibrous Systems Described by Distribution Functions.** More generally, the fibers in either the horizontal or vertical layer are considered to be aligned parallel to one another, and the separation between the fibers can be given by a distribution function. The effect of fibers positioned far from the fiber under consideration decreases rapidly with the distance, so that an infinite system can be considered and the spatial integrations can be carried out to the limit of  $r \rightarrow \infty$ . The correction factor  $F$  is thus (White and Kumar, 1990)

$$F(\gamma) = 1 + 8f \int_0^\infty [g(R) - 1] J_0\left(4\alpha R \sin \frac{\gamma}{2}\right) R dR, \quad (15a)$$

where  $f$  is the solid volume fraction and  $g(R)$  is the ratio of the local fiber number density at a nondimensional distance  $R$  from the representative fiber to the average (bulk) number density. Similarly Eq. (9) is modified as follows to account for decreasing influence of the scattering from fibers located at large distances:

$$\begin{aligned} \frac{HV}{H+V} C_{fw} + C_{bck} = C_{fw} \frac{8f_v f_h}{f_v + f_h} \int_0^\infty & [g(R) - 1] \\ & \times [J_0(4\alpha R) + 1] R dR, \quad \alpha \ll 1, \quad (15b) \end{aligned}$$

where Eqs. (12a) and (12b) have been used. Two cases of  $g(R)$  are considered below, for low volume fractions or widely dispersed fibers such as in a low-density insulation material, and high volume fractions or relatively closely packed fibers as in a woven material.

For low volume fractions the number density is assumed uniform for  $r \geq d$  ( $R \geq 1$ ) and is zero for values of  $r < 1$  ( $R < 1$ ). This model is called the gas model and Eq. (15a) is readily integrated as (White and Kumar, 1990)

$$F(\gamma) = 1 - \frac{8f}{4\alpha \sin \frac{\gamma}{2}} J_1\left(4\alpha \sin \frac{\gamma}{2}\right), \quad (16a)$$

$$F(\gamma) = 1 - 4f \left[ 1 - \frac{1}{8} \left(4\alpha \sin \frac{\gamma}{2}\right)^2 \right], \quad \alpha \rightarrow 0. \quad (16b)$$

The corresponding dependent scattering efficiency for small values of  $\alpha$  using Eqs. (9), (10a), (12b), (15b), and (16a) is

$$\begin{aligned} \frac{Q_{sN}}{Q_{si}} = 1 - 4 \frac{f_v^2 + f_h^2}{f_v + f_h} & \left[ J_0^2(2\alpha) + J_1^2(2\alpha) \right. \\ & + \frac{2}{|m^2 + 1|^2 + 2} (J_2^2(2\alpha) - J_1(2\alpha)J_3(2\alpha)) \left. \right] \\ & - \frac{C_{fw} 8f_v f_h}{Q_{si} f_h + f_v} \left[ \frac{1}{4\alpha} J_1(4\alpha) + \frac{1}{2} \right], \quad \alpha \ll 1. \quad (17) \end{aligned}$$

The value of  $C_{fw}$  is obtained from Eq. (12a).

For higher volume fractions a modified distribution function is considered that assigns additional solid volume near the fiber. This attempts to account for higher density near the fiber that is expected to decrease in an oscillatory fashion with increasing radius from the fiber. As before, the nondimensional number density  $g(R)$  is assumed to be unity for  $R > 1$ . This model is called the packed model where an additional delta function at  $R = 1$  is specified as (White and Kumar, 1990)

$$\lim_{\delta \rightarrow 0} \int_{1-\delta}^{1+\delta} R g(R) dR = \frac{1}{2} \left( 1 - \frac{1}{2\pi} \right) = 0.4204. \quad (18)$$

This distribution function yields

$$\begin{aligned} F(\gamma) = 1 - \frac{8f}{4\alpha \sin \frac{\gamma}{2}} & J_1\left(4\alpha \sin \frac{\gamma}{2}\right) \\ & + 8 \times 0.4204 f J_0\left(4\alpha \sin \frac{\gamma}{2}\right), \quad (19a) \\ = 1 - 4f & \left[ 0.1592 + 0.0852 \left(4\alpha \sin \frac{\gamma}{2}\right)^2 \right], \\ & \alpha \rightarrow 0. \quad (19b) \end{aligned}$$

The corresponding dependent scattering efficiency using Eqs. (9), (10a), (12b), (15b), and (19a) is

$$\begin{aligned} \frac{Q_{sN}}{Q_{si}} = 1 - 4 \frac{f_v^2 + f_h^2}{f_v + f_h} & \left[ J_0^2(2\alpha) + J_1^2(2\alpha) \right. \\ & + \frac{2}{|m^2 + 1|^2 + 2} (J_2^2(2\alpha) - J_1(2\alpha)J_3(2\alpha)) \left. \right] + 8 \\ & \times 0.4204 \frac{f_v^2 + f_h^2}{f_v + f_h} \left[ J_0^2(2\alpha) + \frac{2}{|m^2 + 1|^2 + 2} J_2^2(2\alpha) \right] \\ & - \frac{C_{fw} 8f_v f_h}{Q_{si} f_h + f_v} \left[ \frac{1}{4\alpha} J_1(4\alpha) + \frac{1}{2} - 0.4204 [J_0(4\alpha) + 1] \right], \\ & \alpha \ll 1. \quad (20) \end{aligned}$$

## Results

Numerical results are presented for a few representative cases of fibers of small diameters such that the size parameter  $\alpha \ll 1$ . Figure 3 considers the case of evenly spaced horizontal and ver-

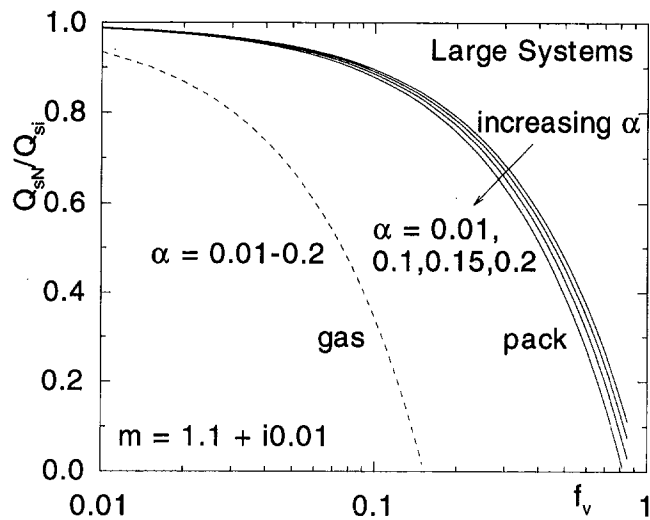


Fig. 4 Effect of volume fraction on the scattering efficiency  $Q_{sN}$  of fibrous systems containing horizontal and vertical fibers for horizontal volume fraction  $f_h$  equal to the vertical volume fraction  $f_v$

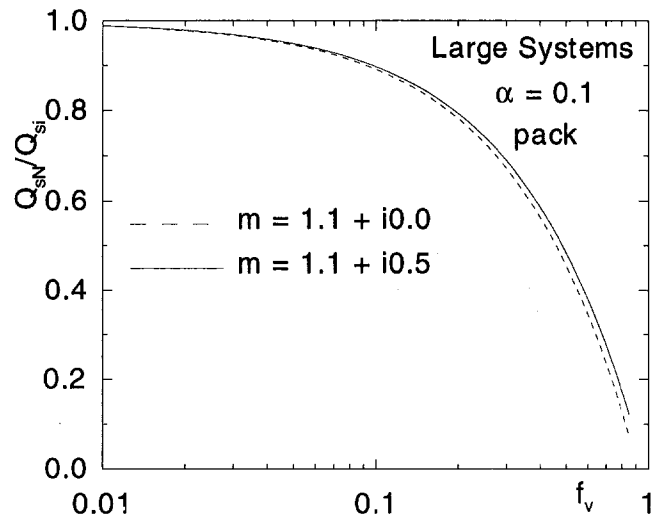


Fig. 5 Effect of refractive index on the scattering efficiency  $Q_{sN}$  of fibrous systems containing horizontal and vertical fibers for horizontal volume fraction  $f_h$  equal to the vertical volume fraction  $f_v$

tical fibers located in one plane. Here the single sheet of woven fabric is modeled via Eq. (14) and 10 fibers each in vertical and horizontal planes are considered. The scattering efficiency ratio is evaluated as a function of the spacing for different size parameters. It is seen that for very small sized fibers the dependent scattering efficiency is high since the scattered radiation adds constructively in all directions. As the fiber size increases, the scattered radiation interferes both constructively and destructively, and the dependent scattering efficiency is lower. In addition, the scattering efficiency decreases as the separation between the fibers increases. Similar results have been observed for unidirectional parallel fibers (White and Kumar, 1990).

Figure 4 examines the dependent scattering efficiency for a fibrous system modeled as a random system of perpendicular and horizontal fibers via the gas and packed models for the distribution function  $g(R)$ . Here the volume fractions for the vertical and horizontal fibers are taken to be the same,  $f_v = f_h$ . It is seen that as the volume fraction increases the dependent scattering efficiency decreases. The decrease is larger for larger sized fibers and the dependent scattering efficiency equals to the independent one as the volume fraction asymptotes to zero. The gas model, which is expected to be more accurate at lower values of volume fraction, yields physically unacceptable negative values of scattering efficiency for volume fractions greater than approximately 0.15. The packed model covers a larger range and does not give negative values except at large volume fractions for large size

parameters. These deficiencies of the two models have been noted and discussed in the literature (Tien and Drolen, 1987; Kumar and Tien, 1990). Experimental validation is required before either of these models for  $g(R)$  or others available from the literature are accepted.

The cross-polarization interference effects in fabrics are highlighted by the results of Table 1. Two different cases are considered, the first where half the fibers are in the horizontal direction and the other half in the vertical direction in the form of a woven fabric, and the second where all the fibers are oriented parallel in one direction. Due to the additional cross-polarization interference in the forward and backward scattering directions, the dependent scattering efficiency from the fabric is higher. The interference in these directions is constructive and therefore the magnitude of the total scattered energy is higher than that of the unidirectional fibers where the cross-polarization is absent.

The effect of the refractive index on the dependent scattering efficiency is examined in Fig. 5. Higher index of absorption  $\kappa$  leads to slightly higher values of dependent scattering efficiencies.

## Summary

A theoretical model of radiative properties of an idealized fabric developed in this paper indicates how the scattering characteristics of a system of woven fibers are affected by the location and orientation of the fibers with respect to each other. The mechanism of interference of the scattered waves from different fibers has been ignored in the classical formulations of scattering theory of fibrous systems. The present theoretical framework analyzes this effect and the resultant model incorporates these interference effects. Further research is needed to validate these models experimentally.

## References

- Al-Nimr, M. A., and Arpaci, V. S., 1992, "Radiative Properties of Interacting Particles," *ASME JOURNAL OF HEAT TRANSFER*, Vol. 114, pp. 950-957.
- Bohren, C. F., and Huffman, D. R., 1983, *Absorption and Scattering of Light by Small Particles*, Wiley-Interscience, New York.
- Kerker, M., 1981, *The Scattering of Light and Other Electromagnetic Radiation*, Dover, New York.
- Koylu, U. O., and Faeth, G. M., 1993, "Radiative Properties of Flame Generated Soot," *ASME JOURNAL OF HEAT TRANSFER*, Vol. 115, pp. 409-417.
- Ku, J. C., and Shim, K. H., 1991, "Optical Diagnostics and Radiative Properties

Table 1  $Q_{sN}/Q_{si}$  for  $n + i\kappa = 2 + i0.1$

Table 1: $Q_{sN}/Q_{si}$ for $n + i\kappa = 2 + i0.1$		
size $\alpha$	fabric $f_v = f_h = 0.05$	parallel $f = 0.1$
0.001	0.9564	0.9363
0.005	0.9564	0.9363
0.01	0.9564	0.9363
0.02	0.9563	0.9362
0.03	0.9562	0.9361
0.04	0.9561	0.9359
0.05	0.9560	0.9356
0.06	0.9557	0.9353
0.07	0.9555	0.9350
0.08	0.9552	0.9346
0.09	0.9549	0.9341



of Simulated Soot Agglomerates," ASME JOURNAL OF HEAT TRANSFER, Vol. 113, pp. 953-959.

Kumar, S., and Tien, C. L., 1989, "Effective Diameter of Agglomerates for Radiative Extinction and Scattering," *Combustion Science and Technology*, Vol. 66, pp. 199-216.

Kumar, S., and Tien, C. L., 1990, "Dependent Absorption and Extinction of Radiation by Small Particles," ASME JOURNAL OF HEAT TRANSFER, Vol. 112, pp. 178-185.

Lee, S. C., 1990, "Dependent Scattering of an Obliquely Incident Plane Wave by a Collection of Parallel Cylinder," *Journal of Applied Physics*, Vol. 68, pp. 4952-4957.

Lee, S. C., 1992, "Dependent Scattering by Parallel Fibers: Effects of Multiple Scattering and Wave Interference," *Journal of Thermophysics and Heat Transfer*, Vol. 6, No. 4, pp. 589-595.

Ma, Y., Varadan, V. K., and Varadan, V. V., 1990, "Enhanced Absorption Due

to Dependent Scattering," ASME JOURNAL OF HEAT TRANSFER, Vol. 112, pp. 402-407.

Pitts, W. C., and Murbach, M. S., 1986, "Thermal Design of Aeroassisted Orbital Transfer Vehicle Heat Shields for a Conical Drag Brake," *Journal of Spacecraft and Rockets*, Vol. 23, No. 4, pp. 442-448.

Tien, C. L., and Drolen, B. L., 1987, "Thermal Radiation in Particulate Media With Dependent and Independent Scattering," *Annual Review of Numerical Fluid Mechanics and Heat Transfer*, Vol. 1, pp. 349-417.

Walberg, G. D., 1988, "A Review of Aerobraking for Mars Missions," presented at the 39th Congress of the International Astronautical Federation (Bangalore, India), IAF Paper 88-196, Oct.

White, S. M., and Kumar, S., 1990, "Interference Effects on Scattering by Parallel Fibers at Normal Incidence," *Journal of Thermophysics and Heat Transfer*, Vol. 4, No. 3, pp. 305-310.

# Subcooled Flow Film Boiling Across a Horizontal Cylinder: Part I—Analytical Model

X. S. Chou

Research Assistant.

L. C. Witte

Professor,  
Fellow ASME

Heat Transfer and Phase Change  
Laboratory,  
Department of Mechanical Engineering,  
University of Houston,  
Houston, TX 77204-4792

*An analytical model of stable subcooled flow film boiling on the front of a horizontal cylinder and a model for the wake region downstream of the flow separation points were developed. The flow and temperature fields upstream of the separation points were represented by a "local-similarity" solution obtained through a rigorous mathematical transformation. The transformed governing equations were solved numerically using a finite-difference scheme. Numerical solutions for the vapor layer thickness, the velocity, and the temperature fields were obtained for both the liquid and vapor layers. The results showed that the liquid boundary layer was thicker than the vapor film. Increases in the liquid subcooling and in the free-stream velocity decreased the vapor layer thickness. The influence of convection in the vapor layer is small yielding a near-linear temperature distribution. A two-dimensional vapor wake model was developed based on mass and energy balances. Numerical solutions, including the vapor layer thickness and the temperature field of the front part and the wake part, were matched at the separation points. The results showed that increases in the liquid subcooling decreased the vapor layer thickness. Heat transfer in the wake region can amount up to 20 percent of the heat transfer in the forward region and should not be neglected especially at high subcooling.*

## Introduction

The theory of flow film boiling across bluff bodies that induce flow separation and wake formation is still not complete, even though it has been studied for many years, especially for subcooled systems. Bromley et al. conducted the first systematic theoretical and experimental studies on pool film boiling (Bromley, 1950), flow film boiling (Bromley et al., 1953), and subcooled flow film boiling (Motte and Bromley, 1957). Witte (1968) theoretically studied film boiling from a sphere. Nishikawa et al. (1976) investigated pool film boiling from a vertical plate including the effects of variable thermophysical properties. Srinivasan and Rao (1984) conducted a numerical study on film boiling over a flat plate including the radiation contribution. Witte and Orozco (1984) proposed a physical model for subcooled flow film boiling from a sphere or a cylinder that included nonlinear vapor velocity effects. Chappidi et al. (1990) theoretically examined subcooled flow film boiling from a wedge considering the streamwise pressure gradient imposed on the flow and the streamwise buoyancy force acting on the vapor film. Sakurai et al. (1990) investigated, both theoretically and experimentally, subcooled pool film boiling over a horizontal cylinder and established a correlation that predicts heat transfer very well. Liu et al. (1992) obtained a correlation of flow film boiling across a cylinder for subcooled systems. Shoji and Montasser (1993) modified Witte and Orozco's model (1984) to suit uniform wall heat flux conditions during flow film boiling from cylinders and spheres. Most of the previous analyses are for surfaces that do not involve flow separation and wake formation, or simply omit the heat transfer in the wake region. The previous flow-film-boiling models underestimate the available experimental data by a significant amount, especially for subcooled systems.

This study provides a model for subcooled flow film boiling across a horizontal cylinder that covers the entire cylinder surface

including the front region (called Part One) and the wake region (called Part Two).

A local-similarity solution for the velocity and temperature fields over the front part of cylinder was obtained without resorting to the conventional assumptions that make a solution more tractable. By doing this the influence of subcooling and velocity on the temperature and velocity fields, and the vapor film thickness were obtained. The solution yielded separation points in the vapor flow that lead to the formation of a wake as well as other details of the velocity and temperature fields. The influences of various system parameters can be illuminated using this solution.

The solution over the front part of the cylinder provides input for a model that represents the physical behavior of the vapor in the wake region, past the separation points. In the analysis that follows, a physical model is proposed that will allow for the prediction of heat transfer behavior including the local heat transfer characteristics in the wake region. Prior to this study, this has not been done.

In a companion paper (Chou et al., 1995), the heat transfer results from this analysis (combined front and wake parts of the cylinder) will be compared with experimental data.

## Part One: Solution for Front of Cylinder

The basic physical model is shown schematically in Fig. 1. The vapor is assumed to form a continuous film layer around the cylinder. A liquid boundary layer rides over the vapor layer; it conforms to a potential flow at points far from the vapor-liquid interface. By joining the two symmetric vapor separation points, as shown in this figure, the flow field can be divided into two parts, which are defined as "Part One" and "Part Two" for purposes of analysis. Part One is basically a boundary-layer-type problem since both the vapor film and the liquid layer are fairly thin compared to the cylinder radius (for subcooled systems). Part Two is a wake-type problem, where the vapor film thickness can be much thicker than that over the front part. The boundary-layer theory is available for the first part, whereas it is not applicable to the second part. Solutions, including the vapor layer thickness and the temperature field, of the two parts must be matched at the separation points.

Contributed by the Heat Transfer Division for publication in the JOURNAL OF HEAT TRANSFER. Manuscript received by the Heat Transfer Division September 1993; revision received April 1994. Keywords: Boiling, Forced Convection, Wakes. Associate Technical Editor: R. Viskanta.

**Governing Equations.** The curvilinear orthogonal coordinates  $(x, y)$ , the origin  $(0, 0)$ , and the angle  $\zeta$  are shown in Fig. 1. The following assumptions are made:

- The vapor-liquid interface is smooth and is at the local saturation temperature. (It has been observed that as subcooling increases, the interface becomes smoother and velocity has a much smaller influence.)
- The cylinder surface temperature  $T_w$ , the liquid free-stream velocity  $V_\infty$ , and the bulk liquid temperature  $T_\infty$  are uniform. (It is just an assumption so that the boundary condition can be established.)
- The vapor film layer and the adjacent liquid boundary layer are thin and laminar. (This can be verified by calculations as will be shown later.)
- Viscous dissipation and liquid compression work are negligible. The vapor expansion work is close to that for an ideal gas. (The velocities are relatively low in most film boiling applications as are system pressures.)
- Steady state and steady flow conditions apply.
- Variable physical properties are functions of temperature.
- A cross-cylinder potential flow field exists outside the liquid boundary layer. (Both vapor and liquid layers are thin compared with the cylinder diameter based on the calculations described later.)

The governing equations, including mass, momentum, and energy conservation, in the vapor layer ( $j = v$ ) and the liquid layer ( $j = L$ ) are

$$\frac{\partial}{\partial x}(\rho u)_j + \frac{\partial}{\partial y}(\rho v)_j = 0, \quad (1)$$

$$\begin{aligned} & \rho_j \left( u_j \frac{\partial u_j}{\partial x} + v_j \frac{\partial u_j}{\partial y} \right) \\ &= \frac{2\rho_{L\infty} V_\infty^2}{R} \sin\left(\frac{2x}{R}\right) + g(\rho_{L\infty} - \rho_j) \sin\left(\frac{x}{R}\right) \\ & \quad + \frac{\partial}{\partial y} \left( \mu_j \frac{\partial u_j}{\partial y} \right), \quad (2) \end{aligned}$$

$$\begin{aligned} & (\rho c_p)_j \left( u_j \frac{\partial T_j}{\partial x} + v_j \frac{\partial T_j}{\partial y} \right) \\ &= \left[ -\frac{2\rho_{L\infty} V_\infty^2}{R} u \sin\left(\frac{2x}{R}\right) \right]_{j=v} + \frac{\partial}{\partial y} \left( k_j \frac{\partial T_j}{\partial y} \right), \quad (3) \end{aligned}$$

where the index  $j$  denotes whether the vapor or the liquid region is being described. Note that based on the assumptions the first term of the right-hand side of Eq. (3), the expansion work term, exists for the vapor layer only; this term is zero for the liquid layer.

The boundary conditions and the vapor (without subscript)–liquid (with subscript  $L$ ) interface conditions are

$$y = 0; \quad u = 0, \quad v = 0, \quad T = T_w, \quad (4)$$

$$y = \delta; \quad u = u_L, \quad \mu \frac{\partial u}{\partial y} = \mu_L \frac{\partial u_L}{\partial y}, \quad T = T_L = T_{s1}(x),$$

$$\rho \left( v - u \frac{d\delta}{dx} \right) = \rho_L \left( v_L - u_L \frac{d\delta}{dx} \right) = m, \quad (5)$$

$$-k \frac{\partial T}{\partial y} + q_r = -k_L \frac{\partial T_L}{\partial y} - \rho \left( v - u \frac{d\delta}{dx} \right) h_{fg}, \quad (6)$$

$$y = \delta + \delta_L; \quad u_L = 2V_\infty \sin\left(\frac{x}{R}\right), \quad T_L = T_\infty. \quad (7)$$

## Nomenclature

$A$  = interface shape factor, see Eq. (35)  
 $c_p$  = specific heat, J/(kgK)  
 $c_1, c_2$  = constants  
 $D$  = diameter of cylinder heater, m  
 $f$  = dimensionless velocity function  
 $h$  = local heat transfer coefficient =  $q/(T_w - T_s)$ , W/(m<sup>2</sup>K)  
 $h_{fg}$  = latent heat of evaporation, J/kg  
 $i$  = enthalpy, J/kg  
 $Ja_L$  = Jakob number of liquid =  $c_{pL} \Delta T_{sub} / h'_{fg}$ , where  $h'_{fg} = h_{fg}(1 + 0.4c_p \Delta T_{sat} / h_{fg})^2$ , J/kg  
 $k$  = thermal conductivity, W/(mK)  
 $M, N$  = see Eq. (11)  
 $m$  = mass flux, kg/(m<sup>2</sup>s)  
 $Nu$  = Nusselt number of vapor, see Eq. (40)  
 $P$  = system pressure (pressure in bulk liquid), Pa  
 $Pr$  = Prandtl number of vapor =  $\nu \rho c_p / k$   
 $q$  = heat flux, W/m<sup>2</sup>  
 $Q$  = heat transfer, W  
 $Q_{front}$  = front heat transfer, W  
 $Q_{wake}$  = wake heat transfer, W  
 $R$  = radius of cylinder heater, m  
 $Re_L$  = Reynolds number of liquid =  $V_\infty D / \nu_L$   
 $R'$  =  $(\rho_w / \bar{\rho}) R$ , m  
 $s$  = sign indicator defined in Eqs. (18) and (19)

$T$  = temperature, K  
 $u$  = x-component velocity, m/s  
 $V_\infty$  = free-stream velocity in bulk liquid, m/s  
 $V_n$  = vapor velocity normal to the interface into liquid, m/s  
 $v$  = y-component velocity, m/s  
 $X_0$  = function of  $\zeta$ , defined in Eq. (12)  
 $X$  = coordinate along the heater surface in the wake region, m  
 $x$  = coordinate along the heater surface in the front region, m  
 $Y$  = coordinate normal to the heater surface in the wake region, m  
 $y$  = coordinate normal to the heater surface in the front region, m  
 $\alpha$  = liquid absorptivity  
 $\gamma$  = function of  $\zeta$   
 $\Delta T_{sat}$  = heater surface superheat =  $T_w - T_s$ , K  
 $\Delta T_{sub}$  = liquid subcooling =  $T_s - T_\infty$ , K  
 $\delta$  = thickness of vapor film layer, m  
 $\delta_L$  = thickness of liquid layer, m  
 $\epsilon_w$  = emissivity of heater surface  
 $\zeta$  = angle measured from stagnation point, see Eq. (10)  
 $\eta$  = similarity variable, see Eq. (10)  
 $\theta$  = dimensionless temperature, see Eq. (20)

$\mu$  = viscosity, kg/(ms)  
 $\nu$  = kinematic viscosity, m<sup>2</sup>/s  
 $\rho$  = density, kg/m<sup>3</sup>  
 $\tau$  = dimensionless coordinate =  $X/X_p$   
 $\sigma_s$  = Stefan–Boltzmann constant, W/(m<sup>2</sup>K<sup>4</sup>)  
 $\Phi$  = function of  $\zeta$   
 $\psi$  = stream function  
 $\omega$  = dimensionless coordinate =  $Y/\delta$

## Subscripts

$c$  = angle given in Eqs. (18) and (19)  
 $i$  = local vapor–liquid interface  
 $in$  = in-flow  
 $L$  = liquid  
 $n$  = normal direction at the vapor–liquid interface into the liquid  
 $out$  = outflow  
 $r$  = radiation  
 $s$  = saturation at system pressure  
 $si$  = saturation at local pressure  
 $sp$  = flow separation point in vapor layer  
 $w$  = wall of cylinder surface  
 $\delta$  = vapor–liquid interface  
 $\infty$  = bulk liquid

## Superscript

– = average

## Subscript

$j = j = v$  (vapor);  $j = L$  (liquid)

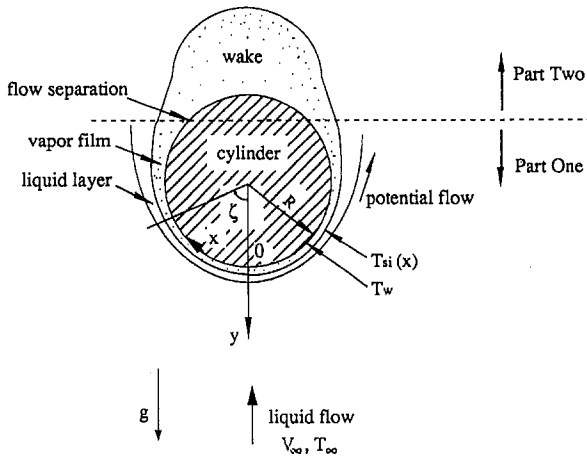


Fig. 1 Physical model of flow film boiling across a cylinder

**Local-Similarity Transformations.** The partial differential Eqs. (1) to (7) are difficult to solve. To simplify the equations, a local-similarity transformation was developed in this study. The idea of local-similarity is a well-known technique in forced convection boundary layer problems for computing the heat transfer in the nonseparated region on bluff bodies like spheres, cylinders, etc. Burmeister (1983) describes local similarity solutions for bodies where similarity does not exist exactly. Sparrow and Yu (1971) give an excellent exposition of this method, and the uncertainties that can arise from it. Wang and Shi (1984) apply the method to a film boiling case. Generally, buoyancy is a major contributor to the nonsimilarity of the solution, along with the geometry. The validity of local-similarity improves for forced-convection cases as the influence of buoyancy declines.

Sakurai et al. (1990) developed a similarity transformation for a pool-boiling solution in which the liquid velocity is zero. However, their transformation cannot be used to solve the present flow boiling problem since the liquid velocity and the pressure gradient are not zero in this study.

The detailed steps of the present local-similarity transformation are given by Chou (1992), and a summary of this transformation is presented in this section. The stream functions  $\psi$  and  $\psi_L$  are introduced as

$$u_j = \left( \frac{\rho_s}{\rho} \frac{\partial \psi}{\partial y} \right)_j, \quad v_j = - \left( \frac{\rho_s}{\rho} \frac{\partial \psi}{\partial x} \right)_j \quad (8)$$

The stream function  $\psi$  is assumed to be separated by two single-variable functions  $\Phi(\zeta)$  and  $f(\eta)$  so that

$$[f(\eta)]_j = \left[ \frac{\psi}{M\Phi(\zeta)} \right]_j \quad (9)$$

where  $\zeta$  and  $\eta$  are the new independent variables, which are similar to the Dorodnitsyn-Stewartson variables (1942, 1950) for variable properties and were used for cylinders (Sakurai et al., 1990), defined as

$$\zeta = \frac{x}{R}, \quad \eta_j = N_j \frac{\gamma_j(\zeta)}{R} \int_{\delta(j=L)}^{0(j=v)} \left( \frac{\rho}{\rho_s} \right)_j dy \quad (10)$$

and

$$M_j = (\nu_s)_j [g(\rho_{L\infty} - \rho_s)R^3 / (\nu_s^2 \rho_s)]_j^{1/4}, \quad N_j = (M/\nu_s)_j \quad (11)$$

In the vapor layer,  $\Phi$  and  $\gamma$  are functions determined by the following relations, which arise from "local similarity" during the transformations:

$$\Phi \gamma' + \Phi' \gamma = X_0 \gamma^2, \quad (12)$$

$$\Phi' = 3\gamma, \quad (13)$$

$$c_1 \sin 2\zeta + c_2 \sin \zeta = sc_2 \Phi \gamma^3, \quad (14)$$

where  $c_1 = 2\rho_{L\infty} V_\infty^2 / RM^2$ , and  $c_2 = g(\rho_{L\infty} - \rho) / M^2 \approx g\rho_{L\infty} / M^2$  (for  $\rho / \rho_{L\infty} \ll 1$ ).

In Eqs. (13) and (14), the constant "3" and "c<sub>2</sub>" are chosen so that if  $V_\infty$  becomes zero, the functions  $\Phi$  and  $\gamma$  will be consistent with the ones in the transformation of Sakurai et al. (1990) for pool boiling ( $V_\infty = 0$ ). The three Eqs. (12)–(14) yield a unique solution for the three functions  $\Phi$ ,  $\gamma$ , and  $X_0$ ,

$$\Phi = \left[ \frac{4}{c_2^{1/3}} \int_{\zeta_c}^{\zeta} |c_1 \sin 2\zeta' + c_2 \sin \zeta'|^{1/3} d\zeta' \right]^{3/4}, \quad (15)$$

$$\gamma = \left[ \frac{1}{c_2 \Phi} |c_1 \sin 2\zeta + c_2 \sin \zeta| \right]^{1/3}, \quad (16)$$

$$X_0 = 2 + s \frac{\frac{4}{3}(2c_1/c_2 \cos 2\zeta + c_2 \cos \zeta)}{|c_1/c_2 \sin 2\zeta + \sin \zeta|^{4/3}} \times \int_{\zeta_c}^{\zeta} |c_1/c_2 \sin 2\zeta' + \sin \zeta'|^{1/3} d\zeta' \quad (17)$$

$$s = 1, \quad \zeta_c = 0, \quad \text{for } (c_1 \sin 2\zeta + c_2 \sin \zeta) > 0, \quad (18)$$

$$s = -1, \quad \zeta_c = \cos^{-1} \left( -\frac{Rg}{4V_\infty^2} \right),$$

$$\text{for } (c_1 \sin 2\zeta + c_2 \sin \zeta) < 0, \quad (19)$$

where, in Eq. (19),  $\zeta_c$  is the root of the equation  $c_1 \sin(2\zeta) + c_2 \sin \zeta = 0$ . The term,  $(c_1 \sin 2\zeta + c_2 \sin \zeta)$ , represents a combined effect of pressure gradient and buoyancy.

Similar expressions result for the liquid layer; they are omitted for the sake of brevity. The details are presented by Chou and Witte (1992). Furthermore, the following variables for the vapor (without subscript) and the liquid (with subscript  $L$ ) layers are introduced:

$$\theta = \frac{T - T_s}{\Delta T_{\text{sat}}}, \quad \theta_L = \frac{T_L - T_\infty}{\Delta T_{\text{sub}}},$$

$$q_{rp} = \frac{\sigma_s}{1/\epsilon_w + 1/\alpha - 1} [T_w^4 - T_{si}^4(\zeta)], \quad (20)$$

where  $q_{rp}$  is the radiation heat flux between two parallel plates (with temperature  $T_w$  and  $T_{si}(\zeta)$ , respectively), and  $\alpha$  is the interface liquid absorptivity which is assumed unity (i.e.,  $\alpha \approx 1$ ) since the absorption distance for heat radiation is usually very short in a liquid. The actual radiation heat flux  $q_r$  is assumed to be a modification of  $q_{rp}$ , which is

$$q_r(\zeta) = q_{rp} \gamma(\zeta) / \bar{\gamma}, \quad (21)$$

where  $\bar{\gamma} = 1/\zeta_{sp} \int_0^{\zeta_{sp}} \gamma d\zeta$  and  $\zeta_{sp}$  is the angle at the vapor flow separation point, which is determined numerically. Assumption (21) is introduced to make the local-similarity transformation possible. Numerical calculations show that radiation is not important for the cases studied; therefore, assumption (21) will cause little deviation.

Based on the transformation Eqs. (8)–(21), the governing Eqs. (1)–(3), the boundary conditions (4) and (7), and the interface conditions (5) and (6) are finally transformed into

$$\left[ \left( \frac{\rho \mu}{\rho_s \mu_s} f'' \right)' + 3ff'' - X_0 f'^2 + \frac{sc_2 R^3}{N^2 \rho} \right]_j = 0, \quad (22)$$

$$\left[ \left( \frac{\rho k}{\rho_s k_s} \theta' \right)' + 3 \text{Pr}_s \frac{c_p}{c_{ps}} f \theta' \right]_j - \left( \frac{R^2 \rho_s \nu_s I_0}{\rho k_s \Delta T_{\text{sat}}} f' \right)_{j=v} = 0, \quad (23)$$

$$f(0) = 0, \quad f'(0) = 0, \quad \theta(0) = 1, \quad (24)$$

$$(f_L)_i = K_s R_s \frac{\Phi'}{\Phi_L} (f)_i, \quad (f'_L)_i = K_s^2 \frac{\Phi \gamma}{\Phi_L \gamma_L} (f')_i, \quad (25)$$

$$(f''_L)_i = K_s^3 R_i^2 R_s^{-1} \frac{\Phi \gamma^2}{\Phi_L \gamma_L^2} (f'')_i, \quad (26)$$

$$(\theta)_i = \frac{(T_{si} - T_s)}{\Delta T_{\text{sat}}}, \quad (\theta_L)_i = \frac{(T_{si} - T_{\infty})}{\Delta T_{\text{sub}}}, \quad (27)$$

$$Sp_s = -Q_i (f/\theta')_i + S_i / (\theta')_i + A_i Sc_s (\theta'_L/\theta')_i, \quad (28)$$

$$f'_L(\eta_{\delta L}) = \frac{2RV_{\infty} \sin \zeta}{N_L M_L \gamma_L \Phi_L}, \quad \theta_L(\eta_{\delta L}) = 0, \quad (29)$$

where

$$I_0 = c_2 \Phi \left( s \Phi \gamma^2 - \frac{\sin \zeta}{\gamma} \right),$$

$$K_s = \left[ \frac{(\rho_{L\infty} - \rho_s) / \rho_s}{(\rho_{L\infty} - \rho_{Ls}) / \rho_{Ls}} \right]^{1/4}, \quad R_s = \left( \frac{\rho_s \mu_s}{\rho_{Ls} \mu_{Ls}} \right)^{1/2},$$

$$Sp_s = \frac{c_{ps} \Delta T_{\text{sat}}}{h_{fgs} Pr_s}, \quad Sc_s = \frac{c_{pLs} \Delta T_{\text{sub}}}{h_{fgs}},$$

$$R_i = \left[ \left( \frac{\rho \mu}{\rho_L \mu_L} \right)_i \right]^{1/2}, \quad Q_i = \frac{3 \rho_s k_s}{h_{fgs}} \left( \frac{h_{fg}}{\rho k} \right)_i,$$

$$S_i = \frac{Rk_s}{h_{fgs} \gamma M} \left( \frac{q_{fp}}{\rho k} \right)_i, \quad A_i = \frac{k_s \rho_s}{k_{Ls} \rho_{Ls} K_s R_s Pr_{Ls}} \left( \frac{k_L \rho_L}{k \rho} \right)_i \frac{\gamma_L}{\gamma},$$

$$\eta_{\delta L} = (\eta_L)_{y=\delta+bl}.$$

The transformed Eqs. (22) to (29) become a set of ordinary differential equations locally for any given angle  $\zeta$  that yields a local-similarity solution. The quantity  $\zeta$  may be regarded as a constant parameter at any streamwise location. The equations corresponding to any given  $\zeta$  value are independent of the equations at any other  $\zeta$ . By assigning a succession of  $\zeta$  values, the streamwise dependence of velocity and temperature fields can be determined.

**Numerical Method and Numerical Results.** The transformed Eqs. (22)–(29) have been numerically solved using a finite-difference method. Once the dimensionless velocity function,  $f$ , is obtained in Eqs. (22) and (23), the stream function,  $\psi$ , can be found from Eq. (9), which in turn gives both the  $u$ - and  $v$ -components of velocity at all points based on Eq. (8).

Energy is balanced at the vapor–liquid interface (Eq. (6)) to determine the vapor film thickness. The thickness of the liquid boundary layer is taken as the point where either the velocity becomes 99 percent of the potential flow velocity or the temperature becomes 99 percent of the bulk liquid temperature (the thicker one of the two is selected). Both the vapor layer and the liquid layer thicknesses are successively obtained by using an iteration method. The steps are repeated for each angle  $\zeta$ . The flow separation points of the vapor layer are evaluated by using the condition,

$$\left( \frac{\partial u}{\partial y} \right)_{y=0} = 0.$$

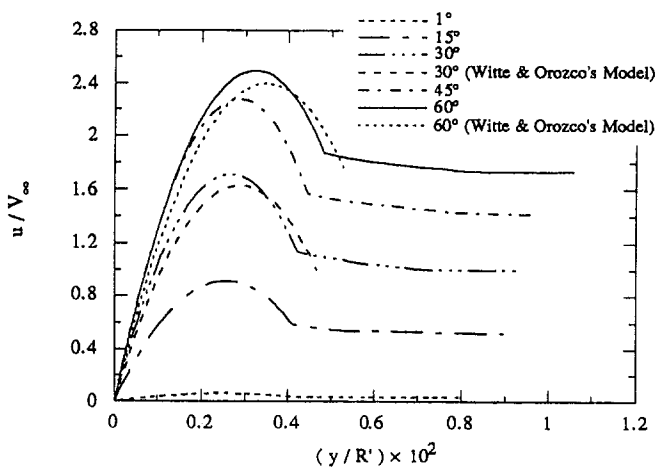
Additionally, the derivative changes sign through the separation points.

Although the transformed governing equations were solved in dimensionless form, it should be noted that specific cases for water were calculated to illustrate the nature of the results. Because of the influence of property variations, the numerical results for velocity and temperature profiles can differ for different input parameters even though dimensionless numbers like  $Ja_L$ ,  $Re_L$ ,  $Pr$ , etc., might be held constant. Thus, we have only included in this paper some calculations with water to show how various parameters affect the general solution. The values of the dimen-

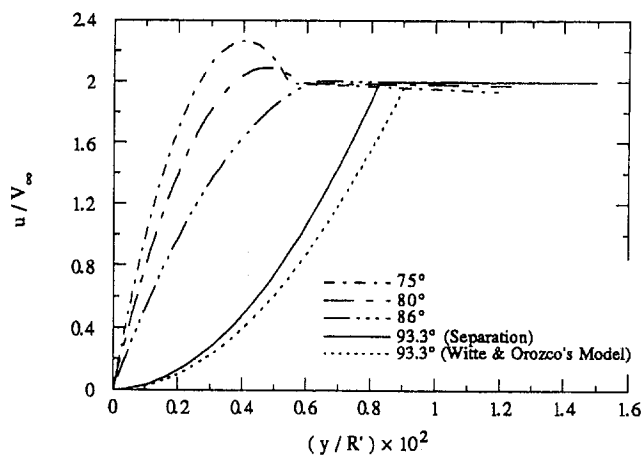
sionless numbers are included in the captions for convenience so that the reader doesn't need to calculate them. Physical properties of water were evaluated by using thermophysical property software (NBS-NRC Tables) called during the computations. Water was chosen because its properties are well known throughout large ranges of temperature and pressure.

Numerical results show that increased liquid subcooling significantly thins both the vapor and liquid layers. The vapor separation angle  $\zeta_{sp}$  is increased with increased subcooling. The liquid layer is thicker than the vapor layer over the front part of cylinder in most of the cases.

Figures 2(a, b) present the velocity profiles in vapor and liquid at different angles over the cylinder from the near-stagnation point ( $\zeta = 1$  deg) to the separation point ( $\zeta = 93.3$  deg) for the given case. The dimensionless numbers,  $Pr$  and  $Re_L$ , given in the figures are evaluated at the average temperatures of vapor and liquid, respectively. The discontinuous velocity gradient points indicate the location of the vapor–liquid interface as shown in the figures. The velocity in the vapor, for the given case, first increases with the angles  $\zeta$  from 1 to 60 deg, and then decreases with angles from 60 to 93.3 deg. The highest vapor velocity curve is found at about 60 deg. In the liquid boundary layer, except for

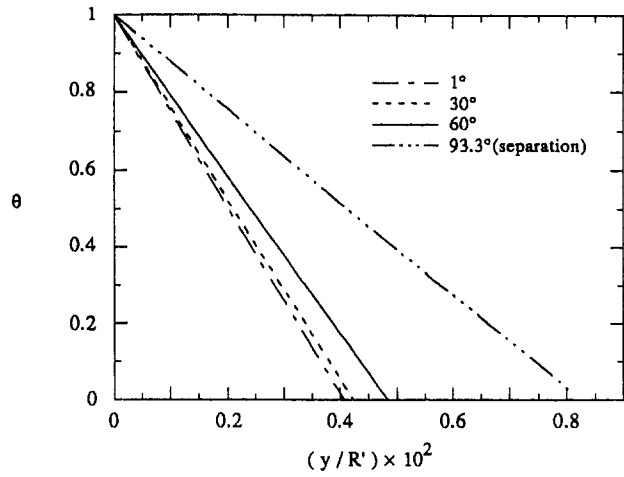


(a)  $\zeta = 1^\circ$  to  $60^\circ$

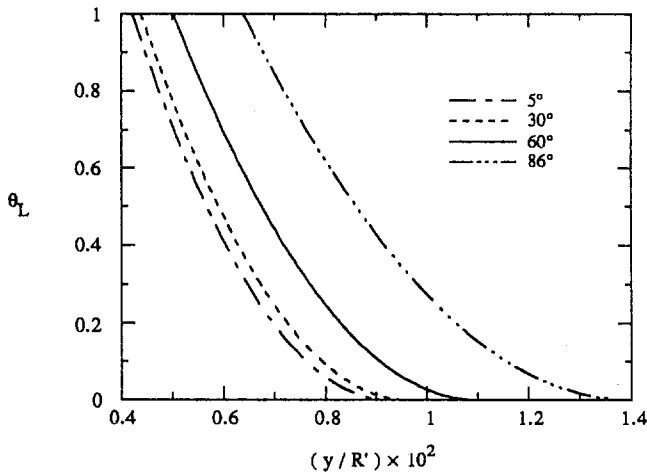


(b)  $\zeta = 75^\circ$  to  $93.3^\circ$

**Fig. 2 Velocity profiles in vapor and liquid layers at different angles: (a)  $\zeta = 1$  to  $60$  deg; (b)  $\zeta = 75$  to  $93.3$  deg. Water,  $R = 10$  mm,  $\epsilon_w = 0.12$ ,  $V_{\infty} = 1$  m/s,  $\Delta T_{\text{sat}} = 400^\circ\text{C}$ ,  $\Delta T_{\text{sub}} = 30^\circ\text{C}$ ,  $P = 0.313$  MPa,  $Pr = 0.94$ ,  $Re_L = 82,000$ .**



(a) vapor layer



(b) liquid layer

Fig. 3 Temperature profiles at different angles: (a) vapor layer; (b) liquid layer. Water,  $R = 10$  mm,  $\epsilon_w = 0.12$ ,  $V_\infty = 1$  m/s,  $\Delta T_{\text{sat}} = 400^\circ\text{C}$ ,  $\Delta T_{\text{sub}} = 30^\circ\text{C}$ ,  $P = 0.313$  MPa,  $Pr = 0.94$ ,  $Re_L = 82,000$ .

the stagnation region, the velocity curves are somewhat steeper at the lower part of the cylinder than those near the separation point. The velocity gradients in the liquid layer exhibit the influence of vapor drag. The velocity profiles based on Witte and Orozco's model (1984), for the same case, are also plotted in Fig. 2(a, b) for three angles 30, 60, and 93.3 deg in order to compare them with the results of the current model. Witte and Orozco's velocity profiles end at the vapor-liquid interface since the potential velocity is assumed at the interface; therefore, no vapor drag induced velocity gradients in the liquid exists. The peak vapor velocities are higher and the vapor film thicknesses are smaller as a result of the current model than that of Witte and Orozco for a given angle, thus a higher heat transfer is obtained from the current model.

The temperature profiles in the vapor film at various angles around the cylinder from the cylinder bottom to the vapor separation point are shown in Fig. 3(a). A nondimensional temperature of unity represents the cylinder wall temperature, and a nondimensional temperature in the vapor of zero represents the saturation temperature. The temperature profiles in the vapor layer are virtually linear. The linear temperature distributions suggest that conduction dominates the heat transfer through the

vapor film, while convection and radiation across the vapor film are small compared with conduction, based on the numerical computations for these conditions. Additionally, the vapor expansion work term in Eq. (3) is relatively small according to the numerical results.

The temperature profiles in the liquid layer at different angles are shown in Fig. 3(b). The nondimensional temperature of unity represents saturation temperature. The lowest nondimensional temperature in the liquid of zero represents the bulk liquid temperature. The temperature profiles are no longer linear. Convection plays a role in the total heat transfer within the liquid layer.

Although illustrative plots are not included, the effects of bulk liquid velocity, superheat, cylinder diameter and system pressure were also studied (for details, see Chou, 1992). Numerical results show that the velocities of the vapor and liquid layers are increased with bulk liquid velocity. The vapor film thickness is reduced with increased bulk liquid velocity. For a given angle  $\zeta$ , the vapor layer thickness  $\delta$  increases with the superheat  $\Delta T_{\text{sat}}$  and the cylinder diameter,  $D$ . The effect of superheat on the vapor layer thickness is nearly linear. For a given angle  $\zeta$ , increasing the system pressure  $P$  has only a small effect on the thickness of the vapor layer in the calculated pressure range.

## Part Two: Wake Solution and Heat Transfer Results

As previously described, the wake is defined as the region downstream of the separation points in vapor flow. The two-dimensional vapor wake cross section is schematically shown in Fig. 4. The curvilinear orthogonal coordinates ( $X$ ,  $Y$ ) and the separation point,  $X_{sp}$ , are also shown in the figure.

The vapor is assumed to form a continuous, smooth and steady film layer (vapor bubble) in the wake. Since vapor flow separates at the angle  $\zeta_{sp}$ , the arc length  $X_{sp}$  of the separated region on the wall, measured from the origin, should be  $(\pi - \zeta_{sp})R$ . The vapor layer thickness of the wake region must match the solution of the front part of the heater at the separation point  $X_{sp}$ . The cylinder surface temperature and the vapor-liquid interface temperature are assumed uniform, and are  $T_w$  and  $T_s$ , respectively.

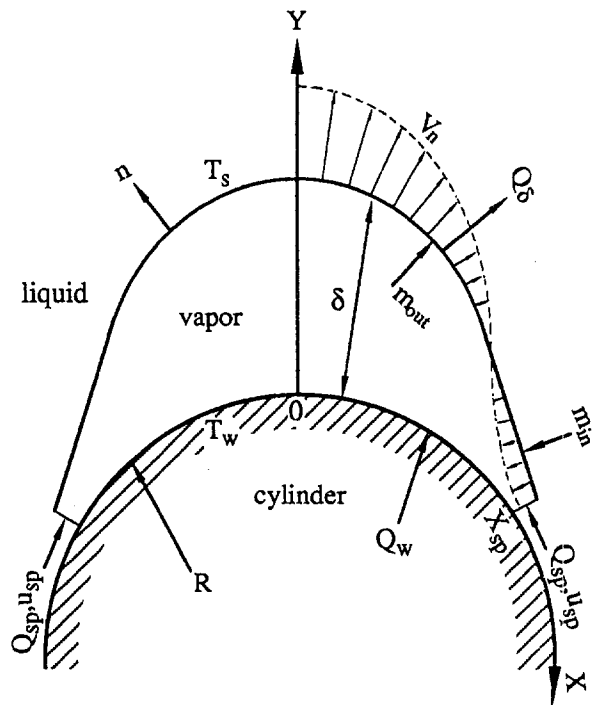


Fig. 4 Two-dimensional wake model

Based on the two-dimensional model, both an energy balance and a mass balance are applied as follows.

**Energy Balance.** Considering the right-hand half of a symmetric vapor bubble as shown in Fig. 4, for steady state, the heat inflow from the front part at the separation point,  $Q_{sp}$ , and the heat conducted in from the hot cylinder wall,  $Q_w$ , should balance the net heat outflow across the vapor-liquid interface,  $Q_\delta$ ; i.e.,

$$Q_{sp} + Q_w = Q_\delta \quad (30)$$

where

$$Q_{sp} = \int_0^{\delta_{sp}} \left( k \frac{\partial T}{\partial X} \right)_{sp} dY + \int_0^{\delta_{sp}} (\rho u i)_{sp} dY$$

$$Q_w = \int_0^{X_{sp}} \left( -k \frac{\partial T}{\partial Y} \right)_w dX$$

$$Q_\delta = \int_0^{X_{sp}} \left( -k_s \frac{\partial T}{\partial n} \right) \sqrt{1 + \delta'^2} dX + \int_0^{X_{sp}} (\rho_s V_n i_s) \sqrt{1 + \delta'^2} dX$$

$$X_{sp} = (\pi - \zeta_{sp})R, \quad \delta' = d\delta/dX,$$

$$e_n = (-\delta' e_x + e_y)/(1 + \delta'^2)^{1/2}.$$

The term  $\sqrt{1 + \delta'^2} dX$ , in the equation for  $Q_\delta$ , is the infinitesimal unit of the arc length along the vapor-liquid interface.

**Mass Balance.** The control volume is the same as that in the energy balance analysis given above. For a steady-state vapor bubble, the mass inflow from the front part at the separation point,  $m_{sp}$ , and the mass inflow across the lower part of the bubble interface,  $m_{in}$ , should balance the mass outflow across the upper part of the bubble interface,  $m_{out}$ ; i.e.,

$$m_{sp} + m_{in} = m_{out}$$

where

$$m_{sp} = \int_0^{\delta_{sp}} (\rho u)_{sp} dY$$

$$m_{out} - m_{in} =$$

$$\int_0^{X_{sp}} \rho_s V_n \sqrt{1 + \delta'^2} dX \quad (\text{net mass flux across the interface})$$

Therefore, we have

$$\int_0^{X_{sp}} \rho_s V_n \sqrt{1 + \delta'^2} dX = \int_0^{\delta_{sp}} (\rho u)_{sp} dY \quad (31)$$

Combining energy and mass balance Eqs. (30) and (31) gives

$$\begin{aligned} & \int_0^{\delta_{sp}} \left( k \frac{\partial T}{\partial X} \right)_{sp} dY + \int_0^{\delta_{sp}} (\rho u i)_{sp} dY + \int_0^{X_{sp}} \left( -k \frac{\partial T}{\partial Y} \right)_w dX \\ & = \int_0^{X_{sp}} \left( -k_s \frac{\partial T}{\partial n} \right) \sqrt{1 + \delta'^2} dX + i_s \int_0^{\delta_{sp}} (\rho u)_{sp} dY \end{aligned}$$

Regrouping this equation gives

$$\int_0^{X_{sp}} k_w \left( \frac{\partial T}{\partial Y} \right)_w dX - \int_0^{X_{sp}} k_s \frac{\partial T}{\partial n} \sqrt{1 + \delta'^2} dX = Q'_{sp} \quad (32)$$

where

$$Q'_{sp} = \int_0^{\delta_{sp}} \left[ k \frac{\partial T}{\partial X} + \rho u (i - i_s) \right]_{sp} dY$$

$Q'_{sp}$  is evaluated at the separation section ( $X = X_{sp}$ ) and thus can be obtained using the numerical results on the front of the cylinder at the separation point.

Note that Eq. (32) can be derived in another way; i.e., by applying an energy balance in which the saturation enthalpy is used as the reference point of convective heat flux. The purpose of using Eqs. (30) and (31) is to demonstrate how energy and mass are balanced simultaneously.

By applying the nondimensional temperature  $\theta = (T - T_s)/(T_w - T_s)$ , and by using variable transformations  $\tau = X/X_{sp}$  and  $\omega = Y/\delta$  that result in a regular flat interface, Eq. (32) can be transformed into

$$\begin{aligned} \Delta T_{sat} X_{sp} \int_0^1 \left\{ \frac{k_w}{\delta} \left( \frac{\partial \theta}{\partial \omega} \right)_{\omega=0} \right. \\ \left. + k_s \left[ \frac{1}{X_{sp}^2} \frac{d\delta}{d\tau} \left( \frac{\partial \theta}{\partial \tau} - \frac{1}{\delta} \frac{d\delta}{d\tau} \frac{\partial \theta}{\partial \omega} \right) - \frac{1}{\delta} \frac{\partial \theta}{\partial \omega} \right]_{\omega=1} \right\} d\tau = Q'_{sp} \quad (33) \end{aligned}$$

To solve Eq. (33), the following additional assumptions are made:

- $\theta = 1 - \omega$

(linear temperature distribution across the vapor film) (34)

- $\delta(\tau) = A[1 + \cos(\pi\tau)] + \delta_{sp}$ , where  $A = [\delta(0) - \delta_{sp}]/2$   
(cosine function for the interface shape) (35)

Previously, numerical results for the forward part of the cylinder showed that the vapor temperature distribution is virtually linear. The fact that the vapor has very small heat capacity also suggests that heat conduction dominates wake heat transfer and the temperature profile across the vapor film should approach a linear distribution. As far as the reason why we choose the cosine interface shape, the cosine function (35) gives a closed curve, which satisfies the following boundary conditions:  $\delta = \delta_{sp}$  at  $X = X_{sp}$ ;  $\delta' = 0$  at  $X = 0$ ; and  $\delta = \delta_{max}$  at  $X = 0$ . By applying the assumed temperature and interface profiles, and by integrating Eq. (33), we get

$$\begin{aligned} \frac{\pi^2 k_s \Delta T_{sat}}{X_{sp}} [A + \delta_{sp} - \sqrt{\delta_{sp}(2A + \delta_{sp})}] \\ - \frac{(k_w - k_s) \Delta T_{sat} X_{sp}}{\sqrt{\delta_{sp}(2A + \delta_{sp})}} = Q'_{sp}. \quad (36) \end{aligned}$$

Equation (36) yields a unique solution for the variable "A," which determines a cosine interface shape given in Eq. (35).

**Numerical Results.** The vapor film thicknesses over the entire cylinder surface at different liquid subcooling are shown in Fig. 5. It can be seen from the figure that the increase of subcooling largely reduces the vapor thickness. At the separation point, the vapor layer thickness of the wake part matches the solution of the front part.

It is observed from the numerical results that if subcooling is increased up to a certain level ( $\Delta T_{sub} > 110^\circ\text{C}$  for a typical case like Fig. 6 in which  $T_s = 135^\circ\text{C}$ ), the vapor film thickness in Part One becomes virtually uniform. If subcooling further increases to a higher level, the vapor film thickness in the wake part (Part Two) also becomes uniform; therefore, at this high-subcooling condition, the vapor film acquires an almost constant thickness over the entire cylinder surface. Obviously, such a high level of subcooling is difficult to achieve in experimental studies and is also beyond actual applications in industries.

The local heat transfer coefficient ( $h$ ) over the front part of cylinder can be calculated, for any given angle  $\zeta$ , by using the following equation:

$$h = -(k \partial T / \partial y)_{y=0} / \Delta T_{sat} = -\frac{N \rho_w k_w \gamma}{R \rho_s} \theta'(0) \quad (37)$$

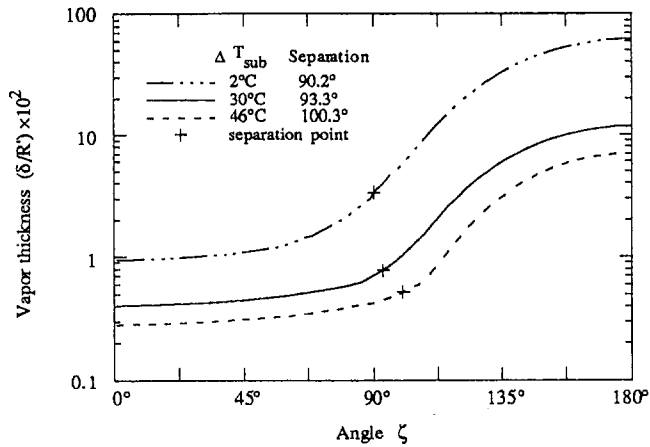


Fig. 5 Angular dependence of vapor film thickness around a cylinder:  $R = 10$  mm,  $V_\infty = 1$  m/s,  $\epsilon_w = 0.12$ ,  $P = 0.313$  MPa,  $\Delta T_{\text{sat}} = 400^\circ\text{C}$ , water,  $Pr = 0.94$ ,  $Re_L = 82000$ ,  $Ja_L = 0.01 \sim 0.08$

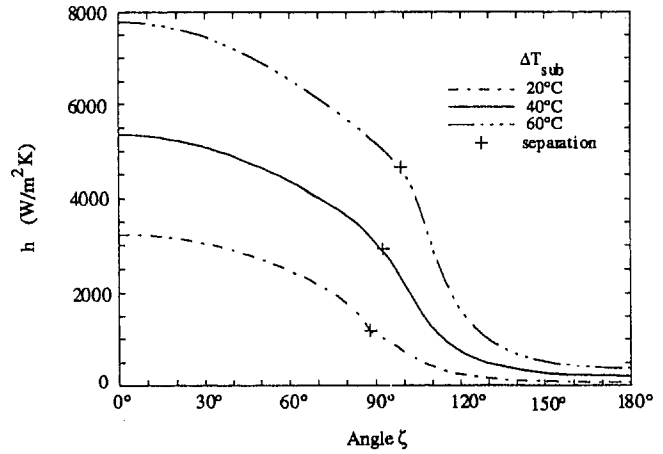


Fig. 6 Local heat transfer coefficient around a cylinder:  $P = 0.313$  MPa,  $V_\infty = 2.95$  m/s,  $R = 3.2$  mm,  $\epsilon_w = 0.12$ ,  $\Delta T_{\text{sat}} = 515^\circ\text{C}$ , water,  $Re_L = 77,400$ ,  $Pr = 0.85$ ,  $Ja_L = 0.03 \sim 0.1$

The local heat transfer coefficient ( $h$ ) in the wake can be calculated using the same procedure as used for the front part. This culminates in the equation,  $h = k_w/\delta$ .

The numerical results of the local heat transfer coefficients on the front and in the wake of the cylinder are shown in Fig. 6 for a typical set of operating parameters. The plot shows the local heat transfer over the entire cylindrical surface from the bottom (angle 0 deg) to the top (angle 180 deg). Again, water has been chosen because of the availability of property data. The liquid subcooling is  $20^\circ\text{C}$ ,  $40^\circ\text{C}$ , and  $60^\circ\text{C}$ , respectively. The separation points for different subcoolings are also shown in the figure. The solutions for the front and the wake must be matched at the separation points.

As shown in Fig. 6, the local heat transfer decreases with increased angle in response to increased vapor film thickness. The highest local heat transfer coefficient occurs at the bottom of a cylinder (angle 0 deg), while the lowest one occurs at the top (angle 180 deg). The effects of subcooling on heat transfer are observed to be significant. It can be seen from the figure that  $h$  is more than twice as large at  $\Delta T_{\text{sub}} = 60^\circ\text{C}$  than at lower subcooling  $\Delta T_{\text{sub}} = 20^\circ\text{C}$ .

The average heat transfer coefficient,  $\bar{h}$ , is determined by integrating the local heat transfer coefficient ( $h$ ) over the entire cylinder surface. The integration domain includes two parts, which are the front of the cylinder and the wake. In other words, the average heat transfer coefficient of a cylinder can be calculated by using the following equation:

$$\bar{h} = \frac{Q}{2\pi R(T_w - T_s)}, \quad (38)$$

where  $Q$  is the total heat transfer over the entire cylinder surface given by

$$Q = \int_0^\pi h(\zeta) \Delta T_{\text{sat}} R d\zeta \quad (39)$$

The overall Nusselt number ( $Nu$ ), also called the average Nusselt number, for a cylinder can then be calculated using the following equation:

$$Nu = \frac{\bar{h}D}{k}, \quad (40)$$

where  $k$  is evaluated at the vapor film temperature, that is,  $(T_w + T_s)/2$ . The numerical solutions for the average Nusselt number at one set of system variables is shown in Fig. 7. It is clear that the Nusselt number is a strong function of liquid subcooling.

$Q_{\text{front}}$  is defined as the heat transfer in the front part up to the separation point, while  $Q_{\text{wake}}$  is that heat transfer from the cylinder surface in the wake. A review of the literature indicates that the wake heat transfer was neglected in previous theoretical analyses as described earlier in this paper. The present model contributes, for the first time, a solution for heat transfer over an entire cylinder surface including the wake region.

The numerical solutions for wake heat transfer compared to the front heat transfer are shown in Fig. 8. The relative magnitude ( $Q_{\text{wake}}/Q_{\text{front}}$ ) of wake and front heat transfer is increased with increased subcooling. The magnitude is up to about 20 percent at high subcooling and, therefore, it should not be neglected, especially at high subcooling. This result helps explain why previous flow-film-boiling models underestimated experimental data by a significant amount.

## Conclusions

Based on the results obtained from this study, the following conclusions are made:

1 A local-similarity solution successfully predicts flow-film-boiling behavior on the front part of a cylinder. The local-similarity transformation can be used not only for this study but also for similar problems. The validity of the local-similarity solution

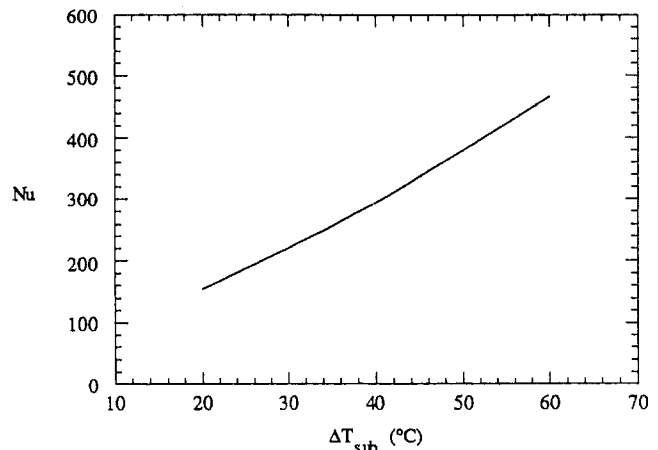


Fig. 7 The effect of liquid subcooling on average Nusselt number:  $P = 0.313$  MPa,  $V_\infty = 2.95$  m/s,  $R = 3.2$  mm,  $\epsilon_w = 0.12$ ,  $\Delta T_{\text{sat}} = 515^\circ\text{C}$ , water,  $Re_L = 77,400$ ,  $Pr = 0.85$ ,  $Ja_L = 0.03 \sim 0.1$



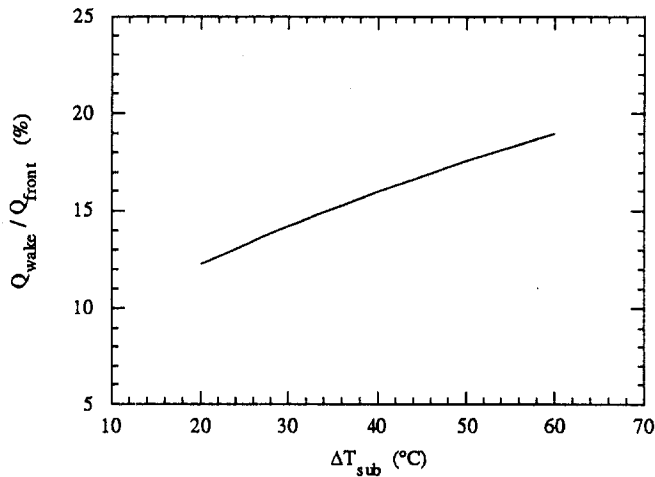


Fig. 8 Relative magnitudes of wake and front heat transfer at different subcooling:  $P = 0.313$  MPa,  $V_\infty = 2.95$  m/s,  $R = 3.2$  mm,  $\epsilon_w = 0.12$ ,  $\Delta T_{sat} = 515^\circ\text{C}$ , water,  $Re_L = 77,400$ ,  $Pr = 0.85$ ,  $Ja_L = 0.03 \sim 0.1$

improves for forced-convection cases when the influence of buoyancy declines.

2 Over the front part of a cylinder, the vapor film is thin compared with the cylinder diameter, while in the wake part behind a cylinder, the vapor film is relatively thick compared with that over the front part of a cylinder. The vapor film is thinner than the adjacent liquid boundary layer over the front part of a cylinder.

3 The vapor-flow separation angle is increased with increased liquid subcooling. The increase of subcooling has a significant effect on thinning both the vapor and liquid layers. A thinner vapor film is found at higher liquid velocity, lower wall superheat, smaller cylinder diameter, or lower system pressure.

4 If subcooling is increased up to a certain high level, the vapor film thickness approaches uniformity over the front part of a cylinder. This uniformity is extended to the wake part as well if subcooling further increases.

5 There exists some degree of vapor drag on the liquid layer over the lower part of a cylinder. The drag is decreased downstream, and becomes negligible near the separation points.

6 The temperature profiles are virtually linear in the vapor film over the front part of a cylinder, but not in the liquid layer. Heat convection and radiation are minor contributors to total heat transfer.

7 Heat transfer in the wake region, one of the major findings in this study, can amount up to 20 percent of the front heat transfer at high subcooling.

## Acknowledgments

This work was performed in its early stages with support from DoE Office of Basic Energy Sciences grant DE-FG05-88ER13893 and NSF grant CBT-8803569. In the latter stages it was funded in part from a Texas Advanced Technology Project, ATP 2040, and a Texas Advanced Research Project, ARP-00365204.

## References

- Bromley, L. A., 1950, "Heat Transfer in Stable Film Boiling," *Chem. Eng. Progr.*, Vol. 46, May, pp. 221–227.
- Bromley, L. A., Leroy, N. R., and Robbers, J. A., 1953, "Heat Transfer in Forced Convection Film Boiling," *Ind. Eng. Chem.*, Vol. 45, No. 1, Dec., pp. 2639–2646.
- Burmeister, L. C., 1983, *Convective Heat Transfer*, Wiley, pp. 310, 335–337.
- Chappidi, P. R., Gunnerson, F. S., and Pasamehmetoglu, K. O., 1990, "Forced Convection Film Boiling Drag and Heat Transfer of a Wedge," Paper No. AIAA-90-1374.
- Chou, X. S., 1992, "Subcooled Flow Film Boiling Across a Horizontal Cylinder," Ph.D. Dissertation, University of Houston, Houston, Texas.
- Chou, X. S., and Witte, L. C., 1992, "A Theoretical Model for Flow Film Boiling Across Horizontal Cylinders," Paper No. AIAA-92-4051.
- Chou, X. S., Sankaran, S., and Witte, L. C., 1995, "Subcooled Flow Film Boiling Across a Horizontal Cylinder: Part II—Comparison to Experimental Data," *ASME JOURNAL OF HEAT TRANSFER*, Vol. 117, this issue, pp. 175–178.
- Dorodnitsyn, A., 1942, "On the Boundary Layer of a Compressible Gas," *Prikladnaia Matematika i Mekhanika*, Vol. 6, pp. 449–485.
- Liu, Q. S., Shiotsu, M., and Sakurai, A., 1992, "A Correlation for Forced Convection Film Boiling Heat Transfer From a Horizontal Cylinder Under Subcooled Conditions," *Fundamentals of Subcooled Flow Boiling*, ASME HTD-Vol. 217, pp. 21–32.
- Motte, E. I., and Bromley, L. A., 1957, "Film Boiling of Flow Subcooled Liquids," *Ind. Eng. Chem.*, Vol. 49, No. 11, Nov., pp. 1921–1928.
- Nishikawa, K., Ito, T., and Matsumoto, K., 1976, "Investigation of Variable Thermophysical Property Problem Concerning Pool Film Boiling From Vertical Plate With Prescribed Uniform Temperature," *Int. J. Heat Mass Transfer*, Vol. 19, pp. 1173–1182.
- Sakurai, A., Shiotsu, M., and Hata, K., 1990, "A General Correlation for Pool Film Boiling Heat Transfer From a Horizontal Cylinder to Subcooled Liquid: Part 1—A Theoretical Pool Film Boiling Heat Transfer Model Including Radiation Contributions and Its Analytical Solution," *ASME JOURNAL OF HEAT TRANSFER*, Vol. 112, May, pp. 430–440.
- Shoji, M., and Montasser, O., 1993, "Theoretical Analysis of Uniform Wall Heat Flux and Uniform Wall Temperature Forced Convection Film Boiling Heat Transfer," *Journal of the Faculty of Engineering, The University of Tokyo (B)*, Vol. XLII, No. 1, pp. 41–56.
- Sparrow, E. M., and Yu, H. S., 1971, "Local Non-similarity Thermal Boundary-Layer Solutions," *ASME JOURNAL OF HEAT TRANSFER*, Nov. 1971, pp. 328–334.
- Srinivasan, J., and Rao, N. S., 1984, "Numerical Study of Heat Transfer in Laminar Film Boiling by the Finite-Difference Method," *Int. J. Heat Mass Transfer*, Vol. 27, No. 1, pp. 77–84.
- Stewartson, K., 1950, "Correlated Incompressible and Compressible Boundary Layers," *Proc. Roy. Soc. London A*, Vol. 200, pp. 84–100.
- Wang, B. X., and Shi, D. H., 1984, "Film Boiling in Laminar Boundary-Layer Flow Along a Horizontal Plate Surface," *Int. J. Heat Mass Transfer*, Vol. 27, No. 7, pp. 1025–1029.
- Witte, L. C., 1968, "Film Boiling From a Sphere," *I. and E. C.—Fundamentals*, Vol. 7, No. 3, Aug., pp. 517.
- Witte, L. C., and Orozco, J., 1984, "The Effect of Vapor Velocity Profile Shape on Flow Film Boiling From Submerged Bodies," *ASME JOURNAL OF HEAT TRANSFER*, Vol. 106, pp. 191–197.

# Subcooled Flow Film Boiling Across a Horizontal Cylinder: Part II—Comparison to Experimental Data

X. S. Chou  
Research Assistant.

S. Sankaran<sup>1</sup>  
Research Assistant.

L. C. Witte  
Professor,  
Fellow ASME

Heat Transfer and Phase Change  
Laboratory,  
Department of Mechanical Engineering,  
University of Houston,  
Houston, TX 77204-4792

*In this paper, the results of a rigorous heat transfer analysis of subcooled flow film boiling over a heated cylinder are compared to experimental data. The analysis includes both the influence of the front part of the heater and the wake region behind the heater. Experiments using Freon-113 were conducted at subcooling levels up to 58°C and at velocities up to 3.81 m/s. The configuration was upflowing Freon-113 in crossflow over a 0.635-cm electric heater. A comparison of these data as well as other available experimental data to the analysis of Chou and Witte showed good agreement as long as the subcooling level of the liquid was substantial—that is, for liquid Jakob numbers above about 0.04. This represents a considerable improvement over other models that have been developed to predict subcooled flow boiling heat transfer. A method using a temperature correction to a constant-property heat transfer solution that corresponds to the full variable-property solution is also presented, and applied to water and Freon-113.*

## Introduction

In a companion paper, Chou and Witte (1995), subcooled flow film boiling across a horizontal cylinder has been completely analyzed, including for the first time a heat transfer analysis of the wake region behind the cylinder. In this paper the results of this complete analysis are compared to experimental data for highly subcooled Freon-113 obtained in our laboratory as well as other available experimental data.

The analysis of Chou and Witte included the effects of variable thermophysical vapor properties upon the kinematics of the flow around the cylinder as well as on the heat transfer from the heated surface. Such an analysis requires a very complex analytical procedure that is costly and not well suited for general analysis. Consequently a method of correcting the variable-property solution so that a much simpler constant-property solution can be used to represent the average heat transfer from a horizontal heater will be presented.

## Experimental Apparatus

Experimental boiling data were obtained using a flow loop designed and fabricated to produce steady, low-temperature flows over an electric heater. Complete details of the apparatus are given by Sankaran (1990) and Sankaran and Witte (1990). Figure 1 shows a layout of the flow loop. Liquid velocity was controlled by a variable speed 450 gpm pump. The flow passed through various flow-straightening sections before passing through a transparent Plexiglas test section across which the heater was suspended. The test section was 8 × 8 cm; the 0.635-cm-dia heater suspended across it represented less than 8 percent blockage. Equally important, the loop has a preconditioning section upstream of the test section that removes the boundary layers from the walls of the loop. Thus the flow represented a close approximation to an infinite flow field as it entered the test section.

A water-cooled Filtrine POC-500 W of 16 kW cooling capacity was used to maintain the flowing coolant at the desired temperature. Freon-113 temperatures down to 0°C were possible with the use of this chiller. The system was designed such that the temperature of the working fluid would rise less than 1.0°C/min at the maximum heating rates.

Flow rates used to calculate flow velocities in the test section were measured with an annubar element. A pitot tube traverse across the test section was used to verify that the calibration curve of the annubar was accurate. Thermocouples and pressure taps were installed at various points in the loop to yield the operating conditions of the working fluid.

The electric heater and its connections are depicted in Fig. 2; the heater was 0.635 cm in diameter and consisted of a thin-walled Hastelloy-C outer heating shell (0.04 mm thickness) fitted over a machined lava insert. The lava insert provided for structural rigidity as well as additional thermal mass. It also served as the vehicle for situating five 36-gage chromel-alumel thermocouples at various strategic locations just under the heating surface. Three of the thermocouples were located at 90-deg intervals around the periphery of the heater at the midpoint of the test section. Two other thermocouples were located near the point where the heater intersected the wall to help monitor the uniformity of the heater temperature. After grooves were machined into the lava insert, and the thermocouples positioned properly in it, then the insert was heated at 1100°C for 24 hours so that the lava expanded to create very good contact between all elements of the heater system.

Two thermocouples mounted on the bus bars outside the test section wall were used to estimate the end losses of the heaters during operation. The heat losses through the ends of the heater were less than 2 percent of the total heat dissipated even for the highest heat fluxes encountered.

Power was supplied to the heater by a DC motor-generator set capable of providing up to 1500 amps of electric current at low voltages. The energy being dissipated in the heater was found by simultaneous measurements of voltage and current provided to the heater.

## Experimental Conditions

Table 1 shows the range of conditions over which experiments were performed. It was found that the velocity was limited to

<sup>1</sup> Currently Postdoctoral Fellow, Princeton University.

Contributed by the Heat Transfer Division for publication in the JOURNAL OF HEAT TRANSFER. Manuscript received by the Heat Transfer Division September 1993; revision received April 1994. Keywords: Boiling, Forced Convection, Wakes. Associate Technical Editor: R. Viskanta.

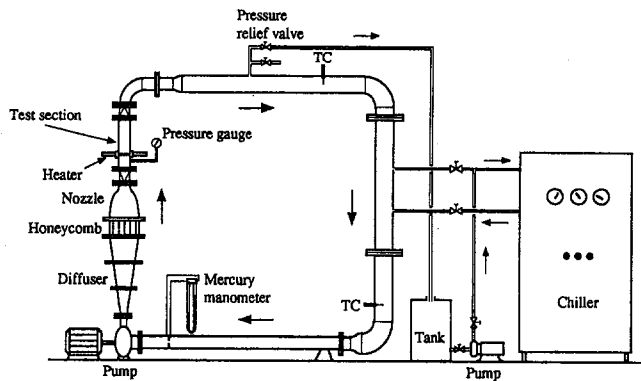


Fig. 1 Schematic diagram of the experimental flow loop

about 3.8 m/s with this apparatus. Only the data that lay in the fully developed film boiling regime were used for purposes of comparison to the analytical results described herein. This was done to insure that effects such as liquid–solid contact that occur near the minimum film boiling point did not substantially influence the data.

An error analysis based on the techniques described by Moffat (1988) showed that heat flux could be determined to within  $\pm 3$  percent, while the temperature uncertainty is estimated at  $\pm 1.5^\circ\text{C}$  in  $T_\infty$ , and  $< 2$  percent in  $T_w$ , which translates to  $\pm 6^\circ\text{C}$  at  $300^\circ\text{C}$ . Velocity in the test section could be determined to within  $\pm 3$  percent.

### Comparison of Different Models With Experimental Data

Five sets of experimental data, one correlation, and three analytical models are used for comparison. Deviations and limitations of the models are discussed.

**Experimental Data.** In the literature, limited experimental data for film boiling across a cylinder are available especially for subcooled and flowing liquids. Table 2 lists five sets of subcooled-flow-film-boiling experimental data reported since 1957 to compare with the analytical models.

It should be noted that the data of Sankaran (1990) listed in Table 2 are consistent with the data in Table 1. Data obtained at a velocity of 2.95 m/s were used in Table 2 for Sankaran's data. Additionally, for comparison purposes, the water data of Liu et al. (1992, Fig. 4, p. 23) were selected for a fixed velocity and superheat to compare with the analytical models at the same condition. They obtained many more data but they are at either lower velocity or lower subcooling than those selected for comparison here.

Data obtained with electric heaters were evaluated at an average wall temperature for comparison with the analysis. In the

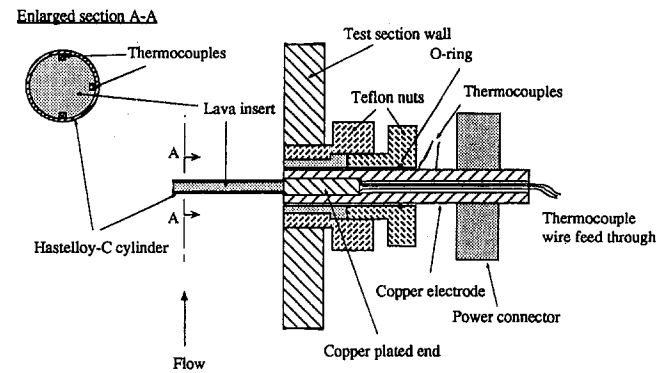


Fig. 2 Cross-sectional view of the heater section and connections

case of Chang and Sankaran's data, the average wall temperature is the mean of measurements made at the forward stagnation point, the equator, and the back stagnation point on the cylinder. Sankaran (1990) reported in some cases that the temperature difference between the back and front of cylinder could reach as high as  $120^\circ\text{C}$ , at wall temperatures in the range of  $400$ – $500^\circ\text{C}$ .

**Analytical Models and Correlation.** In addition to the experimental data, a correlation and three analytical models, which include the present model and two previous models, are listed as follows for comparison:

- 1 Liu et al. correlation (1992)
- 2 Bromley et al. model (1953)
- 3 Witte and Orozco model (1984)
- 4 Chou and Witte model (1995)

The correlation of Liu et al. (1992) was based on their experimental data and correlated those data very well. The range of liquid Jakob number,  $Ja_L$ , for the correlation is shown in Table 2 for the operating case. The correlation range of water subcooling is from zero (saturated case) to  $40^\circ\text{C}$ , which is their maximum water subcooling. Their data, in general, fell below the  $Ja_L$  range for which the Chou/Witte analysis applies; thus, only a few of their data were used for comparison.

To compare the three models with the experimental data, the same ranges of operating parameters were used. The fluid used for the calculations were the same as experimental fluids. Variable physical properties were used in the computations using the Chou/Witte model. Calculations for water showed that the difference between variable properties and constant properties in heat transfer is about 10 to 20 percent; therefore, variable-property calculations are needed for more accurate heat transfer results. The results of a study of the relationship between variable-property and constant-property calculations will be presented later.

### Nomenclature

$c_p$  = specific heat, J/(kgK)  
 $D$  = diameter of cylinder heater, m  
 $h_{fg}$  = latent heat of evaporation, J/kg  
 $\bar{h}$  = average heat transfer coefficient of a cylinder, W/(m<sup>2</sup>K)  
 $h'_{fg}$  = latent heat of evaporation, J/kg  
 $h''_{fg} = h'_{fg}(1 + 0.4c_p\Delta T_{sat}/h'_{fg})^2$ , J/kg  
 $Ja$  = Jakob number of vapor =  $\frac{c_p\Delta T_{sat}}{h'_{fg}}$   
 $Ja_L$  = Jakob number of liquid =  $\frac{c_{pL}\Delta T_{sub}}{h'_{fg}}$

$k$  = thermal conductivity, W/(mK)  
 $Nu$  = Nusselt number of vapor =  $\frac{\bar{h}D}{k}$   
 $Pr$  = Prandtl number of vapor =  $\frac{\nu\rho c_p}{k}$   
 $Re_L$  = Reynolds number of liquid =  $\frac{V_\infty D}{\nu_L}$   
 $T$  = temperature, K  
 $T_m$  = film mean temperature =  $0.5(T_w + T_s)$ , K  
 $V_\infty$  = free-stream velocity in bulk liquid, m/s

$\Delta T_{sat}$  = heater surface superheat =  $T_w - T_s$ , K  
 $\Delta T_{sub}$  = liquid subcooling =  $T_s - T_\infty$ , K  
 $\nu$  = kinematic viscosity, m<sup>2</sup>/s  
 $\rho$  = density, kg/m<sup>3</sup>

### Subscripts

$L$  = liquid  
 $s$  = saturation at system pressure  
 $w$  = wall of cylinder surface  
 $\infty$  = bulk liquid

**Table 1 Range of operating conditions**

Run No.	$V_{\infty}$ (m/s)	$T_s$ (°C)	$\Delta T_{\text{sub}}$ (°C)
1	2.95	60.0	50.0
2	2.95	61.0	51.0
3	2.95	59.5	54.5
4	3.53	65.5	58.6
5	3.81	68.1	57.6
6	3.53	65.5	57.0
7	2.95	60.0	56.5
8	2.95	60.0	55.6
9	2.95	59.5	49.3
10	2.95	61.0	42.0

**Data Comparison**

Figure 3 shows a comparison between available experimental data, the correlation, and the three models alluded to before. The data are plotted as average vapor Nusselt number versus liquid Jakob number, which represents the subcooling level of the liquid. Three different Reynolds numbers are used that represent as close a match as possible to experimental conditions. The model by Bromley et al. (1953) did not consider the liquid subcooling effect; therefore, it can be used only for the very small subcooling cases as shown in the figure. The Witte and Orozco model (1984) did not consider the heat transfer in the wake, while the Chou/Witte model does.

As shown in Fig. 3, Motte and Bromley's data (1957) scattered in their subcooling range. Both the Chou/Witte model and Witte/Orozco model predict lower heat transfer than the data, with the Chou/Witte model predicting slightly higher than Witte/Orozco. It should be pointed out that Motte and Bromley's data overlap the  $Ja_L$  range where the Chou/Witte model begins to lose its applicability, as will be discussed later. Yilmaz and Westwater's data (1980) as well as Chang's data (1987) covered relatively narrow ranges of the liquid Jakob number in the low subcooling ranges. In fact, the data of Chang and Yilmaz and Westwater fall at  $Ja_L$  values less than the applicable range of the Chou/Witte model. Hence, comparative calculations were not performed for those data.

Figure 3 shows that the Chou/Witte model is in better agreement with the subcooled-flow-film boiling experimental data than the previous models. The merit of the Chou/Witte model is much more obvious at high Jakob number than at low Jakob number. The model of Bromley et al. is significantly lower than the experimental data, especially with increasing Jakob number. The model by Witte and Orozco is better than Bromley's model; however, it diverges from the data when subcooling is increased. The Chou/Witte model, although it is still lower than the data, yields higher heat transfer results than the previous models. The difference between the Chou/Witte model and the Witte/Orozco model is greater at higher Jakob numbers, and the two models are closer at lower subcooling since the wake heat transfer is less important at lower Jakob numbers. In the Witte/Orozco model, the average deviation is about 38 percent from Sankaran's data; about 29 percent from Motte and Bromley's data; and about 33 percent from the data of Liu et al. which is much better than Bromley's model. In the Chou/Witte model, the average deviation is about 18 percent from Sankaran's data, about 22 percent from Motte and Bromley's data; and about 23 percent from the data of Liu et al. In other words, the Chou/Witte model gives closer predictions to experimental data than previous models, especially at high subcooling.

Figure 3 also shows selected data from Liu et al., along with the correlation that was developed by Liu to fit their data. Their correlation indeed fits their data better in the low  $Ja_L$  range than does the Chou/Witte model. However, it is clear that at the higher  $Ja_L$  end of Liu's data, the Chou/Witte model results appear to

**Table 2 Range of experimental data**

Year	Contributor(s)	Fluid	$Re_L$	$Ja_L$	Pr	Ja
1957	Motte & Bromley	Ethyl Alcohol	$(2.1-2.9) \times 10^5$	0.015-0.056	0.06	0.49-0.61
1980	Yilmaz & Westwater	Freon-113	42100	0.024-0.028	0.5-0.54	0.33-0.43
1987	Chang	Freon-11	22700-38600	0.009-0.019	0.54-0.91	0.38-0.48
1990	Sankaran	Freon-113	50500	0.08-0.2	0.37-0.55	0.47-0.6
1992	Liu, Shiotsu & Sakurai	Water	1230	0-0.07	0.95	0.34

coincide well with the experimental data. Because Liu's correlation was based on data limited to relatively low  $Ja_L$  and  $Re_L$  ranges, it was deemed inappropriate to extend it into the range where it could be compared to Sankaran's data.

**Applicable Ranges of the Present Model.** The Chou/Witte model gives a better prediction for the experimental data at higher subcooling than at lower subcooling. The external potential flow assumption for the front part of cylinder is acceptable only for thin vapor films. Based on the Chou/Witte numerical results, the film thickness over the front part of cylinder is relatively thin compared to the cylinder radius for medium to high subcooling. Additionally, the Chou/Witte model is only applicable for flow boiling. In other words, a nonzero liquid velocity ( $V_{\infty}$ ) is required since this velocity term is in the denominator during the mathematical transformations for solving the governing equations. The Chou/Witte analysis does not address the issue of possible liquid-solid contact, which was observed in recent experiments in the authors' lab, especially near the minimum film boiling point. Thus the analysis will apply for the flow film boiling regime sufficiently far away from the  $q_{\text{min}}$  point so that this issue is not important.

In summary, the present model is in better agreement with the available experimental data than previous flow-film-boiling models. The applicable ranges of the present model are medium to high subcooling ( $Ja_L > 0.04$ ) and nonzero liquid velocity. The lowest liquid velocity used in the Chou/Witte calculations for water was about 0.1 m/s.

**A Temperature Correction for the Constant-Property Solution**

Constant-property calculations are much simpler than variable-property calculations because the temperature dependency

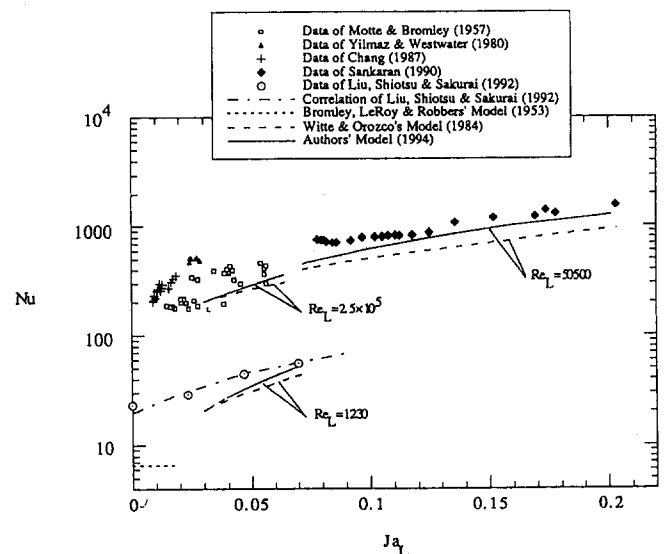


**Fig. 3 Comparison of the models to the experimental data**

of properties at each iteration step is not considered for constant-property solutions. Thus, a technique for "correcting" a constant-property solution to bring it into agreement with a variable-property solution was sought. The concept was that the influence of the various significant thermophysical properties ( $\mu$ ,  $\rho$ , etc.) could be represented in an average sense as a dependence upon an appropriate thermal conductivity ratio. An obvious selection for this ratio is  $k_w/k_s$ , where  $k_w$  and  $k_s$  are evaluated at the wall and the saturation temperatures, respectively.

Figure 4 shows a comparison of the constant-property solution to the variable-property solution in relation to selected water data taken from Liu et al. The plot uses liquid Reynolds number,  $Re_L$ , as the abscissa because of the way in which the data were obtained; the data were taken under constant subcooling conditions at various velocities. Very good agreement between the Chou/Witte variable-property solution and Liu's data exists. However, the constant-property solution is significantly lower than the variable-property one. Through trial-and-error it was found that  $Nu = Nu(T_m)(k_w/k_s)^{0.24}$  corrects the constant-property solution best so that it essentially agrees with the variable-property case.

Figure 5 shows a similar comparison for Freon-113 with the exception that  $Ja_L$  is the abscissa. This reflects the fact that Sankaran's data were obtained in terms of liquid subcooling at relatively constant  $Re_L$ . Again, we can see that the constant-property case falls short of the data and the variable-property case. And, as before, it was found through trial-and-error that the term  $(k_w/k_s)^{0.11}$  "corrects" the best.

Although this technique for correcting the constant-property solution has been developed only for the two liquids over a limited range of parameters stated in Fig. 4 and 5, it shows a way to "correct" for the variable-property effect on heat transfer in subcooling flow film boiling.

## Conclusions

- 1 The effect of variable physical properties is important. The difference in heat transfer results between variable properties and constant properties is about 10 to 20 percent for water. However, it is shown that heat transfer that accounts for the variable properties of water can be approximately obtained from constant-property solutions multiplied by a

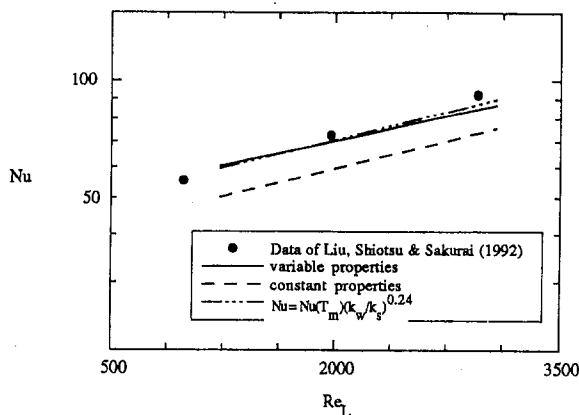


Fig. 4 Comparison of variable-property and constant-property solutions: water,  $Ja_L = 0.07$ ,  $Ja = 0.34$ ,  $Pr = 0.95$

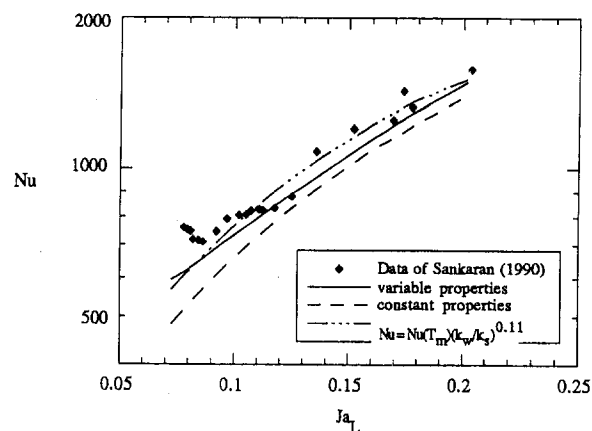


Fig. 5 Comparison of variable-property and constant-property solutions: Freon-113,  $Re_L = 50,500$

correction coefficient,  $(k_w/k_s)^{0.24}$ , and a similar representation can be made for Freon-113.

- 2 The Chou/Witte model yields higher heat transfer results and is in better agreement with available experimental data than previous flow-film-boiling models, reflecting the influence of wake heat transfer and variable properties.
- 3 The Chou/Witte model gives better predictions at higher subcooling than at lower subcooling. The applicable ranges of the present model are for medium to high subcooling ( $Ja_L > 0.04$ ) and nonzero liquid velocity.

## Acknowledgments

This work was performed in its early stages with support from DoE Office of Basic Energy Sciences grant DE-FG05-88ER13893 and NSF grant CBT-8803569. In the latter stages it was funded in part from a Texas Advanced Technology Project, ATP 2040, and a Texas Advanced Research Project, ARP-00365204.

## References

- Bromley, L. A., Leroy, N. R., and Robbers, J. A., 1953, "Heat Transfer in Forced Convection Film Boiling," *Ind. Eng. Chem.*, Vol. 45, No. 1, Dec., pp. 2639-2646.
- Chang, K. H., 1987, "The Instability of Vapor Films in Flow Boiling From Cylinders," Ph.D. Dissertation, University of Houston, Houston, TX.
- Chou, X. S., 1992, "Subcooled Flow Film Boiling Across a Horizontal Cylinder," Ph.D. Dissertation, University of Houston, Houston, TX.
- Chou, X. S., and Witte, L. C., 1995, "Subcooled Flow Film Boiling Across a Horizontal Cylinder: Part I. Analytical Model," *ASME JOURNAL OF HEAT TRANSFER*, Vol. 117, this issue, pp. 167-174.
- Liu, Q. S., Shiotsu, M., and Sakurai, A., 1992, "A Correlation for Forced Convection Film Boiling Heat Transfer From a Horizontal Cylinder Under Subcooled Conditions," *Fundamentals of Subcooled Flow Boiling*, ASME HTD-Vol. 217, pp. 21-32.
- Moffat, R. J., 1988, "Describing the Uncertainties in Experimental Results," *Experimental Thermal and Fluid Science*, Vol. 1, pp. 3-17.
- Motte, E. I., and Bromley, L. A., 1957, "Film Boiling of Flow Subcooled Liquids," *Ind. Eng. Chem.*, Vol. 49, No. 11, Nov., pp. 1921-1928.
- Sankaran, S., 1990, "Highly Subcooled Flow Boiling From a Cylinder in Cross-flow," Ph.D. Dissertation, University of Houston, Houston, TX, p. 89.
- Sankaran, S., and Witte, L. C., 1990, "Highly Subcooled Flow Boiling of Freon-113 Over Cylinders," *Proc. AIAA/ASME Heat Transfer and Thermophysics Conference*, ASME HTD-Vol. 136, pp. 29-34.
- Witte, L. C., and Orozco, J., 1984, "The Effect of Vapor Velocity Profile Shape on Flow Film Boiling From Submerged Bodies," *ASME JOURNAL OF HEAT TRANSFER*, Vol. 106, pp. 191-197.
- Yilmaz, S., and Westwater, J. W., 1980, "Effects of Velocity on Heat Transfer to Boiling Freon-113," *ASME JOURNAL OF HEAT TRANSFER*, Vol. 102, pp. 26-32.

# Stratified Flow Film Boiling Inside Horizontal Tubes

A. M. C. Chan

Ontario Hydro Technologies,  
800 Kipling Ave.,  
Toronto, Ontario M8Z 5S4 Canada  
Mem. ASME

*Stratified flow film boiling inside a horizontal tube was investigated. A one-dimensional flow model was used to solve for the local vapor film thickness and vapor velocity in the vapor channel in the circumferential direction. Analytical solutions for the local vapor film thickness and heat transfer coefficient at the bottom of the tube were derived. The solutions were compared with expressions obtained for other external geometries. A simple experiment was also performed to provide local heat transfer data for direct comparison. It was found that the local heat transfer coefficient normalized with respect to  $h_0$  can be represented by a single curve for different liquid inventory and initial wall temperatures. The curve was expressed in the form of a polynomial and it provides a simple way of calculating the local heat transfer coefficient in stratified flow film boiling in horizontal tubes.*

## 1.0 Introduction

Film boiling is the mode of boiling in which the heating surface is covered by a thin vapor film. Since energy is transported to the fluid primarily by conduction through the vapor film, and the vapor has a low thermal conductivity, film boiling is characterized by low heat transfer coefficients and large temperature differences between the heating surface and the boiling liquid. These characteristics are not desirable in most heat transfer applications. However, film boiling is often encountered in the handling of cryogenic fluids and less frequently during the operation of equipment where high-temperature sources exist.

Considerable experimental and analytical work has been performed on stable film boiling on external geometries. This includes vertical surfaces (Bromley, 1950; Chang, 1959; Hsu and Westwater, 1958), horizontal surfaces (Chang, 1959; Berenson, 1961; Hamill and Baumeister, 1966), horizontal cylinders (Bromley, 1950; Breen and Westwater, 1962; Baumeister and Hamill, 1967), and spheres (Merte and Clark, 1961; Frederking et al., 1964; Toda and Mori, 1982). Film boiling on the inside of a horizontal tube, however, receives very little attention. The only known investigation was reported by Kruger and Rohsenow (1966). The local vapor film thickness in stratified flow film boiling inside a horizontal tube (Fig. 1) was obtained using a force balance similar to Bromley's analysis (1950) for horizontal cylinders. A simple expression for the vapor film thickness was derived (Kruger and Rohsenow, 1966):

$$\delta = \beta \left[ \frac{\mu_g k_g \Delta T D}{\rho_g (\rho_f - \rho_g) g h'_{fg}} \right]^{0.25} \left( \frac{\theta}{\sin \theta} \right)^{0.25} \quad (1)$$

The local vapor film thickness at different angular positions was found to be independent of the liquid level or the amount of liquid present in the tube. Since one would expect  $\delta$  to be different for given  $\theta$  when the tube is filled to different levels, Eq. (1) thus appears to be too simplistic and physically unrealistic.

In the present paper, stratified flow film boiling in a horizontal tube is investigated more vigorously. A detailed flow model is used to solve for the local vapor film thickness and vapor velocity in the circumferential direction. This allows the calculation of the local heat transfer coefficient inside the tube. A simple experiment, which provides local heat transfer data at the inside bottom of a tube for direct comparison, is also described.

## 2.0 Mathematical Model

**2.1 Formulation.** The flow model used is shown in Fig. 1. It is a cross section taken from the film boiling region for stratified flow in a horizontal tube. The liquid bulk is separated from the tube wall by a thin vapor film. This film thickness,  $\delta(\theta)$ , varies under the influence of the hydrostatic pressure head, vapor thrust, surface tension, and vapor flow. Vapor is produced at the interface by boiling and it flows one dimensionally in the circumferential direction as shown. Vapor flow in the axial direction is neglected.

Considering the vapor film or channel, the kinematic equations for the vapor phase can be written as follows:

*Mass Conservation*

$$\rho_g \frac{\partial \delta}{\partial t} + \rho_g \frac{\partial}{\partial x} (\delta u_x) = \frac{k_g \Delta T_w}{h'_{fg}} \frac{1}{\delta} \quad (2)$$

where constant vapor density is assumed and heat transport is assumed to be by molecular conduction across the vapor film only, i.e.,  $h = k_g/\delta$ .

*Momentum Conservation*

$$\frac{\partial}{\partial t} (\delta u_x) + \frac{\partial}{\partial x} (\delta u_x^2) = - \frac{1}{\rho_g} \frac{\partial}{\partial x} (\delta P) - \frac{1}{\rho_g} (\tau_g + \tau_i) + \frac{k_g \Delta T_w}{\rho_g h'_{fg}} \frac{u_i}{\delta} \quad (3)$$

where  $P$  is the local pressure,  $\tau_g$  and  $\tau_i$  are shear stresses on the wall and vapor-liquid interface, respectively, and  $u_i$  is the interfacial velocity. The last term on the right-hand side is the momentum transfer term due to phase change.  $P$  can be shown to be given by

$$P - P_a = \rho_f g (h_L - y) - \frac{1}{\rho_g} \left( \frac{k_g \Delta T_w}{h'_{fg}} \right)^2 - \sigma \left[ 1 + \left( \frac{\partial \delta}{\partial x} \right)^2 \right]^{-1.5} \frac{\partial^2 \delta}{\partial x^2} \quad (4)$$

$P_a$  is the tube pressure above the liquid layer, which is considered constant. The terms in the right-hand side of Eq. (4) are contributions from hydrostatic head ( $P_{HH}$ ), vapor thrust ( $P_{VT}$ ), and surface tension ( $P_{ST}$ ), respectively.  $P_{HH}$  is maximum at  $y = 0$  and reduces to zero at the liquid surface (i.e.,  $y = h_L$ ).  $P_{VT}$  results from mass transfer due to evaporation (Wallis, 1969).  $P_{ST}$  is usually small except near  $\theta = 0$  and can be ignored in general.

Contributed by the Heat Transfer Division and presented at the Fluids Engineering Conference, Washington, DC, June 20–24, 1993. Manuscript received by the Heat Transfer Division March 1993; revision received November 1993. Keywords: Boiling, Multiphase Flows, Stratified Flows. Associate Technical Editor: L. Witte.

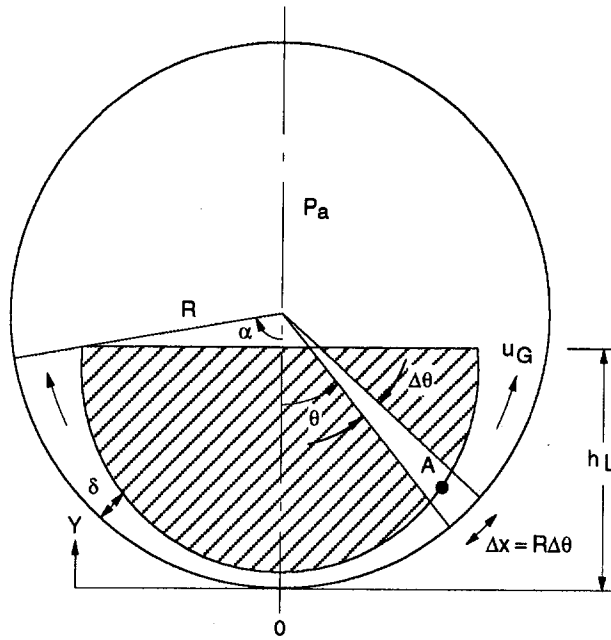


Fig. 1 Film boiling model

For quasi-steady-state solutions, Eqs. (2) and (3) can be simplified to:

$$\delta \frac{\partial u_g}{\partial x} + u_g \frac{\partial \delta}{\partial x} = \frac{k_g \Delta T_w}{\rho_g h'_{fg}} \frac{1}{\delta} \quad (5)$$

and

$$\delta u_g \frac{\partial u_g}{\partial x} + a \frac{\partial \delta}{\partial x} = \frac{\rho_f}{\rho_g} g \delta \sin \theta - \frac{1}{\rho_g} (\tau_s + \tau_i) - \frac{k_g \Delta T_w}{\rho_g h'_{fg}} \frac{u_g - u_i}{\delta} \quad (6)$$

where

$$a = \frac{\rho_f}{\rho_g} g (h_L - R + R \cos \theta) + \left( \frac{k_g \Delta T_w}{\rho_g h'_{fg}} \frac{1}{\delta} \right)^2$$

Equation (6) was obtained using Eq. (5) and  $y = R(1 - \cos \theta)$ . It can be further simplified if we assume

$$\tau_s = \tau_i = \frac{1}{2} \rho_g \bar{f} u_g^2$$

and

$$u_i = \frac{1}{2} u_g$$

where  $\bar{f}$  is an average friction factor.

Equation (6) becomes

$$\delta u_g \frac{\partial u_g}{\partial x} + a \frac{\partial \delta}{\partial x} = \frac{\rho_f}{\rho_g} g \delta \sin \theta - \bar{f} u_g^2 - \frac{k_g \Delta T_w}{2 \rho_g h'_{fg}} \frac{u_g}{\delta} \quad (7)$$

The set of equations to be solved is thus given by Eqs. (5) and (7).

**2.2 Solution Procedure.** Since Eqs. (5) and (7) are nonlinear, numerical solutions are sought. There are a number of ways to finite-difference the set of equations. A simple explicit solution scheme is described here. Equations (5) and (7) are discretized as follows:

$$(u_g)_{j+1} = R \Delta \theta \left[ \frac{1}{\delta} \left( \frac{k_g \Delta T_w}{\rho_g h'_{fg}} - u_g \frac{\partial \delta}{\partial x} \right) \right] + (u_g)_j \quad (8)$$

and

$$\left( \frac{\partial \delta}{\partial x} \right)_{j+1} = \left\{ \frac{1}{A} \left[ \frac{\rho_f}{\rho_g} g \delta \sin \theta - \bar{f} u_g^2 - \frac{k_g \Delta T_w}{2 \rho_g h'_{fg}} \frac{u_g}{\delta} - u_g \left( \frac{k_g \Delta T_w}{\rho_g h'_{fg}} - u_g \frac{\partial \delta}{\partial x} \right) \right] \right\}, \quad (9)$$

It should be noted that

$$\delta_{j+1} = R \Delta \theta \left( \frac{\partial \delta}{\partial x} \right)_{j+1} + \delta_j \quad (10)$$

where  $j = 0$  and  $J$  correspond to  $x = 0$  and  $R\alpha$  respectively and  $\Delta x = R\Delta\theta$  (Fig. 1).

To calculate  $u_g$  and  $\delta$  as a function of  $x$  using Eqs. (8)–(10), boundary conditions at  $x = 0$  (or  $\theta = 0$ ) have to be specified. By symmetry considerations, we have

$$(u_g)_0 = 0 \quad \text{and} \quad \left( \frac{\partial \delta}{\partial x} \right)_0 = 0 \quad (11)$$

An additional boundary condition,  $\delta_0$ , is estimated by solving Eqs. (5) and (7) near  $x = 0$ , i.e.,  $x = R\theta \rightarrow 0$ . Making use of the boundary conditions as given in Eq. (11), Eqs. (5) and (7) can be written respectively as

$$\delta'^2 = \frac{R \Delta \theta k_g \Delta T_w}{\rho_g h'_{fg}} \frac{1}{u_g'} \quad (12)$$

$$u_g'^2 \left[ 1 + \frac{\bar{f} R \Delta \theta}{\delta'} \right] + \left[ \frac{k_g \Delta T_w}{2 \rho_g h'_{fg}} \frac{R \Delta \theta}{\delta'^2} \right] u_g' - [\rho_f g R (\Delta \theta)^2 / \rho_g] = 0 \quad (13)$$

where  $\delta'$  and  $u_g'$  are defined at  $x = R\theta \rightarrow 0$ .

$u_g'$  is obtained by solving the quadratic equation (Eq. (13)),

$$u_g' = \left\{ -B \Delta \theta + [(B \Delta \theta)^2 + 4(1 + A \Delta \theta) C (\Delta \theta)^2]^{0.5} \right\} / 2(1 + A \Delta \theta) \quad (14)$$

where

## Nomenclature

$C_p$  = specific heat at constant pressure  
 $D$  = diameter of tube  
 $f$  = friction coefficient  
 $g$  = gravitational acceleration  
 $h$  = heat transfer coefficient  
 $h_L$  = liquid level  
 $h_{fg}$  = latent heat of evaporation  
 $h'_{fg} = h_{fg} + 0.5 C_{pg} \Delta T_w$  = latent heat plus vapor sensible heat content  
 $k$  = conductivity  
 $P$  = pressure  
 $R$  = radius of tube

$T$  = temperature  
 $u$  = velocity  
 $x = R\theta$  = position along vapor channel  
 $\alpha$  = angle defining the liquid level  
 $\beta$  = coefficient in Eq. (1)  
 $\Delta T$  = temperature difference  
 $\Delta T_w = T_w - T_{sat}$  = wall superheat  
 $\delta$  = vapor film thickness  
 $\theta$  = angle from bottom of tube  
 $\mu$  = viscosity  
 $\rho$  = density

$\sigma$  = surface tension  
 $\tau$  = shear stress

## Subscripts

$a$  = ambient  
 $f$  = liquid phase  
 $g$  = vapor phase  
 $i$  = interface  
 $j$  = index of discretization  
 $0$  = bottom of tube  
 $sat$  = saturation  
 $w$  = wall

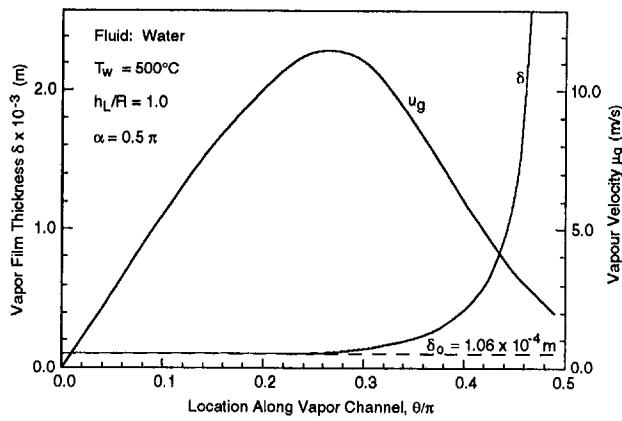


Fig. 2 Local vapor film thickness and vapor velocity

$$A = (\bar{f}R)/\delta'$$

$$B = (k_g \Delta T_w R) / (2 \rho_g h'_{fg} \delta'^2)$$

$$C = (\rho_f g R) / \rho_g$$

It should be noted that only the positive root is chosen in Eq. (14) since  $u'_g$  is positive by definition. Substituting  $u'_g$  into Eq. (12), we have

$$\delta'^2 = [4B(1 + A\Delta\theta)]\delta'^2 / \{-B + [B^2 + 4(1 + A\Delta\theta)C]^{0.5}\} \quad (15)$$

For  $\Delta\theta \rightarrow 0$ ,  $\delta'$  becomes  $\delta_0$ , and Eq. (15) can be reduced to

$$1 = 4B / \{-B + [B^2 + 4C]^{0.5}\} \quad (16)$$

Rearranging terms in Eq. (16), the vapor film thickness at the bottom of the tube is obtained:

$$\delta_0 = 1.107 \{R[k_g \Delta T_w / h'_{fg}]^2 / [g \rho_f \rho_g]\}^{0.25} \quad (17)$$

It is interesting to note that  $\delta_0$  depends only on the tube geometry ( $R$ ) and wall superheat ( $\Delta T_w$ ). It is independent of the liquid level ( $h_L$ ).

Having defined the boundary conditions (Eqs. (11) and (17)), Eqs. (8) and (10) can be solved explicitly for  $u_g$  and  $\delta$  along the vapor channel. This will be discussed below.

Assuming that heat is transported across the vapor film primarily by conduction in film boiling, and that a linear temperature profile exists in the vapor film, the heat transfer coefficient across the film is given by

$$h = \frac{k_g}{\delta} \quad (18)$$

At the bottom of the tube, i.e.,  $\theta = 0$ , we have

$$h_0 = \frac{k_g}{\delta_0} = 0.9 \left[ \frac{k_g^2 \rho_f \rho_g g (h'_{fg})^2}{R (\Delta T_w)^2} \right]^{0.25} \quad (19)$$

It should be noted that the thermodynamic properties of vapor that appear in the above equations are evaluated at an average film temperature given by

$$T_g = \frac{1}{2}(T_w + T_{sat}) \quad (20)$$

**2.3 Results and Discussions.** Equations (8) and (10) were solved explicitly by marching the solutions along the vapor channel from  $x = 0$  to  $R^*\alpha$  using boundary conditions as defined by Eqs. (11) and (17). Different water levels and initial wall temperatures were used. Typical results are shown in Fig. 2 for  $T_w = 500^\circ\text{C}$  and  $h_L/R = 1.0$  (i.e.,  $\alpha = \pi/2$ ).

Plotted in Fig. 2 are the vapor velocity and vapor film thickness along the vapor channel in the circumferential direction inside a

horizontal tube.  $\delta_0$  was obtained using Eq. (17). It can be seen that the thickness of the vapor film remains essentially constant over a relatively long distance from the bottom of the tube. The vapor velocity, on the other hand, increases linearly from zero value at the bottom due to evaporation. The vapor film begins to increase in thickness about midway in the vapor channel, first slowly and then rapidly toward the end of the channel. The vapor velocity changes in response to the change in the flow channel area as the film thickness increases. As  $\delta$  increases,  $u_g$  passes through a maximum and then decreases rapidly toward the end of the channel.

Results for different liquid levels are shown in Fig. 3 for an initial wall temperature of  $500^\circ\text{C}$ . It can be seen that  $\delta$  behaves the same in all cases.

Knowing the film thickness along the vapor channel, the local heat transfer coefficient can be readily calculated using Eq. (18). This is shown in Figs. 4 and 5 for different  $h_L$  and  $T_w$ . Shown in Figs. 4 and 5 are the normalized local heat transfer coefficient versus the normalized position along the vapor channel. Five liquid levels and four initial wall temperatures were used. It is interesting to note that the normalized results tend to collapse into one curve in each figure, and the curves in the two figures are close to being identical. It is, therefore, possible to use just one single curve to represent the normalized heat transfer coefficient along the vapor channel for different water levels and initial wall temperatures. This unified curve can be expressed in the form of a polynomial,

$$h/h_0 = 1 + a_1(\theta/\alpha) + a_2(\theta/\alpha)^2 + a_3(\theta/\alpha)^3 + a_4(\theta/\alpha)^4 + a_5(\theta/\alpha)^5 \quad (21)$$

where

$$a_1 = -0.133$$

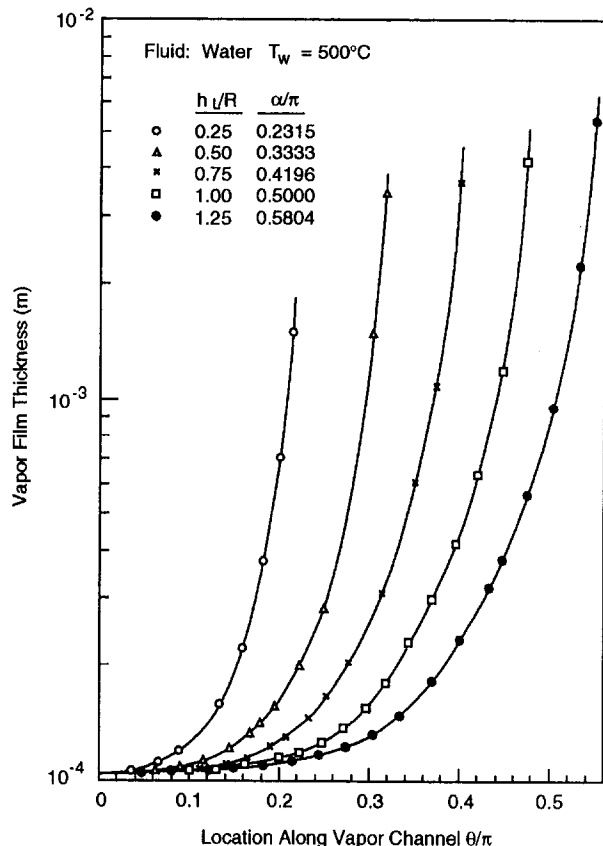


Fig. 3 Local vapor film thickness for different water levels



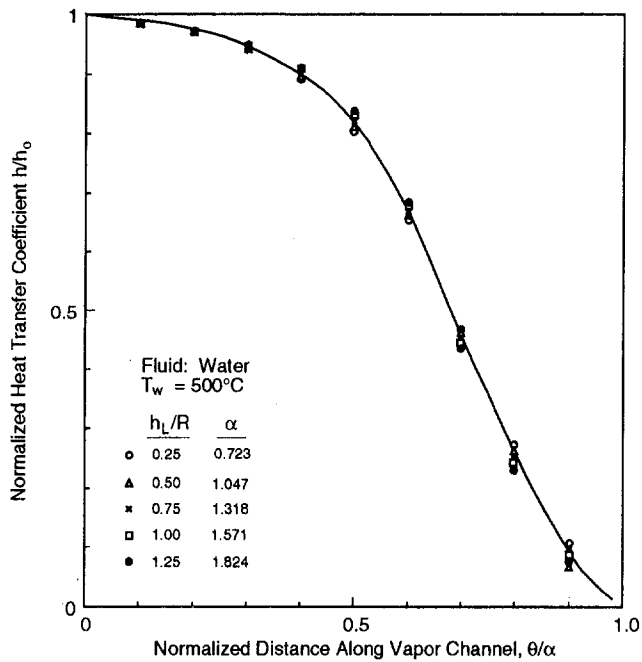


Fig. 4 Normalized local heat transfer coefficient for different water levels

$$a_2 = -0.253$$

$$a_3 = 2.981$$

$$a_4 = -10.898$$

$$a_5 = 7.439$$

Equation (21) provides an easy way of predicting the local heat transfer coefficient in stratified flow film boiling in horizontal tubes. The amount of liquid present ( $h_L$ ) is defined by  $\alpha$  and values of  $\delta_0$  and consequently  $h_0$  are determined by the initial wall temperature (Eqs. (17) and (19)). To obtain the average film boiling heat transfer coefficient, Eq. (21) can be integrated between  $x = 0$  and  $R\alpha$ .

From the discussion above, it is obvious that our ability to predict the local heat transfer coefficient depends very much on  $h_0$ . As  $h_0$  is derived analytically using a simplified flow model, it is important that  $h_0$  be verified experimentally.

### 3.0 Verification of $h_0$

To verify  $h_0$ , a simple experiment was performed. The experimental setup used is shown schematically in Fig. 6. It consists of a piece of stainless steel tube with an inner diameter of 26 mm and a wall thickness of 2.54 mm. Part of the tube was cut open at the top for a length of 50.8 mm. Two ceramic disks were cemented to the ends of the open section, forming a cavity as shown. A hopper made from a thin stainless steel sheet was welded to the opening, as shown in Fig. 6. This is to prevent possible contact of water droplets with the test section outer surface due to spluttering resulting from surface quenching.

To measure  $h_0$ , temperature drop across the tube wall at the bottom was measured using type *K* stainless steel sheathed thermocouples as shown in Fig. 6. Thermocouples were attached from the outer surface so as not to disturb the boiling inner surface. Only two embedded thermocouples were used at distances of 0.0508 mm and 1.27 mm, respectively, from the inner surface. A novel thermocouple instrumenting technique was used: The thermocouple was prepared by exposing and sealing the wires with a silver cap approximately 0.125 mm thick to form a silver end cap assembly. The assembly was then press fitted into a

mounting hole drilled into the wall from the outside to the pre-defined depth. Care was taken to ensure good thermal contact between the silver cap and the bottom of the hole. Details of the technique and an estimation of the measurement errors were given by Elphick et al. (1986). In general, the thermal disturbance due to the presence of the thermocouple assembly was found to be about 0.3 (Elphick et al., 1986). This corresponded to wall temperature measurement errors of less than 1°C in the present situation. The temperature at the tube outer surface was measured by spot-welding an exposed junction thermocouple to the wall. A grounded junction thermocouple located about 3 mm from the bottom inside the cavity was used to obtain the water temperature. All the thermocouples used were fine gage (0.508-mm-dia) thermocouples for fast response.

The experiment was performed by first heating the test section by Joule heating using an AC transformer (5 volts, 1600 amp). A power variac was used to control the power input. After the test section achieved the desired initial temperature, the power was turned off and a known quantity of distilled water was poured into the cavity rapidly through a funnel at one end of the cavity. The transient response of the thermocouples was recorded using a chart recorder. A total of 18 tests were done for different initial tube wall temperatures and water volumes. The parameters were varied as follows:

$$T_w = 300\text{--}550^\circ\text{C}$$

$$h_L/D = 0.1\text{--}0.7$$

The transient temperature measurements across the tube wall for a typical test run ( $T_w = 500^\circ\text{C}$ ) are shown in Fig. 7. It can be seen that when water was first introduced into the cavity at time *A*, surface quenching could occur due to the unstable water/vapor interface. A rapid drop in wall temperature was thus registered by  $T_1$ . However, because of the high surface temperature and high heat capacity in the wall, film boiling was restored at point *B*. Stable film boiling existed between time *C* and *D*. Surface quenching occurred at a later stage when the quenching criterion (Chan and Banerjee, 1981) was satisfied.

In the stable film boiling region, *C*–*D*, the heat transfer coefficient at the bottom of the tube can be readily deduced using the equation,

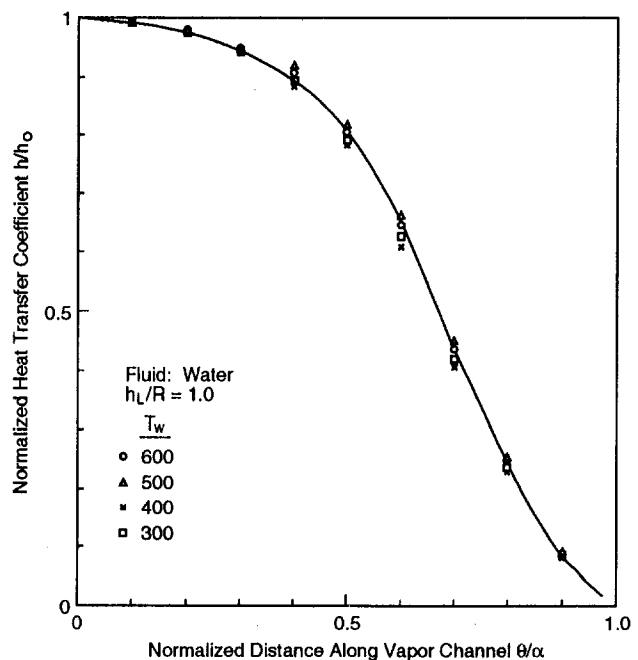


Fig. 5 Normalized local heat transfer coefficient for different initial wall temperatures

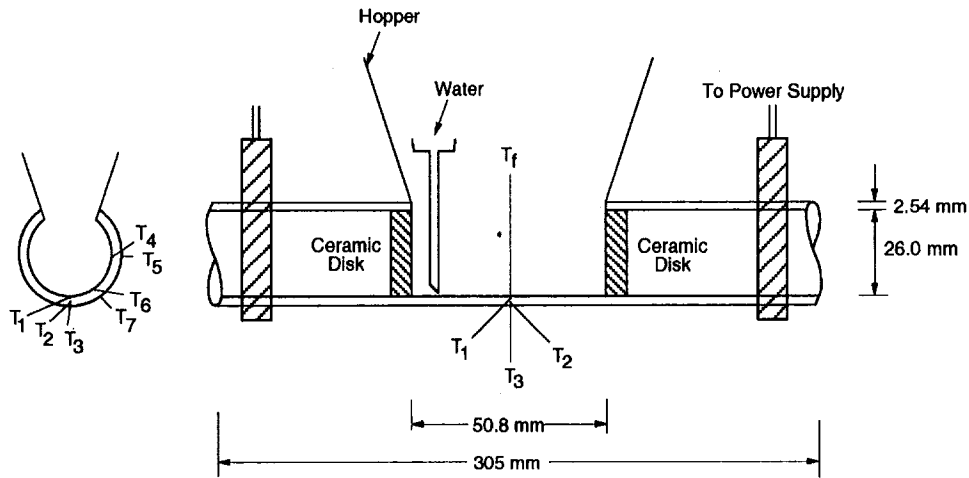


Fig. 6 Schematic diagram of experimental setup

$$h_0 = \frac{k_w \partial T / \partial r}{\partial T_w} \quad (22)$$

where

$$\begin{aligned} \partial T &= T_2 - T_1 \\ \partial r &= \Delta r_2 - \Delta r_1 \\ \partial T_w &\approx T_1 - T_f \end{aligned}$$

Equation (22) was used to calculate  $h_0$  for all the test runs. The results were compared with the analytical solution obtained (Eq. (19)). This is shown in Fig. 8. The uncertainty in  $h_0$  deduced is given in the appendix.

Also shown in Fig. 8 are analytical solutions for a horizontal plate ( $h_{HP}$ ) (Berenson, 1961) and a horizontal cylinder ( $h_{HC}$ ) (Bromley, 1950). It can be seen that  $h_0$  for film boiling inside a horizontal tube ( $h_{HT}$ ) is significantly higher than the corresponding values for horizontal plates and cylinders.  $h_{HT}$  is also a stronger function of  $\Delta T_w$  than  $h_{HP}$  and  $h_{HC}$ . The difference in  $h_0$  values among the different geometries, however, tends to decrease as  $\Delta T_w$  increases. It can also be seen that the experimental results compare favorably with the present solution ( $h_{HT}$ ). The wide data scatter can be attributed to the fact that the data were obtained under transient conditions. Stable film boiling only existed for a short duration in many cases, especially at low initial wall temperatures.

The film boiling heat transfer coefficient at the bottom of a horizontal tube, as derived by Kruger and Rohsenow (1966), was also obtained. A coefficient  $\beta = 1.33$  (Eq. (1)) was used. It

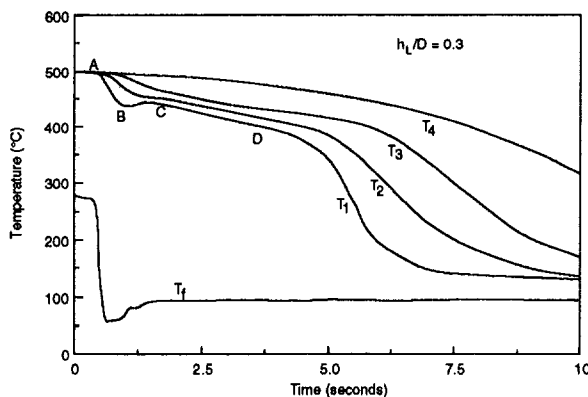


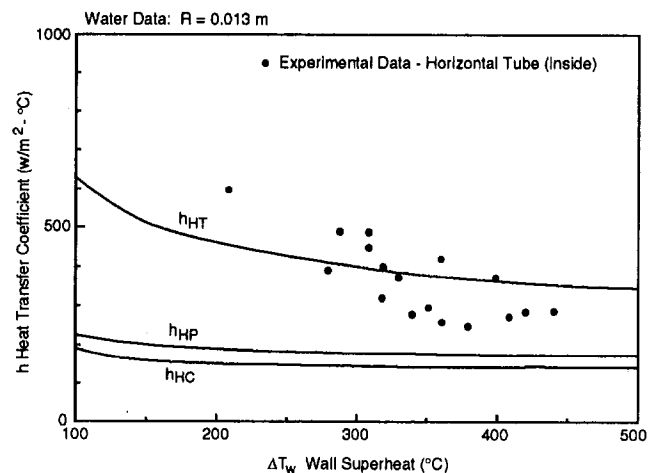
Fig. 7 Transient temperature responses for a typical test run

was found to be very close to  $h_{HP}$  shown in Fig. 8. It should be noted that  $\beta = 1.33$  was recommended by Kruger and Rohsenow (1966) based on a set of R113 test data. It may not apply here with water as the boiling fluid.

#### 4.0 Conclusions

Stratified flow film boiling inside a horizontal tube was investigated. A one-dimensional flow model was used to obtain numerically the local vapor film thickness and vapor velocity under the liquid mass in the circumferential direction. Analytical solutions were derived for the vapor film thickness and heat transfer coefficient at the bottom of the tube. A simple experiment was performed to provide local heat transfer data for direct comparison.

From the results obtained, the following observations can be made:



$$h_{HT} = 0.9 \left\{ \frac{\text{kg}^2 \text{g} \rho_f \rho_g h_{fg}^2}{R \Delta T_w^2} \right\}^{0.25} \text{ - Horizontal Tube (Inside)}$$

$$h_{HP} = 0.425 \left\{ \frac{\text{kg}^3 h_{fg}^3 \rho_g \rho_f (\rho_f - \rho_g)}{\mu_g \Delta T_w \sqrt{g(\rho_f - \rho_g)}} \right\}^{0.25} \text{ - Horizontal Plate}$$

$$h_{HC} = 0.62 \left\{ \frac{\text{kg}^3 h_{fg}^3 \rho_g \rho_f (\rho_f - \rho_g)}{\mu_g D \Delta T_w} \right\}^{0.25} \text{ - Horizontal Cylinder}$$

Fig. 8  $h$  versus  $\Delta T_w$  plot for different geometries

- 1 The heat transfer coefficient at the inside bottom of the tube ( $h_0$ ) as obtained in the present analysis was found to be independent of the amount of liquid present ( $h_L$ ). The coefficient depends only on the wall superheat and tube radius.
- 2 The expression for  $h_0$  as derived compared fairly well with the set of test data obtained in the present study. It was found to be substantially higher than the corresponding solutions obtained for a horizontal plate or a horizontal cylinder.
- 3 The normalized heat transfer coefficient along the vapor channel in the circumferential direction can be represented by a single curve (Eq. (21)) for different liquid levels and initial wall temperatures.
- 4 The average heat transfer coefficient for stable film boiling inside a horizontal tube can be obtained by integrating Eq. (21).

## References

- Baumeister, K. J., and Hamill, T. D., 1967, "Film Boiling From a Thin Wire as an Optimal Boundary-Value Process," ASME Paper No. 67-HT-62.
- Berenson, P. J., 1961, "Transition Boiling Heat Transfer From a Horizontal Surface," ASME JOURNAL OF HEAT TRANSFER, Vol. 83C, pp. 351-358.
- Breen, B. P., and Westwater, J. W., 1962, "Effect of Diameter of Horizontal Tubes on Film Boiling Heat Transfer," *Chemical Engineering Progress*, Vol. 58, pp. 67-72.
- Bromley, L. A., 1950, "Heat Transfer in Stable Film Boiling," *Chemical Engineering Progress*, Vol. 46, pp. 221-227.
- Chan, A. M. C., and Banerjee, S., 1981, "Refilling and Rewetting of a Hot Horizontal Tube: Part III, Application of a Two-Fluid Model to Analyze Rewetting," ASME JOURNAL OF HEAT TRANSFER, Vol. 103, pp. 653-659.
- Chang, Y. P., 1959, "Wave Theory of Heat Transfer in Film Boiling," ASME JOURNAL OF HEAT TRANSFER, Vol. 81C, pp. 1-12.
- Elphick, I. G., Chan, A. M. C., and Shoukri, M., 1986, "Modelling the Steady State and Transient Response of Thermocouple Assemblies in Solids," *Pressure and Temperature Measurements*, ASME FED-Vol. 44/HTD-Vol. 58, pp. 51-56.
- Frederking, T. H. K., Chapman, R. C., and Wang, S., 1964, "Heat Transport and Fluid Motion During Cooldown of Single Bodies to Low Temperatures," *Int. Advances in Cryogenic Engineering*, Vol. 10, pp. 353-359.

Hamill, T. D., and Baumeister, K. J., 1966, "Film Boiling Heat Transfer From a Horizontal Surface as an Optimal Boundary Value Process," *Proc. 3rd Int. Heat Transfer Conf.*, Vol. 4, pp. 59-64.

Hsu, Y. Y., and Westwater, J. W., 1958, "Film Boiling From Vertical Tubes," *AIChE Journal*, Vol. 4, pp. 58-62.

Kruger, R. A., and Rohsenow, W. M., 1966, "Film Boiling Inside Horizontal Tubes," *Proc. 3rd International Heat Transfer Conference*, Vol. V, pp. 60-68.

Merte, H., and Clark, J. A., 1961, "Boiling Heat Transfer Data for Liquid Nitrogen at Standard and Near-Zero Gravity," presented at the Cryogenic Engineering Conf., Ann Arbor, MI.

Toda, S., and Mori, M., 1982, "Subcooled Film Boiling and the Behaviour of Vapor Film on a Horizontal Wire and a Sphere," *Proc. 7th Int. Heat Transfer Conf.*, Vol. 4, pp. 173-178.

Wallis, G. B., 1969, *One Dimensional Two-Phase Flow*, McGraw-Hill, New York, Chap. 7.

## APPENDIX

### Uncertain Analysis

The uncertainties associated with the measured and experimentally deduced parameters are given below:

Parameter	Uncertainty
$T_1, T_2$	1°C
$T_f$	0.5°C
$r_1, r_2$	0.0254 mm
$k_w$	5 percent
$h_0$	<35 percent

The uncertainty in  $h_0$  was evaluated using the following equation:

$$\begin{aligned}
 (\Delta h_0/h_0)^2 = & (\Delta k_w/k_w)^2 + ((\Delta T_2)^2 + (\Delta T_1)^2)/(T_2 - T_1) \\
 & + ((\Delta T_1)^2 + (\Delta T_f)^2)/(T_1 - T_f) \\
 & + ((\Delta r_2)^2 + (\Delta r_1)^2)/(r_1 - r_2)
 \end{aligned}$$

It should be noted that the uncertainty in  $h_0$  is dominated by the second term on the right-hand side because of the relatively small values of  $(T_2 - T_1)$  in the experiment.

Shou-Shing Hsieh  
Professor and Chairman.  
Mem. ASME

Mao-Yu Wen  
Graduate Student.

Department of Mechanical Engineering,  
National Sun Yat-Sen University,  
Kaohsiung, Taiwan 80424

# An Experimental Study of Flow Boiling Heat Transfer in Rib-Roughened Tube Annuli

*Heat transfer measurements were performed on six rib-type roughened tube annuli (4.67–9.01 mm  $D_h$ , 6–16 ribs, rib pitch 19.7–63.0 mm, rib height 4 mm, rib width 15 mm, rib angle 20–60 deg) with two phases of refrigerant R-114 under evaporating conditions. Based on the same heat transfer area of the test section, the effects of heat flux, quality, and rib spacing on flow boiling heat transfer coefficient were presented and discussed. Correlations of two-phase enhancement factor  $F$  and suppression factor  $S$  were developed by modifications and extensions of Chen's model for the present geometric configurations.*

## 1 Introduction

A lot of work has been carried out to obtain an understanding of boiling heat transfer from a smooth surface. These fundamental studies clearly brought out the complexities of the flow boiling mechanisms (see Collier, 1981, for a comprehensive survey). At present, many aspects of boiling heat transfer on a smooth surface are well explored and reasonably good correlations have been developed for the design of efficient heat exchange equipment. However, there are many saturated flow boiling correlations (over 30) in the literature. Some of the well-known correlations were summarized by Kandlikar (1983, 1990). With roughened surfaces, boiling heat transfer is more complicated. Due in part to this complexity, heat transfer in roughened tube annuli has received less attention than that in smooth tube annuli. The lack of design data for heat transfer coefficients, especially in flow boiling, is now one of the limitations in the design of efficient evaporators for use in the refrigeration and process industries (Webb and Pais, 1992).

This work is a continuation of our previous study regarding evaporative heat transfer and enhancement performance of rib-roughened tube annuli with R-114 (Wen and Hsieh, 1994). In that paper, the influence of mass velocity, heat flux, and rib geometry on pressure drop and heat transfer characteristics were examined. It was found that flow nucleate boiling is enhanced in terms of a lower wall superheat being required for incipient boiling, and a great number of more stable bubbles exist than in smooth tube annuli. Moreover, the gradual suppression of the nucleation mechanism reduces the heat transfer coefficients with increasing quality.

In this paper, several correlations related to saturated flow boiling in rib-roughened tube annuli with R-114 will be developed. Over the last few years a large data bank for saturated and subcooled flow boiling in tubes and annuli have been made to fit correlations that cover all the data. In spite of the aim to reduce the number of physical properties required in the correlations and to extend the range of applicability as well as to different types of fluid and to both saturated and subcooled boiling, such correlations are still unavailable in roughened tubes and annuli.

Flow boiling combines nucleate boiling and forced convection evaporation. One may predict the heat transfer coefficient using a forced convection boiling model, such as that proposed by Chen (1963). The Chen model is based on

$$h_{TP} = Sh_{pb} + Fh_{fc} \quad (1)$$

$Sh_{pb}$  is the nucleate boiling contribution:  $h_{pb}$  is for pool boiling on a single tube of the geometries of interest. The suppression factor  $S$  ( $< 1.0$ ) reflects the fact that a lower effective superheat is available in flow boiling than in pool boiling. Due to the thin boundary layer,  $S$  was assumed to be a function of the two-phase Reynolds number  $Re_{TP} \cdot Fh_{fc}$  is the forced convective contribution where  $h_{fc}$  is the liquid-only  $h$ , while  $F$  is the forced convective enhancement factor. The value of  $F$  is always greater than unity.

Prediction of refrigeration performance requires the nucleate boiling coefficient,  $h_{pb}$ ,  $S$ , and  $F$  for the tube geometries and refrigerants of interest. Except for smooth (bare) tubes/or annuli, no correlations exist for predicting  $h_{pb}$  as a function of temperature and refrigerant type as well as for  $S$  and  $F$  for any of the surface geometries shown in Fig. 1. Hence, actual pool boiling data are needed for the refrigerant at the evaporator operating condition, as well as  $S$  and  $F$  dependences on surface geometry, in order to use Eq. (1).

## 2 Objective of the Present Work

The objective of this study is mainly to develop correlations for R-114 in tube annuli geometries. Before this can be done, a database of pool as well as flow boiling data is needed. This paper presents the necessary boiling data for this study.

Tubes with rib-type surfaces that provide more stable nucleation sites are attractive for augmentation of boiling heat transfer. The mouth of the cavity between two consecutive ribs determines the superheat required to nucleate, while the internal shape and volume together with the wetting characteristics of the cavity walls determine the stability of the cavity. Therefore a model for correlating flow boiling heat transfer in augmented tubes is needed that applies to various geometries.

The ability of a correlation to apply to new fluids is also an important feature. In spite of this, only one working fluid, R-114, was used in this study. This is because: (1) Its operating pressure is close to atmospheric, thus minimizing leakage; (2) R-114 is highly stable compared to other refrigerants; (3) it belongs to the group of refrigerants having the lowest toxicity; and the most important, to meet these needs, the following work was conducted:

- 1 Experimental results were compared with existing correlations for a smooth tube.
- 2 The effects of heat flux, quality, and rib spacing on flow boiling heat transfer coefficients were displayed.
- 3 Correlations of two-phase enhancement factor  $F$  and suppression factor  $S$  were developed to predict the convection heat transfer coefficient using Chen's model,  $h_{TP} = Sh_{pb} + Fh_{fc}$ .

Contributed by the Heat Transfer Division for publication in the JOURNAL OF HEAT TRANSFER. Manuscript received by the Heat Transfer Division May 1993; revision received February 1994. Keywords: Augmentation and Enhancement, Boiling, Forced Convection. Associate Technical Editor: L. C. Witte.

### 3 Correlation Development

The present correlation was based on Chen's postulate that both convection and nucleate boiling play a role in flow boiling heat transfer. For use in Eq. (1),  $h_{fc}$  is calculated from the Dittus-Boelter equation with the assumption that the entire mass flows as liquid in the channel

$$h_{fc} = 0.023 (k_f/D_h) \left[ \frac{G(1-X)D_h}{\mu_l} \right]^{0.8} \left( \frac{C_{pl}\mu_l}{k_f} \right)^{0.4} \quad (2)$$

$h_{pb}$  is found from the present experiments, while  $S$  is the suppression factor. The actual superheat is not constant across the boundary layer. Thus, the mean superheat ( $\Delta T_e$ ) of the fluid in which the bubble grows is lower than the wall superheat ( $\Delta T_{sat}$ ). The difference between this lower  $\Delta T_e$  and the  $\Delta T_{sat}$  is small for the case of pool boiling and was generally neglected but is significant in the flow boiling case and cannot be neglected since the boundary layer is much thinner and the temperature gradients much steeper. Consequently, Chen defines  $S$  as the ratio of  $\Delta T_e$  to  $\Delta T_{sat}$

$$S = \left( \frac{\Delta T_e}{\Delta T_{sat}} \right)^{0.99} \quad (3)$$

Therefore,  $F$  can be written as

$$F = \left( \frac{h_{TP}}{h_{fc}} \right)_{S=0} \quad \text{or} \quad F = \frac{h_{TP} - Sh_{pb}}{h_{fc}} \quad (4)$$

Both  $S$  and  $F$  could be calculated from Eqs. (3) and (4).

Once  $F$  was obtained, it was plotted against  $X_{II}$  (see Fig. 9), which is defined as follows:

$$X_{II} = \left( \frac{1-X}{X} \right)^{0.9} \left( \frac{\rho_v}{\rho_l} \right)^{0.5} \left( \frac{\mu_l}{\mu_v} \right)^{0.1} \quad (5)$$

A two phase  $Re_{TP}$  is given by Whalley (1987) as

$$Re_{TP} = Re_l F^{1.25} \quad (6)$$

$S$  was plotted versus  $Re_{TP}$ , as shown in Fig. 10, for correlation purposes.

### 4 Experimental Apparatus and Procedure

A horizontal test section with R-114 flowing in a closed loop is shown in Fig. 1. The flow loop consists of a pre-evaporator, preheater, dryer, test section, receiver, condenser, pump, and af-

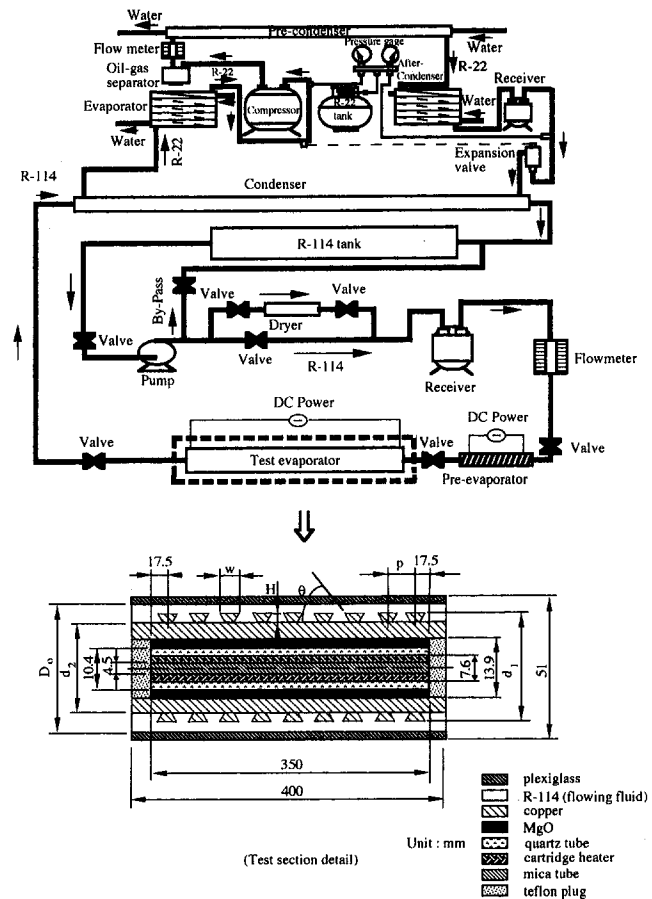


Fig. 1 Schematic of experimental apparatus

ter-pump. The test section is a conventional double-pipe heat exchanger (see Fig. 1 for details).  $D_o$  is 45 mm and  $d_2$  of the inner tube was 19 mm. The outside tube was a plexiglass pipe (45 mm i.d., 51 mm o.d.) to facilitate flow visualization. Copper ribs (the size and geometry are given in Table 1) on a copper ( $k = 111$  W/m K) tube (350 mm  $\times$  19.0 mm  $\times$  13.9 mm) comprised the augmented surface. Heating was provided by conducting direct current through electric wire packed into the cop-

### Nomenclature

$A$  = heat transfer area =  $2\pi r_c L$   
 $A_c$  = sectional area  
 $D_h$  = hydraulic diameter of annulus =  $2(r_o - r_c)$   
 $G$  = mass velocity at inlet of tube annuli =  $\dot{m}/A_c$   
 $H$  = rib height  
 $h$  = local wall heat transfer coefficient, in Eq. (10)  
 $h_{fc}$  = forced convection heat transfer coefficient for the entire liquid flow  
 $\bar{h}$  = averaged local wall heat transfer coefficient, in Eq. (11)  
 $i_{fg}$  = latent heat of vaporization  
 $k$  = thermal conductivity  
 $L$  = length of test tube  
 $M$  = molecular weight  
 $\dot{m}$  = mass rate of flow  
 $Nu$  = Nusselt number =  $D_h h_{TP}/k_f$

$\bar{P}$  = average pressure over the test section =  $(P_1 + \dots + P_7)/7$   
 $P$  = pressure  
 $P_r$  = reduced pressure (absolute pressure/critical pressure)  
 $p$  = rib pitch  
 $Q$  = heat transfer rate  
 $\dot{q}$  = wall heat flux  
 $Re_l$  = liquid Reynolds number =  $GD_h(1-X)/\mu_l$   
 $r_c$  = radius of equivalent circular tube defined in Eq. (2)  
 $T$  = temperature  
 $\bar{T}_{sat}$  = saturated temperature corresponding to the average pressure,  $\bar{P}$  over the test section  
 $\bar{T}_w$  = average wall temperature along the test tube =  $(T_{w_1} + \dots + T_{w_7})/7$

$T_w$  = average wall temperature along circumferential wall =  $(T_{top} + T_{mid} + T_{bot})/3$   
 $X$  = quality  
 $V$  = voltage  
 $w$  = rib width  
 $\theta$  = rib angle  
 $\mu$  = dynamic viscosity  
 $\rho$  = density  
 $\sigma$  = surface tension

### Subscripts

cec = convective evaporation contribution  
 $i$  = inside diameter  
 $l$  = liquid  
 $o$  = outside diameter  
 $sat$  = saturated  
 $TP$  = two-phase  
 $v$  = vapor

**Table 1 The size of test tubes and working fluid (R-114) properties**

Size of test tube annuli	Test tube	Tube (No.)	d <sub>1</sub> (mm)	d <sub>2</sub> (mm)	D <sub>h</sub> (mm)	Number of rib elements	p (mm)	w (mm)	H (mm)	θ	A (cm <sup>2</sup> )
	Rib	1	27	19	9.01	6	63.0	15	4	20°	4.28
	Rib	2	27	19	6.93	9	39.4	15	4	30°	4.22
	Rib	3	27	19	7.80	10	35.0	15	4	40°	4.20
	Rib	4	27	19	5.76	13	26.3	15	4	45°	4.26
	Rib	5	27	19	4.72	13	23.3	15	4	55°	4.20
	Rib	6	27	19	4.67	16	19.7	15	4	60°	4.21
	Smooth	7	—	—	6.50	—	—	—	—	—	4.24

R-114 Properties (saturated)	Properties	Unit	Value	Properties	Unit	Value
	Molecular weight	kg/kmol	170.92	Heat of evaporation	kcal/kg	30.17
	Pressure	kg/cm <sup>2</sup>	2.55	Liquid thermal conductivity	mW/m · K	64.0
	Saturated temperature	°	30.0	Liquid viscosity	μPa · s	334.8
	Liquid density	kg/m <sup>3</sup>	1440.8	Vapor viscosity	μPa · s	11.82
	Vapor density	kg/m <sup>3</sup>	13.38	Surface tension	N/m	0.01
	Liquid specific heat	kJ/kg · K	1.11	Prandtl number	—	5.38

per tube. A two-walled structure (MgO + quartz) was sandwiched between the copper tube and the electric wire as an electrical shield. Quartz was used as an electrical insulation. MgO can distribute the heat energy uniformly.

The pre-evaporator preheated R-114 to saturation (within ±0.3°C). As R-114 flowed through the test section, it was uniformly heated by dc power, provided by a 100 V, 550-amp capacity dc rectifier. After exiting the test section, R-114 passed to the R-22 cooled condenser, where it was condensed and subcooled prior to being returned to the pump to complete the circuit.

Figure 2 shows the locations of temperature and pressure measurements of the test section. Bulk fluid temperatures at inlet and outlet were measured with 40 gage Cu-Cn thermocouples located at midstream. The inlet and outlet pressures were measured with a calibrated pressure gage, respectively. Intermediate bulk fluid temperatures were measured at a certain distance (50 mm each) downstream (see Fig. 2 for details). The R-114 flow rate was measured by a rotameter located between the condenser and pre-evaporator. Thermocouples measured wall temperature at 13 locations along the test section. These thermocouples were carefully buried in the outside wall of the inner tube. A detailed cross-sectional view of the thermocouple setup designed for more accurate temperature measurements was also shown in Fig. 2. Based on calibration of the entire temperature measurement system, including thermocouple and digital voltmeter, the error associated with the temperature data was estimated to be ±0.5°C. Table 2 shows the ranges of variables over which the experiments were conducted and the associated measurement uncertainties. The error reported in this paper is the absolute value of the maximum expected deviation for the all test runs. The detailed procedure to evaluate the experimental uncertainty is reported by Kline and McClintock (1953).

Saturated pool/flow boiling data were taken on a smooth tube annulus and the six tube annuli described in Table 1. Tests were conducted at a  $\bar{T}_{sat}$  of 30.0°C using R-114. The important properties of R-114 are in Table 1.  $D_h$  is defined as

$$D_h = 2(r_o - r_e) \quad (7)$$

which corresponds to a bare inner tube of radius  $r_e$ . A bare tube of radius  $r_e$  provides the same surface as the ribbed tube, i.e.,

$$r_e = \left[ 2 \left( r_i + \frac{H}{2} \right) \frac{H}{\sin \theta} + (r_i + H)w + r_i \left( (p - w) + \frac{2H}{\tan \theta} \right) \right] / p \quad (8)$$

Also shown in Table 1 is the tube numbering system (i.e., tubes 1 through 7), which is used to identify each tube. Before each test, the tubes were cleaned with acetone. A test was started by boiling the liquid for 2–3 hours to drive out any absorbed air in the system.

### 5 Data Reduction

Tubes with different rib pitches and rib angles and smooth tubes were tested with R-114 at an average pressure of 2.68 (kg/cm<sup>2</sup>). Each tube was tested at an inlet pressure of approximately 2.41 (kg/cm<sup>2</sup>) and an inlet temperature of approximately 30°C.

For each test run,  $h$ 's were calculated at six axial locations on the basis of bulk fluid saturation temperature, tube heat flux, and tube inside wall temperature. Three thermocouples were mounted just downstream of specified pressure tap (see Fig. 2 for sections B-B and D-D); hence, the readings were averaged

$$T_{\bar{w}} = (T_{top} + T_{mid} + T_{bot})/3 \quad (9)$$

Wall temperatures at all other locations were based on the single measurement,  $T_{mid}$ . Circumferential variations in  $T_w$  were normally negligible in the forced convection vaporization region, and somewhat larger (but still less than 0.2°C) in the nucleate boiling region. The local  $h$  at the axial locations was then calculated as follows:

$$h_{TP} = Q/A(T_{\bar{w}} - T_{sat}) \quad (10)$$

When  $h$ 's were calculated for roughened tubes, the surface area in Eq. (10) was  $2\pi r_e L$ . The  $\bar{h}_{TP}$  was determined by the following formula:

$$\bar{h}_{TP} = Q/A(\bar{T}_{\bar{w}} - \bar{T}_{sat}) \quad (11)$$

It is necessary to note that  $h_{TP}$  was calculated based on  $T_{sat}$  instead of mean bulk temperature of the refrigerant. Nevertheless, the error was evaluated to be less than 1 percent. The active heating length  $L$  was 0.35 m. Mass flux was also based on the cross-sectional area calculated from the equivalent diameter  $D_h$ . Qual-

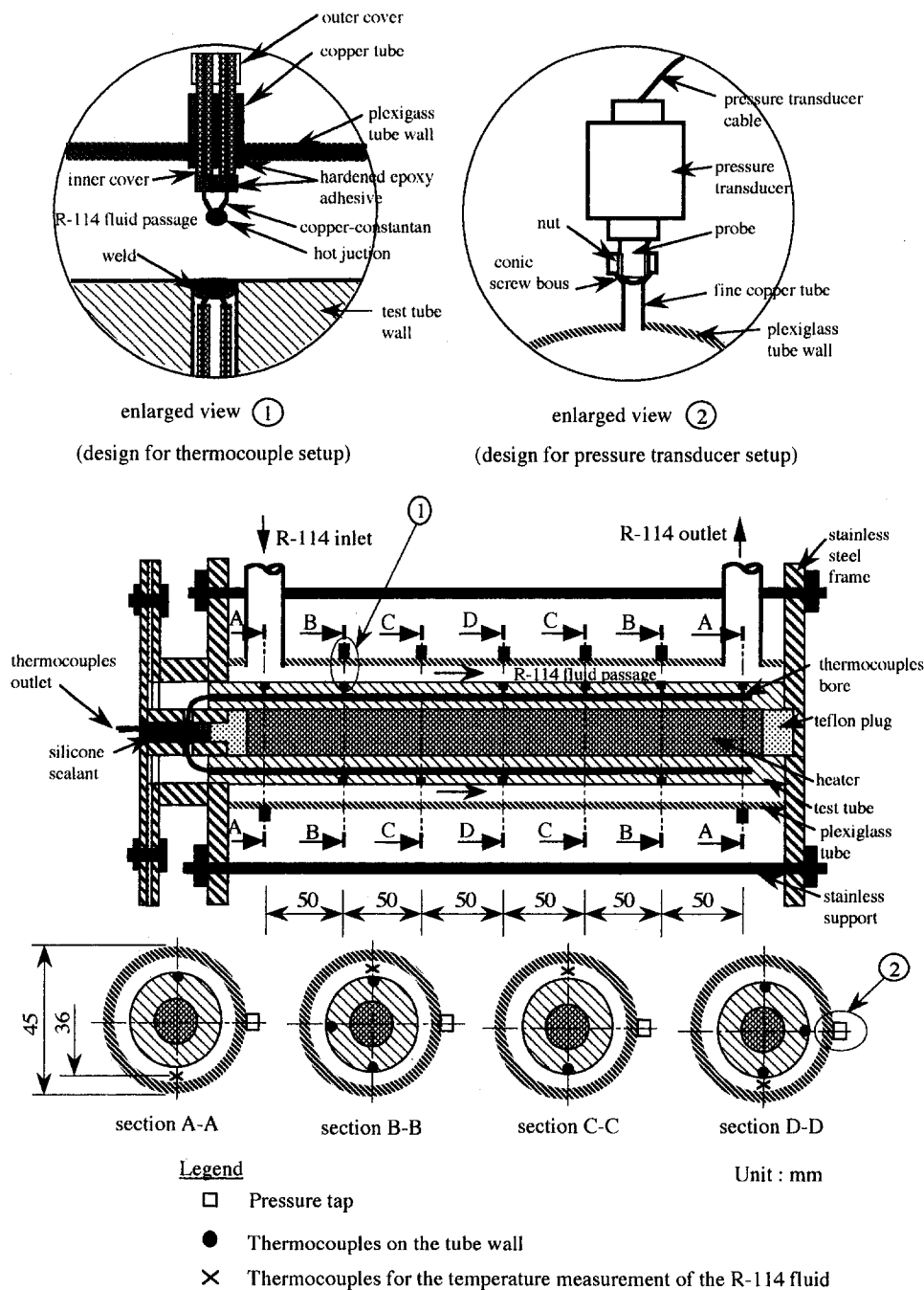


Fig. 2 Locations of temperature/pressure measurements for the test evaporator (not to scale)

ities at each axial location were calculated from inlet conditions and energy balances along the tube length. The uncertainties in the heat transfer coefficient and quality calculations are also listed in Table 2. The pressure drop data were measured over a length of 0.05 m for the test section (0.35 m). The effect of natural convection in the experiments reported herein can be considered to be negligible because the Grashof number is much less than  $Re^2$  even at the lowest mass velocity.

## 6 Results and Discussion

Tests were carried out for the seven tube annuli geometries with R-114. The ranges of heat flux and mass velocity are also listed in Table 2. To avoid burnout of the test section, qualities at the outlet were not allowed to exceed 80 percent. Several single-phase heated tube annuli tests were performed for R-114

prior to nucleate pool/or flow boiling tests and results were compared to the Dittus-Boelter equation. It was found that the  $h$ 's were in good agreement within an average deviation of  $\pm 25$  percent. Table 3 lists the values measured/calculated of the relevant parameters such as inlet and outlet flow qualities, geometric parameter as well as the enhancement performance ratio. For each test, an energy balance was made for entire loop. The energy gained by the R-114 across the test section was compared to the sum of the power input and heat losses to the surroundings. For all tests, the energy balance was satisfied within 9.3 percent. The system was judged to have reached a steady-state condition when the temperature, pressure, and mass flux rates of R-114 remained unchanged for about 2 hours.

**6.1 Comparison Against Published Results.** Figure 3(a) depicts the comparison of the experimental  $h$  data with the Shah

**Table 2 Ranges of experiments and measurement uncertainties**

Parameters	Range	Uncertainty
Mass velocity, G	63.55 - 160.12 (kg/m <sup>2</sup> s)	± 3.1%
Heat flux supplied to test section, q̇	2.01 - 2.95 × 10 <sup>4</sup> (W/m <sup>2</sup> )	± 4.3%
Local quality in the test section, x	0.015-0.8	± 5.7%
Average pressure over the test section, P̄	2.53-2.83 (kg/cm <sup>2</sup> )	± 4.5%
Wall temperature, T <sub>w</sub>	32-45 (°C)	± 1.0%
Average wall heat transfer coefficient, h̄ <sub>TP</sub>	4.1-8.9 × 10 <sup>3</sup> (W/m <sup>2</sup> ·°C)	± 7.1%
Enhancement performance ratio, $\frac{(h_a/h_p)}{(\Delta P_a/\Delta P_p)}$	0.93-1.41	± 9.4%
Definition: $\bar{P} = \frac{P_{in} + P_{out}}{2}$ , $\bar{h}_{TP} = Q/A(\bar{T}_w - \bar{T}_{sat})$		

correlation (1982) for the cases shown for a smooth tube. The Shah correlation reduces to the Dittus-Boelter correlation for single-phase liquids. Most of the data were within ±20 percent of the predicted values. A series of repeatability tests indicated a maximum variation about ±7.1 percent in the heat transfer coefficients. A comparison of experimental ΔP data with the Lockhart and Martinelli (1949) correlation is shown in Fig. 3(b). No correlation was made for the acceleration part because it is so small compared to its counterpart (friction force part). The data are within ±30 percent of the predicted values with the maximum deviation occurring at the low mass velocity. The large deviation from the correlation is not unusual for two-phase flow.

It is of interest to compare the present data with measurements for roughened tubes/or annuli by other investigators. However, the survey by Pais and Webb (1991) shows that there are very few

published data that could be compared. Figure 4(a) shows the R-11 test results for the GEWA K26 tube of Webb and Pais (1992) at 26.7°C compared to the present R-114 pool boiling data. The present data are 1–14 percent higher than those of Webb and Pais for Tube 1 to Tube 6. Figure 4(a) also shows the pool boiling coefficients for a smooth tube. In addition, present test data of pool boiling including roughened/smooth tubes qualitatively coincide with the results correlated by Borishanski (1969), and by Ratiani and Shekrladze (1972). Figure 4(b) presents flow boiling data compared to the correlation (Kandlikar, 1990) at G = 63.55 kg/m<sup>2</sup> s. As predicted by Kandlikar, the flow boiling data show the same dependence on q̇ as does pool boiling.

**6.2 Pool/Flow Boiling Data.** All data were obtained with R-114 at a pressure of 2–3 atm. The onset of nucleate boiling was observed through the plexiglass, and was defined as the applied heat flux where first nucleation was observed on the instrumented tube annuli. When heat flux is plotted versus (T̄<sub>w</sub> - T̄<sub>sat</sub>), the “incipient boiling” condition is indicated by a change in slope since the heat transfer mechanism changes from single-phase convection to two-phase convection with the activation, growth, and departure of vapor bubbles. Here T̄<sub>sat</sub> is the mean saturated temperature based on the average pressure over the test section.

Four out of seven data of the geometry studied are presented in the form of q̇ versus (T̄<sub>w</sub> - T̄<sub>sat</sub>) on Figs. 5(a) and 5(b) for flow/pool boiling, respectively. Figure 5(a) shows saturated flow boiling data at four mass velocities (63.55, 93.74, 129.86, and 160.12 kg/m<sup>2</sup>s) from tube No. 2. The data shown pertain to the increasing-heat flux mode. A “partial nucleate boiling” in which the heat transfer mechanism may be sensitive to variations in mass velocity was noted. This may be attributed to the contribution of roughened surfaces on the part of forced convection in “partial nucleate boiling” region where forced convection and nucleate boiling are both significant. Immediately after this region an asymptote to the fully developed nucleate boiling model was found. The fully developed mode is essentially insensitive

**Table 3 Measured/calculated values of the relevant parameters**

Tube No. 1										Tube No. 2											
G (kg/m <sup>2</sup> s)	q (W/m <sup>2</sup> )	P <sub>in</sub> (kg/cm <sup>2</sup> )	X <sub>1</sub>	X <sub>2</sub>	h̄ <sub>TP</sub> (W/m <sup>2</sup> K)	(h̄ <sub>TP</sub> ) <sub>meas</sub> / ((h̄ <sub>TP</sub> ) <sub>unif</sub> / (ΔP) <sub>meas</sub> / (ΔP) <sub>unif</sub> )	GP*	E(%)			G (kg/m <sup>2</sup> s)	q (W/m <sup>2</sup> )	P <sub>in</sub> (kg/cm <sup>2</sup> )	X <sub>1</sub>	X <sub>2</sub>	h̄ <sub>TP</sub> (W/m <sup>2</sup> K)	(h̄ <sub>TP</sub> ) <sub>meas</sub> / ((h̄ <sub>TP</sub> ) <sub>unif</sub> / (ΔP) <sub>meas</sub> / (ΔP) <sub>unif</sub> )	GP*	E(%)		
63.55	2.01x10 <sup>4</sup>	2.01	0.055	0.705	5.40x10 <sup>3</sup>	1.29	24.69	7.2			63.55	2.01x10 <sup>4</sup>	2.01	0.054	0.692	5.44x10 <sup>3</sup>	1.34	9.234	7.5		
63.55	2.43x10 <sup>4</sup>	2.01	0.057	0.746	6.61x10 <sup>3</sup>	1.06	24.69	8.2			63.55	2.43x10 <sup>4</sup>	2.01	0.057	0.743	6.82x10 <sup>3</sup>	1.09	9.234	8.1		
63.55	2.95x10 <sup>4</sup>	2.01	0.058	0.755	7.12x10 <sup>3</sup>	0.99	24.69	9.1			63.55	2.95x10 <sup>4</sup>	2.01	0.058	0.763	7.28x10 <sup>3</sup>	1.01	9.234	9.0		
93.74	2.01x10 <sup>4</sup>	2.01	0.057	0.723	6.99x10 <sup>3</sup>	1.07	24.69	6.8			93.74	2.01x10 <sup>4</sup>	2.01	0.056	0.718	7.19x10 <sup>3</sup>	1.09	9.234	7.6		
93.74	2.43x10 <sup>4</sup>	2.01	0.058	0.754	7.64x10 <sup>3</sup>	1.03	24.69	7.6			93.74	2.43x10 <sup>4</sup>	2.01	0.059	0.762	7.85x10 <sup>3</sup>	1.05	9.234	7.9		
93.74	2.95x10 <sup>4</sup>	2.01	0.061	0.789	8.20x10 <sup>3</sup>	0.99	24.69	9.2			93.74	2.95x10 <sup>4</sup>	2.01	0.060	0.782	8.41x10 <sup>3</sup>	1.00	9.234	8.9		
129.68	2.01x10 <sup>4</sup>	2.01	0.061	0.741	7.75x10 <sup>3</sup>	1.01	24.69	6.5			129.68	2.01x10 <sup>4</sup>	2.01	0.060	0.737	7.86x10 <sup>3</sup>	1.04	9.234	6.7		
129.68	2.43x10 <sup>4</sup>	2.01	0.060	0.762	8.21x10 <sup>3</sup>	0.98	24.69	7.9			129.68	2.43x10 <sup>4</sup>	2.01	0.060	0.771	8.37x10 <sup>3</sup>	1.02	9.234	6.6		
129.68	2.95x10 <sup>4</sup>	2.01	0.061	0.803	8.43x10 <sup>3</sup>	0.93	24.69	8.7			129.68	2.95x10 <sup>4</sup>	2.01	0.061	0.814	8.61x10 <sup>3</sup>	0.94	9.234	8.8		

Tube No. 3										Tube No. 4											
G (kg/m <sup>2</sup> s)	q (W/m <sup>2</sup> )	P <sub>in</sub> (kg/cm <sup>2</sup> )	X <sub>1</sub>	X <sub>2</sub>	h̄ <sub>TP</sub> (W/m <sup>2</sup> K)	(h̄ <sub>TP</sub> ) <sub>meas</sub> / ((h̄ <sub>TP</sub> ) <sub>unif</sub> / (ΔP) <sub>meas</sub> / (ΔP) <sub>unif</sub> )	GP*	E(%)			G (kg/m <sup>2</sup> s)	q (W/m <sup>2</sup> )	P <sub>in</sub> (kg/cm <sup>2</sup> )	X <sub>1</sub>	X <sub>2</sub>	h̄ <sub>TP</sub> (W/m <sup>2</sup> K)	(h̄ <sub>TP</sub> ) <sub>meas</sub> / ((h̄ <sub>TP</sub> ) <sub>unif</sub> / (ΔP) <sub>meas</sub> / (ΔP) <sub>unif</sub> )	GP*	E(%)		
63.55	2.01x10 <sup>4</sup>	2.01	0.054	0.729	5.56x10 <sup>3</sup>	1.35	5.545	7.7			63.55	2.01x10 <sup>4</sup>	2.01	0.054	0.766	5.75x10 <sup>3</sup>	1.39	3.294	4.4		
63.55	2.43x10 <sup>4</sup>	2.01	0.057	0.779	6.97x10 <sup>3</sup>	1.11	5.545	8.8			63.55	2.43x10 <sup>4</sup>	2.01	0.056	0.821	6.96x10 <sup>3</sup>	1.16	3.294	6.4		
63.55	2.95x10 <sup>4</sup>	2.01	0.058	0.798	7.43x10 <sup>3</sup>	1.03	5.545	9.3			63.55	2.95x10 <sup>4</sup>	2.01	0.057	0.857	7.45x10 <sup>3</sup>	1.05	3.294	7.5		
93.74	2.01x10 <sup>4</sup>	2.01	0.056	0.731	7.25x10 <sup>3</sup>	1.10	5.545	7.5			93.74	2.01x10 <sup>4</sup>	2.01	0.057	0.744	7.31x10 <sup>3</sup>	1.11	3.294	4.9		
93.74	2.43x10 <sup>4</sup>	2.01	0.059	0.784	7.96x10 <sup>3</sup>	1.07	5.545	8.2			93.74	2.43x10 <sup>4</sup>	2.01	0.059	0.798	8.01x10 <sup>3</sup>	1.05	3.294	6.4		
93.74	2.95x10 <sup>4</sup>	2.01	0.062	0.820	8.58x10 <sup>3</sup>	1.02	5.545	8.9			93.74	2.95x10 <sup>4</sup>	2.01	0.061	0.861	8.62x10 <sup>3</sup>	1.04	3.294	8.2		
129.68	2.01x10 <sup>4</sup>	2.01	0.062	0.733	7.95x10 <sup>3</sup>	1.01	5.545	7.2			129.68	2.01x10 <sup>4</sup>	2.01	0.061	0.737	8.21x10 <sup>3</sup>	0.99	3.294	4.7		
129.68	2.43x10 <sup>4</sup>	2.01	0.063	0.789	8.47x10 <sup>3</sup>	0.99	5.545	8.0			129.68	2.43x10 <sup>4</sup>	2.01	0.062	0.781	8.52x10 <sup>3</sup>	0.98	3.294	6.9		
129.68	2.95x10 <sup>4</sup>	2.01	0.064	0.852	8.66x10 <sup>3</sup>	0.96	5.545	8.5			129.68	2.95x10 <sup>4</sup>	2.01	0.064	0.869	8.72x10 <sup>3</sup>	0.96	3.294	7.6		

Tube No. 5										Tube No. 6											
G (kg/m <sup>2</sup> s)	q (W/m <sup>2</sup> )	P <sub>in</sub> (kg/cm <sup>2</sup> )	X <sub>1</sub>	X <sub>2</sub>	h̄ <sub>TP</sub> (W/m <sup>2</sup> K)	(h̄ <sub>TP</sub> ) <sub>meas</sub> / ((h̄ <sub>TP</sub> ) <sub>unif</sub> / (ΔP) <sub>meas</sub> / (ΔP) <sub>unif</sub> )	GP*	E(%)			G (kg/m <sup>2</sup> s)	q (W/m <sup>2</sup> )	P <sub>in</sub> (kg/cm <sup>2</sup> )	X <sub>1</sub>	X <sub>2</sub>	h̄ <sub>TP</sub> (W/m <sup>2</sup> K)	(h̄ <sub>TP</sub> ) <sub>meas</sub> / ((h̄ <sub>TP</sub> ) <sub>unif</sub> / (ΔP) <sub>meas</sub> / (ΔP) <sub>unif</sub> )	GP*	E(%)		
63.55	2.01x10 <sup>4</sup>	2.01	0.058	0.806	5.86x10 <sup>3</sup>	1.41	2.490	5.2			63.55	2.01x10 <sup>4</sup>	2.01	0.055	0.801	5.75x10 <sup>3</sup>	1.32	1.299	3.8		
63.55	2.43x10 <sup>4</sup>	2.01	0.060	0.849	7.12x10 <sup>3</sup>	1.19	2.490	6.1			63.55	2.43x10 <sup>4</sup>	2.01	0.057	0.843	6.81x10 <sup>3</sup>	1.15	1.299	4.1		
63.55	2.95x10 <sup>4</sup>	2.01	0.062	0.861	7.56x10 <sup>3</sup>	1.15	2.490	7.5			63.55	2.95x10 <sup>4</sup>	2.01	0.058	0.855	7.77x10 <sup>3</sup>	1.14	1.299	5.3		
93.74	2.01x10 <sup>4</sup>	2.01	0.058	0.768	7.45x10 <sup>3</sup>	1.13	2.490	4.8			93.74	2.01x10 <sup>4</sup>	2.01	0.056	0.758	7.36x10 <sup>3</sup>	1.09	1.299	3.9		
93.74	2.43x10 <sup>4</sup>	2.01	0.060	0.799	8.22x10 <sup>3</sup>	1.09	2.490	5.4			93.74	2.43x10 <sup>4</sup>	2.01	0.058	0.781	8.09x10 <sup>3</sup>	1.06	1.299	4.7		
93.74	2.95x10 <sup>4</sup>	2.01	0.061	0.841	8.71x10 <sup>3</sup>	1.07	2.490	6.7			93.74	2.95x10 <sup>4</sup>	2.01	0.060	0.831	8.51x10 <sup>3</sup>	1.05	1.299	4.8		
129.68	2.01x10 <sup>4</sup>	2.01	0.063	0.751	8.30x10 <sup>3</sup>	1.04	2.490	4.6			129.68	2.01x10 <sup>4</sup>	2.01	0.059	0.739	8.46x10 <sup>3</sup>	0.97	1.299	3.4		
129.68	2.43x10 <sup>4</sup>	2.01	0.065	0.805	8.64x10 <sup>3</sup>	1.02	2.490	5.2			129.68	2.43x10 <sup>4</sup>	2.01	0.061	0.797	8.51x10 <sup>3</sup>	0.96	1.299	3.8		
129.68	2.95x10 <sup>4</sup>	2.01	0.066	0.876	8.89x10 <sup>3</sup>	1.01	2.490	6.6			129.68	2.95x10 <sup>4</sup>	2.01	0.063	0.854	8.69x10 <sup>3</sup>	0.95	1.299	4.3		

$$* : GP = \frac{(p-w) + \frac{2H}{\tan \theta}}{\sqrt{g(\rho_1 - \rho_v)}} \frac{1}{\sin \theta}$$



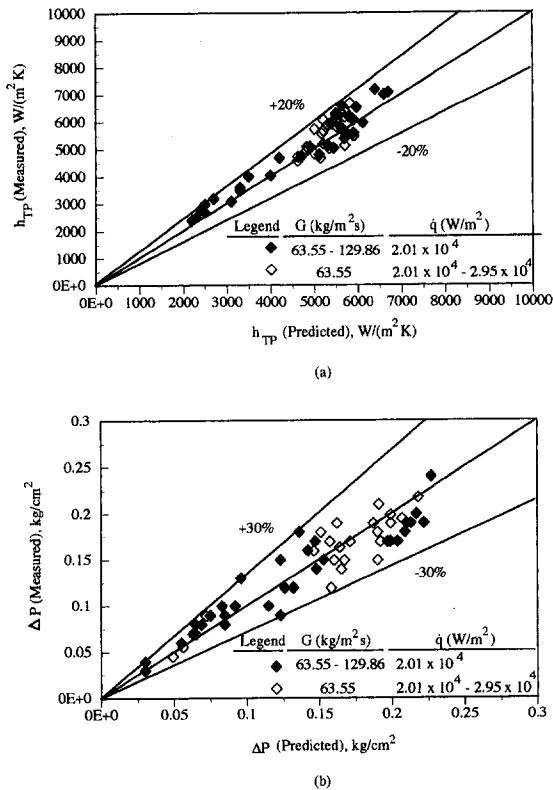


Fig. 3 Comparisons between measured and (a) predicted evaporation heat transfer coefficients (Shah, 1982), (b) predicted pressure drops (Lockhart and Martinelli, 1949) for smooth tube

to variations in  $G$  and depends strongly on the heat flux. All of these features are consistent with the findings of earlier investigators for smooth tubes (e.g., Bergles and Rohsenow, 1964). However, a significant enhancement of nucleate boiling was observed with the rib-roughened tubes, regardless of whether there is an increase in  $G$ , as compared to those of smooth tubes (see Wen and Hsieh, 1994). This enhancement, shown by the lower wall superheats, could be attributed to a preferential stripping of the R-114 near the roughened surface resulting in a local  $(T_w - T_{sat})$  increase. Consequently, the effective wall superheat decreases, which is termed a "loss of wall superheat." With a smaller effective wall superheat, nucleate boiling would be suppressed more rapidly with roughened annuli than with smooth annuli under the same flow condition.

Figure 5(b) shows typical pool/flow boiling data for annuli No. 1, No. 3, No. 5, and No. 7 at  $G = 63.55 \text{ kg/m}^2\text{s}$ . The differences between pool and flow boiling are quite obvious. Moreover, among these four tube annuli, it is found annulus No. 5 has the best  $\dot{q}$  for both flow/pool boiling. It is because Tube No. 5 could generate more smaller vapor pockets, which will be triggered into active bubble growth to reduce the wall superheat for incipient boiling compared to those for the other test tubes. It could be understood that the cumulative active nucleation site density is a function of a specified contact angle (cavity mouth angle), but it is not clear why annulus No. 5 has more active nucleation sites resulting in the best  $\dot{q}$ . This needs further examination in a future study. The effect of spacing of transverse ribs as well as rib angles on flow boiling and pool boiling heat transfer by this typical plot was further noted.

Figure 6 shows the effect of  $X$ ,  $G$ ,  $\dot{q}$ , and rib spacing on the  $h$ . In Fig. 6(a) the  $h$ 's are plotted versus  $X$  for different  $\dot{q}$  and tubes. For a given  $G$  in the "partial nucleate boiling" region, the  $h$ 's at various  $\dot{q}$  are distinctly different at low qualities, approximately merging into a single line beyond certain transition qualities, which was also observed in the other references (see Ross

et al., 1987, and Jung et al., 1989). In "partial nucleate boiling," both forced convection and nucleate boiling are significant. The gradual suppression of the latter leads to a temporary reduction of the  $h$ 's. Later they will increase until finally merging into a single line with increasing quality, which was also observed by Jung et al. (1989). This indicates that, in "partial nucleate boiling,"  $h$  is strong function of the heat flux. However, in convective evaporation region,  $h$  is independent of the heat flux.

The effects of rib spacing on heat transfer are shown by Fig. 6(b). It was found that the flow boiling  $h$  increases are mainly due to  $G$  increases. It is also shown that  $h$  decreased with increasing rib spacing but the decrease seems insignificant. The trends of these decreases are in parallel for different  $G$ 's and heat fluxes  $\dot{q}$ . This indicates that there exists a plot like Fig. 7 for a correlation of heat transfer coefficient versus a geometric parameter for all six roughened rib tubes under study. The data are correlated in Fig. 7 using the following relationship:

$$Nu = 17.1 \left( \frac{\dot{q}}{i_{f,g} G} \right)^{0.71} \left[ \frac{(p-w) + \frac{2H}{\tan \theta}}{\sqrt{\frac{\sigma}{g(\rho_l - \rho_v)}}} \frac{1}{\sin \theta} \right]^{0.22} \times \left( \frac{\rho_v}{\rho_l} \right)^{-0.566} \quad (12)$$

The correlation was derived by using standard procedures, and the dimensionless group  $(\dot{q}/i_{f,g} G)$  known as boiling number and  $\rho_v/\rho_l$  will be familiar from other established boiling correlations. Although the range of  $\rho_v/\rho_l$  of the present study was limited, its effect is well known and is, therefore, included for completeness. The third dimensionless group

$$\left[ \frac{\left( (p-w) + \frac{2H}{\tan \theta} \right) \left( \frac{1}{\sin \theta} \right)}{\sqrt{\frac{\sigma}{g(\rho_l - \rho_v)}}} \right]$$

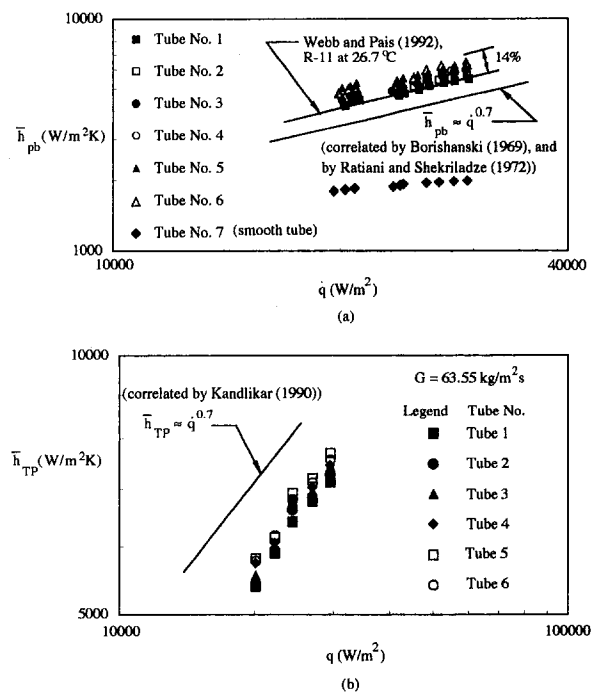


Fig. 4 Comparison against the published results for (a) pool boiling, (b) flow boiling

**Table 4 Summary of correlations for flow boiling heat transfer of augmented tubes**

Authors	Correlation	Tube geometry	Test fluid and parameter ranges	Comments
This study	$Nu = 17.1 \left( \frac{\dot{q}}{i_{fg}} \right)^{0.71} \left( \frac{\rho_v}{\rho_l} \right)^{-0.566}$ $\left[ \frac{(p-w) + \frac{2H}{\tan \theta}}{\frac{\sigma}{\sin \theta}} \right]^{0.22} \frac{1}{\sqrt{g(\rho_l - \rho_v)}}$		R-114; X=0.015-0.8 P=2.53-2.83 kg/m <sup>2</sup> G=63.55-2.95x10 <sup>4</sup> kg/cm <sup>2</sup> s q̇=2.01-1.95x10 <sup>4</sup> W/m <sup>2</sup> ΔT <sub>sub</sub> =0	Correlation predicts 98% of points within ±30% and 85% of points within ±12%.
Akhanda and James (1991)	$\frac{Nu_{exp}}{Nu_{calc}} = 130.0 \left( \frac{q/A}{\lambda_{p,v}} \right)^{0.73} \left( \frac{\lambda}{C_{pl} \Delta T} \right)^{0.55}$ $\left( \frac{\rho_v}{\rho_l} \right)^{0.7} \frac{s}{\sqrt{g(\rho_l - \rho_v)}} \frac{e}{l}^{0.10}$ $(1 + \sin \theta)^{0.15}$		Distilled and deionized water; P=1 atm G=0.2-1.4 m/s q̇=in nucleate boiling below the burnt-out heat flux ΔT <sub>sub</sub> =5, 15, and 30 °C	Experimental data were correlated to within ±30%
Kandlikar (1991)	$h_{TP} = \text{larger of } \begin{cases} h_{TP,NBD} \\ h_{TP,CBD} \end{cases}$ $h_{TP,NBD} = 0.6683 Co^{-0.2} (1-X)^{0.8} h_{lo} E_{CB} + 1058.0 Bo^{0.7} (1-X)^{0.8} F_n h_{lo} E_{NB}$ $h_{TP,CBD} = 1.1360 Co^{-0.9} (1-X)^{0.8} h_{lo} E_{CB} + 667.2 Bo^{0.7} (1-X)^{0.8} F_n h_{lo} E_{NB}$	Refer to 1. Khanpara et al. (1987) 2. Robertson and Lovegrove (1983) 3. Cohen and Carey (1990) (Geometry 1 and 3)	Refer to the literature of left term (Tube geometry)	All experimental data reported by Khanpara et al. (1987), Robertson and Lovegrove (1983), and Cohen and Carey (1990) were correlated to within ±30% for different fixed augmentation factors E <sub>CB</sub> and E <sub>NB</sub> .

represents all the dimensions necessary to illustrate the present rib geometric configuration. In addition, it includes a term that is proportional to the bubble departure diameter and incorporates surface tension and buoyant forces, which are dominant in a hydrodynamic situation. The numerator of this dimensionless

group,  $[(p-w) + (2H/\tan \theta)](1/\sin \theta)$ , is a measure proportional to the availability of space for bubble growth between ribs, and, furthermore,  $[(p-w) + (2H/\tan \theta)](1/\sin \theta) / \sqrt{(\sigma/g(\rho_l - \rho_v))}$  can be considered as the Bond number, which is typical of pool conditions. Since the Bond number is closely connected to the pool boiling peak heat flux, it is not surprising that the Nu correlation developed for the enhanced roughened surfaces studied herein has some dependence on it. In addition, the exponent of the boiling number in the nucleate boiling is seen to be 0.71 in the present study for both convective and nucleate boiling regions. These two findings strongly suggest that the underlying mechanism for the nucleate boiling in two-phase flow can be related to the pool boiling. Figure 8 shows the performance plot for Eq. (12). The correlation predicts 98 percent of points within ±30 percent and 85 percent of points within ±12 percent. Agreement is particularly good for annuli Nos. 2, 4, and 5. Although there was considerable scatter in the data, the prediction seems still good and useful. Table 4 summarizes the present correlation and those of enhanced tubes previously studied.

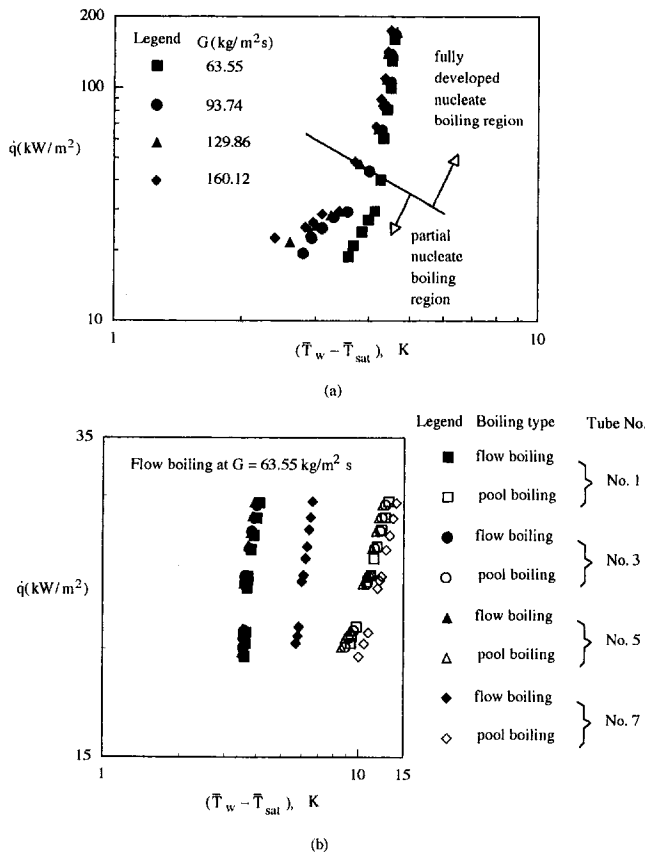


**Fig. 5 (a) Flow boiling curves at four mass velocities for the test tube No. 2; (b) pool boiling/flow boiling curves for four test tubes**

**6.3 Determination of Two-Phase Enhancement Factor *F*.** Since the present results indicate the suppression of nucleate boiling for R-114, a plot of  $h_{TP}/h_{fc}$  and  $h_{ecc}/h_{fc}$  against  $1/X_{tt}$  and quality is made to account for the effects of various roughened surface conditions. In Fig. 9,  $h_{TP}$  is a measured quantity and  $X_{tt}$  is given by Eq. (5). Figures 9(a) and 9(b) show the results without/with nucleate boiling suppression, respectively. Also shown in Fig. 9 is Chen's *F* function. The dimensionless *h*'s are scattered at low qualities where partial boiling occurs; they fall into a single line for the evaporation region (see Fig. 9(a)) as previously observed for R-12 (Jung et al., 1989). Chen's *F* function underpredicts the present data by 15–25 percent with the larger deviation observed at higher qualities. However, its slope is parallel to the present data. Based on the experimental evidence and the observations of other investigators, a new *F* function was determined in the evaporative region. The resulting *F* function has the following form:

$$F = 1 + c_1 \left( \frac{1}{X_{tt}} \right)^{n_1} \quad (13)$$

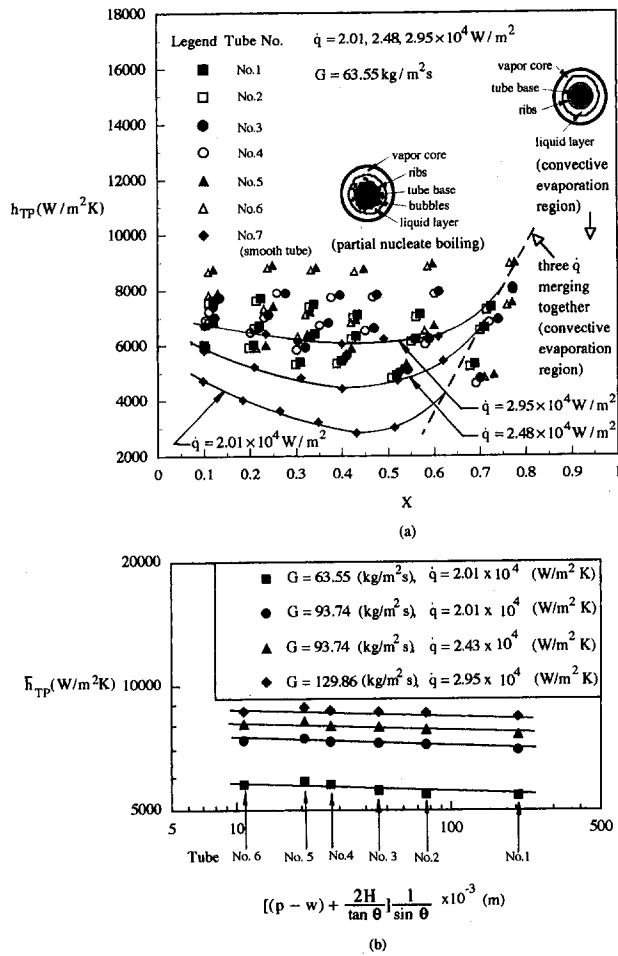


Fig. 6 Effect of (a) quality and (b) rib spacing on flow boiling heat transfer coefficients

where constants  $c_1$ , exponents  $n_1$ , and standard deviations  $s_1$  are also tabulated in Table 5. The data for each case can be correlated with an  $s_1$  of less than 0.32.  $s_1$  is based on the difference between the calculated and experimental results for the  $F$  function. These correlations represent the experimental data with a maximum deviation of 8.95 percent. In accordance with Eq. (13), the data for the present roughened/smooth tubes can be correlated as follows:

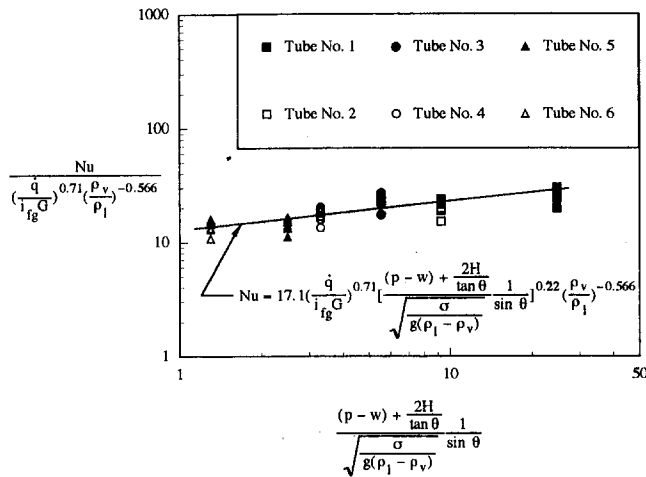


Fig. 7 A correlation of flow boiling heat transfer performance for six roughened tubes

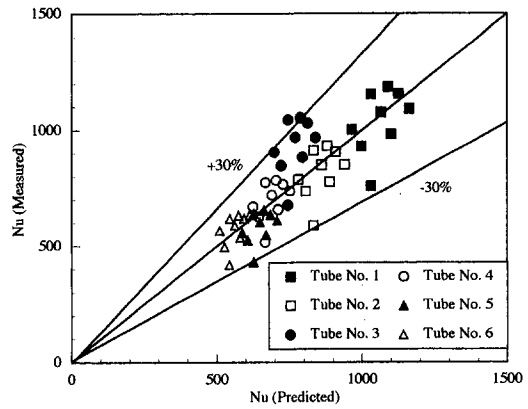


Fig. 8 Comparison between the predicted Nusselt numbers using the present correlation and experimental values

$$F = 1 + 1.96(1/X_{tt})^{0.82}, \text{ for roughened tubes} \quad (14)$$

$$F = 1 + 1.81(1/X_{tt})^{0.80}, \text{ for smooth tube} \quad (15)$$

At the 95 percent confidence level,  $n_1 = 0.172 \pm 0.02013$ . This shows that the  $F$  dependence on  $1/X_{tt}$  is not altered for the seven tubes under consideration. The revised  $F$  function also shown in Fig. 9(b) predicts the data in the convective evaporation region. The exponents in Eqs. (14) and (15) for roughened and smooth tubes are not altered and they are in good agreement with that of Jung et al. (1989).

#### 6.4 Determination of Suppression Factor $S$ . Following Chen's definition of $S$ , Eq. (3), the present results plotted against

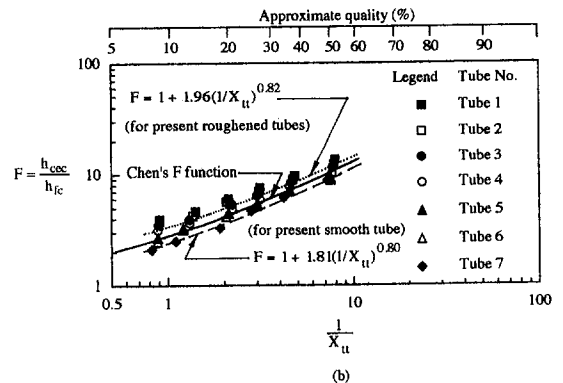
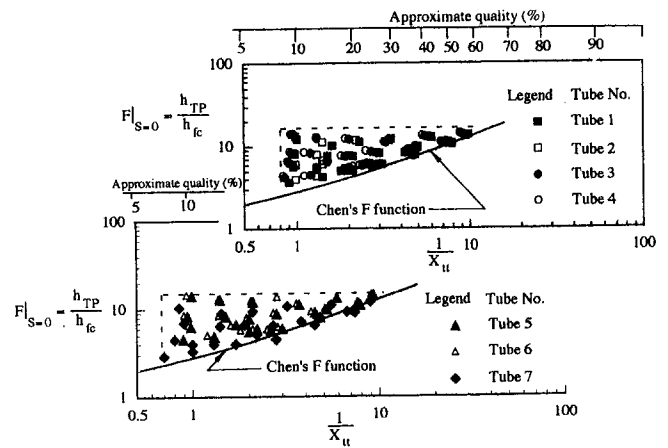


Fig. 9 (a) Dimensionless parameter  $h_{TP}/h_{fc}$ , and (b) forced convective heat transfer enhancement factor  $F$  versus  $1/X_{tt}$

$Re_{TP}$  are shown in Fig. 10. It might be also expected that the revised suppression factor  $S$  would approach unity at low flows and zero at high flows. With the present roughened annuli, the suppression factor  $S$  would be expected to have a higher value than its corresponding one for a smooth annulus (i.e., Chen's  $S$  correlation) under the same flow condition due to a loss of wall superheat. It is therefore postulated that in all ranges of flow, a new  $S$  can be represented in the following form:

$$S = \frac{1}{1 + c Re_{TP}^{n_2}} \quad (16)$$

where constants  $c_2$ , exponents  $n_2$ , and standard deviations  $s_2$  listed in Table 5 are obtained from the experimental results. The data for each case can be correlated with a standard deviation of less than 0.26. This correlation is based on the original data with a maximum error of 11.7 percent. In accordance with Eq. (16), the data for the present roughened/smooth tubes can be correlated in the form

$$S = \frac{1}{1 + 0.0000225 Re_{TP}^{1.14}}, \quad \text{for roughened tubes} \quad (17)$$

$$S = \frac{1}{1 + 0.000012 Re_{TP}^{1.02}}, \quad \text{for smooth tube} \quad (18)$$

According to a 95 percent confidence level,  $n_2 = 0.177 \pm 0.01647$ . The revised  $S$  function also shown in Fig. 10 predicts the data in the nucleate boiling region.

Chen's correlation is also included in Fig. 10; it coincides well only with the present data for the smooth tube. The discrepancy between Chen's correlation and the rib-roughened data may be caused by the loss of wall superheat for the roughened tubes.

## 7 Conclusions

Based on the study of the roughened tube annuli effects on horizontal saturation flow boiling heat transfer with R-114, the following conclusions can be drawn:

1 It was found that six rib-roughened tube annuli have considerable heat transfer enhancement for R-114 at 30°C for flow as well as pool boiling. The enhancement performance ratios ranged from 0.93–1.41 depending on the quality, specified mass velocity, heat flux, and roughened surface geometry.

2 A full suppression of nucleate boiling was observed. Two distinct heat transfer regions exist. In the partial boiling region, a strong heat flux dependence of  $h_{TP}$  was noted while in the convective evaporation region  $h_{TP}$  for various heat fluxes seemed to collapse into a single line depending solely upon quality.

3 In the "partial nucleate boiling" region at low qualities the nucleate boiling effect is quite strong for roughened surfaces, while it is suppressed more rapidly compared to the smooth surface due to a loss of wall superheat.

4 New  $F$  and  $S$  functions were obtained for the present roughened tubes and one plain tube. It was found that  $F$  and  $S$

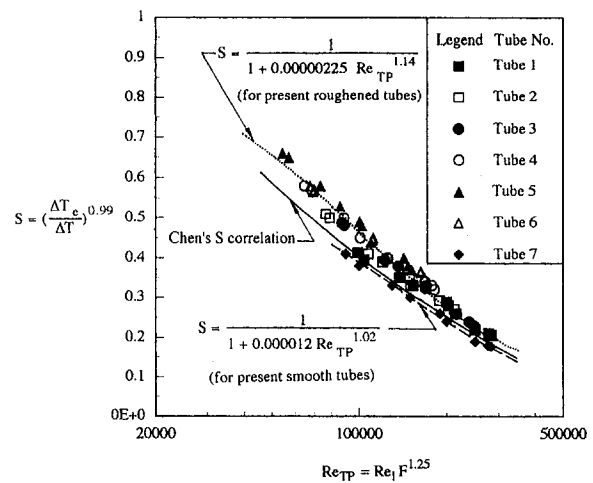


Fig. 10 Suppression factor  $S$  versus two-phase Reynolds number  $Re_{TP}$

for the present roughened tubes predict a higher value than Chen's correlation. In addition, the following correlations:

$$F = 1 + 1.96(1/X_H)^{0.82},$$

$$S = \frac{1}{1 + 0.0000225 Re_{TP}^{1.14}} \quad \text{for roughened tubes}$$

$$F = 1 + 1.81(1/X_H)^{0.80},$$

$$S = \frac{1}{1 + 0.000012 Re_{TP}^{1.02}} \quad \text{for smooth tube}$$

can be used to predict the flow boiling heat transfer coefficient for the present tube geometries by using the Chen model,  $h_{TP} = Sh_{pb} + Fh_{fc}$ .

5 The effects of transverse and longitudinal rectangular ribbing on the heat transfer performance were investigated and the results were correlated in the form of Eq. (12) within  $\pm 30$  percent of the experimental data.

## References

- Akhanda, M. A. R., and James, D. D., 1991, "An Experimental Study of the Relative Effects of Transverse and Longitudinal Ribbing of the Heat Transfer Surface in Forced Convective Boiling," *ASME JOURNAL OF HEAT TRANSFER*, Vol. 113, pp. 209–215.
- Bergles, A. E., and Rohsenow, W. M., 1964, "The Determination of Forced-Convection Surface-Boiling Heat Transfer," *ASME JOURNAL OF HEAT TRANSFER*, Vol. 86, pp. 365.
- Borishanski, V. M., 1969, "Correlation of the Effect of Pressure on the Critical Heat Flux and Heat Transfer Rates Using the Theory of Thermodynamic Similarity," in: *Problems of Heat Transfer and Hydraulics of Two-Phase Media*, Z. Z. Kutateladze, ed., Pergamon, Oxford, United Kingdom, pp. 16–37.
- Chen, J. C., 1963, "A Correlation for Boiling Heat Transfer to Saturated Fluids in Convective Flow," *ASME Paper No. 63-HT-34*.
- Collier, J. G., 1981, *Convective Boiling and Condensation*, 2nd ed., McGraw-Hill, New York.
- Jung, D. S., McLinden, M., Radermacher, R., and Didion, D., 1989, "A Study of Flow Boiling Heat Transfer With Refrigerant Mixtures," *Int. J. Heat Mass Transfer*, Vol. 32, pp. 1751–1764.
- Kandlikar, S. G., 1983, "An Improved Correlation for Predicting Two-Phase Flow Boiling Heat Transfer Coefficient in Horizontal and Vertical Tubes," in: *Heat Exchangers for Two-Phase Flow Applications*, ASME, New York.
- Kandlikar, S. G., 1990, "A General Correlation for Saturated Two-Phase Flow Boiling Heat Transfer Inside Horizontal and Vertical Tubes," *ASME JOURNAL OF HEAT TRANSFER*, Vol. 112, pp. 219–228.
- Kandlikar, S. G., 1991, "A Model for Correlating Flow Boiling Heat Transfer in Augmented Tubes and Compact Evaporators," *ASME JOURNAL OF HEAT TRANSFER*, Vol. 113, pp. 966–972.
- Kline, S. J., and McClintock, F. A., 1953, "Describing Uncertainties in Single-Sample Experiments," *Mech. Eng.*, Vol. 75, Jan., pp. 3–8.
- Lockhart, R. W., and Martinelli, R. C., 1949, "Proposed Correlation of Data for

Table 5 Coefficients, exponents, and deviations, for  $F$  function correlations of Eq. (13) and  $S$  function of Eq. (16)

Test tube No.	$c_1$	$n_1$	$s_1$	$c_2$	$n_2$	$s_2$
roughened tubes	No. 1	2.32	0.79	0.317	0.0000278	0.941
	No. 2	2.07	0.80	0.154	0.0000102	1.02
	No. 3	1.95	0.81	0.122	0.00000389	1.08
	No. 4	1.70	0.82	0.082	0.00000729	1.04
	No. 5	1.57	0.84	0.212	0.00000177	1.15
	No. 6	1.41	0.86	0.149	0.00000166	1.05
smooth tube	No. 7	1.79	0.80	0.168	0.0000120	1.02

Isothermal Two-Phase Two-Component Flow in Pipes," *Chemical Engineering Progress*, Vol. 45, pp. 39–48.

Pais, C., and Webb, R. L., 1991, "Literature Survey on Single-Tube Pool Boiling on Enhanced Surfaces," *ASHRAE Transactions*, Vol. 97, pp. 79–89.

Ratiani, G. V., and Shekrladze, I. G., 1972, "Study of the Process of Fully Developed Boiling of Liquids," *Heat Transfer—Soviet Research*, Vol. 4, pp. 126–141.

Ross, H., Radermacher, R., Marzo, M. D., and Didion, D., 1987, "Horizontal Flow Boiling of Pure and Mixed Refrigerants," *Int. J. Heat Mass Transfer*, Vol. 30, pp. 979–992.

Shah, M. M., 1982, "Chart Correlation for Saturated Boiling Heat Transfer Equations and Further Study," *ASHRAE Transactions*, Vol. 88, pp. 185–196.

Webb, R. L., and Pais, C., 1992, "Nucleate Pool Boiling Data for Five Refrigerants on Plain, Integral-Fin and Enhanced Tube Geometries," *Int. J. Heat Mass Transfer*, Vol. 35, pp. 1891–1904.

Wen, M.-Y., and Hsieh, S.-S., 1994, "Evaporative Heat Transfer and Enhancement Performance of Rib-Roughened Tube Annuli With Refrigerant 114," *Int. J. Heat Mass Transfer*, Vol. 37, pp. 425–436.

Whalley, P. B., 1987, *Boiling, Condensation, and Gas-Liquid Flow*, Oxford University Press, Oxford.

**L. W. Swanson**  
Senior Research Engineer,  
Heat Transfer Research, Inc.,  
1500 Research Parkway,  
College Station, TX 77840  
Mem. ASME

**G. P. Peterson**  
Tenneco Professor and Head of  
Mechanical Engineering,  
Mechanical Engineering Department,  
Texas A&M University,  
College Station, TX 77843  
Fellow ASME

# The Interfacial Thermodynamics of Micro Heat Pipes

*Successful analysis and modeling of micro heat pipes requires a complete understanding of the vapor-liquid interface. A thermodynamic model of the vapor-liquid interface in micro heat pipes has been formulated that includes axial pressure and temperature differences, changes in local interfacial curvature, Marangoni effects, and the disjoining pressure. Relationships were developed for the interfacial mass flux in an extended meniscus, the heat transfer rate in the intrinsic meniscus, the "thermocapillary" heat-pipe limitation, as well as the nonevaporating superheated liquid film thickness that exists between adjacent menisci and occurs during liquid dry out in the evaporator. These relationships can be used to define quantitative restrictions and/or requirements necessary for proper operation of micro heat pipes. They also provide fundamental insight into the critical mechanisms required for proper heat pipe operation.*

## Introduction

In order to analyze and understand the operation of a heat pipe, it is necessary first to understand the phenomena that control the behavior of the various interfaces, particularly that occurring at the vapor-liquid interface. This behavior, which is primarily governed by the surface tension, wettability, and contact angle, results in a pressure imbalance occurring at or near the interface and provides the capillary pumping action required for proper heat pipe priming and operation. The interfaces existing at the boundaries of the liquid, vapor, and solid phases are typically thought of as a clearly delineated line, or in the case of the interface between the liquid and a vapor phase, as a meniscus. However, the meniscus is actually a very small region on the order of  $10 \text{ \AA}$  where the density of the liquid phase changes continuously with respect to that of the vapor phase. For simplicity, the meniscus is assumed to be an infinitely thin dividing surface separating the bulk vapor and liquid phases. Under this assumption, the extensive properties for the system as a whole differ from the sum of the values for the two bulk phases by an excess or deficiency assigned to the interface region (Adamson, 1990). In the past, this type of model has been applied to the entire extended meniscus, which is composed of an intrinsic meniscus of constant mean curvature (macroscopic region), a transition region, and a thin liquid film predominantly influenced by the solid substrate (microscopic region). All three of these regions play an important role in the steady-state operation of micro heat pipes. The current investigation was motivated by the increasing interest in micro heat pipes (Peterson et al., 1991, 1993), and the work of Wayner et al. (1976) and Wayner (1982, 1991), in which expressions for superheated adsorbed layers and thin films were developed.

Previous steady-state investigations of the behavior of micro heat pipes have typically utilized a traditional pressure balance type of model (Babin et al., 1990; Wu et al., 1991; Longtin, 1991). Other investigations of the transient behavior have applied kinetic theory to predict the interfacial mass flux but have still relied upon an overall pressure balance (Wu and Peterson, 1991). As a result of these models, several interesting characteristics have been identified. Most notable among these are the prediction of reverse liquid flow in the arteries during startup, and the importance of the wetting angle in determining the overall transport capability. Although these pressure balance techniques have resulted in relatively good

correlation with the existing experimental results, they have not provided sufficient insight into the fundamental differences in behavior between these very small heat pipes and larger heat pipes with more conventional wicking structures. As the feature size of micro heat pipes continues to decrease in characteristic radius to levels of 20 microns or less (Mallik and Peterson, 1992), it will be necessary to formulate additional models that will more accurately describe the behavior of the thin film interfacial region (Peterson et al., 1991). This can be done by applying microscopic interfacial concepts similar to those developed by P. C. Wayner, Jr., and his co-workers over the past twenty years.

Wayner et al. (1976) formulated a thermodynamic model of a superheated nonevaporating thin film directly above the interline of an extended meniscus. The thickness of the film was related to the pressure and temperature in the liquid and vapor phases immediately adjacent to the interface as well as the dispersion forces due to the presence of the solid substrate. This approach was extended in subsequent studies by including other types of surface and body forces, e.g., Wayner (1991).

Wayner and his co-workers also conducted a number of experimental studies of evaporation in the extended meniscus (DasGupta et al., 1993; Sujanani and Wayner, 1992; Truong and Wayner, 1987). Using ellipsometry, the presence of this thin film was verified and its thickness was determined for a number of different liquid-substrate combinations. In many of these studies, the dispersion forces were specifically characterized by a semi-empirical dispersion constant, which was determined using the measured film thickness. This method of characterizing the dispersion forces is very useful because most substrates of practical use have a rough oxide layer of unknown thickness on the surface. The current lack of understanding of the oxide layer and molecular structure of the substrate near the surface prohibits the use of purely theoretical methods to determine the dispersion forces; methods based solely on bulk substrate properties are not adequate. Once the dispersion forces are known, the extended meniscus can be modeled using the augmented Young-Laplace equation, which eliminates the need for contact-angle measurements.

These experiments have also provided valuable information on how the dispersion forces influence evaporation, fluid flow, and interfacial phenomena (i.e., curvature) in the liquid near the interline. For the particular geometries studied, the evaporation in the interline region was found to go through a maximum point and eventually fall to zero at the interline. The increase in both the curvature and attractive dispersion forces associated with the high heat fluxes were responsible for the pressure gradient that caused fluid to flow into the interline region.

Contributed by the Heat Transfer Division for publication in the JOURNAL OF HEAT TRANSFER. Manuscript received by the Heat Transfer Division June 1993; revision received April 1994. Keywords: Heat Pipes and Thermosyphons, Moving Boundaries, Phase-Change Phenomena. Associate Technical Editor: A. Faghri.

This paper focuses on formulating a thermodynamic model of the vapor–liquid interface that can be applied specifically to micro heat pipes. This is done by combining the concepts discussed in earlier studies both by Peterson and Wayner. The equilibrium thermodynamic model of the vapor–liquid interface developed in this paper includes the effects of an axial temperature difference, changes in local interfacial curvature, Marangoni surface effects, and intermolecular forces due to the solid substrate.

### Thermodynamic Formulation

An equilibrium thermodynamic description of the vapor–liquid interface in heat pipes can be formulated by writing the caloric equations of state for (a) the liquid phase near the interface, (b) the interface region, and (c) the vapor phase near the interface. Figure 1 illustrates a micro heat pipe with an equilateral triangular cross section. The vapor–liquid interface shown applies to a wetting fluid that has receded somewhat, with a relatively flat liquid film between the intrinsic menisci. This type of interfacial configuration is assumed to exist throughout the micro heat pipe, even in the condenser region. For a wetting fluid, vapor that condenses on the film flows or spreads into the intrinsic menisci creating a smooth liquid film. Ideal charging of the micro heat pipe will be referred to as a condition when the intrinsic menisci in the triangular channels meet in the condenser, forming an inscribed hemispherical meniscus (e.g., see Duncan, 1993, and Khrustalev and Faghri, 1993).

A classic thermodynamic derivation for the internal energy in the interface region, which is based on a mathematical dividing surface and surface excess quantities, can be found from Adamson (1990). A similar approach is taken in this paper with the addition of the disjoining pressure, which accounts for intermolecular forces due to the close proximity of a solid substrate in the thin film region. This approach therefore does not require any data specifying the apparent contact angle. Other assumptions in the model include:

- (i) Thermodynamic equilibrium exists between the liquid phase, the interface region, and the vapor region.
- (ii) Surface tension is not affected by interfacial curvature.

Under these assumptions, the Gibbs–Duhem equation for the liquid phase near the interface region is

$$d\mu_l = -\bar{S}_l dT + \bar{V}_l dP_l \quad (1)$$

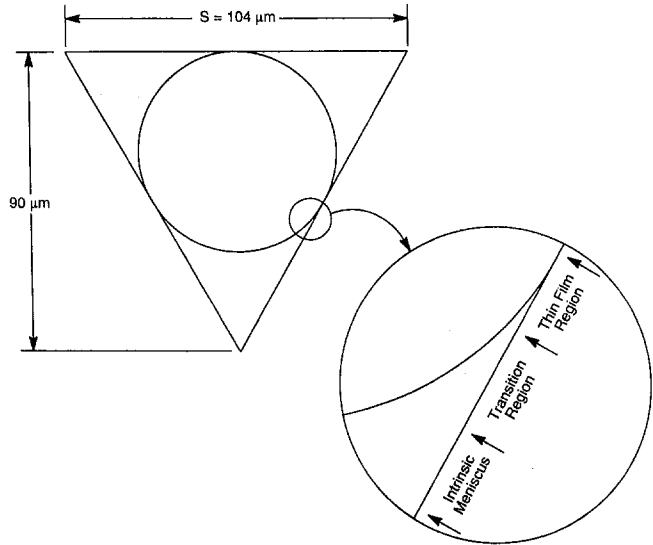


Fig. 1 Equilateral triangular micro heat pipe

where the subscript  $l$  refers to properties of the liquid phase and the quantities with an overbar represent specific molar quantities. A similar expression can be written for the vapor phase,

$$d\mu_v = -\bar{S}_v dT + \bar{V}_v dP_v \quad (2)$$

where the subscript  $v$  signifies properties of the vapor. Note that the pressure in the liquid phase differs from that in the vapor phase due to the curved interface (capillary pressure) and the disjoining pressure. The augmented Young–Laplace equation, or normal-stress condition at the interface, that accounts for these forces is

$$P_v = P_l + 2\sigma K + \Pi \quad (3)$$

In this expression,  $\Pi$  is the disjoining pressure and  $K$  is the mean curvature of the interface. The mean curvature is defined mathematically in the nomenclature and is equal to one-half the sum of the principle curvatures (e.g., see Brand, 1948). A formal derivation of the classical Young–Laplace equation can be found

### Nomenclature

$A$  = Hamaker constant  
 $C_i$  = coefficients found in Eq. (18)  
 $G$  = interfacial mass flux  
 $\bar{h}_{vl}$  = latent heat of vaporization per unit mole  
 $h_{vl}$  = latent heat of vaporization per unit mass  
 $K$  = mean curvature ( $2K = -\nabla \cdot \mathbf{n}$ , where  $\mathbf{n}$  is the unit normal vector normal to the vapor–liquid interface pointing into the vapor phase)  
 $l_{\text{eff}}$  = effective heat-pipe length  
 $\dot{m}$  = liquid mass flow between the interface and tube wall (mass flow rate)  
 $M$  = molecular weight  
 $P_l$  = pressure on the liquid side of the meniscus  
 $P_v$  = pressure on the vapor side of the meniscus  
 $q$  = heat transfer rate

$r$  = radial coordinate  
 $r_c$  = radius of curvature (capillary radius)  
 $R$  = ideal gas constant divided by the molecular weight  
 $s$  = characteristic length of a micro heat pipe with an equilateral triangular cross-section  
 $\bar{S}_l$  = molar specific entropy in the liquid phase  
 $\bar{S}_v$  = molar specific entropy in the vapor phase  
 $T$  = temperature  
 $T_{\text{sat}}$  = saturation temperature  
 $\bar{V}_l$  = molar specific volume in the liquid phase  
 $\bar{V}_v$  = molar specific volume in the vapor phase  
 $x$  = axial coordinate  
 $\delta$  = liquid film thickness

$\gamma$  = change in surface tension with temperature =  $(d\sigma/dT)_0$   
 $\mu$  = chemical potential  
 $\nu$  = kinematic viscosity  
 $\Pi$  = disjoining pressure  
 $\rho$  = mass density  
 $\sigma$  = surface tension

### Subscripts

avg = average  
 $c$  = capillary  
 $e$  = evaporator  
 $\text{eff}$  = effective  
 $h$  = hydraulic  
 $i$  = interfacial region  
 $l$  = liquid phase  
 $\text{max}$  = maximum  
 $\text{sat}$  = saturation  
 $v$  = vapor phase  
 $0$  = reference conditions in the condenser

from Adamson (1990). Taking the total derivative of this expression and noting  $d\sigma = \gamma dT$  produces

$$dP_v = dP_l + 2K\gamma dT + 2\sigma dK + d\Pi. \quad (4)$$

Substituting Eq. (4) into Eq. (2) generates a vapor-phase differential chemical potential of

$$d\mu_v = -\bar{S}_v dT + \bar{V}_v [dP_l + 2K\gamma dT + 2\sigma dK + d\Pi]. \quad (5)$$

At equilibrium  $d\mu_l = d\mu_v$ ; equating Eqs. (1) and (5) yields

$$-\bar{S}_l dT + \bar{V}_l dP_l = -\bar{S}_v dT + \bar{V}_v dP_l + 2\bar{V}_v K\gamma dT + 2\sigma \bar{V}_v dK + \bar{V}_v d\Pi. \quad (6)$$

Rearranging this expression assuming that  $\bar{V}_v - \bar{V}_l \approx MRT/P_v$  and noting that  $\bar{S}_v - \bar{S}_l = \bar{h}_{vl}/T$  gives

$$dP_l = \frac{h_{vl} P_v}{RT^2} dT - 2K\gamma dT - 2\sigma dK - d\Pi. \quad (7)$$

This expression for the change in liquid pressure will be used later to explain the thermodynamic behavior of the intrinsic meniscus in micro heat pipes.

A similar procedure yields an expression for the vapor pressure near the interface,

$$\frac{dP_v}{P_v} = \frac{\bar{h}_{vl}}{MR} \frac{dT}{T^2} - \frac{2\sigma \bar{V}_l}{MRT} dK - \frac{2K\bar{V}_l \gamma}{MR} \frac{dT}{T} - \frac{\bar{V}_l}{MRT} d\Pi. \quad (8)$$

Integrating Eq. (8) produces

$$\ln \frac{P_v}{P_{sat}} = \frac{h_{vl}}{R} \left( \frac{1}{T_{sat}} - \frac{1}{T} \right) - \frac{2\sigma \bar{V}_l}{MRT} (K - K_0) - \frac{2K\bar{V}_l \gamma}{MR} \ln \frac{T}{T_{sat}} - \frac{\bar{V}_l}{MRT} (\Pi - \Pi_0), \quad (9)$$

where  $K_0$  and  $\Pi_0$  refer to the mean curvature and disjoining pressure at a reference saturation temperature and pressure. Equation (9) is a general expression that can be used to explain a number of different physical phenomena. This equation reduces to the well-known Clausius-Claperton equation under the following conditions: The Marangoni term is negligible (third term on the right hand side), the interface is flat ( $K = K_0 = 0$ ), and the interface is far away from the substrate ( $\Pi = \Pi_0 = 0$ ). Secondly, when the interface is far away from the solid substrate under saturated conditions,

$$\ln \frac{P_v}{P_{sat}} = -\frac{2\sigma \bar{V}_l}{MRT} K. \quad (10)$$

This expression relates the interfacial vapor pressure to the mean curvature of the interface and is the general form for the Kelvin equation assuming a flat interface as a reference value ( $K_0 = 0$ ). The more common form of the Kelvin equation results when Eq. (10) is applied to spherical droplets ( $K = -1/r_c$ ). Finally, for thin flat films under isothermal conditions Eq. (9) reduces to

$$\Pi = \Pi_0 - \frac{MRT}{\bar{V}_l} \ln \frac{P_v}{P_{sat}}. \quad (11)$$

This is an expression for the disjoining pressure where  $\Pi_0$  is the disjoining pressure for a flat interface at the saturation temperature. A similar relationship for adsorption has been derived by Adamson (1990) from the Gibbs equation. Equation (11) can be used to explain how the interfacial vapor pressure changes with the disjoining pressure.

For a wetting film the disjoining pressure is positive. If the film thickness is less than the film thickness at the saturation pressure ( $\Pi > \Pi_0$ ), there is a net attractive force that causes the interfacial vapor pressure to be less than its saturation value. This can induce adsorption or condensation that will continue until the film reaches its saturation thickness. However, if the condensate

flows or spreads into the adjacent intrinsic menisci, the film can remain at a thickness less than its saturation value. Thus, for thin films, condensation may be enhanced by the presence of a solid substrate. It should be noted that in most cases the film thickness will probably be large enough that the disjoining pressure can be neglected ( $>1000 \text{ \AA}$ ). In this case, a lower interfacial vapor pressure due to interfacial curvature can enhance condensation because the meniscus is curved toward the wedge apex ( $K$  is positive). This effect can be explained by the Kelvin equation described earlier [Eq. (10)].

The relationship above shows that evaporation is suppressed by a positive disjoining pressure (attractive intermolecular potential) unless the film is thicker than its saturation value. For thicker wetting films, the molecules are less tightly bound to the surface resulting in a reduced disjoining pressure ( $\Pi < \Pi_0$ ). Films thicker than their saturation value therefore tend to evaporate. However, if a fluid becomes partially or fully nonwetting at the saturation temperature of interest, the disjoining pressure decreases below its reference value or becomes negative forcing the interfacial vapor pressure to increase. Consequently, partially or nonwetting liquids can enhance evaporation in thin films.

It is important to note that the effects of the various forces discussed to this point have been for very restricted conditions (i.e., constant interfacial superheat). Under more practical circumstances, most of the conditions discussed contribute to the overall behavior of the extended menisci in micro heat pipes. For small pressure differences and superheats, a Taylor series expansion can be used to approximate the nonlinear terms in Eq. (9). Using the ideal gas law and rearranging yields

$$P_v - P_{sat} = \frac{\rho_v}{\rho_l} (\Pi_0 - \Pi) + \left( \frac{\rho_v \bar{h}_{vl}}{T_{sat}} - \frac{2K\gamma \rho_v}{\rho_l} \right) (T - T_{sat}) - \frac{2\sigma \rho_v}{\rho_l} (K - K_0). \quad (12)$$

The Kucherov-Rikenglaz equation (1960) is an expression commonly used to evaluate the vapor mass flux at the interface. A clear concise derivation of this expression is given by Carey (1992). For pure fluids, small vapor pressure differences and superheats (i.e., those in this paper), the Kucherov-Rikenglaz equation can be linearized yielding

$$G = \left( \frac{2C}{2-C} \right) \left( \frac{1}{2\pi RT_{sat}} \right)^{1/2} \times \left[ (P_v - P_{sat}) - \frac{P_{sat}}{2T_{sat}} (T - T_{sat}) \right]. \quad (13)$$

This expression gives the transport of vapor to or from a vapor-liquid interface under slightly subcooled or superheated conditions. For a pure fluid the accommodation coefficient ( $C$ ) found in Eq. (13) can be set equal to unity (Mills, 1965). Note that the mass flux given by expression (13) is positive for evaporation. During evaporation, Eq. (13) shows that the interfacial mass flux increases as the pressure difference increases and decreases as the interfacial superheat increases. The mechanisms responsible for this behavior require some explanation. It is obvious that the mass flux in the vapor phase should increase when the interface is superheated because of the increase in the interfacial vapor pressure. However, although the vapor pressure is higher, the more energetic molecules surrounding the interface allow less molecules to penetrate into the bulk vapor. Consequently, the temperature driving force is an impediment to mass transfer as reflected by Eq. (13). Because the saturation pressure and temperature at the interface are related, the net effect of these opposing driving forces is a positive evaporation heat flux. Similar although opposite arguments apply to condensation. The relationship between the vapor-pressure driving force and the interfacial superheat, and other driving forces as well, is given by Eq. (12). Combining Eqs. (12) and (13) generates an expression



reflecting the influence of the various forces on the interfacial mass flux,

$$G = \frac{\rho_v}{\rho_l} \left( \frac{2C}{2-C} \right) \left( \frac{1}{2\pi RT_{\text{sat}}} \right)^{1/2} \left[ \Pi_0 - \Pi - 2\sigma(K - K_0) + \left( \frac{\rho_l h_{vl}}{T_{\text{sat}}} - 2K\gamma - \frac{\rho_l R}{2} \right) (T - T_{\text{sat}}) \right]. \quad (14)$$

This expression is equivalent, although less restrictive, to that derived by Carey (1992) and is well suited to qualitative discussion assuming reference conditions apply to a flat saturated film that is thick enough to neglect the disjoining pressure. Note that the coefficient multiplying the interfacial superheat is always positive.

Under subcooled conditions, condensation occurs, causing the film to become thicker; thus, the disjoining pressure remains negligible. Because the mass flux is negative, a meniscus with a positive mean curvature (curvature toward the wedge apex in a micro heat pipe channel) tends to enhance condensation. The subcooling in a condensate meniscus tends to increase as the meniscus gets closer to the wall, although the mean curvature decreases. Eventually, the mean curvature goes to zero and the meniscus forms a thick flat film, which lies between adjacent menisci in the condenser section of the micro heat pipe.

Under superheated conditions, the mass flux is positive and a positive mean curvature has a deleterious effect on evaporation. This effect is constant in the intrinsic meniscus but falls off sharply to zero at the interline. As the intrinsic meniscus gets closer to the wall the superheat increases, causing the evaporative heat flux to increase. Eventually, the interface gets close enough to the wall that the attractive dispersion forces cause the disjoining pressure to increase. This also has a deleterious effect on evaporation because the surface molecules are held more tightly to the interface. Although the superheat continues to increase as the meniscus get closer to the interline, the disjoining pressure eventually becomes large enough to overcome the superheat driving force and cause the evaporative heat flux to pass through a maximum point. Beyond this maximum, the evaporative heat flux decreases until the superheat term in Eq. (14) is equal to the disjoining pressure. This creates a nonevaporating superheated thin film that separates adjacent menisci in the evaporator section of the micro heat pipe. Note that the maximum point in the evaporative heat flux near the interline has been reported by a number of investigators for a variety of small capillary structures (Wayner and Croccio, 1971; Stephan and Busse, 1992; Swanson and Herdt, 1992).

**Intrinsic Meniscus Region.** Equation (7) can be used to formulate relationships for the intrinsic meniscus or macroscopic interface in micro heat pipes where the disjoining pressure effects can be neglected. Comparing Eq. (7) with a rearranged form of Eq. (4) and integrating produces the well-known Clausius–Clapeyron equation for the local vapor pressure at the interface. The axial temperature difference between the bulk vapor in the evaporator and the condenser is therefore caused by the thermodynamic pressure drop, which can be approximated by the vapor-phase frictional pressure drop. This approximation assumes that the vapor–liquid interface is nearly stationary relative to the vapor and momentum losses/recovery in the evaporator/condenser are small. The frictional pressure drop can be determined by an expression such as the Darcy–Weisbach equation or an expression specifically describing the pressure loss in micro channels. Because the mean curvature in the intrinsic meniscus is constant at any axial position,  $2K = 1/r_c$ . Substituting the Clausius–Clapeyron equation into Eq. (7) and integrating between the condenser and the evaporator regions of the pipe yields

$$\frac{\sigma}{r_{c,e}} = \frac{\sigma}{r_{c,0}} + \Delta P_l + \Delta P_v \left( 1 - \frac{\gamma T_0}{r_{c,e} \rho_l h_{vl}} \right). \quad (15)$$

The reference state is defined in the condenser where  $r_c = r_{c,0}$  and  $P_{v,0} = P_{l,0} + 1/r_{c,0}$ . Note that  $1/r_{c,0} = 2/r_{\text{sphere}}$ , where  $r_{\text{sphere}}$  is the radius of curvature of the inscribed hemispherical meniscus described earlier. The linearized Clausius–Clapeyron equation ( $\Delta T/T_{c,0} = \text{small}$ ) has also been used to approximate the temperature driving force for the Marangoni term in Eq. (15). This expression simply shows that the capillary pressure in the evaporator has to be large enough to compensate for the capillary pressure in the condenser, the pressure drop in both the vapor and liquid phases, as well as the Marangoni effect in the axial direction (note that  $\gamma$  is negative). Aside from the Marangoni term, this expression is the same as that derived in the traditional manner using a force balance (e.g., see Chi, 1976; Dunn and Reay, 1982).

The steady-state heat transfer rate in a micro heat pipe can be determined after relationships for the frictional pressure losses in the liquid and vapor phases have been developed. The equilateral triangular geometry given by Fig. 1 has been used to develop these relationships. The viscous pressure drop for a liquid in triangular channels has been evaluated by Ayyaswami et al. (1974) and used by Xu and Carey (1990) for wetting fluids in small V-shaped grooves. The expression developed by Xu and Carey (1990) was applied in this paper with the following assumptions: (1) axial flow along the groove channel, (2) constant radius of curvature at any axial position, (3) linear functional dependence of the capillary radius in the axial direction, and (4) negligible vapor shearing at the vapor–liquid interface. Under these assumptions the liquid pressure drop becomes

$$\Delta P_l = 44.08 \frac{q_{\text{eff}} \nu_l}{h_{vl} r_{c,\text{avg}}^4}, \quad (16)$$

where the average capillary radius is

$$r_{c,\text{avg}} = \frac{r_{c,e} + r_{c,0}}{2},$$

and the effective heat-pipe length is

$$l_{\text{eff}} = \frac{l_e + l_c}{2} + l_a.$$

The mass transfer rate has been set equal to the heat transfer rate divided by the latent heat of vaporization in Eq. (16). The hydraulic diameter of the liquid has been used in Eq. (16) assuming the apparent contact angle of the liquid is equal to zero (wetting fluid).

The viscous pressure drop in the vapor phase has been evaluated in a similar manner using the Darcy–Weisbach expression assuming the flow is laminar,

$$\Delta P_v = \frac{32\nu_v l_{\text{eff}} q}{h_{vl} D_h^2 A_{c,v}}, \quad (17)$$

where the vapor-phase cross-sectional area is

$$A_{c,v} = 0.433s^2 - 2.055r_c^2,$$

and the vapor-phase hydraulic diameter is

$$D_h = \frac{4A_{c,v}}{3s - 4.109r_c}.$$

Combining Eqs. (15)–(17) and rearranging yields an expression for the heat transfer rate,

$$q = \frac{\sigma h_{vl}}{C_1 r_{c,e} - C_2} \left( 1 - \frac{r_{c,e}}{r_{c,0}} \right), \quad (18)$$

where the coefficients  $C_1$  and  $C_2$  are

$$C_1 = 44.08 \frac{l_{\text{eff}} \nu_l}{r_{c,\text{avg}}^4} + 2\nu_v l_{\text{eff}} \frac{(3s - 4.109r_{c,\text{avg}})^2}{(0.433s^2 - 2.055r_{c,\text{avg}}^2)^3},$$

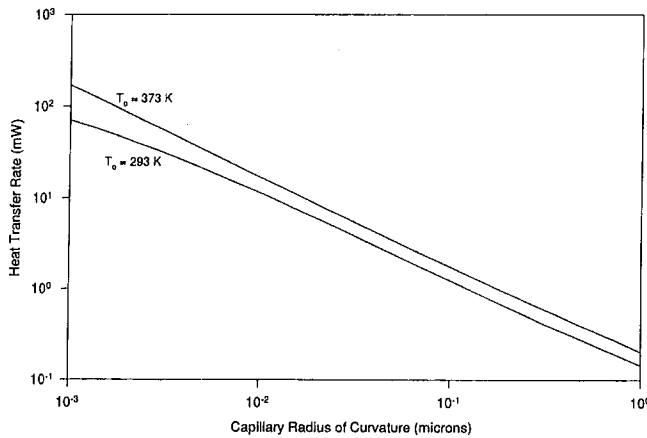


**Fig. 2 Effect of evaporator capillary radius and condenser temperature on the heat transfer rate for a single channel. Methanol is the working fluid.**

and

$$C_2 = \frac{2\nu_v l_{\text{eff}} \gamma T_0}{\rho_v h_{vl}} \frac{(3s - 4.109r_{c,\text{avg}})^2}{(0.433s^2 - 2.055r_{c,\text{avg}})^3}$$

Note that  $C_1$  and  $C_2$  are functions of the capillary radius in the evaporator and the characteristic length of the micro-heat-pipe triangular cross section ( $s = 104 \mu\text{m}$  in Fig. 1).

The heat transfer rate for a single capillary channel [Eq. (18)] has been plotted as a function of the evaporator capillary radius for different condenser temperatures in Fig. 2 using methanol as the working fluid.  $l_{\text{eff}}$  and  $r_{c,0}$  have been set equal to 2 cm and  $15 \mu\text{m}$ , respectively. As expected, the heat transfer rate increases as the evaporator capillary radius decreases because of the larger capillary driving force. The figure also shows that the heat transfer rate increases with increasing condenser temperature. This trend is caused primarily by a favorable change in thermophysical properties with temperature over the condenser temperature range plotted in the figure. For temperatures above approximately 373 K, the heat transfer rate actually begins to decrease as the condenser temperature increases because the reduction in surface tension with increasing temperature starts to dominate the trends given by Eq. (18). The figure also shows that the heat transfer rate is  $\sim 1.5 \text{ mW}$  at a capillary radius of  $0.1 \mu\text{m}$  where the dispersion forces become important. This represents the maximum heat transfer rate that can be determined using the intrinsic meniscus formulation. Below this threshold, the liquid pressure drop based solely on the intrinsic meniscus [Eq. (15)] no longer applies because the capillary pressure or mean curvature is not constant over most of the groove cross section. However, Fig. 2 can still be used to estimate the heat transfer rate if the capillary radius is defined as an integrated or effective capillary radius, which accounts for dispersion forces. Also note that although the liquid in this region is on the order of  $0.1 \mu\text{m}$  deep, extremely large heat fluxes can occur in this region as pointed out by Wayner and Croccio (1971), Stephan and Busse (1992), and Swanson and Herdt (1992). The large heat flux in this region, however, may not affect the heat transfer rate significantly because the large heat fluxes may be negated by the small evaporation surface area in this region.

At first glance, the results shown in Fig. 2 appear to disagree with those reported by Khurstalev and Faghri (1993). Khurstalev and Faghri found that for  $r_{c,e} < 0.1 D_{h,v}$ , the heat transfer rate no longer increased as the evaporator capillary radius decreased, but remained constant equal to a maximum value. We believe the difference in the two results depends on the pipe geometry (length) and the amount liquid charging, both of which determine the vapor volume and maximum attainable saturation density in the pipe. In other words, the assumption of thermodynamic

equilibrium at the interface does not allow the density at the interface to be greater than its saturation value. If insufficient vapor volume is available to allow the high saturation densities necessary for high evaporation rates (shorter pipes, high liquid charging), both the evaporation rate (or heat transfer rate) will reach a maximum for fairly large evaporator capillary radii. We believe this is what has occurred for the conditions studied by Khurstalev and Faghri. On the other hand, if enough vapor volume is available to support high saturation densities and evaporation rates at the interface (long pipes, low liquid charging), the evaporator capillary radius can become very small as proposed in this paper.

The maximum heat transfer rate can be determined using Eq. (18) by setting the evaporator capillary radius equal to zero. This produces

$$q_{\text{max}} = -5.15 \times 10^{-3} \frac{\sigma \rho_v h_{vl}^2 s^4}{\gamma T_0 \nu_v l_{\text{eff}}} \quad (19)$$

This expression defines a "thermocapillary" heat pipe limitation because it includes the ratio  $\gamma/\sigma$  traditionally found in the Marangoni number. For most working fluids, thermocapillary convection causes liquid on the vapor-liquid interface to flow from a hot region (evaporator) to a cold region (condenser). Thus, thermocapillary convection has an adverse effect on liquid flow from the condenser to the evaporator. The thermocapillary limitation represents the point at which surface flow from the evaporator to the condenser is large enough to prevent liquid from returning to the evaporator. This phenomenon is caused by the axial temperature gradient that exists between the evaporator and condenser.

The maximum heat transfer rate defined by the thermocapillary limitation is plotted in Fig. 3 as a function of the condenser temperature. Even though the condenser temperature appears explicitly in the denominator, the heat transfer rate increases with increasing condenser temperature primarily because of the change in the thermophysical properties with temperature. The figure shows that the heat transfer rates predicted by this limitation are generally very large and may not ever be attained even at the lower end of the operational temperature range for methanol.

**Thin Nonevaporating Superheated Films.** Equation (14) can be used to determine thickness of the nonevaporating thin superheated film found between the extended menisci. As stated earlier, this condition occurs in the evaporator section of the micro heat pipe. When the mass flux is equal to zero, Eq. (14) can be rearranged to give a general expression for the disjoining pressure as a function of the disjoining pressure at saturation, the interfacial vapor pressure and temperature, and the mean interfacial curvature. The film thickness, which is related to the disjoining pressure, is fundamentally dependent on the electromag-

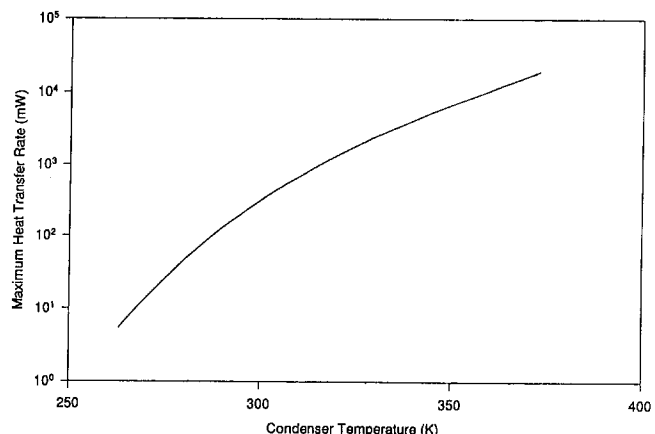


**Fig. 3 "Thermocapillary" heat-pipe limitation for methanol**

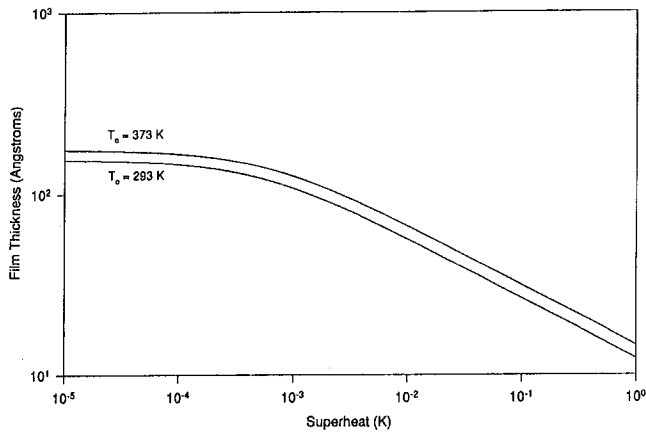


Fig. 4 Flat thin film thickness between adjacent menisci in the evaporation region

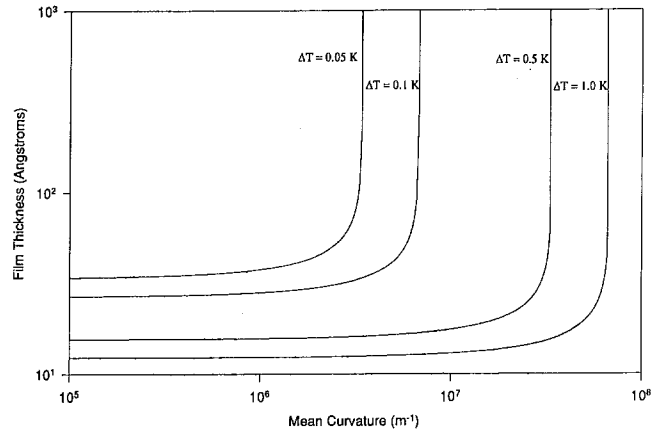


Fig. 5 Local film thickness as a function of the mean curvature for different values of the superheat ( $T_0 = 293$  K)

netic interactions between the vapor, liquid, and solid (e.g., see Ivanov, 1988; Israelachvili, 1985). For demonstrative purposes, a potential interaction reflecting only the nonretarded van der Waals forces will be assumed. The integrated form of this potential is related to the disjoining pressure by  $\Pi = -A/6\pi\delta^3$ , where  $A$  is the Hamaker constant (e.g., see Israelachvili, 1985). Note that this expression for the disjoining pressure is restrictive and applies to thin films in the range of  $10 \text{ \AA} < \delta < 300 \text{ \AA}$ . Using this form of the disjoining pressure and solving for the film thickness gives

$$\delta = \left[ \frac{\frac{-A}{6\pi}}{\Pi_0 + \left( \frac{\rho_l h_{vl}}{T_{sat}} - 2K\gamma - \frac{\rho_l R}{2} \right) \times (T_w - T_{sat}) - 2\sigma(K - K_0)} \right]^{1/3} \quad (20)$$

This is an expression for the film thickness as a function of the superheat, mean curvature, and the disjoining pressure at the saturation temperature. The interface temperature has been set equal to the wall temperature because very little heat is conducted through the film to a nonevaporating interface, making the interface temperature very nearly equal to the wall temperature. Note that the Hamaker constant,  $A$ , is negative for a wetting liquid. Equation (20) is a more general form of an expression derived earlier by Wayner et al. (1976) for superheated nonevaporating thin films.

Figure 4 shows the film thickness for the flat methanol film between intrinsic menisci when  $\Pi_0$  is set equal to  $2/r_{sphere}$ , which is the capillary pressure throughout the pipe under isothermal conditions ( $q = 0$ ). In this case, the reference mean curvature ( $K_0$ ) was set equal to zero characteristic of the flat interface between adjacent menisci under isothermal conditions. The Hamaker constant for methanol,  $-1.07 \times 10^{-19}$  J, was determined using methods described by Israelachvili (1992). Under these conditions, Eq. (20) reduces to a form very similar to that given by Wayner et al. (1976). The figure shows that the film thickness is asymptotic to its isothermal value at superheats less than  $10^{-4}$  K. For superheats greater than  $2 \times 10^{-3}$  K, the film thickness tends to decrease linearly as the superheat increases. It is interesting to note that to sustain superheats on the order of 0.1 K, a flat film has to be extremely thin (approximately 20 Å).

As for the nonevaporating thin film between adjacent menisci, dryout in micro heat pipes represents a situation where no evaporation occurs at the vapor-liquid interface. When dryout occurs, no liquid flows into the dry portion of the evaporator and Eq. (20) can be used to describe what is likely a nonevaporating thin film in this region. In the previous section, Eq. (18) showed that

the heat transfer rate for the intrinsic meniscus increases as the capillary radius decreases (or mean curvature increases) in micro heat pipes. This expression breaks down for capillary radii on the order of  $0.1 \mu\text{m}$  because disjoining pressure effects become important and the entire meniscus begins to resemble a thin film. As the meniscus recedes farther into the wedge channel in the evaporator the curvature and disjoining pressure become large enough to compensate for the superheat and force evaporation at the vapor-liquid interface to cease. When the entire meniscus becomes a nonevaporating thin film, dryout has occurred in the evaporator.

Figure 5 gives the film thickness as a function of the mean curvature for different values of the superheat when  $\Pi_0$  is set equal to its isothermal value described earlier. The condenser temperature has been set equal to 293 K. For the smaller values of the mean curvature ( $< 10^6 \text{ m}^{-1}$ ), the film thickness is asymptotic to values corresponding to those for a flat film shown in Fig. 4. The figure also shows that superheats greater than  $0.1$  K are required to sustain films with mean curvatures larger than  $7 \times 10^6 \text{ m}^{-1}$ . Furthermore, in a micro heat pipe, the mean curvature is limited to values of the superheat that produce a finite film thickness. For each value of the superheat, Fig. 5 indicates that the mean curvature is asymptotic to a maximum value when the film thickness gets large. The value of  $K_{max}$  for each superheat can be determined by setting the denominator in Eq. (20) equal to zero. The locus of maxima for the mean curvature are plotted in Fig. 6 as a function of the superheat. At low values of the superheat, the maximum mean curvature is asymptotic to a constant equal to the mean curvature in the condenser under iso-

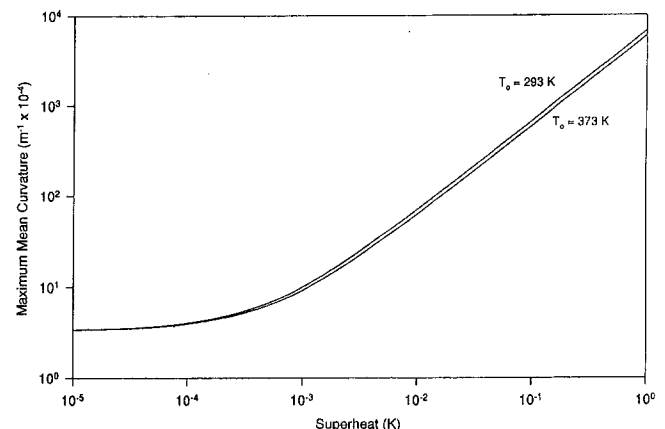


Fig. 6 Locus of maxima in the mean curvature as a function of superheat

thermal conditions. For large values of the superheat, the maximum curvature tends to increase linearly as the superheat increases. Because this curve represents the largest attainable mean curvature for a given superheat, it can be used to estimate the dryout heat transfer rate in micro heat pipes. As stated earlier, the mean curvature can be written in terms of an effective capillary radius, which can then be used in Eq. (18) to determine the dryout heat transfer rate. It is important to note that because the film thickness and mean curvature are actually coupled, the differential form of the mean curvature ( $2K = -\nabla \cdot n$ ) should be used to determine the local interface morphology under dryout conditions. This, however, is beyond the scope of this paper and currently under investigation.

## Conclusions

A thermodynamic model of the vapor–liquid interface in heat pipes has been developed to define the boundary conditions necessary for coupling the transport phenomena in the vapor and liquid phases. The model, which helps provide additional insight into the behavior of the extended meniscus in capillary structures, includes changes in local interface curvature, Marangoni surface effects, and disjoining pressure.

When the vapor–liquid interface is treated as an intrinsic meniscus (no disjoining pressure effects), the results show that the heat transfer rate is strongly dependent on the magnitude of the evaporator capillary radius. This formulation breaks down when the evaporator capillary radius is less than  $0.1 \mu\text{m}$  where the dispersion forces are the same order of magnitude as the capillary forces. Nevertheless, allowing the evaporator capillary radius to go its limiting value of zero generates a so-called “thermocapillary” heat-pipe limitation. The heat transfer rates predicted by this limitation are generally very large and therefore are not likely to be attained in most practical applications of micro heat pipes.

Including dispersion forces in the thermodynamic formulation of the vapor–liquid interface produces a relationship that applies to nonevaporating superheated films. These films connect adjacent menisci and cover the entire dry portion of extended meniscus when dryout occurs in the evaporator. The results show that under dryout conditions the mean curvature in the evaporator approaches a maximum value (minimum capillary radius), which increases as the wall superheat increases.

## Acknowledgment

The authors would like to acknowledge the support of the Air Force Astronautics Laboratory under UES/AFOSR Contract #F49620-88-C-0053/SB5881-0378, and the assistance of Ms. Rebecca Von Gonten, Mr. Jeong-Mann Ha, and Hongbin Ma. The authors also appreciate the insightful comments and recommendations made by the manuscript reviewers.

## References

- Adamson, A. W., 1990, *Physical Chemistry of Surfaces*, 5th ed., Wiley, Los Angeles, CA.
- Ayyaswamy, P. S., Catton, I., and Edwards, D. K., 1974, “Capillary Flow in Triangular Grooves,” *ASME Journal of Applied Mechanics*, Vol. 41, pp. 332–336.

- Babin, B. R., Peterson, G. P., and Wu, D., 1990, “Steady-State Modeling and Testing of a Micro Heat Pipe,” *ASME JOURNAL OF HEAT TRANSFER*, Vol. 112, pp. 595–601.
- Brand, L., 1948, *Vector and Tensor Analysis*, Wiley, New York.
- Carey, V. P., 1992, *Liquid–Vapor Phase Change Phenomena*, Hemisphere Publishing Corp., Washington, DC.
- Chi, S. W., 1976, *Heat Pipe Theory and Practice*, McGraw-Hill, New York.
- DasGupta, S., Schonberg, J. A., and Wayner, P. C., Jr., 1993, “Investigation of an Evaporating Extended Meniscus Based on the Augmented Young–LaPlace Equation,” *ASME JOURNAL OF HEAT TRANSFER*, Vol. 115, pp. 201–208.
- Duncan, A. B., 1993, “An Experimental and Analytical Evaluation of Etched Micro Heat Pipes,” Ph.D. Dissertation, Texas A&M University, College Station, TX.
- Dunn, P. D., and Reay, D. A., 1982, *Heat Pipes*, 3rd ed., Pergamon Press, New York.
- Israelachvili, J. N., 1985, *Intermolecular and Surface Forces*, Academic Press, London.
- Ivanov, I. B., 1988, *Thin Liquid Films: Fundamentals and Applications*, Marcel Dekker, Inc., New York.
- Khrustalev, D., and Faghri, A., 1993, “Thermal Analysis of a Micro Heat Pipe,” *ASME HTD-Vol. 236*, pp. 19–30; accepted for publication in the *ASME JOURNAL OF HEAT TRANSFER*.
- Kucherov, R. Y., and Rikenglaz, L. E., 1960, “The Problem of Measuring the Condensation Coefficient,” *Doklady Akad. Nauk SSSR*, Vol. 133, No. 5, pp. 1130–1131.
- Longtin, J. P., 1991, “Analysis and Testing of Etched Micro Heat Pipes,” M.S. Thesis, University of Cincinnati, Cincinnati, OH.
- Mallik, A. K., and Peterson, G. P., 1992, “On the Use of Micro Heat Pipes as an Integral Part of Semiconductor Devices,” *AMSE Journal of Electronic Packaging*, accepted for publication.
- Mills, A. F., 1965, “The Condensation of Steam at Low Pressure,” Technical Report on NSF GP-2520, Series No. 6, Issue No. 39, Space Sciences Laboratory, University of California, Berkeley.
- Peterson, G. P., Duncan, A. B., Ahmed, A. K., Mallik, A. K., and Weichold, M. H., 1991, “Experimental Investigation of Micro Heat Pipes in Silicon,” *ASME DSC-Vol. 32*, pp. 341–348.
- Peterson, G. P., Duncan, A. B., and Weichold, M. H., 1993, “Experimental Investigation of Micro Heat Pipes Fabricated in Silicon Wafers,” *ASME JOURNAL OF HEAT TRANSFER*, Vol. 115, pp. 751–756.
- Stephan, P. C., and Busse, C. A., 1992, “Analysis of the Heat Transfer Coefficient of Grooved Heat Pipe Evaporator Walls,” *Int. J. Heat Mass Transfer*, Vol. 35, No. 2, pp. 383–391.
- Sujanani, M., and Wayner, P. C., Jr., 1992, “Transport Processes and Interfacial Phenomena in an Evaporating Meniscus,” *Chem. Eng. Comm.*, Vol. 118, pp. 89–110.
- Swanson, L. W., and Herdt, G. C., 1992, “Model of the Evaporating Meniscus in a Capillary Tube,” *ASME JOURNAL OF HEAT TRANSFER*, Vol. 114, pp. 434–441.
- Truong, J. G., and Wayner, P. C., Jr., 1987, “Effects of Capillary and Van der Waals Dispersion Forces on the Equilibrium Profile of a Wetting Liquid: Theory and Experiment,” *J. Chem. Phys.*, Vol. 87, No. 7, pp. 4180–4188.
- Wayner, P. C., Jr., and Croccio, C. L., 1971, “Heat and Mass Transfer in the Vicinity of the Triple Interline of a Meniscus,” *AIChE J.*, Vol. 17, No. 3, pp. 569–574.
- Wayner, P. C., Jr., Kao, Y. K., and LaCroix, L. V., 1976, “The Interline Heat-Transfer Coefficient of an Evaporating Wetting Film,” *Int. J. Heat Mass Transfer*, Vol. 19, pp. 487–492.
- Wayner, P. C., Jr., 1982, “Adsorption and Capillary Condensation at the Contact Line in Change of Phase Heat Transfer,” *Int. J. Heat Mass Transfer*, Vol. 25, No. 5, pp. 707–713.
- Wayner, P. C., Jr., 1991, “The Effects of Interfacial Mass Transport on Flow in Thin Liquid Films,” *Colloids and Surfaces*, Vol. 52, pp. 71–84.
- Wu, D., and Peterson, G. P., 1991, “Investigation of the Transient Characteristics of a Micro Heat Pipe,” *AIAA Journal of Thermophysics and Heat Transfer*, Vol. 5, No. 2, pp. 129–134.
- Wu, D., Peterson, G. P., and Chang, W. S., 1991, “Transient Experimental Investigation of Micro Heat Pipes,” *AIAA J. of Thermophysics and Heat Transfer*, Vol. 5, No. 4, pp. 539–545.
- Xu, X., and Carey, V. P., 1990, “Film Evaporation From a Micro-grooved Surface—An Approximate Heat Transfer Model and Its Comparison With Experimental Data,” *AIAA J. of Thermophysics and Heat Transfer*, Vol. 4, No. 4, pp. 512–520.

# Two-Dimensional Rotating Heat Pipe Analysis

C. Harley

A. Faghri

Department of Mechanical and Materials Engineering,  
Wright State University,  
Dayton, OH 45435

*A detailed transient numerical simulation of rotating heat pipes is presented. This two-dimensional, axisymmetric formulation accounts for the thin liquid condensate film on the inner surface of the rotating pipe wall, the vapor flow in the vapor space, and the unsteady heat conduction in the pipe wall. The thin liquid film is coupled to the vapor velocity at the liquid-vapor interface, and the effects of the vapor pressure drop and the interfacial shear stress are included in the Nusselt-type condensation analysis.*

## Introduction

Rotating heat pipes use the centrifugal force generated by the motion of the pipe to pump the working fluid from the condenser to the evaporator instead of the capillary force in a conventional, stationary wicked heat pipe, or gravity in a wickless thermosyphon. The rotating heat pipe was first proposed by Gray (1969), who demonstrated that such a heat pipe is capable of transferring significantly more heat than a similar stationary heat pipe. With the addition of a slight internal taper, a component of the centrifugal force is used to pump the liquid working fluid to the evaporator, which results in significantly thinner condensate films and higher heat transfer coefficients.

The foundation for thin-film condensation analyses, developed by Nusselt (1916), concerns laminar filmwise condensation on flat plates and circular tubes under the influence of gravity. Nusselt's analysis neglected the shear stress at the liquid-vapor interface and assumed a linear temperature profile in the liquid film. The analysis was expanded by Sparrow and Hartnett (1961) to include centrifugal effects of vapor condensation on a rotating cone. Sparrow and Hartnett assumed a constant interfacial shear stress, and the analysis was only applicable in the constant film thickness region for cones with large cone angles. However, in a rotating heat pipe, the interfacial shear force is an unknown variable, which is dependent upon the counterflowing vapor.

Ballback (1969) extended the Nusselt condensation analysis for rotating heat pipes by assuming that the liquid film was very thin and had a slope much smaller than the cone angle. These assumptions, along with neglecting the vapor shear stress and the thermal resistance of the wall, allowed Ballback to find a closed-form expression for the total heat transfer from the condenser section of a rotating heat pipe.

This work was further developed by Daley (1970), who included the thermal resistance of the wall. Daley determined that the temperature drop across the wall results in a thinner liquid film and a higher heat transfer rate. However, neither Ballback nor Daley accounted for the effects of interfacial shear on the liquid film.

The problem associated with the interfacial shear stress was addressed by Daniels and Al-Jumaily (1975), who incorporated a variable shear formulation into the Nusselt analysis for rotating heat pipes. This formulation uses the shear stress correlations developed for axisymmetric flow in smooth pipes, which was recommended by Bergelin et al. (1949).

As in conventional stationary heat pipes, there is an axial vapor pressure drop across the rotating heat pipe. This pressure drop was accounted for by Marto (1976) by relating the vapor pressure drop to both momentum and interfacial shear. The effects of interfacial shear stress were included by using the conventional pipe flow friction factor analysis.

A more complete rotating heat pipe vapor flow analysis was performed by Faghri et al. (1993). A two-dimensional axisymmetric formulation was used to determine the influence of rotation rate on the vapor pressure drop and interfacial shear stresses. Faghri et al. found that conventional pressure drop and shear stress correlations do not apply in rotating heat pipes, since the vapor flow profiles are significantly different from those patterns seen in stationary heat pipes. However, heat transfer in the pipe wall or the counterflowing liquid film were not considered.

The present formulation accounts for the vapor pressure drop and the interfacial shear stress of the counterflowing vapor, which is coupled to the thin liquid film and pipe wall for the entire heat pipe. However, rather than using the existing correlations to determine the shear stress or vapor pressure drop, the actual values are determined from the complete transient two-dimensional vapor flow analysis. Furthermore, the effect of coupled two-dimensional heat conduction in the pipe wall is included by solving the entire heat pipe as a single-domain problem, instead of only modeling the condenser section.

## Mathematical Modeling

**Vapor and Wall.** In the present analysis, it is assumed that the effects of gravity are negligible in comparison to those of the centrifugal force. Therefore, the orientation of the rotating heat pipe with respect to the gravity vector is not considered. The coordinate system and labeling convention for this model are shown in Fig. 1.

The general three-dimensional governing equations are simplified through the axisymmetric assumption, in which all gradients with respect to  $\theta$  are neglected. Therefore, the differential conservation equations for two-dimensional, axisymmetric, transient, compressible flow in the vapor space of the rotating heat pipe with constant viscosity are as follows:

*Mass:*

$$\frac{\partial \rho}{\partial t} + \frac{1}{r} \frac{\partial}{\partial r} (\rho r v_r) + \frac{\partial}{\partial z} (\rho w_z) = 0 \quad (1)$$

*r-Momentum:*

$$\rho \left( \frac{\partial v_r}{\partial t} + v_r \frac{\partial v_r}{\partial r} - \frac{u_r^2}{r} + w_z \frac{\partial v_r}{\partial z} \right) = - \frac{\partial p}{\partial r} + \mu \left[ \frac{4}{3} \frac{\partial^2 v_r}{\partial r^2} + \frac{4}{3r} \frac{\partial v_r}{\partial r} - \frac{4}{3} \frac{v_r}{r^2} + \frac{1}{3} \frac{\partial^2 w_z}{\partial r \partial z} + \frac{\partial^2 v_r}{\partial z^2} \right] + \rho g_r \quad (2)$$

*$\theta$ -Momentum:*

$$\rho \left( \frac{\partial u_r}{\partial t} + v_r \frac{\partial u_r}{\partial r} + \frac{v_r u_r}{r} + w_z \frac{\partial u_r}{\partial z} \right) = \mu \left[ \frac{\partial^2 u_r}{\partial r^2} + \frac{1}{r} \frac{\partial u_r}{\partial r} - \frac{u_r}{r^2} + \frac{\partial^2 u_r}{\partial z^2} \right] \quad (3)$$

Contributed by the Heat Transfer Division for publication in the JOURNAL OF HEAT TRANSFER. Manuscript received by the Heat Transfer Division November 1993; revision received April 1994. Keywords: Conjugate Heat Transfer, Heat Pipes and Thermosyphons, Rotating Flows. Associate Technical Editor: R. Viskanta.

*z*-Momentum:

$$\rho \left( \frac{\partial w_v}{\partial t} + v_v \frac{\partial w_v}{\partial r} + w_v \frac{\partial w_v}{\partial z} \right) = - \frac{\partial p}{\partial z} + \mu \left[ \frac{\partial^2 w_v}{\partial r^2} + \frac{1}{r} \frac{\partial w_v}{\partial r} + \frac{1}{3r} \frac{\partial v_v}{\partial z} + \frac{1}{3} \frac{\partial^2 v_v}{\partial z \partial r} + \frac{4}{3} \frac{\partial^2 w_v}{\partial z^2} \right] + \rho g_z \quad (4)$$

Energy:

$$\rho c_p \left( \frac{\partial T}{\partial t} + v_v \frac{\partial T}{\partial r} + w_v \frac{\partial T}{\partial z} \right) = k \left[ \frac{1}{r} \frac{\partial}{\partial r} \left( r \frac{\partial T}{\partial r} \right) + \frac{\partial^2 T}{\partial z^2} \right] + \left( \frac{\partial p}{\partial t} + v_v \frac{\partial p}{\partial r} + w_v \frac{\partial p}{\partial z} \right) + \mu \Phi \quad (5)$$

The viscous dissipation term is given by

$$\Phi = 2 \left[ \left( \frac{\partial v_v}{\partial r} \right)^2 + \left( \frac{v_v}{r} \right)^2 + \left( \frac{\partial w_v}{\partial z} \right)^2 \right] + \left[ r \frac{\partial}{\partial r} \left( \frac{u_v}{r} \right) \right]^2 + \left( \frac{\partial u_v}{\partial z} \right)^2 + \left( \frac{\partial v_v}{\partial z} + \frac{\partial w_v}{\partial r} \right)^2 - \frac{2}{3} \left( \frac{1}{r} \frac{\partial}{\partial r} (r v_v) + \frac{\partial w_v}{\partial z} \right)^2 \quad (6)$$

The vapor pressure and temperature are related by the equation of state:

$$p = \rho R_g T_v \quad (7)$$

The following energy equation describes the transient two-dimensional heat transfer in the heat pipe wall:

$$\rho_w c_{pw} \frac{\partial T}{\partial t} = k_w \left[ \frac{1}{r} \frac{\partial}{\partial r} \left( r \frac{\partial T}{\partial r} \right) + \frac{\partial^2 T}{\partial z^2} \right] \quad (8)$$

where  $\rho_w$  and  $c_{pw}$  are the density and specific heat of the pipe wall material, respectively. It should be mentioned that the variations of vapor space radius  $R_v$  and the heat pipe wall thickness along the heat pipe have been neglected in the formulations given above due to the small taper angle  $\alpha$  and the relatively short heat pipe length.

### Liquid Film

The assumptions used in the general, Nusselt-type thin-film condensation analysis for rotating heat pipes are:

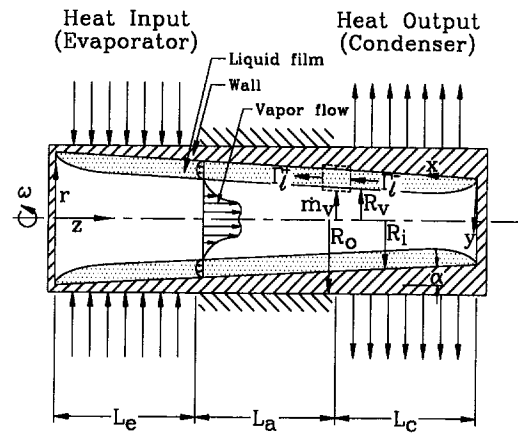


Fig. 1 Rotating heat pipe configuration and coordinate system

- 1 The vapor condensation is filmwise.
- 2 Inertial and convective effects in the liquid are negligible.
- 3 The liquid film thickness is much smaller than the vapor space radius.
- 4 The vapor density is much smaller than the liquid density.
- 5 The taper angle is small.
- 6 The circumferential velocity and temperature gradients are negligible.

Static force balances in the  $x$  and  $y$  directions give

$$\frac{\partial \tau_l}{\partial y} - \frac{\partial p_l}{\partial x} + \rho_l (\omega^2 r) \sin \alpha = 0 \quad (9)$$

$$- \frac{\partial p_l}{\partial y} - \rho_l (\omega^2 r) \cos \alpha = 0 \quad (10)$$

where  $\tau_l$  is the liquid shear at any radial position in the film,  $r$  is the distance from the heat pipe centerline to the control volume, and  $\alpha$  is the taper angle. The last terms in Eqs. (9) and (10) result from the rotation of the heat pipe. The component of the centrifugal force parallel to the wall provides the driving force for the condensate flow. The boundary conditions for these equations are

$$y = 0: \quad w_l = 0 \quad (11)$$

### Nomenclature

$c_p$  = specific heat at constant pressure, J/(kg-K)  
 $h$  = convective heat transfer coefficient, W/(m<sup>2</sup>-K)  
 $h_{fg}$  = latent heat of evaporation, J/kg  
 $k$  = thermal conductivity, W/(m-K)  
 $L$  = length, m  
 $\dot{m}$  = mass flow rate, kg/s  
 $\dot{m}'_v$  = evaporation or condensation mass flow rate per unit width, kg/(m-s)  
 $p$  = pressure, N/m<sup>2</sup>  
 $Q$  = heat rate, W  
 $q$  = heat flux, W/m<sup>2</sup>  
 $q_s$  = heat source, W/m<sup>2</sup>  
 $r$  = radial coordinate, m  
 $R_i$  = inner pipe radius, m  
 $R_o$  = outer pipe radius, m  
 $R_v$  = vapor space radius =  $R_i - \delta$ , m

$R_g$  = gas constant, J/(kg-K)  
 $t$  = time, s  
 $T$  = temperature, K  
 $u$  = tangential velocity component, m/s  
 $v$  = radial velocity component, m/s  
 $w$  = axial velocity, m/s  
 $x$  = rectangular coordinate, m  
 $y$  = rectangular coordinate, m  
 $z$  = axial coordinate, m  
 $\alpha$  = taper angle, deg  
 $\Gamma_l$  = liquid mass flow rate per unit width, kg/(m-s)  
 $\delta$  = film thickness, m  
 $\epsilon$  = emissivity  
 $\mu$  = dynamic viscosity, kg/(m-s)  
 $\rho$  = density, kg/m<sup>3</sup>  
 $\sigma$  = Stefan-Boltzmann constant, W/(m<sup>2</sup>-K<sup>4</sup>)

$\tau$  = shear stress, N/m<sup>2</sup>  
 $\Phi$  = viscous dissipation term  
 $\omega$  = rotation rate, rad/s

### Subscripts

$a$  = adiabatic  
 $c$  = condenser  
 $e$  = evaporator  
 $l$  = liquid  
 $o$  = outer wall  
 $sat$  = saturation  
 $t$  = total  
 $v$  = vapor  
 $w$  = wall  
 $0$  = reference  
 $\infty$  = ambient  
 $\delta$  = liquid-vapor interface

$$y = \delta: \quad \tau_l = \mu_l \frac{\partial w_l}{\partial y} = -\tau_{v,\delta} \cos \alpha \quad (12)$$

where  $\tau_{v,\delta}$  is the shear stress at the liquid–vapor interface due to the counterflowing vapor. Integrating the  $y$ -direction static force balance, Eq. (10), yields an expression for the local liquid pressure within the condensate film

$$p_l = p_v|_\delta + \rho_l(\omega^2 r)(\delta - y) \cos \alpha \quad (13)$$

where  $\delta$  is the condensate film thickness. Differentiating Eq. (13) with respect to  $x$  gives

$$\frac{\partial p_l}{\partial x} = \frac{\partial p_v}{\partial x} \Big|_\delta + \rho_l(\omega^2 r) \frac{d\delta}{dx} \cos \alpha \quad (14)$$

Substituting this pressure relation into the  $x$ -direction static force balance, Eq. (9), results in

$$\frac{\partial \tau_l}{\partial y} = \mu_l \frac{\partial^2 w_l}{\partial y^2} = \frac{\partial p_v}{\partial x} \Big|_\delta + \rho_l(\omega^2 r) \left( \cos \alpha \frac{d\delta}{dx} - \sin \alpha \right) \quad (15)$$

Integrating this relation twice with respect to  $y$ , subject to the boundary conditions (11) and (12), yields

$$w_l = \frac{1}{\mu_l} \frac{\partial p_v}{\partial x} \Big|_\delta \left( \frac{y^2}{2} - y\delta \right) + \frac{\rho_l}{\mu_l} (\omega^2 r) \left( \sin \alpha - \cos \alpha \frac{d\delta}{dx} \right) \left( y\delta - \frac{y^2}{2} \right) - \frac{y\tau_{v,\delta}}{\mu_l} \cos \alpha \quad (16)$$

Assuming that the slope of the condensate film is much less than the taper angle gives

$$\sin \alpha - \cos \alpha \frac{d\delta}{dx} \approx \sin \alpha \quad (17)$$

and the liquid velocity relation becomes

$$w_l = \frac{1}{\mu_l} \frac{\partial p_v}{\partial x} \Big|_\delta \left( \frac{y^2}{2} - y\delta \right) + \frac{\rho_l}{\mu_l} (\omega^2 r) \left( y\delta - \frac{y^2}{2} \right) \sin \alpha - \frac{y\tau_{v,\delta}}{\mu_l} \cos \alpha \quad (18)$$

The mass flow rate of the liquid condensate per unit width can be found as

$$\Gamma_l = \int_0^\delta \rho_l w_l dy \quad (19)$$

Substituting Eq. (18) for  $w_l$  into Eq. (19), the liquid mass flow rate per unit width can be expressed as

$$\Gamma_l = \left[ \rho_l(\omega^2 r) \sin \alpha + \frac{dp_v}{dz} \Big|_\delta \right] \frac{\rho_l \delta^3}{3\mu_l} + \frac{\rho_l \mu_v}{2\mu_l} \delta^2 \cos \alpha \frac{\partial w_v}{\partial r} \Big|_{r=R_c} \quad (20)$$

At any axial position in the falling liquid film, mass enters the fixed control volume, shown in Fig. 1, by condensation or evaporation of the vapor and by liquid flow from the upstream control volumes. Since the liquid flow is assumed to be quasi-steady and incompressible, all mass entering the control volume must leave in the falling liquid film. This relationship can be written as

$$\Gamma_l^- + \dot{m}'_v = \Gamma_l^+ \quad (21)$$

where  $\dot{m}'_v$  is the vapor condensation or evaporation mass flow rate per unit width over the length of the control volume. The superscript (–) indicates conditions at the entrance to the control

volume and (+) indicates conditions at the exit of the control volume.

Since the radial vapor velocity is assumed known from the solution of the momentum equation in the vapor space, the condensate mass flow rate per unit length,  $\dot{m}'_v$ , is also assumed known. Using this, and the definition of the liquid mass flow rate, Eq. (20), the conservation of mass relation (21) can be written as

$$\left[ \rho_l(\omega^2 r) \sin \alpha + \frac{dp_v}{dz} \Big|_\delta \right] \frac{\rho_l \delta^3}{3\mu_l} + \frac{\rho_l \mu_v}{2\mu_l} \delta^2 \cos \alpha \frac{\partial w_v}{\partial r} \Big|_{r=R_c} = \Gamma_l^- + \rho_\delta v_\delta dz \quad (22)$$

Equation (22) is a third-order polynomial in  $\delta$ . The solution of this polynomial is found by setting the film thickness at the condenser end cap to zero. As a result of the condensate film formulation in terms of the vapor velocity, the transient nature of the condensation problem is preserved.

In the liquid film, the general energy equation is

$$\rho_l c_{pl} \left( \frac{\partial T_l}{\partial t} + v_l \frac{\partial T_l}{\partial r} + w_l \frac{\partial T_l}{\partial z} \right) = \frac{1}{r} \frac{\partial}{\partial r} \left( r k_l \frac{\partial T_l}{\partial r} \right) + \frac{\partial}{\partial z} \left( k_l \frac{\partial T_l}{\partial z} \right) \quad (23)$$

However, under the assumptions used in the Nusselt-type condensation analysis and using a coordinate transformation into the  $x$ – $y$  system shown in Fig. 1, this general equation simplifies to

$$\frac{\partial^2 T_l}{\partial y^2} = 0 \quad (24)$$

The simplified energy equation yields a linear temperature profile across the liquid film. This implies that the latent heat of the condensing vapor is removed only by conduction through the liquid. While this formulation for the condensate liquid flow was derived for the condenser section, it also applies in the evaporator section of the rotating heat pipe because no assumptions were made on the sign of the  $\dot{m}'_v$ . Therefore, in the evaporator, mass is removed from the liquid film by evaporation, and Eq. (22) still applies. It should be noted that this falling film analysis is valid for only the ‘critical’ liquid fill ratio, which is defined as the amount of liquid that produces a liquid film with a zero film thickness at  $z = 0$  and  $L_r$ .

## Boundary Conditions

At the end caps of the rotating heat pipe, the condensate film thickness is zero, and the no-slip condition for velocity and the adiabatic condition for temperature are in effect. In addition, the application of the no-slip condition for tangential velocity results in a linear variation of velocity with respect to the radial position:

$$z = 0: \quad v_v = w_v = \frac{\partial T}{\partial z} = 0, \quad u_v = r\omega, \quad \delta = 0 \quad (25)$$

$$z = L_r: \quad \delta = v_v = w_v = \frac{\partial T}{\partial z} = 0, \quad u_v = r\omega \quad (26)$$

At the centerline ( $r = 0$ ), the radial and tangential vapor velocities and the radial gradients of the axial velocity and temperature are zero:

$$u_v = v_v = \frac{\partial w_v}{\partial r} = \frac{\partial T_v}{\partial r} = 0 \quad (27)$$

To ensure saturation conditions in the evaporator section (and in the adiabatic section since the exact transition point is determined iteratively), the Clausius–Clapeyron equation is used to determine the interfacial temperature as a function of pressure. The

radial vapor velocity at the interface is then found through the evaporation rate required to satisfy heat transfer requirements.

$$r = R_v(z \leq L_e + L_a):$$

$$T_{\text{sat}} = \left( \frac{1}{T_0} - \frac{R_g}{h_{fg}} \ln \frac{p_v}{p_0} \right)^{-1} \quad (28)$$

$$v_\delta = \frac{\left( k_l \frac{T_\delta - T_w}{\delta} - k_\delta \frac{\partial T_v}{\partial r} \right)}{(h_{fg} + c_p \delta T_{\text{sat}}) \rho_\delta} \quad (29)$$

$T_\delta$  is the temperature at the liquid–vapor interface,  $T_w$  is the temperature at the liquid–wall interface,  $k_\delta$  is the harmonic average of the vapor and liquid thermal conductivities at the liquid–vapor interface,  $\rho_\delta$  is the vapor density at the liquid–vapor interface, and  $T_0$  and  $p_0$  are the saturation reference temperature and pressure of the vapor, respectively. It is important to mention that this saturation relation does not fix a temperature or pressure at any point in the rotating heat pipe, but simply defines a relation between the known vapor pressure and the unknown saturation temperature at the liquid–vapor interface.

Due to the no-slip condition, the vapor velocity at the liquid–vapor interface must be the same as the condensate velocity at the interface, and the mechanical force balance at the liquid–vapor interface must be satisfied. Even though the shear stresses are continuous across the liquid–vapor interface, the velocity gradients are discontinuous since there is a viscosity difference between the vapor and liquid phases.

$$r = R_v:$$

$$u_v = R_v \omega, w_v = -w_l(\delta) \cos \alpha \quad (30)$$

$$\tau_l = -\tau_{v,\delta} \cos \alpha = -\mu_v \left. \frac{\partial w_v}{\partial r} \right|_{r=R_v} \cos \alpha \quad (31)$$

The interfacial liquid velocity is found from Eq. (18). The matching shear stress condition, Eq. (31), is implicitly satisfied in the formulation for the falling film thickness.

At the liquid–vapor interface in the active portions of the condenser section, vapor condenses and releases its latent heat energy. This process is simulated by applying a heat source at the interface grids in the condenser section (Cao and Faghri, 1990). The interface velocity can be obtained through a mass balance at the interface. To account for temperature continuity, the liquid temperature is set equal to the vapor temperature at the liquid–vapor interface. Therefore, at  $r = R_v$  ( $z > L_e + L_a$ )

$$q_s = (h_{fg} + c_{p\delta} T_\delta) \rho_\delta v_\delta \quad (32)$$

$$T_l = T_\delta |_{r=R_v} \quad (33)$$

where  $c_{p\delta}$  is the harmonic average of the vapor and liquid specific heats at the liquid–vapor interface. At the liquid–wall interface ( $r = R_w$ ), the heat flux into and out of the interface must be equal:

$$-k_w \frac{\partial T}{\partial r} = k_l \frac{T_\delta - T_w}{\delta} \quad (34)$$

which is automatically satisfied with the conjugate solution technique. At the outer pipe wall surface, the boundary conditions depend on both the axial position and the mechanism of heat transfer being studied (convection or radiation):

*Evaporator:*

$$k_w \left. \frac{\partial T}{\partial r} \right|_{r=R_o} = q_e \quad (35)$$

*Adiabatic:*

$$\left. \frac{\partial T}{\partial r} \right|_{r=R_o} = 0 \quad (36)$$

*Condenser:*

$$-k_w \left. \frac{\partial T}{\partial r} \right|_{r=R_o} = \begin{cases} h(T_o - T_\infty) & \text{convection} \\ \sigma \epsilon (T_o^4 - T_\infty^4) & \text{radiation} \end{cases} \quad (37)$$

## Initial Conditions

Since this model simulates the transient operation of a rotating heat pipe, the initial physical conditions are required for a solution of the problem. The temperature of the heat pipe is assumed to be uniform at the initial temperature and the heat pipe is assumed to be stationary before the simulation begins. The initial temperature is also assumed to be above the free molecular/continuum flow transition temperature based on the vapor space diameter (Cao and Faghri, 1993).

The liquid film is determined by the radial vapor velocity, so at the initial thermal equilibrium condition, there will be no liquid along the walls of the condenser and adiabatic sections. In reality, the working fluid will be pooled at the bottom of the evaporator section, but the model in this paper does not consider the possibility of a liquid pool under any operating condition.

## Numerical Procedure

The numerical procedure followed in this model is an application of SIMPLE as extended to compressible flow by Cao and Faghri (1990). The sequence of numerical steps taken is:

- 1 Input the initial temperature, total heat input, and condenser ambient conditions.
- 2 Initialize the pressure, temperature, and velocity fields.
- 3 For the first time step, find the film thickness with Eq. (22) assuming the vapor velocity and pressure drop are equal to zero.
- 4 Solve the vapor momentum equations to obtain  $v^*$ ,  $u^*$ , and  $w^*$  using the guessed pressure distribution.
- 5 Solve for the new pressure field and update the previous pressure field by employing the continuity Eq. (1). Notice that since the axisymmetric assumption is used, there is no contribution to the pressure correction from the tangential velocity field.
- 6 Calculate  $v$ ,  $u$ , and  $w$  in the vapor from their starred values using the velocity correction formulas.
- 7 With the known vapor velocity fields, determine the condensate film thickness using the quasi-steady Nusselt-type analysis, Eq. (22).
- 8 Solve the energy equation for the vapor with Eq. (5).
- 9 Solve the energy equation in the wall using Eq. (8).
- 10 Determine the new  $\rho$  from the equation of state.
- 11 Steps 4–10 are repeated until successive iterations differ by a small preassigned value (in this case, 0.1 percent of the maximum field value).

Grid independence of the two-dimensional rotating heat pipe code was verified by systematically varying the number of axial and radial grids. The comparison was performed with both a  $20 \times 40$  and  $30 \times 50$  (radial  $\times$  axial) mesh with less than 2 percent maximum difference between the solutions. The present grid ( $20 \times 40$ ) was chosen since it optimizes the accuracy of the result with minimal required computational time.

## Results and Discussion

The complete rotating heat pipe simulation was performed for the heat pipe experimentally studied by Daniels and Al-Jumaily (1975) for a heat input of  $Q = 800$  W and a rotational rate of  $\omega = 600$  rpm. The dimensions of this heat pipe are  $L_e = 0.325$  m,  $L_c = 0.05$  m,  $L_a = 0.123$  m,  $L_c = 0.152$  m,  $R_v = 0.02125$  m,  $R_o$



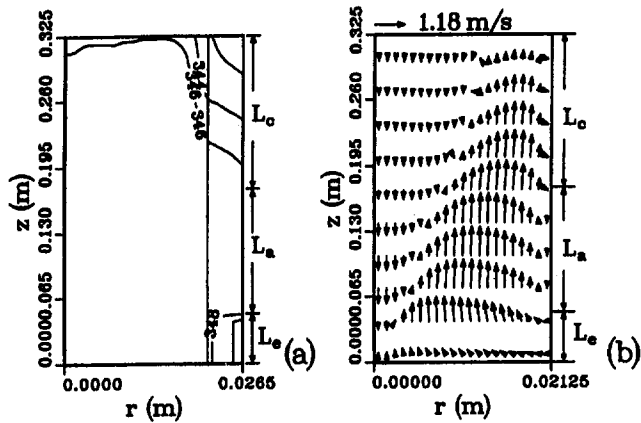


Fig. 2 Numerical simulation of the low-temperature rotating heat pipe: (a) temperature contours (K); (b) velocity vectors in the  $r$ - $z$  plane (m/s)

= 0.02650 m, and  $\alpha = 2$  deg. The heat pipe wall is copper and the working fluid is Freon-113. A true comparison with actual experimental data is impossible due to the assumption for the outer heat transfer coefficient. An approximate heat transfer coefficient ( $600 \text{ W}/(\text{m}^2\cdot\text{K})$ ) was determined from an examination of the wall temperature profile given by Daniels and Al-Jumaily. Since both the wall temperature and total heat input were given, the assumption of an ambient temperature is needed to obtain the external convective heat transfer coefficient.

The two-dimensional steady-state temperature contours and velocity vectors are shown in Fig. 2. In Fig. 2(a), the uniform nature of the temperature profiles can be clearly seen. The heat pipe vapor core is nearly isothermal, with temperature variations of less than  $6^\circ\text{C}$ . Due to rotation, the radial location of the maximum axial velocity has shifted toward the liquid-vapor interface, as shown in Fig. 2(b). This shift results in a region of higher vapor velocity near the liquid-vapor interface and a region of reverse flow near the centerline. These effects were also observed by Faghri et al. (1993) in their study of rotating heat pipe vapor flow dynamics.

The axial variation of the outer wall temperature is shown in Fig. 3(a). This assumed heat transfer coefficient resulted in the isothermal operation of the rotating heat pipe, which can be seen in Fig. 3(b), where the centerline vapor temperature is nearly constant along the length of the rotating heat pipe. Daniels and Al-Jumaily (1975) determined the vapor temperature with two pressure transducers located on the centerline at the two end caps, where the vapor was assumed to be saturated. As can be seen in Fig. 3(b), the assumption of a saturated vapor is valid since the vapor velocity is low enough to neglect compressibility effects.

The transient variation of the axial vapor velocity along the centerline is shown in Fig. 4(a), where the flow reversal can be clearly seen. The centerline vapor velocity is initially positive, and becomes negative as the blowing rate increases due to heat conduction in the pipe wall. Initially, the vapor velocity in the heat pipe is very small since the heat added at the outer wall surface of the evaporator has not yet been transferred through the pipe wall to the liquid working fluid by conduction. Additionally, since the heat pipe is stationary at  $t = 0.0$  s, there is a time lag between the application of the rotation and the observation of the rotational effects. In this case, the rotation is applied at  $t = 0.0$  s, and the inertial effects of the rotating pipe wall are neglected. However, the angular acceleration of the vapor is considered in the formulation, and it can be seen in Fig. 4(a) that the inertial effects of the rotating vapor cannot be neglected because the variation of the vapor flow is controlled by heat conduction in the pipe wall.

Since the heat pipe uses a low-temperature working fluid with a moderate external condenser heat transfer coefficient, the heat

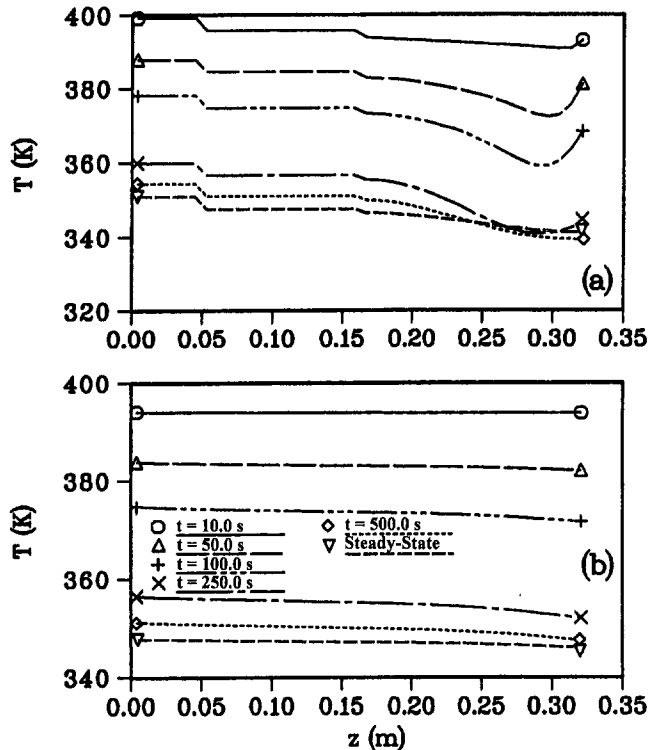


Fig. 3 Numerical simulation of the low-temperature rotating heat pipe: (a) transient outer pipe wall temperatures; (b) transient centerline vapor temperatures

pipe operates isothermally. Furthermore, the large molecular weight of Freon-113 and the large vapor density result in very small vapor velocities, the maximum value of which is  $1.19 \text{ m/s}$ , as shown in Fig. 2(b). These two factors suggest that the axial

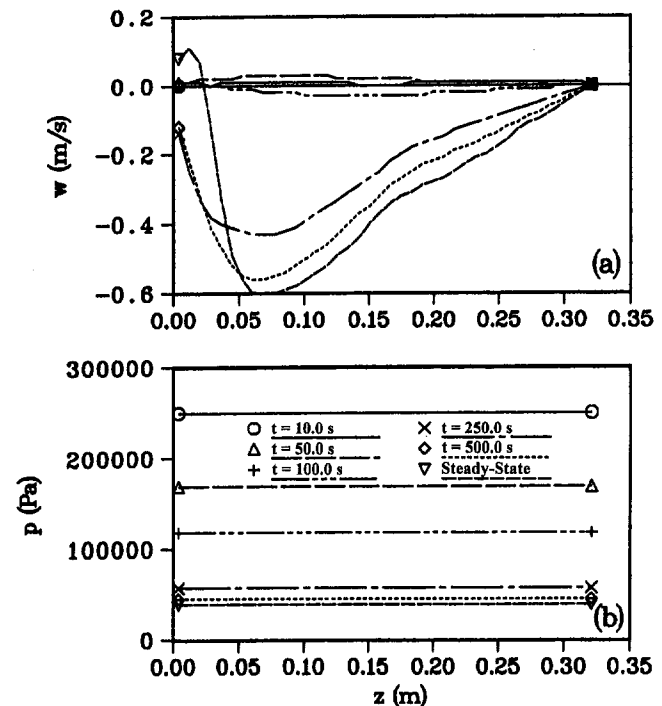


Fig. 4 Numerical simulation of the low-temperature rotating heat pipe: (a) transient axial centerline vapor velocities; (b) transient axial centerline vapor pressures

vapor pressure drop should be very small, which is indeed the case as shown in Fig. 4(b). In fact, the radial pressure variation is nearly negligible. This fact was seen by Faghri et al. at lower rotational speeds.

The vapor flow dynamics are shown in Figs. 5–7. In Fig. 5, the effect of rotation on the transient axial vapor velocity is shown. In the evaporator section, Fig. 5(a), the blowing caused by evaporation of the working fluid balances the centrifugal force. This results in a “wider” vapor flow core with a lower axial velocity. It should be noted that the axial velocity at the liquid–vapor interface is not zero due to the counter-flowing liquid film. This results in a slightly higher shear stress at the interface than that predicted by other studies, which neglect the contribution of the liquid film. In the adiabatic section, vapor flow reversal at the centerline can be observed, indicating a shift of the maximum vapor velocity toward the liquid–vapor interface. Since no phase change occurs in the adiabatic section, unless axial heat conduction in the pipe wall is significant, there is no blowing velocity at the wall to balance the centrifugal force, which results in a narrower annular vapor flow core than in the evaporator. However, in the condenser, the condensation of the working fluid aids the centrifugal force, resulting in a very narrow vapor flow core, as shown in Fig. 5(c).

The radial vapor velocity variation can be seen in Fig. 6. In the evaporator, Fig. 6(a), the effect of conduction in the pipe wall can be seen in the increase of the blowing velocity with

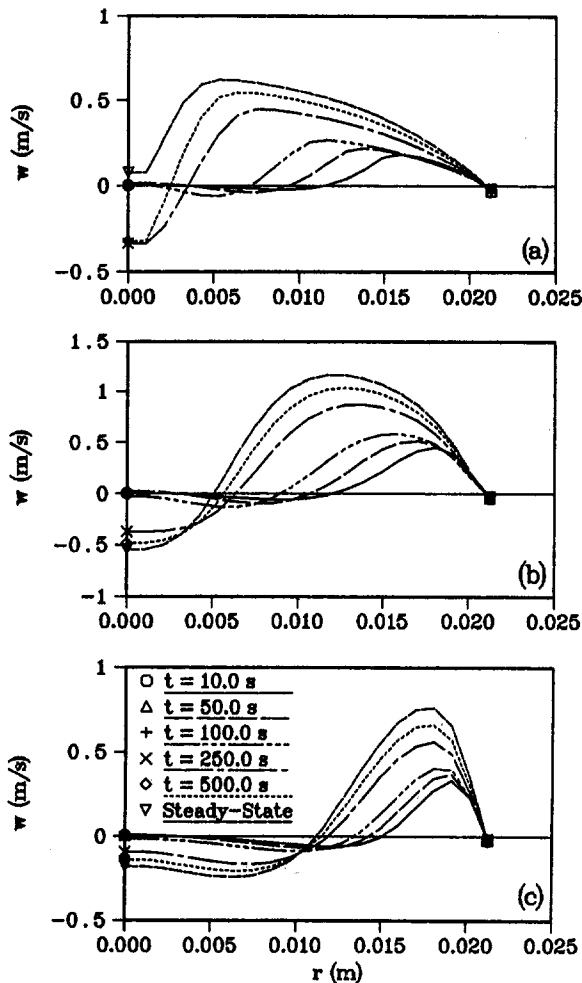


Fig. 5 Transient radial variation of the axial vapor velocity at: (a)  $z/L = 0.075$ ; (b)  $z/L = 0.35$ ; (c)  $z/L = 0.775$

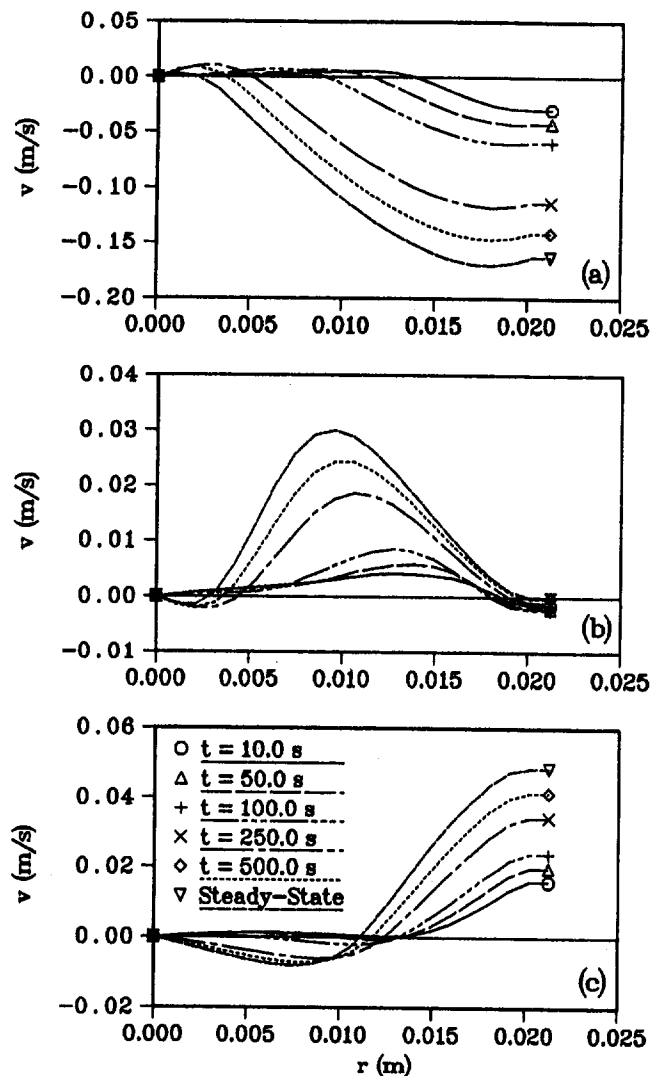


Fig. 6 Transient radial variation of the radial vapor velocity at: (a)  $z/L = 0.075$ ; (b)  $z/L = 0.35$ ; (c)  $z/L = 0.775$

time. It should also be noted that this simulation does not assume a constant blowing velocity at the liquid–vapor interface. The blowing velocity variation allows a more complete prediction to be made for the flow patterns in the evaporator and adiabatic sections. In the adiabatic section, Fig. 6(b), the effect of rotation can be seen as the radial vapor velocity is nonzero at the radial position of the maximum axial velocity. Furthermore, transient axial conduction in the pipe wall results in a slight blowing velocity during the early times in the adiabatic section.

Finally, the transient radial variations of the tangential vapor velocity are shown in Fig. 7. The most significant observation to be made from these figures is that a rotating heat pipe does not undergo solid-body rotation, i.e., the radial variation of the tangential vapor velocity is nonlinear. The solid-body rotation assumption has been made in several previous studies of rotating heat pipes and is clearly incorrect for this case. Additionally, it should be noted that the shape of the tangential velocity variations are not constant in the three heat pipe sections. In the evaporator, Fig. 7(a), the blowing velocity induced by the phase change of the working fluid dominates the flow patterns, resulting in a nearly constant tangential velocity region over a large portion of the vapor space cross section. In the adiabatic section, Fig. 7(b), the flow pat-

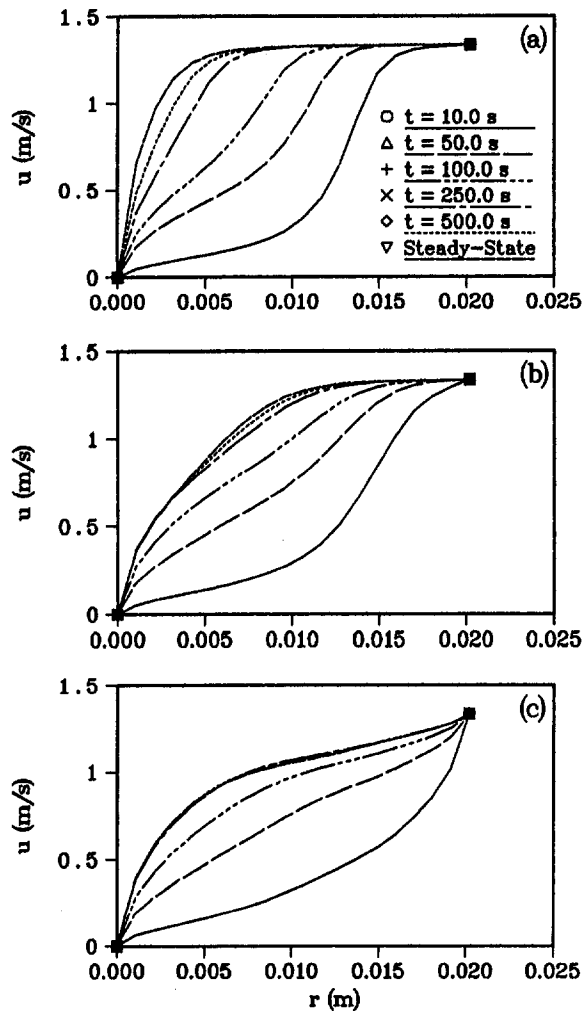


Fig. 7 Transient radial variation of the tangential vapor velocity at: (a)  $z/L = 0.075$ ; (b)  $z/L = 0.35$ ; (c)  $z/L = 0.775$

tern can be seen to have a more gradual radial variation. In the condenser section, Fig. 7(c), condensation of the working fluid increases the gradient of the tangential vapor velocity at

the liquid–vapor interface. It should be noted that the tangential vapor velocity is constant at the liquid–vapor interface due to the no-slip condition.

## Conclusions

A transient two-dimensional model of a rotating heat pipe has been presented. It was shown that the complex vapor flow patterns in a rotating heat pipe are strongly dependent upon the operating temperature and vapor density due to coupled boundary conditions. These flow patterns influence the vapor temperature and thus the performance of the heat pipe. The influence of interfacial vapor shear stress on the liquid film thickness and subsequent thermal resistance across the film was also discussed. Finally, the vapor flow dynamics showed that the vapor velocity field is significantly different from that of conventional heat pipes without rotation.

## References

- Ballback, L., 1969, "The Operation of a Rotating Wickless Heat Pipe," M.Sc. Thesis, U.S. Naval Postgraduate School (AD 701674), Monterey, CA.
- Bergelin, C., Kegel, B., Carpenter, F., and Gayley, C., 1949, *Proc. Heat Transfer Fluid Mech.*, IMechE.
- Cao, Y., and Faghri, A., 1990, "Transient Two-Dimensional Compressible Analysis for High-Temperature Heat Pipes With Pulsed Heat Input," *Numerical Heat Transfer, Part A*, Vol. 18, pp. 483–502.
- Cao, Y., and Faghri, A., 1993, "Simulation of the Early Startup Period of High-Temperature Heat Pipes From the Frozen State by the Rarefied Vapor Self-Diffusion Model," *ASME JOURNAL OF HEAT TRANSFER*, Vol. 115, pp. 239–246.
- Daley, T., 1970, "The Experimental Design and Operation of a Rotating Wickless Heat Pipe," M.Sc. Thesis, U.S. Naval Postgraduate School (AD 709923), Monterey, CA.
- Daniels, T., and Al-Jumaily, F., 1973, "Theoretical and Experimental Analysis of a Rotating Wickless Heat Pipes," *1st Int. Heat Pipe Conf.*, Stuttgart, Germany, Paper 3-2.
- Daniels, T., and Al-Jumaily, F., 1975, "Investigations of the Factors Affecting the Performance of a Rotating Heat Pipe," *Int. J. Heat Mass Transfer*, Vol. 18, pp. 961–973.
- Faghri, A., Gogineni, S., and Thomas, S., 1993, "Numerical Analysis of Vapor Flow in an Axially Rotating Heat Pipe," *Int. J. Heat Mass Transfer*, Vol. 36, No. 9, pp. 2293–2303.
- Gray, V. H., 1969, "The Rotating Heat Pipe—A Wickless, Hollow Shaft for Transferring High Heat Fluxes," *Proc. ASME/AICHE Heat Transfer Conf.*, Minneapolis, pp. 1–5; ASME Paper No. 69-HT-19.
- Marto, P., 1976, "Performance Characteristics of Rotating Wickless Heat Pipes," *2nd Int. Heat Pipe Conf.*, Bologna, Italy, pp. 281–291.
- Nussult, W., 1916, "Die Oberflaechenkondensation des Wasser-Dampfes," *Z. Ver. Dt. Ing.*, Vol. 60, pp. 541.
- Sparrow, E., and Hartnett, J., 1961, "Condensation on a Rotating Cone," *ASME JOURNAL OF HEAT TRANSFER*, Vol. 83C, No. 1, pp. 101–102.

# Analysis of Asymmetric Disk-Shaped and Flat-Plate Heat Pipes

K. Vafai  
Professor,  
Fellow ASME

N. Zhu

Department of Mechanical Engineering,  
The Ohio State University,  
Columbus, OH 43210

W. Wang

CETE, College of Education,  
The Ohio State University,  
Columbus, OH 43210

*An analytical investigation and conceptual design of a disk-shaped asymmetric heat pipe is presented in this work. Using the conservative formulations for the steady incompressible vapor and liquid flow for a disk-shaped heat pipe, an in-depth integral analysis is applied. Analytical results for the asymmetric vapor velocity profile, the vapor and liquid pressure distributions, and the vapor temperature distribution in the heat pipe are obtained and compared to those of rectangular flat-plate heat pipe. The analysis establishes the physics of the process and the intrawick interactions for the disk-shaped heat pipe. The effects of variations in the thicknesses of the vapor channel and the wick as well as the heat pipe on the performance of both disk-shaped and rectangular flat-plate heat pipes are analyzed in detail and compared with each other. The factors limiting heat pipe performance are discussed and the results show that the disk-shaped heat pipe, while utilizing a smaller surface area and being more adaptable to several application areas, significantly increases the heat transfer capability per unit surface area compared to rectangular flat-plate heat pipe.*

## Introduction

Heat pipes have been studied extensively in the last three decades. Almost all of the studies, both numerical and experimental, have focused on the operation and performance of cylindrical heat pipes or concentric annular heat pipes having a symmetric heat source and sink (Tien, 1975; Winter and Barsch, 1971; Faghri, 1986). While theoretical bases of these symmetric heat pipes have been well established for a wide variety of application areas, the application of heat pipes to asymmetric heat sources and the investigation of asymmetric heat pipes has been mostly neglected.

Ooijen and Hoogendoorn (1979) studied the vapor flow numerically in a flat-plate heat pipe with adiabatic top wall. Assuming the same injection and suction velocity, they solved the momentum equations for steady laminar incompressible two-dimensional vapor flow using a finite-difference method. In their work no change of phase was involved and the wick and the liquid flow were neglected. Vafai and Wang (1992) investigated the operation and overall performance of an asymmetric rectangular flat-plate heat pipe using a detailed integral analysis. The study was based on steady, incompressible vapor and liquid flow with pseudo-three-dimensional vapor flow field bifurcated on the  $x$ - $y$  plane due to the asymmetric nature of heat source and sinks. The analytical results for the shifted vapor velocity profiles on the  $x$ - $y$  plane, the overall axial pressure distributions in both vapor and liquid phases, and the axial vapor temperature distribution in the heat pipe were obtained. The good qualitative agreement between the results obtained and those based on the solution of the field equations for the conventional symmetric cases (Dunn and Reay, 1982; Ivanovskii et al., 1982) and asymmetric case (Ooijen and Hoogendoorn, 1979) demonstrated that the in-depth integral method provides accurate results on modeling the flow and heat transfer characteristics of asymmetric flat plate heat pipes.

Compared to the rectangular flat-plate heat pipe the disk-shaped heat pipe is more adaptable to several application areas due to its geometry and smaller surface area. Maezawa et al.

(1981) studied the heat transfer characteristics of a disk-shaped rotating, wickless heat pipe. They concentrated their study on the condensate layer and found the condensate velocity distribution by establishing the force balance within the condensate layer. Having no wick in the heat pipe and utilizing centrifugal forces for condensate return, they applied Nusselt's theory of laminar film condensation to the condensate layer and obtained the heat transfer rate by assuming a linear temperature distribution within the condensate film. In their study the disk-shaped heat pipe is considered to be a special type of rotating heat pipe with symmetric heat source and sink.

In the present work the vapor and liquid flow in a disk-shaped heat pipe heated asymmetrically, the overall heat pipe performance, as well as the conceptual design are investigated analytically. Using the conservative formulations for the steady incompressible vapor and liquid flow in the heat pipe, an in-depth integral analysis is employed to obtain the velocity profiles and overall pressure distributions for both vapor and liquid phases. The heat transfer capability for different sizes of the disk-shaped heat pipe is obtained based on the capillary limit and is compared with that of the rectangular flat-plate heat pipe proposed by Vafai and Wang (1992). The effects of variations in the thickness of the wick and the vapor channel as well as the overall thickness of the heat pipe on the performance of both disk-shaped and rectangular flat-plate heat pipes are analyzed and compared to each other.

A specific application will be considered for the disk-shaped heat pipe used in our analysis, namely, Boron Neutron Capture Therapy (BNCT), which has an important medical application. A description of this application is given in the literature (Vafai and Wang, 1992). The disk-shaped heat pipe, with heavy water as working fluid, is more suitable for the BNCT application than the rectangular flat-plate heat pipe due to its size, geometry, and thermal performance and will be used to remove the high heat flux generated by the proton bombardments of the lithium target. However, it should be noted that all of the analytical results are completely general and apply to various configurations of both symmetric and asymmetric disk-shaped heat pipes.

## Analysis and Formulation

The schematic diagram of the heat pipe under study is shown in Fig. 1. The heat generated from the proton bombardment of the lithium target is imposed on a portion of the bottom part of

Contributed by the Heat Transfer Division for publication in the JOURNAL OF HEAT TRANSFER. Manuscript received by the Heat Transfer Division August 1993; revision received April 1994. Keywords: Augmentation and Enhancement, Heat Pipes and Thermosyphons, Phase-Change Phenomena. Associate Technical Editor: A. Faghri.

the heat pipe and causes the vaporization and subsequent pressurization of the liquid in the wick. Part of the vapor is condensed on the opposite surface of the evaporator; however, most of it is condensed downstream of the evaporator. The vapor space is divided into several channels by vertical wicks, which transport liquid from the upper wick to the lower wick. Any one of the internal channels can be considered as a building block for the disk-shaped heat pipe. Therefore, we will concentrate on the fluid flow considerations within one of these channels (Fig. 1*b*). Once the fluid flow characteristics within one of the channels are determined, the fluid flow characteristics of the entire heat pipe can be easily established. The results of this analysis are applicable to any number of channels, any specified thickness of the wick, as well as any specified thickness of the disk-shaped heat pipe.

In our analysis the position coordinates, velocities, pressures, and temperature are nondimensionalized by  $h^2 v_1 / \nu_v$ ,  $h$ ,  $\Phi$ ,  $v_1$ ,  $\nu_v / h$ ,  $\rho_v v_1^2$ , and  $h_{fg} / \bar{R}$ , where  $\nu_v$  is the vapor kinematic viscosity,  $v_1$  is the vapor injection velocity, which is related to the input power through  $v_1 = Q / \rho_v A_e h_{fg}$ ,  $\rho_v$  is the vapor density,  $h$  and  $\Phi$  are the height and angle of the vapor space for any one of the vapor flow channels,  $h_{fg}$  is the latent heat of the working fluid, and  $\bar{R}$  is the ideal gas constant.

In the heat pipe research performed to date, researchers have made some traditional assumptions in modeling and analysis. An important assumption made by various researchers is that the capillary porous wick is always saturated with liquid phase working fluid and vapor flows only in the core region during the operation of the heat pipe. Hence, evaluation of the effective thermal conductivity and formulation of the capillary pressure were simplified. This assumption will be employed in the present investigation. We will also make the following common assumptions, which are usually made in analyzing the heat pipes:

- 1 Vapor and liquid flow are steady, laminar, and subsonic.
- 2 Transport properties for the vapor and liquid are taken as constants.
- 3 The vapor injection and suction rate are uniform in the evaporator and condenser sections.
- 4 The vapor velocity component in the  $\theta$  direction is negligible since the injection and suction on the vertical wicks are negligible. However, the  $\theta$  component of the liquid velocity is considered in the analysis.

**1 Vapor Phase Analysis.** Based on these assumptions, the continuity Eq. (1) and the  $r$ -direction momentum Eq. (2) govern the vapor flow

$$\frac{\partial u_v^+}{\partial r^+} + \frac{\partial v_v^+}{\partial y^+} + \frac{u_v^+}{r^+} = 0 \quad (1)$$

$$u_v^+ \frac{\partial u_v^+}{\partial r^+} + v_v^+ \frac{\partial u_v^+}{\partial y^+} = -\frac{\partial p_v^+}{\partial r^+} + \frac{1}{\text{Re}_h^2} \left[ \frac{\partial^2 u_v^+}{\partial (r^+)^2} + \frac{1}{r^+} \frac{\partial u_v^+}{\partial r^+} - \frac{u_v^+}{(r^+)^2} + \text{Re}_h^2 \frac{\partial^2 u_v^+}{\partial (y^+)^2} + \frac{1}{\Phi^2 (r^+)^2} \frac{\partial^2 u_v^+}{\partial (\theta^+)^2} \right] \quad (2)$$

In these equations  $\text{Re}_h = v_1 h / \nu_v$  is defined as the injection Reynolds number. The associated boundary conditions of the problem are

$$u_v^+(r^+, y^+, 0) = u_v^+(r^+, y^+, 1) = 0 \quad (3)$$

$$u_v^+(r^+, 0, \theta^+) = u_v^+(r^+, 1, \theta^+) = 0 \quad (4)$$

$$u_v^+(0, y^+, \theta^+) = u_v^+(R^+, y^+, \theta^+) = 0 \quad (5)$$

$$v_v^+(r^+, 0, \theta^+) = -v_2^+,$$

$$v_v^+(r^+, 1, \theta^+) = \begin{cases} -v_1^+ & (0 \leq r^+ \leq \varphi R^+) \\ +v_2^+ & (\varphi R^+ \leq r^+ \leq R^+), \end{cases} \quad (6)$$

As indicated in Eq. (6), within the  $0 \leq r^+ \leq \varphi R^+$  region, the lower wick acts as the evaporator and the upper wick as the condenser. However, both upper and lower wicks act as condensers within the  $\varphi R^+ \leq r^+ \leq R^+$  region. The parameter  $\varphi$  will be established later.

(a) *Velocity Profile.* Based on the numerical results given by Narayana (1986), Faghri (1986), and Sorour et al. (1987), a parabolic velocity profile will be used for vapor flow within the heat pipe. The dimensionless velocity profile  $u_v^+(r^+, y^+, \theta^+)$  will be represented by a functional product in the  $r^+$ ,  $y^+$ , and  $\theta^+$  directions; that is

$$u_v^+(r^+, y^+, \theta^+) = U_v^+(r^+) [a_0 + a_1 y^+ + a_2 (y^+)^2] \times [c_0 + c_1 \theta^+ + c_2 (\theta^+)^2] \quad (7)$$

where  $U_v^+(r^+)$  denotes the maximum velocity for  $u_v^+(r^+, y^+, \theta^+)$  on every transverse surface along the  $r^+$  axis. Because of the symmetric conditions in the  $\theta^+$  direction (i.e., boundary conditions (3)), the constants  $c_0$ ,  $c_1$ , and  $c_2$  for the  $\theta^+$  component of  $u_v^+(r^+, y^+, \theta^+)$  are easily specified as

$$[c_0 + c_1 \theta^+ + c_2 (\theta^+)^2] = 4\theta^+(1 - \theta^+) \quad (8)$$

## Nomenclature

$A_e$  = evaporator area,  $\text{m}^2$   
 $A_{\text{total}}$  = total external surface area of the heat pipe,  $\text{m}^2$   
 $f(r)$  = location of the maximum vapor velocity,  $m$   
 $f^+(r^+)$  = dimensionless location of the maximum vapor velocity  
 $h$  = height of vapor space for the heat pipe,  $m$   
 $h_{fg}$  = latent heat of working fluid,  $\text{kJ/kg}$   
 $h_{\text{total}}$  = thickness of the heat pipe =  $h + 2h_w$ ,  $m$   
 $h_w$  = thickness of the wick,  $m$   
 $h_w^+$  = dimensionless thickness of the wick =  $h_w/h$   
 $K$  = permeability,  $\text{m}^2$

$K^+$  = dimensionless permeability =  $K/h_w^2$   
 $k_e$  = effective thermal conductivity of the liquid-saturated wick,  $\text{W/mK}$   
 $p_0$  = saturation pressure,  $\text{Pa}$   
 $p_l$  = liquid pressure,  $\text{Pa}$   
 $p_v$  = vapor pressure,  $\text{Pa}$   
 $p_l^+$  = dimensionless liquid pressure =  $p_l/\rho_l v_1^2$   
 $p_v^+$  = dimensionless vapor pressure =  $p_v/\rho_v v_1^2$   
 $p_{0v}^+$  = dimensionless saturate vapor pressure =  $p_{0v}/\rho_v v_1^2$   
 $\Delta p_{\text{cap}}$  = capillary pressure head generated by the wick,  $\text{Pa}$   
 $\Delta p_l$  = overall liquid pressure drop along the heat pipe,  $\text{Pa}$

$\Delta p_v$  = overall vapor pressure drop along the heat pipe,  $\text{Pa}$   
 $\Delta p_l^+$  = overall dimensionless liquid pressure drop along the heat pipe =  $p_l^+ - p_{0v}^+$   
 $\Delta p_v^+$  = overall dimensionless vapor pressure drop along the heat pipe =  $p_v^+ - p_{0v}^+$   
 $Q_{\text{max}}$  = maximum input heat power under capillary limit,  $\text{W}$   
 $q_{b,\text{max}}$  = maximum heat flux for boiling limit,  $\text{W/m}^2$   
 $r, y$  = coordinates,  $m$   
 $r^+, y^+$  = dimensionless coordinates;  $r^+ = r\nu_v/h^2 v_1$ ,  $y^+ = y/h$   
 $r_n$  = nucleation radius of the vapor bubbles,  $m$

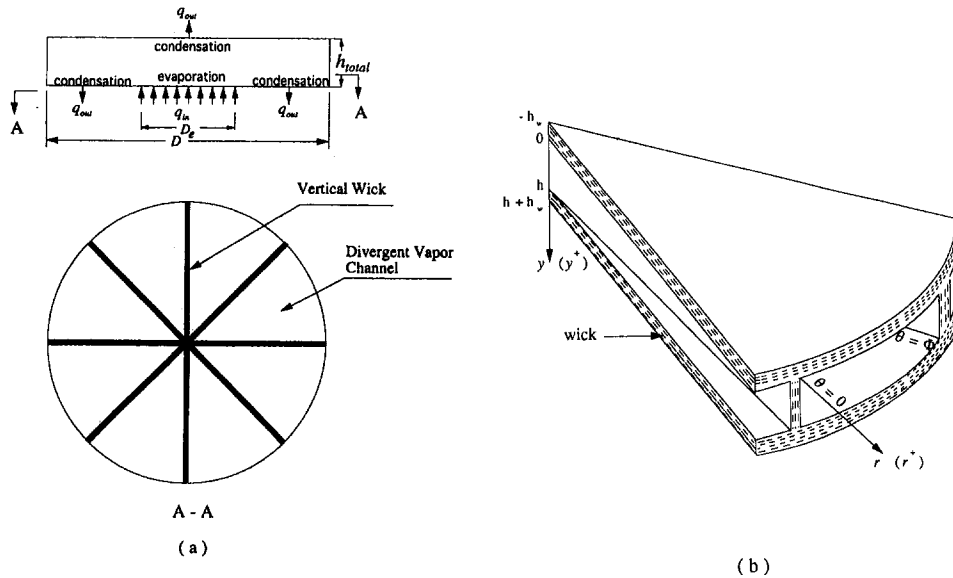


Fig. 1 Schematic of the disk-shaped heat pipe: (a) geometry of the heat pipe, (b) the coordinate system used in the analysis

where  $\theta^+ = \theta/\Phi$ . Since the angular component of  $u_v^+(r^+, y^+, \theta^+)$  given by Eq. (8) is uncoupled from  $r^+$  and  $y^+$ , the  $r^+$  and  $y^+$  component of  $u_v^+(r^+, y^+, \theta^+)$  can be determined by concentrating only on the  $r^+ - y^+$  plane. Therefore, the velocity profile in the  $r^+ - y^+$  plane is

$$u_v^+(r^+, y^+) = U_v^+(r^+) [a_0 + a_1 y^+ + a_2 (y^+)^2]. \quad (9)$$

The vapor flow in the heat pipe does not have a symmetric velocity profile in the  $r^+ - y^+$  plane. The location of the maximum vapor velocity will be shifted toward the upper plate due to the vapor injection from the heating side of the lower plate. As the vapor flows downstream, the location of the maximum velocity will gradually shift toward the centerline due to the presence of symmetric cooling conditions. To account for this feature, the velocity profile in  $y^+$  direction will be divided into two parts based on the location of the maximum velocity (Fig. 2): the upper part ( $0 \leq y^+ \leq f^+(r^+)$ ) and the lower part ( $f^+(r^+) \leq y^+ \leq 1$ ). The location of the maximum velocity,  $y^+ = f^+(r^+)$ ,

is also the location corresponding to zero shear stress for the velocity distribution on the  $r^+ - y^+$  plane. Applying boundary condition (4) and

$$u_v^+(r^+, f^+(r^+)) = U_v^+(r^+), \quad \left. \frac{\partial u_v^+(r^+, y^+)}{\partial y^+} \right|_{y^+=f^+(r^+)} = 0$$

to Eq. (9) will result in the following velocity profiles:

$$u_v^+(r^+, y^+) = \begin{cases} U_v^+(r^+) \left[ 2 \frac{y^+}{f^+(r^+)} - \left( \frac{y^+}{f^+(r^+)} \right)^2 \right] & (0 \leq y^+ \leq f^+(r^+)) \\ U_v^+(r^+) \left[ 2 \left( \frac{1 - y^+}{1 - f^+(r^+)} \right) - \left( \frac{1 - y^+}{1 - f^+(r^+)} \right)^2 \right] & (f^+(r^+) \leq y^+ \leq 1). \end{cases} \quad (10)$$

### Nomenclature (cont.)

$r_w$  = porous radius of wick, m  
 $R$  = radius of the disk-shaped heat pipe, m  
 $R^+$  = dimensionless radius of the disk-shaped heat pipe  
 $\bar{R}$  = ideal gas constant = 8.31433 kJ/(kmole · K)  
 $Re_h$  = injection Reynolds number =  $v_1 h / \nu_v$   
 $T_v$  = vapor temperature, °C  
 $T_v^+$  = dimensionless vapor temperature =  $T_v R / h_{fg}$   
 $T_{0v}^+$  = dimensionless saturate vapor temperature =  $T_{0v} R / h_{fg}$   
 $\Delta T_v^+$  = dimensionless vapor temperature drop along the heat pipe =  $T_v^+ - T_{0v}^+$   
 $u_l$  = liquid velocity, m/s  
 $u_v$  = vapor velocity, m/s

$u_l^+$  = dimensionless liquid velocity =  $u_l / v_1$   
 $u_v^+$  = dimensionless vapor velocity =  $u_v / v_1$   
 $U_v^+$  = dimensionless vapor velocity component in  $r^+$  direction  
 $v_1$  = vapor injection velocity, m/s  
 $v_2$  = vapor suction velocity, m/s  
 $v_1^+$  = dimensionless vapor injection velocity =  $v_1 h / \nu_v$   
 $v_2^+$  = dimensionless vapor suction velocity =  $v_2 h / \nu_v$   
 $\epsilon$  = wick porosity  
 $\theta$  = coordinate  
 $\theta^+$  = dimensionless coordinate =  $\theta / \Phi$   
 $\nu_l$  = kinematic viscosity of liquid,  $m^2/s$   
 $\nu_v$  = kinematic viscosity of vapor,  $m^2/s$   
 $\nu^+$  = dimensionless kinematic viscosity =  $\nu_l / \nu_v$

$\rho_l$  = liquid density,  $kg/m^3$   
 $\rho_v$  = vapor density,  $kg/m^3$   
 $\rho^+$  = dimensionless density =  $\rho_l / \rho_v$   
 $\sigma_l$  = surface tension of the working liquid, N/m  
 $\varphi$  = square root of the ratio of the evaporator area to the heat pipe area;  $\varphi^2 = A_e / \pi R^2$   
 $\Phi$  = angle of each divergent vapor channel of disk-shape heat pipe

### Subscripts

$e$  = evaporator  
 $l$  = liquid phase  
 $v$  = vapor phase  
 $w$  = wick

### Superscripts

$+$  = dimensionless quantities

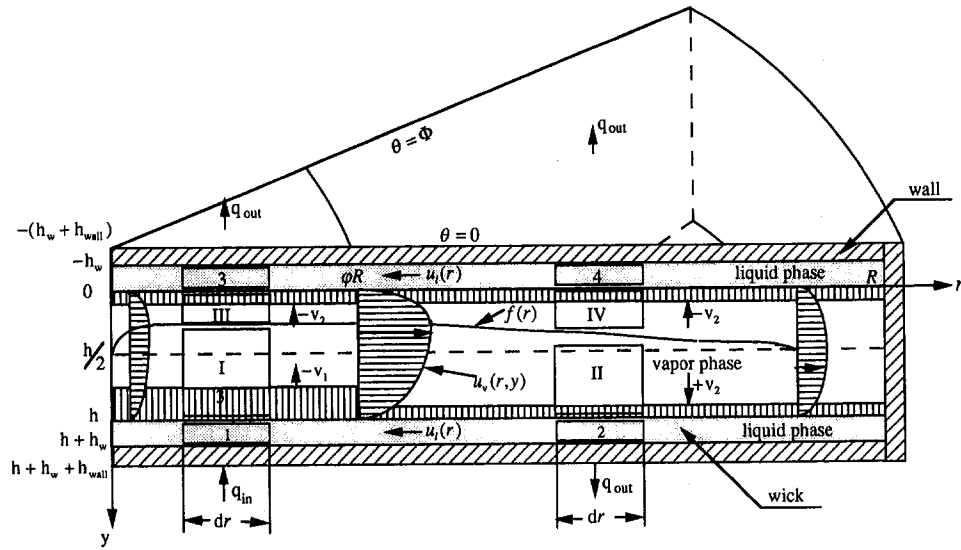


Fig. 2 Different regimes, which are analyzed for the vapor and liquid phases in the  $r$ - $y$  plane of the heat pipe

The two unknowns  $U_v^+(r^+)$  and  $f^+(r^+)$  in Eq. (10) will be determined by integrating the continuity Eq. (1) and the momentum Eq. (2). Integrating the continuity Eq. (1) with respect to  $y^+$  from 0 to 1 and substituting the velocity profile given by Eq. (10) into the integrated equation and applying boundary conditions given by Eqs. (4) and (6) will result in an expression for  $U_v^+(r^+)$ :

$$U_v^+(r^+) = \begin{cases} \frac{3(v_1^+ - v_2^+)}{4} r^+ & (0 \leq r^+ \leq \varphi R^+) \\ -\frac{3v_2^+}{2} \frac{1}{r^+} [(r^+)^2 - (R^+)^2] & (\varphi R^+ \leq r^+ \leq R^+) \end{cases} \quad (11)$$

As expected,  $U_v^+(r^+)$  is related to vapor injection and suction velocities. Recognizing the fact that  $U_v^+(r^+)$  must be continuous at  $r^+ = \varphi R^+$  will result in

$$\varphi = \sqrt{\frac{2v_2^+}{v_1^+ + v_2^+}} \quad (12)$$

Using Eq. (12), Eq. (11) can be written as

$$U_v^+(r^+) = \begin{cases} \frac{3}{2} \frac{1 - \varphi^2}{2 - \varphi^2} \text{Re}_h r^+ & (0 \leq r^+ \leq \varphi R^+) \\ -\frac{3}{2} \frac{\varphi^2}{2 - \varphi^2} \frac{\text{Re}_h}{r^+} [(r^+)^2 - (R^+)^2] & (\varphi R^+ \leq r^+ \leq R^+) \end{cases} \quad (13)$$

The  $f^+(r^+)$  will be determined by integrating the  $r^+$ -momentum Eq. (2) with respect to  $y^+$  for either the lower part or the upper part of the vapor space. It should be noted that in the  $0 \leq r^+ \leq \varphi R^+$  region, there is a mass flow crossing the interface between the two control volumes I and III within the vapor phase (Fig. 2) due to the vapor injection from the lower wick and suction from the upper wick. However, in the  $\varphi R^+ \leq r^+ \leq R^+$  region, due to the symmetric boundary conditions on both upper and lower wicks, there is no mass exchange between the two control volumes II and IV. Since the dimension in the  $r^+$  direction is much larger than the transverse length in the vapor channel, the shear stress in the  $r^+$  direction will be neglected (Narayana, 1986; Faghri, 1986). We have also been able to confirm that the shear stress in the  $r^+$  direction is negligible when it was accounted for in the analysis. The above-mentioned considerations will result in the following set of equations for the upper part of the vapor space:

$$\begin{aligned} \frac{d}{dr^+} \int_0^{f^+(r^+)} (u_v^+(r^+, y^+, \theta^+))^2 dy^+ - U_v^+(r^+) J(\theta^+) \frac{d}{dr^+} \int_0^{f^+(r^+)} u_v^+(r^+, y^+, \theta^+) dy^+ + \int_0^{f^+(r^+)} \frac{1}{r^+} (u_v^+(r^+, y^+, \theta^+))^2 dy^+ \\ - U_v^+(r^+) J(\theta^+) \int_0^{f^+(r^+)} \frac{1}{r^+} u_v^+(r^+, y^+, \theta^+) dy^+ - U_v^+(r^+) J(\theta^+) v_2^+ = - \int_0^{f^+(r^+)} \frac{\partial p_v^+}{\partial r^+} dy^+ + \int_0^{f^+(r^+)} \frac{\partial^2 u_v^+(r^+, y^+, \theta^+)}{\partial (y^+)^2} dy^+ \\ - \frac{1}{\text{Re}_h^2} \left[ \int_0^{f^+(r^+)} \frac{u_v^+(r^+, y^+, \theta^+)}{(r^+)^2} dy^+ - \frac{1}{\Phi^2} \int_0^{f^+(r^+)} \frac{\partial^2 u_v^+(r^+, y^+, \theta^+)}{\partial (\theta^+)^2} dy^+ \right] \quad (0 \leq r^+ \leq \varphi R^+) \quad (14a) \end{aligned}$$

and

$$\begin{aligned} \frac{d}{dr^+} \int_0^{f^+(r^+)} (u_v^+(r^+, y^+, \theta^+))^2 dy^+ - (U_v^+(r^+))^2 (J(\theta^+))^2 \frac{df^+(r^+)}{dr^+} + \int_0^{f^+(r^+)} \frac{1}{r^+} (u_v^+(r^+, y^+, \theta^+))^2 dy^+ \\ = - \int_0^{f^+(r^+)} \frac{\partial p_v^+}{\partial r^+} dy^+ + \int_0^{f^+(r^+)} \frac{\partial^2 u_v^+(r^+, y^+, \theta^+)}{\partial (y^+)^2} dy^+ - \frac{1}{\text{Re}_h^2} \left[ \int_0^{f^+(r^+)} \frac{u_v^+(r^+, y^+, \theta^+)}{(r^+)^2} dy^+ \right. \\ \left. - \frac{1}{\Phi^2} \int_0^{f^+(r^+)} \frac{\partial^2 u_v^+(r^+, y^+, \theta^+)}{\partial (\theta^+)^2} dy^+ \right] \quad (\varphi R^+ \leq r^+ \leq R^+) \quad (14b) \end{aligned}$$

where  $J(\theta^+) = 4\theta^+(1 - \theta^+)$ . Using the vapor velocity profile and the average vapor pressure in each transverse plane in Eqs. (14a) and (14b) will result, after a very lengthy analysis, in the following expression for the rate of change of  $f^+(r^+)$

$$\frac{df^+(r^+)}{dr^+} = \begin{cases} \left\{ \left[ \frac{2(1 - \varphi^2)J(\theta^+)}{2 - \varphi^2} + \frac{10}{3 \text{Re}_h^3(r^+)^2} \left( 1 + \frac{8}{\Phi^2 J(\theta^+)} \right) \right] f^+(r^+) + \frac{10}{\text{Re}_h f^+(r^+)} - \frac{5\varphi^2}{2 - \varphi^2} \right. \\ \left. + \frac{10(2 - \varphi^2)f^+(r^+)}{3(1 - \varphi^2)J(\theta^+) \text{Re}_h^2 r^+} \frac{dp_v^+}{dr^+} \right\} \frac{2 - \varphi^2}{(1 - \varphi^2)J(\theta^+)r^+} & (0 \leq r^+ \leq \varphi R^+) \\ \left\{ \left[ \frac{6\varphi^2 J(\theta^+)}{5(2 - \varphi^2)} (3(r^+)^2 + (R^+)^2) - \frac{1}{\text{Re}_h^3} \left( 1 + \frac{8}{\Phi^2 J(\theta^+)} \right) \right] f^+(r^+) - \frac{3(r^+)^2}{\text{Re}_h} - \frac{1}{f^+(r^+)} \right. \\ \left. + \frac{2 - \varphi^2}{\varphi^2 J(\theta^+)} \frac{(r^+)^3}{(r^+)^2 - (R^+)^2} \frac{f^+(r^+)}{\text{Re}_h^2} \frac{dp_v^+}{dr^+} \right\} \frac{20(2 - \varphi^2)}{21\varphi^2 J(\theta^+)r^+[(r^+)^2 - (R^+)^2]} & (\varphi R^+ \leq r^+ \leq R^+). \end{cases} \quad (15)$$

Since  $U^+(0) = U^+(R^+) = 0$ , and the velocity distributions at  $r^+ = 0$  and  $r^+ = R^+$  are uniform, the boundary conditions for the function  $f^+(r^+)$  are taken as  $f^+(0) = f^+(R^+) = 1/2$ . The use of Eqs. (8), (10), (13), and (15) in Eq. (7) will provide us with the complete velocity profile within the disk-shaped heat pipe assembly.

(b) *Pressure Distribution.* The pressure distribution in the vapor phase can be obtained by integrating the  $r^+$ -momentum Eq. (2) within a channel bounded by porous wicks. Introducing continuity Eq. (1), the velocity profile given by Eqs. (8), (10), (13), and (15) and boundary conditions given by Eq. (6) into the integrated momentum equation will result, after a very lengthy analysis, in the following expression for the pressure gradient:

$$\frac{dp_v^+}{dr^+} = \begin{cases} -\frac{2(1 - \varphi^2)}{(2 - \varphi^2)} \text{Re}_h \left\{ \left[ \frac{24(1 - \varphi^2)}{25(2 - \varphi^2)} \text{Re}_h + \frac{1}{f^+(1 - f^+)} \right] r^+ + \frac{4}{\text{Re}_h^2 \Phi^2 r^+} \right\} & (0 \leq r^+ \leq \varphi R^+) \\ -\frac{2\varphi^2}{(2 - \varphi^2)} \text{Re}_h \left\{ \left[ \frac{24}{25} \frac{\varphi^2}{(2 - \varphi^2)} \text{Re}_h - \frac{1}{f^+(1 - f^+)} \right] r^+ - \frac{4}{\text{Re}_h^2 \Phi^2 r^+} + \frac{8}{25(2 - \varphi^2)} \frac{\varphi^2 \text{Re}_h (R^+)^2}{r^+} \right\} \frac{(r^+)^2 - (R^+)^2}{(r^+)^2} & (\varphi R^+ \leq r^+ \leq R^+). \end{cases} \quad (16)$$

The coupled Eqs. (15) and (16) are solved by using the Runge-Kutta method for the pressure drop  $\Delta p_v^+(r^+)$  and  $f^+(r^+)$ . A good approximation for the  $f^+(r^+)$  is developed by using Bernoulli's equation at  $y^+ = f^+(r^+)$  and is used as startup for the numerical calculations. The use of Bernoulli's equation will result in

$$\frac{df^+(r^+)}{dr^+} = \begin{cases} \left\{ \left[ -11(1 - \varphi^2)J(\theta^+) + \frac{20(2 - \varphi^2)}{3 \text{Re}_h^3(r^+)^2} \left( 1 + \frac{8}{J(\theta^+)\Phi^2} \right) \right] f^+(r^+) \right. \\ \left. + \frac{20(2 - \varphi^2)}{\text{Re}_h} \frac{1}{f^+(r^+)} - 10\varphi^2 \right\} \frac{1}{(1 - \varphi^2)J(\theta^+)r^+} & (0 < r^+ \leq \varphi R^+) \\ \left\{ \left[ (9(r^+)^2 - 7(R^+)^2)J(\theta^+) - \frac{20(2 - \varphi^2)}{3\varphi^2 \text{Re}_h^3} \left( 1 + \frac{8}{J(\theta^+)\Phi^2} \right) \right] f^+(r^+) \right. \\ \left. - \frac{20(2 - \varphi^2)}{\varphi^2 \text{Re}_h} \frac{(r^+)^2}{f^+(r^+)} \right\} \frac{1}{7J(\theta^+)r^+((r^+)^2 - (R^+)^2)} & (\varphi R^+ \leq r^+ < R^+). \end{cases} \quad (17)$$

(c) *Temperature Distribution.* The vapor temperature distribution can be related to the vapor pressure distribution by using the Clausius-Clapeyron equation. In this work, the vapor is assumed to behave as an ideal gas and the volume of the liquid

within the vapor phase is neglected (Winter and Barsch, 1971; Ivanovskii et al., 1982). The dimensionless temperature profile based on the Clausius-Clapeyron equation can be found from

$$\Delta T_v^+(r^+) = (T_{0v}^+)^2 \left[ \frac{\ln p_v^+(r^+) - \ln p_{0v}^+}{1 - T_{0v}^+(\ln p_{0v}^+ - \ln p_v^+(r^+))} \right] \quad (18)$$

where  $T_{0v}^+ = T_{0v}/(h_{fg}/R)$  is the dimensionless saturation temperature.

## 2 Liquid Phase Analysis

(a) *Velocity Profile.* Since both upper and lower wicks in the  $\varphi R^+ \leq r^+ \leq R^+$  region act as condensers, the condensate in both upper and lower wicks of the  $\varphi R^+ \leq r^+ \leq R^+$  region (sections 4 and 2 of Fig. 2) flows directly toward section 3 and section 1, respectively, along the horizontal wicks. There is no liquid exchange through the vertical wicks in the  $\varphi R^+ \leq r^+ \leq R^+$  region due to the symmetric boundary conditions. Therefore, the condensate will have only one velocity component,  $u_l^+$ , along the

$r^+$  direction in the  $\varphi R^+ \leq r^+ \leq R^+$  region. However, within the  $0 \leq r^+ \leq \varphi R^+$  region the condensate in both upper and lower wicks possesses two distinct velocity components,  $u_l^+$  in the  $r^+$  direction and  $w_l^+$  in the  $\theta^+$  direction, since the lower wick (evaporator) gets part of the liquid supply from the upper wick through the vertical wicks. Applying mass conservation for the conden-

sate in both upper and lower wicks and eliminating  $w_l^+$  by adding the lower and upper wick mass conservation equations together will result in the following equations for the velocity distribution in the  $r^+$  direction:



$$\begin{cases} \frac{d(u_l^+(r^+))}{dr^+} + \frac{u_l^+(r^+)}{r^+} - \frac{v_l^+ - v_2^+}{2h_w^+ \rho^+} = 0 \\ (0 \leq r^+ \leq \varphi R^+) \\ \frac{d(u_l^+(r^+))}{dr^+} + \frac{u_l^+(r^+)}{r^+} + \frac{v_2^+}{h_w^+ \rho^+} = 0 \\ (\varphi R^+ \leq r^+ \leq R^+) \end{cases} \quad (19)$$

where  $\rho^+ = \rho_l/\rho_v$  and  $h_w^+ = h_w/h$ . Solving Eq. (19) subject to the following boundary conditions:

$$u_l^+(0) = u_l^+(R^+) = 0$$

results in the liquid phase velocity distribution

$$u_l^+(r^+) = \begin{cases} \frac{v_l^+ - v_2^+}{4\rho^+ h_w^+} r^+ & (0 \leq r^+ \leq \varphi R^+) \\ -\frac{v_2^+}{2\rho^+ h_w^+} \frac{(r^+)^2 - (R^+)^2}{r^+} & (\varphi R^+ \leq r^+ \leq R^+). \end{cases} \quad (20)$$

The continuity of  $u_l^+(r^+)$  at  $r^+ = \varphi R^+$  will reconfirm the result given in Eq. (12).

(b) *Pressure Distribution.* The pressure distribution in the wick along the  $r^+$  direction can be related to the liquid velocity distribution by Darcy's law. The dimensionless Darcy's law is

$$\frac{dp_l^+(r^+)}{dr^+} = \frac{1}{K^+} u_l^+(r^+) \quad (21)$$

where  $K^+ = K/h_w^2$  is the dimensionless permeability. It should be noted that in using Darcy's law some important aspects related to boundary and inertial effects are neglected (Vafai and Tien, 1981; Tien and Vafai, 1989). Substituting Eq. (20) into Eq. (21) and using the boundary condition

$$p_l^+(R^+) = p_v^+(R^+)$$

will result in

$$p_l^+(r^+) = \begin{cases} p_v^+(R^+) + \frac{\nu^+}{4K^+(h_w^+)^3} \frac{\varphi^2 \text{Re}_h}{(2 - \varphi^2)} \left[ \frac{1 - \varphi^2}{\varphi^2} (r^+)^2 + 2(R^+)^2 \ln(\varphi) \right] & (0 \leq r^+ \leq \varphi R^+) \\ p_v^+(R^+) + \frac{\nu^+}{4K^+(h_w^+)^3} \frac{\varphi^2 \text{Re}_h}{(2 - \varphi^2)} \left[ (R^+)^2 - (r^+)^2 - 2(R^+)^2 \ln\left(\frac{R^+}{r^+}\right) \right] & (\varphi R^+ \leq r^+ \leq R^+). \end{cases} \quad (22)$$

**3 Maximum Heat Transfer Capability.** There are limits on the maximum heat input that a heat pipe is capable of removing. For a low-temperature heat pipe usually only the boiling limit and capillary limit will be in effect (Tien, 1975). The maximum heat flux for boiling limit can be calculated as follows (Chi, 1976):

$$q_{b,\max} = \frac{k_e T_v}{\rho_v h_{fg} h_w} \left( \frac{2\sigma_l}{r_n} - \Delta p_{\text{cap}} \right) \quad (23)$$

where  $k_e$  is the effective thermal conductivity of the liquid-saturated wick,  $\sigma_l$  the surface tension of the working liquid in the wick,  $r_n$  the nucleation radius of the vapor bubbles, and  $\Delta p_{\text{cap}}$  is the capillary pressure head. Assuming that there are no noncondensable gases within the heat pipe, the value of  $r_n$  can be taken as  $2.54 \times 10^{-7}$  m (Chi, 1976). Some typical values can be considered to evaluate the maximum heat flux for boiling limit. For example, for the heavy water heat pipe under current study, which operates at 80°C, the wick pore radius is taken as  $r_w = 0.019$  cm, permeability  $K = 1.8 \times 10^{-9}$  m<sup>2</sup>, porosity  $\varepsilon = 0.8$ , and the effective thermal conductivity is taken as  $k_e = 13.84$  W/mK. The maximum heat flux for boiling limit is then calculated as

$$q_{b,\max} = 1.85 \times 10^6 \text{ W/m}^2 = 185 \text{ W/cm}^2$$

This value is larger than the maximum heat transfer rate limited by the capillary limit. Thus we will concentrate on the capillary limit. For a heat pipe under steady-state operation, the capillary pressure head needed for the return of condensate from the condenser to the evaporator is balanced by the sum of total vapor pressure drop and total liquid pressure drop and gravitational pressure head; that is

$$\Delta p_{\text{cap}} = \Delta p_{v,\text{total}} + \Delta p_{l,\text{total}} + \Delta p_{g,\text{total}}. \quad (24)$$

The gravitational head  $\Delta p_{g,\text{total}}$  can be neglected for the horizontal heat pipe, and the overall vapor and liquid pressure drops are established as

$$\Delta p_{v,\text{total}} = p_v(0) - p_v(R) \quad (25)$$

$$\Delta p_{l,\text{total}} = p_l(R) - p_l(0), \quad (26)$$

Therefore, the capillary pressure head is presented as

$$\Delta p_{\text{cap}} = \Delta p_{v,\text{total}} + \Delta p_{l,\text{total}} = p_v(0) - p_l(0). \quad (27)$$

When the input heat flux increases, the total pressure drops in both vapor and liquid regions increase; thus the capillary pressure head increases to meet the heat transfer and flow conditions. However, there exists a maximum capillary pressure head given by

$$\Delta p_{\text{cap,max}} = \frac{2\sigma_l}{r_w} \quad (28)$$

where  $r_w$  is the capillary radius of the porous wick. If the capillary pressure head needed is larger than  $\Delta p_{\text{cap,max}}$ , the heat pipe operation will dry out the wick. Therefore the heat that the disk-shaped or the flat-plate heat pipe transfers when it reaches the

capillary limit is the maximum heat transfer,  $Q_{\max}$ . As long as  $\Delta p_{\text{cap,max}}$  is specified,  $Q_{\max}$  can be determined according to this analysis. The maximum heat transfer capability per unit external surface area of the heat pipe is then determined based on  $Q_{\max}$  and is discussed later.

**4 Simplified Analytical Solution.** Noticing that the values of the injection Reynolds number under current study are very large relative to other parameters, as an approximation we can neglect the affected terms in Eqs. (17) and reach the following expressions for  $f^+(r^+)$ :

$f^+(r^+)$

$$= \begin{cases} -\frac{10\varphi^2 e^{-A/2(r^+)^2}}{(1-\varphi^2)J(\theta^+)(r^+)^{11}} \int (r^+)^{10} e^{A/2(r^+)^2} dr^+ \\ (0 \leq r^+ \leq \varphi R^+) \\ c(r^+)^{1+B}((R^+)^2 - (r^+)^2)^{(1/7-B/2)} \\ (\varphi R^+ \leq r^+ \leq R^+) \end{cases} \quad (29)$$

where

$$A = \frac{20(2-\varphi^2)}{3(1-\varphi^2)J(\theta^+) \text{Re}_h^3} \left(1 + \frac{8}{J(\theta^+)\Phi^2}\right) \quad (30)$$

$$B = \frac{20(2-\varphi^2)}{21\varphi^2 J(\theta^+) \text{Re}_h^3 (R^+)^2} \left(1 + \frac{8}{J(\theta^+)\Phi^2}\right) \quad (31)$$

and  $c$  is the integration constant, which is determined by the continuous condition of  $f^+(r^+)$  at  $r^+ = \varphi R^+$ . Similarly, Eq. (16) can be simplified to obtain the following expression for the vapor pressure:

$$p_v^+(r^+) = \begin{cases} p_v^+(0) - \frac{24}{25} \left(\frac{1-\varphi^2}{2-\varphi^2} \text{Re}_h R^+\right)^2 \left(\frac{r^+}{R^+}\right)^2 & (0 \leq r^+ \leq \varphi R^+) \\ p_v^+(0) - \frac{8}{25} \left(\frac{\varphi^2}{2-\varphi^2} \text{Re}_h R^+\right)^2 \left[3\left(\frac{r^+}{R^+}\right)^2 + \left(\frac{R^+}{r^+}\right)^2 - 4 \ln \frac{r^+}{R^+} - 2\left(3 - 2 \ln \varphi - \frac{1}{\varphi^2}\right)\right] \\ (\varphi R^+ \leq r^+ \leq R^+) \end{cases} \quad (32)$$

The liquid pressure profile is therefore given as follows:

$$p_l^+(r^+) = \begin{cases} p_l^+(0) + \frac{\nu^+ \text{Re}_h (R^+)^2}{4K^+(h_w^+)^3} \frac{1-\varphi^2}{2-\varphi^2} \left[\left(\frac{r^+}{R^+}\right)^2 + \frac{2\varphi^2}{1-\varphi^2} \ln \varphi\right] - \left(\frac{4}{5} \frac{\varphi^2 \text{Re}_h}{2-\varphi^2} R^+\right)^2 \left(2 \ln \varphi + \frac{1}{\varphi^2} - 1\right) \\ (0 \leq r^+ \leq \varphi R^+) \\ p_l^+(0) + \frac{\nu^+ \text{Re}_h (R^+)^2}{4K^+(h_w^+)^3} \frac{\varphi^2}{2-\varphi^2} \left[1 - \left(\frac{r^+}{R^+}\right)^2 - 2 \ln \left(\frac{R^+}{r^+}\right)\right] - \left(\frac{4}{5} \frac{\varphi^2 \text{Re}_h}{2-\varphi^2} R^+\right)^2 \left(2 \ln \varphi + \frac{1}{\varphi^2} - 1\right) \\ (\varphi R^+ \leq r^+ \leq R^+) \end{cases} \quad (33)$$

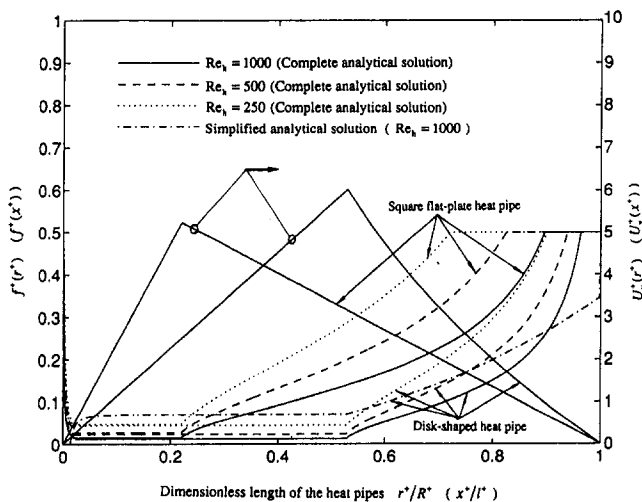


Fig. 3 Variations of the maximum vapor velocity and its location along heat pipe channels

## Results and Discussion

The results based on this analysis for the disk-shaped heat pipe are presented and compared with those of square flat-plate heat pipe analyzed by Vafai and Wang (1992). To make the comparison meaningful at all times the diameter of the disk-shaped heat pipe is taken equal to the length of the square flat-plate heat pipe, i.e.,  $R = l$ . On the same basis, the heat input areas (the evaporator section) and the values of  $h$  and  $h_w$  for both disk-shaped and square flat-plate heat pipes are taken to be equal. Comparisons between the performance of the disk-shaped and the square flat-plate heat pipes as a function of  $h$ ,  $h_w$ , and  $R$  (or  $l$ ) are presented later. The respective dimensions of the heat pipes, based on our application, are chosen as:  $R = l = 0.46$  m,  $h = 0.0254$  m, and  $h_w = 2 \times 10^{-3}$  m. The working fluid is heavy water, which has the following thermophysical properties:  $h_{fg} = 2128$  kJ/kg,  $\rho_v = 0.3055$  kg/m<sup>3</sup>,  $\rho_l = 1078.3$  kg/m<sup>3</sup>,  $\mu_v = 1.1876 \times 10^{-5}$  Ns/m<sup>2</sup>, and  $\mu_l = 41.6 \times 10^{-5}$  Ns/m<sup>2</sup>. The results for both disk-shaped and square flat-plate heat pipes have been calculated for  $\text{Re}_h$  values of 250, 750, and 1000, which corresponds to the input heat powers of 46.25 kW, 92.5 kW, and 185 kW,

respectively. It is important to note that due to the analytical nature of the solution, various ranges of the pertinent parameters along with different heat pipe sizes can be readily analyzed.

Figure 3 shows the variation of the maximum vapor velocity  $U_v^+(r^+)$  [ $U_v^+(x^+)$  for the square flat-plate heat pipe] along the  $r^+$  axis [ $x^+$  axis for the square flat-plate heat pipe]. As mentioned earlier, to have meaningful comparisons the heat input areas (the evaporator area) for both disk-shaped and square flat-plate heat pipes were selected to be equal. This obviously will translate to different  $\varphi$  values for the disk-shaped and the square flat-plate heat pipes. For both disk-shaped and square flat-plate heat pipes, vapor accelerates in the  $0 \leq r^+ \leq \varphi R^+$  [ $0 \leq x^+ \leq \varphi l^+$ ] region corresponding to the evaporator section and decelerates in the  $\varphi R^+ \leq r^+ \leq R^+$  [ $\varphi l^+ \leq x^+ \leq l^+$ ] region corresponding to the condenser section, due to the vapor injection and suction over the corresponding regions. The acceleration within evaporator section of the disk-shaped heat pipe is smaller than that of the square flat-plate heat pipe, and the deceleration within condenser section of the disk-shaped heat pipe is larger than that of the square flat-plate heat pipe. This is because the rate of increase of the net vapor mass flow within the evaporator section of the disk-shaped heat pipe is smaller than that of the square flat-plate heat pipe; and the rate of decrease of the net vapor mass flow within

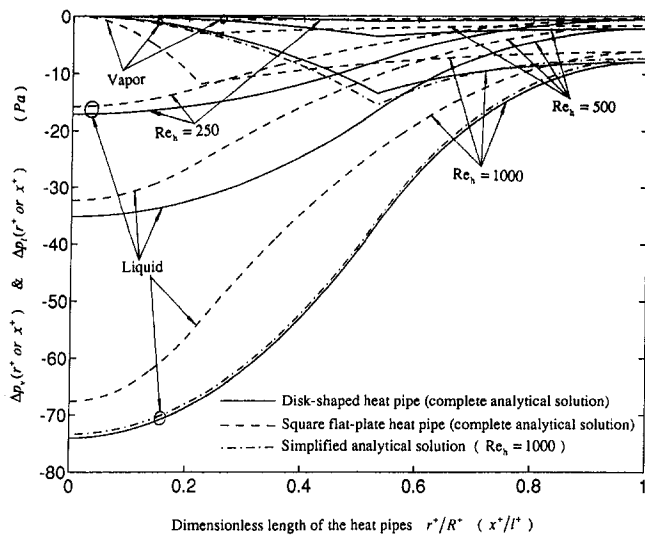


Fig. 4 Vapor and liquid pressure distributions for both disk-shaped and square flat-plate heat pipes

the condenser section of the disk-shaped heat pipe is larger than that of the square flat-plate heat pipe, due to the divergent vapor channel and the larger suction velocity of the disk-shaped heat pipe.

The locations of the maximum vapor velocity for both the disk-shaped heat pipe,  $f^+(r^+)$ , and the square flat-plate heat pipe,  $f^+(x^+)$ , are also shown in Fig. 3 and compared to each other. As expected, the location of the maximum vapor velocity is shifted toward the cooling side of either disk-shaped or flat-plate heat pipe in the  $0 \leq r^+ \leq \varphi R^+$  [ $0 \leq x^+ \leq \varphi l^+$ ] region while it returns to the center line of the heat pipe in the  $\varphi R^+ \leq r^+ \leq R^+$  [ $\varphi l^+ \leq x^+ \leq l^+$ ] region. For larger values of  $Re_h$ , the location of the maximum vapor velocity is shifted more prominently toward the cooling side, and it takes longer in the  $\varphi R^+ \leq r^+ \leq R^+$  [ $\varphi l^+ \leq x^+ \leq l^+$ ] region to return to the centerline. This is due to the fact that for larger input heat fluxes, larger amounts of vapor mass need to be condensed. The simplified analytical solution for  $Re_h = 1000$  is also shown in this figure.

For the disk-shaped heat pipe,  $f^+(r^+)$  is pulled a little closer to the cooling side and takes a relatively shorter distance in the  $\varphi R^+ \leq r^+ \leq R^+$  region to return to the centerline. This is because both heat pipes have the same value of injection velocity  $v_1^+$ , but the disk-shaped heat pipe has a larger suction velocity  $v_2^+$  since it has less surface area than the square flat-plate heat pipe. Furthermore, although the distances from  $r^+ = \varphi R^+$  [ $x^+ = \varphi l^+$ ] to the location where  $f^+(r^+)$  [ $f^+(x^+)$ ] returns to the center line are different for disk-shaped and square flat-plate heat pipes, our results have demonstrated that the amounts of vapor mass sucked within these distances are the same for both heat pipes at a given value of  $Re_h$ . For example, for  $Re_h = 1000$ , the injection velocity is  $v_1 = 1.53$  m/s for both disk-shaped and square flat-plate heat pipes, but the suction velocities will be  $v_2 = 0.2487$  m/s for the disk-shaped heat pipe and  $v_2 = 0.1887$  m/s for the square flat-plate heat pipe. The surface areas needed for  $f^+(r^+)$  [ $f^+(x^+)$ ] to return to the centerline are  $a = 0.4306$  m<sup>2</sup> for the disk-shaped heat pipe and  $a = 0.5721$  m<sup>2</sup> for the square flat-plate heat pipe. Therefore the condensed mass flow rates within these surface areas are the same for both disk-shaped and square flat-plate heat pipes and given by  $\rho a v_2 = 0.0165$  kg/s. This means for the same input heat power and the same evaporator surface area  $A_e$ , i.e., for the same input heat flux, the disk-shaped heat pipe will condense the vapor mass more efficiently with less cooling surface than the larger square flat-plate heat pipe.

Figure 4 shows the vapor and liquid pressure distributions for both disk-shaped and square flat-plate heat pipes, where  $\Delta p_v(r) = p_v(r) - p_v(0)$  and  $\Delta p_l(r) = p_l(r) - p_l(0)$ . As in conventional

heat pipes, there is a vapor pressure drop in the evaporator region due to vapor acceleration in that region and a vapor pressure recovery in the condenser region due to the vapor deceleration in that region. The larger the injection Reynolds number, the larger the vapor and liquid pressure drops. Compared to the square flat-plate heat pipe, the vapor pressure of disk-shaped heat pipe decreases more slowly in the evaporator region and increases faster in the condenser region due to its smaller vapor acceleration within evaporator region and larger vapor deceleration within condenser region. This is in agreement with the maximum vapor velocity distribution shown in Fig. 3. The overall liquid pressure drop for the disk-shaped heat pipe is a little larger than that of the square flat-plate heat pipe. This is because of the convergence of the liquid flow channel, which leads to a larger capillary pressure head for the disk-shaped heat pipe. The simplified analytical solution for  $Re_h = 1000$  is also shown in this figure.

Figure 5 shows the vapor temperature distribution along the heat pipes. The temperature distribution is given relative to the saturation temperature  $T_{0v}^+$ , which is the temperature when the effect of the vapor pressure drop is neglected, in the form of  $\Delta T_v^+ = T_v^+ - T_{0v}^+$ . As shown in Fig. 5, there is a vapor temperature drop in the evaporator region and a temperature recovery in the condenser region due to the effect of vapor pressure drop. This is consistent with the numerical and experimental results of conventional cylindrical heat pipes reported by Tien and Rohani (1974) and Busse (1973). For both disk-shaped and square flat-plate heat pipes, the vapor temperature is quite uniform ( $\Delta T \ll 1^\circ\text{C}$ ). This demonstrates the successful operation of both of these heat pipes for high input heat fluxes encountered in such applications as that of BNCT.

Figure 6 shows the effects of variations in the thickness of the wick and the vapor channel as well as the overall thickness of the heat pipe on the maximum heat input power that can be transferred per unit surface area by both types of heat pipes. In this figure as well as in Fig. 7,  $A_{\text{total}}$  refers to the total external area of each heat pipe and  $h_{\text{total}}$  is the thickness of each heat pipe,  $h_{\text{total}} = h + 2h_w$ . Figure 6(a) presents  $Q_{\text{max}}/A_{\text{total}}$  as a function of the wick thickness, while Fig. 6(b) shows  $Q_{\text{max}}/A_{\text{total}}$  as a function of the vapor channel thickness. Figure 6(c) shows  $Q_{\text{max}}/A_{\text{total}}$  as a function of the total thickness of the heat pipe,  $h_{\text{total}}$ . As expected,  $Q_{\text{max}}/A_{\text{total}}$  increases with an increase in  $h_{\text{total}}$  for a fixed value of  $h_w/h_{\text{total}}$ . In both Figs. 6(a) and 6(b),  $h_{\text{total}}$  is fixed as a constant for both types of heat pipe. It should be noted that the results in Figs. 6(a) and 6(b) were calculated independently. As seen in Fig. 6, there is an optimum value of  $h_w/h_{\text{total}}$  [Fig. 6(a)]

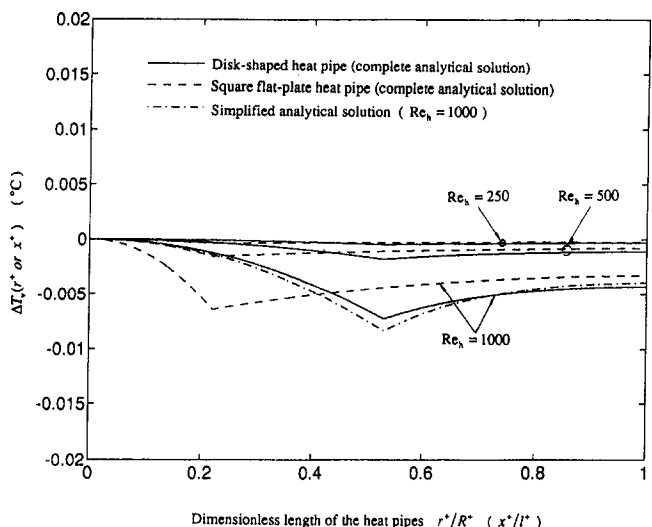


Fig. 5 Vapor temperature distributions for both disk-shaped and square flat-plate heat pipes

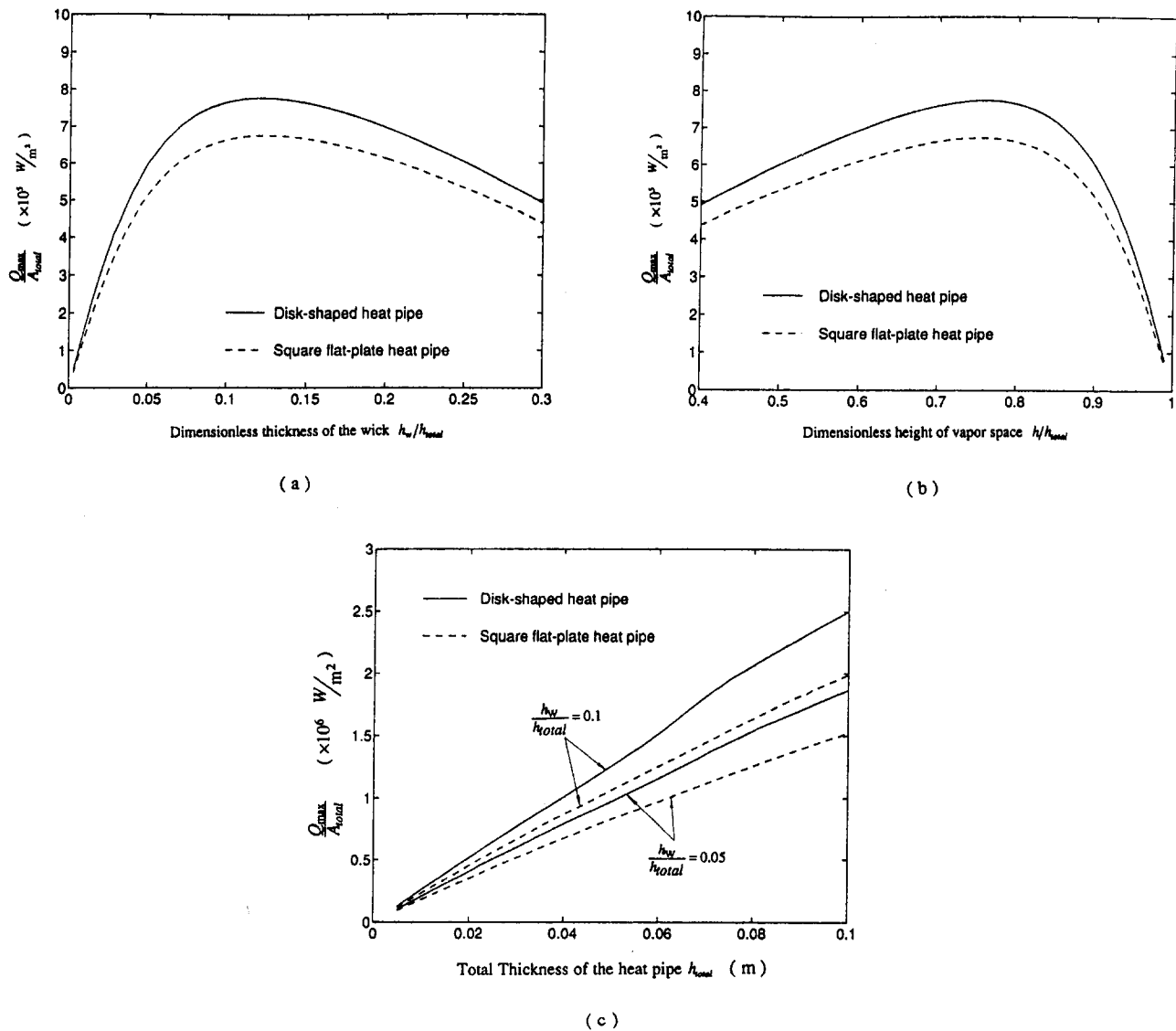


Fig. 6 Variations of maximum heat transfer per unit surface area as a function of (a) wick thickness, (b) thickness of the vapor space, (c) total thickness of the heat pipe

and an optimum value of  $h/h_{\text{total}}$  [Fig. 6(b)] at which  $Q_{\max}/A_{\text{total}}$  reaches its maximum value. The values of  $h_w$  in these two optimum cases are exactly the same ( $h_w = 0.12h_{\text{total}}$ ), and the difference between the corresponding values of  $Q_{\max}/A_{\text{total}}$  from each figure is less than 0.001 percent. This demonstrates that for a given heat pipe thickness there exists a wick thickness relating to the optimum performance of the disk-shaped or flat-plate heat pipe.

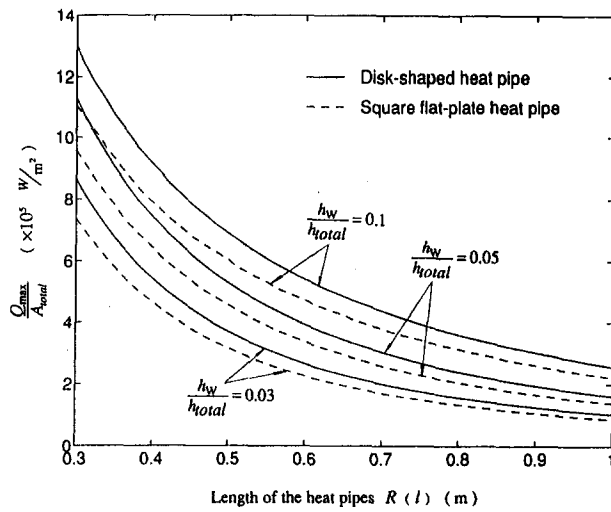
Figure 7 shows the maximum heat transfer per unit surface area as a function of the total length of each type of heat pipe while  $h_{\text{total}}$  is fixed as a constant. As seen in Fig. 7(a),  $Q_{\max}/A_{\text{total}}$  increases as  $h_w/h_{\text{total}}$  increases. However, after  $h_w/h_{\text{total}}$  reaches a certain value,  $Q_{\max}/A_{\text{total}}$  decreases as  $h_w/h_{\text{total}}$  increases [Fig. 7(b)]. This reconfirms that there is an optimum wick thickness, which gives the maximum  $Q_{\max}/A_{\text{total}}$  for both disk-shaped and square flat-plate heat pipes, as demonstrated in Figs. 6(a) and 6(b). Furthermore, it can be seen that for any length heat pipe the  $Q_{\max}/A_{\text{total}}$  of the disk-shaped heat pipe is about 20 percent larger than that of the square flat-plate heat pipe, despite the smaller total external surface area of the disk-shaped heat pipe compared to that of the square flat-plate heat pipe.

The simplified analytical solution for the disk-shaped heat pipe is also presented (Figs. 3, 4, and 5). It can be seen that there is

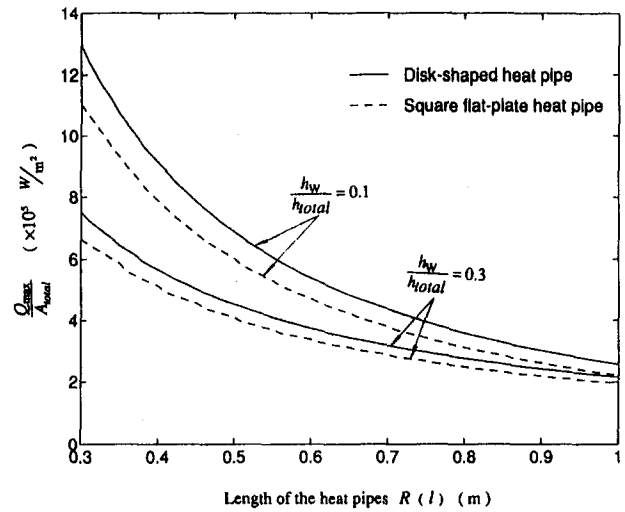
a relatively good agreement between the simplified analytical solution and the complete analytical solution for large injection Reynolds numbers. It should be noted that this simplified analytical solution does neglect some physical features. Nevertheless, it does provide us with a reasonable expression over a good portion of the heat pipe.

### Conclusions

The vapor and liquid velocity and pressure distributions in an asymmetric disk-shaped heat pipe have been analyzed in depth in this work and analytical solutions for these quantities have been presented. The conceptual design and intrawick interactions for the disk-shaped heat pipe have been investigated in detail. The overall performance of both disk-shaped and square flat-plate heat pipes and the factors limiting their performance have been analyzed and the maximum heat transfer capability for both types of heat pipes with different sizes have been established. The effects of variations in the wick thickness and the vapor channel thickness as well as the overall thickness of the heat pipe on the performance of both types of heat pipes have been analyzed. The results show that the disk-shaped heat pipe, while utilizing a smaller surface area, significantly increases the heat transfer capability compared to the flat-plate heat pipe.



(a)



(b)

Fig. 7 Variations of maximum heat transfer per unit surface area as a function of the total length of the heat pipe

## References

- Bankston, C. A., and Smith, H. J., 1973, "Vapor Flow in Cylindrical Heat Pipes," *ASME JOURNAL OF HEAT TRANSFER*, Vol. 95, pp. 371-376.
- Busse, C. A., 1973, "Theory of the Ultimate Heat Transfer Limit of Cylindrical Heat Pipes," *Int. J. Heat Mass Transfer*, Vol. 16, pp. 169-186.
- Chen, M. M., and Faghri, A., 1990, "An Analysis of the Vapor Flow and the Heat Conduction Through the Liquid-Wick and Pipe Wall in a Heat Pipe With Single or Multiple Heat Sources," *Int. J. Heat Mass Transfer*, Vol. 33, pp. 1945-1955.
- Chi, S. W., 1976, *Heat Pipe Theory and Practice*, McGraw-Hill, New York, pp. 89-95.
- Dunn, P. D., and Reay, D. A., 1982, *Heat Pipes*, 3rd ed., Pergamon Press, New York.
- Faghri, A., 1986, "Vapor Flow Analysis in a Double-Walled Concentric Heat Pipe," *Numerical Heat Transfer*, Vol. 10, pp. 583-595.
- Horner-Richardson, K. D., 1991, "Heat Pipe Furnace Element and Epitaxy Susceptor Development," *Thermacore, Inc. Final Report to Electronic Systems Division*, Air Force Systems Command, USAF, Hanscom AFB, MA017311.
- Ivanovskii, M. N., Sorokin, I. V., 1982, *The Physical Principles of Heat Pipes*, Clarendon Press, Oxford-New York.
- Maezawa, S., Suzuki, Y., and Tsuchida, A., 1981, "Heat Transfer Characteristics of Disk-Shaped Rotating, Wickless Heat Pipe," *Proc. IV Int. Heat Pipe Conference*, Pergamon Press, Oxford, United Kingdom, pp. 725-733.
- Narayana, K. B., 1986, "Vapor Flow Characteristics of Slender Cylindrical Heat Pipes—a Numerical Approach," *Numerical Heat Transfer*, Vol. 10, pp. 79-93.
- Ooijen, H., and Hoogendoorn, C. J., 1979, "Vapor Flow Calculations in a Flat-Plate Heat Pipe," *AIAA Journal*, Vol. 17, pp. 1251-1259.
- Rosenfeld, J. H., 1987, "Modeling of Heat Transfer Into a Heat Pipe for a Localized Heat Input Zone," *AIChE Symposium Series*, No. 257, Vol. 83, pp. 71-76.
- Sorour, M. M., Hassab, M. A., and Estafanous, S., 1987, "Developing Laminar Flow in a Semi-porous Two Dimensional Channel With Nonuniform Transpiration," *Int. J. Heat Fluid Flow*, Vol. 8, pp. 44-53.
- Tien, C. L., and Rohani, A. R., 1974, "Analysis of the Effect of Vapor Pressure Drop on Heat Pipe Performance," *Int. J. Heat Mass Transfer*, Vol. 17, pp. 61-67.
- Tien, C. L., 1975, "Fluid Mechanics of Heat Pipes," *Annular Review of Fluid Mechanics*, Vol. 7, pp. 167-185.
- Tien, C. L., and Vafai, K., 1989, "Convective and Radiative Heat Transfer in Porous Media," *Advances in Applied Mechanics*, Vol. 27, pp. 225-282.
- Vafai, K., and Tien, C. L., 1981, "Boundary and Inertia Effects on Flow and Heat Transfer in Porous Media," *Int. J. Heat Mass Transfer*, Vol. 24, pp. 195-203.
- Vafai, K., and Wang, W., 1992, "Analysis of Flow and Heat Transfer Characteristics of an Asymmetrical Flat Plate Heat Pipe," *Int. J. Heat Mass Transfer*, Vol. 35, pp. 2087-2099.
- Winter, E. R. F., and Barsch, W. O., 1971, "The Heat Pipe," *Advances in Heat Transfer*, Vol. 7, pp. 219-320.

This section contains shorter technical papers. These shorter papers will be subjected to the same review process as that for full papers.

## Heat Conduction in an Energy-Generating Slab Subject to a Nonuniform Heat Transfer Coefficient

G. F. Jones,<sup>1</sup> E. V. McAssey, Jr.,<sup>1</sup> and  
B. W. Yang<sup>2</sup>

### Nomenclature

- $A$  = aspect ratio =  $H/d$   
 $Bi$  = Biot number =  $hd/k$   
 $d$  = thickness of slab, m  
 $h$  = heat transfer coefficient,  $Wm^{-2} K^{-1}$   
 $H$  = length, m  
 $k$  = thermal conductivity,  $Wm^{-1} K^{-1}$   
 $p$  = exponent, Eq. (13)  
 $q'''$  = rate of energy generation,  $Wm^{-3}$   
 $t$  = length of insulated region of slab, m  
 $T$  = temperature, K  
 $x, y$  = coordinates, m  
 $\beta$  = ratio =  $H/H_v$   
 $\eta$  =  $x/d$   
 $\xi$  =  $y/d$   
 $\phi$  = dimensionless temperature, Eq. (7)

### Subscripts

- 0 = asymptotic limit  
 $v$  = distance over which  $h$  changes  
 $\infty$  = bulk fluid

### Introduction

This note describes an analytical investigation conducted to explain experimental results obtained during flow boiling tests in an electrically heated vertical annulus. At low pressures ( $<1500$  kPa), Ledinegg flow instability (Lahey and Moody, 1973) is generally the limiting parameter in the operation of a heated channel. The present experimental program was undertaken to establish the flow limit for a vertical annulus under subcooled-boiling conditions with downflow. Tests were conducted in chan-

nels with and without internal insulating ribs. The ribs positioned the annular section and divided the annulus into subchannels. Heat input to the channel was accomplished by DC heating of the channel walls. The tests without ribs yielded flow-instability flow rate limits in agreement with earlier single tube results (Dougherty et al., 1990). However, the addition of internal ribs resulted in the occurrence of unexpected critical heat flux (CHF) events.

Ledinegg (or excursive) flow instability occurs at the minimum point of the pressure drop-velocity curve (onset of flow instability point). The experimental program was undertaken to determine the onset of flow instability (OFI) flow rate as a function of operating parameters such as surface heat flux, inlet temperature, and exit pressure. Data were obtained for both single tube and annular test sections (Yang et al., 1994). Figure 1 presents the results for the annular test section both with and without ribs. For the ribless test section, the channel geometry was maintained by pins mounted on the inner tube. For the ribbed test section, nonconducting rectangular ribs were mounted on the inner tube. The results for both configurations agreed fairly well. For the ribbed test section, the OFI velocity occurred at a slightly higher value for the same operating conditions than the ribless tests. The major difference between these test sections was the fact that three CHF points were recorded. Two of these points at fluxes of  $1.5 MW/m^2$  and  $1.89 MW/m^2$  (see Fig. 1) also corresponded to OFI points. The point at  $1.5 MW/m^2$  surface heat flux destroyed the test section. CHF predictions (Knoebel et al., 1971) based upon ribless data indicated that a CHF margin of almost 180 percent existed for these operating conditions. Since these data directly related to reactor safety, it was imperative that the results be explained.

Test data showed that the overheating was not caused by flow maldistribution or changes in test section geometry. The latter

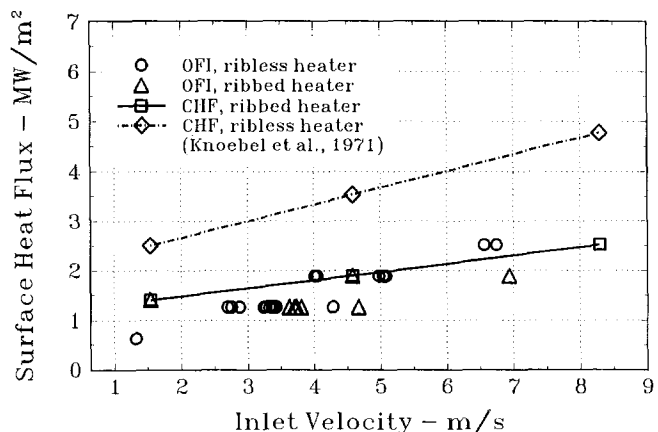


Fig. 1 Heater flux versus velocity for OFI and CHF points

<sup>1</sup> Villanova University, Villanova, PA 19085.

<sup>2</sup> Columbia University, New York, NY 10027.

Contributed by the Heat Transfer Division of THE AMERICAN SOCIETY OF MECHANICAL ENGINEERS. Manuscript received by the Heat Transfer Division February 1994; revision received July 1994. Keywords: Boiling, Conduction, Flow Instability. Associate Technical Editor: Y. Bayazitoglu.

result was verified by x-ray examination and a fiber optic probe. In the region under the rib, the gap was very small so that effective cooling of the heater was greatly reduced. In addition, the junction between the rib and heater at the rib root and tip created a low-velocity region in which the heat transfer coefficient was reduced. Therefore, the cause of the overheating was primarily due to rib blockage and flow stagnation. These factors resulted in a locally high heat flux ("flux peak") even though the electrical dissipation in the heater was uniform. The magnitude of this peaking has been investigated using an analytical model of the test article.

### Analytical Model

Since the heater tube thickness is small compared with its radius of curvature and since each heater is axially symmetric, either tube wall can be represented by a two-dimensional slab with generation as shown in Fig. 2. In this figure, the heater is represented by a slab of length equal to one eighth of the heater circumference. The steady-state, constant property, heat conduction equation for the slab is given by

$$\frac{\partial^2 T}{\partial x^2} + \frac{\partial^2 T}{\partial y^2} + \frac{q'''}{k} = 0 \quad (1)$$

The boundary conditions are given by

$$\left. \frac{\partial T}{\partial x} \right|_{x=-t} = \left. \frac{\partial T}{\partial x} \right|_{x=H} = \left. \frac{\partial T}{\partial y} \right|_{y=0} = 0 \quad (2)$$

$$-k \left. \frac{\partial T}{\partial y} \right|_{y=d} = 0, \quad -t \leq x < 0,$$

$$-k \left. \frac{\partial T}{\partial y} \right|_{y=d} = h(x)(T(x, d) - T_\infty), \quad 0 \leq x \leq H \quad (3)$$

In Eq. (2), the boundary conditions at  $x = -t$  and  $x = H$  are based upon symmetry. At  $y = 0$ , the surface is insulated. The adiabatic condition given in Eq. (3) is based upon the assumption of negligible convection under the fin. A series solution for Eq. (1) was obtained because of the anticipated need to conduct parametric studies. Unfortunately, because of the large difference in size between  $t$  and  $H$ , the solution exhibited stiff characteristics. To improve the solution, the boundary conditions in the region  $0 \leq x \leq H$  were modified as follows:

$$\left. \frac{\partial T}{\partial x} \right|_{x=H} = \left. \frac{\partial T}{\partial y} \right|_{y=0} = 0, \quad T(0, y) = T_1(y) \quad (4)$$

$$-k \left. \frac{\partial T}{\partial y} \right|_{y=d} = h(x)(T(x, d) - T_\infty) \quad (5)$$

In Eq. (4),  $T_1(y)$  is an unknown temperature distribution along the line  $x = 0$ . In the region under the rib, the temperature distribution is essentially a function of  $x$ . Far from the rib, in the region of constant  $h$ , the temperature is independent of  $x$ . A consequence of variable  $h$  is that if  $dh/dx$  near  $x = 0$  is small, the temperature gradients in the  $y$  direction in the neighborhood of  $x = 0$  may be negligible compared to those in the  $x$  direction. With  $T_1$  constant along  $x = 0$ , the solution is simplified since only a single Fourier series is required. This assumption is verified by comparing results with a full two-dimensional solution for several important cases. The value of  $T_1$  is determined by matching the temperature and heat flux in the  $x$  direction along  $x = 0$  for the regions  $-t \leq x \leq 0$  and  $0 \leq x \leq H$ .

The dimensionless form of the governing equation becomes

$$\frac{\partial^2 \phi}{\partial \eta^2} + \frac{\partial^2 \phi}{\partial \xi^2} + 1 = 0, \quad (6)$$

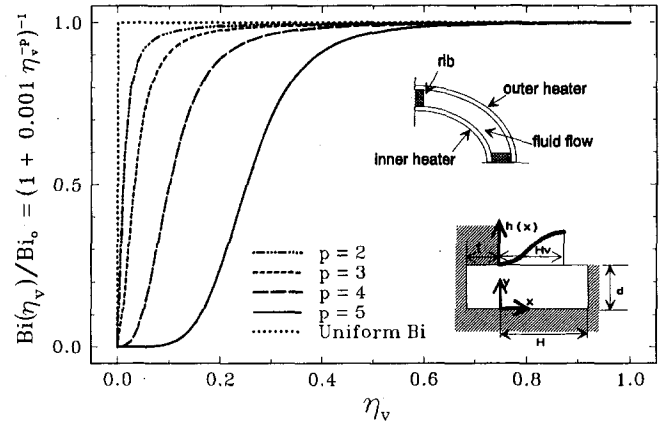


Fig. 2 The function  $Bi(\eta_v)$ ; geometry is shown as an inset

where

$$\phi = \frac{T - T_1}{q'''d^2/k}, \quad \eta = \frac{x}{d}, \quad \xi = \frac{y}{d}. \quad (7)$$

The boundary conditions are written in dimensionless form as

$$\left. \frac{\partial \phi}{\partial \eta} \right|_{\eta=A} = 0, \quad \phi(0, \xi) = 0, \quad (8)$$

and

$$\left. \frac{\partial \phi}{\partial \xi} \right|_{\xi=0} = 0, \quad \left. \frac{\partial \phi}{\partial \xi} \right|_{\xi=1} + Bi(\eta)\phi(\eta, 1) = Bi(\eta)\phi_\infty, \quad (9)$$

where

$$\phi_\infty = \frac{(T_\infty - T_1)}{q'''d^2/k}, \quad A = \frac{H}{d}. \quad (10)$$

For large  $\eta$ ,  $\partial^2 \phi / \partial \eta^2$  in Eq. (6) is of the order  $\eta^{-2}$ . With negligible conduction in the  $\eta$  direction, Eq. (6) becomes an ordinary differential equation, and with the boundary conditions given above, has a solution given by

$$\frac{T(\eta, \xi) - T_\infty}{q'''d^2/k} = \frac{1 - \xi^2}{2} + \frac{1}{Bi(\eta)} \quad (11)$$

For  $\eta$  not large, Eq. (6) can be solved by classical methods (cf. Ma et al., 1991) to yield

$$\begin{aligned} \phi(\eta_v, \xi) = & A_v^2 \left( \beta \eta_v - \frac{\eta_v^2}{2} \right) + \sum_{n=0}^{\infty} B_n \cosh \left[ \left( n + 1/2 \right) \pi \frac{\xi}{\beta A_v} \right] \\ & \times \sin \left[ \left( n + 1/2 \right) \pi \frac{\eta_v}{\beta} \right], \\ & 0 \leq \eta_v \leq \beta, \quad 0 \leq \xi \leq 1, \quad (12) \end{aligned}$$

which satisfies Eq. (8) and the first of Eqs. (9). In Eq. (12), a new dimensionless  $x$  coordinate appears,  $\eta_v = x/H_v$ , since  $H_v$  is the correct length scale for conduction in the  $x$  direction for  $x$  not large. The term  $\beta = A/A_v$ , which relates the slab length to the length scale for the change in  $h$ , is greater than or equal to unity. The function  $Bi(\eta_v)$  is given by Eq. (13) (see Fig. 2).  $Bi(\eta_v)$  approaches  $Bi_0 = h_0 d/k$ , to within 0.1 percent at  $\eta_v = 1$ .

$$Bi(\eta_v)/Bi_0 = (1 + 0.001\eta_v^2)^{-1}, \quad (13)$$

The coefficients  $B_n$  in Eq. (12) are obtained by applying the second of Eqs. (9), which is the boundary condition at  $y = d$ . An equation for the unknown temperature,  $\phi_\infty$ , is obtained by writing the integral form of the heat conduction equation for the

slab over the range  $-t \leq x \leq H$ . This results in a system of  $N + 1$  equations for  $\phi_\infty$  and the  $N$  values of  $B_n$ . Once the temperature distribution,  $\phi(\eta_v, \xi)$ , is evaluated from Eq. (12), the heat flux at the surface ( $y = d$ ) is given by

$$\frac{q(\eta_v)}{q''d} = \text{Bi}(\eta_v)[\phi(\eta_v, 1) - \phi_\infty] \quad (14)$$

### Results and Discussion

The system of equations describing the problem contains five dimensionless parameters,  $A_v$ ,  $\beta$ ,  $\text{Bi}_0$ ,  $p$ , and  $t/d$ . To illustrate the solution, the values of parameters  $A_v$ ,  $t/d$ ,  $\text{Bi}_0$  were taken as 5–10, 0.48, and 6.1, respectively, based on data reported for a series of flow boiling experiments (Yang et al., 1994). The parameter  $p$  is selected from a range of 2 to 5, the former value representing a large rate of change of  $h(x)$  near  $x = 0$  and the latter small.

The system of equations was solved using LU decomposition (Carnahan et al., 1969). For cases with  $\beta = 1$ ,  $N$  of 40 was sufficient to insure convergence to better than three significant figures. For those cases where  $\beta > 1$ ,  $N$  of 60 was needed for the same precision because of the larger length of the domain. To test the validity of the assumption of uniform  $T_1$  at  $x = 0$ , a full two-dimensional solution was obtained using second-order finite differences for all internal and boundary nodes. Typically, 15 nodes were used over the width  $d$  and 121 over the length  $H$ . Larger numbers of nodes were tested and found to affect the solution by less than a percent. Table 1 presents a comparison of results at  $\eta = 0$  for a range of parameters. From this table, it can be seen that the assumption is reasonable.

Figure 3 presents dimensionless heat flux distributions for the full range of the  $p$  parameter,  $A_v$  of 5 and 10, and  $\beta$  of 1 and 1.5. All the heat flux curves possess maxima ("flux peaks") as a consequence of the monotonically increasing  $\text{Bi}$  and monotonically decreasing  $\phi$  in Eq. (14). Figure 3(a, c, d) also presents a comparison of the peaks obtained from the full two-dimensional results (finite difference solution). As with Table 1, the agreement is quite good.

**Table 1 A comparison of solution methods**

$A_v$	$\beta$	$p$	Analytical Results	Full 2D Results (Finite Difference Solution)		
			$\frac{(T_1 - T_\infty)}{q''d^2/k}$	$\frac{(T(0,0) - T_\infty)}{q''d^2/k}$	$\frac{(T(0,d/2) - T_\infty)}{q''d^2/k}$	$\frac{(T(0,d) - T_\infty)}{q''d^2/k}$
5	1.0	2	0.898	1.04	0.961	0.786
5	1.0	3	1.28	1.36	1.30	1.22
5	1.0	4	1.79	1.82	1.79	1.75
10	1.5	2	0.953	1.09	1.02	0.872
10	1.5	3	1.45	1.52	1.48	1.42
10	1.5	4	2.16	2.20	2.17	2.15

For all cases, the flux peak varies between 1.6 and 2.0 depending upon the values of  $p$ ,  $A_v$ , and  $\beta$ . Figure 3(b) shows that the constant  $h$  case yields a peak of approximately 2.75. Although sufficient instrumentation was not available to determine flux distributions around the annulus, in three cases local flux peaks were high enough to cause CHF events. These events were identified by either temperature excursions or physical failure of the test section. Figure 3(a) shows the band of experimental peak flux data. Figure 1 presents data showing the variation of surface heat flux at the flow instability point versus test inlet velocity. In this figure, the three cases in which CHF occurred are also identified. Figure 1 also presents (dotted line) theoretical predictions of CHF based upon Knoebel et al. (1971). For each case, the actual flux would have to be approximately 1.8 times the applied flux in order to achieve the CHF. This magnitude of flux is in agreement with the results in Fig. 3. It can also be seen from Fig. 1 that a flux peaking of 2.75, predicted by the constant heat transfer coefficient model, would have resulted in many more CHF events, which was not the case.

In summary, a solution has been developed that considers the effect of ribs on an otherwise uniform flux distribution along a convectively cooled surface. Predictions from the solution agree with limited experimental data. In particular, the heat transfer

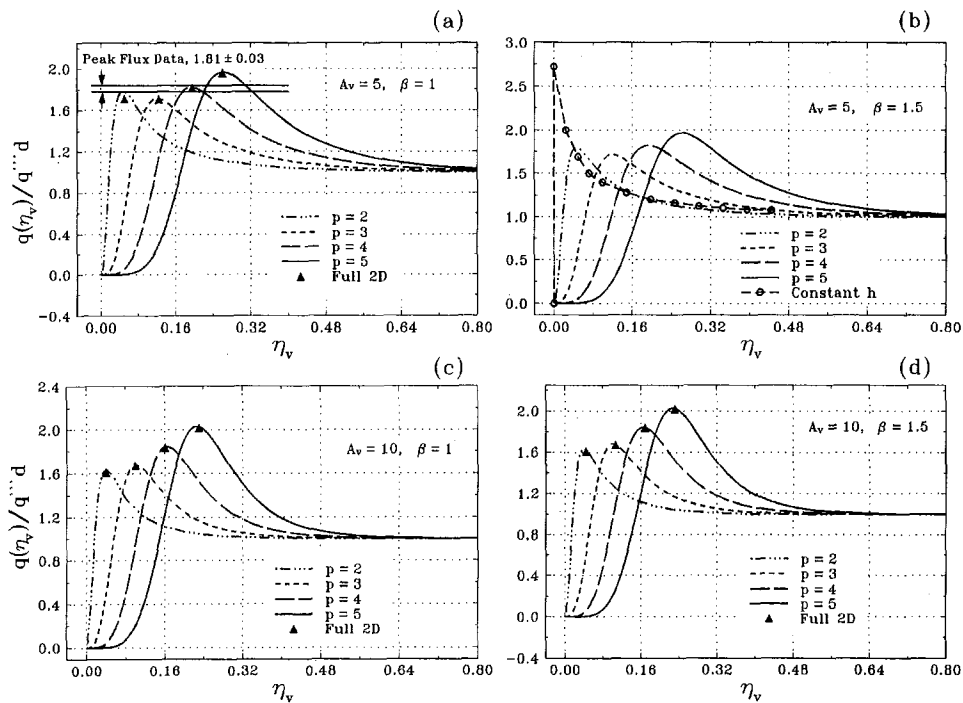


**Fig. 3 Heat flux distribution for  $\text{Bi}_0 = 6.1$  and  $t/d = 0.48$ . Full two-dimensional and constant  $h$  solution are numerical (this work), and data are from Yang et al. (1994).**



coefficient is appropriately modeled by Eq. (13) where  $p$  ranges from about 2 to 4 for the cases studied.

## References

- Carnahan, B., Luther, H. A., and Wilkes, J. O., 1969, *Applied Numerical Methods*, Wiley, New York.
- Dougherty, T., Fighetti, C., Reddy, G., Yang, B., Jafri, T., McAssey, E., and Qureshi, Z., 1990, "Flow Boiling in Vertical Down-Flow," *Proceedings of the Ninth International Heat Transfer Conference*, Jerusalem, Israel, Vol. 2.
- Knoebel, D. H., Harris, S. D., and Biderman, R. M. 1971, "Forced Convection Subcooled Critical Heat Flux," 12th National Heat Transfer Conference, Tulsa, OK.
- Lahey, R. T., and Moody, F. J., 1973, *The Thermal Hydraulics of a Boiling Water Reactor*, The American Nuclear Society, Hinsdale, IL.
- Ma, S. W., Behbahani, A. I., and Tsuei, Y. G., 1991, "Two-Dimensional Rectangular Fin With Variable Heat Transfer Coefficient," *Int. J. Heat Mass Transfer*, Vol. 34, 79-85.
- Yang, B. W., Dougherty, T., Fighetti, C., Kokolis, S., Reddy, G. D., McAssey, E. V., and Coutts, A., 1994, "Flow Instability and Critical Heat Flux in a Ribbed Annulus," *Proceedings of the Tenth International Heat Transfer Conference*, Brighton, United Kingdom.

## Heat Transfer Across a Bilayer Composite Cylinder With Partial Debonding

C. Y. Wang<sup>1</sup>

### Nomenclature

- $a$  = normalized inner radius  
 $A$  = constant coefficient  
 $b$  = normalized interface radius  
 $B$  = constant coefficient  
 $h$  = mean convection constant  
 $H$  = function defined by Eq. (13)  
 $h_{int}$  = interface heat transfer coefficient  
 $J$  = function defined by Eq. (15)  
 $k$  = thermal conductivity  
 $n, N$  = integers  
 $q$  = heat flux  
 $r$  = radial coordinate  
 $R$  = outer radius  
 $T$  = temperature  
 $T_\infty$  = ambient temperature  
 $T_{01}, T_{02}$  = solution without debonding  
 $\alpha = k_1/k_2$   
 $\beta = Rh_{int}/k_2$   
 $\gamma = k_2/Rh$   
 $\delta$  = half debonding angle  
 $\theta$  = cylindrical coordinate  
 $'$  = dimensional quantity  
 $( )_{1,2}$  = inner and outer regions

### Introduction

Bilayer composite sheathing has definite advantages. Since each layer is in contact with a different medium, their properties may be selected to suit the different requirements of each me-

<sup>1</sup> Institute of Applied Mechanics, Taiwan University, Taipei, Taiwan; permanent address: Michigan State University, East Lansing, MI.

Contributed by the Heat Transfer Division of THE AMERICAN SOCIETY OF MECHANICAL ENGINEERS. Manuscript received by the Heat Transfer Division September 1993; revision received March 1994. Keywords: Conduction. Associate Technical Editor: L. S. Fletcher.

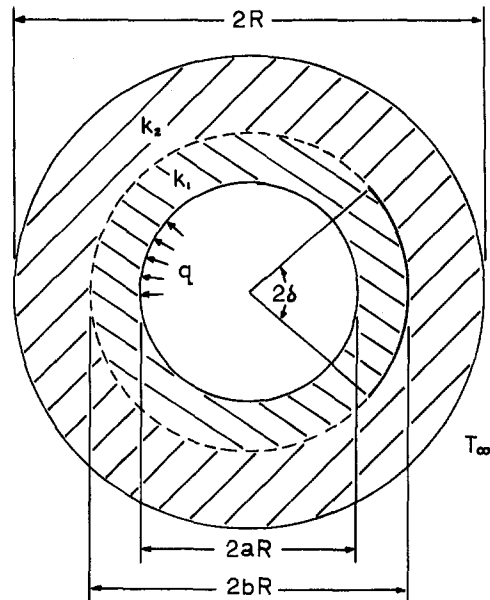


Fig. 1 Cross section of a debonded bilayer cylinder

dium. In certain cases partial debonding may occur, perhaps due to physical stress or some manufacturing defect. Figure 1 shows the cross section of a bilayer cylinder with partial debonding. The problem is two dimensional with mixed boundary conditions. The purpose of the present study is to examine the thermal effects of partial debonding, which has not been investigated before, through a highly efficient eigenfunction and point-match method.

The interface is assumed to be perfectly bonded except for a completely separated or debonded gap (Fig. 1). Across the gap the heat flux is proportional to the temperature difference (Schneider, 1985)

$$\frac{k_1}{R} \frac{\partial T'_1}{\partial r} = \frac{k_2}{R} \frac{\partial T'_2}{\partial r} = -h_{int}(T'_1 - T'_2) \quad (1)$$

Although there exist more sophisticated models for the contact region of compound cylinders (Madhusadana, 1986; Lemczyk and Yovanovich, 1987), in the present study we use a simpler model to illustrate the method. We assume the heat loss across the outer surface is through convection or low-level radiation:

$$-\frac{k_2}{R} \frac{\partial T'_2}{\partial r} = h(T'_2 - T_\infty) \quad (2)$$

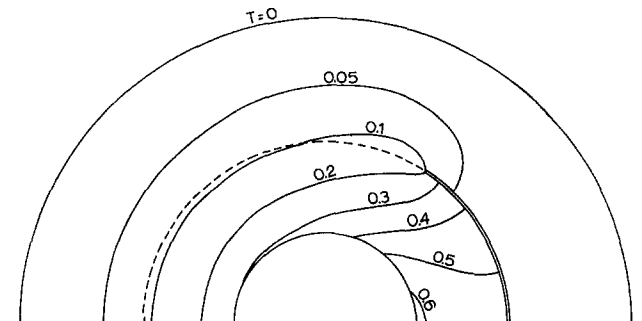


Fig. 2 Typical isotherms,  $a = 0.3, b = 0.6, \alpha = 0.5, \beta = \gamma = 0, \delta = 1$

coefficient is appropriately modeled by Eq. (13) where  $p$  ranges from about 2 to 4 for the cases studied.

## References

- Carnahan, B., Luther, H. A., and Wilkes, J. O., 1969, *Applied Numerical Methods*, Wiley, New York.
- Dougherty, T., Fighetti, C., Reddy, G., Yang, B., Jafri, T., McAssey, E., and Qureshi, Z., 1990, "Flow Boiling in Vertical Down-Flow," *Proceedings of the Ninth International Heat Transfer Conference*, Jerusalem, Israel, Vol. 2.
- Knoebel, D. H., Harris, S. D., and Biderman, R. M. 1971, "Forced Convection Subcooled Critical Heat Flux," 12th National Heat Transfer Conference, Tulsa, OK.
- Lahey, R. T., and Moody, F. J., 1973, *The Thermal Hydraulics of a Boiling Water Reactor*, The American Nuclear Society, Hinsdale, IL.
- Ma, S. W., Behbahani, A. I., and Tsuei, Y. G., 1991, "Two-Dimensional Rectangular Fin With Variable Heat Transfer Coefficient," *Int. J. Heat Mass Transfer*, Vol. 34, 79-85.
- Yang, B. W., Dougherty, T., Fighetti, C., Kokolis, S., Reddy, G. D., McAssey, E. V., and Coutts, A., 1994, "Flow Instability and Critical Heat Flux in a Ribbed Annulus," *Proceedings of the Tenth International Heat Transfer Conference*, Brighton, United Kingdom.

## Heat Transfer Across a Bilayer Composite Cylinder With Partial Debonding

C. Y. Wang<sup>1</sup>

### Nomenclature

- $a$  = normalized inner radius  
 $A$  = constant coefficient  
 $b$  = normalized interface radius  
 $B$  = constant coefficient  
 $h$  = mean convection constant  
 $H$  = function defined by Eq. (13)  
 $h_{int}$  = interface heat transfer coefficient  
 $J$  = function defined by Eq. (15)  
 $k$  = thermal conductivity  
 $n, N$  = integers  
 $q$  = heat flux  
 $r$  = radial coordinate  
 $R$  = outer radius  
 $T$  = temperature  
 $T_\infty$  = ambient temperature  
 $T_{01}, T_{02}$  = solution without debonding  
 $\alpha = k_1/k_2$   
 $\beta = Rh_{int}/k_2$   
 $\gamma = k_2/Rh$   
 $\delta$  = half debonding angle  
 $\theta$  = cylindrical coordinate  
 $'$  = dimensional quantity  
 $( )_{1,2}$  = inner and outer regions

### Introduction

Bilayer composite sheathing has definite advantages. Since each layer is in contact with a different medium, their properties may be selected to suit the different requirements of each me-

<sup>1</sup> Institute of Applied Mechanics, Taiwan University, Taipei, Taiwan; permanent address: Michigan State University, East Lansing, MI.

Contributed by the Heat Transfer Division of THE AMERICAN SOCIETY OF MECHANICAL ENGINEERS. Manuscript received by the Heat Transfer Division September 1993; revision received March 1994. Keywords: Conduction. Associate Technical Editor: L. S. Fletcher.

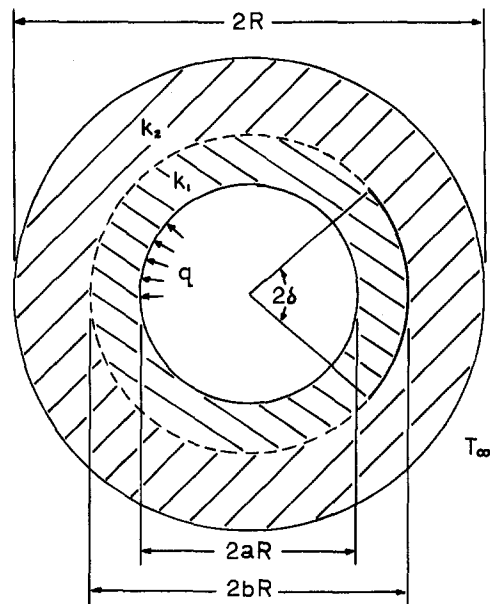


Fig. 1 Cross section of a debonded bilayer cylinder

dium. In certain cases partial debonding may occur, perhaps due to physical stress or some manufacturing defect. Figure 1 shows the cross section of a bilayer cylinder with partial debonding. The problem is two dimensional with mixed boundary conditions. The purpose of the present study is to examine the thermal effects of partial debonding, which has not been investigated before, through a highly efficient eigenfunction and point-match method.

The interface is assumed to be perfectly bonded except for a completely separated or debonded gap (Fig. 1). Across the gap the heat flux is proportional to the temperature difference (Schneider, 1985)

$$\frac{k_1}{R} \frac{\partial T'_1}{\partial r} = \frac{k_2}{R} \frac{\partial T'_2}{\partial r} = -h_{int}(T'_1 - T'_2) \quad (1)$$

Although there exist more sophisticated models for the contact region of compound cylinders (Madhusadana, 1986; Lemczyk and Yovanovich, 1987), in the present study we use a simpler model to illustrate the method. We assume the heat loss across the outer surface is through convection or low-level radiation:

$$-\frac{k_2}{R} \frac{\partial T'_2}{\partial r} = h(T'_2 - T_\infty) \quad (2)$$

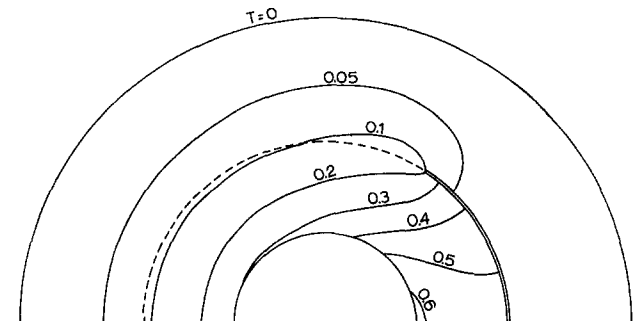


Fig. 2 Typical isotherms,  $a = 0.3, b = 0.6, \alpha = 0.5, \beta = \gamma = 0, \delta = 1$

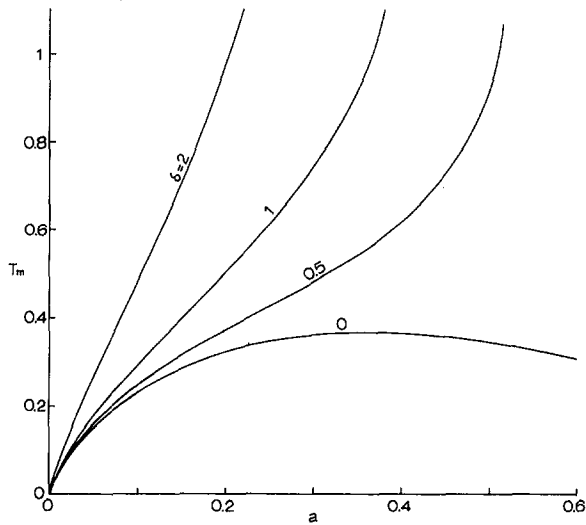


Fig. 3 Effects of  $\delta$  and  $a$  ( $b = 0.6, \alpha = 1, \beta = \gamma = 0$ )

The temperature is normalized by

$$T_i(r, \theta) = \frac{k_1}{qR} (T'_i(r, \theta) - T_\infty) \quad i = 1, 2 \quad (3)$$

The governing equation is then

$$\nabla^2 T_i = 0 \quad i = 1, 2 \quad (4)$$

with the boundary conditions

$$\frac{\partial T_1}{\partial r} \Big|_{r=a} = -1, \quad \gamma \frac{\partial T_2}{\partial r} \Big|_{r=1} + T_2|_{r=1} = 0 \quad (5)$$

Along the interface we have the following mixed conditions:

For  $\delta < \theta \leq \pi$  and  $r = b$ , the temperatures and the heat flux match:

$$T_1 = T_2, \quad \alpha \frac{\partial T_1}{\partial r} = \frac{\partial T_2}{\partial r} \quad (6)$$

For  $0 \leq \theta < \delta$  and  $r = b$ , we have

$$\frac{\partial T_2}{\partial r} = -\beta(T_1 - T_2), \quad \alpha \frac{\partial T_1}{\partial r} = \frac{\partial T_2}{\partial r} \quad (7)$$

Equations (4)–(7) are to be solved with the given parameters  $a, b, \alpha, \beta, \gamma, \delta$ .

First we find the solution without debonding:

$$T_{01}(r) = \alpha a(\gamma - \ln b) - a \ln(r/b),$$

$$T_{02}(r) = \alpha a(\gamma - \ln r) \quad (8)$$

The general solution for the inner layer, satisfying the inner boundary condition, is

$$T_1(r, \theta) = T_{01}(r) + A_0 + \sum_{n=1}^{\infty} A_n \cos(n\theta) \left[ \left(\frac{r}{b}\right)^n + \left(\frac{rb}{a^2}\right)^{-n} \right] \quad (9)$$

Similarly, the general solution for the outer layer, satisfying the outer boundary condition, is

$$T_2(r, \theta) = T_{02}(r) + B_0(\gamma - \ln r) + \sum_{n=1}^{\infty} B_n \cos(n\theta) \left[ (\gamma n - 1)(rb)^n + (\gamma n + 1) \left(\frac{r}{b}\right)^{-n} \right] \quad (10)$$

Using Eqs. (9), (10) and the second interface conditions of Eqs. (6), (7) we find

$$B_0 = 0, \quad A_n = B_n \frac{[(\gamma n - 1)b^{2n} - \gamma n - 1]}{\alpha[1 - (b/a)^{-2n}]} \quad n \neq 0 \quad (11)$$

Then the other interface conditions give the dual series, for  $\delta < \theta \leq \pi$ ,

$$A_0 + \sum_{n=1}^{\infty} B_n \cos(n\theta) H_n = 0 \quad (12)$$

$$H_n = \frac{[(\gamma n - 1)b^{2n} - \gamma n - 1][1 + (b/a)^{-2n}]}{\alpha[1 - (b/a)^{-2n}]} - [(\gamma n - 1)b^{2n} + \gamma n + 1] \quad (13)$$

and for  $0 \leq \theta < \delta$

$$\beta A_0 + \sum_{n=1}^{\infty} B_n \cos(n\theta) J_n = \frac{\alpha a}{b} \quad (14)$$

$$J_n = \beta \frac{[(\gamma n - 1)b^{2n} - \gamma n - 1][1 + (b/a)^{-2n}]}{\alpha[1 - (b/a)^{-2n}]} + \left(\frac{n}{b}\right) [(\gamma n - 1)b^{2n} - \gamma n - 1] - \beta [(\gamma n - 1)b^{2n} + \gamma n + 1] \quad (15)$$

We use point match at  $N$  equally spaced locations along the half interface yielding  $N$  algebraic equations, which are solved for the  $N$  unknowns  $A_0, B_1, \dots, B_{N-1}$ . The error of truncation is determined by comparing the match of  $T_i$  along the interface, which in general is about 3 percent for  $N = 60$ .

Typical isotherms are shown in Fig. 2. Due to debonding, regions of high local temperatures are created near the inside surface. The maximum temperature  $T_m = T_1(a, 0)$  is much higher than the corresponding maximum when debonding is absent. Since  $T_m$  is a function of six parameters,  $a, b, \alpha, \beta, \gamma, \delta$ , a complete tabulation will not be attempted. Figure 3 shows the effects of varying  $\delta$  or  $a$ , keeping other parameters fixed. Note that when  $\delta = 0$  or there is no debonding,  $T_m$  reaches a maximum. This is due to the fact that an increase in  $a$  (the inner radius) increases the amount of heat through increased area, but decreases the temperature through decreased thermal resistance. With debonding, the maximum temperature almost always increases with  $a$ , reaching infinity as  $a \rightarrow b$ . In general  $T_m$  increases with increased  $\alpha$  and  $\gamma$  and decreased  $\beta$  and  $b$ . The effects of  $\alpha, \beta, \gamma$  are about the same order as that of  $T_{01}$ , but if debonding is present and  $a \approx b$ , the temperature increase may reach unacceptable levels.

In conclusion, the eigenfunction and collocation method is well suited for problems with debonding. Finite difference or finite element integrations can be performed, but the amount of computation needed would be more than the square of that used in the present paper.

## References

- Lemczyk, T. P., and Yovanovich, M. M., 1987, "New Models and Methodology for Predicting Thermal Contact Resistance in Compound Cylinders and Finned Tubes," *Heat Trans. Eng.*, Vol. 8, No. 2, pp. 35–48.
- Madhusadana, C. V., 1986, "On Heat Flow Across Cylindrical Joints," *Proc. 8th Int. Heat Trans. Conf.*, Vol. 2, pp. 651–658.
- Schneider, P. J., 1985, "Conduction," in: *Handbook of Heat Transfer*, W. M. Rohsenow, J. P. Hartnett, and E. N. Ganic, eds., McGraw-Hill, New York, Chap. 4.

# Agitation and Heat Transfer Studies in Suspensions

A. Ramasubramanian<sup>1</sup> and S. K. Pandey<sup>2</sup>

## Nomenclature

- $B$  = empirical constant  
 $C_s$  = heat capacity of the suspension at constant pressure,  $J/(kg \cdot K)$   
 $D_i$  = diameter of the impeller, m  
 $h_0$  = outside heat transfer coefficient in suspension,  $W/(m^2 \cdot K)$   
 $K_s$  = thermal conductivity of the suspension,  $W/(m \cdot K)$   
 $N$  = speed of agitation, rpm  
 $Nu$  = Nusselt number  
 $Re$  = Reynolds number  
 $\rho_s$  = density of the suspension,  $kg/m^3$   
 $\mu_s$  = viscosity of the suspension,  $kg/(m \cdot s)$

## Introduction

Agitation of two-phase solid-liquid suspensions inside a cylindrical vessel is carried out in many chemical process industries where it is often necessary to heat or cool such suspensions due to the process requirements. Agitation results in enhanced heat transfer, mass transfer, simultaneous heat and mass transfer, and chemical reaction rates. This finds wide applications in the design of equipment, especially the heterogeneous, solid-liquid stirred reactors in which the reactions are highly exothermic or endothermic by nature. Manufacture of maleic anhydride and sodium fluoride in agitated vessels are examples. Besides, sulfonation reactions are often carried out in agitated vessels with turbine agitators.

Cummings and West (1950) were the first investigators to study the rate of heat transfer from the wall into the agitated slurries. They presented qualitative results based on few measurements and observed a decrease in rate of heat transfer in comparison with heat transfer into pure liquids. Engel and Hougen (1963) hydrolyzed isoamyl acetate dispersed in a large volume of water where the reaction was catalyzed by an acidic ion exchange resin, kept in suspension by rapid stirring in a batch reactor. The overall resistance to hydrolysis was observed to be the sum of the resistance of the liquid surrounding the catalyst particles and the catalyst itself, influenced by the degree of agitation only for the catalyst particles below  $100 \mu m$  diameter. The overall resistance also increased at agitator speeds exceeding 600 rpm and the complete suspension of the catalyst could be attained at agitator speeds of 175 rpm and above. Sohn and Chen (1981) observed the enhancement of effective thermal conductivity in shear flow and dispersed two-phase suspensions as a consequence of microconvection. The two suspensions studied were high-density polyethylene pellets in a liquid mixture of silicone oil and kerosene and polystyrene particles in silicone oil and Freon-113 mixtures. Fundamental equations governing the two-phase solid-liquid systems have been described by Frantisak et

al. (1968) but solution of these analytical expressions for heat transfer to agitated suspensions is practically impossible in the absence of experimental data to calculate diffusion coefficients, Prandtl number, velocity profile, and mixing characteristics for any realistic system. Voncken (1965) has tried to define the fluid flow in mixing systems, but the description is largely qualitative. In the absence of mathematical solutions, dimensional analysis has been used as a tool to define the system variables both by Frantisak et al. (1968) and Ramasubramanian (1990). They have observed a decrease in heat transfer rates with increase in solid particle concentration in suspensions purely on the basis of experimental observations. Shah and Rao (1969) and Trivedi et al. (1975) studied heat transfer in a jacketed, agitated vessel and both the studies have reported an increase in heat transfer rate with increase in solid particle concentration in suspensions. Thus, the literature provides sectorial investigations and little quantitative information, which is also controversial in nature, as mentioned above. Hence, the present investigation aimed to study the effect of impeller speed and solid particle concentration on heat transfer coefficients in suspensions.

## Experimental Apparatus and Procedure

A schematic diagram of the experimental setup is shown in Fig. 1. A flat-bottomed cylindrical vessel of 304 stainless steel having 300 mm i.d. and 450 mm height with hemispherical lid was used as a test vessel. Openings were provided at the top cover for insertion of a copper-constantan thermocouple, a long-necked mercury thermometer, an impeller shaft, the cooling water inlet and outlet, and the test fluid. Agitation was caused by using a six-bladed, flat blade turbine impeller having diameter equal to  $\frac{1}{3}$  of the tank diameter and blade dimensions as  $30 \text{ mm} \times 22 \text{ mm}$ . Impeller speed was varied from 100 to 500 rpm by means of a variable speed d.c. motor provided with a separate control panel. Swirling and vortex formation inside the liquid pool were prevented by using four baffles, each of them having width equal to 30 mm and height equal to 420 mm. These baffles were welded to the inside wall of the test vessel, dividing the periphery into four equal segments.

Two immersion heaters of capacity 2 kW each were fitted at the bottom of the vessel, which provided energy input to the agitated solid-liquid suspension. Energy input to these heaters

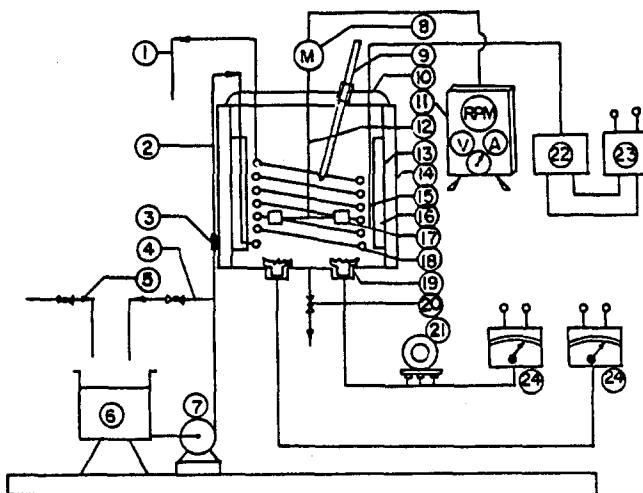


Fig. 1 Schematic diagram of the experimental setup: 1. cooling water outlet; 2. cooling water inlet; 3. rotameter for cooling water; 4. bypass line for flow control; 5. inlet pipe to water tank; 6. water storage tank; 7. centrifugal pump; 8. DC motor for agitator; 9. mercury thermometer; 10. agitated vessel top cover; 11. DC motor control panel; 12. agitator shaft; 13. agitator vessel; 14. thermal insulation layer; 15. copper-constantan thermocouple; 16. baffles; 17. turbine impeller; 18. helical coil of copper; 19. immersion heaters; 20. drain valve; 21. auto transformer; 22. DC voltage stabilizer; 23. AJCO thermocouple calibrator; 24. wattmeters

<sup>1</sup> Formerly M. Tech. student, Department of Chemical Engineering, Regional Engineering College, Tiruchirappalli—620 015, Tamil Nadu, India; presently, Assistant Engineer (Chemical), TATA Consulting Engineers, Bombay—400 025, India.

<sup>2</sup> Assistant Professor, Department of Chemical Engineering, Regional Engineering College, Tiruchirappalli—620 015, Tamil Nadu, India.

Contributed by the Heat Transfer Division of THE AMERICAN SOCIETY OF MECHANICAL ENGINEERS. Manuscript received by the Heat Transfer Division September 1992; revision received January 1994. Keywords: Multiphase Flows, Thermophysical Properties, Turbulence. Associate Technical Editor: R. Viskanta.

**Table 1 Range of experimental variables**

Variable	Range
Speed of agitation, $N$	100–500 rpm
Reynolds number, $D_i^2 N \rho_s / \mu_s$	$2.2 \times 10^4$ – $2.0 \times 10^5$
Prandtl number, $C_s \mu_s / K_s$	3.73–6.42
Weight fraction (solids)	0.02–0.10
Volume fraction (solids)	0.014–0.145
Particle size	–295 to +211 $\mu\text{m}$

was controlled by using auto-transformers and was measured with the help of precision grade wattmeters. A helical coil of six turns was fabricated out of the copper pipe, 9 mm i.d., 12 mm o.d., and 4200 mm length. Average outside coil diameter was 205 mm with 30 mm spacing between the consecutive coil turns. The helical coil was submerged in the pool of solid–liquid suspension and water was circulated through it at room temperature with the help of a centrifugal pump and its flow rate measured by means of a calibrated rotameter. The test vessel was lagged thoroughly with asbestos rope and magnesia powder followed by a layer of glass wool. An energy balance was carried out that indicated negligible energy losses to the surroundings.

Prior to experimental data runs, sand and powdered coal samples were separately subjected to sieve analysis. Particles in the size range –295 to +211  $\mu\text{m}$  were collected in order to minimize the effect of particle size during heat transfer studies in suspensions. Sand and coal particles were dispersed separately in the carrier fluid, water, in the concentration range varying from 0 to 10 wt. percent in increments of 2.0 wt. percent. Each suspension was agitated at constant speed and flow rate of cooling water through the coil and energy input to the suspension was also maintained constant during the period, required by the system to reach thermal equilibrium. Under the steady-state conditions, inlet and outlet water temperatures and the temperature of the suspension close to the top and bottom liquid surfaces were recorded before changing over to the next impeller speed. The difference between the temperatures of the suspension at the top and bottom levels was observed to be insignificant.

**Results and Discussion**

Experimental investigation pertains to the determination of heat transfer characteristics of the suspensions with the variation of agitator speed and concentration of solid particles. Data analysis has been carried out on the basis of one hundred and twenty experimental runs. Several data runs were repeated to check the consistency of results, which represented the data within  $\pm 5$  percent experimental error. Table 1 indicates the range of experimental variables.

**Effect of Agitator Speed.** Heat transfer coefficient was observed to increase with an increase in speed of agitation for all the compositions of sand–water and coal–water suspensions. This is attributed to the fact that higher speed of agitation intensifies the turbulence inside the heat transfer equipment, which leads to the effective transfer of heat. Data analysis suggests the following exponential relationship between Nusselt and Reynolds number:

$$Nu = B(Re)^n$$

The exponent,  $n$ , was found to be 0.7 for both coal–water and sand–water suspensions, which is in good agreement with observations for all the single and two-phase liquid mixtures, as studied by Pandey (1978) during her earlier investigations as well as data for distilled water during the present investigation. The constant  $B$  varies with physicochemical properties of the liquid and it remained constant only for a given composition of solid particles in suspension.

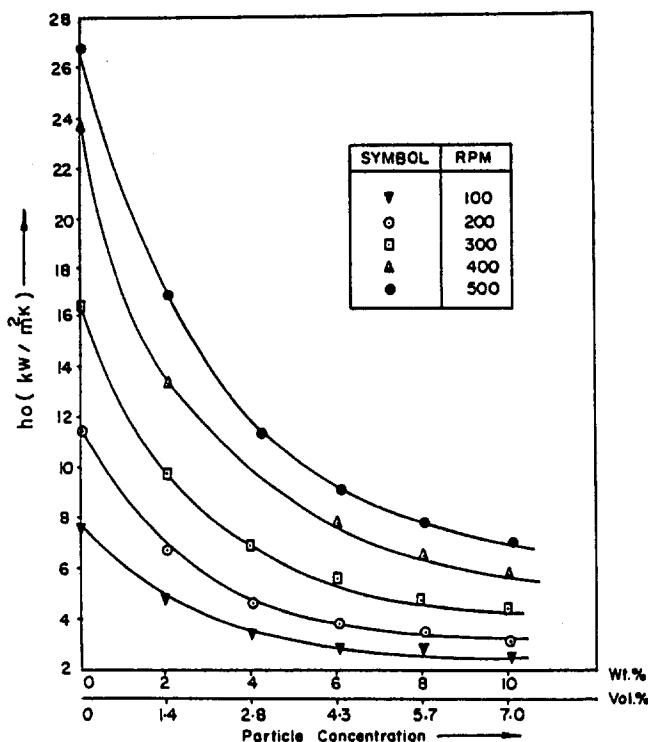


**Fig. 2 Effect of particle concentration on heat transfer coefficient for sand–water suspensions**

**Effect of Particle Concentration.** Figures 2 and 3 represent the variation of heat transfer coefficient,  $h_o$ , with particle concentration in sand–water and coal–water suspensions, respectively. The outside heat transfer coefficients,  $h_o$ , were calculated by accounting all the resistances in the path of heat transfer (Bird

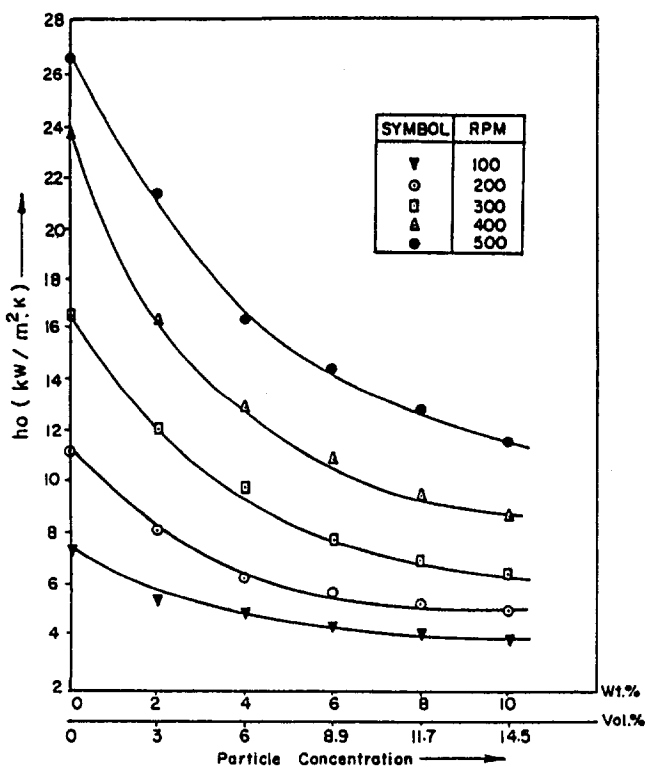


**Fig. 3 Effect of particle concentration on heat transfer coefficient for coal–water suspensions**

et al., 1960). A decrease in heat transfer coefficient has been observed with an increase in solid particle concentration at each speed of the impeller during the current investigations. These results conform with the findings of Cummings and West (1950) and Frantisak et al. (1968) but contradict the results reported by Shah and Rao (1969) and Trivedi et al. (1975). Shah and Rao (1969) and Trivedi et al. (1975) have proposed the strong dependence of heat transfer rate on thermal conductivity of the solid particles in suspension. Since thermal conductivity and heat capacity of both sand and coal particles are less than those of the carrier fluid, an increase in particle concentration is only expected to decrease the net thermal conductivity and heat capacity of the suspension. However, Sohn and Chen (1981) and Chung and Leal (1982) have reported significant enhancement in effective thermal conductivity in low Reynolds number, rotating Couette flow using neutrally buoyant solid–fluid suspensions (these studies were confined to only microconvective effects, which cannot be separated from other effects in case of any two-phase heat transfer process). In addition to this, the viscosity of the suspension would increase with increasing solid concentration and loss in particle velocity would also occur (although loss would be small, due to the solid concentration of less than 10 percent) due to the interparticle friction and any agglomeration. Change in these parameters would cause a decrease in Reynolds number and would offset the effects of turbulence created by agitation.

Conductivity, particle size, and concentration of the suspensions are the most important parameters, deciding the role of particles during heat transfer in suspensions. Further, particle velocity and particle population in any zone of the vessel depend on particle size, density, suspension concentration, and agitator depth at any given speed of agitation. Since all the other conditions for both sand and coal particles in their respective suspensions were kept identical except the particle density, larger particle population of coal (due to its lower density) could increase the frequency of particle collisions among themselves and also with the heat transfer surface. This has caused induced turbulence and an increase in heat transfer rate in case of coal–water suspensions in spite of the lower thermal conductivity of the dry coal in comparison to dry sand. However, no quantitative comparison of the experimental results was possible with the results of the previous researchers as these are the first of their kind for heat transfer studies.

## References

- Bird, R. B., Stewart, W. E., and Lightfoot, E. N., 1960, *Transport Phenomena*, Wiley, New York, p. 393.
- Chung, Y. C., and Leal, L. G., 1982, "An Experimental Study of the Effective Thermal Conductivity of a Sheared Suspension of Rigid Spheres," *Int. J. Multiphase Flow*, Vol. 8, No. 6, pp. 605–625.
- Cummings, G. H., and West, A. S., 1950, "Heat Transfer Data for Kettles With Jackets and Coils," *Industrial and Engineering Chemistry*, Vol. 42, No. 11, pp. 2303–2313.
- Engel, A. J., and Hogen, O. A., 1963, "Mass Transfer and Contactor Efficiency in a Stirred Liquid–Liquid Reactor," *AIChE Journal*, Vol. 9, No. 6, pp. 724–729.
- Frantisak, F., Smith, J. W., and Dohnal, J., 1968, "Heat Transfer to Solid–Liquid Suspensions in an Agitated Vessel," *Industrial & Engineering Chemistry, Process Design and Development*, Vol. 7, No. 2, pp. 188–193.
- Pandey, S. K., 1978, "Heat Transfer Studies for Agitated Liquids," *Chemical Engineering World*, Vol. XIII, No. 9, pp. 47–50.
- Ramasubramanian, A., 1990, "Heat Transfer Studies in Suspensions," M. Tech. Thesis, Dept. of Chemical Engineering, Regional Engineering College, Tiruchirappalli—620 015, India.
- Shah, P. V., and Rao, M. R., 1969, "Heat Transfer to Agitated Suspensions in Baffled Jacketed, Agitated Vessel," *Indian Journal of Technology*, Vol. 7, pp. 166–173.
- Sohn, C. W., and Chen, M. M., 1981, "Microconvective Thermal Conductivity in Disperse Two-Phase Mixtures as Observed in a Low Velocity Couette Flow Experiment," *ASME JOURNAL OF HEAT TRANSFER*, Vol. 103, pp. 47–51.
- Trivedi, R. N., Pandey, G. N., and Tripathi, G., 1975, "Heat Transfer to Solid–Liquid Suspensions in Jacketed Agitated Vessels," *Indian Journal of Technology*, Vol. 13, pp. 53–58.
- Voncken, R. M., 1965, "Homogenization of Miscible Liquids, Part 1," *British Chemical Engineering*, Vol. 10, No. 1, pp. 13–18.

# Three-Fluid Heat Exchanger Effectiveness—Revisited

D. P. Sekulić<sup>1</sup> and I. Kmečko<sup>2</sup>

## Nomenclature

- $A$  = heat transfer surface area, m<sup>2</sup>  
 $c_p$  = specific heat of fluid at constant pressure, J/kg K  
 $C_{j,2}^*$  = heat capacity rate ratio =  $(\dot{m}c_p)_j(\dot{m}c_p)_2^{-1}$ ,  $j = 1$  or  $3$   
 $H$  = enthalpy rate, J/s  
 $i_k$  = fluid stream indicator,  $i_k = \pm 1$ ,  $k = 1, 2$ , or  $3$   
 $L$  = heat exchanger length, m  
 $\dot{m}$  = mass flow rate, kg/s  
NTU = number of heat transfer units =  $(UA)_{1,2}(\dot{m}c_p)_1^{-1}$   
 $\dot{Q}$  = heat transfer rate, W  
 $R^*$  = conductance ratio =  $(UA)_{23}(UA)_{1,2}^{-1}$   
 $T$  = temperature, K  
 $U$  = overall heat transfer coefficient, W/m<sup>2</sup> K  
 $x$  = Cartesian axial coordinate, m  
 $\epsilon$  = heat exchanger effectiveness as defined in Eq. (4)  
 $\vartheta_{1(3)}$  = temperature effectiveness =  $(T_{1(3),out} - T_{1(3),in})(T_{2,in} - T_{1(3),in})^{-1}$   
 $\xi$  = dimensionless coordinate =  $x/L$   
 $\Theta_k$  = dimensionless temperature =  $(T_k - T_{1,in})(T_{2,in} - T_{1,in})^{-1}$ ,  $k = 1, 2$ , or  $3$

## Subscripts

- 1, 2, 3 = streams 1, 2, or 3  
in = inlet  
max = maximum value  
out = outlet

## Superscripts

- = dimensionless quantity  
3FHE = three-fluid heat exchanger  
P1–P4 = stream couplings

## Introduction

Previous attempts to define the effectiveness of a three-fluid heat exchanger can be traced in the technical literature (Sorlie, 1962; Willis, 1966; Aulds and Barron, 1967; Willis and Chapman, 1968; Horváth, 1977; Barron and Yeh, 1976). The first logical step in that direction seemed to be the straightforward extension of the standard definition of a two-fluid heat exchanger effectiveness to the three-fluid heat exchanger case (Sorlie, 1962):

$$\epsilon = \frac{\dot{Q}_{3FHE}}{\dot{Q}_{max}^{3FHE}} \quad (1)$$

where  $\dot{Q}_{3FHE}$  and  $\dot{Q}_{max}^{3FHE}$  are supposed to represent the actual "heat transfer rate" and the maximum "heat transfer rate" in a three-fluid heat exchanger, respectively.

It is interesting to note, however, that a thorough analysis of the concept of the three-fluid heat exchanger effectiveness does

<sup>1</sup> Visiting Professor, Department of Mechanical and Aerospace Engineering, University of Tennessee, Knoxville, TN 27966; permanent address: Department of Mechanical Engineering, University of Novi Sad, YU 21121 Novi Sad; Mem. ASME.

<sup>2</sup> Research Assistant, Department of Mechanical Engineering, University of Novi Sad, Novi Sad, YU 21121.

Contributed by the Heat Transfer Division of THE AMERICAN SOCIETY OF MECHANICAL ENGINEERS. Manuscript received by the Heat Transfer Division February 1994; revision received July 1994. Keywords: Heat Exchangers, Associate Technical Editor: T. J. Rabas.

et al., 1960). A decrease in heat transfer coefficient has been observed with an increase in solid particle concentration at each speed of the impeller during the current investigations. These results conform with the findings of Cummings and West (1950) and Frantisak et al. (1968) but contradict the results reported by Shah and Rao (1969) and Trivedi et al. (1975). Shah and Rao (1969) and Trivedi et al. (1975) have proposed the strong dependence of heat transfer rate on thermal conductivity of the solid particles in suspension. Since thermal conductivity and heat capacity of both sand and coal particles are less than those of the carrier fluid, an increase in particle concentration is only expected to decrease the net thermal conductivity and heat capacity of the suspension. However, Sohn and Chen (1981) and Chung and Leal (1982) have reported significant enhancement in effective thermal conductivity in low Reynolds number, rotating Couette flow using neutrally buoyant solid–fluid suspensions (these studies were confined to only microconvective effects, which cannot be separated from other effects in case of any two-phase heat transfer process). In addition to this, the viscosity of the suspension would increase with increasing solid concentration and loss in particle velocity would also occur (although loss would be small, due to the solid concentration of less than 10 percent) due to the interparticle friction and any agglomeration. Change in these parameters would cause a decrease in Reynolds number and would offset the effects of turbulence created by agitation.

Conductivity, particle size, and concentration of the suspensions are the most important parameters, deciding the role of particles during heat transfer in suspensions. Further, particle velocity and particle population in any zone of the vessel depend on particle size, density, suspension concentration, and agitator depth at any given speed of agitation. Since all the other conditions for both sand and coal particles in their respective suspensions were kept identical except the particle density, larger particle population of coal (due to its lower density) could increase the frequency of particle collisions among themselves and also with the heat transfer surface. This has caused induced turbulence and an increase in heat transfer rate in case of coal–water suspensions in spite of the lower thermal conductivity of the dry coal in comparison to dry sand. However, no quantitative comparison of the experimental results was possible with the results of the previous researchers as these are the first of their kind for heat transfer studies.

## References

- Bird, R. B., Stewart, W. E., and Lightfoot, E. N., 1960, *Transport Phenomena*, Wiley, New York, p. 393.
- Chung, Y. C., and Leal, L. G., 1982, "An Experimental Study of the Effective Thermal Conductivity of a Sheared Suspension of Rigid Spheres," *Int. J. Multiphase Flow*, Vol. 8, No. 6, pp. 605–625.
- Cummings, G. H., and West, A. S., 1950, "Heat Transfer Data for Kettles With Jackets and Coils," *Industrial and Engineering Chemistry*, Vol. 42, No. 11, pp. 2303–2313.
- Engel, A. J., and Hougen, O. A., 1963, "Mass Transfer and Contactor Efficiency in a Stirred Liquid–Liquid Reactor," *AIChE Journal*, Vol. 9, No. 6, pp. 724–729.
- Frantisak, F., Smith, J. W., and Dohnal, J., 1968, "Heat Transfer to Solid–Liquid Suspensions in an Agitated Vessel," *Industrial & Engineering Chemistry, Process Design and Development*, Vol. 7, No. 2, pp. 188–193.
- Pandey, S. K., 1978, "Heat Transfer Studies for Agitated Liquids," *Chemical Engineering World*, Vol. XIII, No. 9, pp. 47–50.
- Ramasubramanian, A., 1990, "Heat Transfer Studies in Suspensions," M. Tech. Thesis, Dept. of Chemical Engineering, Regional Engineering College, Tiruchirappalli—620 015, India.
- Shah, P. V., and Rao, M. R., 1969, "Heat Transfer to Agitated Suspensions in Baffled Jacketed, Agitated Vessel," *Indian Journal of Technology*, Vol. 7, pp. 166–173.
- Sohn, C. W., and Chen, M. M., 1981, "Microconvective Thermal Conductivity in Disperse Two-Phase Mixtures as Observed in a Low Velocity Couette Flow Experiment," *ASME JOURNAL OF HEAT TRANSFER*, Vol. 103, pp. 47–51.
- Trivedi, R. N., Pandey, G. N., and Tripathi, G., 1975, "Heat Transfer to Solid–Liquid Suspensions in Jacketed Agitated Vessels," *Indian Journal of Technology*, Vol. 13, pp. 53–58.
- Voncken, R. M., 1965, "Homogenization of Miscible Liquids, Part 1," *British Chemical Engineering*, Vol. 10, No. 1, pp. 13–18.

# Three-Fluid Heat Exchanger Effectiveness—Revisited

D. P. Sekulić<sup>1</sup> and I. Kmečko<sup>2</sup>

## Nomenclature

- $A$  = heat transfer surface area, m<sup>2</sup>  
 $c_p$  = specific heat of fluid at constant pressure, J/kg K  
 $C_{j,2}^*$  = heat capacity rate ratio =  $(\dot{m}c_p)_j(\dot{m}c_p)_2^{-1}$ ,  $j = 1$  or  $3$   
 $H$  = enthalpy rate, J/s  
 $i_k$  = fluid stream indicator,  $i_k = \pm 1$ ,  $k = 1, 2$ , or  $3$   
 $L$  = heat exchanger length, m  
 $\dot{m}$  = mass flow rate, kg/s  
NTU = number of heat transfer units =  $(UA)_{1,2}(\dot{m}c_p)_1^{-1}$   
 $\dot{Q}$  = heat transfer rate, W  
 $R^*$  = conductance ratio =  $(UA)_{23}(UA)_{1,2}^{-1}$   
 $T$  = temperature, K  
 $U$  = overall heat transfer coefficient, W/m<sup>2</sup> K  
 $x$  = Cartesian axial coordinate, m  
 $\epsilon$  = heat exchanger effectiveness as defined in Eq. (4)  
 $\vartheta_{1(3)}$  = temperature effectiveness =  $(T_{1(3),out} - T_{1(3),in})(T_{2,in} - T_{1(3),in})^{-1}$   
 $\xi$  = dimensionless coordinate =  $x/L$   
 $\Theta_k$  = dimensionless temperature =  $(T_k - T_{1,in})(T_{2,in} - T_{1,in})^{-1}$ ,  $k = 1, 2$ , or  $3$

## Subscripts

- 1, 2, 3 = streams 1, 2, or 3  
in = inlet  
max = maximum value  
out = outlet

## Superscripts

- = dimensionless quantity  
3FHE = three-fluid heat exchanger  
P1–P4 = stream couplings

## Introduction

Previous attempts to define the effectiveness of a three-fluid heat exchanger can be traced in the technical literature (Sorlie, 1962; Willis, 1966; Aulds and Barron, 1967; Willis and Chapman, 1968; Horváth, 1977; Barron and Yeh, 1976). The first logical step in that direction seemed to be the straightforward extension of the standard definition of a two-fluid heat exchanger effectiveness to the three-fluid heat exchanger case (Sorlie, 1962):

$$\epsilon = \frac{\dot{Q}_{3FHE}}{\dot{Q}_{max}^{3FHE}} \quad (1)$$

where  $\dot{Q}_{3FHE}$  and  $\dot{Q}_{max}^{3FHE}$  are supposed to represent the actual "heat transfer rate" and the maximum "heat transfer rate" in a three-fluid heat exchanger, respectively.

It is interesting to note, however, that a thorough analysis of the concept of the three-fluid heat exchanger effectiveness does

<sup>1</sup> Visiting Professor, Department of Mechanical and Aerospace Engineering, University of Tennessee, Knoxville, TN 27966; permanent address: Department of Mechanical Engineering, University of Novi Sad, YU 21121 Novi Sad; Mem. ASME.

<sup>2</sup> Research Assistant, Department of Mechanical Engineering, University of Novi Sad, Novi Sad, YU 21121.

Contributed by the Heat Transfer Division of THE AMERICAN SOCIETY OF MECHANICAL ENGINEERS. Manuscript received by the Heat Transfer Division February 1994; revision received July 1994. Keywords: Heat Exchangers, Associate Technical Editor: T. J. Rabas.

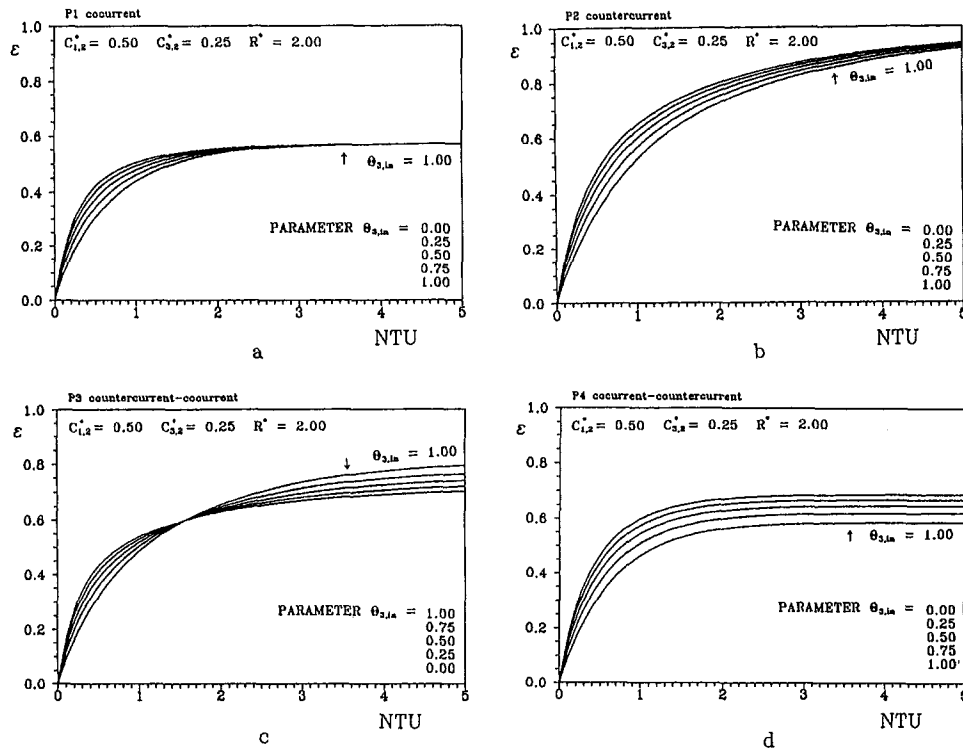


Fig. 1 Overall three-fluid heat exchanger effectivenesses: stream couplings P1-P4

not exist. Consequently, the major objective of this note is to provide a basis for further studies of a thermal performance figure of merit for a class of thermal devices in which three fluids simultaneously change mutual enthalpy levels without external heat and work interactions.

### The Overall Three-Fluid Heat Exchanger Effectiveness Revisited

The analysis is going to be performed on a class of parallel stream three-fluid heat exchangers with two thermal communications (only the central fluid, Fluid 2, is in simultaneous thermal contact with the two lateral fluids, Fluids 1 and 3). This class of heat exchangers has four possible stream couplings: cocurrent flow (P1, all three streams flow in the positive fluid flow direction,  $i_k^{P1} \xi (= i_k^{P1} x/L)$ ,  $i_k^{P1} = +1$ ,  $k = 1, 2, 3$ ), countercurrent flow (P2, Fluid 2 flows in the direction opposite to the other two fluids, i.e.,  $i_2^{P2} \xi$ ,  $i_2^{P2} = -1$ ), countercurrent-cocurrent flow (P3, Fluid 1 flows in the direction opposite to the other two fluids,  $i_1^{P3} \xi$ ,  $i_1^{P3} = +1$ ) and cocurrent-countercurrent flow (P4, Fluid 3 flows in the direction opposite to the other two fluids,  $i_3^{P4} \xi$ ,  $i_3^{P4} = -1$ ).<sup>3</sup>

In order to define the actual "heat transfer rate," one should formulate the purpose of a three-fluid heat exchanger. The most frequent situation is when one (central) fluid stream has to be used in a heat exchanger device to change simultaneously the enthalpy levels of the other two (lateral) fluid streams. Correspondingly, the purpose of the device has to be expressed in terms of enthalpy rate exchanges, not in terms of heat transfer rates (Sekulić, 1990). Having this in mind, let us assume that the purpose of a three-fluid heat exchanger is to achieve the pre-

scribed total enthalpy rate change of the two lateral fluids. In that case, the engineering goal can be expressed in dimensionless form as follows:

$$\Delta \bar{H}_{1\&3} = C_{1,2}^* \Theta_{1,\text{out}} + C_{3,2}^* (\Theta_{3,\text{out}} - \Theta_{3,\text{in}}) \quad (2)$$

where  $\Delta \bar{H}_{1\&3} = (\Delta \bar{H}_1 + \Delta \bar{H}_3) [(\dot{m}c_p)_2 (T_{2,\text{in}} - T_{1,\text{in}})]^{-1}$ ,  $C_{j,2}^* = (\dot{m}c_p)_j / (\dot{m}c_p)_2^{-1}$ ,  $j = 1$  or  $3$ , and  $\Theta_{k,\text{in(out)}} = (T_{k,\text{in(out)}} - T_{1,\text{in}}) / (T_{2,\text{in}} - T_{1,\text{in}})^{-1}$ . This goal can be accomplished at the expense of a change of the enthalpy rate of the central fluid:

$$\Delta \bar{H}_2 = 1 - \Theta_{2,\text{out}} \quad (3)$$

where  $\Delta \bar{H}_2 = \Delta \bar{H}_2 [(\dot{m}c_p)_2 (T_{2,\text{in}} - T_{1,\text{in}})]^{-1}$  is the dimensionless enthalpy rate change of Fluid 2.

It is easy to demonstrate that the equality of the two expressions given by Eqs. (2) and (3) follows the overall energy (enthalpy) balance of a three-fluid heat exchanger.

Following the procedure and the rules adopted for the proper definition of a figure of merit (i.e., (i) the figure of merit should represent the measure of performance with respect to the desired engineering task, (ii) it should be expressed in dimensionless form, and (iii) it should range between 0 and 1), one should define the effectiveness as a ratio of an actual enthalpy rate change in a three-fluid heat exchanger  $\Delta \bar{H}_{1\&3}$  to the maximum possible enthalpy rate change  $(\Delta \bar{H}_{1\&3})_{\text{max}}$ :

$$\begin{aligned} \epsilon &= \frac{\Delta \bar{H}_{1\&3}}{(\Delta \bar{H}_{1\&3})_{\text{max}}} = \frac{\Delta \bar{H}_{1\&3}}{(\Delta \bar{H}_2)_{\text{max}}} \\ &= \frac{C_{1,2}^* \Theta_{1,\text{out}} + C_{3,2}^* (\Theta_{3,\text{out}} - \Theta_{3,\text{in}})}{(1 - \Theta_{2,\text{out}})_{\text{max}}} \end{aligned} \quad (4)$$

In Eq. (4), the equality between Eqs. (2) and (3) is taken into account.

Therefore:

$$0 \leq \epsilon = \frac{1 - \Theta_{2,\text{out}}}{(1 - \Theta_{2,\text{out}})_{\text{max}}} \leq 1 \quad (5)$$

<sup>3</sup> Note that only couplings P1-P3 have to be considered as distinct flow arrangements (i.e., cocurrent, countercurrent, and countercurrent-cocurrent or cocurrent-countercurrent flow arrangement, respectively), regardless of the fact that the couplings P3 and P4 may have different performances for the same set of governing parameters. Couplings P3 and P4 represent distinct physical situations with different performances for the same set of parameters and hence should be included in the analysis.



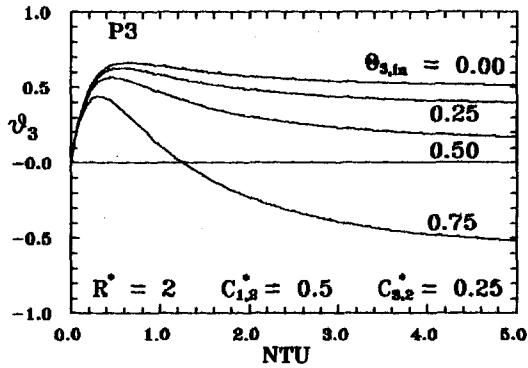
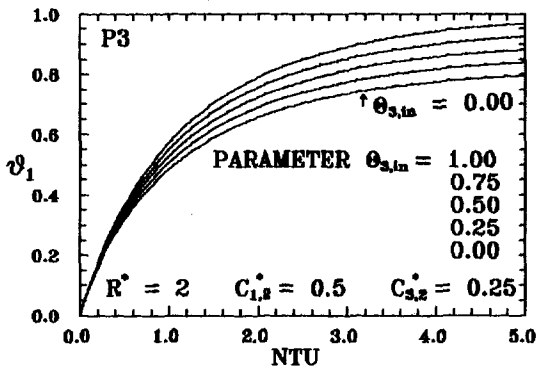


Fig. 2 Temperature effectiveness indicators, coupling P3: (a) Fluid 1, (b) Fluid 3

The next important step is to determine the denominator in Eq. (4). The physical meaning of the denominator can be expressed as follows:

$$(\Delta \bar{H}_2)_{\max} = \lim_{NTU \rightarrow \infty} (\Delta \bar{H}_2) = \lim_{NTU \rightarrow \infty} (1 - \Theta_{2,\text{out}}), \quad (6)$$

i.e., the maximum possible enthalpy rate change of the central fluid can be accomplished in a countercurrent heat exchanger (P2) with infinite large thermal size. The exit temperature for Fluid 2 for infinitely large countercurrent heat exchanger in Eq. (6) can be determined using the analytical solution given by Sekulic (1994). It can be readily shown (using the analytical solution from Sekulic (1994) and determining the limes) that Eq. (6) takes the form as follows:

$$(\Delta \bar{H}_2)_{\max} = C_{3,2}^* (1 - \Theta_{3,\text{in}}) + C_{1,2}^* \quad (7)$$

Introducing Eq. (7) into the expression for overall effectiveness given by Eq. (4), leads to:

$$\epsilon = \frac{C_{3,2}^* (\Theta_{3,\text{out}} - \Theta_{3,\text{in}}) + C_{1,2}^* \Theta_{1,\text{out}}}{C_{3,2}^* (1 - \Theta_{3,\text{in}}) + C_{1,2}^*} \quad (8)$$

The dimensionless outlet temperatures  $\Theta_{3,\text{out}}$ , and  $\Theta_{1,\text{out}}$  for all four possible stream couplings (P1–P4) can be calculated using the corresponding exact analytical solutions known from the literature (Sorlie, 1962; Schneller, 1970; Sekulic, 1994).

The overall effectiveness definition as given by Eq. (8) is valid for any flow arrangement of the three-fluid heat exchanger class under study (i.e., three-fluid heat exchanger with two thermal communications). This definition holds for thermally balanced or unbalanced streams regardless of the mutual relation between the heat capacity rate magnitudes. It is important to note that both existing concepts of the three-fluid heat exchanger effectiveness (Sorlie, 1962; Willis, 1966) give the same results as Eq. (8) when  $C_{1,2}^* + C_{3,2}^* < 1$ , but their definitions lead to erroneous evaluation of the exchanger performance when  $C_{1,2}^* + C_{3,2}^* > 1$ .

According to Sorlie (1962), the outlet temperature of Fluid 2 for an infinitely large countercurrent heat exchanger is a function of the relevant heat transfer area ratio of an actual heat exchanger and respective overall heat conductances. However, the assumption of an infinitely large heat exchanger should not be dependent upon the exchanger parameters. Willis (1966) assumed that the exit temperature of Fluid 2 should be numerically equal to the mixed-mean inlet temperature of Fluids 1 and 3. As a consequence, his three-fluid heat exchanger effectiveness can exceed unity.

### Analysis

The three-fluid heat exchanger effectiveness given by Eq. (8) reduces to the two-fluid heat exchanger effectiveness if one thermal communication vanishes (i.e., the communication between Fluids 2 and 3). In that situation, the first terms in both the nominator and the denominator vanish, and effectiveness equals the dimensionless outlet temperature of Fluid 1. It can be shown that the dimensionless outlet temperature of the lateral Fluid 1 in that case reduces to the effectiveness of cocurrent or countercurrent flow arrangements, depending on the mutual flow direction of the remaining two fluid streams.

In order to provide insight into the nature of overall three-fluid heat exchanger effectiveness, let us consider this figure of merit for the same set of parameters but for different fluid flow arrangements. The set of relevant parameters is as follows:  $C_{1,2}^* = 0.5$ ,  $C_{3,2}^* = 0.25$ ,  $R^* = (UA)_{2,3}(UA)_{1,2}^{-1} = 2.0$ ,  $\Theta_{3,\text{in}} = 0.0, 0.25, 0.5, 0.75$ , and  $1.0$ , and  $NTU = (UA)_{1,2}(\dot{m}c_p)_2^{-1} = 0.0-5.0$ . In Fig. 1, the overall effectiveness curves are presented for all four stream couplings (P1–P4).

Several conclusions may be drawn from the inspection of these diagrams. The first important conclusion is that the countercurrent flow arrangement (coupling P2) has, as expected, the most

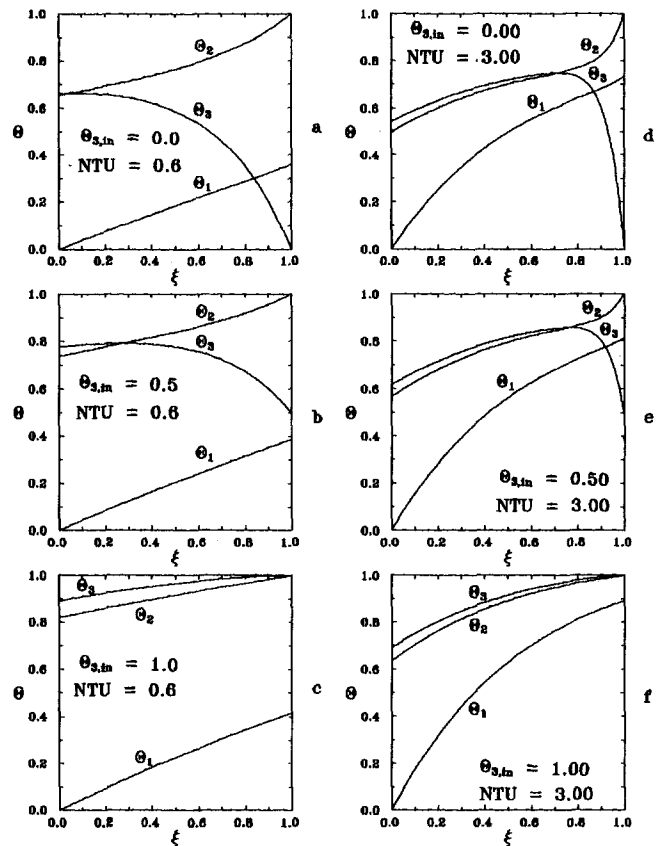


Fig. 3 Temperature distributions within the three-fluid heat exchanger, coupling P3, NTU = 0.6: (a)  $\Theta_{3,\text{in}} = 0$ , (b)  $\Theta_{3,\text{in}} = 0.5$ , (c)  $\Theta_{3,\text{in}} = 1.0$ ; NTU = 3.0: (d)  $\Theta_{3,\text{in}} = 0$ , (e)  $\Theta_{3,\text{in}} = 0.5$ , (f)  $\Theta_{3,\text{in}} = 1.0$

favorable performance compared to the other three stream couplings. The cocurrent arrangement (coupling P1) has the worst performance, the same conclusion as for two-fluid heat exchangers. The rank of performance for the remaining two couplings depends on the range of thermal size values (expressed in terms of NTU parameters) under consideration, and the value of the dimensionless inlet temperature of Fluid 3.

A very interesting, unexpected feature of the effectiveness behavior for the countercurrent-cocurrent coupling (P3) takes place in the region of moderately large NTUs. That is, the inversion of the effectiveness level with respect to the dimensionless inlet temperature of the third fluid occurs at  $NTU' = 1.575$  (for the particular selection of parameters as mentioned above). To understand the meaning of this behavior and to demonstrate how the overall three-fluid heat exchanger effectiveness reflects the exchanger performance, one needs to consider the actual physical situation within a heat exchanger. This study should involve both the so-called temperature effectivenesses (Sorlie, 1962), and the actual temperature distributions within the heat exchanger.

Temperature effectivenesses are *indicators* of the outlet temperature levels of both lateral fluids. They indicate how close (or far) the lateral fluids outlet temperatures approach (or differ from) the inlet temperature of the central fluid, i.e.,

$$\vartheta_1 = \Theta_{1,out} \quad (9)$$

$$\vartheta_3 = \frac{\Theta_{3,out} - \Theta_{3,in}}{1 - \Theta_{3,in}} \quad (10)$$

Note that the temperature effectiveness indicator does not necessarily satisfy the third rule imposed for the proper definition of a figure of merit. That is, it can take either positive or negative values, even smaller than  $-1$ , depending on the given inlet temperature conditions and the set of relevant parameters.

In Fig. 2 the two temperature effectiveness indicators are presented for the same set of parameters that have been used to demonstrate the nature of overall heat exchanger effectiveness (see Fig. 1).

The temperature effectiveness indicator of Fluid 1 (see Fig. 2a) monotonously increases if either the thermal size of a heat exchanger or the dimensionless inlet temperature of the third fluid increases for the given set of heat capacity rate ratios and conductance ratio. The temperature effectiveness indicator of Fluid 3 (see Fig. 2b), however, increases, reaches a maximum value, and further decreases with the increase in NTU of the heat exchanger, the other parameters remaining fixed as before. For this particular set of parameters, the temperature effectiveness indicator of the third fluid reaches even negative values for either large dimensionless inlet temperatures of Fluid 3 or large thermal sizes. This means that Fluid 3 was actually cooled instead of being heated.

In order to understand why temperature effectiveness indicators and overall effectiveness were interrelated in the described manner, one should consider the actual temperature distributions (i.e.,  $\Theta = \Theta(\xi)$ ,  $\xi = x/L$ ) of all three fluids in a three-fluid heat exchanger of a given flow arrangement. In Fig. 3, these temperature distributions are presented for the cases of Fig. 2 for only three values of  $\Theta_{3,in}$  (0, 0.5, and 1) and two values of NTU (0.6 and 3.0).

At NTU = 0.6, if the inlet temperature  $\Theta_{3,in}$  is equal to zero (see Fig. 3a), both lateral fluids are going to be heated. Fluid 3 will have the outlet temperature slightly higher than the central fluid (i.e., the temperature cross is very close to the exit) and a very small portion of the heat exchanger surface might be considered as "wasted." An increase in the inlet temperature of Fluid 3 will cause a shift of the temperature cross (see Fig. 3b for  $\Theta_{3,in} = 0.5$ ) within the heat exchanger, and Fluid 3 will have higher temperature than Fluid 2 within a substantial portion of the exchanger. Fluid 2 (idealized perfectly mixed at every cross section) is being cooled by Fluid 1 and Fluid 3 simultaneously in the portion of the heat exchanger close to the inlets of Fluids 2 and 3. The temperature of Fluid 3 becomes higher than that of Fluid 2 close to the exit depending upon the heat capacity rate

ratios, NTU and  $\Theta_{3,in}$ . In addition, the enthalpy rate change of the third fluid will be substantially smaller and the temperature effectiveness indicator of this fluid will decrease (see Fig. 2b). The temperature effectiveness indicator of Fluid 1, though, will increase slightly (Fig. 2a). If both fluids, Fluids 3 and 2, are going to have the same inlet temperature (i.e.,  $\Theta_{3,in} = 1.0$ , see Fig. 3c), the previous goal (i.e., to heat both lateral fluids by the central fluid) is going to be completely lost, and the third fluid will be cooled throughout the heat exchanger.

The nature of the temperature distribution behavior at large NTU is, however, quite different (see Fig. 3d-f). At NTU = 3, the increase in  $\Theta_{3,in}$  from 0 to 1 will result in monotonous increase of outlet temperatures of both Fluids 1 and 3. There is, however, a remarkable difference in temperature distributions of these two fluid streams. While the temperature of Fluid 1 has monotonous increase along the heat exchanger, the temperature of Fluid 3 will increase, reach a maximum value, and then decrease (see Fig. 3d, e). Note that the flow direction of Fluid 3 is from right to left (i.e., coupling P3). For both  $\Theta_{3,in} = 0$  and 0.5, the temperature cross between Fluids 3 and 2 is present. At  $\Theta_{3,in} = 1.0$ , the temperature of Fluid 3 will monotonically decrease from the inlet to the outlet of the heat exchanger. Consequently, the temperature effectiveness of Fluid 1 will again monotonically increase with an increase in  $\Theta_{3,in}$  (see Fig. 2a), i.e., the same as has been noticed for small values of NTUs. Temperature effectiveness of Fluid 3, however, will deteriorate even faster than was the case at small values of NTUs (see Fig. 2b).

## Concluding Remarks

The overall three-fluid heat exchanger effectiveness provides an insight into the overall performance of the exchanger with respect to its defined engineering goal. This figure of merit though reflects only the combined consequences of enthalpy changes of all three fluids involved.

## References

- Aulds, D. D., and Barron, R. F., 1967, "Three-Fluid Heat Exchanger Effectiveness," *Int. J. Heat Mass Transfer*, Vol. 10, pp. 1457-1462.
- Barron, R. F., and Yeh, S. L., 1976, "Longitudinal Conduction in a Three-Fluid Heat Exchanger," ASME Paper No. 76-WA/HT-9.
- Horváth, C. D., 1977, "Three-Fluid Heat Exchangers of Two and Three Surfaces," *Periodica Polytechnica*, Vol. 21, pp. 33-44.
- Schneller, J., 1970, "Berechnung von Dreikomponenten-Wermeaustauschsystemen," *Chem.-Ing.-Techn.*, Vol. 42, pp. 1245-1251.
- Sekulić, D. P., 1990, "A Reconsideration of the Definition of a Heat Exchanger," *Int. J. Heat Mass Transfer*, Vol. 33, pp. 2748-2750.
- Sekulić, D. P., 1994, "A Compact Solution of the Parallel Flow Three-Fluid Heat Exchanger Problem," *Int. J. Heat Mass Transfer*, Vol. 37, pp. 2183-2187.
- Sorlie, T., 1962, "Three-Fluid Heat Exchanger Design Theory, Counter and Parallel Flow," TR. No. 54, Department of Mechanical Engineering, Stanford University, CA.
- Willis, N. C., Jr., 1966, "Analysis of Three-Fluid, Crossflow Heat Exchanger," PhD thesis, Rice University, Houston, TX.
- Willis, N. C., Jr., and Chapman, A. J., 1968, "Analysis of Three-Fluid Crossflow Heat Exchangers," *ASME JOURNAL OF HEAT TRANSFER*, Vol. 90, pp. 333-339.

## Turbulent Mixed Convection Heat and Mass Transfer in a Wetted Channel

Wei-Mon Yan<sup>1</sup>

### Nomenclature

- $b$  = half channel width, m
- $c_p$  = specific heat, J/(kg·K)

<sup>1</sup> Department of Mechanical Engineering, Hua Fan College of Humanities and Technology, Shih-Ting, Taipei, Taiwan 22305.

Contributed by the Heat Transfer Division of THE AMERICAN SOCIETY OF MECHANICAL ENGINEERS. Manuscript received by the Heat Transfer Division July 1993; revision received February 1994. Keywords: Evaporation, Mixed Convection, Turbulence. Associate Technical Editor: Y. Jaluria.

favorable performance compared to the other three stream couplings. The cocurrent arrangement (coupling P1) has the worst performance, the same conclusion as for two-fluid heat exchangers. The rank of performance for the remaining two couplings depends on the range of thermal size values (expressed in terms of NTU parameters) under consideration, and the value of the dimensionless inlet temperature of Fluid 3.

A very interesting, unexpected feature of the effectiveness behavior for the countercurrent-cocurrent coupling (P3) takes place in the region of moderately large NTUs. That is, the inversion of the effectiveness level with respect to the dimensionless inlet temperature of the third fluid occurs at  $NTU' = 1.575$  (for the particular selection of parameters as mentioned above). To understand the meaning of this behavior and to demonstrate how the overall three-fluid heat exchanger effectiveness reflects the exchanger performance, one needs to consider the actual physical situation within a heat exchanger. This study should involve both the so-called temperature effectivenesses (Sorlie, 1962), and the actual temperature distributions within the heat exchanger.

Temperature effectivenesses are *indicators* of the outlet temperature levels of both lateral fluids. They indicate how close (or far) the lateral fluids outlet temperatures approach (or differ from) the inlet temperature of the central fluid, i.e.,

$$\vartheta_1 = \Theta_{1,out} \quad (9)$$

$$\vartheta_3 = \frac{\Theta_{3,out} - \Theta_{3,in}}{1 - \Theta_{3,in}} \quad (10)$$

Note that the temperature effectiveness indicator does not necessarily satisfy the third rule imposed for the proper definition of a figure of merit. That is, it can take either positive or negative values, even smaller than  $-1$ , depending on the given inlet temperature conditions and the set of relevant parameters.

In Fig. 2 the two temperature effectiveness indicators are presented for the same set of parameters that have been used to demonstrate the nature of overall heat exchanger effectiveness (see Fig. 1).

The temperature effectiveness indicator of Fluid 1 (see Fig. 2a) monotonously increases if either the thermal size of a heat exchanger or the dimensionless inlet temperature of the third fluid increases for the given set of heat capacity rate ratios and conductance ratio. The temperature effectiveness indicator of Fluid 3 (see Fig. 2b), however, increases, reaches a maximum value, and further decreases with the increase in NTU of the heat exchanger, the other parameters remaining fixed as before. For this particular set of parameters, the temperature effectiveness indicator of the third fluid reaches even negative values for either large dimensionless inlet temperatures of Fluid 3 or large thermal sizes. This means that Fluid 3 was actually cooled instead of being heated.

In order to understand why temperature effectiveness indicators and overall effectiveness were interrelated in the described manner, one should consider the actual temperature distributions (i.e.,  $\Theta = \Theta(\xi)$ ,  $\xi = x/L$ ) of all three fluids in a three-fluid heat exchanger of a given flow arrangement. In Fig. 3, these temperature distributions are presented for the cases of Fig. 2 for only three values of  $\Theta_{3,in}$  (0, 0.5, and 1) and two values of NTU (0.6 and 3.0).

At NTU = 0.6, if the inlet temperature  $\Theta_{3,in}$  is equal to zero (see Fig. 3a), both lateral fluids are going to be heated. Fluid 3 will have the outlet temperature slightly higher than the central fluid (i.e., the temperature cross is very close to the exit) and a very small portion of the heat exchanger surface might be considered as "wasted." An increase in the inlet temperature of Fluid 3 will cause a shift of the temperature cross (see Fig. 3b for  $\Theta_{3,in} = 0.5$ ) within the heat exchanger, and Fluid 3 will have higher temperature than Fluid 2 within a substantial portion of the exchanger. Fluid 2 (idealized perfectly mixed at every cross section) is being cooled by Fluid 1 and Fluid 3 simultaneously in the portion of the heat exchanger close to the inlets of Fluids 2 and 3. The temperature of Fluid 3 becomes higher than that of Fluid 2 close to the exit depending upon the heat capacity rate

ratios, NTU and  $\Theta_{3,in}$ . In addition, the enthalpy rate change of the third fluid will be substantially smaller and the temperature effectiveness indicator of this fluid will decrease (see Fig. 2b). The temperature effectiveness indicator of Fluid 1, though, will increase slightly (Fig. 2a). If both fluids, Fluids 3 and 2, are going to have the same inlet temperature (i.e.,  $\Theta_{3,in} = 1.0$ , see Fig. 3c), the previous goal (i.e., to heat both lateral fluids by the central fluid) is going to be completely lost, and the third fluid will be cooled throughout the heat exchanger.

The nature of the temperature distribution behavior at large NTU is, however, quite different (see Fig. 3d-f). At NTU = 3, the increase in  $\Theta_{3,in}$  from 0 to 1 will result in monotonous increase of outlet temperatures of both Fluids 1 and 3. There is, however, a remarkable difference in temperature distributions of these two fluid streams. While the temperature of Fluid 1 has monotonous increase along the heat exchanger, the temperature of Fluid 3 will increase, reach a maximum value, and then decrease (see Fig. 3d, e). Note that the flow direction of Fluid 3 is from right to left (i.e., coupling P3). For both  $\Theta_{3,in} = 0$  and 0.5, the temperature cross between Fluids 3 and 2 is present. At  $\Theta_{3,in} = 1.0$ , the temperature of Fluid 3 will monotonically decrease from the inlet to the outlet of the heat exchanger. Consequently, the temperature effectiveness of Fluid 1 will again monotonically increase with an increase in  $\Theta_{3,in}$  (see Fig. 2a), i.e., the same as has been noticed for small values of NTUs. Temperature effectiveness of Fluid 3, however, will deteriorate even faster than was the case at small values of NTUs (see Fig. 2b).

## Concluding Remarks

The overall three-fluid heat exchanger effectiveness provides an insight into the overall performance of the exchanger with respect to its defined engineering goal. This figure of merit though reflects only the combined consequences of enthalpy changes of all three fluids involved.

## References

- Auld, D. D., and Barron, R. F., 1967, "Three-Fluid Heat Exchanger Effectiveness," *Int. J. Heat Mass Transfer*, Vol. 10, pp. 1457-1462.
- Barron, R. F., and Yeh, S. L., 1976, "Longitudinal Conduction in a Three-Fluid Heat Exchanger," ASME Paper No. 76-WA/HT-9.
- Horváth, C. D., 1977, "Three-Fluid Heat Exchangers of Two and Three Surfaces," *Periodica Polytechnica*, Vol. 21, pp. 33-44.
- Schneller, J., 1970, "Berechnung von Dreikomponenten-Wermeaustauschsystemen," *Chem.-Ing.-Techn.*, Vol. 42, pp. 1245-1251.
- Sekulić, D. P., 1990, "A Reconsideration of the Definition of a Heat Exchanger," *Int. J. Heat Mass Transfer*, Vol. 33, pp. 2748-2750.
- Sekulić, D. P., 1994, "A Compact Solution of the Parallel Flow Three-Fluid Heat Exchanger Problem," *Int. J. Heat Mass Transfer*, Vol. 37, pp. 2183-2187.
- Sorlie, T., 1962, "Three-Fluid Heat Exchanger Design Theory, Counter and Parallel Flow," TR. No. 54, Department of Mechanical Engineering, Stanford University, CA.
- Willis, N. C., Jr., 1966, "Analysis of Three-Fluid, Crossflow Heat Exchanger," PhD thesis, Rice University, Houston, TX.
- Willis, N. C., Jr., and Chapman, A. J., 1968, "Analysis of Three-Fluid Crossflow Heat Exchangers," *ASME JOURNAL OF HEAT TRANSFER*, Vol. 90, pp. 333-339.

## Turbulent Mixed Convection Heat and Mass Transfer in a Wetted Channel

Wei-Mon Yan<sup>1</sup>

### Nomenclature

- $b$  = half channel width, m
- $c_p$  = specific heat, J/(kg·K)

<sup>1</sup> Department of Mechanical Engineering, Hua Fan College of Humanities and Technology, Shih-Ting, Taipei, Taiwan 22305.

Contributed by the Heat Transfer Division of THE AMERICAN SOCIETY OF MECHANICAL ENGINEERS. Manuscript received by the Heat Transfer Division July 1993; revision received February 1994. Keywords: Evaporation, Mixed Convection, Turbulence. Associate Technical Editor: Y. Jaluria.

$D$  = mass diffusivity,  $m^2/s$   
 $D_h$  = hydraulic diameter =  $4b$ , m  
 $h_{fg}$  = latent heat of vaporization, J/kg  
 $g$  = gravitational acceleration,  $m/s^2$   
 $Gr_e$  = effective Grashof number =  $Gr_T + Gr_M$   
 $Gr_M$  = Grashof number for mass transfer =  $g(M_a/M_v - 1)(w_w - w_0)D_h^3/\nu^2$   
 $Gr_T$  = Grashof number for heat transfer =  $g\beta(T_w - T_0) \cdot D_h^3/\nu^2$   
 $M$  = molar mass,  $kg/(K \cdot mol)$   
 $Nu_l$  = local Nusselt number for latent heat transport, Eq. (12)  
 $Nu_s$  = local Nusselt number for sensible heat transport, Eq. (12)  
 $Nu_x$  = overall Nusselt number =  $Nu_s + Nu_l$ , Eq. (11)  
 $p_m$  = motion or dynamic pressure =  $p - p_0$   
 $Pr$  = Prandtl number =  $\nu/\alpha$   
 $Q$  = total heat transfer rate  
 $Q_0$  = total heat transfer rate for dry wall  
 $q''_e$  = total energy flux, Eq. (10),  $W/m^2$   
 $q''_{li}$  = latent heat flux (or net enthalpy flux) =  $\dot{m}''_w \cdot h_{fg}$ ,  $W/m^2$   
 $q''_{st}$  = sensible heat flux,  $W/m^2$   
 $Re$  = Reynolds number =  $\bar{u} \cdot 4b/\nu$   
 $Sc$  = Schmidt number =  $\nu/D$   
 $Sc_t$  = turbulent Schmidt number  
 $Sh$  = interfacial Sherwood number  
 $T$  = temperature, K,  $^{\circ}C$   
 $u$  = axial velocity, m/s  
 $u_f$  = fully developed velocity at inlet, m/s  
 $v$  = transverse velocity, m/s  
 $w$  = mass fraction of water vapor  
 $x, y$  = coordinates in the  $x$  and  $y$  directions, respectively, m  
 $\alpha$  = thermal diffusivity,  $m^2/s$   
 $\lambda$  = thermal conductivity,  $W/m \cdot ^{\circ}C$   
 $\mu$  = dynamic viscosity,  $N \cdot s/m^2$   
 $\tau$  = shear stress, kPa  
 $\rho$  = density,  $kg/m^3$   
 $\phi$  = relative humidity at inlet

### Subscripts

$a$  = of air  
 $t$  = turbulent  
 $v$  = of vapor  
 $w$  = condition at wall  
 $0$  = condition at inlet

### Introduction

Latent heat transfer associated with liquid film evaporation in turbulent mixed convection heat transfer is important in many engineering applications. Noticeable examples include the cooling of microelectronic equipment, the process of the evaporative cooling for waste heat disposal, the simultaneous diffusion of metabolic heat and perspiration in controlling our body temperature, and double-diffusive convection in ocean flows.

A vast amount of work, both theoretical and experimental, exists in the literature to study the effects of thermal buoyancy force on the turbulent forced convection channel flows, as is evident in the reviews by Petukhov et al. (1982) and Jackson et al. (1989). Only those related to the present work are briefly reviewed here. Thermal buoyancy effects on turbulent forced convection in an ascending flow in heated vertical pipes were examined by Carr et al. (1973) and Connor and Carr (1978). Their results showed that at high Grashof numbers a limiting profile shape was approached, with maximum velocity shifting toward the heated wall. The interactions of natural and forced convection in the turbulent, downward flow in a heated vertical pipe were investigated by Axcell and Hall (1978) and Easby (1978). They

observed a marked enhancement in heat transfer rate but decrease in the friction coefficient compared with the corresponding results of turbulent forced convection. Turbulent mixed convection flows between vertical parallel plates subjected to different wall temperatures was investigated by Nakajima et al. (1980). In order to simulate the problem, they adopted a modified mixing length model to examine the effects of aiding and opposing buoyancy forces on fully developed turbulent forced convection. Abdelmeguid and Spalding (1979) applied, for the first time, a two-equation model for turbulent mixed convection pipe flows. Their model adopted a simple treatment near the wall, utilizing the wall function. Recently, Cotton and Jackson (1990) and Tanaka et al. (1987) applied a low-Reynolds-number  $k-\epsilon$  turbulent model to predict the turbulent mixed convection heat transfer and flow in vertical pipes. They were fairly successful in predicting heat transfer distribution with the experimental results.

As far as mixed convection heat and mass transfer are concerned, laminar mixed convection heat and mass transfer in wetted ducts was investigated by Lin et al. (1988) and Yan (1991). In their analyses, they found that the heat transfer along the wetted wall is dominated by the transfer of latent heat in association with film evaporation.

In spite of its importance in engineering applications, the turbulent mixed convection heat and mass transfer in a wetted channel has not been adequately studied. This motivates the present work.

### Analysis

In this work, the geometry of the system under consideration is a vertical parallel plate channel with a half-channel-width  $b$ . The channel walls are wetted by thin liquid water films. The loss of evaporated water in the film is compensated by injection of additional liquid through the porous channel wall. With good control of the water injection and the appropriate choice of the porosity of porous channel wall, the film on the wetted surface can be regarded as stationary and at the same uniform temperature as the channel wall temperature  $T_w$ . The flow of moist air enters the channel from the bottom or top with a fully developed velocity  $u_f$  and a uniform temperature  $T_0$ . The flow is influenced by the combined buoyancy forces due to differences in temperature and concentration of water vapor between the wetted wall and the ambient.

Steady turbulent mixed convection heat and mass transfer can be explored, with the usual boundary layer approximation, by the following conservation equations of mass, axial momentum, energy, and concentration:

$$\partial(\rho u)/\partial x + \partial(\rho v)/\partial y = 0 \quad (1)$$

$$\rho u \partial u/\partial x + \rho v \partial u/\partial y$$

$$= -dp_m/dx + \partial[(\mu + \mu_t)\partial u/\partial y]/\partial y + \text{sign}(\rho_0 - \rho)g \quad (2)$$

$$\rho c_p u \partial T/\partial x + \rho c_p v \partial T/\partial y = \partial[(\lambda + \lambda_t)\partial T/\partial y]/\partial y \quad (3)$$

$$\rho u \partial w/\partial x + \rho v \partial w/\partial y = \partial[\rho(D + D_t)\partial w/\partial y]/\partial y \quad (4)$$

It is noted in Eq. (2) that the third term on the right-hand side means the buoyancy forces due to the variations in temperature and concentration. For upward flow, the "sign" is taken as plus, while for downward flow, the "sign" is minus. The  $\mu_t$  and  $\lambda_t$  are the turbulent viscosity and conductivity, respectively. In this work, the turbulent mass diffusivity  $D_t$  is modeled through the relation  $D_t = \nu_t/Sc_t$ . The turbulent Schmidt number  $Sc_t$  is taken to be 1 (Bejan, 1984).

The boundary conditions for this marching-type problem are:

$$x = 0: \quad u = u_f(y), \quad T = T_0, \quad w = w_0 \quad (5)$$

$$y = 0: \quad \partial u/\partial y = \partial T/\partial y = 0 \quad (6)$$

$$y = b: \quad u = 0, \quad v = v_w(x), \quad T = T_w, \quad w = w_w \quad (7)$$

In Eq. (7), the transverse velocity of the air–vapor mixture is deduced by assuming the interface is semipermeable (Eckert and Drake, 1972),

$$v_w = -(D + D_r)/(1 - w_w) \cdot \partial w / \partial y \quad (8)$$

Moreover, by assuming the interface to be in thermodynamic equilibrium and the air–vapor mixture an ideal gas mixture, the mass fraction of the water vapor can be evaluated by

$$w_w = M_v p_w / [M_a (p_0 - p_w) + M_v p_w] \quad (9)$$

where  $p_w$  is the partial pressure of the water vapor at the wetted wall.

Energy transport between the wetted wall and the moist air in the presence of mass transfer depends on two related factors: the fluid temperature gradient at the wetted wall, resulting from the sensible heat transfer, and the rate of mass transfer, resulting from the latent heat transfer (Eckert and Drake, 1972). The total heat flux from the wetted wall is given by

$$q_x'' = q_{s,x}'' + q_{l,x}'' \\ = (\lambda \partial T / \partial y)_w + [\rho D / (1 - w_w)] \cdot (\partial w / \partial y)_w \cdot h_{f,g} \quad (10)$$

The local Nusselt number can be defined as

$$\text{Nu}_x = q_x'' \cdot D_h / [\lambda (T_w - T_b)] = \text{Nu}_s + \text{Nu}_l \quad (11)$$

where  $\text{Nu}_s$  and  $\text{Nu}_l$  are, respectively, the local Nusselt numbers for sensible and latent heat transfer, and are defined as

$$\text{Nu}_s = D_h \cdot (\partial T / \partial y)_w / (T_w - T_b), \\ \text{Nu}_l = D_h \cdot (\rho v_w) / [\lambda (T_w - T_b)] \quad (12)$$

Similarly, the local Sherwood number then becomes

$$\text{Sh} = D_h \cdot (\partial w / \partial y)_w / (w_w - w_b) \quad (13)$$

For simulation of turbulence in the flow, a modified low-Reynolds-number  $k-\epsilon$  turbulence model proposed by Myong et al. (1989) is adopted to eliminate the usage of wall functions in the computation and thus to permit direct integration of the transport equations to wetted wall. Due to the space limit, the turbulence modeling is omitted. The detailed description is available in the work of Yan (1993).

## Solution Method

The governing Eqs. (1)–(4) are solved numerically using a fully implicit numerical scheme in which the axial convective term is approximated by upwind difference and the transverse convection and diffusion terms by central difference. This scheme is employed to transform the governing equations into the finite difference equations. Each system of finite difference equations forms a tridiagonal set, which can be efficiently solved by the Thomas algorithm. Considering the large gradient of the variables at the entrance and near the gas–liquid interface, a non-uniform grid system, in both axial and transverse directions, was

employed to accommodate the drastic variations of  $u$ ,  $T$ , and  $w$ . The grid lines are clustered together in the regions near the inlet and the gas–liquid interface. The transverse distribution of grid nodes is arranged by locating the first five nodes in the gas side within the viscous sublayer adjacent to the gas–liquid interface and expanding the rest of the grid points to the channel centerline using a factor of 1.04. To produce grid-independent results, it was found from the separate computational runs that the differences in the local Nusselt number  $\text{Nu}_l$  from computations using either  $201 \times 121$  or  $101 \times 81$  grids are always less than 1 percent. To check the numerical scheme further, the results for limiting case of turbulent mixed convection heat transfer in a vertical pipe was first obtained. The predicted results agree well with those of Tanaka et al. (1987) and Cotton and Jackson (1990). Additionally, a comparison was also made by comparing the results for laminar mixed convection heat and mass transfer in a vertical channel with the results provided by Yan (1991). The predicted axial variations of local Nusselt numbers are indistinguishable from those in Yan (1991). Through these program tests, the proposed numerical algorithm is considered to be suitable for the problem.

## Results and Discussion

In this study, the calculations are specifically performed for moist air flowing in a vertical channel. As shown by Lin et al. (1988), not all the values for the nondimensional groups appearing in the analysis, i.e.,  $\text{Pr}$ ,  $\text{Sc}$ ,  $\text{Gr}_T$ ,  $\text{Gr}_M$ , etc., can be arbitrarily assigned. In fact, they are interdependent for a given mixture under certain specific condition. In this work, the physical parameters—wall temperature, relative humidity of ambient air, and inlet Reynolds number—are chosen as the independent variables. Eight cases shown in Table 1 were selected to investigate the buoyancy forces on the turbulent forced convection heat and mass transfer in a vertical channel. All of the cases are based on a vertical channel of half channel width  $b = 0.05$  m.

To study the relative contributions of heat transfer through sensible and latent heat exchanges in the flow, both sensible heat Nusselt number  $\text{Nu}_s$  and latent heat Nusselt number  $\text{Nu}_l$  are presented in Figs. 1(a) and 1(b). For comparison purposes, the results of dry wall are also plotted in Fig. 1(a) by the dashed curves. Comparing cases I and III or cases II and IV in Fig. 1 indicates that for upward flow, the upward buoyancy forces would cause a significant reduction in  $\text{Nu}_s$  or  $\text{Nu}_l$ . This stems from the fact the aiding buoyancy forces would modify turbulent flow to such an extent that both turbulent shear stress and turbulent energy transport are reduced, leading to a deterioration of heat transfer. Meanwhile, for downward flow, the heat transfer is progressively augmented by the retarding buoyancy forces as the fluid moves downstream. By comparing the solid and dashed curves in Fig. 1(a), it is obvious that the presence of moisture on the wetted wall tends to diminish the sensible heat Nusselt number for buoyancy-aiding flows. For buoyancy-opposing flows, the presence of moisture on the wetted wall may enhance or decrease  $\text{Nu}_s$ . Near the entrance,  $\text{Nu}_l$  is larger than at the wet-

Table 1 Values of major parameters for various cases

Case	$T_0$ , °C	$T_w$ , °C	Re	$\text{Gr}_T$	$\text{Gr}_M$	Pr	Sc	$\phi$ , percent	$\text{Gr}_e/\text{Re}^2$
I	20	40	$2 \times 10^4$	$2.369 \times 10^7$	$8.316 \times 10^6$	0.709	0.597	50	0.080
II	20	60	$2 \times 10^4$	$4.739 \times 10^7$	$2.640 \times 10^7$	0.709	0.597	50	0.184
III	20	40	$2 \times 10^4$	$-2.369 \times 10^7$	$-8.316 \times 10^6$	0.709	0.597	50	-0.080
IV	20	60	$2 \times 10^4$	$-4.739 \times 10^7$	$-2.640 \times 10^7$	0.709	0.597	50	-0.184
V	20	40	$5 \times 10^4$	$2.369 \times 10^7$	$8.316 \times 10^6$	0.709	0.597	50	0.0128
VI	20	60	$5 \times 10^4$	$4.739 \times 10^7$	$2.640 \times 10^7$	0.709	0.597	50	0.0295
VII	20	40	$5 \times 10^4$	$-2.369 \times 10^7$	$-8.316 \times 10^6$	0.709	0.597	50	-0.0128
VIII	20	60	$5 \times 10^4$	$-4.739 \times 10^7$	$-2.640 \times 10^7$	0.709	0.597	50	-0.0295

In this work, the half channel width  $b$  is 0.05 m.

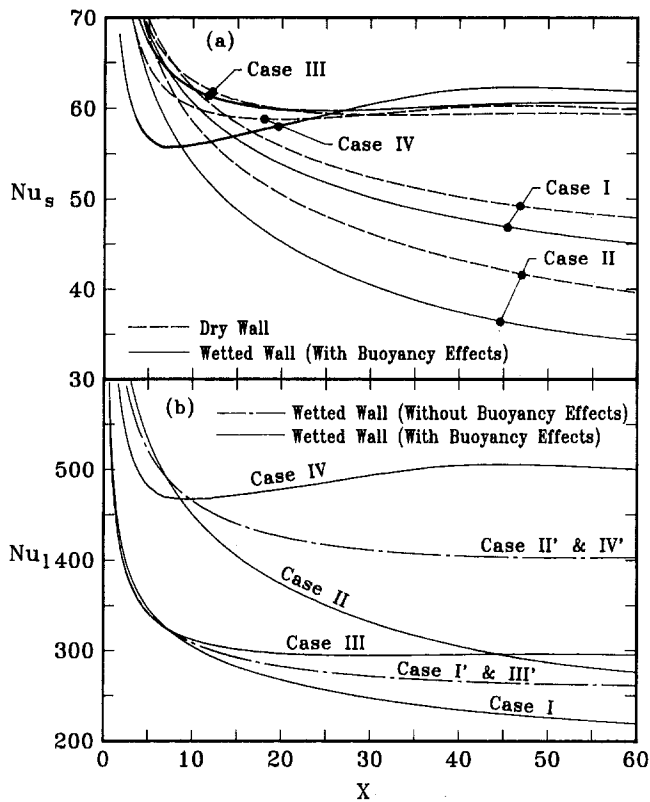


Fig. 1 Local Nusselt number distributions for (a) sensible heat; (b) latent heat

ted wall. The reverse trend is found in the downstream region. Hence, the correlations applicable to mixed convection heat transfer can not be applied to the moist surface conditions. In Fig. 1(b), the flow with a higher  $T_w$  shows a larger  $Nu_l$  (by comparing cases I and II or cases III and IV). This is brought about by the larger latent heat transport in connection with the larger liquid film evaporation for higher  $T_w$ . Besides, a larger  $Nu_l$  results for a buoyancy-retarding flow (i.e., downward flow). It becomes apparent, by comparing the magnitudes of  $Nu_s$  and  $Nu_l$ , that heat transfer resulting from the latent heat exchange is much more effective.

The effects of the combined buoyancy forces of thermal and mass diffusion on the local Sherwood number distributions are presented in Fig. 2 for both upward and downward flows. In Fig. 2, cases I, II, V, and VI are upward flow (aiding flow) while cases III, IV, VII, and VIII are descending flow (opposing flow). It is noted that for aiding flow,  $Sh$  decreases with the increase in wall temperature  $T_w$  (by comparing cases I and II or cases V and VI). This stems from the double effects. One is due to the higher blowing (evaporating) effect. The other is owing to the larger buoyancy forces for a higher  $T_w$ , which would modify turbulent flow to a larger extent that both turbulent shear stress and turbulent energy transport are reduced, leading to a larger deterioration of heat and mass transfer. For opposing flow, except the region near the entrance, a larger  $Sh$  results in a higher  $T_w$  (i.e., larger opposing buoyancy forces). This is similar to the general conception that for turbulent mixed convection heat transfer, the heat transfer increases with the buoyancy forces in the buoyancy-opposing flow. It was found from the separate computational runs that the heat and mass transfer analogy can not be applied in this work.

The most pronounced influences on the turbulent transport processes are noted by examining the distributions of the shear stress across the channel. Figure 3 presents the shear stress pro-

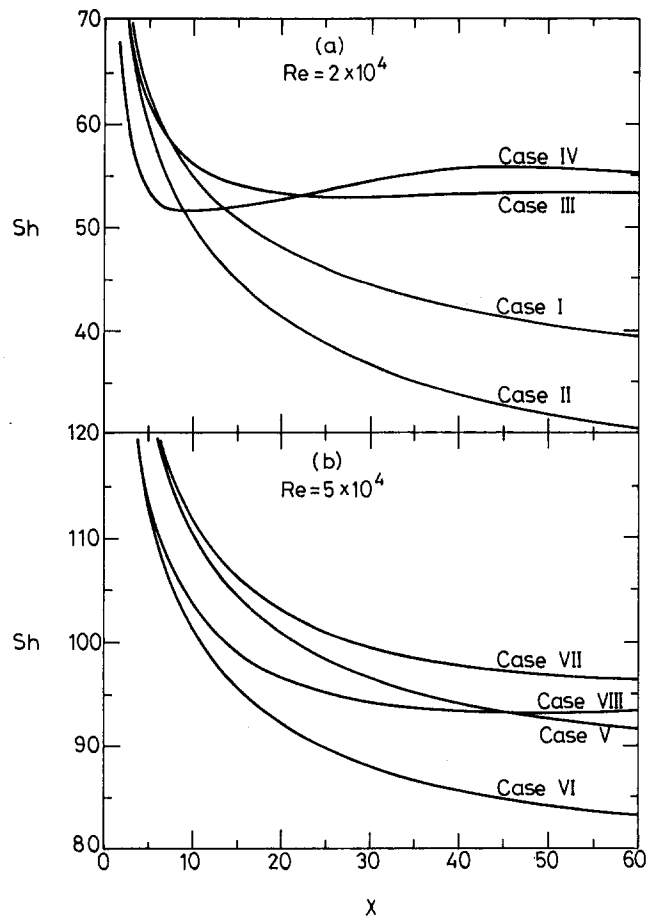


Fig. 2 Local Sherwood number along the wetted wall

file, normalized by the wall shear stress  $\tau_w$ . For pure forced convection, the relationship between the shear stress and transverse position is linear. However, with buoyancy effects taken into account, the profile becomes greatly distorted. For opposing flow (case III, IV, VII, and VIII), a shear stress maximum would move from the wall to the region where mean flow kinetic energy is fed into the turbulence, as is evident from the results in Fig. 4.

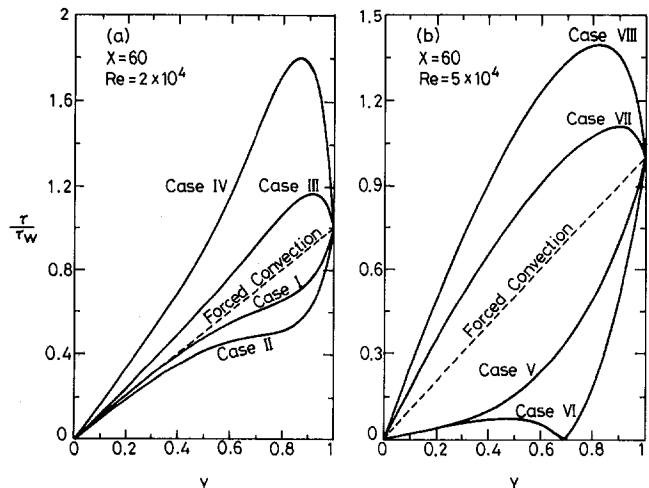


Fig. 3 Variations of shear stress across the channel

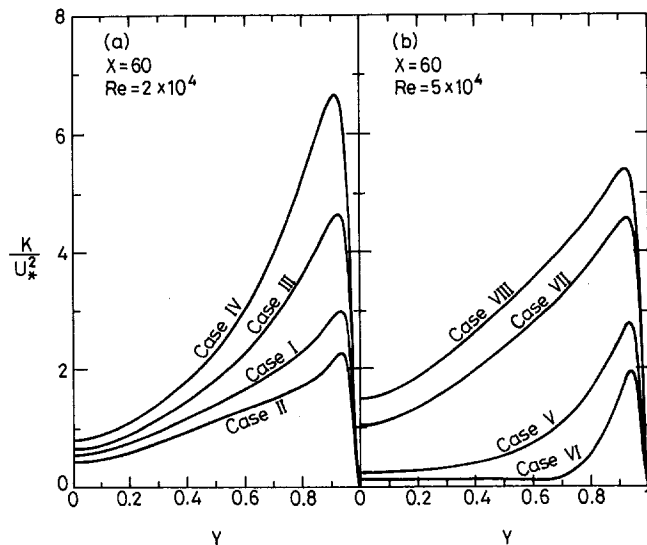


Fig. 4 Turbulent kinetic energy distributions across the channel

In this maximum shear stress region, the production of turbulent energy, expressed as  $\tau \partial u / \partial y$ , will be much larger than that in a purely forced convection flow and hence the eddy diffusivities of heat and momentum will be increased (Easby, 1978). This in turn results in the enhancement of heat and mass transfer. But for aiding flow, the shear stress decreases with the increase in  $T_w$  (by comparing cases I and II or cases V and VI).

Shown in Fig. 4 are the variations of turbulent kinetic energy  $k$  across the channel at  $x/b = 60$ . As is explained in Fig. 3, for the opposing flow the  $k$  value in the region of maximum turbulent energy production increases with  $T_w$ . But for aiding flow, the buoyancy forces reduce the production of turbulent kinetic energy in the flow, which in turn causes a lower level of turbulent kinetic energy.

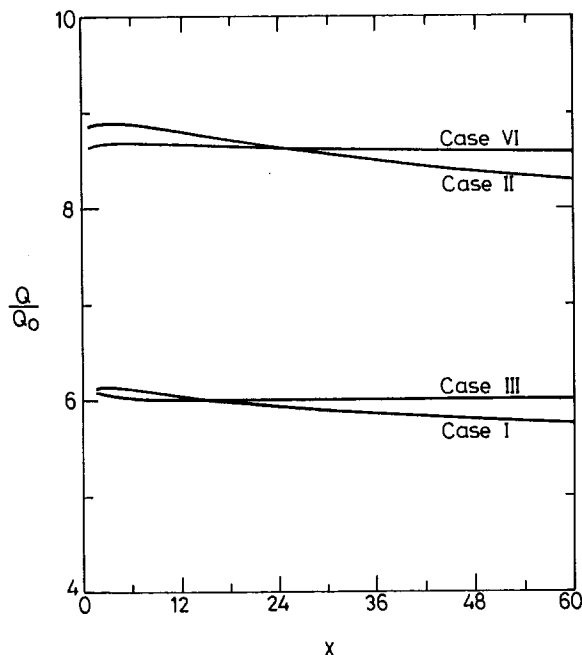


Fig. 5 Effect of various conditions on the total heat transfer rate

To illustrate the effectiveness of latent heat transfer through mass diffusion, the total heat transfer rate from the wetted channel to the moist air is compared with the result for the situation in which the channel wall is dry. The results for  $Q/Q_0$  are given in Fig. 5.  $Q_0$  represents the total heat transfer rate under dry wall conditions. The tremendous capacity of energy transport through mass diffusion is demonstrated by noting that  $Q/Q_0$  can be as large as 8 for  $T_w = 60^\circ\text{C}$ .

## Conclusions

The effects of combined buoyancy forces of thermal and mass diffusion on the turbulent forced convection heat and mass transfer in the upward and downward flows were numerically examined in detail. Results are presented for air-water system under different wall temperature and Reynolds number. Particular attention is paid to investigating the role of latent heat transport associated with the film vaporization in turbulent mixed convection heat and mass transfer. Predicted results show that the heat transfer along the wetted wall is dominated by the latent heat transfer. Additionally, the buoyancy forces would cause a deterioration of the heat and mass transfer coefficients in the buoyancy-aiding flow compared with the corresponding results of turbulent forced convection, and vice versa in the buoyancy-opposing flow.

## Acknowledgments

The financial support of this research by the National Science Council, Taiwan, through contract No. NSC 82-0401-E211-003 is greatly appreciated.

## References

- Abdelmeguid, A. M., and Spalding, D. B., 1979, "Turbulent Flow and Heat Transfer in Pipe With Buoyancy Effects," *J. Fluid Mechanics*, Vol. 94, pp. 383-400.
- Axcell, B. P., and Hall, W. B., 1978, "Mixed Convection to Air in a Vertical Pipe," *6th Int. Heat Transfer Conference*, Toronto, Canada, Vol. 2, pp. 37-42.
- Bejan, A., 1984, *Convective Heat Transfer*, Wiley, New York.
- Carr, A. D., Connor, M. A., and Buhr, H. O., 1973, "Velocity, Temperature, and Turbulence Measurement in Air for Pipe Flow With Combined Free and Forced Convection," *ASME J. OF HEAT TRANSFER*, Vol. 95, pp. 445-452.
- Connor, M. A., and Carr, A. D., 1978, "Heat Transfer in Vertical Tubes Under Conditions of Mixed Free and Forced Convection," *6th Int. Heat Transfer Conference*, Toronto, Canada, Vol. 2, pp. 43-48.
- Cotton, M. A., and Jackson, J. D., 1990, "Vertical Tube Air Flows in the Turbulent Mixed Convection Regime Calculated Using a Low-Reynolds-Number  $k-\epsilon$  Model," *Int. J. Heat Mass Transfer*, Vol. 33, pp. 275-286.
- Easby, J. P., 1978, "The Effect of Buoyancy on Flow and Heat Transfer for a Gas Passing Down a Vertical Pipe at Low Turbulent Reynolds Number," *Int. J. Heat Mass Transfer*, Vol. 21, pp. 791-801.
- Eckert, E. R. G., and Drake, R. M., Jr., 1972, *Analysis of Heat and Mass Transfer*, McGraw-Hill, New York, Chaps. 20 and 22.
- Jackson, J. D., Cotton, M. A., and Axcell, B. P., 1989, "Studies of Mixed Convection in Vertical Tubes," *Int. J. Heat Fluid Flow*, Vol. 10, pp. 2-15.
- Lin, T. F., Chang, C. J., and Yan, W. M., 1988, "Analysis of Combined Buoyancy Effects of Thermal and Mass Diffusion on Laminar Forced Convection Heat Transfer in a Vertical Tube," *ASME J. OF HEAT TRANSFER*, Vol. 110, pp. 337-344.
- Myong, H. K., Kasagi, N., and Hira, M., 1989, "Numerical Prediction of Turbulent Pipe Flow Heat Transfer for Various Prandtl Number Fluids With the Improved  $k-\epsilon$  Turbulence Model," *JSME Int. J.*, Vol. 32, pp. 613-622.
- Nakajima, M., Fukui, K., Ueda, H., and Mizushima, T., 1980, "Buoyancy Effects on Turbulent Transport in Combined Free and Forced Convection Between Vertical Parallel Plates," *Int. J. Heat Mass Transfer*, Vol. 23, pp. 1325-1336.
- Petukhov, B. S., Polyakov, A. F., and Martynenko, O. G., 1982, "Buoyancy Effect on Heat Transfer in Forced Channel Flows," *7th Int. Heat Transfer Conference*, Munich, Federal Republic of Germany, pp. 343-362.
- Tanaka, H., Maruyama, S., and Hatano, S., 1987, "Combined Forced and Natural Convection Heat Transfer for Upward Flow in a Uniformly Heated, Vertical Pipe," *Int. J. Heat Mass Transfer*, Vol. 30, pp. 165-174.
- Yan, W. M., 1991, "Mixed Convection Heat Transfer Enhancement Through Latent Heat Transport in Vertical Parallel Plate Channel Flows," *Can. J. Chem. Engng.*, Vol. 69, pp. 1277-1282.
- Yan, W. M., 1993, "Turbulent Mixed Convection Heat and Mass Transfer in a Wetted Channel," *ASME HTD-Vol. 246*, pp. 65-71.

# Unsteady Conjugated Mixed Convection in a Vertical Channel

Wei-Mon Yan<sup>1</sup> and Kuan-Tzong Lee<sup>2</sup>

## Nomenclature

- $A$  = wall-to-fluid thermal diffusivity ratio =  $\alpha_w/\alpha_f$   
 $b$  = half channel width  
 $C_{p,f}$  = specific heat of fluid  
 $C_{p,w}$  = specific heat of wall  
 $g$  = gravitational acceleration  
 $Gr$  = Grashof number, Eq. (5)  
 $K$  = wall-to-fluid thermal conductivity ratio =  $k_w/k_f$   
 $k_f$  = fluid thermal conductivity  
 $k_w$  = wall thermal conductivity  
 $Nu$  = local Nusselt number, Eq. (12)  
 $P$  = dimensionless pressure defect =  $p_m/(\rho_f \bar{u}^2)$   
 $p_m$  = pressure defect (dynamic pressure) =  $p - p_0$   
 $Pr$  = Prandtl number =  $\nu_f/\alpha_f$   
 $q_{w0}$  = outer wall heat flux  
 $Re$  = Reynolds number =  $\bar{u}b/\nu_f$   
 $T$  = temperature  
 $T_b$  = bulk fluid temperature  
 $T_e$  = initial or inlet temperature  
 $T_{w0}$  = external wall temperature  
 $t$  = time  
 $U$  = dimensionless axial velocity =  $u/\bar{u}$   
 $u$  = axial velocity  
 $\bar{u}$  = mean velocity at entrance  
 $V$  = dimensionless transverse velocity =  $vRe/\bar{u}$   
 $v$  = transverse velocity  
 $X$  = dimensionless axial coordinate =  $x/(b \cdot Re)$   
 $x$  = axial coordinate  
 $Y$  = dimensionless transverse coordinate =  $y/b$   
 $y$  = transverse coordinate  
 $\alpha_f$  = thermal diffusivity of fluid  
 $\alpha_w$  = thermal diffusivity of wall  
 $\beta$  = thermal expansion of fluid  
 $\beta^*$  = wall conduction parameter  
 $\Delta$  = dimensionless wall thickness =  $\delta/b$   
 $\theta$  = dimensionless temperature =  $(T - T_e)/(q_{w0}b/k_f)$  for UHF;  $(T - T_e)/(T_{w0} - T_e)$  for UWT  
 $\nu_f$  = kinematic viscosity of fluid  
 $\rho_f$  = fluid density at inlet temperature  
 $\rho_w$  = density of wall  
 $\tau$  = dimensionless time =  $t\alpha_f/b^2$

## Subscripts

- $e$  = at inlet or initial condition  
 $f$  = of fluid  
 $w$  = of wall

## Introduction

The problems of combined free and forced convection heat transfer in internal flows are encountered in industrial, techno-

logical, and natural surroundings. Outstanding examples include solar energy collection systems, cooling in electronic equipment, cooling and distillation systems in chemical processes, and ventilation systems. Existing literature for vertical parallel-plate channels deals mostly with the limiting case of zero wall thickness. Little information is available for the unsteady conjugated problem. This paper examines the wall effects on unsteady mixed convection in a vertical channel.

Quintiere and Muller (1973) presented the overall heat transfer results for finite vertical parallel plates. They found a significant effect of the inlet pressure condition on the heat transfer and flow behaviors at high Rayleigh numbers. Steady mixed convection heat transfer between vertical parallel plates with asymmetrically heated conditions was studied by Aung and Worku (1986a, 1986b, 1987), Habchi and Acharya (1986), and Gau et al. (1992a). Aung and Worku (1986a) showed that the hydrodynamic entry length initially increases rapidly with  $Gr/Re$  and then approaches an asymptotic value at large  $Gr/Re$ . But the buoyancy effect diminishes the thermal development distance. A criterion for the occurrence of the flow reversal was presented by Aung and Worku (1986b). Aung and Worku (1987) also showed that for a symmetric wall heating condition buoyancy introduces a lesser degree of skewness in the velocity distribution and flow reversal is more prone to occur in uniform wall temperature situation. In particular, no flow reversal is predicted for  $Gr/Re$  up to 500. Habchi and Acharya (1986) indicated that the local Nusselt number increases with increasing value of  $Gr/Re^2$ . The correlations of the average Nusselt number for buoyancy aiding and opposing flows were proposed by Gau et al. (1992a). Ingham et al. (1988a, 1988b) developed a numerical method to treat the flow reversal in buoyancy-aiding and opposing flows. They noted that poor heat transfer results when flow is retarded by an opposing buoyancy, but for a large and negative  $Gr/Re$  heat transfer is rather effective. Additionally, they found that by solving the corresponding elliptic equations, the parabolic solution method produces a good approximation of the flow for  $Re \geq 50$ . A closed-form solution was obtained by Cheng et al. (1990) for laminar fully developed mixed convection between parallel plates. Mixed convection between vertical parallel plates with and without flow reversal was examined by Jeng et al. (1992) over the range of  $Re$  from 1 to 1000. Their results showed that the matching technique using the boundary-layer equations can accurately calculate the heat transfer along the heated wall for  $Re \geq 50$ . Recently, mixed convection flow and heat transfer processes in a heated vertical channel were studied experimentally and numerically by Gau et al. (1992b) and Lin et al. (1993), respectively. Their results showed that when  $Gr/Re^2$  is relatively large, the flow may become unstable.

The impacts of the wall effect on unsteady forced convection heat transfer in laminar channel flows have been studied by numerous researchers (Succo, 1987a, 1987b; Lin and Kuo, 1988; Lee and Yan, 1993). They showed that the wall effect has a significant impact on the unsteady heat transfer, especially for the early transient period. Recently, Lin et al. (1991) presented the results of unsteady laminar mixed convection heat transfer in a vertical channel with a low  $Gr/Re$  so that no flow reversal occurs. Their results revealed that the wall heat capacity has a significant effect on the characteristics of heat transfer and flow. Nevertheless, wall conduction still remains untreated. Despite the relative importance in engineering applications, the unsteady conjugated mixed convection heat transfer has not received much attention. This motivates the present study to investigate the unsteady conjugated mixed convection in a vertical channel.

## Analysis

The geometry of the problem under consideration, as schematically shown in Fig. 1, is a two-dimensional vertical channel with half channel width  $b$  and wall thickness  $\delta$ . An insulated section of the channel is allow to develop. Flow enters the heated

<sup>1</sup> Associate Professor, Department of Mechanical Engineering, Hua Fan College of Humanities and Technology, Shih-Ting, Taipei, Taiwan 22305.

<sup>2</sup> Instructor, Department of Mechanical Engineering, Oriental Institute of Technology, Pan-Chiao, Taipei, Taiwan 22064.

Contributed by the Heat Transfer Division and presented at the 29th National Heat Transfer Conference, Atlanta, Georgia, August 9-11, 1993. Manuscript received by the Heat Transfer Division August 1993; revision received February 1994. Keywords: Conjugate Heat Transfer, Mixed Convection, Transient and Unsteady Heat Transfer. Associate Technical Editor: Y. Jaluria.



section with a uniform temperature ( $T = T_c$ ) and a fully developed velocity profile. Initially, the whole system comprising the flowing fluid and the confining channel wall is maintained at a uniform temperature  $T_c$ . At  $t = 0$ , the thermal condition of the outer surface of the heated section is changed and is maintained at either uniform heat flux  $q_{w0}$  or uniform wall temperature  $T_{w0}$ . Attention is focused on the temporal developments of the hydrodynamic and thermal characteristics in the system after the sudden heat input to the channel wall. To facilitate the analysis, the following simplifying assumptions are made:

- 1 The Boussinesq approximation is valid (Aung and Worku, 1986a; Lin et al., 1991).
- 2 The flow is of boundary-layer type. This is justified by Ingham et al. (1988a, 1988b) and Jeng et al. (1992) for  $Re \geq 50$  and small  $Gr/Re$ , which is the situation in this work.
- 3 A long vertical channel is considered so that the outlet effect can be neglected.
- 4 The fluid is Newtonian and the viscous dissipation effect can be neglected.
- 5 High Peclet number flow is treated here so that the axial conduction in the fluid is negligibly small (Shah and London, 1978).

Based on the above assumptions, the problem can be formulated by the following governing equations:

Continuity equation

$$\partial U/\partial X + \partial V/\partial Y = 0 \quad (1)$$

Axial-momentum equation

$$(1/Pr) \cdot \partial U/\partial \tau + U \partial U/\partial X + V \partial U/\partial Y = -dP/dX + \partial^2 U/\partial Y^2 + (Gr/Re) \cdot \theta \quad (2)$$

Energy equation of the fluid

$$\partial \theta_f/\partial \tau + Pr \cdot (U \partial \theta_f/\partial X + V \partial \theta_f/\partial Y) = \partial^2 \theta_f/\partial Y^2 \quad (3)$$

Energy equation of the wall

$$(1/A) \cdot \partial \theta_w/\partial \tau = (1/Re^2) \cdot \partial^2 \theta_w/\partial X^2 + \partial^2 \theta_w/\partial Y^2 \quad (4)$$

where the dimensionless quantities are defined as follows:

$$\begin{aligned} X &= x/(bRe) & Y &= y/b \\ U &= u/\bar{u} & V &= vRe/\bar{u} \\ Re &= \bar{u}b/\nu_f & K &= k_w/k_f \\ A &= \alpha_w/\alpha_f & \Delta &= \delta/b \\ \theta &= (T - T_c)/(q_{w0}b/k_f) & Gr &= g\beta b^4 q_{w0}/(\nu_f^2 k_f) \text{ for UHF} \\ \theta &= (T - T_c)/(T_{w0} - T_c) & Gr &= g\beta b^3 (T_{w0} - T_c)/\nu_f^2 \text{ for UWT} \\ P &= p_m/(\rho_f \bar{u}^2) & Pr &= \nu_f/\alpha_f \\ \tau &= t\alpha_f/b^2 \end{aligned} \quad (5)$$

In Eq. (4), the order of the coefficient  $1/Re^2$  is about  $10^{-4}$  to  $10^{-6}$ . Hence, the axial wall conduction term is small relative to the transverse diffusion term and is neglected in this study. In reality, the strength of axial conduction in the wall is measured by a parameter  $\beta^* = k_w \delta/k_f b = K\Delta$  (Faghri and Sparrow, 1980). In this work, the maximum value of  $\beta^*$  is 10. As shown in Fig. 2(d) of Faghri and Sparrow (1980), the preheating due to axial wall conduction for the case of  $\beta^* = 10$  is only apparent near the entrance ( $X = 0$ ). But away from the inlet, the effect of axial wall conduction is negligibly small. It is worth noting that for mixed convection flows in vertical channels, the parameter that governs the importance of the buoyancy force depends on the axial scaling. In the studies of Aung and Worku (1986a,

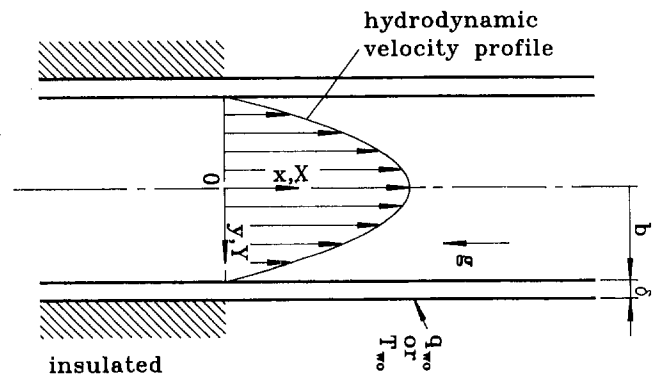


Fig. 1 Schematic diagram of the physical model

1986b, 1987), the parameter of  $Gr/Re$  appears in the axial momentum equation, while in the study of Lin et al. (1993), the parameter of  $Gr/Re^2$  appears in the formulation.

Equations (1)–(4) are subjected to the following initial and boundary conditions:

$$\tau = 0: U = 1.5(1 - Y^2), \quad \theta_f = \theta_w = 0 \quad (6)$$

$$\tau > 0:$$

$$X = 0: U = 1.5(1 - Y^2), \quad \theta_f = \theta_w = 0 \quad (7)$$

$$Y = 0: \partial U/\partial Y = \partial \theta_f/\partial Y = 0 \quad (8)$$

$$Y = 1: U = 0, \quad \theta_f = \theta_w, \quad \partial \theta_f/\partial Y = K \partial \theta_w/\partial Y \quad (9)$$

$$Y = 1 + \Delta: \partial \theta_w/\partial Y = 1/K \text{ for UHF} \quad (10a)$$

$$\theta_w = 1 \text{ for UWT} \quad (10b)$$

In the study of unsteady convective heat transfer in internal flows, the conventional Nusselt number  $Nu^*$  is evaluated by

$$Nu^* = q_{w0}b/[(T_{wi} - T_b)k_f] \quad (11)$$

But because  $Nu^*$  cannot realistically reflect the magnitude and the direction of the energy exchange between the fluid and the channel wall (Lin and Kuo, 1988), a much more informative definition must be sought to interpret the results, which in this work is

$$Nu = hb/k_f = q_{w0}b/[(T_{wi} - T_c)k_f] \text{ for UHF} \quad (12a)$$

$$Nu = hb/k_f = (\partial \theta_f/\partial Y)|_{Y=1} \text{ for UWT} \quad (12b)$$

## Solution Method

Because the flow under consideration is of the boundary-layer type, the solution for Eqs. (1)–(4) can be marched in the downstream direction. A fully implicit numerical scheme in which the diffusion and transverse convective terms are approximated by central differences, the unsteady term by backward differences, and axial convective term by upwind differences, is employed to transform the governing equations into finite-difference equations. Each system of the finite-difference equations forms a tri-diagonal matrix equation, which can be efficiently solved by the Thomas algorithm (Patankar, 1980). The detailed numerical method is available in Yan and Lee (1993).

To obtain enhanced accuracy in the numerical computation, grids are nonuniformly spaced in axial and transverse directions to account for the drastic variations of temperature and velocity near the wall–fluid interface and the region near the channel entrance. The grids are highest in density near the interface in the transverse direction and the highest concentration near the entrance in the axial direction. To insure accuracy and reduce computation time, a nonuniform time step is used. The first time interval  $\Delta \tau_1$  is taken to be 0.0001 and 0.00001 for UHF and

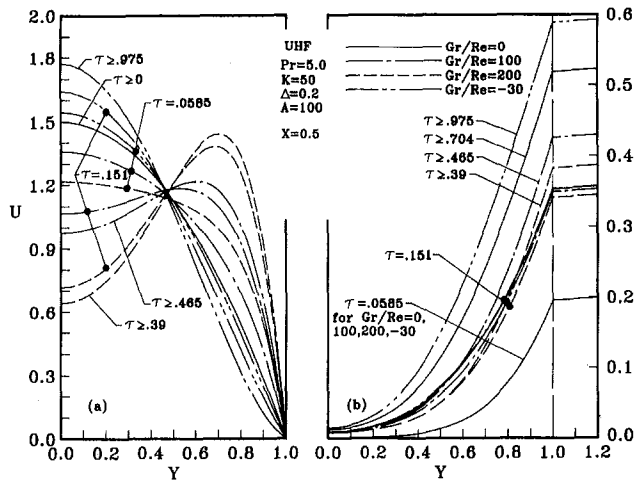


Fig. 2 Comparisons of transient distributions of velocity and temperature profiles between case A and case B for UHF

UWT, respectively, and every subsequent interval is enlarged by 3 percent over the previous one. In the transverse direction, 81 grid points were deployed where 31 grid points were packed in the wall and 51 in the fluid, while in the axial direction 101 grid lines were used. To verify the adequacy of the numerical scheme described above for the problem considered, results for the limiting case of UHF with extremely thin wall thickness were first obtained. The predicted steady-state axial variations of wall temperature are indistinguishable from those plotted in Fig. 6 of Aung and Worku (1987). Further comparison is made for the fully developed velocity profiles. It is observed that the predicted results differ from the exact solutions of Cheng et al. (1990) by less than 1 percent. To check the grid independence, a comparison for various grid arrangements was made. It was found from the separate numerical runs that the differences in local Nusselt number  $Nu$  for the computations using either  $101 \times 81$  or  $201 \times 161$  grids were within 1 percent. The  $101 \times 81$  grid is therefore considered to be suitable for the present work and will be used in the subsequent computations. The above described program test indicates that the adopted solution procedures are suitable for the present study.

## Results and Discussion

The preceding analysis indicates that the transient conjugated heat transfer in mixed convection channel flows depends on the ratio of Grashof number to Reynolds number  $Gr/Re$ , wall-to-fluid thermal conductivity ratio  $K$ , dimensionless wall thickness  $\Delta$ , wall-to-fluid thermal diffusivity ratio  $A$ , and Prandtl number  $Pr$ . In this work, the following conditions are selected in the computations:  $Pr = 5$  (water),  $Gr/Re$  ranging from  $-30$  to  $200$ ,  $K$  from  $0.5$  to  $50$ , and  $A$  from  $10$  to  $1000$ . The results of a typical case for  $Gr/Re = 100$ ,  $K = 50$ ,  $A = 100$ , and  $\Delta = 0.2$  were discussed in detail and were compared with those ignoring the wall effect (i.e., zero wall thickness).

The temporal developments of velocity and temperature profiles are shown in Fig. 2 at  $X = 0.5$  for case A (zero wall thickness) and case B (finite wall thickness). In Fig. 2(a), the velocity profiles develop from the parabolic one in the initial transient to the distorted one at the steady state. Maximum velocity is off the centerline and is shifted toward the channel wall due to the aiding buoyancy force. It is also clear in Fig. 2(a) that during the transient period case A (zero wall thickness) shows a larger buoyancy effect and a greater degree of distortion in the velocity profile. But as the flow reaches steady state, the velocity profiles for these two treatments approach one single curve. Typical developing temperature profiles, corresponding to the velocity profiles, are given in Fig. 2(b). During the transient period,

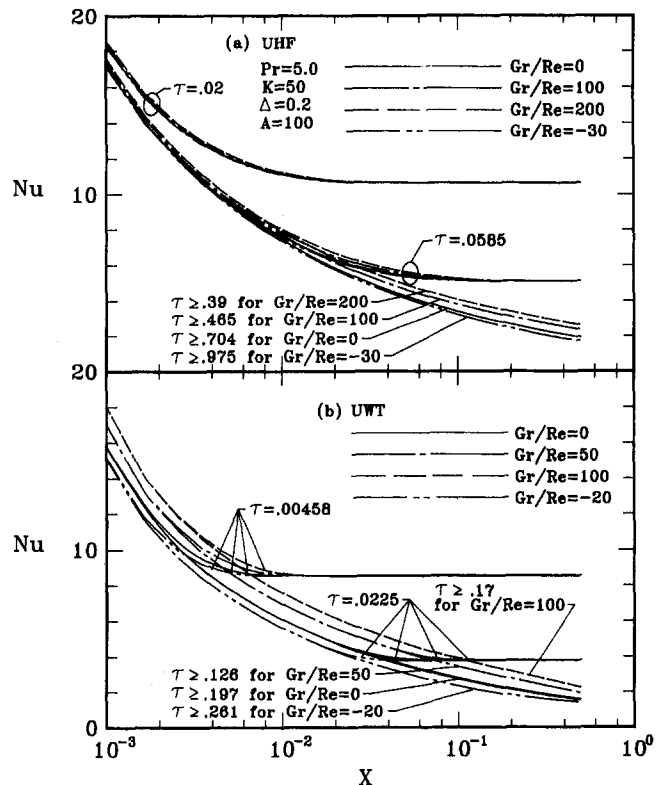


Fig. 3 Effects of  $Gr/Re$  on the unsteady axial distributions of local Nusselt number for UHF and UWT

a lower temperature is noted for case B (finite wall thickness). This is due to the heat input to the channel wall being mostly stored in the wall during the early transient period. This is known as the thermal lag of the system. Therefore, the time required for

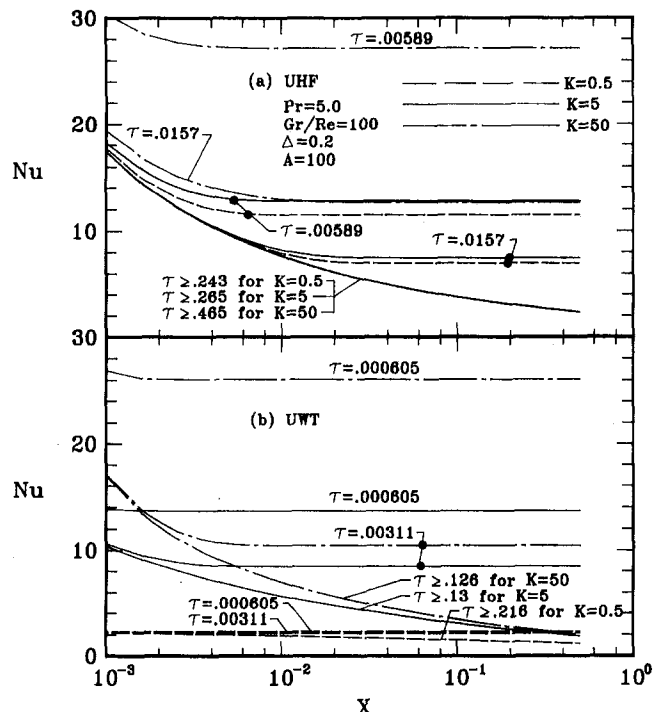


Fig. 4 Effects of wall-to-fluid conductivity ratio  $K$  on the transient distributions of local Nusselt number for UHF and UWT

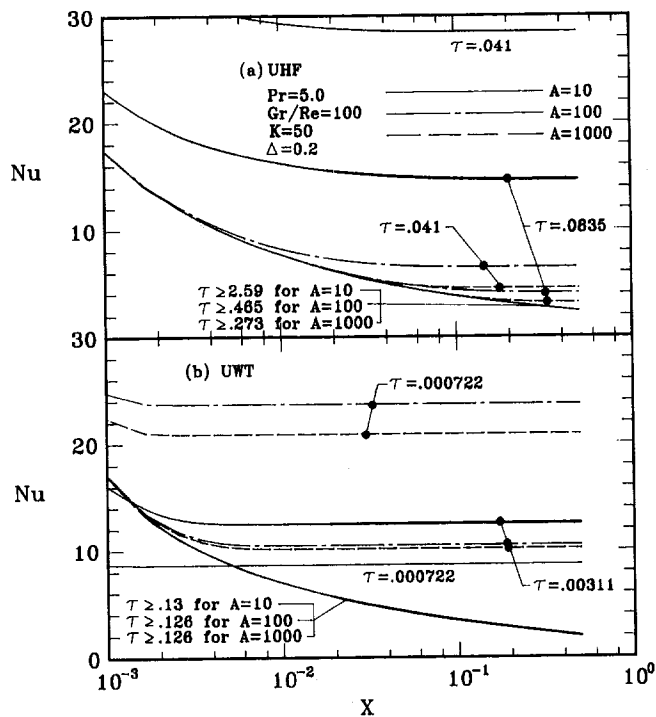


Fig. 5 Effect of wall-to-fluid diffusivity ratio  $A$  on the transient distributions of local Nusselt number for UHF and UWT

the system to reach the steady-state condition is much longer for a finite wall system.

The effects of  $Gr/Re$  on the unsteady distributions of local  $Nu$  for UHF and UWT are displayed in Fig. 3 for  $K = 50$ ,  $\Delta = 0.2$ , and  $A = 100$ . In the initial transient period, the curves of local  $Nu$  for different  $Gr/Re$  approach a constant value at large  $X$ . This is due to the fact that the convection effect has not arrived at this region and the heat transfer is still dominated by conduction. But as the time proceeds, a larger  $Nu$  results for a higher  $Gr/Re$  owing to the larger buoyancy effect. It is also noted in Fig. 3(a) that for the buoyancy-aiding flow, the time required for the system to reach steady state is shorter for a larger  $Gr/Re$ . This is not the case for UWT (Fig. 3b).

Figure 4(a) gives the effects of wall-to-fluid conductivity ratio  $K$  on the temporal distributions of local Nusselt number at different times for UHF. It is clear that during the transient period, the increase in  $K$  results in an increase in  $Nu$ . This behavior is attributed to the fact that for a larger  $K$  ( $= A\rho_w C_{pw} / \rho_f C_{pf}$ ) with  $A$  fixed, an increase in  $K$  results in a slow rise in interfacial temperature at this time instant. According to the definition of the Nusselt number, Eq. (12a),  $Nu$  is thus large for a large  $K$ . Thermal lag in the system due to the wall effect can also be found in Fig. 4(a). Clearly, a significant increase in thermal lag results as  $K$  is raised from 0.5 to 50. Also noted in Fig. 4(a), no matter what  $K$  is, the steady-state distributions of  $Nu$  approach a single curve. This is due to the fact that at steady state the heat flux at the wall-fluid interface is equal to the imposed constant heat flux at the boundary for different  $K$ . Figure 4(b) gives the comparative results of local  $Nu$  for different  $K$ . During the unsteady state, an increasing  $K$  contributes to an increase in  $Nu$ , while at steady state, unlike the results of UHF, the distributions of  $Nu$  do not approach a single curve. Near the entrance, the  $Nu$  for different  $K$  exhibits a significant discrepancy, but the deviation diminishes as the flow goes downstream. The similar trend was also found by Lee and Yan (1993) for the results of purely forced convection.

The last parameter to be discussed is the wall-to-fluid diffusivity ratio  $A$ . Its effect on the transient distributions of the local

Nusselt number for UHF and UWT is shown in Fig. 5. For UHF, it is found from Fig. 5(a) that the time required for the system to arrive at the steady-state condition is much longer for the system with a smaller  $A$ . But for UWT, the effect of  $A$  on the time required for system to reach the steady state is insignificant. It is worth noting that the curves for various  $A$  collapse onto a single curve as the flow reaches the steady-state condition. This is because the governing equations for the system at steady state are independent of  $A$ .

## Conclusions

In the present study, the unsteady mixed convection heat transfer in a vertical channel subjected to either uniform heat flux or uniform wall temperature is presented over a wide range of parameters. The solutions take transverse wall conduction and wall heat capacity effects into account. Comparisons of the results between zero wall thickness and finite wall thickness for the case of UHF are discussed in detail. What follows is a brief summary of the major results:

- 1 The ignorance of the wall effect in the unsteady mixed convection heat transfer would cause a substantial error, especially for the early transient period. Under steady-state condition, the error in neglecting heat transfer in the channel wall, however, is rather small.
- 2 For UHF, during the transient period, the increase in  $K$  or decrease in  $A$  results in a higher  $Nu$ . But the effects of  $K$  and  $A$  on the  $Nu$  diminish at the steady-state condition.
- 3 For UWT, the effects of  $A$  on the time required for system to reach the steady-state condition are insignificant.

## Acknowledgments

The financial support of this work by the National Science Council, Taiwan, through contract No. NSC 82-0401-E211-003 is greatly appreciated.

## References

- Aung, W., and Worku, G., 1986a, "Developing Flow and Flow Reversal in a Vertical Channel With Asymmetric Wall Temperature," *ASME JOURNAL OF HEAT TRANSFER*, Vol. 108, pp. 299-304.
- Aung, W., and Worku, G., 1986b, "Theory of Fully Developed Combined Convection Including Flow Reversal," *ASME JOURNAL OF HEAT TRANSFER*, Vol. 108, pp. 485-488.
- Aung, W., and Worku, G., 1987, "Mixed Convection in Ducts With Asymmetric Wall Heat Fluxes," *ASME JOURNAL OF HEAT TRANSFER*, Vol. 109, pp. 947-951.
- Cheng, C. H., Kou, H. S., and Huang, W. H., 1990, "Flow Reversal and Heat Transfer of Fully Developed Mixed Convection in Vertical Channels," *J. Thermophysics and Heat Transfer*, Vol. 4, pp. 375-383.
- Faghri, M., and Sparrow, E. M., 1980, "Simultaneous Wall and Fluid Axial Conduction in Laminar Pipe-Flow Heat Transfer," *ASME JOURNAL OF HEAT TRANSFER*, Vol. 102, pp. 58-63.
- Gau, C., Yih, K. A., and Aung, W., 1992a, "Measurements of Heat Transfer and Flow Structure in Heated Vertical Channels," *J. Thermophysics Heat Transfer*, Vol. 6, pp. 707-712.
- Gau, C., Yih, K. A., and Aung, W., 1992b, "Reversal Flow Structure and Heat Transfer Measurement for Buoyancy-Assisted Convection in a Heated Vertical Duct," *ASME JOURNAL OF HEAT TRANSFER*, Vol. 114, pp. 928-935.
- Habchi, S., and Acharya, S., 1986, "Laminar Mixed Convection in an Asymmetrically or Symmetrically Heated Vertical Channel," *Numerical Heat Transfer*, Vol. 9, pp. 605-618.
- Ingham, D. B., Keen, D. J., and Heggs, P. J., 1988a, "Two Dimensional Combined Convection in Vertical Parallel Plate Ducts, Including Situations of Flow Reversal," *Int. J. Numerical Methods in Engineering*, Vol. 26, pp. 1645-1664.
- Ingham, D. B., Keen, D. J., and Heggs, P. J., 1988b, "Flows in Vertical Channels With Asymmetric Wall Temperatures and Including Situations Where Reverse Flows Occur," *ASME JOURNAL OF HEAT TRANSFER*, Vol. 110, pp. 910-917.
- Jeng, Y. N., Chen, J. L., and Aung, W., 1992, "On the Reynolds-Number Independence of Mixed Convection in a Vertical Channel Subjected to Asymmetric Wall Temperature With and Without Flow Reversal," *Int. J. Heat Fluid Flow*, Vol. 13, pp. 329-339.
- Lee, K. T., and Yan, W. M., 1993, "Transient Conjugated Forced Convection Heat Transfer With Fully Developed Laminar Flow in Pipe," *Numerical Heat Transfer*, Part A, Vol. 23, pp. 341-359.
- Lin, T. F., and Kuo, J. C., 1988, "Transient Conjugated Heat Transfer in Fully Developed Laminar Pipe Flows," *Int. J. Heat Mass Transfer*, Vol. 31, pp. 1093-1102.

Lin, T. F., Yin, C. P., and Yan, W. M., 1991, "Transient Laminar Mixed Convection Heat Transfer in Vertical Flat Ducts," *ASME JOURNAL OF HEAT TRANSFER*, Vol. 113, pp. 384–390.

Lin, T. F., Chang, T. S., and Chen, Y. F., 1993, "Development of Oscillatory Asymmetric Recirculating Flow in Transient Laminar Opposing Mixed Convection in a Symmetrically Heated Vertical Channel," *ASME JOURNAL OF HEAT TRANSFER*, Vol. 105, pp. 342–352.

Patankar, S. V., 1980, *Numerical Heat Transfer and Fluid Flow*, Chaps. 4 and 5, Hemisphere/McGraw-Hill, New York.

Quintiere, J., and Muller, W. K., 1973, "An Analysis of Laminar Free and Forced Convection Between Finite Vertical Parallel Plates," *ASME JOURNAL OF HEAT TRANSFER*, Vol. 95, pp. 53–59.

Shah, R. K., and London, A. L., 1978, *Laminar Flow Forced Convection in Duct*, Academic Press, New York.

Sucec, J., 1987a, "Unsteady Conjugated Forced Convection Heat Transfer in a Duct With Convection From the Ambient," *Int. J. Heat Mass Transfer*, Vol. 30, pp. 1963–1970.

Sucec, J., 1987b, "Exact Solution for Unsteady Conjugated Heat Transfer in the Thermal Entrance Region of a Duct," *ASME JOURNAL OF HEAT TRANSFER*, Vol. 109, pp. 295–299.

Yan, W. M., and Lee, K. T., 1993, "Unsteady Conjugated Mixed Convection in a Vertical Channel," *ASME HTD-Vol. 247*, pp. 1–7.

## Buoyancy Effect on the Flow Reversal of Three-Dimensional Developing Flow in a Vertical Rectangular Duct—A Parabolic Model Solution

C.-H. Cheng,<sup>1</sup> C.-J. Weng,<sup>2</sup> and W. Aung<sup>3</sup>

### Introduction

The buoyancy effect on convective heat transfer in vertical passages has recently received considerable attention because of its profound influence on the flow pattern and thermal characteristics of fluid flow. Based on the existing information, it is recognized that when wall heating is sufficiently intense, buoyancy force can cause reversed flow even in buoyancy-assisted situations. Hanratty et al. (1958) performed experimental observation on the flow reversal in vertical circular tubes. Their studies clearly reveal reversed flow patterns in low Reynolds number flows. More recently, flow reversal is further observed experimentally by Gau et al. (1993a) for flow in an asymmetrically heated vertical parallel-plate channel.

Meanwhile, fully developed flow solutions presented by Aung and Worku (1986b) and Cheng et al. (1990) for flows in parallel-plate channels and presented by Cheng and Weng (1991) for flows in vertical rectangular ducts all exhibit the reversed flow pattern as the ratio of  $Gr/Re$  exceeds a threshold value. On the other hand, the buoyancy effect on the developing flows has also been studied extensively by researchers. For example, Aung and Worku (1986a) applied the boundary layer model to the analysis of developing flow in vertical channels. Gau et al. (1993b) and Cheng and Yang (1993) evaluated this effect in a finite-height vertical duct by solving the elliptic Navier–Stokes equations.

In these boundary layer analyses (e.g., Aung and Worku, 1986a), the streamwise diffusion terms in the governing equations are assumed to be negligible. Thus, the equations are parabolic in nature and can be solved by using finite-difference methods and a forward-marching procedure. If the boundary conditions at the inlet are given, the solutions can be calculated up to the fully developed region or to a point where the reversed flow is first detected. In boundary layer analyses, however, once the reversed-flow point is reached, the numerical computation usually diverges. Therefore, these analyses yield solutions merely up to the point of reversed flow, but in general fail to march across this point. To overcome this difficulty, Ingham et al. (1988) employed FLARE-like marching techniques to advance the numerical calculation into the downstream region. The FLARE approximation, proposed by Reyhner and Flugge-Lotz (1968), suggests that the axial convective term  $u\partial u/\partial x$  in the two-dimensional boundary layer momentum equation should be represented in the reversed flow regions by  $C|u|\partial u/\partial x$ , where  $C$  is zero or a small positive constant and  $u$  is just the axial velocity component. Compared with the elliptic models adopted by Gau et al. (1993b) and Cheng and Yang (1993), the parabolic boundary layer model requires much less computation effort but still appears to give smooth and plausible solutions for many flows with flow reversal. Such an advantage becomes particularly important in the study for three-dimensional flow.

Considering a vertical rectangular duct with one wall maintained at a higher temperature ( $T_H$ ) while the other three walls are at ambient temperature ( $T_L$ ), Cheng and Weng (1993) presented the numerical solutions of the developing flow in the situations involving no reversed flow. The fully developed solutions earlier provided by Cheng and Weng (1991) can precisely portray the asymptotic behavior of the developing flow of Cheng and Weng (1993). However, the three-dimensional flow reversal is not found and hence not adequately investigated because in the study of Cheng and Weng (1993), the ratio  $Gr/Re$  is not sufficiently high to produce reversed flows.

To extend the analysis of Cheng and Weng (1991, 1993) into situations of higher Grashof numbers in which three-dimensional flow reversal takes place, the parabolic boundary layer model of Cheng and Weng (1993) needs to be properly revised to predict the velocity and temperature fields. The FLARE method used previously for the two-dimensional problems (Ingham et al., 1988) is modified for the calculation of the present three-dimensional flow. As shown in Fig. 1, fluid enters a vertical rectangular duct of cross-sectional area  $x_0 \times y_0$  at ambient temperature ( $T_L$ ) with uniform velocity ( $\omega_0$ ). The flow traverses upward and is heated by the hotter wall in a buoyancy-assisted situation. In certain circumstances, for instance when the ratio  $Gr/Re$  is sufficiently large, flow reversal occurs downstream near the colder walls. The fully developed region is finally reached after a development length. The numerical solutions in the far downstream region should in principle approach asymptotically the fully developed solutions given by Cheng and Weng (1991). Such an agreement would illustrate the validity of the present theoretical model and the accuracy of the computation methods employed.

In this analysis, the maximum value of  $Gr/Re$  is 1100, and the aspect ratio ( $B = y_0/x_0$ ) is varied between 0.5 and 2. In addition, the Prandtl number is 0.71.

### Theoretical Analysis

The flow is considered to be steady and laminar, and the fluid properties are assumed to be constant except for the density in the buoyancy term of the momentum equation for the vertical direction. The mathematical formulation of the three-dimensional, boundary layer model for a Boussinesq fluid has been provided by Cheng and Weng (1993). Introduction of the modified FLARE method into the axial vertical momentum equation and the energy equation leads to the following dimensionless governing equations:

<sup>1</sup> Associate Professor, Department of Mechanical Engineering, Tatung Institute of Technology, Taipei, Taiwan.

<sup>2</sup> Graduate student, Department of Mechanical Engineering, Tatung Institute of Technology, Taipei, Taiwan.

<sup>3</sup> Division of Engineering Education and Centers, National Science Foundation, 4201 Wilson Boulevard, Arlington, VA 22230; Adjunct Professor, Department of Mechanical Engineering, University of Maryland, College Park, MD 20742.

Contributed by the Heat Transfer Division of THE AMERICAN SOCIETY OF MECHANICAL ENGINEERS. Manuscript received by the Heat Transfer Division May 1993; revision received May 1994. Keywords: Electronic Equipment, Flow Separation, Mixed Convection. Associate Technical Editor: Y. Jaluria.

Lin, T. F., Yin, C. P., and Yan, W. M., 1991, "Transient Laminar Mixed Convection Heat Transfer in Vertical Flat Ducts," *ASME JOURNAL OF HEAT TRANSFER*, Vol. 113, pp. 384–390.

Lin, T. F., Chang, T. S., and Chen, Y. F., 1993, "Development of Oscillatory Asymmetric Recirculating Flow in Transient Laminar Opposing Mixed Convection in a Symmetrically Heated Vertical Channel," *ASME JOURNAL OF HEAT TRANSFER*, Vol. 105, pp. 342–352.

Patankar, S. V., 1980, *Numerical Heat Transfer and Fluid Flow*, Chaps. 4 and 5, Hemisphere/McGraw-Hill, New York.

Quintiere, J., and Muller, W. K., 1973, "An Analysis of Laminar Free and Forced Convection Between Finite Vertical Parallel Plates," *ASME JOURNAL OF HEAT TRANSFER*, Vol. 95, pp. 53–59.

Shah, R. K., and London, A. L., 1978, *Laminar Flow Forced Convection in Duct*, Academic Press, New York.

Sucec, J., 1987a, "Unsteady Conjugated Forced Convection Heat Transfer in a Duct With Convection From the Ambient," *Int. J. Heat Mass Transfer*, Vol. 30, pp. 1963–1970.

Sucec, J., 1987b, "Exact Solution for Unsteady Conjugated Heat Transfer in the Thermal Entrance Region of a Duct," *ASME JOURNAL OF HEAT TRANSFER*, Vol. 109, pp. 295–299.

Yan, W. M., and Lee, K. T., 1993, "Unsteady Conjugated Mixed Convection in a Vertical Channel," *ASME HTD-Vol. 247*, pp. 1–7.

## Buoyancy Effect on the Flow Reversal of Three-Dimensional Developing Flow in a Vertical Rectangular Duct—A Parabolic Model Solution

C.-H. Cheng,<sup>1</sup> C.-J. Weng,<sup>2</sup> and W. Aung<sup>3</sup>

### Introduction

The buoyancy effect on convective heat transfer in vertical passages has recently received considerable attention because of its profound influence on the flow pattern and thermal characteristics of fluid flow. Based on the existing information, it is recognized that when wall heating is sufficiently intense, buoyancy force can cause reversed flow even in buoyancy-assisted situations. Hanratty et al. (1958) performed experimental observation on the flow reversal in vertical circular tubes. Their studies clearly reveal reversed flow patterns in low Reynolds number flows. More recently, flow reversal is further observed experimentally by Gau et al. (1993a) for flow in an asymmetrically heated vertical parallel-plate channel.

Meanwhile, fully developed flow solutions presented by Aung and Worku (1986b) and Cheng et al. (1990) for flows in parallel-plate channels and presented by Cheng and Weng (1991) for flows in vertical rectangular ducts all exhibit the reversed flow pattern as the ratio of  $Gr/Re$  exceeds a threshold value. On the other hand, the buoyancy effect on the developing flows has also been studied extensively by researchers. For example, Aung and Worku (1986a) applied the boundary layer model to the analysis of developing flow in vertical channels. Gau et al. (1993b) and Cheng and Yang (1993) evaluated this effect in a finite-height vertical duct by solving the elliptic Navier–Stokes equations.

In these boundary layer analyses (e.g., Aung and Worku, 1986a), the streamwise diffusion terms in the governing equations are assumed to be negligible. Thus, the equations are parabolic in nature and can be solved by using finite-difference methods and a forward-marching procedure. If the boundary conditions at the inlet are given, the solutions can be calculated up to the fully developed region or to a point where the reversed flow is first detected. In boundary layer analyses, however, once the reversed-flow point is reached, the numerical computation usually diverges. Therefore, these analyses yield solutions merely up to the point of reversed flow, but in general fail to march across this point. To overcome this difficulty, Ingham et al. (1988) employed FLARE-like marching techniques to advance the numerical calculation into the downstream region. The FLARE approximation, proposed by Reyhner and Flugge-Lotz (1968), suggests that the axial convective term  $u\partial u/\partial x$  in the two-dimensional boundary layer momentum equation should be represented in the reversed flow regions by  $C|u|\partial u/\partial x$ , where  $C$  is zero or a small positive constant and  $u$  is just the axial velocity component. Compared with the elliptic models adopted by Gau et al. (1993b) and Cheng and Yang (1993), the parabolic boundary layer model requires much less computation effort but still appears to give smooth and plausible solutions for many flows with flow reversal. Such an advantage becomes particularly important in the study for three-dimensional flow.

Considering a vertical rectangular duct with one wall maintained at a higher temperature ( $T_H$ ) while the other three walls are at ambient temperature ( $T_L$ ), Cheng and Weng (1993) presented the numerical solutions of the developing flow in the situations involving no reversed flow. The fully developed solutions earlier provided by Cheng and Weng (1991) can precisely portray the asymptotic behavior of the developing flow of Cheng and Weng (1993). However, the three-dimensional flow reversal is not found and hence not adequately investigated because in the study of Cheng and Weng (1993), the ratio  $Gr/Re$  is not sufficiently high to produce reversed flows.

To extend the analysis of Cheng and Weng (1991, 1993) into situations of higher Grashof numbers in which three-dimensional flow reversal takes place, the parabolic boundary layer model of Cheng and Weng (1993) needs to be properly revised to predict the velocity and temperature fields. The FLARE method used previously for the two-dimensional problems (Ingham et al., 1988) is modified for the calculation of the present three-dimensional flow. As shown in Fig. 1, fluid enters a vertical rectangular duct of cross-sectional area  $x_0 \times y_0$  at ambient temperature ( $T_L$ ) with uniform velocity ( $\omega_0$ ). The flow traverses upward and is heated by the hotter wall in a buoyancy-assisted situation. In certain circumstances, for instance when the ratio  $Gr/Re$  is sufficiently large, flow reversal occurs downstream near the colder walls. The fully developed region is finally reached after a development length. The numerical solutions in the far downstream region should in principle approach asymptotically the fully developed solutions given by Cheng and Weng (1991). Such an agreement would illustrate the validity of the present theoretical model and the accuracy of the computation methods employed.

In this analysis, the maximum value of  $Gr/Re$  is 1100, and the aspect ratio ( $B = y_0/x_0$ ) is varied between 0.5 and 2. In addition, the Prandtl number is 0.71.

### Theoretical Analysis

The flow is considered to be steady and laminar, and the fluid properties are assumed to be constant except for the density in the buoyancy term of the momentum equation for the vertical direction. The mathematical formulation of the three-dimensional, boundary layer model for a Boussinesq fluid has been provided by Cheng and Weng (1993). Introduction of the modified FLARE method into the axial vertical momentum equation and the energy equation leads to the following dimensionless governing equations:

<sup>1</sup> Associate Professor, Department of Mechanical Engineering, Tatung Institute of Technology, Taipei, Taiwan.

<sup>2</sup> Graduate student, Department of Mechanical Engineering, Tatung Institute of Technology, Taipei, Taiwan.

<sup>3</sup> Division of Engineering Education and Centers, National Science Foundation, 4201 Wilson Boulevard, Arlington, VA 22230; Adjunct Professor, Department of Mechanical Engineering, University of Maryland, College Park, MD 20742.

Contributed by the Heat Transfer Division of THE AMERICAN SOCIETY OF MECHANICAL ENGINEERS. Manuscript received by the Heat Transfer Division May 1993; revision received May 1994. Keywords: Electronic Equipment, Flow Separation, Mixed Convection. Associate Technical Editor: Y. Jaluria.

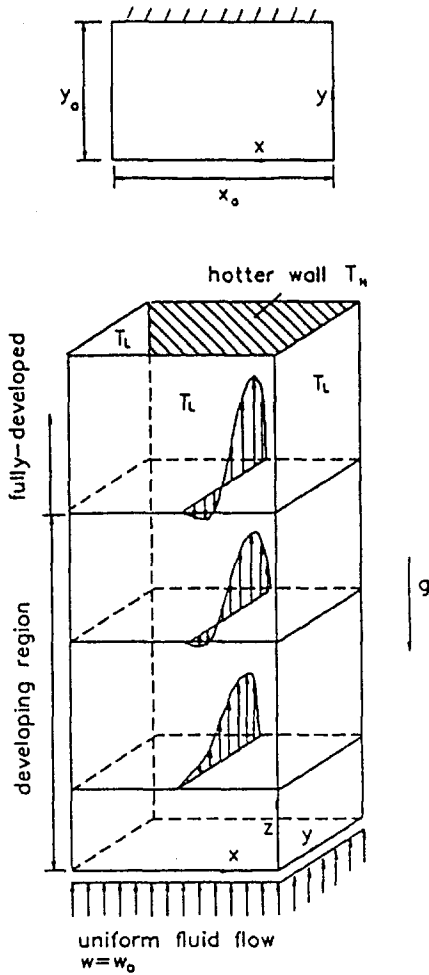


Fig. 1 Reversed flow in a vertical duct with one heated wall

In the above,  $p_L$  is the pressure in the ambient fluid,  $d\bar{P}/dZ$  is the streamwise gradient of the dimensionless mean pressure, and  $C = 0$  for  $w(x, y) < 0$  and  $C = 1$  for  $w(x, y) \geq 0$  in the FLARE formulation. Note that in the present modified version of the FLARE approximation the momentum equations in the two transverse directions, Eqs. (2) and (3), are expressed in the original forms so as to reduce the potential error of the approximation. As a matter of fact, it has been found that the introduction of the FLARE approximation into the convective terms of these two equations leads to a difference of less than 1 percent in the respective results.

The flow entering the duct at the inlet plane is considered to have a uniform velocity profile ( $w_0$ ) and at ambient temperature ( $T_L$ ) and pressure ( $p_L$ ). Thus, by using the dimensionless parameters, these boundary conditions can be written as

$$U = V = 0, \quad W = 1, \quad \bar{P} = 0, \quad \theta = 0 \quad \text{at } Z = 0 \quad (6)$$

On the other hand, on the solid walls, the no-slip condition is specified for all velocity components. Three of the walls of the duct are maintained at ambient temperature ( $\theta = 0$ ), while the wall at  $Y = 1$  is at a higher temperature ( $\theta = 1$ ).

The numerical methods for solving the equations have been described in detail by Cheng and Weng (1993). It is worth noting that the axial pressure  $d\bar{P}/dZ$  at each cross section is adjusted iteratively to make the axial velocity profile  $W(X, Y)$  satisfy the overall mass conservation. When reversed flow occurs, however, the iteration procedure used by Cheng and Weng (1993) needs some modifications to prevent divergence of the solution.

The computation starts from the inlet at  $Z = 0$ , and then is advanced continuously in the axial direction. By following this axial marching procedure, the solutions at each cross section are obtained by using the known values at the previous cross section. The computation is terminated when the fully developed flow region is reached. The flow is fully developed when the relative changes of the axial velocity profiles between consecutive cross sections are less than  $10^{-4}$  at all grid points.

## Results and Discussion

Figure 2 shows the developing axial velocity and temperature distributions at different axial locations by using the lines of equal axial velocity ( $W$ ) and the isothermal lines, for  $B = 1$  and  $Gr/Re = 200$  and  $350$ . Since the solutions are symmetric with respect to the middle plane ( $X = 1/2$ ), each cross section is divided into two and the velocity and temperature distributions are displayed on the left and right halves, respectively. It is noticed that the fluid near the hotter wall is accelerated by the buoyancy force. Consequently, the reversed flow is first found at the corners of the colder walls. The reversed flow develops gradually in the axial direction and then occupies the low-temperature zone of the cross section. The development of the thermal boundary layer on the hotter wall can also be observed from the temperature fields. Note that a higher  $Gr/Re$  leads to a larger region of an earlier appearing flow reversal.

The threshold value of  $Gr/Re$  for reversed flow to occur obviously increases with the aspect ratio ( $B$ ), as the value of  $B$  is varied from 1 to 2.

The development of the velocity profiles at the middle plane ( $X = 1/2$ ) for various aspect ratios and Grashof numbers is shown in Fig. 3. The dashed curves in this figure represent the present numerical results. Observe that the curves of  $Z \rightarrow \infty$  exactly approach the analytical fully developed solutions presented by Cheng and Weng (1991).

The solutions for temperature distribution can be used to calculate the local heat transfer rate. The local Nusselt number,  $Nu_{x,z}$ , denoting the dimensionless local heat flux on the hotter wall, is defined by

$$\frac{\partial U}{\partial X} + \frac{\partial V}{\partial Y} + \frac{\partial W}{\partial Z} = 0 \quad (1)$$

$$\frac{\partial U^2}{\partial X} + \frac{\partial(VU)}{\partial Y} + \frac{\partial(WU)}{\partial Z} = -B^2 \frac{\partial P}{\partial X} + B^2 \frac{\partial^2 U}{\partial X^2} + \frac{\partial^2 U}{\partial Y^2} \quad (2)$$

$$\frac{\partial(UV)}{\partial X} + \frac{\partial V^2}{\partial Y} + \frac{\partial(WV)}{\partial Z} = -\frac{\partial P}{\partial Y} + B^2 \frac{\partial^2 V}{\partial X^2} + \frac{\partial^2 V}{\partial Y^2} \quad (3)$$

$$\begin{aligned} \frac{\partial(UW)}{\partial X} + \frac{\partial(VW)}{\partial Y} + \frac{\partial W^2}{\partial Z} + \left[ C|W| \frac{\partial W}{\partial Z} - W \frac{\partial W}{\partial Z} \right] \\ = -\frac{d\bar{P}}{dZ} + B^2 \frac{\partial^2 W}{\partial X^2} + \frac{\partial^2 W}{\partial Y^2} + \frac{Gr}{Re} \theta \end{aligned} \quad (4)$$

$$\begin{aligned} \frac{\partial(U\theta)}{\partial X} + \frac{\partial(V\theta)}{\partial Y} + \frac{\partial(W\theta)}{\partial Z} + \left[ C|W| \frac{\partial \theta}{\partial Z} - W \frac{\partial \theta}{\partial Z} \right] \\ = \frac{1}{Pr} \left( B^2 \frac{\partial^2 \theta}{\partial X^2} + \frac{\partial^2 \theta}{\partial Y^2} \right) \end{aligned} \quad (5)$$

where the dimensionless parameters have been defined as

$$X = x/x_0, \quad Y = y/y_0, \quad Z = z/(y_0 Re), \quad B = y_0/x_0,$$

$$U = uy_0^2/(\nu x_0), \quad V = vy_0/\nu, \quad W = w/w_0, \quad P = py_0^2/(\rho\nu^2),$$

$$\bar{P} = (\bar{p} - p_L)/(\rho w_0^2), \quad \theta = (T - T_L)/(T_H - T_L)$$

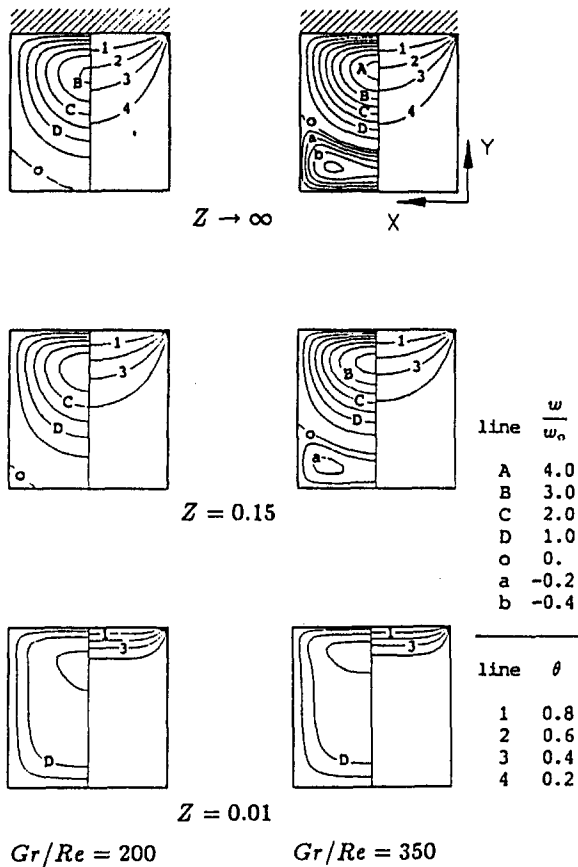


Fig. 2 Developing axial velocity ( $w/w_0$ , left half) and temperature ( $\theta$ , right half) distributions for  $Pr = 0.71$ ,  $B = 1$ ,  $Gr/Re = 200$  and  $350$

$$Nu_x = \frac{y_0}{T_H - T_L} \frac{\partial T}{\partial y} \Big|_{y=y_0} = \frac{\partial \theta}{\partial Y} \Big|_{Y=1} \quad (7)$$

$Nu_x$  is a function of  $X$  along the wall surface, and may be calculated at different axial locations. Integration of  $Nu_x$  with respect to  $X$  from  $X = 0$  to  $X = 1$  yields the average Nusselt number,  $\bar{Nu}$ , on the hotter wall, i.e.,

$$\bar{Nu} = \frac{1}{x_0} \int_0^{x_0} \left( \frac{y_0}{T_H - T_L} \frac{\partial T}{\partial y} \Big|_{y=y_0} \right) dx = \int_0^1 Nu_x dX \quad (8)$$

The data of  $\bar{Nu}$  at different axial locations indicate the axial variation of heat transfer.

Variation of heat transfer and pressure along the streamwise direction for  $B = 1$  and  $Pr = 0.71$  is shown in Fig. 4. The value of the Nusselt number, which increases with  $Gr/Re$ , approaches asymptotically a constant, minimum value as the fully developed region is reached. Note that a higher value of  $B$  indicates a smaller dimensionless area of cross section; therefore, a higher cross-sectional temperature gradient and hence, a higher Nusselt number may be expected. Furthermore, an adverse pressure gradient develops downstream when the value of  $Gr/Re$  is sufficiently high. This adverse pressure gradient provides the driving force to the occurrence of reversed flow.

To have a deeper insight into the development of the adverse pressure gradient downstream, Table 1 displays the variation of pressure gradient ( $-dP/dZ$ ) in the  $Z$  direction for  $B = 2$  under various values of  $Gr/Re$ . The fully developed flow solutions (Cheng and Weng, 1991) are also given in this table for comparison. As  $Gr/Re$  is sufficiently large, an adverse pressure gradient (i.e.,  $-dP/dZ < 0$ ) can be seen downstream. In general,

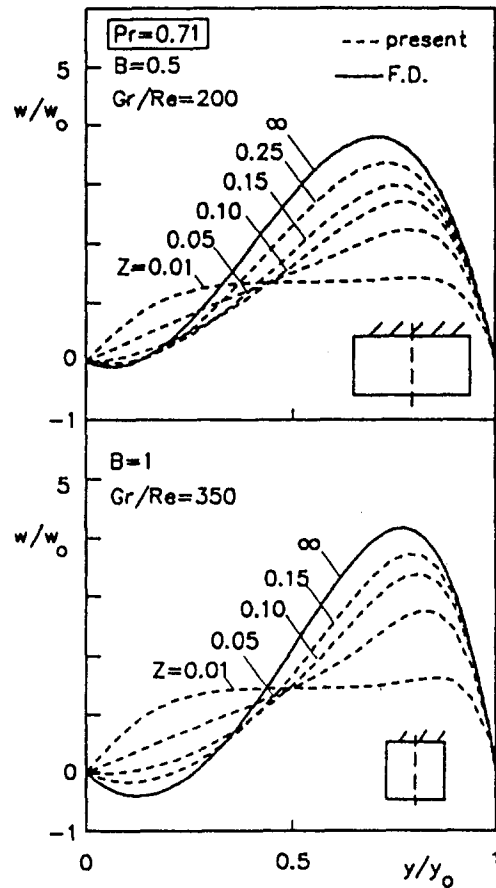


Fig. 3 Developing axial velocity profiles at the middle plane ( $X = 1/2$ ) for  $Pr = 0.71$

the magnitude of this adverse pressure gradient increases with  $Gr/Re$ .

## Conclusions

The buoyancy-induced flow reversal phenomenon in the developing regions of vertical rectangular ducts has been studied numerically. The parabolic boundary layer model is adopted to predict the three-dimensional developing flow. A modified

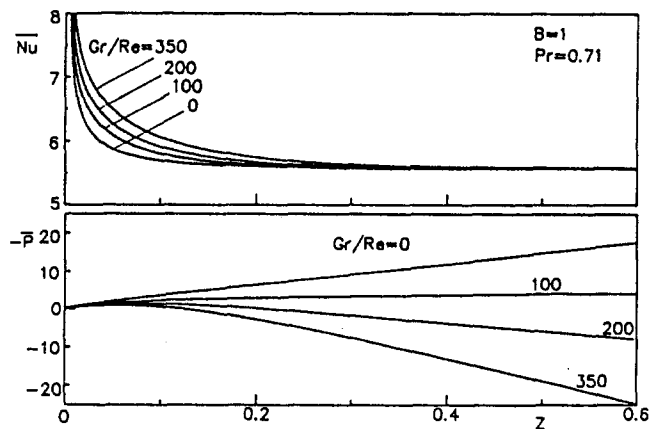


Fig. 4 Variation of average Nusselt number and dimensionless pressure defect in streamwise direction, for  $B = 1$  and  $Pr = 0.71$

**Table 1**  $-\bar{d}P/dZ$  as a function of Gr/Re and Z for Pr = 0.71 and B = 2

z	Gr/Re						
	0	100	300	500	700	900	1100
0.001	206.18	199.81	189.13	180.56	171.47	165.98	161.34
0.01	82.82	74.78	64.16	57.03	52.00	47.87	44.47
0.1	69.50	58.52	38.12	20.68	6.81	-4.60	-14.08
0.5	69.49	58.27	35.82	13.36	-9.09	-31.51	-53.83
$\infty$	69.49	58.27	35.82	13.36	-9.09	-31.54	-53.98
F.D.*	69.97	58.79	36.44	14.10	-8.25	-30.60	-52.94

\* Presented by Cheng and Weng (1991).

FLARE approximation is introduced into the governing equations in order to advance the marching computation procedure into the downstream region in which reversed flow occurs.

It is found that the strength and the extent of the reversed flow are dependent mainly on the ratio Gr/Re and the aspect ratio of the cross section B. In general, the threshold value of Gr/Re for the occurrence of flow reversal becomes higher when the value of B is increased. Due to the buoyancy-assisted flow effects, an adverse pressure gradient develops downstream as Gr/Re is sufficiently high. The adverse pressure gradient is the major supporting force to the flow reversal.

The Nusselt number on the hotter wall increases appreciably with Gr/Re. The value of the Nusselt number approaches asymptotically a constant, minimum value as the fully developed region is reached. The existing analytical solution of fully developed flow and numerical solution of developing flow without flow reversal (Cheng and Weng, 1991, 1993) are found to agree closely with the limiting cases of the solutions reported in this study.

### Acknowledgments

Financial support for this study from the National Science Council, Taiwan, under Grant No. NSC 81-0401-E036-509, is gratefully acknowledged.

### References

- Aung, W., and Worku, G., 1986a, "Developing Flow and Flow Reversal in a Vertical Channel With Asymmetric Wall Temperatures," *ASME JOURNAL OF HEAT TRANSFER*, Vol. 108, pp. 299-304.
- Aung, W., and Worku, G., 1986b, "Theory of Fully Developed Combined Convection Including Flow Reversal," *ASME JOURNAL OF HEAT TRANSFER*, Vol. 108, pp. 485-488.
- Cheng, C. H., Kou, H. S., and Huang, W. H., 1990, "Flow Reversal and Heat Transfer of the Fully Developed Mixed Convection in Vertical Channels," *AIAA J. Thermophysics and Heat Transfer*, Vol. 4, pp. 375-383.
- Cheng, C. H., and Weng, C. J., 1991, "Flow Reversal of Combined Convection in a Vertical Rectangular Duct With Unequally Isothermal Walls," *Int. Comm. Heat Mass Transfer*, Vol. 18, pp. 127-140.
- Cheng, C. H., and Weng, C. J., 1993, "Developing Flow of Mixed Convection in a Vertical Rectangular Duct With One Heating Wall," *Numerical Heat Transfer*, Part A, Vol. 24, pp. 479-493.
- Cheng, C. H., and Yang, J. J., 1993, "Buoyancy-Induced Recirculation Bubbles and Heat Convection of Developing Flow in Vertical Channels With Fin Arrays," *Int. J. Heat Fluid Flow*, Vol. 15, pp. 11-19.
- Gau, C., Yih, K. A., and Aung, W., 1992, "Reversed Flow Structure and Heat Transfer Measurements for Buoyancy Assisted Convection in a Heated Vertical Duct," *ASME JOURNAL OF HEAT TRANSFER*, Vol. 114, pp. 928-935.
- Gau, C., Yih, K. A., and Aung, W., 1993, "Numerical and Analytical Study of Reversed Flow and Heat Transfer in a Heated Vertical Duct," *Mixed Convection Heat Transfer*, M. Keyhani and R. Kumar, eds., ASME HTD-Vol. 247, pp. 9-19.
- Hanratty, T. J., Rosen, E. M., and Kabel, R. L., 1958, "Effect of Heat Transfer on Flow Field at Low Reynolds Numbers in Vertical Tubes," *Industrial Engineering Chemistry*, Vol. 50, pp. 815-820.
- Ingham, D. B., Keen, D. J., and Heggis, P. J., 1988, "Flow in Vertical Channels With Asymmetric Wall Temperature and Including Situations Where Reverse Flows Occur," *ASME JOURNAL OF HEAT TRANSFER*, Vol. 110, pp. 910-917.
- Reyhner, T. A., and Flugge-Lotz, I., 1968, "The Interaction of a Shock Wave With a Laminar Boundary Layer," *International Journal of Non-linear Mechanics*, Vol. 3, pp. 173-199.

## On the Superposition Rule for Configuration Factors

K. G. T. Hollands<sup>1</sup>

### Nomenclature

- a = dimension, see Fig. 3  
A = area  
 $dA_{1m}$  = general elemental surface at 1 oriented such that its normal is  $\hat{m}$  (Fig. 1)  
 $dA_{1m+}$ ,  $dA_{1m-}$  = opposite faces of  $dA_{1m}$  (Fig. 1)  
b, c = dimensions, see Fig. 3  
 $F_{u-v}$  = configuration factor from surface u to surface v, e.g.,  $F_{(dA_{1i-})-2}$  is the configuration factor from  $dA_{1i-}$  to 2, as shown in Fig. 2(b)  
h = dimension, see Fig. 3  
H = in Eq. (12),  $H = h/a$ ; in Eq. (13),  $H = h/r$   
 $\hat{i}, \hat{j}, \hat{k}$  = unit vectors in x, y, and z directions, respectively  
 $\hat{m}$  = general unit vector, =  $\hat{i}, \hat{j}, \hat{k}$ , or  $\hat{n}$   
 $\hat{n}$  = unit vector normal to surface  $dA_1$  of interest  
 $P = \sqrt{Z^2 - 4R^2}$   
 $\vec{q}$  = radiant flux vector  
 $q_i, q_j, q_k, q_n$  = components of  $\vec{q}$  (i.e., net radiant fluxes) in  $\hat{i}, \hat{j}, \hat{k}$  and  $\hat{n}$  directions, respectively  
r = dimension, see Fig. 3; also magnitude of  $\vec{r}$   
 $\vec{r}$  = vector joining  $dA_1$  and  $dA_2$   
R = r/a  
x, y, z = rectangular coordinates of  $dA_1$   
 $\theta_i, \theta_j, \theta_k$  = direction angles of  $\hat{n}$  (see Fig. 2d)  
 $\varphi_1(\hat{m})$  = angle between  $\vec{r}$  and  $\hat{m}$   
 $\varphi_2$  = angle between normal to  $dA_2$  and  $\vec{r}$

### Introduction

As is well known, the task of calculating configuration factors is assisted by a number of special analytical tools, or rules, such as reciprocity, additivity, flux algebra, and contour integration. These rules permit analysts to avoid or simplify the arduous task of analytic integration. The superposition principle, first elaborated by Sparrow (1963), is one such rule: It enables the analyst to calculate the configuration factor between a finite area ( $A_2$ ) and an infinitesimal area ( $dA_1$ ) (see Fig. 1) from a weighted sum of three other configuration factors. The weights are the direction cosines of the normal to  $dA_1$ , and the three other configuration factors are those between  $A_2$  and each of three mutually perpendicular infinitesimal areas at the same location as  $dA_1$ , as shown in Fig. 2, in which  $dA_1$  has been located at the origin.

The superposition rule does not appear to be widely used; it is not described in recent textbooks, either undergraduate or graduate level, nor is it contained in heat transfer handbooks. The reason is probably the complexity of its application and the restrictions on its use. As originally described (Sparrow, 1963), it required that the finite area  $A_2$  be viewed completely from each of the three mutually perpendicular areas. This requirement is quite restrictive; ordinarily  $A_2$  will lie partly behind at least one of these three areas. Sparrow and Cess (1970) relaxed that restriction. They argued that one can sum the configuration factors

<sup>1</sup> Department of Mechanical Engineering, University of Waterloo, Waterloo, Ontario Canada N2L 3G1.

Contributed by the Heat Transfer Division of THE AMERICAN SOCIETY OF MECHANICAL ENGINEERS. Manuscript received by the Heat Transfer Division August 1993; revision received February 1994. Keywords: Radiation. Associate Technical Editor: M. Modest.



**Table 1**  $-\bar{d}P/dZ$  as a function of Gr/Re and Z for Pr = 0.71 and B = 2

z	Gr/Re						
	0	100	300	500	700	900	1100
0.001	206.18	199.81	189.13	180.56	171.47	165.98	161.34
0.01	82.82	74.78	64.16	57.03	52.00	47.87	44.47
0.1	69.50	58.52	38.12	20.68	6.81	-4.60	-14.08
0.5	69.49	58.27	35.82	13.36	-9.09	-31.51	-53.83
$\infty$	69.49	58.27	35.82	13.36	-9.09	-31.54	-53.98
F.D.*	69.97	58.79	36.44	14.10	-8.25	-30.60	-52.94

\* Presented by Cheng and Weng (1991).

FLARE approximation is introduced into the governing equations in order to advance the marching computation procedure into the downstream region in which reversed flow occurs.

It is found that the strength and the extent of the reversed flow are dependent mainly on the ratio Gr/Re and the aspect ratio of the cross section B. In general, the threshold value of Gr/Re for the occurrence of flow reversal becomes higher when the value of B is increased. Due to the buoyancy-assisted flow effects, an adverse pressure gradient develops downstream as Gr/Re is sufficiently high. The adverse pressure gradient is the major supporting force to the flow reversal.

The Nusselt number on the hotter wall increases appreciably with Gr/Re. The value of the Nusselt number approaches asymptotically a constant, minimum value as the fully developed region is reached. The existing analytical solution of fully developed flow and numerical solution of developing flow without flow reversal (Cheng and Weng, 1991, 1993) are found to agree closely with the limiting cases of the solutions reported in this study.

### Acknowledgments

Financial support for this study from the National Science Council, Taiwan, under Grant No. NSC 81-0401-E036-509, is gratefully acknowledged.

### References

- Aung, W., and Worku, G., 1986a, "Developing Flow and Flow Reversal in a Vertical Channel With Asymmetric Wall Temperatures," *ASME JOURNAL OF HEAT TRANSFER*, Vol. 108, pp. 299-304.
- Aung, W., and Worku, G., 1986b, "Theory of Fully Developed Combined Convection Including Flow Reversal," *ASME JOURNAL OF HEAT TRANSFER*, Vol. 108, pp. 485-488.
- Cheng, C. H., Kou, H. S., and Huang, W. H., 1990, "Flow Reversal and Heat Transfer of the Fully Developed Mixed Convection in Vertical Channels," *AIAA J. Thermophysics and Heat Transfer*, Vol. 4, pp. 375-383.
- Cheng, C. H., and Weng, C. J., 1991, "Flow Reversal of Combined Convection in a Vertical Rectangular Duct With Unequally Isothermal Walls," *Int. Comm. Heat Mass Transfer*, Vol. 18, pp. 127-140.
- Cheng, C. H., and Weng, C. J., 1993, "Developing Flow of Mixed Convection in a Vertical Rectangular Duct With One Heating Wall," *Numerical Heat Transfer, Part A*, Vol. 24, pp. 479-493.
- Cheng, C. H., and Yang, J. J., 1993, "Buoyancy-Induced Recirculation Bubbles and Heat Convection of Developing Flow in Vertical Channels With Fin Arrays," *Int. J. Heat Fluid Flow*, Vol. 15, pp. 11-19.
- Gau, C., Yih, K. A., and Aung, W., 1992, "Reversed Flow Structure and Heat Transfer Measurements for Buoyancy Assisted Convection in a Heated Vertical Duct," *ASME JOURNAL OF HEAT TRANSFER*, Vol. 114, pp. 928-935.
- Gau, C., Yih, K. A., and Aung, W., 1993, "Numerical and Analytical Study of Reversed Flow and Heat Transfer in a Heated Vertical Duct," *Mixed Convection Heat Transfer*, M. Keyhani and R. Kumar, eds., ASME HTD-Vol. 247, pp. 9-19.
- Hanratty, T. J., Rosen, E. M., and Kabel, R. L., 1958, "Effect of Heat Transfer on Flow Field at Low Reynolds Numbers in Vertical Tubes," *Industrial Engineering Chemistry*, Vol. 50, pp. 815-820.
- Ingham, D. B., Keen, D. J., and Heggis, P. J., 1988, "Flow in Vertical Channels With Asymmetric Wall Temperature and Including Situations Where Reverse Flows Occur," *ASME JOURNAL OF HEAT TRANSFER*, Vol. 110, pp. 910-917.
- Reyhner, T. A., and Flugge-Lotz, I., 1968, "The Interaction of a Shock Wave With a Laminar Boundary Layer," *International Journal of Non-linear Mechanics*, Vol. 3, pp. 173-199.

## On the Superposition Rule for Configuration Factors

K. G. T. Hollands<sup>1</sup>

### Nomenclature

- a = dimension, see Fig. 3  
 A = area  
 $dA_{1m}$  = general elemental surface at 1 oriented such that its normal is  $\hat{m}$  (Fig. 1)  
 $dA_{1m+}$ ,  $dA_{1m-}$  = opposite faces of  $dA_{1m}$  (Fig. 1)  
 b, c = dimensions, see Fig. 3  
 $F_{u-v}$  = configuration factor from surface u to surface v, e.g.,  $F_{(dA_{1i-})-2}$  is the configuration factor from  $dA_{1i-}$  to 2, as shown in Fig. 2(b)  
 h = dimension, see Fig. 3  
 H = in Eq. (12),  $H = h/a$ ; in Eq. (13),  $H = h/r$   
 $\hat{i}, \hat{j}, \hat{k}$  = unit vectors in x, y, and z directions, respectively  
 $\hat{m}$  = general unit vector, =  $\hat{i}, \hat{j}, \hat{k}$ , or  $\hat{n}$   
 $\hat{n}$  = unit vector normal to surface  $dA_1$  of interest  
 $P = \sqrt{Z^2 - 4R^2}$   
 $\vec{q}$  = radiant flux vector  
 $q_i, q_j, q_k, q_n$  = components of  $\vec{q}$  (i.e., net radiant fluxes) in  $\hat{i}, \hat{j}, \hat{k}$  and  $\hat{n}$  directions, respectively  
 r = dimension, see Fig. 3; also magnitude of  $\vec{r}$   
 $\vec{r}$  = vector joining  $dA_1$  and  $dA_2$   
 R = r/a  
 x, y, z = rectangular coordinates of  $dA_1$   
 $\theta_i, \theta_j, \theta_k$  = direction angles of  $\hat{n}$  (see Fig. 2d)  
 $\varphi_1(\hat{m})$  = angle between  $\vec{r}$  and  $\hat{m}$   
 $\varphi_2$  = angle between normal to  $dA_2$  and  $\vec{r}$

### Introduction

As is well known, the task of calculating configuration factors is assisted by a number of special analytical tools, or rules, such as reciprocity, additivity, flux algebra, and contour integration. These rules permit analysts to avoid or simplify the arduous task of analytic integration. The superposition principle, first elaborated by Sparrow (1963), is one such rule: It enables the analyst to calculate the configuration factor between a finite area ( $A_2$ ) and an infinitesimal area ( $dA_1$ ) (see Fig. 1) from a weighted sum of three other configuration factors. The weights are the direction cosines of the normal to  $dA_1$ , and the three other configuration factors are those between  $A_2$  and each of three mutually perpendicular infinitesimal areas at the same location as  $dA_1$ , as shown in Fig. 2, in which  $dA_1$  has been located at the origin.

The superposition rule does not appear to be widely used; it is not described in recent textbooks, either undergraduate or graduate level, nor is it contained in heat transfer handbooks. The reason is probably the complexity of its application and the restrictions on its use. As originally described (Sparrow, 1963), it required that the finite area  $A_2$  be viewed completely from each of the three mutually perpendicular areas. This requirement is quite restrictive; ordinarily  $A_2$  will lie partly behind at least one of these three areas. Sparrow and Cess (1970) relaxed that restriction. They argued that one can sum the configuration factors

<sup>1</sup> Department of Mechanical Engineering, University of Waterloo, Waterloo, Ontario Canada N2L 3G1.

Contributed by the Heat Transfer Division of THE AMERICAN SOCIETY OF MECHANICAL ENGINEERS. Manuscript received by the Heat Transfer Division August 1993; revision received February 1994. Keywords: Radiation. Associate Technical Editor: M. Modest.

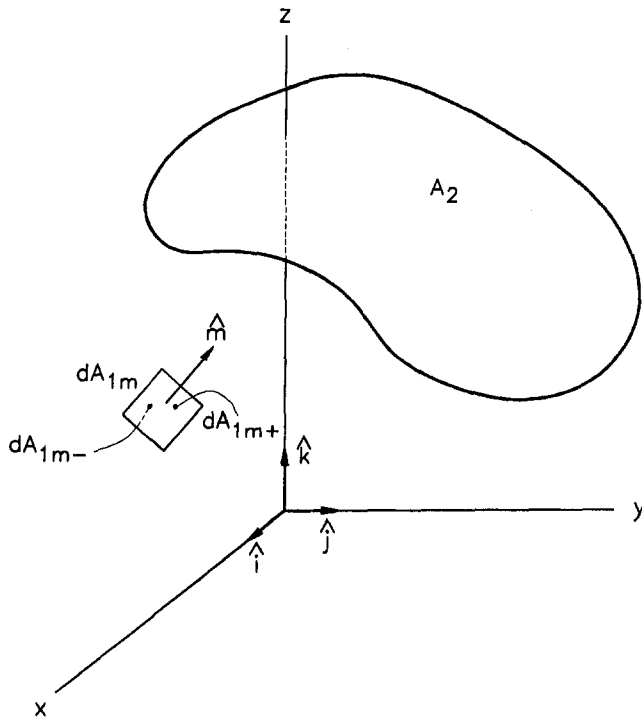


Fig. 1 General surface element  $dA_{1m}$  facing finite area  $A_2$ ; showing distinction between two sides of  $dA_{1m}$

from each side of the three mutually perpendicular areas, and then enter these three sums into the weighted sum formula. But this means that in general six configuration factors must be first determined to apply the rule, and this may have made the task of applying the rule too daunting for common use.

This paper will show that the configuration factors from each side of the three areas should be *subtracted*, rather than *summed*, before being entered into the weighted sum formula. This means that if the two configuration factors, one from each side, are equal because of symmetry, their difference will be zero, and considerable simplification is achieved. Whereas Sparrow derived the rule as a consequence of the method of contour integration, the rule is rederived here from the properties of the radiant flux vector. This places it in a somewhat different context, and makes it clear why the difference is required.

### Rule Derivation Using the Radiant Flux Vector

It will be recalled that the radiant flux vector  $\vec{q}$  at general point  $P_1$  is the vector sum of the *net* radiant flux on three mutually perpendicular elemental surfaces at  $P_1$ , each flux multiplied by its corresponding unit normal. Thus if we choose unit vectors  $\hat{i}$ ,  $\hat{j}$ , and  $\hat{k}$  along the  $x$ ,  $y$ , and  $z$  axes, respectively, to be the three unit normals, then

$$\vec{q} = q_i \hat{i} + q_j \hat{j} + q_k \hat{k} \quad (1)$$

where  $q_i$ ,  $q_j$ , and  $q_k$  are the net fluxes in the  $x$ ,  $y$ , and  $z$  directions, respectively. The important property of  $\vec{q}$  is that, once  $\vec{q}$  at  $P_1$  has been determined, the net radiant flux  $q_n$  on any arbitrarily oriented elemental surface at  $P_1$  can be determined directly. Thus if  $\hat{n}$  is the unit normal to the arbitrarily orientated surface,  $q_n$  is given by

$$q_n = \vec{q} \cdot \hat{n} \quad (2)$$

Let  $A_2$  (Fig. 1) be some black isothermal surface in space, let the space between  $A_2$  and  $P_1$  be transparent, and let the rest of space be at absolute zero. Let  $dA_{1m}$  be both sides of a general

elemental surface at 1 oriented such that its unit normal is general unit vector  $\hat{m}$ . As shown in Fig. 1, let  $dA_{1m+}$  be the side that has  $\hat{m}$  directed *out*, and let  $dA_{1m-}$  be the side that has  $\hat{m}$  directed *in*. In other words  $dA_{1m+}$  and  $dA_{1m-}$  are opposite faces of the same surface,  $dA_{1m}$ , and  $dA_{1m+} = dA_{1m-} = \frac{1}{2} dA_{1m}$ . If the emissive power at 2 is unity, then the net radiant flux  $q_m$  at 1 in direction  $\hat{m}$  can be written

$$q_m = (A_2 F_{2-(d1m-)} - A_2 F_{2-(d1m+)}) / dA_{1m+}$$

or

$$q_m = F_{(d1m-)-2} - F_{(d1m+)-2} \quad (3)$$

We write Eq. (3), which applies to general  $\hat{m}$ , four times: for  $\hat{m} = \hat{i}$ ,  $\hat{j}$ ,  $\hat{k}$  and  $\hat{n}$  in turn; thus

$$q_i = F_{(d1i-)-2} - F_{(d1i+)-2} \quad (4a)$$

$$q_j = F_{(d1j-)-2} - F_{(d1j+)-2} \quad (4b)$$

$$q_k = F_{(d1k-)-2} - F_{(d1k+)-2} \quad (4c)$$

$$q_n = F_{(d1n-)-2} - F_{(d1n+)-2} \quad (4d)$$

We consider  $dA_{1n+}$  to be the surface side from which we are trying to evaluate the configuration factor to  $A_2$ . Substituting Eq. (4) into Eq. (2), and re-arranging gives

$$F_{(d1n+)-2} = F_{(d1n-)-2} + \sum_{m=i,j,k} (F_{(d1m+)-2} - F_{(d1m-)-2}) \cos \theta_m \quad (5)$$

where  $\theta_i$ ,  $\theta_j$  and  $\theta_k$  (shown in Fig. 2) are the direction angles of  $\hat{n}$ : i.e.,  $\hat{n} = (\cos \theta_i, \cos \theta_j, \cos \theta_k)$ . Equation (5) is the "superposition rule" for configuration factors, in its most general form. It expresses a configuration factor at 1 in terms of seven other configuration factors.

### Application of the Rule

In applying the superposition rule it will normally be assumed that the plane of  $dA_{1n}$  does not cut through  $A_2$ , i.e., that  $A_2$  lies completely on one side of  $dA_{1n}$ —say the side having unit outward normal  $\hat{n}$ . From this it follows that  $F_{(d1n-)-2} = 0$ . Dropping the subscript plus sign on the left-hand side of Eqs. (5) as understood, Eq. (5), with this assumption, becomes

$$F_{d1n-2} = \sum_{m=i,j,k} (F_{(d1m+)-2} - F_{(d1m-)-2}) \cos \theta_m \quad (6)$$

The simplest applications of the superposition rule arise in cases where  $A_2$  has some special properties with respect to point 1. For convenience in notation, let point 1 lie at the origin O (Fig. 1). We consider in turn, cases where  $A_2$  is symmetric about one or more of the coordinate planes, or where  $A_2$  lies completely on one side of one or more coordinate planes; or both. This will imply that one or more pairs of the configuration factors in Eq. (6) are either equal (making the difference equal to zero) or zero.

**Case 1:  $A_2$  is Symmetric About Two Coordinate Planes.** Suppose  $A_2$  is symmetric with respect to both the  $yz$  plane and the  $xz$  plane. Then  $F_{(d1i+)-2} = F_{(d1i-)-2}$  and  $F_{(d1j+)-2} = F_{(d1j-)-2}$ , and  $F_{(d1k-)-2} = 0$  by the same restriction that makes  $F_{(d1n-)-2} = 0$ . Then Eq. (6) becomes, for this case, simply

$$F_{d1n-2} = F_{(d1k+)-2} \cos \theta_k \quad (7)$$

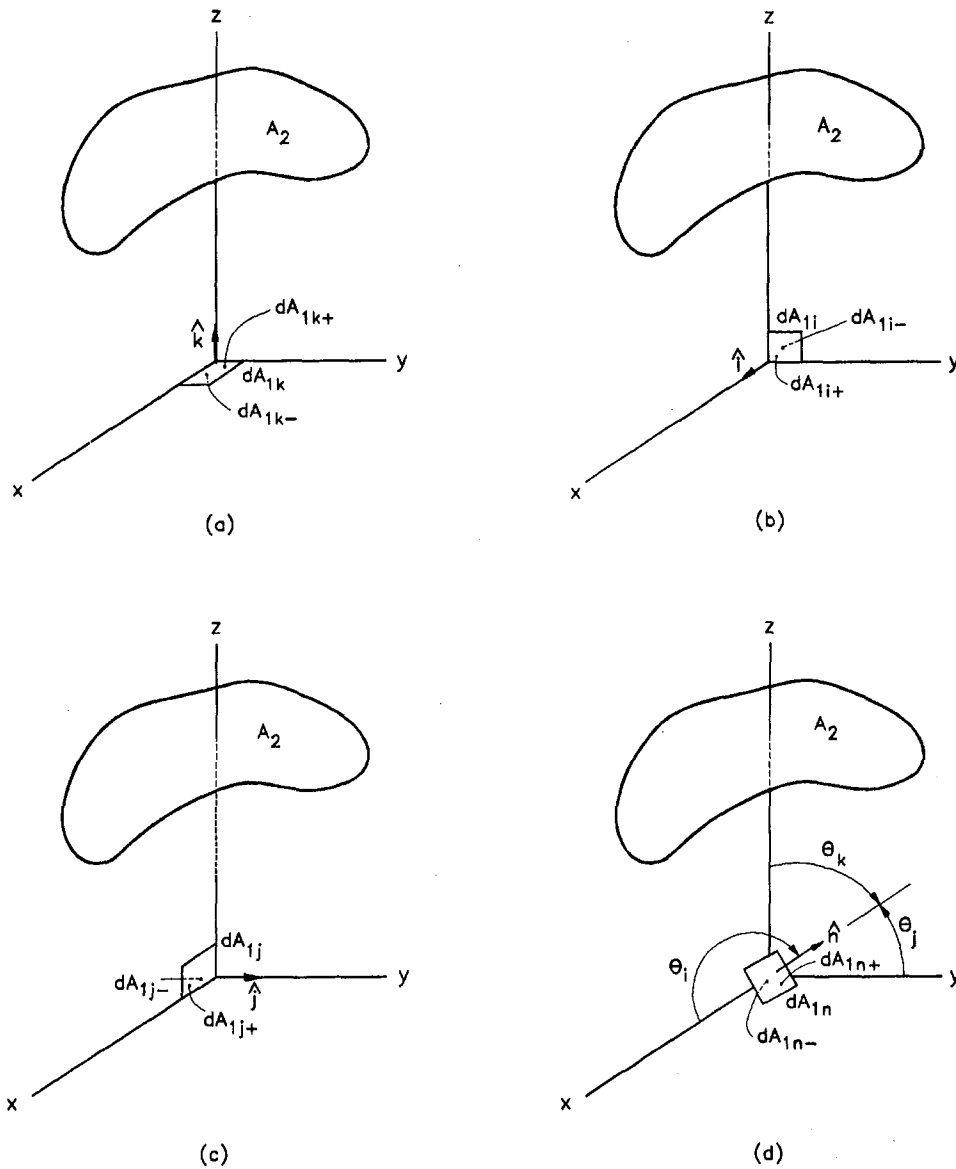


Fig. 2 Three perpendicular positions and one oblique position for  $dA_{1m}$ . This figure relates to Eq. (5), which is the general statement of the superposition rule.

A specific example is when  $A_2$  is a sphere of radius  $r$  with center at point  $(0, 0, h)$ ,  $h$  being less than  $r$ . Here  $F_{(d1k+)-2} = (r/h)^2$ , so, from Eq. (7)

$$F_{d1n-2} = \frac{1}{H^2} \cos \theta_k \quad (8)$$

where  $H = (h/r)$ .

For the same problem, the method of Sparrow and Cess (1970) would have given a different answer. Their method would amount to using Eq. (6) with the minus sign replaced by a plus sign. For the case of  $A_2$  being a sphere,  $F_{(d1j+)-2}$ ,  $F_{(d1j-)-2}$ ,  $F_{(d1i+)-2}$ , and  $F_{(d1i-)-2}$  are all equal to the form factor  $F_{d1-h}$  from an infinitesimal area to a hemisphere of radius  $r$  whose base, centered distance  $h$  away, is in the same plane as the infinitesimal area, a situation for which Siegel and Howell (1992) tabulate the formula:

$$F_{d1-h} = \frac{1}{\pi} \left( \tan^{-1} \frac{1}{\sqrt{H^2 - 1}} - \frac{\sqrt{H^2 - 1}}{H^2} \right) \quad (9)$$

Thus the method of Sparrow and Cess would give

$$F_{d1n-2} = \frac{2}{\pi} \left( \tan^{-1} \frac{1}{\sqrt{H^2 - 1}} - \frac{\sqrt{H^2 - 1}}{H^2} \right) \cos \theta_i + \frac{2}{\pi} \left( \tan^{-1} \frac{1}{\sqrt{H^2 - 1}} - \frac{\sqrt{H^2 - 1}}{H^2} \right) \cos \theta_j + \frac{1}{H^2} \cos \theta_k \quad (10)$$

an answer decidedly different from Eq. (8). The veracity of Eq. (8) is checked by the fact that is identical to the formula derived by using first principle arguments by Feingold and Gupta (1970), who used the artifice of differentiating the configuration factor from a sphere to a circle. It is also the formula given in Modest's (1993) configuration factor catalogue.

Equation (7) can be applied to cases where  $A_2$  is a rectangle, a regular polygon with an even number of sides, an ellipse, an oblate or prolate ellipsoid, a pyramid, or a symmetrically placed cylinder with its axis along either the  $x$  or  $y$  axis. In addition it

applies to any solid of revolution about the  $\hat{k}$  axis, including rings, toruses, cones, cylinders, paraboloids, hyperboloids, etc. The only restriction on Eq. (7) (aside from the necessary symmetry) is that the plane of  $dA_{1n}$  must not cut  $A_2$ .

**Case 2:  $A_2$  Lies Symmetrically About One Coordinate Plane and Totally on One Side of Two Others.** If  $A_2$  is symmetric about the  $zy$  plane and lies completely on one side of the  $xy$  and  $xz$  planes (say the sides having  $z \geq 0$  and  $y \geq 0$ ), then  $F_{(d1i+)-2} = F_{(d1i-)-2}$  and  $F_{(d1j-)-2} = F_{(d1k-)-2} = 0$ , so Eq. (6) becomes, for this case,

$$F_{d1n-2} = F_{(d1j+)-2} \cos \theta_j + F_{(d1k+)-2} \cos \theta_k \quad (11)$$

As a specific example of this case, consider the situation where  $A_2$  is a circle parallel to the  $xy$  plane, having radius  $r$  and center at  $(0, a, h)$ , as shown in Fig. 3(a). In this situation  $F_{(d1j+)-2}$  and  $F_{(d1k+)-2}$  are functions of  $r, a,$  and  $h$  tabulated by Seigel and Howell (1992) for example. Thus  $F_{d1n-2}$  can be determined from Eq. (11), yielding, finally

$$F_{d1n-2} = \frac{1}{2} \left\{ (\cos \theta_k - H \cos \theta_j) + \frac{1}{P} (HZ \cos \theta_j) - (1 + H^2 + R^2) \cos \theta_k \right\} \quad (12)$$

where  $H = h/a, R = r/a, Z = 1 + H^2 + R^2,$  and  $P = \sqrt{Z^2 - 4R^2}.$

As a further specific example of this case, consider the situation where  $A_2$  is a hemisphere of radius  $r$  with its base on the  $xz$  plane, and its center at  $(0, 0, h),$  with  $h > r.$  Applying the tabulated formula (Seigel and Howell, 1992) for  $F_{(d1j+)-2},$  and noting that  $F_{(d1k+)-2} = \frac{1}{2}(r/h)^2,$  we obtain from Eq. (11),

$$F_{d1n-2} = \frac{1}{2H^2} \cos \theta_k + \frac{1}{\pi} \left( \tan^{-1} \frac{1}{\sqrt{H^2 - 1}} - \frac{\sqrt{H^2 - 1}}{H^2} \right) \quad (13)$$

where  $H = h/r.$

**Case 3:  $A_2$  Lies on One Side of All Three Coordinate Planes.** A third special case of interest arises when  $A_2$  does not intersect any of the coordinate planes (although it may touch these planes). This is the case originally treated by Sparrow

(1963), and the results presented for this case are identical to those obtained using Sparrow's method. Suppose  $A_2$  lies totally in the first octant (the region having  $x > 0, y > 0,$  and  $z > 0).$  In this case  $F_{(d1m-)-2} = 0$  for  $m = i, j,$  and  $k.$  So Eq. (6) becomes

$$F_{d1n-2} = F_{(d1i+)-2} \cos \theta_i + F_{(d1j+)-2} \cos \theta_j + F_{(d1k+)-2} \cos \theta_k \quad (14)$$

As a specific example, consider the case where  $A_2$  is a rectangle with edges along both the  $xy$  and  $yz$  planes (Fig. 3(b)). Configuration factors  $F_{(d1i+)-2}, F_{(d1j+)-2}$  and  $F_{(d1k+)-2}$  are all tabulated function of the various dimensions (Seigel and Howell, 1992), so  $F_{d1n-2}$  can be determined from Eq. (14), yielding, after some simplification:

$$F_{d1n-2} = \frac{1}{2\pi} \left\{ \left( \tan^{-1} \frac{b}{c} \right) \cos \theta_i + \left( \tan^{-1} \frac{a}{c} \right) \cos \theta_j + \frac{a \cos \theta_k - c \cos \theta_i}{\sqrt{c^2 + a^2}} \tan^{-1} \frac{b}{\sqrt{c^2 + a^2}} + \frac{b \cos \theta_k - c \cos \theta_j}{\sqrt{b^2 + c^2}} \tan^{-1} \frac{a}{\sqrt{c^2 + b^2}} \right\} \quad (15)$$

Dimensions  $a, b,$  and  $c$  are defined in Fig. 3(b). Using Eq. (15) and flux algebra, one can find  $F_{d1n-2}$  for any rectangular  $A_2$  regardless of its position, provided only that  $A_2$  does not pass through the plane of  $dA_1.$

### Alternate Derivation of the Superposition Rule

The radiant flux vector and contour integration are advanced topics in the study of radiation heat transfer, while the configuration factor is an introductory one. From a heuristic point of view, therefore, it would be better if the superposition rule could be developed without reference to either, so that students can start to use it without studying advanced topics. Presented in this section is a derivation of Eq. (5) that does not make reference to the radiant flux vector. Let  $\varphi_1(\hat{m})$  be the angle between  $\hat{m}$  and the vector  $\vec{r}$  joining  $dA_1$  to  $dA_2.$  Then

$$\cos \varphi_1(\hat{m}) = \hat{m} \cdot \vec{r} / r \quad (16)$$

where  $r = |\vec{r}|.$

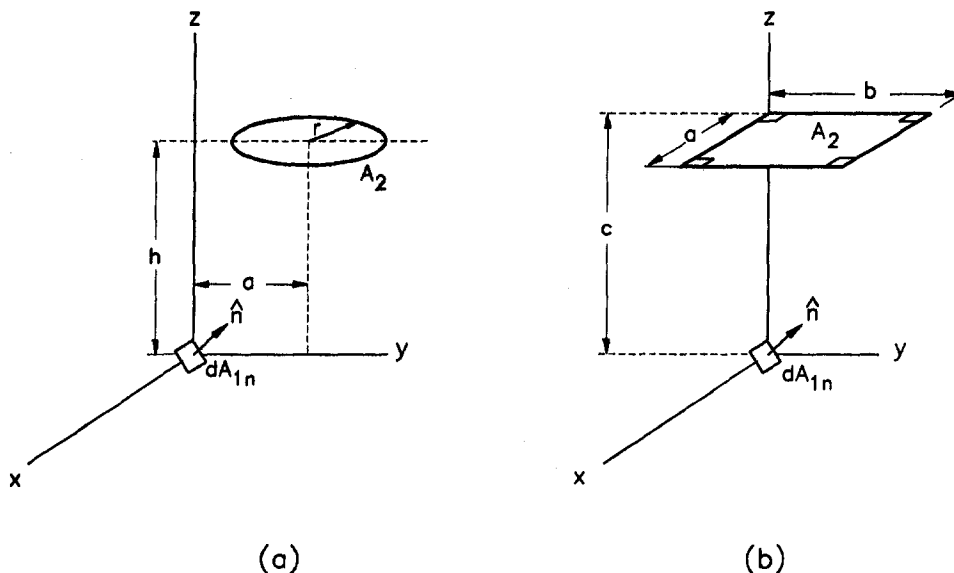


Fig. 3 Plot defining quantities in configuration factor Eqs. (12) and (15), derived using the superposition rule

So, specializing to the case where  $\hat{m} = \hat{n}$ :

$$\iint_{A_2} \frac{\cos \varphi_2 \cos \varphi_1(\hat{n}) dA_2}{\pi r^2} = \iint_{A_2} \frac{(\hat{n} \cdot \vec{r}) \cos \varphi_2}{\pi r^3} dA_2 \quad (17)$$

Substituting  $\hat{n} \cdot \vec{r} = \cos \theta_i \hat{i} \cdot \vec{r} + \cos \theta_j \hat{j} \cdot \vec{r} + \cos \theta_k \hat{k} \cdot \vec{r}$ , then substituting Eq. (16) with  $\hat{m} = \hat{i}, \hat{j}$ , and  $\hat{k}$  in turn, and then simplifying gives

$$\begin{aligned} \iint_{A_2} \frac{\cos \varphi_1(\hat{n}) \cos \varphi_2 dA_2}{\pi r^2} \\ = \sum_{m=i,j,k} \cos \theta_m \iint_{A_2} \frac{\cos \varphi_1(\hat{m}) \cos \varphi_2 dA_2}{\pi r^2} \end{aligned} \quad (18)$$

At this point it is useful, for general vector  $\hat{m}$ , to consider how the plane through  $dA_1$  perpendicular to  $\hat{m}$  cuts  $A_2$  into two parts: a part  $A_{1m-}$  seen by  $d1m-$  but not seen by  $d1m+$ , and a part  $A_{2m-}$  seen by  $d1m+$  but not seen by  $d1m-$ . (One of  $A_{2m-}$  and  $A_{2m+}$  may be zero.) We can then write Eq. (18) as

$$\begin{aligned} \iint_{A_{2m+}} \frac{\cos \varphi_1(\hat{n}) \cos \varphi_2 dA_2}{\pi r^2} + \iint_{A_{2m-}} \frac{\cos \varphi_1(\hat{n}) \cos \varphi_2 dA_2}{\pi r^2} \\ = \sum_{m=i,j,k} \cos \theta_m \left\{ \iint_{A_{2m+}} \frac{\cos \varphi_1(\hat{m}) \cos \varphi_2 dA_2}{\pi r^2} \right. \\ \left. + \iint_{A_{2m-}} \frac{\cos \varphi_1(\hat{m}) \cos \varphi_2 dA_2}{\pi r^2} \right\} \end{aligned} \quad (19)$$

Now

$$\iint_{A_{2m+}} \frac{\cos \varphi_1(\hat{m}) \cos \varphi_2}{\pi r^2} dA_2 = F_{(d1m+)-2} \quad (20)$$

and, since  $\varphi_1(-\hat{m}) = \pi - \varphi_1(\hat{m})$ ,

$$\begin{aligned} \iint_{A_{2m-}} \frac{\cos \varphi_1(\hat{m}) \cos \varphi_2 dA_2}{\pi r^2} \\ = - \iint_{A_{2m-}} \frac{\cos \varphi_1(-\hat{m}) \cos \varphi_2 dA_2}{\pi r^2} = -F_{(d1m-)-2} \end{aligned} \quad (21)$$

So Eq. (5) follows directly by applying Eqs. (20) and (21) for  $\hat{m} = \hat{i}, \hat{j}, \hat{k}$ , and  $\hat{n}$  in turn, and then substituting for the integrals in Eq. (19).

## Conclusions

The configuration factor from an infinitesimal area to a finite area is subject to a superposition rule, the use of which can provide some simplification to configuration factor evaluation. The rule expresses the configuration factor from an arbitrarily oriented infinitesimal area in terms of a weighted sum (Eq. (5)) of the configuration factors from six other infinitesimal areas, many of which can be readily evaluated from symmetry or other arguments, or are tabulated. In its most useful form (Eq. (6)), the rule requires that the infinitesimal area view the finite area entirely (i.e., that none of the latter lies behind the former). The rule is derivable from the vector property of the radiant flux vector as well as from contour integration. It can also be derived without reference to either.

## References

- Feingold, A., and Gupta, K. G., 1970, "New Analytical Approach to the Evaluation of Configuration Factors in Radiation From Spheres and Infinitely Long Cylinders," *ASME JOURNAL OF HEAT TRANSFER*, Vol. 92, pp. 69-76.
- Modest, M. F., 1993, *Radiation Heat Transfer*, McGraw-Hill, New York, p. 785.
- Seigel, R., and Howell, J. R., 1992, *Thermal Radiation Heat Transfer*, 3rd ed., McGraw-Hill, New York, pp. 1027-1037.
- Sparrow, E. M., 1963, "A New and Simpler Formulation for Radiative Angle Factors," *ASME JOURNAL OF HEAT TRANSFER*, Vol. 85, pp. 81-88.
- Sparrow, E. M., and Cess, R. D., 1970, *Radiation Heat Transfer*, revised ed., Wadsworth Publishing Company, Belmont, CA, pp. 122-126.

# Saturated Flow Boiling Heat Transfer in Internally Spirally Knurled/Integral Finned Tubes

Mao-Yu Wen<sup>1</sup> and Shou-Shing Hsieh<sup>2</sup>

## Nomenclature

- $A$  = heat transfer area =  $\pi D_e L$
- $C$  = oil concentration, kg oil/kg mixture
- $D_e$  = mean diameter defined as the inside diameter of a smooth round tube that has a flow cross-sectional area equal to the augmented tubes
- $G$  = mass flux
- $h$  = local wall heat transfer coefficient, Eq. (2)
- $\bar{h}$  = averaged local heat transfer coefficient, Eq. (3)
- $k$  = thermal conductivity
- $L$  = length of test tube
- $P$  = pressure
- $\bar{P}$  = average pressure over the test section =  $(P_{in} + P_{out})/2$
- $q_w$  = wall heat flux based on primary heat transfer surface including roughened surface area
- $T$  = temperature
- $\bar{T}_{sat}$  = saturated temperature at the average pressure over the test section
- $\bar{T}_{wi}$  = average temperature for the inner surface of the tube =  $T_{wo} + q_w D_e [\ln(D_o/D_e)/2k]$
- $X$  = quality
- $\bar{X}$  = quality averaged over the test section
- $\theta$  = enhancement performance ratio, Eq. (4)

## Subscripts

- $a$  = augmented tube with pure refrigerant
- $a'$  = augmented tube with refrigerant-oil mixture
- $i$  = inside diameter
- $in, w$  = inlet of the heated water
- $o$  = outside diameter
- $s$  = smooth tube with pure refrigerant
- $s'$  = smooth tube with refrigerant-oil mixture
- sat = saturated
- TP = two-phase
- wi = inner wall
- wo = outer wall

## 1 Introduction

Various techniques have been investigated during the past few decades for augmenting two-phase heat transfer in refrigeration and air-conditioning systems (see Bergles et al., 1981). Internally spirally knurled, integral finned tubes (shown in Table 1) are quite effective in enhancing the flow boiling heat transfer due to their excellent thermal-hydraulic performance. However, boiling heat transfer within such tubes has not been widely studied and few papers have been published. Of particular concern in this note is evaporation heat transfer of refrigerants R-114, R-22, and R-134a during flow boiling on horizontal tubes.

<sup>1</sup> Graduate student, Department of Mechanical Engineering, National Sun Yat-Sen University, Kaohsiung, Taiwan 80424.

<sup>2</sup> Professor and Chairman, Department of Mechanical Engineering, National Sun Yat-Sen University, Kaohsiung, Taiwan 80424; Mem. ASME.

Contributed by the Heat Transfer Division of THE AMERICAN SOCIETY OF MECHANICAL ENGINEERS. Manuscript received by the Heat Transfer Division September 1993; revision received March 1994. Keywords: Augmentation and Enhancement, Boiling, Forced Convection. Associate Technical Editor: L. C. Witte.

So, specializing to the case where  $\hat{m} = \hat{n}$ :

$$\iint_{A_2} \frac{\cos \varphi_2 \cos \varphi_1(\hat{n}) dA_2}{\pi r^2} = \iint_{A_2} \frac{(\hat{n} \cdot \vec{r}) \cos \varphi_2}{\pi r^3} dA_2 \quad (17)$$

Substituting  $\hat{n} \cdot \vec{r} = \cos \theta_i \hat{i} \cdot \vec{r} + \cos \theta_j \hat{j} \cdot \vec{r} + \cos \theta_k \hat{k} \cdot \vec{r}$ , then substituting Eq. (16) with  $\hat{m} = \hat{i}, \hat{j}$ , and  $\hat{k}$  in turn, and then simplifying gives

$$\begin{aligned} & \iint_{A_2} \frac{\cos \varphi_1(\hat{n}) \cos \varphi_2 dA_2}{\pi r^2} \\ &= \sum_{m=i,j,k} \cos \theta_m \iint_{A_2} \frac{\cos \varphi_1(\hat{m}) \cos \varphi_2 dA_2}{\pi r^2} \quad (18) \end{aligned}$$

At this point it is useful, for general vector  $\hat{m}$ , to consider how the plane through  $dA_1$  perpendicular to  $\hat{m}$  cuts  $A_2$  into two parts: a part  $A_{1m-}$  seen by  $d1m-$  but not seen by  $d1m+$ , and a part  $A_{2m-}$  seen by  $d1m+$  but not seen by  $d1m-$ . (One of  $A_{2m-}$  and  $A_{2m+}$  may be zero.) We can then write Eq. (18) as

$$\begin{aligned} & \iint_{A_{2m+}} \frac{\cos \varphi_1(\hat{m}) \cos \varphi_2 dA_2}{\pi r^2} + \iint_{A_{2m-}} \frac{\cos \varphi_1(\hat{m}) \cos \varphi_2 dA_2}{\pi r^2} \\ &= \sum_{m=i,j,k} \cos \theta_m \left\{ \iint_{A_{2m+}} \frac{\cos \varphi_1(\hat{m}) \cos \varphi_2 dA_2}{\pi r^2} \right. \\ & \quad \left. + \iint_{A_{2m-}} \frac{\cos \varphi_1(\hat{m}) \cos \varphi_2 dA_2}{\pi r^2} \right\} \quad (19) \end{aligned}$$

Now

$$\iint_{A_{2m+}} \frac{\cos \varphi_1(\hat{m}) \cos \varphi_2}{\pi r^2} dA_2 = F_{(d1m+)-2} \quad (20)$$

and, since  $\varphi_1(-\hat{m}) = \pi - \varphi_1(\hat{m})$ ,

$$\begin{aligned} & \iint_{A_{2m-}} \frac{\cos \varphi_1(\hat{m}) \cos \varphi_2 dA_2}{\pi r^2} \\ &= - \iint_{A_{2m-}} \frac{\cos \varphi_1(-\hat{m}) \cos \varphi_2 dA_2}{\pi r^2} = -F_{(d1m-)-2} \quad (21) \end{aligned}$$

So Eq. (5) follows directly by applying Eqs. (20) and (21) for  $\hat{m} = \hat{i}, \hat{j}, \hat{k}$ , and  $\hat{n}$  in turn, and then substituting for the integrals in Eq. (19).

## Conclusions

The configuration factor from an infinitesimal area to a finite area is subject to a superposition rule, the use of which can provide some simplification to configuration factor evaluation. The rule expresses the configuration factor from an arbitrarily oriented infinitesimal area in terms of a weighted sum (Eq. (5)) of the configuration factors from six other infinitesimal areas, many of which can be readily evaluated from symmetry or other arguments, or are tabulated. In its most useful form (Eq. (6)), the rule requires that the infinitesimal area view the finite area entirely (i.e., that none of the latter lies behind the former). The rule is derivable from the vector property of the radiant flux vector as well as from contour integration. It can also be derived without reference to either.

## References

- Feingold, A., and Gupta, K. G., 1970, "New Analytical Approach to the Evaluation of Configuration Factors in Radiation From Spheres and Infinitely Long Cylinders," *ASME JOURNAL OF HEAT TRANSFER*, Vol. 92, pp. 69-76.
- Modest, M. F., 1993, *Radiation Heat Transfer*, McGraw-Hill, New York, p. 785.
- Seigel, R., and Howell, J. R., 1992, *Thermal Radiation Heat Transfer*, 3rd ed., McGraw-Hill, New York, pp. 1027-1037.
- Sparrow, E. M., 1963, "A New and Simpler Formulation for Radiative Angle Factors," *ASME JOURNAL OF HEAT TRANSFER*, Vol. 85, pp. 81-88.
- Sparrow, E. M., and Cess, R. D., 1970, *Radiation Heat Transfer*, revised ed., Wadsworth Publishing Company, Belmont, CA, pp. 122-126.

# Saturated Flow Boiling Heat Transfer in Internally Spirally Knurled/Integral Finned Tubes

Mao-Yu Wen<sup>1</sup> and Shou-Shing Hsieh<sup>2</sup>

## Nomenclature

- $A$  = heat transfer area =  $\pi D_e L$
- $C$  = oil concentration, kg oil/kg mixture
- $D_e$  = mean diameter defined as the inside diameter of a smooth round tube that has a flow cross-sectional area equal to the augmented tubes
- $G$  = mass flux
- $h$  = local wall heat transfer coefficient, Eq. (2)
- $\bar{h}$  = averaged local heat transfer coefficient, Eq. (3)
- $k$  = thermal conductivity
- $L$  = length of test tube
- $P$  = pressure
- $\bar{P}$  = average pressure over the test section =  $(P_{in} + P_{out})/2$
- $q_w$  = wall heat flux based on primary heat transfer surface including roughened surface area
- $T$  = temperature
- $\bar{T}_{sat}$  = saturated temperature at the average pressure over the test section
- $\bar{T}_{wi}$  = average temperature for the inner surface of the tube =  $T_{wo} + q_w D_e [\ln(D_o/D_e)/2k]$
- $X$  = quality
- $\bar{X}$  = quality averaged over the test section
- $\theta$  = enhancement performance ratio, Eq. (4)

## Subscripts

- $a$  = augmented tube with pure refrigerant
- $a'$  = augmented tube with refrigerant-oil mixture
- $i$  = inside diameter
- $in, w$  = inlet of the heated water
- $o$  = outside diameter
- $s$  = smooth tube with pure refrigerant
- $s'$  = smooth tube with refrigerant-oil mixture
- sat = saturated
- TP = two-phase
- wi = inner wall
- wo = outer wall

## 1 Introduction





Various techniques have been investigated during the past few decades for augmenting two-phase heat transfer in refrigeration and air-conditioning systems (see Bergles et al., 1981). Internally spirally knurled, integral finned tubes (shown in Table 1) are quite effective in enhancing the flow boiling heat transfer due to their excellent thermal-hydraulic performance. However, boiling heat transfer within such tubes has not been widely studied and few papers have been published. Of particular concern in this note is evaporation heat transfer of refrigerants R-114, R-22, and R-134a during flow boiling on horizontal tubes.

<sup>1</sup> Graduate student, Department of Mechanical Engineering, National Sun Yat-Sen University, Kaohsiung, Taiwan 80424.

<sup>2</sup> Professor and Chairman, Department of Mechanical Engineering, National Sun Yat-Sen University, Kaohsiung, Taiwan 80424; Mem. ASME.

Contributed by the Heat Transfer Division of THE AMERICAN SOCIETY OF MECHANICAL ENGINEERS. Manuscript received by the Heat Transfer Division September 1993; revision received March 1994. Keywords: Augmentation and Enhancement, Boiling, Forced Convection. Associate Technical Editor: L. C. Witte.

**Table 1 Tube characteristics**

Tube configurations	Smooth tube	Internally spirally knurled tubes		Internally integral finned tube	
		 (tube with 5-leg aluminum insert)	 (tube with 10-leg aluminum insert)	 (corrugated tube)	
Tube No.	1	2	3	4	5
Nominal tube O.D., cm	1.6	1.6	1.6	1.6	1.6
Nominal tube I.D., cm	1.4	1.4	1.4	1.4	1.4
Nominal heat transfer area, cm <sup>2</sup>	660	667	674	707	772
Nominal flow area, cm <sup>2</sup>	6.16	5.81	5.60	7.07	6.17
Helix angle, degrees	—	—	—	30°	76°
Insert thickness/fin height (e), mm	—	1.0	0.8	0.7	0.38
Tube pitch, mm	—	—	—	2.6	1.2

Tetrafluoroethane (R-134a) has been suggested as a substitute for R-12, which is thought to contribute to ozone depletion. Thus, R-134a was chosen as one of the working fluids in this study. Moreover, in refrigerators with oil-filled compressors, some of the oil is entrained with the refrigerant vapor, so that the fluid that boils in the evaporator is not pure refrigerant, but a refrigerant-oil mixture. The literature dealing with the effect of oil content on flow boiling of refrigerants is quite limited. Furthermore, no studies were found dealing with refrigerant (R-134a)–oil (RS 68S refrigeration lubricant) in augmented tubes. Such a study is one of the objectives of this study.

In this note, the results of experiments for saturated flow boiling of R-114, R-22, and R-134a in a water-heated, horizontal heat exchanger with internally spirally knurled/or integral finned tubes are described. Tests were performed with  $G$  up to 430 kg/(m<sup>2</sup> s), averaged  $q_w$  from the heated water up to 30 kW/m<sup>2</sup>, oil concentration,  $C$ , of 0–5.4 percent. To meet the capacity of the present thermostat that controlled the heated water to evaporate the refrigerants, a specific mean pressure of 2.23 kg/cm<sup>2</sup> for R-114, 6.02 kg/cm<sup>2</sup> for R-22, and 4.08 kg/cm<sup>2</sup> for R-134a was chosen. The ranges of experiments for the calculated values in the  $X$ ,  $\bar{h}_{TP}$ , and enhancement performance ratio,  $(h_a/h_s)/(\Delta P_a/\Delta P_s)$ , were 0.05–0.93, 0.19–9.5 × 10<sup>3</sup> W/m<sup>2</sup>K, and 0.45–1.43, respectively.

## 2 Experimental Apparatus and Instrumentation

The test setup consists primarily of a standard refrigeration cycle. The test section is made of a conventional double-pipe heat exchanger. The size and geometry for a series of copper test tubes ( $k = 111$  W/m K) were given in Table 1. Bulk fluid temperatures at the inlet and exit of the test section were measured with 40 gage Cu–Cn thermocouples located at midstream. The inlet and outlet pressures were measured with a calibrated pressure gage. Intermediate bulk fluid temperatures were measured at 20 cm intervals along the tube. The refrigerant flow rate was measured by a rotameter located between the condenser and oil-gas separator. Thermocouples measured wall temperature at 28 locations along the test section. These thermocouples were carefully buried into the outside wall of the inner tube. Moreover, thermocouples measured the heated water and refrigerant along the test section at 36 locations and 45–54 locations, respectively. Further information about the experimental apparatus and instrumentation is available from Wen and Hsieh (1994).

For each test run, seven axial  $h$ 's were calculated on the basis of  $\bar{T}_{sat}$ ,  $q_w$ , and  $T_{wi}$ . Four thermocouples were mounted just downstream of each pressure tap; hence, the readings were averaged as

$$T_{\bar{w}o} = (T_{top} + 2T_{mid} + T_{bot})/4 \quad (1)$$

The  $q_w$  and  $T_{wi}$  can be obtained by the general calculations. The peripherally local  $h$  was then calculated as:

$$h_{TP} = q_w / (T_{wi} - T_{sat}) \quad (2)$$

When  $h$  was calculated for roughened tubes, the  $q_w$  in Eq. (2) was based on primary heat transfer surface and roughened surface (see Table 1). The details of the calculation procedure for  $h$  can be seen in Hsieh and Wen (1995). The  $\bar{h}_{TP}$  was determined by the following formula:

$$\bar{h}_{TP} = q_w / (\bar{T}_{wi} - \bar{T}_{sat}) \quad (3)$$

The active heating length  $L$  in the test section is 1.5 m.  $G$  was also based on the cross-sectional area calculated from  $D_e$ . Qualities at each axial location were calculated from inlet conditions and energy balances along the tube length. Pressure drop,  $\Delta P$ , data were measured over a length of 0.21 m for the test section (1.5 m). The mass fraction of oil in the refrigerant is determined by the ratio between the weight of oil and refrigerant-oil mixture. An uncertainty analysis was made to consider the error caused by the interpolation procedure of the measuring instruments. The estimated uncertainties in  $G$ ,  $q_w$ ,  $x$ ,  $\bar{P}$ ,  $C$ ,  $\bar{h}_{TP}$ , and  $(h_a/h_s)/(\Delta P_a/\Delta P_s)$  are ±4.2, ±4.4, ±4.9, ±4.1, ±0.1, ±6.3, and ±8.2 percent, respectively.

## 3 Results and Discussion

The  $h$ 's for the single-phase liquid flow about the smooth tube were in good agreement with the Dittus–Boelter (1930) correlation, and the  $h$ 's in tube Nos. 2, 3, 4, and 5 were higher than that for the smooth tube by about 40, 70, 55, and 65 percent, respectively.

Averaged enhancement factors  $(\bar{h}_{TP,a}/\bar{h}_{TP,s})$  were calculated by forming ratios of experimentally measured  $h$ 's for the augmented tube and a smooth tube at the same conditions. Figure 1 exhibits the effects of  $G$  on the factor  $(\bar{h}_{TP,a}/\bar{h}_{TP,s})$  for two different  $q_w$ . The ratios decrease rapidly with increasing  $G$  in the range 42 to 150 kg/m<sup>2</sup>s at a lower heat flux level. When  $G$  is higher than 250 kg/m<sup>2</sup>s, the ratios are generally much smaller, and both the differences between the augmented tubes and between the fluids are not notable. However, it suggests that the lower  $G$  has a higher enhancement factor. This is because the two-phase flow regime is wavy at a lower  $G$  for the smooth tube and, consequently, the top of the tube should be dry, which causes  $\bar{h}_{TP,s}$  to be extremely low. Moreover, at a lower  $G$ , due to an aluminum insert inside the spirally knurled tubes, the heat flux from the heated water would rapidly redistribute itself. But, under the

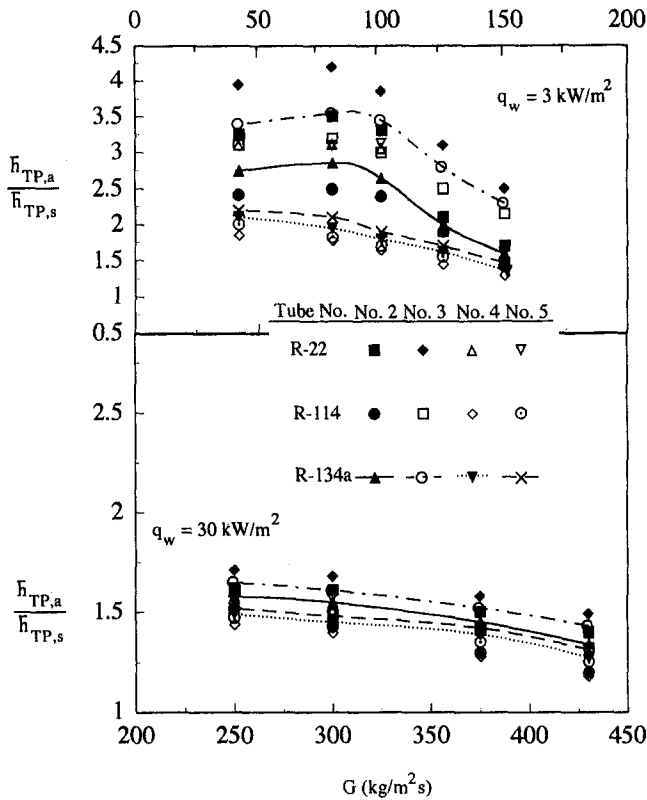


Fig. 1 Ratios of the averaged heat transfer coefficient in the augmented tubes to the smooth tube versus mass flow rate at two different heat fluxes

same condition, the internally integral finned tubes supplied capillary pumping phenomenon at the top. This caused the tube wall to be wetted intermittently. Therefore, the  $\bar{h}_{TP,a}$ 's are significantly improved. In addition, at the higher  $G$ , an annular liquid film is formed over the tube perimeter in the present tubes and, consequently, the  $h$ 's are increased in both the smooth and augmented tubes. The  $h$ 's in the augmented tubes are higher than those in the smooth tube also at higher  $G$ , but the differences are much smaller than those at the lower  $G$  stated above. This results in the higher factor ( $\bar{h}_{TP,a}/\bar{h}_{TP,s}$ ) at the lower  $G$ .

The effects of  $q_w$  and  $\Delta P$  can be combined into one parameter called the enhancement performance ratio,  $\theta_{a/s}$ , which has been chosen for performance comparisons (Azer et al., 1980; Reid et al., 1987). The ratio is:

$$\theta_{a/s} = \frac{\bar{h}_{TP,a}/\bar{h}_{TP,s}}{\Delta P_a/\Delta P_s} \quad (4)$$

Figure 2 shows  $\theta_{a/s}$  versus  $G$ . It is clear that the  $q_w$  enhancement was significantly higher than the  $\Delta P$  increase ( $\theta_{a/s} > 1$ ) at  $G < 100 \text{ kg/m}^2\text{s}$ . At  $G > 100 \text{ kg/m}^2\text{s}$ , the  $\theta_{a/s}$  was below 1.0. Comparing Fig. 2 with Fig. 1, it is observed that all curves shift downward, that is  $\theta_{a/s} < \bar{h}_{TP,a}/\bar{h}_{TP,s}$ . This behavior is consistent with a general  $\Delta P$  increase in augmented tubes relative to smooth tubes. The internally spirally knurled tubes (tube No. 1 and No. 3) and integral finned tubes (tube No. 4 and No. 5) show quite similar heat transfer performance, but the overall performance of the tube No. 2 and No. 4 is superior to tube No. 3 and No. 5, respectively, because of their lower  $\Delta P$ .

No studies were found that used R-134a with RL 68S mineral oil, so comparisons were not possible. Figure 3(a, b) show the heat transfer results for evaporation of a R-134a/RL 68S for both tube Nos. 2 and 4, respectively. For comparison, the pure R-134a data shown earlier are also included. It is found that  $q_w$  increased with increasing  $G$ . The effect of oil does not appear to be a strong

function of  $G$  as the increase in  $h$  appears fairly uniform at  $G < 150 \text{ kg/m}^2\text{s}$ . At higher  $G$ , an annular liquid film is formed over the tube perimeter; this increases  $h$ . It is also seen that the effect of oil on  $\bar{h}_{TP}$  is very dependent on  $C$  at  $G > 150 \text{ kg/m}^2\text{s}$ . Below 1.0 percent oil,  $\bar{h}_{TP}$  is very close to that with pure refrigerant, but with a slight tendency toward enhancement. At higher  $C$ , there is a degradation of  $q_w$  by as much as 20 percent when compared to the pure refrigerant case. This is because when the oil concentration is increased, the oil formed a film on the heat transfer surface, which resulted in a diffusion resistance. It reduced the bubble growth rate, and resulted in a lower  $h$ . Additionally, the specific heat of R-134a/RL 68S mixture is higher than the pure R-134a and, consequently, the boiling point of the mixture is increased. This caused a large increase in the wall superheat and results in a decrease of  $h$ .

The effects of  $C$  on  $\theta_{a/s}$  are presented in Fig. 4. It shows  $\theta_{a/s}$  versus  $G$  for various  $C$  at 3 and 30  $\text{kW/m}^2$  in two tube geometries. The  $\theta_{a/s}$  for no oil is also included for comparison. For both tubes, the values of  $\theta_{a/s}$  with oil are generally less than  $\theta_{a/s}$ , indicating that overall performance is degraded with the addition of oil. The tube shear stress is increased by the high viscosity oil, which increased  $\Delta P$ , but decreased  $h$ . However, the increase of  $\Delta P$  caused by the oil film is higher than the decrease of  $h$  for the present study. This is because  $\theta_{a/s}$  is degraded with the addition of oil. The trend in  $\theta_{a/s}$  is downward with increasing  $G$ , but all curves are relatively flat at  $C$  of 2.5–5.0 percent. Tube No. 2 is superior to that of No. 4 in overall performance. This may be due to the radial spines that separate the tube into five compartments. The radial spines increased the surface area by about 100 percent and created more nucleation sites for evaporation. It was also found that tube No. 2 has a performance advantage relative to the smooth tube at  $G < 125 \text{ kg/m}^2\text{s}$ . At  $G <$

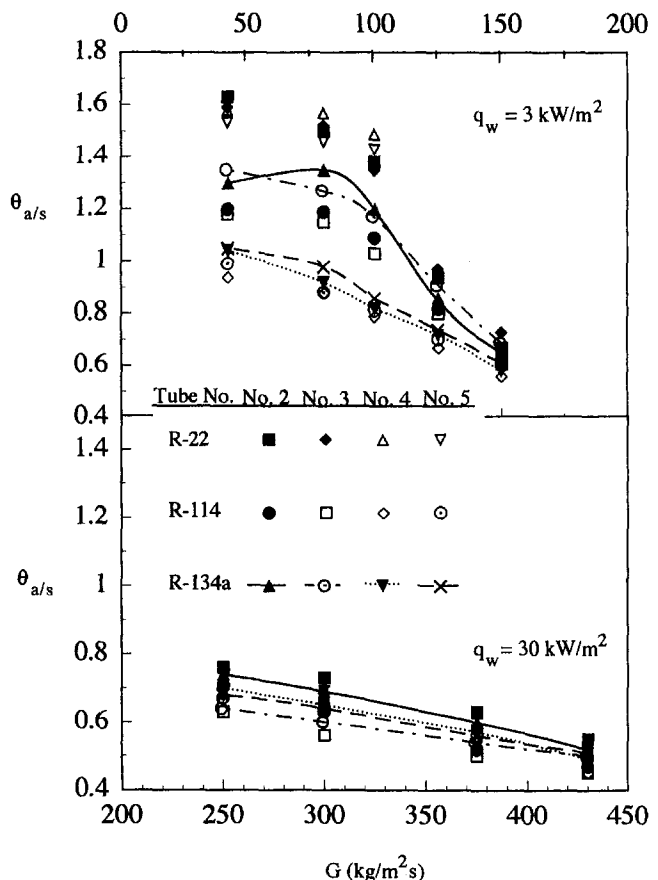


Fig. 2 Enhancement performance ratio,  $\theta_{a/s}$ , versus mass flow rate at two different heat fluxes



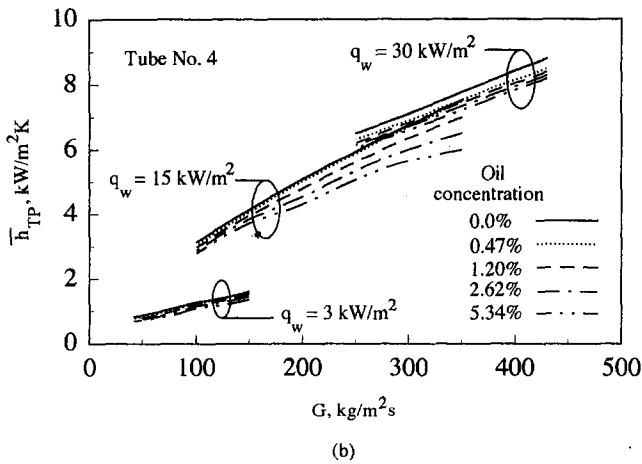
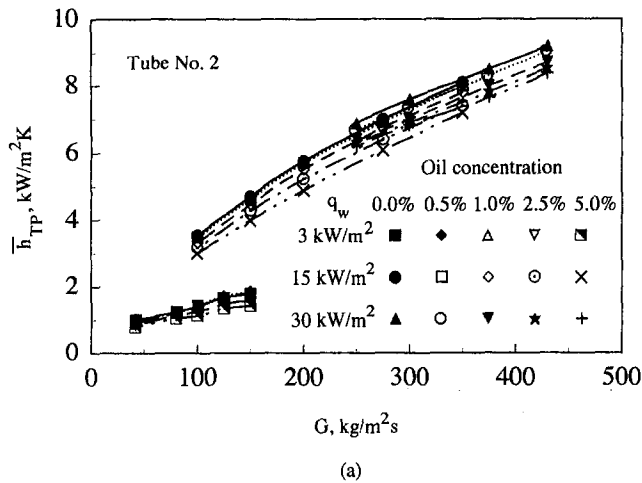


Fig. 3 Evaporation heat transfer coefficient versus mass flow rate with mixture of R-134a plus RL68S oil

150 kg/m<sup>2</sup>s,  $\theta_{a/s}$  tends to fall rapidly with increasing  $G$ . There is very little influence of  $G$  above 250 kg/m<sup>2</sup>s. Although  $\theta_{a/s}$  for tubes Nos. 2 and 4 only were shown in Fig. 4, similar results were obtained for tubes Nos. 3 and 5.

This note suggests that tubes with lower  $G$  have a higher  $\bar{h}_{TP,a}/\bar{h}_{TP,s}$ . The heat transfer enhancements for R-22 are generally

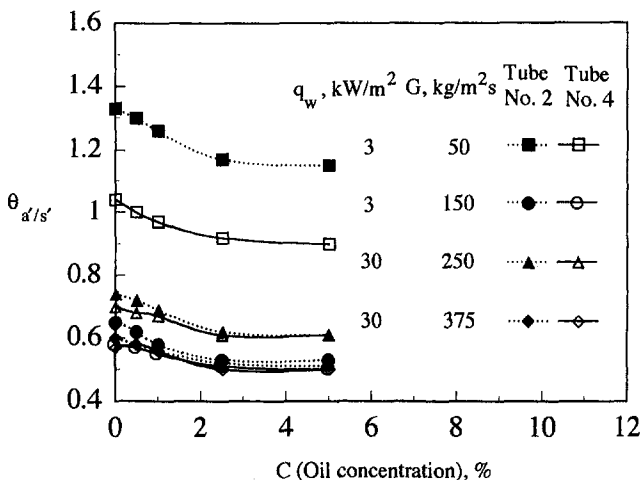


Fig. 4 Effects of oil content on the enhancement performance ratio,  $\theta_{a/s}$ , in two tube geometries for different oil concentration

higher than those for R-114 and R-134a. Tubes with lower pressure drop (Nos. 2 and 4) are superior in overall performance to those with higher pressure drop (Nos. 4 and 5) even though their heat transfer performance is similar. The enhancement performance ratio decreases with an increase in oil concentration. The heat transfer performance with an R-134a/RL 68S mixture have the same trend as that of the pure refrigerant but the magnitude of the effect is different. In general, oil content decreases the heat transfer and increases the pressure drop for the cases studied.

### Acknowledgments

A research grant from the Division of Energy and Resources Laboratories, Industrial Technology Research Institute (R.O.C.) is sincerely appreciated. Special thanks go to Kuen Ling Machinery Refrigerating Co., Ltd., for providing the internally spirally knurled/integral finned tubes.

### References

Azer, N. Z., Lin, S. T., and Fan, L. T., 1980, "Augmentation of Forced Flow Boiling Heat Transfer With Kenics Motionless Mixers," *Industrial and Engineering Chemistry Process Design and Development*, Vol. 19, pp. 246-250.  
 Bergles, A. E., Collier, J. G., Delhaye, J. M., Hewitt, G. F., and Mayinger, 1981, *Two-Phase Flow and Heat Transfer in the Power and Process Industries*, Hemisphere Publishing Co., Washington, DC.  
 Dittus, F. W., and Boelter, L. M. K., 1930, "Heat Transfer in Automobile Radiators of the Tubular Type," *Univ. Calif., Berkeley, Pub. in Eng.*, Vol. 2, pp. 443-450.  
 Hsieh, S.-S., and Wen, M.-Y., 1995, "An Experimental Study of Flow Boiling Heat Transfer in Rib-Roughened Tube Annuli," *ASME JOURNAL OF HEAT TRANSFER*, Vol. 117, this issue, pp. 185-194.  
 Lockhart, R. W., and Martinelli, R. C., 1949, "Proposed Correlation of Data for Isothermal Two-Phase Two-Component Flow in Pipes," *Chemical Engineering Progress*, Vol. 45, pp. 39-48.  
 Reid, R. W., Pate, M. B., and Bergles, A. E., 1987, "A Comparison of Augmentation Techniques During In-Tube Evaporation of R-113," in: *Boiling and Condensation in Heat Transfer Equipment*, E. G. Ragi, T. M. Rudy, T. J. Rabas, and J. M. Robertson, eds., ASME, New York, pp. 21-30.  
 Shah, M. M., 1982, "Chart Correlation for Saturated Boiling Heat Transfer Equations and Further Study," *ASHRAE Transactions*, Vol. 88, pp. 185-196.  
 Wen, M.-Y., and Hsieh, S.-S., 1994, "Evaporative Heat Transfer and Enhancement Performance of Rib-Roughened Tube Annuli With Refrigerant 114," *Int. J. of Heat Mass Transfer*, Vol. 37, pp. 425-436.

## Toward a Universal Critical Heat Flux (CHF) Correlation for Uniformly Heated Round Tubes

G. A. Tingate<sup>1</sup>

### Nomenclature

- $D$  = internal diameter of test section, mm
- $G$  = mass velocity of coolant, Mg/m<sup>2</sup>s
- $L$  = heated length of test section, mm
- $P$  = nominal pressure of coolant, MPa
- $m_1$  = coefficient of Eq. (1)
- $m_2$  = coefficient of Eq. (3)
- $\alpha$  = coefficient of Eq. (3)
- $\Delta h_i$  = inlet subcooled enthalpy of coolant, MJ/Mg

<sup>1</sup> Formerly a Research Engineer with the Australian Atomic Energy Commission at Lucas Heights near Sydney, now retired. Present address: 175 Nicholson Parade, Cronulla, NSW 2230, Australia.

Contributed by the Heat Transfer Division of THE AMERICAN SOCIETY OF MECHANICAL ENGINEERS. Manuscript received by the Heat Transfer Division July 1993; revision received February 1994. Keywords: Direct-Contact Heat Transfer, Forced Convection, Multiphase Flows. Associate Technical Editor: L. C. Witte.

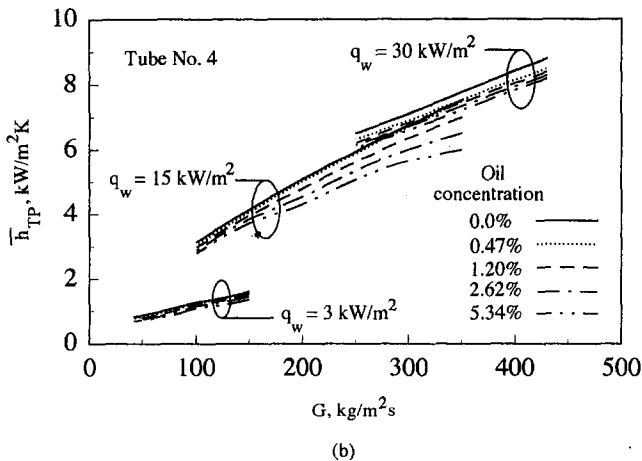
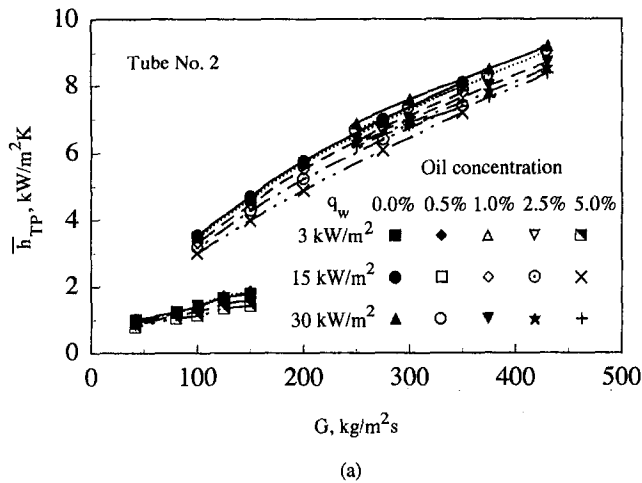


Fig. 3 Evaporation heat transfer coefficient versus mass flow rate with mixture of R-134a plus RL68S oil

150 kg/m<sup>2</sup>s,  $\theta_{a/s}$  tends to fall rapidly with increasing  $G$ . There is very little influence of  $G$  above 250 kg/m<sup>2</sup>s. Although  $\theta_{a/s}$  for tubes Nos. 2 and 4 only were shown in Fig. 4, similar results were obtained for tubes Nos. 3 and 5.

This note suggests that tubes with lower  $G$  have a higher  $\bar{h}_{TP,a}/\bar{h}_{TP,s}$ . The heat transfer enhancements for R-22 are generally

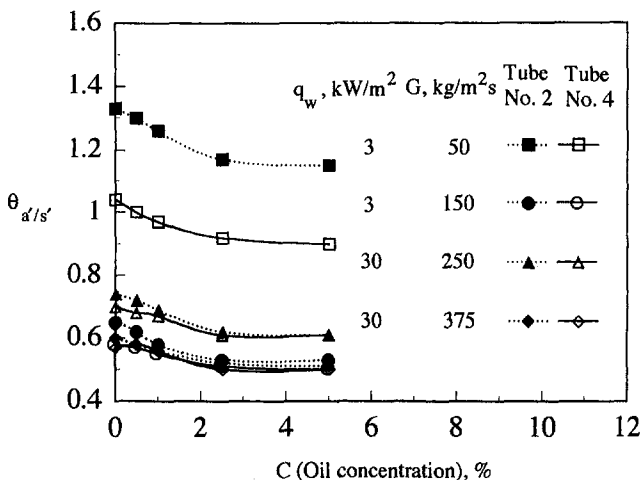


Fig. 4 Effects of oil content on the enhancement performance ratio,  $\theta_{a/s}$ , in two tube geometries for different oil concentration

higher than those for R-114 and R-134a. Tubes with lower pressure drop (Nos. 2 and 4) are superior in overall performance to those with higher pressure drop (Nos. 4 and 5) even though their heat transfer performance is similar. The enhancement performance ratio decreases with an increase in oil concentration. The heat transfer performance with an R-134a/RL 68S mixture have the same trend as that of the pure refrigerant but the magnitude of the effect is different. In general, oil content decreases the heat transfer and increases the pressure drop for the cases studied.

### Acknowledgments

A research grant from the Division of Energy and Resources Laboratories, Industrial Technology Research Institute (R.O.C.) is sincerely appreciated. Special thanks go to Kuen Ling Machinery Refrigerating Co., Ltd., for providing the internally spirally knurled/integral finned tubes.

### References

- Azer, N. Z., Lin, S. T., and Fan, L. T., 1980, "Augmentation of Forced Flow Boiling Heat Transfer With Kenics Motionless Mixers," *Industrial and Engineering Chemistry Process Design and Development*, Vol. 19, pp. 246-250.
- Bergles, A. E., Collier, J. G., Delhaye, J. M., Hewitt, G. F., and Mayinger, 1981, *Two-Phase Flow and Heat Transfer in the Power and Process Industries*, Hemisphere Publishing Co., Washington, DC.
- Dittus, F. W., and Boelter, L. M. K., 1930, "Heat Transfer in Automobile Radiators of the Tubular Type," *Univ. Calif., Berkeley, Pub. in Eng.*, Vol. 2, pp. 443-450.
- Hsieh, S.-S., and Wen, M.-Y., 1995, "An Experimental Study of Flow Boiling Heat Transfer in Rib-Roughened Tube Annuli," *ASME JOURNAL OF HEAT TRANSFER*, Vol. 117, this issue, pp. 185-194.
- Lockhart, R. W., and Martinelli, R. C., 1949, "Proposed Correlation of Data for Isothermal Two-Phase Two-Component Flow in Pipes," *Chemical Engineering Progress*, Vol. 45, pp. 39-48.
- Reid, R. W., Pate, M. B., and Bergles, A. E., 1987, "A Comparison of Augmentation Techniques During In-Tube Evaporation of R-113," in: *Boiling and Condensation in Heat Transfer Equipment*, E. G. Ragi, T. M. Rudy, T. J. Rabas, and J. M. Robertson, eds., ASME, New York, pp. 21-30.
- Shah, M. M., 1982, "Chart Correlation for Saturated Boiling Heat Transfer Equations and Further Study," *ASHRAE Transactions*, Vol. 88, pp. 185-196.
- Wen, M.-Y., and Hsieh, S.-S., 1994, "Evaporative Heat Transfer and Enhancement Performance of Rib-Roughened Tube Annuli With Refrigerant 114," *Int. J. of Heat Mass Transfer*, Vol. 37, pp. 425-436.

## Toward a Universal Critical Heat Flux (CHF) Correlation for Uniformly Heated Round Tubes

G. A. Tingate<sup>1</sup>

### Nomenclature

- $D$  = internal diameter of test section, mm
- $G$  = mass velocity of coolant, Mg/m<sup>2</sup>s
- $L$  = heated length of test section, mm
- $P$  = nominal pressure of coolant, MPa
- $m_1$  = coefficient of Eq. (1)
- $m_2$  = coefficient of Eq. (3)
- $\alpha$  = coefficient of Eq. (3)
- $\Delta h_i$  = inlet subcooled enthalpy of coolant, MJ/Mg

<sup>1</sup> Formerly a Research Engineer with the Australian Atomic Energy Commission at Lucas Heights near Sydney, now retired. Present address: 175 Nicholson Parade, Cronulla, NSW 2230, Australia.

Contributed by the Heat Transfer Division of THE AMERICAN SOCIETY OF MECHANICAL ENGINEERS. Manuscript received by the Heat Transfer Division July 1993; revision received February 1994. Keywords: Direct-Contact Heat Transfer, Forced Convection, Multiphase Flows. Associate Technical Editor: L. C. Witte.

**Table 1** Experimental values selected for analysis

Coolant	P, MPa	Number of values selected
Freon-12	1.069	391
Water	6.895	272
Water	13.790	252

$\lambda$  = latent heat of evaporation, MJ/Mg

$\phi$  = CHF, MW/m<sup>2</sup>

$\phi_0$  = CHF when  $\Delta h_i = 0$ , MW/m<sup>2</sup>

$\phi_c/\phi_e$  = calculated-to-experimental CHF ratio

## Introduction

In 1968 the author commenced a study of CHF correlations for uniformly heated round tubes with Freon-12 and water cooling. Use was made of experimental data from two sources: Stevens et al. (1964) giving the results of some 780 experiments with Freon-12 at 1.069 MPa, and Thompson and Macbeth (1964) giving the results of some 4400 experiments with water ranging from atmospheric pressure to 19.0 MPa. Values were selected to give more manageable proportions, while maintaining as balanced a representation as possible, as indicated in Table 1.

The Freon-12 values were given the closest attention, as they provided the best coverage of the many possible combinations of the variables, and also appeared to offer the best hope of an accurate correlation.

Several promising forms of equation were optimized and tested in turn, but with limited success. Considerable improvements in accuracy were found to be possible, but only by increasing the number and complexity of the terms. It was hoped that this procedure would enable key terms to be identified, and so lead to the elimination of any redundant terms without reducing the accuracy. This did not eventuate; instead all attempts to eliminate "unconvincing" terms resulted in sacrificing most of the accuracy gained by their inclusion. Furthermore no discernible pattern could be found in the coefficients of any of the equations for the three coolants. Thus the equations were no better in this regard than those given by Thompson and Macbeth (1964), who encountered the same obstacle. During the study a strong suspicion developed that the computer was merely doing its best to substitute the more complex equations for the heat balance equation; if so it would be contributing nothing to the CHF correlation.

All the equations in the original study were in the form of the sum of two main terms. The first term,  $\phi_0$ , was a function of all the main variables except  $\Delta h_i$ , while the second term included  $\Delta h_i$ . Both linear and nonlinear relationships between  $\phi$  and  $\Delta h_i$  were considered. Initially the two main terms were analyzed separately to establish trends, but thereafter they were optimized together.

Interest in the problem was renewed in 1991, when a strong case was found for analyzing and optimizing the two terms separately. This led to the present study, which is based almost entirely on the original data, but is limited to a linear relationship between  $\phi$  and  $\Delta h_i$ . Even so it led to a reasonably accurate correlation (Eq. (4)), which was optimized separately for each of the three coolants. In the case of the Freon-12 coolant it was possible to improve the accuracy further (Eq. (5)). This was not possible with water cooling because of the limitations of the selected experimental data.

## Considerations Leading to Present Study

The study was resumed after considering the possibility that the coolant in an annular section adjacent to the wall reaches or closely approaches a quality of 1.0 at the dryout point. If so the

way would be opened for an alternative mathematical representation of the problem, based on heat balance equations. In such an analysis two distinct lengths of the test section would have to be taken into account. Over the first length, where the bulk coolant is subcooled, heat is transferred to the central section by mixing. If vapor is present some or all will condense in contact with subcooled liquid. Over the second length, where the bulk coolant is at saturation temperature, heat is transferred by mixing but without condensation. The two mixing regimes are also relevant to the equations associated with the original study, and indicate a need for an appropriate reappraisal.

## Development of Preliminary Equation

This equation is based on the general (but not universal) linear equation

$$\phi = \phi_0 + m_1 \Delta h_i \quad (1)$$

The existence of the two regimes adds weight to this form of equation, if not to its linearity.

A detailed check was first carried out on the selected data for the linearity of this relationship, and it was found to be sufficiently consistent and widespread to justify proceeding further on this basis. Optimum values of  $\phi_0$  and  $m_1$  were next determined by linear regression for each grouping, with a view to evaluating their dependence on the main variables. It was found that  $m_1$  is closely proportional to  $(GD/L)^{2/3}$ . The optimized value of the index was 0.66 for Freon-12 and 0.73 for water, but  $2/3$  was adopted for both. The optimized equation for Freon-12 is

$$m_1 = 0.0266(GD/L)^{2/3} \quad (2)$$

It was immediately apparent that  $\phi_0$  does not depend directly on  $GD/L$ . Instead it is strongly dependent on  $G$  for the larger values of  $L/D$  but is virtually independent of  $G$  for the smaller values of  $L/D$ , suggesting an equation of the form

$$\phi_0 = m_2 G^\alpha \quad (3)$$

where  $m_2$  and  $\alpha$  are functions of  $D$  and  $L$  to be determined.

It was found that  $\alpha$  is directly proportional to  $L/D$ . The optimized value for Freon-12 is 0.00146, and for the three coolants combined is 0.00157. The latter value was adopted for the rest of the study. It was also found that  $m_2$  is closely proportional to  $(D/L)^{1/2}$ , the optimized value of the index for Freon-12 being 0.49.

Combining the two optimized terms, the preliminary equation for Freon-12 at 1.069 MPa becomes

$$\phi = 0.00949\lambda(0.737G)^{0.00157L/D}(D/L)^{1/2} + 0.0266(GD/L)^{2/3}\Delta h_i \quad (4)$$

The first coefficient of each term was calculated along the same lines for each of the two water pressures. The three pairs of optimized coefficients are given in Table 2.

The accuracy of Eq. (4) was next investigated by calculating  $\phi$  and  $\phi_c/\phi_e$  for each case, using the appropriate coefficients for each coolant. The general accuracy left much to be desired, as may be seen from Table 3.

**Table 2** Coefficients of Eq. (4)

Coolant	Pressure, MPa	$\lambda$ , MJ/Mg	Coefficient of	
			First term	Second term
Freon-12	1.069	125.6	0.00949	0.0266
Water	6.895	1512.8	0.01274	0.0333
Water	13.790	1080.7	0.01003	0.0355

**Table 3 General accuracy of Eq. (4)**

Range of values of $\phi_c/\phi_e$	Percentage of values of $\phi_c/\phi_e$ within range for		
	Freon-12 1.069 MPa	Water 6.895 MPa	Water 13.790 MPa
0.95–1.05	43	19	12
0.90–1.10	77	36	24
0.85–1.15	88	51	38
0.80–1.20	95	63	50

On inspection of the values of  $\phi_c/\phi_e$  of each group, 66 percent were found to be virtually independent of  $\Delta h_i$  for Freon-12, but only 34 percent for water. Thus the Freon-12 results offered the best prospect of a significant improvement to Eq. (4). The water results were not analyzed further.

**Development of Improved Equation for Freon-12 at 1.069 MPa**

The average value of  $\phi_c/\phi_e$  was calculated for each group and the results were plotted. Three trends were apparent: a marked separation between the largest and smallest diameters, a dramatic increase in  $\phi_c/\phi_e$  as  $G$  falls below 0.4, and a reversal (increase) as  $L$  falls below 500. For values of  $G$  greater than 0.4 it was found that  $\phi_c/\phi_e$  could be represented by a family of parallel straight lines of slope 0.0143 $G$ .

Experimental results with values of  $G$  less than 0.4 and  $L$  less than 500 were therefore excluded from the rest of the study, and the points at which the parallel lines met the origin were analyzed, leading to the equation

$$\phi = \frac{0.0131\lambda(0.737G)^{0.00157L/D}(D/L)^{1/2}}{D^{0.1} + 0.0000272L + 0.0143G} + 0.0266(GD/L)^{2/3}\Delta h_i \quad (5)$$

The general accuracy has been improved, as evidenced by the values of  $\phi_c/\phi_e$ : 31 percent in the range 0.98–1.02, 68 percent in the range 0.95–1.05, and 95 percent in the range 0.90–1.10. The errors are not equally distributed about the zero point (Fig. 1), the average value being 1.5 percent. The standard deviation is 5.4 percent.

A similar form of denominator was optimized for the second term, but it made virtually no difference to the calculated values of  $\phi$ . Thus with Eq. (5) the study has been taken as far as it can on the basis of a linear relationship between  $\phi$  and  $\Delta h_i$ .

**Comparison With Other Correlations**

Bertoletti et al. (1964) report on an equation that has been applied to 368 cases taken from Stevens et al. (1964). It gave 96 percent in the range 0.85–1.15, compared with 95 percent in the range 0.90–1.10 for Eq. (5) with 292 cases, of which 281 were taken from Stevens et al.

Katto (1978) has considered four characteristic regimes of CHF, and has developed dimensionless equations for each regime with various coolants and pressures, including the experimental values of Stevens et al. (1964). The general accuracy is comparable with that of Bertoletti et al. (1964).

All the equations examined have one significant feature in common. In each term containing  $G$  the index is a constant, in contrast to a variable index of  $G$  in the first term of Eq. (5).

**Discussion**

In developing Eq. (5), use was made of experimental results over the following ranges:

$D$ : 5.2–16.0

$G$ : 0.4–14.5

$L$ : 500–3556

$\Delta h_i$ : 0.0–33.6.

Although it would have been desirable to optimize the coefficients with more evenly balanced combinations of these variables, the indications are that much of the residual inaccuracy is attributable to the nonlinear relationship between  $\phi$  and  $\Delta h_i$ .

The experimental results of Katto and Yokoya (1987) provide an extensive coverage of both positive and negative values of  $\Delta h_i$ . Their results indicate a marked nonlinear relationship when  $\Delta h_i$  is negative, and some of the smaller positive values are affected similarly. In contrast a strong linear relationship holds for the larger positive values.

Before attempting to adapt the second term of Eq. (5) to a nonlinear relationship, it would be desirable to segregate all the results exhibiting a linear relationship, and use them to re-optimize the coefficients. It might also be worthwhile trying out alternative forms of the denominator of the first term of Eq. (5).

Meanwhile, from the similar values of the coefficients in Table 2, the general form of Eq. (5) may be applicable to other coolants and pressures, provided the coefficients are re-optimized for groups of data each with the one coolant at the one pressure.

Separate studies would be required for the data with values of  $G$  less than 0.4, and with values of  $L$  less than 500. At the very least these studies would involve changing the denominator of the first term of Eq. (5).

In the original study the coefficients were all optimized together, giving much the same accuracy over the full range of variables, including the smallest values of  $G$  and  $L$ . This is a strong indication that the computer had come up with an approximate numerical substitute for the heat balance equation.

Although the accuracy of Eq. (5) is equal to or somewhat better than for the other equations examined, the key difference

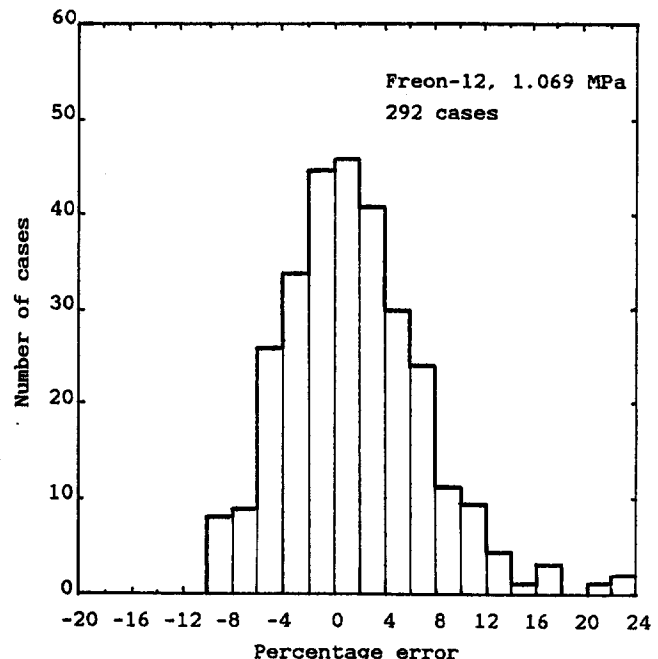


Fig. 1 Error distribution for Eq. (5)

is analytical and lies in the variable index of  $G$  in the first term of Eq. (5).

## References

- Bertoletti, S., Gaspari, G. P., Lombardi, C., Peterlongo, G., and Tacconi, F. A., 1964, "Heat Transfer Crisis With Steam-Water Mixtures," CISE-R-99.
- Katto, Y., 1978, "A Generalized Correlation of Critical Heat Flux for the Forced Convection Boiling in Vertical Uniformly Heated Round Tubes," *Int. J. Heat Mass Transfer*, Vol. 21, pp. 1527-1542.
- Katto, Y., and Yokoya, S., 1987, "A Data Set of Critical Heat Flux of Boiling R-12 in Uniformly Heated Vertical Tubes Including Very Large Length-to-Diameter Ratios," Nihon University Report, University of Tokyo.
- Stevens, G. F., Elliott, D. F., and Wood, R. W., 1964, "An Experimental Investigation Into Forced Convection Burn-out in Freon, With Reference to Burn-out in Water: Uniformly Heated Round Tubes With Vertical Up-flow," AEEW-R 321.
- Thompson, B., and Macbeth, R. V., 1964, "Boiling Water Heat Transfer Burnout in Uniformly Heated Round Tubes: A Compilation of World Data With Accurate Correlations," AEEW-R 356.